

This document was produced  
by scanning the original publication.

Ce document est le produit d'une  
numérisation par balayage  
de la publication originale.

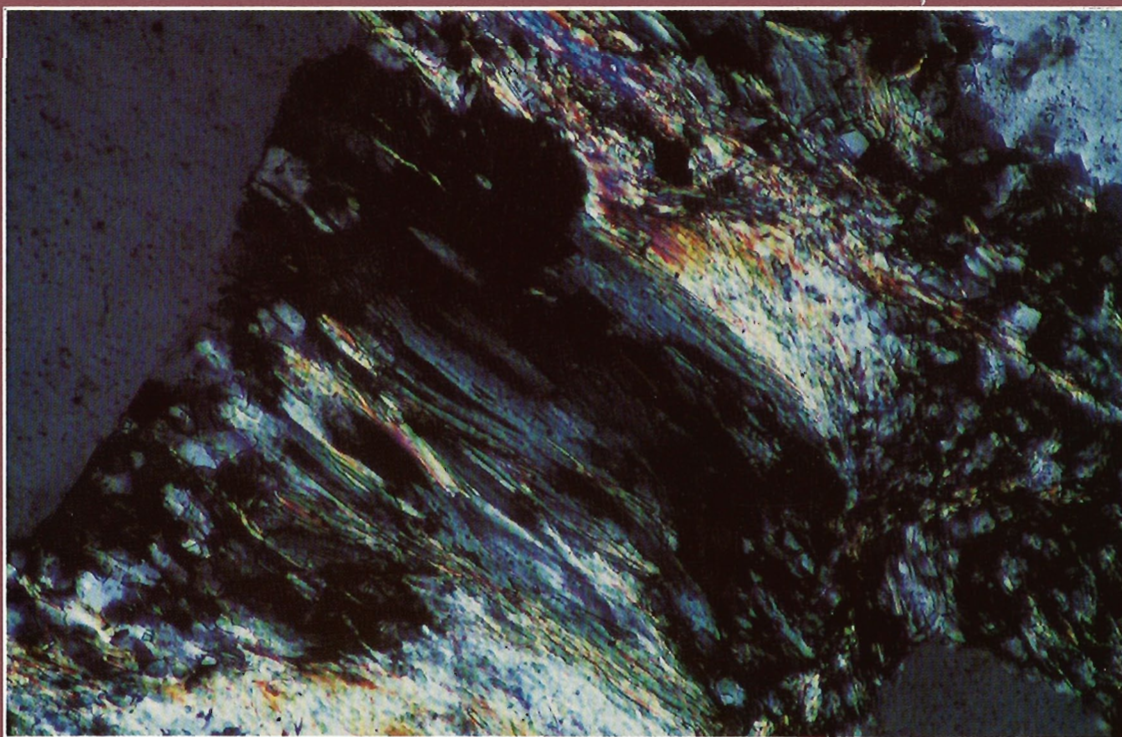


GEOLOGICAL SURVEY OF CANADA  
COMMISSION GÉOLOGIQUE DU CANADA

PAPER/ÉTUDE  
93-1E

CURRENT RESEARCH, PART E

RECHERCHES EN COURS, PARTIE E



1993



Energy, Mines and  
Resources Canada

Énergie, Mines et  
Ressources Canada

Canada

## **NOTE TO CONTRIBUTORS**

Submissions to the Discussion section of Current Research are welcome from both the staff of the Geological Survey of Canada and from the public. Discussions are limited to 6 double-spaced typewritten pages (about 1500 words) and are subject to review by the Chief Scientific Editor. Discussions are restricted to the scientific content of Geological Survey reports. General discussions concerning sector or government policy will not be accepted. All manuscripts must be computer word-processed on an IBM compatible system and must be submitted with a diskette using WordPerfect 5.0 or 5.1. Illustrations will be accepted only if, in the opinion of the editor, they are considered essential. In any case no redrafting will be undertaken and reproducible copy must accompany the original submissions. Discussion is limited to recent reports (not more than 2 years old) and may be in either English or French. Every effort is made to include both Discussion and Reply in the same issue. Current Research is published in January and July. Submissions should be sent to the Chief Scientific Editor, Geological Survey of Canada, 601 Booth Street, Ottawa, Canada, K1A 0E8.

## **AVIS AUX AUTEURS D'ARTICLES**

Nous encourageons tant le personnel de la Commission géologique que le grand public à nous faire parvenir des articles destinés à la section discussion de la publication Recherches en cours. Le texte doit comprendre au plus six pages dactylographiées à double interligne (environ 1500 mots), texte qui peut faire l'objet d'un réexamen par le rédacteur scientifique en chef. Les discussions doivent se limiter au contenu scientifique des rapports de la Commission géologique. Les discussions générales sur le Secteur ou les politiques gouvernementales ne seront pas acceptées. Le texte doit être soumis à un traitement de texte informatisé par un système IBM compatible et enregistré sur disquette WordPerfect 5.0 ou 5.1. Les illustrations ne seront acceptées que dans la mesure où, selon l'opinion du rédacteur, elles seront considérées comme essentielles. Aucune retouche ne sera faite au texte et dans tous les cas, une copie qui puisse être reproduite doit accompagner le texte original. Les discussions en français ou en anglais doivent se limiter aux rapports récents (au plus de 2 ans). On s'efforcera de faire coïncider les articles destinés aux rubriques discussions et réponses dans le même numéro. La publication Recherches en cours paraît en janvier et en juillet. Les articles doivent être envoyés au rédacteur en chef scientifique, Commission géologique du Canada, 601, rue Booth, Ottawa, Canada, K1A 0E8.



GEOLOGICAL SURVEY OF CANADA  
COMMISSION GÉOLOGIQUE DU CANADA

PAPER / ÉTUDE  
93-1E

---

**CURRENT RESEARCH, PART E**  
**RECHERCHES EN COURS, PARTIE E**

---

**Includes/comprend:**

**Cordillera and Pacific Margin**  
**Cordillère et marge du Pacifique**

**Interior Plains and Arctic Canada**  
**Plaines intérieures et région arctique du Canada**

**Canadian Shield**  
**Bouclier canadien**

**Eastern Canada and National and General Programs**  
**Est du Canada et programmes nationaux et généraux**

1993

©Minister of Supply and Services Canada 1993

Available in Canada through  
authorized bookstore agents and other bookstores

or by mail from

Canada Communication Group - Publishing  
Ottawa, Canada K1A 0S9

and from

Geological Survey of Canada offices:

601 Booth Street  
Ottawa, Canada K1A 0E8

3303-33rd Street N.W.,  
Calgary, Alberta T2L 2A7

100 West Pender Street  
Vancouver, B.C. V6B 1R8

A deposit copy of this publication is also available for reference  
in public libraries across Canada

Cat. No. M44-93/1E  
ISBN 0-660-58871-4

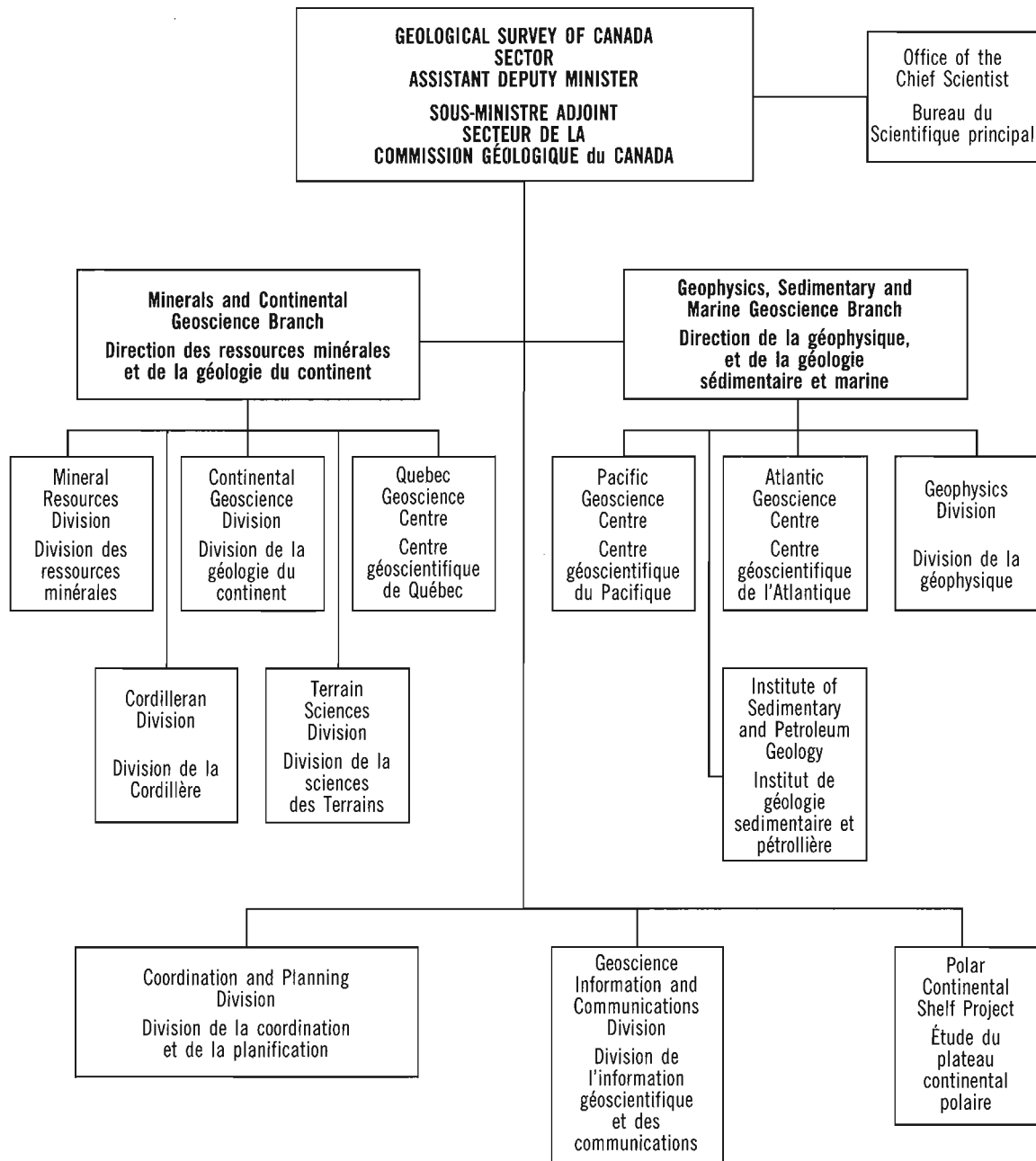
Price subject to change without notice

#### **Cover description**

Photomicrograph of hydrothermally altered felsic volcanic rocks, alteration zone 1, Brunswick No. 12 deposit; Berlin blue=chlorite, yellow=muscovite, upper left grey mineral=quartz phenocryst. Field of view 90  $\mu\text{m}$  wide, crossed nichols. Photo by Wayne Goodfellow. GSC 1993-173. For further information on the Brunswick No. 12 deposit, see papers by Lentz and Goodfellow in this volume.

#### **Description de la photo couverture**

Microphotographie d'une volcanite felsique affectée par une altération hydrothermale dans la zone d'altération n<sup>o</sup> 1 du gisement Brunswick n<sup>o</sup> 12; bleu de Berlin = chlorite, jaune = muscovite, minéral gris dans le coin gauche supérieur = phénocrystal de quartz. Le champ de la photographie, en nicols croisés, a une largeur de 90  $\mu\text{m}$  (Photo : Wayne Goodfellow, GSC 1993-173.) Le lecteur intéressé à obtenir de l'information sur le gisement Brunswick n<sup>o</sup> 12 est prié de se référer aux articles de Lentz et Goodfellow dans le présent volume.



## Separates

A limited number of separates of the papers that appear in this volume are available by direct request to the individual authors. The addresses of the Geological Survey of Canada offices follow:

601 Booth Street  
OTTAWA, Ontario  
K1A 0E8  
(FAX: 613-996-9990)

Institute of Sedimentary and Petroleum Geology  
3303-33rd Street N.W.  
CALGARY, Alberta  
T2L 2A7  
(FAX: 403-292-5377)

Cordilleran Division  
100 West Pender Street  
VANCOUVER, B.C.  
V6B 1R8  
(FAX: 604-666-1124)

Pacific Geoscience Centre  
P.O. Box 6000  
9860 Saanich Road  
SIDNEY, B.C.  
V8L 4B2  
(Fax: 604-363-6565)

Atlantic Geoscience Centre  
Bedford Institute of Oceanography  
P.O. Box 1006  
DARTMOUTH, N.S.  
B2Y 4A2  
(FAX: 902-426-2256)

Québec Geoscience Centre  
2700, rue Einstein  
C.P. 7500  
Ste-Foy (Québec)  
G1V 4C7  
(FAX: 418-654-2615)

When no location accompanies an author's name in the title of a paper, the Ottawa address should be used.

## Tirés à part

On peut obtenir un nombre limité de «tirés à part» des articles qui paraissent dans cette publication en s'adressant directement à chaque auteur. Les adresses des différents bureaux de la Commission géologique du Canada sont les suivantes:

601, rue Booth  
OTTAWA, Ontario  
K1A 0E8  
(facsimilé : 613-996-9990)

Institut de géologie sédimentaire et pétrolière  
3303-33rd St. N.W.,  
CALGARY, Alberta  
T2L 2A7  
(facsimilé : 403-292-5377)

Division de la Cordillère  
100 West Pender Street  
VANCOUVER, British Columbia  
V6B 1R8  
(facsimilé : 604-666-1124)

Centre géoscientifique du Pacifique  
P.O. Box 6000  
9860 Saanich Road  
SIDNEY, British Columbia  
V8L 4B2  
(facsimilé : 604-363-6565)

Centre géoscientifique de l'Atlantique  
Institut océanographique Bedford  
B.P. 1006  
DARTMOUTH, Nova Scotia  
B2Y 4A2  
(facsimilé : 902-426-2256)

Centre géoscientifique de Québec  
2700, rue Einstein  
C.P. 7500  
Ste-Foy (Québec)  
G1V 4C7  
(facsimilé : 418-654-2615)

Lorsque l'adresse de l'auteur ne figure pas sous le titre d'un document, on doit alors utiliser l'adresse d'Ottawa.

# CONTENTS

## **CORDILLERA AND PACIFIC MARGIN CORDILLÈRE ET MARGE DU PACIFIQUE**

---

- 1 S. TRIBE  
Kunghit Island mylonite of the southern Louscoone Inlet fault system,  
Queen Charlotte Islands, British Columbia
- 9 D.C. HARRIS  
Confirmation of antimony in co-type nuffieldite, Lime Creek, British Columbia  
and a second Canadian occurrence at Izok Lake, Northwest Territories
- 11 R.M. BUSTIN and M. MASTALERZ  
Preliminary results of the variation in maceral chemistry of a coking coal  
from the Mist Mountain Formation, southeastern Canadian Cordillera
- 15 J.V. BARRIE and K.W. CONWAY  
Postglacial geology of Dixon Entrance, northwestern British Columbia continental shelf
- 23 C. LOWE, D.A. SEEMANN, D.B. HEARTY, and D.W. HALLIDAY  
New regional gravity data from the southern Yukon and Northwest Territories
- 33 J.F. SLACK  
Models for tourmalinite formation in the Middle Proterozoic Belt and  
Purcell supergroups (Rocky Mountains) and their exploration significance
- 41 R.H. LINDEN and J.J. CLAGUE  
Paleoseismic implications of sediment cores from Comox Lake, British Columbia
- 47 J.J. CLAGUE and W.W. SHILTS  
Two landslide-dammed lakes in the Cascade Mountains, southwestern British Columbia
- 55 J.W. HAGGART and E.S. CARTER  
Cretaceous (Barremian-Aptian) Radiolaria from Queen Charlotte Islands,  
British Columbia: newly recognized faunas and stratigraphic implications
- 67 R.A. KOSTASCHUK and J.L. LUTERNAUER  
Preliminary measurements of subtidal dune migration and sediment movement  
on Roberts Bank, Fraser River delta, British Columbia
- 73 P. VAN DER HEYDEN, R. SHIVES, B. BALLANTYNE, D. HARRIS,  
C. DUNN, D. TESKEY, A. PLOUFFE, and C. HICKSON  
Overview and preliminary results for the Interior Plateau Program,  
Canada-British Columbia Agreement on Mineral Development 1991-1995

## **INTERIOR PLAINS AND ARCTIC CANADA PLAINES INTÉRIEURES ET RÉGION ARCTIQUE DU CANADA**

---

- 83 L. DYKE and S. WOLFE  
Ground temperatures and recent coastal change at the north end of Richards Island,  
Mackenzie Delta, Northwest Territories
- 93 P.J. LEE  
Oil and gas pool size probability distributions - J-shaped, lognormal, or Pareto?
- 97 C. CLARKSON, M. LAMBERSON, and R.M. BUSTIN  
Variation in surface area and micropore size distribution with composition of medium  
volatile bituminous coal of the Gates Formation, northeastern British Columbia: implications  
for coalbed methane potential
- 105 P. THÉRIAULT, B. BEAUCHAMP, and R. STEEL  
Syntectonic deposition of the Carboniferous Borup Fiord Formation,  
northwestern Ellesmere Island, Northwest Territories
- 113 W.W. NASSICHUK, D.N. SKIBO, M.G. FOWLER, K.R. STEWART, and L.R. SNOWDON  
Update of Canada-Russia collaboration on Arctic pollutants
- 123 T.J. KATSUBE and D.R. ISSLER  
Pore-size distributions of shales from the Beaufort-Mackenzie Basin, northern Canada
- 133 M.M. BURGESS, D.E. LAWRENCE, and K.L. MACINNES  
Hot spots on wood chip insulated permafrost slopes, Norman Wells pipeline,  
northwestern Canada
- 141 J.M. AYLSWORTH, I.M. KETTLES, and B.J. TODD  
Peatland distribution in the Fort Simpson area, Northwest Territories with a  
geophysical study of peatland-permafrost relationships at Antoine Lake

## **CANADIAN SHIELD BOUCLIER CANADIEN**

---

- 151 KIDD CREEK STUDY GROUP  
Co-operative research on the Kidd Creek volcanogenic massive sulphide deposit,  
Timmins, Ontario
- 157 B.I. CAMERON, M.D. HANNINGTON, D.I. BRISBIN, and E.R. KOOPMAN  
Preliminary mineral chemical studies of phyllosilicates in host rocks of the  
Kidd Creek massive sulphide deposit, Timmins, Ontario
- 165 I.M. KETTLES  
Till geochemistry in the Manitouwadge area, Ontario
- 175 V. RUZICKA  
Comparative metallogenic studies of the Alberta and Saskatchewan parts of Athabasca Basin



- 185 M. SCHAU and S. TELLA  
An introduction to the "Aqxarneq gneisses" and retraction of the term  
"Chesterfield Fault Zone", District of Keewatin, Northwest Territories
- 191 J.M. BEDNARSKI  
Preliminary report of the Quaternary geology of the Canadian Shield of northeastern Alberta
- 197 K.L. CURRIE and J. GITTINS  
Preliminary report on peralkaline silica-undersaturated rocks in the Kipawa syenite  
gneiss complex, western Quebec
- 207 M.I. LEGAULT and B.W. CHARBONNEAU  
Geophysical, geochemical, and petrographical study of Contwoyto Batholith,  
Lupin gold mine area, Northwest Territories
- 219 G. CHAI and O.R. ECKSTRAND  
Origin of the Sudbury Igneous Complex, Ontario - differentiate of two separate magmas
- 231 S.S. GANDHI and D. HALLIDAY  
Gravity survey of the Sue-Dianne deposit, Northwest Territories
- 239 A.N. RENCZ, D. BARIL, and P.H. THOMPSON  
Integrating LANDSAT, aeromagnetic, and geological data for regional bedrock  
mapping, Winter Lake-Lac de Gras map area, Northwest Territories

## **EASTERN CANADA AND NATIONAL AND GENERAL PROGRAMS EST DU CANADA ET PROGRAMMES NATIONAUX ET GÉNÉRAUX**

---

- 249 D.R. LENTZ and W.D. GOODFELLOW  
Mineralogy and petrology of the stringer sulphide zone in the Discovery Hole  
at the Brunswick No. 12 massive sulphide deposit, Bathurst, New Brunswick
- 259 D.R. LENTZ and W.D. GOODFELLOW  
Geochemistry of the stringer sulphide zone in the Discovery Hole at the  
Brunswick No. 12 massive sulphide deposit, Bathurst, New Brunswick
- 271 I.M. KETTLES and C.G. RODRIGUES  
Evaluation of glacial Lake Iroquois shoreline data from south-central and eastern Ontario
- 275 M. DOUMA and F.M. NIXON  
Geophysical characterization of glacial and postglacial sediments in a  
continuously cored borehole near Ottawa, Ontario
- 281 G. CAMIRÉ, M.R. LA FLÈCHE et M. MALO  
Géochimie des roches volcaniques cambro-ordoviциennes du Groupe de  
Shickshock: incidences sur la stratigraphie et le contexte géotectonique  
de la Gaspésie septentrionale

291	M.A.J. PIASECKI Tectonics along the Dog Bay Line - a Silurian terrane boundary in northeastern Newfoundland
299	M.A. WILLIAMSON, T.J. KATSUBE, Z. HUANG, M. FOWLER, K.D. MCALPINE, F.C. THOMAS, R. FENSOME, and M. AVERY Hydrocarbon charge history of east coast offshore basins: modelling geological uncertainty
307	P.G. KILLEEN and K.A. PFLUG Detection of <sup>234</sup> Pa in low-level radioactive waste by gamma-ray spectral logging
313	N. SCROMEDA and T.J. KATSUBE Effect of vacuum-drying and temperature on effective porosity determination for tight rocks
321	T.J. KATSUBE and N. SCROMEDA Formation factor determination procedure for shale sample V-3 from the Scotian Shelf
331	J.M. LOMAN, T.J. KATSUBE, J.M. CORREIA, and M.A. WILLIAMSON Effect of compaction on porosity and formation factor for tight shales from the Scotian Shelf
337	A. TREMBLAY, S. FAURE, and B. DUBÉ Gold occurrences of the Rocky Brook-Millstream fault, northern Appalachians, New Brunswick
347	R.J. WETMILLER and J.A. DRYSDALE Eastern Canadian earthquakes 1992
351	R.G. NORTH and F.M. ANGLIN Automatic location of earthquakes in eastern Canada
361	P. ST-ANTOINE, A. CHAGNON et M.M. SAVARD Étude de la minéralogie des argiles dans l'encaissant carbonaté du gîte de Gays River, Nouvelle-Écosse
369	Author Index

CORDILLERA  
AND PACIFIC  
MARGIN

CORDILLÈRE  
ET MARGE DU  
PACIFIQUE



# Kunghit Island mylonite of the southern Louscoone Inlet fault system, Queen Charlotte Islands, British Columbia

Selina Tribe<sup>1</sup>

Cordilleran Division, Vancouver

*Tribe, S., 1993: Kunghit Island mylonite of the southern Louscoone Inlet fault system, Queen Charlotte Islands, British Columbia; in Current Research, Part E; Geological Survey of Canada, Paper 93-1E, p. 1-8.*

---

**Abstract:** The Kunghit Island mylonite (KIM) outcrops on western Kunghit Island on strike with the Louscoone Inlet fault system (LIFS). The mylonite lies within the Upper Triassic Karmutsen Formation and was metamorphosed to greenschist facies. Microscopic structures indicate this mylonite formed as a northwest striking, steeply to vertically dipping fault zone of oblique dip-slip movement with a sinistral strike-slip component. No evidence of dextral strike slip movement was found in the mylonite. A crenulation overprinting the primary foliation attests to a younger episode of north-south compression. Field relations bracket deformation between Early Jurassic and Late Tertiary time. The close association of Kunghit Island mylonite and other shear zones on strike with Louscoone Inlet fault system in the southern islands with plutonic rocks, suggests that deformation reflects intrusion of the San Christoval plutonic suite. Once established, Kunghit Island mylonite and other parts of Louscoone Inlet fault system could have accommodated later deformation.

**Résumé :** La mylonite de Kunghit Island affleure dans l'ouest de l'île Kunghit, dans le prolongement du système de failles de Louscoone Inlet. La mylonite se trouve à l'intérieur de la Formation de Karmutsen (Trias supérieur) et a été métamorphisée au faciès des schistes verts. Les structures microscopiques indiquent que cette mylonite est apparue sous la forme d'une zone de failles de direction nord-ouest et de pendage abrupt à vertical, à rejet pente oblique et à rejet longitudinal (décrochement) senestre. Aucun indice de décrochement dextre n'a été relevé dans la mylonite. Une schistosité de crénulation qui se superpose à la schistosité primaire atteste d'un épisode plus récent de compression nord-sud. Les relations établies sur le terrain situent la déformation entre le Jurassique précoce et le Tertiaire tardif. L'étroite association entre la mylonite de Kunghit Island et d'autres zones de cisaillement qui se situent dans le prolongement du système de failles de Louscoone Inlet dans les îles au sud d'une part et les roches plutoniques d'autre part suggère que la déformation témoigne de l'intrusion de la suite plutonique de San Christoval. Une fois établies, la mylonite de Kunghit Island et d'autres parties du système de failles de Louscoone Inlet ont pu être le siège d'une déformation ultérieure.

---

<sup>1</sup> Department of Geological Sciences, University of British Columbia, 6339 Stores Road, Vancouver, British Columbia V6T 2B4

## INTRODUCTION

The Louscoone Inlet fault system (LIFS) is the longest fault system in the Queen Charlotte Islands (Fig. 1) and has been considered to be a dextral strike-slip fault (Sutherland Brown, 1968; Yorath and Chase, 1981; Lewis, 1991). An absence of unequivocally offset structures across the fault and the paucity of outcrop make characterization of fault system difficult. On western Kunghit Island a mylonite outcrops on strike with the southern extension of the Louscoone Inlet fault system. This mylonite was mapped and sampled in the summer of 1992, the aim being to determine its shear sense and to relate this information to the fault system.

The Louscoone Inlet fault system forms part of the system first defined by Sutherland Brown (1968) as the Rennell Sound-Louscoone Inlet fault zone, extending from Rennell Sound in the northwest to Howe Bay on Kunghit Island in the southeast (Fig. 1). Sutherland Brown postulated 19-90 km of dextral strike-slip movement along the system, with eastern block subsidence. This interpretation was based on restoring the separation of large scale structures assumed to have been adjacent on either side of the fault.

Yorath and Chase (1981) considered the Louscoone Inlet fault to be the dextrally offset southern extension of the Sandspit fault. Young (1981) considered the Rennell-Louscoone fault system to be a Cenozoic dextral wrench fault associated with plate tectonic interactions to the west. Both these studies were based heavily on Sutherland Brown's work (1968).

In 1987 the Geological Survey of Canada initiated the Queen Charlotte Basin Frontier Geoscience Project which resulted in key structural areas being mapped in greater detail, leading to modification of earlier ideas. Thompson et al. (1991) and Lewis and Ross (1991) found the Louscoone Inlet fault system to terminate south of Rennell Sound and not to be the southern extension of Sandspit fault. Lewis and Ross (1991) reported several mylonite zones in the Upper Triassic Karmutsen Formation and Kunga Group in the central islands. These zones are steeply dipping, northwest trending structures often with a northeast-side-up movement, based on field indicators and microstructures. They found no evidence for strike-slip faulting in northern and central Queen Charlotte Islands.

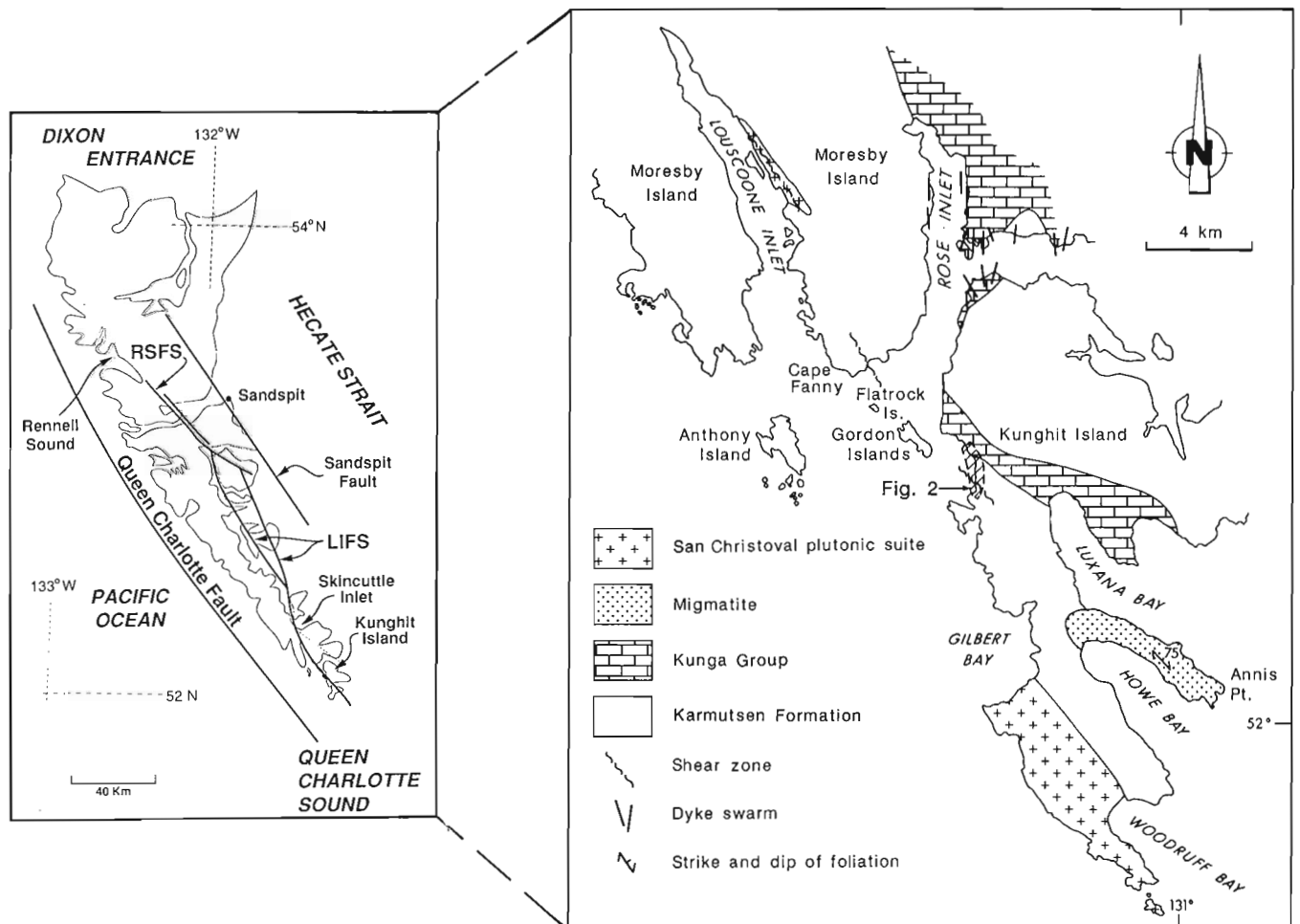


Figure 1. Map showing study area, major structures and regional geology of the Queen Charlotte Islands.

Lewis (1991) subsequently mapped part of the central Louscoone Inlet fault system in the vicinity of eastern Skin-cuttle Inlet and, on the basis of consistent structural fabrics in a mylonite, proposed dextral strike-slip faulting with at least 10-20 km of offset. He also proposed a model whereby strike-slip displacement decreases to the north with displacement taken up by extensional faulting to the east.

In the summer of 1992 field work was undertaken to examine the southern part of the fault system, with the portion that passes through northern Kunghit Island receiving particular attention (Fig. 1). This paper outlines the results of this work and was done as an undergraduate research project.

## REGIONAL GEOLOGY OF QUEEN CHARLOTTE ISLANDS

Queen Charlotte Islands are a group of some fifty islands located off the west coast of Canada. The following outline of the regional geology is taken from Lewis et al. (1991). The geology can be expressed with reference to four major stratigraphic packages. The lowermost package is unnamed Permian strata and Upper Triassic Karmutsen Formation basalt, Upper Triassic to Lower Jurassic calcareous and clastic sedimentary rocks (Sadler, Peril, and Sandilands formations of Kunga Group), and Lower to lower Middle Jurassic clastic sedimentary rocks (Maude Group). This package was folded during a southwest directed shortening event in the Middle Jurassic. Unconformably above these strata is the second package, of Middle to Late Jurassic calc-alkaline volcanic strata of Yakoun Group and epiclastic sediments of Moresby Group. In Late Jurassic time the region experienced block faulting and widespread plutonism. The elongate San Christoval plutonic suite (SCPS) trends northwest on the west side of the islands and consists of diorite and quartz diorite. On the east side of the islands, Burnaby Island Plutonic Suite forms small individual plutons of gabbro, diorite, quartz monzonite, and trondhjemite. Isotopic data indicate that both these plutonic suites were emplaced and uplifted in Middle to Late Jurassic time (Anderson and Reichenbach, 1991).

The third stratigraphic package consists of clastic sediments of Longarm, Haida, Skidegate, and Honna formations and records marine transgression in Cretaceous time (Haggart, 1991). In Tertiary time extensive calc-alkaline volcanism produced the Masset Formation, the fourth and youngest stratigraphic package. Closely associated in time and space with the Tertiary volcanic rocks is the Kano plutonic suite, which occurs as small intrusions and north-striking dyke swarms throughout the islands (Souther and Jessop, 1991). Active Tertiary structures are northwest- to northeast-striking faults such as the Sandspit and Louscoone faults, along which dextral strike-slip faulting has been suggested to have occurred. The dominant northerly trend of the dykes indicates a component of east-west extension.

## GEOLOGY OF THE KUNGHIT ISLAND MYLONITE

This mylonite outcrops on western Kunghit Island (Fig. 1) along a rugged shoreline open to the Pacific Ocean. One narrow area on the south margin of the zone allows approach and landing suitable for small craft such as a Zodiac. Continuous intertidal exposure trends north for about 2 km with a width of 7-20 m. Beach gravels and dense forest obscure exposures inland. Average orientation of the foliation throughout the mylonite zone is  $140^{\circ}/80^{\circ}$  east. Mineral lineations in the plane of the foliation plunge from  $12-56^{\circ}$  north-west with the majority plunging  $35-40^{\circ}$  north-northwest. Shoreline orientation provides an oblique transect through the mylonite zone. Kunghit Island mylonite can be divided into five northwest trending zones on the basis of lithology and structure (Fig. 2).

### *Mesosopic structures*

Domain 1, in the south, is made up entirely of pillow basalt and pillow breccia of the Upper Triassic Karmutsen Formation. Although deformed in a brittle manner with quartz and calcite veining, primary volcanic depositional features such as pillows are recognizable. Bedding is oriented  $126^{\circ}/47^{\circ}$  southwest, in agreement with attitudes on surrounding shoreline exposures. Domains 1 and 2 are separated by an 8 m wide area of no exposure, immediately north of which lithologies dip southeast; it is unknown whether there is a gradation in lithology and deformation or a major discontinuity between the two domains.

Domain 2 extends for about 250 m across strike and comprises mafic schist with minor limestone, sandstone, and elongate pods of felsic plutonic rock. The mafic schists appear to have been derived from the Karmutsen Formation, but it is not certain if they were originally pillowed flows, and thus a continuation of the rocks to the south, or if they were a different volcanic facies such as massive flows. Limestone and sandstone lenses, with uncommon crinoid ossicles, are interstratified with Karmutsen Formation in this area. They are considered to be part of Karmutsen Formation for two reasons: the sedimentary lithologies do not appear similar to either Sadler or Peril formations; and Sutherland Brown (1968) reported interstratified beds of limestone and clastic sediments with crinoid ossicles within Karmutsen Formation elsewhere in the islands.

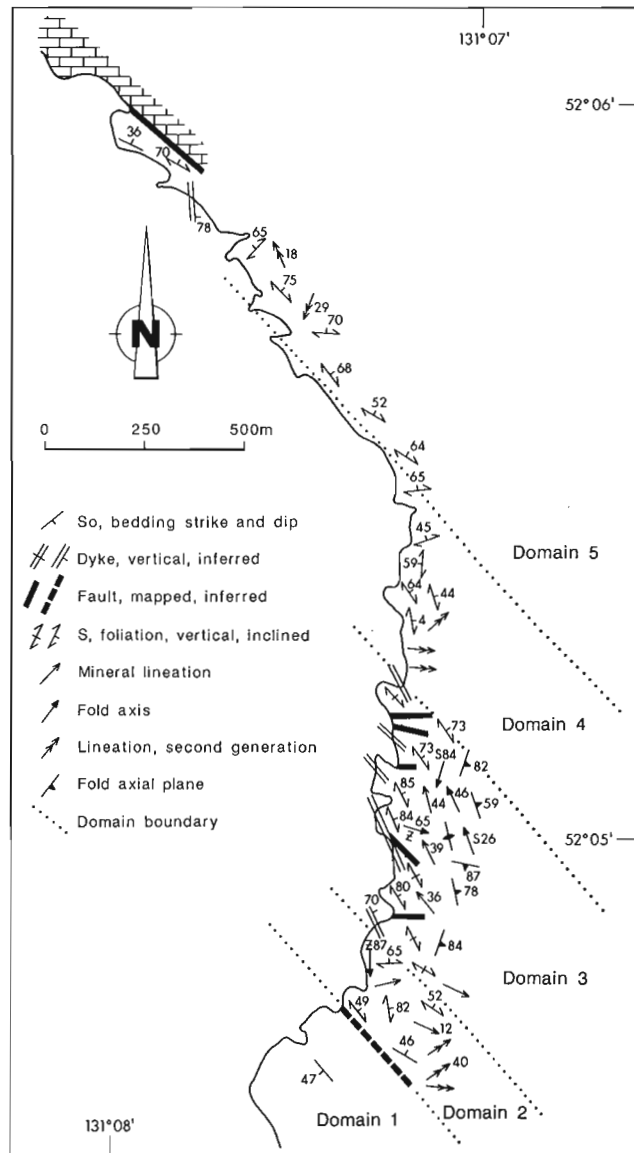
Average foliation in this domain trends northwest and dips approximately  $40^{\circ}$  northeast and is best developed in the mafic schists and limestones. Overprinting the foliation is a crenulation with fold axes plunging up to  $55^{\circ}$  east. Crenulations have an amplitude of about 1 cm and wavelength of 3-4 cm. Locally, rods developed in limestone and sandstone, and pencil structures, formed by the intersection of bedding and foliation, occur trending east. Aplitic material occurs as unfoliated 0.25-1.0 m wide veins intruded parallel to the foliation. The mafic schists grade northward into the dense, well foliated mafic rock of domain 3 over a distance of about 100 m.

Domain 3 is everywhere composed of a mylonite: dense, dark green rock with a well developed and consistent north-west striking foliation, dipping steeply northeast to vertical. Locally the mylonitic foliation is folded into S and Z folds. For most of these rocks the earliest recognizable foliation is evident as parallel streaks of different mineral composition. Mineral lineations consistently plunge 40° northwest. In places, poorly developed feldspar and epidote porphyroclasts, 0.2-3.0 cm across, occur along the foliation. Boudins, 2 cm wide, extend parallel to the lineation in places. Crenulations were not observed. Moving northward into domain 4 the mylonitic foliation becomes discontinuous over a distance of 150 m.

Domain 4 consists of discontinuous mylonite and crenulated schists. Mylonitic rocks have the same character as in domain 3 although foliation is more variable striking 060-190° and dipping from 4-70° north or northeast. Interbedded with mylonitic rocks are crenulated mafic schists with fold axes trending east. In some places the earliest recognizable foliation has a very shallow dip. Although no faults were discovered in outcrop, the rocks in this domain seem contorted because of the variable foliation attitudes. Small amounts of dioritic rock occur within this zone, exhibiting a poor foliation. Domain 4 extends for about 500 m across the strike of the northwest foliation and grades into domain 5.

Domain 5 is distinguished by the disappearance of mylonitization, a decrease in schistosity, and the appearance of primary bedding. Lithologies are Karmutsen Formation mafic schists of variable schistosity and poorly to moderately foliated rocks of Triassic Sadler and Peril formations. Schistosity strikes approximately northwest. Weak crenulation fold axes of variable orientations are overprinted on this schistosity. In the north end of the map area bedding in Karmutsen Formation is oriented 115°/36° east and is in fault contact with Kunga Group. This fault trends 132°/80° east and displays no indicators of sense of past movement.

Brittle faults and dykes are found throughout Kunghit Island mylonite. Faults are 10-60 cm wide, trend consistently easterly, and have vertical to subvertical dips. Most of these faults are marked by an orange weathering, fine grained fault gouge. Slickensides or offset indicators are absent on these faults. All dykes trend northwest with vertical to subvertical dips, their orientation parallel and subparallel to the mylonitic foliation they have intruded. These dykes are 1.0-1.5 m wide with fine grained, intermediate to mafic, aphyric to feldspar-phyric, unfoliated lithologies.



**Figure 2.** Geology and mesoscopic structure map of the Kunghit Island mylonite. Patterned area at north end is Kunga Group, remainder of map area is Karmutsen Formation.

**Microstructures**

Thin sections were made of oriented samples chosen to give a survey of all rock types through Kunghit Island mylonite and were cut parallel to the mineral elongation lineation and perpendicular to the foliation to reveal the kinematic plane. Structures such as winged porphyroclasts, S & C foliations, and C', or extensional crenulation cleavages, were sought in this study and are described below. Virtually all thin sections show well-developed foliations: a pervasive, closely spaced foliation called the C1 foliation, and a less well-developed C2 foliation spaced 0.5-10 mm apart.

A thin section from domain 1 shows a brecciated fine grained, dark brown lithology with interstices filled with glass or calcite, epidote, and quartz. Breccia fragments are 0.25-0.40 mm across, generally too fine grained to optically determine the mineralogy. No foliation is visible in thin section. This sample is interpreted to be a fractured pillow breccia.

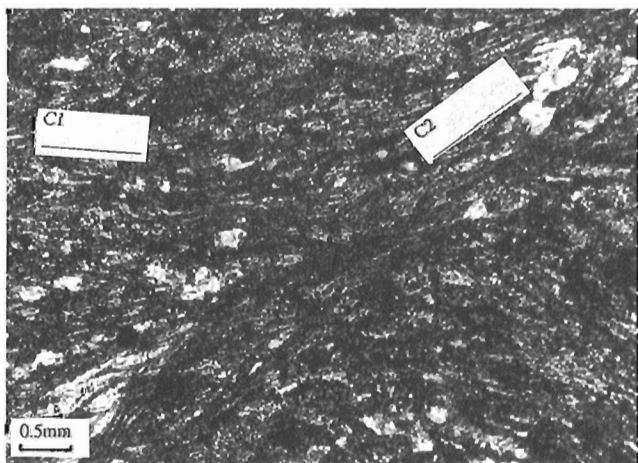
Domain 2 has the most variable lithology of all domains and includes carbonate, plutonic and mylonitic rocks. Carbonate rocks consist of recrystallized calcite grains and quartz porphyroclasts with symmetric and asymmetric pressure shadows of quartz and calcite fibres. C1 foliation trends 087°/50° north and is delineated by opaque matter. Spaced



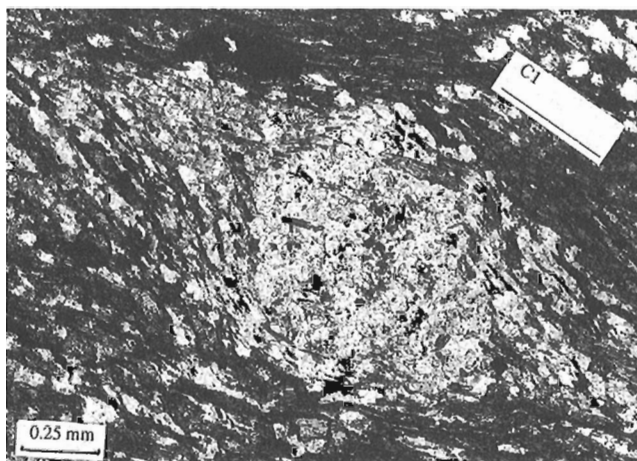
approximately 0.5 mm apart, the C2 foliation trends  $063^{\circ}/54^{\circ}$  north and is also delineated by opaque matter. C2 intersects C1 at an average angle of  $24^{\circ}$  in the kinematic plane with sinistral geometry. Plutonic material is medium grained quartz diorite of hornblende, plagioclase, and quartz, highly altered to chlorite and epidote in places. Small fractures containing breccia fragments cut the quartz diorite. Some plagioclase grains show a slight bending of their twin lamellae indicating a small amount of ductile deformation. No foliation is present in thin section. Mylonitic rocks are fine grained with quartz, epidote, chlorite, and hornblende. C1 foliation is oriented  $126^{\circ}/83^{\circ}$  southwest and is marked by acicular hornblende, tabular epidote, and opaque matter. C2 foliation is spaced 0.5 mm and is oriented  $099^{\circ}/68^{\circ}$  south. C2 intersects C1 in the kinematic plane at an angle of  $28^{\circ}$  with sinistral geometry. Porphyroclasts of epidote, hornblende and feldspar have pressure shadows of fibrous quartz, calcite, and chlorite grains. About 25% of the porphyroclasts have asymmetric delta pressure shadows indicating sinistral shear; the remainder having symmetrical or ambiguous pressure shadows.

All sections from domain 3 have very similar mineralogy and structures. Mylonitic foliations are well developed and marked by bands of equant quartz and calcite, tabular epidote, acicular hornblende and chlorite, and opaque minerals. Most quartz occurs as recrystallized equant grains 0.025-0.1 mm across showing a small amount of undulose strain. Pervasive C1 foliation has an average trend of  $145^{\circ}/86^{\circ}$  south and the C2 foliation spaced from 0.25 to 0.75 mm apart has a trend of  $063^{\circ}/54^{\circ}$  north to  $126^{\circ}/70^{\circ}$  southwest. The two intersect in the kinematic plane at an angle of  $24-28^{\circ}$  with sinistral shear geometry in all thin sections (Fig. 3).

Feldspar (albite) forms delta porphyroclasts with asymmetric to symmetric pressure shadows, most of which indicate sinistral shear (Fig. 4). One thin section shows several symmetric feldspar porphyroclasts fractured at high angles ( $70-90^{\circ}$ ) and extended parallel to the trace of the C1 foliation. Interstices between these formerly joined feldspar fragments



**Figure 3.** Photomicrograph of mylonite in domain 3 showing C1 and C2 foliations intersecting to give sinistral shear sense. Foliations are marked by acicular hornblende, epidote, chlorite and quartz grains. Plane light, north is to the top.



**Figure 4.** Photomicrograph of feldspar porphyroclasts in domain 3. Pressure shadow tails are composed of quartz, epidote, and calcite. C1 foliation is visible in the groundmass of hornblende, epidote, chlorite and quartz. Plane light, north is to the top.

are filled with relatively coarse grained (0.25-0.5 mm) undulose strained quartz. Elongation measured by displacement of fractured pieces ranges from 16-35% with an average elongation of 24%.

Most of the thin sections from domain 4 have the same mineralogies and foliations as in domain 3. Sinistral shear is indicated by C1 and C2 foliation geometries and by offset grains along microfractures.

No thin sections were examined from domain 5 because mesoscopic structures show a drastic decrease in deformation and primary bedding is visible.

## DISCUSSION

Kunghit Island mylonite is a shear zone with penetrative foliation that parallels its margins. Deformation increases from both sides toward the centre, from undeformed volcanic and sedimentary rock through crenulated schists to mylonite.

Some of the most helpful and obvious structures in a mylonite are the C-S fabrics. Kunghit Island mylonite's foliation and compositional bedding strike subparallel to each other, which explains the paucity of mesoscopic and microscopic C-S fabrics. Almost all sections show a dominant foliation, slightly wavy in places, which is interpreted to be the C and the S fabrics together and is called the C1 foliation. Some sections, especially from domain 3, the shear zone centre, have a second foliation, the C2 foliation, which is interpreted to be an extensional crenulation cleavage (Platt and Vissers, 1980). Extensional crenulation cleavages mark ductile shear bands which have the geometry of Reidel shear fractures. These ductile shear bands, or C2 foliation surfaces, intersect the C1 foliation in the same way C-S fabrics do, allowing the sense of shear to be determined. Intersections of C1 and C2 foliations in all the mylonite specimens indicate sinistral shear.

**Table 1.** Type and number of porphyroclasts developed in sample from Kunghit Island mylonite

Domain	Sample No.	# of Sinistral	# of Dextral	Comments
2	9	2 fair	2 fair	many symmetric
3	26	3 good, 2 moderate	0	
3	2	13 good	0	
3	5	1 good, 2 fair	2 fair	many symmetric
3	7	4 good	2 fair	
3	12	4 good	0	

Porphyroclasts are best developed from feldspar grains and exhibit delta pressure shadows of quartz, calcite, and some epidote. Most porphyroclasts show sinistral shear although there are a few which show dextral shear. Dextral varieties are always poorly to moderately developed and are accompanied by ambiguous or poorly to moderately developed sinistral porphyroclasts (Table 1).

The vast majority of quartz grains are equant with an angle of mis-match between lattices always greater than 10°, making them discrete grains. Thus all quartz was recrystallized during deformation. Most of these recrystallized quartz grains exhibit a small amount of undulose extinction, suggesting deformation continued after recovery. Recrystallized quartz occurring with fractured feldspar grains indicates deformation was accommodated by semi-brittle processes.

Crenulation is visible in outcrop only in schistose rocks. The mylonitic rocks presumably are too competent and dense to show it, although in thin section they do show a second foliation. C2 foliation is interpreted to be a second shearing foliation, or extensional crenulation foliation. Microscopic C2 foliation strikes 060-126° and dips 50-70°. Although this attitude agrees with the trend of crenulation axes in outcrop (050-110°), it is not certain if the two are related to the same event. Crenulation can be viewed in two ways: as a later response to the same deformation episode but one wherein the strain axes have rotated; or as a later, unrelated episode of deformation with new strain axes. Mesoscopic buckling crenulation indicates the local maximum compressive stress axis plunged gently south. In Skincuttle Inlet, Lewis (1991) mapped mylonites and found an overprinting crenulation with east trending axes. Possibly the crenulation in Skincuttle Inlet and in Kunghit Island mylonite are due to the same event.

Vertical to subvertical, east-striking brittle faults attest to a later stage of brittle deformation in this region, related or unrelated to the mylonitization event.

Mineralogy of Kunghit Island mylonite comprises feldspar, quartz, opaques, chlorite, epidote, and clinoamphibole, mostly hornblende with minor actinolite, metamorphosed at moderate to high greenschist facies conditions. Presence of amphibole and chlorite grains growing into and along the C surfaces, and quartz and epidote porphyroblasts, indicates deformation also occurred at greenschist facies. Peak temperatures were presumably 400-450°C and pressure about 2-6 kb. Hydrous mineralogy and pressure shadows indicate fluids were present during metamorphism.

Shear zone margins strike 140° and their dip can be taken as the dip of the mesoscopically visible foliation, which is about 80° northeast. This geometry indicates the local maximum compressive stress axis was plunging gently west. Asymmetric pressure shadows in thin section indicate that the plane of flattening was oriented at a small and variable angle, 0-25°, to the shear planes. Because the shear planes and strain axes are not orthogonal to each other, Kunghit Island mylonite is considered a product of non-coaxial strain.

## STRUCTURAL GEOLOGY OF THE SOUTHERN QUEEN CHARLOTTE ISLANDS

Mapping of the southern Queen Charlotte Islands in the summer of 1992 revealed other shear zones on strike with the Louscoone Inlet fault system (Fig. 1). On the east shore of Louscoone Inlet a shear zone strikes northwest and consists of schistose Karmutsen Formation and foliated quartz diorite. This shear zone is traceable through Cadman Point and then southeastward inland, where it is hard to recognize. To the south, no shoreline exposure of deformed rocks occurs until immediately east of Cape Fanny where a 0.5-2 km wide zone of schistose Karmutsen Formation and foliated plutonic rock outcrops. This outcrop is on strike with Kunghit Island mylonite. Flatrock and Gordon islands, which lie just south of the strike of this shear zone and Kunghit Island mylonite, contain undeformed Karmutsen Formation, although Gordon Islands has a few northwest trending brittle fault zones. Taken together, the data suggest the Kunghit Island mylonite is a segment of the Louscoone Inlet fault system.

Southeast of Kunghit Island mylonite is the Luxana Bay migmatite forming the peninsula south of Luxana Bay. The northern and northwestern shores of Luxana Bay consist of undeformed to moderately schistose Karmutsen Formation and Kunga Group rocks. Shoreline exposures toward Annis Point comprise schistose Karmutsen Formation grading into a dark green mylonite and then into a migmatite. Foliation in the migmatite has a constant attitude of 130°/75° northeast. The southernmost part of Kunghit Island is underlain by undeformed diorite, the Woodruff Bay segment of San Christoval plutonic suite (Anderson and Reichenbach, 1991).

## TIMING

Timing of deformation of Kunghit Island mylonite is constrained by the ages of lithologies affected by the deformation. The Kunghit Island mylonite is principally in Upper Triassic Karmutsen Formation, supported by the fact that its mineralogy is the characteristic assemblage of greenschist facies metamorphism of mafic rocks. Foliation of Kunga Group sedimentary rocks in domain 5 has the same attitude as the mylonitic foliation in domain 3, thus the two foliations are assumed to have developed in response to the same event. Deformation must have occurred after Late Triassic or Early Jurassic time.

Several groups of dykes belonging to the Middle Eocene to Middle Miocene Carpenter Bay dyke swarm occur on northern Kunghit Island (Souther and Jessop, 1991). Lithologies of dykes cutting Kunghit Island mylonite and their proximity to the above mentioned dyke groups suggest they are also part of the Carpenter Bay swarm. Because dykes in the mylonite are unfoliated they provide an upper limit to the age of the deformation event(s) responsible for the mylonitization and the crenulation. Field relations therefore suggest deformation occurred between Early Jurassic and Late Tertiary time.

Kunghit Island mylonite is thought to be a southern extension of Louscoone Inlet fault system because it occurs on strike with that feature. The time of deformation bracketed by field relations in Kunghit Island mylonite are in agreement with ages cited for activity along Louscoone Inlet fault system: Sutherland Brown (1968) considered the Louscoone Inlet fault system active in Cretaceous time because Honna and Longarm formations were thicker in the faulted area, whereas Lewis (1991) considered the fault system to be active from Triassic to Tertiary based on ages of rocks affected by faulting.

Pods of weakly deformed quartz diorite in Kunghit Island mylonite as well as the close association of Karmutsen Formation with foliated quartz diorite in Louscoone Inlet and with the migmatite of southern Luxana Bay, suggest deformation is related to intrusion of the San Christoval plutonic suite (SCPS) in Middle to Late Jurassic time. Alternatively, the northwest striking attitude of the mylonite suggests it may be a result of the Middle Jurassic southwest directed contractional event recorded elsewhere in the Queen Charlotte Islands (Thompson et al., 1991). Once established, Kunghit Island mylonite may have become a zone of weakness which was exploited to accommodate strains from subsequent tectonic and structural events.

Irving et al. (1992) determined that the Queen Charlotte Islands were tilted 9-16° towards the north and northwest in Tertiary time based on the paleomagnetism of Tertiary dyke swarms. Accounting for this tilt, mineral lineations in Kunghit Island mylonite would have plunged from 24-31° northeast suggesting the mylonite had a moderate strike-slip component.

## CONCLUSIONS

Kunghit Island mylonite is a northwest striking, steeply dipping fault zone recording oblique dip-slip movement with a component of sinistral strike slip formed within Karmutsen Formation. Deformation occurred at greenschist facies conditions and was accommodated by semi-brittle processes. The mylonite's orientation suggests that the local maximum stress axis responsible for mylonitization plunged gently west. Crenulations visible in outcrop indicate a post-mylonitization event with a local maximum compressive stress axis plunging shallowly toward the south.

Kunghit Island mylonite is a southern segment of Louscoone Inlet fault system and field relations bracket the age of deformation between Early Jurassic and Late Tertiary time, in agreement with ages of Louscoone Inlet fault system activity cited elsewhere. No evidence is found to support the theory that Kunghit Island mylonite is a dextral strike-slip feature. This does not rule out the possibility of dextral strike-slip faulting on other Louscoone Inlet fault segments, or in Kunghit Island mylonite prior to the mylonitization event. Once established Kunghit Island mylonite and Louscoone Inlet fault system probably accommodated later strains. The mylonite may have formed in response to the southwest directed shortening event in Middle Jurassic time and/or as a result of San Christoval plutonic suite intrusion in Middle to Late Jurassic time.

## ACKNOWLEDGMENTS

Many thanks to Jim Haggart of the Geological Survey of Canada for field support and for suggesting this project. John V. Ross is thanked for helpful guidance, comments and discussions and Glenn Woodsworth for a thoughtful review. Michael Bromley and Tonia Oliveric provided excellent figures, and Jim Haggart clarified the final version.

## REFERENCES

- Anderson, R.G. and Reichenbach, I.**  
1991: U-Pb and K-Ar framework for Middle to Late Jurassic (172- $\geq$ 158 Ma) and Tertiary (46-27 Ma) plutons in Queen Charlotte Islands, British Columbia; in *Evolution and Hydrocarbon Potential of the Queen Charlotte Basin, British Columbia*, (ed.) G.J. Woodsworth; Geological Survey of Canada, Paper 90-10, p. 59-87.
- Haggart, J.W.**  
1991: A synthesis of Cretaceous stratigraphy, Queen Charlotte Islands, British Columbia; in *Evolution and Hydrocarbon Potential of the Queen Charlotte Basin, British Columbia*, (ed.) G.J. Woodsworth; Geological Survey of Canada, Paper 90-10, p. 253-277.
- Irving, E., Souther, J.G., and Baker, J.**  
1992: Tertiary extension and tilting in the Queen Charlotte Islands, evidence from dyke swarms and their paleomagnetism; *Canadian Journal of Earth Sciences*, v. 29, p. 1878-1898.
- Lewis, P.D.**  
1991: Dextral strike-slip faulting and associated extension along the southern portion of the Louscoone Inlet fault system, southern Queen Charlotte Islands, British Columbia; in *Current Research, Part A*; Geological Survey of Canada, Paper 91-1A, p. 383-391.

**Lewis, P.D., Haggart, J.W., Anderson, R.G., Hickson, C.J., Thompson, R.I., Dietrich, J.R., and Rohr, K.M.M.**

1991: Triassic to Neogene geologic evolution of the Queen Charlotte region; *Canadian Journal of Earth Science*, v. 28, p. 854-869.

**Lewis, P.D. and Ross, J.V.**

1991: Mesozoic and Cenozoic structural history of the central Queen Charlotte Islands, British Columbia; in *Evolution and Hydrocarbon Potential of the Queen Charlotte Basin*, British Columbia, (ed.) G.J. Woodsworth; Geological Survey of Canada, Paper 90-10, p. 31-50.

**Platt, J.P. and Vissers, R.L.M.**

1980: Extensional structures in anisotropic rocks; *Journal of Structural Geology*, v. 2, p. 397-410.

**Souther, J.G. and Jessop, A.**

1991: Dyke swarms in the Queen Charlotte Islands, British Columbia, and implications for hydrocarbon exploration; in *Evolution and Hydrocarbon Potential of the Queen Charlotte Basin*, British Columbia, (ed.) G.J. Woodsworth; Geological Survey of Canada, Paper 90-10, p. 465-487.

**Sutherland Brown, A.**

1968: *Geology of the Queen Charlotte Islands*; British Columbia Department of Energy, Mines and Petroleum Resources, Bulletin 54, 226 p.

**Thompson, R.I., Haggart, J.W., and Lewis, P.D.**

1991: Late Triassic through Early Tertiary evolution of the Queen Charlotte Basin, British Columbia, with a perspective on hydrocarbon potential; in *Evolution and Hydrocarbon Potential of the Queen Charlotte Basin*, British Columbia, (ed.) G.J. Woodsworth; Geological Survey of Canada, Paper 90-10, p. 3-29.

**Yorath, C.J. and Chase, R.L.**

1981: Tectonic history of the Queen Charlotte Islands and adjacent areas—a model; *Canadian Journal of Earth Sciences*, v. 18, p. 1717-1739.

**Young, I.F.**

1981: Structure of the western margin of the Queen Charlotte Basin, British Columbia; M.Sc. thesis, University of British Columbia, Vancouver.

---

Geological Survey of Canada Project 870070

# Confirmation of antimony in co-type nuffieldite, Lime Creek, British Columbia and a second Canadian occurrence at Izok Lake, Northwest Territories

Donald C. Harris

Minerals Resources Division

*Harris, D.C., 1993: Confirmation of antimony in co-type nuffieldite, Lime Creek, British Columbia and a second Canadian occurrence at Izok Lake, Northwest Territories; in Current Research, Part E; Geological Survey of Canada, Paper 93-1E, p. 9-10.*

---

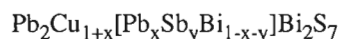
**Abstract:** Microprobe analysis of co-type nuffieldite has confirmed the presence of antimony as well as its presence in nuffieldite at Izok Lake, Northwest Territories. These results support previously reported synthetic studies indicating antimony is an essential component for the stabilization of the mineral.

**Résumé :** L'analyse par microsonde de la nuffieldite cotype a confirmé la présence d'antimoine ainsi que sa présence dans la nuffieldite au lac Izok (Territoires du Nord-Ouest). Ces résultats appuient les études de synthèse antérieures selon lesquelles l'antimoine est un élément essentiel pour la stabilisation du minéral.

## INTRODUCTION

Nuffieldite, a rare copper-lead-bismuth sulphosalt was discovered by Kingston (1968) in specimens of quartz veins in the Lime Creek quartz diorite stock, near Alice Arm, Cassiar District, British Columbia. With the limited amounts of material available and the use of various analytical methods to analyze minute quantities, an ideal formula of  $Pb_{10}Bi_{10}Cu_4S_{27}$  was proposed for nuffieldite.

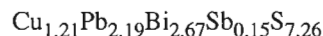
Moelo (1989) reported a second occurrence of nuffieldite near Les Houches (Chamonix Valley, Haute-Savoie, France) and electron microprobe analysis showed a significant antimony content (2.2%) giving a structural formula as:



with  $x = 0.37$ ,  $y = 0.24$ . The presence of antimony and because nuffieldite has not been synthesized in the  $PbS-Bi_2S_3-Cu_2S$  system strongly indicated that antimony is an essential component. Synthetic studies by Maurel and Moelo (1990) in the  $Cu-Pb-Bi-Sb-S$  system, indeed showed that nuffieldite is easily obtained at  $435^\circ$ , at various values of sulphur fugacities and antimony contents (up to 5 wt.%).

## PRESENT STUDIES

During a study of a massive Zn-Cu-Pb sulphide deposit at Izok Lake, Northwest Territories where a new sulphosalt, izoklakeite, was discovered (Harris et al., 1986), a second unreported Canadian occurrence of nuffieldite was identified and microprobe analysis gave Cu 5.6, Pb 34.1, Bi 39.4, Sb 2.3, S 16.9, totals 98.3 wt.%. In order to confirm that antimony is also present in nuffieldite from the type Lime Creek locality, a co-type specimen was obtained from the National Mineral Collection, Systematic Reference Series, Cat. No. 13448 and analyzed by microprobe. The analyses of eleven spots on three fragments gave Cu 5.81, Pb 34.12, Bi 42.00, Sb 1.33, S 17.52, totals 100.78 wt.%. Based on the structural formula of  $Cu_{1+x}Pb_{2x}Bi_{3-x-y}Sb_yS_7$ , the above analysis for Pb+Bi+Sb = 5 atoms, gives:



where Pb gives  $x = 0.19$ , Cu gives  $x = 0.21$ , Sb gives  $y = 0.15$ , Bi gives  $3-x-y = 2.67$  for  $x = 0.18$ ,  $y = 0.15$ .

Thus for type nuffieldite  $x = 0.18$ ,  $y = 0.15$  as compared to  $x = 0.37$ ,  $y = 0.24$  for nuffieldite from Les Hauches (France) and  $x = 0.21$ ,  $y = 0.25$  for nuffieldite from Izok Lake.

## CONCLUSIONS

The analyses of nuffieldite from the type locality and that from the second Canadian occurrence at Izok Lake supports the studies of Moelo (1989) and Maurel and Moelo (1990) that antimony is an essential component in nuffieldite.

## ACKNOWLEDGMENTS

The author is grateful to A.C. Roberts for the X-ray powder diffraction identifications and J.M. Beaulne, CANMET for the polished sections.

## REFERENCES

- Harris, D.C., Roberts, A.C., and Criddle, A.J.**  
1986: Izoklakeite, a new mineral species from Izok Lake, Northwest Territories; *Canadian Mineralogist*, v. 24, p. 1-5.
- Kingston, P.W.**  
1968: Studies of mineral sulphosalts: XXI – Nuffieldite, a new species; *Canadian Mineralogist*, v. 9, p. 439-452.
- Maurel, C. and Moelo, Y.**  
1990: Synthèse de la nuffieldite dans le système Bi-Pb-Sb-Cu-S; *Canadian Mineralogist*, v. 28, p. 745-749.
- Moelo, Y.**  
1989: Antimonie dans la nuffieldite associée à de la freidrichite (commune des Houches, Alpes de Haute-Savoie), redefinition cristallographique de la nuffieldite; *Académie des Sciences, Comptes Rendus Hebdomadaires des Séances, Paris*, t. 309, série II, p. 1659-1664.

Geological Survey of Canada Project 680023

# Preliminary results of the variation in maceral chemistry of a coking coal from the Mist Mountain Formation, southeastern Canadian Cordillera

R.M. Bustin<sup>1</sup> and M. Mastalerz<sup>1</sup>

Institute of Sedimentary and Petroleum Geology, Calgary

*Bustin, R.M. and Mastalerz, M., 1993: Preliminary results of the variation in maceral chemistry of a coking coal from the Mist Mountain Formation, southeastern Canadian Cordillera; in Current Research, Part E; Geological Survey of Canada, Paper 93-1E, p. 11-14.*

---

**Abstract:** Electron microprobe and reflectance micro-fourier transform infrared spectroscopy (micro-FTIR) techniques have been combined with organic petrology to determine the elemental chemistry and functional groups in macerals of a medium volatile bituminous coal from the Mist Mountain Formation in the southeastern Canadian Cordillera. Both sporinite and vitrinite have reflectance values averaging 1.30% and elemental compositions of about 88.5 to 88.9% C and 4.0 to 4.3% O. Semifusinite has an average reflectance of 1.84% and is comprised on average of about 89.6% C and 3.9% O. Fusinite has an average reflectance of 2.98% and an average elemental composition of 90.0% C and 3.7% O. The sulphur content of vitrinite (0.84%) and semifusinite (0.91%) is substantially higher than fusinite (0.39%).

Micro-FTIR spectra of all macerals have strong aromatic out-of-plane bands in the 700 to 900 cm<sup>-1</sup> region. The aliphatic bands at a wave number of about 2925 cm<sup>-1</sup> in sporinite and vitrinite are similar, and only slightly more intense than in semifusinite. Neither macrinite nor fusinite have absorbencies in this region.

**Résumé :** On a combiné les techniques de la sonde électronique et de la microspectroscopie infrarouge à transformée de Fourier (micro-FTIR) par réflectance et la pétrologie organique pour déterminer la composition chimique élémentaire et les groupes fonctionnels des macéraux d'un charbon bitumineux volatil moyen de la Formation de Mist Mountain dans le sud-est de la Cordillère canadienne. La sporinite et la vitrinite ont des réflectances moyennes de 1,30 % et des compositions élémentaires d'environ 88,5 à 88,9 % de C et 4,0 à 4,3 % de O. La semifusinite a une réflectance moyenne de 1,84 % et se compose en moyenne d'environ 89,6 % de C et 3,9 % de O. La fusinite a une réflectance moyenne de 2,98 % et une composition élémentaire moyenne de 90,0 % de C et de 3,7 % de O. Les teneurs en soufre de la vitrinite (0,84 %) et de la semifusinite (0,91 %) sont beaucoup plus élevées que celle de la fusinite (0,39 %).

Les spectres micro-FTIR de tous les macéraux présentent de fortes bandes hors plan aromatiques entre 700 et 900 cm<sup>-1</sup>. Les bandes aliphatiques, au nombre d'onde d'environ 2 925 cm<sup>-1</sup>, sont semblables dans la sporinite et la vitrinite, et légèrement plus intenses que dans la semifusinite. Le pouvoir d'absorption de la macrinite et de la fusinite est nul dans cette région.

---

<sup>1</sup> Department of Geological Sciences, University of British Columbia, Vancouver, British Columbia V6T 1Z4

## INTRODUCTION

Organic matter in sedimentary rocks and coal is a heterogeneous mixture of components of varying physical and chemical properties, most of which reflect characteristics inherited from the organic precursors or are acquired during subsequent diagenesis. The characteristics of the microscopic organic components (macerals) comprising coal are of fundamental importance in determining technological utility and petroleum generating potential. Because macerals are complexly inter-grown in coal and commonly vary little in density, mechanical separation based on specific gravity and subsequent chemical analysis may yield results of limited quality. In addition, for the mechanical separation of macerals it is commonly necessary to crush the samples to such a fine particle size that the separates are highly susceptible to oxidation, making it difficult to evaluate the quality of separation. As a result of recent advances in analytical instrumentation it is now possible to characterize directly the major light elements (C, O, N) and other elements in macerals utilizing the electron microprobe (Bustin et al., 1993). A promising method complementary to elemental analysis is the use of micro-fourier transform infrared spectroscopy (micro-FTIR) to determine functional groups.

In this study the electron microprobe and micro-FTIR are used to chemically characterize medium volatile bituminous coal from the Mist Mountain Formation in the southeastern Canadian Cordillera. Much of the impetus for the current study is to attempt to resolve the chemical composition of semifusinite, which is relatively abundant in these coals and important in determining coking characteristics. In this preliminary paper we document the variability in chemical composition within and between the main maceral groups of a specific coal. The logic of our investigation is that in order to assess the significance of any chemical variations between samples, seams or varying ranks, the degrees of variation within and between maceral groups of a single coal must be established.

## METHODS

A sample of medium volatile bituminous coal from the Mist Mountain Formation near Coleman, Alberta, was crushed and prepared into a polished block according to standard coal preparation techniques (Bustin et al., 1985). The block was photographed using a 20x oil immersion objective. Reflectance of vitrinite, semifusinite, and fusinite was measured using a Leitz MPV II microscope. After measuring reflectance, the immersion oil was removed and the samples were sputter-coated with a 0.023  $\mu\text{m}$  thick layer of carbon.

A Cameca SX-50 electron microprobe with the PAP matrix correction routine (Pouchou and Pichoir, 1991) was used to analyze major and minor elements in coal; a PC2 (NiC) pseudo crystal was used for analyzing light elements (C, O, N). The conditions of the analyses were: an accelerating voltage of 10 kV, a beam current of 10 nA, and a beam size of 5  $\mu\text{m}$ . Vitrinite (anthracite rank), magnesite, boron nitride, and barite were used as carbon, oxygen, nitrogen, and

sulphur standards, respectively. Iron, Silica, and aluminum contents were also determined, with siderite as a standard for iron, wollastonite as a standard for silica, and anorthite as a standard for aluminum. Hydrogen content was calculated by difference. A full description of the analytical routine for electron microprobe analysis of light elements in coal is given in Bustin et al. (1993). Following microprobe analysis the samples were carefully repolished to remove the carbon coat from the sample.

Functional groups in macerals were determined from micro-FTIR spectra collected using a Nicolet 710 micro-FTIR spectrometer equipped with a NICPLAN microscope. A 35x IR objective was used which, together with photomicrographs taken earlier, permitted micro-FTIR analysis of the same macerals that were previously analyzed optically and by microprobe. All spectra were obtained in reflectance mode, 128 scans were co-added and rationed to a background of 128 scans and Kramer-Kronig transformation was applied to all spectra. Bands were assigned according to Painter et al. (1981) and Wang and Griffith (1985) and subsequently areas under the peaks in the 2800 to 3000  $\text{cm}^{-1}$  (aliphatic stretching) and 700 to 900  $\text{cm}^{-1}$  (aromatic out-of-plane vibration) were integrated and are used here as semiquantitative measures of aliphatic (Hal) and aromatic hydrogen (Har). The values of Har/Hal used here represent a ratio of these integration areas and not absolute aromatic and aliphatic hydrogen contents.

Most previous micro-FTIR studies of macerals have utilized transmission micro-FTIR (Landais and Rochdi, 1990; Pradier et al., 1992). The difficulty with transmission micro-FTIR is in obtaining thin sections of organic matter thin enough (<25  $\mu\text{m}$ ) and free enough of artifacts for analysis. Our studies suggest that the reflectance micro-FTIR not only alleviates sample preparation problems and allows analysis of the exact same area as was identified petrographically and analyzed with the microprobe, but may also have greater potential for quantitative analysis without a severe loss of information due to spectral reflectance.

## RESULTS AND DISCUSSION

The elemental chemistry of the macerals together with vitrinite reflectance are summarized in Table 1. There is no significant variation in the elemental chemistry between sporinite and vitrinite and there is significant overlap in the elemental composition of semifusinite with fusinite and vitrinite. Only at the 60 percentile (t-test) is there a statistical argument for differences in the elemental chemistry of semifusinite, and fusinite. The difference in light elemental chemistry between vitrinite/sporinite and semifusinite/fusinite is significant at the 99 percentile (t-test). The mean values of C increase and O decrease as anticipated from vitrinite through sporinite, semifusinite and fusinite. Neither H nor H/C content vary systematically. Such results probably reflect the overall low H content of the coal. Of the other elements analyzed, only N and S occur in potentially significant quantities. Sulphur varies from a mean of 0.39% in fusinite to 0.91% in semifusinite. It must be pointed out that such values represent the S content of what microscopically (at about

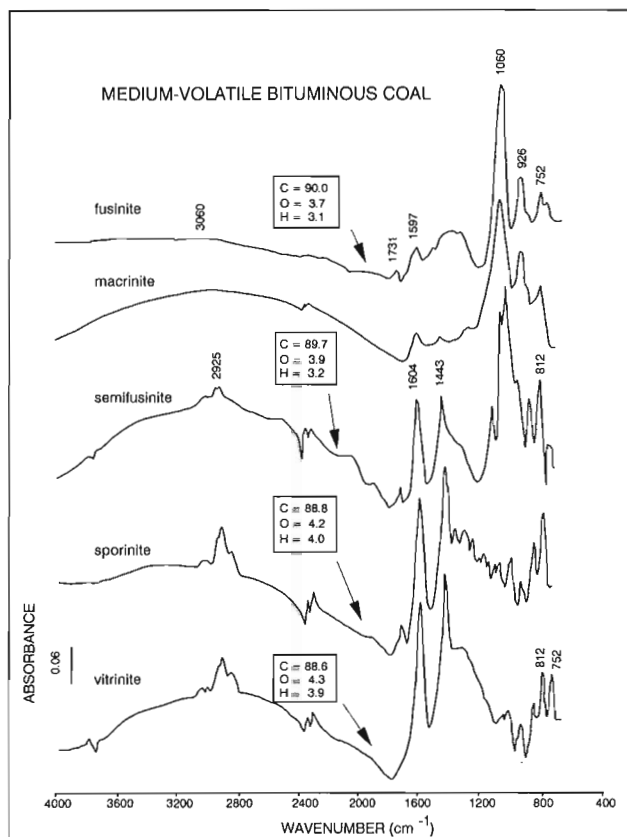


**Table 1.** Chemical composition of macerals in medium volatile bituminous coal from the Mist Mountain Formation (wt. %)

	Vitrinite	Semifusinite	Fusinite	Sporinite
Ro	1.3	1.84	2.98	1.3
C	88.56 (0.21)	89.73 (2.22)	90.02 (1.74)	88.82 (0.22)
O	4.25 (0.30)	3.87 (2.44)	3.69 (1.51)	4.04 (0.28)
N	0.31 (0.82)	0.00	0.00	0.25 (0.21)
S	0.84 (0.09)	0.91 (0.25)	0.39 (0.06)	0.78 (0.12)
Fe	0.03 (0.05)	0.13 (0.05)	0.02 (0.04)	0.03 (0.05)
Si	0.09 (0.03)	0.09 (0.27)	0.09 (0.03)	0.10 (0.04)
Al	0.03 (0.02)	0.07 (0.12)	0.03 (0.03)	0.03 (0.02)
H	6.21 (0.32)	5.20 (2.74)	5.73 (0.37)	5.95 (0.32)
H/C	0.84	0.70	0.77	0.85
O/C	0.04	0.03	0.03	0.03
n	40	20	15	5
n, number of microprobe analyses ( ), standard deviation				

500 x magnification) appears to be homogenous organic matter, free of mineral matter. Some submicroscopic Fe sulphides may be present as suggested by the correspondence of the highest Fe and S in semifusinite. Of all the elements analyzed, N is the most elusive. Assuming such results are representative, our data suggest that N is very unevenly distributed (as found in some N-fixing plants), even within a single maceral. Alternatively our method of N analysis which currently depends on a nonorganic matrix N standard, may require refinement.

In Figure 1 representative micro-FTIR spectra are shown and in Table 2 the integrated areas of 2800 to 3000  $\text{cm}^{-1}$  (aliphatic stretching) and 700 to 900  $\text{cm}^{-1}$  (aromatic out-of-plane vibration) are summarized. The aliphatic band at 2925  $\text{cm}^{-1}$  in sporinite and vitrinite are very similar and only slightly more intense than in semifusinite. No absorption occurs in this range in fusinite or macrinite. The aromatic bands with a peak at 1604  $\text{cm}^{-1}$  and aliphatic bands with a peak at 1443  $\text{cm}^{-1}$  have much higher absorbencies in vitrinite than in fusinite or macrinite. There is very little variation in the IR spectra between sporinite and vitrinite. Aromatic out-of-plane bands are prominent in all the macerals. The ratio of aromatic hydrogen ( $H_{ar}$ ) to aliphatic hydrogen ( $H_{al}$ ), approximated from integration of the 2800-3000  $\text{cm}^{-1}$  and 700-900  $\text{cm}^{-1}$  bands, increases from sporinite, to vitrinite, to semifusinite, and on to infinity in fusinite which has no measurable bands in the 2800-3000  $\text{cm}^{-1}$  range.



**Figure 1.** Reflected micro-fourier infrared spectra of representative macerals from medium volatile bituminous coal of the Mist Mountain Formation. One hundred and twenty-eight scans followed by background correction and Kramers-Kronig transformation.

## CONCLUSIONS

The variations in maceral chemistry documented in this study confirm and extend many previous general conclusions or inferences based on whole sample analysis (i.e., Dormans et al., 1957; Dyrkacz et al., 1991). In particular, the general increase in aromatics and decrease in aliphatics, and increase in C and decrease in O and H from vitrinite, through semifusinite, to fusinite is apparent from our preliminary results presented here. Although such general results are well established, the microscopic techniques used in this study enable quantitative assessment of the variation that exists not only between but also within the maceral groups. In particular the large variation in chemistry within the semifusinite group and the extent of overlap within the fusinite group are noteworthy. In addition, the similarity between sporinite and vitrinite in elemental chemistry and in functional groups is surprising and suggests that there may also be little difference in the coking characteristics of these macerals at the medium volatile bituminous coal rank.

**Table 2.** Functional groups, elemental composition, and reflectance of macerals in medium volatile bituminous coal of the Mist Mountain Formation

	Vitrinite	Semifusinite	Fusinite	Sporinite
H <sub>al.</sub> *	4.3	1.6	0.0	4.4
H <sub>ar.</sub> *	6.3	4.9	2.2	6.3
H <sub>ar./al.</sub> *	1.47	3.06	-	1.43
C	88.6	89.7	90.0	88.8
O	4.3	3.9	3.7	4.2
H	3.9	3.2	3.1	4.0
R <sub>max</sub>	1.30	1.84	2.98	1.30
n	40	20	15	10
n, number of microprobe analyses *, integration areas				

Work in progress will more fully assess the variation in maceral chemistry of major coal seams of the Mist Mountain Formation and will address such factors as depositional environment and oxidation on coal chemistry.

## REFERENCES

- Bustin, R.M., Cameron, A., Grieve, D., and Kalkreuth, W.**  
1985: Coal petrology, its principles, methods and applications; Geological Association of Canada, Short Course Notes, 2nd edition, 230 p.
- Bustin, R.M., Mastalerz, M., and Wilks, K.R.**  
1993: Direct determination of carbon, oxygen and nitrogen content in coal using the electron microprobe; Fuel, v. 72, p. 181-185.
- Dormans, H.N.M., Huntjens, F.J., and van Krevelen, D.W.**  
1957: Chemical structure and properties of coal – composition of the individual macerals (vitrinites, fusinites, micrinites and exinites); Fuel, v. 36, p. 321-339.
- Dyrkacz, G.R., Bloomquist, C.A.A., and Ruscic, L.**  
1991: An investigation of the vitrinite maceral group in microlithotypes using density gradient separation methods; Energy and Fuels, v. 5, p. 155-163.
- Landais, P. and Rochdi, A.**  
1990: Reliability of semiquantitative data extracted from Transmission Microscopy – Fourier Transform Infrared spectra of coal; Energy and Fuels, v. 4, p. 290-295.
- Painter, P.C., Snyder, R.W., Starsinic, M., Coleman, M.M., Kuehn, D.W., and Davis, A.**  
1981: Concerning the application of Ft-i.r. to the study of coal: a critical assessment of band assignments and the application of spectral analysis programs; Applied Spectroscopy, v. 35, p. 475-485.
- Pouchou, J.L. and Pichoir, F.**  
1991: Quantitative analysis of homogenous or stratified microvolume applying the model "PAP"; in Electron Probe Quantitation, (ed.) K.F.J. Heinrich, and D.E. Newbury; Plenum Press, New York, p. 31-75.
- Pradier, B., Landais, P., Rochdi, A., and Davis, A.**  
1992: Chemical basis of fluorescence alteration of crude oils and kerogens – II. Fluorescence and infrared micro-spectrometric analysis of vitrinite and liptinite; Organic Geochemistry, v. 18, p. 241-249.
- Wang, S.H. and Griffith, P.R.**  
1985: Resolution enhancement of diffuse reflectance i.r. spectra of coals by Fourier self-deconvolution. 1. C-H stretching and bending modes; Fuel, v. 64, p. 229-236.

Energy, Mines and Resources Canada Research Agreement 029 4 92.

# Postglacial geology of Dixon Entrance, northwestern British Columbia continental shelf

J.V. Barrie and K.W. Conway  
Pacific Geoscience Centre, Sidney

*Barrie, J.V. and Conway, K.W., 1993: Postglacial geology of Dixon Entrance, northwestern British Columbia continental shelf; in Current Research, Part E; Geological Survey of Canada, Paper 93-1E, p. 15-21.*

---

**Abstract:** Dixon Entrance is a submerged asymmetrical U-shaped valley located on the northern border of the Pacific Canadian margin. It is separated from Hecate Strait and Queen Charlotte Sound to the south by a very shallow shelf. Nonetheless, the post glacial stratigraphy is similar to that interpreted for Hecate Strait and Queen Charlotte Sound. A regionally extensive late Wisconsinan till is overlain by glaciomarine muds formed between approximately 14.0 and 12.9 ka. Glacial ice had completely retreated from the Dixon Entrance by 12.9 ka. Relative sea level lowering followed deglaciation resulting in the deposition of a coarse grained lag unit to depths greater than 450 m. Holocene sedimentation has been limited and restricted to the southern entrance to Clarence Strait and an isolated lobe in west-central Dixon Entrance.

**Résumé :** L'entrée Dixon est une vallée asymétrique submergée en forme de U située à la limite nord de la marge pacifique du Canada. Au sud, un banc très peu profond la sépare du détroit d'Hecate et du détroit de la Reine-Charlotte. Néanmoins, la stratigraphie postglaciaire est semblable à celle interprétée pour le détroit d'Hecate et le détroit de la Reine-Charlotte. Un till du Wisconsinien tardif d'étendue régionale repose sous des boues glaciomarines formées il y a entre 14,0 et 12,9 ka environ. La glace glaciaire s'était complètement retirée de l'entrée Dixon il y a 12,9 ka. Une baisse relative du niveau marin a suivi la déglaciation, laissant un dépôt de résidus de déflation grossiers à des profondeurs supérieures à 450 m. La sédimentation holocène a été limitée à l'entrée sud du détroit de Clarence et à un lobe isolé dans le centre-ouest de l'entrée Dixon.

## INTRODUCTION

Dixon Entrance is a broad trough which lies between southernmost Alaska and northern Graham Island of the Queen Charlotte Islands (Fig. 1). Unlike the primarily shallower shelves to the south (Hecate Strait and Queen Charlotte Sound) Dixon Entrance is a deep asymmetrical U-shaped valley with the deepest portion in the north towards the disputed "A-B" boundary with the United States. Here the seafloor displays rugged topography, a consequence of scouring by westward-flowing glaciers (Bornhold and Barrie, 1991). The entrance widens and abruptly deepens to the west at the shelf edge formed by the North American plate boundary to the west. Consequently, it is completely exposed to the north Pacific Ocean. At the southeastern corner the Entrance sharply abuts Hecate Strait where a shallow (<30 m) platform forms the northern shelf of Hecate Strait (Fig. 1). Dixon Entrance is macrotidal, due to location and morphology, with a tidal range of 3.5 m at the mouth to 5.0 m along its eastern shore (Thomson, 1981).

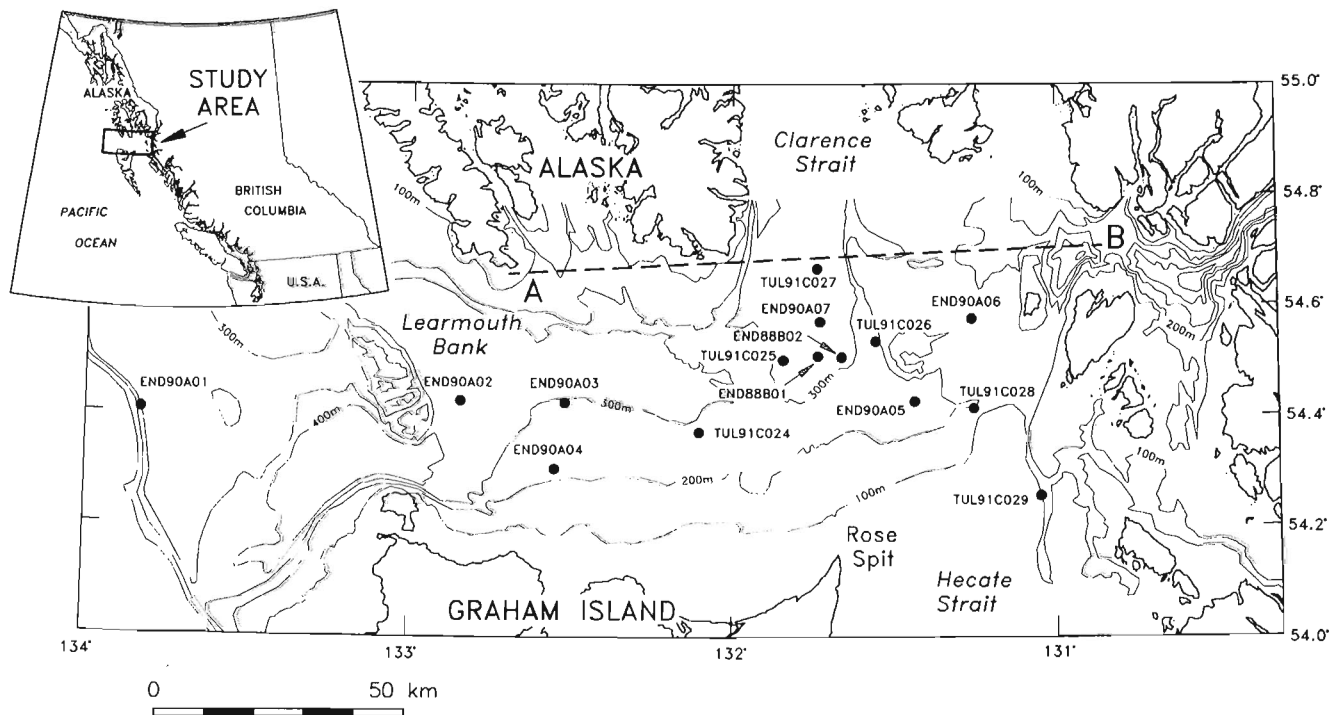
Dixon Entrance is, therefore, physiographically disconnected from the central and southern shelves of the western Canadian margin. Relative sea levels along the nearshore margin were lower by 100 m or greater (Luternauer et al., 1989b; Barrie et al., 1991; Josenhans et al., 1993) at the end of the last glaciation (prior to ca. 10.5 ka) thus isolating Dixon Entrance from the rest of the British Columbia margin. Dixon Entrance may then exhibit a different postglacial history from previously described regions and, in view of its greater depth,

have a more continuous record of the postglacial history of the northwestern Pacific region. Core data may provide an expanded stratigraphic record and yield insights into climatic changes at the onset of the Holocene and, in particular, the Younger Dryas interval (eg. Mathewes et al., 1993).

In order to map the surficial geology of Dixon Entrance and allow the investigation of the outlined scientific questions, two scientific cruises were completed in September and October 1990 (CFAV *Endeavour*) and June 1991 (CSS *John P. Tully*). During these field programs a gridded network of high resolution seismic survey lines was completed with a line spacing of 9 km. In addition 15 piston cores (Fig. 1) and 14 vibrocores were obtained throughout Dixon Entrance. Our purpose here is to compare the stratigraphic chronology as interpreted from the deeper water piston cores of Dixon Entrance with the present understanding of the late Quaternary geology of Hecate Strait (Barrie et al., 1991; Barrie and Bornhold, 1989) and Queen Charlotte Sound (Luternauer et al., 1989a) to the south.

## SURFICIAL GEOLOGY OF THE WESTERN CANADIAN MARGIN – HECATE STRAIT AND QUEEN CHARLOTTE SOUND

The postglacial stratigraphy of the Pacific margin, south of Dixon Entrance, can be broadly divided into three dominant units that overlie what is interpreted to be late Wisconsinan till. Glaciomarine mud (unit A) containing approximately equal



**Figure 1.** Dixon Entrance, showing the bathymetry (100 m contours) and the location of the piston cores used in this study.

proportions of sand, silt and clay with ice-rafted debris occurs in depths generally greater than 200 m. Initial deposition of the glaciomarine sediments began during deglaciation between 14.0 and 13.0 ka. A radiocarbon date of 14 160 BP was reported in a glaciomarine unit just overlying a till in Hecate Strait (Barrie et al., 1991). The depositional environment changed somewhere between 13.6 and 12.9 ka (Luternauer et al., 1989a) with the complete retreat of the late Wisconsinan glaciers from the continental shelf, ending the ice rafting.

Overlying the glaciomarine mud (unit A) in the troughs of Queen Charlotte Sound and Hecate Strait is a sedimentary sequence up to 20 m thick. This sequence, designated unit B, was sub-divided by Luternauer et al. (1989a) into 3 sub-units which reflect the radiocarbon age and texture of the sediments. B<sub>1</sub>, lowermost in the package, has been dated to between 13.0 and 12.0 ka BP in age. This mud unit is thought to have developed as sea levels were falling on the shelf and, unlike unit A, contains no material of ice rafted origin.

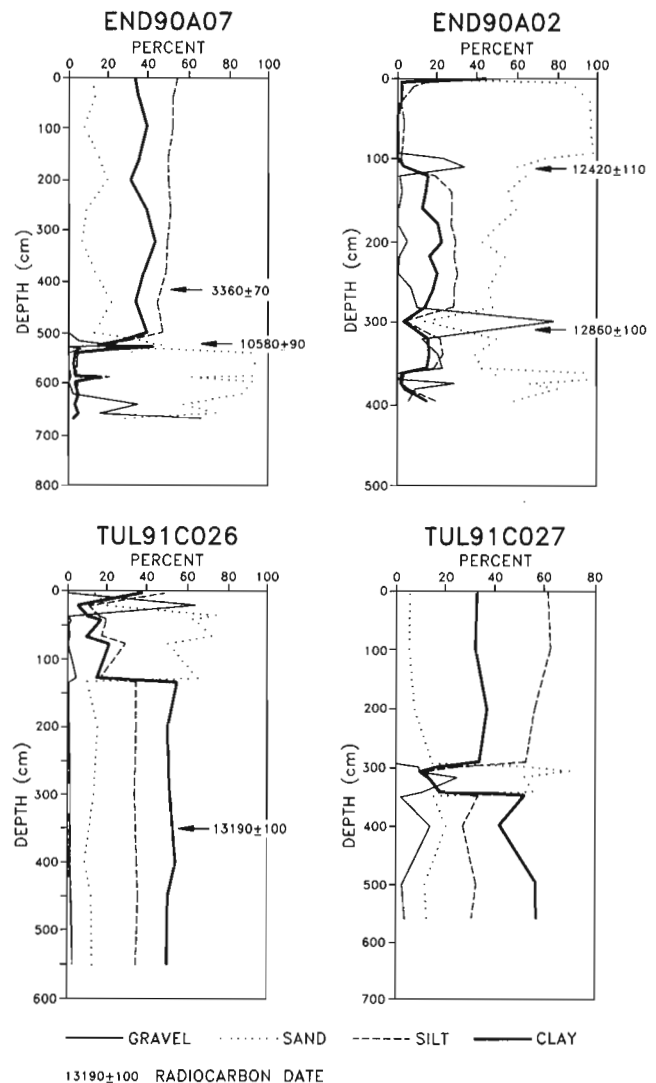
Unit B<sub>2</sub> overlies B<sub>1</sub> or, where B<sub>1</sub> sediments are not found, overlies unit A. This sandy mud unit, 0.01 to 4.0 m in thickness, represents a lag formed between 12.9 ka and approximately 10.5 to 10.2 ka. Between water depths of 160 and 100 m, at the edge of the shelf banks, unit B<sub>2</sub> thickens into a wedge of laminated sands (Barrie, 1991). This unit is thought to have been deposited over a period of several hundred years when sea level was at least 100 m lower than at present (Luternauer et al., 1989b; Barrie et al., 1991). The upper contact of unit B<sub>2</sub> is sharp, implying that the conditions that caused the formation of the lag in the deeper waters and the rapid deposition in shallower waters, were abruptly terminated. The rapid transgression that began shortly after 10.5 ka (7 to 10 cm/a, Luternauer et al., 1989b) brought about this dramatic change. At a few locations in the troughs, unit B<sub>3</sub> overlies unit B<sub>2</sub>; a mud unit of limited areal distribution which was deposited between about 10.5 and 9.7 ka.

Finally, sedimentation during the Holocene has resulted in up to 40 m of olive, clay-rich mud (unit C) in the troughs of Queen Charlotte Sound and Hecate Strait and a thin (usually less than 10 m) transgressive sand and gravel unit on the bank tops. Present day sedimentation on these shelves is minimal.

## SURFICIAL GEOLOGY OF DIXON ENTRANCE

The previously described stratigraphy for the shelf areas south of Dixon Entrance can be directly correlated into the Entrance. The glaciomarine mud (unit A) contains in decreasing order clay (50%), silt (35%), sand (10%) and ice-rafted gravel (5%), consistently finer than samples from the glaciomarine mud (unit A) to the south (Fig. 2). Two C<sup>14</sup> dates within this unit (13 960 BP in Core TUL91C024 and 13 190 BP in Core TUL91C026 (Fig. 3b); Table 1) fall within the time interval of deposition for the glaciomarine mud in the southern areas, that being between 14.0 and 12.9 ka.

Unit B<sub>1</sub> sediments were not observed. Unit B<sub>2</sub>, however, occurred in all cores and was consistently thicker in section and coarser than previously seen in Hecate Strait and Queen Charlotte Sound (Fig. 3a, b). This low sea level stand, lag unit varies between 0.5 to greater than 3.0 m in thickness with consistently greater than 50% sand and the remainder consisting of equal amounts of gravel, silt and clay (Fig. 2). Four C<sup>14</sup> dates within this unit range between 12 860 and 10 580 BP (Table 1), consistent with the interpretation from other areas. These data suggest that not only was relative sea level lower during this time in Dixon Entrance, but wave and current energy at the seabed was much higher than at similar water depths in Hecate Strait and Queen Charlotte Sound.



**Figure 2.** Textural plots from selected Dixon Entrance cores illustrating the down-core textural variation between the three main lithologic units in the study area. Examples of Units are: Unit A – glaciomarine – base of TUL91C026; Unit B<sub>2</sub> – lowstand sediments – all of END90A02; Unit C – Holocene mud – top of END90A07; all three units – TUL91C027. The stratigraphy of these same cores are presented in Figure 3a and b.

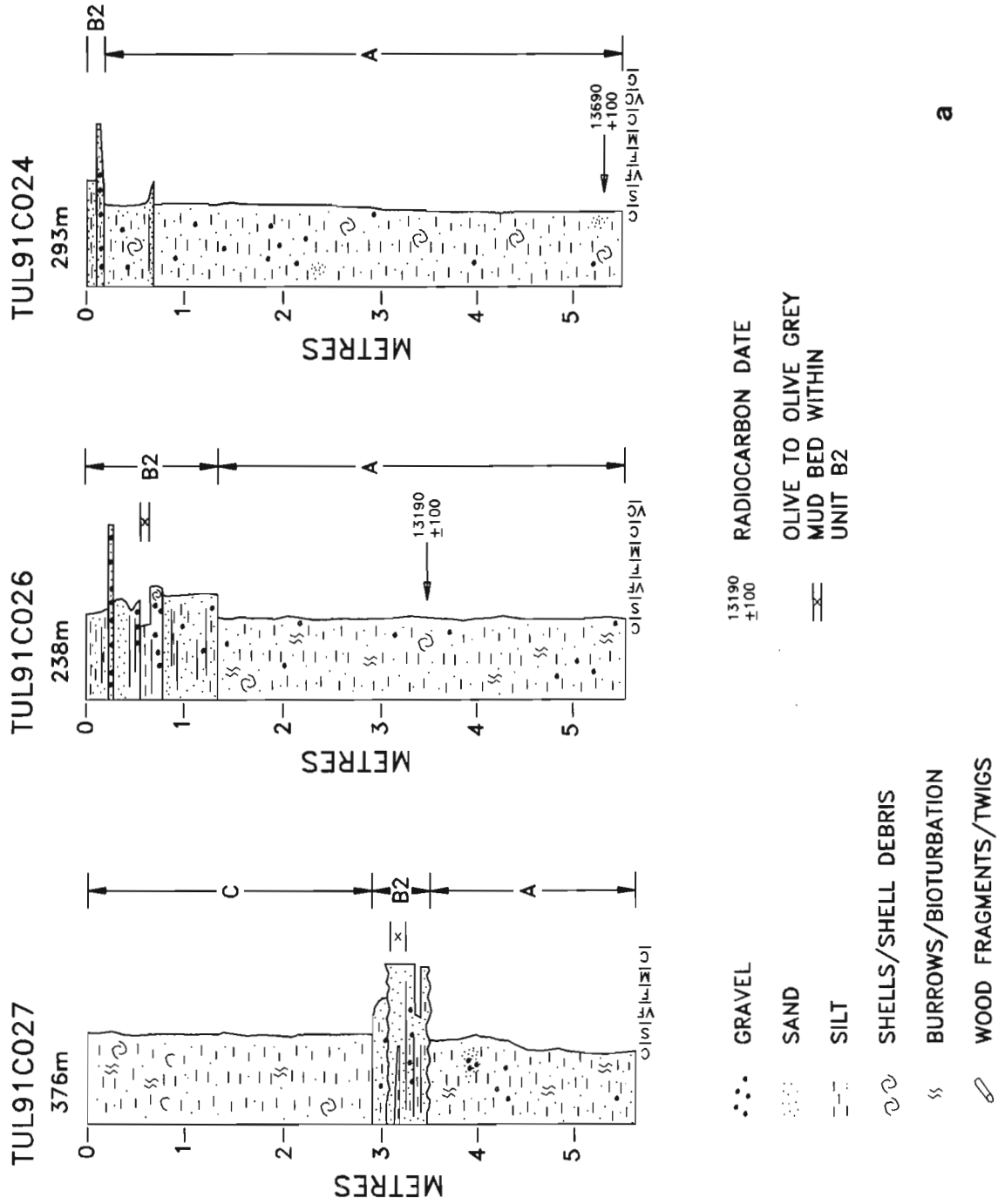
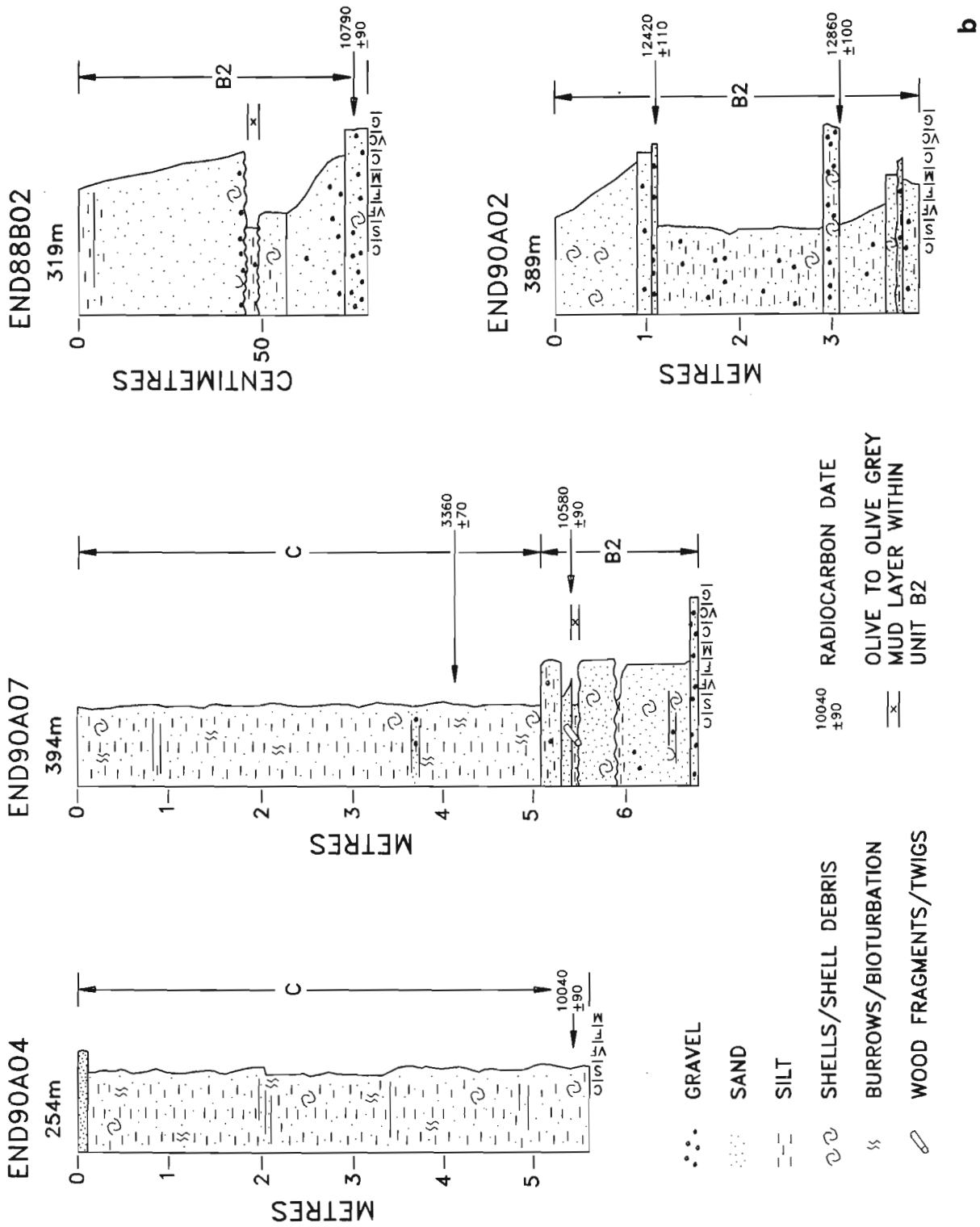


Figure 3. a and 3b. Stratigraphy, lithologic unit designation and chronology of selected Dixon Entrance cores.



**Table 1.** Radiocarbon dates obtained from samples taken from cores recovered in Dixon Entrance. Lithological units are discussed in text

Core	Sample Depth (cm)	Dated Specimen	Radiocarbon Date	Lab #	Lithologic Unit
END88B02	77	serpulid tube	10790 $\pm$ 90	TO-2251	B <sub>2</sub>
END90A02	108	<i>Chlamys rubida</i>	12420 $\pm$ 110	TO-2252	B <sub>2</sub>
END90A02	30	<i>Nuculana fossa</i>	12860 $\pm$ 100	TO-2253	B <sub>2</sub>
END90A04	543	<i>Y. thraciaeformis</i>	10040 $\pm$ 90	TO-2254	C
END90A07	411	shell fragments	3360 $\pm$ 70	TO-2256	C
END90A07	543	twig	10580 $\pm$ 90	TO-2254	B <sub>2</sub>
TUL91C021	527	<i>Nuculana fossa</i>	13960 $\pm$ 100	TO-3489	A
TUL91C026	348	<i>Nuculana fossa</i>	13190 $\pm$ 100	TO-3491	A

One anomaly found in the cores from Dixon Entrance is a thin (less than 10 cm) olive to dark grey laminated mud that is consistently found within unit B<sub>2</sub> (Fig. 3a, b). This appears to represent a regional event as it is found throughout the full east-west extent of the Entrance. Being below the Holocene section and deposited near the top of the low sea level lag, this event would date to the early Holocene (sometime after 10.5 ka).

Unit C in Dixon Entrance is absent in many areas and does not have the consistent sedimentology or distribution as found in the troughs of Hecate Strait and Queen Charlotte Sound. Only in the trough that extends south out of Clarence Strait in Alaska (Fig. 1) is there any appreciable accumulation of unit C muds. Core END90A07 (Fig. 3b) is typical of unit C with bioturbated and laminated mud consisting primarily of silt with lesser amounts of clay and generally less than 10% sand (Fig. 2). An isolated mound of unit C is also found in west-central Dixon Entrance at approximately 250 m water depth. Here the laminated mud contains a greater concentration of sand (10 to 20%), as seen in Core END90A04 (Fig. 3b). Elsewhere in Dixon Entrance late Wisconsinan till or unit B<sub>2</sub> outcrops at the seabed. Unit B<sub>2</sub> often forms the top of the stratigraphic sequence, even to depths of 450 m or greater (Core END90A01, (Fig. 1)).

## DISCUSSION AND SUMMARY

The postglacial stratigraphy and chronology in Dixon Entrance is similar to that observed for the rest of the north-western Canadian continental shelf. Deglaciation ended between 14.0 and 13.0 ka with the complete retreat of the late Wisconsinan ice from the Entrance by approximately 12.9 ka.

From this time until approximately 10.5 to 10.2 ka, sea levels were lowered, resulting in the deposition of a coarse grained sediment lag to depths greater than 450 m. The total amount of relative sea level lowering is not presently known, but the thick and coarse unit B<sub>2</sub> suggests the possibility of greater late Wisconsinan lowering than predicted for Hecate Strait and Queen Charlotte Sound to the south (i.e. Barrie et al., 1991).

The anomalous bed found near the top of B<sub>2</sub> suggests a regional alternation of depositional environment from coarse traction deposition and winnowing conditions to fine suspension sedimentation, and then a return to more energetic conditions and coarser sedimentation. Based on stratigraphic position, these events appear to have occurred prior to the establishment of post-transgressive conditions within Dixon Entrance. This sequence possibly reflects a complexity to the rapid transgression occurring after 10.5 ka, recorded only in Dixon Entrance. Alternatively, the sequence may relate to an oceanographic change resulting in changes to bottom current intensity in Dixon Entrance at this time. Changes in local oceanographic circulation probably accompanied the opening of Hecate Strait into Dixon Entrance as sea levels rose.

Holocene hemipelagic mud (unit C) was deposited only in the trough at the southern end of Clarence Strait and a limited lobe in the west-central part of the entrance, the origin of which is not known at present. A thin transgressive sand and gravel unit was deposited over most of Dixon Entrance to depths greater than 450 m. The clean, coarse grained seabed sediments found throughout most of Dixon Entrance suggest that the hydrodynamic energy levels have remained high since transgression, a result of the macrotidal environment, and the absence of any significant present-day sediment source.



## **ACKNOWLEDGMENTS**

We would like to thank the Captains and crews of **CFAV Endeavour** and **CSS Tully** for their support in the collection of the cores in Dixon Entrance and the participants of cruises PGC90-03 and PGC91-06. B. Swayer and R. Franklin produced the graphics and the manuscript was critically reviewed by H. Josenhans and M. Best. This project was supported by the Office of Energy Research and Development (OERD) and the Department of External Affairs.

## **REFERENCES**

- Barrie, J.V.**  
1991: Contemporary and relict titaniferous sand facies on the western Canadian continental shelf; *Continental Shelf Research*, v. 11, p. 67-79.
- Barrie, J.V. and Bornhold, B.D.**  
1989: Surficial geology of Hecate Strait, British Columbia continental shelf; *Canadian Journal of Earth Sciences*, v. 26, p. 1241-1254.
- Barrie, J.V., Bornhold, B.D., Conway, K.W., and Luternauer, J.L.**  
1991: Surficial geology of the northwestern Canadian continental shelf; *Continental Shelf Research*, v. 11, p. 701-715.
- Bornhold, B.D. and Barrie, J.V.**  
1991: Surficial sediments on the continental shelf off British Columbia; *Continental Shelf Research*, v. 11, p. 685-700.
- Luternauer, J.L., Conway, K.W., Clague, J.J., and Blaise, B.**  
1989a: Late Quaternary geology and geochronology of the central continental shelf of western Canada; *Marine Geology*, v. 89, p. 57-68.
- Luternauer, J.L., Clague, J.J., Conway, K.W., Barrie, J.V., Blaise B., and Mathewes R.W.**  
1989b: Late Pleistocene terrestrial deposits on the continental shelf of western Canada: evidence for rapid sea-level change at the end of the last glaciation; *Geology*, v. 17, p. 357-360.
- Josenhans, H.W., Barrie J.V., Conway, K.W., Patterson, T., Mathewes, R.W., and Woodsworth, G.J.**  
1993: Surficial geology of the Queen Charlotte Basin: evidence of submerged proglacial lakes at 170 m on the continental shelf of western Canada; in *Current Research, Part A; Geological Survey of Canada, Paper 93-1A*, p. 119-127.
- Mathewes, R.W., Heusser, L.E., and Patterson, R.T.**  
1993: Evidence for a Younger Dryas-like cooling event on the British Columbia coast; *Geology*, v. 17, p. 101-104.
- Thomson, R.E.**  
1981: *Oceanography of the British Columbia Coast; Canada Special Publication of Fisheries and Aquatic Sciences*, No. 56, p. 291.

Geological Survey of Canada Project 890052



# New regional gravity data from the southern Yukon and Northwest Territories

C. Lowe, D.A. Seemann, D.B. Hearty<sup>1</sup>, and D.W. Halliday<sup>1</sup>

Pacific Geoscience Centre, Sidney

*Lowe, C., Seemann, D.A., Hearty, D.B., and Halliday, D.W., 1993: New regional gravity data from the southern Yukon and Northwest Territories; in Current Research, Part E; Geological Survey of Canada, Paper 93-1E, p. 23-31.*

---

**Abstract:** In 1991 and 1992, 3637 gravity measurements were obtained in the southern Yukon and Northwest Territories. The measurements are approximately 10 km apart and are accurate to 1-2 mGal. Station coordinates were determined using a Global Positioning System or an Inertial Survey System, and are generally considered accurate to within  $\pm 3$  m.

The data, presented as a contoured Bouguer anomaly map, show many significant features including: an unexpected Bouguer high over the northern Yukon-Tanana and adjacent Nisling and Stikine terranes; prominent linear anomalies and steep gradients along the mapped traces of the Denali Fault and portions of the Tintina Fault systems; generally low values over the Selwyn Basin, and an arcuate zone of high gravity gradients over the Redstone Arch and the western Mackenzie Platform. Elongate, suboval Bouguer lows are associated with post-accretionary granitic batholiths and are found in all terranes and throughout the miogeocline. The geological implications of these features are discussed.

**Résumé :** En 1991 et 1992, 3 637 mesures gravimétriques ont été effectuées dans le sud du Yukon et des Territoires du Nord-Ouest. Les mesures, précises à 1-2 mgal près, sont espacées d'environ 10 km. Les coordonnées des stations ont été déterminées par un système de positionnement global ou par un système inertiel de levé et sont en général considérées exactes à 3 m près.

Les données, présentées sous la forme d'une carte en contours de l'anomalie de Bouguer, révèlent de nombreuses caractéristiques importantes comme : une zone inattendue de valeurs élevées de l'anomalie de Bouguer dans le nord du terrane de Yukon-Tanana et des terranes voisins de Nisling et de Stikine; des anomalies linéaires importantes et de forts gradients le long des traces cartographiées de la faille de Denali et de parties du système de failles de Tintina; des valeurs généralement faibles dans le bassin de Selwyn, et une zone de forts gradients gravimétriques en forme d'arc dans l'arche de Redstone et l'ouest de la plate-forme de Mackenzie. On observe des zones de valeurs faibles de l'anomalie de Bouguer, de forme subovale et allongée, associées à des batholites granitiques postaccrétionnaires dans tous les terranes et dans l'ensemble du miogéocline. Les conséquences géologiques de ces caractéristiques sont analysées.

---

<sup>1</sup> Geophysics Division

## INTRODUCTION

Prior to 1991, regional gravity surveying in the Canadian Cordillera was primarily carried out by the Geological Survey of Canada (formerly the Earth Physics Branch) at an annual rate of 600-800 measurements. A three year program of "enhanced" gravity surveying was initiated in the Cordillera in 1991 in response to a Canada-United States agreement on gravity mapping. Partners in the program are the Geological Survey of Canada, the Geodetic Survey of Canada, the Department of National Defence, and the United States Defence Mapping Agency. Two years of the program have now been completed and 3637 new gravity measurements are available for the southern Yukon and Northwest Territories. The final survey of the program will take place in 1993 in northwestern British Columbia and in the St. Elias Mountains area of the Yukon Territory. The location of the three survey areas comprising this project are shown in Figure 1. The new data, which effectively complete regional coverage of the Cordillera, are the most comprehensive geophysical data-set in these regions. They will be used to help understand and constrain tectonic models, to develop better geoid models, and to provide data for correcting inertial guidance systems.

## DATA ACQUISITION

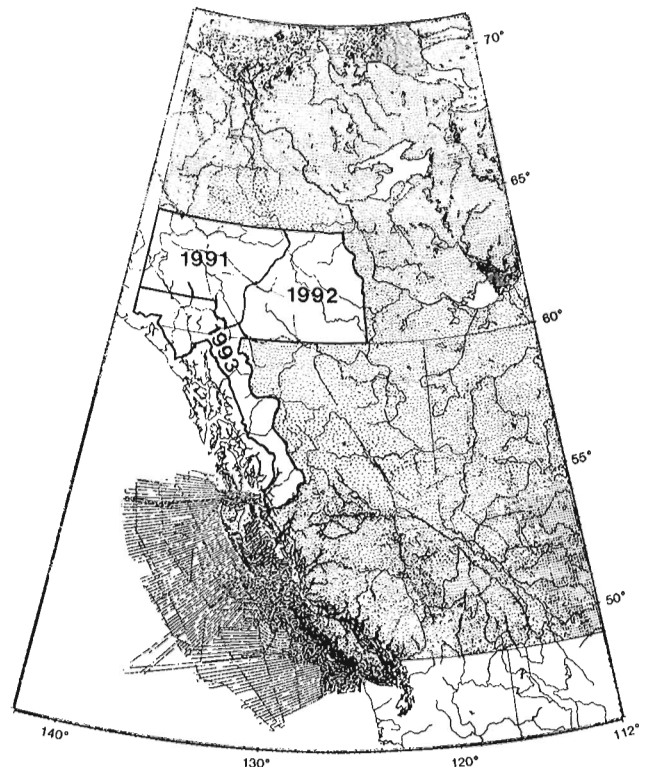
### 1. Gravity data

The 1991 survey (Operation Bouguer 91) consisted of 1812 gravity observations in the western part of the Yukon Territory from 60°N to 64°N. The 1992 survey (Operation Bouguer 92) consisted of 1825 gravity observations in the eastern Yukon and Northwest Territories (Fig. 1). During both surveys gravity data were obtained using Lacoste & Romberg (model G) gravity meters. The meters were calibrated prior to each survey on the Calgary-Inuvik calibration line. Daily gravity traverses, began and ended, at national gravity control points, established throughout the survey areas. The maximum accepted daily closure error on a traverse was 0.5 mGal. In the 1991 survey only one traverse failed to meet this criterion, and it was subsequently repeated. All gravity traverses in the 1992 survey met the prescribed error closure criteria. Accuracy checks were performed by repeating gravity measurements at selected stations. The mean gravity difference in the 1991 survey was 0.065 mGal (for 204 repeat observations) and 0.048 mGal in the 1992 survey (for 284 repeat observations). An average gravity reading takes approximately 1-2 minutes.

### 2. Positioning data

#### (i) Operation Bouguer 91

Of the 1812 gravity stations collected in this survey, 1620 were positioned using an Inertial Survey System (ISS), 69 using the Global Positioning System (GPS), and the remaining stations using conventional altimetry and 1:50 000 scale maps. The inertial work was conducted using two Litton Auto Surveyor Lass II Inertial Survey Systems, mounted on Hughes 500 helicopters. Two visits to each station were



**Figure 1.** Gravity coverage in western Canada, showing the location of the three regions in the enhanced mapping project.

required. On the first visit, gravity, altimetric height, and wet and dry bulb temperatures were measured, while on the second visit, ISS-equipped helicopters accurately located the stations. Approximately 134 stations were not revisited, primarily due to inclement weather, and were subsequently positioned using the measured altimetric heights and 1:50 000 scale maps.

Stations with GPS positioning required only one helicopter visit. Approximately 15 minutes of satellite position data were recorded on Ashtech XII 12 channel, dual-frequency, CA code receivers. The receivers were operated in differential mode, i.e. data were recorded simultaneously at the gravity station and at two base-stations deployed in the area. A comparison of ISS and GPS data at 89 stations showed an overall agreement in station elevation of  $\pm 1.24$  m rms, i.e. well within the  $\pm 3$  m specification required for reconnaissance gravity surveys. Consequently, the two-visit ISS system was abandoned for future surveys in favour of the more cost-effective GPS.

#### (ii) Operation Bouguer 92

The majority of station positions in this survey were determined using the GPS system as described above. However, unlike the 1991 survey, dual frequency P-code receivers were now used and the antenna, rather than mounted on a tripod over the gravity station, was mounted on the tail-fin of the helicopter. This also permitted use of GPS for navigation between gravity stations. The horizontal and

vertical offsets between the antenna and the gravity station were accurately measured and a correction was applied in the subsequent processing. Altimetric heights and 1:50 000 scale maps were used to locate the few stations which did not have sufficiently accurate GPS control (due to poor satellite geometry, or an insufficient number of satellites).

## **DATA PROCESSING**

### ***1. Gravity data***

The gravity data were reduced to the International Gravity Standardization Net 1971 (Morelli, 1974) and theoretical gravity values were calculated using the Geodetic Reference System 1967 gravity formula. Simple Bouguer anomalies were calculated using a standard density of 2670 kg/m<sup>3</sup>. Regional terrain corrections were applied out to a distance of 25 km from each station, using a digital elevation file. The resulting complete Bouguer anomalies (Fig. 2) are considered accurate to 1-2 mGal. The data are available from the Geophysical Data Centre (Geological Survey of Canada, Ottawa).

### ***2. Positioning data***

GPS data processing was carried out in the field using Ashtech software. Stations with vertical errors in excess of  $\pm 2.5$  m were repeated. The geoidal undulation, used to transform GPS (ellipsoidal) elevations to orthometric (geoidal) elevations was calculated using the UNB'90 geoid model (Vanicek et al., 1990) for Operation Bouguer 91, and the GSD92A geoid model (after Veronneau and Mainville, 1992) for Operation Bouguer 92. The latter model incorporated the 1991 gravity data and hence was a significant improvement over the UNB'90 model. ISS data were processed using the Positional and Azimuth Determining System (PADS) software package, supplied with the Litton instruments. Horizontal station coordinates are generally considered accurate to  $\pm 2$  m and station elevations to  $\pm 3$  m. More specific acquisition and processing details are given in the survey reports of Putter (1991), Gregory (1992), Halliday (1992), and Seemann (1993).

## **REGIONAL GEOLOGY**

The 1991 and 1992 surveys of the northern Canadian Cordillera traverse geologically diverse regions with distinctive bedrock and tectonic histories. In the east Proterozoic and Phanerozoic sediments of the Selwyn Basin and Mackenzie Platform comprise the Foreland Belt of the outer miogeocline (ancestral North America), whereas to the west of the transcurrent Tintina Fault System, the Cordillera comprises a series of distinct terranes (Fig. 3). Some terranes are considered truly exotic in character (e.g. Stikinia and Cache Creek Terrane), some pericratonic (e.g. Nisling Terrane), and others displaced fragments of continental North America (e.g. Cassiar Terrane). Terrane accretion has been ongoing since the Mesozoic, and has continued in response

to subduction and compression processes across the nearby boundary between the North American and Pacific plates. Terranes record distinctive stratigraphy, thicknesses, and deformational histories which effect the gravity field. Two processes introduce complexities within these terranes obscuring the lithological and density differences between them. Several episodes of igneous intrusion occurred concurrently with the Mesozoic and Cenozoic terrane accretion processes. Since accretion, hundreds of kilometres of displacement has occurred on large-scale, dextral transcurrent faults, including the Tintina and Denali fault systems. While in general these faults form terrane boundaries, in some instances they have cut and significantly off-set individual terranes.

## **PREVIOUS GEOPHYSICAL SURVEYS**

Although the regional framework has been established, through geological mapping at the 1:250 000 scale, little is known of the subsurface geology. Drillholes are infrequent and usually less than a kilometre deep.

### ***Seismic refraction and reflection data***

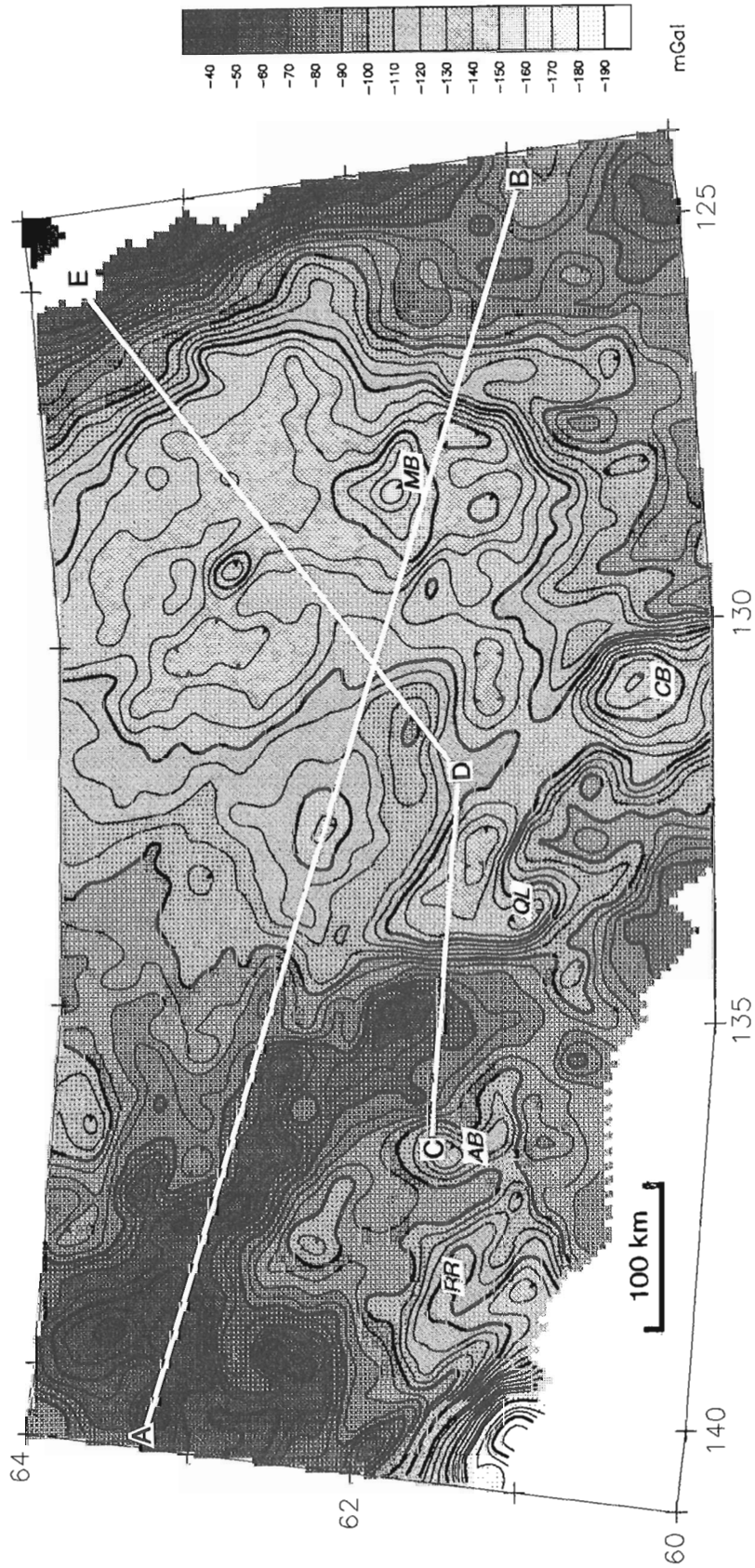
Hales and Asada (1966) calculated a crustal thickness of 36-42 km along a northwest-trending, unreversed seismic refraction profile from Skagway (Alaska) towards Kluane Lake (Yukon), and a thickness of some 35 km along a more northerly profile from Skagway. No other reflection or refraction data exist.

### ***Seismicity data***

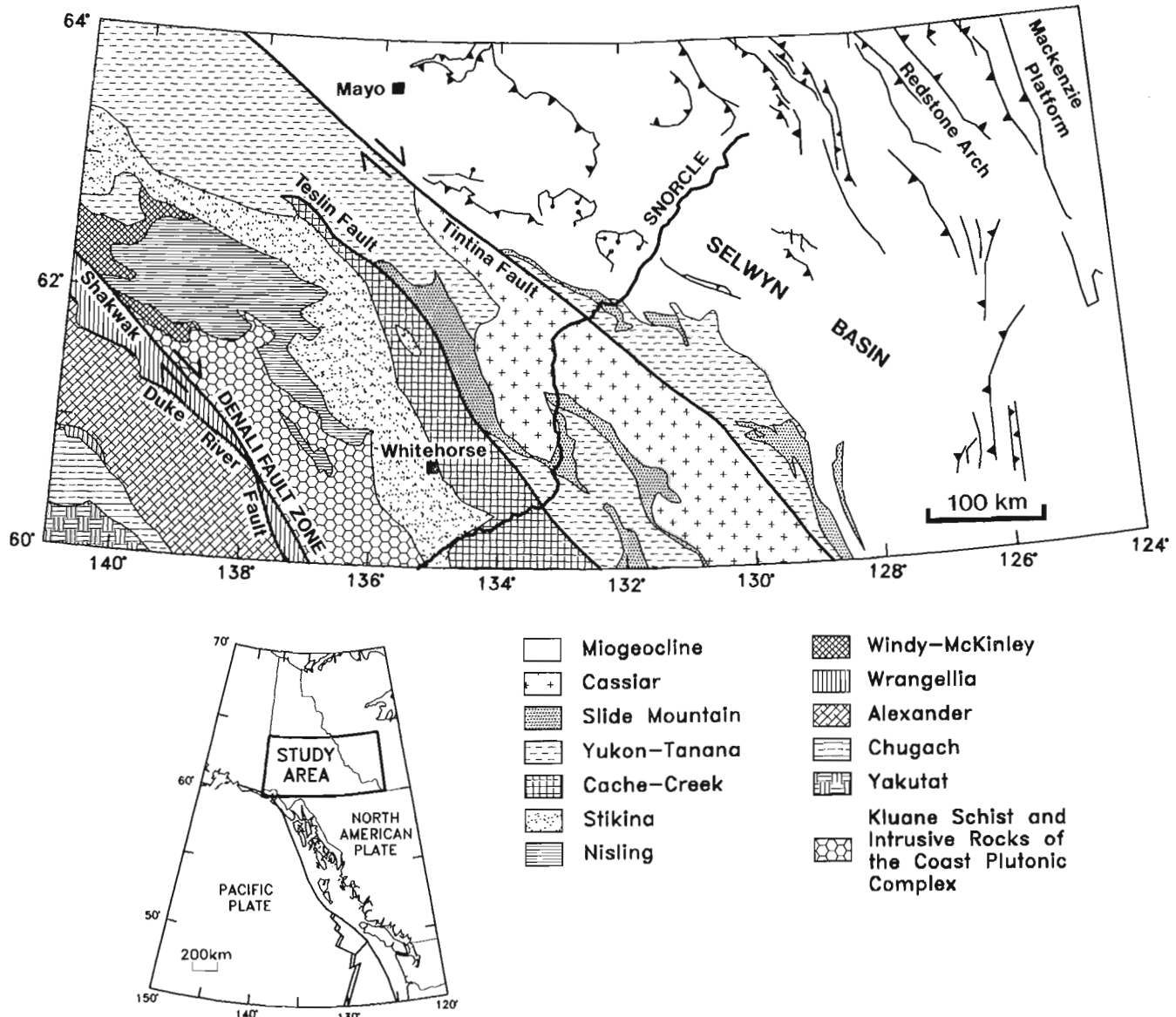
A good record of modern seismicity data is available for the entire region (Horner, 1983; Wetmiller et al., 1988; Horner et al., 1990). In general, the present seismic network allows all events with a magnitude  $\geq 2.5$  to be located with accuracies of  $\pm 20$  km, but is insufficient for accurate focal depth determinations. Recent analysis of this seismicity shows significant activity along the Denali Fault System, decreasing to the east. No events larger than magnitude 4 have been recorded between the Denali and Tintina faults. The northern Yukon-Tanana Terrane and the Selwyn Basin immediately northeast of the Tintina Fault are conspicuous; the former is aseismic and the latter a region of very low seismicity. Seismicity levels increase again over the Mackenzie Platform. Focal mechanism studies on two large earthquakes in this region indicate shallow-dipping thrust events within the Phanerozoic cover (Wetmiller et al., 1988).

### ***Aeromagnetics***

High resolution aeromagnetic coverage is available for the western and central Yukon Territory, but large portions of the miogeocline remain unsurveyed. These data provide good horizontal resolution of structure, via variations in the magnetic field (intensity, wavelength, and fabric). Terranes having high proportions of volcanic units (e.g. Stikinia) are,



**Figure 2.** Bouguer anomaly map of gravity data collected during the 1991 and 1992 enhanced mapping surveys (see Fig. 1). Shading differences occur at intervals of 10 mGal, contour interval is 5 mGal. White lines A-B and C-D-E denote the trace of profiles presented in Figure 4. Batholiths are abbreviated as follows; Ruby Range, RR; Aishihik, AB; Quiet Lake, QL; Cassiar, CB; and Mount Billings, MB.



**Figure 3.** Terranes and tectonic elements in northwestern Canada, after Wheeler et al. (1991), Gordey and Anderson (1993) and Lowe et al. (manuscript in preparation). The location of the proposed SNORCLE transect is shown as a solid line.

in general, magnetically noisy compared to sediment dominated terranes (e.g. Cassiar). Contrasts in magnetic intensity and fabric are noted across major faults, e.g. the Denali and the Tintina. While no clear magnetic fabric is observed over much of the miogeocline, many terranes display a northwesterly trending fabric parallel to geologic structure. Tempelman-Kluit and Currie (1978) measured the magnetic susceptibility and density of a large number of rock samples in the northwestern part of the 1991 study region. Results for some common rock types are shown in Table 1.

Lowe et al. (manuscript in preparation) provide a comprehensive summary of the available geophysical data for the 1991 survey region and discuss the implications of these data on the deep geology and tectonics of the region. A LITHOPROBE multidisciplinary geoscience traverse to investigate the deep architecture of the lithosphere in the northern Cordillera (Slave-Northern Cordillera Lithospheric Evolution (SNORCLE) transect, Fig.3) has been proposed (Clowes, 1993). If undertaken, the study should afford us the opportunity to test a number of suggestions and hypotheses discussed here.

**Table 1.** Range, mean, and population size (PS) of measured densities ( $\text{kg/m}^3$ ), and magnetic susceptibilities ( $10^3 \times \text{SI units}$ ) for a number of rock types in the southern Yukon. Compiled from data in Tempelman-Kluit and Currie (1978).

Rock type	Density			Susceptibility		
	Range	Mean	PS	Range	Mean	PS
Ultramafic	2500-3190	2950	22	0.0- 55.5	31.8	11
Basalt	2500-3050	2760	90	0.0-102.5	19.0	99
Diorite	2600-3100	2790	74	0.0- 53.6	7.8	68
Granodiorite	2590-3150	2710	167	0.0- 71.2	8.6	166
Granite	2560-2710	2620	43	0.0- 33.6	5.3	50
Rhyolite	2310-2930	2610	51	0.0- 23.6	2.9	52
Schist	2540-2940	2750	29	0.0- 29.5	1.7	177
Shale	2560-2690	2630	4	0.7- 1.3	0.5	4
Sandstone	2670-2740	2700	4	0.0- 64.9	4.5	18
Conglomerate	2430-3230	2700	12	0.2- 48.0	8.4	39
Mudstone	2660-2720	2700	3	1.2- 2.5	1.7	3
Carbonate	2610-2720	2690	6	0.0- 23.1	2.4	24

Note: a magnetic susceptibility of 0.0 denotes a reading that was below the threshold of the meter ( $\sim 0.0005 \times 10^3 \text{ SI units}$ ).

## PRELIMINARY OBSERVATIONS AND CORRELATIONS

The average free-air anomaly (not shown) for both survey regions is approximately 1 mGal, indicating isostatic compensation of topography. Generally, high Bouguer values (-70 to -40 mGal) are observed over northwestern areas west of Tintina Fault, and low Bouguer values (<-100 mGal) over much of the miogeocline east of Tintina Fault (Fig. 2). These low values are bound on the east by an arcuate zone of steep gradients with high Bouguer values overlying the Redstone Arch and Mackenzie Platform in the extreme east.

Southwest of the Denali Fault very low Bouguer values (<-190 mGal) are observed over the northeastern St. Elias Mountains (Fig. 2). This is one of the most tectonically active regions in Canada, with estimates of uplift in the range 0.02 - 0.04 m/a (Barnes, 1991). The actual cause of the uplift is variously attributed to glacial rebound and/or compression related to subduction of the Pacific Plate beneath the North American Plate. In nearby Alaska, seismic refraction studies (Fuis and Pflaker, 1991; Fuis et al. 1991) yield crustal velocities to depths of 57 km. Thick, low-density crust could explain the observed gravity low in this region.

Major fault systems such as the Denali and Tintina are recognized in the gravity data. The trace of the Denali Fault is associated with strong WNW-trending linear anomalies bounded by steep gradients (up to 5 mGal/km). In the southwest Yukon it comprises two primary fault segments, the Shakwak and Duke River faults. Duke River Fault juxtaposes Alexander Terrane to the southwest and a segment of Wrangellia to the northeast (Fig. 3). Shakwak Fault juxtaposes rocks of the Wrangellia and Alexander terranes in the southwest against Jura-Cretaceous cover rocks to Wrangellia, the Coast Plutonic Complex, and the Kluane

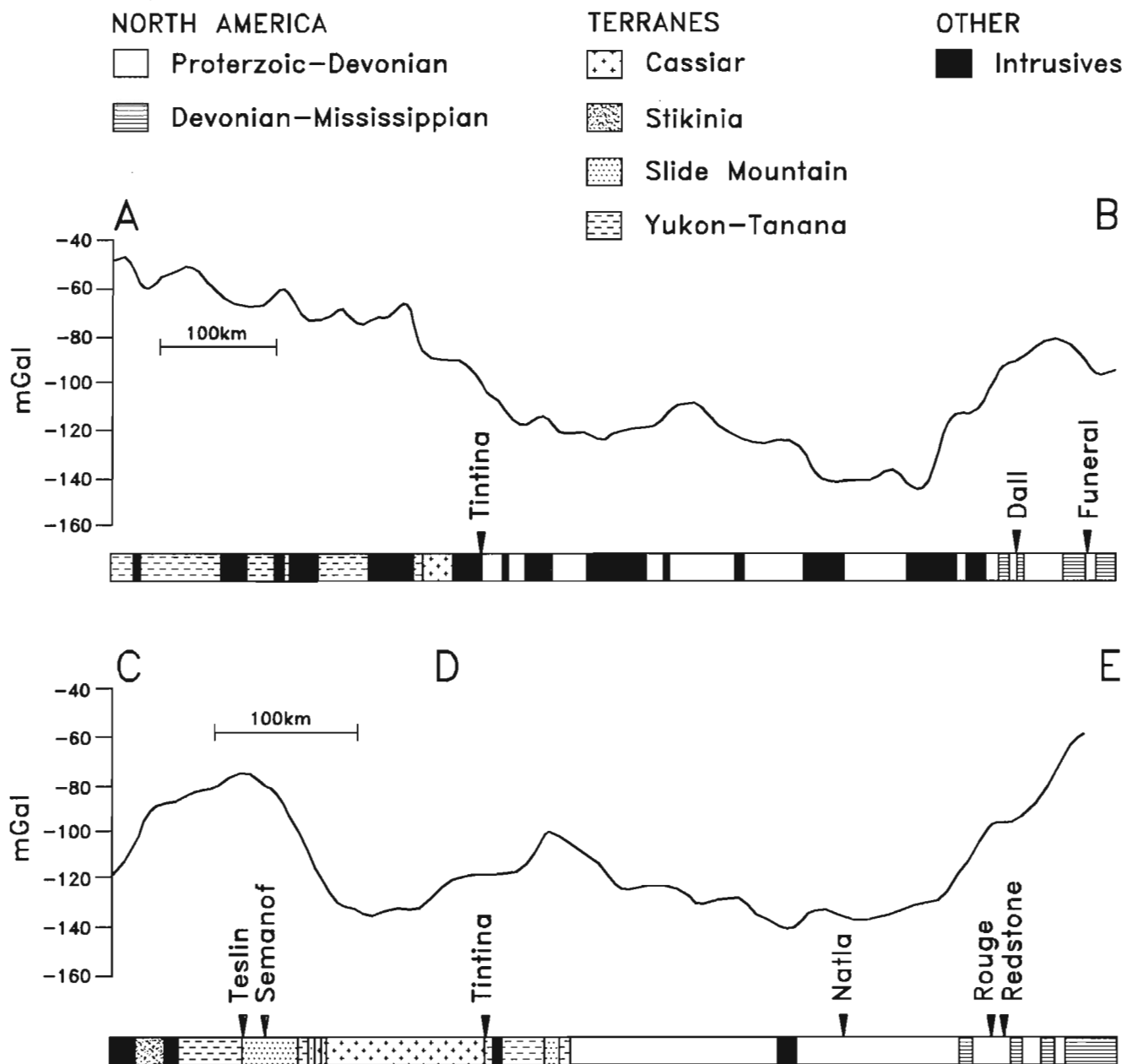
schist in the northeast, (Fig. 3). Deposits of Quaternary sediments infill the Shakwak trench, a pronounced physiographic depression, and produce a strong Bouguer low (minimum -130 mGal). The zone between the Shakwak and Duke River faults is highly tectonized, and intruded by a number of mafic and ultramafic bodies. This region is the locus of high Bouguer values (maximum -55 mGal). The fault system is considered a major intraplate crustal break (St. Amand, 1957; Muller, 1967; Eisbacher, 1976; Campbell and Dodds 1983). There are few constraints on the magnitude or timing of displacement on the Denali Fault System; seismicity indicates active deformation across the fault (Horner, 1983), but the youngest geologic evidence of motion is Middle Holocene (Clague, 1979).

The northwest-trending Tintina Fault (Fig. 3) is a major transcurrent fault system. Tempelman-Kluit et al. (1976) and Gabrielse (1991) estimated at least 450 km of Late Cretaceous and/or Early Tertiary dextral displacement across this fault. While weak, northeasterly-trending gravity gradients, and clear linears are observed along some segments of the fault trace (e.g. between 61.25° and 62.00°N), elsewhere no obvious lineations are recognized. In contrast, south of 60°N, where the Tintina merges with the Northern Rocky Mountain Trench, there is a pronounced gravity low. Some differences in the gravity field on either side of the fault are visible. To the east, gradients are gentle, a broad, open contour pattern dominates, and Bouguer values are typically low (-100 to -145 mGal). West of the fault the gravity field is dominated by short wavelength anomalies (typically <80 km), steep gradients, and generally high Bouguer values (-90 to -40 mGal). These patterns suggest densities are more homogeneous over the miogeocline than over terranes west of the fault. The geometry of the fault at depth is a source of some speculation. D.J. Tempelman-Kluit (pers. comm., 1993) favours a thin-skinned interpretation based on



continuity of deformation style across the fault. Others (e.g. Gabrielse, 1985; Price and Carmichael, 1986; Lowe et al., manuscript in preparation) suggest it represents a major crustal (and/or lithospheric) break. The latter interpretations are based on the geological evidence for large offsets across the fault; the differences across the fault, observed over a spectrum of wavelengths, in a number of geophysical parameters (e.g. magnetics, seismicity, and gravity); and the linearity of the surface trace of the fault over large distances (>1900 km).

Bouguer data highlight differences in terranes between the Denali and Tintina fault systems. The most conspicuous feature is a pronounced gravity high (maximum -40 mGal) overlying the northern Yukon-Tanana Terrane and adjacent parts of the Stikine and Nisling terranes (Fig. 3 and Profile A-B). Here the surface geology is dominated by quartzofeldspathic lithologies, and density determinations (Tempelman-Kluit and Currie, 1978) on a large number of rock samples indicate moderate values of 2700-2800 kg/m<sup>3</sup> (Table 1). Both features indicate the source of the gravity



**Figure 4.** Gravity transects along profiles A-B and C-D-E, located in Figure 2. The geological legend refers to map units shown as a strip along the base of each profile. The major faults are indicated. Note the correspondence between low gravity values and intrusive bodies, the Bouguer high over the Yukon-Tanana Terrane, low gravity values over the Selwyn Basin, and the sharp rise in gravity over the Redstone Arch (near Redstone Fault).

anomaly occurs at some depth in the crust. It is broadly coincident with a sub-oval magnetic low and an apparently aseismic region. A number of different models may account for the gravity anomaly including: relative thinning of the crust beneath the anomalous region (bringing hot, high-density mantle material to shallower depths); underplating of the anomalous region with dense ultramafics; or alternatively, accretion of terranes in the anomalous area onto an allochthonous basement (either another (mafic-rich) terrane such as Slide Mountain, or true oceanic crust). Some support exists for each hypothesis, but given the poor vertical resolution of gravity data and the lack of independent depth constraints, discrimination between hypotheses must await acquisition of high resolution seismic data, such as that proposed in Lithoprobe's SNORCLE transect.

The miogeocline, to the east of the Tintina Fault, comprises sedimentary strata in the Selwyn Basin and Mackenzie Platform (Fig. 3). These sediments, which range in age from Proterozoic to Jurassic, have been thrust faulted and folded. The strata comprise several overlapping, but not coincident, large depocentres developed through (?)mid-Proterozoic, Late Proterozoic, Early Cambrian, and Late Devonian extension (Eisbacher, 1981; Thompson et al., 1987; Gordey and Thompson, 1991). The extent of the mid-Proterozoic and Upper Proterozoic assemblages beneath the western part of the region is unknown.

Low Bouguer values (-110 to -180 mGal) are associated with much of the western miogeocline (Selwyn Basin) with minima presumably reflecting areas of greatest sediment thickness. These low values are bound to the east and south by an arcuate zone of steep gradients (up to 1.4 mGal/km) that may map the boundary between regions of relatively thick (west) and thin (east) sediment cover. The high values to the east coincide, in part, with the Redstone Arch and the western Mackenzie Platform (compare Fig. 2 and 3). Variations in gradient along the arcuate zone reflect variations in topography of the underlying basement.

Post-accretionary granitic intrusives intrude all tectonic units and are often associated with sub-oval, northwest-trending Bouguer lows. Examples include, the Ruby Range (RR) batholith in the Coast Plutonic Complex, the Aishihik batholith (AB) in Stikinia, the Quiet Lake (QL) and Cassiar (CB) batholiths in the Cassiar Terrane, and the Mount Billings (MB) batholith in the Selwyn Basin (Fig. 2). The elongation presumably identifies the direction of minimum compressive stress at the time of emplacement of the bodies. Profiles A-B and C-D-E (Fig. 4) cross a number of Triassic/Jurassic to Upper Cretaceous granodioritic to granitic bodies and highlight clearly this association between the intrusive bodies and Bouguer lows. In general, the more felsic the body, the lower the associated anomaly – a feature reflected in the density data (Table 1). The shape of the anomaly associated with a batholith often differs from its mapped extent giving an indication of its surface geometry. Bouguer data suggest the Quiet Lake batholith and the Glenlyon Range batholith outcropping to the northwest are connected at depth. The lows associated with these bodies are truncated to the west by a strong west-trending gradient zone (up to 2 mGal/km), suggesting a steep intrusive contact or fault.

## CONCLUSIONS

The 3637 new gravity measurements have been acquired in the southern Yukon and Northwest Territories as part of a three-year enhanced gravity mapping project. The measurements are spaced approximately 10 km apart and are considered accurate to 1-2 mGal. Station coordinates are generally estimated to within  $\pm 3$  m. The new data are in the public domain and available through the Geophysical Data Centre (Geological Survey of Canada, Ottawa).

A preliminary examination of these data highlights a number of geological correlations and offers some new insights into the deeper geology. Linear anomalies and strong Bouguer gradients are associated with the mapped trace of the Denali Fault System and with portions of the Tintina Fault System. A Bouguer high overlies the northern Yukon-Tanana Terrane and adjacent portions of the Nisling and Stikine terranes. This high is incompatible with the mapped surface geology and with measured rock densities, suggesting the anomalous mass was accreted onto a basement which is geologically distinct from neighbouring regions, or alternatively, that it is an area of recent extension and crustal thinning. East of the Tintina Fault gravity data indicate a relatively homogenous crust. There, Bouguer values are generally low, especially over the Selwyn Basin, but increase over the Redstone Arch, where sediment thickness decreases dramatically. Granitic plutons intrude all geological units and are invariably associated with low anomaly values.

## ACKNOWLEDGMENTS

Funding for the field programs was provided by the United States Defence Mapping Agency and the Geological Survey of Canada. Field surveying was carried out by personnel from the Canadian Department of National Defense, under the capable direction of Capt. E.K. Putter (1991) and Capt. S.J. Gregory (1992). The participation of all field staff is gratefully acknowledged. C.Lowe and D.A. Seemann have benefitted from discussions with many Yukon geologists: Jim Mortensen (UBC, Vancouver), Charlie Roots (YGO, Whitehorse), and Steve Gordey (GSC, Vancouver). Ralph Currie and Tark Hamilton (GSC, Sidney) reviewed an earlier version of this manuscript and suggested a number of improvements. We thank Richard Franklin for drafting some diagrams.

## REFERENCES

- Barnes, D.F.**  
1991: Small or undetectable gravity changes accompanying vertical crustal movements in northern southeast Alaska and adjacent Canada; EOS, v. 72, p. 111.
- Campbell R.B. and Dodds, C.J.**  
1983: Terranes and major faults of the Saint Elias Mountains, Yukon Territory, British Columbia and Alaska; Geological Association of Canada, Annual meeting Victoria, Program with Abstracts, p. A10.
- Clague, J.J.**  
1979: The Denali Fault System in southwest Yukon Territory - a geologic hazard?; in Current Research, Part A; Geological Survey of Canada, Paper 79-1A, 169-178.

**Clowes, R.M. (ed.)**

1993: LITHOPROBE Phase IV proposal - Studies of Evolution of a Continent; Published by the LITHOPROBE secretariat, University of British Columbia, Vancouver, British Columbia.

**Eisbacher, G.H.**

1976: Sedimentology of the Dezadeash Flysch and its implications for strike-slip faulting along the Denali Fault, Yukon Territory and Alaska; *Canadian Journal of Earth Sciences*, v. 13, p. 1495-1513.

1981: Sedimentary tectonics and glacial record in the Windermere Supergroup, Mackenzie Mountains, northwestern Canada; Geological Survey of Canada, Paper 80-27.

**Fuis, G.S. and Plafker, G.**

1991: Evolution of deep structure along the Trans-Alaska Crustal Transect, Chugach Mountains and Copper River Basin, Southern Alaska; *Journal of Geophysical Research*, v. 96, p. 4229-4253.

**Fuis, G.S., Ambos, E.L., and Mooney, W.D.**

1991: Crustal structure of accreted terranes in southern Alaska, Chugach Mountains and Copper River Basin, from seismic refraction results; *Journal of Geophysical Research*, v. 96, p. 4187-4227.

**Gabrielse, H.**

1985: Major dextral transcurrent displacements along the northern Rocky Mountain Trench and related lineaments in north-central British Columbia; *Geological Society of America Bulletin*, v. 96, p. 1-14.

1991: Tintina and Northern Rocky Mountain Trench System, in *Structural styles*; Chapter 17 in *Geology of the Cordilleran Orogen in Canada*, H. Gabrielse and C.J. Yorath (ed.); Geological Survey of Canada, *Geology of Canada*, no. 4, p. 651-653.

**Gordey, S.P. and Thomson, R.I.**

1991: Ancestral North America; Chapter 17 in *Structural styles Geology of the Cordilleran Orogen in Canada*, H. Gabrielse and C.J. Yorath (ed.); Geological Survey of Canada, no. 4, p. 625-628.

**Gordey, S.P. and Anderson, R.G.**

1993: Evolution of the northern Cordilleran Miogeocline, Nahanni Map area (1051), Yukon and Northwest Territories; Geological Survey of Canada, Memoir 428.

**Gregory, S.J. (Capt.)**

1992: 'OP Bouguer 92' field operations report; Mapping and Charting Establishment, Department of National Defense, Ottawa.

**Hales, A.L. and Asada, T.**

1966: Crustal structure in coastal Alaska; in *The Earth Beneath the Continents*, (ed.) J.A. Steinhart and T. Jefferson-Smith (ed.). American Geophysical Union, *Geophysical Monograph* v. 10, p. 420-432.

**Halliday, D.W.**

1992: 'OP Bouguer 91', Project 91112 Gravity data processing report; Geophysics Division, Geological Survey of Canada, Ottawa.

**Horner, R.B.**

1983: Seismicity in the St. Elias region of northwestern Canada and southeastern Alaska; *Seismological Society of America Bulletin*, v. 73, p. 1117-1137.

**Horner, R.B., Wetmiller, R.J., Lamontagne, M., and Plouffe, M.**

1990: A fault model for the Nahanni Earthquakes from aftershock studies; *Seismological Society of America Bulletin*, v. 80, p. 1553-1570.

**Morelli, C. (comp.)**

1974: International Gravity Standardisation Net 1974; International Association of Geodesy, Special Publication No. 4, Paris

**Muller, J.E.**

1967: Kluane Lake map-area, Yukon Territory; Geological Survey of Canada, Memoir 340.

**Price, R.A. and Carmichael, D.M.**

1986: Geometric test for Late Cretaceous - Paleogene intracontinental transform faulting in the Canadian Cordillera. *Geology*, 14, 468-471.

**Putter, E.K. (Capt.)**

1991: 'OP Bouguer 91' field operations report; Mapping and Charting Establishment, Department of National Defence, Ottawa.

**Seemann, D.A.**

1993: 'OP Bouguer 92' Project 92112 Gravity data processing report; Geophysics Division, Geological Survey of Canada, Ottawa.

**St. Amand, P.**

1957: Geological and geophysical synthesis of the tectonics of portions of British Columbia, the Yukon Territory, and Alaska; *Geological Society of America Bulletin*, v. 68, p. 1343-1370.

**Tempelman-Kluit, D.J. and Currie, R.G.**

1978: Reconnaissance rock geochemistry of Aishihik Lake, Snag, and Stewart River map areas in the Yukon Crystalline Terrane, Geological Survey of Canada, Paper 77-8.

**Tempelman-Kluit, D.J., Gordey, S.P., and Read, B.C.**

1976: Stratigraphic and structural studies in the Pelly Mountains, Yukon Territory; in *Report of Activities, Part A*; Geological Survey of Canada, Paper 76-1A, 97-106.

**Thompson, B., Mercier, E., and Roots, C.**

1987: Extension and its influence on Canadian Cordilleran passive-margin evolution; in *Continental extensional tectonics*, (ed.) M.P. Coward, J.F. Dewey, and P.L. Hancock, Geological Society of London, Special Publication, No. 28, 409-417.

**Vanicek, P., Zhang, C., and Ong, P.**

1990: Computation of a file of Geoid heights using Molodenski's Truncation method; Contract Report Number 90-001; Geodetic Survey Division, Surveys, Mapping, and Remote Sensing Sector, EMR, Ottawa, p. 29.

**Veronneau, M. and Mainville, A.**

1992: Computation of a Canadian Geoid model using the FFT technique to evaluate Stokes' and Vening-Meinesz formulas in a planar approximation; Internal Report, Geodetic Survey Division, EMR, Ottawa, p. 11.

**Wetmiller, R.J., Horner, R.B., Hasagawa, H.S., North, R.G.,****Lamontagne, M., Wiechert, D.H., and Evans, S.G.**

1988: An analysis of the 1985 Nahanni earthquakes; *Seismological Society of America Bulletin*, v. 78, p. 590-616.

**Wheeler, J.O., Brookfield, A.J., Gabrielse, H., Monger, J.W.H.,****Tipper, H.W., and Woodsworth, G.J. (comp.)**

1991: Terrane map of the Canadian Cordillera; Geological Survey of Canada, Map 1713A.

Geological Survey of Canada Project 910017, 86009



# Models for tourmalinite formation in the Middle Proterozoic Belt and Purcell supergroups (Rocky Mountains) and their exploration significance<sup>1</sup>

John F. Slack<sup>2</sup>

*Slack, J.F., 1993: Models for tourmalinite formation in the Middle Proterozoic Belt and Purcell supergroups (Rocky Mountains) and their exploration significance; in Current Research, Part E; Geological Survey of Canada, Paper 93-1E, p. 33-40.*

---

**Abstract:** Tourmalinites in the Middle Proterozoic Belt and Purcell supergroups apparently formed by both subseafloor replacement and by reaction between exhalative boron and aluminous sediments in a submarine brine pool. Stratiform tourmalinites, which may form by either process, are favourable exploration guides where they contain sulphide minerals and(or) anomalous amounts (>10 vol.%) of fine grained, Mn-rich garnet (indicating precipitation in a brine pool). Discordant tourmalinites, which form only by replacement, are also prospective where they contain sulphides, especially sphalerite and galena. Coexisting brown and black discordant tourmalinites may be an additional exploration guide, indicating subseafloor mixing of Mg-rich seawater and Fe-rich hydrothermal fluid under high fluid/rock conditions.

**Résumé :** Les tourmalinites observées dans les supergroupes de Belt et de Purcell (Protérozoïque moyen) se seraient apparemment formées par substitution sous le fond marin ainsi que par réaction entre des sédiments borés et alumineux d'origine exhalative à l'intérieur d'un «bassin» de saumure sous-marin. Les tourmalinites stratiformes, qui pourraient se former par l'un ou l'autre des deux processus, sont des guides d'exploration favorables lorsqu'elles renferment des sulfures et (ou) des quantités anormales (>10 % en volume) de grenat à grain fin, riche en Mn (indiquant une précipitation dans un bassin de saumure). Les tourmalinites discordantes, qui ne se forment que par substitution, sont aussi prometteuses lorsqu'elles renferment des sulfures, surtout de la sphalérite et de la galène. Les tourmalinites discordantes brunes et noires coexistantes peuvent constituer un autre guide d'exploration, indiquant un mélange d'eau de mer riche en Mg et de fluide hydrothermal riche en fer, sous le fond marin, dans des conditions de rapport fluide/roche élevé.

---

<sup>1</sup> Contribution No. 16, Sullivan-Aldridge Project

<sup>2</sup> United States Geological Survey, National Center, MS 954, Reston VA 22092

## INTRODUCTION

Since the pioneering work of Ethier and Campbell (1977) on tourmalinites in the Middle Proterozoic Belt and Purcell supergroups, exploration efforts have focused on these unusual rocks as prospecting guides. Tourmalinites are now well documented in association with a variety of stratabound mineral deposits, including those containing Cu, Pb, Zn, Ag, Au, W, Co, and U (see Slack et al., 1993, for references). Over the past decade, several genetic models have been proposed for tourmalinites, each of which has different exploration implications. The present paper reviews these models and their relevance to tourmalinites in the Belt and Purcell supergroups, and proposes criteria for distinguishing barren tourmalinites from those that may have associated stratabound mineralization.

## BELT-PURCELL TOURMALINITES

### *Distribution*

Diverse occurrences of tourmaline-rich rocks and tourmalinites are known in the Middle Proterozoic Belt and Purcell supergroups (Fig. 1). Most of the occurrences are in the Aldridge Formation (Canada) and the stratigraphically equivalent Prichard Formation (United States), which together are the lowest recognized units within this dominantly clastic metasedimentary sequence (e.g., Harrison, 1972; Cressman, 1989; Höy, 1993). By far the most famous locality is in the footwall of the Sullivan Pb-Zn-Ag deposit, British Columbia, where tourmalinites and related tourmaline-bearing metasedimentary rocks form part of a large discordant feeder zone beneath overlying massive sulphide ores (Shaw and Hodgson, 1980; Hamilton et al., 1982). Stratigraphically, these footwall tourmalinites are in the uppermost part of the lower Aldridge Formation; smaller tourmalinites are also present in the hangingwall of the orebody, where their original extent has been largely obscured by younger alteration (Shaw et al., 1993). Elsewhere in Purcell Supergroup in British Columbia, tourmalinites are known in both the lower and middle Aldridge, including some occurrences in the uppermost part of the middle Aldridge; tourmalinites near Estella mine on the east side of the Rocky Mountain trench (Fig. 1) are also in the middle Aldridge Formation (T. Höy, pers. commun., 1992). In Belt Supergroup in the United States, tourmalinites occur mainly in Prichard Formation of western Montana and northern Idaho (Beaty et al., 1988; Cressman, 1989), and in the possibly equivalent Yellowjacket Formation in eastern Idaho (Modreski and Connor, 1991). One tourmalinite locality is also known in carbonate-rich rocks of Newland Formation (a stratigraphic equivalent of the Prichard), in the Helena embayment area at Cement Gulch, Montana (J.M. Leask, pers. commun., 1992).

### *Field relations*

Tourmalinites in the Belt and Purcell supergroups may be divided into two major types, discordant and stratiform. Minor tourmaline occurrences in small veins or joint fillings

and in granites or pegmatites (e.g., Beaty et al., 1988) are not considered here. The discordant tourmalinites form clearly crosscutting bodies several metres to hundreds of metres in diameter. Examples include the tourmalinized feeder zone of the stratiform Sullivan deposit, tourmalinized wall rocks of the nearby discordant Stemwinder deposit, and tourmalinites at the Goatfell and Fors prospects to the south (Fig. 1). Many of these tourmalinites clearly replace clastic metasediments and discordant bodies of breccia or conglomerate (Hamilton et al., 1982), and some are associated with Middle Proterozoic Moyie-type gabbroic intrusions and/or stratabound albite-rich rocks or albitites.

The stratiform tourmalinites are centimetres to metres in thickness and locally may be traced along strike for tens to hundreds of metres. Stratiform (bedded) tourmalinites are known at the Neg, St. Joe, Can Am, and Estella prospects in British Columbia, and at the Fork and related occurrences in the Plains area of western Montana. In general, stratiform tourmalinites are not spatially related to Moyie-type gabbroic intrusions. The St. Joe and Fork tourmalinites are unusual in being associated with highly carbonaceous argillites.

### *Textures and mineral assemblages*

Tourmalinites in the Belt and Purcell supergroups vary greatly in texture from aphanitic and cherty to somewhat coarse and granoblastic. Most are dark grey to black in hand specimen, although pale to dark brown tourmalinites occur in a few areas (e.g., Sullivan mine, Fors prospect, Estella locality). Some of the fine grained, cherty tourmalinites have been worked by Native Americans into arrowheads and spear points, and a few tourmalinite outcrops (e.g., Neg) show clear evidence of excavation and development. The cherty tourmalinites consist mainly of quartz and tourmaline, the latter with a grain size typically <10 µm (Ethier and Campbell, 1977). Relatively coarse (1-2 mm) tourmalines occur in tourmalinites within the aureole of a granite pluton at the Vulcan prospect (Fig. 1); similar coarse tourmalines (to 5 mm) have been identified adjacent to Moyie-type gabbroic intrusions at the Sullivan mine. The grain size of the cherty tourmalinites apparently reflects primary hydrothermal precipitation, while that of the coarser varieties is mainly a function of recrystallization during superimposed hydrothermal alteration and/or contact metamorphism.

Many of the tourmalinites show primary sedimentary structures such as fine-scale laminations, graded beds (Fig. 2A), cross laminations, and flame structures; tourmalinized rip-up clasts in a tourmaline-free matrix occur locally (Fig. 2B). Tourmalinites from the Morning Glory prospect in Montana display an unusual spotted texture in which laminations 3-5 mm thick contain irregular clots of dark, presumably Fe-rich tourmalinite that are partially replaced by pale, presumably Mg-rich tourmalinite (Fig. 2C); similar spotted tourmalinites occur at Mt. Mahon. At the Fork locality, Montana, thin (1-2 mm) veinlets of quartz+tourmaline+ilmenite±pyrite form unequivocal feeders for associated stratiform tourmalinites (Fig. 2D). These vein-related occurrences, and similar ones observed in the St. Joe tourmalinites, strongly suggest an epigenetic, replacement origin for some

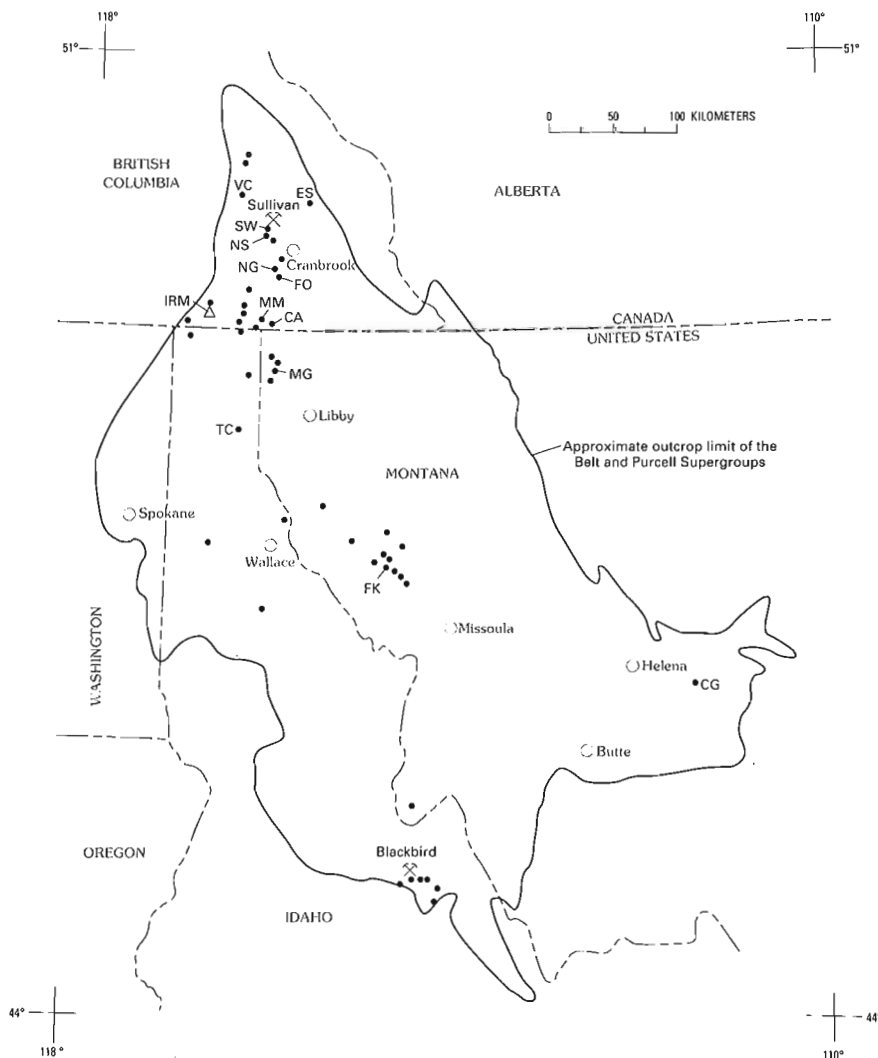
of the stratiform Belt-Purcell tourmalinites. Support for this hypothesis comes from the selective replacement of matrix minerals (interpreted as original clays and/or feldspars) observed in tourmaline-bearing siltstones from the Morning Glory prospect (Fig. 2E); similar features have been noted in tourmalinized sediments from the Sullivan-North Star alteration zone (Leitch et al., 1991).

Most of the tourmalinites have a simple mineralogy consisting of subequal amounts of quartz and tourmaline, together with minor accessory phases such as zircon, titanite, rutile, allanite, and ilmenite. Petrographic study of nearly 150 thin sections from samples collected by the author during the 1992 field season in British Columbia and Montana shows that some Belt-Purcell tourmalinites also contain substantial pyrrhotite, garnet, feldspar, epidote, chlorite, biotite, and/or muscovite (see Hamilton et al., 1982; Shaw and Hodgson, 1986; Leitch and Turner, 1991; Leitch, 1992b). The garnets are particularly distinctive, forming generally small (<3 mm) euhedral grains that may account for as much as 30 volume percent of some samples (Fig. 2F); microprobe analyses of similar garnets from the Sullivan mine (R.L. Barnett, Cominco Ltd. report, 1982; Leitch, 1992b) and from surface

outcrops at the Morning Glory prospect (J.F. Slack, unpub. data) reveal very Mn-rich compositions. Such garnet-rich tourmalinites may be boron facies of spessartine-quartz rocks or coticles (e.g., Spry, 1990) that are locally prominent in the immediate footwall of the Sullivan orebody (R.L. Barnett, Cominco Ltd. report, 1982; J.F. Slack, unpub. data).

### Geochemistry

Whole-rock geochemical data for tourmalinites from the Sullivan mine have been presented by Hamilton et al. (1982) and recently by Shaw et al. (1993). Compared to relatively unaltered clastic metasedimentary rocks of Aldridge Formation, Sullivan tourmalinites are significantly enriched in MgO and B<sub>2</sub>O<sub>3</sub>, and depleted in Na<sub>2</sub>O, CaO, and K<sub>2</sub>O; MnO shows a minor enrichment. Shaw et al. (1993) recalculated their tourmalinite analyses on a sulphide-free basis, and determined that total Fe (as Fe<sub>2</sub>O<sub>3</sub>) is not appreciably different between the mine tourmalinites and unaltered Aldridge metasedimentary rocks. Electron microprobe analyses of tourmalines from the footwall tourmalinite and from other alteration zones associated with the Sullivan deposit (Ethier and Campbell,

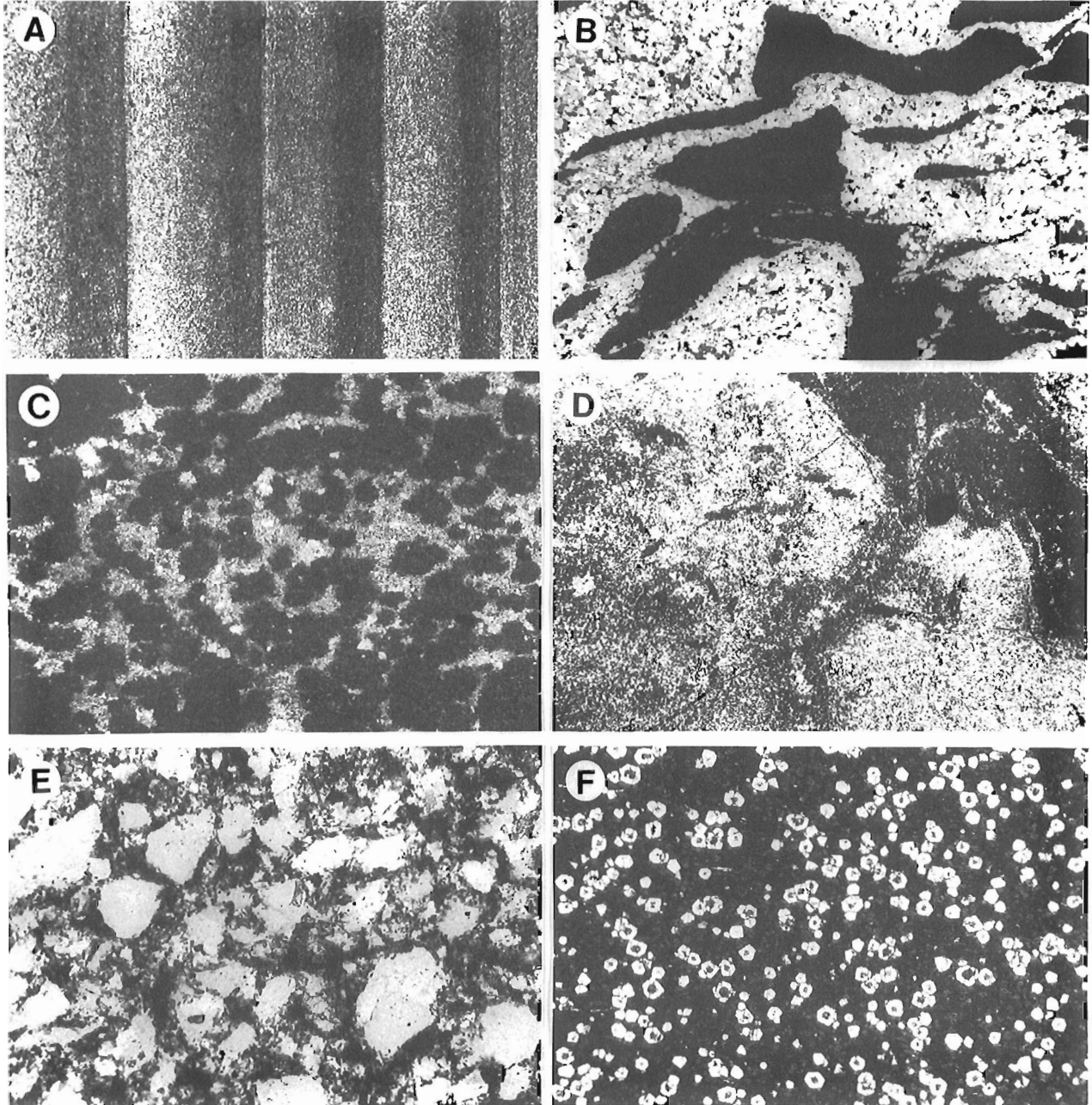


**Figure 1.**

Locations of stratabound tourmaline-rich rocks and tourmalinites (dots) in the Middle Proterozoic Belt and Purcell supergroups. Abbreviations: CA – Canam; CG – Cement Gulch; ES – Estella; FK – Fork; FO – Fors; IRM – Iron Range Mountain; MG – Morning Glory; MM – Mount Mahon; NG – Neg; NS – North Star; SW – Stemwinder; TC – Trestle Creek; VC – Vulcan. Distribution of Belt-Purcell outcrop after Cressman (1989); Phanerozoic rocks (including the Idaho batholith) are not shown.

1977; Leitch, 1992b; J.F. Slack, unpub. data) show compositions mainly intermediate along the schorl-dravite solid-solution join. Most of the Mg-rich tourmalines analyzed to date are relatively coarse, apparently recrystallized grains that occur in massive pyrrhotite ore, adjacent to gabbroic intrusions, or

within (or near) younger alteration facies (e.g., albite-chlorite). Local brown cherty tourmalinites in the footwall of the deposit probably are also Mg-rich, based on analyses obtained on brown tourmalines from other stratabound sulphide deposits (cf. Taylor and Slack, 1984).



**Figure 2.** Photomicrographs of thin sections (all plane transmitted light). **A** – Graded bedding defined by quartz-rich (light) and tourmaline-rich (dark) layers in tourmalinite from the Morning Glory prospect, Montana (field of view = 1 cm); **B** – Tourmalinized rip-up clasts (black) in a tourmaline-free matrix from the Mount Mahon property, British Columbia (field of view = 1 cm); **C** – Spotted tourmalinite from the Morning Glory prospect, Montana, showing dark, Fe-rich (?) tourmalinite partially replaced by pale, Mg-rich (?) tourmalinite (field of view = 4 mm); **D** – Quartz-tourmaline veinlet and related replacive tourmalinite (dark) from the Fork locality, Montana (field of view = 1 cm); **E** – Tourmaline preferentially replacing matrix minerals (probably clays or feldspars) in a tourmalinized siltstone from Morning Glory, Montana (field of view = 4 mm); **F** – Garnet-rich tourmalinite from the immediate footwall (3907 Bypass) of the Sullivan Zn-Pb deposit, British Columbia, showing tourmaline concentrations (dark) in the cores of many of the garnets (field of view = 1 cm).



## MODELS FOR TOURMALINITE FORMATION

### *Constraints from aluminum solubility*

The high alumina content of tourmaline (typically 28-35 wt%  $\text{Al}_2\text{O}_3$ ) significantly constrains models of tourmalinite formation. Any model involving precipitation of tourmaline directly from an aqueous phase, such as metalliferous hydrothermal fluids, must provide for transport of significant aluminum in solution. In hydrothermal fluids at low to moderate temperature, however, aluminum shows appreciable solubility only under conditions of low or high pH, high fluoride or sulphate content, and high concentration of organic acid complexes (e.g., Robertson and Hem, 1969; Driscoll, 1989; Wesolowski and Palmer, 1992). Available field and petrographic data on tourmalinites in the Belt and Purcell supergroups do not support the existence of such geochemical conditions (e.g., lack of metamorphosed acid-sulphate or K-feldspar alteration zones, lack of fluorite or barite gangue, etc.), although their former presence cannot be entirely ruled out. Similarly, it is difficult to evaluate the possible role of organic complexes (e.g., acetate) in the formation of the tourmalinites, though it is noted that the St. Joe and Fork occurrences appear to be preferentially associated with highly carbonaceous argillites. Given present data, however, it seems likely that the formation of most (if not all) Belt-Purcell tourmalinites was controlled by the availability of aluminum at the local site of deposition. The most readily accessible source of the aluminum probably was in detrital clays and feldspars in the clastic sediments of the Aldridge and Prichard formations.

### *Subseafloor replacement of clastic sediments*

A growing body of field and geochemical data suggest that most tourmalinites form by the selective replacement of permeable clastic sediments on or beneath the seafloor. Evidence for this interpretation comes from the preferential replacement of the clay and/or feldspar matrix of siltstones and argillites by tourmaline, and the broadly similar bulk compositions of tourmalinites and their host sediments (Slack et al., 1993). A model preferred by the author involves migration of boron-rich hydrothermal fluids along permeable, sandy beds and the selective replacement of argillaceous beds (or laminae) in the upper parts of unconsolidated sedimentary sequences. This replacement may have taken place at or near the sediment-water interface, or tens to hundreds of metres beneath it. Based on the presence of tourmaline in weakly metamorphosed tourmalinites of the Belt and Purcell supergroups, the primary boron-bearing phase in these replacement tourmalinites is considered to have been tourmaline (see also Plimer, 1988; Slack and Coad, 1989; Slack et al., 1993).

The Sullivan tourmalinites display a variety of colours that suggest variable fluid compositions. Most of the tourmalinites are dark grey to black, but some are medium to dark brown. Assuming that the brown tourmalinites are magnesian (cf. Taylor and Slack, 1984), their compositions imply the involvement of significant amounts of entrained Mg-rich seawater along the margins and top of the footwall feeder

zone. The occurrence in the feeder zone of both black, Fe-rich tourmalinites and brown, Mg-rich tourmalinites in complex parageneses (J.F. Slack and D.R. Shaw, unpub. data) suggests mixing of Fe-rich hydrothermal fluids and Mg-rich seawater under relatively high fluid/rock conditions (see Slack and Coad, 1989); alternatively, these relations could be due to multiple periods of tourmalinization. The more Fe-rich compositions of tourmalines in other Belt-Purcell tourmalinites (Beatty et al., 1988) probably reflect relatively low fluid/rock conditions in which the chemistry of the tourmalines was controlled largely by the bulk composition of the host sediments (cf. Slack et al., 1993).

### *Syngenetic-exhalative processes*

Most previous studies concluded that tourmalinites form by syngenetic-exhalative processes coeval with sedimentation and/or volcanism (e.g., Ethier and Campbell, 1977; Slack et al., 1984; Plimer, 1988). These interpretations were based on the stratiform geometry of the tourmalinites, their common associations with stratabound sulphide deposits and other chemical sediments, and their local preservation of sedimentary structures such as graded beds, cross-laminations, and rip-up clasts. As a result of recent whole-rock geochemical work, however, we now know that such features are better explained by subseafloor replacement (i.e., tourmalinization) of original sedimentary structures (see Slack et al., 1993).

Some tourmalinites nevertheless appear to have formed by exhalative activity. Support for this hypothesis comes mainly from the common association of tourmalinites with coticles and, in some cases, with massive sulphide deposits (e.g., Slack, 1982; Spry, 1990). The very Fe- and Mn-rich nature of coticles, relative to their host sediments, suggests derivation of the Fe and Mn from hydrothermal oxides and/or hydroxides that precipitated within the water column (or at the sediment-water interface), probably in a brine pool setting. Detailed microprobe analyses by Stanton and Williams (1978) of the garnets in laminated coticule rocks ("spessartine quartzites") of the Broken Hill district, Australia, show a systematic chemical microstratigraphy that reinforces this model. By analogy, the boron in coticule-associated tourmalinites is also believed to have precipitated at or above the sediment-water interface. Primary boron precipitates in these rocks may have been jimboite [ $\text{Mn}_3\text{B}_2\text{O}_6$ ] and/or sussexite [ $\text{MnBO}_2(\text{OH})$ ], based on their occurrence in bedded manganese ores of Switzerland and Japan (Epprecht et al., 1959; Kato and Matsubara, 1980), and perhaps the hypothetical iron analogs of these minerals (as yet unknown in nature). It is suggested that coticule-associated tourmalinites originally formed from exhalative Fe-Mn borates and intermixed detrital clays (e.g., smectite, illite, chlorite) that were later converted to tourmaline and spessartine-rich garnet by post-depositional diagenetic and/or metamorphic processes.

The presence of abundant Mn-rich garnet locally in the footwall of the Sullivan orebody implies the former existence of a brine pool prior to exhalative Pb-Zn mineralization. Studies of drill core in 1992 by the author, together with examination of underground samples collected by D.R. Shaw in 1976-1980, suggest that this postulated brine pool was

present during the exhalative (?) formation of the uppermost footwall tourmalinites, based on the occurrence within them of abundant (10-30%) fine grained garnet (Fig. 2F). Garnet-rich tourmalinites have also been found at Mt. Mahon and the Morning Glory prospect, both of which are in the middle Aldridge/Prichard, stratigraphically well above those identified at the Sullivan horizon. These stratigraphically higher tourmalinites, which are believed to represent the products of younger brine pools in the Belt-Purcell basin, may be genetically related to other stratabound mineralization in the middle Aldridge Formation, such as the hematite±magnetite deposits on Iron Range Mountain near Kitchener, British Columbia (see Blakemore, 1902; Young and Uglow, 1926).

### *Hydrothermal colloids and gels*

Ethier and Campbell (1977) proposed that the footwall tourmalinites at Sullivan formed from a hydrothermal colloid or gel. Their interpretation was based on the extremely fine grained, felted nature of the Sullivan tourmalinites, and on their textural similarity to some crystallized gels. Colloids and gels have the ability to transport significant amounts of Al (and Si) at relatively low temperature and moderate pH (e.g., de Kimpe et al., 1981), and thus are attractive media for precipitating aluminosilicate minerals like tourmaline at or near the sediment-water interface. The former existence of colloids or gels in ancient seafloor environments is documented in bedded manganese deposits of the Franciscan Complex, California, by the occurrence of small isotropic domains that have compositions of Mn-rich chlorite and smectite (Huebner and Flohr, 1990). Modern aluminosilicate gels are also known in Lake Magadi, Kenya (Eugster and Jones, 1968). Although there is no proof for the role of colloids or gels in the formation of the Belt-Purcell tourmalinites, the author considers it likely that they were precursors of at least some of the tourmalinites. The best candidates are those associated (or in contact) with coticles, such as in the immediate footwall of the Sullivan deposit, in the North Star alteration zone, and at the Morning Glory prospect. Evidence for the former existence of colloids or gels in these Mn-rich tourmalinites would be revealed by very low concentrations of rare earth elements (see Huebner and Flohr, 1990), a possibility currently being tested through detailed geochemical studies by the author.

## **EXPLORATION APPLICATIONS**

### *The coticle connection*

Many massive sulphide deposits contain coticles (e.g., Spry, 1990), although they also are common in terranes that lack massive sulphides. In some areas, tourmalinites are closely associated (and interlayered) with coticles, especially in sequences containing clastic metasedimentary and minor mafic metavolcanic rocks. This relationship suggests that in these types of settings, both the coticles and tourmalinites are former seafloor hydrothermal precipitates in which the Fe, Mn, and B were derived from submarine-hydrothermal exhalations. Modern analogs are unknown, but geochemical studies

suggest a general affinity of boron for manganese in seafloor environments, such as on the East Pacific Rise where anomalous boron contents (300-800 ppm on a carbonate-free basis) are preferentially associated with Al-poor Fe-Mn precipitates (Boström and Peterson, 1969). Concentration and preservation of Fe-Mn-B exhalites may require venting into a thermally and chemically insulated brine pool, with detrital clays providing the necessary aluminum for the formation of spessartine garnet and tourmaline (see Slack et al., 1993).

The abundance of fine grained, Mn-rich garnet in tourmalinites immediately underlying massive sulphide ores at Sullivan (Fig. 2F) contrasts with the general lack of garnet in tourmalinites from deeper in the footwall (J.F. Slack, unpub. data). This mineralogical contrast suggests that two fundamental types of tourmalinite may exist there, one formed by epigenetic replacement of Aldridge sediments, and the other by exhalation from submarine vents (see also Shaw and Hodgson, 1980). The great majority of the footwall tourmalinites are believed to be replacements of argillites, siltstones, and conglomerates. Stratiform tourmalinites that contain appreciable (>10%) fine grained garnet, however, are considered to be the products of Fe-Mn-B precipitation in a dense brine pool. The bedded Pb-Zn-Ag ores, which locally contain abundant Mn-rich garnet in disseminations and laminations, are also believed to have formed in a brine-pool environment (Hamilton et al., 1982; Leitch, 1992a). A logical corollary is that appreciable Mn-rich garnet in other stratiform lithologies is an indication of a brine pool origin.

### *Suggested prospecting guides*

Base-metal exploration in the Aldridge and Prichard formations has routinely relied on the presence of tourmalinite as a broad prospecting guide (e.g., Beaty et al., 1988). Most of these tourmalinites, however, seem unrelated to stratiform Pb-Zn deposits or occurrences and thus, apparently, have limited exploration significance. Criteria to distinguish these presumably barren tourmalinites from productive (sulphide-associated) tourmalinites are therefore needed. The following discussion is intended as a preliminary evaluation of tourmalinites as exploration guides in the Belt and Purcell supergroups.

The regional distribution of tourmalinites in the Aldridge and Prichard formations probably is controlled, at least in part, by synsedimentary growth faults (cf. Höy, 1982). Such growth faults may have been important not only as conduits for boron-bearing fluids but also for focusing metalliferous hydrothermal brines that could have formed exhalative Pb-Zn deposits. In the Sullivan mine area, tourmalinites and related sulphide deposits at Stemwinder and North Star occur within a 6-km-long, north-trending alteration zone that includes the Sullivan fault (Leitch et al., 1991; Turner et al., 1992). The Sullivan fault is one of several reactivated growth faults that probably controlled emplacement of the district-scale Moyie gabbroic intrusions and the formation of the Sullivan-Stemwinder-North Star deposits (Turner et al., 1992; Höy, 1993). By analogy, the alteration zones associated with these deposits – including the tourmalinites – are also believed to have been controlled by major growth faults.

Some of the tourmalinites, both discordant and stratiform, may have formed by dewatering of the Aldridge-Prichard basin independent of mineralization. According to Russell (1983), fluids generated by dewatering generally have low temperatures (<200°C) compared to those associated with seafloor hydrothermal systems (~200-300°C). Although both types of fluids may leach and transport metals in the subsurface, the higher temperature systems are more likely to yield major exhalative base-metal deposits, based on the homogenization temperatures measured in fluid inclusions from weakly metamorphosed sedex-type deposits (Gardner and Hutcheon, 1985; Ansdell et al., 1989), including Sullivan (Leitch, 1992a). Reconnaissance oxygen isotope data by Nesbitt et al. (1984) suggested that the Sullivan footwall tourmalinite formed at <100°C, but more recent work by Beaty et al. (1988) implies formational temperatures of 200-300°C. These higher temperatures are consistent with fluid inclusion data from wispy quartz-pyrrhotite veinlets in the footwall tourmalinite at Sullivan that are believed to have precipitated from the same hydrothermal fluid that formed the tourmalinite (Leitch, 1992a).

Some criteria exist for distinguishing potentially productive from barren tourmalinites. Preliminary field and petrographic studies indicate that the most obvious criterion is the presence of sulphide minerals, especially sphalerite and galena, in both the discordant and stratiform types of tourmalinite. The occurrence of anomalous amounts (>10%) of fine grained, Mn-rich garnet within the stratiform tourmalinites (or in adjacent wall rocks) is also considered important as evidence of exhalative hydrothermal activity, because of the preferential precipitation of Mn at the sediment-water interface, rather than deep in the subsurface. Whole-rock analyses of tourmalinites may also prove valuable, based on the geochemistry of ore-related tourmalinites at Broken Hill, Australia, that show elevated Fe (non-sulphide), Zn, Mn, and P, relative to barren tourmalinites in the district (Slack et al., 1993); the occurrence of positive Eu anomalies on chondrite-normalized REE plots (Lottermoser, 1989) is another possible criterion. The key is recognizing tourmalinites that formed from exhalative hydrothermal fluids at or near the sediment-water interface, as potential guides to nearby exhalative base-metal ores. In contrast are the vast majority of other tourmalinites in the Belt and Purcell supergroups (both discordant and stratiform) that probably formed by subseafloor replacement of clastic sediments. Unlike the exhalative tourmalinites, the replacive tourmalinites are not true time-stratigraphic markers and cannot be used as definitive indicators of exhalative activity.

The favorability of the discordant tourmalinites is more difficult to assess and is still under study. Discordant tourmalinites in the footwall of the Sullivan deposit are clearly productive based on their general association with the base-metal ores. The presence of abundant pyrrhotite and local base-metal sulphides in the stratigraphically higher parts of the footwall tourmalinite may be a critical feature, compared to the lack of sulphides in barren discordant tourmalinites from elsewhere in the Belt and Purcell supergroups. Petrographic studies suggest that most of the sulphides in the discordant Sullivan tourmalinite precipitated together with

the tourmaline, rather than during a later hydrothermal event. The presence of these sulphides may reflect deposition of tourmalinite from a high-temperature, seafloor hydrothermal system that mixed with cold seawater in the shallow subsurface. Such mixing of hydrothermal fluids and seawater is also thought to be responsible for the formation of the colour variations of the discordant tourmalinites at Sullivan and the Fors prospect, British Columbia, in which the brown tourmalinites reflect the influence of Mg-rich seawater over Fe-rich hydrothermal fluids in a high fluid/rock environment. Similar coexisting brown and black discordant tourmalinites in other parts of the Belt and Purcell supergroups therefore may be additional prospecting guides.

## ACKNOWLEDGMENTS

I thank D. Anderson, J.C. Finch, T. Höy, J.M. Leask, C.H.B. Leitch, P.J. Modreski, D.L. Pighin, P.W. Ransom, J.P. Thorson, R.J.W. Turner, and D.R. Shaw for discussions, suggestions, and information. Logistical help during field work was provided by D. Anderson and P.W. Ransom in British Columbia, and by J.C. Finch and P.W. Rankin in Montana. The manuscript has benefited from comments by D. Anderson, M.P. Foose, J.M. Hamilton, T. Höy, C.H.B. Leitch, P.W. Ransom, R.R. Seal II, and R.J.W. Turner.

## REFERENCES

- Ansdell, K.M., Nesbitt, B.E., and Longstaffe, F.J.  
1989: A fluid inclusion and stable isotope study of the Tom Ba-Pb-Zn deposit, Yukon Territory, Canada; *Economic Geology*, v. 84, p. 841-856.
- Beaty, D.W., Hahn, G.A., and Threlkeld, W.E.  
1988: Field, isotopic, and chemical studies of tourmaline-bearing rocks in the Belt-Purcell Supergroup: Genetic constraints and exploration significance for Sullivan type ore deposits; *Canadian Journal of Earth Sciences*, v. 25, p. 392-402.
- Blakemore, W.  
1902: The iron ore deposits near Kitchener, B.C.; *Journal of the Canadian Mining Institute*, v. 5, p. 76-80.
- Boström, K. and Peterson, M.N.A.  
1969: The origin of aluminum-poor ferromanganous sediments in areas of high heat flow on the East Pacific Rise; *Marine Geology*, v. 7, p. 427-447.
- Cressman, E.R.  
1989: Reconnaissance stratigraphy of the Prichard Formation (Middle Proterozoic) and the early development of the Belt basin, Washington, Idaho, and Montana; United States Geological Survey, Professional Paper 1490, 80 p.
- de Kimpe, C.R., Kodama, H., and Rivard, R.  
1981: Hydrothermal formation of a kaolinite-like product from noncrystalline aluminosilicate gels; *Clays and Clay Minerals*, v. 29, p. 446-450.
- Driscoll, C.T.  
1989: The chemistry of aluminum in surface waters; in *The Environmental Chemistry of Aluminum*, (ed.) G. Sposito; Boca Raton, CRC Press, Inc., p. 241-277.
- Epprecht, W.Th., Schaller, W.T., and Vlisidis, A.C.  
1959: Über Wiserit, Sussexit und ein weiteres Mineral aus den Mangangerzen vom Gonzen (bei Sargans); *Schweizerische Mineralogische und Petrographische Mitteilungen*, v. 39, p. 85-104.
- Ethier, V.G. and Campbell, F.A.  
1977: Tourmaline concentrations in Proterozoic sediments of the southern Cordillera of Canada and their economic significance; *Canadian Journal of Earth Sciences*, v. 14, p. 2348-2363.

- Eugster, H.P. and Jones, B.F.**  
1968: Gels composed of sodium-aluminum silicate, Lake Magadi, Kenya; *Science*, v. 161, p. 160-163.
- Gardner, H.D. and Hutcheon, I.**  
1985: Geochemistry, mineralogy, and geology of the Jason Pb-Zn deposits, Macmillan Pass, Yukon, Canada; *Economic Geology*, v. 80, p. 1257-1276.
- Hamilton, J.M., Bishop, D.T., Morris, H.C., and Owens, O.E.**  
1982: Geology of the Sullivan orebody, Kimberley, B.C., Canada; in *Precambrian Sulphide Deposits*, (ed.) R.W. Hutchinson, C.D. Spence, and J.M. Franklin; Geological Association of Canada, Special Paper 25, p. 597-665.
- Harrison, J.E.**  
1972: Precambrian Belt basin of northwestern United States: Its geometry, sedimentation, and copper occurrences; *Geological Society of America Bulletin*, v. 83, p. 1214-1240.
- Höy, T.**  
1982: The Purcell Supergroup in southeastern British Columbia: Sedimentation, tectonics and stratiform lead-zinc deposits; in *Precambrian Sulphide Deposits*, (ed) R.W. Hutchinson, C.D. Spence, and J.M. Franklin; Geological Association of Canada, Special Paper 25, p. 127-147.  
1993: Geology of the Purcell Supergroup in the Fernie west-half map area, southeastern British Columbia; *British Columbia Ministry of Energy, Mines and Petroleum Resources, Bulletin* 84, 157 p.
- Huebner, J.S. and Flohr, M.J.K.**  
1990: Microbanded manganese formations: Protoliths in the Franciscan Complex, California; *United States Geological Survey, Professional Paper* 1502, 72 p.
- Kato, A. and Matsubara, S.**  
1980: Manganese borate minerals from Japan; *Journal of the Mineralogical Society of Japan*, v. 14, Special Issue No. 3, p. 86-97 [in Japanese with English abstract].
- Leitch, C.H.B.**  
1992a: A progress report of fluid inclusion studies of veins from the vent zone, Sullivan stratiform sediment-hosted Zn-Pb deposit, British Columbia; in *Current Research, Part E*; Geological Survey of Canada, Paper 92-1E, p. 71-82.  
1992b: Mineral chemistry of selected silicates, carbonates, and sulphides in the Sullivan and North Star stratiform Zn-Pb deposits, British Columbia, and in district-scale altered and unaltered sediments; in *Current Research, Part E*; Geological Survey of Canada, Paper 92-1E, p. 83-93.
- Leitch, C.H.B. and Turner, R.J.W.**  
1991: The vent complex of the Sullivan stratiform sediment-hosted Zn-Pb deposit, British Columbia: Preliminary petrographic and fluid inclusion studies; in *Current Research, Part E*; Geological Survey of Canada, Paper 91-1E, p. 33-44.
- Leitch, C.H.B., Turner, R.J.W., and Höy, T.**  
1991: The district-scale Sullivan-North Star alteration zone, Sullivan mine area, British Columbia: a preliminary petrographic study; in *Current Research, Part E*; Geological Survey of Canada, Paper 91-1E, p. 45-57.
- Lottermoser, B.G.**  
1989: Rare earth element study of exhalites within the Willyama Supergroup, Broken Hill block, Australia; *Mineralium Deposita*, v. 24, p. 92-99.
- Modreski, P.J. and Connor, J.J.**  
1991: Tourmalinite and iron-formation in the Yellowjacket Formation, Idaho cobalt belt, Lemhi County, Idaho (abstract); *United States Geological Survey, Circular* 1062, p. 57.
- Nesbitt, B.E., Longstaffe, F.J., Shaw, D.R., and Muehlenbachs, K.**  
1984: Oxygen isotope geochemistry of the Sullivan massive sulfide deposit, Kimberley, British Columbia; *Economic Geology*, v. 79, p. 933-946.
- Plimer, I.R.**  
1988: Tourmalinites associated with Australian Proterozoic submarine exhalative ores; in *Base Metal Sulfide Deposits in Sedimentary and Volcanic Environments*, (ed.) G.H. Friedrich and P.M. Herzig; Berlin, Springer-Verlag, p. 255-283.
- Robertson, C.E. and Hem, J.D.**  
1969: Solubility of aluminum in the presence of hydroxide, fluoride, and sulfate; *United States Geological Survey, Water-Supply Paper* 1827-C, 37 p.
- Russell, M.J.**  
1983: Major sediment-hosted exhalative zinc + lead deposits: Formation from hydrothermal convection cells that deepen during crustal extension; in *Sediment-Hosted Stratiform Lead-Zinc Deposits*, (ed.) D.F. Sangster; Mineralogical Association of Canada Short Course Handbook, v. 8, p. 251-282.
- Shaw, D.R. and Hodgson, C.J.**  
1980: Wall-rock alteration at the Sullivan mine, Kimberley, British Columbia (abstract); *Canadian Institute of Mining and Metallurgy Bulletin*, v. 73, no. 821, p. 75.  
1986: Wall-rock alteration at the Sullivan mine, Kimberley, B.C.; in *The genesis of stratiform sediment-hosted lead and zinc deposits, conference proceedings*, (ed.) R.J.W. Turner and M.T. Einaudi; Stanford University Publications, School of Earth Sciences, v. XX, p. 13-21.
- Shaw, D.R., Hodgson, C.J., Leitch, C.H.B., and Turner, R.J.W.**  
1993: Geochemistry of tourmaline, muscovite, and chlorite-garnet-biotite alteration, Sullivan Zn-Pb deposit, British Columbia; in *Current Research, Part A*; Geological Survey of Canada, Paper 93-1A, p. 97-107.
- Slack, J.F.**  
1982: Tourmaline in Appalachian-Caledonian massive sulphide deposits and its exploration significance; *Transactions of the Institution of Mining and Metallurgy*, v. 91, sec. B (Applied Earth Science), p. B81-B89.
- Slack, J.F. and Coad, P.R.**  
1989: Multiple hydrothermal and metamorphic events in the Kidd Creek volcanogenic massive sulphide deposit, Timmins, Ontario: evidence from tourmalines and chlorites; *Canadian Journal of Earth Sciences*, v. 26, p. 694-715.
- Slack, J.F., Herriman, N., Barnes, R.G., and Plimer, I.R.**  
1984: Stratiform tourmalinites in metamorphic terranes and their geologic significance; *Geology*, v. 12, p. 713-716.
- Slack, J.F., Palmer, M.R., Stevens, B.P.J., and Barnes, R.G.**  
1993: Origin and significance of tourmaline-rich rocks in the Broken Hill district, Australia; *Economic Geology*, v. 88, p. 505-542.
- Spry, P.G.**  
1990: Geochemistry and origin of cotecules (spessartine-quartz rocks) associated with metamorphosed massive sulfide deposits; in *Regional Metamorphism of Ore Deposits and Genetic Implications*, (ed.) P.G. Spry and L.T. Bryndzia; Utrecht, The Netherlands, VSP Publishers, p. 49-75.
- Stanton, R.L. and Williams, K.L.**  
1978: Garnet compositions at Broken Hill, New South Wales, as indicators of metamorphic processes; *Journal of Petrology*, v. 19, p. 514-529.
- Taylor, B.E. and Slack, J.F.**  
1984: Tourmalines from Appalachian-Caledonian massive sulfide deposits: textural, chemical, and isotopic relationships; *Economic Geology*, v. 79, p. 1703-1726.
- Turner, R.J.W., Höy, T., Leitch, C.H.B., and Anderson, D.**  
1992: Guide to the tectonic, stratigraphic and magmatic setting of the Middle Proterozoic stratiform sediment-hosted Sullivan Zn-Pb deposit, southeastern British Columbia; *British Columbia Ministry of Energy, Mines and Petroleum Resources, Information Circular* 1992-23, 53 p.
- Wesolowski, D.J. and Palmer, D.A.**  
1992: Experimental studies of aluminum solubility and speciation in brines; in *Water-Rock Interaction, Proceedings of the 7th International Symposium on Water-Rock Interaction*, (ed.) Y.K. Kharaka and A.S. Maest; Rotterdam, A.A. Balkema, v. 1, p. 185-188.
- Young, G.A. and Uglow, W.L.**  
1926: The iron ores of Canada, Volume I. British Columbia and Yukon; *Geological Survey of Canada, Economic Geology Series No. 3*, 253 p.

# Paleoseismic implications of sediment cores from Comox Lake, British Columbia

R.H. Linden<sup>1</sup> and John J. Clague  
Terrain Sciences Division, Vancouver

*Linden, R.H. and Clague, J.J., 1993: Paleoseismic implications of sediment cores from Comox Lake, British Columbia; in Current Research, Part E; Geological Survey of Canada, Paper 93-1E, p. 41-46.*

---

**Abstract:** Cores from Comox Lake, British Columbia, provide information on sedimentation associated with the failure of the Cruickshank River delta during the 1946 Vancouver Island earthquake (M7.2). A sediment gravity flow triggered by the earthquake deposited a layer of muddy sand with large amounts of wood and other plant detritus far beyond the Cruickshank delta front. The stratigraphy of the cores and radiocarbon ages on detrital plant material from sediments below the sandy layer suggest that Comox Lake has not experienced an earthquake as strong and as close as that in 1946 for at least 3000 years.

**Résumé :** Des carottes en provenance du lac Comox, en Colombie-Britannique, ont fourni de l'information sur la sédimentation associée au glissement qui s'est produit dans le delta de la rivière Cruickshank à la suite du séisme (M7,2) qui a secoué l'île de Vancouver en 1946. L'écoulement par gravité des sédiments, déclenché par le séisme, a déposé une couche de sable boueux et de grandes quantités de bois et d'autres débris végétaux loin en aval du front du delta. La stratigraphie des carottes et la datation au radiocarbone des débris végétaux provenant de sédiments sous la couche de sable portent à croire que le lac Comox n'avait pas été le théâtre d'un séisme aussi intense et aussi proche que celui de 1946 depuis au moins 3 000 ans.

---

<sup>1</sup> Coastal Geoscience Research Corporation, 2601 Scott Street, Victoria, British Columbia V8R 4J1

**INTRODUCTION**

Southwestern British Columbia is seismically active, and there is concern that future large earthquakes may damage major population centres and associated development in the region. Assessments of the likelihood of such events are based largely on the record of historical seismicity. This record, however, is short (on the order of 100 years), limiting its predictive capability.

Seismic risk evaluations can be improved with information on the frequency and magnitude of prehistoric earthquakes. The lakes of southwestern British Columbia offer opportunities for obtaining such information. Holocene sediment fills in many of these lakes are likely to preserve a record of past earthquakes because they are water saturated and,

commonly, fine grained. Strong seismic shaking may trigger extensive subaqueous slumps and flows that transport large quantities of sediment from the margins of the lakes into deeper water (Shilts and Clague, 1992). Such failures also can resuspend silt, clay, and fine organic particles which then settle out onto the lake floor to produce a texturally anomalous layer (Doig, 1986, 1990, 1991).

An example of earthquake-induced disturbance of lake sediments is presented in this paper. We describe two cores from Comox Lake, 20 km southeast of the epicentre of the 1946 Vancouver Island earthquake (M7.2; Rogers and Hasegawa, 1978) (Fig. 1). The cores are from an area of the lake floor that was affected by a sediment gravity flow triggered by this earthquake (Clague et al., 1989; Shilts and Clague, 1992).



Figure 1. Location map.

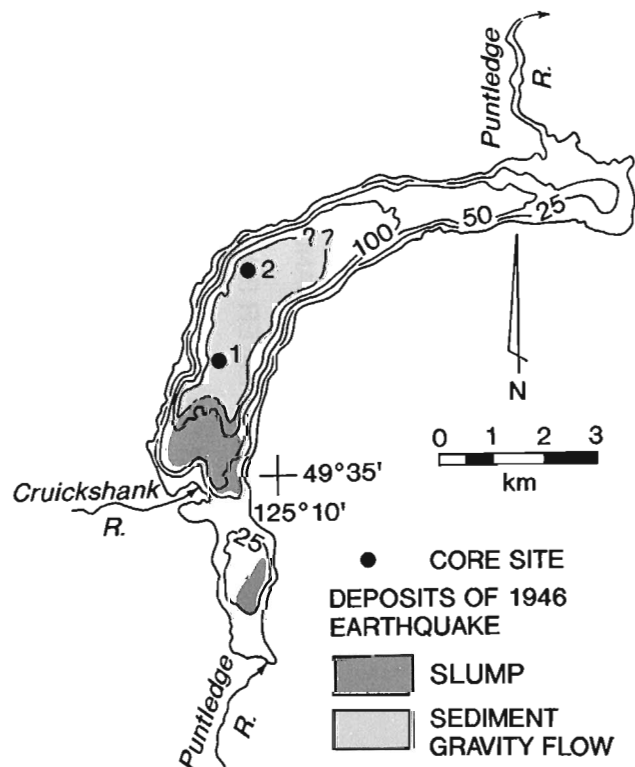
## STUDY AREA

Comox Lake is a relatively narrow, deep lake located on east-central Vancouver Island, 6 km southwest of Courtenay, British Columbia (Fig. 1). It extends northward and eastward through the easternmost ranges of Vancouver Island to a drift-covered lowland bordering the Strait of Georgia. Two large deltas, consisting mainly of sand and gravel, have been built into the southern part of the lake by Puntledge and Cruickshank rivers (Fig. 2). North of Cruickshank River, the lake is bordered by steep rock slopes. These give way farther east to lower, gentler slopes underlain by Pleistocene deltaic gravel and sand. The lake is as much as 125 m deep north of the Cruickshank delta, but is much shallower both farther east and off the Puntledge delta.

Some of the slopes bordering the lake have been logged. First-growth trees along the shore were cut in the 1930s using barges. A camp established on the Cruickshank delta in 1933 provided access to rich stands of trees in the valleys of Puntledge and Cruickshank rivers.

In 1912, the river draining Comox Lake was dammed to provide power to nearby coal mines, raising the level of the lake. Later, a higher dam was built, further increasing water levels.

Hodgson (1946, p. 308) reported that the 1946 earthquake triggered a large landslide in Comox Lake. It can be concluded from Hodgson's description and photographs that a



**Figure 2.** Map of Comox Lake and environs, showing core locations and the distribution of landslide deposits emplaced during the 1946 Vancouver Island earthquake. Bathymetric contours = 25, 50, and 100 m.

considerable mass of sediment slumped from the front of the Cruickshank delta into the depths of the lake. These deposits, as well as related sediment gravity flow deposits and a second slump off the Puntledge delta, have been identified through subbottom acoustic profiling (Clague et al., 1989; Linden, 1990; Shilts and Clague, 1992); they collectively cover most of the southern half of the lake floor.

## METHODS

Cores were collected with a 10 m long MacKerith corer. This is a pneumatically powered, remotely operated device that can be deployed from a small launch. A 9.11 m plastic tube is driven into the sediments from an attached, self-anchoring platform, using compressed air. Upon completion of this operation, the air supply is reversed, which causes the tube to withdraw from the enclosing sediments; air bags then move the device to the lake surface.

Two cores, each 7.8 m in length, were collected in water depths of 120 m, north of the Cruickshank delta (Fig. 2). Both core sites are in the area covered by the 1946 debris flow. Site 1 (49°36.19'N, 125°11.01'W) is 2.5 km north of the mouth of Cruickshank River; site 2 (49°37.19'N, 125°10.42'W) is 1.9 km north-northeast of site 1. The sites were chosen on the basis of subbottom and bathymetric surveys and were located using Del Norte trisponder navigation.

Plastic core tubes were sectioned in the field into 1.2 m lengths and transported to the laboratory where they were refrigerated. The cores then were split lengthwise, described, photographed, and sampled for particle-size analysis, natural remnant magnetism (NRM), and radiocarbon dating. Samples for NRM were collected every 3 cm in the manner described by Carmichael et al. (1990). Declination, inclination, and intensity were measured with a Schonstedt DSM-1 spinner magnetometer at Royal Roads Military College, again using the methodology of Carmichael et al. (1990). Accelerator mass spectrometry radiocarbon dating was done at IsoTrace Laboratory (University of Toronto).

## RESULTS

### Core descriptions

Four lithostratigraphic units are recognized in the cores (Fig. 3). All units are similar in colour (olive grey, moist Munsell colour = 5Y 4/1), and are discriminated mainly on the basis of texture.

The uppermost unit (no. 1 = 0-80 cm in core 1, 0-1 cm in core 2) consists of massive, organic-rich mud and silty mud with scattered small twigs, wood fragments, conifer needles, and other detrital plant remains. Unit 1 is slightly coarser and much thicker in core 1, which is proximal to the Cruickshank delta, than in core 2. It gradationally overlies unit 2 in core 1; in contrast, the contact between the two units is fairly sharp in core 2.

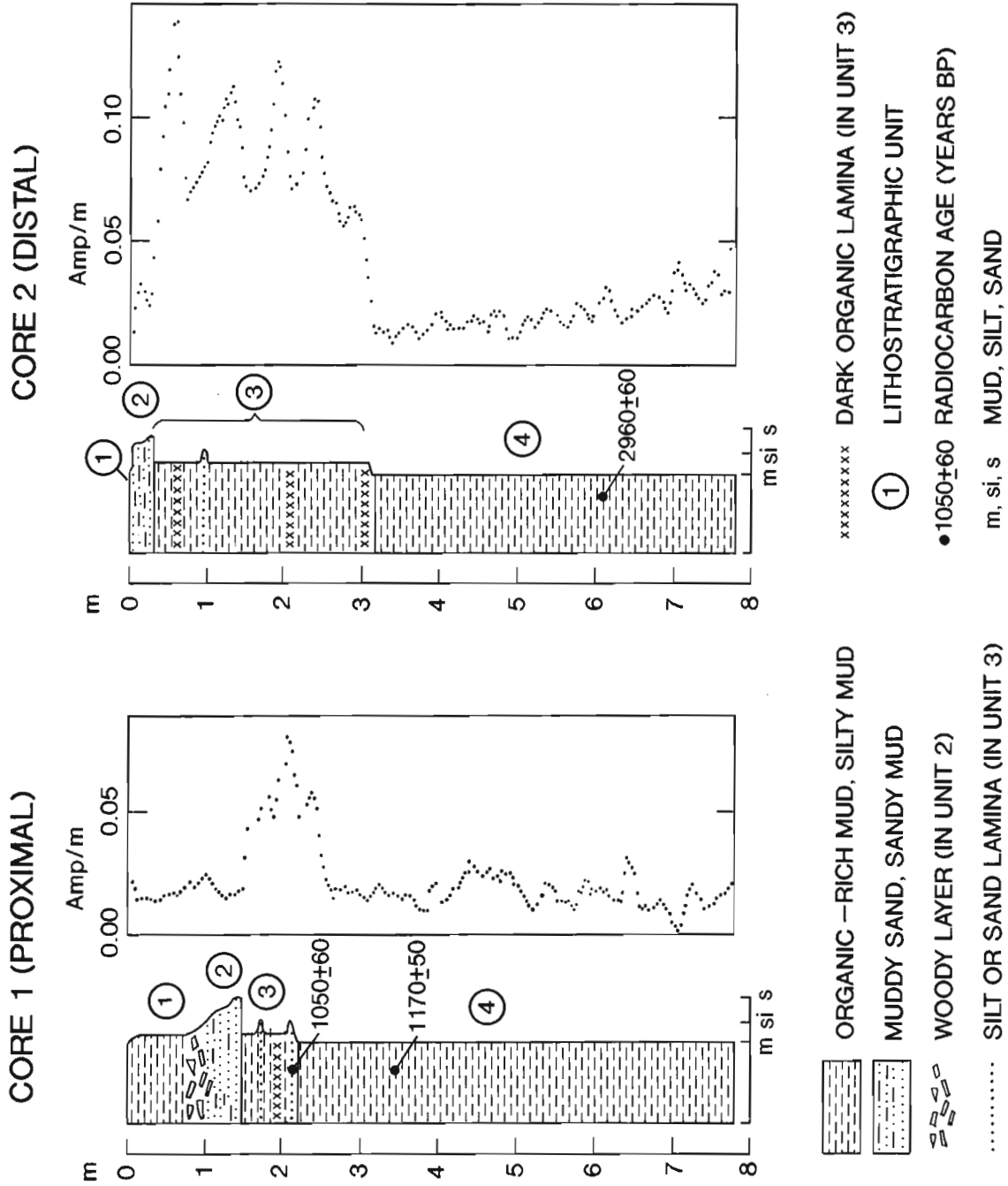


Figure 3. Description and magnetization intensity of cores from Comox Lake (see Fig. 2 for locations). The numbered lithostratigraphic units are described in the text.



Unit 2 (80-160 cm in core 1, 1-37 cm in core 2), the coarsest unit in the sequence, comprises sandy and silty sediments. In core 1, it fines upward from muddy medium sand to fine sandy mud; the uppermost 20 cm is very rich in wood and other plant detritus. In core 2, it comprises structureless sandy mud. The basal contact of unit 2 in both cores is sharp.

Unit 3 (160-231 cm in core 1, 37-304 cm in core 2) consists of organic-rich mud and silty mud with conspicuous, darker, silt laminae and scattered wood fragments. The dark laminae and silty texture distinguish this unit from unit 4, which it gradationally overlies; these differences are most evident in core 1.

The lowest unit (no. 4 = 231-778 cm in core 1, 304-780 cm in core 2) comprises massive organic mud. It is similar to, although perhaps slightly finer and less woody than, unit 1.

### *Natural remnant magnetism*

Magnetization intensities are less than 0.025 amp/m in units 1 and 2 (i.e. above 160 cm in core 1 and 35 cm in core 2; Fig. 3). In contrast, intensities are greater than 0.05 amp/m in unit 3 and the upper part of unit 4 (between 160 and 245 cm in core 1 and between 35 and 310 cm in core 2). Below this zone, magnetization intensities return to the low values found in units 1 and 2.

### *Radiocarbon ages*

Part of a conifer cone at 352 cm in core 1 yielded a radiocarbon age of  $1170 \pm 50$  BP (TO-3329), and a piece of wood at 216 cm in the same core was dated at  $1050 \pm 60$  BP (TO-3328). A fragment of wood at a depth of 608 cm in core 2 gave an age of  $2960 \pm 60$  BP (TO-3327).

## **DISCUSSION**

The sandy and silty sediments of unit 2 were deposited by a sediment gravity flow caused by the collapse of the Cruickshank delta during the 1946 earthquake. It is thicker and coarser in core 1 than in core 2. Abundant wood at the top of unit 2 (in core 1) may have been carried in the flow, or it may have settled onto the lake floor soon after the earthquake.

Organic-rich silty mud of unit 1 may have been deposited by one or more small flows soon after the earthquake. Alternatively, it may record the fine tail of the main flow or normal, postearthquake sedimentation, although these explanations seem less likely because this unit is almost absent in core 2.

The origin of unit 3 is problematic. It, like unit 4, consists of organic-rich mud. It differs from unit 4, however, in containing dark silty laminae. The higher magnetization intensity in unit 3, relative to unit 4, may be due to its slightly coarser texture and higher mineral content.

One possible interpretation is that unit 3 was deposited during the period immediately before the 1946 earthquake, when lake levels rose due to damming of the outlet (i.e. after 1912), and when the shoreline and adjacent slopes were logged (mainly in the 1930s). It would be expected that a rise in lake level and removal of the forest cover would lead to increased erosion of sediments and soils bordering the lake, with attendant increased sedimentation on the lake floor. If this is true, average sedimentation rates for unit 3 at the two core sites are extremely high, on the order of 2-17 cm/yr (the range reflects uncertainties in the age of the unit, as well as differences in its thickness at the two sites).

Another interpretation is that unit 3 records a period when climate was different from that prevailing during deposition of unit 4. Sediment inputs into the lake by Puntledge and Cruickshank rivers, for example, may have been higher during the Little Ice Age which spans the last several hundred years and ended in the late nineteenth century. If this explanation is correct, the deposition of unit 3 may have begun several hundred years ago, and average sedimentation rates would be much lower than mentioned above (<1 cm/yr).

With available information, we are unable to choose between these possibilities, and, in fact, there may be other explanations. It should be pointed out, however, that wood from the base of unit 3 yielded a radiocarbon age of  $1050 \pm 60$  BP. If accepted at face, this age indicates that unit 3 spans a period of about 1000 years. It, however, is only slightly younger than the radiocarbon age 136 cm lower in the same core. It thus is possible that the dated wood from unit 3 does not closely delimit the age of the enclosing sediments (i.e. it has been recycled from soil or sediment on slopes bordering the lake or in the Puntledge or Cruickshank valley).

Unit 4 records "normal" lacustrine deposition of clay, silt, and fine organic matter from suspension or small turbidity flows or both. The two radiocarbon ages from this unit indicate a relatively low average sedimentation rate (a fraction of a centimetre per year). None of the turbidity flows were comparable in size to the large flow triggered by the 1946 earthquake. This suggests that there have been no failures of the Cruickshank delta comparable to that in 1946 for at least 3000 years. From this, we conclude that Comox Lake has not experienced an earthquake that is both as big (M7.2) and as close (epicentral distance = 20 km) as the 1946 event over the same period. This, of course, does not preclude the possibility that smaller earthquakes have occurred near the lake or that comparable or even larger earthquakes have occurred more than a few tens of kilometres away<sup>1</sup>. It does show, however, that Comox Lake has been severely affected by only one earthquake in 3000 years and that this happened in 1946.

<sup>1</sup> Magnitude 6.0 and 7 earthquakes, with epicentres about 100 km west of Comox Lake, occurred in 1957 and 1918, respectively (Milne et al., 1978).

## **ACKNOWLEDGMENTS**

J. Mothersill (Royal Roads Military College) supplied the MacKerith corer and helped collect the cores. He also provided the NRM measurements. J. Veillette reviewed a draft of the paper and contributed to its improvement. C. Davis and T. Oliveric drafted the figures.

## **REFERENCES**

### **Carmichael, C.M., Mothersill, J.S., and Morris, W.A.**

1990: Paleomagnetic and pollen chronostratigraphic correlations of late glacial and postglacial sediments in Lake Ontario; *Canadian Journal of Earth Sciences*, v. 27, p. 131-147.

### **Clague, J.J., Shilts, W.W., and Linden, R.H.**

1989: Application of subbottom profiling to assess seismic risk on Vancouver Island, British Columbia; in *Current Research, Part E*; Geological Survey of Canada, Paper 89-1E, p. 237-242.

### **Doig, R.**

1986: A method for determining the frequency of large-magnitude earthquakes using lake sediments; *Canadian Journal of Earth Sciences*, v. 23, p. 930-937.

### **Doig, R. (cont'd.)**

1990: 2300 yr history of seismicity from silting events in Lake Tadoussac, Charlevoix, Quebec; *Geology*, v. 18, p. 820-823.

1991: Effects of strong seismic shaking in lake sediments, and earthquake recurrence interval, Témiscaming, Quebec; *Canadian Journal of Earth Sciences*, v. 28, p. 1349-1352.

### **Hodgson, E.A.**

1946: British Columbia earthquake, June 23, 1946; *Royal Astronomical Society of Canada, Journal*, v. 40, p. 285-319.

### **Linden, R.H.**

1990: Subbottom survey of Comox, Horne and Nitinat lakes, Vancouver Island, B.C.; unpublished report to Geological Survey of Canada, Vancouver, B.C., 17 p. and 4 appendixes.

### **Milne, W.G., Rogers, G.C., Riddihough, R.P., McMechan, G.A., and**

### **Hyndman, R.D.**

1978: Seismicity of western Canada; *Canadian Journal of Earth Sciences*, v. 15, p. 1170-1193.

### **Rogers, G.C. and Hasegawa, H.S.**

1978: A second look at the British Columbia earthquake of June 23, 1946; *Seismological Society of America, Bulletin*, v. 68, p. 653-676.

### **Shilts, W.W. and Clague, J.J.**

1992: Documentation of earthquake-induced disturbance of lake sediments using subbottom acoustic profiling; *Canadian Journal of Earth Sciences*, v. 29, p. 1018-1042.

Geological Survey of Canada Project 870017

# Two landslide-dammed lakes in the Cascade Mountains, southwestern British Columbia

John J. Clague and William W. Shilts<sup>1</sup>  
Terrain Sciences Division, Vancouver

*Clague, J.J. and Shilts, W.W., 1993: Two landslide-dammed lakes in the Cascade Mountains, southwestern British Columbia; in Current Research, Part E; Geological Survey of Canada, Paper 93-1E, p. 47-54.*

---

**Abstract:** Two prehistoric landslides in the Cascade Mountains of southwestern British Columbia blocked streams and impounded lakes that contain remnants of a drowned forest. Radiocarbon ages on drowned trees indicate that Foley Lake formed less than 310 years ago, and Silver Lake formed, or grew greatly in size, 800-1000 years ago. Some trees growing on Foley Lake landslide debris are as much as 152 years old; thus the landslide was not triggered by the 1872 earthquake, which was the largest earthquake in this region in at least the last 200 years. Similarly, the Silver Lake landslide may be slightly younger than a very large earthquake, 1000-1100 years ago, that triggered a tsunami in Puget Sound and numerous landslides in the nearby Olympic Mountains of western Washington.

**Résumé :** Deux glissements de terrain préhistoriques dans la chaîne des Cascades dans le sud-ouest de la Colombie-Britannique ont obstrué des cours d'eau et formé des lacs contenant des vestiges d'une forêt submergée. La datation au radiocarbone d'arbres submergés indique que le lac Foley s'est formé il y a moins de 310 ans et que le lac Silver s'est formé ou s'est beaucoup agrandi il y a entre 800 et 1 000 ans. Certains arbres qui poussent sur les débris du glissement de terrain du lac Foley remontent jusqu'à 152 ans; le glissement n'a donc pas été déclenché par le séisme de 1872, qui a été le plus gros séisme dans cette région depuis au moins 200 ans. De même, le glissement de terrain du lac Silver pourrait être un peu plus récent qu'un très fort séisme qui s'est produit il y a entre 1 000 et 1 100 ans et qui a provoqué un tsunami dans le détroit de Puget et de nombreux glissements de terrain dans les monts Olympic voisins, dans l'ouest de l'État de Washington.

---

<sup>1</sup> Mineral Resources Division

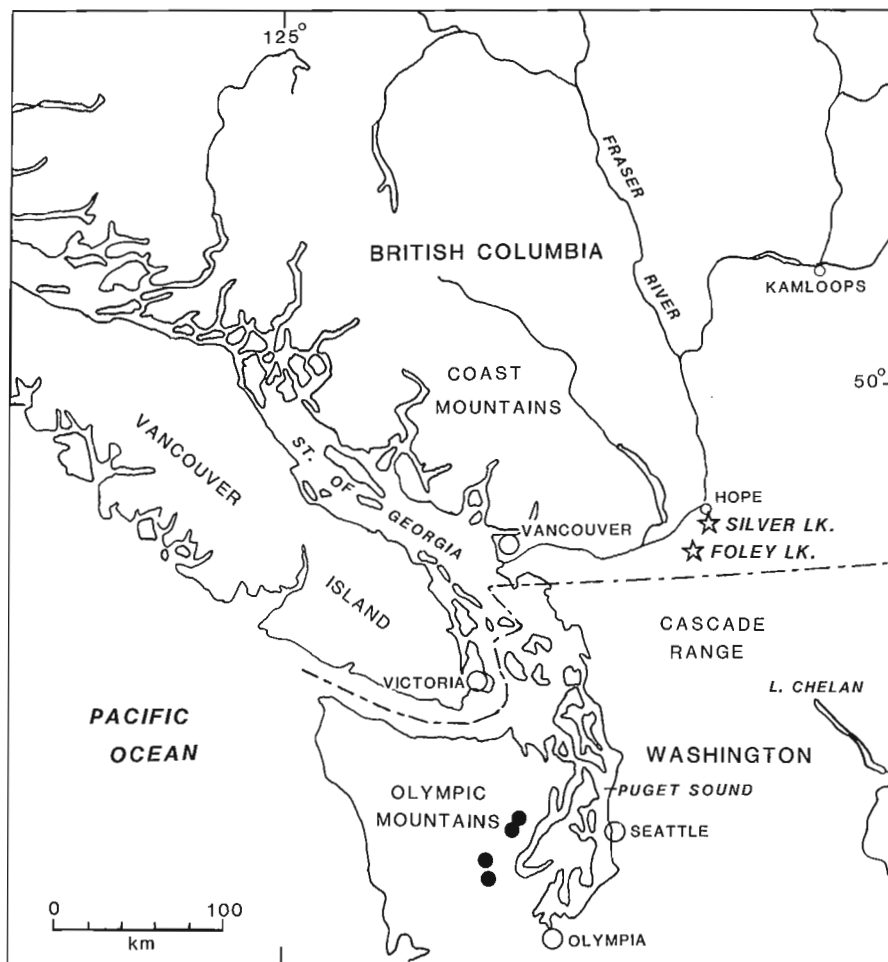
## INTRODUCTION

Many landslides in the Cordillera of western North America have blocked streams and impounded lakes (Evans, 1986; Costa and Schuster, 1988). At least 19 such damming events have occurred in British Columbia since 1880, mainly on the flanks of Plio-Pleistocene volcanoes and in valleys incised into thick Quaternary sediments (Evans, 1986). Lakes dammed by historic landslides commonly drained soon after they formed; consequently, little evidence of the events remains other than the breached dams.

In contrast, many, large, prehistoric, bedrock failures in British Columbia have dammed lakes that have persisted to the present (Evans, 1986). Two of these lakes (Foley and Silver), both in the Cascade Mountains of southwestern British Columbia (Fig. 1), are of particular interest because they contain drowned trees. Among other things, it is possible to determine the age of the landslides that formed these lakes by radiocarbon dating the outermost annual rings of the drowned trees. These two lakes and the landslides that formed them are the subject of this paper.

Historic landslides in British Columbia have been triggered by anomalous groundwater flow, high rainfall, freeze-thaw activity, and erosion of steep slopes by streams. Earthquakes were not involved in any of the 19 historic damming events. On the other hand, some of the large, prehistoric, landslide dams in this region may have formed during earthquakes. Certainly, this is common in other mountainous regions. For example, an earthquake in Calabria, Italy, in 1873 triggered landslides that impounded about 15 lakes (Cotecchia, 1978; R.L. Schuster, pers. commun., 1993), and the 1929 Buller earthquake in New Zealand created at least 16 landslide-dammed lakes (Adams, 1981; Perrin and Hancox, 1992; see also Costa and Schuster, 1991, for other examples).

Recently, evidence has been presented that several lakes in the Olympic Mountains of western Washington, similar to those described in this paper, were dammed by landslides 1000-1300 years ago (Schuster et al., 1992), probably as a result of a large earthquake centred near Seattle (Fig. 1; Atwater and Moore, 1992). Another large earthquake in Washington in 1872 triggered many landslides, including one

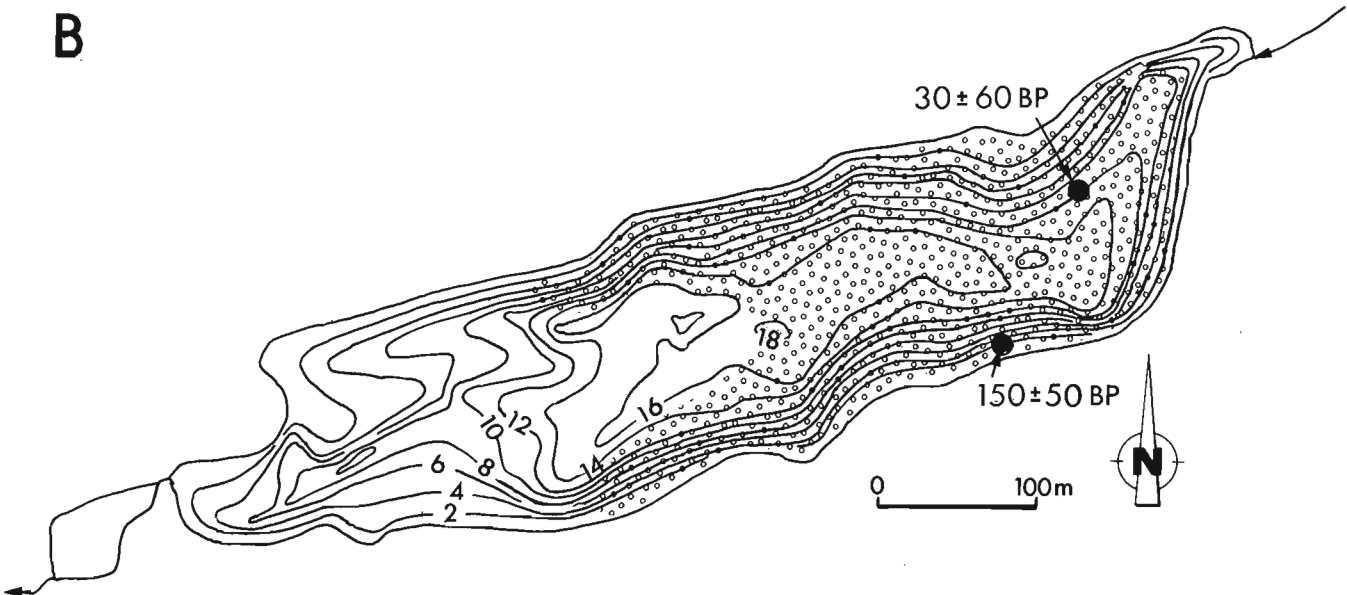
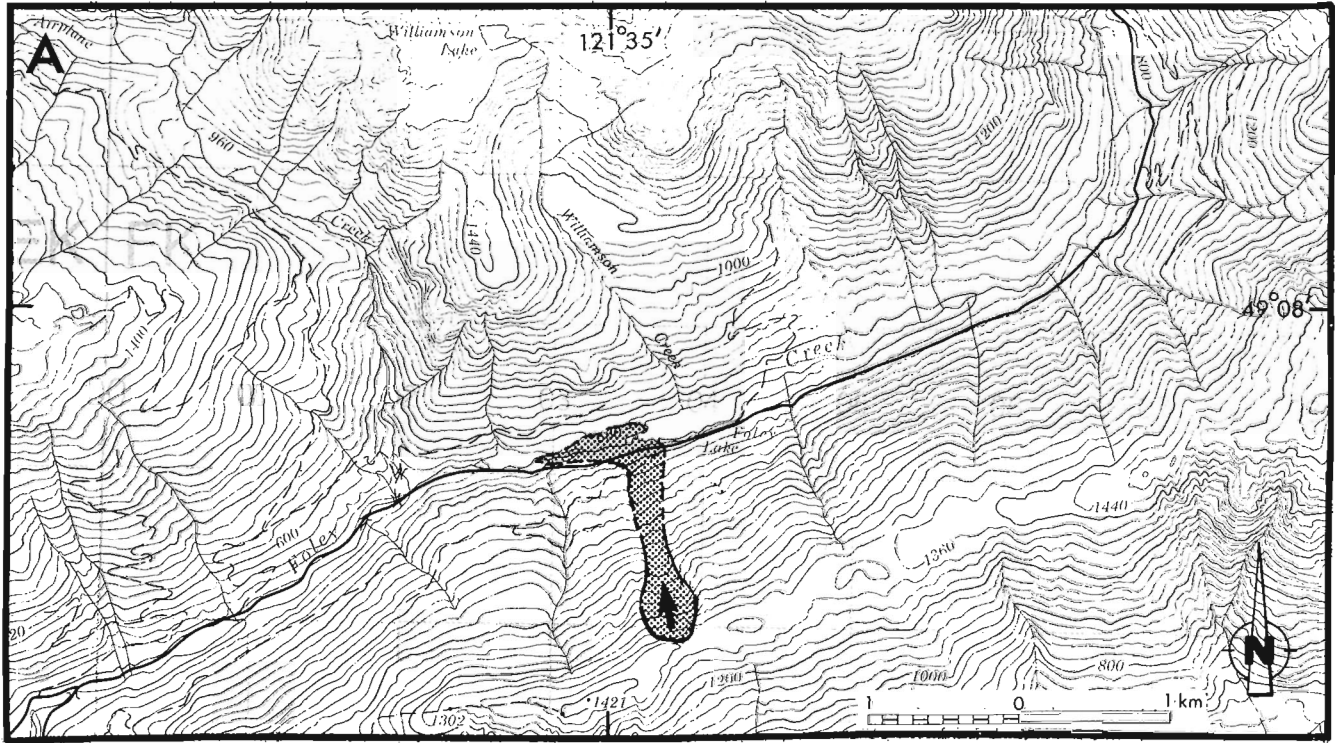


**Figure 1.** Locations of Foley and Silver lakes, as well as landslide-dammed lakes in the Olympic Mountains (darkened circles) that are discussed in the paper.

from Cheam Peak, only 10 km from Foley Lake, one of the lakes discussed in this paper (Chilliwack Progress, August 19, 1915). A major impetus for the present study was to determine whether or not Foley and Silver lakes formed during either of these earthquakes.

### FOLEY LAKE

Foley Lake (49°08'N, 121°35'W; 550 m asl) is located 110 km east of Vancouver in the valley of Foley Creek, a tributary of Chilliwack River (Fig. 1, 2A). The lake is 800 m

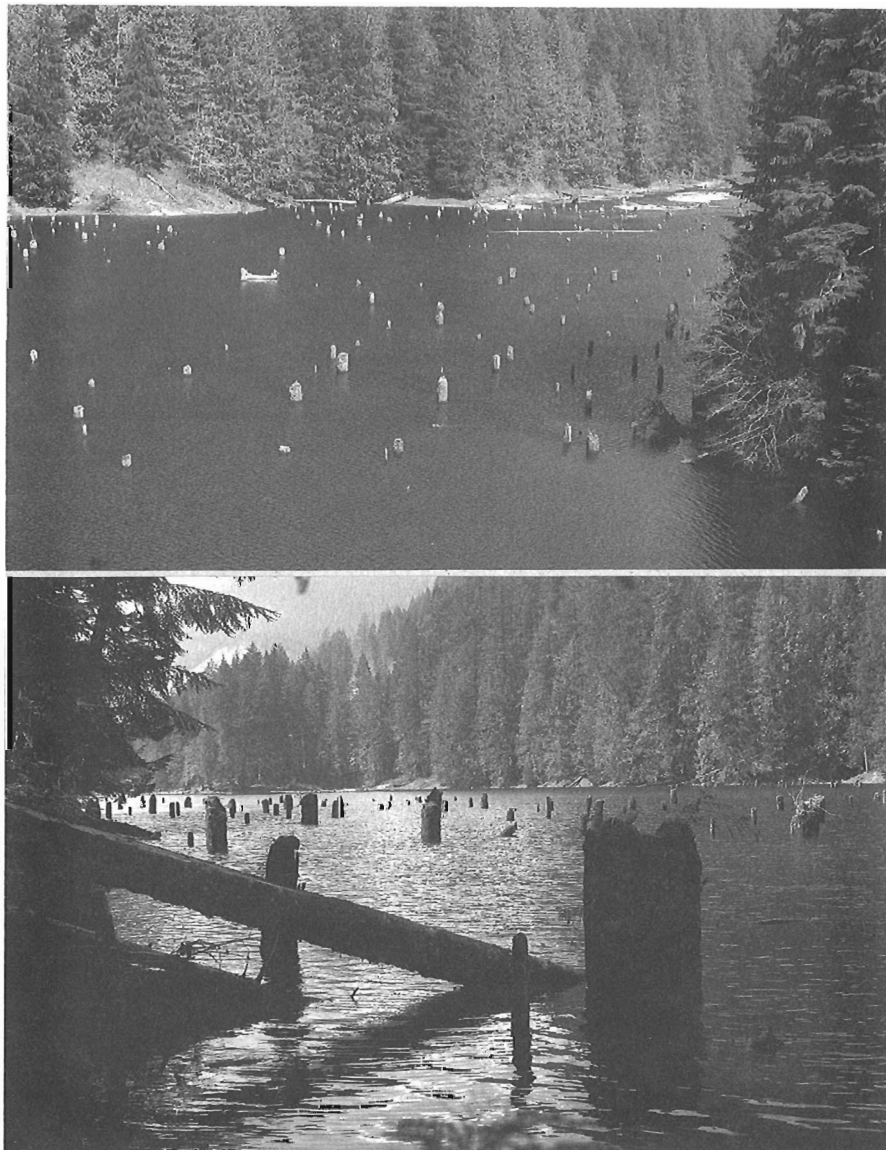


**Figure 2.** **A.** Topographic map showing the scarp (line with arrow) and path (stippled) of the Foley Lake landslide. Contour interval = 40 m. **B.** Bathymetric map of Foley Lake compiled from an echo-sounding survey in October 1991. Contour interval = 2 m. Circle pattern shows approximate extent of drowned trees. Darkened circles are radiocarbon-dated trees (ages in radiocarbon years BP; see Table 1).

long, up to 200 m wide, and has a maximum depth of 18 m (Fig. 2B). It is dammed at its west end by debris emplaced by a rock avalanche from the south wall of Foley Creek valley. A conspicuous scarp extending from ca. 1050 m to 1300 m asl, just below the crest of the ridge that separates the valleys of Foley Creek and Chilliwack River, marks the source of the landslide. The failure occurred in Upper Paleozoic meta-pelitic rocks (mainly phyllite; Monger, 1970), mantled by colluvium and till. Several hundred thousand, to perhaps one million, cubic metres of rock became detached and moved down the 30° slope into the valley below. There, the debris came to rest as a hummocky lobe several hundred metres long and up to 200 m wide; the lobe extends beneath the western part of Foley Lake (Fig. 2B). Since the landslide occurred, a small gravelly delta has been built into the lake at its east end.

Large numbers of standing trees (mainly western red cedar and Douglas fir) are present in the eastern half of the lake (Fig. 2B, 3). Since the landslide, most of these have decayed to close to the lake surface or have been topped by logging operators; a few, however, still project far above the water.

The age of the landslide that impounded Foley Lake is constrained by two radiocarbon dates on drowned trees and by the ages of living trees on the landslide debris. Radiocarbon ages of  $30 \pm 60$  BP and  $150 \pm 50$  BP were obtained on the outermost preserved rings of two drowned trees (Table 1). The range of possible calendric ages, based on the calibration curves of Stuiver and Pearson (1986) and taking into account the  $2\sigma$  error terms, is 50-310 years (Table 1). The landslide must be older than 152 years, however, because trees this old



**Figure 3.** Drowned trees in Foley Lake, April 1991. The canoe in the upper photo provides scale.

are growing on the debris lobe impounding the lake. The data thus indicate that the landslide occurred sometime between about 1680 and 1840 AD.

## SILVER LAKE

Silver Lake (49°19'N, 121°25'W; 350 m asl) lies 8 km south of the town of Hope and 120 km east of Vancouver, in the valley of Silverhope Creek (Fig. 1). The lake is 1.5 km long and up to 400 m wide; its maximum depth is 12 m (Fig. 4). It is bordered on the south by the broad floodplain and delta of Silverhope Creek. In contrast, Silverhope Creek flows out of the lake in a narrow, steep, bouldery channel. This channel is constrained to the east by a colluvial apron and to the west by a bedrock hill occupying the centre of the valley. Rock slopes east and north of Silver Lake are steep (typically >40°) and culminate in peaks with elevations of 1500-1840 m. Gentler, till- and colluvium-mantled slopes rise southwest of the lake.

An echo-sounding survey in the fall of 1991 revealed the morphology of the lake floor (Fig. 4B). Much of the northern third of the lake has an irregular, hummocky bottom with relief of several metres (Fig. 5). This is interpreted to be rockfall or rock-avalanche debris derived from slopes to the northeast. Southward, the bottom gradually becomes flatter as the cover of silty and sandy sediments carried into the lake by Silverhope Creek thickens. Echo sounding indicates that the floor of the southern third of the lake is a bench that slopes gently upward from about 6-7 m at its north end to 4 m adjacent to the Silverhope delta (Fig. 5). A large number of in-situ tree stumps are present on this bench; many of these extend upward to the water surface. Similar submerged tree stumps also occur farther north near the eastern and western shores of the lake.

The large boulders and blocks that choke the outlet of Silver Lake (Fig. 6A) and cover part of the adjacent colluvial apron were deposited during a rockfall from cliffs northwest of the lake (Fig. 4B). One or more large masses of granodiorite or quartz diorite became detached from the cliff and cascaded down a ravine onto the colluvial apron below (Fig. 6B). Presumably, some of the debris on the lake floor near the outlet (Fig. 4B) also was deposited during this event. Farther south, however, blocky debris occurs on the lake floor outside the path of the landslide and is a substrate for several drowned trees. It thus seems likely that there has been more than one landslide into the Silver Lake basin.

The landslide either created Silver Lake or, more likely, raised its level 6-7 m (see below). The rising waters drowned a forest and began to overflow across the newly formed debris dam.

The age of this event is approximated by radiocarbon ages of  $890 \pm 60$  BP and  $1010 \pm 100$  BP on the outermost preserved rings of two drowned trees (Table 1). The range of possible calendric ages, again based on Stuiver and Pearson (1986), and taking into account  $2\sigma$  error terms, is 770-1090 years; the two age determinations overlap between 830 and 960 years ago.

It is possible that this event did not actually create Silver Lake, but rather raised the level of a much smaller lake already present in the basin. The gently sloping bench that forms the floor of the southern third of the lake may be a remnant of a pre-830 year old floodplain or delta graded to a lake level 6-7 m lower than the present. If so, the rockslide 800-1000 years ago raised the level of the lake, as well as base level in Silverhope valley to the south. In response, Silverhope Creek prograded northward across the old delta-floodplain into the newly formed lake.

**Table 1.** Radiocarbon ages from Foley and Silver lakes

Radiocarbon age (years BP) <sup>a</sup>	$\delta^{13}\text{C}$ (‰)	Calibrated age (years) <sup>b</sup>	Laboratory no.	Site	Location Lat.	Long.	Dated material
30 ± 60	-26.1	<110	GSC-5239	Foley Lk.	49°07.7'	121°34.3'	Drowned tree <sup>c</sup>
150 ± 50	-27.7	50-310 <sup>d</sup>	GSC-5260	Foley Lk.	49°07.7'	121°34.3'	Drowned tree <sup>e</sup>
890 ± 60	-22.9	830 (770-960)	GSC-5444	Silver Lk.	49°18.6'	121°24.4'	Drowned tree <sup>f</sup>
1010 ± 100	-26.2	970 (830-1090)	GSC-5204	Silver Lk.	49°18.8'	121°24.8'	Drowned tree <sup>g</sup>

<sup>a</sup>Error terms are  $2\sigma$ .

<sup>b</sup>Reference datum is 1993. Calculated from dendro-calibrated data of Stuiver and Pearson (1986).

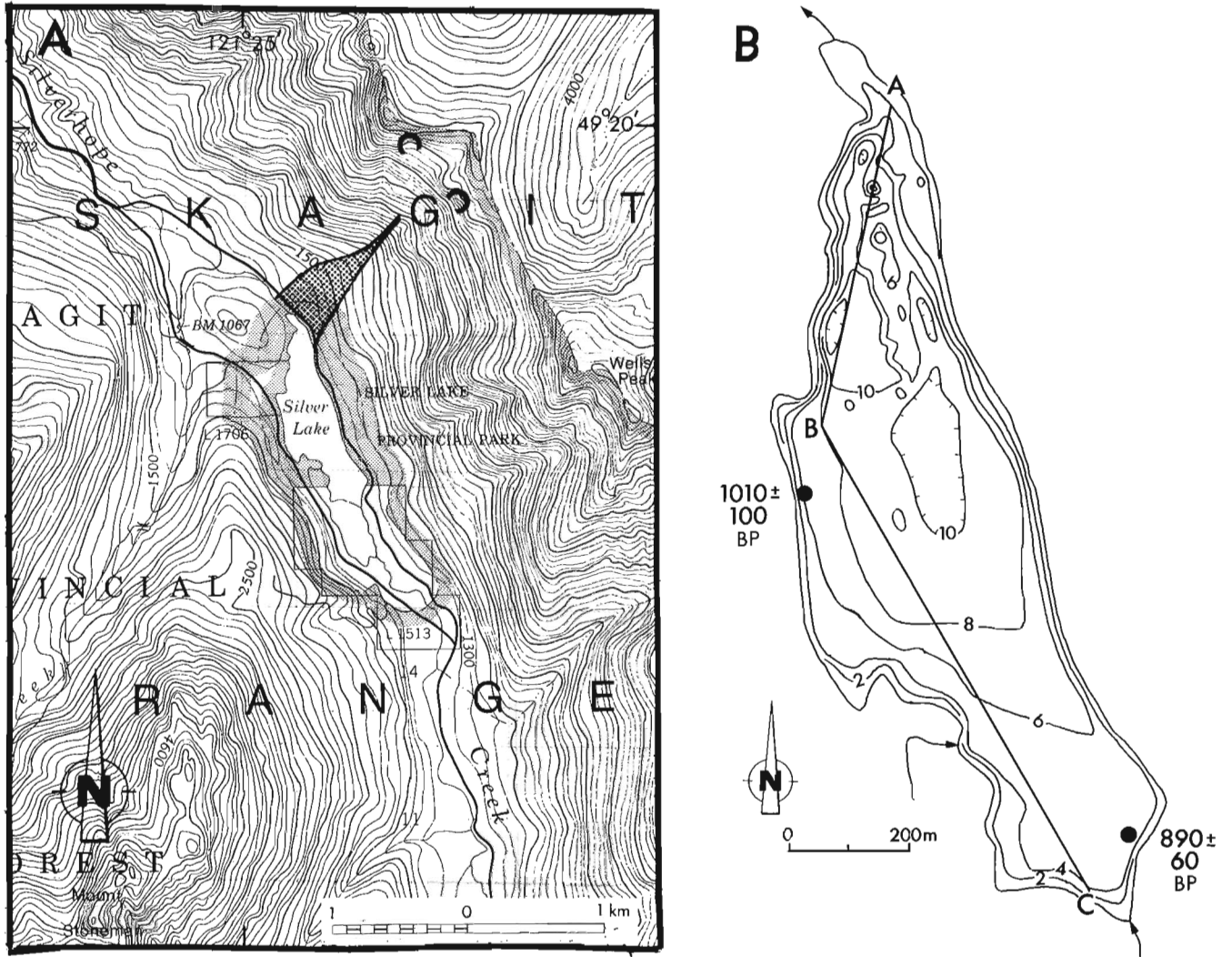
<sup>c</sup>Outermost 20 rings of conifer; identified as *Abies* sp. by H. Jetté (GSC Wood Identification Report No. 91.37).

<sup>d</sup>There are four possible calendar ages corresponding to a radiocarbon age of 150 BP: 50, 190, 250, and 310 years. If the  $2\sigma$  error term is taken into consideration, the possible range is 0-330 years.

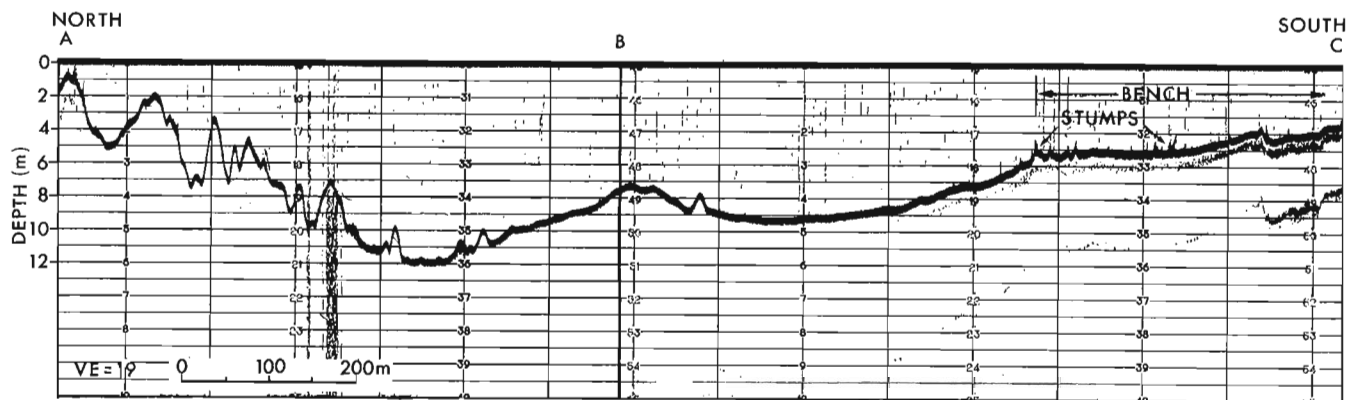
<sup>e</sup>Outermost 10 rings of conifer; identified as *Abies* sp. by H. Jetté (GSC Wood Identification Report No. 91.44).

<sup>f</sup>Outermost 18 rings of conifer; identified as *Pseudotsuga menziesii* by H. Jetté (GSC Wood Identification Report No. 92.61).

<sup>g</sup>Outermost 10 rings of conifer; identified as *Pseudotsuga menziesii* by R.J. Mott (GSC Wood Identification Report No. 90.53).



**Figure 4.** A. Topographic map showing the path (stipple) of the Silver Lake landslide. Two possible source areas are marked by half circles, the northern area being the more likely of the two. Contour interval = 100 feet (30.5 m). B. Bathymetric map of Silver Lake compiled from an echo-sounding survey in October 1991. Contour interval = 2 m. Darkened circles are radiocarbon-dated trees (ages in radiocarbon years BP; see Table 1). Also shown is the line of the profile reproduced in Figure 5.



**Figure 5.** Echo-sounding profile of Silver Lake (see Fig. 4B for location). Note the hummocky bottom at the north end of the lake and the gently sloping bench at the south end (see text for discussion). Horizontal scale and vertical exaggeration (VE) are approximate.

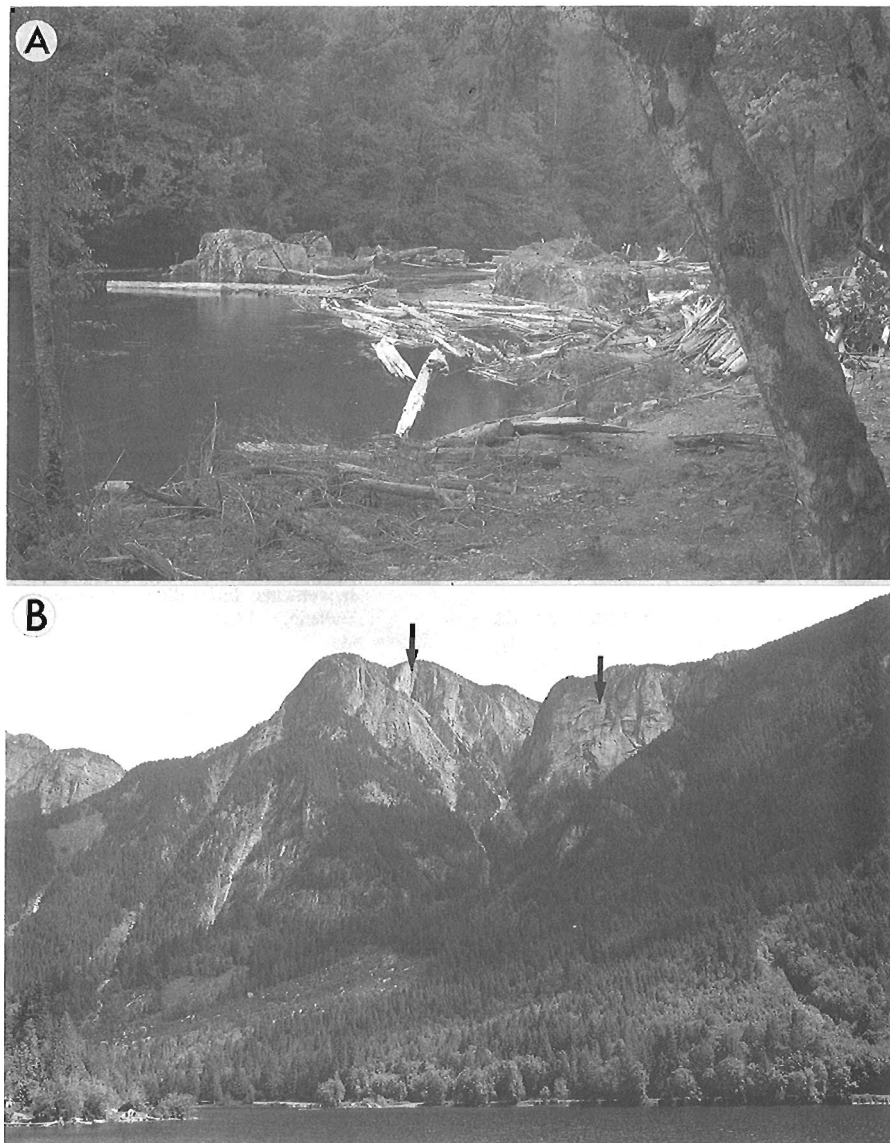


## DISCUSSION

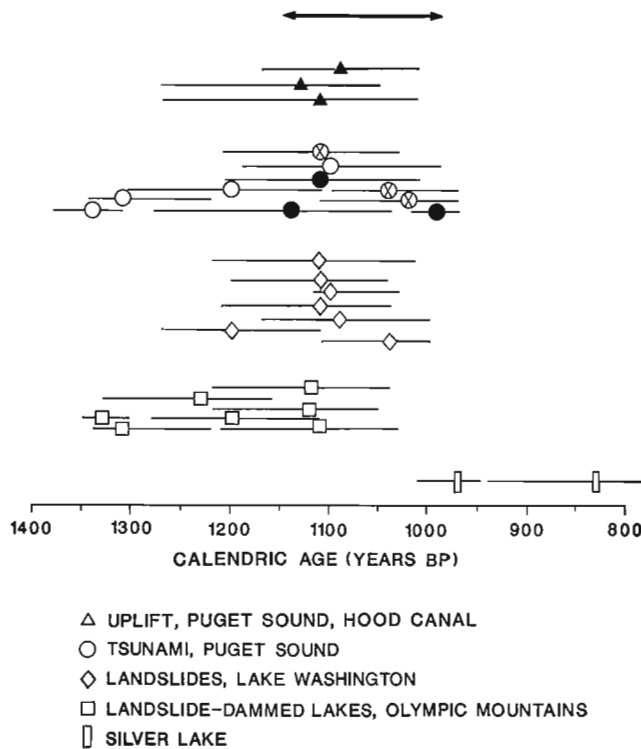
At the beginning of this study, it was thought that the damming of Foley Lake might be related to the 1872 earthquake, centred in north-central Washington just south of the International Boundary. This is clearly not the case, however, because the landslide damming Foley Lake occurred before 1840 AD. Radiocarbon dating indicates that the lake is no more than 310 years old, but the cause of the landslide remains unknown.

A large earthquake in the Seattle area, 190 km south of Silver Lake (Fig. 1), produced surface deformation (uplift and subsidence), landslides, and a tsunami sometime between

1000 and 1100 years ago (Atwater and Moore, 1992; Bucknam et al., 1992; Jacoby et al., 1992). Three, or possibly four, landslide-dammed lakes in the Olympic Mountains, 60-85 km west and southwest of Seattle, contain trees that were drowned at this time, and it has been suggested that these lakes also are products of this earthquake (Schuster et al., 1992). It is tempting to ascribe the Silver Lake rockfall to this event, because the radiocarbon ages from Silver Lake are close to those in Washington that have been attributed to the earthquake. Close inspection, however, indicates that the former are slightly younger (ca. 100-200 years) than the latter (Fig. 7). The older Silver Lake radiocarbon age does overlap many of the Washington ages, if laboratory error terms are taken into account, but this is not true for the younger Silver



**Figure 6.** **A.** Boulder-choked outlet of Silver Lake. **B.** View of the source area of the Silver Lake landslide from the south end of the lake, June 1991. Two possible sources are indicated by arrows; the more likely of the two is to the left; note the colluvial apron on the lower part of slope above Silver Lake.



**Figure 7.** Plot of Silver Lake calibrated (calendric) ages and calibrated ages of a tsunami and landslides triggered by a large prehistoric earthquake near Seattle, Washington (data from Atwater and Moore, 1992; Jacoby et al., 1992; Schuster et al., 1992). Datum for all ages is 1993. Horizontal bars represent age range based on  $1\sigma$  error terms of radiocarbon dates. Relationship of dated sample to event: darkened circles and darkened triangles = minimum age; circles containing x = approximate age; all other symbols = maximum age.

Lake radiocarbon age. The available evidence thus suggests that the Silver Lake rockfall postdates, although not by much, a major earthquake that triggered numerous landslides farther south.

The two case histories described in this paper show how difficult it is to determine the cause of a prehistoric landslide. In an area of high seismicity, such as southwestern British Columbia, it is tempting to conclude that most large prehistoric landslides have been triggered by earthquakes. This assumption, however, may not be correct; consider, for example, that the three largest historic landslides in Canada - Frank, Alberta, 1903; Hope, British Columbia, 1965; and Devastation Glacier, British Columbia, 1975 - were not caused by earthquakes. Only by demonstrating that many large landslides occurred at the same time, or at the time of an independently dated earthquake, can a seismic trigger be reasonably inferred. In the former case, the possibility that the landslides were triggered by a catastrophic, regional rainstorm must also be ruled out.

This problem is aggravated by the fact that radiocarbon dating, which is the most common technique for determining the age of prehistoric landslides, is inherently imprecise; it is

very difficult to prove that two events are contemporaneous on the basis of radiocarbon ages alone. This is illustrated by the Foley Lake event. The radiocarbon ages from Foley Lake indicate that the lake formed 50 to 310 years ago; one might conclude from this that the landslide that impounded the lake was triggered by the 1872 earthquake, which is probably the largest earthquake to affect this area in the last two centuries. In this case, however, other evidence proves that the landslide is older than 152 years and thus unrelated to the 1872 earthquake.

## ACKNOWLEDGMENTS

I thank Roger McNeely (Geological Survey of Canada, GSC) for radiocarbon dating the Foley and Silver Lake wood samples. Reviews by S.G. Evans (GSC), J. Veillette (GSC), and R.L. Schuster (U.S. Geological Survey) improved the paper and are much appreciated.

## REFERENCES

- Adams, J.E.  
1981: Earthquake-dammed lakes in New Zealand; *Geology*, v. 9, p. 215-219.
- Atwater, B.F. and Moore, A.L.  
1992: A tsunami about 1000 years ago in Puget Sound, Washington; *Science*, v. 258, p. 1614-1617.
- Bucknam, R.C., Hemphill-Haley, E., and Leopold, E.B.  
1992: Abrupt uplift within the past 1700 years at southern Puget Sound, Washington; *Science*, v. 258, p. 1611-1614.
- Costa, J.E., and Schuster, R.L.  
1988: The formation and failure of natural dams; *Geological Society of America Bulletin*, v. 100, p. 1054-1068.  
1991: Documented historical landslide dams from around the world; United States Geological Survey, Open-File Report 91-239, 486 p.
- Cotecchia, V.  
1978: Systematic reconnaissance mapping and registration of slope movements; *International Association of Engineering Geology Bulletin*, v. 17, p. 5-37.
- Evans, S.G.  
1986: Landslide damming in the Cordillera of western Canada; in *Landslide Dams: Processes, Risk and Mitigation*, R.L. Schuster (ed.); American Society of Civil Engineers, Geotechnical Special Publication 3, p. 111-130.
- Jacoby, G.C., Williams, P.L., and Buckley, B.M.  
1992: Tree ring correlation between prehistoric landslides and abrupt tectonic events in Seattle, Washington; *Science*, v. 258, p. 1621-1623.
- Monger, J.W.H.  
1970: Hope map-area, west half (92H W1/2), British Columbia; Geological Survey of Canada, Paper 69-47, 75 p.
- Perrin, N.D. and Hancox, G.T.  
1992: Landslide-dammed lakes in New Zealand--Preliminary studies on their distribution, cause and effects; in *Landslides [Proceedings of the Sixth International Symposium, Christchurch]*, D.H. Bell (ed.); A.A. Balkema, Rotterdam, v. 2, p. 1457-1466.
- Schuster, R.L., Logan, R.L., and Pringle, P.T.  
1992: Prehistoric rock avalanches in the Olympic Mountains, Washington; *Science*, v. 258, p. 1620-1621.
- Stuiver, M. and Pearson, G.W.  
1986: High-precision calibration of the radiocarbon time scale, AD 1950-500 BC; *Radiocarbon*, v. 28, p. 805-838.

# Cretaceous (Barremian-Aptian) Radiolaria from Queen Charlotte Islands, British Columbia: newly recognized faunas and stratigraphic implications

James W. Haggart and Elizabeth S. Carter<sup>1</sup>  
Cordilleran Division, Vancouver

*Haggart, J.W. and Carter, E.S., 1993: Cretaceous (Barremian-Aptian) Radiolaria from Queen Charlotte Islands, British Columbia: newly recognized faunas and stratigraphic implications; in Current Research, Part E; Geological Survey of Canada, Paper 93-1E; p. 55-65.*

---

**Abstract:** Radiolarian faunas have been identified from Lower Cretaceous rocks of Queen Charlotte Islands (NTS 103B, F). Microfossils were obtained from fine grained clastic rocks of the Longarm and Haida formations and taxa indicative of the Hauterivian, Barremian, Aptian, and Albian stages were identified. The faunas include the first Cretaceous radiolarians noted from the northern part of the Canadian Insular Belt and the first diverse radiolarian assemblages of Barremian and Aptian age from west coast North America. These collections are critically important in the development of a radiolarian biochronology for the Lower Cretaceous of the North American Cordillera. The faunas demonstrate that deposition of fine clastic rocks was widespread across the Queen Charlotte Islands region during most of the Early Cretaceous and argue against diastrophism at that time.

**Résumé :** On a reconnu des faunes de radiolaires dans des roches du Crétacé inférieur des îles de la Reine-Charlotte (SNRC 103B, F). On a prélevé des microfossiles dans des roches détritiques à grain fin des formations de Longarm et de Haida et identifié des taxons indicateurs de l'Hauterivien, du Barrémien, de l'Aptien et de l'Albien. Les faunes comprennent les premiers radiolaires du Crétacé observés dans la partie nord du Domaine insulaire canadien et les premières associations de radiolaires variés du Barrémien et de l'Aptien de la côte ouest de l'Amérique du Nord. Ces collections sont très importantes pour établir la biochronologie des radiolaires du Crétacé inférieur de la Cordillère nord-américaine. La présence de ces faunes révèle que l'accumulation de roches détritiques à grain fin a été étendue dans l'ensemble des îles de la Reine-Charlotte pendant la plus grande partie du Crétacé ancien et infirme qu'il y a eu diastrophisme à cette époque.

---

<sup>1</sup> Geology Department, Portland State University, Portland, Oregon 97207-0751 U.S.A.

## INTRODUCTION

Upper Triassic and Lower Jurassic strata from the Insular Belt of western Canada (Fig. 1) have provided extensive, well-preserved radiolarian faunas, described in several recent publications (Carter et al., 1988; Carter, 1991, 1993). These faunas have proved very useful for correlation of strata on Queen Charlotte Islands, and have also aided in international correlation and the development of an integrated macro- and microfossil biostratigraphy for the Insular Belt (see Pessagno et al., 1987; Carter et al., 1989; Tipper et al., 1991).

In contrast, radiolarian faunas from Cretaceous strata of the Insular Belt have received relatively little study. Radiolarians from contemporaneous deposits in the southern Alaska region (Karl et al., 1979; Plafker et al., 1989) and southwestern Vancouver Island (Brandon, 1989) have been noted briefly, but no systematic analysis of radiolarians in Cretaceous rocks of the Insular Belt has been undertaken. Elsewhere in North America, Cretaceous radiolarians have been described from northwestern Manitoba (Rüst, 1892), central California (Campbell and Clark, 1944; Foreman, 1968), and the Coast Ranges of northern California (Pessagno, 1976, 1977, etc.). Although radiolarian faunas are common in Berriasian-Valanginian and post-Aptian strata of the California Coast Ranges, they are very poorly developed in the Hauterivian, Barremian, and Aptian stages there, and this is the interval of interest to the present study. In the deep sea, Early Cretaceous radiolarians of Tethyan origin have been studied from DSDP sites in the central and northwestern Pacific (Foreman, 1973, 1975; Schaaf, 1981). More recently, contemporaneous faunas of mid- to high latitude origin have been studied from ODP Leg 113 in the Weddell Sea (Ling and Lazarus, 1990) and Leg 123 off northwestern Australia (Indian Ocean) (Baumgartner, 1992).

In this paper we briefly summarize recent collections from Cretaceous strata of Queen Charlotte Islands (Fig. 1) which have produced radiolarian faunas, some beautifully preserved. Several of the collections contain diverse faunas indicative of the Barremian, Aptian, and Albian stages, and are previously undocumented from North America. The importance of the radiolarian faunas to models of Cretaceous sedimentation in the Queen Charlotte Islands region is also discussed.

## STRATIGRAPHY

The stratigraphy of the Cretaceous rocks of Queen Charlotte Islands has been generally reviewed by Haggart (1991). Most Cretaceous strata of the islands are placed within the Queen Charlotte Group (Haggart, 1993) and include two major stratigraphic packages, the Longarm Formation of Valanginian to Aptian age, and the conformably overlying Haida Formation of Albian to Turonian age (Fig. 2). Both these units are heterogeneous assemblages of laterally widespread strata, representing principally shallow-marine, shelf environments. Younger Cretaceous deposits, and probably older as well, are known locally from the islands (Haggart, 1991, 1992). Haggart (1991, 1993) has suggested that the

Cretaceous stratigraphic sequence reflects essentially uninterrupted sedimentation within the islands region, with depositional systems in place continuously through most of Cretaceous time. Volcanism in the region was of only local extent, and tectonic activity was minimal.

The Longarm and Haida formations both consist of basal coarse conglomerate and sandstone which fine upward into mudstone. The two units include similar but diachronous facies, deposited in separate areas of Queen Charlotte Islands in response to eastward-directed transgression (Haggart, 1991). Detritus was derived from the east and accumulated in a forearc basin open to the west (Haggart, 1991, 1993; Gamba, 1993). Abundant mollusc fossils in the coarse-clastic portions of the Longarm and Haida formations allow detailed correlation of these shallow-marine rocks (e.g., McLearn, 1972).

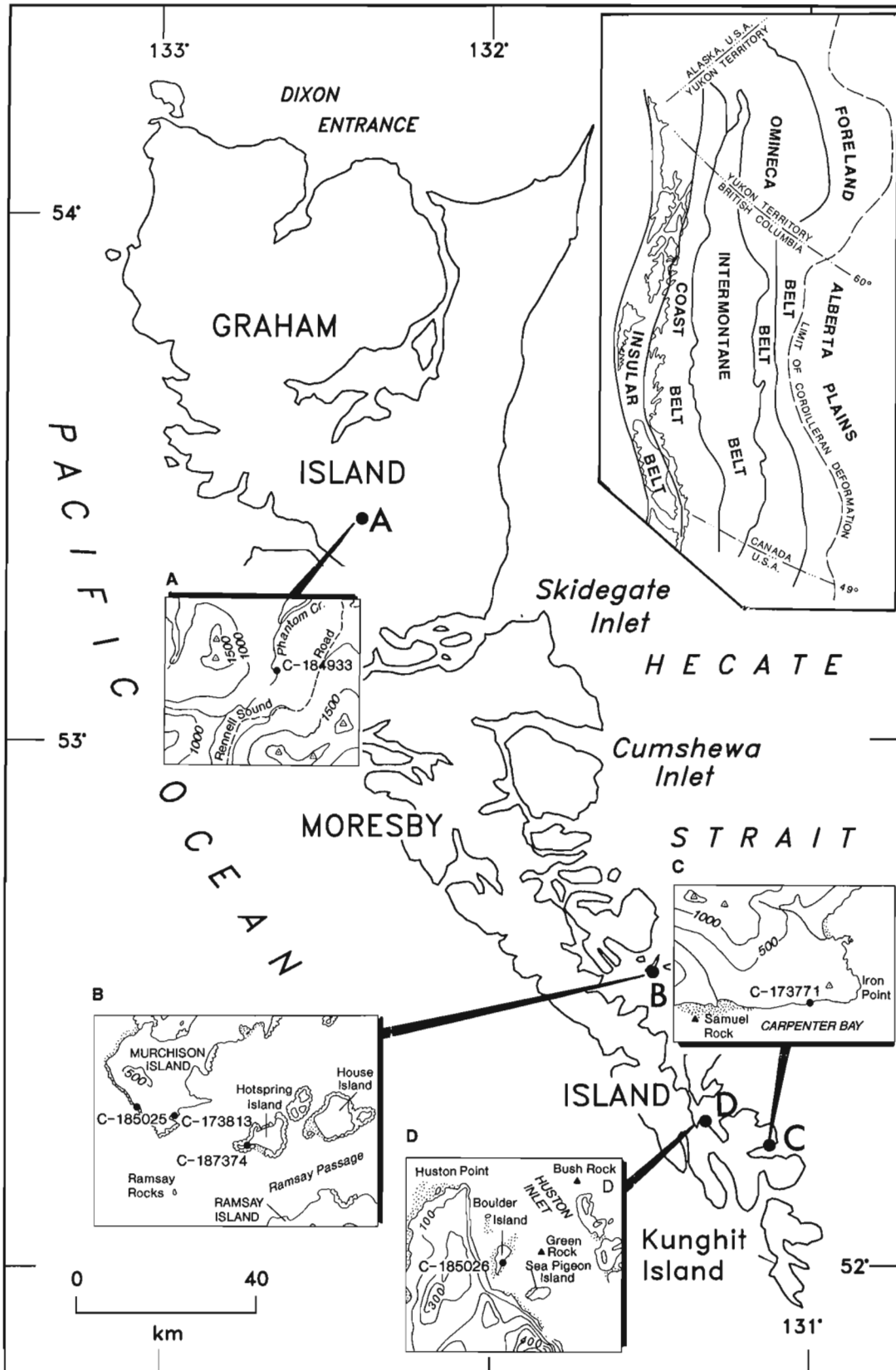
Haggart (1991) has proposed that the areally limited and poorly fossiliferous mudstone successions preserved at the top of both the Longarm and Haida successions reflect widespread, deeper-marine sedimentation which occurred west of the shallow-marine deposits that form the principal exposures preserved on Queen Charlotte Islands (Fig. 2). Little of this shale basin is preserved today, however, due to uplift of the western part of the islands and preferential destruction of the fine-clastic facies.

The radiolarians described in this report were collected from exposures of this deeper-water mudstone sequence at six different localities on Queen Charlotte Islands (Fig. 1 and Appendix). Five samples are from exposures of Longarm Formation on or adjacent to Moresby Island; the sixth sample is from Haida Formation on central Graham Island. Outcrops consist of thick sequences of grey to black mudstone and silty mudstone, with some coarse clastic interbeds, interpreted as storm deposits and debris flows (Haggart, 1991; Gamba, 1993). Given the tectonized nature of the Cretaceous deposits, the fossil localities are generally not found in stratigraphic continuity with the better-dated, coarse clastic facies. However, stratigraphic and structural mapping allows us to confidently place the collections into a composite stratigraphic association (Fig. 3).

## PROCESSING

The samples (all carbonate concretions) were crushed and processed with acetic acid in the paleontology laboratory of the Cordilleran Division, Geological Survey of Canada, Vancouver. Radiolarians were picked, mounted on cardboard slides/metal stubs, and identified using binocular microscope and SEM photographs. All photographs were taken with a Cambridge S100 scanning electron microscope at the Pacific Geoscience Centre, Sidney, B.C.

The radiolarians are best preserved in the calcareous concretions which characterize the purest mudstone facies. The matrix surrounding the concretions is typically non-calcareous to very weakly calcareous. Radiolarians are moderately to well preserved and faunal diversity/sample is closely related to the quality of preservation. Radiolarians were identified



**Figure 1.** Map of Queen Charlotte Islands, British Columbia, Canada, showing locations of Cretaceous sections with preserved radiolarians. Inset shows position of islands within Insular Belt of the Canadian Cordillera (after Monger et al., 1982).

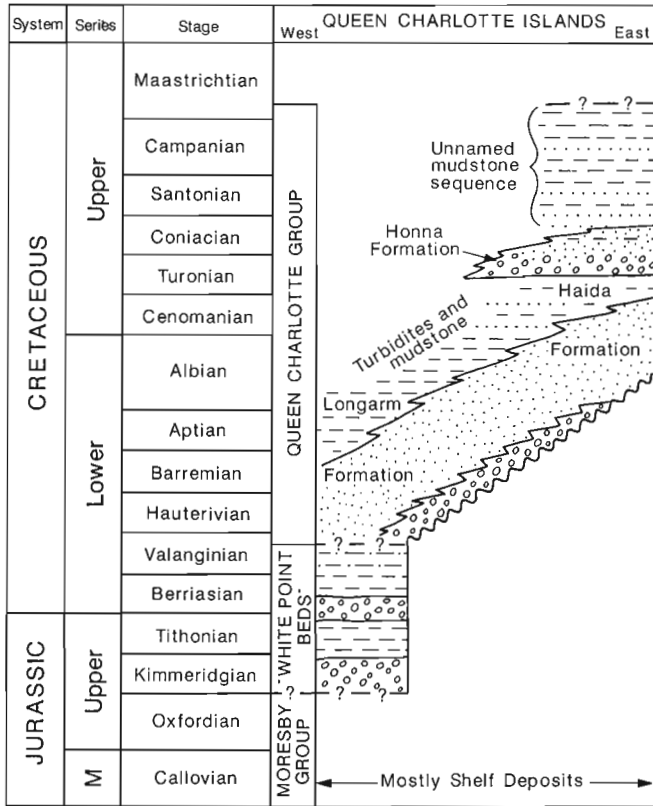
by comparison with described species in the literature and through discussions with colleagues. The commonly known radiolarian taxa from these localities are listed in Table 1 and are placed in a composite range chart (Table 2).

Figured specimens are deposited in the National Collection of Type Invertebrates of the Geological Survey of Canada, presently housed at Ottawa.

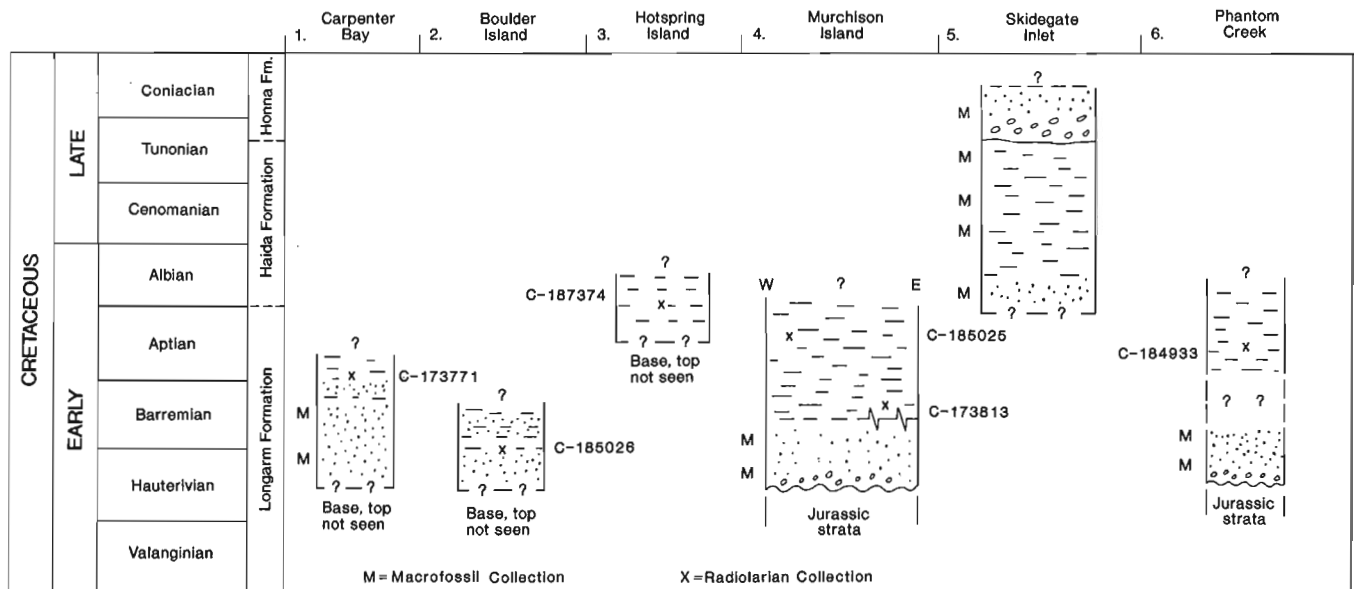
**DISCUSSION**

*Radiolarian faunas*

The radiolarian assemblages discussed below are the first reported from Lower Cretaceous strata of British Columbia. These assemblages generally contain few common index species and age dating has been quite difficult. Most indicators present are fairly long ranging, and the problem is compounded by the conflicting taxon ranges reported by various authors. There are a significant number of species having affinities with well known indicators, but many other species appear to be new. In all samples, the most abundant and diverse genera are *Acaeniotyle*, *Archaeodictyomitra*, *Holocryptocanium*, *Napora*, *Orbiculiforma*, *Parvicingula*, *Praeconocaryomma*, *Stichocapsa(?)*, *Thanarla*, *Triactoma*, *Xitus* and a variety of spongy, disc-like and tetrahedrally-shaped radiolarians. Dominant species include *Acaeniotyle umbilicata*, *Archaeodictyomitra vulgaris*, *Holocryptocanium barbui*, *Napora durhami*, *Thanarla conica*, and several new forms identified as *Crucella* sp. aff. *C. messina*, *Parvicingula(?)* n. sp., and *Stichocapsa(?)* sp. aff. *S.(?) pseudodecora*. Of these, *Crucella* sp. aff. *C. messina* (Pl. 1, fig. 8) is almost identical to a form figured by Foreman (1975, pl. 2d, fig. 9) as *Crucella* sp. This species belongs to the *Acaeniotyle umbilicata* assemblage of Foreman (1975), which is Barremian to Albian in age. *Crucella* sp. aff. *C. messina* is also known from the Hauterivian of Romania (P. Dumitrica, pers. comm. to E.S. Carter, 1993) and the Aptian of Australia (L. O'Dogherty, pers. comm. to E.S. Carter, 1993). This species is found both with and without a patagium, but older (Hauterivian) forms generally lack this feature (P. Dumitrica,



**Figure 2.** Cretaceous stratigraphic framework for Queen Charlotte Islands (after Haggart, 1991, 1993).



**Figure 3.** Positions of radiolarian collections within stratigraphic sections (schematic).

**Table 1.** Distribution of Early Cretaceous radiolarians at localities on Queen Charlotte Islands. An 'x' indicates presence of species; a '-' indicates the species has been searched for but not found.

Taxa	GSC Locality					
	C-185026	C-173771	C-173813	C-184933	C-185025	C-187374
<i>Acaeniotyle diaphorogona</i> FOREMAN						x
<i>Acaeniotyle</i> sp. aff. <i>A. florea</i> OZVOLDOVA	x					x
<i>Acaeniotyle umbilicata</i> RÜST	x	x	x	-	x	x
<i>Alievium gemmatus</i> (WU)			x	x		
<i>Alievium horridus</i> (SQUINABOL)						x
<i>Archaeodictyomitra pseudosclaris</i> (TAN SIN HOK)	x	-				x
<i>Archaeodictyomitra vulgaris</i> PESSAGNO			x	-	x	x
<i>Angulobrachia</i> (?) <i>media</i> STEIGER ms	x					
<i>Crucella</i> sp. aff. <i>C. messina</i> PESSAGNO	x	x	-	-	x	x
<i>Cyclastrum luminosum</i> JUD ms						x
<i>Cyrtocapsa grutterinki</i> TAN SIN HOK		-				x
<i>Holocryptocanium barbui</i> DUMITRICA	-	x	x	x	x	x
<i>Hymeniastrum ancora</i> RÜST					x	x
<i>Lithotractus pusillus</i> (CAMPBELL & CLARK)			x			
<i>Mita</i> sp.					-	x
<i>Napora durhami</i> PESSAGNO		?			x	x
<i>Napora praespinifera</i> PESSAGNO			-	-		x
<i>Napora</i> sp. aff. <i>N. praespinifera</i> PESSAGNO			x	x		
<i>Novaxitus</i> (?) sp. aff. <i>N. (?) tuberculatus</i> (WU)					x	x
<i>Orbiculiforma decora</i> PETERCÁKOVÁ	x					
<i>Orbiculiforma</i> sp. cf. <i>O. depressa</i> WU	x					
<i>Orbiculiforma</i> sp. cf. <i>O. multangula</i> PESSAGNO		-				x
<i>Parvicingula</i> (?) n. sp.	x	x	x	x	x	x
<i>Patulula solara</i> JUD ms?	x					
<i>Pantanellium squinaboli squinaboli</i> (TAN SIN HOK)		x				
<i>P. squinaboli cantuchapai</i> PESSAGNO & MACLEOD		x				
<i>Patulibracchium</i> sp. (in LING & LAZARUS)						x
<i>Podobursa triacantha</i> (FISCHLI)		x				
<i>Praeconocaryomma</i> sp. cf. <i>P. uhlensis</i> PESSAGNO		-				x
<i>Staurocyclia martini</i> RÜST	x	x	?			-
<i>Stylosphaera luca</i> JUD ms	x					
<i>Stichomitra</i> sp. cf. <i>S. asymbatos</i> FOREMAN		x			x	-
<i>Sethocapsa</i> sp. aff. <i>S. dorysphaeroides</i> NEVIANI						x
<i>Sethocapsa leiostraca</i> FOREMAN		-				x
<i>Stichocapsa</i> (?) <i>perspicua</i> (SQUINABOL)						x
<i>Stichocapsa</i> (?) sp. aff. <i>S. (?) pseudodecora</i> TAN SIN HOK		-	x	x	-	x
<i>Stephanastrum</i> sp. aff. <i>S. inflexum</i> RÜST					x	x
<i>Thanarla conica</i> (ALIEV)	x	x	x	-	x	x
<i>Tricolocapsa</i> sp. cf. <i>T. simplex</i> TAN SIN HOK		x		x		
<i>Xitus plenus</i> PESSAGNO					?	x
<i>Xitus spicularis</i> (ALIEV)		x	x		?	?

pers. comm. to E.S. Carter, 1993). *Parvicingula(?)* n. sp. (Pl. 1, fig. 12) has a large cephalis, 6-8 post-abdominal chambers, three or four rows of offset pores per chamber, and a partial outer layer of irregular bars arranged in a manner similar to the Xitidae; this species is abundant in every sample. *Stichocapsa(?)* sp. aff. *S.(?) pseudodecora* has a strong apical horn, is more inflated distally than *S. pseudo-decora*, and frequently possesses multiple robust spines on the terminal chamber.

Comments on sample diversity and preservation, taxa abundance, and species useful for determining age in the individual radiolarian assemblages are summarized below.

GSC loc. C-173771 contains a diverse, well-preserved radiolarian fauna. In addition to species recorded in Table 1, several species of *Orbiculiforma*, *Praeconocaryomma*, and *Xitus* are present, together with a new form somewhat similar to *Crolanium*. Well known indicators whose first appearance datum (FAD) could constrain a lower age are lacking, but the overall assemblage composition suggests this sample is probably younger than C-185026 (below). All specimens of *Crucella* sp. aff. *C. messina* possess a patagium and this may indicate they are younger than Hauterivian (see general comments above). The upper age limit is constrained by *Pantanellium squinaboli squinaboli* and *Podobursa triacantha*, both of which do not range above the Lower Aptian. Age: Barremian to early Aptian.

**Table 2.** Range chart of selected Early Cretaceous radiolarian species. The composite ranges illustrated are derived from both the published literature and discussions with colleagues. Numbers above range interval refer to the following sources: 1) Jud (1991); 2) Pessagno (1977); 3) Sanfilippo and Riedel (1985); 4) Schaaf (1981); 5) Ozvoldova (1990); 6) P. Dumitrica (pers. comm., 1993); 7) L. O'Dogherty (pers. comm., 1993); 8) Ling and Lazarus (1990). '←' indicates range extends below Valanginian; '→' indicates range extends above Albian.

	VAL.	HAUT.	BARR.	APT.	ALB.
<i>Acaeniotyle diaphorogona</i> FOREMAN	←				3
<i>Acaeniotyle umbilicata</i> RÜST	←		1		3
<i>Alievium gemmatus</i> (WU)			7		
<i>Archaeodictyomitra pseudosclaris</i> (TAN SIN HOK)			1		7
<i>Archaeodictyomitra vulgaris</i> PESSAGNO				2	
<i>Crucella</i> sp. aff. <i>C. messina</i> PESSAGNO	?	6		7	?
<i>Cyclastrum luminosum</i> JUD ms			1		
<i>Cyrtocapsa grutterinki</i> TAN SIN HOK			4		5
<i>Holocryptocanium barbui</i> DUMITRICA	←				4
<i>Hymeniastrum ancora</i> RÜST	←		1	?	
<i>Lithotractus pusillus</i> (CAMPBELL & CLARK)	←		1	?	
<i>Mita</i> spp.					2 →
<i>Napora durhami</i> PESSAGNO				4	2
<i>Napora praespinifera</i> PESSAGNO					2
<i>Napora</i> sp. aff. <i>N. praespinifera</i> PESSAGNO				7	
<i>Orbiculiforma decora</i> PETERCÁKOVÁ			7		
<i>Orbiculiforma</i> sp. cf. <i>O. depressa</i> WU				?	?
<i>Orbiculiforma multangula</i> PESSAGNO					2
<i>Patulula solara</i> JUD ms?	←	1			
<i>Pantanellium squinaboli squinaboli</i> (TAN SIN HOK)	←		1	7	
<i>P. squinaboli cantuchapai</i> PESSAGNO & MACLEOD	←		1	?	
<i>Patulibracchium</i> sp. (in LING & LAZARUS)				?	8 ?
<i>Podobursa triacantha</i> (FISCHLI)	←			4	
<i>Praeconocaryomma uhlensis</i> PESSAGNO				2	
<i>Staurocyclia martini</i> RÜST				4	
<i>Stylosphaera luca</i> JUD ms	←		1		
<i>Stichomitra asymbatos</i> FOREMAN					4 →
<i>Sethocapsa</i> sp. aff. <i>S. dorysphaeroides</i> NEVIANI				7	
<i>Sethocapsa leiostraca</i> FOREMAN	←		1		
<i>Stichocapsa(?) perspicua</i> (SQUINABOL)				1 ?	
<i>Stichocapsa(?)</i> sp. aff. <i>S.(?)pseudodecora</i> TAN SIN HOK				? 4	?
<i>Stephanastrum inflexum</i> RÜST			1	4	
<i>Thanarla conica</i> (ALIEV)				2	
<i>Tricolocapsa</i> sp. cf. <i>T. simplex</i> TAN SIN HOK				7	
<i>Xitus plenus</i> PESSAGNO					2
<i>Xitus spicularis</i> (ALIEV)					4,5



The sample from GSC loc. C-173813 contains a low-diversity, moderately preserved siliceous fauna dominated by *Holocryptocanium barbui*, *Thanarla conica*, and several species of *Praeconocaryomma*. The first appearance of *Stichocapsa(?)* sp. aff. *S.(?) pseudodecora* is recorded in this sample. A Barremian age is suggested by *Alievium gemmatum* and *Napora* sp. aff. *N. praespinifera*; *Archaeodictyomitra vulgaris* and *Thanarla conica* indicate the sample is not younger than Aptian. Age: probably late Barremian to early Aptian.

The sample from GSC loc. C-184933 contains a low-diversity, moderately preserved siliceous fauna including *Napora* sp. aff. *N. praespinifera* (Barremian-Aptian, see Table 2), and a form identified as *Tricolocapsa* sp. cf. *T. simplex* which, according to O'Dogherty (pers. comm. to E.S. Carter, 1993), is common in the Aptian of Australia and Spain. Age: probably late Barremian to early Aptian.

GSC loc. C-185025 produced a low-diversity, moderately preserved siliceous fauna. Age-diagnostic taxa are limited: *Hymeniastrum ancora* suggests a late Barremian or younger age, whereas species such as *Napora durhami*, together with *Archaeodictyomitra vulgaris* and *Thanarla conica*, indicate this sample is more likely Aptian. Age: Aptian.

GSC loc. C-185026 contains a moderately diverse assemblage of fair to well preserved radiolarians. A few species are indicated in Table 1 but the majority are either new or too recrystallized to identify accurately. The sample age is loosely constrained by the presence of *Crucella* sp. aff. *C. messina* (without patagium), *Staurocyclia martini* (late Barremian to early Aptian, so far as known), and by *Orbiculiforma decora* and a form similar to *Patulula solara*, of Hauterivian to Barremian and Berriasian to Hauterivian ages, respectively (L. O'Dogherty, pers. comm. to E.S. Carter, 1993). Age: Hauterivian-Barremian.

The sample from GSC loc. C-187374 is a rich one, containing diverse, well preserved radiolarians. Some taxa are documented in Table 1, but the majority of species have not been reported in the literature. The assemblage contains abundant *Xitus* and *Stichocapsa(?)* sp. aff. *S.(?) pseudo-decora*, both widely variable. The presence of *Stichocapsa(?) perspicua* and a form similar to *Sethocapsa dorysphaeroides* suggests this sample is probably not older than Aptian (perhaps late). In addition, *Archaeodictyomitra vulgaris*, *Praeconocaryomma uhlenensis*, and *Thanarla conica* are not presently known to range above the Aptian (Pessagno, 1977). On the other hand, species such as *Napora praespinifera*, *Orbiculiforma multangula*, *Xitus plenus*, and *Mita* sp. alternately suggest an Albian age. Further study of Queen Charlotte Islands Barremian-Albian radiolarian faunas may eventually require that the ranges of some of the above taxa be emended. Age: Late Aptian to early Albian.

The faunal assemblages discussed above all correspond to the *Parvicingula-Thanarla conica* Zone (Zone 6) of Pessagno (1977), which is primarily of local applicability. Correlation with broader-based zonal schemes (e.g., Foreman, 1975; Schaaf, 1981; Sanfilippo and Riedel, 1985) is not possible at this time because most age-diagnostic taxa are absent from the Queen Charlotte Islands assemblages.

### Stratigraphic implications

The described radiolarian collections provide important new information about the extent and duration of mudstone deposition in Queen Charlotte Islands during Early Cretaceous time. Haggart (1991, 1993) has argued that most Cretaceous rocks preserved on Queen Charlotte Islands are shallow-marine, coarse-clastic transgressive deposits which accumulated on the eastern margin of a forearc basin. According to this model, the basin deepened to westward, and more-offshore rocks should have been deposited west of the shallow-marine outcrop belt. However, except for the Cenomanian-Early Turonian interval (Fig. 3, section 5), direct evidence for these inferred coeval, but more offshore, deposits has been mostly lacking.

The new radiolarian collections document that deeper-water mudstone deposition was widespread on Queen Charlotte Islands through Barremian and Aptian time (Fig. 3). The thick sequences of mudstone strata always succeed the transgressive, shallow-water sequences in stratigraphic sections, indicating that the shale basin was extensive to westward.

Previously, strata of Barremian-Aptian age have been considered rare or lacking on the islands, and this has been interpreted as evidence of diastrophism (Sutherland Brown, 1968; Yorath and Chase, 1981). Haggart (1991) has proposed instead that this part of the Insular Belt was characterized by tectonic stability during the late Early Cretaceous and that deposition in the islands region was continuous throughout most of Cretaceous time. The presence of widespread, deeper-water Barremian-Aptian mudstone sequences on the islands, documented by the radiolarian collections, underscores the relative lack of tectonic activity in the islands region during the late Early Cretaceous interval, and further supports the interpretation of a conformable relationship between the shallow water Longarm and Haida formations.

### CONCLUSIONS

1. Radiolarian faunas of Hauterivian, Barremian, Aptian, and possibly Albian age have been identified from fine clastic deposits of Queen Charlotte Islands, British Columbia.
2. Barremian and Aptian radiolaria from Queen Charlotte Islands are the first extensive and diverse faunas of this age from the west coast of North America.
3. Radiolarian faunas document the existence of widespread mudstone deposition in the Queen Charlotte Islands region during late Early Cretaceous time and support the interpretation of an extensive deeper-water basin situated west of the present-day outcrop belt. Interpretations of diastrophism in the Queen Charlotte Islands region during this time are unwarranted.

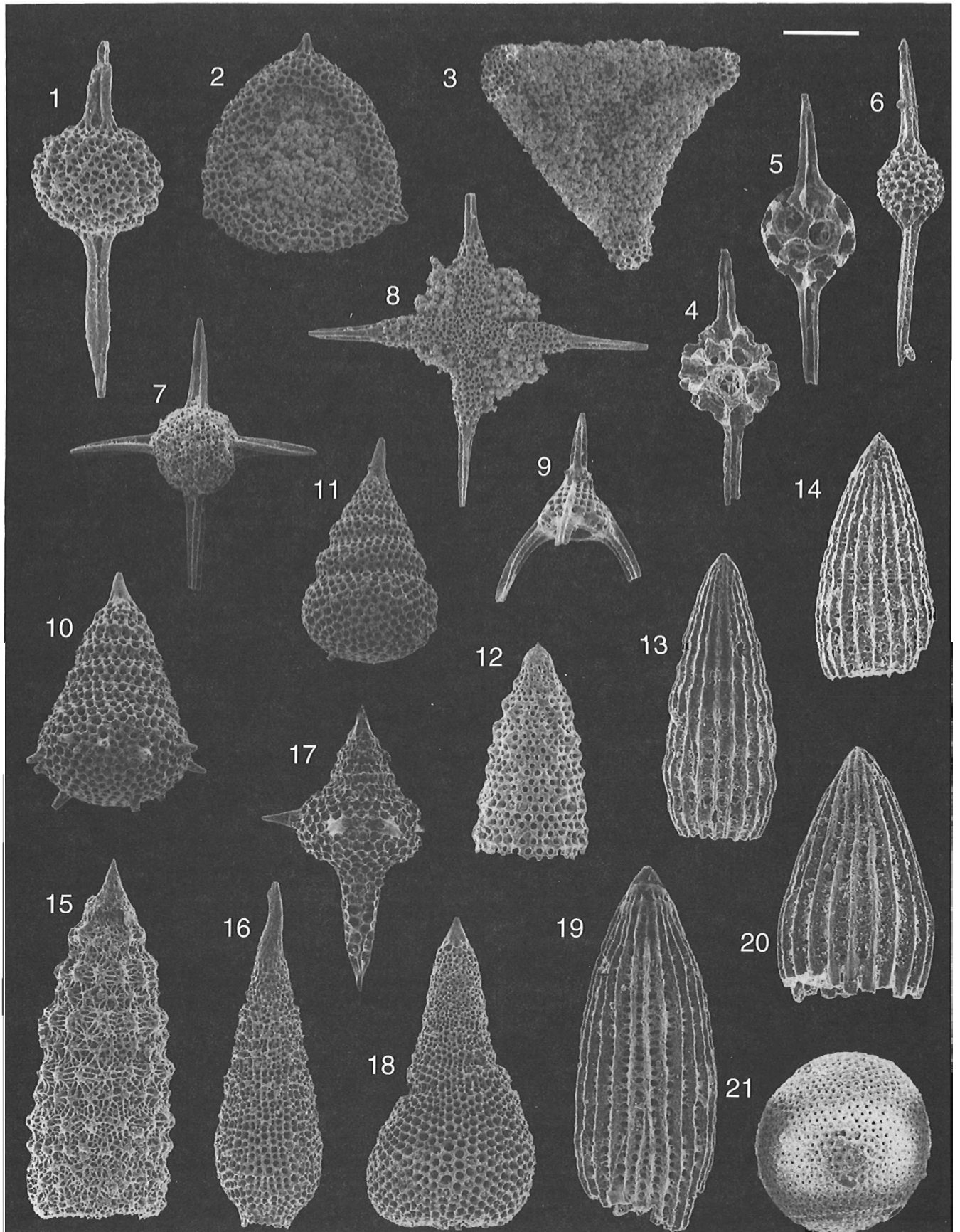


Plate 1

### Plate 1

Scanning electron micrographs of late Early Cretaceous radiolarians from Queen Charlotte Islands. Figure 11 from Haida Formation, all other specimens from Longarm Formation. Scale bar = number of microns for each specimen illustrated.

- Figure 1.** *Acaeniotyle umbilicata* RÜST. GSC No. 107611, GSC loc. C-173771, Carpenter Bay, Moresby Island. Scale bar = 100 µm.
- Figure 2.** *Cyclastrum luminosum* JUD ms. GSC No. 107612, GSC loc. C-187374, Hotspring Island. Meshwork in central area obscured by pyrite. Scale bar = 100 µm.
- Figure 3.** *Hymeniastrum ancora* RÜST. GSC No. 107613, GSC loc. C-187374, Hotspring Island. Outer meshwork of test obscured by pyrite. Scale bar = 135 µm.
- Figure 4.** *Pantanellium squinaboli cantuchapai* PESSAGNO and MACLEOD. GSC No. 107614, GSC loc. C-173771, Carpenter Bay, Moresby Island. Scale bar = 80 µm.
- Figure 5.** *Pantanellium squinaboli squinaboli* (TAN SIN HOK). GSC No. 107615, GSC loc. C-173771, Carpenter Bay, Moresby Island. Scale bar = 80 µm.
- Figure 6.** *Stylosphaera luca* JUD ms. GSC No. 107616, GSC loc. C-185026, Boulder Island. Scale bar = 135 µm.
- Figure 7.** *Acaeniotyle* sp. aff. *A. florea* OZVOLDOVA. GSC No. 107617, GSC loc. C-187374, Hotspring Island. Scale bar = 135 µm.
- Figure 8.** *Crucella* sp. aff. *C. messina* PESSAGNO. GSC No. 107618, GSC loc. C-187374, Hotspring Island. Patagium partially preserved with pyrite. Scale bar = 135 µm.
- Figure 9.** *Napora durhami* (PESSAGNO). GSC No. 107619, GSC loc. C-187374, Hotspring Island. Scale bar = 100 µm.
- Figures 10, 11.** *Stichocapsa*(?) sp. aff. *S.*(?) *pseudodecora* TAN SIN HOK. GSC No. 107620 and GSC No. 107621, respectively, both GSC loc. C-187374, Hotspring Island. Scale bar = 100 µm.
- Figure 12.** *Parvicingula*(?) n. sp. GSC No. 107622, GSC loc. C-184933, Phantom Creek, central Graham Island. Scale bar = 100 µm.
- Figure 13.** *Archaeodictyomitra pseudosclaris* (TAN SIN HOK). GSC No. 107623, GSC loc. C-187374, Hotspring Island. Scale bar = 80 µm.
- Figure 14.** *Archaeodictyomitra vulgaris* PESSAGNO. GSC No. 107624, GSC loc. C-173813, Murchison Island. Scale bar = 68 µm.
- Figure 15.** *Xitus plenus* PESSAGNO. GSC No. 107625, GSC loc. C-187374, Hotspring Island. Scale bar = 100 µm.
- Figure 16.** *Stichocapsa*(?) *perspicua* (SQUINABOL). GSC No. 107626, GSC loc. C-187374, Hotspring Island. Scale bar = 135 µm.
- Figure 17.** *Podobursa triacantha* (FISCHLI). GSC No. 107627, GSC loc. C-173771, Carpenter Bay, Moresby Island. Scale bar = 135 µm.
- Figure 18.** *Sethocapsa* sp. aff. *S. dorysphaeroides* NEVIANI. GSC No. 107628, GSC loc. C-187374, Hotspring Island. Scale bar = 135 µm.
- Figure 19.** *Mita* sp. GSC No. 107629, GSC loc. C-187374, Hotspring Island. Scale bar = 80 µm.
- Figure 20.** *Thanarla conica* (ALIEV). GSC No. 107630, GSC loc. C-187374, Hotspring Island. Scale bar = 68 µm.
- Figure 21.** *Holocryptocanium barbui* DUMITRICA. GSC No. 107631, GSC loc. C-173771, Carpenter Bay, Moresby Island. Scale bar = 80 µm.

## ACKNOWLEDGMENTS

We are grateful to Peter Krauss (GSC, Vancouver) for expert sample processing, and to Marji Johns (Pacific Geoscience Centre) for SEM support. Drafted figures were prepared by Tonia Oliveric and the tables were formatted and typed by Bev Vanlier. Glenn Woodsworth's careful review clarified several ambiguous points.

Discussions between E.S. Carter and Luis O'Dogherty, Paulian Dumitrica, and Ruth Jud at the Université de Lausanne (February 1993) were critical to the understanding of many lesser known radiolarian species documented in this paper; their help and generosity is greatly appreciated.

This work has been supported by GSC Project 880038.

## REFERENCES

- Baumgartner, P.O.**  
1992: Lower Cretaceous radiolarian biostratigraphy and biogeography off northwestern Australia (ODP sites 765 and 766 and DSDP site 261), Argo Abyssal Plain and Lower Exmouth Plateau; Proceedings of the Ocean Drilling Program, Scientific Results, v. 123, p. 299-342.
- Brandon, M.T.**  
1989: Deformational styles in a sequence of olistostromal mélanges, Pacific Rim Complex, western Vancouver Island, Canada; Geological Society of America Bulletin, v. 101, p. 1520-1542 + unpublished appendix of 25 p.
- Campbell, A.S. and Clark, B.L.**  
1944: Radiolaria from Upper Cretaceous of Middle California; Geological Society of America, Special Papers, No. 57, 61 p.
- Carter, E.S.**  
1991: Late Triassic radiolarian biostratigraphy of the Kunga Group, Queen Charlotte Islands, British Columbia; in *Evolution and Hydrocarbon Potential of the Queen Charlotte Basin, British Columbia*, (ed.) G.J. Woodsworth; Geological Survey of Canada, Paper 90-10, p. 195-201.  
1993: Biochronology and paleontology of uppermost Triassic (Rhaetian) radiolarians, Queen Charlotte Islands, British Columbia, Canada; Ph.D. thesis, Université de Lausanne, Switzerland, 175 p.
- Carter, E.S., Cameron, B.E.B., and Smith, P.L.**  
1988: Lower and Middle Jurassic radiolarian biostratigraphy and systematic paleontology, Queen Charlotte Islands, British Columbia; Geological Survey of Canada, Bulletin 386, 109 p., 18 pls.
- Carter, E.S., Orchard, M.J., and Tozer, E.T.**  
1989: Integrated ammonoid-conodont-radiolarian biostratigraphy, Late Triassic Kunga Group, Queen Charlotte Islands, British Columbia; in *Current Research, Part H*; Geological Survey of Canada, Paper 89-1H, p. 23-30.
- Foreman, H.P.**  
1968: Upper Maastrichtian radiolaria of California; Special Papers in Palaeontology, No. 3, The Palaeontological Association, London, 82 p.  
1973: Radiolaria from DSDP Leg 20; in *Initial Reports of the Deep Sea Drilling Project*, (ed.) B.C. Heezen, I.D. MacGregor, et al.; v. 20, p. 249-305. United States Government Printing Office, Washington.  
1975: Radiolaria from the North Pacific, Deep Sea Drilling Project, Leg 32; in *Initial Reports of the Deep Sea Drilling Project*, (ed.) R.L. Larson, R. Moberly, et al.; v. 32, p. 579-676. United States Government Printing Office, Washington.
- Gamba, C.A.**  
1993: Stratigraphy and sedimentology of the Late Jurassic to Early Cretaceous Longarm Formation, Queen Charlotte Islands, British Columbia; in *Current Research, Part A*; Geological Survey of Canada, Paper 93-1A, p. 139-148.
- Haggart, J.W.**  
1991: A synthesis of Cretaceous stratigraphy, Queen Charlotte Islands, British Columbia; in *Evolution and Hydrocarbon Potential of the Queen Charlotte Basin, British Columbia*, (ed.) G.J. Woodsworth; Geological Survey of Canada, Paper 90-10, p. 253-277.  
1992: Progress in Jurassic and Cretaceous stratigraphy, Queen Charlotte Islands, British Columbia; in *Current Research, Part A*; Geological Survey of Canada, Paper 92-1A, p. 361-365.  
1993: Latest Jurassic and Cretaceous paleogeography of the northern Insular Belt, British Columbia; in *Mesozoic Paleogeography of the Western United States-II*, (ed.) G.C. Dunne and K.A. McDougall; Society of Economic Paleontologists and Mineralogists, Pacific Section, Special Volume 71.
- Jud, R.**  
1991: Biochronology and systematics of Early Cretaceous radiolaria of the western Tethys; Ph.D. thesis, Université de Lausanne, Switzerland.
- Karl, S., Decker, J., and Jones, D.L.**  
1979: Early Cretaceous radiolarians from the McHugh Complex, south-central Alaska; United States Geological Survey, Circular 804-B, p. B88-B90.
- Ling, H.Y. and Lazarus, D.B.**  
1990: Cretaceous Radiolaria from the Weddell Sea: Leg 113 of the Ocean Drilling Program; Proceedings of the Ocean Drilling Program, Scientific Results, v. 113, p. 353-363.
- McLearn, F.H.**  
1972: Ammonoids of the Lower Cretaceous Sandstone member of the Haida Formation, Skidegate Inlet, Queen Charlotte Islands, western British Columbia; Geological Survey of Canada, Bulletin 188, 78 p., 45 pls.
- Monger, J.W.H., Price, R.A., and Tempelman-Kluit, D.J.**  
1982: Tectonic accretion and the origin of the two metamorphic and plutonic belts in the Canadian Cordillera; *Geology*, v. 10, p. 70-75.
- Ozoldova, L.**  
1990: Occurrence of Albian Radiolaria in the underlier of the Vienna Basin; *Geologicky Zbornik, Geologica Carpathica, Bratislava*, v. 41, no. 2, p. 137-154.
- Pessagno, E.A., Jr.**  
1976: Radiolarian zonation and stratigraphy of the Upper Cretaceous portion of the Great Valley sequence, California Coast Ranges; *Micropaleontology*, Special Publication no. 2, 95 p.  
1977: Lower Cretaceous radiolarian biostratigraphy of the Great Valley sequence and Franciscan Complex, California Coast Ranges; Cushman Foundation for Foraminiferal Research, Special Publication no. 15, 87 p.
- Pessagno, E.A., Jr., Blome, C.D., Carter, E.S., MacLeod, N., Whalen, P.A., and Yeh, K.-Y.**  
1987: Preliminary radiolarian zonation for the Jurassic of North America; in *Studies of North American Jurassic Radiolaria. Part 2*; Cushman Foundation for Foraminiferal Research, Special Publication No. 23, p. 1-18.
- Pfaffer, G., Lull, J.S., Nokleberg, W.J., Pessel, G.H., Wallace, W.K., and Winkler, G.R.**  
1989: Geologic map of the Valdez A-4, B-3, B-4, C-3, C-4, and D-4 quadrangles, northern Chugach Mountains and southern Copper River basin, Alaska; United States Geological Survey, Open File Report No. 89-569, 1 map, scale 1:125 000.
- Rüst, D.**  
1892: Contributions to Canadian micro-palaeontology, Part IV; Geological and Natural History Survey of Canada, Ottawa, p. 99-116.
- Sanfilippo, A. and Riedel, W.R.**  
1985: Cretaceous radiolaria; in *Plankton Stratigraphy*, (ed.) H.M. Boli, J.B. Saunders, and K. Perch-Nielsen; Cambridge University Press, Cambridge, v. 2, p. 573-630..
- Schaaf, A.**  
1981: Late Early Cretaceous Radiolaria from Deep Sea Drilling Project Leg 62; in *Initial Reports of the Deep Sea Drilling Project*, (ed.) L.N. Stout; United States Government Printing Office, Washington, v. 62, p. 419-470.
- Sutherland Brown, A.**  
1968: Geology of the Queen Charlotte Islands, British Columbia; British Columbia Department of Mines and Petroleum Resources, Bulletin 54, 226 p., 18 pls.

Tipper, H.W., Smith, P.L., Cameron, B.E.B., Carter, E.S.,  
Jakobs, G.K., and Johns, M.J.

1991: Biostratigraphy of the Lower Jurassic formations of the Queen Charlotte Islands, British Columbia; in *Evolution and Hydrocarbon Potential of the Queen Charlotte Basin, British Columbia*, (ed.) G.J. Woodsworth; Geological Survey of Canada, Paper 90-10, p. 203-235.

Yorath, C.J. and Chase, R.L.

1981: Tectonic history of the Queen Charlotte Islands and adjacent areas – a model; *Canadian Journal of Earth Sciences*, v. 18, p. 1717-1739.

Geological Survey of Canada Project 880038

## APPENDIX: LOCALITY REGISTER

Information is provided here for illustrated material. Field numbers in parentheses follow GSC locality number.

GSC loc. C-173771 (HFB-89-62 R). Kunghit Island map area (NTS 103 B/3), UTM: 356900E, 5790300N, shoreline exposures 1.6 km east of mouth of unnamed creek draining north side of Carpenter Bay near Samuel Rock. Longarm Formation, massive fine grained sandstone. Radiolarians from calcareous concretion. Other fossils present: *Acroteuthis* sp., *Pinna* sp., indeterminate brachiopods.

GSC loc. C-173813 (HFB-89-104 R). Ramsay Island map area (NTS 103 B/11), UTM: 333100E, 5828200N, intertidal platform just west of large Tertiary dyke, about 0.5 km east of southwest corner of Murchison Island. Longarm Formation, mudstone structurally overlying sandstone and siltstone with Barremian bivalves. Radiolarians from calcareous concretion.

GSC loc. C-184933 (HFB-90-JH-142A R). Yakoun Lake map area (NTS 103 F/8), UTM: 678000E, 5915800N, exposures in bed of Phantom Creek. Haida Formation, mudstone. Radiolarians from calcareous concretion.

GSC loc. C-185025 (HFB-90-220 R). Ramsay Island map area (NTS 103 B/11), UTM: 332400E, 5828400N, west shore of Murchison Island. Longarm Formation, strongly intruded and deformed mudstone stratigraphically overlying sandstone and siltstone with Hauterivian-Barremian bivalves. Radiolarians from calcareous concretion. Indeterminate belemnites present locally.

GSC loc. C-185026 (HFB-90-224 R). Burnaby Island map area (NTS 103 B/6), UTM: 343500E, 5795750N, southernmost exposures on east side of Boulder Island, Skincuttle Inlet. Longarm Formation(?), mudstone unit interstratified(?) with sandstone and siltstone. Radiolarians from calcareous concretion. Indeterminate belemnites present locally.

GSC loc. C-187374 (HFB-90-302 R). Ramsay Island map area (NTS 103 B/11), UTM: 334350E, 5827650N, intertidal peninsula on southwest side of Hotspring Island. Longarm Formation, mudstone unit. Radiolarians from calcareous concretion.



# Preliminary measurements of subtidal dune migration and sediment movement on Roberts Bank, Fraser River delta, British Columbia

R.A. Kostaschuk<sup>1</sup> and J.L. Luternauer  
Cordilleran Division, Vancouver

*Kostaschuk, R.A. and Luternauer, J.L., 1993: Preliminary measurements of subtidal dune migration and sediment movement on Roberts Bank, Fraser River delta, British Columbia; in Current Research, Part E; Geological Survey of Canada, Paper 93-1E, p. 67-72.*

---

**Abstract:** Dunes on Roberts Bank are migrating slowly and transporting sediment to the northwest in the direction of the flood tidal current. There is no obvious source of sand replenishment, suggesting net erosion of the surface and possible undercutting of the slope. Such a process may lead to failure of the slope adjacent to coastal developments. Preliminary measurements suggest migrating dunes may bury submarine transmission cables by as much as 4 m during a neap tidal period.

**Résumé :** Les dunes sur le banc Roberts migrent lentement, transportant des sédiments vers le nord-ouest en direction du courant de marée montante. Il n'existe aucune source évidente de renouvellement du sable, ce qui porte à croire qu'il y a nette érosion de la surface et havage possible du talus. Un tel phénomène pourrait provoquer un glissement du talus près des aménagements côtiers. Les premières mesures semblent indiquer que les dunes en migration pourraient enfouir des câbles de transmission sous-marins sous jusqu'à 4 m de sable pendant une période de morte-eau.

---

<sup>1</sup> Department of Geography, University of Guelph, Guelph, Ontario N1G 2W1

## INTRODUCTION

The Fraser River delta, British Columbia, is the largest and most important delta on the west coast of Canada (Fig. 1). The subaqueous slope of the delta supports a variety of coastal structures and the stability of the slope has become a concern (e.g., McKenna et al., 1992; Kostaschuk et al., 1992; Hart et al., 1992a, b; Luternauer et al., in press). A field of large, subaqueous dunes occurs on the southern slope of the delta on Roberts Bank (Fig. 2), indicating movement of sediment

to the northwest by tidal currents (Luternauer, 1980). There are no obvious fluvial or coastal sources of sediment for the dune field, suggesting the possibility of net sediment loss and erosion of the slope in the area (Luternauer, 1980). This could lead to undercutting of the upper portion of the slope, placing the Tsawwassen Ferry Terminal and Westshore Terminals (Coal Port) at risk to foundation movement or failure (Luternauer, 1980). British Columbia Hydro is also concerned that migrating dunes can bury submarine transmission cables in the area, causing heat gain and a loss of efficiency. Unfortunately, a lack of data on dune and sediment movement

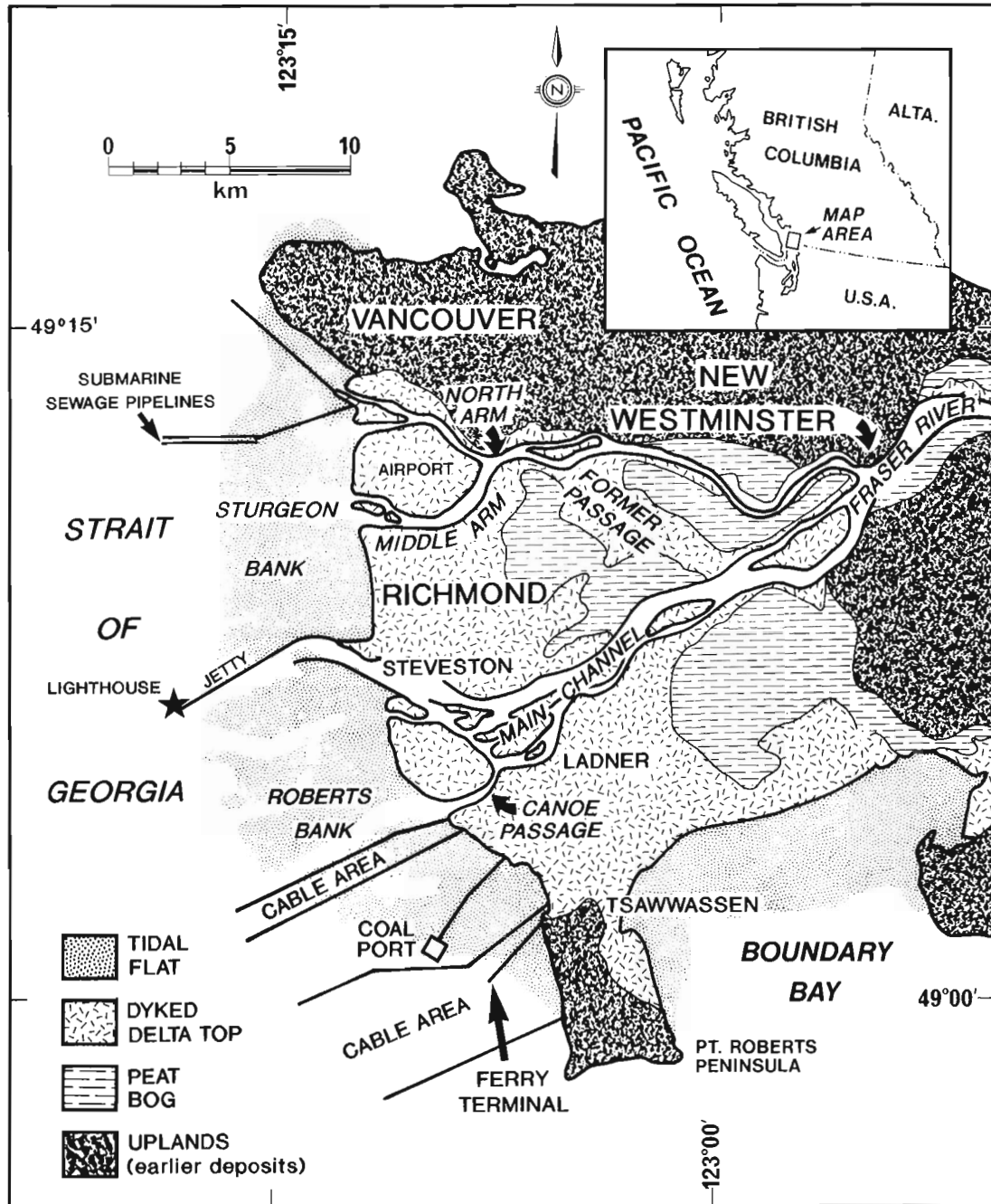


Figure 1. Location and setting of Fraser River delta.



makes it difficult to test these hypotheses. This paper presents the preliminary results of a recent investigation to estimate dune migration and sediment transport rates.

## SETTING

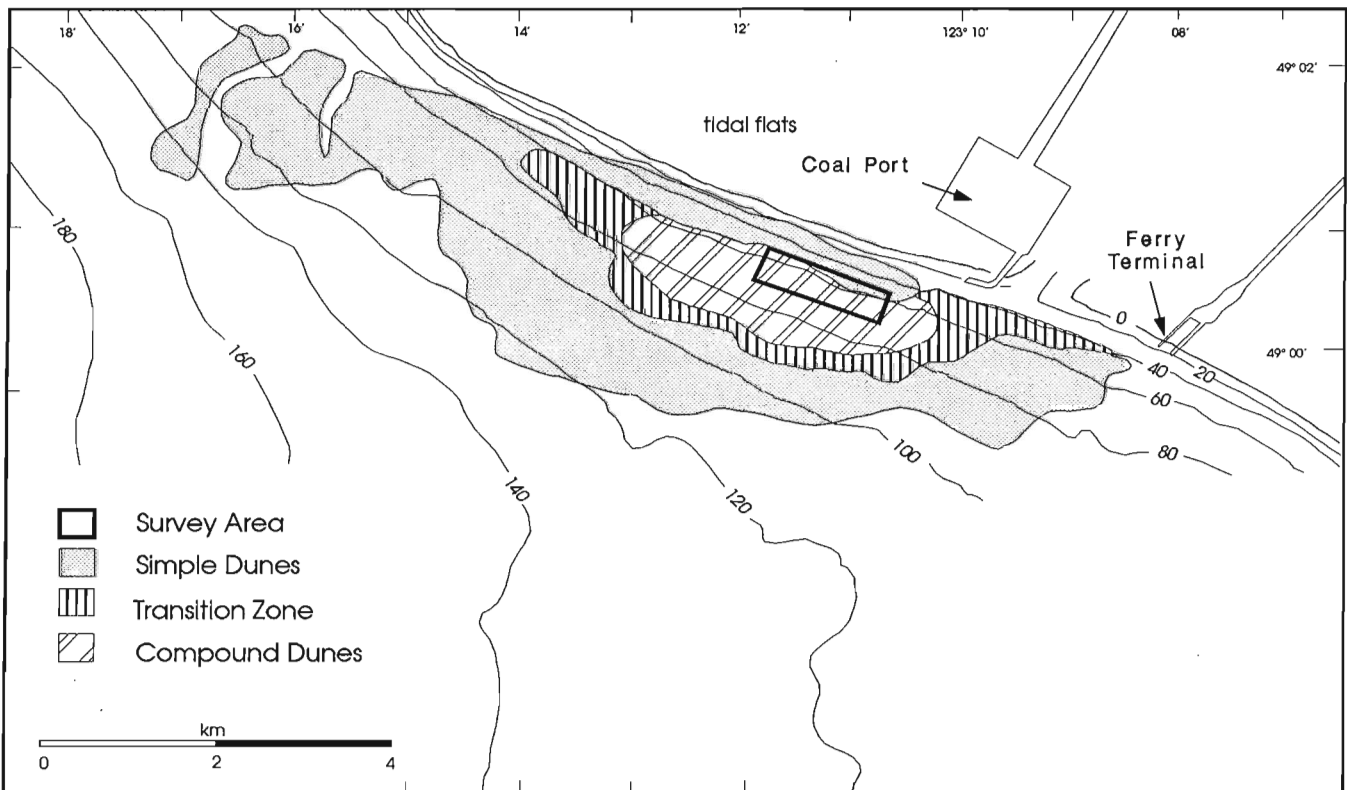
The Fraser River drains 250 000 km<sup>2</sup> of rugged terrain into the Strait of Georgia. The mean annual discharge is 3400 m<sup>3</sup>/s near the mouth and the river transports an average of 17.4 million tonnes of suspended sediment to the delta (McLean and Church, 1986). Most sediment transport takes place during the spring snowmelt freshet, and over one third of this is sand. The Strait of Georgia is a high-energy, semi-enclosed marine basin. Tides in the strait near the delta are mixed, semidiurnal with a mean range of 2.6 m and a maximum range of 5.4 m. Tidal streams along the delta move toward the northwest on the flood and to the southeast on the ebb (Thomson, 1981).

A series of distributary channels dissect the sandy sediments of the subaerial Fraser Delta. Gently sloping, sandy tidal flats extend up to 9 km from the edge of the subaerial delta to the subtidal slope. The subtidal slope inclines at 1-23° and extends 5-10 km seaward of the tidal flats to depths of 300 m. Sediments on the subtidal slope are dominantly mud next to Sturgeon Bank and dominantly sand next to Roberts Bank (Luternauer, 1980).

Werth von Deichmann (1992) used sidescan sonar, seismic profiles, echosoundings and sediment grab samples to describe the general morphology and surficial geology of the dunes. The dune field consists of simple and compound forms (Fig. 2). Simple dunes are single, discrete features and compound dunes develop from the coalescence of simple dunes (Ashley et al., 1990). The large compound dunes are in the central portion of the field, with simple features surrounding them. A transition zone consisting of both simple and compound features separates the two main groups. Compound dunes have crests with an irregular shape and simple dunes have straight crests. All dunes have steep lee sides oriented toward the northwest, in the same direction as the dominant flood tidal current. The composition of surficial sediments varies from sand (>90% sand) to muddy sand (50-90% sand) and sandy mud (50-90% mud). The central portion of the study area consists of sand that grades into muddy sand to the southeast. To the northwest the sand grades into sandy mud.

## METHODS

Two replicate surveys of a portion of the dune field by Public Works Canada on July 24 and October 2, 1992, are the database for this study. The study section is 375 m wide and 1.5 km in length, and water is between 55 and 75 m deep (Fig. 2). The sounder is a Ross Model 800, accurate to



**Figure 2.** Study area on Roberts Bank slope, southwestern Fraser River delta. Bathymetry is in metres. Spatial distribution of dunes is from Werth von Deichmann (1992).

±0.15 m for the depths in this study. A Krup-Atlas Polarfix laser system provides positions with an accuracy of ±1.5 m. Echosounding lines are set at 10 m intervals and run parallel to the slope contours.

A computer mapping program (Digital Ground Model) uses sounding data to generate three-dimensional block diagrams. Profiles along the centre of the study section allow measurement of dune geometry and changes in bed elevation. Dunes are easy to recognize from one survey to the next, providing estimates of migration distance between surveys.

The relation of Simons et al. (1965) estimates sediment transport per unit crest width within migrating dunes,  $G_d$ :

$$G_d = \rho_s(1 - P) \beta HM \quad (1)$$

in which  $\rho_s$  is sediment density,  $P$  is bed porosity,  $\beta$  is a dune shape factor,  $H$  is dune height and  $M$  is dune migration distance (or rate). Sediment density is constant at  $2650 \text{ kg/m}^3$ . Van den Berg (1987) reviewed the literature and found  $P = 0.4$  and  $\beta = 0.6$  in most cases.

## RESULTS

The block diagram (Fig. 3) shows that dunes have straight crests with an orientation perpendicular to bathymetric contours. Depressions and ridges occur within both crest and trough areas. There are 32 dunes on the centreline profile (Fig. 4), most of which are simple in form. Measurements of bed elevation indicate net mean aggradation of 0.54 m between surveys and up to 3.1 m aggradation in a dune trough. The mean value is well above the vertical error estimate ±0.15 m, indicating that instrument error cannot account for the aggradation.

Figure 5 presents frequency distributions and descriptive statistics of the 32 measurements of dune height, length and migration, plus sediment transport estimates. All of the data have a positive skew, with higher frequencies in the lower values. Dune height ranges from 0.3 to 3.5 m, lengths between 13.8 and 108 m, and migration from 0 to 25 m. All dunes migrated toward the northwest. The mean height, length and migration of the dunes are well above the vertical

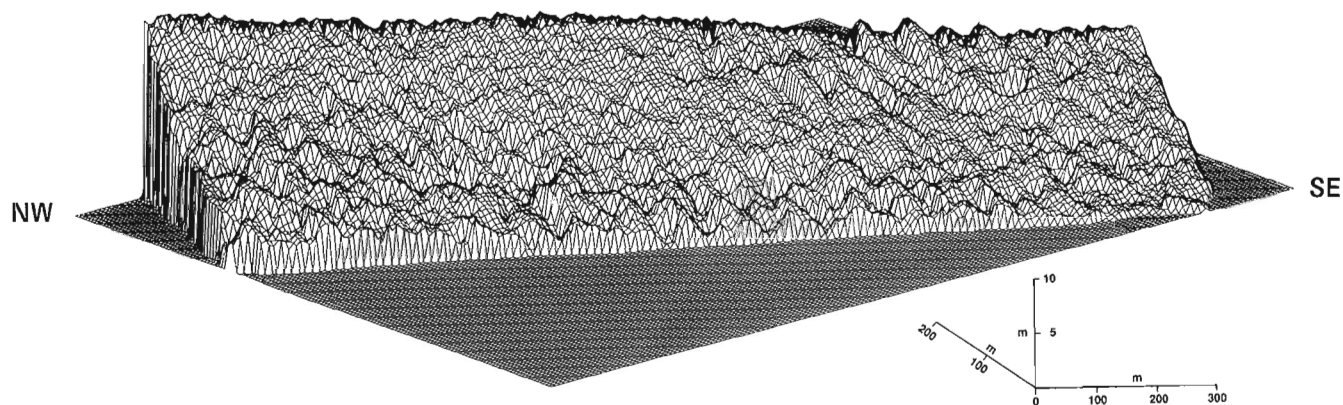


Figure 3. Digital Ground Model of the survey area on July 24, 1992.

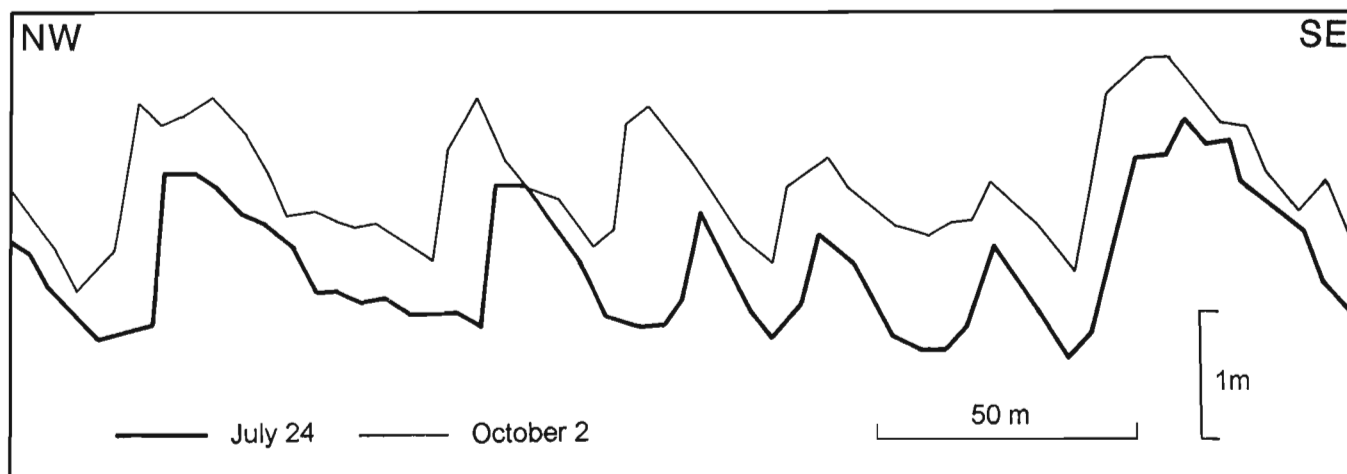


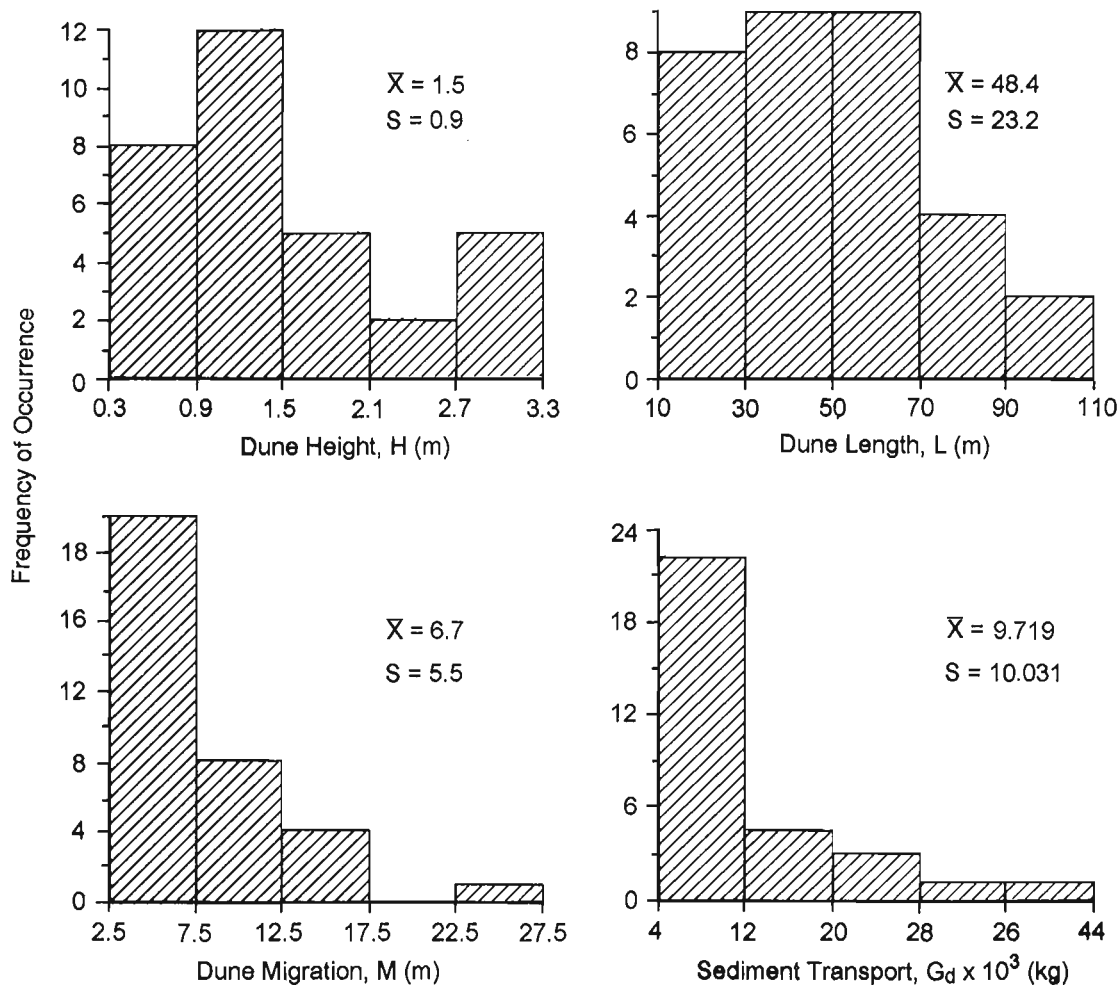
Figure 4. Dune profiles along the centreline of the survey area.

and horizontal survey error estimates. Sediment transport between the survey dates was estimated by applying Equation (1), assuming standard values for sediment density, porosity and dune shape. Transport estimates range from 5 to 40 545 kg.

**DISCUSSION**

The study section falls within the sand sediment region and the zone of compound dunes identified by Werth von Deichmann (1992) (Fig. 2). We classify most of the dunes in our survey as simple features, which does not agree with Werth von Deichmann. Our dunes are also larger. These disagreements could result from a lower precision in the earlier surveys, or a different interpretation of what constitutes a compound dune. It is also possible that the character of this portion of the dune field changed in the period between Werth von Deichmann's survey (1991) and our survey.

The orientation of dune lee sides and dune migration direction show dominant sediment transport to the northwest, corresponding with directions measured by Werth von Deichmann. These results support Luternauer's (1980) hypothesis that flood currents dominate sediment movement. Luternauer also hypothesizes a net sediment loss, and hence bed erosion, in the dune field. Our data conflict on this issue. Horizontal sediment movement is clearly to the northwest, suggesting a degradation of the bed in the apparent absence of fluvial or coastal sand replenishment. The bed elevation measurements, however, show a net aggradation over the study period. It is possible that the aggradation only occurred in the portion of the dune field in which we conducted our survey, with degradation occurring in other regions. The area could also aggrade during neap tides, such as our survey period, but erode during spring tides. Despite the evidence for aggradation during our study, dune migration and sediment transport to the northwest show a net sediment loss. This suggests that the area we surveyed is probably degrading over the longer term. Resolution of the issue of bed erosion in the dune field will require rigorously monitoring bed elevations over a period of years.



**Figure 5.** Histograms and descriptive statistics for 32 dunes measured along the survey centreline.  $\bar{x}$  is the sample mean and  $s$  is the standard deviation.

The combination of dune migration and bed aggradation can result in burial of submarine cables to a significant depth over a short period. We measured moving dunes of up to 3.5 m in height, so a cable at the elevation of the dune trough risks burial by as much as 3.5 m of sand. Addition of the measured mean aggradation of 0.54 m results in a maximum accumulation of over 4 m. Mean dune height of 1.5 m and a mean aggradation of 0.54 m combine for a cable burial of over 2 m.

## ACKNOWLEDGMENTS

Special thanks to Warren Williams and Al Cadenhead and his crew at Public Works Canada for conducting the dune surveys. Kostaschuk's Natural Sciences and Engineering Research Council Operating Grant and Luternauer's Geological Survey of Canada Project 860022 provided funding. V. Barrie reviewed the draft manuscript.

## REFERENCES

- Ashley, G.M., Boothroyd, J.C., Bridge, J.S., Clifton, H.E., Dalrymple, R.W., Elliott, T., Flemming, B.W., Harms, J.C., Harris, P.T., Hunger, R.E., Kreisa, R.D., Lancaster, N., Middleton, G.V., Paola, C., Rubin, D.M., Smith, J.D., Southard, J.B., Terwindt, J.H.J., and Twitchell, Jr., D.C.  
 1990: Classification of large-scale subaqueous bedforms: a new look at an old problem; *Journal of Sedimentary Petrology*, v. 60, p. 160-172.
- Hart, B.C., Prior, D.B., Barrie, J.V., Currie, R.A., and Luternauer, J.L.  
 1992a: A river mouth submarine landslide and channel complex, Fraser delta, Canada; *Sedimentary Geology*, v. 81, p. 73-87.
- Hart, B.S., Prior, D.B., Hamilton, T.S., Barrie, J.V., and Currie, R.G.  
 1992b: Patterns and styles of sedimentation, erosion and failure, Fraser delta slope, British Columbia; in *Geotechnique and Natural Hazards [Proceedings of the First Canadian Symposium on Geotechnique and Natural Hazards]*, Canadian Geotechnical Society, Vancouver, May 1992, p. 365-372.
- Kostaschuk, R.A., Luternauer, J.L., McKenna, G.T., and Moslow, T.F.  
 1992: Sediment transport in a submarine channel system: Fraser River delta, Canada; *Journal of Sedimentary Petrology*, v. 62, p. 273-282.
- Luternauer, J.L.  
 1980: Genesis of morphologic features on the western delta front of the Fraser River, British Columbia; in *Coastlines of Canada*, (ed.) S.B. McCann; Geological Survey of Canada, Paper 80-10, p. 381-396.
- Luternauer, J.L., Clague, J.J., Hunter, J.A.M., Pullan, S.E., Roberts, M.C., Woeller, D.J., Kostaschuk, R.A., Moslow, T.F., Monahan, P.A., and Hart, B.S.  
 in press: The Fraser River delta, British Columbia: architecture, geological dynamics and human impact; in *Deltas of the World, Proceedings Special Session at Coastal Zone '93, 8th Symposium on Coastal and Ocean Management*, New Orleans, July 19-12, 1993.
- McKenna, G.T., Luternauer, J.L., and Kostaschuk, R.A.  
 1992: Large-scale mass-wasting events on the Fraser River delta front near Sand Heads, British Columbia; *Canadian Geotechnical Journal*, v. 29, p. 151-156.
- McLean, D.G. and Church, M.A.  
 1986: A re-examination of sediment transport observations in the lower Fraser River; Environment Canada, Water Resources Branch, Inland Waters Directorate, Sediment Survey Section, IWD-HQ-WRB-SS-86-6.
- Simons, D.B., Richardson, E.V., and Nordin, C.F.  
 1965: Bed-load equation for ripples and dunes; United States Geological Survey, Professional Paper 462H.
- Thomson, R.E.  
 1981: *Oceanography of the British Columbia Coast*; Department of Fisheries, Ottawa, 291 p.
- van den Berg, J.H.  
 1987: Bedform migration and bed-load transport in some rivers and tidal environments; *Sedimentology*, v. 34, p. 681-698.
- Werth von Deichmann, L.  
 1992: A detailed morphological description of an anomalous sand wave field on the southern slopes of Roberts Bank, Fraser Delta, British Columbia; B.Sc. thesis, Department of Oceanography, University of British Columbia, Vancouver, 102 p.

# Overview and preliminary results for the Interior Plateau Program, Canada-British Columbia Agreement on Mineral Development 1991-1995

Peter van der Heyden, Rob Shives<sup>1</sup>, Bruce Ballantyne<sup>1</sup>, Don Harris<sup>1</sup>,  
Colin Dunn<sup>1</sup>, Dennis Teskey<sup>2</sup>, Alain Plouffe<sup>3</sup>, and Cathie Hickson  
Cordilleran Division, Vancouver

*van der Heyden, P., Shives, R., Ballantyne, B., Harris, D., Dunn, C., Teskey, D., Plouffe, A., and Hickson, C., 1993: Overview and preliminary results for the Interior Plateau Program, Canada-British Columbia Agreement on Mineral Development 1991-1995; in Current Research, Part E; Geological Survey of Canada, Paper 93-1E, p. 73-79.*

---

**Abstract:** The Interior Plateau program is a multidisciplinary initiative that is part of the Canada-British Columbia Agreement on Mineral Development 1991-1995, a subsidiary agreement under the Economic Development Agreement. The Interior Plateau may be favourable for mineral deposits, but exploration has been hampered by a blanket of plateau basalt and glacial drift. As part of a regional program to assess the potential for buried mineralization, the Geological Survey of Canada (GSC) will conduct regional airborne magnetic and radiometric surveys, bedrock and surficial geological mapping, till geochemistry, and a biogeochemical survey. Preliminary work in 1992 included orientation work for the multiparameter geophysical and biogeochemical surveys, orientation surficial mapping and till geochemistry, and bedrock mapping along the western margin of Interior Plateau. All GSC projects will be active in 1993, and will conclude in 1994-1995. The resulting data will be published as yearly reports and maps and will be summarized in a volume in 1996.

**Résumé :** Le programme du Plateau intérieur est une initiative multidisciplinaire de l'Entente Canada-Colombie-Britannique sur l'exploitation minérale de 1991-1995, entente auxiliaire qui s'inscrit dans le cadre de l'Entente de développement économique. Le Plateau intérieur pourrait receler des gisements de minéraux, mais la présence d'un manteau de basalte des plateaux et de dépôts glaciaires a nuit à l'exploration. Dans le cadre d'un programme régional d'évaluation de la minéralisation enfouie potentielle, la Commission géologique du Canada (CGC) entreprendra des levés magnétiques et radiométriques aériens régionaux, des levés biochimiques, des travaux de cartographie de la géologie de la surface et du substratum rocheux et une étude de la géochimie des tills. Les travaux préliminaires effectués en 1992 comprennent les travaux d'orientation pour les levés géophysiques et biogéochimiques à paramètres multiples, les travaux initiaux de cartographie de la surface et d'étude de la géochimie des tills, et la cartographie du substratum rocheux le long de la marge ouest du Plateau intérieur. Tous les projets de la CGC seront en marche en 1993 et se termineront en 1994-1995. Les résultats seront publiés sous la forme de rapports annuels et de cartes, et seront résumés dans un volume en 1996.

---

<sup>1</sup> Mineral Resources Division, Ottawa

<sup>2</sup> Geophysics Division, Ottawa

<sup>3</sup> Terrain Sciences Division, Ottawa

## INTRODUCTION

The Interior Plateau Subprogram is a new initiative, funded and operated under the guidelines of the Canada-British Columbia Agreement on Mineral Development 1991-1995 (MDA). The Geological Survey of Canada (GSC) and the British Columbia Geological Survey Branch (BCGS) will carry out a number of multidisciplinary projects throughout the Interior Plateau region of British Columbia (Fig. 1). GSC projects include a regional total field aeromagnetic survey, two 1:50 000-scale bedrock mapping projects, a surficial geology and till geochemistry project, an airborne multiparameter (gamma ray, magnetic, VLF-EM) survey, and a biogeochemical survey (Table 1, Fig. 2). The objective of these projects is to provide new data to upgrade the existing geological, geophysical, and geochemical databases. The integration of the new geoscientific information will aid mineral exploration and will better support mineral potential assessments and informed resource management and land-use decisions in the Interior Plateau region.

Mineral exploration in the Interior Plateau region in the past has been severely hampered by inaccessibility, dense vegetation, extensive glacial drift, a blanket of Miocene lava flows, an obsolete geological database, and lack of modern geophysical/geochemical coverage. Geological environments favourable for economic mineral deposits exist in areas adjoining the Interior Plateau study area (e.g., porphyry style deposits such as Endako and Gibraltar, the Equity Silver deposit and epithermal precious metal deposits such as Silver Queen and Blackdome; Fig. 1). Extrapolation of structural trends, plutonic suites, and stratigraphy from these adjoining areas suggests there is potential for similar, undiscovered

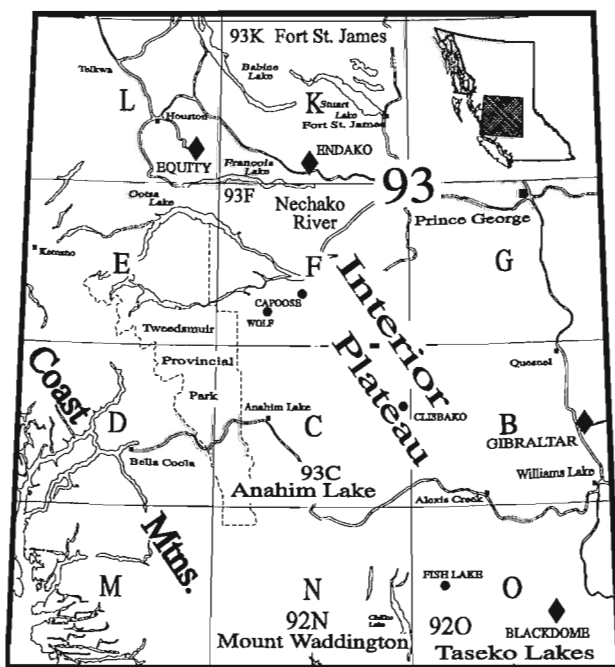


Figure 1. Features of the Interior Plateau region, showing major producing mines (shown by diamonds) and other significant mineral deposits.

Table 1. Schedule of sub-projects in the Interior Plateau program

Project/Coordinator	1992	1993	1994	1995
AEROMAGNETIC TOTAL FIELD SURVEY D. Teskey			Orientation Survey	FINAL MAPS (1:50,000 1:100,000) and PROJECT VOLUME
			Full Survey	
			Report and Map Preparation	
1:50,000 BEDROCK MAPPING P. van der Heyden C. Hickson				
SURFICIAL GEOLOGY AND TILL GEOCHEMISTRY SURVEYS A. Plouffe				
BIOGEOCHEMICAL SURVEY C. Dunn				
AIRBORNE MULTIPARAMETER SURVEYS (Gamma ray, Magnetic and VLF) J. R. Shives B. Ballantyne D. Harris				

deposits in the Interior Plateau region. The primary aim of the Interior Plateau program is to further delineate this potential for undiscovered mineral deposits.

This report gives a brief overview of projects carried out by the GSC, including preliminary results for the multiparameter and biogeochemical surveys, for the surficial geology and till geochemistry project, and for one of the bedrock mapping projects. BCGS Mineral Development Agreement projects carried out in 1992-1993 are summarized by Diakow and van der Heyden (1993, and references therein). GSC projects, for which preliminary results are presented in this report, were initiated in 1992: All GSC projects will be active in 1993-1994, and will conclude in 1994-1995. Annual reports and maps will be published for projects active during a given year. A final volume synthesizing the Interior Plateau program is planned for publication in 1995-1996.

## REGIONAL AEROMAGNETIC SURVEY

The Aeromagnetic Surveys Section, Geophysics Division (Dennis Teskey) is co-ordinating a regional aeromagnetic survey of an area in the Interior Plateau that will cover 59 adjoining 1:50 000 map areas (Fig. 2). The airborne survey will be contracted and flown in the summer of 1993. Processing and interpretation of the digital data will be followed by publication of high-resolution total field maps at 1:100 000-scale and specific maps at 1:50 000-scale, scheduled for release in 1994. Data processing and interpretation, an integral part of this project, are necessary to minimize effects of thin but extensive Miocene flood basalts that may mask patterns caused by older strata and deeper structures.

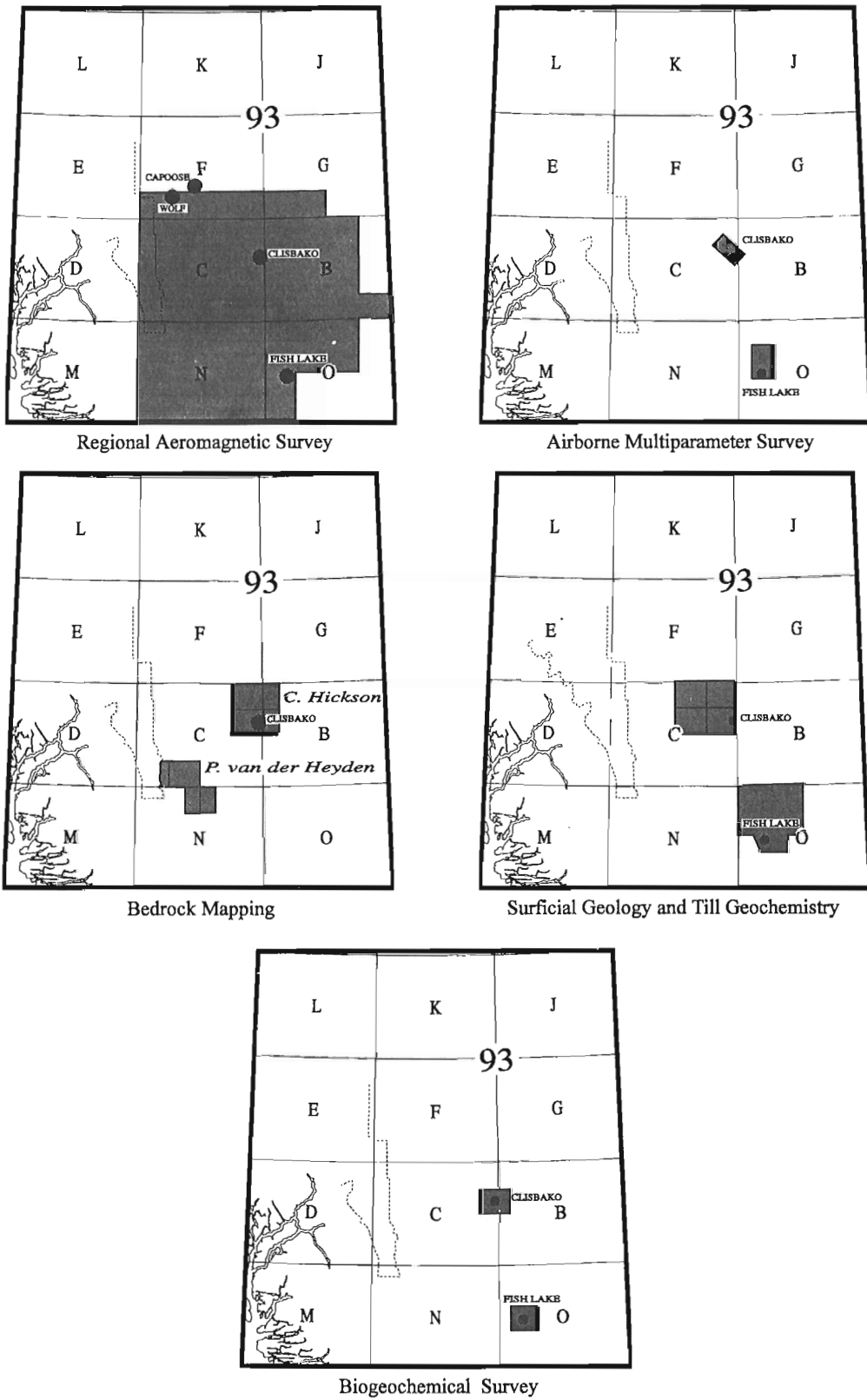


Figure 2. Location of projects in the Interior Plateau region.

## **MULTIPARAMETER GEOPHYSICAL/ GEOCHEMICAL SURVEYS**

An integrated exploration method and model for the discovery of blind porphyry systems has been developed and applied in the Cordillera (Ballantyne et al., 1992; Harris and Ballantyne, 1992; Pilon et al., 1992; Plouffe, 1992; Shives, 1992). The exploration model uses various airborne and ground geophysical and geochemical techniques in a multiparameter, multimedia approach. Under the current Mineral Development Agreement the methodology continues to be tested. In the Interior Plateau, Mineral Resources Division (Rob Shives) will provide digital, high resolution airborne gamma ray spectrometric, total field magnetic, and VLF-EM data for two key exploration targets: epithermal precious metal occurrences in the Clisbako River area (93B,C) and porphyry copper-gold prospects in the Fish Lake area (92O) (Fig. 2).

Similar multiparameter surveys completed in the Mount Milligan area of the Quesnel Trough, east of the Interior Plateau (GSC Open File 2535) show that ground and airborne gamma ray spectrometric methods can be used to explore for both porphyry and precious metal epithermal systems. Gamma ray spectrometry delineates anomalous radioelement concentrations (K, U, Th) caused by mineralizing processes in bedrock or in derived surficial materials. Radioelement enrichment or depletion, in concert with magnetic and VLF-EM signatures, can thus be interpreted and used as a guide for mineral exploration.

Several features present within the planned Interior Plateau survey areas should respond well to these techniques: variable degrees of potassic alteration are present at the Clisbako River, Fish Lake and Mega deposits; the Fish Lake region contains various intrusive phases and the deposit itself has distinct magnetite enrichment; and structural features, such as the Yalakom fault, may be delineated by the VLF-EM technique. The combination of airborne chemical (gamma ray), magnetic and conductive methods thus offers a powerful mineral exploration and mapping tool within the Interior Plateau. The results of these surveys will enhance ongoing and future mapping and industry exploration programs. Planned outputs will include colour contour maps and profiles of radioelement, magnetic and VLF-EM data.

Ground orientation and follow-up studies, an integral project component and conducted in collaboration with other Mineral Development Agreement projects, will include ground spectrometry (Rob Shives), mineralogical studies (Don Harris), and multimedia geochemical sampling (Bruce Ballantyne). These will enable interpretation of the airborne patterns, demonstrate practical applications of the data, and will foster the transfer of a relatively simple, inexpensive ground technique to mappers and explorationists.

During September 1992 a brief ground orientation survey was initiated in the Fish Lake deposit area, in conjunction with preliminary surficial mapping and till sampling by Alain Plouffe and Bruce Ballantyne. Field work included collection of drill core, outcrop and overburden samples within the Fish Lake deposit area and regionally to the north. Gamma

ray spectrometry and magnetic susceptibility measurements were made on drill core and local outcrops. No orientation work was done in the Clisbako River area.

Preliminary results of the magnetic susceptibility (MS) measurements demonstrate the strong relationship between magnetite and higher ore grades within the Fish Lake deposit. These magnetic susceptibility measurements are easily and accurately made using a small, hand held instrument. This method should be routinely used during core logging to guide descriptive logging and sampling.

To test the ability of gamma ray spectrometry to distinguish lithologies and alteration types in drill core, two methods were tested. Results showed that the conventional use of a lead container to shield the gamma ray detector from background radioactivity (thus increasing signal to noise) is useful only when very long count times are used (20 minutes or longer). This is because the drill core provides a relatively small source of low radioactivity. Minor K variations did correlate with alteration assemblages, but this method is not considered practical from an industry point of view. A second method was devised whereby an entire core box provides the source. This yielded interpretable but still only qualitative results. Detailed correlation between descriptive logs and our "in situ" measurements are in progress. The core-box method shows that detectable variations in K, U, and Th exist in the various intrusive phases and alteration types within the Fish Lake deposit. However, we suggest that the best way to measure these variations would be to use the better constrained, fully quantitative ability of borehole gamma ray logging (Killeen, 1991). The multiparameter capability of borehole logging also allows distinction of complex intrusive phases, alteration assemblages and structural features.

Near the Fish Lake deposit, excavation of diamond drill-hole water sump pits has exposed weathered, in-situ bedrock. This regolith was examined for gold and the associated heavy mineral suite. Regolith exposed in bulldozer trenches in the Albert Zone, northeast of the Fish Lake deposit, was sampled to examine possibly liberated Au grains and heavy minerals. This zone is reported to have epithermal characteristics. Gold grain morphology, composition and heavy mineral suites from these bedrock exposures will be compared to those found in their associated, down-ice tills.

## **BEDROCK MAPPING**

### ***Geology, eastern Coast Belt and western Intermontane Belt near 52°N***

In 1992 Cordilleran Division (Peter van der Heyden and Arthur Calderwood) commenced bedrock mapping in the Charlotte Lake (93C/3) and Junker Lake east-half (93C/4E) map areas (Fig. 2); the Bussel Creek east-half (92N/14E) and Tatla Lake west-half (92N/15W) map areas will be mapped during the 1993 field season (Peter van der Heyden and Peter Mustard, Cordilleran Division). Exploration prospects in these areas include the Copper Queen Cu-Mo showing (Minfile 093C-001 and 093C-004), Ada Cu showing (Minfile 093C-005), Mountain Boss Au-Ag-Cu developed prospect



(Minfile 092N-010), Briton Fe prospect (Minfile 092N-011), Bluebell Au-Graphite prospect (Minfile 092N-012), Orwill Au-Ag-Cu-Zn-Pb-Sb-Bi prospect (Minfile 092N-033), PIN Cu showing (Minfile 092N-053), KLIN Au showing (Minfile 092N-022), and Golden Rose Au-As showing (Minfile 092N-046).

Charlotte Lake (93C/3) and Junker Lake east-half (93C/4E) map areas (Fig. 3) are underlain predominantly by granitoid and metamorphic rocks of the eastern Coast Belt. Extensive glacial drift and felsenmeer (ca. 80% of the total surface area) obscures relationships between three primary map units: a Middle-Late Jurassic metamorphic and plutonic basement complex, Early Cretaceous(?) volcanic rocks, and a younger, economically important pluton. The following notes summarize preliminary results of the 1992-93 field season.

The study area is dominated by a regionally extensive Middle-Late Jurassic complex (the Atnarko Complex of van der Heyden, 1990, 1991) consisting of screens and pendants of greenschist and amphibolite facies metavolcanic schist and gneiss, enclosed in variably foliated diorite, quartz diorite and tonalite. A metarhyolite from the metavolcanic succession yielded a concordant 190 Ma U-Pb date, and two phases of the host tonalite yielded 160 Ma (van der Heyden, 1991) and 145 Ma (unpublished data, 1993) U-Pb ages, respectively. Foliations and ductile shear zones in the complex trend northeasterly and dip steeply; this trend is orthogonal with respect to the regional northwesterly trend of the Coast Belt.

Relatively unmetamorphosed Lower Cretaceous(?) volcaniclastic rocks appear to lie nonconformably on the basement complex north of Charlotte Lake. The contact itself was not observed, but it appears to be marked by a volcanic boulder conglomerate. The volcanic rocks are unmetamorphosed near the basement tonalite, and granitoid dykes are absent from the volcanic rocks.

The northwestern part of the study area is underlain by biotite-muscovite-garnet granite and related porphyritic and pegmatitic/aplitic intrusions, which cut the basement complex. Contact relations with the Lower Cretaceous(?) volcanic rocks are unclear; the contact may be a fault. The contact zone with the older tonalite is marked by malachite-azurite-magnetite-quartz veins in an area that probably includes the Ada copper showing (Minfile No. 093C-005; location uncertain).

The study area is cut by numerous northeasterly, northerly, and northwesterly trending shear zones. Several of these appear to have localized hydrothermal activity related to the younger granitic intrusions. The Copper Queen copper-molybdenum showing (Minfile No. 093C-001 and 093C-004) in the southwestern Charlotte Lake map area may represent a fault-controlled, copper and molybdenum bearing hydrothermal stockwork.

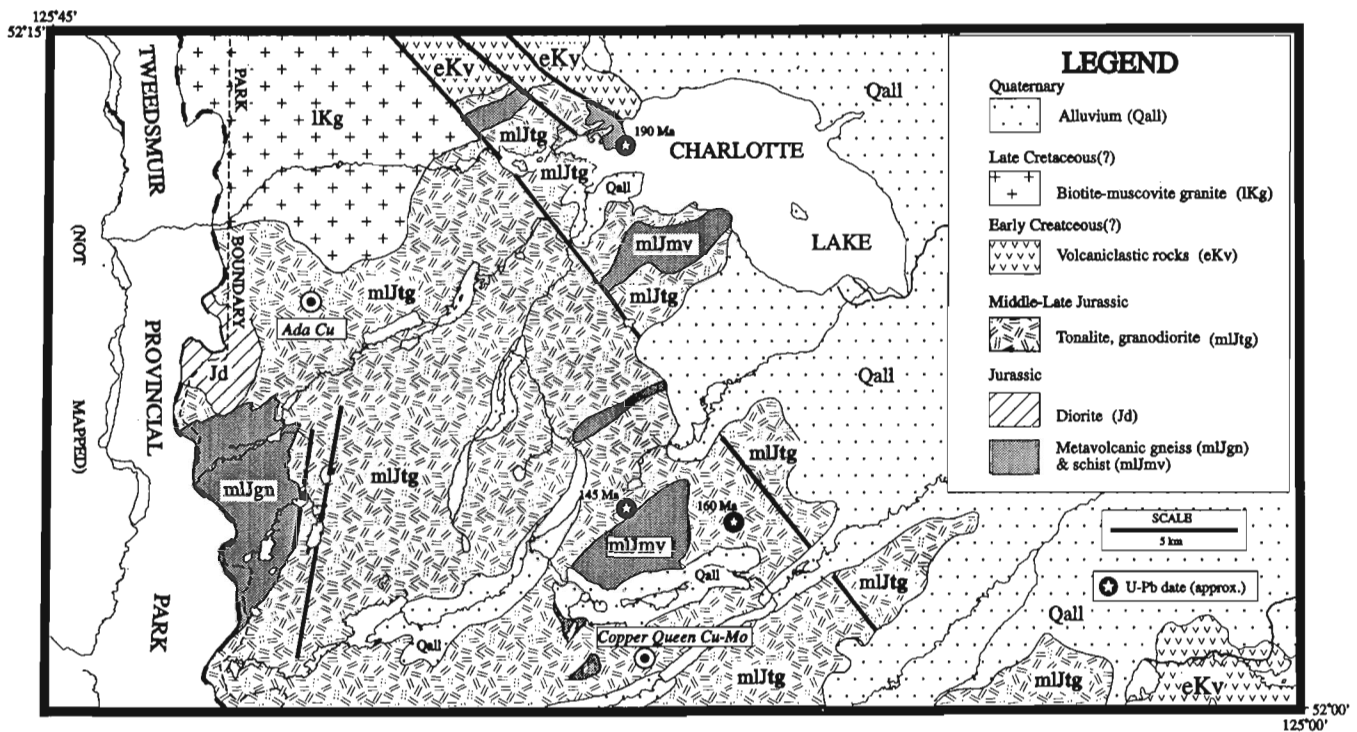


Figure 3. Simplified geology, Charlotte Lake (93C/3) and Junker Lake east-half (93C/4E) map areas.

### *Eocene volcanic stratigraphy*

In much of central British Columbia, Eocene magmatism is manifest as a broad field of continental volcanic rocks and associated plutons, many of which appear related to extensional tectonics. Several former producing mines and scattered prospects throughout the Interior Plateau represent epithermal-type precious metal mineralization related to this magmatic and tectonic episode (e.g., Blackdome, Wolf). Very little is known about the age, distribution, chemistry, and regional correlation of these magmatic rocks.

Starting in the summer of 1993, the Cordilleran Division (Cathie Hickson) will commence a bedrock mapping project in the central region of the Interior Plateau (93C/9, 16 and 93B/12, 13; Fig. 2). The focus will be on elucidating the Eocene stratigraphy and geochemistry of the study area, and on providing regional correlations with Eocene volcanic rocks to the northwest and to the southeast. Eocene rocks in the area contain several precious metal occurrences; the most notable occur in the Clisbako River area.

### **SURFICIAL GEOLOGY AND TILL GEOCHEMISTRY**

Terrain Sciences Division (Alain Plouffe) is engaged in a two-part project that addresses regional surficial geochemistry and Pleistocene glacial stratigraphy, ice flow pattern indicators, and till lithologies. The project area comprises the northwest quadrant of Taseko Lakes (92O) and the eastern sector of Anahim Lake (93C) map areas (Fig. 2). Regional till sampling by the BCGS, in the eastern sector of Anahim Lake map area (Giles and Kerr, 1993; Proudfoot, 1993), was completed in 1992. Reconnaissance sampling in the Taseko River valley, and a detailed survey on the Fish Lake property, were initiated in the fall of 1992, in order to assess the mineralization signature in till. Regional sampling will be continued in accessible areas of NTS map sheets 92O/5 and 92O/12 during the 1993 field season.

The silt plus clay size fractions (<63 m or -230 mesh) of all till samples collected in 1992 were analyzed by ICP-AES (Ag, Al, As, Ba, Be, Bi, Ca, Cd, Co, Cr, Cu, Fe, Ga, Hg, K, La, Mg, Mn, Mo, Na, Ni, P, Pb, Sb, Sc, Sr, Ti, Tl, U, V, W, and Zn) and INAA (Ag, As, Au, Ba, Br, Ca, Co, Cr, Fe, Hf, Hg, Ir, Mo, Na, Rb, Sb, Sc, Se, Sn, Sr, Ta, Th, U, W, Zn, La, Ce, Nd, Sm, Eu, Tb, Yb, and Lu) in a commercial laboratory. Study of the heavy mineral assemblages in surficial sediments of the area is presently in progress.

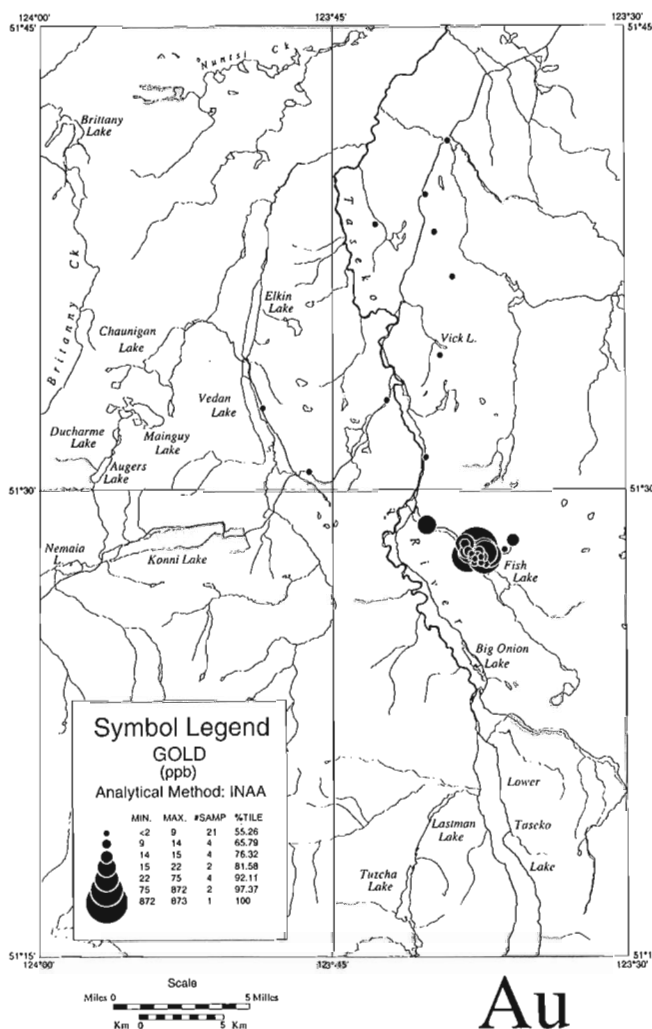
The dot value geochemical map depicted in Figure 4 is an example of the type of product which will be released in a final open file publication. The final product will also include information about ice flow directions and bedrock geology. Such maps will document background concentrations of various elements in till over different bedrock lithologies, and will have applications in drift prospecting, establish baseline data for environmental assessments, and define anomalous areas for mineral exploration.

### **BIOGEOCHEMICAL SURVEY**

Mineral Resources Division (Colin Dunn) is evaluating the effectiveness of biogeochemistry as a prospecting tool by sampling vegetation at several mineralized sites in the Interior Plateau region. The study areas, located in the Fish Lake and Clisbako River areas (Fig. 2), encompass roughly the equivalent of two 1:50 000-scale map sheets. In a previous case study over the QR deposit in the Quesnel trough, the biogeochemical survey demonstrated that reconnaissance level biogeochemical mapping using data obtained from tree top tissues is a rapid, cost-effective, and efficient means of detecting mineralized bedrock concealed by dense forest and overburden.

The Interior Plateau project will involve detailed ground and airborne biogeochemical reconnaissance surveys. A brief orientation survey, carried out by Rob Scagel (Pacific Phytometric Consultants, Surrey, B.C.) in 1992, will be followed

Fish Lake Area - Till Geochemical Sampling Program



**Figure 4.** Dot value geochemical map for Au concentrations in the silt plus clay (<63 m or -230 mesh) size fraction of till samples, NTS sheets 92O/5 and 92O/12.

by a full survey in 1993, in collaboration with other project leaders in the area. Approximately 50 elements will be analyzed (see above under surficial geology and till geochemistry), and results will be compiled on geochemical maps which will focus attention on areas with anomalous metal concentrations. The results will be interpreted in light of geophysical, surficial, and bedrock geological data obtained from the related surveys.

During the 1992 orientation survey, outer bark and the top 3 years growth of lodgepole pine (*Pinus contorta*) were collected from 21 sites near Eocene epithermal precious metal mineralization in the Clisbako River area. In addition, samples of shrub birch, willow and alder were obtained. Trace element concentrations in general are fairly low, although there is weak enrichment of Au, Mo, As, Cs, and Ni in the pine tops. Bark samples yield higher concentrations of Au, Ag, As, and Cd, and confirm the elevated background levels of Mo. Birch twigs are locally enriched in Au and As. Ash samples of alder yield unusually high levels of Au (300 ppb) and Mo (73 ppm) near the North Zone.

A similar suite of tissue types was collected from 26 sites around the Fish Lake exploration site operated by Taseko Mines Ltd. Similar levels of trace metals to those found at Clisbako River are present in the trees. The pine tops from the immediate vicinity of the Fish Lake prospect yield weak enrichments of Au, Mo, Cu, Cs, and Ni. The pine barks yield some enrichment of Au (up to 67 ppb in ash), Cu, and As. Trees growing over the surrounding plateau basalts are relatively enriched in Cr, Fe, Na, Sc, and REEs.

## CONCLUSIONS

The Interior Plateau Program is a multidisciplinary initiative that is part of the Canada-British Columbia Agreement on Mineral Development 1991-1995, a subsidiary agreement under the Economic and Regional Development Agreement. The GSC will carry out a regional aeromagnetic survey, airborne multiparameter surveys, bedrock and surficial geological mapping, and a biogeochemical survey, in areas that are favourable for mineral deposits but are mostly covered by extensive plateau basalts and glacial drift. The resulting data will be essential for accurate mineral potential assessments and informed resource management and land-use decisions in the Interior Plateau region.

## ACKNOWLEDGMENTS

We thank the exploration staff of Taseko Mines Ltd. and Valerie Gold Resources Ltd. for full co-operation and assistance prior to and during initial fieldwork for the multiparameter

geophysical and surficial geology surveys. Arthur Calderwood, Steve Metcalfe, Doreen Chan, and James McKinnon Matthews provided able and cheerful assistance during the Charlotte Lake-Junker Lake mapping project; Rob Owens (Alpine Helicopters), and John Way (Wayco Aviation) are thanked for flying us safely to and from our various field locations. Dirk Tempelman-Kluit reviewed an earlier version of the manuscript; Bev Vanlier typed the final version. Table 1 and Figures 1 and 2 are based on earlier versions drafted by Larry Diakow (BCGS).

## REFERENCES

- Ballantyne, S.B., Harris, D.C., Shives, R.B.K., Ford, K.L., Holman P.B., Plouffe, A., Judge, A.S., and Pilon, J.A.**  
1992: An integrated approach and model for the discovery of blind Cu-Au porphyry systems; in Forum 92 Program with Abstracts; Geological Survey of Canada, p. 18.
- Diakow, L.J. and van der Heyden, P.**  
1993: An overview of the Interior Plateau Program; in Geological Fieldwork 1992; British Columbia Ministry of Energy, Mines and Petroleum Resources, Paper 1993-1, p. 53-56.
- Giles, T.R. and Kerr, D.E.**  
1993: Surficial geology in the Chilanko Forks and Chezacut areas (93C/1,8); in Geological Fieldwork 1992; British Columbia Ministry of Energy, Mines and Petroleum Resources, Paper 1993-1, p. 483-490.
- Harris, D.C. and Ballantyne, S.B.**  
1992: Applied mineralogy and geochemical surveys of copper-gold porphyry systems in northern Quesnel Trough, British Columbia; in Forum 92 Program with Abstracts; Geological Survey of Canada, p. 20.
- Killeen, P.G.**  
1991: Borehole geophysics: Taking Geophysics into the Third Dimension; Geos, v. 20, No.2, Insert.
- Pilon, J.A., Plouffe, A., Judge, A.S., and Ballantyne, S.B.**  
1992: Ground penetrating radar surveys for quaternary geology studies and mineral exploration in central British Columbia; in Forum 92 Program with Abstracts; Geological Survey of Canada, p. 22.
- Plouffe, A.**  
1992: Quaternary stratigraphy and history, central British Columbia; in Forum 92 Program with Abstracts; Geological Survey of Canada, p. 22-23.
- Proudfoot, D.N.**  
1993: Drift exploration and surficial geology of the Clusko River and Toil Mountain map sheets (93C/19,16); in Geological Fieldwork 1992; British Columbia Ministry of Energy, Mines and Petroleum Resources, Paper 1993-1, p. 491-498.
- Shives, R.B.K.**  
1992: Airborne and ground gamma ray spectrometric mapping in the Quesnel Trough, British Columbia; in Forum 92 Program with Abstracts; Geological Survey of Canada, p. 24.
- van der Heyden, P.**  
1990: Eastern margin of the Coast Belt in west-central British Columbia; in Current Research, Part E; Geological Survey of Canada, Paper 90-1E, p. 171-182.  
1991: Preliminary U-Pb dates and field observations from the eastern Coast Belt near 52°N, British Columbia; in Current Research, Part A; Geological Survey of Canada, Paper 91-1A, p. 79-84.



INTERIOR PLAINS  
AND ARCTIC  
CANADA

PLAINES INTÉRIEURES  
ET RÉGION ARCTIQUE  
DU CANADA



# Ground temperatures and recent coastal change at the north end of Richards Island, Mackenzie Delta, Northwest Territories

Larry Dyke and Stephen Wolfe<sup>1</sup>  
Terrain Sciences Division

*Dyke, L. and Wolfe, S., 1993: Ground temperatures and recent coastal change at the north end of Richards Island, Mackenzie Delta, Northwest Territories; in Current Research, Part E; Geological Survey of Canada, Paper 93-1E, p. 83-91.*

---

**Abstract:** Coastal retreat and redeposition of sediments, as well as breaching and infilling of lakes, has resulted in a wide variation in ground temperatures in the shallow seabottom and adjacent shoreline at North Head, Richards Island, Northwest Territories. The ground thermal regime beneath the coastal sediments suggest that coastal processes have been vigorous for at least the last 250 years. The most significant change is the deposition of a platform of redeposited sediments, over a former embayment, that has probably lengthened about 3 km in the past 50 years. Ground temperatures are presently adjusting to this process.

**Résumé :** Le recul du littoral, la resédimentation, ainsi que la percée et le colmatage de lacs ont entraîné de fortes variations de la température dans le sol du fond marin peu profond et du littoral contigu au cap North, dans l'île Richards (T.N.-O.). Le régime thermique du sol sous les sédiments littoraux porte à croire que les processus littoraux sont importants depuis au moins 250 ans. Le changement le plus significatif est l'accumulation, au-dessus d'une ancienne baie, d'une plate-forme de sédiments redéposés qui s'est probablement allongée de 3 km depuis 50 ans. Les températures du sol s'ajustent actuellement à ce processus.

---

<sup>1</sup> Department of Geography, University of Guelph, Guelph, Ontario N1G 2W1

## INTRODUCTION

Rising relative sea level along the Beaufort Sea coasts of the Tuktoyaktuk Peninsula and Richards Island is promoting coastal erosion of frozen, unconsolidated sediments in these areas. Cliff tops are retreating up to several metres per year and occasionally more than 10 m per year (Harper, 1990; Mackay, 1986; Forbes and Frobels, 1985). In addition, nearshore bathymetry is apparently keeping pace with terrestrial retreat. Longshore currents are active in the region, as suggested by prominent spits extending from islands and promontories exposed to storm waves. Consequently, sediment is transported away from the locally eroding coast and is redeposited in nearby depocentres. Therefore, offshore erosion locally accompanies coastal retreat and sediment is removed to form aggradational features elsewhere.

Permafrost is responding to the erosion and redeposition of sediment. Where coastal retreat is active, the depth to ice-bonded permafrost deepens as the surface is subjected to warmer temperatures resulting from submergence. Conversely, ice-bonded permafrost may be aggrading in areas of sediment deposition, where water depths are reduced sufficiently to permit bottom-fast winter sea ice to form. Therefore, ice-bonded permafrost may be aggrading into formerly frozen sediments that were previously thawed by submergence. In addition, recooling of sediments that were warmed but not thawed may also occur. Finally, the retreating coastline also intersects lakes. These may drain or be inundated, depending on the lake bottom elevation relative to sea level. Subsurface temperatures in the former lake basins respond to these changes, further complicating the subbottom temperature distribution in the Beaufort Sea. This paper reviews the effects of coastal dynamics on subsurface temperatures and permafrost and describes several examples of the thermal response to coastal retreat and deposition at North Head, Richards Island, in the Beaufort Sea region.

Oil pipeline construction has been considered in the vicinity of North Head, Richards Island (Fig. 1). As a consequence, considerable attention has been given to the

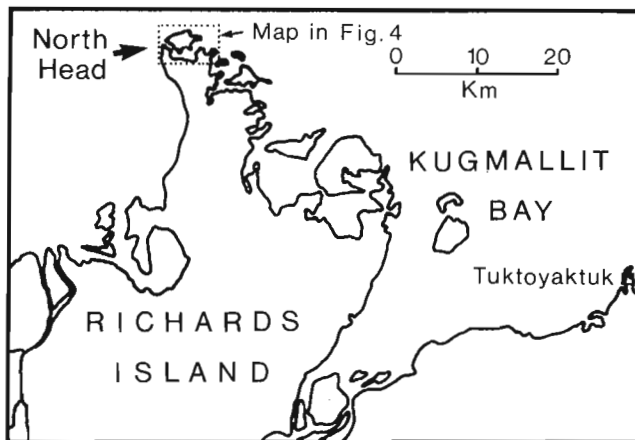


Figure 1. Location of North Head.

evolution of this portion of the Beaufort Sea coastline (Hill et al., 1986; Dallimore et al., 1988). On the west side of North Head, detailed temperature cross-sections have been made for two 1.5 km transects across an eroding and a stable segment of coast (Kurfurst and Dallimore, 1991; Kurfurst, 1986, 1987). Ground temperatures and stratigraphy are also available at several locations immediately to the east. These include relic lake basins and a depositional platform (Wolfe, 1989; Dallimore, 1991). Together, this information provides a representative sampling of the range of ground thermal regimes in a dynamic coastal permafrost setting.

## NORTH HEAD ERODING AND STABLE COASTS

Coastal erosion at North Head is most rapid along the northwest-facing portion of the coast. Subsurface temperatures along the borehole transect across this segment of coast (see Fig. 4, below) reveal an abrupt subsurface temperature increase in submerged sediments. As coastal retreat progresses, a point initially at the shoreline is covered in winter with an increasing thickness of bottom-fast ice. Across this zone, average annual temperatures increase from about  $-8^{\circ}\text{C}$  near the shoreline to about  $1^{\circ}\text{C}$  offshore, at the point of maximum thickness of bottom-fast ice (Fig. 2). The zone is about 100 m wide at this site. Using the maximum measured retreat rate of  $3.2\text{ m/a}$  (Dallimore et al., 1988), it would require

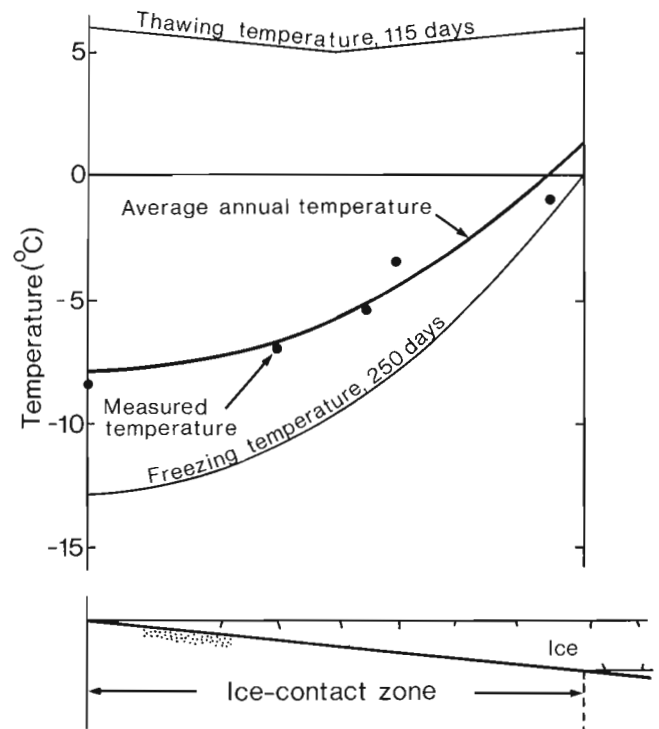


Figure 2. The average annual temperature on the seafloor for the zone with bottom-fast winter sea ice in the North Head area. The freezing and thawing indices used to construct this curve are also shown (from Dyke, 1991).



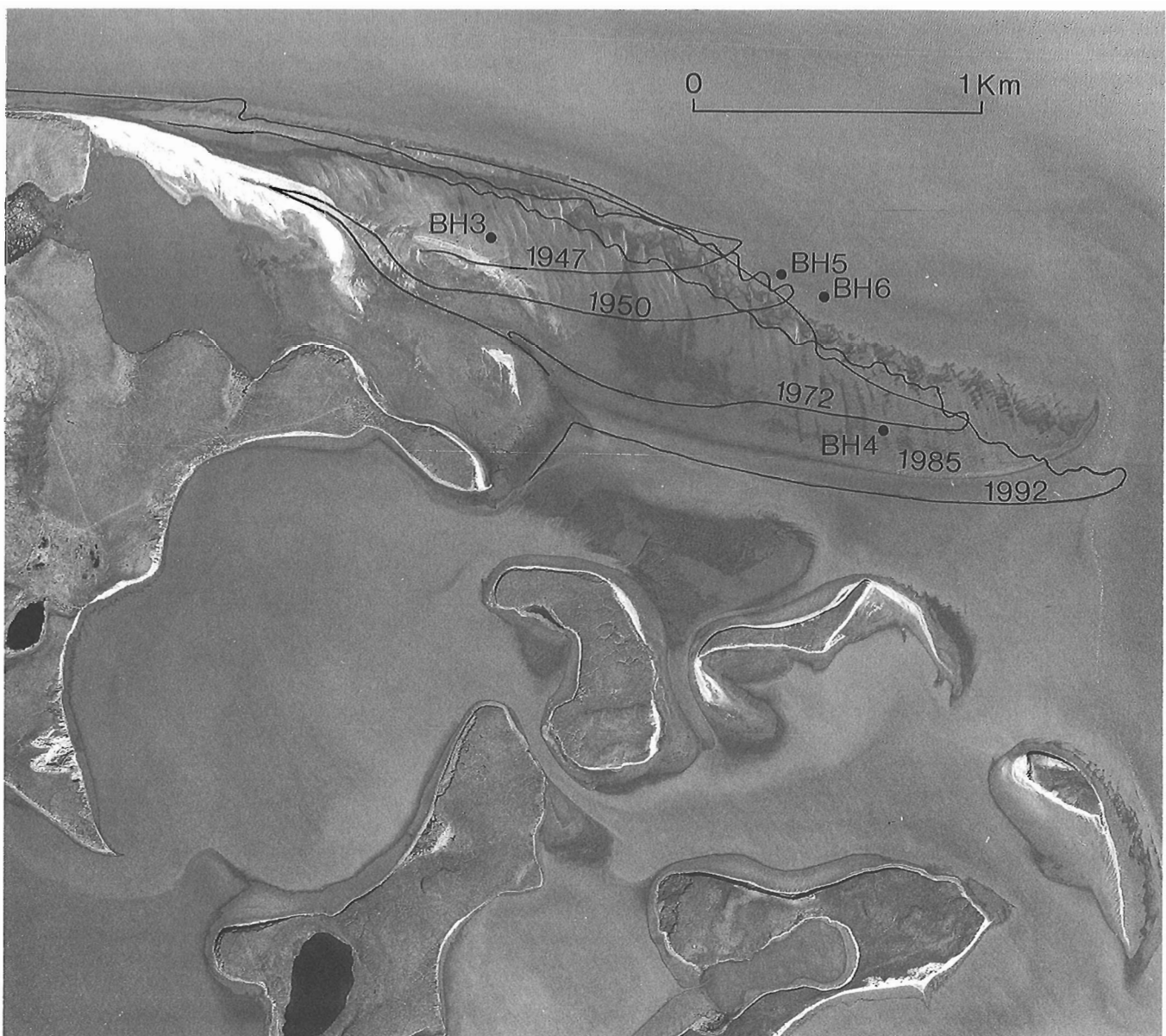
about 30 years for a point initially at the shoreline to be located beneath the offshore limit of this zone. This rate is rapid enough to result in continued warming beneath the seaward edge of the bottom-fast ice zone. Seaward of this point, the seabottom temperature remains above 0°C and thawing begins. With further retreat, thawing continues and a history of coastal retreat is reflected in the rate with which the top of ice bonding deepens with distance offshore.

In contrast, the borehole transect across the stable coast site crosses a bottom-fast sea ice zone about 1 km wide (see Fig. 4, below). The water depth increases steadily across this zone and, like the shoreline at this site, has probably not changed significantly in the last 50 years. Consequently, ground temperatures at this site are likely in equilibrium with surface conditions and clearly reflect the influence of

increasing thickness of bottom-fast ice. Figure 2 includes the measured temperatures at the depth of zero annual change taken from boreholes on this transect (derivation of the average annual temperature curve in Figure 2 is discussed under "Early stages of permafrost aggradation"). The relationship between temperature and ice thickness in Figure 2 describes the major temperature change that any point will undergo during coastal retreat or sediment accumulation.

### NORTH HEAD SPIT AND PLATFORM

A sand and gravel spit and silty sand platform (the term platform is used to describe the broad, flat extension of the spit) are presently aggrading eastward from the extreme

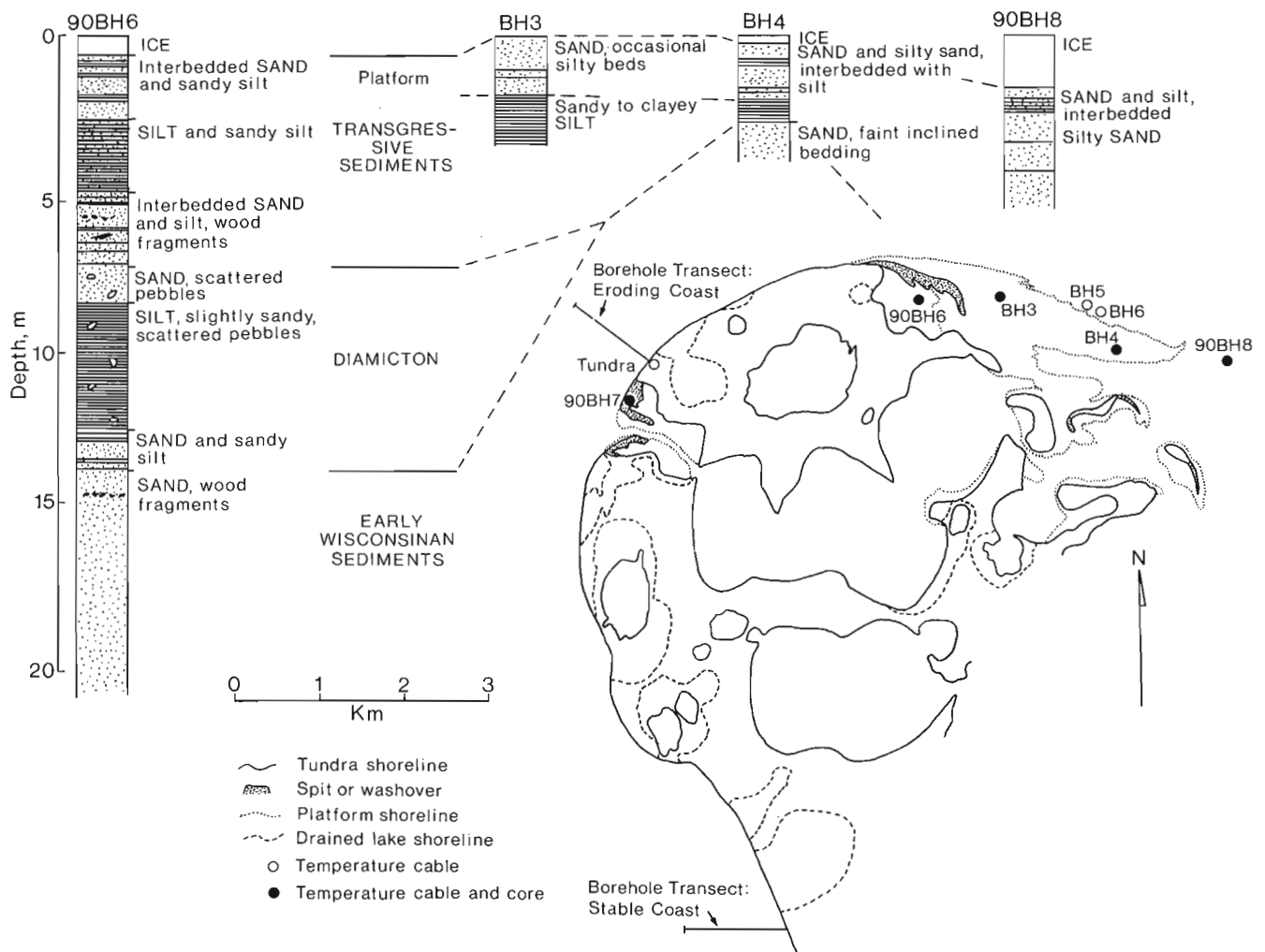


**Figure 3.** A 1985 vertical airphoto (National Air Photo Library photograph A26754-199) showing the extent of the sediment platform at North Head for various times back to 1947.

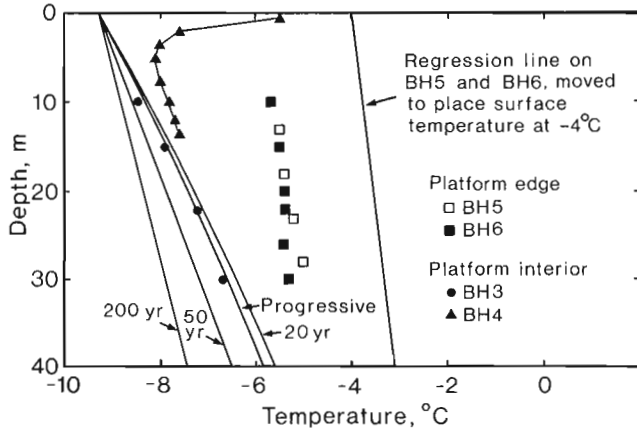
northern end of Richards Island. Dallimore and Wolfe (unpub. report) have linked the development of the platform to coastal retreat along the northwest portion of North Head. Wolfe (1989) has suggested that rapid platform growth was initiated sometime between 1937 and 1947, based on the increasing size as seen on successive airphotos (1947 to 1992 outlines shown on Fig. 3). Two boreholes on the platform, each about 4 m deep, penetrate a topmost unit of sand and interbedded sand and silt about 1.5 m thick (BH3 and BH4 in Fig. 4). This unit is thought to represent sediments deposited during construction of the platform. A sandy to clayey silt unit occurs beneath the platform deposit in each borehole and may be of lacustrine or nearshore marine origin. In BH4 these sediments lie in sharp contact with a lower massive sand thought to be part of the transgressed sediments (Kittigazuit sands) predating the Early Wisconsinan Toker Point glaciation (Rampton, 1988). This lower contact represents the surface of the submerged sediments, after coastal erosion has removed higher land separating the Beaufort Sea from the present lagoon.

The apparent onset of sedimentation at the site of the platform about 50 years ago coincides with an inferred increase in coastal retreat rates along the northwest side of North Head. This increase is based on a prediction of the retreat rate required to produce the existing frost table profile along the transect at the retreating coast 3 km west of the North Head spit (Dyke, 1991). The additional flux of sediment may have upset a previous sediment balance and resulted in rapid construction of the platform. While the cause of the increased retreat rate is open to speculation, the recent formation of the platform is confirmed by an analysis of subsurface temperature profiles, as described below.

Figure 5 shows temperatures with depth for four locations on the North Head platform. The following discussion compares the temperature profiles from two boreholes located along the seaward edge of the platform (BH5 and BH6) with the two located in the interior (BH3 and BH4) as shown in Figure 4. The two seaward edge temperature profiles are about 150 m apart and were located in approximately 50 cm of water on a fine sand bar forming the seaward boundary of



**Figure 4.** Stratigraphic descriptions of boreholes on the North Head platform and location of all boreholes referred to in text. Platform shoreline for 1985 is plotted.



**Figure 5.** Ground temperature measurements for boreholes BH3, BH4, BH5, and BH6 in the North Head area. The regression line shows the temperature profile assumed to have existed at BH3 prior to platform aggradation. The family of curves show present ground temperatures that would result from a 5°C cooling 20, 50, and 200 years ago and a progressive cooling of 1°C every 10 years starting 50 years ago.

the platform. As shown in Figure 5, they have essentially identical temperature profiles. A linear regression on those measurements considered to be below the depth of annual temperature change (about 10 m) gives a mean annual surface temperature of about -6°C and a temperature gradient of about 0.02°C/m. The near-linearity and match of this gradient with the gradient beneath tundra at the location shown in Figure 4 (see Fig. 7 for tundra ground temperatures) suggest that the BH5 and BH6 temperatures are very close to equilibrium with the surface thermal regime. These platform-edge temperature profiles are assumed to supply an equilibrium temperature gradient against which the interior profiles can be compared. The shallow, near-equilibrium temperature gradient suggests that the thermal regime at this location has remained relatively unchanged for more than 50 years.

The platform has grown distally to the east and laterally to the south. The deepest interior borehole (BH3) shows a thermal gradient of up to 0.1°C/m and an approximate average annual ground surface temperature of -9°C. This thermal gradient is much greater than the gradients in boreholes BH5 and BH6 beneath the seaward edge of the platform. The temperature profile at BH3 thus suggests that temperatures are in the process of adjusting to a surface temperature change from some warmer temperature to about -9°C. This cooling could have been initiated by construction of the platform and subsequent subaerial exposure of platform sediments.

The surface temperature at BH3 prior to the initiation of platform growth can be inferred with the aid of the shallow stratigraphy. Platform sands overlie silts at a depth of about 1.5 m at this location and the present ground surface elevation is about 0.5 m above mean sea level. If the silts represent sediments transgressed by the construction of the platform, then the platform aggraded into water depths of about 1.0 m. Cooling transmitted to the seabottom after growth of this

thickness of ice would give an average annual temperature of -4°C, based on the temperature-ice thickness relationship presented in Figure 2.

Based on this estimate of the former seabottom temperature, a cooling of about 5°C has accompanied the construction of the platform. Using the thermal gradient defined by BH5 and BH6, and shifting the associated profile to place the surface temperature at -4°C gives a temperature profile for the BH3 location prior to the onset of platform aggradation (Fig. 5). This profile can now be used as an initial condition for the calculation of a temperature profile that matches the present profile at BH3.

A solution for the one-dimensional heat flow equation is used to calculate temperature changes from the initial condition shown in Figure 5. While this technique can only deal with an instantaneous change at the sediment surface, this restriction can be effectively circumvented by approximating a progressive change with a series of steps. The accuracy of the calculation is probably much more dependent on the values selected for thermal properties of the sediments. Thermal conductivities for frozen fine sand and silty sand from borehole 90BH6 range from 2.2 to 3.5 W/m°C with an average of 3.0 W/m°C. The range of heat capacities over the range of moisture contents encountered is less (1.2 to 1.5 J/cm<sup>3</sup>•°C, with an average of 1.4 J/cm<sup>3</sup>•°C). Therefore the variability in thermal diffusivity is primarily related to the thermal conductivity (thermal diffusivity = thermal conductivity/heat capacity, and characterizes the rate at which a material changes temperature).

The results of several temperature histories are plotted in Figure 5. All include a total cooling of 5°C over the times elapsed since the initiation of temperature change. Three curves show temperatures for an initial 5°C drop 20, 50, and 200 years ago. The other curve shows the temperatures caused by a progressive drop of 1°C every 10 years starting 50 years ago. All curves descend from -9°C, although the family of curves has been shifted slightly to the left to permit a clearer comparison with temperatures at BH3. The progressive cooling and sudden cooling 20 years ago both produce gradients similar to BH3. Spreading the 5°C cooling in various ways over 50 years produces curves lying between the 20- and 50-year single step changes. Temperature gradients for single step coolings 50 years ago or more are all shallower than the gradient at BH3. Despite the difficulty in choosing any one model for the surface temperature history, the thermal event represented by the advance of the platform sediments probably did not happen more than 50 years ago.

While of limited depth, BH4 temperatures below about 10 m closely approach temperatures in BH3, but remain slightly warmer. This part of the platform has likely formed over a time interval shorter than that indicated by BH3.

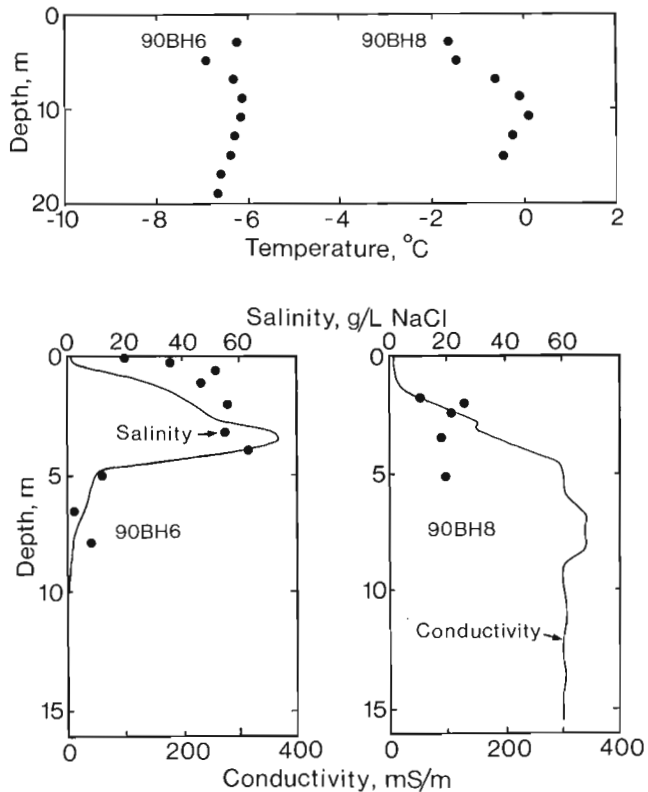
## BREACHED LAKES

Temperatures beneath the sediment platform document changes in previously frozen ground but are of insufficient depth to determine if permafrost reaggradation has occurred.

However, permafrost aggradation is almost certainly occurring beneath former lake basins in the North Head area. Lakes breached by coastal retreat either drain or are inundated, depending on the lake bottom elevation relative to sea level. If a lake with an associated talik drains, permafrost aggrades into the underlying material. If a lake is inundated by the sea, the lake bottom may be raised by sedimentation and brought into contact with winter sea ice for a sufficient period each year to also permit permafrost to aggrade.

The existence of a drained lake basin inland of the distal end of the spit suggests that the lagoon enclosed by the spit may coincide with part of a former lake (Fig. 4). The lagoon bottom was cored and subsurface temperatures were measured in the anticipation that evidence of permafrost aggradation might be found (borehole 90BH6, Fig. 4). About 7 m of interbedded silts and sands overlie a diamicton thought to be the Toker Point till. Occasional wood fragments, including a fragment of a log, are contained in these sediments. While lakes on northern Richards Island are seldom deeper than 5 m (Dallimore, pers. comm., 1993), the presence of large wood fragments about 6 m below the lagoon suggests that the former lake bottom was at least this deep.

Only one temperature observation is available for this borehole. Below 10 m temperatures range between -6°C and -7°C (Fig. 6), consistent with an equilibrium temperature anticipated beneath the 50 cm ice thickness at this site. It is not possible to determine when permafrost aggradation began. However, permafrost appears to have aggraded into

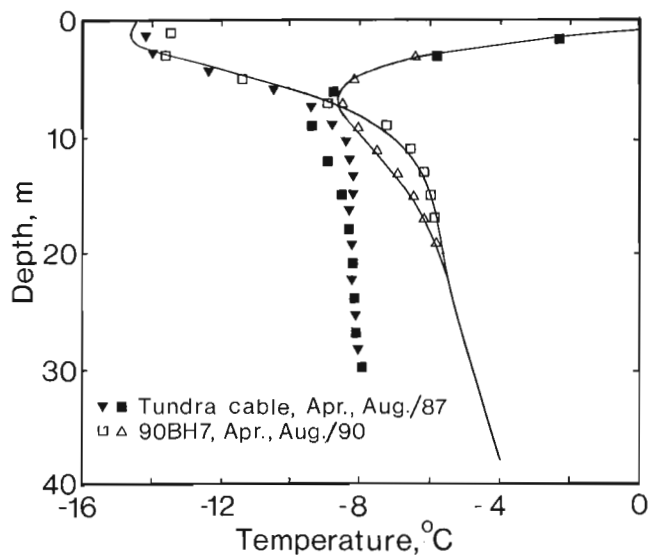


**Figure 6.** Borehole temperatures, salinity, and logged electrical conductivity for 90BH6 and 90BH8.

the sediments after inundation by the sea because of the elevated salinities (up to 65 g/L NaCl) in the first 5 m of frozen sediment (Fig. 6). In addition, the probable existence of ice-bonded sediments to a depth well in excess of 20 m suggests that ice-bonded permafrost may have aggraded into these sediments considerably before the growth of the platform.

Ground temperature profiles from a drained lake on the west side of North Head suggest that permafrost aggradation is occurring there. The profiles are taken from a borehole located immediately inland of a beach berm formed in washover sands that extend a few hundred metres inland across the lake bottom (90BH7, Fig. 4). About 2 m of sand and gravel overlie 1 m of black, fetid clay which may represent lake bottom sediments. The top of the clay is about at present sea level. It was probably exposed to sea water for a short time before becoming ice bonded because of the moderate salinity (up to 20 g/L NaCl) confined to this unit.

Temperature profiles for two dates are shown in Figure 7. Profiles computed using the temperature oscillation equation (Jumikis, 1977) have been fitted to these profiles to allow comparison with equilibrium temperatures beneath the nearby tundra. Because the 90BH7 temperatures show an overall steeper gradient than the tundra borehole temperatures, a constant gradient has been added to the oscillation model to improve the fit. This gradient is 0.1 °C/m, considerably higher than the gradient suggested by the tundra borehole. This suggests that permafrost is still aggrading below the extrapolated depth of about 80 m. To reach this depth, a sudden temperature drop, from slightly above 0°C to -9°C, about 250 years ago is required if the breached lake bottom was initially permafrost-free. The lake was probably breached at this time but the associated rate of coastal retreat cannot be determined because the original outline of the lake is unknown.



**Figure 7.** Comparison of ground temperatures between a borehole in upland tundra at North Head and borehole 90BH7 in a drained lake.

## EARLY STAGES OF PERMAFROST AGGRADATION

Wolfe (1989) estimates that the North Head sediment platform has extended eastward at an average rate of 40 m/a. Ground temperatures at BH3 and BH4 imply that ice bonding extends over 100 m beneath much of the platform. However, the platform is presently prograding into water deep enough to promote thawing of ice-bonded sediments. Therefore, at some location along the axis of the platform, a transition from an area undergoing cooling of frozen ground to an area undergoing permafrost aggradation must occur. This distribution is further suggested by 1.7 m of ice-bonded sand and silty sand overlying thawed sediment to a depth of at least 15 m, about 1 km east of the eastern end of the platform (borehole 90BH8, Fig. 4, ground temperatures shown in Fig. 6). Most notably, the 1.7 m of ice-bonded sediment was found in contact with 1.5 m of sea ice. It is suspected that this thickness of ice bonding is too great to form in one freezing season beneath the measured ice thickness. Therefore, the site is probably in the earliest stages of permafrost aggradation.

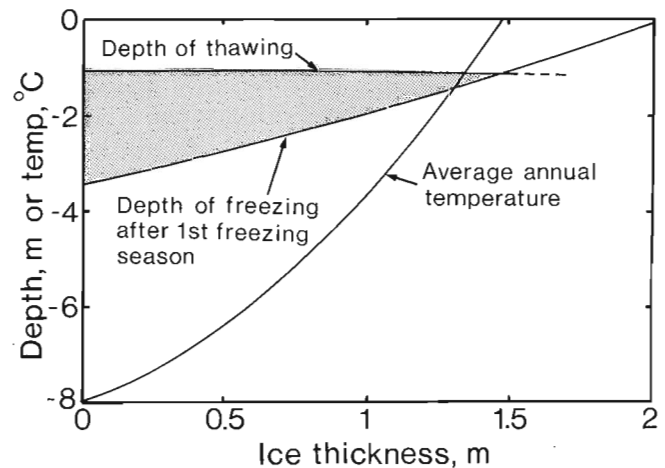
To determine if permafrost can be expected under the conditions described above, a model for predicting permafrost aggradation (Dyke, 1988) was applied to this site. Permafrost aggradation is initiated as the water depth is reduced by sedimentation. Once the seabottom comes into contact with winter sea ice, freezing of the topmost seabottom sediment occurs. As shallowing continues, frost penetration will be sufficiently thick to survive the following summer season, forming ice-bonded permafrost. Subbottom temperatures are controlled primarily by the thickness of winter sea ice in contact with the seafloor. If the average sub-zero temperature for the duration of freezing is known, then that portion of the freezing index remaining after the formation of the sea ice can be determined. This index increases as the water depth and resulting thickness of bottom-fast ice decreases. The index is expressed as the freezing temperature curve in Figure 2.

The frost penetration depth after one freezing season is shown in Figure 8. The temperature for the duration of thawing (thawing temperature curve in Fig. 2) is then applied to determine the thaw depth in the previously formed frozen zone. This thawing depth is also shown in Figure 8. A wedge of frozen ground remains and is represented by the shaded area in Figure 8 and depicts the thermal condition under which permafrost can aggrade. That portion of the next freezing index remaining after the thawed zone is refrozen, when normalized to a full year, supplies the average annual temperature at the sea floor for any location in the zone of ice contact with the seafloor. The curve of these temperatures is shown in Figure 2 and is repeated in Figure 8 and can be used to calculate permafrost thickness after any elapsed time.

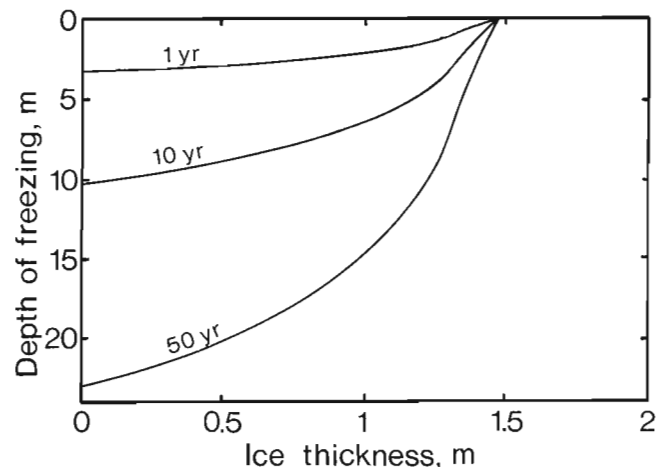
Figure 8 suggests that permafrost will form in water depths of 1.5 m or less. Permafrost thicknesses for elapsed times of 1, 10, and 50 years are plotted on Figure 9 to show the tendency of permafrost to aggrade under these conditions. These estimates are in good agreement with observations of growth of permafrost beneath drained lakes on Richards

Island (Mackay, 1985). The thickness of permafrost is most sensitive to ice thicknesses corresponding to the onset of permafrost. However, this figure is only applicable where the seabottom has suddenly been brought into contact with the sea ice, with no further change in ice thickness.

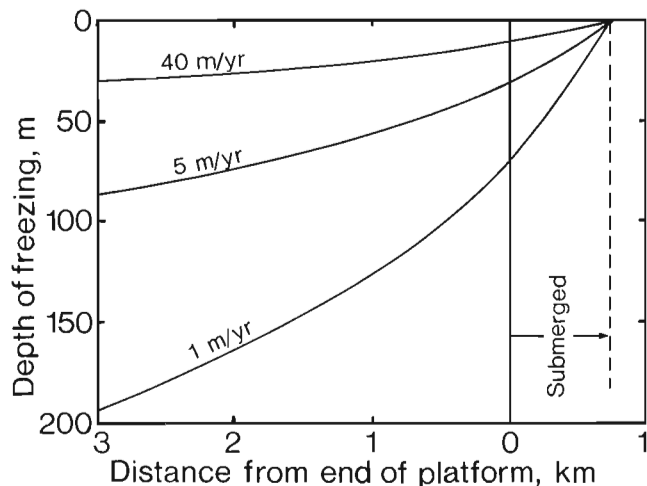
In a dynamic coastal environment, any zone of contact with winter sea ice has probably moved laterally to reach its present position. In the case of a prograding feature, the seafloor rises gradually, experiencing decreasing average annual temperatures. If the rate of progradation and the slope of the underwater portion of the feature are known, then the average annual temperature experienced by a site on the seafloor, between the time the temperature falls below 0°C and subaerial exposure, can be determined.



**Figure 8.** Relationship of bottom-fast sea ice thickness to predicted depth of freezing into unfrozen ground after one freezing season. Also shown is the depth of annual thaw. The amount of cooling remaining after refreezing the thawed ground is used to calculate the average annual temperature at the seafloor for a given sea ice thickness. The shaded area is the frozen ground that would remain.



**Figure 9.** The depth of freezing into unfrozen ground under the average annual temperatures in Figure 8 for 1, 10, and 50 years.



**Figure 10.** The depth of freezing into unfrozen ground that would occur for different rates of platform aggradation, assuming the seabottom temperature distribution of Figure 8.

For the North Head sediment platform, an underwater extension presumably progrades along with the subaerial portion. If borehole 90BH8 is located at the distal end of the platform, then the submerged portion is about 0.75 km long. If it is further assumed that the feature has been prograding continuously at 40 m/a, then an average annual temperature during progradation for any present site can be determined. Figure 10 shows predicted profiles of the thickness of permafrost beneath the platform, for different rates of progradation. For a rate of 40 m/a, permafrost is predicted to be about 10 m thick at the subaerial distal end of the platform. In reality, permafrost is probably much thicker at the end of the platform. The temperature profile for BH4 (Fig. 5), which is about 1 km away, implies that permafrost is over 100 m thick. This is most likely due to the fact that much of the platform has formed over previously frozen sediment and is continuing to prograde into deeper water. Therefore, a boundary between previously existing thick permafrost and a much thinner wedge probably exists somewhere between borehole BH4 and borehole 90BH8.

## SUMMARY

Field measurements and comparison of successive airphotos indicate that shoreline retreat in the North Head area has been occurring at a rate of up to 3 m/a for the last 50 years. Over the same interval, the eroded sediments have been redeposited to form a platform eastward of the retreating cliffs. Changes in the slope of the nearshore frost table at the most rapidly eroding part of the North Head sea cliffs indicate that the retreat rate increased from 1 m/a to 3 m/a approximately 50 years ago (Dyke, 1991). The correspondence between the time of this increase and the appearance of the platform suggests that the two events are linked.

While the link between the increase in retreat rate and platform growth is somewhat speculative, the recent growth of the platform is confirmed by the subsurface thermal

regime. Ground temperature profiles indicate that the adjustment to cooling of about 5°C (from -4°C to -9°C) is still progressing. This cooling is most likely caused by subaerial exposure from sediment accumulation. Furthermore, the occurrence of a thin layer of ice-bonded sediment over deeper thawed sediment at the distal end of the platform may represent the onset of permafrost. If this ice-bonded sediment is permafrost, then it must be very recent. Its existence in line with the principle construction direction of the platform suggests that platform sedimentation is continuing at least 0.75 km offshore of the subaerial extent of the platform.

The platform overlies older sediments that may have been the floor of a previous embayment. Temperatures beneath the present seaward edge of the platform and lagoon bottom indicate that these surfaces have existed in their present water depth (about 0.5 m) prior to the construction of the platform. Subbottom temperatures beneath the lagoon suggest that the breached lake was probably filled a few hundred years ago, once it was connected with the Beaufort Sea. Hence, the coast immediately east of North Head may have been stable. In contrast, erosion of the northwest exposure of North Head has been continuous for at least 150 years. Shoreline erosion has also been continuous over this time interval on the west side of North Head as indicated by permafrost aggradation in a drained lake bottom.

Overall, the thermal regime of nearshore sediments in the North Head area are highly variable. This variability is controlled by the erosional and depositional history over the last few hundred years. An evaluation of the subbottom temperature profiles provides an additional means of determining the rates of nearshore coastal processes. At some localities, ground temperatures suggest that significant changes in bathymetry have occurred in the last 50 years.

## ACKNOWLEDGMENTS

The borehole data analyzed in this paper was collected with the aid of funding from the National Science and Engineering Research Council of Canada in 1988 and from the Northern Oil and Gas Action Program, Department of Indian and Northern Affairs in 1990. In both years indispensable logistical support was provided by Polar Continental Shelf Project from Tuktoyaktuk and Inuvik Research Center from Inuvik. The paper has been greatly improved thanks to a thorough review by S.R. Dallimore.

## REFERENCES

- Dallimore, S.R. (ed.)  
1991: Geological, geotechnical and geophysical studies of an onshore-offshore transect of the Beaufort Shelf; Geological Survey of Canada, Open File 2408.
- Dallimore, S.R., Kurfurst, P.J., and Hunter, J.A.M.  
1988: Geotechnical and geothermal conditions of nearshore sediments, southern Beaufort Sea, Northwest Territories, Canada; Permafrost, Fifth International Conference, Proceedings Volume 1, p. 127-131.

**Dyke, L.D.**

- 1988: Permafrost aggradation along an emergent coast, Churchill, Manitoba; Permafrost, Fifth International Conference, Proceedings Volume 1, p. 138-142.
- 1991: Temperature changes and thaw of permafrost adjacent to Richards Island, Mackenzie Delta, N.W.T.; Canadian Journal of Earth Sciences, v. 28, p. 1834-1842.

**Forbes, D.L. and Frobel, D.**

- 1985: Coastal erosion and sedimentation in the Canadian Beaufort Sea; in Current Research, Part B; Geological Survey of Canada, Paper 85-1B, p. 69-80.

**Harper, J.R.**

- 1990: Morphology of the Canadian Beaufort Sea Coast; Marine Geology, v. 91, p. 75-91.

**Hill, P.R., Forbes, D.L., Dallimore, S.R., and Morgan, P.**

- 1986: Shoreface development in the Canadian Beaufort Sea; Proceedings of the Symposium on Cohesive Shores, National Research Council, Canada, p. 428-448.

**Jumikis, A.R.**

- 1977: Thermal Geotechnics; Rutgers University Press, New Brunswick, New Jersey.

**Kurfurst, P.J. (ed.)**

- 1986: Geotechnical investigations of the nearshore zone, North Head, Richards Island, N.W.T.; Geological Survey of Canada, Open File 1376.

- 1987: Geotechnical Investigations off Northern Richards Island, N.W.T. – 1987; Geological Survey of Canada, Open File 1376.

**Kurfurst, P.J. and Dallimore, S.R.**

- 1991: Engineering geology of nearshore areas off Richards Island, N.W.T.: a comparison of stable and actively eroding coastlines; Canadian Geotechnical Journal, v. 28, p. 179-188.

**Mackay, J.R.**

- 1985: Permafrost growth in recently drained lakes, Western Arctic Coast; in Current Research, Part B; Geological Survey of Canada, Paper 85-1B, p. 177-189.
- 1986: Fifty years of coastal retreat west of Tuktoyaktuk, District of MacKenzie; in Current Research, Part A; Geological Survey of Canada, Paper 86-1A, p. 727-735.

**Rampton, V.N.**

- 1988: Quaternary Geology of the Tuktoyaktuk Coastlands, Northwest Territories; Geological Survey of Canada, Memoir 423.

**Wolfe, S.A.**

- 1989: Investigation of nearshore conditions across an aggrading coastal shoreline in permafrost, Richards Island, N.W.T.; M.Sc. thesis, Queen's University, Kingston, Ontario, 188 p.

---

Geological Survey of Canada Project 920045.





# Oil and gas pool size probability distributions – J-shaped, lognormal, or Pareto?

P.J. Lee

Institute of Sedimentary and Petroleum Geology, Calgary

*Lee, P.J., 1993: Oil and gas pool size probability distributions – J-shaped, lognormal, or Pareto?; in Current Research, Part E; Geological Survey of Canada, Paper 93-1E, p. 93-96.*

---

**Abstract:** Until recently, suitable data sets were unavailable to test the hypothesis that oil and gas pool size distributions are Pareto or log-geometric. The following observations from the Western Canada Sedimentary Basin challenge the Pareto hypothesis: (1) a single lognormal population can exhibit a J-shaped distribution; (2) a natural basin population, which consists of various lognormal and nonparametric populations, may also exhibit a J-shaped distribution; and (3) there is no constant ratio between two adjacent size classes in the two J-shaped distributions.

**Résumé :** Jusqu'à récemment, il n'existait aucun ensemble convenable de données pour vérifier l'hypothèse selon laquelle les tailles des gisements de gaz naturel et de pétrole ont des distributions de Pareto ou des distributions log-géométriques. Les observations suivantes relatives au Bassin sédimentaire de l'Ouest du Canada contestent l'hypothèse de Pareto : (1) une seule population log-normale peut avoir une distribution en J; (2) la population d'un bassin naturel, qui comporte diverses populations log-normales et non paramétriques, peut aussi avoir une distribution en J; et (3) il n'y a pas de rapport constant entre deux classes de taille successives dans les deux distributions en J.

## INTRODUCTION

Petroleum resource evaluation is usually performed using probabilistic statistical analysis which essentially assumes that sample data sets can be represented by specific types of probability distributions. The choice of a probability distribution for oil and gas pools or fields was a controversial topic in past decades for two reasons: (1) the statistical methods required to test data sets sampled by the biased exploration process were not developed; and (2) the number of data sets available for this type of study remained quite limited.

The nonparametric discovery process model has been applied to evaluate data sets (Wang and Nair, 1988, Lee and Wang, 1990). The results from this model favour lognormal distributions.

Drew et al. (1980, 1982, 1988), Schuenemeyer and Drew (1983), and Drew (1990) observed from the Permian basin that the mode of a pool size distribution, expressed in terms of the number of pools, shifts toward the small pool size class (left side) as exploration progresses. They also observed that the ratio between the number of pools in two adjacent size classes (base 2) fluctuates somewhat. These researchers had suggested that, in theory, pool size distribution should exhibit a J-shaped distribution and the ratio between two adjacent size classes should remain constant.

A J-shaped distribution with a constant ratio between two adjacent size classes supports the hypothesis that pool size distribution is Pareto or log-geometric, if base 2 is used. If this hypothesis is correct, the ratio between adjacent size classes is estimated from the large pool size classes where all pools have been discovered. This ratio can then be applied to estimate the number of pools in the small pool size classes.

Recently, additional data sets have been obtained and analyzed using the superpopulation approach. Data sets for entire basins are also available for both superpopulation and finite population analysis. From these studies, it is now possible to examine play and basin pool size probability distribution. This paper reports the results of these observations.

For purposes of this discussion, a play is defined as a natural and single geological population, whereas a basin is a natural population containing one or more plays and is not truncated by depth or political boundaries.

## POPULATION POOL SIZE DISTRIBUTIONS

### *Pool size distribution of a play*

The Beaverhill Lake oil play of the Western Canada Sedimentary Basin was selected for this study because of its exploration maturity. The play has 36 oil discoveries with numerous drill-stem oil recoveries from economically unsuccessful exploratory wells. Although not classified as commercial, the oil resources of those recoveries are significant. In petroleum resource evaluations, these exploratory wells are considered pools. The discovery sequence, which consists of commercial and noncommercial pools, forms a fairly complete data set that has no economic truncations.

**Table 1.** Grouped distributions derived from the lognormal and nonparametric discovery process models for the Beaverhill Lake play. (The ratios between two adjacent size classes are recorded in brackets).

Size class (10 <sup>6</sup> m <sup>3</sup> )	Number of pools discovered	Total number of pools predicted by	
		LDSCV	NDSCV
<0.001	18	73	68
	(0.9)	(2.7)	(2.1)
0.001-0.01	20	27	32
	(1.0)	(1.2)	(1.3)
0.01-0.1	20	22	25
	(1.3)	(1.4)	(1.6)
0.1-1	15	16	16
	(1.9)	(1.6)	(2.0)
1-10	8	10	8
	(1.0)	(1.3)	(1.0)
10-100	8	8	8
	(2.7)	(2.7)	(2.7)
>100	3	3	3

The play's data set was evaluated using the lognormal (LDSCV) and nonparametric (NDSCV) discovery process models (Lee and Wang, 1985, 1990). The lognormal model assumes that the distribution of pool sizes can be approximated by a lognormal distribution, whereas the nonparametric model does not require a prior probability distribution. The results (base 10 is used for the size class) are summarized in Table 1.

Table 1 shows that the sample and population exhibit a J-shaped distribution. The ratios between two adjacent size classes are derived from the sample and the results of the LDSCV and NDSCV, and are listed within brackets. The ratios between the two largest and the two smallest size classes may be ignored: the two smallest because the smallest class contains more than one size class, the two largest classes because this play contains large outliers.

The LDSCV yields ratios ranging from 1.2 to 1.6, whereas the NDSCV yields ratios ranging from 1.0 to 2.0. The sample ratio ranges from 1.0 to 1.9. It is not surprising that the LDSCV yields a more uniform ratio than the NDSCV, because the LDSCV adopts a continuous lognormal distribution, whereas the NDSCV follows the estimated empirical distribution. However, the sample ratio is much smaller (mean = 1.3) than those derived by the LDSCV (mean = 1.4)

and NDSCV (mean = 1.5). This is due to the fact that the discoveries are from a biased sample derived from a selective exploration process.

**Table 2.** Grouped distribution derived from the superpopulation and finite population approaches for the 25 Devonian mature gas plays. (The ratios between two adjacent size classes are recorded in brackets).

Size class (10 <sup>6</sup> m <sup>3</sup> )	Number of pools discovered	Total number of pools predicted by	
		Super- population	Finite population*
<64	1158	7658	7859
	(4.9)	(8.7)	(8.6)
64-128	239	882	919
	(1.3)	(1.5)	(1.8)
128-256	191	595	502
	(1.2)	(1.6)	(1.6)
256-512	155	374	316
	(1.6)	(1.7)	(1.8)
512-1024	98	223	175
	(1.8)	(2.0)	(2.3)
1024-2048	54	113	77
	(1.6)	(2.1)	(2.0)
2048-4096	33	54	39
	(1.3)	(1.7)	(1.6)
4096-8192	25	32	25
	(1.2)	(1.5)	(1.2)
8192-16384	21	21	21
	(2.1)	(2.1)	(2.1)
16384-32768	10	10	10
	(1.0)	(1.0)	(1.0)
32768-65536	10	10	10
	(10)	(10)	(10)
>65536	1	1	1

\*Note: The finite population has a lower and upper limit; only the lower limit is presented here.

### ***Pool size distribution of a basin***

A total of 25 gas plays have been identified from the Devonian system of the Western Canada Sedimentary Basin (Reinson et al., 1993). For the superpopulation case, individual undiscovered pool sizes for each play were evaluated using the LDSCV or NDSCV. The estimated pool sizes from these 25 plays were then merged as a single population and classified by a size class of base 2. For the finite population case, all discovered pool sizes were combined into one single population which was analyzed by the finite population model (Bickel et al., 1992). Table 2 presents the output.

It is evident that the grouped distributions for both the superpopulation and finite population approaches are J-shaped. Again ignoring the ratios between the two largest and the two smallest size classes: (1) the ratio derived from the superpopulation approach ranges from 1.0 to 2.1 (mean = 1.7); (2) the ratio derived from the lower limit of the finite population approach ranges from 1.0 to 2.3 (mean = 1.7); and (3) the sample ratio ranges from 1.0 to 2.1 (mean = 1.5). The sample ratio, again, is smaller than that of the population. Furthermore, the finite population approach does not require any prior probability distribution and it yields ratios that are more irregular.

### **CONCLUDING REMARKS**

Based on the above observations, the following remarks can be made: (1) the Beaverhill Lake example demonstrates that a single and natural lognormal population can be J-shaped; (2) the 25 gas plays which have different means and variances of lognormal and empirical distributions also exhibit a J-shaped distribution; and (3) from the examples studied, there is no apparent trend for all ratios.

Does the lack of a trend imply a constant ratio? In these cases the number of pools would be under- or overestimated if an average ratio or any ratio is used for the prediction of the entire population. Is it possible that the ratio varies randomly from class to class without any pattern? The constant ratio hypothesis remains unproven.

The previous remarks suggest that a J-shaped distribution estimated by statistical methods or observed from a sample data set does not necessarily support a Pareto distribution. The Devonian system and Beaverhill Lake play examples challenge this application of the Pareto hypothesis.

### **ACKNOWLEDGMENTS**

The author would like to thank Kirk Osadetz, Katrina Olsen-Heise, and Tim Bird for their suggestions and discussions.

---

## REFERENCES

---

**Bickel, P.J., Nair, V.N., and Wang, P.C.C.**

1992: Nonparametric inference under biased sampling from a finite population; *The Annals of Statistics*, v. 20, no. 2, p. 853-878.

**Drew, L.J.**

1990: Oil and gas forecasting: reflections of a petroleum geologist; Oxford University Press, New York, 252 p.

**Drew, L.J., Attanasi, E.D., and Schuenemeyer, J.H.**

1988: Observed oil and gas field size distributions: a consequence of the discovery process and prices of oil and gas; *Mathematical Geology*, v. 20, no. 8, p. 939-953.

**Drew, L.J., Schuenemeyer, J.H., and Bawiec, W.J.**

1982: Estimation of the future rates of oil and gas discoveries in the Gulf of Mexico; U.S. Geological Survey, Professional Paper 1252, 26 p.

**Drew, L.J., Schuenemeyer, J.H., and Root, D.H.**

1980: Petroleum resource appraisal and discovery rate forecasting in partially explored region – an application to the Denver Basin; U.S. Geological Survey, Professional Paper 1138-A, 13 p.

**Lee, P.J. and Wang P.C.C.**

1985: Prediction of oil and gas pool sizes when discovery record is available; *Mathematical Geology*, v. 17, no. 2, p. 95-113.

1990: An introduction to petroleum resource evaluation methods; CSPG Short course for the 1990 CSPG Convention on Basin Perspectives, Calgary, Canada.

**Reinson, G.E., Lee, P.J., Warters, W., Osadetz, K.G., Bell, L.L.,**

**Price, P.R., Trollope, F., Campbell, R.I., and Barclay, J.E.**

1993: Devonian gas resources of Western Canada Sedimentary Basin - play definition and resource assessment; Geological Survey of Canada, Bulletin 452, 157 p.

**Schuenemeyer, J.H. and Drew, L.J.**

1983: A procedure to estimate the parent population of the size of oil and gas fields as revealed by a study of economic truncation; *Mathematical Geology*, v. 15, no. 1, p. 145-161.

**Wang, P.C.C. and Nair, V.N.**

1988: Statistical analysis of oil and gas discovery data; in *Quantitative analysis of mineral and energy resources*, (ed.) C.F. Chung, A.G. Fabbri, R. Sindig-Larsen, and D.R. Dordrecht, p. 199-214.

---

Geological Survey of Canada Project 750023

# Variation in surface area and micropore size distribution with composition of medium volatile bituminous coal of the Gates Formation, northeastern British Columbia: implications for coalbed methane potential

C. Clarkson<sup>1</sup>, M. Lamberson<sup>1</sup>, and R.M. Bustin<sup>1</sup>  
Institute of Sedimentary and Petroleum Geology, Calgary

*Clarkson, C., Lamberson, M., and Bustin, R.M., 1993: Variation in surface area and micropore size distribution with composition of medium volatile bituminous coal of the Gates Formation, northeastern British Columbia: implications for coalbed methane potential; in Current Research, Part E; Geological Survey of Canada, Paper 93-1E, p. 97-104.*

---

**Abstract:** The micropore CO<sub>2</sub> surface area, monolayer capacity, pore size distribution, and CH<sub>4</sub> monolayer capacity of a suite of medium volatile bituminous coals of the Gates Formation were investigated in order to assess the effect of composition (maceral and mineral) on coalbed methane potential. The CO<sub>2</sub> surface areas range from 57.6 to 123.86 m<sup>2</sup>/g (raw coal basis) and generally increase with increasing vitrinite content (raw coal and mineral matter free basis) and decrease with increasing mineral matter content. The lowest CO<sub>2</sub> surface area was obtained from the coal with the highest inertinite content. The CH<sub>4</sub> monolayer capacities determined by high pressure CH<sub>4</sub> adsorption are correlative but generally lower than CO<sub>2</sub> monolayer capacities. The micropore size distribution and mean pore size vary little with composition and thus the variation in surface area must reflect the greater abundance of micropores in vitrinite compared to other macerals.

**Résumé :** On a étudié la surface et la capacité d'adsorption d'une monocouche de CO<sub>2</sub>, la distribution de la taille des pores et la capacité d'adsorption d'une monocouche de CH<sub>4</sub> dans une série de charbons bitumineux volatils moyens de la Formation de Gates en vue d'évaluer l'effet de la composition (macéraux et minéraux) sur le potentiel de dégagement de méthane des couches de houille. La surface d'adsorption du CO<sub>2</sub> varie de 57,6 à 123,86 m<sup>2</sup>/g (charbon brut); en général, elle augmente en fonction de la teneur en vitrinite (charbon brut exempt de matière minérale) et diminue avec l'accroissement de la teneur en matière minérale. La surface d'adsorption du CO<sub>2</sub> la plus petite est celle du charbon le plus riche en inertinite. La capacité d'adsorption d'une monocouche de CH<sub>4</sub>, déterminée par adsorption de CH<sub>4</sub> sous haute pression, est correlative de la capacité d'adsorption de la monocouche de CO<sub>2</sub>, mais généralement moins élevée. La distribution de la taille et la taille moyenne des micropores varient peu en fonction de la composition, de sorte que la variation de la surface doit être liée à l'abondance plus élevée des micropores dans la vitrinite que dans les autres macéraux.

---

<sup>1</sup> Department of Geological Sciences, University of British Columbia, Vancouver, British Columbia V6T 1Z4

## INTRODUCTION

Previous studies have identified factors such as pressure, rank, tectonic structure (fractures), amount of mineral matter, and hydrological conditions as crucial elements in the assessment of coalbeds as a resource for CH<sub>4</sub> (Kim, 1977; Meissner, 1984; Dawson and Clow, 1992; Ayers and Kaiser, 1992). Methane occurs in coals in three possible ways: as free gas within cleat fractures or pores; as a solute in groundwater within the coalbed; and as adsorbed molecules on the coal internal surface (Rightmire, 1984). The third, adsorbed gas, is the primary mechanism for CH<sub>4</sub> retention in coal. Methane adsorption is dependent on the internal surface area, which is dependent on the pore size distribution and number of pores within the coal. The porosity of higher rank coals is primarily microporous (Gan et al., 1972; Mahajan and Walker, 1978) and the micropores (pore diameter <2 nm) contribute much of the surface area in such coals. Details of how compositional variation and maceral content affect CH<sub>4</sub> retention in coal have received little study. The objective of our ongoing research is to characterize and eventually quantify the effect of maceral and mineral compositional variability on the CH<sub>4</sub> adsorption characteristics and thus the coalbed methane potential of western Canadian coals. In this paper we present some preliminary results from our effort to determine the relationship between coal composition and CH<sub>4</sub> adsorption, CO<sub>2</sub> surface areas (surface areas determined using CO<sub>2</sub> as an adsorbate gas), and micropore size distribution for a suite of medium volatile bituminous coals. The coals chosen for this study are from the Lower Cretaceous Gates Formation from the Bullmoose Mine in northeastern British Columbia.

## METHODS

Seven lithotypes were located in the Bullmoose C seam and one from the A1 seam, approximately 50 m stratigraphically below the C seam (Lamberson and Bustin, 1992).

Petrography (maceral and mineral), proximate, sulphur, low-temperature ash (LTA), x-ray diffraction (XRD, mineral), equilibrium moisture, high pressure CH<sub>4</sub> adsorption, and low pressure CO<sub>2</sub> adsorption analyses were performed. The samples were crushed to less than a 250 µm screen size for all analyses.

Methane adsorption analysis was performed by Core Laboratories (Calgary, Alberta) using a high pressure volumetric adsorption technique similar to that of Mavor et al. (1990). Methane adsorption isotherms (corrected to an ash-free basis) and monolayer capacities were measured following the procedures outlined by Lamberson and Bustin (1992).

CO<sub>2</sub> adsorption analysis was performed at University of British Columbia using a Micromeritics ASAP 2000 surface area analyzer. Samples were evacuated at 70°C for at least 16 hours prior to analysis to remove residual volatiles. Each sample (with sample tube) was then transferred to an analysis port on the instrument, back-filled with helium to remove entrained volatiles, and re-evacuated. Then a preliminary leak

test was performed; this consisted of opening the sample tube to a pressure transducer which monitored pressure buildup due to the release of volatiles from the sample. If a critical pressure increase was not achieved over a set period of time, then the analysis was continued. Upon passing the preliminary leak test, a free space analysis was performed using helium gas at analysis temperature, followed by a more stringent leak test. After the secondary leak test was passed, the sample was cooled to analysis temperature, exposed to fixed doses of CO<sub>2</sub> gas, allowed to come to equilibrium, and the adsorbed volume of CO<sub>2</sub> gas was calculated. The analysis was performed over a relative pressure range of about 0.0006 to 0.01 at 25°C, and 0.0006 to 0.032 at 0°C. Relative pressure is P/P<sub>0</sub>, where P is the equilibrium pressure and P<sub>0</sub> is the input saturation pressure for CO<sub>2</sub> at the analysis temperature. CO<sub>2</sub> adsorption isotherms (plots of volume of gas adsorbed versus partial pressure) were thus obtained.

The isotherm data were used to determine CO<sub>2</sub> monolayer capacities (volumes), surface areas, and micropore size distributions. The Dubinin-Radushkevich equation (Sato, 1981; Gregg and Sing, 1982; Lowell and Shields, 1984; Marsh, 1987) was used to determine CO<sub>2</sub> monolayer capacities from the 25°C isotherm data. Surface areas were obtained from the monolayer capacity using a monolayer cross-sectional area of  $17 \times 10^{-20} \text{m}^2$  for CO<sub>2</sub>.

The Dubinin-Astakov equation (Gregg and Sing, 1982; Marsh, 1987) was used to obtain pore size distribution data. The pore size distributions were obtained using an analysis bath temperature of 0°C to obtain a larger relative pressure range than at 25°C (0.0006-0.032 versus 0.0006-0.01).

## RESULTS

### *Standard industrial analyses, rank, and composition*

The results of proximate, sulphur, equilibrium moisture, and ash yield (for CH<sub>4</sub> adsorption test samples only) analyses are given in Table 1. A complete discussion of these results is given by Lamberson and Bustin (in press). Sulphur values range from 0.18 to 0.77%, whereas weight per cent volatiles (dry, mineral matter free basis) range from 17.38 to 30.53%.

Random reflectance performed on three samples, LTC-1, LTC-15, LTA1-6, yielded values of 0.97, 0.96, and 1.03, respectively (Lamberson and Bustin, in press). These values straddle the high volatile A – medium volatile bituminous boundary as established for western Canadian coals (Cameron, 1991). Rank, as estimated by the American Society of Testing and Materials (ASTM) coal classification for higher rank coals, based on a fixed carbon percentage (dry, mineral matter free basis), is medium volatile to low volatile bituminous.

Compositions of all samples are given in Figure 1 and Table 2. The maceral percentages were calculated on a volume per cent, mineral matter free basis, and were recalculated to include mineral matter using the Parr formula (Lamberson and Bustin, 1992). Liptinite content of the coals is very low (0-3%, mmf), thus the coals are composed mainly

**Table 1.** Proximate analysis, sulphur, equilibrium moisture, and ash yield data for all samples (Lamberson and Bustin, in press).

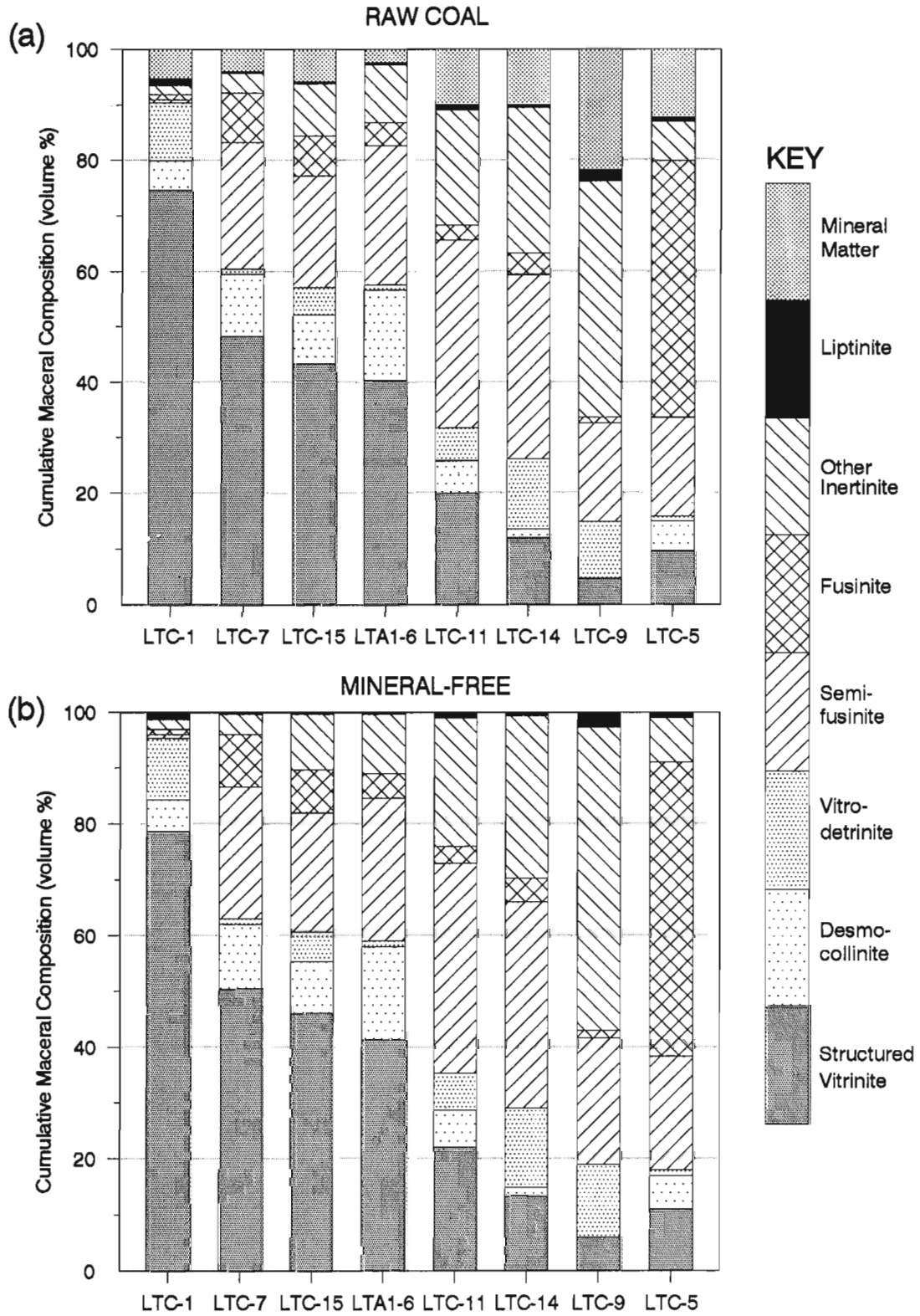
Sample	Proximate Analysis						Total Sulphur (wt. %)	Equilibrium Moisture (wt. %)	Ash Yield Adsorption Test (wt. %)
	Ash Yield (wt. %)	Moisture (%, as rcv'd)	Volatile Matter (wt. %, daf)	Fixed Carbon (wt. %, daf)	Volatile Matter (wt. %, dmmf)	Fixed Carbon (wt. %, dmmf)			
LTC-1	7.98	1.05	28.62	71.38	27.95	72.05	0.66	2.08	9.20
LTC-7	6.77	0.96	24.64	75.36	24.01	75.99	0.65	1.70	7.04
LTC-15	9.61	0.71	26.74	73.26	25.89	74.11	0.77	1.70	10.27
LTA1-6	3.61	0.87	24.03	75.97	23.70	76.30	0.37	1.95	4.37
LTC-11	20.46	0.87	23.23	76.77	21.46	78.54	0.43	1.60	17.11
LTC-14	17.63	0.68	22.75	77.25	21.25	78.75	0.45	1.40	17.02
LTC-9	33.83	0.84	20.90	79.10	17.38	82.62	0.31	1.50	33.68
LTC-5	22.15	0.48	32.16	67.84	30.53	69.47	0.19	1.40	20.70

wt. %, weight per cent  
as rcv'd, as received  
daf, dry, ash free  
dmmf, dry, mineral matter free (ASTM)

**Table 2.** Petrographic compositions of all samples on a mineral matter free and raw coal basis (Lamberson and Bustin, in press).

Maceral	LTC-1	LTC-7	LTC-15	LTA1-6	LTC-11	LTC-14	LTC-9	LTC-5
<b>Volume %, Mineral Matter Free</b>								
Structured Vitrinite	78.7	50.3	46.0	41.3	22.0	13.3	6.0	11.0
Desmocollinite	5.7	11.7	9.3	16.7	6.7	1.7	0.0	6.0
Vitrodetrinite	11.0	1.0	5.3	1.0	6.7	14.0	13.0	1.0
Semifusinite	0.7	23.7	21.3	25.7	37.7	37.0	22.7	20.3
Fusinite	1.0	9.3	7.7	4.3	3.0	4.3	1.3	52.7
Other inertinite	1.7	3.7	10.0	10.7	23.0	29.0	54.3	8.0
Total Liptinite	1.3	0.3	0.3	0.3	1.0	0.7	2.7	1.0
Total Vitrinite	95.3	63.0	60.7	59.0	35.3	29.0	19.0	18.0
Total Inertinite	3.3	36.7	39.0	40.7	63.7	70.3	78.3	81.0
Struc: Deg Vitrinite <sup>1</sup>	4.7	4.0	3.1	2.3	1.7	0.9	0.5	1.6
Struc: Deg Inertinite <sup>2</sup>	1.0	9.0	2.9	2.8	1.8	1.4	0.4	9.1
<b>Volume %, Raw Coal</b>								
Structured Vitrinite	74.5	48.3	43.3	40.3	19.8	12.0	4.7	9.7
Desmocollinite	5.4	11.2	8.8	16.3	6.0	1.5	0.0	5.3
Vitrodetrinite	10.4	1.0	5.0	1.0	6.0	12.6	10.2	0.9
Semifusinite	0.6	22.7	20.1	25.0	33.9	33.3	17.8	17.8
Fusinite	0.9	9.0	7.2	4.2	2.7	3.9	1.0	46.2
Other Inertinite	1.6	3.5	9.4	10.4	20.7	26.1	42.6	7.0
Total Liptinite	1.3	0.3	0.3	0.3	0.9	0.6	2.1	0.9
Total Vitrinite	90.3	60.5	57.1	57.6	31.8	26.1	14.9	15.8
Total Inertinite	3.2	35.2	36.7	39.7	57.3	63.3	61.4	71.1
Ash Yield (volume %)	5.2	4.0	5.9	2.4	10.0	9.9	21.7	12.3

<sup>1</sup>Structured Vitrinite: Degraded Vitrinite  
<sup>2</sup>Structured Inertinite: Degraded Inertinite



**Figure 1.** Maceral and mineral matter contents of samples on a) raw coal and b) mineral matter free basis (Lamberson and Bustin, in press).



of the three components vitrinite, inertinite, and mineral matter. Mineral matter free vitrinite content ranges from 18 to 95%, and inertinite ranges from 3 to 81%. On a raw coal basis, vitrinite content ranges from 15 to 90%, inertinite ranges from 3 to 71%, and mineral matter varies from 2 to

22%. LTC-1 has the highest vitrinite and lowest mineral matter and inertinite content; LTC-5 has the highest inertinite content; LTC-9 has the highest mineral matter content. Table 2 gives the ratio of unstructured to structured macerals and the results of XRD and LTA analysis are given in Table 3.

**Table 3.** X-ray diffraction (mineral) and low temperature ash data for all samples (Lamberson and Bustin, in press).

Sample	Lithotype	Low-temp. ash yield (weight %)	Quartz	Kaolinite	Dolomite	Ferroan Dolomite
LTC-1	Bright	7.20	major	major	-	minor
LTC-7	Banded bright	7.51	major	major	-	minor
LTC-15	Banded coal	11.28	major	major	minor	-
LTA1-6	Banded dull	2.83	dominant	minor	-	minor
LTC-11	Banded dull	18.57	major	major	-	minor
LTC-14	Dull	19.15	major	minor	minor	-
LTC-9	Dull	37.59	major	minor	-	-
LTC-5	Fibrous	33.43	minor	-	dominant	-

Note: detection limit of XRD technique is approximately 5%.  
 dominant, essentially the only mineral present  
 major, strong peaks present (15-40%)  
 minor, weak peaks, but detectable (5-15%?)

**Table 4.** Methane and carbon dioxide monolayer volumes and carbon dioxide surface on a raw coal, ash free, and mineral matter free basis (Lamberson and Bustin, in press).

Sample	Monolayer Volume (cm <sup>3</sup> /g)						Surface Area (m <sup>2</sup> /g)		
	Methane			Carbon Dioxide			Carbon Dioxide		
	Raw Coal	Ash Free <sup>1</sup>	M. M. F. <sup>2</sup>	Raw Coal	Ash Free <sup>1</sup>	M. M. F. <sup>2</sup>	Raw Coal	Ash Free <sup>1</sup>	M. M. F. <sup>2</sup>
LTC-1	19.30	21.25	20.37	25.68 (5) <sup>3</sup>	28.28	27.10	117.68	129.60	124.19
LTC-7	22.02	23.69	22.94	26.54 (2)	28.55	27.65	121.22	130.40	126.27
LTC-15	20.52	22.87	21.80	27.12 (2)	30.22	28.81	123.86	138.04	131.58
LTA1-6	18.67	19.53	19.14	24.53 (2)	25.65	25.14	112.10	117.22	114.90
LTC-11	12.25	14.78	13.61	21.26 (4)	25.65	23.62	97.14	117.19	107.92
LTC-14	15.47	18.64	17.18	21.21 (2)	25.56	23.55	96.90	116.78	107.60
LTC-9	7.85	11.84	10.02	16.03 (2)	24.17	20.46	72.61	109.48	92.70
LTC-5	8.10	10.19	9.23	12.61 (5)	15.90	14.37	57.60	72.64	65.64

<sup>1</sup> Corrected using as yield, weight %  
<sup>2</sup> M.M.F., Mineral Matter Free; corrected using ash yield, volume % - Parr Formula  
<sup>3</sup> Number of times analysis was performed, value represents average

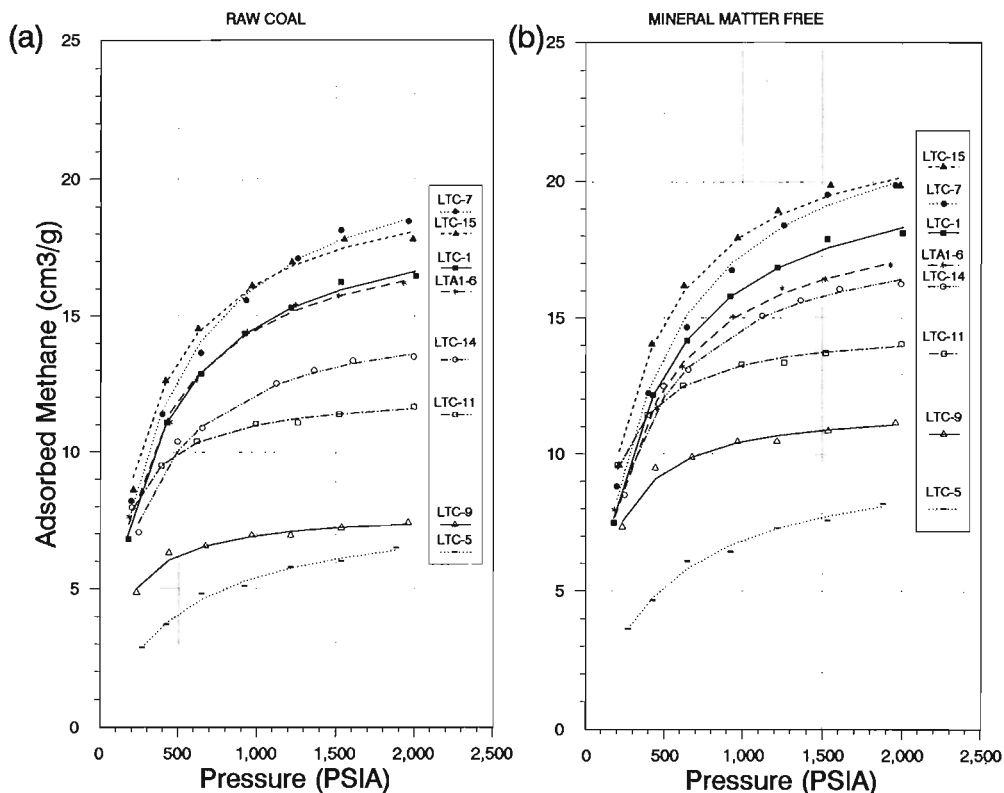


Figure 2. Methane adsorption isotherms produced on a a) raw coal and b) mineral matter free basis under equilibrium moisture at 22°C (Lamberson and Bustin, in press).

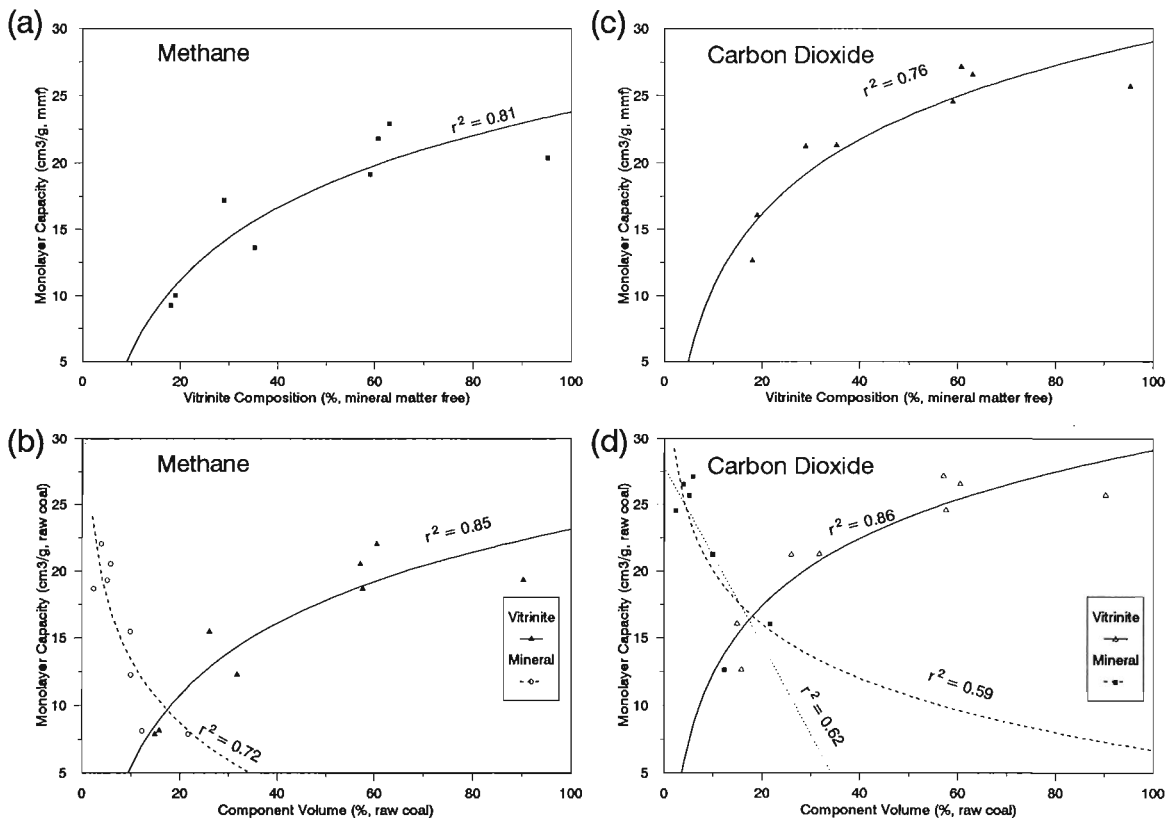


Figure 3. Plots of a), b) methane and c), d) carbon dioxide monolayer capacities (volumes) on a a), c) mineral matter free and b), d) raw coal basis (Lamberson and Bustin, in press).

### Adsorption studies

Mean CO<sub>2</sub> surface areas measured at 25°C vary from 57.6 to 123.86 m<sup>2</sup>/g (Table 4) and mean CO<sub>2</sub> monolayer capacities vary from 12.61 to 27.12 cm<sup>3</sup>/g (raw coal basis). These values have also been corrected for mineral matter using the Parr formula (Table 4; Lamberson and Bustin, in press). Experimental error is approximately ±0% for the measured values. Methane adsorption isotherms plotted on a raw coal and ash-corrected basis are given in Figure 2, and CH<sub>4</sub> monolayer capacities are given in Table 4.

Plots of CH<sub>4</sub> and CO<sub>2</sub> monolayer capacities versus vitrinite content on a raw coal and mineral matter free basis are given in Figure 3. The correlation between vitrinite content and CH<sub>4</sub> and CO<sub>2</sub> monolayer capacities appears to be exponential, but more analysis is needed to clarify this. A plot of low pressure CO<sub>2</sub> monolayer capacities versus high pressure CH<sub>4</sub> monolayer capacities (raw coal and mineral matter free basis) is given in Figure 4.

Dubinin-Astakhov differential pore volume curves are given for all samples in Figure 5. These curves are plots of the differential pore volume, an expression of how the pore volume changes with the equivalent pore diameter. A representative transformed Dubinin-Radushkevich plot, a plot of Log V vs. Log<sup>2</sup> (P<sub>0</sub>/P), is given in Figure 6.

## DISCUSSION

The plot of high pressure CH<sub>4</sub> and low pressure CO<sub>2</sub> monolayer capacities versus vitrinite and mineral matter content (Fig. 3) reveals several relationships. The CO<sub>2</sub> and CH<sub>4</sub> monolayer capacities (and thus CO<sub>2</sub> surface areas) show a general decrease with increased mineral matter or inertinite content and an increase with increased vitrinite content. The sample with the smallest CO<sub>2</sub> surface area was the sample with the lowest inertinite content (LTC-5). The largest surface areas and CH<sub>4</sub> adsorption recorded, however, were not the samples with the greatest vitrinite content, but those with a mixture of vitrinite and inertinite (LTC-7 and LTC-15). Lamberson and Bustin (in press) suggest that a possible explanation is that partial charring/burning, evidenced by the presence of structured inertinite and structured vitrinite, may

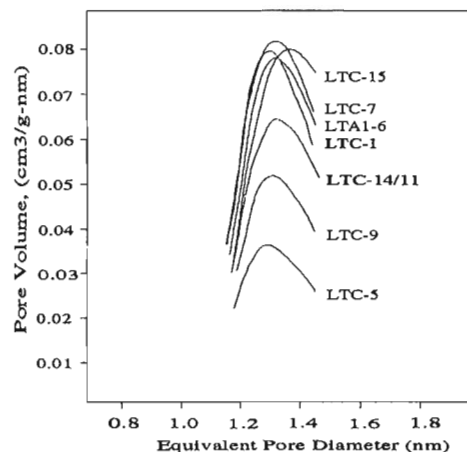


Figure 5. Dubinin-Radushkevich differential pore volume plots for all samples.

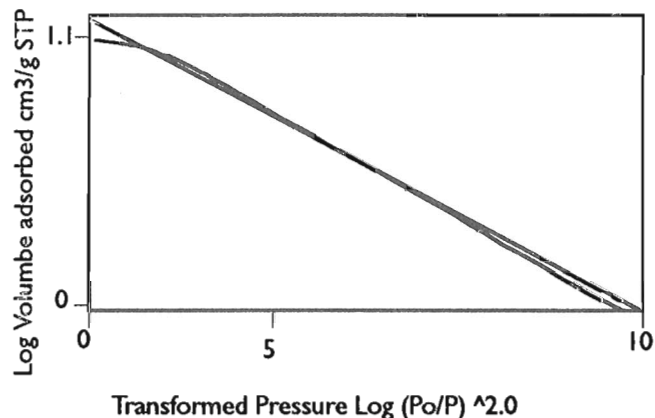


Figure 6. Representative transformed Dubinin plot.

increase the microporosity in these transitional materials as a result of the loss of volatile matter. The charring may be somewhat analogous to the formation of micropores of various sizes in activated carbon as a result of burn-off (Dubinin and Stoeckli, 1980).

LTC-1, the sample with the highest vitrinite and lowest mineral content, would be expected to have the highest CO<sub>2</sub> surface area and CH<sub>4</sub> adsorption based on the assumption that surface area generally increases with vitrinite content, but this is not observed. The transformed Dubinin-Radushkevich plot for this sample (Fig. 6) reveals that maximum deviation in linearity of the plot occurs at relative pressures approaching 0.032 whereas sample LTC-15 as marked does not show a deviation from linearity. Marsh (1987) attributes the presence of a second linear segment in some Dubinin-Radushkevich plots to either the absence of part of the pore size distribution at larger pore sizes or the filling of the entire microporosity at lower relative pressures. Although a second linear section is not observed in this study, the deviation from the initial, essentially linear section may also be due to either of the

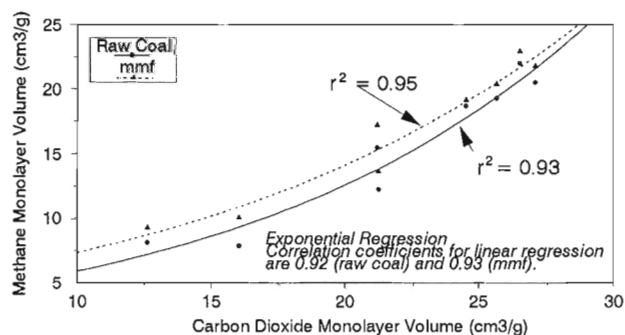


Figure 4. Relationship between methane and carbon dioxide monolayer capacities on a raw coal and mineral matter free basis (Lamberson and Bustin, in press).

above reasons; the lack of microporosity accounting for the lower surface area of LTC-1. All the samples showed some deviation from linearity at the upper relative pressures, but the deviation was greater for LTC-1 than for either LTC-15 or LTC-7.

The increase in surface area with vitrinite content could be due to either variations in the pore size distribution between samples or an absolute increase in number of micropores with vitrinite content. The differential pore volume plot shown in Figure 6 suggests that in coals of this study, an absolute increase in number of micropores in vitrinite relative to other macerals accounts for the larger surface area of vitrinite. The shape (nature) of the pore size distribution curve, as well as the mean equivalent diameter, is relatively uniform for each sample and thus pore size distribution varies little with composition. Our results in general support earlier conclusions that vitrinite is essentially microporous whereas inertinite is mainly meso-macroporous (Harris and Yust, 1979).

High pressure CH<sub>4</sub> monolayer capacities are consistently lower than the low pressure CO<sub>2</sub> monolayer capacities (Table 4), but the two monolayer capacities have an exponential relationship (Fig. 4). The reason for the lower CH<sub>4</sub> monolayer capacities may be the tighter packing of the quadropolar CO<sub>2</sub> molecule during adsorption than the nonpolar CH<sub>4</sub> molecule (Sato, 1981; Lamberson and Bustin, 1992).

## CONCLUSIONS

From the presented data, it is obvious that maceral composition is an important control upon the nature of porosity in coals. Methane adsorption is likewise affected by coal composition, and thus coal composition must be included among parameters, such as rank, pressure, etc., used in the assessment of coalbeds as a resource for CH<sub>4</sub>. It is also clear from the above discussion that much work must be done to explore the relationship between coal composition, the nature of its porosity and resulting surface area, and methane adsorption.

Our ongoing studies are designed to determine the relationship between CO<sub>2</sub> surface area, pore size distribution and rank, CO<sub>2</sub> and CH<sub>4</sub> monolayer capacities at low to medium pressures, and the effect of oxidation upon the surface area available to adsorbate gas and pore size.

## REFERENCES

- Ayers, W.B. and Kaiser, W.R.**  
1992: Coalbed methane occurrence and producibility, Fruitland Formation, Navajo Lake area, San Juan Basin, New Mexico; in Proceedings of The Canadian Coal and Coalbed Methane Geoscience Forum, Parksville, B.C., February 2-5, 1992, p. 3-20.
- Cameron, A.R.**  
1991: Comparison of petrographic and chemical characteristics in western Canadian coals; Geological Society of America, Abstracts and Programs, v. 23, no. 5, p. A143.
- Dawson, F.M. and Clow, J.T.**  
1992: Coalbed methane research, Elk Valley coalfield; in Proceedings of The Canadian Coal and Coalbed Methane Geoscience Forum, Parksville, B.C., February 2-5, 1992, p. 57-71.
- Dubin, M.M. and Stoeckli, H.F.**  
1980: Homogenous and heterogenous micropore structures in carbonaceous adsorbents; Journal of Colloid and Interface Science, v. 75, p. 34-42.
- Gan, H., Nandi, S.P., and Walker, P.L., Jr.**  
1972: Nature of Porosity in American coals; Fuel, v. 51, p. 272-277.
- Gregg, S.J. and Sing, K.S.W.**  
1982: Adsorption, Surface Area and Porosity, Second Edition; Academic Press, New York, 303 p.
- Harris, L.A. and Yust, C.S.**  
1979: Ultrafine structure of coal determined by electron microscopy: Preprint paper; American Chemical Society, Division of Fuel Chemistry, v. 24, p. 210-217.
- Kim, A.G.**  
1977: Estimating methane content of bituminous coalbeds from adsorption data; U.S. Bureau of Mines, Report of Investigations 8245, 22 p.
- Lamberson, M.N. and Bustin, R.M.**  
1992: Coalbed methane characteristics of Gates Formation lithotypes, northeastern British Columbia; in Proceedings of the Canadian Coal Coalbed Methane Geoscience Forum, Parksville, B.C., February 2-5, 1992, p. 87-101.  
in press: Coalbed methane characteristics of Gates Formation coals, northeastern British Columbia; American Association of Petroleum Geologists, Bulletin.
- Lowell, S. and Shields, J.E.**  
1984: Powder Surface Area and Porosity, Second Edition; Chapman and Hall, London, 234 p.
- Mahajan, O.P. and Walker, P.L., Jr.**  
1978: Porosity of coal and coal products, in Analytical Methods for Coal and Coal Products, Volume I, (ed.) C. Karr, Jr.; Academic Press, New York, p. 125-162.
- Marsh, H.**  
1987: Adsorption methods to study microporosity in coals and carbons: a critique; Carbon, v. 29, no. 1, p. 49-58.
- Mavor, M.J., Owen, L.B., and Pratt, T.J.**  
1990: Measurement and evaluation of isotherm data; Proceedings of 65th Annual Technical Conference and Exhibition of the Society of Petroleum Engineers, SPE 20728, p. 157-170.
- Meissner, F.F.**  
1984: Cretaceous and lower Tertiary coals as sources for gas accumulations in the Rocky Mountain area; in Source rocks of the Rocky Mountain Region, 184 Guidebook, Rocky Mountain Association of Geologists, p. 401-431.
- Rightmire, C.T.**  
1984: Coalbed methane resource; in Coalbed Methane Resources of the United States, (ed.) C.T. Rightmire, G.E. Eddy, and J.N. Kirr; AAPG Studies in Geology Series 17, p. 1-13.
- Sato, T.**  
1981: Methane recovery from coalbeds: surface and physical properties of western United States coals; M.Sc. thesis, The University of New Mexico, 78 p.

# Syntectonic deposition of the Carboniferous Borup Fiord Formation, northwestern Ellesmere Island, Northwest Territories

P. Thériault<sup>1</sup>, B. Beauchamp, and R. Steel<sup>1</sup>  
Institute of Sedimentary and Petroleum Geology, Calgary

*Thériault, P., Beauchamp, B., and Steel, R., 1993: Syntectonic deposition of the Carboniferous Borup Fiord Formation, northwestern Ellesmere Island, Northwest Territories; in Current Research, Part E; Geological Survey of Canada, Paper 93-1E, p. 105-112.*

---

**Abstract:** The Carboniferous Borup Fiord Formation, exposed in the vicinity of Hare Fiord on northwestern Ellesmere Island, comprises two distinct facies assemblages: (i) a conglomerate assemblage, deposited in alluvial fans and proximal braided streams; and (ii) a sandstone assemblage, deposited in more distal braided stream and floodplain environments. Facies relationships and paleocurrent directions show that the formation accumulated in a tectonic subbasin, the longitudinal axis of which corresponded approximately, both in location and orientation, to the present axis of Hare Fiord. This subbasin represents one of probably many continental depressions to have characterized the Early Carboniferous evolution of Sverdrup Basin.

**Résumé :** La Formation de Borup Fiord du Carbonifère, qui affleure près du fjord Hare dans le nord-est de l'île d'Ellesmere, comprend deux associations de faciès distinctes : (i) une association de conglomérats, déposée dans des cônes de déjection et des cours d'eau anastomosés proximaux; et (ii) une association de grès, déposée dans des cours d'eau anastomosés et des plaines d'inondation plus distaux. Les relations entre les faciès et les directions des paléocourants montrent que la formation s'est déposée dans un sous-bassin tectonique dont la position et l'orientation de l'axe longitudinal correspondaient approximativement à celles de l'axe actuel du fjord Hare. Le sous-bassin est une des dépressions continentales probablement nombreuses qui ont caractérisé l'évolution du bassin de Sverdup au Carbonifère précoce.

---

<sup>1</sup> Geological Institute Avd. A, University of Bergen, Allégaten 41, 5007 Bergen, Norway

## INTRODUCTION

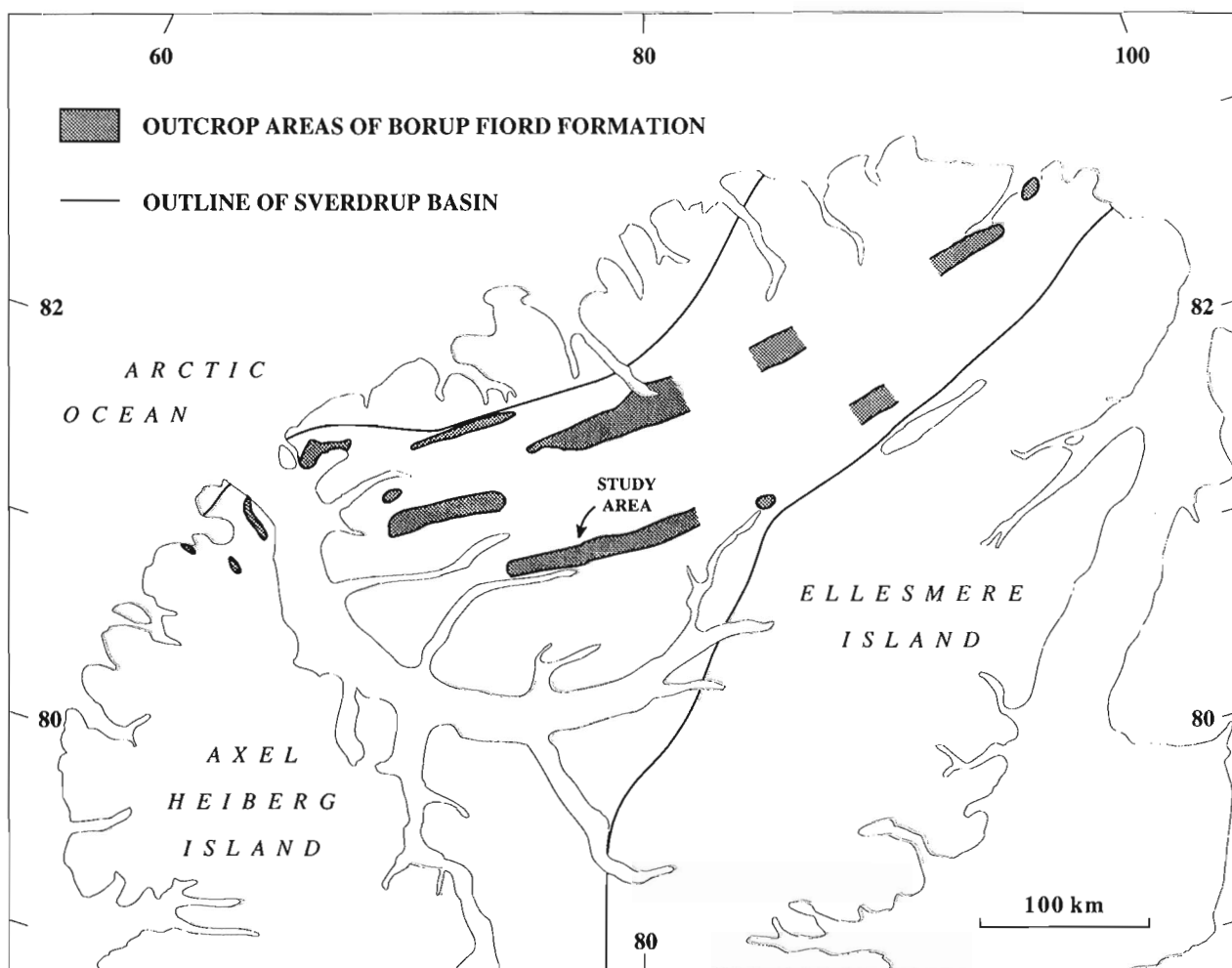
The Borup Fiord Formation is a Lower Carboniferous unit that outcrops on northern Ellesmere and northern Axel Heiberg islands (Fig. 1). It was deposited largely in fluvial environments during an early rift phase that heralded the development of Sverdrup Basin, now a major depocentre underlying the northern part of the Canadian Arctic Archipelago. Facies relationships, paleocurrent orientations, and a synrift tectonic context suggest that the Borup Fiord Formation accumulated in a number of small tectonic subbasins (Mayr, 1992). Unfortunately, because of intense Tertiary deformation related to the Eurekan Orogeny, the outline and geometry of these subbasins is no longer observable. The outcrop belts illustrated in Figure 1 may not represent Early Carboniferous depocentres.

The present study, which deals with sedimentological and stratigraphic data obtained largely from one of the outcrop areas (Fig. 1, 2), provides a preliminary account of the sedimentary history and paleogeographic setting of the Borup Fiord Formation during the early development of Sverdrup

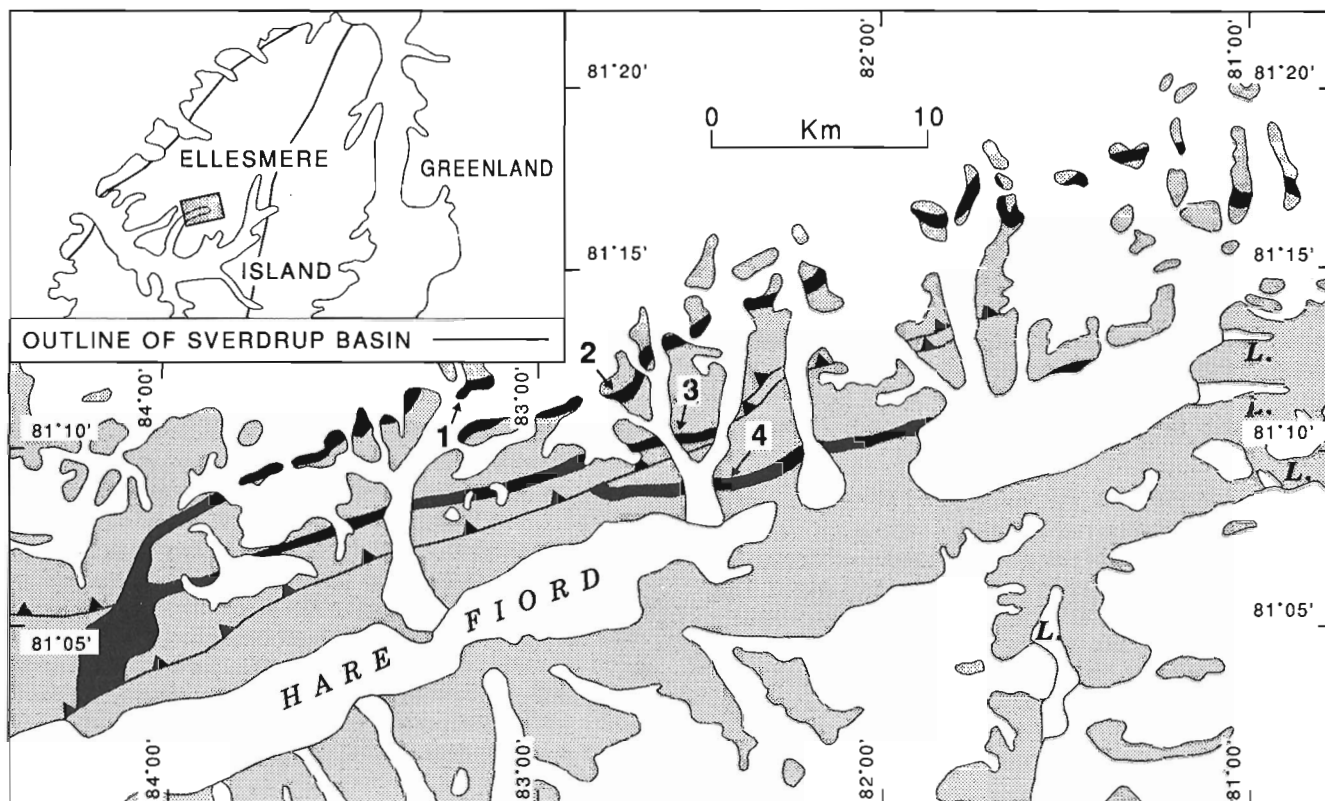
Basin. Future work will aim at identifying important depositional sequences and cycles within the formation, and at determining their degree of correlatability between the different outcrop areas.

## GEOLOGICAL SETTING

Sverdrup Basin is a successor rift basin located in the Canadian Arctic Archipelago. It was initiated in the Early Carboniferous with the gradual extension and collapse of the Franklinian Mobile Belt, and terminated in the middle Tertiary with the Eurekan Orogeny. Following compressional deformation in the Devonian, a reorientation of lithospheric stresses led to the development of several small, localized tectonic subbasins throughout Sverdrup Basin, within which the fluviolacustrine Viséan Emma Fiord Formation accumulated under subhumid climatic conditions (Davies and Nassichuk, 1988). Some of these subbasins are probably transpressive in origin, because a regional angular unconformity on top of the Emma Fiord (Thorsteinsson, 1974)



**Figure 1.** Known outcrop areas of the Borup Fiord Formation, based on Thorsteinsson (1974), Mayr (1992).



**Figure 2.** The study area on northwestern Ellesmere Island, showing the outcrop distribution of the Borup Fiord Formation. Numbers 1 to 4 are localities of stratigraphic sections displayed in Figure 3. Lakes are indicated by "L".

implies that the subbasin floors were uplifted in late Viséan or early Serpukhovian time, likely in relation to a phase of transpression.

Regional stress fields were later reorganized during the Early Carboniferous, resulting in the development of subbasins in central areas of Sverdrup Basin. Fluvial clastics of the Serpukhovian Borup Fiord Formation infilled the base of these subbasins in a semi-arid climate, contrasting with the earlier Viséan climate. Extensional faulting at the basin margin at that time was minor and may have controlled the local deposition of paleosol-hosting, undated fine clastics within relatively subdued subbasins (lower sandstone assemblage of the basal Canyon Fiord Formation; Thériault, 1991).

A rifting event in Early Bashkirian time intensely affected both central and marginal areas of Sverdrup Basin. This event resulted in a major transgression and the accumulation of marine limestones and evaporites near the basin centre above the Borup Fiord redbeds (Nansen and Otto Fiord formations; Thorsteinsson, 1974; Nassichuk and Davies, 1980), and fluvial conglomerates at the basin margin within well developed longitudinal subbasins (conglomerate assemblage of the basal Canyon Fiord Formation; Thériault, 1991).

Later, a Moscovian to Gzhelian regression led to the progradation of marine limestone throughout the bulk of the basin (Nansen Formation, basal Antoinette Formation, and

middle limestone member of the Canyon Fiord Formation; Thorsteinsson, 1974), and only subordinate marine and fluvial sandstone at the basin margin (upper clastic member of the Canyon Fiord Formation; Beauchamp, 1987).

## STRATIGRAPHY

The Borup Fiord Formation is a synrift, clastic-dominated unit exposed along the axis of Sverdrup Basin, on northern Ellesmere and northern Axel Heiberg islands. It has been assigned a Serpukhovian age, based on small foraminifers recovered from marine carbonates in the upper part of the formation (Thorsteinsson, 1974) at the type section north of Hare Fiord. The age is also based on its stratigraphic position between the Viséan Emma Fiord Formation (Davies and Nassichuk, 1988) and the Lower Bashkirian basal limestones of the Nansen Formation (Thorsteinsson, 1974). In the study area, and at nearly all other Borup Fiord localities, the Emma Fiord Formation is absent, such that the Borup Fiord Formation rests unconformably upon lower to middle Paleozoic basement strata. It is overlain by the Nansen Formation, and locally overlain by the Otto Fiord Formation.

Forty stratigraphic sections, measuring 40 to 1100 m and passing through the Borup Fiord Formation and basal Nansen Formation, were described in the course of field seasons in 1991 and 1992. Most of the work (23 measured sections) was

carried out in an area north of Hare Fiord (Fig. 2), where the Borup Fiord Formation outcrops as four narrow bands, each contained within separate, north-dipping Tertiary thrust sheets. The resulting stratal repetition due to thrusting is such that facies variations in the formation could not only be studied from east to west within each outcrop band, but also from north to south within the different thrust sheets. Because fluvial paleoflow in Borup Fiord time was found to be directed toward the south-southeast (see Table 1), the most rapid and well defined facies transitions are in a general north-northwest to south-southeast orientation, across outcrop belts. East-west facies changes within each belt are more subtle and follow no obvious pattern. In this context, the four localities outlined on Figure 2 are the sites of representative stratigraphic intervals for each of the four bands.

As seen in Figure 3, the Borup Fiord Formation passes rapidly from a conglomerate-dominated succession in the two northern bands (sections 1 and 2), to a sandstone-dominated succession in the two southern bands (sections 3 and 4). This overall lithofacies transition is interpreted to represent a proximal-to-distal graded fluvial profile, as supported by the following five lines of evidence: (1) general southward thickening of the formation (Fig. 2); (2) south-southeast-directed paleocurrents (Table 1); (3) southward decrease in the ratio of conglomerate units versus sandstone and mudstone units (Table 1); (4) southward decrease in the clast competence of conglomerate units (Table 1); and (5) caliche paleosols more common in the sandstone assemblage (Fig. 2). The four different lithofacies of the Borup Fiord Formation are often finely interlayered, which is not shown in the schematic representation of Figure 3. Sections 1 and 2 comprise no limestone, but as much as 90 to 95% conglomerate.

At the large scale, the succession can be subdivided into a few trends or sequences. For example, the sandstone assemblage of section 3 (Fig. 3) is organized, from base to top, into a 100 m thick coarsening-upward megasequence, a 130 m fining-upward megasequence, and a 150 m coarsening-upward megasequence. The two upper megasequences are characteristic of the entire outcrop band containing section 3, but the basal coarsening-upward sequence is restricted to the vicinity of section 3. At section 4, in the southernmost outcrop

band, only one coarsening-upward megasequence occurs at that scale. It measures 220 m, and correlates clearly with the second coarsening-upward megasequence at section 3. A basal fining-upward megasequence, also correlating with that at section 3, can be seen locally along the southernmost outcrop band.

Based on an overall slight increase in clast size upsection at sections 1 and 2, the conglomerate assemblage appears to be arranged into a coarsening-upward megasequence. This megasequence may or may not correlate with the uppermost coarsening-upward megasequence in the two southern outcrop bands.

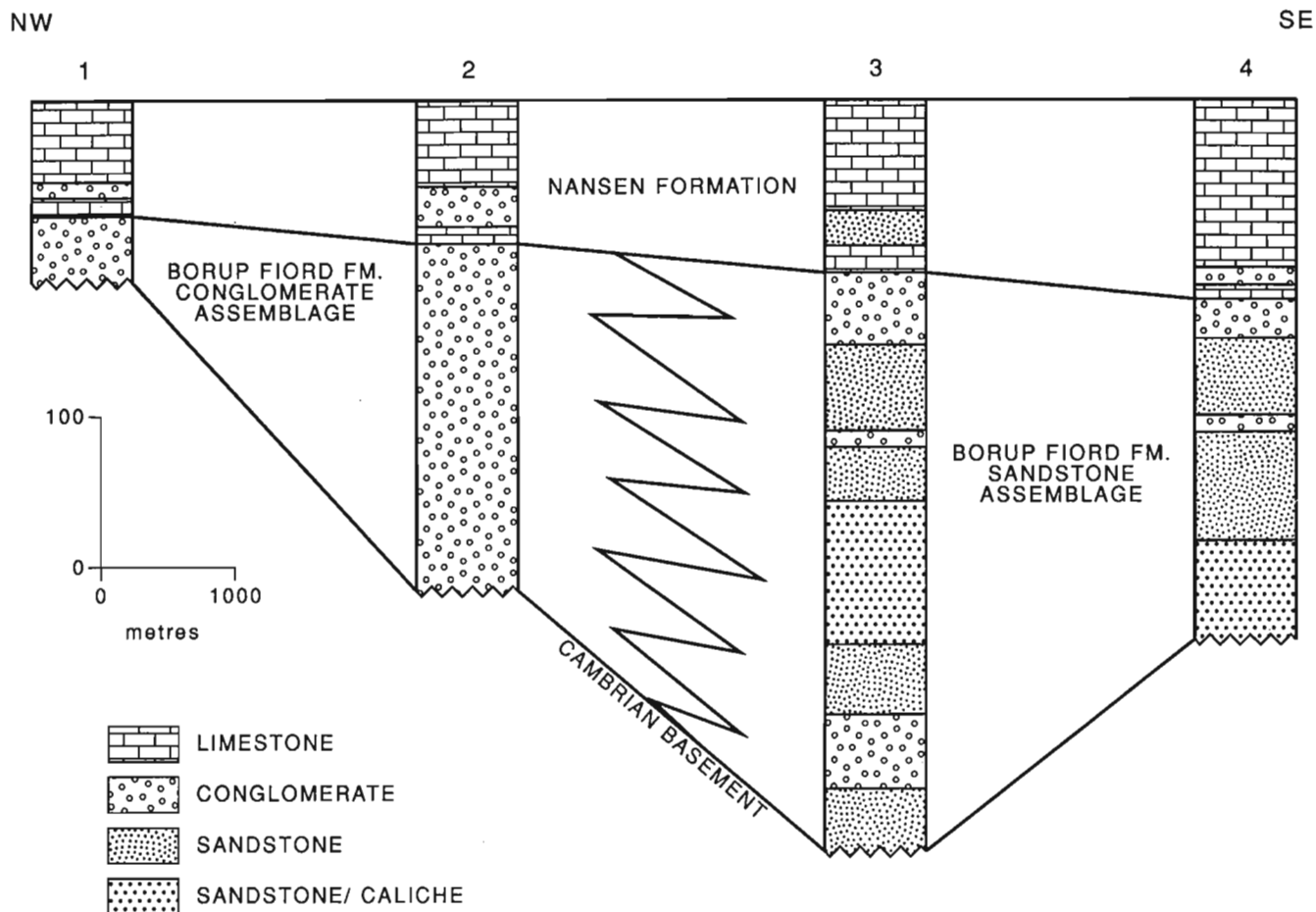
The origin of the megasequences within both lithofacies assemblages of the Borup Fiord Formation is almost certainly due to tectonic activity, although it is not yet possible to determine in which way tectonism acted on sedimentation to yield the observed sequences. Fining-upward and coarsening-upward megasequences can be seen in all syntectonic fluvial successions, and no clear consensus has been reached to explain them. One current model states that sedimentation reacts to significant events of fault-controlled subsidence by an initial, rapid progradation of fine axial facies above coarser marginal facies, followed by a gradual retrogradation of axial facies and accompanied progradation of marginal facies (Blair and Bilodeau, 1988; Steel and Ryseth, 1990). In response to one such tectonic cycle, the ideal stratigraphic succession would develop into overlying fining-upward (thinner) and coarsening-upward (thicker) megasequences. Although this model seems quite attractive, it should be applied with care, as it does not take into account important controls such as sediment supply and climate. It also fails to consider the time response of sedimentation to tectonic activity and changes in subsidence rates.

The contact between the Borup Fiord Formation and the Nansen Formation is shown as being diachronous from the southeast to the northwest in the study area (Fig. 3). This relationship is supported by the south-southeast-facing depositional slope inferred from paleocurrents, but remains to be tested with biostratigraphy. Moreover, the sharpness of the Borup Fiord/Nansen contact (Fig. 4) varies greatly throughout the study area, from being transitional over a thickness of 75 m, to being a disconformity with up to 200 m

**Table 1.** Statistical parameters at different localities of the Borup Fiord Formation; CGL, conglomerate; SST, sandstone; MDST, mudstone; MPS, maximum particle size.

Locality (Section)	Paleocurrents	CGL/SST+MDST	CGL MPS
1	160-190°	0.94	19 cm
2	145-200°	0.92	18 cm
3	135-155°	0.21	9 cm
4	115-165°	0.18	6 cm





**Figure 3.** Northwest-southeast cross-section of the Borup Fiord Formation and basal Nansen Formation. See Figure 2 for locations of stratigraphic sections.

of relief (i.e., Girty Creek area, in the central part of the southern outcrop band). In general, the contact is conformable within the three outcrop bands to the north, and disconformable in the southern band. The disconformity and its correlative conformity represent a significant sequence boundary, which is thought to have resulted from a regional rift-related phase of tectonic subsidence.

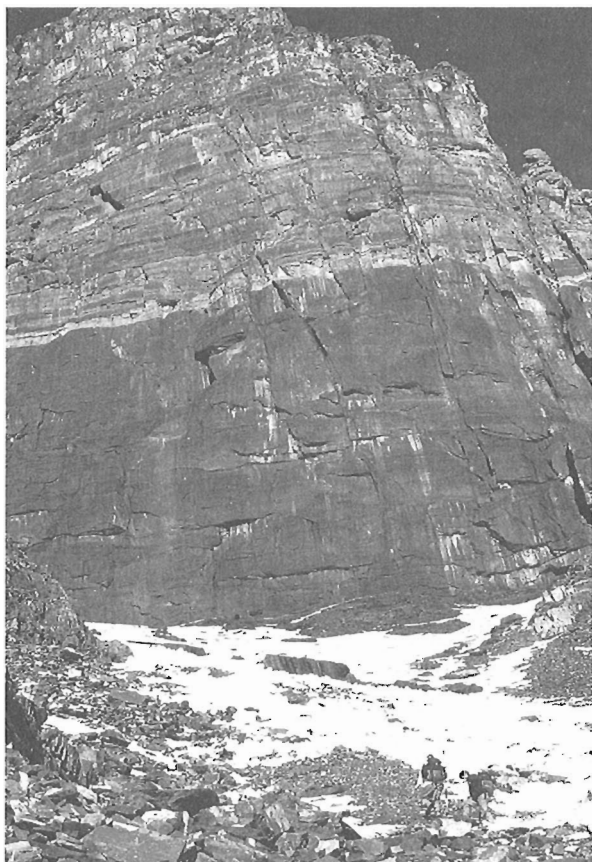
## SEDIMENTOLOGY

As discussed above, the Borup Fiord Formation has been subdivided into two distinct lithofacies assemblages. The first, a conglomerate assemblage, typified by the successions at sections 1 and 2, consists of conglomerate and subordinate interlayers of siltstone and sandstone. The second, a sandstone assemblage, exposed at sections 3 and 4, comprises interlayers of sandstone, siltstone, caliche paleosol, and conglomerate.

### *Conglomerate assemblage*

This lithofacies assemblage characterizes all exposed Borup Fiord strata within the two northern outcrop bands, and forms a southward thickening, coarse clastic wedge that is invariably exposed throughout the length of the two northern outcrop bands (Fig. 1). It either thins northward into a feather edge before disappearing under the ice cap, or thins out completely to be replaced by an interval of Nansen limestones resting unconformably on Cambrian basement. Exposures form spectacular, often inaccessible cliffs and mountain faces, and are of a weathered reddish-brown to greyish-brown.

The conglomerates (Fig. 5), which constitute more than 90% of the assemblage, are medium- to very thick-bedded, sheetlike or in the form of shallow lenses, and are internally massive with minor tabular crossbeddings. Crossbedded units also contain common normal grading, which is characterized by a pebbly to cobbly, well-sorted openwork base grading into a pebbly, poorly sorted and matrix-rich upper part. Both



**Figure 4.** Conglomerate-dominated Borup Fiord Formation (dark-coloured cliff) overlain by marine limestones of the Nansen Formation (light-coloured cliff), north of the head of Hare Fiord, 3 km northeast of section 2. The Borup Fiord Formation is 68 m thick. The Borup Fiord-Nansen contact is transitional over a thickness of 10 m. ISPG 2806-10

clast-supported and matrix-supported conglomerates are present. Clasts are subspherical to subplaty in shape, and are variably arranged into disorganized or imbricate fabrics. Where imbricated, the B-axis of clasts shows a preferred orientation towards the southeast or south-southeast (Table 1 – nearly 500 separate clasts were measured for orientational purposes at 12 different stations in sections 1 and 2). The clasts are also subangular in general, and composed of 95 to 99% varicoloured chert with less than 5% brownish sandstone and clear polycrystalline quartz. Maximum particle size values (MPS – the average size of the ten largest clasts measured in one bed) were found to vary between 15 and 25 cm at section 1 (average of 19 cm from 9 stations), and between 7 and 35 cm at section 2 (average of 18 cm from 30 stations). Matrix, 5 to 20% in content, is unsorted and sand-rich.

The coarseness and massive/disorganized nature of many conglomerate units, together with the scarcity of interlayered sandstones or mudstones, suggest that they represent mass-flow and sheetflood deposits of alluvial fan origin. The odd lenticular, crossbedded and/or normally-graded unit is likely to be of stream-channel origin.

The conglomerate assemblage also contains 5 to 10% of relatively thin sandstone and siltstone intervals. These are up to 5 m thick, but are most often in the 20 to 50 cm range and laterally discontinuous. They are composed of any of the following lithologies: (1) siltstone to fine sandstone, with or without minor pebbles and/or caliche nodules; (2) pebbly sandstone; and (3) nodular caliche. These lithologies occur as units that are internally massive, and are interpreted as sheetflood alluvial fan deposits. They likely accumulated on relatively inactive parts of the alluvial fans, at times when the site of coarse sediment accumulation had shifted laterally.



**Figure 5.**

Clast-supported cobble conglomerate from the conglomerate assemblage of Borup Fiord Formation, north of the head of Hare Fiord, northwestern Ellesmere Island. Hammer for scale. ISPG 3806-7

### *Sandstone assemblage*

The sandstone assemblage of the Borup Fiord Formation is widely exposed throughout the two southern outcrop bands, and is typified by sections 3 and 4. Exposures are good yet partly recessive, and are invariably of a weathered deep reddish-brown. The assemblage consists predominantly of sandstones and siltstones, along with less common intervals of conglomerate and caliche paleosol. These lithologies are complexly interlayered but appear, ideally, to follow small-scale fining-upward cycles of the type conglomerate-sandstone-siltstone-caliche. In most instances, one or two of the lithologies are absent from a given cycle, giving the succession a more random character. A further complication is that most fining-upward cycles, which measure between 5 and 20 m on average, have smaller-scale cycles or rhythms encompassed within them.

The conglomerates in the sandstone assemblage are predominantly fine- to thick-bedded, lenticular in shape, massive or tabular crossbedded, and clast-supported. Crossbedded units also show common normal grading. Clasts are subspherical to subplaty in shape, and are either disorganized or imbricate. Imbrication directions are preferentially oriented toward the south-southeast (Table 1 – nearly 400 separate clasts were measured at 9 different stations in sections 3 and 4). The clasts are also subrounded in outline, and composed of 80 to 95% chert, 1 to 10% sandstone, and 1 to 10% polycrystalline quartz. Maximum particle size is between 2 and 18 cm at section 3 (average of 9 cm from 29 stations), and between 1 and 15 cm at section 4 (average of 6 cm from 27 stations). Matrix ranges in content from 5 to 15%, and is poorly to moderately sorted and sand-rich.

The conglomerate units within the sandstone assemblage are interpreted as stream-channel deposits of distal alluvial fan or proximal braided stream environments. The fact that no paleocurrents with northeast-southwest orientations were recovered from the conglomerates of sections 3 and 4

suggests that these units are distal counterparts of the transverse fluvial system interpreted farther north for sections 1 and 2, and that they are not part of an axial-flow system.

Caliche paleosols are locally abundant in the sandstone assemblage (Fig. 6). They are hosted by fine sandstones and siltstones, in which they occur as nodular, nodular-massive, and massive varieties. Nodular caliches are up to 2 m thick, and are commonly overlain by a horizon of nodular-massive or massive caliche that locally reaches 1.5 m in thickness. The thicker caliche profiles outcrop as resistant benches that can be followed laterally for hundreds of metres, if not kilometres (such as profiles 2-3 near the base of the sandstone-caliche intervals displayed in Fig. 3). Pedogenic caliche development occurred during periods of low sedimentation rates.

The sandstone units of the sandstone assemblage are sheetlike to slightly lenticular, have bed thicknesses in the order of 5 to 50 cm, and vary from internally massive to low-angle trough crossbedded to tabular crossbedded. They are very fine grained to pebbly, quartz-rich, and relatively well sorted. Many beds contain variable amounts of caliche nodules. Desiccation cracks are often found on the bedding planes of scree blocks. Siltstone units are commonly present as interlayered intervals together with fine sandstones. They are invariably massive, 5 to 30 cm thick on average, and host varying amounts of granules, pebbles, and caliche nodules.

The sandstones and siltstones of the sandstone assemblage are interpreted as being mainly the sheetflood overbank deposits of braided streams that flowed southeastward and another similar braided system that flowed southwestward. These orientations were recovered from well-exposed crossbeds at three localities other than section 4, along the southern outcrop band. They suggest that the southern part of the study area lies near the intersection of the transverse fluvial system discussed above and an axial fluvial system running along the axis of maximum subsidence of a middle Carboniferous subbasin.



**Figure 6.**

Pebbly sandstone lying on top of nodular caliche in the sandstone assemblage of Borup Fiord Formation, north of the head of Hare Fiord, northwestern Ellesmere Island. Hammer for scale on caliche layer. ISPG 3806-5

## CONCLUDING REMARKS

It is somewhat problematic that the succession at section 3 is thicker than that at section 4 (Fig. 3) and, for that matter, at all localities along the southern band where section 4 was measured. Such geometry could be understood in terms of section 3 and its related outcrop band lying along the longitudinal axis of a subbasin, with the southernmost outcrop band lying on a north-facing paleoslope. However, based on the recovered paleocurrents, this geometry is probably incorrect. Instead, it may be that section 3 is lying in an area along the outcrop band where subsidence was controlled by local faults, perhaps early in Borup Fiord time. The axis of maximum subsidence could have subsequently migrated southward with time, explaining the southward paleoflows in conglomerates of the southern band. Further, it is impossible to determine if the thickness of the succession at section 3 is representative of the outcrop band. The thrust fault lying immediately adjacent to this band cuts down into the formation (Fig. 1), except in the vicinity of section 3, where the thrust fault lies within the Nansen Formation, less than 100 m from its base.

In summary, the Borup Fiord Formation exposed in the vicinity of Hare Fiord was deposited in an Early Carboniferous subbasin characterized by a coarse clastic wedge along its northwestern margin and an adjacent sandstone-dominated succession lying near the subbasin axis. The southeastern margin of the subbasin is concealed in the subsurface somewhere south of Hare Fiord. Work in progress is showing that other similar subbasins existed in Early Carboniferous time and controlled Borup Fiord sedimentation on northern Axel Heiberg Island and northern Ellesmere Island.

## ACKNOWLEDGMENTS

We wish to thank Sylvie Pinard for kindly reviewing the manuscript, and C. Lee, L. Letiecq, C. Sherry, P. Vaillancourt, and V. Wasiuta for their help in the field. Logistical support was provided by the Polar Continental Shelf Project.

## REFERENCES

### Beauchamp, B.

1987: Stratigraphy and facies analysis of the Upper Carboniferous to Lower Permian Canyon Fiord, Belcher Channel and Nansen formations, southwestern Ellesmere Island; Ph.D. thesis, University of Calgary, Calgary, Alberta, June 1987, 370 p.

### Blair, T.C. and Bilodeau, W.L.

1988: Development of tectonic cyclothems in rift, pull-apart, and foreland basins: sedimentary response to episodic tectonism; *Geology*, v. 16, p. 517-520.

### Davies, G.R. and Nassichuk, W.W.

1988: An Early Carboniferous (Viséan) lacustrine oil shale in Canadian Arctic Archipelago; *Bulletin of the American Association of Petroleum Geologists*, v. 92, p. 8-20.

### Mayr, U.

1992: Reconnaissance and preliminary interpretation of Upper Devonian to Permian stratigraphy of northeastern Ellesmere Island, Canadian Arctic Archipelago; Geological Survey of Canada, Paper 91-08, 117 p.

### Nassichuk, W.W. and Davies, G.R.

1980: Stratigraphy and sedimentation of the Otto Fiord Formation; Geological Survey of Canada, Bulletin 286, 87 p.

### Steel, R. and Ryseth, A.

1990 The Triassic – early Jurassic succession in the northern North Sea: megasequence stratigraphy and intra-Triassic tectonics; in *Tectonic Events Responsible for Britain's Oil and Gas Reserves*, (ed.) R.F.P. Hardman and J. Brooks; Geological Society of London, Special Publication No. 55, p. 139-168.

### Thériault, P.

1991: Synrift sedimentation of the Upper Carboniferous Canyon Fiord Formation, SW Ellesmere Island, Canadian Arctic; M.Sc. thesis, University of Ottawa, Ottawa, Ontario, March 1991, 210 p.

### Thorsteinsson, R.

1974: Carboniferous and Permian stratigraphy of Axel Heiberg Island and western Ellesmere Island, Canadian Arctic Archipelago; Geological Survey of Canada, Bulletin 224, 115 p.

# Update of Canada-Russia collaboration on Arctic pollutants

W.W. Nassichuk, D.N. Skibo, M.G. Fowler, K.R. Stewart,  
and L.R. Snowdon

Institute of Sedimentary and Petroleum Geology, Calgary

*Nassichuk, W.W., Skibo, D.N., Fowler, M.G., Stewart, K.R., and Snowdon, L.R., 1993: Update of Canada-Russia collaboration on Arctic pollutants; in Current Research, Part E; Geological Survey of Canada, Paper 93-1E, p. 113-121.*

---

**Abstract:** In 1991, a new project on anthropogenic contaminants in the Arctic Ocean was initiated within the Canada-Russia Agreement on Cooperation in the Arctic and the North. The purpose of the project is to determine the distribution and concentration of heavy metals, radionuclides, polycyclic aromatic hydrocarbons (PAHs), and organochlorines in seafloor sediments off Arctic Canada and Siberia. During 1992, several hundred samples were taken from 54 stations (56 sites) in the eastern Barents Sea. We have also measured the total organic carbon (TOC) present in the uppermost part of the seabed at 55 sites. A significant proportion of the total organic carbon at most sites appears to have been derived from natural terrestrial sources but some was also derived from marine sources. Whether high S1 peaks are due to natural biological productivity or to anthropogenic input can only be decided when further data from measurements on oxidation conditions and more detailed hydrocarbon analyses are available.

**Résumé :** En 1991, un nouveau projet portant sur les contaminants anthropogènes dans l'océan Arctique a été mis sur pied dans le cadre de l'Accord canado-russe sur la collaboration dans l'Arctique et le Nord. Le but du projet est de déterminer la distribution et la concentration des métaux lourds, des radionucléides, des hydrocarbures aromatiques polycycliques (HAP) et des organochlorés dans les sédiments du fond marin au large des côtes arctiques du Canada et de la Sibérie. En 1992, plusieurs centaines d'échantillons ont été prélevés à 54 stations (56 sites) dans l'est de la mer de Barents. Les auteurs ont aussi mesuré le carbone organique total (COT) présent dans la partie supérieure du fond marin à 55 sites. À la plupart des sites, une part importante du COT semble provenir de sources terrestres naturelles, mais une certaine partie provient aussi de sources marines. Il sera possible de savoir si les pics S1 élevés sont attribuables à la productivité biologique naturelle ou à un apport anthropogène une fois que seront disponibles d'autres résultats de mesures sur les conditions d'oxydation et d'analyses plus détaillées des hydrocarbures.

## INTRODUCTION

Ten collaborative projects on geology, geophysics, and geochemistry are active within the geoscience (petroleum) theme of the Canada-Russia Agreement on Cooperation in the Arctic and the North. Since scientific work on this theme began in 1984 under the leadership of W.W. Hutchison, former Director of the Geological Survey of Canada, a number of important maps and reports, co-authored by Russian and Canadian scientists, have been published. Important considerations that led to initiation of the Agreement in 1984 included the significant acceleration in the exploration for and exploitation of oil, gas, and mineral resources in Siberia at that time, and concerns about the consequent impact of these activities on the circum-Arctic environment.

In a speech in Murmansk in 1987, Mr. Gorbachev stressed the importance of co-operative scientific research in the Arctic and, for the first time, he also stressed the importance of protecting the Arctic environment. As suggested by Hoensma (1991), this was a significant turning point for co-operative scientific research in Arctic Russia. In particular, it proved to be a powerful impetus for Russian scientists to participate in joint environmental studies with scientists from other Arctic nations.

Thus, in 1991 the environmental project discussed herein was initiated within the framework of the Canada-Russia Agreement. The intent of the project is to determine, through chemical analysis, the concentration of heavy metals, organic toxins, including some polycyclic aromatic hydrocarbons (PAHs), and organochlorines, including polychlorinated biphenyls (PCBs), in seafloor sediments off Arctic Canada and Siberia. A secondary objective is to determine the character and concentration of radionuclides in Arctic seafloor sediments. It is imperative to increase our knowledge about contaminants in the Arctic so that environmental standards can be instituted in all Arctic regions to safeguard the health of Arctic inhabitants. Even now, relatively elevated concentrations of pesticides, herbicides, and other industrial compounds are present in the Arctic marine ecosystem (Muir et al., 1992; Thomas et al., 1992). Indeed, PCB levels in the blood of part of the Arctic human population might already be dangerously high (Kinloch et al., 1992; Williams-Walsh, 1991). A comprehensive summary of the chemistry, toxicity, mechanisms for dispersal, and pathways to the food chain for all known pollutants in the Arctic environment was produced by Barrie et al. (1992) and this document serves as a particularly important basic reference. Polish and Czechoslovakian government agencies have provided important data on heavy metals in water, glacier ice, plants, and animals from Svalbard at the northernmost end of the Barents Sea (Drbal et al., 1992).

Numerous atmospheric nuclear tests were conducted in the vicinity of Novaya Zemlya up until the Test Ban Treaty in 1962; this was also the site for 40 underground nuclear tests. Radioactive material (fallout) appears to have been distributed widely over the Siberian land mass and over the adjacent Arctic Ocean. Thomas et al. (1992) expressed concerns about the persistence of radionuclides in the

terrestrial Arctic because of the lichen-reindeer-human ecosystem. We have statistical data showing that specific diseases and human death rates from 1960 to 1980, between Murmansk and Chukhotka near the Bering Sea, are much higher than the national Russian average. Although radioactive fallout might well be an important factor affecting those statistics, other anthropogenic airborne and waterborne pollutants cannot be discounted as contributors.

It is also possible that radioactive isotopes from underground tests on Novaya Zemlya have found their way into the Arctic Ocean (Clery, 1993). Further, about 21 nuclear reactors and other nuclear waste were reported to have been dumped in the Barents and Kara seas on the west and east side of Novaya Zemlya, respectively (Cernetig, 1993; MacKenzie, 1993; Wilson, 1993). Little is known about the distribution of radionuclides, heavy metals, and organic toxins in these seas, or indeed in any of the other polar seas adjacent to Siberia. It is crucial to know the degree to which contaminants might have spread elsewhere, possibly into Canadian territory through clockwise circulation of surface waters in the Beaufort Gyre, or farther east, to Greenland, through the northward movement of surface waters in the transpolar drift.

Therefore, our main purpose is to determine the level of anthropogenic contaminants in the shelf areas adjacent to Russia and Canada in a manner in accord with marine environment strategies prepared by the Arctic Monitoring and Assessment Program (AMAP). AMAP was established in 1991 by the "Circum-Polar 8": Canada, Denmark, Finland, Iceland, Norway, Russia, Sweden, and the United States. It is understood, of course, that some heavy metal and organic contaminants in the Arctic environment were derived from natural sources and it is important to distinguish these from anthropogenic contaminants. As we proceed with this project we would like to attract participation by geologists and other scientists elsewhere in the "Circum-Polar 8".

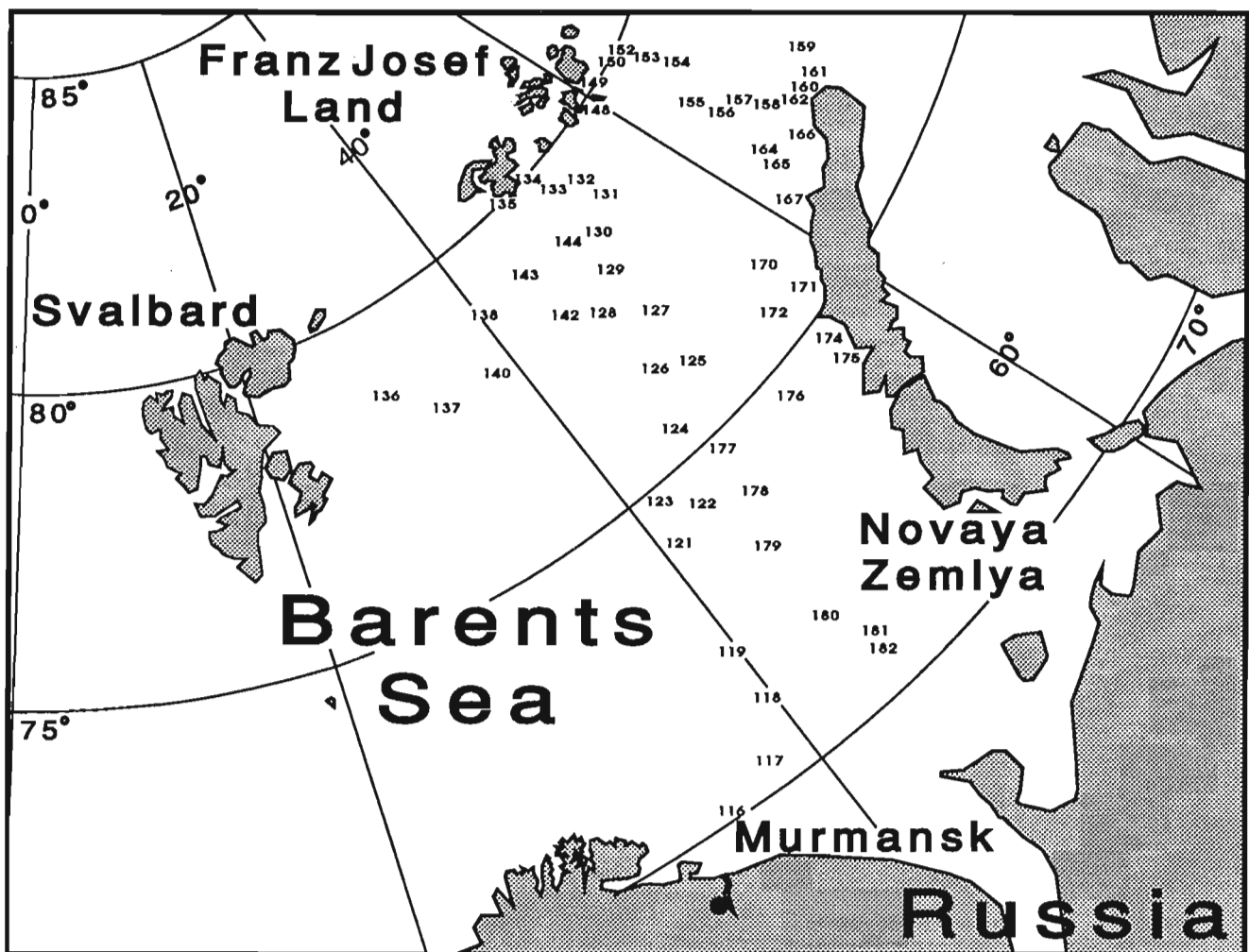
During 1992, Russian environmental geologists D. Dodin and Y. Bordukhov, both of whom are familiar with nickel and copper mining operations in the Noril'sk area south of Taymyr Peninsula, were introduced to the environmental procedures that are in place at the Nanisivik Mine (lead-zinc) on northern Baffin Island and at the Inco Mine (nickel) at Sudbury. In the same year, the project supported K. Saunders (Dalhousie University) in collecting seabed samples from 56 sites in the Barents Sea (Fig. 1) aboard the Russian research vessel "Geolog Fersman". These samples are currently being analyzed for heavy metal, radionuclide, and organic matter concentrations in Geological Survey of Canada laboratories and in other government and industrial laboratories in Canada. Although we have not yet received the final heavy metal or radionuclide data from those laboratories, preliminary information suggests that there are elevated concentrations of specific heavy metals and radionuclides at certain sites in the Barents Sea. We have determined the total organic carbon (TOC) values through Rock-Eval pyrolysis for some 120 samples from the Barents Sea; this report presents analyses of 52 of those from the upper few centimetres of the seabed (Fig. 1). Laboratory analyses for polyaromatic hydrocarbons (PAHs), organochlorines (PCBs) and other pesticides have not been completed.

The concentration and character of organic matter in seabed sediments from the Barents Sea is relevant to our studies for the following reasons:

- 1) Interaction between trace metals and organic matter has long been noted in, for example, the uptake of nickel and vanadium in bitumens and tar sands. It is known that Ni and V exhibit strong covalent bonding with porphyrin complexes. Such bonds are very stable during the evolution of the corresponding bulk sediments - during the lithification, diagenesis, migration, and entrapment stages of organic maturation.
- 2) The combination of mercury and organic materials can be an indicator of anthropogenic contamination. Insofar as organochlorines are concerned, the North Atlantic and Arctic oceans appear to be dominant sinks for PCBs, which are well represented high in the food chain in the Canadian Arctic.
- 3) The study and assessment of radionuclide waste disposal methods has been an important concern to society since the advent of the nuclear age. Particularly during the past

decade, the study of the geochemical behaviour of radionuclides and other trace elements in natural environments has received important attention. In a search for optimal disposal methods, increased attention has been given to the study of "natural analogues" - geological conditions and materials which are known to have provided long term, effective storage of radionuclides. Through such studies, it is hoped to learn how to fabricate safe repositories and to better understand the long-term behaviour of anthropogenic radioactive contamination of the environment. Uranium mines are the most obvious natural geological repositories of radionuclides. Two in particular, Oklo in Gabon (Cowan, 1978; Hageman and Roth, 1978) and Osamu Utsimi in Brazil (Chapman et al., 1992), have been extensively studied recently. The first of these is the only known natural occurrence of a nuclear chain reaction. The second is one of the most naturally radioactive places on the surface of the Earth.

The uptake and retention of radionuclides and trace elements by geological material has been investigated in natural volcanic glasses, clay minerals, bitumens, and resins



**Figure 1.** Map showing location of sites in the Barents Sea where samples were collected from the research vessel "Geolog Fersman" in 1992.

(Lutze and Ewing, 1988). However, only a field study and a literature review are available for waste disposal analogues of bitumen (Hellmuth, 1989a, b).

Natural bitumens are complex organic materials originating mainly from living organisms. Bitumen formation is a step in a series of geological events, associated with the diagenesis of sediments, which can also lead to the formation of petroleum hydrocarbons. The maturation of natural organic materials in the environment can be tracked by the variation in their H/C and O/C atomic ratios. Bitumen molecular constituents are saturated and aromatic hydrocarbons, NSO

compounds (resins), heterocyclic compounds, and high-molecular weight asphaltenes (molecular weight 300 to >10 000). Two main paths of evolution can be defined: diagenetic alteration (mainly temperature dependent), and weathering. With regard to the uptake of radioisotopes, uranium can be fixed by bitumen in concentrations up to a few per cent. Indeed, it is well known that many uranium ore bodies in sediments are closely associated with organic matter, including bitumens, for example, in zones 10 to 13 at the Oklo uranium mine in Gabon, the site of a prehistoric (Precambrian) natural nuclear reactor.

**Table 1.** Results from Rock-Eval/TOC analyses of Barents Sea surface samples collected from the research vessel "Geolog Fersman" in 1992<sup>1</sup>

Sample Site	Water Depth (m)	Interval (cm)	TOC	PI	S1 + S2	T <sub>max</sub>	S1	S2	S3	HI	OI
116-01	189 G *	0-10	0.64	0.21	1.28	394	0.27	1.01	1.16	159	182
119-01	320 G	0-2	1.84	0.26	4.93	385	1.28	3.66	3.98	199	217
121-01	222 G	0-1	1.11	0.23	2.80	395	0.66	2.15	2.34	194	212
122-01	276 G	0-1	1.41	0.22	2.38	404	0.50	1.88	3.35	133	238
123-01	180 G	0-2	1.07	0.21	2.77	394	0.59	2.18	2.00	203	187
124-01	316 G	0-1	3.28	0.31	8.02	384	2.49	5.53	9.63	168	293
124-16	316 C *	15-20	3.15	0.21	6.18	407	1.31	4.87	6.12	155	194
124-17	316 C *	20-25	2.74	0.21	5.26	413	1.11	4.15	5.02	151	183
124-18	316 C *	25-30	2.62	0.21	4.76	405	0.99	3.77	7.86	143	300
129-01	190 C *	0-1	0.64	0.29	1.10	430	0.31	0.79	2.15	123	336
130-01	246 G	0-1	0.96	0.26	1.93	392	0.51	1.42	3.55	149	371
131-01	226 G	0-1.5	1.06	0.30	1.99	377	0.59	1.40	4.49	132	425
132-01	177 G	0-1.5	1.07	0.23	1.20	421	0.27	0.93	2.79	87	262
133-01	456 G	0-1	2.09	0.35	4.34	392	1.50	2.84	7.81	136	374
134-01	40 G	1-3	0.05	0.12	0.21	454	0.03	0.18	0.01	360	20
135-01	134 G	0-1	0.43	0.16	0.86	471	0.14	0.73	0.95	169	219
136-01	228 G *	0-1	1.10	0.13	2.21	475	0.28	1.94	3.12	177	285
137-01	227 G *	0-1	1.78	0.26	4.70	383	1.21	3.50	2.85	196	160
138-01	242 G	0-1	1.21	0.30	2.88	387	0.85	2.03	4.10	168	338
140-01	212 G	0-1	1.21	0.26	2.85	413	0.74	2.11	4.65	174	383
142-01	358 G	0-1	2.45	0.31	5.94	373	1.87	4.07	8.56	166	350
143-01	148 G	0-1	0.54	0.23	0.96	405	0.22	0.74	1.23	138	230
144-01	326 G	0-1	1.44	0.33	2.57	371	0.84	1.73	7.00	120	487
149-01	386 G	0-1	1.97	0.24	3.94	487	0.91	3.03	5.82	153	296

<sup>1</sup>The table contains the standard measured Rock-Eval parameters as well as some derived parameters (Espitalié et al., 1977, 1985): TOC, total organic carbon reported as per cent by weight of the whole rock; T<sub>max</sub>, temperature (°C) at the top of the S2 peak; S1, hydrocarbons evolved (distilled or thermovaporized) at 300°C (mg hydrocarbon per g rock); S2, hydrocarbons evolved during heating at 25°C/min between 300°C and 600°C; S3, organic carbon dioxide evolved at 300°C and up to 390°C; PI, Production Index=S1/(S1+S2); HI, Hydrogen Index=S2/TOC; and OI, Oxygen Index=S3/TOC. In the sample site column the first three digits are represented on Figure 1, and the last two digits represent specific samples from that site. In the water depth column: G, grab; C, core; \*metal can sample (other samples stored in plastic container)



## ROCK-EVAL/TOC PYROLYSIS

The Rock-Eval/TOC anhydrous pyrolysis technique is normally used for the evaluation of shows of oil or gas, oil and gas generation potential, thermal maturity, and indications of the organic matter type in potential petroleum source rocks (Espitalié et al., 1977, 1985, 1985/86; Peters, 1986; Tissot and Welte, 1984, p. 443-447). The Rock-Eval/TOC analysis gives five parameters: S1, S2, S3, TOC, and  $T_{max}$  (Espitalié, 1986). Espitalié et al. (1977) stated that the first peak (S1) represents the free and adsorbed hydrocarbons already present, vaporized at 300°C. The second peak (S2)

represents the hydrocarbons generated directly from the kerogen by thermal cracking during programmed linear temperature increase from 300 to 600°C (a usual heating rate is 25°C/min). Kerogen is organic matter formed by polymerization of organic molecules and is insoluble in common organic solvents. Peak S3 represents organic carbon dioxide (CO<sub>2</sub>) released at 300 to 390°C. According to Espitalié et al. (1977), S1 is a measure of the bitumen content and S2 is a measure of the insoluble kerogen content. The Production Index (PI) ratio S1/(S1+S2) is an evaluation of the transformation of kerogen into oil (in the absence of migration).  $T_{max}$  is the temperature (°C) corresponding to the

Table 1. (cont.)

Sample Site	Water Depth (m)	Interval (cm)	TOC	PI	S1 + S2	$T_{max}$	S1	S2	S3	HI	OI
116-01	189 G *	0-10	0.64	0.21	1.28	394	0.27	1.01	1.16	159	182
150-01	100 G	0-1	1.70	0.17	1.83	426	0.31	1.53	2.52	91	148
152-01	250 G	0-1	1.44	0.24	2.85	498	0.68	2.17	5.81	151	404
153-01	465 G	0-1	1.15	0.25	2.15	548	0.54	1.61	4.67	140	406
153-39	465 C *	0-10	1.02	0.22	2.65	362	0.58	2.08	2.94	204	289
154-01	385 G	0-1	0.81	0.31	1.39	536	0.43	0.96	4.02	119	499
155-01	362 G	0-1	0.89	0.29	1.80	572	0.52	1.28	5.03	144	568
156-01	340 G	0-1	1.67	0.35	2.80	378	0.99	1.81	7.43	108	446
157-01	327 G	0-1	1.30	0.29	2.34	383	0.68	1.66	4.17	127	320
158-01	186 G	0-1	0.73	0.28	1.17	380	0.33	0.85	2.32	116	319
159-27	276 C *	0-5	1.38	0.27	3.24	378	0.86	2.38	1.73	172	125
160-01	38 G	0-1	0.73	0.34	0.42	372	0.14	0.28	1.55	38	211
161-30	200 C *	0-10	1.13	0.24	1.81	381	0.43	1.38	1.90	122	168
165-01	248 G	0-1	2.32	0.38	5.28	373	1.97	3.31	7.55	142	326
167-01	71 G	0-1	0.94	0.36	0.69	372	0.25	0.44	2.09	46	222
170-01	56 G *	0-5	0.22	0.21	0.15	384	0.03	0.12	0.41	54	194
171-10	71 G *	0-2	0.77	0.19	0.55	510	0.11	0.45	1.54	58	199
172-03	110 G	2-3	1.04	0.30	1.45	374	0.44	1.01	2.16	97	209
174-01	108 G	0-1	0.87	0.37	0.88	374	0.33	0.55	1.55	63	178
175-01	79 G	0-2	1.22	0.33	1.40	380	0.46	0.94	2.63	77	216
176-01	167 G	0-2	1.33	0.24	3.14	409	0.73	2.41	2.74	181	206
177-01	230 G	0-1	0.57	0.28	0.93	387	0.26	0.67	1.36	118	239
178-01	284 G	0-1	1.65	0.26	3.92	384	1.00	2.92	5.88	177	356
179-01	356 G	0-1	2.71	0.29	7.39	375	2.13	5.27	9.21	195	341
179-08	356 G *	1-10	4.14	0.30	18.48	363	5.49	13.00	5.22	314	126
179-09	356 G *	0-1	4.59	0.32	21.86	365	6.91	14.95	6.03	325	131
180-01	91 G	0-1	0.09	0.47	0.19	322	0.09	0.10	0.19	118	219
181-01	150 G	0-2	0.89	0.29	2.46	367	0.71	1.75	1.99	196	223
182-08	115 G *	0-2	0.51	0.27	1.32	401	0.36	0.96	1.24	189	245

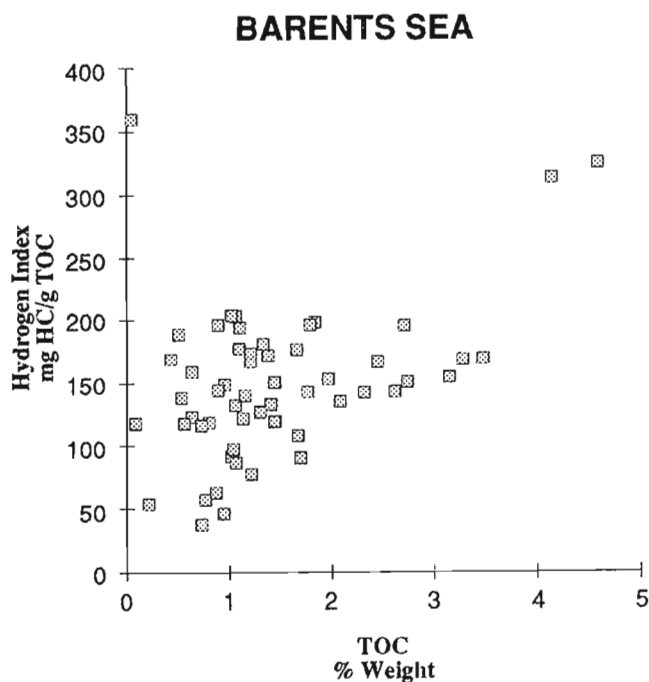
maximum hydrocarbon generation rate during the thermal cracking phase of the experiment. All "S" parameters are measured in milligrams of product per gram of rock sample, which is equivalent to kilograms of product per tonne of rock sample. Total organic carbon (TOC) is measured in weight per cent.

Experimental results have been correlated to other measures of source rock potential (Espitalie et al., 1985; Tissot and Welte, 1984), and source rock potential is generally considered a function of lithology as well as TOC abundance and the S<sub>2</sub> parameter values. The Hydrogen Index (HI) is defined as the ratio S<sub>2</sub>/TOC and the Oxygen Index (OI) as S<sub>3</sub>/TOC. These parameters can be related to atomic H/C and O/C ratios respectively. Rock-Eval/TOC parameters have significance only when threshold values of TOC, S<sub>1</sub>, and S<sub>2</sub> are exceeded. If TOC is less than 0.3% then all parameters have questionable significance (the experiment indicates no source rock potential). Oxygen Index has questionable significance if TOC is less than 0.5%; OI values greater than 150 are meaningless (in terms of source rock potential) and can result from either low or erroneous TOC determination or from a mineral matrix contribution of CO<sub>2</sub> during pyrolysis. Both T<sub>max</sub> and Production Index (S<sub>1</sub>/(S<sub>1</sub>+S<sub>2</sub>)) have questionable significance if S<sub>1</sub> and S<sub>2</sub> values are less than 0.2.

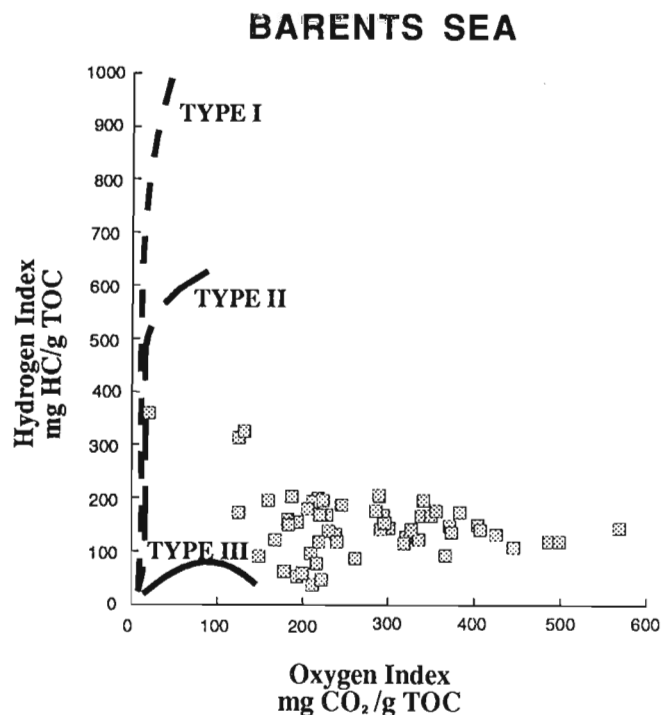
## TOTAL ORGANIC CARBON (TOC) IN BARENTS SEA SAMPLES

Sediment samples were analyzed using a Rock-Eval/TOC anhydrous pyrolysis device (Espitalie et al., 1977). Rock-Eval/TOC data were obtained from both grab and core samples. At 16 sites, samples were stored in standard (500 ml) metal cans for organic analysis. At the remaining sites, samples were stored in plastic containers for metals, inorganic, and radionuclide analysis. To obtain as comprehensive an areal coverage as possible, splits were taken of these samples (44 sample sites) and were also analyzed on the Rock-Eval/TOC equipment. For some stations, both cores and grab samples were taken, and both organic (canned) and inorganic (plastic container) samples were collected.

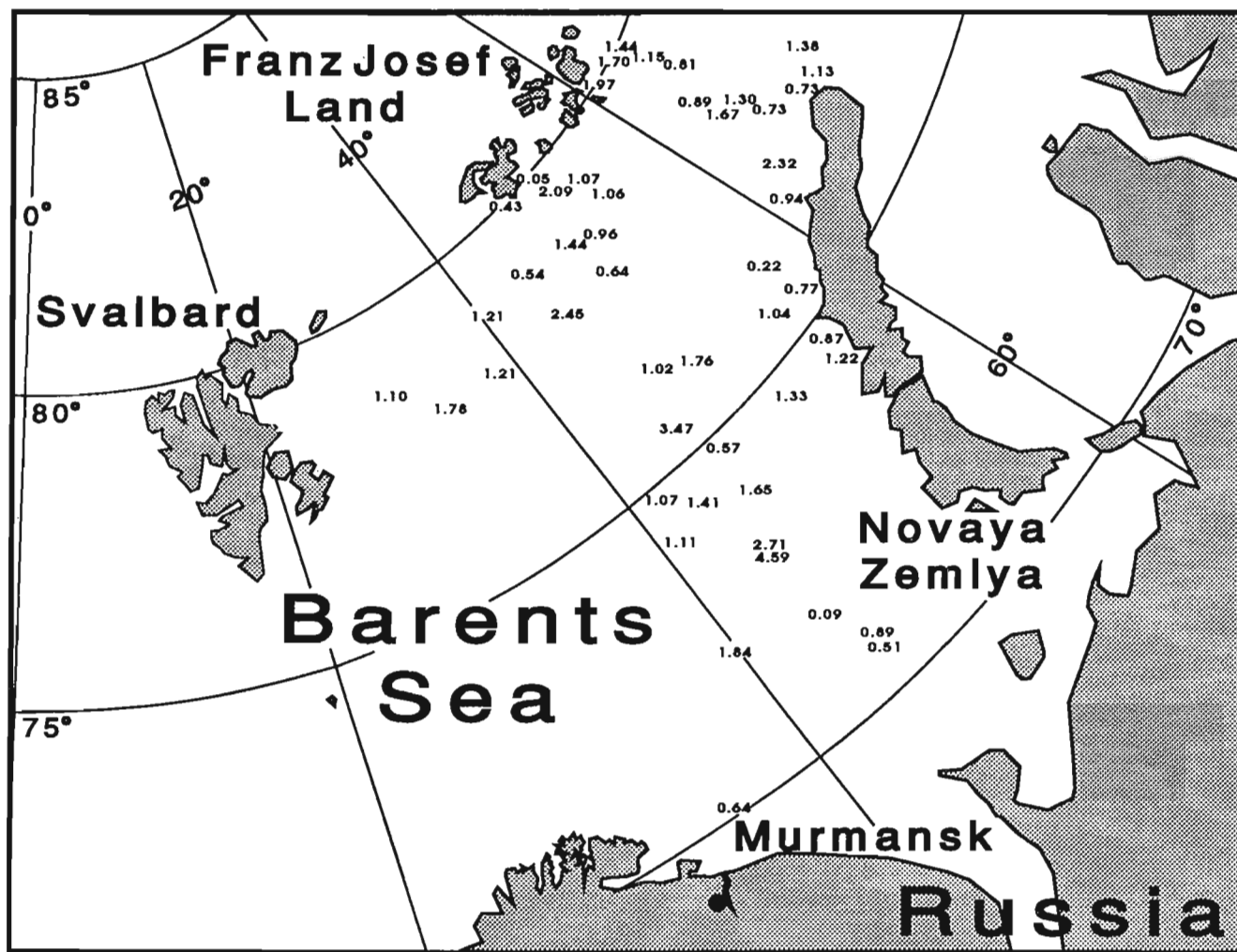
Wet sediment samples collected specifically for organic analysis were stored and transported to Calgary in sealed metal cans. These samples were freeze-dried at the ISPG and screened for organic matter content using a Rock-Eval/TOC instrument. A second sample batch, splits from plastic container samples, were similarly processed. Each sample was run at least in duplicate. The averaged results for the near-surface samples are presented in Table 1. It should be emphasized that the Rock-Eval test was designed for the analysis of older potential source rocks and not recent sediments. Values for some parameters (e.g., S<sub>1</sub> and PI) may have a different interpretation given to them than they would in more ancient sediments.



**Figure 2.** Plot of total organic carbon (TOC) content versus hydrogen index.



**Figure 3.** Plot of oxygen index versus hydrogen index for Barents Sea near surface samples.



**Figure 4.** Map showing TOC content of surface sample from each site sampled from the research vessel "Geolog Fersman".

It is evident from Table 1 that the surface sediments from the Barents Sea show considerable variation in organic carbon content, ranging from 0.05% (site 134) up to 4.59% (site 179). Figure 2 shows that there is some relationship between the total organic carbon content and the amount of organic hydrogen as indicated by the hydrogen index. This relationship would be expected if the level of anoxicity was a major factor in controlling the degree of preservation of organic matter in these bottom sediments. Most samples plot in the Type III-II area on Figure 3, a plot of OI versus HI. This figure indicates that the high TOC and HI samples from site 179 have the lowest oxygen indices, again suggesting they were deposited in more reducing conditions than the other Barents Sea samples.

In Figure 4 the TOC content of surface sediments from each site is shown. Most samples have TOC contents in the 1 to 2% range. Some sites, mostly to the southwest of Novaya Zemlya (e.g., 179, 124, and 142), show values greater than 2%. Nearshore sites, except for 165 near the north end of Novaya Zemlya and 133 adjacent to Franz Josef Land, tend to have lower values. While a more detailed explanation of

these observations must await additional analysis and geological data, one major control appears to be lithology. The samples analyzed range from sands to clays. Organic matter can be best preserved and is most abundant in fine grained samples where localized anoxic conditions that limit bacterial activity can more easily develop. Nearshore sediments are usually deposited under high energy conditions and hence are more oxic. Concentrations of organic and inorganic contaminants should be expected to be highest in fine grained sediments because of the more reducing conditions and because of the absorption of heavy metal cations onto the surfaces of clays. Hence it is likely that these sites with high TOC contents will show the highest levels of anthropogenic contaminants.

## DISCUSSION

Some of the inferences and conclusions in this report are tentative because laboratory analyses for heavy metal and radionuclide contents and sedimentation rates are incomplete.

An array of organic analysis methods (e.g., biomarker analysis, gas chromatographic analysis, solvent extraction) have yet to be applied in a study of these samples. Further, since the presentation of the original Rock-Eval pyrolysis method in 1977, several authors (e.g., Delvaux et al., 1990) have emphasized the difficulty of characterizing kerogen and bitumen on the basis of thermal separation of hydrocarbon products in fractions S1 and S2. Delvaux et al. (1990) have advocated double analysis of a single sample (pyrolysis accompanied by pyrolysis of a solvent extracted sample, Orr, 1983) to better characterize the soluble and insoluble fractions in sedimentary organic matter. The method has been successfully applied to basin margins (i.e., relatively immature diagenetic conditions). Although a wealth of data on fossil sedimentary organic matter can be found in the literature, recent sediments have received considerably less attention and only a few isolated reports deal with the application of Rock-Eval pyrolysis towards their study (e.g., Peters et al., 1981, and recent Ocean Drilling Program Studies).

Unless depositional conditions favour preservation of intact biopolymers, recent marine sediments are characterized by a high abundance of humic compounds. Liebezeit and Wiesner (1990) conducted a study of analytical conditions for temperature-controlled pyrolysis of recent sediments with mixtures of a variety of biopolymers. Preliminary experiments showed that for most recent sediments, a second pyrolysis peak started to form between 520 and 580°C. This is in agreement with Free (1981), who found a similar pattern, especially for compounds containing aromatic structures. Although the range of compounds studied by Liebezeit and Wiesner (1990) may not be sufficiently representative,  $T_{\max}$  or  $T_{\max}$ -HI relations might eventually be of value in identifying at least certain compound classes in recent sediments. Liebezeit and Wiesner (1990) studied samples from the Black Sea and the Neversdorfer See. The Black Sea samples contain a significant amount of condensed compounds (olefins, polycyclics, aromatic hydrocarbons, asphaltic compounds, e.g., Hunt, 1974; Simoneit, 1974) ( $T_{\max} > 400^\circ\text{C}$ ) with minor amounts of polysaccharides/proteins ( $T_{\max}$  300-350°C). For a sapropelic sample with 21.04% TOC (dry weight),  $T_{\max}$  is 411°C, and for a 12.57% TOC coccolith ooze,  $T_{\max}$  is 415°C. The scatter of the  $T_{\max}$  results for our samples indicates the presence of two populations of organic matter present in different proportions. The high  $T_{\max}$  samples are interpreted to be dominated by recycled (reworked) organic matter, whereas the low  $T_{\max}$  samples contain dominantly primary organic material.

While only the  $T_{\max}$  corresponding to maximum pyrolysis yield is reported in Table 1, and the detailed peak shapes are not presented here, the comparisons to other recent sediment examples are striking in the wide range of temperatures recorded. Further research on this subject is warranted and may well improve characterization of the organic matter in the Barents Sea sediments.

Further issues, outside of the scope of this paper, are integration of results with studies of our Russian colleagues (I. Popova and A. Danushevskaya, VNIIOkeanologia, St. Petersburg), correlations with previously completed

Russian studies, and comparisons to recent Ocean Drilling Program results in the Arctic and North Atlantic (Eldholm et al., 1987; Srivastava et al., 1987). These will be taken up in subsequent reports.

## ACKNOWLEDGMENTS

We are grateful to J.S. Bell for discussion and review of the manuscript, R.G. Fanjoy for assistance with Rock-Eval facilities and manipulation of computer files, and Brian Cormier for generation of figures. Ken Saunders (Dalhousie University) participated in collecting samples from the Barents Sea while aboard the Russian research vessel "Geolog Fersman". We are also indebted to R.E. Cranston (Atlantic Geoscience Centre) for his geochemical and technical insights.

## REFERENCES

- Barrie, L., Gregor, D., Hargrave, B., Lake, R., Muir, D., Shearer, R., Tracey, B., and Bidleman, T.  
1992: Arctic contaminants: sources, occurrences and pathways; *The Science of the Total Environment*, v. 122, p. 1-74.
- Cernetig, M.  
1993: A shadow over Siberia; *The Globe and Mail*, Toronto, March 6, p. A1.
- Clery, D.  
1993: Cracks begin to show in Russia's nuclear test site; *New Scientist*, 16 January, p. 8.
- Chapman, N.A., McKinley, I.G., Penna Franca, E., Shea, M.E., and Smellie, J.A.T.  
1992: The Poços de Caldas Project: an introduction and summary of its implications for radioactive waste disposal; *Journal of Geochemical Exploration*, v. 45, p. 1-24.
- Cowan, G.A.  
1978: Migration paths for Oklo reactor products and applications to the problem of geological storage of nuclear wastes; in *Natural Fission Reactors, Proceedings of the Technical Committee, Paris, 1977*; International Atomic Energy Agency, Technical Committee IAEA-TC-119/26; IAEA, Vienna, p. 693-699.
- Drbal, K., Elster, J., and Komárek, J.  
1992: Heavy metals in water, ice and biological material from Spitsbergen, Svalbard; *Polar Research*, v. 11, no. 2, p. 99-101.
- Delvaux, D., Martin, H., Leplat, P., and Paulet, J.  
1990: Comparative Rock-Eval pyrolysis as an improved tool for sedimentary organic matter analysis; *Organic Geochemistry*, v. 16, no. 4-6, p. 1221-1229.
- Eldholm, O., Thiede, J., and Taylor, E.  
1987: Proceedings of the Ocean Drilling Program; Volume 104, Part A - Initial Report, Norwegian Sea, ODP 104, 783 p.
- Espitalié, J.M.  
1986: Use of  $T_{\max}$  as a maturation index for different types of organic matter - Comparison with vitrinite reflectance; in *Thermal Modelling in Sedimentary Basins*, (ed.) J. Burrus; Editions Technip, p. 475-496.
- Espitalié, J., Laporte, J.L., Madec, M., Marquis, F., Leplat, P., Paulet, P., and Boutefeu, A.  
1977: Méthode rapide de caractérisation des roches mères de leur potentiel pétrolier et de leur degré d'évolution; *Revue de l'Institut Français du Pétrole*, v. 32, no. 1, p. 23-42.
- Espitalié, J., Deroo, G., and Marquis, F.  
1985: Rock-Eval pyrolysis and its applications; *Institut Français du Pétrole*, Preprint 333578, 72 p.  
1985/ La pyrolyse Rock-Eval et ses applications; Deuxième partie. *Revue de l'Institut Français du Pétrole*, v. 40, p. 563-579, p. 775-784, v. 41, p. 73-89.  
1986: de l'Institut Français du Pétrole, v. 40, p. 563-579, p. 775-784, v. 41, p. 73-89.

**Free, M.**

1981: Die nichtisotherme Pyrolyse von Sedimentgesteinen und organischen Substanzen zur Aufklärung der Erdgasgenese; Dissertation, Technische Universität Braunschweig, 110 p.

**Hageman, R. and Roth, E.**

1978: Relevance of the studies of the Oklo natural nuclear reactors to the storage of radioactive wastes; *Radiochimica Acta*, v. 22, p. 241-247.

**Hellmuth, K.H.**

1989a: The long-term stability of natural bitumen. A case study of the bitumen impregnated limestone deposit near Holzen, Lower Saxony, FRG; STUK Technical Report No. B-VALO 59.

1989b: Natural analogues of bitumen and bitumenized radioactive waste; STUK Technical Report No. B-VALO 58.

**Hoensma, P.**

1991: *The Soviet Arctic*; Routledge, London and New York, 228 p.

**Hunt, J.M.**

1974: Hydrocarbon Geochemistry of Black Sea; in *The Black Sea - Geology, Chemistry and Biology*; American Association of Petroleum Geologists, Memoir 20, p. 499-504.

**Kinloch, D., Kuhnlein, H., and Muir, D.C.G.**

1992: Inuit foods and diet: a preliminary assessment of benefits and risks; *The Science of the Total Environment*, v. 122, p. 247-278.

**Liebezeit, G. and Wiesner, M.**

1990: Pyrolysis of recent marine sediments-I. Biopolymers; *Organic Geochemistry*, v. 16, no. 4-6, p. 1179-1185.

**Lutze, W. and Ewing, R.C. (ed.)**

1988: *Radioactive Waste Forms for the Future*; North-Holland, Amsterdam, 778 p.

**MacKenzie, D.**

1993: 'Whole' reactors lurk under Barents Sea; *New Scientist*, no. 1860, 13 February, p. 9.

**Muir, D.C.G., Wagemann, R., Hargrave, B.T., Thomas, D.J.,****Peakall, D.B., and Nordstrom, R.J.**

1992: Arctic marine ecosystems contamination; *The Science of the Total Environment*, v. 122, p. 75-134.

**Orr, W.L.**

1983: Comments on pyrolytic hydrocarbon yields in source-rock evaluation, *Advances in Organic Geochemistry 1981*; Proceedings of the 10th International Meeting on Organic Geochemistry, University of Bergen, Norway, 14-18 September, 1981, p. 775-787.

**Peters, K.E.**

1986: Guidelines for evaluating petroleum source rocks using programmed pyrolysis; *Bulletin of the American Association of Petroleum Geologists*, v. 70, p. 318-329.

**Peters, K.E., Rohrback, B.G., and Kaplan, I.R.**

1981: Geochemistry of artificially heated humic and sapropelic sediments-I: Protokerogen; *Bulletin of the American Association of Petroleum Geologists*, v. 65, p. 688-705.

**Simoneit, B.R.**

1974: Organic Analyses of Black Sea Cores; in *The Black Sea - Geology, Chemistry and Biology*; American Association of Petroleum Geologists, Memoir 20, p. 477-498.

**Srivastava, S.P., Arthur, M., Clement, B., et al.**

1987: Proceedings of the Ocean Drilling Program; Volume 105, Part A - Initial Report, Baffin Bay and Labrador Sea; ODP 105, 917 p.

**Thomas, D.J., Tracey, B., Marshall, H., and Norstrom, R.J.**

1992: Arctic terrestrial ecosystem contamination; *The Science of the Total Environment*, v. 122, p. 135-164.

**Tissot, B. and Welte, D.H.**

1984: *Petroleum Formation and Occurrence* (revised 2nd edition); Springer Verlag, New York, 699 p.

**Williams-Walsh, M.**

1991: Arctic villagers have world's highest levels of PCBs in their blood; *The Ottawa Citizen*, Ottawa, June 30, p. E3.

**Wilson, D.**

1993: Nuclear waste dumped at sea, Russia confirms; *The Globe and Mail*, Toronto, March 24, p. A3.

---

Geological Survey of Canada Project 840081



# Pore-size distributions of shales from the Beaufort-Mackenzie Basin, northern Canada

T.J. Katsube and D.R. Issler<sup>1</sup>  
Mineral Resources Division

*Katsube, T.J. and Issler, D.R., 1993: Pore-size distributions of shales from the Beaufort-Mackenzie Basin, northern Canada; in Current Research, Part E; Geological Survey of Canada, Paper 93-1E, p. 123-132.*

---

**Abstract:** Petrophysical characteristics of 41 shale samples from 9 wells (hydrostatically pressured and overpressured sections) in the Beaufort-Mackenzie Basin were studied, using pore-size distribution data obtained from mercury intrusion porosimetry. Results indicate that total porosity and mean pore-size, obtained from the pore-size distribution, vary between 5 to 32% and 9.1 to 331 nm, respectively. In general, pore-size distributions of the samples are unimodal, and are independent from depth. The porosity shows good agreement with compaction trends previously mapped, using sonic logs. Results from three Taglu wells (C-42, G-33, and F-43) indicate that total porosity and mean pore-size decrease with increasing burial depth and compaction. This study forms part of a larger study on the physical and chemical properties of Beaufort-Mackenzie shales, which has a long term objective of constraining the dynamics of shale compaction and overpressure development in the region.

**Résumé :** On a étudié les caractéristiques pétrophysiques de 41 échantillons de shale provenant de 9 puits (sections à la pression hydrostatique et sections à des pressions plus élevées) dans le bassin de Beaufort-Mackenzie à l'aide de données sur la distribution de la taille des pores obtenues par porosimétrie au mercure. Les résultats indiquent que la porosité totale et la taille moyenne des pores, déterminées à partir de la distribution de la taille des pores, varient de 5 à 32 % et de 9,1 à 331 nm, respectivement. En général, les distributions de la taille des pores des échantillons sont unimodales, forme indépendante de la profondeur. La porosité concorde bien avec les tendances de tassement relevées antérieurement par diagraphie sonique. Les résultats de trois puits de l'île Taglu (C-42, G-33 et F-43) indiquent que la porosité totale et la taille moyenne des pores diminuent avec l'accroissement de la profondeur et du tassement. Cette étude s'inscrit dans le cadre d'une étude plus vaste sur les propriétés physiques et chimiques des shales de Beaufort-Mackenzie, dont l'objectif à long terme est de déterminer la dynamique du tassement des shales et de l'évolution des surpressions dans la région.

---

<sup>1</sup> Institute of Sedimentary and Petroleum Geology, Calgary

## INTRODUCTION

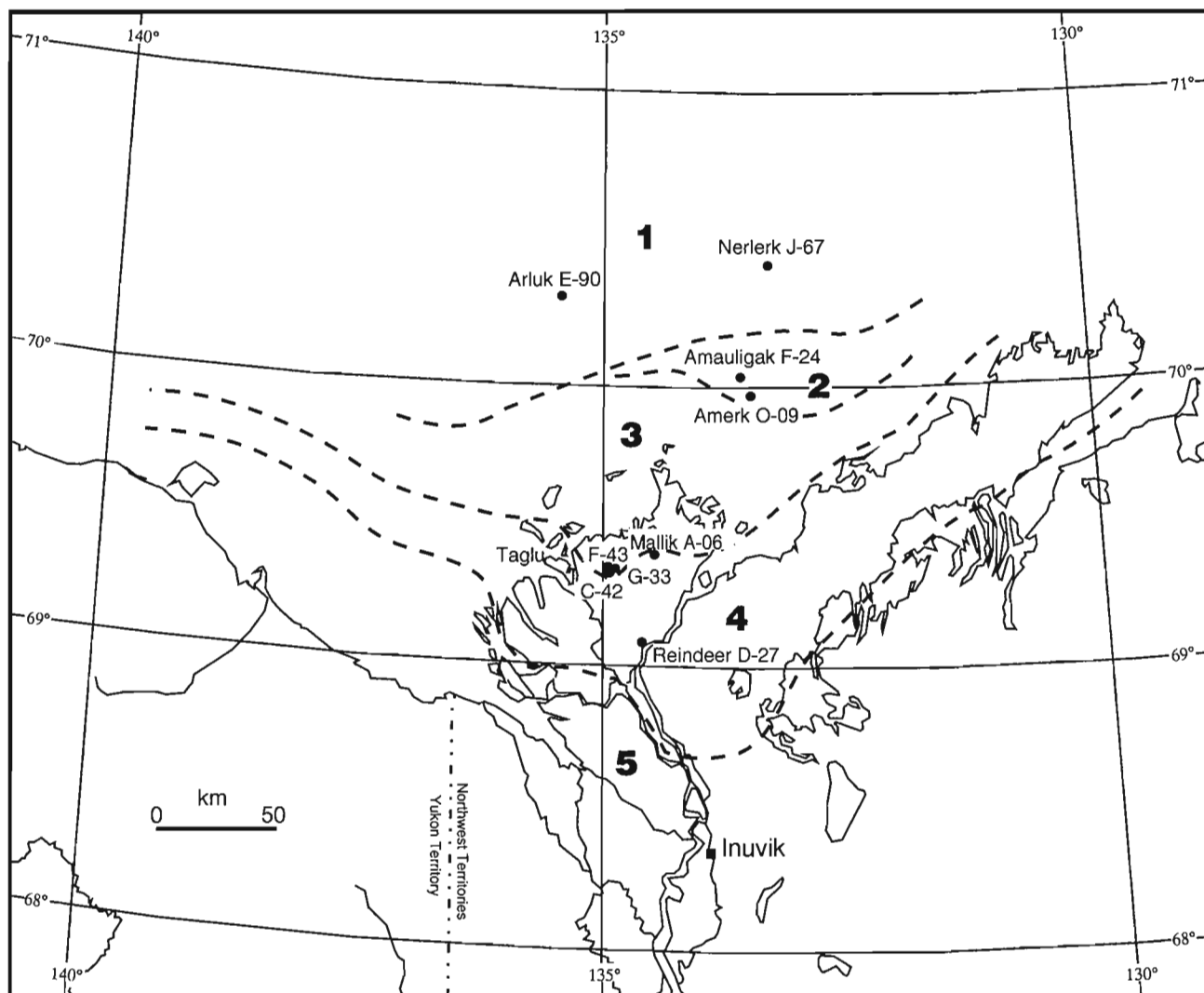
Shales are the most abundant sedimentary rocks, yet their physical properties are least studied. Shales can be a source of hydrocarbons and ore-bearing fluids. Their physical properties are intimately related to changes in pore fluid pressures, and expulsion of hydrocarbons and diagenetic fluids. Shales are also frequently associated with the development of diapirs, faults, and decollements, during their depositional, burial, and compaction history. In spite of the importance of shales in sedimentary basin development, the compaction process is poorly understood, mainly because of insufficient data on physical properties.

In order to improve our understanding of the shale compaction dynamics, scientists from several divisions of the Geological Survey of Canada began a multidisciplinary

physical property study of shales from the Beaufort-Mackenzie Basin (BMB), Northern Canada (Fig. 1). The study consists of investigations of petrophysical properties (including porosity, formation factor, and permeability), organic/inorganic geochemistry, sonic velocity, and thermal conductivity.

The Beaufort-Mackenzie Basin provides an excellent set of conditions for the study of shale compaction, due to the following reasons:

1. It is a relatively young and actively subsiding basin, which is still in the dynamic stage of compaction.
2. Beaufort-Mackenzie Basin shales are relatively uniform in composition, facilitating excellent well log calibration controls.



**Figure 1.** Map showing the location of nine wells in the Beaufort-Mackenzie Basin, northern Canada, from which the shale core samples were obtained. The approximate boundaries of five shale compaction zones (Issler, 1992) are shown by heavy dashed lines. The map was produced using World Data Bank II (Gorny and Carter, 1987) and software provided by Micromaps which uses a USGS ellipsoidal polyconic projection centred on 40°N lat., 90°W long.



Table 1. Sample identification

Well name	K.B. <sup>1</sup> (m)	W.D. <sup>2</sup> (m)	G.L. <sup>3</sup> (m)	Sample I.D. <sup>4</sup>	Depth (m) <sup>5</sup>	
					Meas.	T.V.D.
Amauligak F-24	26.6	32.0	-	B-AM-1 B-AM-2 B-AM-3	4376.5 4395 4695	3106 3119 3341
Amerk O-09	16.1	26.0	-	B-AR-1 B-AR-2 B-AR-3 B-AR-4* B-AR-5* B-AR-6* B-AR-7*	1317 1533 1765 3866 4375 4606 4861	
Arluk E-90	12.2	58.0	-	B-AK-1* B-AK-2*	3452 3938	
Mallik A-06	35.5	-	27.3	B-ML-1 B-ML-2* B-ML-3*	1362 3215 3609	3176 3547
Nerlerk J-67	20.0	45.0	-	B-NR-1* B-NR-2* B-NR-3*	3945 3962 4357.5	3658 3673 4006
Reindeer D-27	32.3	-	27.4	B-RE-1 B-RE-2 B-RE-3 B-RE-4 B-RE-5 B-RE-6* B-RE-7* B-RE-8* B-RE-9* B-RE-10* B-RE-11* B-RE-12* B-RE-13* B-RE-14*	1458 1469 2022 2092 2099 2213 2389 2421 2551 2725 2923 3153 3481 3628	
Taglu C-42	12.3	-	1.7	B-TA-1	2881	
Taglu F-43	12.0	-	1.4	B-TA-2*	3247	
Taglu G-33	7.9	-	1.8	B-TG-1 B-TG-2 B-TG-3 B-TG-4 B-TG-5 B-TG-6 B-TG-7	952 1350 1640 2075 2459 2460 2533	

<sup>1</sup>Kelly Bushing elevation.

<sup>2</sup>Water depth

<sup>3</sup>Ground level elevation.

<sup>4</sup>Samples marked with an (\*) are from overpressured zones. All other samples are from normally-pressured zones.

<sup>5</sup>Measured and true vertical depths are with respect to K.B.

3. Large changes in sedimentation rate across the basin, with significant erosion along the basin margins, produce large spatial variations in shale porosity, providing excellent controls to help understand the porosity evolution in the basin.
4. A reasonable amount of shale core and well controls exist.

Issler (1992) has mapped the variations in shale compaction across the Beaufort-Mackenzie Basin, using sonic logs calibrated with measured core porosity data. This work provides the regional framework for interpreting the petrophysical data.

Following an earlier study on Beaufort-Mackenzie Basin shales (Katsube and Best, 1992), this paper forms the first part of a series of papers which will report the results from the systematic and multidisciplinary physical property study carried out on the shales. In this paper, we present pore-size distribution data for 41 Beaufort-Mackenzie Basin shale core samples, which were obtained using the mercury intrusion porosimetry technique. While previous petrophysical studies of this type have focused mainly on determining the pore structure characteristics of compacted and tight shales (e.g., Katsube et al., 1990, 1991, 1992a, b; Katsube, 1992, 1993; Coyner et al., 1993), the objective of this study is to provide data to understand how pore-size distribution changes with

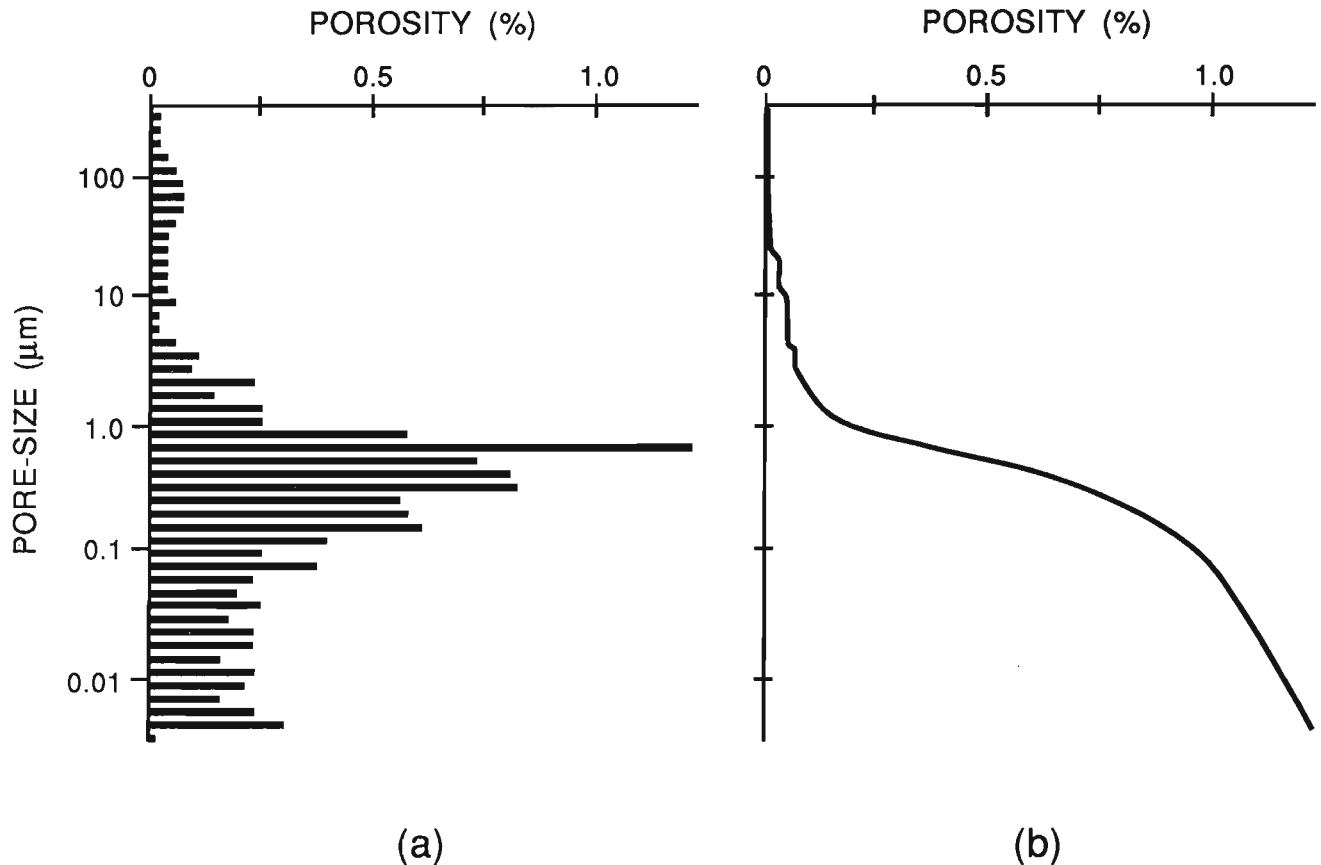
compaction, burial, and overpressure development – information required to determine the shale sealing capacity (Mudford, 1988; Mudford and Best, 1989). For this reason, samples were collected over a broad range of depth (952-4861 m). Only basic experimental results are reported in this paper.

## METHOD OF INVESTIGATION

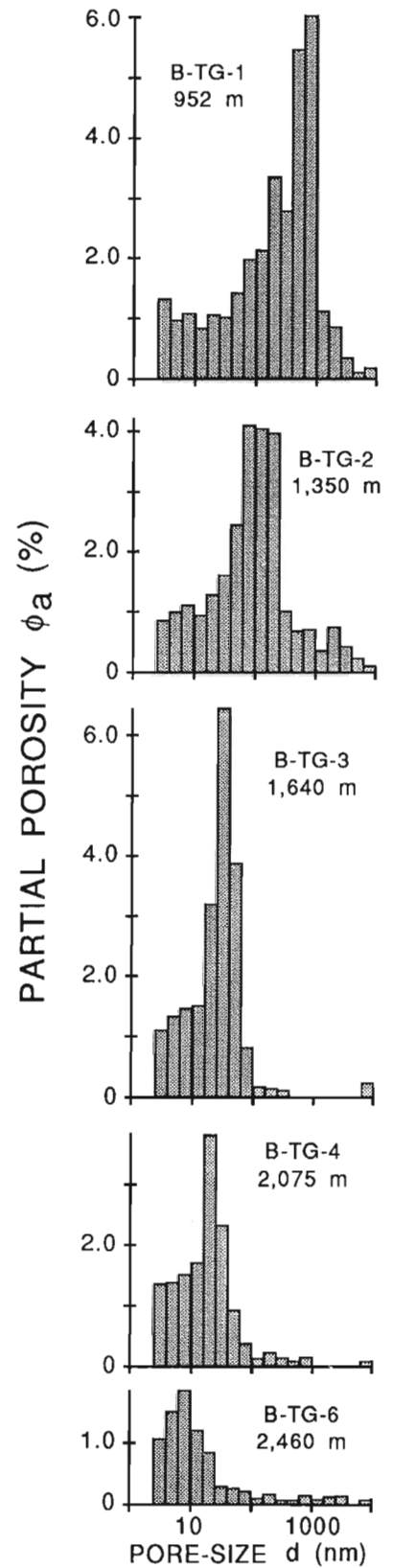
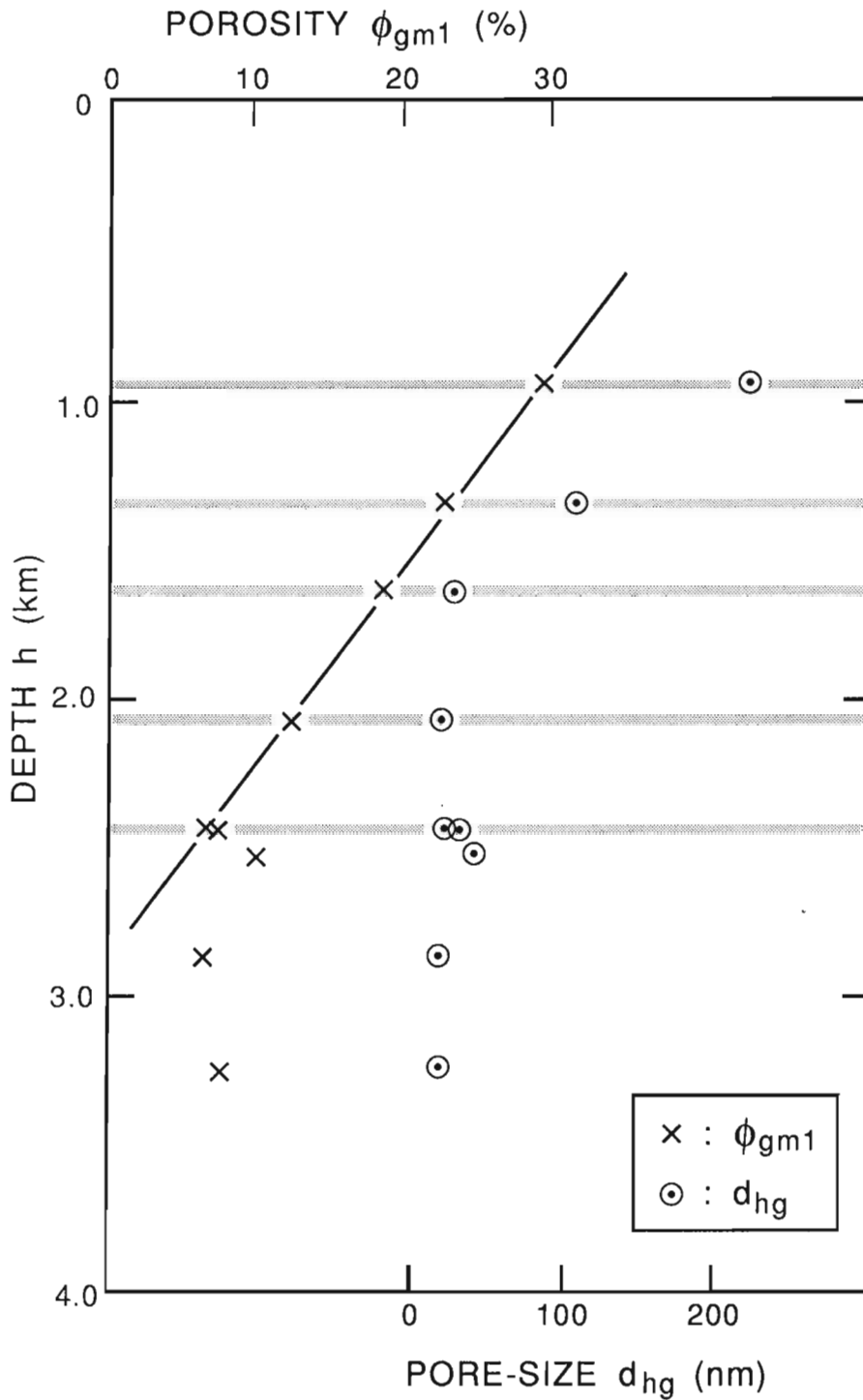
### Sample selection and preparation

The specimens used for mercury porosimetry measurements are fragments of about 5-10 g which were cut from 41 shale core samples. These core samples were obtained from 9 wells in the Beaufort-MacKenzie Basin (Fig. 1), northern Canada. The well name, sample number, and depth from which the samples were obtained are listed in Table 1.

These 41 samples form part of a larger sample set designated for a wide range of physical property measurements (e.g., formation factor, permeability, effective porosity, velocity, thermal conductivity). The wells and sample depths (Table 1) were chosen to cover a wide range of shale porosity values, in both normally pressured and overpressured sections of four different compaction zones



**Figure 2.** Example of mercury porosimetry measurements. (a) Porosity distribution for different pore sizes calculated from the intruded volume of mercury measured at each of the 56 pressure steps between 0.14 MPa to 420 MPa. Pressures are converted to pore sizes. (b) Cumulative porosity curve for the porosity distribution shown in (a).



**Figure 3.** Pore-size distribution, total porosity ( $\phi_{gm1}$ ), and mean pore size ( $d_{hg}$ ) as a function of burial depth for samples from the Taglu C-42, F-43, and G-33 wells (Tables 1 and 2).

**Table 2.** Pore size distribution data for different pore-size ranges, d, obtained by mercury porosimetry for 41 shale samples from the Beaufort-Mackenzie Basin

Sample #	$\phi_a$ (%)																$\phi_{gm1}$	$\phi_{gm2}$	$d_{hg}$	$\delta_{BP}$	$\delta_{SD}$	h			
	$d_a$ (nm)	3.2	5.0	7.9	12.6	20.0	31.6	50.1	79.4	126	200	316	501	794	1259	1995							3162	5012	7943
<b>Reindeer D-27</b>																									
RE-1	0.6	0.8	1.0	0.84	1.38	1.19	1.45	1.41	1.01	1.17	0.68	1.34	1.31	0.30	0.19	0.00	0.00	0.00	0.14	15.0	15.5	95.5	2.34	2.77	1458
RE-2	0.89	0.98	1.08	1.01	1.90	1.41	0.94	0.82	0.56	0.63	0.33	0.54	0.66	0.16	0.12	0.00	0.00	0.00	0.07	12.1	12.8	51.3	2.34	2.69	1469
RE-3	1.21	1.26	1.59	1.00	0.39	0.15	0.13	0.05	0.03	0.03	0.03	0.00	0.00	0.00	0.00	0.00	0.00	0.00	0.03	5.91	6.7	19.5	2.57	2.75	2022
RE-4	1.85	1.38	1.62	1.04	0.47	0.26	0.18	0.18	0.03	0.00	0.00	0.00	0.00	0.00	0.00	0.00	0.00	0.00	0.03	7.04	7.6	14.5	2.61	2.82	2092
RE-5	0.91	1.01	1.70	1.29	0.53	0.20	0.15	0.13	0.08	0.05	0.05	0.03	0.03	0.00	0.00	0.00	0.00	0.00	0.08	6.23	6.7	20.0	2.53	2.71	2099
RE-6	1.05	0.92	1.48	1.33	0.84	0.28	0.20	0.15	0.10	0.08	0.03	0.03	0.00	0.00	0.00	0.00	0.00	0.00	0.10	6.58	7.0	20.4	2.56	2.75	2213
RE-7	0.82	0.92	1.42	2.17	2.20	0.42	0.25	0.15	0.10	0.07	0.02	0.02	0.00	0.00	0.00	0.00	0.00	0.00	0.07	8.66	9.1	19.5	2.50	2.74	2389
RE-8	0.67	0.77	1.07	1.34	2.23	0.89	0.35	0.17	0.07	0.07	0.02	0.07	0.05	0.05	0.00	0.00	0.00	0.00	0.10	7.93	8.5	26.3	2.48	2.71	2421
RE-9	0.84	0.87	1.48	2.79	1.81	0.30	0.20	0.12	0.07	0.07	0.05	0.02	0.07	0.02	0.07	0.02	0.00	0.00	0.07	8.90	9.4	20.9	2.47	2.73	2551
RE-10	0.72	0.87	1.39	2.33	2.63	0.42	0.22	0.12	0.12	0.10	0.02	0.10	0.05	0.05	0.02	0.00	0.00	0.00	0.05	9.25	9.5	20.0	2.46	2.74	2725
RE-11	0.86	1.40	2.46	2.24	0.69	0.25	0.17	0.10	0.12	0.02	0.05	0.05	0.00	0.00	0.00	0.00	0.00	0.00	0.05	8.47	8.9	16.2	2.48	2.70	2923
RE-12	0.73	0.94	1.97	1.52	0.41	0.23	0.15	0.10	0.08	0.08	0.03	0.05	0.10	0.05	0.05	0.05	0.05	0.00	0.08	6.61	7.1	24.0	2.53	2.73	3153
RE-13	1.63	1.45	1.25	0.38	0.31	0.18	0.18	0.13	0.03	0.00	0.00	0.00	0.00	0.00	0.00	0.00	0.00	0.00	0.05	5.58	5.7	9.12	2.55	2.70	3481
RE-14	1.42	1.83	2.19	0.39	0.28	0.21	0.15	0.13	0.08	0.08	0.05	0.05	0.08	0.03	0.00	0.00	0.00	0.00	0.08	7.04	7.4	14.1	2.58	2.79	3628
<b>Taglu G-33</b>																									
TG-1	1.16	0.82	0.90	0.66	0.92	0.86	1.24	1.80	1.95	3.22	2.58	5.32	5.79	0.94	0.73	0.36	0.11	0.19	0.19	29.5	30.6	229	1.87	2.70	952
TG-2	0.66	0.79	0.87	0.75	1.06	1.20	2.24	3.92	3.86	3.77	0.79	0.66	0.68	0.35	0.54	0.39	0.21	0.08	0.08	22.8	23.5	115	2.07	2.71	1350
TG-3	0.91	1.09	1.25	1.32	2.94	6.24	3.71	0.59	0.14	0.09	0.09	0.02	0.02	0.00	0.00	0.00	0.00	0.18	0.18	18.6	19.2	31.6	2.28	2.82	1640
TG-4	1.17	1.21	1.33	1.52	3.57	2.12	0.67	0.36	0.12	0.21	0.10	0.05	0.12	0.00	0.00	0.00	0.00	0.05	0.05	12.6	14.2	26.3	2.38	2.74	2075
TG-5	1.38	1.35	1.78	0.87	0.69	0.31	0.25	0.15	0.13	0.13	0.05	0.08	0.13	0.03	0.08	0.03	0.00	0.13	0.13	7.54	8.3	28.2	2.46	2.78	2459
TG-6	0.89	1.33	1.61	0.97	0.66	0.28	0.26	0.18	0.10	0.13	0.05	0.05	0.13	0.05	0.08	0.08	0.03	0.05	0.05	6.92	7.8	36.3	2.55	2.77	2460
TG-7	0.69	0.79	1.06	1.03	1.99	1.06	1.15	0.79	0.44	0.42	0.12	0.07	0.10	0.05	0.10	0.02	0.00	0.07	0.07	9.95	10.7	44.7	2.46	2.75	2533
<b>Amerk O-09</b>																									
AR-1	0.61	0.76	1.09	1.01	1.44	1.59	2.74	5.44	5.93	5.48	0.97	0.99	0.73	0.36	0.38	0.33	0.50	1.13	1.13	31.5	31.6	117	1.73	2.54	1317
AR-2	1.31	1.19	0.93	0.64	0.78	0.84	1.27	2.03	2.15	2.76	1.65	2.19	2.70	1.69	1.65	1.27	0.04	0.72	0.72	25.8	29.2	331	1.99	2.81	1533
AR-3	0.02	0.29	1.11	0.96	1.53	1.66	2.82	3.67	3.16	3.75	1.93	2.75	2.09	2.09	0.87	0.55	0.23	0.23	0.23	28.3	30.0	200	1.78	2.55	1765
AR-4	1.02	0.90	1.22	1.36	1.46	0.66	0.63	0.46	0.36	0.53	0.27	0.66	0.39	0.07	0.10	0.10	0.00	0.12	0.12	10.3	11.5	70.8	2.43	2.75	3866

Sample #	$d_a$ (nm)	$\phi_a$ (%)														$\phi_{gm1}$	$\phi_{gm2}$	$d_{hg}$	$\delta_{BP}$	$\delta_{SD}$	h					
		3.2	5.0	7.9	12.6	20.0	31.6	50.1	79.4	126	200	316	501	794	1259							1995	3162	5012	7943	
AR-5	0.81	0.84	1.41	2.42	1.13	0.25	0.20	0.10	0.12	0.10	0.07	0.12	0.20	0.10	0.17	0.10	0.15	8.46	9.6	47.9	2.47	2.73	4375			
AR-6	1.00	0.98	1.45	2.20	1.53	0.28	0.28	0.18	0.13	0.13	0.00	0.05	0.05	0.03	0.00	0.00	0.10	8.35	8.8	20.9	2.50	2.74	4606			
AR-7	0.60	0.90	1.32	2.87	1.32	0.25	0.25	0.12	0.12	0.10	0.00	0.07	0.07	0.05	0.00	0.00	0.07	8.16	8.6	21.4	2.50	2.73	4861			
<b>Amauligak F-24</b>																										
AM-1	0.73	0.78	1.05	0.95	1.45	1.45	1.53	0.60	0.20	0.15	0.08	0.08	0.08	0.05	0.50	0.00	0.10	9.76	10.0	47.9	2.50	2.78	4376			
AM-2	1.25	1.01	1.30	1.27	2.81	1.66	0.41	0.22	0.14	0.12	0.02	0.07	0.07	0.07	0.14	0.07	0.10	10.8	12.0	38.0	2.40	2.73	4395			
AM-3	0.73	0.71	0.95	0.85	1.53	1.73	1.46	0.46	0.17	0.15	0.02	0.12	0.15	0.07	0.07	0.10	0.02	9.40	10.1	43.7	2.44	2.71	4695			
<b>Arluk E-90</b>																										
AK-1	1.08	0.98	1.08	1.10	2.20	2.90	1.39	0.65	0.36	0.31	0.14	0.22	0.14	0.02	0.00	0.00	0.07	12.7	13.1	33.1	2.40	2.76	3452			
AK-2	1.80	1.32	1.80	2.01	3.57	0.77	0.43	0.31	0.24	0.14	0.14	0.14	0.17	0.14	0.26	0.24	0.38	14.0	16.8	77.6	2.40	2.88	3938			
<b>Taglu C-42</b>																										
TA-1	2.00	1.45	1.11	0.53	0.44	0.19	0.17	0.11	0.08	0.06	0.00	0.00	0.00	0.00	0.00	0.00	0.15	6.29	7.0	20.4	2.10	2.26	2881			
<b>Taglu F-43</b>																										
TA-2	0.90	0.92	1.20	1.48	1.77	0.72	0.28	0.13	0.10	0.08	0.00	0.00	0.00	0.00	0.00	0.00	0.08	7.65	8.0	20.9	2.506	2.78	3247			
<b>Nerlerk J-67</b>																										
NR-1	1.01	0.71	0.90	0.81	1.34	1.96	4.15	3.39	0.46	0.28	0.12	0.14	0.28	0.18	0.12	0.02	0.09	15.9	16.9	56.2	2.30	2.77	3945			
NR-2	0.77	0.82	1.00	1.02	2.00	4.21	4.33	0.39	0.18	0.23	0.14	0.16	0.25	0.14	0.23	0.16	0.05	16.2	16.7	42.7	2.28	2.73	3962			
NR-3	0.60	0.72	0.97	0.93	1.76	2.71	2.99	0.77	0.26	0.23	0.12	0.12	0.28	0.21	0.42	0.42	0.30	14.0	15.4	85.1	2.32	2.74	4357			
<b>Mallik A-06</b>																										
ML-1	0.14	0.21	0.80	0.78	1.21	1.23	1.66	1.93	1.62	2.23	1.41	2.01	3.24	1.23	0.86	0.31	0.14	21.3	22.9	257	2.05	2.66	1362			
ML-2	0.26	0.44	0.63	0.73	1.41	0.89	0.42	0.13	0.05	0.03	0.00	0.03	0.05	0.00	0.03	0.00	0.00	5.09	5.4	32.3	2.61	2.76	3215			
ML-3	1.15	1.10	1.31	1.02	0.55	0.21	0.21	0.10	0.05	0.00	0.00	0.00	0.00	0.00	0.00	0.00	0.10	5.80	6.4	19.4	2.61	2.79	3609			
$d_a$ = Geometric mean pore-sizes for the different pore-size ranges (nm). $d_{hg}$ = Geometric mean of the entire pore-size distribution (nm). $\phi_a$ = Partial porosity (%). $\phi_{gm1}$ = Total porosity measured by mercury porosimetry for pore sizes up to 10 $\mu$ m (%). $\phi_{gm2}$ = Total porosity measured by mercury porosimetry for pore sizes up to 250 $\mu$ m (%). $\delta_{BP}$ = Bulk density (g/mL). $\delta_{SD}$ = Skeletal density (g/mL). h = Depth (m) from which the sample was obtained.																										

identified by Issler (1992). Depths have been corrected to true vertical depth for the deviated wells, using borehole survey data included in the well history files (Table 1).

The Arluk E-90 and Nerlerk J-67 wells (Fig. 1) are situated in compaction zone 1 (Issler, 1992), which is characterized by very high Pliocene-Pleistocene sedimentation rates (approximately 380-660 m/Ma) with undercompacted and overpressured sediments. The Amaulikak F-24 and Amerk O-09 wells are located in compaction zone 2, where Pliocene-Pleistocene sedimentation rates are somewhat lower (190-380 m/Ma), but where significant undercompaction and overpressure still exist. A major oil accumulation occurs in the Amaulikak area. The Taglu wells are located in compaction zone 3 where the inferred Plio-Pleistocene sedimentation rates vary between 40 to 190 m/Ma, and where deep overpressured zones (generally below 3 km) are overlain by normally compacted strata. The Mallik A-06 well is located within compaction zone 4 (where erosion may range up to 1 km), but close to the boundary with compaction zone 3. This well contains significant overpressure below 2.3 km, and erosion has shifted the porosity profile to lower values at shallow depth (Issler, 1992). The Reindeer D-27 well (located in a section of compaction zone 4) has experienced significant erosion, and overpressure occurs at depth below 2 km.

### Mercury porosimetry technique

Pore-size distribution of these shale specimens was determined by mercury intrusion porosimetry, following the procedures described in previous publications (e.g., Katsube, 1981; Katsube and Walsh, 1987; Katsube and Hume, 1987; Katsube and Best, 1992), using an equilibration time of 30 s for each of the high pressure steps, and 10 s for the low pressure (<0.7 MPa) steps. This technique was first suggested by Washburn (1921). In principle, the mercury porosimeter can generate pressures high enough to force mercury into all accessible pores and measure the volume of mercury taken up by them (Rootare, 1970). Assuming cylindrical pore shapes, the Washburn equation (Rootare, 1970) relates the amount of pressure,  $p$ , required to force mercury into pores with pore-size diameter,  $d$ , greater than or equal to

$$d = -4\gamma\cos(\theta)/p, \quad (1)$$

where  $\gamma$  is the surface tension of mercury, and  $\theta$  is the contact angle. Values of  $\theta=30^\circ$  and  $\gamma=0.48$  N/m were used in this study. These measurements were made by ORTECH (Toronto, Ontario) using a Micromeritics Autopore 9200 mercury porosimeter with an available pressure range of 0.14-420 MPa and an equivalent pore-size range of 10-0.003  $\mu\text{m}$ .

### Determination of pore-size distribution

The mercury injection pressure was incrementally increased from 0.14 MPa to 420 MPa in 56 pressure steps, and the volume of mercury intruded for each step measured. The pressure steps, more or less, equally divide the entire pressure range on a logarithmic scale. Since each pressure step

represents a certain pore size, the volume of mercury intruded for each step can be converted into the porosity of that pore size. Examples of the porosity distribution and accumulated porosity curve for different pore sizes are shown in Figure 2a and 2b (Sample B-TG-1).

The measured pore-size distributions (Fig. 2) have been replotted in a standard format by grouping the data into different size classes, as in previous studies (e.g., Agterberg et al., 1984; Katsube, 1981; Katsube and Walsh, 1987; Katsube and Hume, 1987; Katsube and Best, 1992). The standard display format has each decade of the logarithmic pore-size scale (x-axis) subdivided into five ranges with equal physical spacing (Fig. 3).

## EXPERIMENTAL RESULTS

Results of the pore-size distribution measurements determined by mercury porosimetry are presented in Table 2. Data for partial porosity,  $\phi_a$ , which is the porosity contributed by each pore-size range, are listed in the rows for each sample. The parameter,  $d_a$  (first row), is the geometric mean for each pore-size range (nm). Total porosity,  $\phi_{gm1}$ , is the sum of partial porosity values for pore sizes less than or equal to 10  $\mu\text{m}$ , whereas  $\phi_{gm2}$  is the total porosity expressed as the sum of partial porosity values for pore sizes up to 250  $\mu\text{m}$ . Both  $\phi_{gm1}$  and  $\phi_{gm2}$  represent porosity values corresponding to the effective porosity (Katsube et al., 1992a; Katsube, 1992), that is, the porosity of all interconnected pores in a rock. However,  $\phi_{gm1}$  is more likely to consist of true sample porosity, because  $\phi_{gm2}$  may include measurement errors such as those originating from the space between the specimen and the sample container. The geometric mean of the entire pore-size distribution,  $d_{hg}$ , is calculated using the equation (Katsube, 1992),

$$\log(d_{hg}) = \frac{\left(\frac{1}{n}\right) \sum_{i=1}^n \{\phi_{ai} \log(d_{hgi})\}}{\sum_{i=1}^n \phi_{ai}}, \quad (2)$$

The skeletal density,  $\delta_{SD}$  (Table 2), represents the density of the solid component of the sample, but may actually be less than the true value if isolated pores exist within that solid component.

## DISCUSSION

### General characteristics of porosity data

The total porosity ( $\phi_{gm1}$ ) varies between 31.5% (1317 m depth, Amerk O-09 well) and 5.1% (3215 m depth, Mallik A-07 well), as listed in Table 2, a range similar to that previously reported for the same region (Katsube and Best, 1992). However, the range of variation for the geometric mean pore sizes (9.1-330 nm) is slightly greater for this study compared to that of the previous study (8.4-121 nm).

There are significant lateral variations in porosity across the study area. For example, total porosity is approximately 26% at 1533 m depth offshore at the Amerk O-09 well location, but decreases to only 12-15% at 1458-1469 m depth onshore at the Reindeer D-27 well location (Table 2, Fig. 1). Erosion has removed much of the overlying higher porosity sediments at Reindeer D-27. There also exists a significant relationship between excess pore pressure and porosity. For example, porosity shows little variation (6-9 %) below 2 km depth in the overpressured sediments of the Reindeer D-27 well. Further offshore, overpressured zones preserve porosity values of 14% at approximately 4000 m depth (Arluk E-90 and Nerlerk J-67), and of 8% at 4861 m depth (Amerk O-09, Table 2 and Fig. 1).

### Results for Taglu wells

Variation of pore-size distribution, total porosity ( $\phi_{gm1}$ ) and geometric mean pore size ( $d_{hg}$ ) with depth is shown in Figure 3 for samples from the Taglu wells (C-42, G-33, and F-43; Fig. 1, Table 2). Most of these samples were collected from zones in the hydrostatic pressure regime (Table 1). Total porosity decreases linearly from approximately 30% at 950 m depth down to 6-10% at depths of 2450-3250 m, and  $d_{hg}$  decreases from approximately 230 nm to 20-45 nm over the same depth range. Below 2500-3000 m, both parameters tend to level off, a trend also observed by Katsube and Best (1992). The pore sizes exhibit relatively simple unimodal distributions, with pore-size ranges of 3-30 nm below 2500 m depth, and ranges of 100-1000 nm at 952 m depth. The  $\phi_{gm1}$  and  $d_{hg}$  values for the deepest samples are similar to those for tight shale samples from the Venture gas field, offshore Nova Scotia (Katsube et al., 1990, 1991, 1992a, b).

### CONCLUSIONS

Mercury porosimetry measurements for 41 shale core samples from nine Beaufort-Mackenzie Basin wells show a broad range of pore-size distribution and variation of porosity values, trends which are consistent with a dynamically compacting and eroding sedimentary basin. Porosity varies between approximately 5 to 32 %, and the geometric mean pore size from 9.1 to 331 nm. Measured porosity values compare favourably with previously mapped porosity trends based on the analysis of sonic logs. Vertical and lateral changes in porosity correlate with overpressure development and erosion of the basin margins. More detailed analysis and interpretation of these and additional petrophysical data will be presented in future papers. In particular, these total porosity values will be compared with effective porosity measurements made on separate specimens from the same sample, in order to determine if significant variations exist between porosity values obtained by different methods.

### ACKNOWLEDGMENTS

The authors thank J. Bloch (ISPG, Calgary) for critically reviewing this paper and making useful suggestions. The authors also acknowledge the efficient work of B. Smith

(ORTECH International, Toronto, Ontario) who did the mercury porosimetry measurements. D. Morrow (ISPG, Calgary) assisted in the preparation of the well location map and C. Thompson (ISPG, Calgary) helped us to organize the tables. S. Davis (GSC, Ottawa) drafted most of the diagrams. Core samples were collected from the core repository at the ISPG. Funding for this study was provided through the Office of Energy Research and Development (OERD).

### REFERENCES

- Agterberg, F.P., Katsube, T.J., and Lew, S.N.  
1984: Statistical analysis of granite pore size distribution data, Lac du Bonnet batholith, eastern Manitoba; in Current Research, Part A; Geological Survey of Canada, Paper 84-1A, p. 29-38.
- Coyner, K., Katsube, T.J., Best, M.E., and Williamson, M.  
1993: Gas and water permeability of tight shales from the Venture Gas Field, offshore Nova Scotia; in Current Research, Part D; Geological Survey of Canada, Paper 93-1D, p. 129-136.
- Gorny, A.J. and Carter, R.  
1987: World Data Bank II (WDBII), General Users Guide; U.S. Central Intelligence Agency, Washington, D.C., reproduced by U.S. Department of Commerce, National Technical Information Service, Springfield, Virginia, 7 p.
- Issler, D.R.  
1992: A new approach to shale compaction and stratigraphic restoration, Beaufort-Mackenzie Basin and Mackenzie Corridor, Northern Canada; American Association of Petroleum Geologists Bulletin, v. 76, p. 1170-1189.
- Katsube, T.J.  
1981: Pore structure and pore parameters that control the radionuclide transport in crystalline rocks; in Proceedings of the Technical Program, International Powder and Bulk Solids Handling and Processing, Rosemont, Illinois, p. 394-409.  
1992: Statistical analysis of pore-size distribution data of tight shales from the Scotian Shelf; in Current Research, Part E; Geological Survey of Canada, Paper 92-1E, p. 365-372.  
1993: Nano-pore transport mechanism of tight shales from the Scotian Shelf; in Current Research, Part D; Geological Survey of Canada, Paper 93-1D, p. 121-127.
- Katsube, T.J. and Best, M.E.  
1992: Pore structure of shales from the Beaufort-Mackenzie Basin, Northwest Territories; in Current Research, Part E; Geological Survey of Canada, Paper 92-1E, p. 157-162.
- Katsube, T.J. and Hume, J.P.  
1987: Pore structure characteristics of granitic rock samples from Whiteshell Research Area; in Geotechnical Studies at Whiteshell Research Area (RA-3), CANMET, Report MRL 87-52, p. 111-158.
- Katsube, T.J. and Walsh, J.B.  
1987: Effective aperture for fluid flow in microcracks; International Journal of Rock Mechanics and Mining Sciences and Geomechanics Abstracts, v. 24, p. 175-183.
- Katsube, T.J., Best, M.E., and Mudford, B.S.  
1991: Petrophysical characteristics of shales from the Scotian shelf; Geophysics, v. 56, p. 1681-1688.
- Katsube, T.J., Murphy, T.B., Best, M.E., and Mudford, B.S.  
1990: Pore structure characteristics of low permeability shales from deep formations; in Proceedings of the 1990 SCA (Society of Core Analysts) 4th Annual Technical Conference, August, 1990, Dallas, Texas, SCA-9010, p. 1-21.
- Katsube, T.J., Scromeda, N., and Williamson, M.  
1992a: Effective porosity of tight shales from the Venture Gas Field, offshore Nova Scotia; in Current Research, Part D; Geological Survey of Canada, Paper 92-1D, p. 111-119.
- Katsube, T.J., Williamson, M., and Best, M.E.  
1992b: Shale pore structure evolution and its effect on permeability; in Symposium Volume III of the Thirty-Third Annual Symposium of the Society of Professional Well Log Analysts (SPWLA), The Society of Core Analysts Preprints, Oklahoma City, Oklahoma, June 15-17, 1992, Paper SCA-9214, p. 1-22.

**Mudford, B.S.**

1988: Modelling the occurrence of overpressures on the Scotian Shelf, offshore Eastern Canada; *Journal of Geophysical Research*, v. 93, p. 7845-7855.

**Mudford, B.S. and Best, M.E.**

1989: Venture Gas Field, offshore Nova Scotia; case study of overpressuring in region of low sedimentation rate; *American Association of Petroleum Geologists, Bulletin*, v. 73, p. 1383-1396. Rootare, H.M.

**Mudford, B.S. and Best, M.E. (cont.)**

1970: A review of mercury porosimetry; *Perspectives of Powder Metallurgy*, v. 5, p. 225-252.

**Washburn, E.W.**

1921: Note on a method of determining the distribution of pore sizes in a porous material; *Proceedings of the National Academy of Science*, v. 5, p. 115-116.

---

Geological Survey of Canada Project 870057



# Hot spots on wood chip insulated permafrost slopes, Norman Wells pipeline, northwestern Canada

M.M. Burgess, D.E. Lawrence, and K.L. MacInnes<sup>1</sup>  
Terrain Sciences Division

*Burgess, M.M., Lawrence, D.E., and MacInnes, K.L., 1993: Hot spots on wood chip insulated permafrost slopes, Norman Wells pipeline, northwestern Canada; in Current Research, Part E; Geological Survey of Canada, Paper 93-1E, p. 133-140.*

---

**Abstract:** An insulating layer of wood chips, 0.5 to 1.8 m thick, was used to enhance the stability of 56 thaw-sensitive permafrost slopes along the Norman Wells pipeline. Biological heating within the wood chips was anticipated and observed in the first year after placement. On a few slopes the heating persisted in localized areas (hot spots), recurred after several quiescent years, or only developed in later years. In October 1992, snow melt patterns indicated the presence of hot spots on 23 slopes. This unexpected pervasive heating indicates complex biological activity and suggests the wood chips may have an adverse effect on the thermal performance of slopes.

**Résumé :** Une couche isolante de copeaux de bois de 0,5 à 1,8 m d'épaisseur a permis d'améliorer la stabilité de 56 talus sensibles au dégel en milieu de pergélisol le long du pipeline de Norman Wells. Un réchauffement biologique prévu à l'intérieur des copeaux a été observé au cours de la première année après leur mise en place. Sur quelques talus, le réchauffement a persisté par endroits (points chauds), a repris après plusieurs années de repos ou n'est apparu que plus tard. En octobre 1992, la fonte des neiges a révélé la présence de points chauds sur 23 talus. Ce réchauffement étendu et imprévu est le signe d'une activité biologique complexe et indique que les copeaux peuvent avoir un effet contraire à celui désiré sur le comportement thermique des talus.

---

<sup>1</sup> Department of Indian and Northern Affairs, Yellowknife, Northwest Territories X1A 2R3

## INTRODUCTION

The Norman Wells pipeline, owned and operated by Interprovincial Pipe Line (NW) Ltd. (IPL), is the first completely buried oil pipeline built within the discontinuous permafrost zone of northwestern Canada. The 869 km long pipeline begins in Norman Wells, Northwest Territories, follows the east side of the Mackenzie River south to Fort Simpson, crosses the Mackenzie east of Fort Simpson and then strikes southward to Zama, Alberta. In the northern portion of the route, many steep slopes are encountered at stream crossings.

In total, 165 significant slopes required geotechnical examination and site specific design (McRoberts et al., 1985a). Most of the slopes north of and including the Mackenzie crossing were underlain by permafrost. A layer of wood chips, 0.5 to 1.8 m thick, was used to insulate 56 of these slopes classified as thaw-sensitive. Figure 1 shows a wood chip insulated slope, located at km 79 on the south side of the Great Bear River crossing, in April 1984 following construction. This novel mitigative measure was selected to prevent or retard the thaw of ice-rich permafrost.

The wood chips were harvested locally and placed on the slopes as part of the winter construction activities in 1984 and 1985. A total of 462 hectares was harvested from 26 sites ranging in size from 0.2 to 150 hectares.

This paper briefly reviews the wood chip design, comments on their performance in the first few years after placement, and highlights observations in 1992.

## WOOD CHIP INSULATION DESIGN

Several methods to insulate permafrost slopes were originally assessed by IPL, including gravel over synthetic insulation, wood chips, synthetics, and thermosyphons. Wood chips were selected because of their local availability and ease of placement in cold weather (Pick, 1987). In addition, wood

chips were thought to provide a good geothermal solution; their ability to retain moisture would allow for a high latent heat effect important in retarding seasonal thaw (although this would have a detrimental effect on freezeback in winter). Furthermore the chips would conform to the surface under settlement related to thaw.

Geothermal analyses, preconstruction data, and on-site evaluation during construction were used to determine the thickness of chips required on each slope.

A major known disadvantage of wood chips was the possibility of heat generation due to microbiological activity. Aspen and birch were known in the pulp and paper industry as species that exhibited persistent heating in outside wood chip piles. IPL's construction plans therefore called for selective cutting to avoid use of aspen and birch as much as possible.

In addition to a literature search on the behaviour and properties of wood chips, IPL also established a wood chip test site near Grande Prairie where temperatures were monitored for a full year (July 1983 to July 1984). The test sections were built on sloping terrain using wood chip thicknesses of 1.2 m. In the first summer temperatures quickly rose to 40-50°C, then gradually cooled to 3-4°C the following winter but did not freezeback. The subsequent summer temperatures rose up to 30-40°C. IPL's literature search on wood chip piles suggested that after maximum temperature levels are achieved, the temperature would return relatively quickly to ambient levels.

It was thus anticipated that significant heat generation would only occur in the first one or two years after placement. Questions remained as to how the heat generation rate would reduce with time, with each season, and how the moisture contents and thermal properties would vary over time as the chips degraded.

Therefore an integral aspect of the wood chip design was IPL's establishment of an instrumentation and monitoring program to ensure design assumptions were realized and to



**Figure 1.**

Wood chip insulated slope 29B, Great Bear River South, km 79, postconstruction, April 1984 (photo by D.G. Harry)

evaluate their effectiveness. Seventeen wood chip slopes were instrumented by IPL with temperature cables or piezometers or both at the time of construction.

The federal government's Permafrost and Terrain Research and Monitoring (PTRM) program, co-ordinated by the Department of Indian and Northern Affairs, was also concerned about the performance of this novel technique. The PTRM therefore instrumented one wood chip slope as part of its network of study sites established along the pipeline (Pilon et al., 1989). Visual observations of conditions on the wood chip insulated slopes are an integral component of both IPL and PTRM programs.

### PERFORMANCE 1984 to 1989

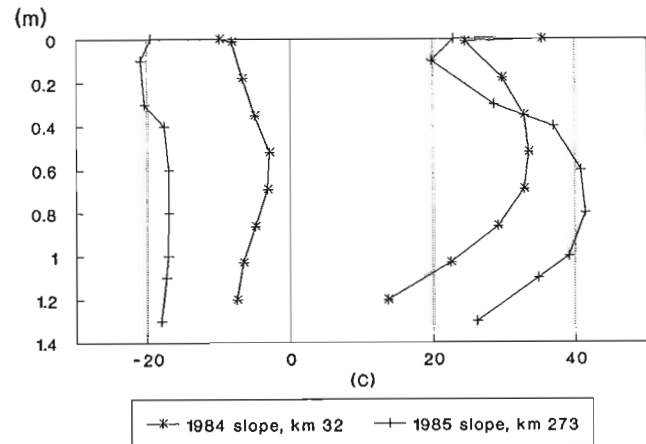
Discussions of the thermal performance of wood chips in the first few years after placement were presented by IPL in McRoberts et al. (1985a, b), Pick (1987), and Hanna and McRoberts (1988), and by the PTRM in MacInnes et al. (1990) and Baker et al. (in prep.).

Wood chips placed on the pipeline in 1984 generally exhibited self-heating during the first summer after placement but not during the second. Wood chips placed in 1985 also showed self-heating in the first summer, but, unlike the 1984 slopes, six of these did not completely cool off the first winter and/or heated up again the following summer.

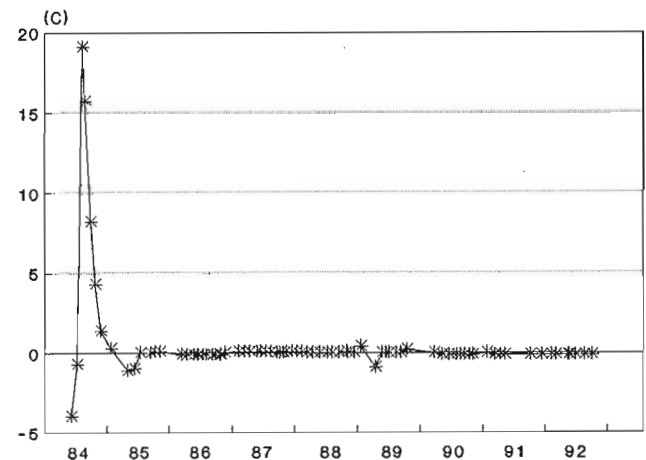
Figure 2 illustrates the maximum/minimum temperature envelope from a temperature cable in the wood chips on 1984 and 1985 insulated slopes during the first year after placement; note the higher temperatures experienced in the centre of the pile. Figure 3, a plot of temperature versus time from the base of the wood chip layer on a 1984 insulated slope, shows that the high temperatures experienced the first summer subsequently dissipated. Figure 4, a similar plot for slope 76 (km 273, placed in 1985), illustrates one of the slopes where heat persisted into the second year. The onset of the snow cover was recognized as an important factor in controlling the temperatures in the chips: a late snowfall allowed heat to dissipate, while an early snowfall favoured heat retention.

Two samples from slope 76, one with evidence of self-heating, the other with self-heating no longer evident, were sent to Forintek Canada Corporation for microbiological identification in 1987. Results from the analyses (K.A. Seifert, unpub. rep., 1987) did not reveal the cause of self-heating, although they did show that the samples were composed of 50% aspen.

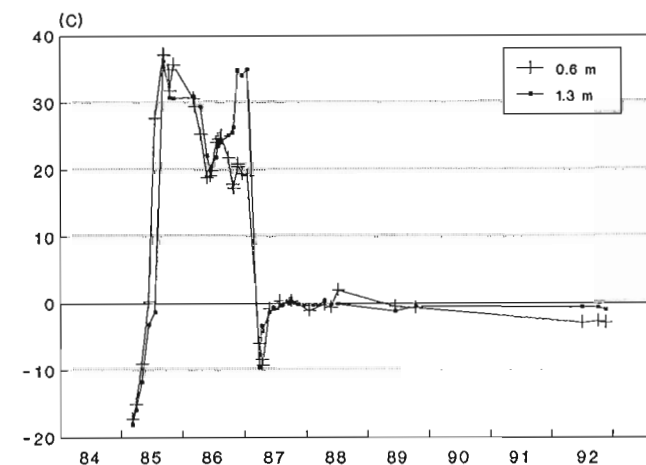
Several remedial measures have been used to cool slopes that exhibited heating that persisted beyond the first summer. These included watering, removal of the insulating snow cover for a few weeks, removal of snow cover and the wood chip layer in the winter to allow the ground to cool, thinning the wood chip layer (thicknesses on several slopes had exceeded design specifications), and the installation of ventilated ducts. (Note: Effects of the remedial work undertaken on slope 76 are evident in Figure 4. In February-March 1987, snow and chips were removed for a month, and



**Figure 2.** Annual temperature envelopes within the wood chip layer during the first year after placement, 1984 and 1985 construction years.



**Figure 3.** Temperatures at the base of wood chip slope 11, km 25.



**Figure 4.** Temperatures at the base and within the wood chip layer of slope 76, upper slope, km 273.

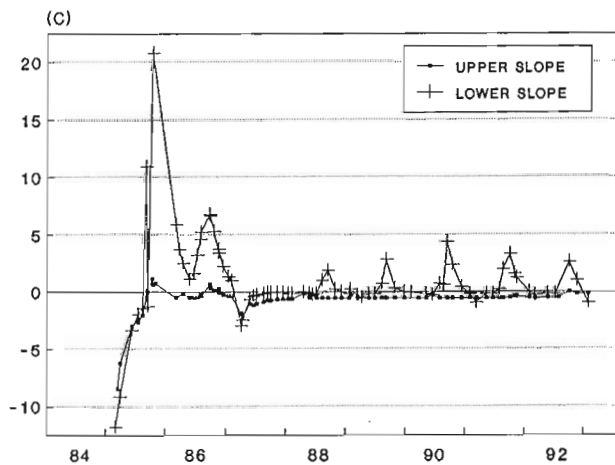
a 0.3 to 0.5 m thinner layer of chips was replaced.) IPL have had varying levels of success in providing short or long term cooling of the whole or specific sections of a slope.

The analysis of wood chip performance in these early years was generally based on an examination of the temperature data from the instrumented slopes. This instrumentation was positioned 3 to 4 m away from the pipeline to ensure that only the performance of the wood chips was being evaluated, i.e. in order to be removed from any thermal influence from the buried pipe. A given instrumented slope could have up to three locations (elevations) with temperature cables, e.g. upper, middle, and lower slope.

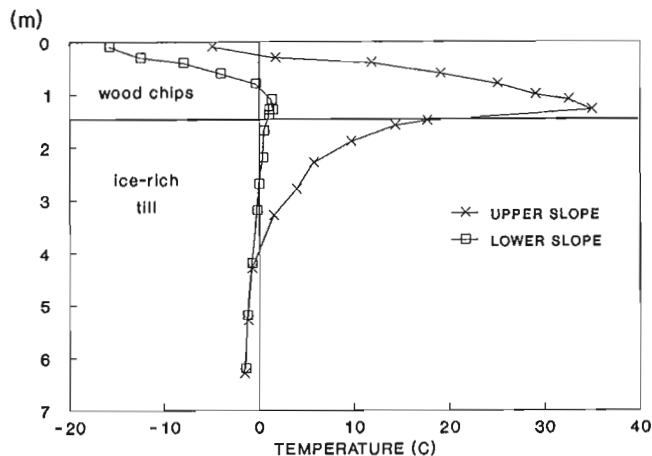
Several slopes with more than one temperature monitoring location showed different thermal behaviour depending on location (Fig. 5). This indicated that heat generation was a localized phenomenon on a slope (although factors controlling location and size were not understood or known) and suggested that the instrumentation on its own could not be solely relied upon to adequately assess the thermal performance of wood chip slopes.

Figure 6 illustrates the effect of a hot spot on the depth of thaw in the ground below the chips. Data from two instrumented locations on slope 76 are plotted; the upper slope instrumentation is located in a hot spot. Thaw depths beneath the hot spot reached about 2.5 m, whereas at the other location, thaw was only about 1 m. The higher temperatures in the hot spots could contribute to the formation of deeper thaw zones which could be a concern for slope stability.

Additional features became evident over time, based on an examination of data from instrumented slopes. At some locations heat generation was inactive for several years (in some cases because remedial measures had been taken) and then reappeared; in others heat generation had been quiescent (except for the first year) and then suddenly appeared.



**Figure 5.** Temperatures near the base of the wood chips from two separate locations on slope 142, Mackenzie River South, km 529.



**Figure 6.** Temperature-depth profiles from two locations on wood chip insulated slope 76, km 273, in January 1987; instrumentation on the upper slope is located in a hot spot.

Areas of persistent or recent heating have been referred to as "hot spots". Pick (1987) noted that differential snow melt patterns allowed visual identification of hot spots and suggested these may be areas of extremely active microbiological decomposition.

### VISUAL OBSERVATIONS OF HOT SPOTS 1990-1992

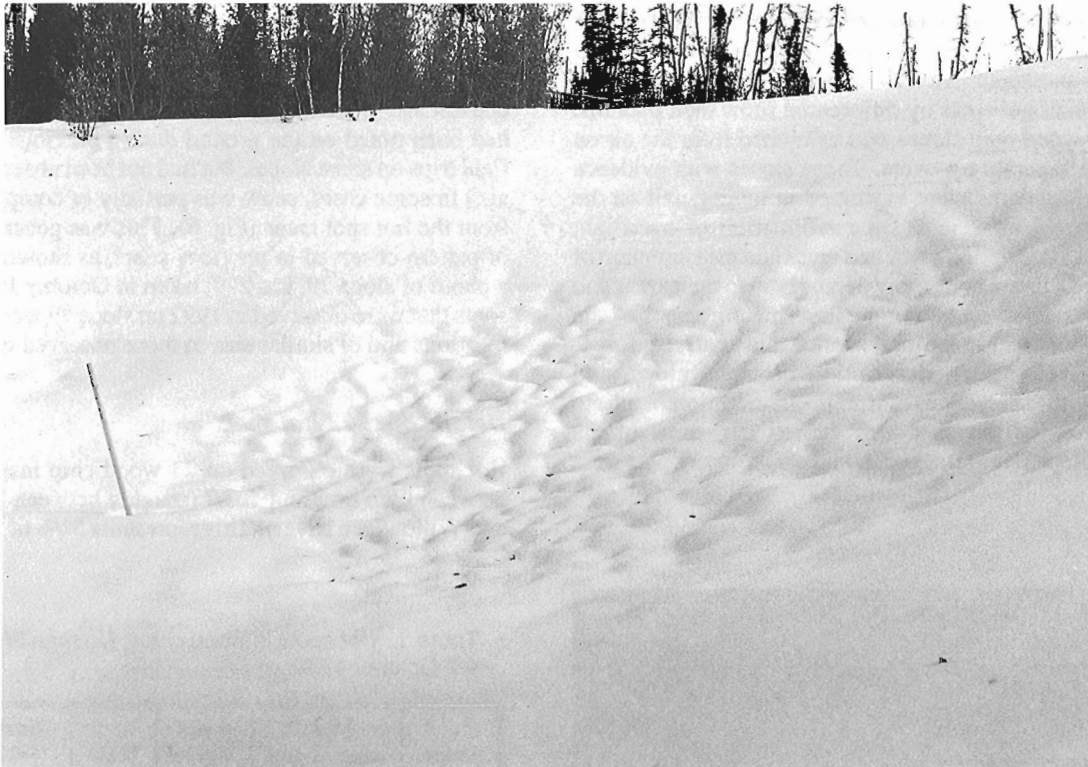
In October 1990, the PTRM noted differential snow melt patterns suggesting wood chip heating on eight slopes (four of which had no instrumentation). IPL reported that six slopes were affected by wood chip heating in the fall of 1991. The late disappearance of the snow cover in May 1992 allowed identification by PTRM of three slopes with hot spots. Examination during sampling of the hot spot on one of these slopes (number 45, km 133) revealed conspicuous white fungal growth in the surface layer (0-25 cm), with a sticky gelatinous material on the wood chips in the lower layer (25-45 cm).

In early October 1992, hot spots were observed by the PTRM on 23 of the 56 wood chip slopes, based on differential snow melt patterns.

#### 1992 observations

Conditions in the fall of 1992 proved to be excellent to observe snow melt patterns. In September 1992 the central Mackenzie region experienced widespread early snow falls (total for the month was 39.9 cm at Norman Wells). Daily temperatures were below 0°C from September 18 until the beginning of October.

The snow cover was preserved for two to three weeks, providing an early thick insulation of hot spots. Snow depths on wood chip slopes ranged from 10-30 cm on most slopes between Norman Wells and Wrigley during the period from

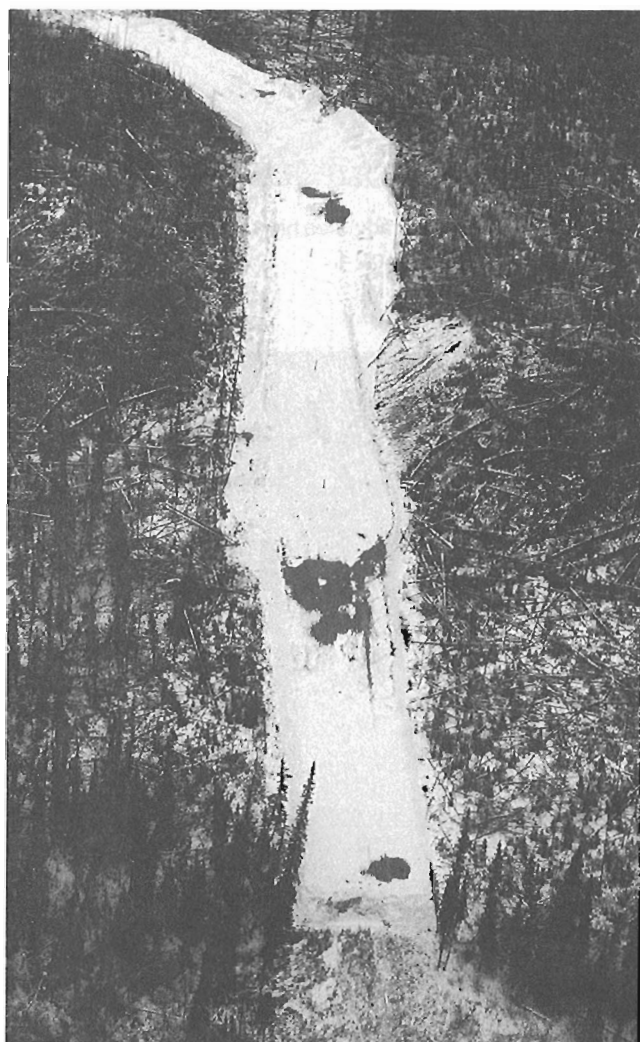


**Figure 7.** Hot spot, slope 45, October 1992. Hummocky, melting wet snow indicates high surface temperature in wood chips.



**Figure 8.** Hot spots, slope 44, October 1992. Extensive snow melt across right-of-way.

October 4-8. Snow melt proceeded from the base of the snowpack as the heat from the hot spots slowly dissipated through the snowpack. These conditions were ideal for the identification of hot spots by differential snow melt patterns. Each of the wood chip slopes was examined from the air on two or three separate fly-overs. Those slopes with evidence of snow melt patterns were examined in more detail on the ground. Ground work included confirmation of overflight observations, description of melted areas and measurement of their size, measurement of snow depths both in melt areas and adjacent unaffected areas, temperature measurement of the wood chips both within the melted areas and unaffected areas (using a thermometer), description of wood chips, and notation of the presence of fungi. In addition a photo documentation of the sites was carried out, most of the significant slopes were flagged, and wood chip samples were taken.



**Figure 9.** Differential snow melt observed on slope 79, km 279, October 1990.

Hot spots were generally in the form of circles or coalescing circles of reduced snow depth (Fig. 7) with altered surface texture and snow properties, i.e. higher moisture content and greater compaction. (Differences in snow texture had been noted on the ground during previous early winter field trips on some slopes, but had not been observed from the air.) In some cases, snow was partially or completely absent from the hot spot areas (Fig. 8). This was generally the type of pattern observed in previous years, as shown in Figure 9, a photo of slope 79, km 279, taken in October 1990. The hot spots that were observed in 1992 on slope 79 were at the same locations and of similar size to those observed in 1990.

**Details of 1992 hot spots**

Hot spots were observed on 23 wood chip insulated slopes between kmp 84.5 and 403.7 (roughly between Fort Norman and Willowlake River). This represents 56% of the slopes in

**Table 1.** Hot spots in wood chips, Norman Wells pipeline, 4-7 October 1992.

Slope	kmp	Ins	# Hot spots	Size	Temp. (°C)	Sample ID
31A	84.5	G		E	12	S7
32A	93.2	G	1	M	12	
33N	94.1	G	1	S		
35	103.1	G	3	S		
36	103.2	G	4	S-L	15	S8
44	133.6	G		E	18	
45	133.7	G	>7	M	15	S9
47	159.5	G	>5	M	18	S10
48B	160.1	G	2			
55	182.2	A	1			
61	191.2	A	1			
63	194.9	G	6	S+M	14	
73	271.4	G		E	18	S6
74	271.6	G	3	S		
75	273.5	G	4	M-L	20	S5
76	273.6	G	1	S		
77	275.5	A	1			
78	275.6	A	4			
79	279.0	G	>9	E		
80	279.3	G	2	S+M	7	
82	286.6	G	6	E	12	S4
112	352.3	G	>5	S+M	6	S2, S3
123	403.7	G	1	E	7	S1

Note: Size: S = 1-3 m, M = 3-6 m, L = +6 m, E = extensive  
 Ins = inspection; G = ground, A = air only  
 Temp = maximum temperature observed in wood chips

this section of the pipeline route. Outside of this area there were either no hot spots or snow and weather conditions were unfavourable for their detection. The total number of insulated slopes along the whole line is 56; hot spots were thus noted on 41% of all the wood chip slopes.

Table 1 summarizes key observations on the hot spots. About one third of the 23 slopes had extensive warm areas, i.e. melt areas extended across more than two thirds of the right-of-way (slopes 31A, 44, 47, 73, 79, 82, and 123). Slope 75 had several large spots and showed the maximum temperature of 20°C.

Temperatures in the hot spots, measured at approximately 20 cm below the surface of the chips, ranged from 7-20°C, while temperatures in surrounding areas were in the 0-5°C range. There were indications from the snow melt patterns within individual circles that the temperature was warmest at the perimeter of the hot spot.

The shape of the melted areas was usually circular with a diameter in the range of 1-13 m. Oval and coalescing forms were also observed, and in a couple of cases melting was continuous across the better part of the right-of-way.

In addition, localized snow melt in very restricted linear patterns indicates that there is localized heat flow from the wood chips via tension cracks.

### *Identification of fungal organisms*

Samples were taken at 10 locations in October 1992 and forwarded to Forintek Canada Corporation for identification of fungal organisms. In almost all cases where samples were taken there was a fungal or rotting odour and the presence of white mycelium was noted.

Samples were also taken from the hot spot on slope 45 (km 133) in May 1992 and sent to Forintek. Forintek has recommended shortening the length of time between sampling and isolation of fungi in the laboratory, as well as several sampling periods throughout the year to allow a more detailed analysis of frequency and diversity of organisms.

### *Winter 92/93 observations*

Unlike previous winters, visible snow melt patterns persisted throughout the winter of 1992-1993 on a few slopes. In addition, new snow melt patterns were also noted.

## **SUMMARY AND CONCLUSION**

Unusual weather conditions in early October 1992 provided an opportunity to detect and document the location of hot spots in wood chip insulated slopes on the Norman Wells pipeline. Prior to 1992 the number of slopes where persistent heat generation had been noted was limited, and it was thought that the heating was localized.

Current observations indicate that hot spots are wider spread and more pervasive than previously recognized, with 23 of the insulated slopes (41%) showing evidence of heating. The extent and implication of this heating to underlying soil temperatures and slope stability cannot yet be determined.

Pipe operating temperatures are generally warmer than those used in the geothermal design of wood chip slopes (Burgess, 1992). This has led to wider and deeper thaw bulbs beneath insulated slopes than had been predicted. Probing by IPL in 1990 confirmed the extent of the thaw zones. Slope stability studies, analyses to reassess the factor of safety, and instrumentation have been a focus of the last two years of research and monitoring. The factor of safety on several insulated slopes has dropped below design levels. The documentation in 1992 of extensive hot spots suggests that heating of wood chips may have more significance on thaw of slopes than previously anticipated.

Further detailed investigations are required to ascertain the effects of these hot spots. It is hoped that additional instrumentation can be installed by PTRM to study the thermal regime in more detail. These data combined with results from fungal analyses may help to understand the complex and dynamic behaviour of the wood chips with time.

The continuity of the monitoring program, with regular trips throughout the year both for visual observations and instrument data collection, has been crucial to achieving the current level of understanding and evaluation of wood chip behaviour. The short-term and long term performance of the wood chips has each revealed itself to be quite different, and much remains to be learnt before this behaviour can be predicted with confidence.

## **ACKNOWLEDGMENTS**

We thank Harry Baker of the National Research Council of Canada for his insights and constructive comments. The government's Permafrost and Terrain Research and Monitoring Program has been primarily funded by the Department of Indian and Northern Affairs' Northern Affairs Program and Northern Oil and Gas Action Program (NOGAP). Additional funding and other assistance has also been provided by Energy, Mines and Resources, the Federal Panel on Energy Research and Development, and IPL. Co-operation in monitoring was established with IPL as part of an Environmental Agreement signed between INAC and IPL.

## **REFERENCES**

- Burgess, M.M.**  
1992: Analysis of the pipe and ditch thermal regime, Norman Wells pipeline; in Proceedings of the 11th International Offshore Mechanical and Arctic Engineering Conference, Calgary, June 1992, v. 5, part B; Paper No. OMAE-92-917, p. 575-584.
- Hanna, A.J. and McRoberts, E.C.**  
1988: Permafrost slope design for a buried oil pipeline; in Proceedings of the Fifth International Conference on Permafrost, Volume 2, Norway, August 1988; Tapir Publishers, p. 1247-1252.

**MacInnes, K.L., Burgess, M.M., Harry, D.G., and Baker, T.H.W.**

1990: Permafrost and terrain research and monitoring: Norman Wells pipeline, volume II research and monitoring results: 1983-1988; Department of Indian and Northern Affairs Canada, Northern Affairs Program, Environmental Studies Report No. 64, 204 p.

**McRoberts, E.C., Hanna, A.J., and Smith, J.**

1985a: Monitoring of thawing permafrost slopes: Interprovincial Pipe Line; in Proceedings of Workshops on Subsea Permafrost and Pipelines in Permafrost, November 1985; National Research Council of Canada, NRCC Technical Memorandum 139, p. 133-151.

**McRoberts, E.C., Nixon, J.F., Hanna, A.J., and Pick, A.R.**

1985b: Geothermal considerations for wood chips used as permafrost slope insulation; in Proceedings, International Symposium on Ground Freezing, Sapporo, Japan, August 1985, v. 1, p. 305-312.

**Pick, A.R.**

1987: Use of wood chips for permafrost slope stabilization; in Proceedings of the Canadian Society of Civil Engineering Centennial Conference, Montreal, Canada, p.345-365.

**Pilon, J.A., Burgess, M.M., Judge, A.S., Allen, V.S., MacInnes, K.L., Harry, D.G., Tarnocai, C., and Baker, H.**

1989: Norman Wells to Zama pipeline permafrost and terrain research and monitoring program: site establishment report; Geological Survey of Canada, Open File 2044, 332 p.

---

Geological Survey of Canada Project 920045-MB



# Peatland distribution in the Fort Simpson area, Northwest Territories with a geophysical study of peatland-permafrost relationships at Antoine Lake

J.M. Aylsworth, I.M. Kettles, and B.J. Todd

Terrain Sciences Division

*Aylsworth, J.M., Kettles, I.M., and Todd, B.J., 1993: Peatland distribution in the Fort Simpson area, Northwest Territories with a geophysical study of peatland-permafrost relationships at Antoine Lake; in Current Research, Part E; Geological Survey of Canada, Paper 93-1E, p. 141-148.*

---

**Abstract:** The distribution of peat bogs and fens in the Fort Simpson area (NTS 95H, NW1/4), in the Mackenzie Valley has been mapped using existing surficial geology maps and recent air photo interpretation. Presence or absence of permafrost is mirrored by the occurrence of peat bogs or fens, respectively. Peatlands comprise approximately 35% of the landmass in the region. Of this, 44% is peat bog and 56% is fen. Borehole logs and results of an EM survey show peat thicknesses of 1.5-8.0 m in bog and 0.6-6 m in fen. An estimate of peat volume for the Fort Simpson area is  $191.9 \times 10^7 \text{ m}^3$ , of which 55% and 45% is in bog and unfrozen fen, respectively. With global warming the  $104.8 \times 10^7 \text{ m}^3$  of peat presently frozen in bog could become an active producer of greenhouse gases. Similar conditions are common throughout the Mackenzie Valley.

**Résumé :** On a cartographié la distribution des tourbières oligotrophes et minérotrophes dans la région de Fort Simpson (SNRC 95H, NW1/4), dans la vallée du Mackenzie, à partir de cartes existantes de la géologie de surface et de photographies aériennes récentes. La présence de tourbières oligotrophes ou de tourbières minérotrophes atteste la présence ou l'absence, respectivement, de pergélisol. Les tourbières constituent environ 35 % des terres de la région. De ce chiffre, 44 % sont des tourbières oligotrophes et 56 % des tourbières minérotrophes. Les diagraphies de forage et les résultats d'un levé EM indiquent que l'épaisseur de la tourbe varie de 1,5 à 8,0 m dans les tourbières oligotrophes et de 0,6 à 6 m dans les tourbières minérotrophes. Le volume de tourbe dans la région de Fort Simpson est évalué à  $191,9 \times 10^7 \text{ m}^3$ , dont 55 % dans des tourbières oligotrophes et 45 % dans des tourbières minérotrophes non gelés. Avec le réchauffement de la planète, les  $104,8 \times 10^7 \text{ m}^3$  de tourbe présentement gelés dans les tourbières pourraient devenir une source active de gaz à effet de serre. Des conditions semblables sont fréquentes partout dans la vallée du Mackenzie.

## INTRODUCTION

Continuing increases in greenhouse gas concentrations will, if unchecked, lead to global warming (Houghten et al., 1990). In boreal forest, sub-arctic, and arctic environments, peatlands form a vast carbon sink and, hence, are also a natural source or sink for greenhouse gases. At present the production of greenhouse gases in peatlands is limited as a high percentage of peatland is permanently frozen (Zoltai et al., 1988). As temperatures increase, however, frozen peat bog in some areas will degrade to unfrozen fen. Within unfrozen fens, degrading peats may produce more than 100 times more methane, for example, than peat in nearby frozen areas (Watson et al., 1990). It is therefore important to know the distribution of bog, fen, and permanently frozen ground and to understand the interrelationships between them in permafrost areas. Of particular importance are peatlands in areas of discontinuous permafrost as these areas are potentially most vulnerable to the effects of global warming.

A 1:1 000 000 scale map showing distribution of peat bogs and fens in the Mackenzie Valley is in preparation (Fig. 1). The compilation, based on existing surficial geology maps, extends from the Mackenzie Delta (68°N) south to the Northwest Territories/Alberta border (60°N), an area of 260 325 km<sup>2</sup>. Information pertaining to physical properties of peat deposits in the valley, including thickness, is available from Geological Survey of Canada's Mackenzie Valley Geotechnical Borehole Database. This database consists of the logs of approximately 14 000 boreholes drilled for highway and pipeline engineering purposes. It forms a generally north-south linear transect of the valley. Along this corridor, average annual ground temperatures range from -10°C in the extreme north to 0° and higher in the southern area near Fort Simpson (Judge, 1973). In the discontinuous permafrost zone in the southern part of the valley the occurrence and thickness of permafrost are extremely variable locally. Here the presence or absence of permafrost is mirrored by the occurrence of peat bogs or fens, respectively. In this paper, the distribution of bog and fen over an area of 2860 km<sup>2</sup> in the Fort Simpson region (NTS 95H northwest quarter), is examined (Fig. 1). Also presented are results of a detailed geophysical study of a peatland site near Antoine Lake. This detailed study, similar to one undertaken by Sartorelli and French (1982), was carried out to gain understanding of subsurface relationships between peat and permafrost in the Fort Simpson area.

### Location

Fort Simpson lies at the confluence of the Liard and Mackenzie rivers in the northern Interior Plains physiographic region (Vincent, 1989). The region is underlain by Devonian-age bedrock of the Fort Simpson Formation comprising predominantly shale and siltstone (Douglas, 1959).

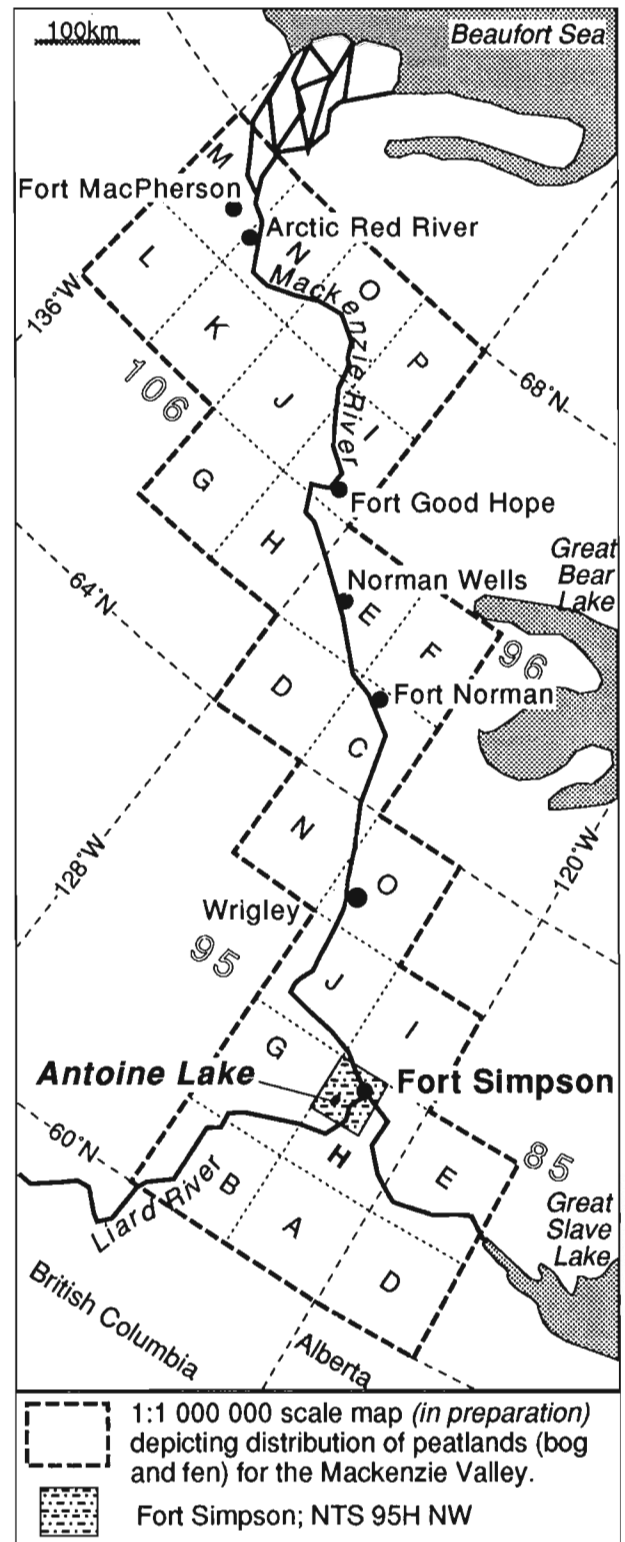


Figure 1. Location map, Mackenzie Valley, Northwest Territories.

Glacial till was deposited during the late Wisconsinan glaciation. During deglaciation, lacustrine fine grained sediments were deposited in Glacial Lake Mackenzie, an isostatically controlled proglacial lake occupying the Mackenzie and lower Liard River valleys (Smith, 1992; Vincent, 1989). Over much of the map area, including the detailed study site at Antoine Lake, lacustrine sediments are overlain by sands and silts of the postglacial Liard River delta (Smith, 1992; Minning et al., 1980). Extensive areas of sand dunes were formed on the delta surface soon after Glacial Lake Mackenzie drained. Modern alluvial sands and gravels as terraces and floodplains lie along the Liard and Mackenzie rivers. Extensive peat deposits have developed on the flat surfaces and in depressions bordering the Liard River and south of the Mackenzie River. The detailed study site at Antoine Lake is entirely covered by peat.

**DISTRIBUTION OF BOG AND FEN IN THE FORT SIMPSON AREA**

Maps showing the distribution of organic units in the Fort Simpson area, based on recent air photo interpretation and from existing surficial geology maps (Minning et al., 1980), are shown in Figures 2 and 3. Organic units are reported to have peat thicknesses exceeding 1.5 m (Minning et al., 1980). Four organic classes have been identified: bog, fen, and two mixed bog/fen units, one with bog dominant (>50%) and the other fen dominant. In turn each of these four classes have been further subdivided according to the percentage of land surface that is covered by thick peat (>1.5 m) – >85%, 50-85%, and 15-49% of surface. Only continuous organic

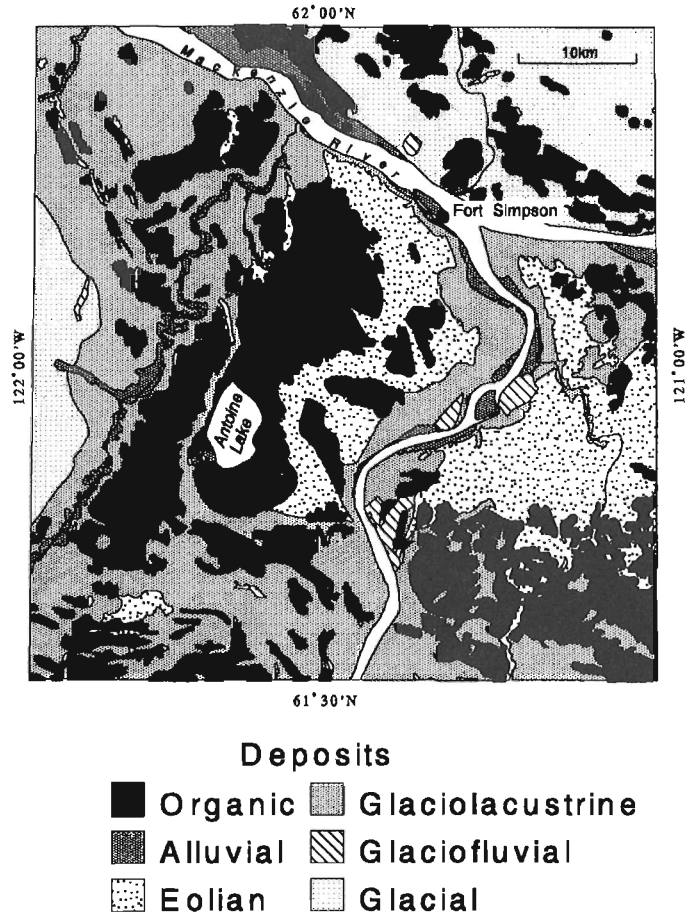


Figure 2. Surficial geology of Fort Simpson area, NTS 95H (NW1/4).

Table 1. Estimate of peat volumes, Fort Simpson area

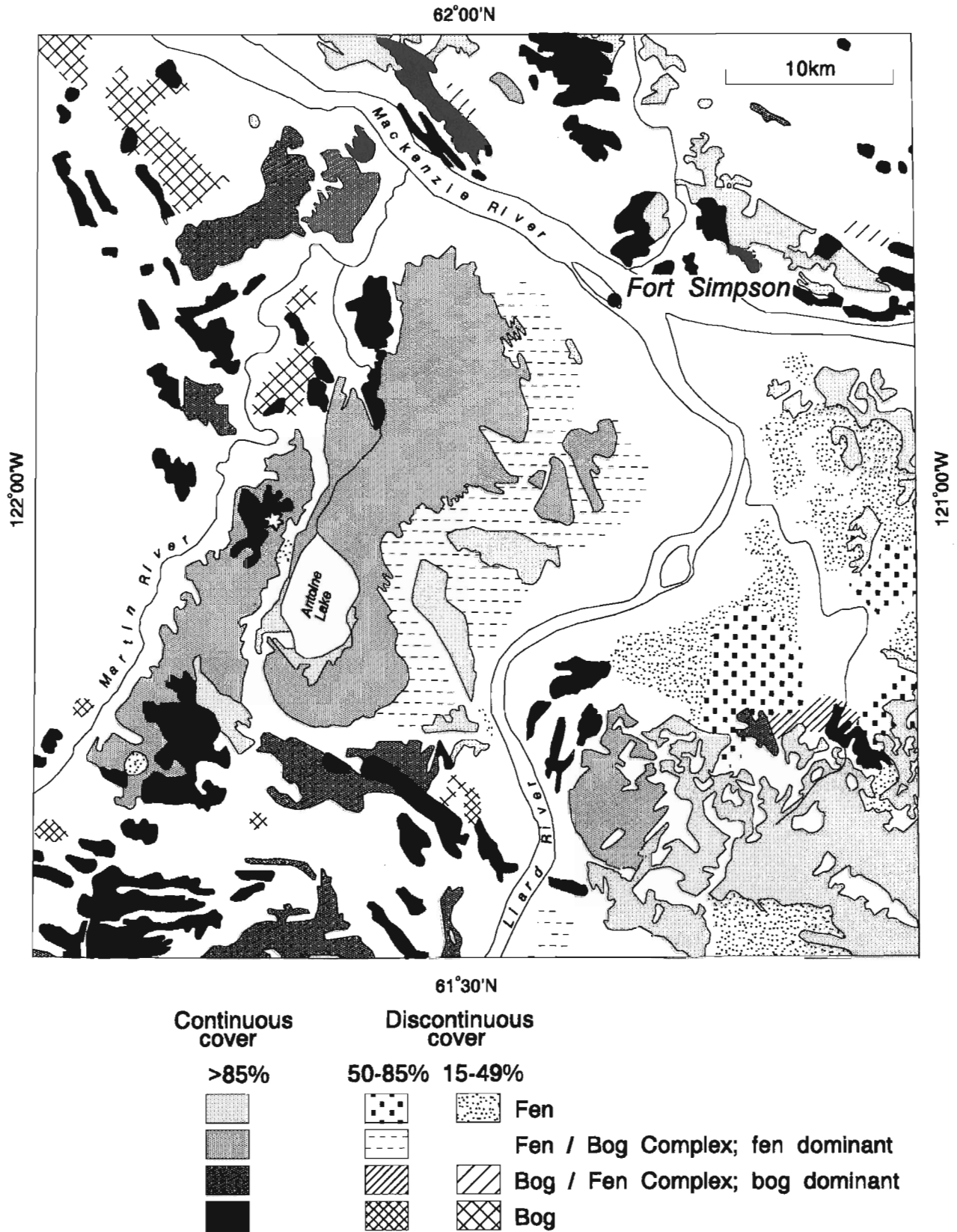
Organic unit	Continuous Cover		Discontinuous Cover					
	>85%		50-85%			15-49%		
	area *	volume **	area*	volume**	area*	volume**	area*	volume**
			95H (NW1/4)	50%	95H (NW1/4)	15%	95H (NW1/4)	
Fen	26498.0	41071.9	5573.0	2786.5	4319.1	12161.0	1824.2	2827.4
Complex	30598.0		12735.0			0.0		
55% fen	16829.0	26085.0	7004.0	3502.0	5428.1			
45% bog	13769.0	33045.6	5731.0	2865.5	6877.2			
Complex	10126.0		728.0			492.0		
55% bog	5569.0	13365.6	400.0	200.0	480.0	271.0	40.7	97.6
45% fen	4557.0	7063.4	328.0	164.0	254.2	221.0	33.2	51.4
Bog	20282.0	48676.8	568.0	284.0	681.6	4464.0	669.6	1607.0
Total Fen	47884.0	74220.2		6452.5	10001.4		1857.3	2878.8
Total Bog	39620.0	95088.0		3349.5	8038.8		710.3	1704.6
Total Organic	87504.0	169308.2		9802.0	18040.2		2567.6	4583.4

\* x 10 000 sq. m.      \*\* x 10 000 cu. m.

NOTE: Calculation of peat volumes is based on average peat thicknesses obtained from borehole logs:

fen = 1.55 m; bog = 2.4 m thick peat

	AREA x10 000 000 sq.m.	95H(NW1/4) VOLUME x10 000 000 sq.m.
Total Fen	56.2	87.1
Total Bog	43.7	104.8
Total Organic	99.9	191.9



**Figure 3.** Organic deposits of Fort Simpson area, NTS 95H (NW1/4). Location of detailed survey site at Antoine Lake indicated by a white star.

cover, considered to be >85% of the surface, has been depicted in Figure 2. Discontinuous organic coverages (50-85% and 15-49%) are shown as patterns in Figure 3.

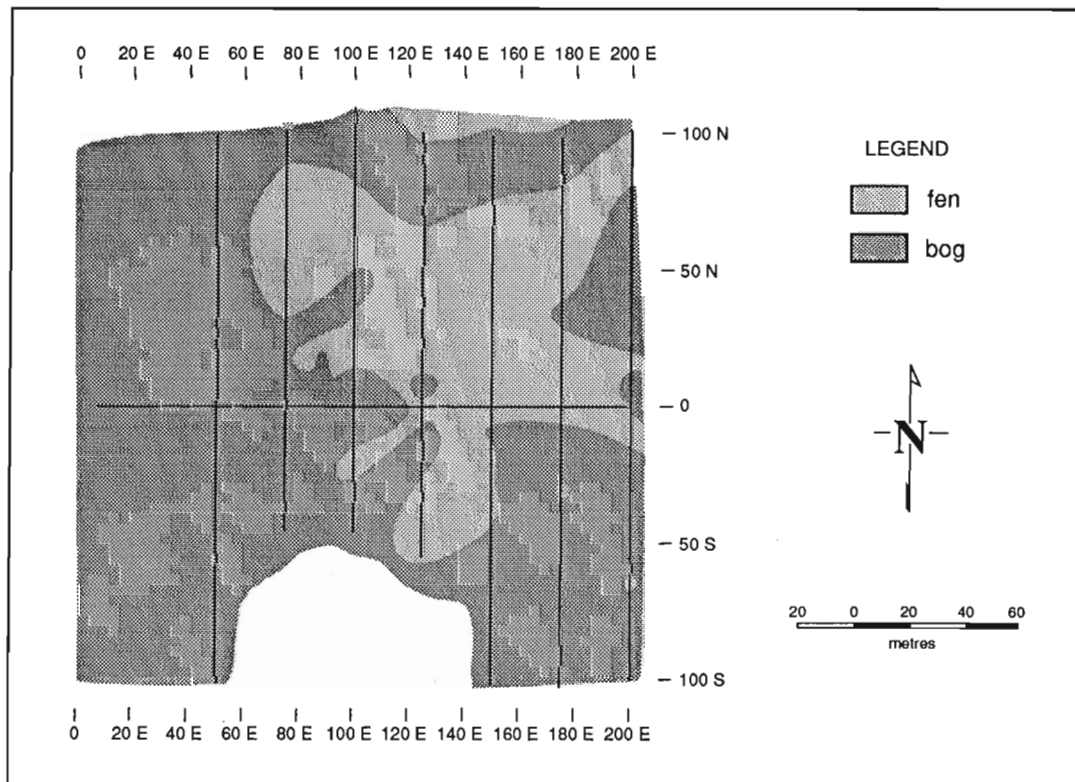
The most extensive areas of organic deposits are either underlain by glaciolacustrine sands, silts and clays, or are underlain by a thin veneer of eolian silt and sand which, in turn, overlies glaciolacustrine sediments. Here the widespread

occurrence of peat reflects the poor surface drainage conditions associated with flat lying areas of impermeable silt and clay. Less extensively, but still commonly, thick organic deposits have developed in depressions in the glacial till surface, especially in fluted or drumlinoid areas. The influence of till morphology is more significant in nearby regions outside of this study area.



**Figure 4.**

Study site at Antoine Lake; baseline shown as black line with Station 100E marked with black star. Eastern end of baseline at right side of photo. GSC 1993-150 B



**Figure 5.** Distribution of bog and fen at the detailed survey site, Antoine Lake, Northwest Territories. East-west trending baseline at "0".

Peat thickness in organic units as well as the thickness of peat occurring as a surface veneer over other surficial units has been summarized from 110 borehole logs in the Fort Simpson area (NTS 95H). In areas mapped as organic units, an average peat thickness of 2.4 m (1.5-5.0 m) was measured in bogs and a lesser average thickness of 1.55 m (0.6-3.2 m) was measured in fens. Visible ice was reported from boreholes in bogs. Boreholes in fens were unfrozen. Peat thicknesses are probably conservative estimates. As most of the boreholes were drilled along highway and pipeline alignments, preferentially avoiding areas where thick peat deposits were known, lesser depths were obtained for organic units than were found for the EM survey described below. In the same general region, Rutter et al. (1973) reported peat thicknesses in fens of over 3.0 m with the underlying ground unfrozen to depths of at least 6 m, the bottom of the boreholes; whereas, for bogs, if peat exceeded 1.8 m, the underlying sediment was generally frozen to at least 6 m.

Peat also occurs as a veneer over other sediments or as discontinuous patches in areas mapped as non-organic units (Fig. 2). For example, in areas mapped as glaciolacustrine deposits, peat veneer, where present, averaged 0.2 m thick. This contrasts with the thick peat cover in areas that are mapped as organic units but are known to overlie glaciolacustrine sediments. These lower values are obtained from the better drained glaciolacustrine plains, such as above the banks of entrenched rivers and creeks. In areas of eolian deposits peats are common in depressions between sand dunes. Thicknesses averaged 1.13 m, and up to 3.05 m were observed. Peat thicknesses in till terrain averaged 0.37 m. Overlying glaciofluvial deposits, thicknesses of peat or organic soil ranged from 0.15 to 1.52 m with an average of 0.76 m. On alluvial deposits, organic soils of up to 0.61 m were measured with an average thickness of 0.26 m.

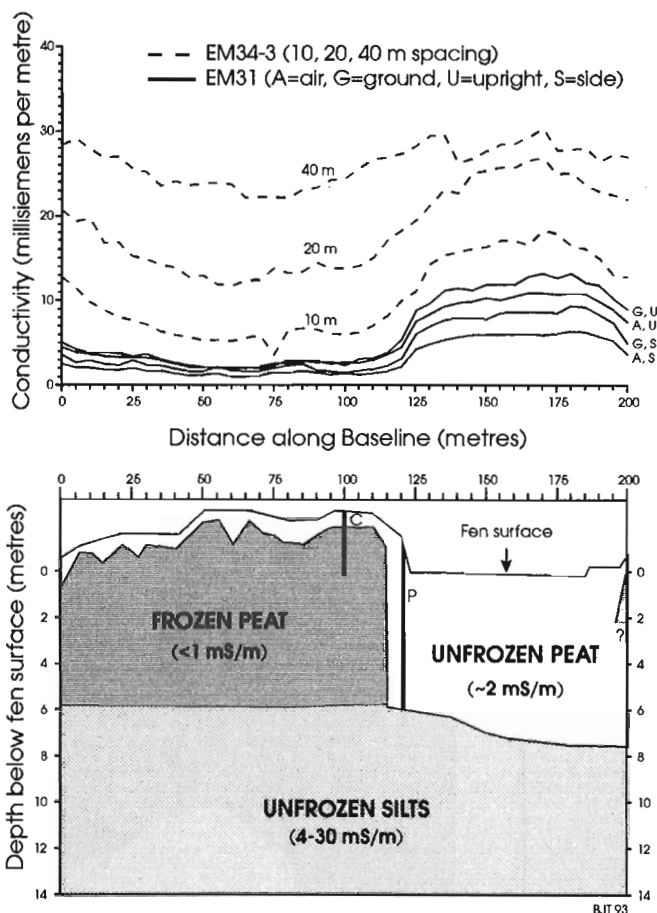
### Calculation of volumes

An estimation of peat volume in fens and bogs for the Fort Simpson area (95 H, NW1/4) was made based on the average peat thicknesses given above, and the area of organic deposits depicted in Figure 3 (Table 1). Peat thicknesses for bog and fen units were 2.4 m and 1.55 m respectively. In mixed units the exact bog/fen ratios were unknown and a conservative 55%/45% ratio was chosen. The areal extent of each organic unit, for both continuous and discontinuous coverage, was determined using an ARC/INFO GIS. The area of 'continuous' organic deposits (>85% of surface) was considered to be the full area of the map polygon. The area of 'discontinuous' organic deposits (50-85% and 15-49% of surface) was chosen conservatively to be 50% and 15% of the full area of the polygon, respectively.

Peatlands comprise approximately 1000 km<sup>2</sup>, or 35% of the landmass of the Fort Simpson area (95H, NW1/4). Of this, 44% is peat bog and 56% is fenland. A conservative estimation of peat volume is  $191.9 \times 10^7 \text{ m}^3$ , of which 55% ( $104.8 \times 10^7 \text{ m}^3$ ) is peat in frozen bog and 45% ( $87.1 \times 10^7 \text{ m}^3$ ) is peat in unfrozen fens.

## A DETAILED STUDY OF PEATLAND IN THE ANTOINE LAKE AREA

A small area of fen and peat plateau bog, generally raised about 2 m above the fen, was selected for geophysical investigation using the electromagnetic (EM) method (Fig. 4). A grid, 200 by 200 m, was set up and the distribution of bog and fen mapped in detail, as survey stations were marked every 5 metres (Fig. 5). The site was then surveyed using two instruments manufactured by Geonics Limited, Mississauga, Ontario. Both instruments measure ground electrical conductivity using the electromagnetic inductive technique. The first instrument, the EM31 ground conductivity meter, operates at a frequency of 39.2 kHz with a fixed coil spacing of 3.66 m. At each survey station, readings were recorded using four different instrument modes to provide depths of signal penetration ranging from 1 to 5 m. Two sets of readings were obtained with the EM31 instrument at hip level, upright and on its side, and another two sets with the unit on the



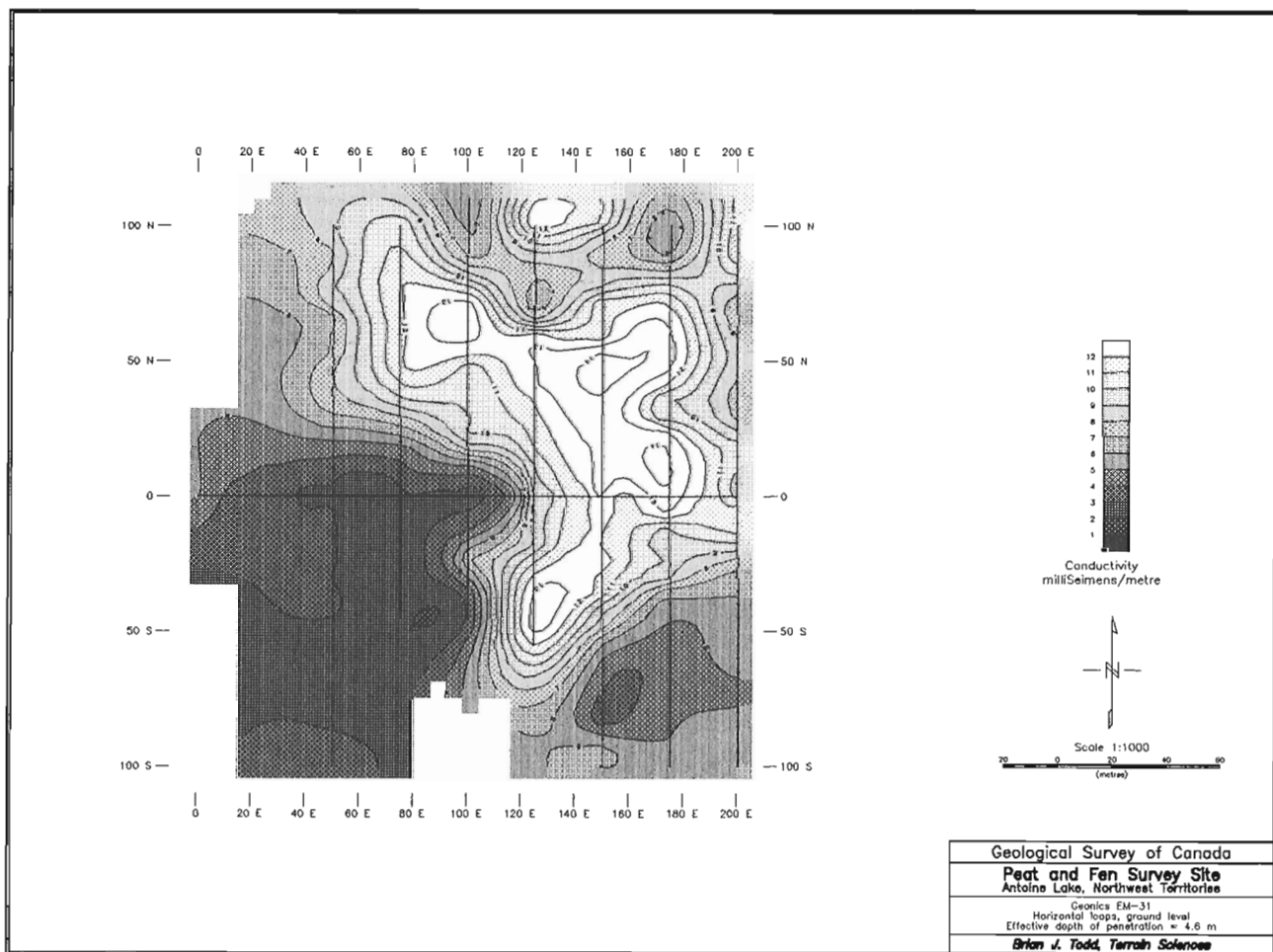
**Figure 6.** The EM31 and EM34-3 conductivity profiles along the baseline (upper diagram). "C" and "P" mark locations of a drillhole and probe hole, respectively. Interpretation of subsurface materials (lower diagram). Also shown in lower diagram is depth to frost table.

ground in the upright and side orientations. The second instrument, an EM34-3, was used at each site with three intercoil spacings (10, 20 and 40 m) at three corresponding frequencies (6.4, 1.6 and 0.4 kHz), yielding a depth of investigation of up to 30 m.

At each survey station, depth to the frost table was measured using a frost probe. On the peat plateau, frost table depths were determined at 5 m intervals at a total of 178 sites. Depth to frost ranged from 0.4 to 2.0 m and averaged 0.7 m. Peat deposits were probed to depths exceeding 2 m at 65 sites in fen. Station 121E on the baseline marks the location of a probe hole through peat to unfrozen grey silty clay, a sample of the latter being obtained at the interface at a depth of 6 m ("P", Fig. 6). In addition, at Station 100E on the baseline, a frozen peat core was recovered to a depth of 3 m from bog using a modified CRREL frozen ground coring barrel driven by a hand-held, Stihl power auger, as described in Veillette and Nixon (1980) ("C", Fig. 6).

Results of the EM31 and EM34-3 survey show that materials of low conductivity are found beneath the peat plateau and of slightly higher conductivity beneath the fen. The EM31 and EM34-3 conductivity profiles along the baseline are shown in Figure 6 and lateral variation in conductivity over the survey grid in Figure 7. The latter was obtained using the EM31 ground conductivity meter on the ground in an upright position, giving an effective depth of signal penetration of approximately 4.6 m. This pattern of variation is similar to others obtained using other instrument modes and orientations.

Subsurface materials along the baseline were modelled further using conductivity data as well as frost probe and drill core data (Fig. 6). EM31 and EM34-3 data were analyzed using the program CONDAPP1 produced by GeoScott Exploration, St. John's, Newfoundland. CONDAPP1 calculates EM31 and EM34-3 responses for layered media in terms of cumulative response functions as described in the Geonics



**Figure 7.** Conductivity map shows results obtained using the EM31 ground conductivity meter on the ground in an upright position. The effective depth of penetration of the signal with this geometry is approximately 4.6 m.

instrument manuals. Geophysical field data from each station were compared to the EM response from a geological model composed of layers of materials of different thicknesses and conductivities. The low conductivity material beneath the peat plateau is interpreted as frozen peat to a depth of 6 m. Beneath the fen, conductivities are slightly higher and unfrozen peat is interpreted to a depth of almost 8 m. At depths below 6-8 m, there are materials of relatively high conductivity. These materials are interpreted as unfrozen postglacial silts, as was retrieved from the drill core.

## CONCLUSIONS

1. Peatlands comprise about 1000 km<sup>2</sup>, or 35 % of the landmass of the Fort Simpson area (95H, northwest quarter). Of this, 44% is peat bog and 56% is fen. A conservative estimation of peat volume is 191.9 x 10<sup>7</sup> m<sup>3</sup>, of which 55% is peat in frozen bog and 45% is peat in unfrozen fens. With global warming the 104.8 x 10<sup>7</sup> m<sup>3</sup> of peat presently frozen in bogs could become an active producer of methane and other greenhouse gases.

2. There are strong geological controls on peat distribution and thicknesses. Peatlands are most extensive over flat-lying, poorly drained, glaciolacustrine and deltaic plains. Thick organic deposits have accumulated in the low areas between sand dunes and in depressions in the till surface. Similar conditions are common throughout the Mackenzie valley.

3. Existing Quaternary maps and, where available, borehole data may be used to make a first estimate of peat volumes and areas on a regional scale. These calculations are facilitated using GIS mapping techniques.

4. EM surveys help characterize subsurface materials in peatland areas, especially when augmented with drill core and frost probe data.

## ACKNOWLEDGMENTS

The authors wish to thank the following: Jean Bisson for assisting with the EM survey at Antoine Lake; J. Traynor for compilation of borehole data; A. Moore for generation of digital maps and derived information; and L. Dyke for helpful advice and for critically reading this manuscript.

## REFERENCES

- Douglas, R.J.W.**  
1959: Trout River, District of Mackenzie, N.W.T.; Geological Survey of Canada, Map 28-1958, 1:506 880 scale.
- Judge, A.S.**  
1973: The thermal regime of the Mackenzie Valley: Observations of the Natural State; Environmental-Social Committee, Northern Pipelines, Task Force on Northern Oil Development, Report No 73-38, 177 p.
- Houghton, J.T., Jenkins, G.J., and Ephraums, J.J. (editors)**  
1990: Climate Change, The IPCC Scientific Assessment; Cambridge Press, New York, 365 p.
- Minning, G.V., Netterville, J.A., and Rutter, N.W.**  
1980: Surficial geology and geomorphology of Fort Simpson, District of Mackenzie, Northwest Territories; Geological Survey of Canada, Map 3-1978; 1: 125 000.
- Rutter, N.W., Boydell, A.N., and Savigny, K.W.**  
1973: Terrain evaluation, Mackenzie Transportation Corridor, Southern part; Environmental-Social Committee, Northern Pipelines, Task Force on Northern Oil Development, Report No. 73-36, 135 p.
- Sartorelli, A.N. and French, R.B.**  
1982: Electro-magnetic induction methods for mapping permafrost along northern pipeline corridors; in Proceedings of 4th Canadian Permafrost Conference, March, 1981, Calgary, (ed) H.M. French, National Research Council, Ottawa, p. 283-295.
- Smith, D.G.**  
1992: Glacial Lake Mackenzie, Mackenzie Valley, Northwest Territories, Canada; Canadian Journal of Earth Sciences, v. 29, p. 1756-1766.
- Watson, R.T., Rodhe, H., Oeschger, H., and Siegenthaler, U.**  
1990: Greenhouse gases and aerosols; in Climate Change: The IPCC Scientific Assessment, (ed.) J.T. Houghton, G.J. Jenkins and J.J. Ephraums, New York: Cambridge Press, p. 1-40.
- Veillette, J.J. and Nixon, F.M.**  
1980: Portable drilling equipment for shallow permafrost sampling; Geological Survey of Canada, Paper 79-21, 35 p.
- Vincent, J-S.**  
1989: Quaternary geology of the northern Canadian Interior Plains; in Chapter 2 of Quaternary Geology of Canada and Greenland, R.J. Fulton (ed.); Geological Survey of Canada, No. 1 (also Geological Society of America, The Geology of North America. v. K-1)
- Zoltai, S.C., Taylor, S., Jeglum, J.K., Mills, G.F., and Johnson, J.D.**  
1988: Wetlands of boreal Canada; in Wetlands of Canada, (ed.) National Wetlands Working Group Canada Committee on Ecological Land Classification; Ecological Land Classification Series, No. 24. Sustainable Development Branch, Environment Canada, Ottawa, Ontario, and Polyscience Publications Inc., Montreal, Quebec, 452 p.

Geological Survey of Canada Project 920046



CANADIAN  
SHIELD

BOUCLIER  
CANADIEN



# Co-operative research on the Kidd Creek volcanogenic massive sulphide deposit, Timmins, Ontario<sup>1</sup>

Kidd Creek Study Group  
Mineral Resources Division, Falconbridge Limited,  
and Laurentian University

*Kidd Creek Study Group, 1993: Co-operative research on the Kidd Creek volcanogenic massive sulphide deposit, Timmins, Ontario; in Current Research, Part E; Geological Survey of Canada, Paper 93-1E, p. 151-156.*

---

**Abstract:** A joint research project is currently being conducted by researchers from Falconbridge Limited, Laurentian University, and the Geological Survey of Canada to provide a thorough documentation of the Kidd Creek volcanogenic massive sulphide deposit. Specific objectives of the project include 1) detailed underground mapping of the mineralization and volcanic stratigraphy in order to reconstruct the depositional environment of the deposit; 2) examination of the petrogenetic history of the volcanics and the identification of key geochemical and isotopic signatures of different units which will facilitate stratigraphic correlation within and outside the mine; and 3) detailed studies of the mineralogy and chemistry of the alteration and mineralization together with investigations of their stable and radiogenic isotope signatures.

**Résumé :** Un projet de recherche conjoint a été entrepris par des chercheurs de la Falconbridge Ltée, de l'Université Laurentienne et de la Commission géologique du Canada pour documenter en détail le gisement de sulfures massifs volcanogènes de Kidd Creek. Les objectifs particuliers du projet sont : 1) cartographie souterraine détaillée de la stratigraphie volcanique et de la zone minéralisée afin de reconstituer le milieu de formation du gisement; 2) étude de l'évolution pétrogénétique des roches volcaniques et identification des principales signatures géochimiques et isotopiques des différentes unités pour faciliter les corrélations stratigraphiques à l'intérieur et à l'extérieur de la mine; 3) études détaillées de la minéralogie et de la chimie de la minéralisation et de l'altération accompagnées d'analyses isotopiques (isotopes stables et radiogéniques) visant à établir la signature de ces phases.

---

<sup>1</sup> Contribution to Canada-Ontario Subsidiary Agreement on Northern Ontario Development (1991-1995), under the Canada-Ontario Economic and Regional Development Agreement.

## INTRODUCTION

Kidd Creek is a world-class Cu-Zn deposit, with 85 million tonnes of past production (at 2.2% Cu and 7.2% Zn) and proven and probable reserves of 44.6 million tonnes (at 3.5% Cu and 5.0% Zn: Brisbin et al., 1990). The deposit accounts for more than one half of the total past production and current reserves of ore from volcanogenic massive sulphide (VMS) deposits in Ontario.

Although considerable knowledge about Kidd Creek has been acquired since the commencement of mining in 1966, important questions about structure, volcanic stratigraphy, primary igneous geochemistry, alteration, and mineralogy remain unanswered, and a comprehensive geological documentation of the deposit is not currently available to the public. The absence of this knowledge raises important questions about what characteristics should be sought in exploration for additional reserves in prospective volcanic rocks in the Timmins region.

To address this problem, a thorough study of the Kidd Creek deposit was initiated in late 1991, supported by the Northern Ontario Mineral Development Agreement and undertaken jointly by researchers from Falconbridge Limited, Laurentian University, and the Geological Survey of Canada. The aim of the study is to provide a complete descriptive model of the deposit, to generate useful guides in exploration for volcanogenic massive sulphide deposits elsewhere in the western Abitibi, and to better understand how, why, and where giant volcanic-associated massive sulphide deposits form. Descriptions of the general geology of Kidd Creek have been published by Matulich et al. (1974), Walker and Mannard (1974), Walker et al. (1975), Coad (1985), and Brisbin et al. (1990). These are discussed below, together with an outline of the current project and a review of preliminary results.

## PROJECT DESCRIPTION

### General geology

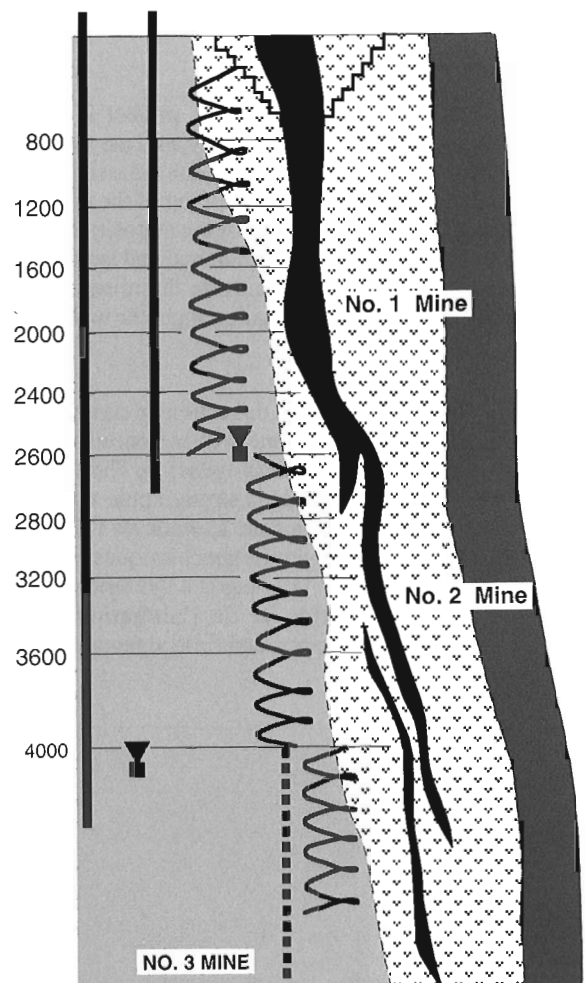
Kidd Creek was discovered in surface drilling in December 1963 and was mined from an open pit until 1979, at which time operations went underground. Ore is now being removed down to the 5300 foot level, and an internal shaft has been completed to a depth of about 7000 feet (Fig. 1). Structure, stratigraphy, alteration, and mineralization have been mapped extensively by the Geology Department at the Kidd Creek mine and other Falconbridge geologists. Further detailed mapping and sampling was completed throughout the No. 1, No. 2, and No. 3 mines during the 1992 field season as the first phase of the Northern Ontario Development Agreement (NODA) Project.

The deposit occurs within an east-trending, steeply dipping sequence of Archean ultramafic, mafic, and felsic metavolcanics and metasediments known as the Kidd-Munro Assemblage (e.g., Jackson and Fyon, 1991). The youngest rhyolites in the assemblage, from Beatty Township, have been dated at  $2714 \pm 2$  Ma (Corfu et al., 1989). A thick sequence

of metasediments (dominantly greywackes) known as the Hoyle Assemblage is believed to lie unconformably on top of the Kidd-Munro volcanics (Jackson and Fyon, 1991), although in the vicinity of Kidd Creek the contact relationships between the volcanics and metasediments are not well constrained. A detrital zircon study of the greywackes is being carried out in the geochronology laboratories of the GSC to determine the relative ages of these rocks.

The felsic volcanics which host Kidd Creek occupy an asymmetric, S-shaped fold structure with westerly younging directions in the mine (Bleeker, 1992; Fig. 2). The deposit plunges steeply to the north, parallel to the hinges of the major fold structures (Bleeker, 1992).

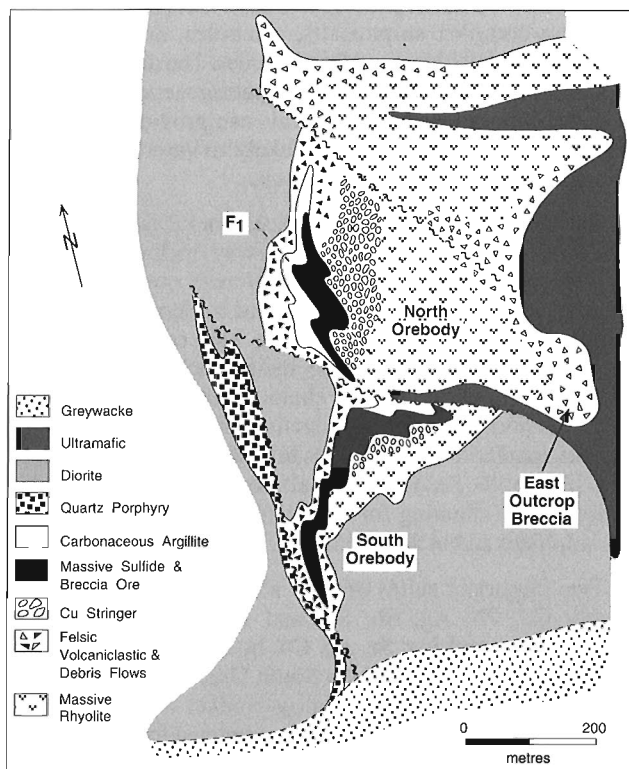
The mineralization occurs in two main orebodies; the North Orebody extends from surface down to 7000 feet and the South Orebody bottoms out near 3400 feet. Both orebodies were thickest at surface, in the open pit, suggesting that much of the original deposit may have been eroded away (Fig. 3). The massive sulphides occur at the top of a locally



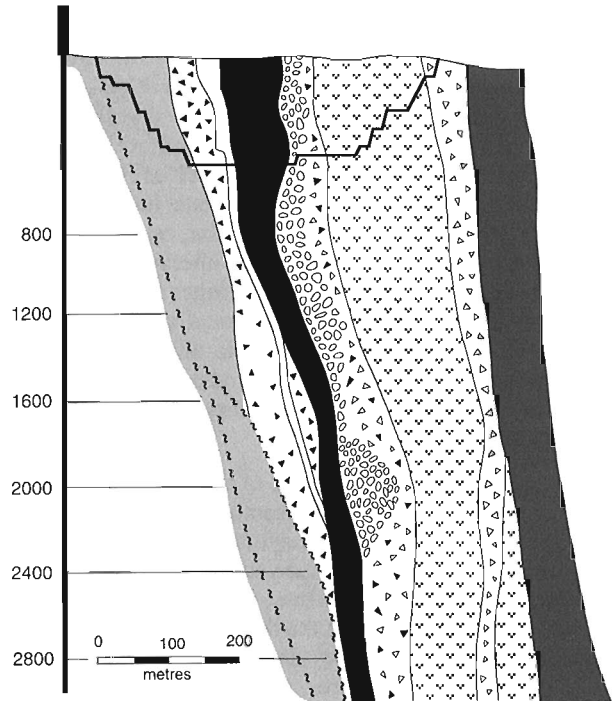
**Figure 1.** Schematic east-west cross-section (looking north) through the Kidd Creek mine, showing underground development and simplified geology (from Brisbin et al., 1990; see Fig. 2 for legend).

thickened felsic volcanic pile, within and overlying a series of massive rhyolite flows (possibly representing a flow-dome sequence). The felsic pile is about 300 m thick at Kidd Creek and pinches out to the north and south of the deposit, suggesting that volcanism and mineralization were localized within a major paleotopographic depression (Bleeker, 1992).

Overlying the massive flows is a thick sequence of felsic volcanoclastics, heterolithic fragmentals, and debris flows that are locally interbedded with and overlain by tuffaceous rhyolite, siltstones, and carbonaceous argillites. A variety of clast types in the heterolithic fragmentals suggests a wide provenance for the debris. The detailed volcanology and sedimentology of these hanging wall units are being examined in order to better define the depositional environment and the geometry of the basin. Massive, autobrecciated rhyolite which occurs at the base of the felsic pile, and is exposed in the East Outcrop (Fig. 2), is interpreted to be a proximal vent facies (Coad 1985). These rocks have been dated at  $2717 \pm 2$  Ma by Barrie and Davis (1990) using an abraded fraction of the zircons from Nunes and Pyke (1981). The youngest rhyolitic unit in the mine is a quartz porphyry in the stratigraphic hanging wall of the deposit, and samples of this unit are currently being dated. A thick sequence of basaltic



**Figure 2.** Simplified geology plan of Kidd Creek mine showing the distribution of principal mine lithologies and orebodies in the No. 1 mine projected to surface (after Walker et al., 1975). Fold structures of the orebodies after Bleeker (1992).



**Figure 3.** East-west longitudinal section through the No. 1 mine at 214600 N, North Orebody (after Walker et al., 1975; see Fig. 2 for legend).

pillow lavas and breccias overlies the felsic volcanics, with an intervening massive diorite unit of intrusive origin (Bleeker, 1992). Intensely altered ultramafic rocks, which may be early extrusives, occur in the footwall (Fig. 2).

### ***Igneous geochemistry***

Stratigraphy within the massive rhyolites is defined locally by a number of tuffaceous, interflow units. The detailed chemical stratigraphy of the rhyolites is being investigated using quantitative models of fractional crystallization to assess their chemical evolution through time and to better define the primary geochemical characteristics of felsic volcanics associated with mineralization.

Anomalous fractionation trends are being examined as a possible exploration tool. For example, the Kidd Creek rhyolites have REE profiles which are typical of productive felsic volcanics in other volcanogenic massive sulphide camps (e.g., Leshner et al., 1986), and their chemistry apparently reflects changes in the subvolcanic magma which may relate to cooling and hydrothermal circulation.

The major and trace element geochemistry and isotopic characteristics of the mafic volcanics, diorite intrusives, and ultramafics are also being studied in order to model compositional variations, determine possible mantle sources, and identify possible comagmatic relationships between the mafic and felsic suites.

### ***Alteration mineralogy and chemistry***

The rhyolites which host Cu-stringer mineralization are strongly depleted in Na<sub>2</sub>O, K<sub>2</sub>O, CaO, and Al<sub>2</sub>O<sub>3</sub> and are enriched in FeO, MgO, and SiO<sub>2</sub>, whereas rhyolites in the hanging wall of the deposit are enriched in K<sub>2</sub>O and Al<sub>2</sub>O<sub>3</sub> (Coad, 1985). This alteration manifests itself as chloritization and intense silicification in the immediate footwall of the massive sulphides, with a halo of sericite, especially in the hanging wall. Several major carbonate alteration events also exist, with abundant siderite in the stringer zone and in the massive sulphides, and more widespread ankerite, ferroan dolomite, and dolomite. Macroscopic alteration has been mapped at several levels in the mine, and essentially the same mineral assemblages are observed throughout the deposit (e.g., Fig. 4).

A complex paragenetic history of the various hydrothermal and metamorphic mineral assemblages has been identified, and considerable effort is required to reconcile the bulk chemistry of the volcanics with the various stages of hydrothermal alteration and metamorphism. Greenschist facies metamorphism and deformation of the rhyolites has resulted in the development of penetrative cleavage and linear fabrics throughout the mine sequence.

The combined effects of metamorphism, remobilization, and late postmagmatic hydrothermal events have complicated the spatial and temporal relationships between minerals within the alteration assemblage. This was confirmed recently by the work of Schandl et al. (1990) who dated at least one K-metasomatic event which is about 100 Ma younger than mineralization. Much of the coarse grained, macroscopic chlorite and sericite has grown in the matrix of fragmental rocks, and in particular along penetrative cleavages, and is related to metamorphic rather than hydrothermal fluids.

Detailed mineralogical studies of the alteration are currently being conducted in order to identify specific phases that can be unequivocally related to hydrothermal activity and to distinguish these from other minerals related to metamorphic and postmagmatic events. Preliminary results suggest that fine-grained chlorite, isolated within structurally undisturbed domains in the altered volcanics, may have preserved a record of hydrothermal alteration with systematic and reproducible compositional variations across the deposit.

### ***Sulphide mineralogy and chemistry***

The main ore types comprise stringer mineralization, massive sulphides, and breccia ore. Cu-stringer ore is best developed in the footwall of the North Orebody and is hosted principally by massive, brecciated rhyolite flows (Fig. 2). These massive flows appear to have been impermeable cap rocks which served to focus high temperature, hydrothermal fluids (Bleeker, 1992). In contrast, the massive ore developed mainly within the overlying fragmental rocks by infilling and wholesale replacement of rhyolite breccias and volcanoclastic debris (Bleeker, 1992). The fragmental units acted locally as permeable aquifers within the felsic pile, and much of the mineralization appears to have been emplaced beneath the paleoseafloor. This is perhaps supported by the absence of a

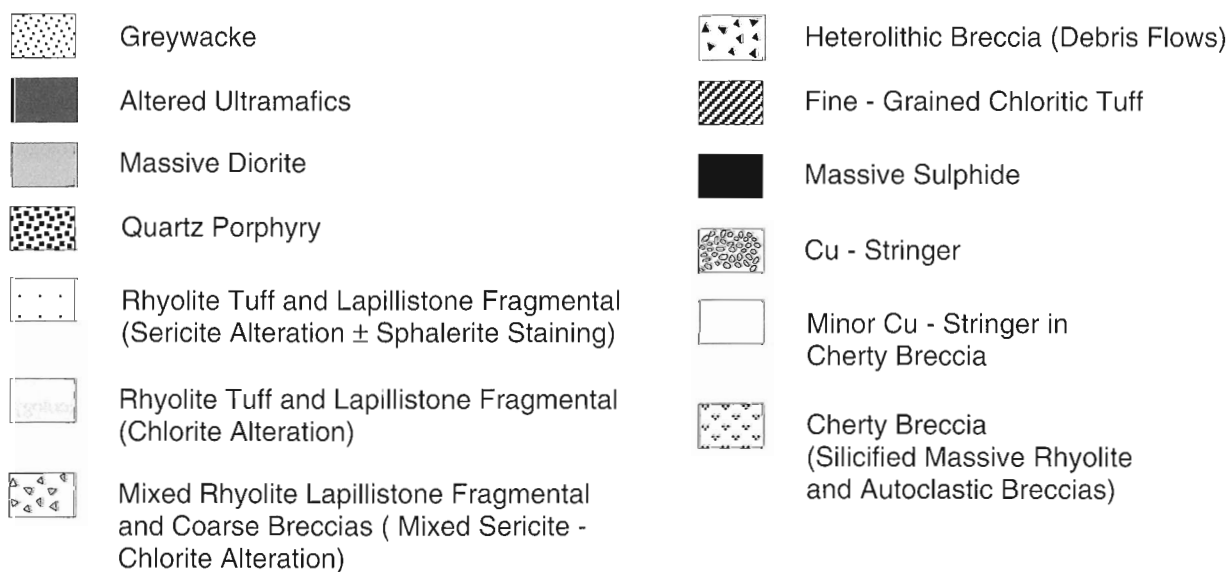
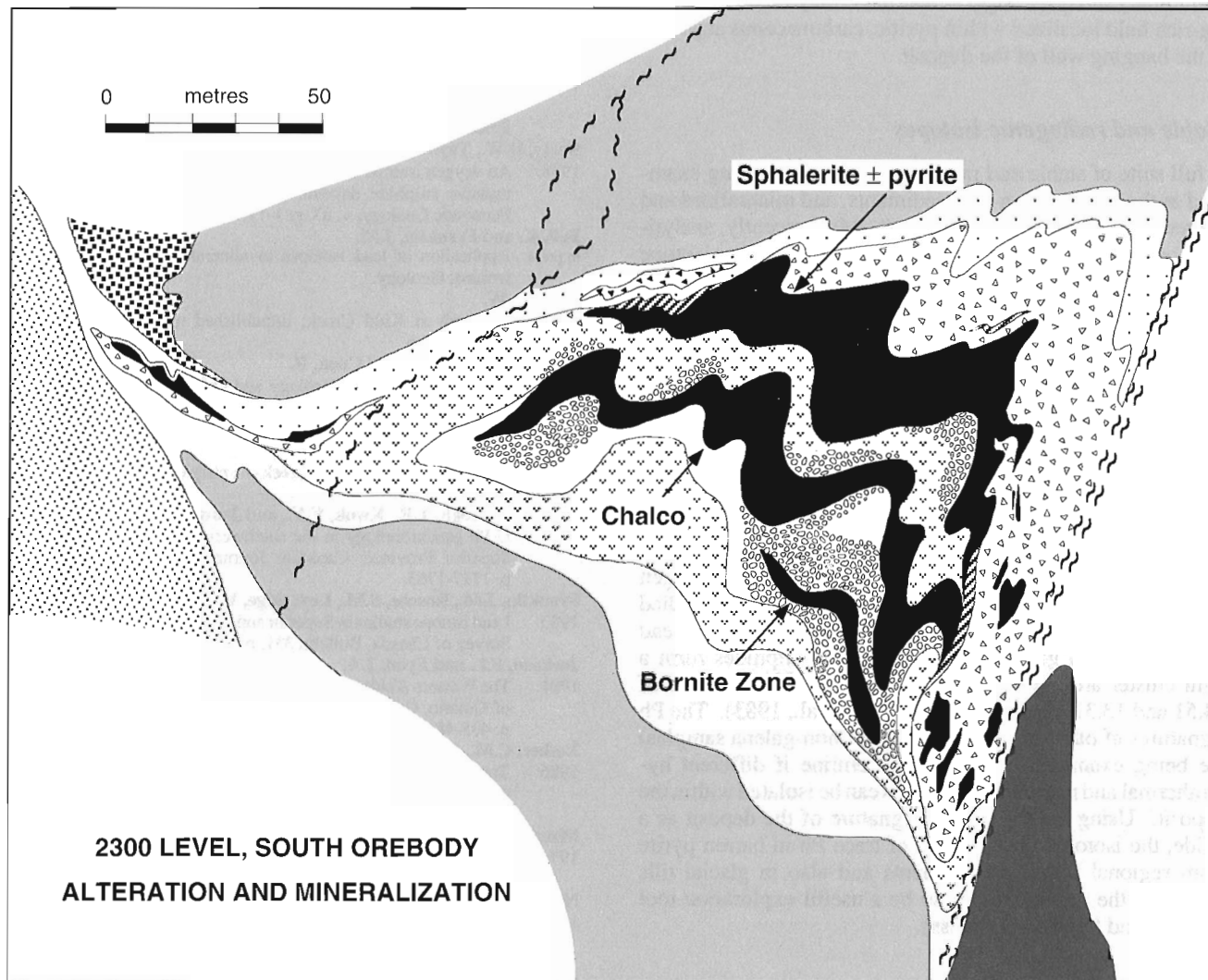
widespread exhalite horizon in the hanging wall which might have been produced by venting of the hydrothermal fluids directly onto the seafloor.

In the North Orebody, the paleoseafloor is represented by hanging wall tuffs, argillites, and a fine grained, sulphide-rich clastic sediment of limited areal extent. Both the North and South orebodies contain distinctly separate lenses of massive sulphide, dominated by a lower Cu-rich lens and an upper Zn-rich lens (e.g., Fig. 4). In addition, the South Orebody hosts the high grade bornite zone between the 1200 and 2800 foot levels (Fig. 4). It consists of massive bornite in the upper levels of the mine and mainly bornite stringer mineralization deeper down. Underground mapping in the bornite zone indicates that it is a late hydrothermal replacement body at the base of the massive sulphides and within the Cu-stringer zone. The composition of the bornite zone differs significantly from the rest of the deposit, and its genesis is one of the focal points of the Kidd Creek project.

To date there has been no comprehensive mineralogical investigation of the entire deposit, although parts of the orebodies have been examined in detail (e.g., the bornite-rich zone of the South Orebody: Thorpe et al., 1976). Apart from the size of Kidd Creek, the enormous variety of ore minerals remains one of the outstanding peculiarities of the deposit; more than 60 different phases have been identified in the ore, including complex sulphosalts, selenides, arsenides, Co-sulphides, As-sulphides, and Sn-sulphides. The detailed mineralogy of the ore can be useful as a petrogenetic indicator in the sense that certain trace minerals can provide clues as to the type of hydrothermal system likely to have been responsible for the formation of the deposit.

A critical examination of the trace mineral assemblages in the Kidd Creek ore is currently underway, including comprehensive microprobe analyses of different ore minerals, in order to identify fine-scale metal and mineral zonation, to document systematic variability in mineral compositions (e.g., FeS contents of sphalerite and pyrrhotite, Co in pyrite, Ag in chalcopyrite), and to characterize the physical and chemical conditions of mineralization. For example, the wide range of sphalerite compositions in Kidd Creek ore (i.e., from 0 to 16 mol.% FeS) lends itself to defining stratigraphic relationships (allowing for lateral zonation) within the massive sulphides and in the sphalerite-rich hanging wall breccias.

Two important suites of trace elements occur in the ore; namely Cd, Pb, Ag, Sb, Sn, and Hg in massive pyrite-sphalerite ore, and Ag, Se, As, Co, In, and Bi in Cu-rich ore and in the bornite zone of the South Orebody. Cadmium is currently being recovered as a by-product from sphalerite-rich ore, and a circuit was recently completed for the recovery of In. The mill also formerly produced a Sn concentrate from cassiterite. The bornite zone is the only part of the deposit with appreciable gold (values up to 1 ppm Au); the average grade of the deposit however is only about 100 ppb Au. The absence of significant gold in high grade Cu-Zn ore at Kidd Creek is an important question which will be addressed by the petrological studies of the sulphides. In contrast, the average Ag content of the massive sulphides is about 100 ppm, and



**Figure 4.** Distribution of mineralization and alteration at the 2300 level, South Orebody (this study).

preliminary analyses suggest that there may be a significant Ag-rich halo localized within pyritic, carbonaceous argillites in the hanging wall of the deposit.

### ***Stable and radiogenic isotopes***

A full suite of stable and radiogenic isotopes is being examined in the ore, hanging wall sediments, and mineralized and altered volcanics around the deposit. Most recently, analytical work has begun on characterization of the sulphur isotope signatures of different ore types. Work by Strauss (1989) and Wellmer (1991) indicates a wide range of carbon isotope compositions of carbonaceous sediments in the vicinity of the mine. Additional work will be carried out to identify possible magmatic versus surficial sources of carbon throughout the Kidd Creek hydrothermal system by examining a variety of carbon-bearing species in the alteration, mineralization, and hanging wall sediments. Beaty et al. (1988) identified an anomalous whole-rock oxygen isotope signature in altered volcanics around the deposit and this constitutes a promising exploration tool. The structure of the hydrothermal system at Kidd Creek is likely preserved in the whole-rock oxygen isotope signatures of the volcanics, and this will be studied further using the work of Beaty et al. (1988) as a guide. Lead isotope ratios in galena from the massive sulphides form a tight cluster around  $^{207}\text{Pb}/^{204}\text{Pb}$  and  $^{206}\text{Pb}/^{204}\text{Pb}$  values of 14.51 and 13.31, respectively (Franklin et al., 1983). The Pb signatures of other ore types (including non-galena samples) are being examined in order to determine if different hydrothermal and metamorphic events can be isolated within the deposit. Using the Pb isotope signature of the deposit as a guide, the isotopic composition of trace Pb in barren pyrite from regional interflow sediments and also in glacial tills overlying the deposit may also be a useful exploration tool (cf. Bell and Franklin, in press).

### **FUTURE WORK**

Work within the mine will be completed in 1993, and regional aspects of the study (e.g., alteration and lithochemical studies) will be carried out in drill core in 1993-94. Borehole geophysical surveys will be carried out in 1993 and may help to clarify important structural and stratigraphic relationships in the mine.

### **ACKNOWLEDGMENTS**

The Kidd Creek Project is a co-operative research effort between the Geological Survey of Canada, Falconbridge Limited, and Laurentian University, with contributions from the following study group (in alphabetical order): D. Archibald, W. Bleeker, D. Brisbin, B. Cameron, R. Cook, J. Franklin, H. Gibson, M. Hannington, E. Koopman, R. Parrish, and B. Taylor.

### **REFERENCES**

- Barrie, C.T. and Davis, D.W.**  
1990: Timing of magmatism and deformation in the Kamiskotia-Kidd Creek area, western Abitibi Subprovince, Canada; *Precambrian Research*, v. 46, p. 217-240.
- Beaty, D.W., Taylor, H.P., and Coad, P.R.**  
1988: An oxygen isotope study of the Kidd Creek, Ontario, volcanogenic massive sulphide deposit: evidence for a high  $^{18}\text{O}$  ore fluid; *Economic Geology*, v. 83, p. 1-17.
- Bell, K. and Franklin, J.M.**  
in press: Application of lead isotopes to mineral exploration in glaciated terrains; *Geology*.
- Bleeker, W.**  
1992: Research at Kidd Creek; unpublished report for Falconbridge Limited, 11 p.
- Brisbin, D., Kelly, V., and Cook, R.**  
1990: Kidd Creek Mine; in *Geology and Ore Deposits of the Timmins District, Ontario (Field Trip 6)*, 8th IAGOD Symposium Field Trip Guidebook, Geological Survey of Canada, Open File 2161, p. 66-76.
- Coad, P.R.**  
1985: Rhyolite geology at Kidd Creek – a progress report; *CIM Bulletin*, v. 78, p. 70-83.
- Corfu, F., Krogh, T.E., Kwok, Y.Y., and Jensen, L.S.**  
1989: U-Pb geochronology in the southwestern Abitibi greenstone belt, Superior Province; *Canadian Journal of Earth Sciences*, v. 26, p. 1747-1763.
- Franklin, J.M., Roscoe, S.M., Loveridge, W.D., and Sangster, D.F.**  
1983: Lead isotope studies in Superior and Southern Provinces; *Geological Survey of Canada, Bulletin* 351, p. 60.
- Jackson, S.L. and Fyon, J.A.**  
1991: The Western Abitibi Subprovince in Ontario; Chapter 11 in *Geology of Ontario, Ontario Geological Survey, Special Volume 4, Part 1*, p. 405-482.
- Leshner, C.M., Goodwin, A.M., Campbell, I.H., and Gorton, M.P.**  
1986: Trace-element geochemistry of ore-associated and barren, felsic metavolcanic rocks in the Superior Province, Canada; *Canadian Journal of Earth Sciences*, v. 23, p. 222-237.
- Matulich, A., Amos, A.C., Walker, R.R., and Watkins, J.J.**  
1974: The Estcall story – geology department; *CIM Bulletin*, v. 67, p. 56-63.
- Nunes, P.D. and Pyke, D.R.**  
1981: Time-stratigraphic correlation of the Kidd Creek orebody with volcanic rocks south of Timmins, Ontario, as inferred from zircon U-Pb ages; *Economic Geology*, v. 76, p. 944-951.
- Thorpe, R.I., Pringle, G.J., and Plant, A.G.**  
1976: Occurrence of selenide and sulphide minerals in bornite ore of the Kidd Creek massive sulphide deposit, Timmins, Ontario; *Geological Survey of Canada, Paper* 76-1A, p. 311-317.
- Schandi, E.S., Davis, D.W., and Krogh, T.E.**  
1990: Are the alteration halos of massive sulphide deposits syngenetic? Evidence from U-Pb dating of hydrothermal rutile at the Kidd volcanic center, Abitibi subprovince, Canada; *Geology*, v. 18, p. 505-508.
- Strauss, H.**  
1989: Carbon and sulphur isotope data for carbonaceous metasediments from the Kidd Creek massive sulphide deposit and vicinity, Timmins, Ontario; *Economic Geology*, v. 84, p. 959-961.
- Walker, R.R. and Mannard, G.W.**  
1974: Geology of the Kidd Creek mine – a progress report; *CIM Bulletin*, v. 67, p. 41-57.
- Walker, R.R., Matulich, A., Amos, A.C., Watkins, J.J., and Mannard, G.W.**  
1975: The geology of the Kidd Creek mine; *Economic Geology*, v. 70, p. 80-89.
- Wellmer, F.W.**  
1991: Graphite sampling for  $^{13}\text{C}$  determinations in the Timmins area (Kidd Twp. and Prosser Twp.); unpublished report for Falconbridge Limited, 29 p.



# Preliminary mineral chemical studies of phyllosilicates in host rocks of the Kidd Creek massive sulphide deposit, Timmins, Ontario<sup>1</sup>

B.I. Cameron<sup>2</sup>, M.D. Hannington, D.I. Brisbin<sup>3</sup>, and E.R. Koopman<sup>2</sup>  
Mineral Resources Division

*Cameron, B.I., Hannington, M.D., Brisbin, D.I., and Koopman, E.R., 1993: Preliminary mineral chemical studies of phyllosilicates in host rocks of the Kidd Creek massive sulphide deposit, Timmins, Ontario; in Current Research, Part E; Geological Survey of Canada, Paper 93-1E, p. 157-164.*

---

**Abstract:** Preliminary electron microprobe analyses of chlorite and white mica have been obtained from drill core through a section of the Kidd Creek massive sulphide deposit. The nonstoichiometric behaviour of these minerals makes them attractive for the study of alteration associated with volcanogenic massive sulphides. The compositions of chlorites analyzed in this study range from 5.95 to 32.67 wt.% FeO, 7.57 to 22.46 wt.% MgO, and up to 1.32 wt.% F. The chemical data for chlorite and sericite indicate a range of alteration conditions corresponding to different paragenetic types, both hydrothermal and metamorphic, different host rocks, and proximity to mineralization.

**Résumé :** Des analyses à la microsonde électronique ont été effectuées sur la chlorite et le mica blanc contenus dans des carottes qui fournissent une coupe du gisement de sulfures massifs de Kidd Creek. Le comportement non stoechiométrique de ces minéraux les rend attrayants pour l'étude de l'altération associée aux sulfures massifs volcanogènes. Les résultats préliminaires de cette étude montrent que les chlorites sont composées de 5,95 à 32,67 % en poids de FeO, de 7,57 à 22,46 % en poids de MgO et d'au plus 1,32 % en poids de F. Les données chimiques pour la chlorite et la séricite révèlent des conditions d'altération variables, correspondant à différents types paragénétiques, tant hydrothermaux que métamorphiques, aux différences des lithologies encaissantes et à la proximité de la minéralisation.

---

<sup>1</sup> Contribution to Canada-Ontario Subsidiary Agreement on Northern Ontario Development (1991-1995), under the Canada-Ontario Economic and Regional Development Agreement.

<sup>2</sup> Geological Survey of Canada, P.O. Box 1163, Timmins, Ontario, P4N 7H9

<sup>3</sup> Falconbridge Limited, Kidd Creek Division, P.O. Box 2002, Timmins, Ontario, P4N 7K1

## INTRODUCTION

The macroscopic alteration at Kidd Creek consists mainly of chloritization and intense silicification in the immediate footwall to the massive sulphides, with a broad halo of sericite ( $\pm$  sphalerite staining) at the margins of this zone (Coad, 1985). In hand specimen, the rhyolite breccias and fragmental rocks (e.g., rhyolite lapillistones) which host mineralization are heterogeneously altered, with individual clasts commonly exhibiting mineralogical zonation from chloritic rims with sericitic cores to silicified rims with chloritic cores. However, the combined effects of hydrothermal alteration, late postmagmatic hydrothermal events, metamorphism, and remobilization have obscured the paragenetic relationships between phyllosilicate minerals in the alteration assemblage. This paper reports on the preliminary examination of the petrographic and chemical characteristics of chlorite and sericite in the footwall and hanging wall rocks the Kidd Creek deposit and the relationship between chlorite-sericite compositions (e.g., Shikazono and Kawahata, 1987) in proximal and distal alteration at the mine scale.

## SAMPLING AND ANALYTICAL METHODS

A brief description of the deposit is given by the Kidd Creek Study Group (1993). Samples for this study were selected from drill core at the 5100' and 4700' levels, stratigraphically near the North Orebody massive sulphides, and at the 3800' level near a relatively small massive sulphide lens farther to the south (known as the Triangle Orebody; Fig. 1). Two felsic footwall lithologies were sampled in five holes; a cherty, brecciated massive rhyolite which is the principal host for the main stringer zone beneath the North Orebody, and a fragmental rhyolite lapillistone which hosts the smaller Triangle Orebody. One sample was collected for comparison from a sill-like diorite body which is interpreted to intrude the felsic complex stratigraphically above the massive sulphides. Major, minor, and trace mineral constituents were identified by X-ray diffraction (XRD) and are reported in Table 1. Individual phases were analyzed by standard procedures on a Cameca-Camebax electron microprobe in the Geological Survey, Ottawa, and averages for different samples are reported in Tables 2 and 3.

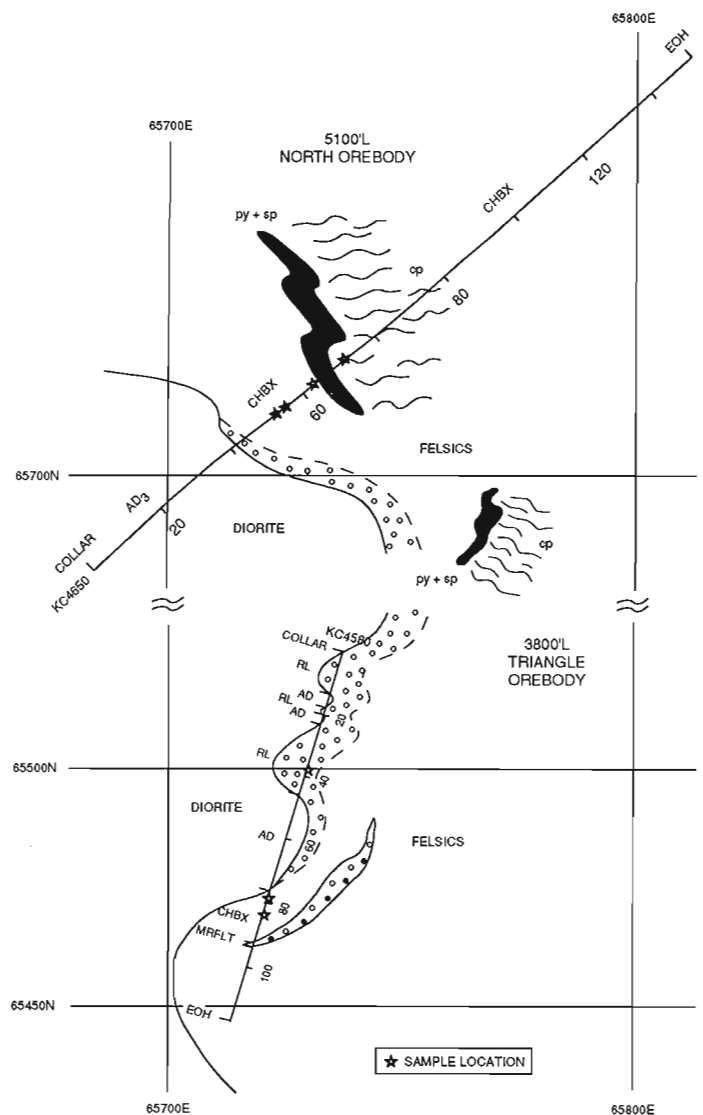
## SAMPLE DESCRIPTIONS AND RESULTS

The 'cherty breccia' unit is a massive, aphanitic, light grey to white rhyolite and is the primary host of stringer mineralization in the footwall to the North Orebody. The 'cherty breccia' typically contains up to 10 vol.% grey chlorite and sericite as fine grained disseminations in the matrix between fragments of cherty breccia, and in late fractures or cleavage planes. Less common green chlorite occurs with remobilized chalcopyrite stringers (1 mm up to 2 cm in width) which occupy and locally crosscut the foliation. Black chlorite (up to 30 vol.%) is common in the matrix of the 'cherty breccia' and in late fractures or cleavages in close proximity to massive sulphides.

The rhyolite lapillistone from the Triangle Orebody comprises a grey-green, monolithic fragmental unit with sericite and chlorite developed in the matrix between individual clasts and as a fine grained dissemination within the clasts. This unit commonly possesses minor sphalerite staining, and weak chalcopyrite stringer mineralization occurs locally in a few samples (typically <1-3 vol.%).

## CHLORITE CHEMISTRY

The Kidd Creek chlorites show a wide range of major element compositions, with FeO contents from 6.0 to 32.7 wt.%, MgO from 7.6 to 22.5 wt.%, SiO<sub>2</sub> from 22.4 to 36.3 wt.%, and



**Figure 1.** Composite plan view of drillhole intersections for KC4650 and KC4580 showing lithological contacts and sample locations. Depths are in metres. CHBX = brecciated massive rhyolite; A/D1 = andesite-diorite; A/D3 = altered andesite-diorite; RL = Rhyolite lapillistone; MRF = Mixed rhyolite fragmental; LT = Lapilli tuff.

**Table 1.** Mineral components determined by XRD

OREBODY	MINERALIZATION	LITHOLOGY	SAMPLE	MINERAL ASSEMBLAGE <sup>1</sup>
NORTH (5100'L)	Mineralized 'cherty breccia' with Cu- stringer (proximal)	CHBX	KC4650-52.1	QUARTZ + CHLORITE GROUP + MICA GROUP
			KC4650-53.6	QUARTZ + CHLORITE GROUP
			KC4650-62.8	CHLORITE GROUP + (Quartz + Mica Group)
			KC4650-72.5	QUARTZ + (Chlorite Group + Mica Group)
TRIANGLE (3800'L)	Weakly mineralized to unmineralized RLST (distal to hanging wall)	RLST	KC4580-39.5	QUARTZ + CHLORITE GROUP
			KC4580-79.7	QUARTZ + (chlorite group + mica group)
			KC4580-81.2	QUARTZ + CHLORITE GROUP + (mica group)
			KC4578-82.2	CHLORITE GROUP + (quartz + mica group + calcite)
			KC4579-84.0	CHLORITE GROUP + (quartz + calcite + mica group)
NORTH (4700' level)			KC4516-62.7	QUARTZ + (mica group + chlorite group + dolomite + Na feldspar)
TRIANGLE (3800'L)	Unmineralized diorite	AD	KC4581-62.7	CHLORITE GROUP + (quartz + Na feldspar + amphibole + calcite)

<sup>1</sup> (minerals in lower case in parenthesis are present in minor or trace amounts)

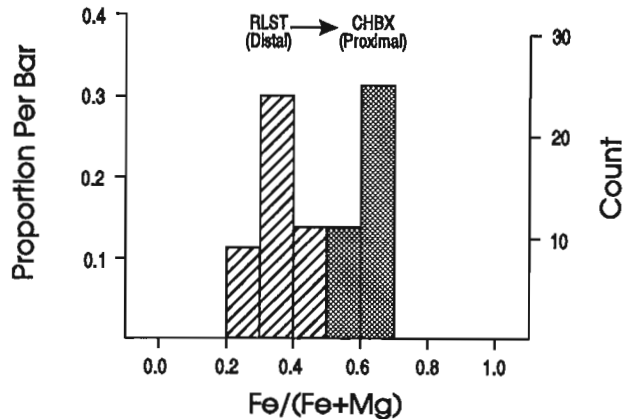
**Table 2.** Kidd Creek chlorite compositions

	KC4650 -52.1 N=7 CHBX	KC4650 -53.6 N=12 CHBX	KC4650 -62.8 N=10 CHBX	KC4650 -72.5 N=4 CHBX	KC4580 -39.5 N=7 RLST	KC4580 -79.7 N=12 RLST	KC4580 -81.2 N=9 RLST	KC4578 -82.2 N=7 RLST	KC4579 -84.0 N=6 RLST	KC4516 -92.0 N=3 RLST	KC4581 -62.7 N=8 AD
Fe/(Fe+Mg)	0.56	0.60	0.61	0.61	0.43	0.39	0.36	0.30	0.29	0.43	0.62
SiO <sub>2</sub>	25.58	23.82	25.60	23.50	26.12	26.23	26.71	27.12	27.36	24.94	24.46
Al <sub>2</sub> O <sub>3</sub>	23.52	22.12	22.65	22.37	23.40	21.89	22.45	21.48	21.10	22.96	19.13
TiO <sub>2</sub>	0.06	0.03	0.03	0.07	0.03	0.08	0.08	0.03	0.04	0.03	0.05
FeO	25.17	27.92	27.96	29.53	20.33	19.97	18.56	16.36	15.93	22.74	31.79
MnO	0.05	0.09	0.07	0.15	0.09	0.13	0.10	0.07	0.08	0.11	0.41
MgO	10.85	10.54	10.01	10.50	14.68	17.74	18.27	21.65	21.71	16.63	10.77
CaO	0.04	0.02	0.04	0.03	0.11	0.04	0.03	0.05	0.02	0.01	0.07
Na <sub>2</sub> O	0.12	0.05	0.10	0.03	0.40	0.03	0.03	0.15	0.03	0.02	0.02
K <sub>2</sub> O	1.03	0.40	0.57	0.09	0.02	0.02	0.14	0.01	0.09	0.01	0.01
F	0.84	0.59	0.67	0.23	0.23	0.62	0.53	0.37	0.47	0.07	0.12
Cl	0.03	0.02	0.01	0.02	0.01	0.01	0.01	0.02	0.02	0.02	0.01
Total	87.29	85.60	87.71	86.52	85.42	85.76	86.91	87.31	86.85	87.24	86.84
Si	5.470	5.279	5.497	5.171	5.467	5.327	5.488	5.483	5.553	5.203	5.438
Al <sup>iv</sup>	2.530	2.721	2.503	2.829	2.533	2.673	2.512	2.517	2.447	2.797	2.562
Al <sup>vi</sup>	3.399	3.059	3.236	2.973	3.239	2.774	2.925	2.603	2.601	2.850	2.452
Fe	4.506	5.184	5.049	5.435	3.630	3.526	3.197	2.767	2.705	3.915	5.912
Mg	3.462	3.490	3.223	3.444	4.653	5.583	5.600	6.525	6.572	5.173	3.571
Mn	0.009	0.016	0.013	0.028	0.015	0.023	0.017	0.013	0.013	0.019	0.078
F	0.567	0.413	0.451	0.157	0.152	0.410	0.340	0.237	0.304	0.046	0.083
Cl	0.013	0.008	0.003	0.006	0.005	0.003	0.004	0.008	0.007	0.006	0.005

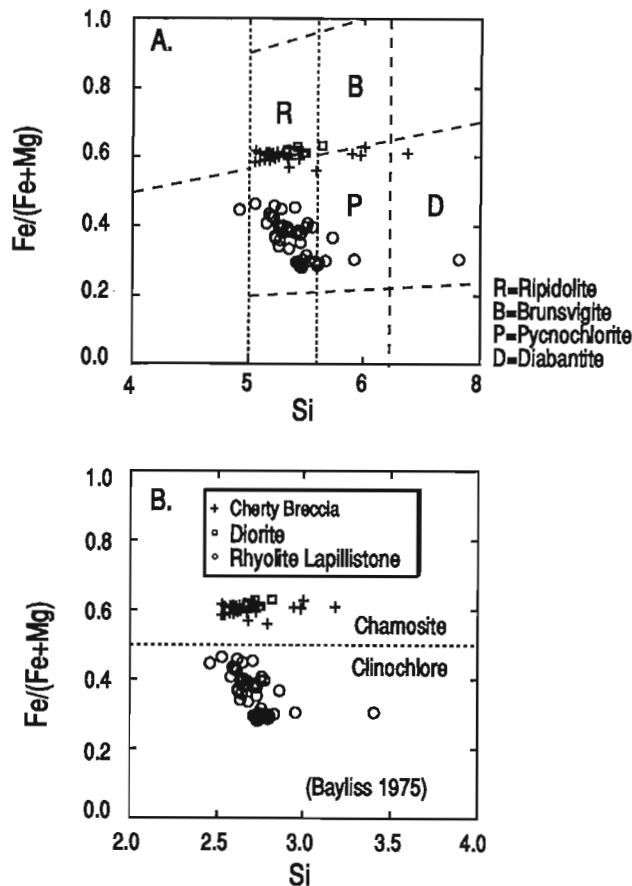
**Table 3.** Kidd Creek white mica compositions

	KC4650	KC4650	KC4650	KC4580	KC4580	KC4578
	-52.1	-62.8	-72.5	-79.7	-81.2	-82.2
	N=6	N=2	N=12	N=4	N=4	N=5
	CHBX	CHBX	CHBX	RLST	RLST	RLST
Fe/(Fe+Mg)	0.39	0.32	0.27	0.22	0.23	0.15
SiO <sub>2</sub>	45.11	50.54	47.72	50.90	49.70	51.92
Al <sub>2</sub> O <sub>3</sub>	33.47	31.17	32.38	34.03	35.37	33.85
TiO <sub>2</sub>	0.10	0.00	0.08	0.19	0.10	0.20
FeO	1.41	1.06	0.99	1.00	0.85	0.73
MnO	0.03	0.02	0.03	0.02	0.01	0.01
MgO	1.22	1.26	1.34	2.05	1.58	2.31
CaO	0.02	0.03	0.02	0.03	0.02	0.01
BaO	0.00	0.00	0.00	1.13	0.88	0.40
Na <sub>2</sub> O	0.75	0.75	0.86	0.25	0.35	0.31
K <sub>2</sub> O	9.86	9.58	9.45	6.97	7.45	6.87
F	1.46	1.53	1.16	0.83	0.80	1.10
Cl	0.02	0.02	0.01	0.01	0.02	0.01
Total	93.45	95.96	94.04	97.41	97.13	97.73
Si	6.218	6.697	6.459	6.540	6.409	6.606
Al <sup>v</sup>	1.782	1.303	1.541	1.460	1.591	1.394
Al <sup>iv</sup>	3.657	3.581	3.625	3.687	3.786	3.682
Fe	0.163	0.118	0.112	0.107	0.091	0.078
Mg	0.250	0.249	0.270	0.393	0.303	0.439

Al<sub>2</sub>O<sub>3</sub> from 18.2 to 32.4 wt.% (e.g., Fig. 2). Fluorine is an important trace constituent in both the chlorite and the sericite (see below), but does not show significant variation between samples of 'cherty breccia' and rhyolite lapillistone. In the 'cherty breccia' chlorites, mean F contents range between 0.23 and 0.84 wt.%, while rhyolite lapillistone chlorites contain F concentrations between 0.07 and 0.62 wt.%. Most of the major element variability is between samples from the 'cherty breccia' (proximal to Cu-stringer mineralization) and the weakly mineralized rhyolite lapillistone. In close proximity to the Cu-stringer zone of the North Orebody, the chlorite in samples of 'cherty breccia' is uniformly Fe-rich (mean Fe/(Fe+Mg) ratios of 0.56 to 0.61 based on mole%), regardless of its paragenesis (e.g., grey matrix chlorite, black cleavage related chlorite, bright green chlorite in remobilized chalcocopyrite stringers). Fe/(Fe+Mg) ratios decrease slightly from the footwall to the hanging wall. The analyzed varieties of 'cherty breccia' chlorite appear to have re-equilibrated with high-temperature hydrothermal fluids either during the main stage of mineralization or, more likely, with a later-stage Fe-rich fluid. In contrast, the chlorite in the six unmineralized to weakly mineralized samples of lapillistone near the small Triangle Orebody have a wider range of bulk chemistry and tend to be more magnesian (mean Fe/(Fe+Mg) ratios of 0.29 to 0.44; Fig. 3). Bright green chlorite in the diorite sill stratigraphically above the massive sulphide is the most Fe-rich (mean Fe/(Fe+Mg) ratio of 0.62) and is likely unrelated to the hydrothermal alteration of the felsic volcanic sequence.



**Figure 2.** Histogram of Fe/(Fe+Mg) in chlorites showing the complete range of all individual analyses.



**Figure 3A and B.** Compositions of Kidd Creek chlorites plotted according to the classification schemes of Hey (1954) and Bayliss (1975).

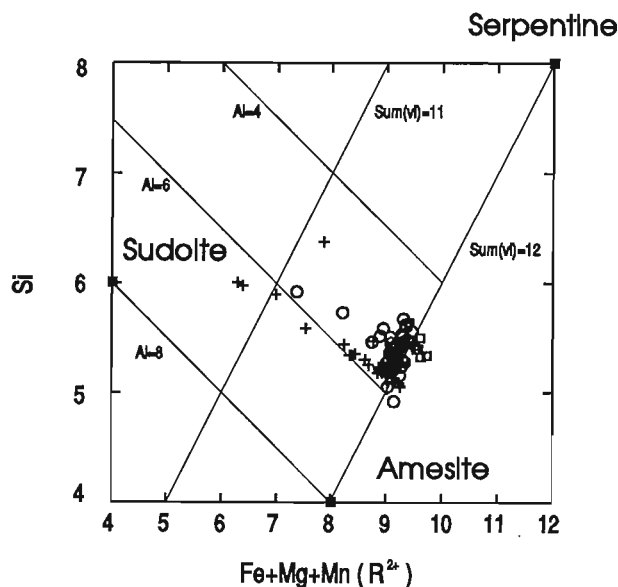
Most of the Kidd Creek chlorites exhibit full octahedral occupancy, typical of metamorphic chlorites (Hillier and Velde, 1991; Fig. 4). The distribution of the data along the serpentine-amesite join corresponds to variation in the amount of Tschermak substitution. However, some of the chlorites in the 'cherty breccia' and rare rhyolite lapillistone samples share similarities with low-temperature diagenetic chlorite by having the most siliceous components characterized by the lowest  $R^{2+}$  totals and with the lowest octahedral occupancy (e.g., Hillier and Velde, 1991).

## WHITE MICA CHEMISTRY

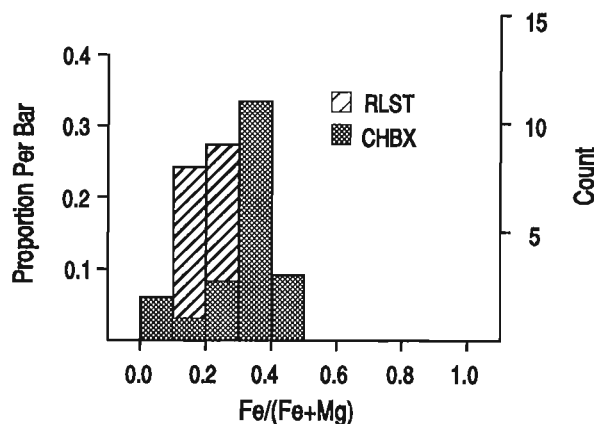
The fine grained white micas (sericite) in both the 'cherty breccia' and rhyolite lapillistone show less variation in their major element chemistry than the chlorites. The  $K_2O$  contents range from 6.5 to 10.3 wt.%, with  $SiO_2$  from 44.3 to 54.8 wt.%, and  $Al_2O_3$  from 28.7 to 35.8 wt.%. Fluorine abundances in the white micas average 1.14 wt.% in comparison to close to detection limits for Cl. White micas from the rhyolite lapillistones have lower  $K_2O$  and  $Na_2O$  contents than the white micas from the 'cherty breccia' and  $BaO$  contents greater than 0.4 wt.% (Table 3). In the 'cherty breccia' samples close to Cu-stringer mineralization, the white micas have mean  $Fe/(Fe+Mg)$  ratios of 0.29 to 0.45, whereas white micas from the unmineralized and weakly mineralized rhyolite lapillistone have mean  $Fe/(Fe+Mg)$  ratios of 0.15 to 0.23 (Table 3; Fig. 5). The mean fluorine

content in white micas from the 'cherty breccia' is slightly higher than in samples from the unmineralized rhyolite lapillistone.

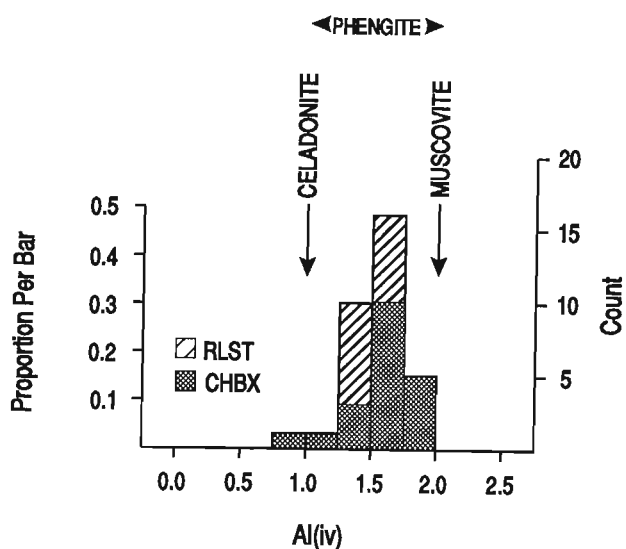
White micas in all the drill holes are phengitic in composition, with a more muscovite than celadonite character (mean  $Al^{iv}=1.5$ ). This is illustrated in Figure 6 which shows variable Si substitution for tetrahedral Al which is coupled with Fe and Mg substitution for Al in the octahedral site (Tschermak substitution). The phengitic micas at Kidd Creek have  $Al^{iv}$  contents between 1.0 and 2.0. Variations in the degree of substitution may reflect differences in the pressure, temperature, and the chemical potential of the major cations. Higher metamorphic temperatures tend to favour the formation of muscovite (Schmidt, 1988).



**Figure 4.** Si versus  $R^{2+}$  crystallochemical classification of chlorites according to Wiewiora and Weiss (1990) showing full octahedral occupancy between compositions corresponding to nonaluminous serpentine and amesite. Total Al and octahedral occupancy are shown by isolines. The spread of the data along the serpentine-amesite join corresponds to the amount of Tschermak substitution. Symbols as in Figure 3.



**Figure 5.** Histogram of  $Fe/(Fe+Mg)$  in white micas showing the complete range of all individual analyses.



**Figure 6.** Histogram of  $Al^{iv}$  in Kidd Creek white micas (after Schmidt, 1988).

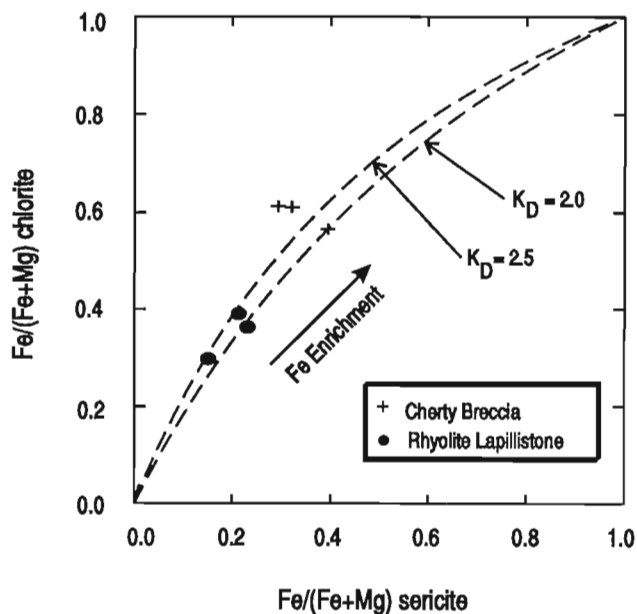
## CHLORITE-SERICITE PAIRS

In six of the drill core samples, data were obtained on the composition of coexisting chlorite-sericite pairs. A distinct Fe-enrichment trend is observed between chlorite-sericite pairs in the rhyolite lapillistone and the 'cherty breccia' samples associated with Cu-stringer mineralization (Fig. 7). The bulk compositions of chlorite-sericite pairs are plotted in Figure 8 with tie lines connecting coexisting minerals. The chlorite and sericite in samples of rhyolite lapillistone show subparallel tie lines with only minor intersections, suggesting precipitation of the coexisting phases in equilibrium. Lateral shifts of the tie lines can be attributed to changes in the bulk chemistry of the host rocks (Ramamohana, 1977). However, tie lines for two chlorite-sericite pairs from the 'cherty breccia' (KC4650-62.8 and 72.5) intersect the general subvertical trend of the bulk compositions of other coexisting pairs and suggest precipitation at different temperatures and/or pressures, and therefore may represent paragenetically different events. This pair of samples also falls well off calculated equilibrium curves which describe the partitioning of Fe between the other chlorite-sericite pairs (Fig. 7).

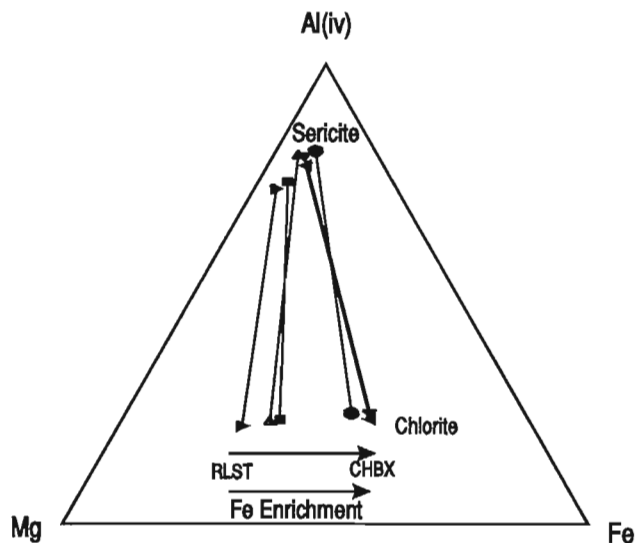
## CHLORITE GEOTHERMOMETRY

Several related chlorite geothermometers have been developed, based on an observed correlation between  $Al^{IV}$  and estimated formation temperatures for hydrothermal chlorites in modern geothermal fields (Cathelineau and Nieva, 1985; Cathelineau, 1988; Jowett, 1991). Table 4 presents the results of the temperature calculations. After correcting  $Al^{IV}$  using the formula  $Al^{IV}(corr) = Al^{IV}(measured) + 0.247(Fe/(Fe+Mg))$  where 0.247 is the slope of the linear regression line on a  $Al^{IV}$  versus  $Fe/(Fe+Mg)$  plot of Kidd Creek chlorites, calculated temperatures range between 365°C and 418°C for 'cherty breccia' chlorites, and between 355°C and 384°C for rhyolite lapillistone chlorites (after Cathelineau 1988). Temperatures using the revised geothermometer of Jowett (1991) give similar ranges. 'Cherty breccia' chlorites range between 350°C and 402°C, while rhyolite lapillistone chlorites fall between 342°C and 370°C.

Large uncertainties implicit in the chlorite geothermometers necessitate the use of caution in their application and interpretation. However, the calculated temperatures fall at the high end of the temperature range for volcanogenic massive sulphide deposits, which might be expected for a large deposit like Kidd Creek. Higher temperatures recorded in Fe-rich chlorites adjacent to Cu-stringer mineralization in 'cherty breccia' samples likely mark the conduit where late Fe-rich hydrothermal fluids were channelized. Lower temperatures calculated from more Mg-rich chlorites in the rhyolite lapillistone samples reflect the cooler margins of a hydrothermal system where seawater mixed with hydrothermal fluid.



**Figure 7.**  $Fe/(Fe+Mg)$  ratios for coexisting pairs of chlorite and sericite in samples of altered 'cherty breccia' and rhyolite lapillistone, showing nearly uniform Fe-enrichment for both chlorites and sericites. Calculated equilibrium curves which describe the partitioning of Fe in the R site between coexisting chlorite and sericite are shown by dashed lines where  $K_D = [X_{ch}/(1-X_{ch})] \cdot [(1-X_{ser})/X_{ser}]$ ,  $X$  is the ionic fraction of Fe in either phyllosilicate, and  $X^{Fe} = Fe/(Fe+Mg)$ . Four of the six mineral pairs fit calculated  $K_D$  values of 2.0 to 2.5, while coexisting chlorite and sericite from two samples of the 'cherty breccia' fall well above these curves.



**Figure 8.**  $Al^{IV}$ -Fe-Mg triangular diagram showing the bulk compositions of coexisting chlorite-sericite pairs. Subparallel tielines indicate precipitation under equilibrium conditions, lateral shifts suggest differences in bulk composition of the altered protolith, whereas crossing tie lines suggest temperature and pressure variations (Ramamohana, 1977).

**Table 4.** Geothermometry on Al saturated Kidd creek chlorites

SAMPLE	LITHOLOGY	Al <sup>iv</sup> Uncorrected	Fe/(Fe+Mg)	Al <sup>iv</sup> (Corr) <sup>1</sup>	Al <sup>iv</sup> (Corr) <sup>2</sup>	T <sup>1</sup> (°C)	T <sup>2</sup> (°C)
KC4650-52.1	Mineralized 'Cherty Breccia'	2.530	0.565	2.670	1.322	368	353
KC4650-62.8		2.503	0.611	2.654	1.313	365	350
KC4650-72.5		2.830	0.612	2.981	1.476	418	402
KC4580-79.7	Weakly Mineralized Rhyolite Lapillistone	2.673	0.387	2.769	1.375	384	370
KC4580-81.2		2.512	0.362	2.602	1.292	357	343
KC4578-82.2		2.517	0.298	2.590	1.288	355	342

Al<sup>iv</sup>(Corr)<sup>1</sup> = Al<sup>iv</sup> + 0.247(Fe/(Fe+Mg))  
Al<sup>iv</sup>(Corr)<sup>2</sup> = Al<sup>iv</sup> + 0.1(Fe/(Fe+Mg)) by Jowett (1991)  
T<sup>1</sup>(°C) = (321.98\*Al<sup>iv</sup>(corr))-61.92 by Cathelineau (1988)  
T<sup>2</sup>(°C) = (319\*Al<sup>iv</sup>(corr))-69 (based on 14 oxygens) by Jowett (1991)

## CONCLUSIONS

Chemical data for chlorite in samples of rhyolite lapillistone at the margins of the massive sulphide and in 'cherty breccia' that host the North Orebody display a distinct Fe-enrichment trend corresponding to proximity to the main Cu-stringer zone underlying massive Zn-sulphides. The most Fe-rich chlorites are associated with Cu-stringer mineralization in the 'cherty breccia' and have calculated formation temperatures greater than 350°C (e.g., KC4650-62.8; Table 4). Recent studies of chlorite compositions in alteration zones at Brunswick No. 12 (Luff et al., 1992), Noranda (Barrett et al., 1991; MacLean and Hoy, 1991), and Sullivan (Leitch, 1992) deposits have yielded similar results.

White micas from the same samples show a wide range of bulk compositions, with a significant increase in Fe/(Fe+Mg) from the rhyolite lapillistone to the mineralized 'cherty breccia'. Similar increases in Na<sub>2</sub>O, K<sub>2</sub>O, and F also appear to be associated with proximity to the stringer zone. Distinctive F-enriched muscovites also occur in the alteration zones beneath comparable massive sulphide deposits in the Iberian Pyrite Belt (Plimer and de Carvalho, 1982).

The bulk compositions of several chlorite-sericite pairs show uniform Fe-enrichment under apparent equilibrium conditions. However, in at least two mineral pairs, the chlorite and sericite partitioned Fe in different proportions and were precipitated under different conditions, and therefore represent paragenetically separate events. A similar result was obtained by Slack and Coad (1989) studying chlorite-tourmaline pairs in the Cu-stringer zone on the 2400' level at Kidd Mine. Difficulties encountered in recognizing a paragenetically distinct group of chlorites and sericites, related unequivocally to alteration of the host rocks at the time of mineralization, are currently being addressed.

## ACKNOWLEDGMENTS

The first author recognizes David Lentz for his advice and guidance on the distribution coefficient calculations. Constructive reviews of earlier versions of this paper by Ian Jonasson and Matthew Leybourne were very helpful. John Stirling of the Electron Microprobe Laboratory and Bob Delabio of the X-ray Diffraction Laboratory at the Geological Survey of Canada are thanked for their assistance. Falconbridge exploration and mine staff, especially Dr. Wouter Bleeker, greatly improved the first author's understanding of the Kidd Creek mine geology.

## REFERENCES

- Barrett, T.J., MacLean, W.H., Cattalani, S., Hoy, L., and Riverin, G.  
1991: Massive sulphide deposits of the Noranda area, Quebec. III. The Ansil Mine; Canadian Journal of Earth Sciences, v. 28, p. 1699-1730.
- Bayliss, P.  
1975: Nomenclature of the trioctahedral chlorites; Canadian Mineralogist, v. 13, p. 178-180.
- Cathelineau, M.  
1988: Cation site occupancy in chlorites and illites as a function of temperature; Clay Minerals, v. 23, p. 471-485.
- Cathelineau, M. and Nieva, D.  
1985: A chlorite solid solution geothermometer: The Los Azufres (Mexico) geothermal system; Contributions to Mineralogy and Petrology, v. 91, p. 235-244.
- Coad, P.R.  
1985: Rhyolite geology at Kidd Creek - a progress report; CIM Bulletin, v. 78, p. 70-83.
- Hey, M.H.  
1954: A new review of the chlorites; Mineralogical Magazine, v. 30, p. 277-292.
- Hillier, S. and Velde, B.  
1991: Octahedral occupancy and the chemical composition of diagenetic (low-temperature) chlorites; Clay Minerals, v. 26, p. 149-168.
- Jowett, C.E.  
1991: Fitting iron and magnesium into the hydrothermal chlorite geothermometer; Geological Association of Canada/Mineralogical Association of Canada, Programme with Abstracts, v. 16, p. A62.

**Kidd Creek Study Group**

1993: Co-operation research on the Kidd Creek volcanogenic massive sulphide deposit, Timmins, Ontario; in *Current Research, Part E*; Geological Survey of Canada, Paper 93-1E.

**Leitch, C.H.B.**

1992: Mineral chemistry of selected silicates, carbonates, and sulphides in the Sullivan and North Star stratiform Zn-Pb deposits, British Columbia, and in district scale altered and unaltered sediments; in *Current Research, Part E*; Geological Survey of Canada, Paper 92-1E, p. 83-93.

**Luff, W.M., Goodfellow, W.D., and Juras, S.J.**

1992: Evidence for a feeder pipe and associated alteration at the Brunswick No. 12 massive sulphide deposit; *Exploration and Mining Geology Journal*, v. 1, p. 167-185.

**MacLean, W.H. and Hoy, L.D.**

1991: Geochemistry of hydrothermally altered rocks at the Horne Mine, Noranda, Quebec; *Economic Geology*, v. 86, p. 506-528.

**Plimer, I.R. and de Carvalho, D.**

1982: The geochemistry of hydrothermal alteration at the Salgadinho copper deposit, Portugal; *Mineralium Deposita*, v. 17, p. 193-211.

**Ramamohana, R.T.**

1977: Distribution of elements between coexisting phengite and chlorite from the greenschist facies of the Tennant Creek area, Central Australia; *Lithos*, v. 10, p. 103-112.

**Schmidt, J.M.**

1988: Mineral and whole-rock compositions of seawater-dominated hydrothermal alteration at the Arctic volcanogenic massive sulphide prospect, Alaska; *Economic Geology*, v. 83, p. 822-842.

**Shikazono, N. and Kawahata, H.**

1987: Compositional differences in chlorite from hydrothermally altered rocks and hydrothermal ore deposits; *Canadian Mineralogist*, v. 25, p. 465-474.

**Slack, J.F. and Coad, P.R.**

1989: Multiple hydrothermal and metamorphic events in the Kidd Creek volcanogenic massive sulphide deposit, Timmins, Ontario: evidence from tourmalines and chlorites; *Canadian Journal of Earth Sciences*, v. 26, p. 694-715.

**Wiewiora, A. and Weiss, Z.**

1990: Crystallochemical classifications of phyllosilicates based on the unified system of projection of chemical composition: II. The chlorite group; *Clay Minerals*, v. 25, p. 83-92.

---

Geological Survey of Canada Project 870058 FB



# Till geochemistry in the Manitowadge area, Ontario<sup>1</sup>

Inez M. Kettles

Terrain Sciences Division

*Kettles, I.M., 1993: Till geochemistry in the Manitowadge area, Ontario; in Current Research, Part E; Geological Survey of Canada, Paper 93-1E, p. 165-173.*

---

**Abstract:** In 1991, 283 till samples were collected in the Manitowadge area, Ontario. Samples were analyzed for their content of distinctive Precambrian and Paleozoic lithologies in the pebble (5.6-16.0 mm) fraction and trace and minor elements in the <0.063 mm and <0.002 mm fractions. Variations in till composition are related to the effects of glacial transport and the composition of underlying or nearby bedrock. In many areas, the till contains a large component of debris derived from Paleozoic carbonate bedrock, glacially transported more than 100 km from the Hudson and James Bay lowland. Where present in large quantities, Paleozoic carbonate tends to suppress the original signature of till derived from Precambrian bedrock which contains higher levels of trace elements. High concentrations of copper, zinc, and other elements are found in till overlying and down ice from the Geco and Willroy mines near Manitowadge. Elsewhere, there are high levels of copper, zinc, and other elements in till in some areas underlain by bedrock of the Manitowadge and Schreiber-Hemlo greenstone belts.

**Résumé :** En 1991, 283 échantillons de till ont été prélevés dans la région de Manitowadge (Ontario). On a analysé les échantillons afin de déterminer les lithologies précambriennes et paléozoïques caractéristiques contenues dans la fraction des cailloux (5,6-16,0 mm), de même que les éléments en traces et les éléments mineurs dans les fractions inférieures à 0,063 mm et à 0,002 mm. Les variations de la composition du till sont liées aux effets du transport glaciaire et à la composition du substratum rocheux sous-jacent ou voisin. À de nombreux endroits, le till comporte une quantité importante de débris dérivés du substratum carbonaté paléozoïque, qui ont été transportés par la glace sur plus de 100 km à partir des basses terres de la baie d'Hudson et de la baie James. Là où elles se rencontrent en abondance, les roches carbonatées paléozoïques tendent à supprimer la signature originale du till dérivé du substratum rocheux précambrien qui contient des teneurs élevées en éléments en traces. Il y a de fortes concentrations de cuivre, de zinc et d'autres éléments dans le till sus-jacent aux mines Geco et Willroy et en aval-glaciaire de ces mines, près de Manitowadge. Ailleurs, dans certaines régions où le substratum rocheux se compose des ceintures de roches vertes de Manitowadge et de Schreiber-Hemlo, le till contient de fortes concentrations de cuivre, de zinc et d'autres éléments.

---

<sup>1</sup> Contribution to Canada-Ontario Subsidiary Agreement on Northern Ontario Development (1991-1995), under the Canada-Ontario Economic and Regional Development Agreement.

## INTRODUCTION

In 1991, the Geological Survey of Canada began a reconnaissance till sampling survey in the Manitowadge area, Ontario (Fig. 1). The program is part of the Northern Ontario Development Agreement (NODA) programme designed to aid and stimulate mineral exploration activities in the region. Other aspects of the NODA project in the Manitowadge area include Precambrian bedrock mapping (Zaleski and Peterson, 1993) and investigation of new and known mineral deposits (D. McKay, pers. comm., 1993).

The Geological Survey of Canada had previously carried out a sampling survey of modern lake bottom sediments and lake waters around the north shore of Lake Superior, including the Manitowadge area (Geological Survey of Canada, 1978, 1979). Samples were reanalyzed in 1990 (Friske et al., 1991a, b).

In addition to the till sampling survey, mapping of surficial deposits is being undertaken in the present study at a scale of 1:50 000 in the Vein Lake area (42E/01). This is an extension of earlier mapping work undertaken by the Ontario Geological Survey (Kristjansson and Geddes, 1986; Geddes and Bajc, 1985).

### *Bedrock and glacial geology*

Most of the study area is underlain by Archean greenstone belts and granitoid plutons of the Wawa subprovince of the Canadian Shield (Williams et al., 1991; Fig. 2). The greenstone belt at Manitowadge is host to the Geco Cu-Zn mine. Part of the Schreiber-Hemlo greenstone belt, which hosts the Hemlo gold deposits further south, is found in the southern part of the study area. Metasedimentary bedrock of the Quetico subprovince underlies the northern part of the study area (Williams, 1991).

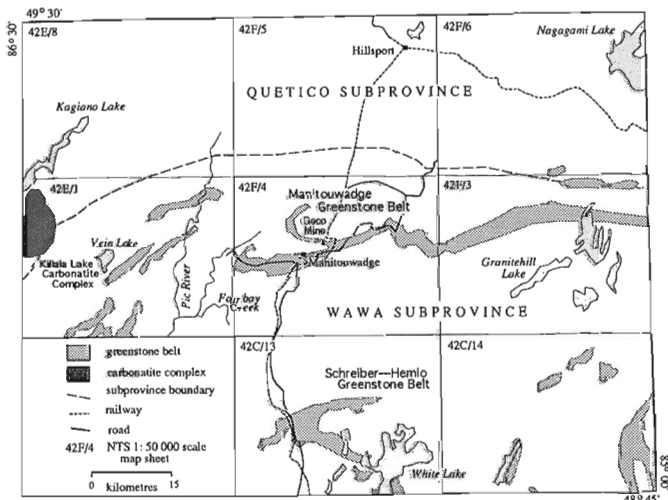


Figure 1. Study area, Manitowadge area, Ont.

All glacial deposits are thought to have been deposited during the Late Wisconsinan (Kristjansson and Geddes, 1986; Geddes and Bajc, 1985). The earliest ice flow direction, determined from striae, was southerly while the latest ice flow was southwestwards (Fig. 3). The most widespread glacial deposit is till. It forms a thin, discontinuous blanket (0.0-1.5 m thick), but in places it may exceed 10 m in thickness.

Also common in the study area are glaciofluvial ice-contact and outwash sand and gravel. Outwash deposits are common in the region east of Manitowadge in low lying areas above the maximum levels of glacial lake incursion (post-Lake Minong) (Kristjansson and Geddes, 1986). Elsewhere in low lying areas, glaciolacustrine deposits consisting of sand, silt, and clay are widespread. In the Manitowadge area, lacustrine sediments have been observed as high as 325 m a.s.l. (R. Geddes, unpub. report, 1987). Eolian dunes are found in some areas where outwash or glaciolacustrine sediments predominate and alluvium sands and silts are well developed along major rivers and streams. Deposits of peat and organic muck are widespread, particularly in areas underlain by glaciolacustrine sediments.

## FIELD AND LABORATORY METHODS

Two hundred and eighty-three till samples were collected in 1991 from hand-dug holes in roadside exposures or at off-road sites. An additional 375 till samples were collected in 1992. Care was taken to sample till that was as unweathered as possible, with most samples being collected below the level of the solum.

Pebbles (5.0-16.0 mm) were separated from most samples for lithological analysis. On average, 230 clasts were examined from each sample; the clasts were grouped into the following six classes and relative percentages calculated: 1) Paleozoic limestones and dolomites; 2) Paleozoic sandstones and siltstones; 3) Proterozoic greywackes and argillites (these clasts are characteristic of the Omarolluk Formation which outcrops in the Belcher Island Fold Belt and Sutton Inlier, described, for example, by Ricketts and Donaldson (1981)); 4) Precambrian metasediments of uncertain provenance; 5) Precambrian intrusive and high grade metamorphic rocks, i.e. coarsely crystalline, clasts; and 6) Precambrian metavolcanic rock, undifferentiated.

The <0.063 mm and <0.002 mm fractions of the samples were analyzed for the following trace and minor elements – Ag, Al, As, Ba, Bi, Ca, Cd, Co, Cr, Cu, Fe, K, La, Mg, Mn, Mo, Na, Ni, Pb, Sb, Sc, Sr, Sn, Te, V, W, Y, and Zn – by Inductively Coupled Plasma and Atomic Emission Spectroscopy (ICP-AES) after use of a nitric acid-aqua regia partial extraction. The <0.063 mm fraction was further analyzed for Au, Pt, and Pd by fire assay and Direct Current Plasma (DCP) spectroscopy.

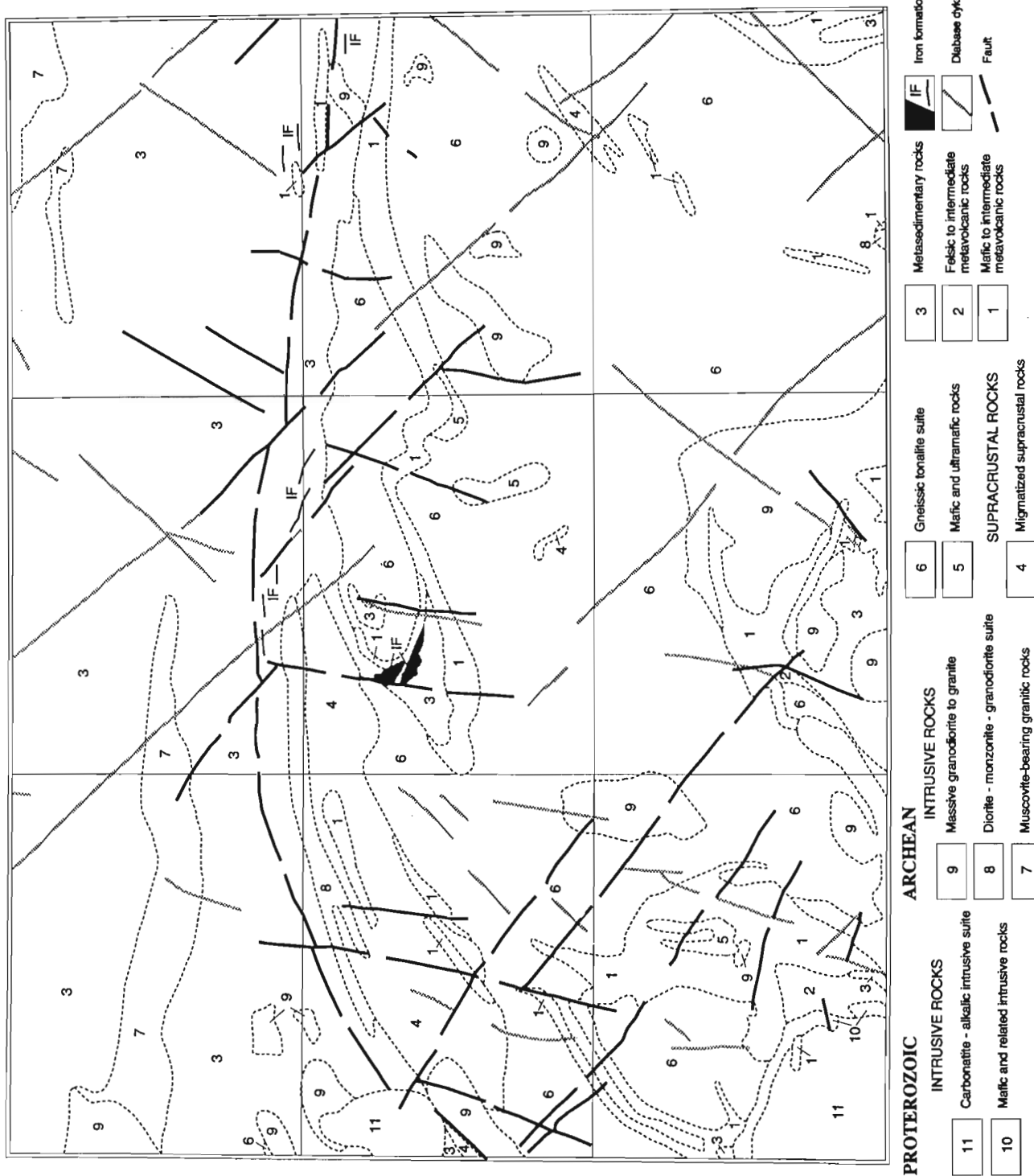


Figure 2. Bedrock geology, Manitowadge area, Ontario, after (Ontario Geological Survey, 1991) Area is same as outlined in Figure 1.

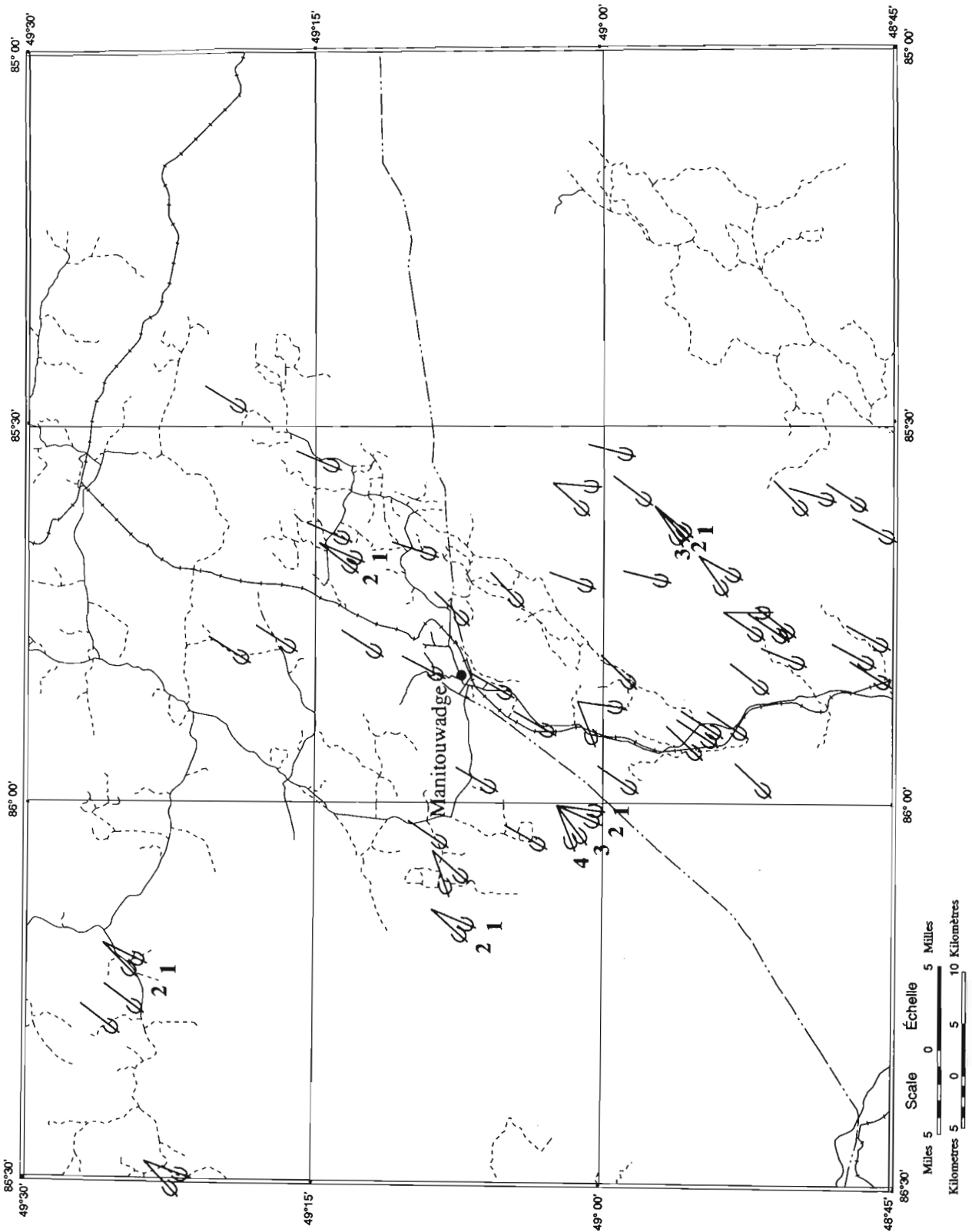


Figure 3. Glacial striation map. Striae measurements from present study and after Kristiansson and Geddes (1986) and Bajc (1985). Where known, relative age relationships indicated as follows: 1 = oldest; 4 = youngest.

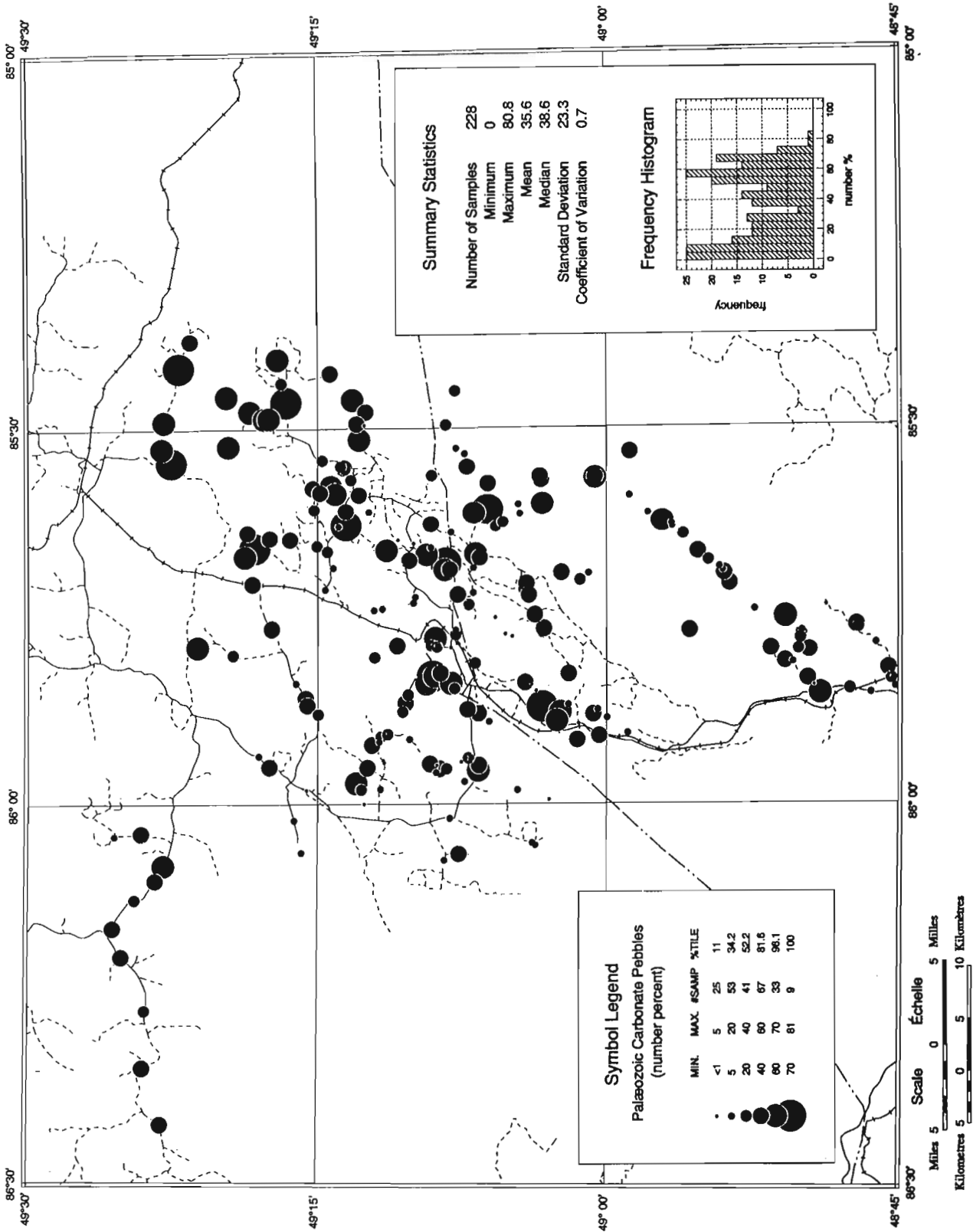


Figure 4. Distribution of clasts (5.0-16.0 mm) of Paleozoic limestone in till in the Manitowadge area, Ontario.

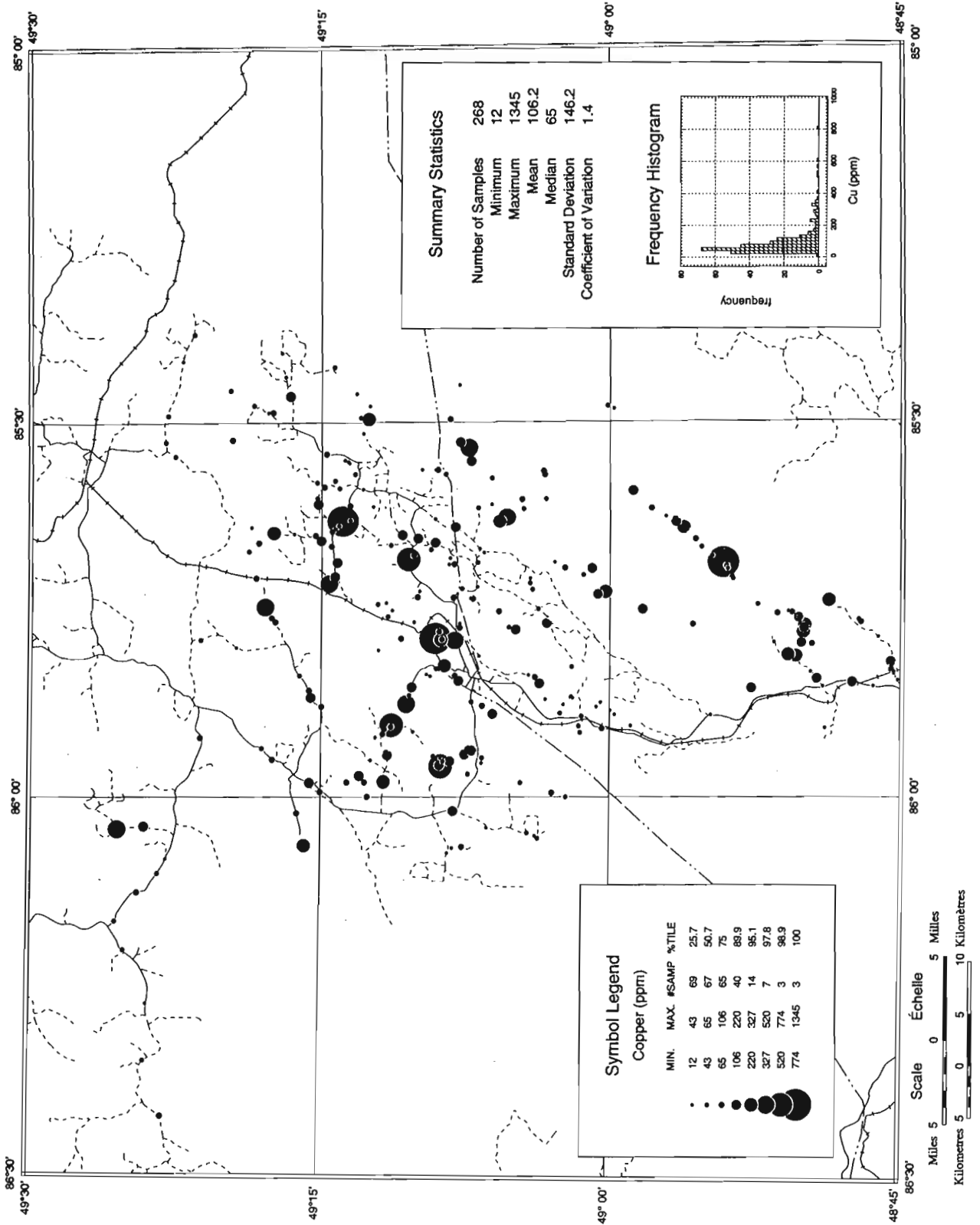


Figure 5. Distribution of copper in the clay-sized (<2 μm) fraction of till in the Manitouwadge area, Ontario.

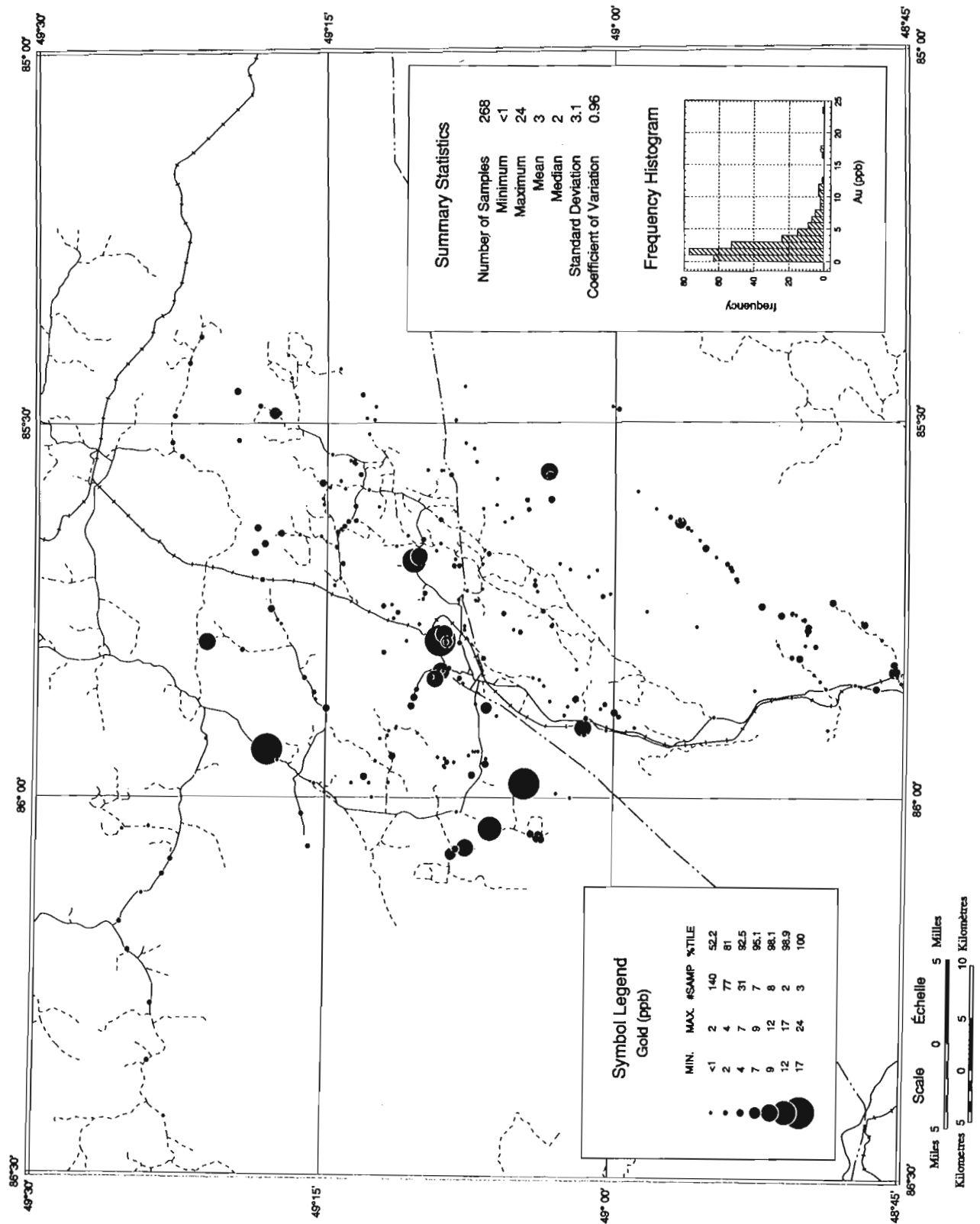


Figure 6. Distribution of gold in the silt plus clay-sized (<63 μm) fraction of till in the Manitouwadge area, Ontario.

## RESULTS

Geochemical and other data lists and trace element distribution maps based on the 1991 till sampling survey have been released as Geological Survey of Canada, Open File 2616 (Kettles, 1993).

The frequency distribution and dispersal patterns of pebbles in till samples from the Manitowadge area was studied to gain knowledge of the relationships of glacial flow to variations in composition. Two major bedrock terranes are represented by clasts in the tills of this region: 1) local Precambrian units, and 2) Paleozoic and Proterozoic terranes of the Hudson Bay and James Bay lowlands. Clasts derived from the Paleozoic and Proterozoic terranes were glacially transported at least 100 km.

The pebble fraction of more than 95% of the 285 till samples collected contained at least 5% Paleozoic carbonate (Fig. 4). The frequency histogram for Paleozoic carbonate clasts shown on Figure 4 indicates that Paleozoic clast frequencies are distinctly bimodal, falling into two broad groups, those with less than 35% Paleozoic carbonate and those with more. In addition, over 60% of the samples contained more than 10% clasts of Proterozoic metasedimentary rock (not shown). In contrast, highest concentrations of local Archean bedrock lithologies were found in till overlying or close to their outcrop areas (Kettles, 1993).

Where there are high concentrations of Paleozoic carbonate in till, the geochemical signature of the fine fraction of till tends to be suppressed (see Kettles, 1993, correlation matrix; Kaszycki, 1989) because unmetamorphosed carbonate bedrock is known to have low trace element concentrations (Mason, 1966, Table 6.5).

Despite the effects of dilution resulting from long distance transport, the distribution of trace and minor elements in the fine fractions of drift may be related in many areas to local bedrock composition. In some cases, high trace element levels in till may reflect high background levels in bedrock. Platinum concentrations (not shown), for example, are generally high in till in Quetico terrane compared to Wawa terrane.

In other areas, high trace element levels in drift may reflect mineralized occurrences in the underlying or nearby bedrock. In Wawa terrane, highest levels of copper (Fig. 5), gold (Fig. 6) and also zinc, lead, silver, palladium, cadmium, and arsenic (not shown) are found in samples collected from till overlying the mafic to intermediate rocks of the Manitowadge greenstone belt, particularly in the vicinity of the Geco and Willroy copper-zinc deposits, and, also, overlying the Hemlo-Schreiber greenstone belt. Elsewhere, there are high levels of gold (Fig. 6) in till in the Fourbay Creek area.

Another major factor which influences the geochemical signature of surface till in any region is surface weathering. In this study, the effects of weathering on composition have been minimized by sampling till below the postglacial solum. As a result, regional patterns of trace element and Paleozoic

and Precambrian clasts or trace elements in drift are believed to be not significantly altered by compositional variation caused by weathering.

## CONCLUSIONS

Variations in till composition may be related to the effects of glacial transport and the composition of underlying or nearby bedrock. In many areas, the till contains a large component of debris derived from Paleozoic carbonate bedrock, glacially transported more than 100 km from the Hudson and James Bay lowland. Where present in large quantities, Paleozoic carbonate tends to suppress the geochemical signature of the fine fraction of till.

Despite the effects of dilution, the signature of mineralized bedrock does stand out in the fine fractions of till in many cases. As would be expected, high concentrations of copper, zinc, gold, and other elements are found in till overlying and down ice from the Geco and other now abandoned mines in the Manitowadge area. Levels of copper, zinc, and other elements are also elevated in till overlying bedrock in other parts of the Manitowadge greenstone belt and also of the Schreiber-Hemlo greenstone belt.

Follow-up mineral exploration work in some areas may prove worthwhile. Additional till samples, collected in 1992 in areas of metal-enriched till overlying the greenstone belts and in the Fourbay Creek region are presently undergoing analysis.

## ACKNOWLEDGMENTS

The author wishes to thank the following: K. Laurus for her able assistance in the field and for carrying out pebble counts in 1991; D.B. McKay for helpful advice; the staff of the geology department of Noranda Geco mine for helpful discussions; S. Bauke for assistance with data compilation; Northwood Geoscience for plotting the proportional symbol maps; D. Pare at Consorminex for carrying out pebble counts; P. Lindsay for co-ordinating the laboratory work; J. Veillette for reviewing this manuscript.

## REFERENCES

- Friske, P.W.B., Hornbrook, E.H.W., Lynch, J.J., McCurdy, M.W., Gross, H., Galletta, A.C., and Durham, C.C.  
 1991a: Regional lake sediment and water geochemical reconnaissance data, northwestern Ontario, (NTS 42D, 42E south); Geological Survey of Canada, Open File 2360.  
 1991b: Regional lake sediment and water geochemical reconnaissance data, northwestern Ontario, (NTS 42C, 42F south), Geological Survey of Canada, Open File 2362.  
 Geddes, R.S. and Bajc, A.F.  
 1985: Quaternary geology of the White Lake (Hemlo area), District of Thunder Bay; Ontario Geological Survey, Map P. 2849, scale 1: 50 000.  
 Geological Survey of Canada  
 1978: Regional lake sediment and water geochemical reconnaissance data, Ontario 1977, NTS 42D, 42E (S 1/2); Geological Survey of Canada, Open File 506.



**Geological Survey of Canada (cont'd.)**

- 1979:** Regional lake sediment and water geochemical reconnaissance data, Ontario 1978, NTS 42C, 42F (S1/2); Geological Survey of Canada, Open File 555.
- Kaszycki, C.A.**  
1989: Surficial geology and till composition, northwestern Manitoba; Geological Survey of Canada, Open File 2118, 150 p.
- Kettles, I.M.**  
1993: Reconnaissance geochemical data for till samples from the Manitowadge area, Ontario; Geological Survey of Canada, Open File 2616, 197 p.
- Kristjansson, F.J. and Geddes, R.S.**  
1986: Quaternary geology of the Manitowadge area, District of Thunder Bay; Ontario Geological Survey, Map P. 3055, scale 1: 50 000.
- Mason, B.**  
1966: Principles of geochemistry; Wiley, New York; 329 p.
- Ontario Geological Survey**  
1991: Bedrock geology of Ontario, east-central sheet; Ontario Geological Survey, Map 2534, scale 1:1 000 000.
- Ricketts, B.D. and Donaldson, J.A.**  
1981: Sedimentary history of the Belcher Group of Hudson Bay; in Proterozoic Basins of Canada, (ed.) F.H.A. Campbell; Geological Survey of Canada, Paper 81-10, p. 235-254.
- Williams, H.R.**  
1991: Quetico Subprovince; in Geology of Ontario; (ed.) P.C. Thurston, H.R. Williams, R.H. Sutcliffe, and G.M. Stott; Ontario Geological Survey, Special Volume 4, pt. 1, p. 383-404.
- Williams, H.R., Stott, G.M., Heather, K.B., Muir, T.L., and Sage, R.P.**  
1991: Wawa Subprovince; in Geology of Ontario, (ed.) P.C. Thurston, H.R. Williams, R.H. Sutcliffe, and G.M. Stott, Ontario Geological Survey, Special Volume 4, pt. 1, p. 485-539.
- Zaleski, E. and Peterson, V.L.**  
1993: Lithotectonic setting of mineralization in the Manitowadge greenstone belt, Ontario: preliminary results; in Current Research, Part C; Geological Survey of Canada, Paper 93-1C, p. 307-317.

---

Geological Survey of Canada Project 910017 FI



# Comparative metallogenic studies of the Alberta and Saskatchewan parts of Athabasca Basin<sup>1</sup>

Vlad Ruzicka  
Mineral Resources Division

*Ruzicka, V., 1993: Comparative metallogenic studies of the Alberta and Saskatchewan parts of Athabasca Basin; in Current Research, Part E; Geological Survey of Canada, Paper 93-1E, p. 175-184.*

---

**Abstract:** Metallogenic studies of the Athabasca Basin in Alberta have been conducted with a comparison to the Saskatchewan part of the basin. In both areas enrichment in specific elements, such as U, Ni, Mo, and Sr, is typically present at the sub-Athabasca unconformity. However, in the Alberta part of the basin some elements, such as chromium, are more enriched in upper parts of the Athabasca sequence distant from the unconformity. Chromium is concentrated inversely to uranium. A conceptual model suggests sedimentary syngenetic processes for chromium concentration, whereas a model for uranium proposes its epigenetic deposition from metalliferous brines at redox fronts. The sources for chromium were, apparently, deeper parts of the basement, composed of mafic to ultramafic rocks, whereas the sources for uraniumiferous fluids were probably younger granitoid domes.

**Résumé :** La partie albertaine du bassin d'Athabasca a été comparée sur le plan métallogénique à la partie du bassin située en Saskatchewan. Dans les deux régions, les teneurs en certains éléments comme U, Ni, Mo et Sr sont en général élevées au niveau de la discordance qui marque la base du bassin. Toutefois, dans la partie albertaine, certains éléments comme le chrome sont plus abondants dans les couches supérieures de la séquence (du bassin) d'Athabasca loin de la discordance. L'enrichissement en chrome présente un comportement inverse de celui de l'uranium. Un modèle conceptuel indique que l'enrichissement en chrome est fonction de processus synsédimentaires, tandis que le dépôt de l'uranium, selon un autre modèle, serait épigénétique et se produirait à la rencontre de fronts d'oxydo-réduction par les saumures métallifères. Les sources du chrome sont apparemment situées dans des parties plus profondes du socle, où celui-ci est composé de roches mafiques à ultramafiques, tandis que les fluides uranifères proviendraient de dômes de granitoïde plus jeunes.

---

<sup>1</sup> Contribution to Canada-Alberta Agreement on Mineral Development (1992-1995), a subsidiary agreement under the Canada-Alberta Economic and Regional Development Agreement.

## INTRODUCTION

The Athabasca Basin region hosts the world's largest high-grade uranium monometallic and polymetallic deposits (Fig. 1). These deposits, which have been found so far only in the Saskatchewan part of the basin, and which in 1992 contributed more than 80% in Canada's uranium production, and, along with exploration for this deposit type, contributed by almost a billion dollars to Canadian economy. The Alberta part of the basin, however, remained for several years as a less attractive target for such exploration and mining activity.

The mineral resources in the basin occur at the sub-Athabasca unconformity, in altered rocks of the basal formations of the Athabasca Group (e.g., the P2 North and the Collins Bay deposits), and in both the altered cover and basement rocks (e.g., the Cigar Lake and Key Lake deposits). Some resources occur entirely in the basement rocks (e.g., the Rabbit Lake and Eagle Point deposits). Only a small portion of the resources occurs some distance above the unconformity entirely within the Athabasca Group sandstones (e.g. the Fond-du-Lac deposit).

The uranium is present either in polymetallic paragenetic association, where uranium minerals are accompanied by minerals of other metallic elements such as Ni, Co, As, Pb, Mo, Zn, Ag, Au, and Pt, or in monometallic assemblages, which consist mainly of pitchblende and coffinite.

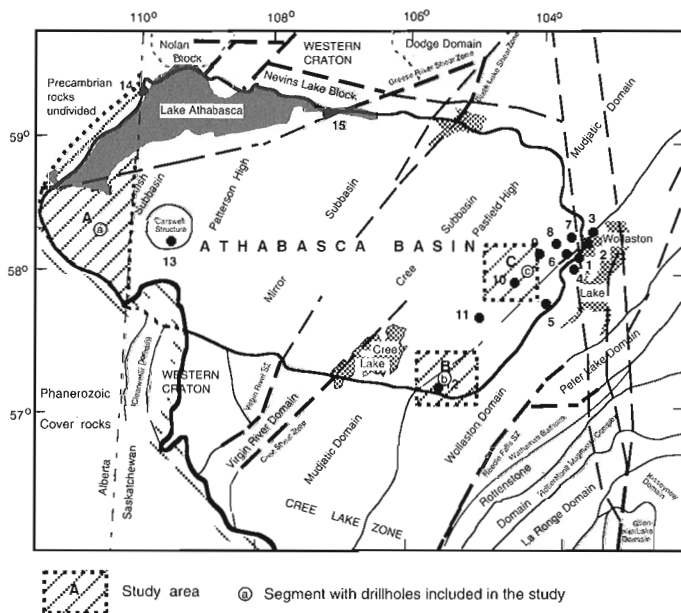
Geology and deposits of the Saskatchewan part of the Athabasca Basin have been the subjects of a number of papers, e.g. Knipping (1974), Hoeve and Sibbald (1978), Tremblay (1982), Ruzicka (1984, 1989), Langford (1986), Wallis et al. (1986), Fouques et al. (1986), Laine (1986), Andrade (1989), Kyser et al. (1989), Ramaekers (1990), and Sibbald et al. (1990). Geology and potential for mineral deposits in the Alberta part of the basin have been investigated particularly by professionals of the Alberta Geological Survey (e.g., Godfrey, 1960, 1986a, b; Godfrey and Watanabe, 1964; Wilson, 1985, 1986, 1987; and Edwards et al., 1991). Exploration for mineral deposits in the area was conducted by several companies, such as Eldorado Nuclear Limited; Norcen Energy Resources Limited; Matagami Mines Limited; National Nickel Limited; and Uranerz Exploration and Mining Limited.

Because of its significance as an important metallogenic province, the Alberta part of the basin has been included in several projects under the current Canada-Alberta Mineral Development Agreement (MDA). At present the writer is conducting metallogenic analysis of the Alberta portion of the Athabasca Basin under this MDA. Some results of the initial field, laboratory, and office studies by the author are presented in this paper.

## METHOD

Metallogenic studies for the selected part of northeastern Alberta have been conducted by comparison with selected areas of the Saskatchewan part of the Athabasca basin (Fig. 1). The work has been focused on interpretation of mineralization processes from lithological and structural observations (mainly on available drill cores), from geophysical (radiometric) measurements, from examination of collected rock samples and their geochemical analyses, and from previous geological studies. In addition to data collected by the writer during the period from 1969 to 1991, the current (1992) studies have included 1726 m of drill core logging; 2687 gamma-ray spectrometric assays for total radioactivity, potassium, uranium, and thorium; geological examination of 150 rock samples; and 3292 geochemical analyses for selected chemical constituents from the collected samples.

The main aim of the studies has been to investigate whether or not the metallogenic observations on the Alberta part of the Athabasca Basin are compatible with the metallogenic features of the Saskatchewan part of the basin.



**Figure 1.** Index map with location of study areas and unconformity-type deposits in the Athabasca Basin (for explanation see text). Base map modified after Sibbald et al., (1990). Deposits (m = monometallic, p = polymetallic): 1 = Rabbit Lake (m), 2 = Collins Bay cluster (p), 3 = Eagle Point (m), 4 = Horseshoe and Raven (m), 5 = West Bear (p), 6 = McClean-Sue cluster (p), 7 = JEB (m), 8 = Dawn Lake (p), 9 = Midwest (p), 10 = Cigar Lake (p), 11 = P2 North (m), 12 = Key Lake (p), 13 = Cluff 'D' (p), Dominique-Peter (m), Dominique-Janine (m), Claude (m), 14 = Maurice Bay (p), 15 = Fond du Lac (m). Study areas: A = Northeastern Alberta (a) Laroque Lake segment, B = Key Lake area (Saskatchewan) (b) Deilmann segment, C = Cigar Lake area (Saskatchewan) (c) Natona Bay segment .

**Table 1a.** Mean values and Standard deviations for analyses of samples from area 'A' (Alberta).

Element	No. of analyses	Mean ppm	Standard Deviation
Al	68	40588.00	37035.00
As	68	120.53	482.96
B	68	63.68	53.33
Ba	68	297.03	560.73
Be	68	0.70	0.90
Ca	68	6435.00	14665.00
Cd	68	1.04	0.21
Co	68	4.68	8.34
Cr	68	196.38	189.92
Cu	68	9.74	25.40
Fe	68	13988.00	16333.00
K	68	12650.00	16492.00
La	68	27.00	26.88
Mg	68	11033.00	21386.00
Mn	68	133.00	331.00
Mo	68	6.71	6.89
Na	68	4431.00	8994.00
Ni	68	79.44	246.64
P	68	323.00	390.00
Pb	68	10.74	16.33
Sr	68	194.81	219.67
Th	68	14.00	20.36
Ti	68	1411.00	1745.00
U	68	4.00	6.90
V	68	43.54	71.44
Y	68	14.96	34.04
Zn	68	19.62	28.18
Zr	68	114.63	139.17

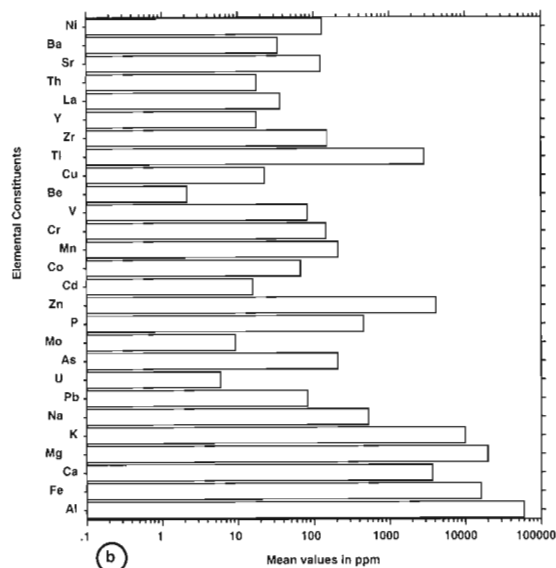
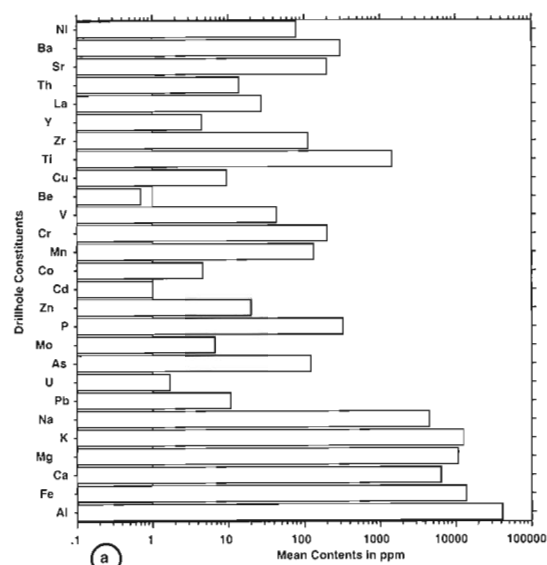
## GEOLOGY AND LITHOCHEMISTRY OF THE STUDY AREAS

Three areas have been selected for the comparative study: area 'A', which is located in NTS 74L/2, about 15 km northeast of Laroque Lake; area 'B', which is located in the proximity of the Key Lake deposit; and area 'C', which is located in the vicinity of the Cigar Lake deposit, at the Natona Bay.

### Area 'A'

The study area 'A' includes the Alberta part of the Athabasca Basin and its immediate vicinity (Fig. 1). Basement rocks, which are part of the Churchill Structural Province, consist of Archean and Aphebian granitoid and metasedimentary rocks. The granitoids typically form domal structures. The basement rocks, which are topped by regolith, are unconformably overlain by unmetamorphosed sedimentary rocks of the Athabasca Group (Wilson, 1985, 1986). The Athabasca

Group has been divided by Wilson (1985) into Fair Point, Manitou Falls, Wolverine Point, Locker Lake, and Otherside formations. Ramaekers (1990), however, classified the basal part of the Wolverine Formation of Wilson (1985) as Lazenby Lake Formation, but did not precisely establish its westernmost extension. The writer's observations on drill core confirm presence of the Fair Point Formation as far as 110°40'W. A total of 873 m of drill core from four drill holes, which intersected both the Athabasca Group and basement rocks, were investigated and multielement analyses from 68 drill core samples are included in this preliminary study (Table 1a). A histogram of mean values for individual constituents from these samples is compiled in Figure 2a.

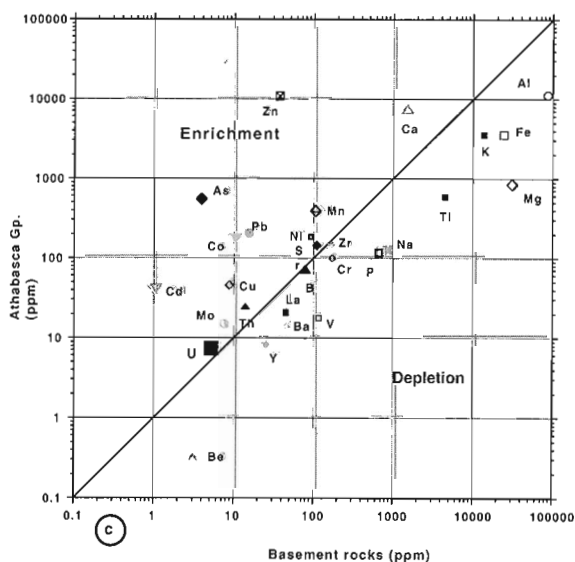
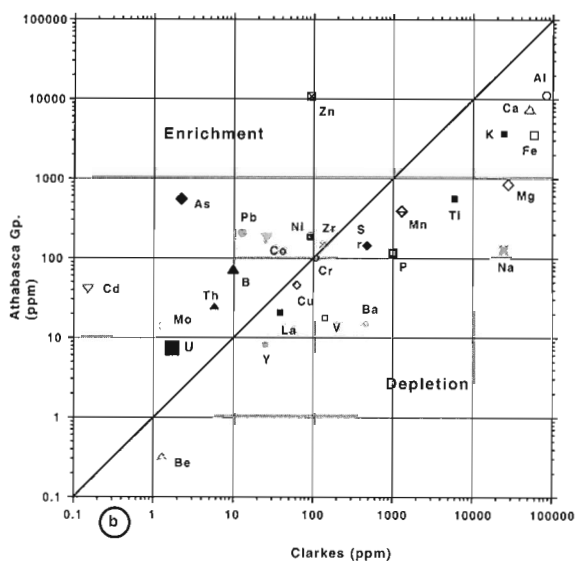
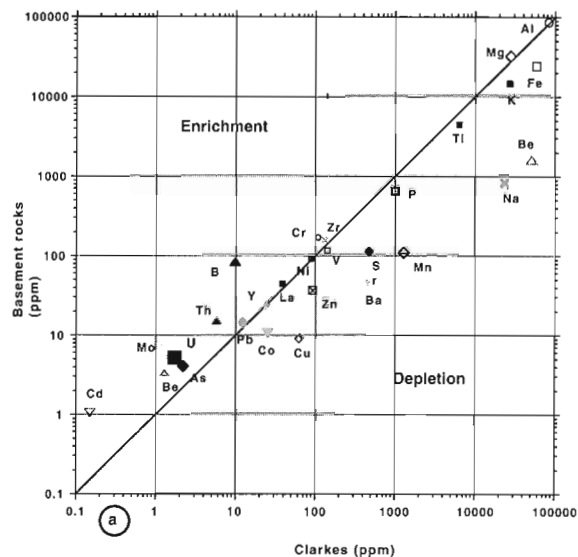


**Figure 2.** Histogram of mean values for selected elemental constituents in selected drillholes: (a) from the Alberta part of the Athabasca Basin, (b) from the Saskatchewan part of the Athabasca Basin.



**Table 1b.** Mean values and Standard deviations for analyses of samples from areas 'B' and 'C' (Saskatchewan).

Element	No. of analyses	Mean ppm	Standard Deviation
Al	45	58519.00	40457.00
As	45	209.40	1370.70
B	45	75.60	67.00
Ba	45	33.89	51.32
Be	45	2.10	2.20
Ca	45	3677.00	17685.00
Cd	45	15.30	91.80
Co	45	68.00	388.50
Cr	45	144.69	100.84
Cu	45	22.40	94.82
Fe	45	16354.00	19247.00
K	45	10096.00	8564.00
La	45	36.00	37.56
Mg	45	20167.00	28529.00
Mn	45	211.00	926.00
Mo	45	9.30	19.70
Na	45	532.00	512.00
Ni	45	126.36	418.33
P	45	449.00	953.00
Pb	45	83.20	329.80
Sr	45	122.98	109.71
Th	45	17.36	16.08
Ti	45	2864.00	3635.00
U	45	6.00	9.10
V	45	80.07	118.14
Y	45	17.29	19.48
Zn	45	4053.50	26825.00
Zr	45	151.69	77.03



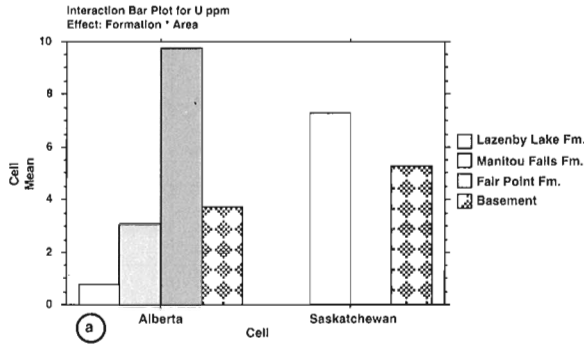
**Legend for Figure 4**



**Figure 4.** Comparison between contents of elemental constituents from selected drillholes in the areas 'B' and 'C' (Saskatchewan parts) of the Athabasca Basin (a) in samples from the basement rocks with the corresponding clarkes of crustal abundance, (b) in samples from the Athabasca Group rocks with the corresponding clarkes of crustal abundance, (c) in samples from the basement and Athabasca Group rocks.

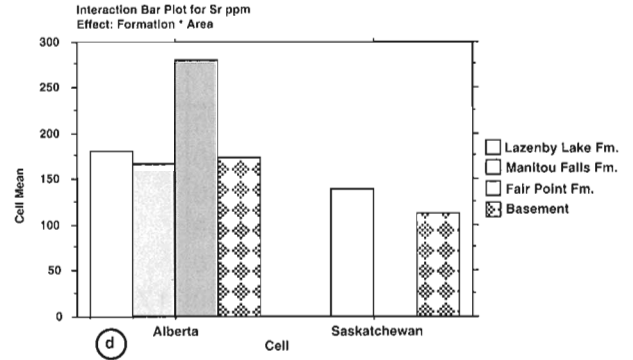
ANOVA Table for U ppm

	DF	Sum of Squares	Mean Square	F-Value	P-Value
Formation	1	8.903	8.903	.155	.6943
Area	0	0.000	*	*	*
Formation * Area	1	32.393	32.393	.565	.4539
Residual	107	6134.837	57.335		



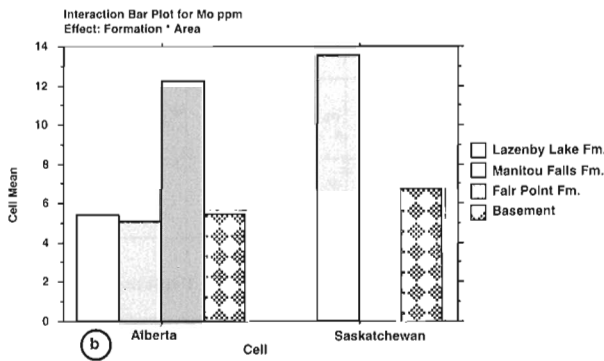
ANOVA Table for Sr ppm

	DF	Sum of Squares	Mean Square	F-Value	P-Value
Formation	1	1809.154	1809.154	.053	.8180
Area	0	0	*	*	*
Formation * Area	1	4820.524	4820.524	.142	.7072
Residual	107	3637517.921	33995.495		



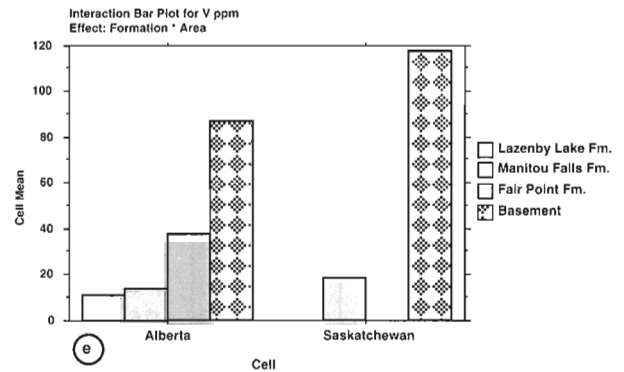
ANOVA Table for Mo ppm

	DF	Sum of Squares	Mean Square	F-Value	P-Value
Formation	1	182.537	182.537	1.012	.3166
Area	0	0.000	*	*	*
Formation * Area	1	246.632	246.632	1.368	.2448
Residual	107	19296.291	180.339		



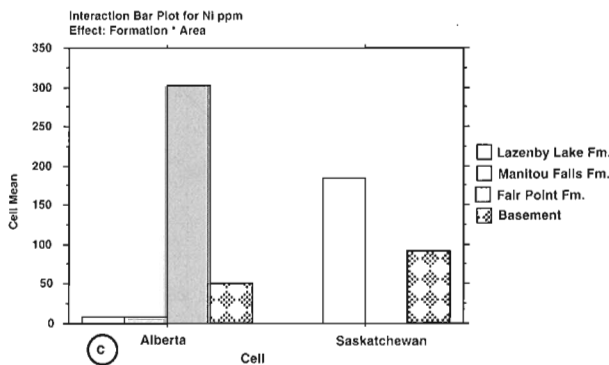
ANOVA Table for V ppm

	DF	Sum of Squares	Mean Square	F-Value	P-Value
Formation	1	139402.013	139402.013	19.223	<.0001
Area	0	0.000	*	*	*
Formation * Area	1	3125.474	3125.474	.431	.5129
Residual	107	775934.277	7251.722		



ANOVA Table for Ni ppm

	DF	Sum of Squares	Mean Square	F-Value	P-Value
Formation	1	11742.933	11742.933	.116	.7345
Area	0	0	*	*	*
Formation * Area	1	86802.340	86802.340	.855	.3572
Residual	107	10863981.897	101532.541		



ANOVA Table for Y ppm

	DF	Sum of Squares	Mean Square	F-Value	P-Value
Formation	1	2852.768	2852.768	3.404	.0678
Area	0	0	*	*	*
Formation * Area	1	136.237	136.237	.163	.6876
Residual	107	89660.683	837.950		

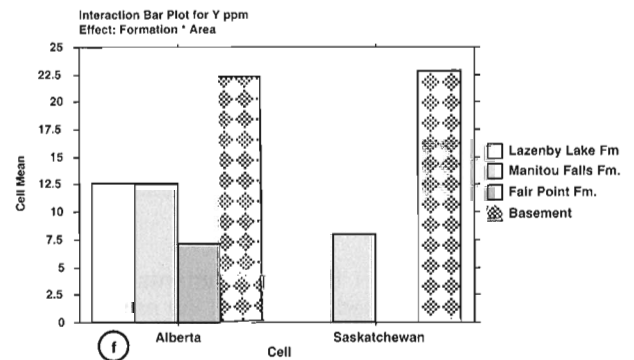


Figure 5. ANOVA Table and Graph for contents of selected elements in geological formations in the Alberta and Saskatchewan parts of the Athabasca Basin: (a) uranium, (b) molybdenum, (c) nickel, (d) strontium, (e) vanadium, (f) yttrium, (g) chromium.



ANOVA Table for Cr ppm

	DF	Sum of Squares	Mean Square	F-Value	P-Value
Formation	1	91011.782	91011.782	5.086	.0261
Area	0	-1.137E-13	*	*	*
Formation * Area	1	13.917	13.917	.001	.9778
Residual	107	1814541.932	17892.915		

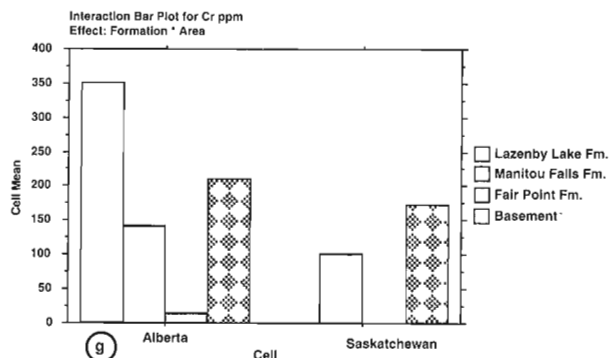


Figure 5 (cont.)

Multielement geochemical analyses of 45 samples from areas 'A' and 'B' are included in this preliminary study (Table 1b). A histogram of mean values for individual constituents from these samples is compiled in Figure 2b.

Lithochemical observations on the basement rocks in areas 'B' and 'C' indicate that, relative to the average crustal elemental abundances (clarkes), these rocks are enriched in certain elements, such as U, As, Cd, Mo, Th, B, Pb, Cr, and Ba (Fig. 4a). The cover rocks exhibit higher concentrations of As (!), B, Mo, Th, Ni, Zr, and Cr, and lower values of Be, Co, Y, Cu, Zn, V, Ti, Al, Fe, Ca, K, Mg, and Mn (Fig. 4b). Relative to the basement rocks, the sedimentary cover rocks are richer in As, Zr, Ni, B, and slightly in U, but have substantially lower amounts of other elements, such as Na, Ba, Mn, Ca, Mg, Mn, Cu, Be, Ti, and V (Fig. 4c). The metallogenic pattern of this area reflects metallogenic processes similar to those in area 'A'.

## DISTRIBUTION OF SELECTED ELEMENTS

Geochemical analyses of samples from the area 'A' (Alberta) have been compared with analyses from the combined areas 'B' and 'C' (Saskatchewan) by statistical analysis of variance (ANOVA model). This statistical treatment determines the significance of the effects in a model by calculating the variability in relationship between contents of the selected constituents in comparable lithostratigraphic units from the areas in question. Area 'A' consists of a crystalline basement unit and the Fair Point, Manitou Falls, and Lazenby Lake formations of the Athabasca Group, whereas investigation of the areas 'B' and 'C' encompassed the crystalline basement and Manitou Falls Formation of the Athabasca Group.

### Uranium

As documented in Figure 5a, the basement rocks in area 'A' contain less uranium than those in areas 'B' and 'C'. The graph also indicates that there is a distinct enrichment of the

basal (Fair Point) formation of the Athabasca Group with uranium relatively to Manitou Falls and particularly Lazenby Lake formations. This enrichment indicates that epigenetic processes involving uranium were in the area 'A' operative and fit to the writer's model for unconformity deposits (Ruzicka, 1984). Pitchblende is the most common uranium mineral present in the samples.

### Molybdenum

Molybdenum is a typical metallic element accompanying uranium in the Athabasca Basin unconformity deposits (Fig. 5b; Ruzicka and LeCheminant, 1987). It concentrates epigenetically in the Athabasca sandstone. Its mean values in studied samples from both parts of the basin exhibit similar levels of concentration, which exceeds about six times its crustal abundance (Fig. 2a, 2b). It occurs mainly in molybdenite and in secondary mineral ilsemannite.

### Nickel

In all areas nickel is paragenetically associated and enriched with uranium, particularly at the sub-Athabasca unconformity (Fig. 5c, 3b, c, 4b, c). It occurs mainly in rammelsbergite, pararammelsbergite, and gersdorffite.

### Strontium

The Alberta part of the Athabasca Basin exhibits higher contents of strontium in all geological units than the Saskatchewan study areas (Fig. 5d). However, even these elevated values represent about one-half of Sr crustal abundance in area 'A' and only about 25% in areas 'B' and 'C'. Factor analyses of elemental constituents in studied samples indicate its relationship with Zr, Th, and La. This feature is related to heavy mineral assemblages derived from granitic (pegmatitic) igneous rocks.

### Vanadium

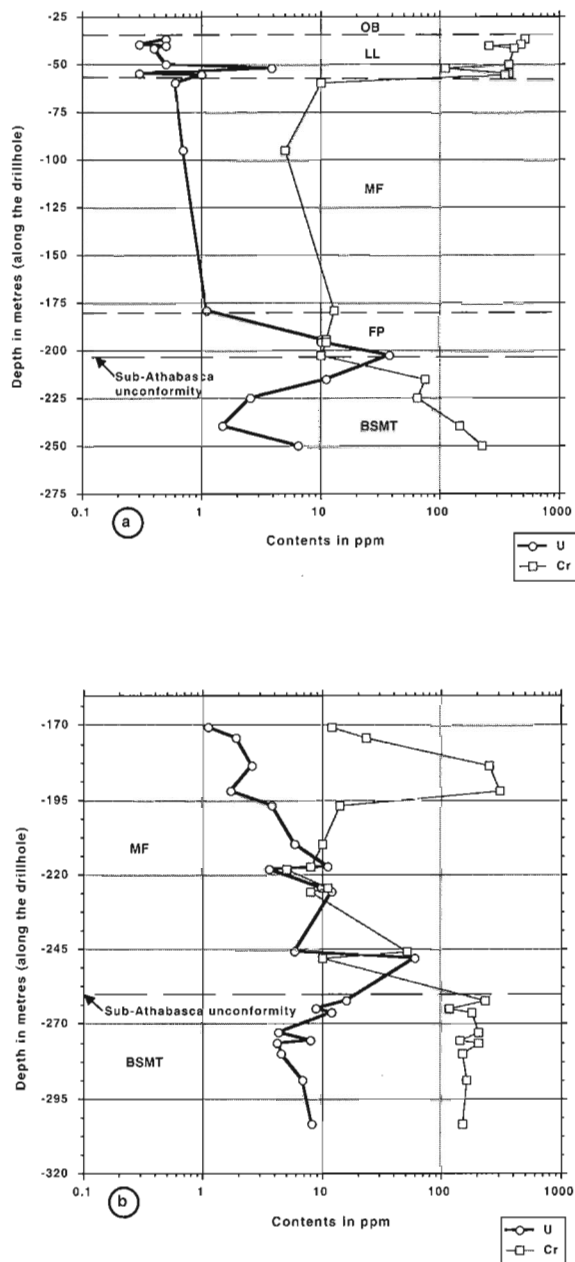
Vanadium is a common constituent in basement rocks in both areas (Fig. 5e). Although its contents are generally lower than its crustal abundance, the basement rocks in Saskatchewan areas 'B' and 'C' exhibit relatively higher levels of this element (in average 118 ppm V) than area 'A' (with an average content of 87 ppm V). This feature is related to more frequent presence of metapelitic rocks in their samples than in samples from area 'A'. However, Wilson (1986) reported an average content of 163 ppm V in seven samples of "mafic mylonite" collected from drillholes, located about 30 km southwest of area 'A'. He described the mafic mylonite as 'dark grey to greenish grey rocks containing chlorite, biotite, epidote and clay groundmass with grains of pyrite and streaks of graphite', which is, apparently, equivalent of the metapelitic layer lithologically controlling mineralization as postulated in models for unconformity deposits (Ruzicka, 1984).

### Yttrium

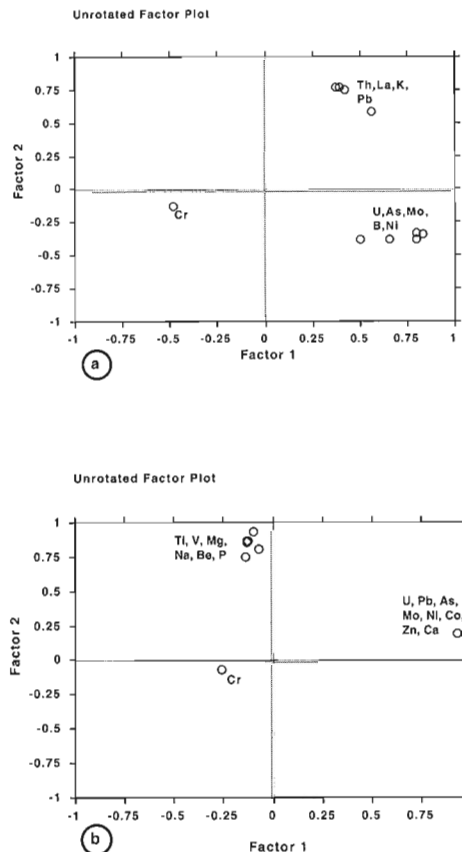
In the Athabasca Group sedimentary rocks yttrium is more common in the Alberta part of the basin (Fig. 5f) than in areas 'B' and 'C'. As in the case of strontium, this feature is apparently related to heavy mineral assemblages derived from granitic (pegmatitic) rocks.

### Chromium

Chromium exhibits a specific distribution. In area 'A' it is distinctly enriched in the Lazenby Lake Formation (Fig. 5g). The mean contents of chromium in samples from this formation exceed its clarkes of crustal abundance by more than 200%, whereas in samples from the underlying Manitou Falls Formation, by only 28%. The mean contents of the chromium in samples from the Fair Point Formation are even lower (by 87.1%) than its clarkes of crustal abundance. The mean contents of the basement rocks in the same area exceed the clarkes by 91%. The mean chromium contents in samples from areas 'B' and 'C' are lower than in the corresponding geological units in Alberta. The chromium is distributed inversely to uranium as demonstrated by vertical logs of selected drillholes from areas 'A' and 'C' (Fig. 6a, b). Distribution of chromium and uranium supports, according to these logs, a model for deposition of chromium by sedimentary syngenetic processes, whereas deposition of uranium is epigenetic and takes place from metalliferous brines at redox fronts.



**Figure 6.** Vertical distribution of U and Cr in samples from selected drillholes: (a) in the Alberta part of the Athabasca Basin, (b) in the Saskatchewan part of the Athabasca Basin. OB = overburden, LL = Lazenby Lake Formation, MF = Manitou Falls Formation, FP = Fair Point Formation, BSMT = Crystalline basement rocks.



**Figure 7.** Unrotated factor plot of elemental constituents: (a) associated with U and Th, and of Cr, from selected drillholes in the Alberta part of the Athabasca Basin, (b) associated with U and Ti, and of Cr, from selected drillholes in the Saskatchewan part of the Athabasca Basin.

The source for chromium was, apparently, deeper parts of the basement, composed of mafic to ultramafic rocks. Chromiferous detritus, derived from these rocks by erosion, was transported to the basin and deposited in a large fan of the Lazenby Lake Formation.

The ANOVA models are supported by results of factor analyses of selected samples. An unrotated factor plot for selected constituents from samples from area 'A' indicates that uranium has geochemical affinity to arsenic, molybdenum, boron, and nickel, whereas chromium exhibits entirely different geochemical behavior (Fig. 7a). An unrotated factor plot for constituents in samples from areas 'B' and 'C' shows also that chromium occupies a specific position, separated from the uranium and titanium groups of elements (Fig. 7b).

The chromium-bearing Athabasca sandstone might be comparable, to a certain degree, to some chromiferous deposits, which occur in the eastern Ugi Graben, in the Olekma-Vitim province of the Russian Republic (Bogdanov and Berlyand-Kozhevnikov, 1990). The chromium mineralization occurs in sandstone of the 100 m thick Precambrian Pravdinskaya Formation either as coastal-marine placers or as concentrations of chrome glauconite and clastic chromite grains associated with a redbed-greybed transition zone of the sandstone.

## DISCUSSION

Ores of the polymetallic deposits in the Athabasca Basin, such as the Key Lake, Cigar Lake, Collins Bay 'B' zone, and Midwest, consist, in addition to several generations of pitchblende and coffinite, of arsenides and sulpharsenides of nickel and cobalt; sulphides of nickel, copper, lead, molybdenum, iron, and zinc; and oxides and hydroxides of iron. Silver, gold, and platinum group minerals occur locally. Chlorite, illite, kaolinite, and siderite are the most common gangue minerals.

Ores of the monometallic deposits in the basin, such as Rabbit Lake and Eagle Point, consist of pitchblende (in massive, globular, and sooty forms), coffinite, and locally, secondary uranium minerals, such as boltwoodite, sklodowskite, and kasolite. Carbonates (calcite, dolomite, siderite), sericite, chlorite, clay minerals (illite, kaolinite), celadonite, and tourmaline (dravite) are common gangue minerals.

Elemental assemblages constituting these polymetallic and monometallic ores are also typical for the basement and cover rocks of the Alberta part of the basin. Furthermore, their characteristic distribution, controlled by the sub-Athabasca unconformity, suggests that the potential for discovery of the unconformity-type deposits in northeastern Alberta is high.

In addition, chromium enrichment of some upper parts of the Athabasca sequence, distant from the unconformity, points to another important metallogenic feature that requires further thorough investigation.

## ACKNOWLEDGMENTS

The study was carried out under the Canada-Alberta Agreement on Mineral Development. Co-operation of Messrs. W.N. Hamilton and W.A.D. Edwards from the Alberta Geological Survey is gratefully acknowledged. Thanks to Dr. R.T. Bell of the Geological Survey of Canada, who critically read the manuscript. Analyses of the samples were made by the Geochemical Laboratories of the Saskatchewan Research Council.

## REFERENCES

- Andrade, N.**  
1989: The Eagle Point uranium deposit, northern Saskatchewan, Canada; in *Uranium Resources and Geology of North America, Proceedings of a Technical Committee Meeting*, Saskatoon, 1987, International Atomic Energy Agency, TECDOC-500, Vienna, p. 455-490.
- Bogdanov, Yu. V. and Berlyand-Kozhevnikov, P.V.**  
1990: Cupriferous and chromiferous Precambrian deposits in Olekma-Vitim Province, U.S.S.R.; in *Program with Abstracts, 8th IAGOD Symposium*, August 12-18, 1990, Ottawa, Canada, p. A223.
- Edwards, W.A.D., Richardson, R.J.H., and Fildes, B.J.**  
1991: Geology and mineral potential of northeastern Alberta; Alberta Research Council, Open File Report 1991-6, 70 p.
- Fouques, J.P., Fowler, M., Knipping, H.D., and Schimann, K.**  
1986: The Cigar Lake uranium deposit: discovery and general characteristics; in *Uranium deposits of Canada*, (ed.) E.L. Evans, The Canadian Institute of Mining and Metallurgy, Special Volume 33, p. 218-229.
- Godfrey, J.D.**  
1960: Northeast corner of Alberta and adjacent area: its development and mineral potential; *The Canadian Institute of Mining and Metallurgy, Transactions*, v. 63, p. 162-171.  
1986a: Geology of the Precambrian Shield in northeastern Alberta, NTS 74L and NTS 74M; Alberta Research Council, Map.  
1986b: Mineral showings of the Precambrian Shield in northeastern Alberta, NTS 74L and NTS 74M; Alberta Research Council, Map.
- Godfrey, J.D. and Watanabe, R.Y.**  
1964: The mineralogical composition of an area of Precambrian Shield in northeastern Alberta; *Proceedings of the 22nd International Geological Congress*, 1964, New Delhi, India, p. 300-328.
- Hoeve, J. and Sibbald, T.I.I.**  
1978: On the genesis of Rabbit Lake and other unconformity-type uranium deposits; *Economic Geology*, v. 73, p. 1450-1473.
- Knipping, H.D.**  
1974: The concepts of supergene versus hypogene emplacement of uranium at Rabbit Lake, Saskatchewan, Canada; in *Formation of Uranium Deposits: International Atomic Energy Agency*, Vienna, p. 531-548.
- Kyser, T.K., Kotzer, T.G., and Wilson, M.R.**  
1989: Isotopic constraints on the genesis of unconformity-type uranium deposits; in *Geological Association of Canada/Mineralogical Association of Canada, Annual Meeting, Montreal; Program with Abstracts*, v. 14, p. A120.
- Laine, R.**  
1986: Uranium deposits of the Carswell structure; in *Uranium deposits of Canada*, (ed.) E.L. Evans; The Canadian Institute of Mining and Metallurgy, Special Volume 33, p. 155-169.
- Langford, F.F.**  
1986: Geology of the Athabasca Basin; in *Uranium deposits of Canada*, (ed.) E.L. Evans; The Canadian Institute of Mining and Metallurgy, Special Volume 33, 123-133.
- Ramaekers, P.**  
1990: Geology of the Athabasca Group (Helikian) in northern Saskatchewan; *Saskatchewan Energy and Mines, Report 195*, 49 p.

**Ruzicka, V.**

1984: Unconformity-related uranium deposits in the Athabasca Basin Region, Saskatchewan; in *Proterozoic Unconformity and Stratabound Uranium Deposits*, International Atomic Energy Agency, IAEA TECDOC - 315, Vienna, p. 219-267.

1989: Monometallic and polymetallic deposits associated with the sub-Athabasca unconformity in Saskatchewan; in *Current Research, Part C*, Geological Survey of Canada, Paper 89-1C, p. 67-79.

**Ruzicka, V. and LeCheminant, G.M.**

1987: Uranium investigations in Canada, 1986; in *Current Research, Part A*; Geological Survey of Canada, Paper 87-1A, p. 249-262.

**Sibbald, T.I.I., Quirt, D.H., and Gracie, A.J.**

1990: Uranium deposits of the Athabasca Basin, Saskatchewan [Field Trip 11]; 8th IAGOD Symposium Field Trip Guidebook, Geological Survey of Canada, Open File 2166, 56 p.

**Tremblay, L.P.**

1972: Geology of the Beaverlodge mining area, Saskatchewan; Geological Survey of Canada, Memoir 367, 265 p.

**Wallis, R.H., Saracoglu, N., Brummer, J.J., and Golightly, J.P.**

1986: The geology of the McClean uranium deposits, northern Saskatchewan; in *Uranium deposits of Canada*, (ed.) E.L. Evans; The Canadian Institute of Mining and Metallurgy, Special Volume 33, p. 193-217.

**Wilson, J.A.**

1985: Geology of the Athabasca Group in Alberta; Alberta Research Council, Bulletin, no. 49, Edmonton, Alberta, 78 p.

1986: Geology of the basement beneath the Athabasca Basin in Alberta; Alberta Research Council, Bulletin, no. 55, Edmonton, Alberta, 61 p.

1987: The geology and economic potential of the Athabasca Basin in Alberta; The Canadian Institute of Mining and Metallurgy, Bulletin 80 (898), p. 29-36.

---

Geological Survey of Canada Project 750010.

# An introduction to the "Aqxarneq gneisses" and retraction of the term "Chesterfield Fault Zone", District of Keewatin, Northwest Territories

Mikkel Schau and Subhas Tella  
Continental Geoscience Division

*Schau, M. and Tella, S., 1993: An introduction to the "Aqxarneq gneisses" and retraction of the term "Chesterfield Fault Zone", District of Keewatin, Northwest Territories; in Current Research, Part E; Geological Survey of Canada, Paper 93-1E, p. 185-189.*

---

**Abstract:** Areas north of Chesterfield Inlet are underlain by high grade metamorphic complexes with components of gabbroic-anorthosite and gabbro that are herein collectively referred to as Aqxarneq gneisses. They are part of a crustal scale, tilted and stacked succession of gneisses that represent upper and middle portions of the continental crust. The Aqxarneq gneisses encompass the previously postulated tectonic boundary between Rae and Hearne geological provinces but this boundary appears to be an Archean feature rather than a mid-Proterozoic boundary. The term "Chesterfield Fault Zone" which refers to a portion in the Aqxarneq gneisses region is retracted.

**Résumé :** Des régions situées au nord de l'inlet Chesterfield reposent sur des complexes de métamorphisme élevé qui ont des composantes d'anorthosite gabbroïque et de gabbro que les auteurs appellent «Gneiss d'Aqxarneq». Ces complexes font partie d'une succession de gneiss empilés et basculés d'échelle crustale qui représentent les parties supérieure et médiane de la croûte continentale. Le Gneiss d'Aqxarneq englobe la limite tectonique supposée des provinces géologiques de Rae et de Hearne, mais cette limite semble remonter à l'Archéen plutôt qu'au Protérozoïque moyen. Le nom «zone de failles de Chesterfield» qui désigne une partie de la région du Gneiss d'Aqxarneq est abandonné.

## INTRODUCTION

The purpose of this paper is to propose a provisional new name to accommodate new tectonic concepts that are developing in the Chesterfield Inlet region (Fig. 1) west of Hudson Bay (cf. Gordon, 1988; Sanborn-Barrie, 1993; Tella et al., 1993, and references therein), to outline the history of nomenclature of high grade rock suites exposed east of Baker Lake, and to suggest withdrawal of some terms. The new term, Aqzarneq gneisses, is proposed here to collectively represent all high grade rock suites in the region. The term "Aqzarneq" refers to the Inuktitut name for Chesterfield Inlet (Birket-Smith, 1933, p. 107).

## AQXARNEQ GNEISSES

The region along Chesterfield Inlet is characterized by high grade rocks and geophysical anomalies. Geological reconnaissance work showed the presence of granulites and several intrusive complexes of gabbroic anorthosites (Wright, 1967; Heywood, 1966, 1967). Results from seismic work led Barr (1969) and Ruffman (1969) to suggest that anomalous or thinned continental crust occurs between the Chesterfield Inlet and Baker Lake. A positive gravity anomaly is present along Chesterfield Inlet, and it is linked with the granulite facies rocks (Gibb and Halliday, 1975). The most striking anomaly is shown in horizontal gradient gravity maps (Goodacre et al., 1987). The idea of a continental suture along such geophysical anomalies was suggested as early as 1971 (Walcott and Boyd, 1971) and the concept is still extant (Hoffman, 1990).

Gordon (1988, p. 4), on the other hand suggested that:

"The Daly Bay Complex lies on an east trending regional gravity high that extends 550 km from Baker Lake to Coats Island. Rocks along this zone include granulite gneiss, gabbro, and anorthosite. Based on observations in the Daly Bay Complex, this zone is interpreted as a belt of Archean lower and middle crustal rocks, tectonically emplaced during the Aphebian."

"It is thus possible that the Daly Bay Complex is only part of a much larger region composed of imbricated slices of middle and lower crustal material. Support for this hypothesis comes from examination of the regional gravity field." (Gordon, 1988, p. 20).

Tella and Annesley (1987, 1988) mapped a 150 km transect across Chesterfield Inlet and showed that the Hanbury Island Shear Zone represents a tectonic remnant of a granulite grade ductile deformation zone consisting of highly strained rocks set within gneissic sheets. They traced the Hanbury rocks along a sinuous line projecting toward the Daly Bay Complex (Gordon, 1988) to the northeast.

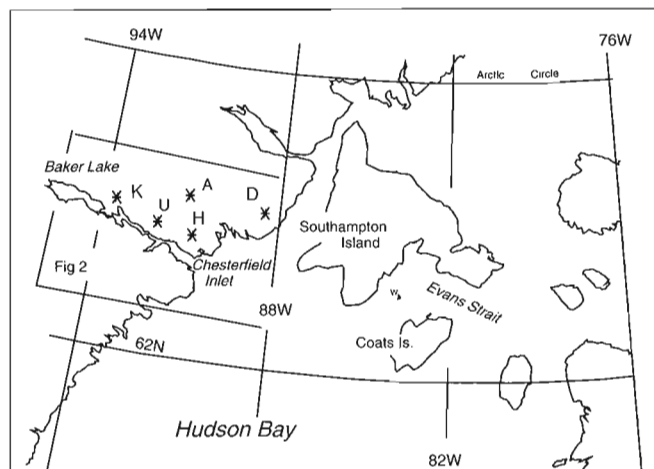
The conceptual model of shallow dipping undulating sheets developed for the region north of Rankin Inlet by Tella and Annesley (1987, 1988) and Tella et al. (1986) was

successfully used to predict distribution of various gneiss domains in the Gibson area (Tella et al., 1992). Mapping in the northern part of the Gibson Lake region discovered the Uvauk Complex (Tella et al., 1993) consisting of heterogeneously and ductilely deformed granulites and gabbroic anorthosites which are on strike with similar rocks of the Kramanituak Complex at Baker Lake to the west, and with the rocks of Hanbury Island and Daly Bay Complex to the east.

The age of formation of the gabbroic anorthosite complexes appear to be Archean, and their tectonic emplacement may be in part Proterozoic. Mangerite from the Kramanituak Complex is 2.57 Ga and probably dates the igneous emplacement (Schau et al., 1980). It was emplaced prior to:

- the deposition of the Dubawnt Group (Schau et al., 1982b),
- a 2.07 Ga lamprophyre dyke (Hunt and Roddick, 1987),
- gabbros which were metamorphosed about 1.98-1.89 Ga (Schau et al., 1982a, b),
- the Bowell Island metadiabase swarm which crosses the southern contact of the complex into to the adjacent metasediments to the south (Schau et al., 1982b) and
- reworked Ingilik Gneiss Rb-Sr isochron indicating local isotopic re-arrangements around 2.07 Ga just north of the Complex (Schau et al., 1982a).
- the formation of the high strain zone north of Baker Lake, which appears to be cut by a late Archean granodiorite (Schau et al., 1982b)

The Kramanituak Complex appears to have been emplaced into its current position before ca. 2 Ga. To the east, the Hanbury Island Shear zone is cut by a pluton with contradictory U/Pb systematics (1.77-2.56 Ga in Tella et al., 1992). Zircons from the Daly Bay Complex have an inherited component of probable Archean age while undeformed



**Figure 1.** General geography of Chesterfield region; K is Kramanituak Complex, U is Uvauk Complex, H is Hanbury Island Shear zone, D is Daly Bay Complex, A is Armit Lake Suite, and W is location of Walrus Island.

pegmatites cutting the high strain rocks at the edge of the Complex have a K/Ar age of 1.95 Ga suggesting that the complex was formed in Archean time and emplacement was complete by 1.95 Ga (Gordon, 1988). More detailed isotopic work is necessary to unravel the complexities, but the tectonic history of the complexes includes an Archean heritage and 1.95 Ga or older emplacement ages.

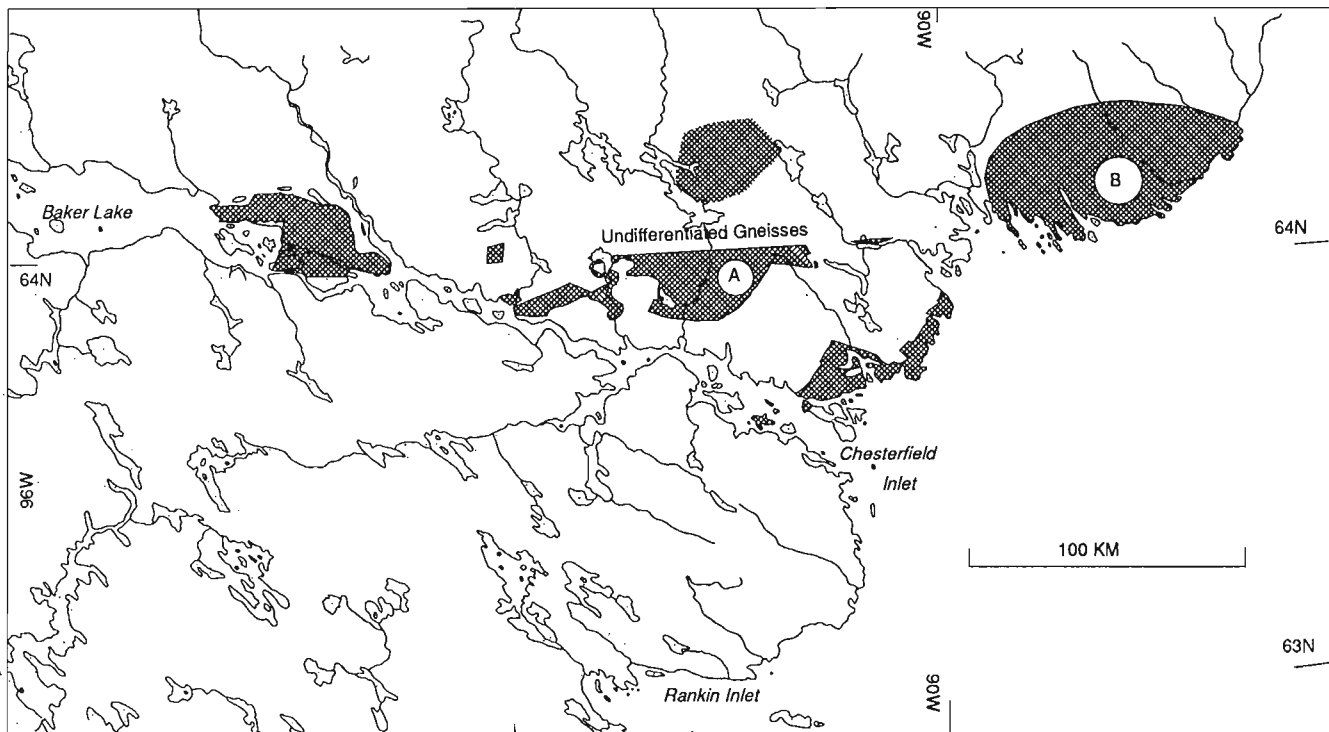
It is proposed that the high grade gneiss complexes should be collectively called the Aqxarneq gneisses (AG). The gneisses occur within a triangular area with a western apex at Baker Lake extending eastward for over 550 km. They are considered to be remnants of late Archean, ductilely deformed and discontinuous high grade gneiss sheets. They include the Kramanituur Complex, the Uvauk Complex, Hanbury Island Shear zone, Daly Bay Complex, and isolated anorthosite exposures on Walrus Island and Coats Island (Fig. 2). Less well known gabbroic complex at Armit Lake may also form part of the Aqxarneq gneisses (Fig. 2). Although gabbroic anorthosites are prominent in most of the complexes, they are not abundant in the areas A and B (Fig. 2). The gneisses are intercalated with relatively lower grade gneisses which are more abundant to the south, and higher grade ones to the north. The widest part of the Aqxarneq gneisses triangle is at least 150 km from south to north. Whether the crustal stacking alluded to above in the northern Keewatin is coeval and conjoined with the shear in the southern Keewatin awaits further structural mapping of gneisses and granulites and modern geochronology in the

intervening district of Keewatin. What is certain, though, is that the tectonic history of these continental rocks extends well into Archean time.

Although parts of the Aqxarneq gneisses are interpreted as allochthonous remnants, the overall tectonic significance is at present uncertain, but we note that gabbroic sills being recognized, elsewhere, are locally important in the middle crust, and they may represent multiple flat reflectors that seismic surveys are recording from the middle crust. For example, recent interpretations of the Bagdad Reflections in the CoCorp seismic data set from the Basin and Range to Colorado Plateau transect suggests that flat seismic reflectors are mostly sheets of basic intrusive rather than extension faults, thus indicating that mafic sills are common in the middle levels of the continental crust (Litak and Hauser, 1992). Possibly, the layered gabbroic-anorthosite components of the Aqxarneq gneisses may in part represent such sills that were subjected to subsequent tectonic dislocations and metamorphic transformations.

### RETRACTION OF THE TERM "CHESTERFIELD FAULT ZONE"

Heywood and Schau (1978) proposed that northeastern Arctic could be divided into distinct crustal blocks separated by steep fault zones in which little to moderate amount of displacement occurred. In this context the Chesterfield Fault



**Figure 2.** The western exposures of the Aqxarneq gneisses shown in dark crosshatch pattern. See text for letters A and B.

Zone (CFZ) was proposed as the southern boundary of the Armit Lake Block (see Fig. 1, Heywood and Schau, 1978). It was based on a fault mapped by Reinhardt and Chandler (1973) at Baker Lake and projected eastward along the southern margin of several anorthosite complexes (Heywood, 1967; Wright 1967).

Heywood and Schau (1978, p. 139) noted that:

"The Chesterfield fault [zone] appears to be a reverse fault system with a vertical separation of as much as 15 km(?) based on preliminary estimates of metamorphic contrast on either side of the system."

Schau and Ashton (1979, 1980) mapped and named an east-striking and steeply dipping brittle fault, at the mouth of Baker Lake, as the western extremity of the Chesterfield Fault Zone. Subsequent mapping to the north and west (Heywood and Schau, 1981; Schau et al., 1982b) delineated a 10 km wide, east-striking and steeply dipping high strain zone which was also referred to as the Chesterfield Fault Zone. It is cut by younger plutons to the east, overlain by younger rock units to the west, splays to the northeast, and cannot be traced for more than 80 km along strike.

We now emphasize that the term Chesterfield Fault Zone is obsolete and that the high grade rocks in this part of the zone are assigned to the Aqvarneq Gneisses.

The area through which the Chesterfield Fault Zone was postulated to pass became part of a Proterozoic suture, the Snowbird Tectonic zone (see p. 553-556, Hoffman, 1988), suture (see Fig. 4 and 5, Hoffman, 1988; Fig. 5, Hoffman, 1990), or line (p. 19-21, Hoffman, 1990), between two continental plates:

"The initial suggestion that the Snowbird [tectonic] zone might be a suture (Walcott & Boyd, 1971; Gibb & Halliday, 1974) was based on associated gravity anomalies" (Hoffman, 1988, p. 554).

The "suture" forms a part of the join between the two adjacent geological provinces: the Hearne to the southeast and the Rae to the northwest.

It is "an anastomosing system of granulite-facies mylonites and associated anorthosite-gabbro-pyroxenite bodies [which] extends for 1500 km from the edge of the shield at longitude 109°W to Hudson Bay at longitude 88°W" (Hoffman, 1990, p. 20).

Further, a "... steep gravity gradient also extends eastward across the northern Hudson Bay basin and converges with the Sugluk suture in Hudson Strait." (Hoffman, 1990, p. 20).

On northeastern Coats Island northeast- and east-trending, steeply dipping, amphibolite grade, high strain zones cut shallow dipping structures with little offset (see Fig. 1 for location). Lithology and structures on Coats Island south of the postulated suture are similar to those on Southampton Island to the north (Heywood and Sanford, 1976; Schau,

1991). The prominent negative gravity anomaly and associated steep gradients, attributed to the suture, are probably due to a sediment-filled Cretaceous graben in Evans Strait (Sanford and Grant, 1990), which is situated just north of Coats Island.

Hoffman (1990, p. 21) suggests that:

"The age of initial juxtaposition of the Hearne and Rae provinces (if they were ever separated) presumably postdates the Taltson magmatic arc (1.99-1.91 Ga) and predates the Baker basin (1.85 Ga)".

Simultaneous with the more recent mapping noted above, Hanmer and others mapped the Snowbird tectonic zone (Hanmer et al., 1991, 1992; Hanmer and Kopfe, 1993) in Saskatchewan and in the southeastern district of MacKenzie and concluded that, if there was a suture, it was not Proterozoic. Instead, Proterozoic brittle faulting was documented in addition to Archean ductile events as old as 3.5 Ga. Tella and Eade (1986) described granulite pods in a pre-existing fault reactivated during the Proterozoic along strike to the northeast. Hanmer and Kopf (1993) concluded that the distribution of lozenge-shaped, dense, mafic granulites is a likely cause for the geophysical anomaly that gave rise to the concept of the Snowbird tectonic zone, which is

"...independent of, and older than, the shearing which produced the mylonites" (Hanmer and Kopf, 1993, p. 43).

The above observations demonstrate that there is no steeply dipping Proterozoic "suture" (formed at ca. 1.875 Ga) that separates two geological provinces east of Baker Lake. It appears that the geophysical anomalies are made of segments with ages as disparate as Middle Archean and Cretaceous. The rocks along the east-trending zone east of Baker Lake shown in (Figures 1 and 2) are best described as the Aqvarneq gneisses and are to be considered as a distinct package of rocks when new tectonic reconstructions are proposed for this region.

## ACKNOWLEDGMENTS

The authors thank Drs. S. Hanmer and T.M. Gordon for their visit in the field and Dr. T.M. Gordon for his reviews of this paper.

## REFERENCES

- Barr, K.G.**  
1969: Evidence for variations in Upper mantle velocity in the Hudson Bay Area; in *Earth Science Symposium on Hudson Bay* (ed.) P.J. Hood; Geological Survey of Canada, Paper 68-53, p. 307-311.
- Birket-Smith, K.**  
1933: Geographical notes on the Barren Grounds; Report of the Fifth Thule Expedition 1921-24, Gyldendalske Boghandel, Nordisk Forlag, Copenhagen, v. 1, no. 4, 128 p.
- Gibb, R.A. and Halliday, D.W.**  
1974: Gravity measurements in southern District of Keewatin and southeastern District of Mackenzie, with maps; Earth Physics Branch, Gravity Map Series 124-131, Ottawa, 36 p.



- Gibb, R.A. and Halliday, D.W.** (cont'd.)  
1975: Gravity measurements in northern District of Keewatin and parts of District of Mackenzie and District of Franklin, N.W.T.; Earth Physics Branch, Gravity Map Series 139-148.
- Goodacre, A.K., Grieve, R.A.F., Halpenny, J.F., and Sharpton, V.L.**  
1987: Horizontal gradient of Bougier Gravity Anomaly Map of Canada; Geological Survey of Canada, Canadian Geophysical Atlas, Map 5, scale 1: 10 000 000.
- Gordon, T.M.**  
1988: Precambrian Geology of the Daly Bay area, District of Keewatin; Geological Survey of Canada, Memoir 422, 21 p.
- Hanmer, S. and Kopf, C.**  
1993: The Snowbird tectonic zone in District of Mackenzie, Northwest Territories; in *Current Research, Part C*; Geological Survey of Canada, Paper 93-1C, p. 41-52.
- Hanmer, S., Darrach, M., and Kopf, C.**  
1992: The East Athabasca mylonite zone: an Archean segment of the Snowbird tectonic zone in Northern Saskatchewan; in *Current Research, Part C*; Geological Survey of Canada, Paper 92-1C, p. 19-29.
- Hanmer, S., Ji, S., Darrach, M., and Kopf, C.**  
1991: Tantato Domain, northern Saskatchewan: a segment of the Snowbird tectonic zone; in *Current Research, Part C*; Geological Survey of Canada, Paper 91-1C, p. 121-133.
- Heywood, W.W.**  
1966: Geological notes on Operation Wager, Northwest Territories; Geological Survey of Canada, Paper 66-10.  
1967: Geological notes, northeastern District of Keewatin and southern Melville Peninsula, District of Franklin, Northwest Territories (parts of 46, 47, 56, 57); Geological Survey of Canada, Paper 66-40.
- Heywood, W.W. and Sanford, B.V.**  
1976: Geology of Southampton, Coats, and Mansel islands, District of Keewatin, Northwest Territories; Geological Survey of Canada, Memoir 382, 35 p.
- Heywood, W.W. and Schau, Mikkel.**  
1978: A subdivision of the northern Churchill Structural Province; in *Current Research, Part A*; Geological Survey of Canada, Paper 78-1A, p. 139-143.  
1981: Geology of Baker Lake Region, District of Keewatin; in *Current Research, Part A*; Geological Survey of Canada, Paper 81-1A, p. 259-264.
- Hoffman, P.F.**  
1988: United Plates of America, the birth of a craton: Early Proterozoic Assembly and Growth of Laurentia; *Annual Review of Earth and Planetary Sciences*, v. 16, p. 543-603.  
1990: Subdivision of the Churchill Province and the extent of the Trans-Hudson Orogen; in *The Early Proterozoic Trans-Hudson Orogen of North America* (ed.) J.F. Lewry, and M.R. Stauffer; Geological Association of Canada, Special Paper 37, p. 15-39.
- Hunt, P.A. and Roddick, J.C.**  
1987: A compilation of K-Ar Ages, Report 17; in *Radiogenic Age and Isotopic Studies, Report 1*, Geological Survey of Canada, Paper 87-2, p. 143-210.
- Litek, R.K. and Hauser, E.C.**  
1992: The Bagdad Reflection Sequence as tabular mafic intrusions: Evidence from seismic modeling of mapped exposures. *Geological Society of America Bulletin*, volume 104, no. 10, p. 1315-1325.
- Reinhardt, E.W. and Chandler, F.W.**  
1973: Gibson-McQuoid Lakes map-area, District of Keewatin; in *Report of Activities, Part A*; Geological Survey of Canada, Paper 73-1A, p. 162-165.
- Ruffman, A.**  
1969: Investigations of the crust in the Hudson Bay region; in *Earth Science Symposium on Hudson Bay*, (ed.) P.J. Hood; Geological Survey of Canada, Paper 68-53, p. 307-311.
- Sanborn-Barrie, M.**  
1993: Structural investigation of high-grade rocks of the Kramanitar complex, Baker Lake area, Northwest Territories; in *Current Research, Part C*; Geological Survey of Canada, Paper 93-1C, p. 137-146.
- Sanford, B.V. and Grant, A.C.**  
1990: New findings relating to the stratigraphy and structure of the Hudson platform; in *Current Research, Part D*; Geological Survey of Canada, Paper 90-1D, p. 17-30.
- Schau, Mikkel**  
1980: Zircon ages from a granulite-anorthosite complex and a layered gneiss complex northeast of Baker Lake, District of Keewatin; in *Rubidium-Strontium and Uranium-Lead Isotopic Age Studies, Report 3*; in *Current Research, Part C*; Geological Survey of Canada, Paper 80-1C, p. 237-238.  
1991: Orthogneisses, paragneisses and high strain zones on northeast Coats Island, District of Keewatin, N.W.T.; in *Current Research, Part C*; Geological Survey of Canada, Paper 91-1C, p. 195-203.
- Schau, M. and Ashton, K.E.**  
1979: Granulites and plutonic complexes northeast of Baker Lake, District of Keewatin; in *Current Research, Part A*; Geological Survey of Canada, Paper 79-1A, p. 311-316.  
1980: Geological map of the granulite and anorthosite complex at the southeast end of Baker Lake (56D1, 56C4, parts of 55M16 and 55N13); Geological Survey of Canada, Open File 712.
- Schau, M., Loveridge W.D., and Stevens, R.D.**  
1982a: Updated Rb-Sr dates from the Ingilik Point Gneiss Complex, Baker Lake region, District of Keewatin; in Rb-Sr and U-Pb Isotopic Age Studies, Report 5; in *Current Research, Part C*; Geological Survey of Canada, Paper 82-1C, p. 169-171.
- Schau, M., Tremblay F., and Christopher, A.**  
1982b: Geology of Baker Lake map area, District of Keewatin: a progress report; in *Current Research, Part A*; Geological Survey of Canada, Paper 82-1A, p. 143-150.
- Tella, S. and Annesley, I.R.**  
1987: Precambrian geology of parts of Chesterfield Inlet map area, District of Keewatin; in *Current Research, Part A*; Geological Survey of Canada, Paper 87-1A, p. 25-36.  
1988: Hanbury Island Shear Zone, a deformed remnant of a ductile thrust, District of Keewatin, N.W.T.; in *Current Research, Part C*; Geological Survey of Canada, Paper 88-1C, p. 283-289.
- Tella, S. and Eade, K.E.**  
1986: The occurrence and possible tectonic significance of high pressure granulite fragments in the Tulemalu Fault Zone, District of Keewatin, N.W.T., Canada; *Canadian Journal of Earth Sciences*, v. 23, p. 1950-1962.
- Tella, S., Annesley, I.R., Borradaile, G.J., and Henderson, J.R.**  
1986: Precambrian geology of parts of Tavani, Marble Island, and Chesterfield Inlet map areas, District of Keewatin: a progress report; Geological Survey of Canada, Paper 86-13, 20 p.
- Tella, S., Schau, M., Armitage, A.E., and Loney, B.C.**  
1993: Precambrian geology and economic potential of the northeastern parts of Gibson Lake map area, District of Keewatin, Northwest Territories; in *Current Research, Part C*; Geological Survey of Canada, Paper 93-1C, p. 197-208.
- Tella, S., Schau, M., Armitage, A.E., Seemayer, B., and Lemkow, D.**  
1992: Precambrian geology and economic potential of the Meliadine Lake-Barbour Bay region, District of Keewatin, Northwest Territories; in *Current Research, Part C*; Geological Survey of Canada, Paper 92-1C, p. 1-11.
- Walcott, R.I. and Boyd, J.B.**  
1971: The gravity field of northern Alberta, and part of Northwest Territories and Saskatchewan, with maps; Earth Physics Branch, Gravity Map Series, no. 103-111, Ottawa, 13 p.
- Wright, G.M.**  
1967: Geology of the southeastern Barren Grounds, parts of the Districts of Mackenzie and Keewatin; Geological Survey of Canada, Memoir 350, 91 p.



# Preliminary report of the Quaternary geology of the Canadian Shield of northeastern Alberta<sup>1</sup>

Jan M. Bednarski

Terrain Sciences Division, Calgary

*Bednarski, J.M., 1993: Preliminary report of the Quaternary geology of the Canadian Shield of northeastern Alberta; in Current Research, Part E; Geological Survey of Canada, Paper 93-1E, p. 191-196.*

---

**Abstract:** Preliminary investigations of Quaternary geomorphology on the Canadian Shield of northeastern Alberta has led to a working model of glacial history. Two regional ice flow patterns, one from the northeast, the other from the east and east-southeast, suggest two lobes of the Laurentide Ice Sheet covered the area. Overall, the ice front retreated towards the east and northeast. A major stillstand or readvance of the ice front produced an extensive moraine system informally named Slave Moraine. The moraine is thought to be correlative with the Cree Lake Moraine of northeastern Saskatchewan.

As the ice front retreated, glacial Lake McConnell inundated Slave River lowlands and Lake Athabasca basin up to ~305 m a.s.l. Subsequent retreat of the ice front created numerous ephemeral lakes and diverted meltwater drainages. Secondary dispersal of glaciogenic sediments by meltwater outflow was important in the eastern part of the study area.

**Résumé :** Les études préliminaires de la géomorphologie quaternaire du Bouclier canadien dans le nord-est de l'Alberta ont permis d'établir un modèle fonctionnel de l'histoire glaciaire. La présence de deux types d'écoulement glaciaire régional, l'un du nord-est, l'autre de l'est et de l'est-sud-est, porte à croire que deux lobes de l'Inlandsis laurentidien ont recouvert la région. Globalement, le front glaciaire a reculé vers l'est et le nord-est. Une halte ou réavancée importante du front glaciaire a produit un vaste système morainique auquel on a donné le nom informel de «moraine de Slave». La moraine serait correlative de la Moraine de Cree Lake qui se situe dans le nord-est de la Saskatchewan.

Pendant le recul du front glaciaire, le Lac glaciaire McConnell a inondé les basses terres de la rivière Slave et le bassin du lac Athabasca jusqu'à environ 305 m au-dessus du niveau de la mer. Le recul subséquent du front glaciaire a créé de nombreux lacs éphémères et détourné le cours des eaux de fonte. La dispersion secondaire des sédiments glaciogéniques par les eaux de fonte a été importante dans la partie est de la région à l'étude.

---

<sup>1</sup> Contribution to Canada-Alberta Agreement on Mineral Development (1992-1995), a subsidiary agreement under the Canada-Alberta Economic and Regional Development Agreement.

## INTRODUCTION

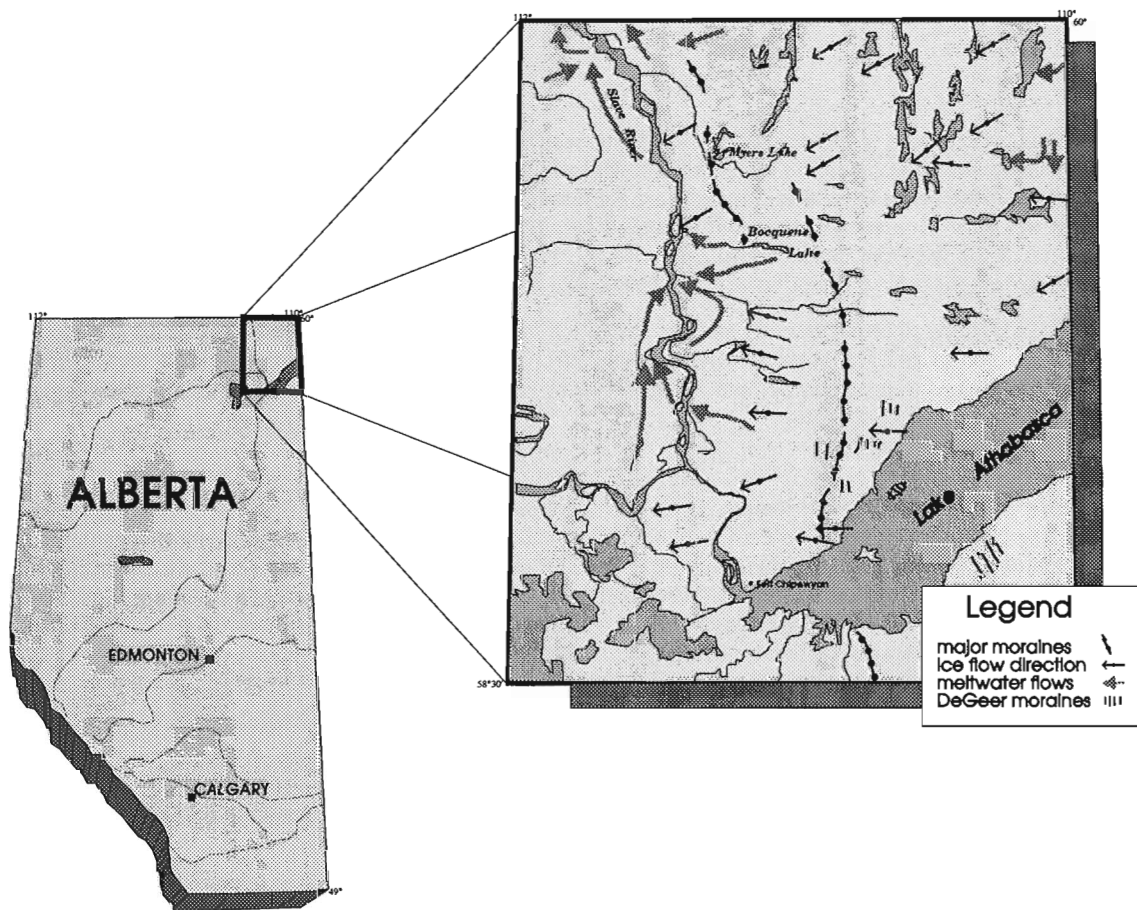
A comprehensive study of the surficial geology on the Shield of Alberta (NTS 74M and part of 74L; Fig. 1) began in the summer of 1992 to assist mineral exploration and provide an inventory of granular resources. Major outputs of the project will consist of a 1:250 000 map of surficial geology and pertinent information on glacial dispersal, drift geochemistry, and till lithology, with selected samples analyzed for kimberlite indicator minerals.

The surficial units are initially interpreted and plotted on 1:60 000 scale aerial photographs and subsequently verified during the field seasons. Glacial drift (including till, outwash, and lacustrine sediments) is sampled along transects at ~5 km intervals, providing average density of one sample per 30 km<sup>2</sup>.

## PHYSIOGRAPHY

The study area is mainly upland of Precambrian Shield which outcrops along extensive ridges that follow the regional structural trends (Fig. 2). Local relief is usually less than 150 m and the overall surface of the Shield slopes gently from >400 m above sea level (a.s.l.) in the east to ~215 m a.s.l. in the west along Slave River. West of Slave River the Precambrian basement is covered by horizontally bedded Middle Devonian rocks.

The Shield uplands are bound by lowlands occupied by Lake Athabasca to the south, Peace/Athabasca Delta to the southwest, and Slave River to the west. Lake Athabasca (213 m a.s.l.) drains to the north via Slave River into Great Slave Lake (156 m a.s.l.). Most of the study area is drained



**Figure 1.** Location and generalized geomorphology of the study area. Note two major ice flow directions: from the northeast in the northern area, and from the east out of Lake Athabasca Basin. An extensive moraine system east of Slave River marks a major stillstand or minor readvance of the retreating Laurentide Ice Sheet.



**Figure 2.** Glacially scoured bedrock in the north central part of the study area. Ice flow was from the lower left to the upper right. Crosscutting channels were incised by glacial meltwater during ice retreat. ISPG 4091-1

by the Slave River system, with the exception of the northeast corner which drains northward into Great Slave Lake via the Taltson River system.

## SURFICIAL MATERIALS

Surficial cover is generally sparse over the Shield, especially on bedrock ridge crests. Depressions between ridges are usually poorly drained and swampy. The most extensive surficial cover occurs in the flat lowlands of Peace/Athabasca Delta and Slave River (Bayrock, 1972a, b). These areas are blanketed by late Pleistocene to Holocene glaciolacustrine, glaciofluvial, and eolian sediments; bedrock outcrops are rare.

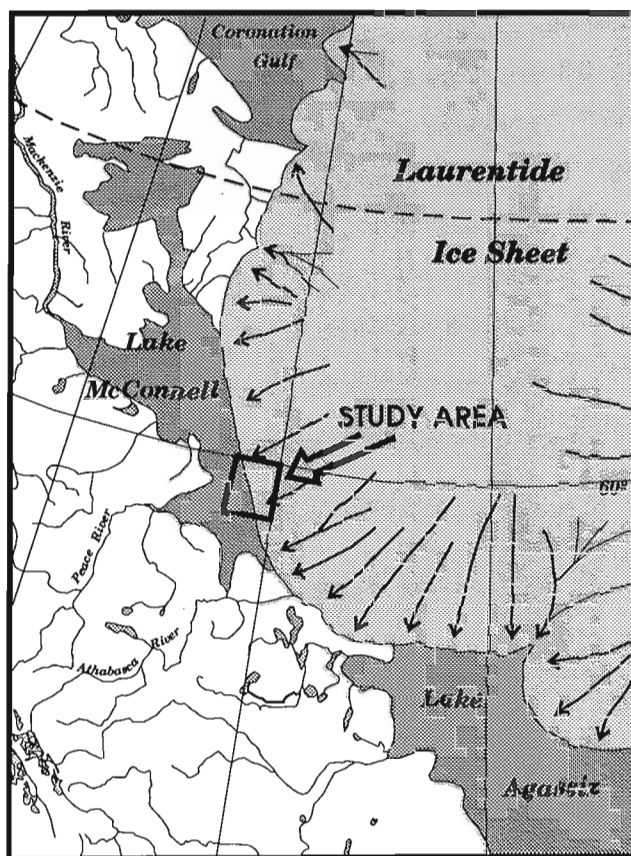
Texturally, the surficial deposits are very sandy, reflecting the crystalline basement outcrops of the area. Till overlying the local rock contains an abundance of large angular to subangular igneous and metamorphic rocks in a sandy to silty-sand matrix. The till has a very similar texture to colluvium or coarse outwash diamictons, however, it can be distinguished by the relative abundance of erratics and striated clasts. Till is very sparse over the Shield and is usually found in lee-side hollows in the bedrock.

Lacustrine, littoral, and eolian deposits are all texturally similar, particularly deposits derived from the Athabasca Group (Wilson, 1985). Genetic interpretations are complicated by the fact that extensive reworking took place during deglaciation. In addition to reworking by meltwater, parts of the region are dominated by eolian sand sheets and dunes. These formed during the early Holocene when strong katabatic winds, blowing off the Laurentide Ice Sheet, remobilized sediment on recently exposed lake bottoms.

## QUATERNARY GEOLOGY

The landform assemblages recognized through preparatory mapping led to a working model of glacial geomorphology. The directions of ice flow measured in this study, and reported by Godfrey (1986), are consistent with westerly- and south-westerly-flowing ice from the Keewatin Sector of the Laurentide ice sheet (Fig. 3). Glacial erosion and dispersal of the bedrock was controlled by both the surface morphology of the ice sheet and local influences of the underlying topography. The structural relief of the Shield has been extensively modified by westerly- and southwesterly-flowing ice, especially in the northern part of the area where intensive glacial erosion crosscut the bedrock structure. Under such conditions till is only preserved in hollows and the lee sides of protuberances.

On the basis of dominant ice flow directions, the study area can be divided into two zones. North of the latitude of Bocquene Lake the dominant ice flow was from the northwest, whereas south of Bocquene Lake the dominant flow was



**Figure 3.** Paleogeography of the Laurentide Ice Sheet about 10 000 years BP (after Dyke and Prest, 1987). Glacial Lake McConnell dominates the margin of the ice sheet in the study area.

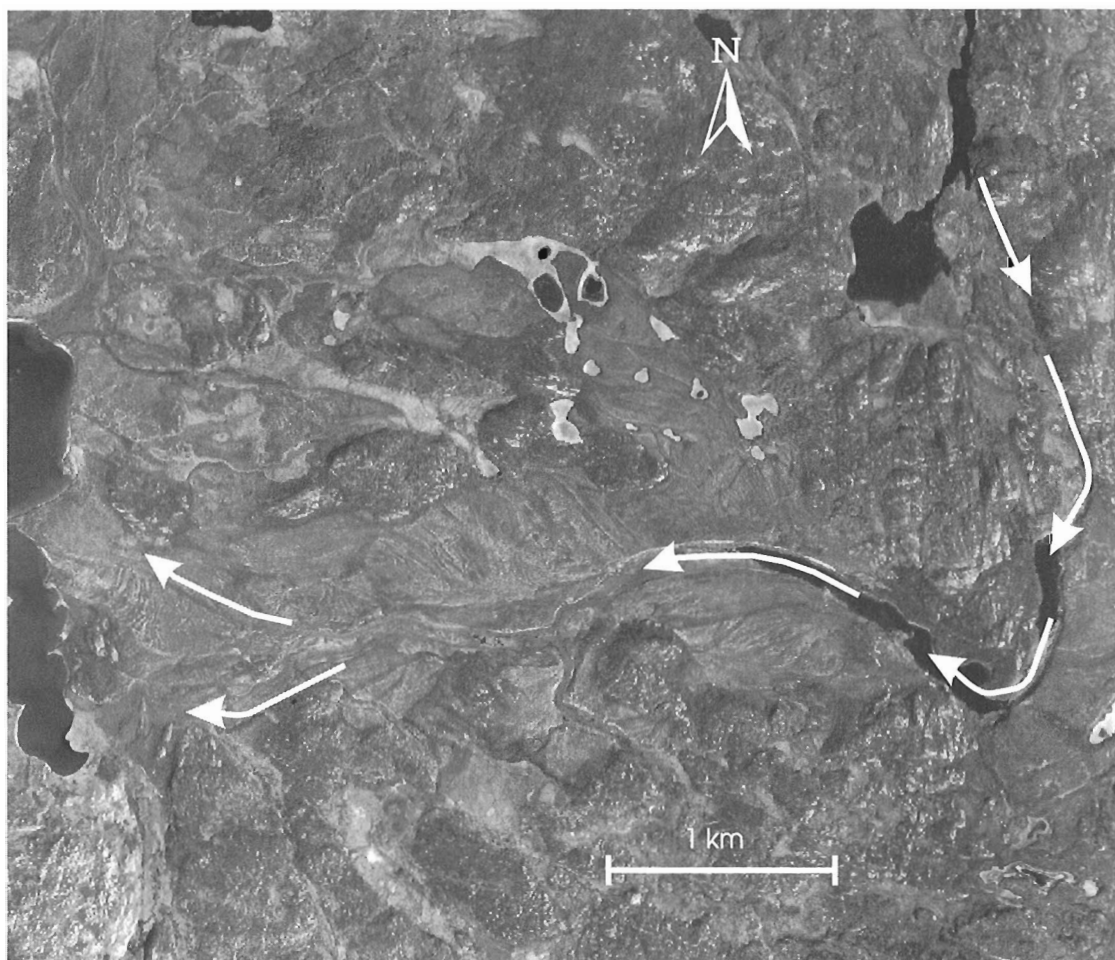


**Figure 4.** An excavation in Slave Moraine on the western end of Myers Lake exposing tens of metres of ice-contact stratified drift. Foreset bedding dips to the west into Lake McConnell. ISPG 4091-2

from the east or east-southeast (Fig. 1). The two zones are also separated by an east-west belt of thicker surficial cover and, hence, are thought to record two lobes of ice emanating from the Laurentide Ice Sheet. The southern lobe occupied the trough currently occupied by Lake Athabasca. Further mapping will determine if the lobes reflect a prevailing configuration of the ice sheet or whether they were solely a deglacial feature.

On the whole, glaciogenic deposition was concentrated along the ice sheet margin and in proglacial depressions as the ice front retreated eastward. The retreat was marked by stillstands, or minor readvances, which resulted in local accumulations of ice-contact gravels. The best example of this is a 120 km moraine system east of Slave River (informally named Slave Moraine here; Fig. 1). The north-trending moraine is tentatively correlated with Cree Lake Moraine of northern Saskatchewan (~10 ka BP; Prest, 1970; Dyke and Prest, 1987).

As the ice front retreated to the position of Slave Moraine, Slave River lowlands were inundated from the north by glacial Lake McConnell, a huge ice-marginal lake (Craig, 1965). The



**Figure 5.** A large braid delta indicating strong outflow to the west, contrary to the present drainage. Southward drainage was diverted by a lobe of ice which was still occupying Lake Athabasca basin.

Laurentide Ice Sheet dammed Lake McConnell to the east and thick lacustrine sediments were deposited in Slave River lowlands (Fig. 3). Raised shorelines indicate that glacial Lake McConnell reached at least 305 m a.s.l. over Lake Athabasca and ~310 m a.s.l. south of Great Slave Lake (Lemmen, 1990a, b). Most of Slave Moraine lies below this elevation and was deposited in a subaqueous environment. A borrow pit at the western end of Myers Lake suggests that Slave Moraine is composed largely of ice-contact glaciofluvial gravels tens of metres thick (Fig. 4). Moreover, DeGeer moraines are associated with the southern section of the Slave Moraine, just north of Lake Athabasca (Fig. 1). These moraines have an amplitude of ~150 m and imply retreat of the ice front in standing water.

Eastward retreat of the ice front from Slave Moraine caused glacial Lake McConnell to overtop the moraine and inundate the proximal lowlands. Raised strandlines are common on both the proximal and distal sides of the moraine with descending beaches marking the regression of Lake McConnell. As Lake McConnell fell, Slave Moraine blocked many westward flowing drainages forming numerous lakes. These lakes eventually drained as moraine segments were breached and incised.

Other ephemeral lakes ponded above the level of Lake McConnell as the ice retreated across the Shield uplands and many depressions were filled with sandy glaciolacustrine sediments deposited at this time. These lakes drained and acquired their present configuration as integrated drainage networks developed during the Holocene.

The retreating ice margin not only impounded lakes but also obstructed and redirected meltwater flow (Fig. 1). Scour channels and outwash indicate a predominantly westward outflow of meltwater from the ice front. Structural troughs were exploited by glacial meltwaters. In some cases Slave Moraine crosscuts the meltwater channels suggesting that the channels were initially subglacial in origin.

Large braided channels and deltas provide evidence of meltwater divergence in the eastern parts of the study area, above the maximum level of Lake McConnell (Fig. 1, 5). These meltwater systems appear to be associated with the interlobate zone described above. The braid patterns on the outwash clearly show that the direction of outflow was to the west, contrary to the southern slope of the land. This abrupt change in outflow direction is the result of obstructing ice, probably the glacier lobe occupying Lake Athabasca trough. Figure 5 shows an example of a characteristic "hooked" channel pattern where early southward flow of meltwater was abruptly redirected westward. This pattern of drainage divergence is repeated several times throughout the area and is very useful in reconstructing the pattern of ice retreat.

By ~8700 BP, ice retreating from the Lake Athabasca trough opened an embayment in Lake McConnell, termed glacial Lake Athabasca by Schreiner (1984), recorded by strandlines at least 90 m above the north shore of Lake Athabasca. Differential isostatic rebound, with the resultant lowering of lake level, caused glacial Lake Athabasca to separate from Lake McConnell along a prominent bedrock sill near Fort Smith (Craig, 1965). Lake McConnell drained

rapidly to the north through the Mackenzie River system. By ~8200 BP Lake McConnell receded north of Fort Smith with a water level of ~204 m a.s.l. (Vanderburgh and Smith, 1988) and the northward flowing Slave River entrenched large channels within the lowlands (Fig. 1). Most lake levels declined throughout the early Holocene as integrated drainage patterns developed. Prominent terraces found ~10 m above many of the larger lakes in the area either relate to this time, or are the result of Recent climate change.

## ECONOMIC GEOLOGY

The main purpose of this project is to interpret the glacial history so that it may be applied to mineral exploration. The Shield of Alberta potentially has significant mineral deposits which were overridden, eroded, and dispersed by glaciers during the Quaternary. The composition of glaciogenic sediments, therefore, should identify target areas with significant mineral enrichment. However, vital information on the probable location of mineral occurrences can only be determined once the ice flow patterns and relative chronology are established.

Till, being a product of direct glacial deposition, is the most desirable sampling medium for analysis. Although till is sparse in the area and usually confined to lee-side protuberances, the recognition of two distinct lobes within the area has important implications for interpreting glacial dispersal.

In areas where till cover is thin and discontinuous, outwash sediments may also be used as a prospecting medium, however, as this is secondary dispersal of glaciogenic sediments, the multifarious evolution of drainage patterns must first be deciphered. This should be possible with the braided channel complexes described in the previous section.

## ACKNOWLEDGMENTS

Adept field assistance was provided by R. Gault. Logistical service by Loon Air, Fort Smith was greatly appreciated. I would also like to thank the people at the Andrew Lake Lodge for their generous hospitality. Critical review by D. Lemmen was much valued.

## REFERENCES

- Bayrock, L.A.**  
 1972a: Surficial geology, Fort Chipewyan NTS 74L; Alberta Research Council Map, scale 1:250 000 with marginal notes.  
 1972b: Surficial geology, Peace Point and Fitzgerald west of 111°20', NTS 84P, 74M; Alberta Research Council Map, scale 1:250 000 with marginal notes.
- Craig, B.G.**  
 1965: Glacial Lake McConnell, and the surficial geology of parts of Slave River and Redstone River map-areas, District of MacKenzie; Geological Survey of Canada, Bulletin 122, 33 p.
- Dyke, A.S. and Prest, V.K.**  
 1987: Late Wisconsinan and Holocene history of the Laurentide Ice Sheet; *Géographie physique et Quaternaire*, v. 41, p. 237-263.

**Godfrey, J.D.**

1986: Geology of the Precambrian Shield in northeastern Alberta; Alberta Research Council, Map 1986-11, scale 1:250 000.

**Lemmen, D.S.**

1990a: Surficial materials associated with glacial Lake McConnell, southern District of MacKenzie; in Current Research, Part D; Geological Survey of Canada, Paper 90-1D, p. 79-83.

1990b: Surficial geology of the Great Slave Lake region, N.W.T.: evolution of the central basin of glacial Lake McConnell; Canadian Association of Geographers, 1990 Annual Meeting, Program and Abstracts, p. 141.

**Prest, V.K.**

1970: Quaternary geology of Canada; in Geology and Economic Minerals of Canada, (ed.) R.J.W. Douglas; Geological Survey of Canada, Economic Geology Report 1, p. 676-764.

**Schreiner, B.T.**

1984: Quaternary geology of the Precambrian Shield, Saskatchewan; Saskatchewan Geological Survey, Report 221, 106 p.

**Vanderburgh, S. and Smith, D.G.**

1988: Slave River delta: geomorphology, sedimentology, and Holocene reconstruction; Canadian Journal of Earth Sciences, v. 25, p. 1990-2004.

**Wilson, J.A.**

1985: Geology of the Athabasca Group in Alberta; Alberta Research Council, Bulletin No. 49, 78 p.

---

Geological Survey of Canada Project 920057 IC



# Preliminary report on peralkaline silica-undersaturated rocks in the Kipawa syenite gneiss complex, western Quebec

K.L. Currie and John Gittins<sup>1</sup>  
Continental Geoscience Division

*Currie, K.L. and Gittins, J., 1993: Preliminary report on peralkaline silica-undersaturated rocks in the Kipawa syenite gneiss complex, western Quebec; in Current Research, Part E; Geological Survey of Canada, Paper 93-1E, p. 197-205.*

---

**Abstract:** The Kipawa syenite gneiss complex forms a thin layer of alkaline igneous rocks, deformed during amphibolite-grade metamorphism, which outcrops over a strike length of more than 50 km. Near massive to L>S nepheline syenite forms a central core flanked by varying thicknesses of biotite syenite gneiss, quartz syenite, gneiss and alkali granite. The rocks were complexly folded and refolded during tectonic transport to the northwest. Along a syenite-marble contact, a zone of peralkaline melasyenite 1500 m long and <5 m thick contains rare Na-rich minerals, (eudialyte, vlasovite) as well as Ca, F, and REE-bearing species including fluorite, mosandrite, hiortdahlite, britholite, and agrellite in deformed segregations and massive pegmatites. These unusual rocks probably formed by metasomatism and partial melting of alkaline igneous rocks during metamorphism about 1000 Ma ago, an event followed by rapid uplift.

**Résumé:** Le complexe de gneiss syénitique de Kipawa forme une mince couche de roches ignées alcalines qui ont été déformées au cours du métamorphisme du faciès des amphibolites et qui affleurent parallèlement à la direction sur plus de 50 km. Une syénite néphélinique quasi massive à L>S forme un noyau central entouré de gneiss syénitique à biotite, de gneiss syénitique quartzifère et de granite alcalin de diverses épaisseurs. Les roches ont été plissées et replissées de façon complexe au cours du transport tectonique vers le nord-ouest. Le long d'un contact de syénite-marbre, une zone de syénite mélanocrate hyperalkaline de 1 500 m de longueur et de moins de 5 m d'épaisseur contient quelques rares minéraux riches en Na (eudialyte, vlasovite) ainsi que des espèces à Ca, à F et à éléments des terres rares, notamment la fluorite, la mosandrite, l'hiortdahlite, la britholite et l'agrellite, dans des ségrégations déformées et des pegmatites massives. Ces roches inhabituelles se sont probablement formées il y a 1 000 Ma par métasomatisme et fusion partielle de roches ignées alcalines au cours d'une période de métamorphisme qu'a suivi un soulèvement rapide.

---

<sup>1</sup> Department of Geology, University of Toronto, Toronto, Ontario M5S 1A1

## INTRODUCTION

Silica-undersaturated rocks with  $(Na+K)/Al > 1.1$  form two major complexes in eastern Canada (Red Wine (Curtis and Currie, 1981) and Mount Saint Hilaire (Currie et al., 1986)) which contain large amounts of acmite, arfvedsonite, eudialyte, and rare Na-Zr and Na-Ti silicates. A third, smaller, occurrence of such rocks near Kipawa, Quebec (Lyll, 1959; Rive, 1973; Tremblay-Clark and Kish, 1978; Allan, 1992) is relatively unknown, although numerous workers have studied its rare and unusual minerals (Aaarden and Gittins, 1974; Ansell et al., 1980; Berry et al., 1972; Gittins et al., 1976; Hicks, 1959; Roberts and Bonardi, 1983; Plant and Roberts, 1979). This report outlines initial field mapping and petrological results of a study of the Kipawa syenite gneiss complex and its unique peralkaline silica-undersaturated rocks.

## GEOLOGICAL SETTING

The Kipawa region lies on the northern fringe of the Grenville Province of the Canadian Shield. According to preliminary reconnaissance studies by A. Davidson (pers. comm., 1992) the Kipawa syenite complex lies within a stack of tectonic slices, transported to the northwest, along the contact of a slice of Proterozoic rocks to the south with a slice of reworked Archean rocks to the north.

To the north, structurally below the syenite complex, the dominant rocks are coarse grained, pink, near massive to gneissic biotite-hornblende granodiorite to quartz monzonite. Sparse primary hornblende is commonly rimmed by biotite and both are oxidized to give characteristic hematitic spotting. Minor schlieren and inclusions of fine grained, buff, granoblastic biotite granitic gneiss, seams of biotite gneiss up to 50 cm wide, and mylonitic granitic gneiss occur locally, as well as concordant pegmatitic lenses ("sweats") constituting up to 30% of the rock.

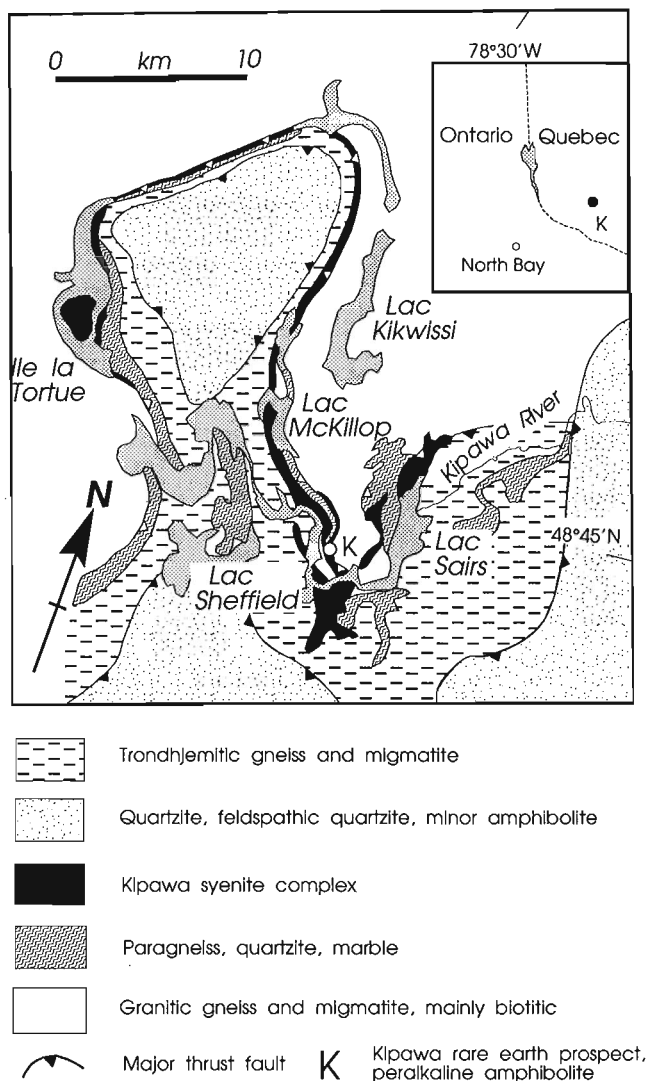
To the south and east, structurally above the syenite complex, moderately foliated grey to pale pink biotite trondhjemite dominates, but a discontinuous, sinuous belt of quartzite, feldspathic quartzite, and quartz-muscovite-potassium feldspar gneiss stretches from Lac Sairs to Ile la Tortue (Fig. 1; Lyll, 1959; Rive, 1973). Two marble layers less than 5 m thick occur west of Lac Sairs. Small bodies of grey muscovite granite are associated with the paragneiss. East of Lac Sheffield a gabbro sill lies in the metasedimentary rocks. Lenses of melanocratic garnet-biotite amphibolite within paragneiss probably formed from mafic intrusions.

## GENERAL GEOLOGY OF THE KIPAWA SYENITE COMPLEX

Syenite and syenite gneiss extend more than 50 km (Fig. 1; Lyll, 1959; Rive, 1973; Tremblay-Clark and Kish, 1978) along the contact between the paragneiss and foliated biotite-amphibole granodiorite. No locality has been found

where syenite is clearly absent from this contact, although locally syenite occurs intercalated with the paragneiss. The syenite exhibits a consistent, crudely symmetrical zoning. A central core of amphibole-pyroxene syenite is flanked by biotite syenite, which is in turn enveloped by quartz syenite and peralkaline granite. The thickness of both the complex and various layers within it varies along strike from a few centimetres to tens of metres.

The amphibole-pyroxene syenite consists of medium grained, granoblastic, grey to buff rock composed of string perthite, oligoclase, small amounts of nepheline, richteritic amphibole, green aegirine, and accessory zircon, sphene, and apatite. Foliation, defined by centimetre-scale compositional



**Figure 1.** Regional setting of the Kipawa syenite complex region (geology modified after Ministère de l'Énergie et des Ressources de Québec Map M-313, Gites Minéraux du Québec, Feuille North Bay, 31L, with additional information from A. Davidson). Relative ages of some units are uncertain. Inset shows the position of the Kipawa syenite complex (K) relative to North Bay and the Ontario-Quebec border.

layering, is ubiquitous but weak, and the dominant fabric is a lineation defined by spindle-shaped aggregates of amphibole and pyroxene up to 2 cm in length. A typical, easily accessible occurrence of this core syenite occurs at the bridge crossing the outlet to Lac McKillop.

This core syenite grades by appearance of biotite, to flanking white to pale grey biotite syenite consisting of granoblastic microcline, albite, an occasional trace of nepheline, distinctive lustrous black biotite and accessory zircon and apatite. Because of strong alignment and local concentration of biotite, this rock commonly appears schistose. Biotite syenite appears to be extremely persistent, although the thickness of this lithology rarely exceeds 2 m. Biotite syenite is well exposed in a road cut about 350 m north of the bridge crossing the outlet of Lac McKillop.

Biotite syenite in turn grades into pink to red syenite which contains varying amounts of quartz, blue riebeckitic amphibole, and acmitic pyroxene. The red colour is a guide to the presence of quartz and strongly sodic minerals. These quartz-bearing syenites and peralkaline granites are considerably more leucocratic than the other syenites, with a colour index generally <10 compared to 20-30 for the core syenite and biotite syenite. Contacts between these peralkaline quartz-bearing rocks and the surrounding granitic gneisses appear to be completely gradational over a width of

tens of metres. The quartz-bearing peralkaline rocks generally appear little deformed, and in a few cases are massive, although weak layering without mineral orientation is more common. These quartz-bearing peralkaline rocks are well exposed in trenches and stripped areas on a Unocal Canada rare-earth prospect east of Lac Sheffield (Allan, 1992).

## GEOLOGICAL SETTING OF THE RARE MINERAL OCCURRENCE

This rare-earth prospect has been known for more than 30 years, but new exposure in these trenches clarifies relations to surrounding units. The apparent succession of units (Fig. 2), from the structural base upward, is (1) mylonitic granodiorite, (2) lineated syenite, (3) marble, (4) peralkaline melasyenite, and (5) peralkaline quartz syenite and granite gneiss.

The granodiorite gneiss at the base of the section contains biotite and relicts of hornblende as well as red hematitic spotting typical of regionally developed granitic gneisses to the north. The upper 5-10 m of this gneiss is mylonitic with well developed quartz ribbons and S-C fabric trending north-northwest and dipping 15-40° to the west. A discontinuous layer of syenite, never more than 2 m thick, containing a small

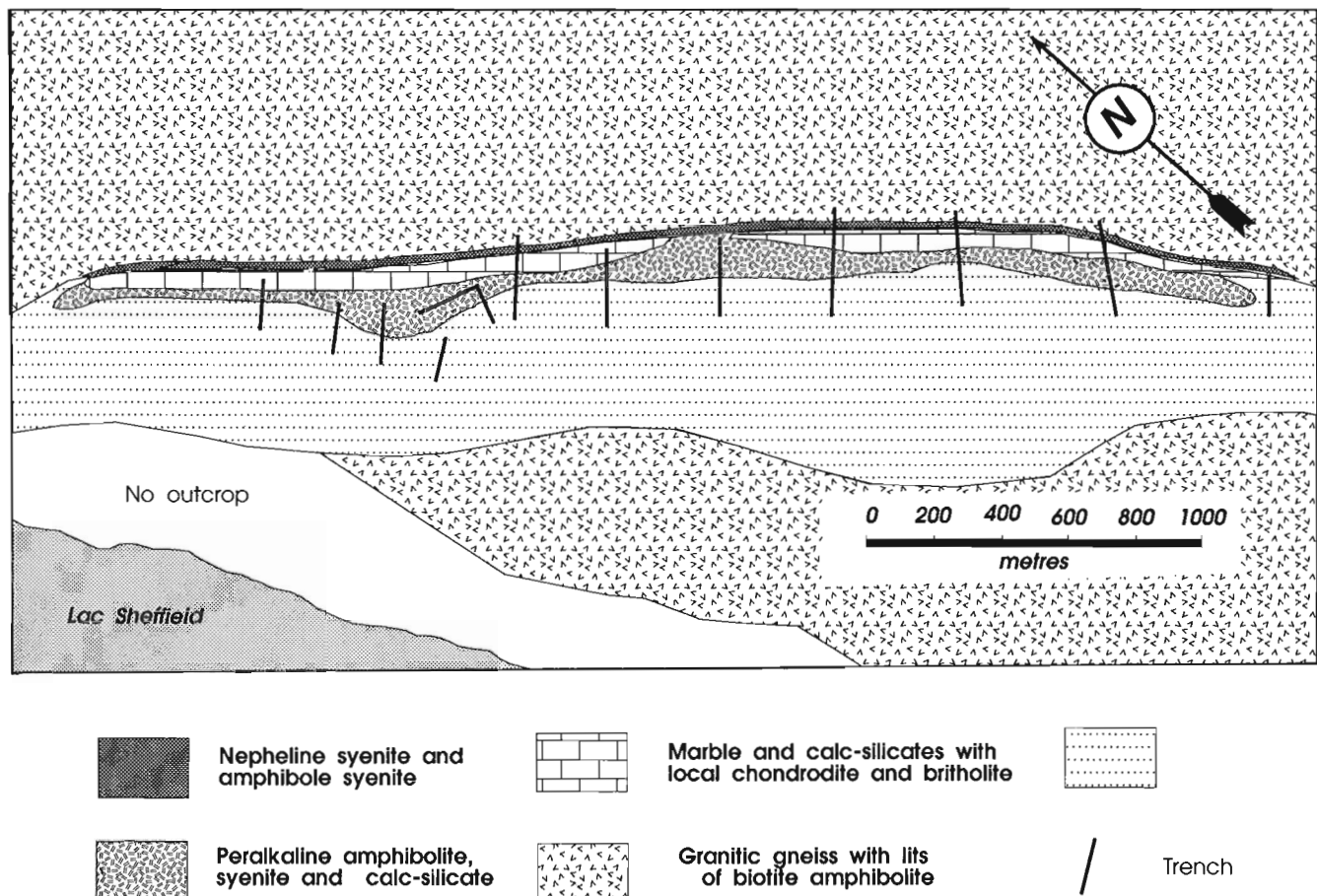
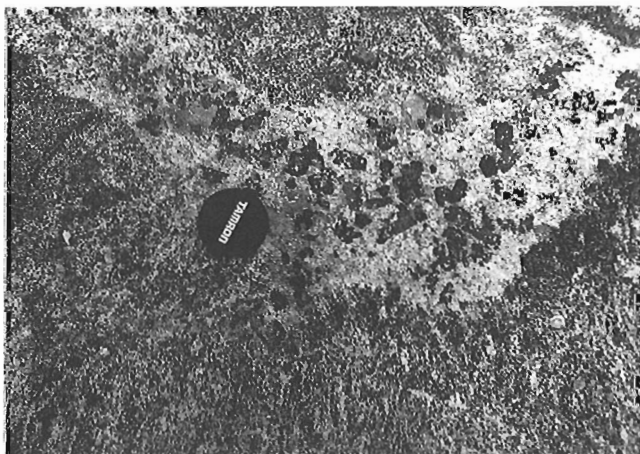


Figure 2. Map of the REE- rare mineral occurrence east of Lac Sheffield (modified from Allan, 1992).

amount of nepheline and exhibiting spindles of amphibole plunging gently to the south-southeast, separates the mylonitic granite from marble above. Mylonite does not extend into the syenite, but stops abruptly, although compositional layering in the syenite is parallel to the mylonitic foliation.

Marble and calc-silicate rocks <5 m in thickness contact syenite over 1300 m of the 1500 m strike length of syenite excavated by the Unocal Canada trenches. This is the only known locality where under-saturated syenite is in contact with marble. Most of the marble is coarse grained and calcitic with minor phlogopite, tremolite, diopside, and graphite, identical to a marble band 4 km further east near Lac Sairs. An upper fringe, 15-30 cm wide is rich in orange chondrodite ( $\text{MgF}_2 \cdot 2\text{Mg}_2\text{SiO}_4$ ) and contains britholite ( $\text{Ce}_5\text{F}(\text{PO}_4)_3$ ) crystals up to 3 cm across. The upper contact of the marble is marked by lenses of granular, massive diopside-phlogopite rock or diopside pyroxenite up to 3 m thick. These calc-silicate lenses contain large crystals of ink-blue alkali amphibole and abundant purple fluorite.

Diopside-dominant rocks grade or pass abruptly into melasyenite of colour index 40-60 which exhibits a remarkable range in texture from massive, pegmatitic and fluorite-rich (Fig. 3), to thinly banded, intricately folded fissile schists (Fig. 4). Eudialyte ( $\text{Na}_4(\text{Ca,Ce})_2(\text{Fe,Mn,Y})\text{ZrSi}_8\text{O}_{22}(\text{F,Cl})_2$ ) occurs as concordant seams of eudialyte-agrellite ( $\text{NaCa}_2\text{Si}_4\text{O}_{10}\text{F}$ ) (Fig. 5), and as disseminations up to a few centimetres across. Hjordahlite ( $\text{Na}_3\text{TiFSi}_2\text{O}_8$ ), mosandrite ( $(\text{Na,Ca,REE})_3\text{Ti}(\text{SiO}_4)_2\text{F}$ ) and vlasovite ( $\text{Na}_2\text{ZrSi}_4\text{O}_{11}$ ) occur in metamorphic segregations. All of these minerals locally form crystals >5 cm in diameter, and appear to be concentrated within or along the edges of calc-silicate boudins and schlieren. Feldspar is relatively minor in the melasyenite commonly less than 20%. The thickness of the melasyenite is less than 5 m although local folding causes apparent widths to be greater.



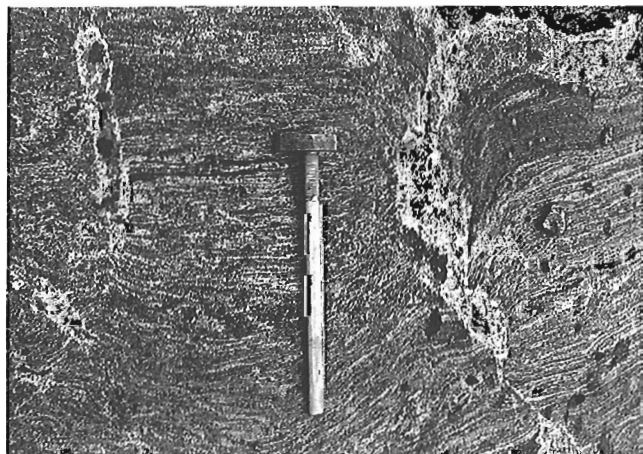
**Figure 3.** Lens of massive peralkaline syenite, containing fluorite, mosandrite, and eudialyte, cutting melasyenite schist. GSC 1992-145D

The melasyenite grades upward into buff or pink rocks in which traces of quartz are present, and the amphibole loses its inky blue shade. These quartz syenites resemble marginal phases of the Kipawa complex elsewhere, but the transition from the marginal phases to country rocks is unusually well exposed. Across 5 to 10 m the number and size of quartz grains gradually increases with distance from the core syenite, biotite increases relative to amphibole, and schlieren of biotite gneiss or schist appear.

An unusual rock on the Kipawa River just south of Lac Sheffield (about 5 km from the rare mineral occurrence) may be related. This mafic rock (colour index ~60), which is also in contact with the core syenite, consists of scapolite and amphibole partly converted to biotite, with minor magnetite. It appears to be derived from an amphibolite.



**Figure 4.** Fissile, folded melasyenite schist with clots of eudialyte as augen. GSC 1992-145B



**Figure 5.** Folded agrellite-eudialite lenses separating boudined melasyenite schist. GSC 1992-145C

## MINERALOGY OF THE KIPAWA SYENITE COMPLEX

The core syenite consists mainly of twinned albite ( $Ab_{99.8}$ ), fine string perthite ( $Or_{96.1}$  and  $Ab_{99.6}$ ) and varying amounts of nepheline ( $Ks_{22.0}$ ). The mafic minerals (Table 1) comprise richteritic amphibole, pleochroic in shades of greenish brown, a grass-green aegirine in which sodium slightly predominates over calcium, and biotite with about 6% Na in the potassium site. Mafic minerals typically contain many small inclusions of feldspar. The texture is xenomorphic granoblastic, and equigranular to seriate. None of the specimens or sections examined show any trace of relict igneous texture. The biotite syenite contains similar feldspars, and red-brown biotite with  $Fe/(Fe+Mg)=0.4$ . The quartz syenite and peralkaline granite exhibit feldspars similar to the core syenite but the albite contains slightly more K (0.011 atoms per formula unit). Both potassium feldspar and plagioclase feldspar are extensively veined and overgrown by albite. Quartz occurs in recrystallized, sutured mosaics of small grains. Mafic minerals exhibit spectacular overgrowth and penetration of biotite and calcic amphibole by riebeckite and later acmite. The mafic minerals are distinctly more alkaline than in other syenite units (midnight blue riebeckite and pale green to brownish acmite), and  $Fe/(Fe+Mg)$  ratios are slightly higher.

Mafic mineralogy of the peralkaline melasyenite is unusual. The blue amphibole is magnesio-richterite with an MgO content ten times that in the nepheline syenite. The pleochroic formula is x=medium blue to lavender, y=pale

greenish blue, and z=grey. Somewhat similar analyses have been reported from metamorphosed peralkaline syenites in Scandinavia (Adamson, 1944). The pyroxene, which exhibits weak to moderate pale green pleochrism, is only mildly sodic (salite), and rich in magnesium. Biotite is poor in Si, rich in Mg, and exhibits a distinctive orange pleochrism.  $Fe/(Fe+Mg)$  ratios are less than half those in the same minerals in the syenite. Amphibole, biotite, and most of the minor minerals contain high contents of F (Table 1). Albite, microcline, and minor nepheline resemble those in the syenite.

A large number of rare mineral species occur in the peralkaline melasyenite, commonly in pegmatitic segregations. A number of them are sufficiently abundant that they locally comprise rock-forming minerals. Agrellite forms folded lenses of large, tabular crystals commonly >2 cm in length associated with eudialyte. Eudialyte forms equant to flattened pink to wine red crystals occurring as patchy disseminations up to 30 cm across in mafic schlieren and as pegmatitic masses with agrellite. Miserite ( $K(Ca,Ce)_4Si_5O_{13}F_3$ ) resembles eudialyte in distribution, but is distinctly browner. Vlasovite forms monomineralic secretion veins up to 5 cm thick within quartz syenite on the margins of the melasyenite. Mosandrite forms tan to honey prismatic crystals up to 10 cm in length found as segregations in the rims of calc-silicate blocks, patchy disseminations in schistose melasyenite, and rare secretion veins in quartz syenite.

**Table 1.** Electron microprobe analyses of mafic minerals from the Kipawa syenite and related units

	amphibole				pyroxene				biotite			
	C	F	S	A	C	F	S	A	C	F	S	A
TiO <sub>2</sub>	41.96	50.41	41.18	54.19	52.22	49.65	48.26	52.45	35.66	34.53	34.44	29.88
Al <sub>2</sub> O <sub>3</sub>	1.26	0.88	1.91	0.18	0.75	3.05	0.72	0.60	3.31	3.42	2.46	2.23
FeO*	13.96	1.21	5.96	1.75	0.97	1.32	3.06	0.75	15.69	13.90	14.47	14.89
MnO	14.71	30.85	29.35	8.62	6.87	24.07	23.05	7.64	15.57	29.50	17.23	14.07
MgO	0.11	1.11	1.03	0.81	0.66	1.26	0.71	0.69	0.08	0.74	0.10	0.75
CaO	10.97	2.56	1.98	16.49	13.35	0.37	1.03	12.97	13.88	2.90	13.74	18.88
Na <sub>2</sub> O	10.32	1.25	4.73	4.73	23.93	2.49	10.46	23.30	0.02	0.02	0.01	0.04
K <sub>2</sub> O	2.07	6.15	5.58	6.89	0.54	11.97	7.51	0.85	0.22	0.06	0.44	0.15
F	0.71	1.81	2.26	2.08	0.02	0.03	0.03	0.02	9.14	9.78	9.57	9.06
Cl	-	1.62	0.67	4.57	-	-	-	-	0.14	1.67	0.83	6.39
Total	96.89#	97.88	95.33#	100.99	99.31	94.25#	95.31#	99.27	95.49#	97.41#	94.18#	97.43
Si	6.305	7.890	6.941	7.907	1.978	1.963	1.934	1.969	2.714	2.813	2.706	2.406
Ti	0.143	0.104	0.242	0.020	0.021	0.091	0.022	0.017	0.189	0.210	0.145	0.135
Al	2.471	0.223	1.183	0.302	0.043	0.061	0.144	0.033	1.407	1.335	1.340	1.413
Fe3	0.000	1.142	0.000	0.000	0.039	0.749	0.529	0.062	0.000	0.000	0.000	0.000
Fe2	1.848	2.897	4.137	1.051	0.172	0.047	0.243	0.171	0.991	2.010	1.132	1.001
Mn	0.015	0.147	0.147	0.101	0.021	0.042	0.024	0.022	0.005	0.051	0.006	0.051
Mg	2.456	0.597	0.497	3.587	0.746	0.022	0.062	0.726	1.575	0.352	1.609	2.266
Ca	1.662	0.210	0.854	0.739	1.961	0.106	0.449	0.937	0.001	0.002	0.001	0.003
Na	0.604	1.866	1.824	1.950	0.039	0.917	0.584	0.062	0.032	0.009	0.066	0.023
K	0.136	0.361	0.485	0.387	0.001	0.001	0.001	0.001	0.888	1.016	0.959	0.931
F	0.000	0.802	0.358	2.012	-	-	-	-	0.034	0.430	0.205	1.627
Cl	0.100	0.008	0.007	0.011	-	-	-	-	0.055	0.060	0.034	0.040
Charges	46	46	46	46	12	12	12	12	22	22	22	22
n	7	8	8	6	6	5	7	6	6	5	6	4

# Totals include ZrO<sub>2</sub>, BaO, SrO, NiO, Cr<sub>2</sub>O<sub>3</sub>, and V<sub>2</sub>O<sub>5</sub>. n=number of analyses averaged

C = country rocks (specimen 91112); F = peralkaline granite and syenite (specimen 91120);  
S = nepheline syenite (specimen 91092); A = peralkaline melasyenite (specimen 91106)

## STRUCTURAL GEOLOGY

Large-scale map patterns in the Kipawa region (Fig. 1) exhibit obvious northwest-trending folds with an amplitude of several kilometres. Small-scale studies on the rare-earth prospect suggest that these large-scale folds represent at least a third period of folding superimposed on older deformation. The oldest recognizable folds ( $F_1$ ) form recumbent sheath-like folds with axes trending 125 to 145°, and amplitudes of a few metres (Fig. 6).  $F_2$  folds trend ~210° are recumbent with long upright limbs, and relatively short overturned limbs suggesting transport from northeast to southwest. Small  $F_1$  folds can be seen almost undisturbed on upright limbs. Both  $F_1$  and  $F_2$  folds are ubiquitously developed in the peralkaline melasyenite producing a variety of spectacular interference folds. Neither generation of fold has been unambiguously identified in the granitic gneiss below the syenite.

$F_1$  and  $F_2$  folds are folded by upright, asymmetric, open to tight folds ( $F_3$ ) with axes trending about 125°. These folds, obvious in the map pattern, affect both granodiorite gneiss and the mylonite which cuts it. A strong mineral and stretching lineation plunging 10-20° toward 125° parallels the axes of these folds. A strong vertical axial plane cleavage locally partially to totally transposed gneissosity.

Brittle, or semi brittle, shatter zones up to a metre thick occur locally within older mylonite along the granite syenite boundary. These zones clearly cut  $F_3$  structures.

The pattern of deformation is consistent with prolonged southeast-over-northwest thrusting under ductile conditions. Orientation of  $F_3$  folds can be explained by lateral constriction of an advancing mass producing longitudinal compression.

## METAMORPHISM

Qualitative observations suggest peak metamorphic conditions in upper amphibolite facies. Kyanite and sillimanite coexist, apparently stably, in the paragneiss (Rive, 1973), and pegmatitic "sweats" are ubiquitous in quartzofeldspathic lithologies. Orthopyroxene is absent from biotite-bearing lithologies. A quantitative estimate of peak P-T conditions can be derived from garnet amphibolite lenses in the paragneiss. The assemblage biotite-garnet-amphibole gives a P-T estimate of 690°C, 9300 bars (Fig. 7) using the method of Mader and Berman (1992), in agreement with the qualitative conclusions outlined above. This P-T estimate also agrees with the presence of metamorphic vlasovite and absence of elpidite (Currie and Zaleski, 1985).

Boudinage of segregations of eudialyte and mosandrite on the limbs of  $F_1$  folds indicate that some Na-rich minerals formed before or during  $F_1$  folding, but major metamorphic mineral growth was syn- $F_2$ , as shown by the ubiquitous occurrence of segregations of Na-rich minerals in  $F_2$  cleavage, and some massive peralkaline pegmatites postdate deformation. Peralkaline compositions of these pegmatites

suggests unusually low melting temperatures (Edgar, 1987). Minor amounts of peralkaline melt formed at metamorphic temperatures as low as 450°C in the Ice River complex of southern British Columbia (Currie, 1975). Small amounts of peralkaline melt may have been locally present throughout deformation and metamorphism of the Kipawa syenite complex.

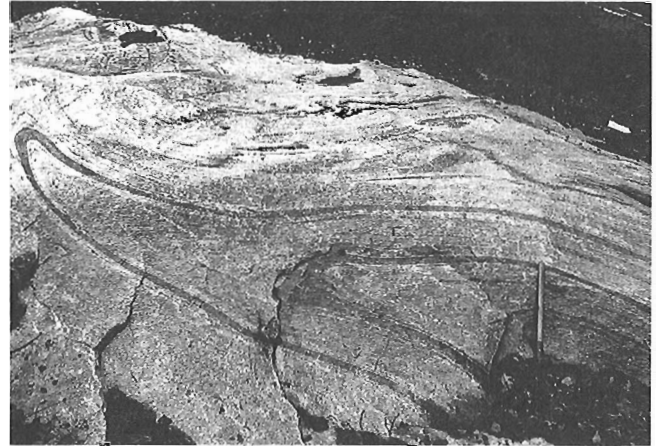


Figure 6. Refolded recumbent isoclinal fold. Hammer is 1 m long. GSC 1992-145E

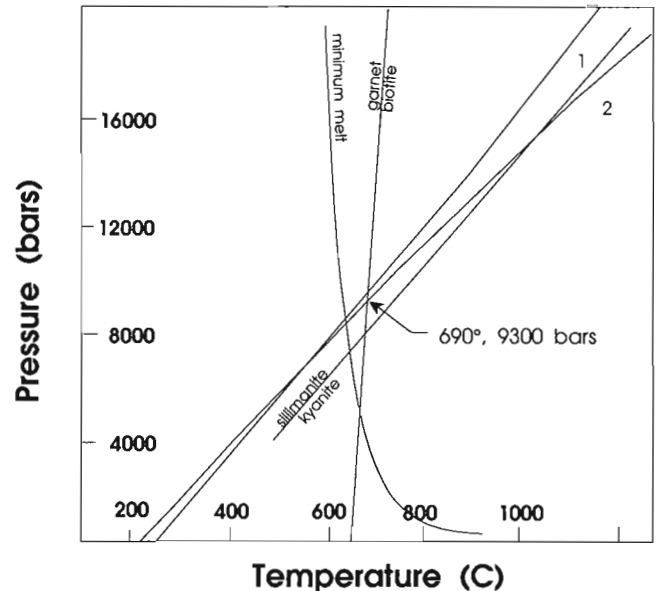


Figure 7. Estimate of peak metamorphic P-T conditions for the Kipawa region based on mineral data from a garnet amphibolite in Lac Sairs. The curve labelled 1 is for the reaction 4 grossular+2 pyrope+12 quartz+3 tschermakite=3 tremolite+12 anorthite, and the curve labelled 2 is for the reaction 2 grossular+pyrope+18 quartz+3 pargasite=3 tremolite+6 anorthite+ 3 albite. Amphibole and garnet activities from Mader and Berman (1992).

**GEOCHEMISTRY**

Bulk rock chemical analyses summarized in Table 2 show the granitic gneiss structurally below the Kipawa syenite gneiss complex has much higher K<sub>2</sub>O content and much lower CaO and Sr content than the trondhjemitic gneiss above the complex. The core syenite is weakly peralkaline, and resembles other syenite gneisses of the Grenville Province, as well as evolved syenites of igneous complexes such as Ice River (Currie, 1975). The F and REE contents are high relative to its host rocks. The quartz syenite and peralkaline granite all exhibit high ferric/ferrous and (Na+K)/Al, ratios, but fall into two contrasting groups. One exhibits high F and REE content and moderate Na and Zr contents, while the other has low F, Al and REE contents and high Zr and Na contents. The chemistry of the peralkaline melasyenite is unique. The magnesium and calcium contents are much higher than normal peralkaline rocks (Fig. 8), and the F, Zr, and REE contents are extreme.

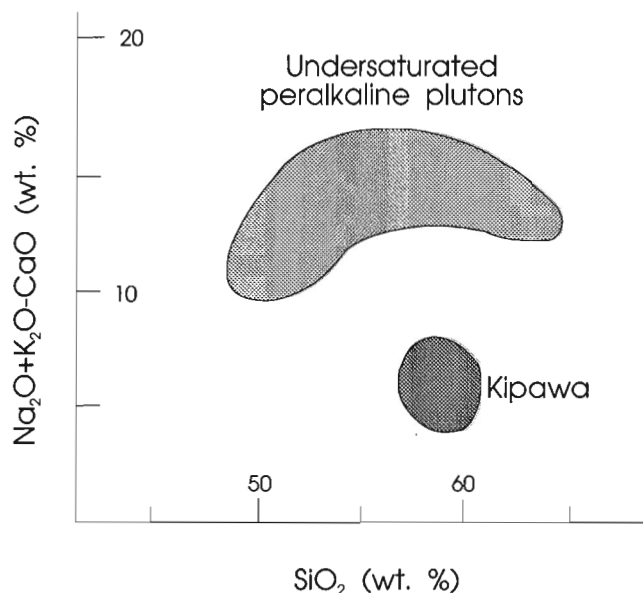
**GEOCHRONOLOGY**

O. van Breemen (pers. comm., 1992) found that large euhedral zircons from metamorphic segregations within the peralkaline granite gave a concordant U-Pb age of ~1000 Ma without significant remnant. Fission-track dating of sphene by G.N. Eby, University of Lowell (pers. comm., 1991), gave essentially identical ages of 1039 ± 88 and 1011 ± 40 Ma (1-sigma error). Aarden and Gittins (1974) obtained K-Ar ages on nepheline of 1276, 1286, and 1309 Ma. Dallmeyer and Rivers (1983) found that K-Ar ages could "remember" old events, even when zircon ages were reset, if argon was retained in the rock during metamorphism. Age of emplacement of the syenite complex may be approximated by the K-Ar nepheline ages. The zircon age indicates the age of formation of the zircon, a late- or post deformation event. The fission track ages suggest uplift and cooling almost coeval with zircon formation.

**Table 2.** Average chemical analyses for the Kipawa syenite and related units

	1	2	3	4	5	6	7	8	9	10
SiO <sub>2</sub>	66.98	71.68	44.83	76.11	2.60	30.51	62.15	52.21	68.73	70.58
TiO <sub>2</sub>	0.56	0.28	3.24	0.39	0.03	0.04	0.34	0.27	0.34	0.50
Al <sub>2</sub> O <sub>3</sub>	13.88	15.25	16.40	12.21	0.30	1.10	17.01	6.75	13.77	9.03
Fe <sub>2</sub> O <sub>3</sub>	3.33	0.49	3.10	2.70	0.21	0.20	2.55	3.85	2.83	6.90
FeO	2.95	1.45	11.03	0.63	0.59	0.81	2.38	2.20	1.23	0.53
MnO	0.13	0.02	0.20	0.03	0.04	0.06	0.12	0.31	0.10	0.11
MgO	0.39	0.63	5.77	0.36	20.40	20.39	0.39	10.37	0.28	0.21
CaO	1.27	2.15	7.78	0.52	30.22	22.69	1.48	14.52	0.69	0.41
Na <sub>2</sub> O	4.35	5.65	3.91	2.53	0.01	0.22	8.15	4.54	5.93	6.53
K <sub>2</sub> O	5.23	1.43	1.56	3.36	0.09	0.83	4.56	1.88	5.07	2.84
H <sub>2</sub> O	0.47	0.62	1.27	0.83	0.40	nd	0.49	0.85	0.37	0.49
CO <sub>2</sub>	0.28	0.08	nd	nd	46.0	20.7	0.10	0.15	0.13	0.10
P <sub>2</sub> O <sub>5</sub>	0.07	0.06	0.61	0.12	0.02	0.01	0.10	0.35	0.05	0.02
F	0.07	0.05	0.19	0.07	0.03	3.46	0.31	2.31	0.25	0.06
Cl	0.03	0.02	0.22	0.02	nd	0.03	0.02	0.04	0.02	0.01
F+Cl=O	-0.04	-0.02	-0.18	-0.03	-0.02	-1.46	-0.14	-0.98	-0.11	-0.03
Total	99.95	99.84	99.93	99.88	100.95	99.57	100.00	99.62	99.68	98.29
	nd = not detected					n = number of analyses averaged				
Ba	765	417	770	646	30	670	922	300	413	37
Sr	87	620	727	169	91	240	159	229	51	21
Rb	98	40	43	118	10	180	152	282	207	340
Nb	18	3	8	17	12	22	24	95	20	6
Zr	360	307	170	273	nd	nd	975	2798	520	13200
Co	3	3	44	6	nd	nd	2	nd	nd	nd
Cr	nd	nd	56	6	nd	nd	nd	28	nd	nd
Ni	nd	nd	56	6	nd	nd	nd	9	nd	nd
Sc	4.4	2.1	16	5.2	nd	nd	3.5	8.4	3.1	1.8
V	nd	11	220	31	nd	nd	nd	19	nd	nd
La	48	22	21	69	10	110	86	556	113	12
Ce	90	55	58	127	25	200	187	1273	227	24
Yb	3.9	2.6	1.8	4.3	1.7	13	10.7	71	12	11
Y	32	22	24	43	12	130	88	540	109	18
n	4	4	3	3	1	1	4	4	3	3

1. Granodioritic gneiss; 2. Trondhjemitic gneiss; 3. Gabbro and amphibolite; 4. Quartzite and meta-arkose;  
5. Marble; 6. Metasomatized (chondrodite) marble; 7. Peralkaline melasyenite; 8. Nepheline syenite;  
9. Mildly peralkaline quartz syenite and granite; 10. Strongly peralkaline quartz syenite and granite



**Figure 8.** K+Na-Ca vs. silica diagram for peralkaline syenites (field for undersaturated peralkaline plutons after Curtis and Currie, 1981).

## DISCUSSION

The Kipawa syenite gneiss complex exhibits an outcrop pattern with length about one thousand times width, implying that the complex forms a thin sheet without apparent breaks in continuity. This planar form appears too regular to result from deformation of an originally equant intrusive complex, and is probably a primary feature. The planar form could result from origin as a lava flow or as a sill emplaced along the discontinuity between the paragneiss and structurally underlying granitic gneiss. If the old K-Ar ages relate to emplacement of the syenite, and the U-Pb age to latest deformation, the lava flow origin is more likely.

Curtis and Currie (1981) showed that strongly metamorphosed alkaline rocks can retain relicts of original mafic minerals. The aegirine and richteritic amphibole of the syenite could be such relicts. The salic minerals have clearly re-equilibrated during metamorphism. The almost pure alkali feldspars suggest that this re-equilibration continued to temperatures below 350°C. The chemistry and mineralogy of the syenite show the silica-undersaturated parts to be mildly peralkaline and chemically strongly differentiated. This is a possible parent for a small amount of strongly peralkaline, Zr-rich differentiate (or anatectic partial melt) in the quartz syenite, although there is a well-known difficulty in deriving quartz-saturated rocks from undersaturated parents. The F-rich melasyenite and quartz syenite, have compositions incompatible with derivation from the core syenite by igneous processes. Metasomatism must be involved. Since both are peralkaline, Na-metasomatism typical of high level alkaline complexes probably played a role, but the chemistry and mineralogy shows that more complex processes must have been involved. The peralkaline character, leading to low

melting temperatures during metamorphism, may be responsible for the massive character of many of these occurrences.

The melasyenite exhibits Na-rich minerals associated with marble and calc-silicates including diopside (Tremblay-Clark and Kish, 1978; Allen, 1992). Igneous plutons containing these Na-rich minerals have very low bulk Mg and Ca contents (commonly <2%), and contain acmite and arfvedsonite as well as major amounts of leucocratic peralkaline syenite. Such rocks are absent from the Kipawa complex. The surroundings of the melasyenite include chondrodite marble, britholite marble, alkali amphiboles in calc-silicate lenses, and scapolite replacing plagioclase in metabasic rocks, indicating addition of Na, F, Cl and REE. It is unclear whether this addition took place solely during igneous emplacement, solely during metamorphism, or was a continuing process. Sodium and REE-rich minerals clearly grew in a F- and Cl-rich environment during deformation, since they form folded secretion veins. Mineral associations such as diopside-richterite and zircon- vlasovite-eudialite appear anomalous for igneous processes.

The peralkaline melasyenite occupies the "stratigraphic" position normally filled by the biotite syenite, that is between the core syenite and the quartz syenite-peralkaline granite. The presence of marble interpolated between the core syenite and the other units of the complex is anomalous. If the melasyenite is ultimately of igneous parentage, this marble must have been brought to its present position during the emplacement process and reacted with its surroundings. Alternately the marble may have been tectonically emplaced subsequent to igneous activity and the present spectacular rocks result from metasomatism and metamorphism. We believe this latter process to be plausible. Sodium was mobilized along a major shear zone during deformation of the Red Wine complex (Curtis and Currie, 1988). Fluorine and chlorine metasomatism are a ubiquitous, if minor, feature of the Grenville Province as indicated by the widespread occurrence of chondrodite and scapolite. Fluorine complexes readily with Zr and REE, and could scavenge these elements from enriched sources, such as the Kipawa syenite, to be dumped where the F reacted with marble to form fluorite. F-metasomatism of trachyte has recently been proposed as the ore-forming mechanism on the Brockman REE prospect of Western Australia (Ramsden et al., 1993).

Many strongly peralkaline undersaturated rocks cannot be explained as differentiates of more abundant magma types due to crystal fractionation (Curtis and Currie, 1981; Currie et al., 1975). The Kipawa syenite gneiss complex suggests that melting of an peralkaline precursor generated by metasomatism could be an alternative way of generating such rocks. This mechanism need not be in conflict with the well-known association of peralkaline complexes with rifting and alkali basalt if it is assumed that the basalt is the heat engine driving the process.

A remarkable concentration of strongly peralkaline undersaturated complexes occurs along the Grenville Front and its extensions. The Kipawa and Red Wine complexes fall south of the front and are deformed and metamorphosed.



Ilimaussaq in Greenland lies north of the extension of this boundary, and is pristine. Norra Karr in Sweden falls to the south and is deformed and metamorphosed. These complexes were emplaced between 1000 and 1400 Ma. They account for all known deformed and metamorphosed strongly peralkaline undersaturated rocks, and about 20 % of the total world inventory of strongly peralkaline undersaturated rocks. The reason for such a high concentration along this boundary is unknown.

## ACKNOWLEDGMENTS

I am greatly indebted to Mr. J.A. Allan and Unocal Canada Ltd. for information on the rare-earth prospect east of Lac Sheffield. The present study would not have been possible without it. Urs Mader performed the geothermometric calculations, and John Stirling assisted with electron microprobe analyses. The manuscript was critically read by Simon Hamner.

## REFERENCES

- Aarden, H.M. and Gittins, J.**  
1974: Hiortdahlite from Kipawa River, Villedieu Township, Temiscaming County, Quebec, Canada; *Canadian Mineralogist*, v. 12, p. 241-247.
- Adamson, O.J.**  
1944: The petrology of the Norra Karr district, an occurrence of alkaline rocks in southern Sweden; *Geologiska Foereningen Stockholm Foerhandlingar*, v. 66, p. 133-255.
- Allan, J.F.**  
1992: Geology and Mineralisation of the Kipawa yttrium-zirconium property, Quebec; *Exploration and Mining Geology*, v. 1, p.283-295.
- Ansell, H.G., Roberts, A.C., and Plant, A.G.**  
1980: Gittinsite, a new calcium zirconium silicate from the Kipawa syenite complex, Quebec; *Canadian Mineralogist*, v. 18, p. 201-203.
- Berry, L.G., Lin, H.C., and Davis, G.C.**  
1972: A new occurrence of miserite from the Kipawa Lake area, Quebec; *Canadian Mineralogist*, v. 11, p. 569.
- Currie, K.L.**  
1975: Geology and petrology of the Ice River alkaline complex, B.C.; *Geological Survey of Canada, Bulletin* 245, 61 p.
- Currie, K.L. and Zaleski, E.**  
1985: The relative stability of elpidite and vlasovite: a P-T indicator for peralkaline rocks; *Canadian Mineralogist*, v. 23, p. 577-582.
- Currie, K.L., Curtis, L.W., and Gittins, J.**  
1975: Petrology of the Red Wine alkaline complexes, central Labrador, and a comparison with the Ilimaussaq complex, southwest Greenland; *Geological Survey of Canada, Paper* 75-1A, p. 271-280.
- Currie, K.L., Eby, G.N., and Gittins, J.**  
1986: The petrology of the Mont Saint Hilaire complex, southern Quebec: an alkaline gabbro-peralkaline syenite association; *Lithos*, v. 19, p. 65-81.
- Curtis, L.W. and Currie, K.L.**  
1981: Geology and petrology of the Red Wine alkaline complex, central Labrador; *Geological Survey of Canada, Bulletin* 294, 61 p.
- Dallmeyer, R.D. and Rivers, T.**  
1983: Recognition of extraneous argon components through incremental release  $^{40}\text{Ar}/^{39}\text{Ar}$  analysis of biotite and hornblende across the Grenvillian metamorphic gradient in southwestern Labrador *Geochimica et Cosmochimica Acta*, v. 47, p.413-428.
- Edgar, A.D.**  
1987: The genesis of alkaline magmas with emphasis on their source regions: inferences from experimental studies; in *Alkaline Igneous Rocks*, (ed.) J.G. Fitton and B.G.J. Upton, Geological Society Special Publication 30, p. 29-52.
- Gittins, J., Brown, M.G., and Sturman, D.**  
1976: Agrellite, a new rock-forming mineral in regionally metamorphosed agpaite alkalic rocks; *Canadian Mineralogist*, v. 14, p. 120-126.
- Hicks, W.D.**  
1959: Eudialyte and eucolite in Canada; *Canadian Mineralogist*, v. 6, p. 297.
- Lyall, H.B.**  
1959: Preliminary report on McLachlin-Booth area, Temiscamingue Electoral District; Quebec Department of Mines, Geological Surveys Branch Preliminary Report 391, 13 p.
- Mader, U.K. and Berman, R.G.**  
1992: Amphibole thermobarometry: a thermodynamic approach; in *Current Research, Part E*; Geological Survey of Canada Paper 92-1E, p. 69-77.
- Plant, A.G. and Roberts, A.C.**  
1979: New data on unnamed  $\text{CaZrSi}_2\text{O}_7$  from Kipawa, Quebec; *Geological Survey of Canada, Paper* 79-1A, p. 391-392.
- Ramsden, A.R., French, D.H., and Chalmers, D.I.**  
1993: Volcanic-hosted rare metals deposit at Brockman, Western Australia: - Mineralogy and geochemistry of the Niobium Tuff; *Mineralium Deposita*, v. 28, p. 1-12.
- Rive, M.**  
1973: Géologie de la région des Lacs Ogascanane et Sairs, Comté de Témiscamingue; Ministère des Richesses Naturelles du Québec, Service de l'Exploration géologique, Rapport Préliminaire 606, 16 p.
- Roberts, A.C. and Bonardi, M.**  
1983: Potassian gaidonnayite from the Kipawa agpaite syenite complex, Quebec; *Geological Survey of Canada, Paper* 83-1A, p. 480-482.
- Tremblay-Clark, P. and Kish, L.**  
1978: Le district radioactif de Kipawa; Ministère des Richesses Naturelles du Québec, Direction Générale des Mines, Rapport Préliminaire DPV-579, 28 p.



# Geophysical, geochemical, and petrographical study of Contwoyto Batholith, Lupin gold mine area, Northwest Territories<sup>1</sup>

M.I. Legault<sup>2</sup> and B.W. Charbonneau  
Mineral Resources Division

*Legault, M.I. and Charbonneau, B.W., 1993: Geophysical, geochemical, and petrographical study of Contwoyto Batholith, Lupin gold mine area, Northwest Territories; in Current Research, Part E; Geological Survey of Canada, Paper 93-1E, p. 207-218.*

---

**Abstract:** Anomalous patterns (gamma-ray spectrometric, magnetic, VLF-EM) from a detailed airborne geophysical survey have been investigated to improve the understanding of the Contwoyto Batholith and to investigate a possible relationship between the intrusion and the gold mineralization at the Lupin mine.

The airborne geophysical survey defines wide ranges in eU/eTh relating to differentiation of peraluminous granites. Low eU/eTh ratio rocks are biotite-rich phases associated with thoriferous monazite and zircon, whereas muscovite-rich high ratio rocks near the mine are depleted in these minerals. Magnetic patterns over the granite indicate relatively low levels of magnetic field near the Lupin mine consistent with lower concentrations of total iron and the almost complete absence of iron oxides. VLF-EM patterns indicate some north-trending conductors which are in places offset along east-west breaks.

Average concentrations of elements associated with the Lupin mineralization (i.e., Au, Ag, Cu, S, As, W, Ca) are extremely low in the granite.

**Résumé :** Les auteurs ont analysé les anomalies (spectrométriques gamma, magnétiques, VLF-EM) reconnues par suite d'un levé géophysique aérien détaillé, afin de mieux comprendre le Batholithe de Contwoyto et d'examiner l'existence d'un lien éventuel entre l'intrusion et la minéralisation aurifère à la mine Lupin.

Le levé géophysique aérien a permis de reconnaître de grands écarts dans le rapport eU/eTh qui sont liés à la différenciation de granites hyperalumineux. Les roches à faible rapport eU/eTh sont des phases riches en biotite associées à la monzonite thorifère et au zircon, tandis que les roches à rapport élevé riches en muscovite près de la mine sont appauvries en ces minéraux. Le réseau magnétique au-dessus du granite indique la présence d'un champ magnétique relativement faible près de la mine Lupin, ce qui s'accorde avec des concentrations plus faibles en fer total et l'absence presque complète d'oxydes de fer. Les configurations VLF-EM indiquent la présence de conducteurs à direction nord qui, par endroits, sont décalés le long de ruptures est-ouest.

Les concentrations moyennes des éléments associés à la minéralisation à la mine Lupin (c.-à-d. Au, Ag, Cu, S, As, W, Ca) sont très faibles dans le granite.

---

<sup>1</sup> Contribution to Canada-Northwest Territories Mineral Development Subsidiary Agreement 1987-91.

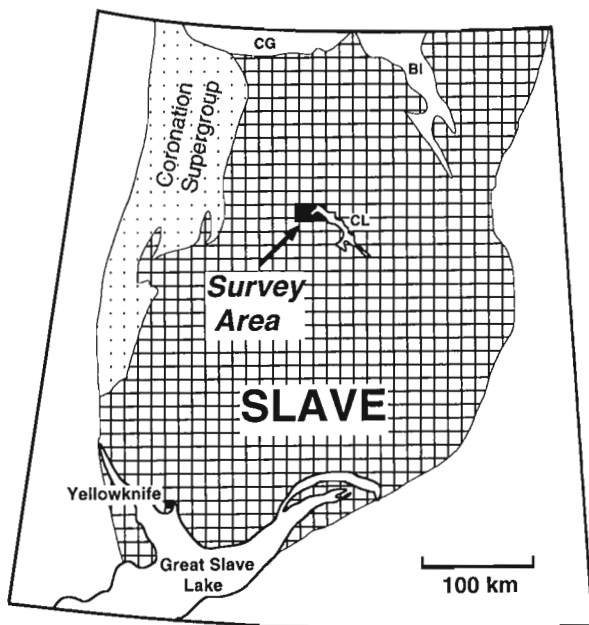
<sup>2</sup> Ottawa-Carleton Geoscience Centre, University of Ottawa, Ottawa, Ontario K1N 6N5

## INTRODUCTION

In the summer of 1988, a detailed airborne geophysical survey (gamma-ray spectrometric-magnetic-VLF, 1200 km<sup>2</sup>) was flown by the GSC over the Lupin gold mine area, west of Contwoyto Lake, Northwest Territories (Fig. 1). The objective of this survey was to improve the understanding of the mineralized area.

The Lupin deposit is hosted by the Contwoyto Formation, which is a turbiditic sequence in which the gold is confined to thin units of iron-formation (Bostock, 1980; Lhotka and Nesbitt, 1989). Two genetic models have been proposed for the Lupin gold deposit: 1) a syngenetic model in which gold is deposited simultaneously with the iron-formation (Kerswill, 1992); and 2) an epigenetic model in which gold is introduced in the iron formation during a later event (Lhotka and Nesbitt, 1989). The spatial association of quartz veins with the gold deposit and the symmetrical zoning in the mineralogy and gold contents around these veins suggest that the mineralization at Lupin resulted from an epigenetic process related to the veins (Lhotka and Nesbitt, 1989; Bullis, 1990).

Because of the possible association of the quartz veins with the Contwoyto Batholith (CB) located west of the north end of Contwoyto Lake, the airborne geophysical survey of the Lupin area focused mainly on this intrusion. Geophysical measurements were taken using gamma-ray spectrometry, total field magnetic intensity and very low frequency electromagnetic (VLF-EM) instruments, with readings every second along east-trending flight lines spaced 250 m apart. Following the airborne survey, a ground study ensued in the summer of 1989, involving geological observations, sampling, and geophysical measurements (Charbonneau and Legault, 1992).



**Figure 1.** Location map indicating the Lupin survey area within the Slave Province. BI-Bathurst Inlet; CG-Coronation Gulf; CL-Contwoyto Lake.

This study is an investigation of airborne and ground geophysical anomalies of the Contwoyto Batholith, and their relationship to petrographical and geochemical observations. The objective of the study is to characterize the granite in order to evaluate the possible relationship between the intrusion and the gold mineralization at Lupin. The literature provides many examples of relationships between peraluminous granites and gold mineralization (Crouzet et al., 1979; Urabe, 1985; Mawer, 1986; MacDonald and O'Reilly, 1988; Bachman et al., 1990).

## GEOLOGY

The Archean supracrustal rocks of the study area are part of the Yellowknife Supergroup (Henderson, 1938; Tremblay, 1976; Bostock, 1980). These rocks include the Contwoyto Formation (unit 2; Fig. 2a) and the Tuk volcanic rocks (unit 1; Fig. 2a) (King et al., 1989). Six phases of plutonism have been distinguished in the Contwoyto Lake area (King et al., 1988; Davis, 1991). Of these six phases, four are present within the survey area. Porphyritic granodiorite (unit 3), biotite-hornblende diorite and tonalite (units 4 and 5), and muscovite-biotite tonalite to monzogranite (unit 6; with some syenogranite phases) are part of a calc-alkaline to peraluminous suite and are interpreted as a product of late- to postaccretion, continental margin magmatism and associated crustal melting (Davis, 1992; Fig. 2a).

The muscovite-biotite tonalite to syenogranite unit is referred to here as the Contwoyto Batholith and it occupies most of the survey area. It is generally equigranular, fine grained to pegmatitic, and contains numerous screens, xenoliths, and schlieren of metasedimentary rock. Associated pegmatites are common and are dominated by large perthitic K-feldspar crystals, quartz, muscovite, and biotite.

The timing of the quartz veins relative to Lupin mineralization and the Contwoyto Batholith is pivotal if the batholith is to have played a direct role in the mineralizing process. Many workers (Mortensen et al., 1988; van Breeman et al., 1990; King et al., 1990; Relf, 1989, 1990; Bullis, 1990) clearly indicate that the quartz veins which are related to gold mineralization are close to the age of the batholith (~2581 Ma). However, many of these studies suggest that the batholith may slightly postdate the gold related quartz veins.

At the Lupin deposit, gold is spatially associated with northeast-trending quartz veins bordered by concentrations of pyrrhotite or pyrite and arsenide. The quartz veins themselves contain <1 ppm Au and are sulphide-poor (Lhotka and Nesbitt, 1989). A zoned sequence of hydrothermal alteration is present in iron-formation adjacent to the quartz veins. Immediately adjacent to the veins calc-silicate alteration is locally developed, followed by an arsenide-rich zone and an iron-sulphide zone; both zones are associated with elevated gold values. Other elements assumed to be introduced by these quartz veins include silver, copper, sulphur, arsenic, tungsten, iron, and calcium (Lhotka and Nesbitt, 1989).

Proterozoic rocks (unit 7) in the map area includes the sedimentary rocks of the Goulburn Group, the magnetite-bearing Morel sills (Tremblay, 1976), and the Bay pluton, which is interpreted to be related to the Booth River Intrusive Suite (Roscoe, 1985) by King et al. (1989)(Fig. 2a).

## AIRBORNE GEOPHYSICAL SURVEY

The airborne geophysical survey was flown with the GSC airborne gamma-ray spectrometer system described by Bristow (1979). In addition to the spectrometer, with 50 L of NaI detectors, the system includes a Geometrics G-803 proton precession magnetometer, and a Herz Totem 1A VLF-EM sensor. Data are presented as a set of twelve maps (11 in colour) and as stacked multiparameter profiles for each flight line (Geological Survey of Canada, 1989).

The VLF pattern is shown by the VLF total field map and VLF quadrature profile map (not shown). The VLF total field map is characterized by numerous sinuous anomalies trending roughly north. Because flight lines are east-west and the VLF station is located to the south (Seattle, Washington), north-trending anomalies strongly influence the map pattern. Numerous correlations with diabase dykes (many of which trend north) are evident on the map. The majority of the dykes are not conductive and some dykes are conductive over part of their length. Other north-south anomalies are not correlated with diabase dykes and their origin is unknown. They may relate to unmapped dykes, other bedrock conductors, conductive overburden and/or lake bottom sediments. Interesting offset features (sutures) trending more or less east-west can be seen in several parts of the survey including one that trends through the Lupin gold mine. These features may be worthy of future investigation.

Geophysical survey results are illustrated in Figures 2b, 2c and 2d, along with the geology (Fig. 2a). The magnetic pattern (Fig. 2b) is strongly influenced by sharp linear anomalies relating to the numerous northwest and north-northwest-trending diabase dykes in the area, however, these anomalies are set in a broad, background pattern of magnetic variation. The broader magnetic pattern indicates lower values over the granitic rocks near the Lupin mine than over portions of the same granite farther to the northwest. There are no obvious anomalies relating to the relatively small iron-formations of the Contwoyto Formation. They also have minimal ferromagnetic contrast with country rocks because much of the iron-formation is composed of silicate (grunerite) and sulphide-rich phases (Bostock, 1980). A prominent circular magnetic anomaly on the eastern boundary of the survey relates to a subsurface mafic intrusion (Tremblay, 1976) that is related to the mafic Proterozoic intrusions of the area. A thin slice of this intrusion is actually faulted up to the surface (Tremblay, 1976).

The Contwoyto Batholith is distinguished from the metasedimentary rocks of the Contwoyto Formation by increased average levels of radioactivity (Fig. 2c). Typical total radioactivity levels over the batholith are 6-10  $\mu\text{R/h}$  compared to levels of less than 6  $\mu\text{R/h}$  over metasedimentary and other igneous rocks in the area. The total-count

radioactivity levels of the batholith are not significantly above crustal levels of radioactivity in Canada (Grasty et al., 1984) and are somewhat lower than typical granites, although uranium contents are high (4 to 5 ppm; not shown).

Average levels of eU/eTh ratio (Fig. 2d) are high and variable over the batholith ranging from the average crustal value of 0.2 up to well over 1.0. The eU/eTh ratio highs trend radially to the northwest away from the Lupin gold mine which lies immediately adjacent to the batholith. These trends are located on metasedimentary screens which are "intersheeted" with the batholith. The largest eU/eTh ratio anomaly is located approximately 3 km from the mine site.

## GROUND STUDY

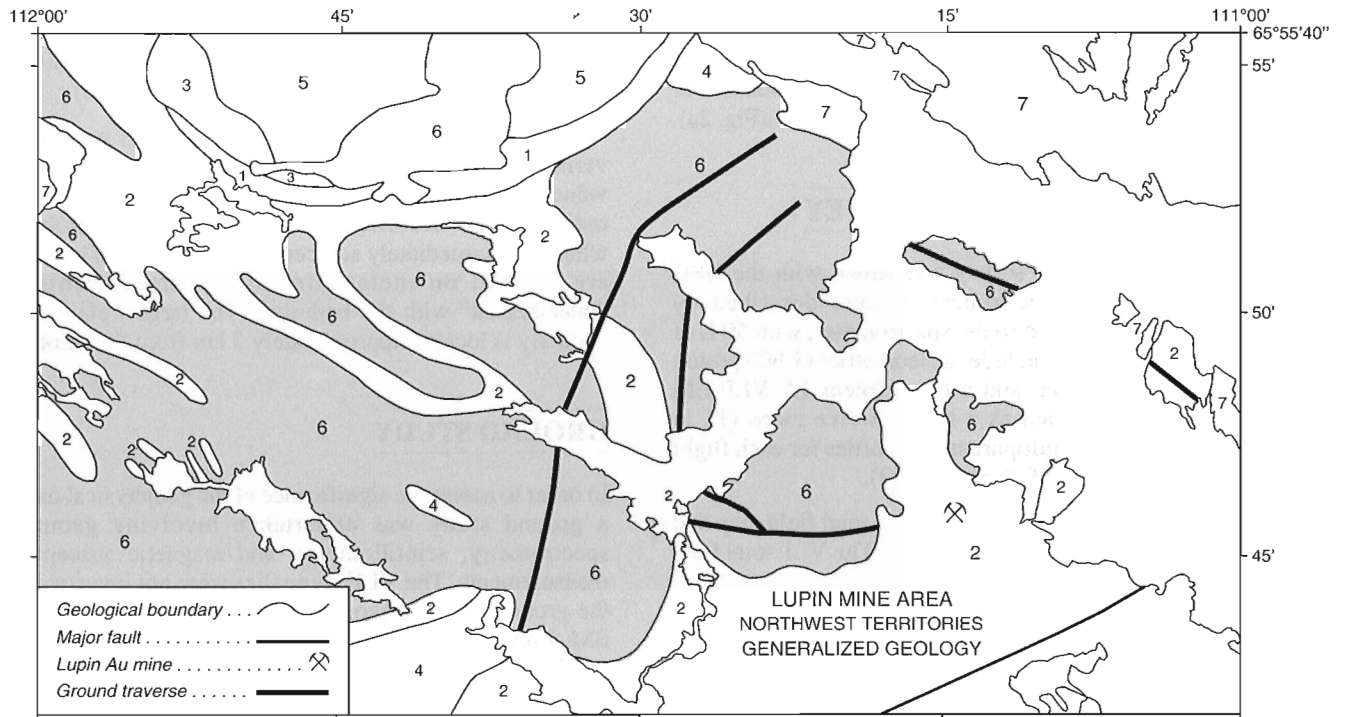
In order to assess the significance of the geophysical patterns, a ground study was undertaken involving gamma-ray spectrometry, scintillometry, and magnetic susceptibility measurements. The VLF anomalies were not investigated on the ground. Ground geophysical equipment utilized were an SM-5 magnetic susceptibility meter (Scintrex) and a DISA 400A gamma-ray spectrometer, a GR101A scintillometer, and a KT-5 magnetic susceptibility meter (all by Exploranium).

Locations of traverses are indicated on Figure 2a. The traverses were designed to cross the major eU/eTh ratio anomalies (Fig. 2c). In addition, several isolated helicopter landings were made on the western part of the batholith. Polished thin sections (30) and geochemical analyses (60) were obtained from 150 large (~1 kg), fresh rock samples collected in the course of this study (Fig. 3). Further work on these samples included slabbing and mineral separations. Petrographical and geochemical work complemented this study and has been reported in more detail by Legault (1991).

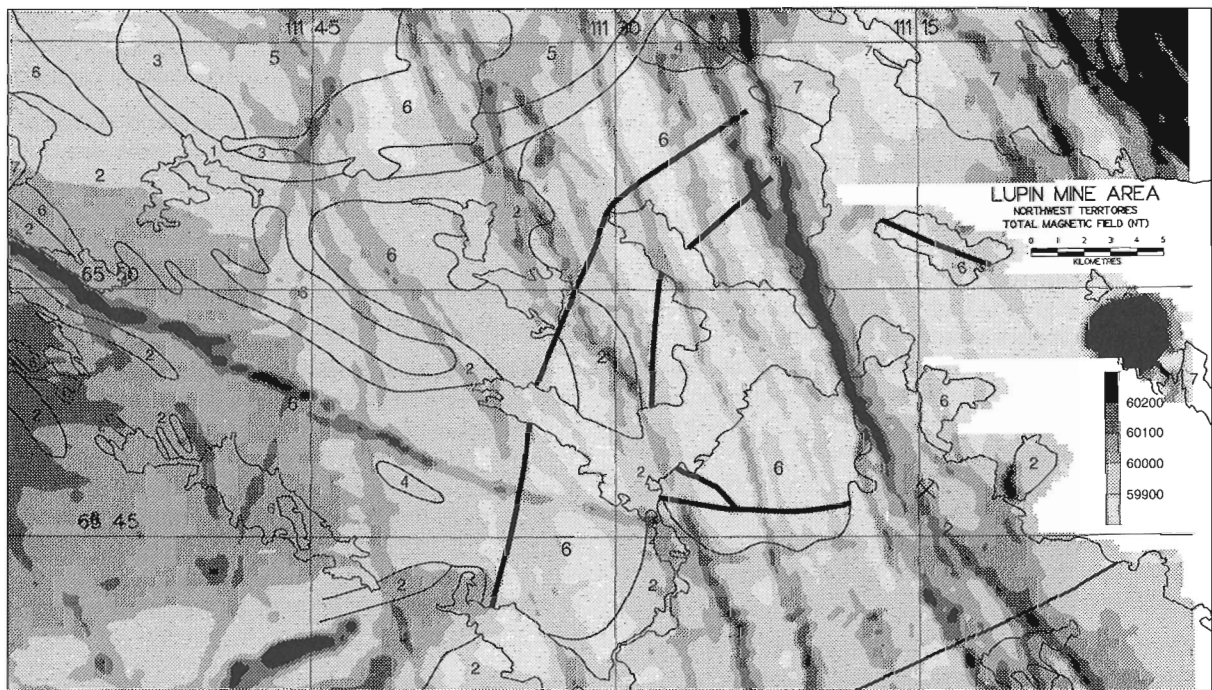
Three hundred in situ gamma ray spectrometric measurements were made in the field, mainly within the Contwoyto Batholith, to characterize the lithological variations; Table 1 summarizes these results. The radiometric values shown are consistent with airborne patterns discussed previously. Traverses over eU/eTh ratio anomalies within the batholith mirror the airborne patterns and indicate that the higher ratios are due to decrease in eTh, not uranium enrichment (Fig. 4).

Magnetic susceptibility measurements in the field correlate with magnetic patterns shown on Figure 2b. The highest values of susceptibility generally relate to portions of the batholith located in the western part of the study area that have lower eU/eTh ratio and also portions of the batholith near the mine that have low eU/eTh ratio (low eU/eTh ratio segments of batholith intervene between the high eU/eTh ratio trends as noted previously on Fig. 2d). The lowest values of susceptibility correlate with the higher eU/eTh ratio rocks which are more prevalent near the mine.

These correlations are illustrated by magnetic susceptibility measurements made on 50 samples with geochemical data. Results show that the magnetic susceptibility decreases with increasing U/Th ratio and correlates positively with  $\text{Fe}_2\text{O}_3(\text{total})$  (Fig. 5).

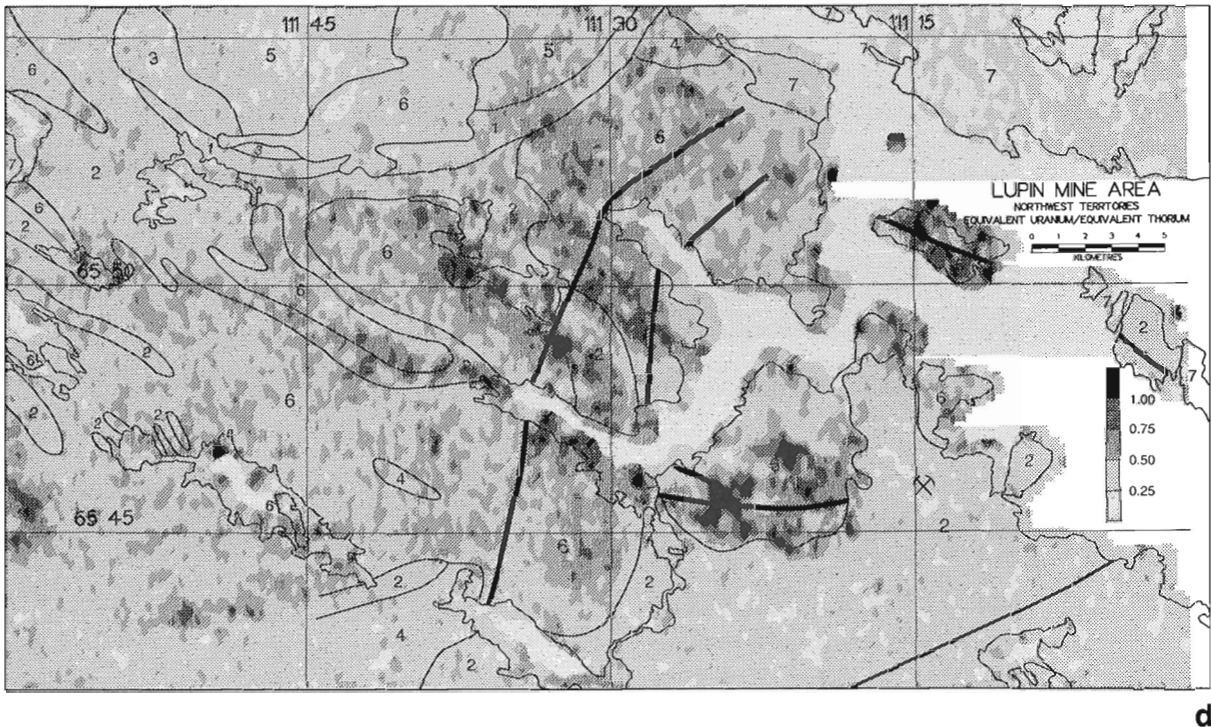
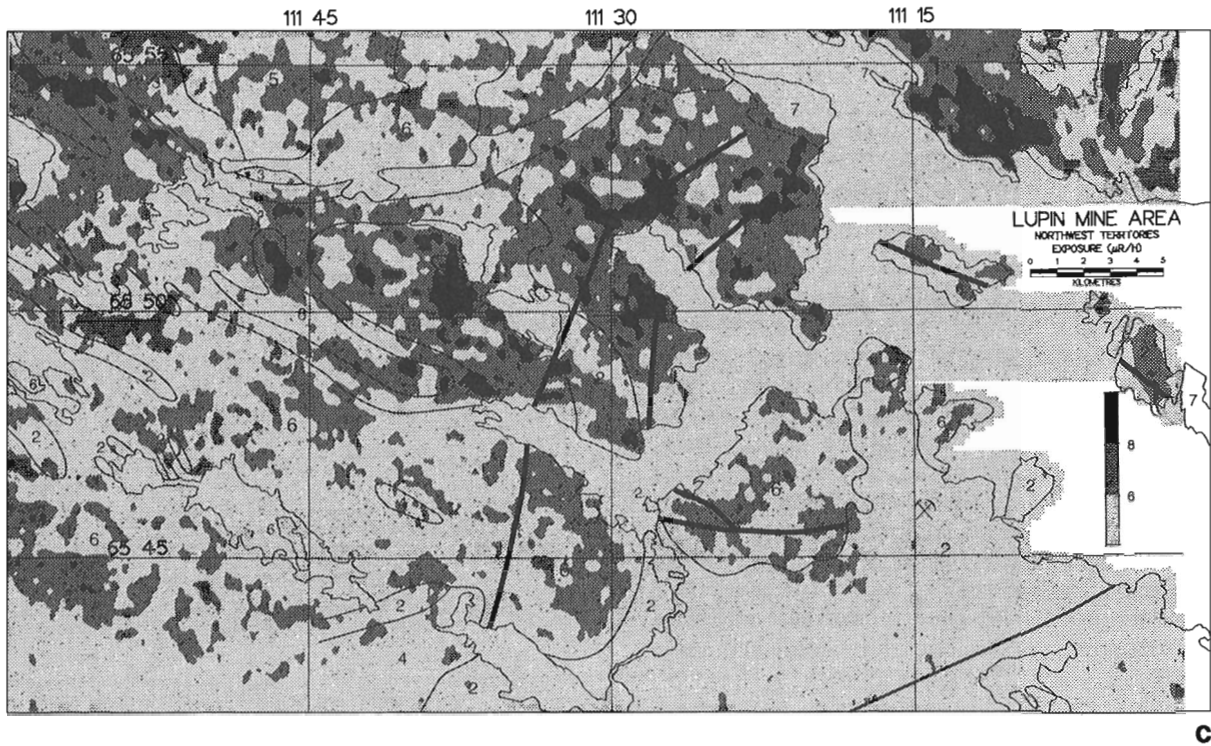


**a**



**b**

**Figure 2. a)** Geology map of the Lupin mine area. Modified from King et al. (1988). **b)** Total magnetic field map. Modified from Geological Survey of Canada (1989).



**Figure 2.** c) Total count radioactivity map. Modified from Geological Survey of Canada (1989). d) eU/eTh ratio map. Modified from Geological Survey of Canada (1989).

## PETROGRAPHY

Variation in magmatic and geochemical evolution of peraluminous granites is usually reflected by the U/Th ratio (Ford and O'Reilly, 1985; Maurice and Charbonneau, 1987; Charbonneau, 1991). When comparing this ratio to the differentiation index (DI) (i.e. normative quartz + albite + orthoclase) of the Contwoyto Batholith, it becomes clear that the U/Th ratio and the DI vary sympathetically (Fig. 6). Therefore, the U/Th ratio reflects fractional crystallization of the batholith.

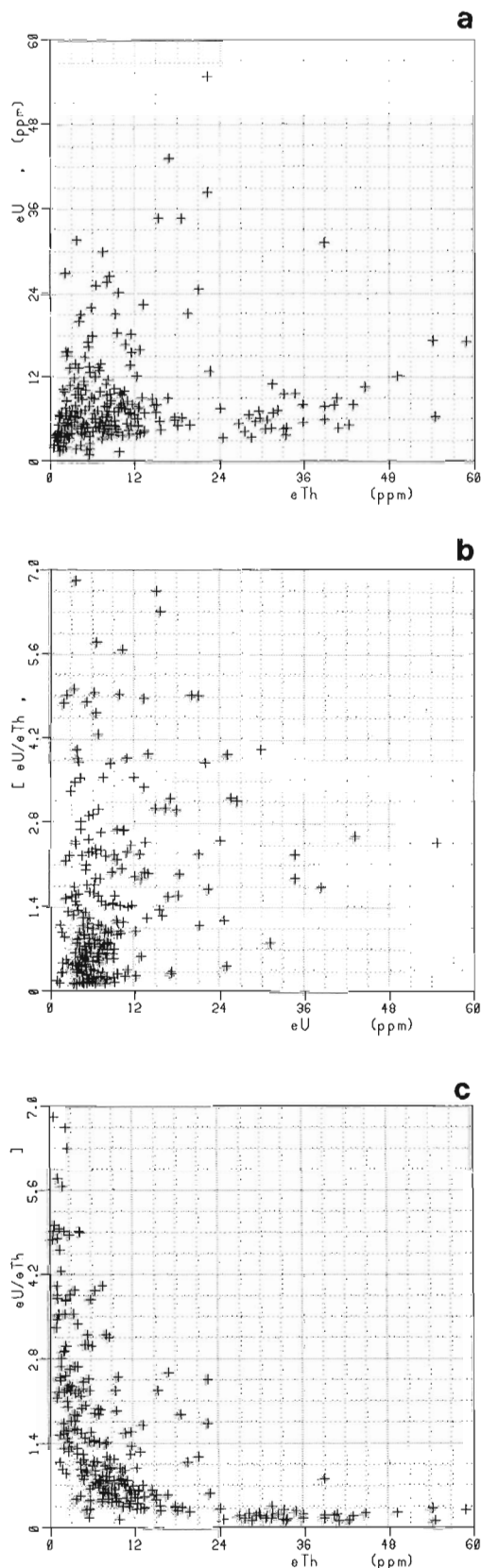
Point counting and petrographical examination of the batholith indicates that the most common composition of the intrusion ranges from granodiorite to monzogranite (Legault, 1991). The essential mineral constituents of the batholith with their average modal percentages ( $\pm$  standard deviation) are quartz ( $33.8 \pm 5.1$ ), plagioclase (albite to oligoclase;  $28.2 \pm 8.2$ ), K-feldspar (microcline;  $22.9 \pm 11.1$ ), sericite ( $5.8 \pm 2.7$ ), muscovite ( $3.4 \pm 3.2$ ), biotite/chlorite ( $3.2 \pm 2.9$ ), with accessory tourmaline, apatite, garnet, sillimanite, rutile, zircon, monazite and a trace of very fine grained, iron oxide opaque minerals. The trace of iron oxides (ilmenite) often occur near chloritized biotite. These mineral percentages are similar to those reported by Tremblay (1976) and Davis (1991).



**Figure 3.** Samples taken for petrographic and geochemical analyses.

**Table 1.** Average gamma-ray spectrometry readings over different lithologies in the study area (n=300)

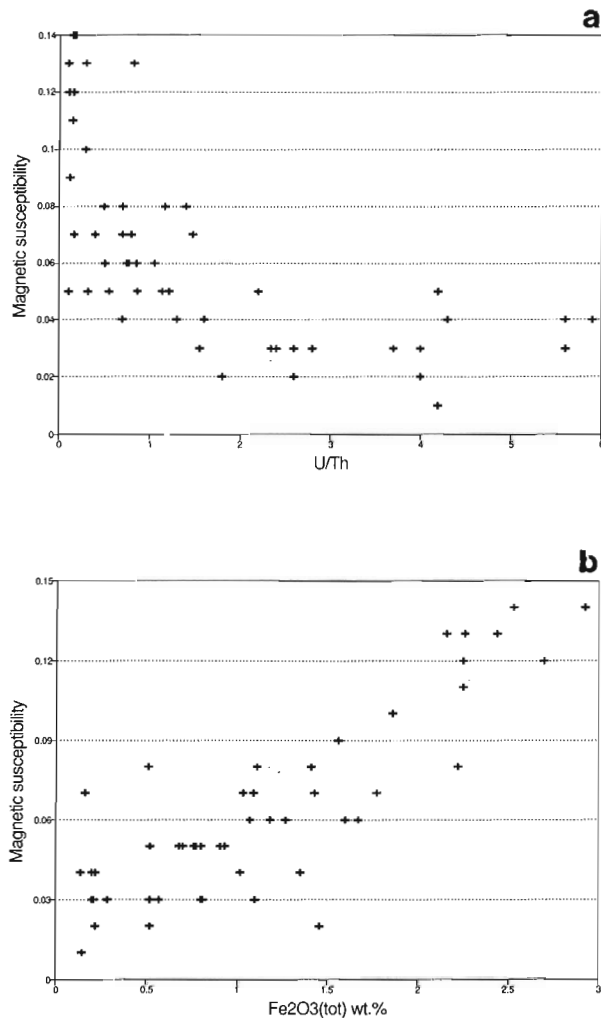
	No.	K %	eU ppm	eTh ppm	eU/eTh	eU/K $\times 10^{-4}$	eTh/K $\times 10^{-4}$
Contwoyto Lake granite	270	3.1	8.6	11.5	0.75	2.8	3.7
Biotite-hornblende diorite and tonalite	12	2.4	1.9	4.9	0.39	0.8	2.0
Porphyritic granodiorite	4	3.1	3.7	22.0	0.17	1.2	7.1
Contwoyto Formation	11	2.2	2.8	9.3	0.30	1.3	4.2
Tuk volcanic rocks	3	1.7	2.0	6.1	0.33	1.2	3.6



**Figure 4.** a) eU versus eTh, b) eU/eTh versus eU, and c) eU/eTh versus eTh. Note the well defined correlation between eU/eTh and eTh and the lack of one between eU/eTh and eU.



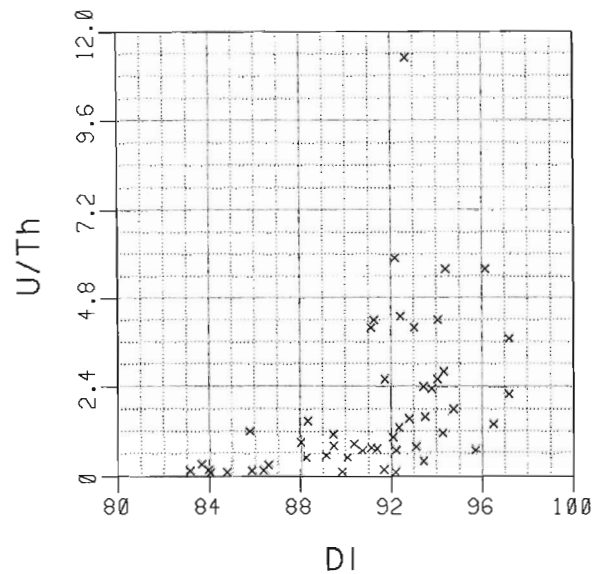
From the standard deviation of the modal mineral proportions and field observations, it is clear that the Contwoyto Batholith is quite heterogeneous (Fig. 7). In thin sections and hand samples, the texture of the batholith varies between idiomorphic and xenomorphic, the former being attributed mostly to the pegmatitic phases. Throughout the batholith, chlorite replaces biotite suggesting regional metamorphic effect, but the degree of chloritization is greatest in rocks with high U/Th ratio suggesting a magmatic/metasomatic component. K-feldspar crystals overgrow plagioclase grains implying that the microcline crystallization extended to late in the paragenetic sequence of the batholith. Graphic, perthitic, and myrmekitic textures were also observed. Perthite and myrmekite are ubiquitous throughout the granite, whereas graphic texture is associated with pegmatitic phases only. The graphic and myrmekitic textures suggest late stage volatile-rich and/or deuteric activity.



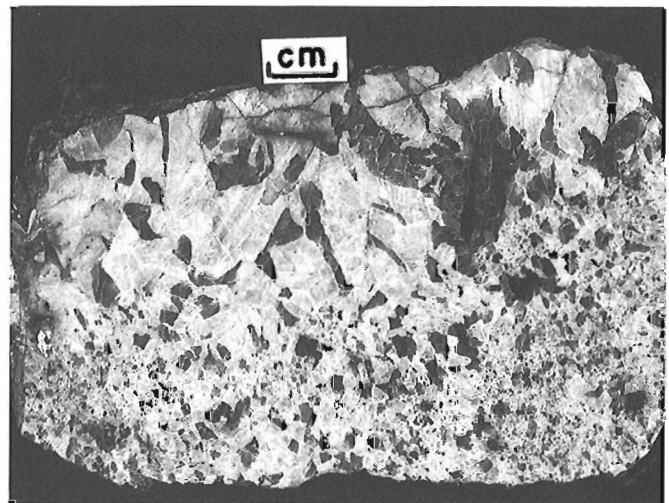
**Figure 5.** Magnetic susceptibility readings versus a) U/Th ratio and b) total iron for 50 samples of Table 2. A magnetic susceptibility reading of 30 is approximately equal to 1 vol.% magnetite.

Examination of thin sections also reveals evidence of nonplastic deformation (i.e., polygonal fracturing of quartz grains, highly fractured tourmaline and garnet crystals).

Petrographical analyses show that low U/Th ratios generally relate to biotite-rich phases, while high-ratio rocks are more muscovite-rich (Fig. 8). Chloritization is more abundant in high-ratio (high DI) rocks although it can be observed in almost all samples. Chloritization has also been reported as being associated with the mineralizing quartz veins (Bullis, 1990). Garnet and tourmaline are associated with the more evolved phases of the batholith (i.e. high DI values). Zircon, monazite, and to a lesser extent apatite reside in the early fractionated phases (i.e., low DI values). This is



**Figure 6.** U/Th ratio versus differentiation index (DI). The DI is the sum of normative quartz, albite, and orthoclase, and relates directly to the evolution of granitoids.



**Figure 7.** Hand sample depicting the wide range in grain size found within the CLG. GSC 1991-170C

related to their low solubility in peraluminous magma (Pagel, 1982). Also, the albite content of plagioclase increases slightly with an increase in U/Th ratio (Fig. 9) as to be expected in the course of magmatic evolution.

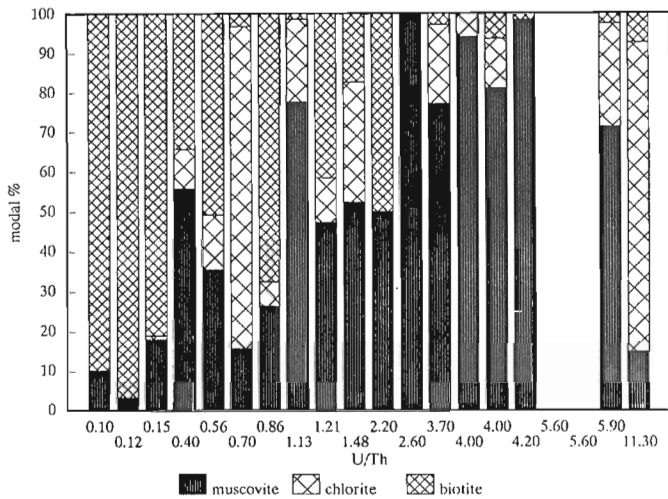
## GEOCHEMISTRY

Average concentrations of major elements in the Contowoyto Batholith (Table 2) indicate that it is similar to two-mica granites from Nockolds (1954) and to low-calcium granites from Turkenian and Wedepohl (1961). However, average sodium ( $\text{Na}_2\text{O}=4.30\%$ ) and aluminium ( $\text{Al}_2\text{O}_3=15.04\%$ ) concentrations in the batholith are quite high, whereas iron ( $\text{FeO}_{\text{total}}=1.14$ ) and calcium ( $\text{CaO}=0.83\%$ ) concentrations

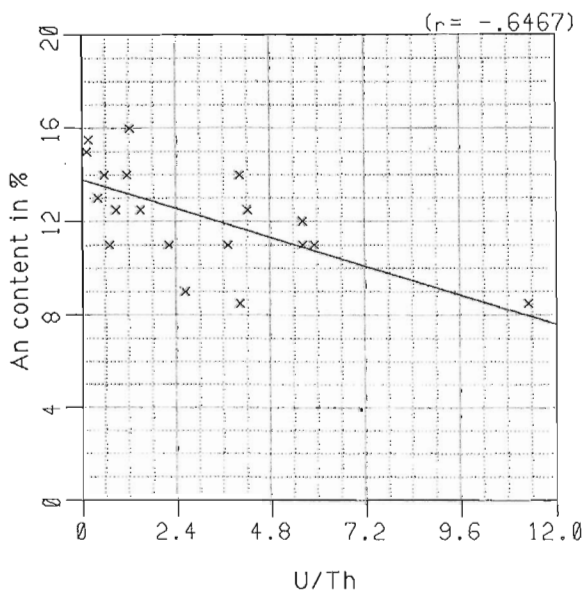
are low. The average trace element concentrations for the Contowoyto Batholith are close to average values for two-mica or low-calcium granites. Geochemical analyses of the batholith also indicate elevated boron (200 ppm) and tin (10 ppm) concentrations and low fluorine (225 ppm) and titanium ( $\text{TiO}_2=0.15\%$ ) values. The strongly peraluminous nature of the batholith, consistent with its mineralogy (i.e., biotite, muscovite, tourmaline, garnet, and sillimanite), is manifested by high values of both normative corundum (up to 4.1%) and A/CNK values (Fig. 10).

**Table 2.** Average values for major, minor, and trace elements of the Contowoyto Batholith granite (n=50). Analysis by X-ray fluorescence spectrometry (+), DC plasma (#), inductively coupled plasma (^), neutron activation (\*), and wet chemical analysis (~).

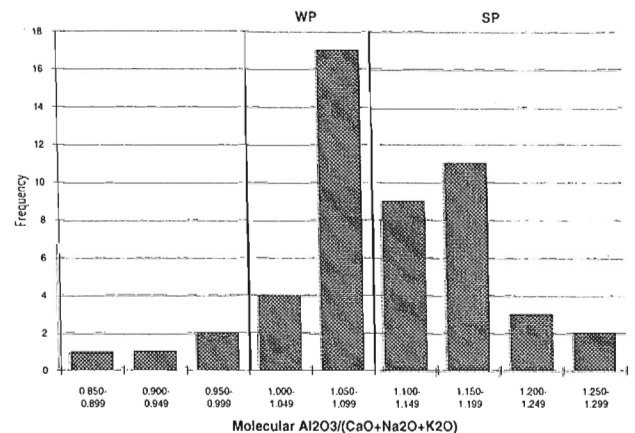
Element	Avg. value	Element	Avg. value
$\text{SiO}_2$ (wt.%)	72.57 +	Au (ppb)	1 #
$\text{TiO}_2$	0.15 +	As (ppm)	2 *
$\text{Al}_2\text{O}_3$	15.04 +	B	200 #
$\text{FeO}(\text{tot})$	1.14 +	Ba	535 +
MnO	0.01 +	Bi	<3 ^
MgO	0.40 +	Ce	41 *
CaO	0.83 +	Cu	2 ^
$\text{Na}_2\text{O}$	4.30 +	F	225 ~
$\text{K}_2\text{O}$	4.56 +	La	23 *
$\text{P}_2\text{O}_5$	0.21 +	Li	69 ^
		Mo	<1 ^
		Pb	15 ^
		Rb	170 +
		Sn	10 +
		Sr	144 +
		Th	11 *
		U	6 *
		W	<3 *
		Zn	32 ^
		Zr	90 +



**Figure 8.** Modal % of muscovite, biotite, and chlorite of thin



**Figure 9.** Anorthite content of plagioclase crystals versus U/Th ratio.



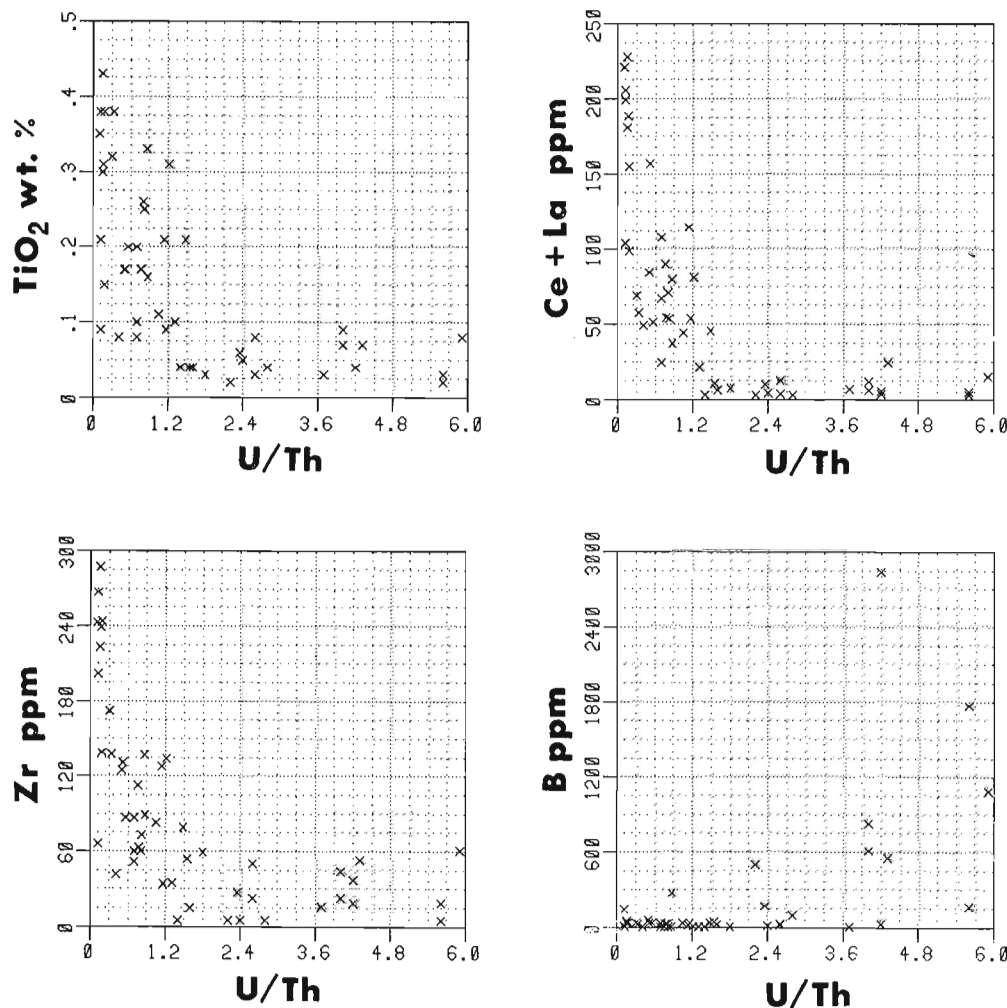
**Figure 10.** Histogram of A/CNK values. Strongly peraluminous (SP) granites are characterized by A/CNK values above 1.10, while weakly peraluminous (WP) granites have a range of 1.00 to 1.10.

The rationale for the geochemical study was to determine if trace elements enriched in the Lupin mineralization (i.e., Au, Ag, Cu, S, As, W) were also elevated in the batholith, and whether they were correlated with the U/Th ratio (DI). The average values of trace elements which have been introduced during the mineralizing process at Lupin reveals that these elements are not enriched in the batholith: Au=<1 ppb, Ag=<0.5 ppm, Cu=2.3 ppm, S=<100 ppm, As=1.7 ppm, W=< 3ppm. However, there may be a slight enrichment in W in the high eU/eTh ratio rocks with three samples above detection limit of 3 ppm (Table 2). Other than the possibility of a weak correlation for W, there is no correlation between these trace elements and the U/Th ratio.

As indicated previously, the U/Th ratio is controlled by thorium depletion, uranium values being random. Some of the more significant chemical variations associated with eU/eTh ratio increases are shown on Figure 11. The low U/Th rocks (high thorium) are biotite-rich and are high in titanium, zirconium (zircon), and Ce+La (monazite). The high U/Th ratio rocks are high in boron (tourmaline). Because

tourmaline often retains gold if gold has moved through a system (Kitaev et al., 1985) and because boron (tourmaline) was noted to increase with the U/Th ratio (DI), tourmaline concentrates were made from ten granite samples. However, levels of gold in these concentrates were also low (~1 ppb).

Variation of Na<sub>2</sub>O and K<sub>2</sub>O contents through out the evolution of the batholith is depicted in Figure 12a. Values for K<sub>2</sub>O vary from 2 to 8 wt.% while Na<sub>2</sub>O ranges from 2 to 6 wt.%. These two elements have an inverse linear relationship. This relationship is explained by the constant amount of feldspar throughout the batholith. Therefore an increase in microcline content implies a reduction in plagioclase and vice-versa. Increases in sodium (albitization) or potassium (K-feldspathization) are common and important alterations associated with gold mineralization (Boyle, 1979). A plot of Na<sub>2</sub>O/K<sub>2</sub>O vs. U/Th indicates no tendency for either sodic or potassium enrichment with an increase in U/Th ratio (DI)(Fig. 12b). This result contrasts, for example, the albitization trend noted in some peraluminous granites in Nova Scotia (Ford and O'Reilly, 1985).



**Figure 11.** Trace element variation diagrams illustrating the relationship between the concentration of certain trace elements and the evolution of the granite.

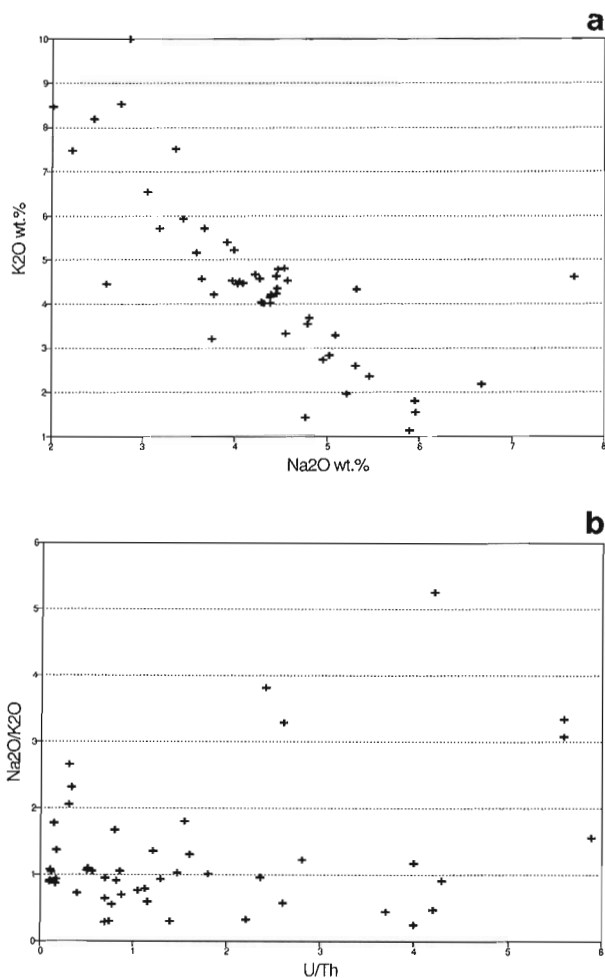


Figure 12. a) K<sub>2</sub>O versus Na<sub>2</sub>O and b) K<sub>2</sub>O/Na<sub>2</sub>O versus U/Th ratio.

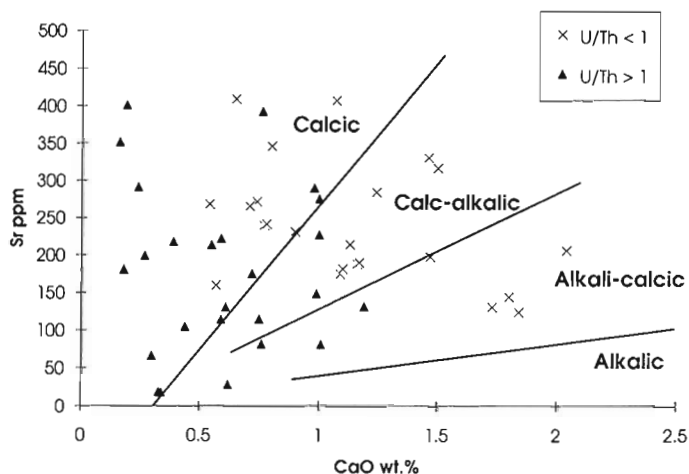


Figure 13. Normalized Sr for CaO = 1.25 wt.% versus CaO. Classification from Keith et al. (1990).

Genetic relationships of magma chemistry to ore deposits have been proposed for some plutons in Nevada by Keith et al. (1990). In their classification, one of the prime indicators for gold fertility is increased Sr/Ca ratio. Based on concentrations of Sr and CaO, peraluminous granites can be classified into four subclasses: alkalic, alkalic-calcic, calcic-alkalic, and calcic. The geochemistry of the Contowoyto Batholith is mainly within the calcic subdivision (68% of data points for the more evolved phases with U/Th >1; Fig. 13). In Nevada the calcic peraluminous granitoids are related empirically to gold.

The degree of oxidation of the Contowoyto Batholith appears to be related to magma evolution and therefore is correlated with the U/Th ratio (Fig. 14). The early phases (i.e. low U/Th) of the batholith crystallized in a reducing environment ( $Fe_2O_3/FeO < 0.9$ ) whereas the more evolved phases (i.e. high U/Th) crystallized in an oxidizing environment ( $Fe_2O_3/FeO > 0.9$ ). There is a broad magnetic anomaly in the western part of the batholith and a low in the east near the mine. Most of the western batholith has a low U/Th ratio (Fig. 2d) and therefore is mostly reduced. In this area, a minute trace of iron oxide (ilmenite) occurs commonly with biotite. Where there is no magnetic anomaly, the batholith has a higher U/Th ratio (Fig. 2d) and is more oxidized. In these rocks, there is also little iron and/or opaque minerals.

### SUMMARY AND CONCLUSIONS

The Contowoyto Batholith is composed of fine- to coarse-grained calcic peraluminous muscovite-biotite monzogranite to granodiorite with accessory apatite,

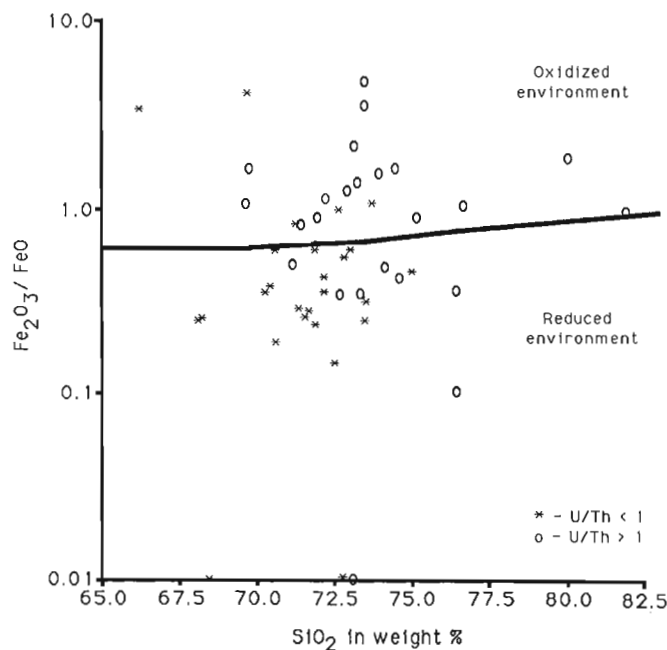


Figure 14. Fe<sub>2</sub>O<sub>3</sub>/FeO ratio versus SiO<sub>2</sub> graph indicating the redox state of the Contowoyto Batholith. Boundary between reduced and oxidized states from Keith et al. (1990).

tourmaline, garnet, sillimanite, rutile, ilmenite, monazite, and zircon. There are abundant associated pegmatitic dykes and pods. The age of the intrusion is relatively close to the age of the mineralizing quartz veins at Lupin.

The batholith has a high and variable U/Th ratio. This ratio has an antipathetic relationship with equivalent thorium concentrations. The petrography reveals that biotite, zircon, apatite, and monazite are mostly confined to the low eU/eTh ratio rocks, while muscovite, chlorite, tourmaline, and garnet are found in the higher ratio rocks. Also, albite content of plagioclase increases slightly with increase in U/Th ratio. Chloritization associated with the mineralizing quartz veins at Lupin is more common in the high eU/eTh ratio rocks.

The U/Th ratio increases with fractionation of the batholith, and is associated with the differentiation index. Low U/Th ratio rocks are higher in TiO<sub>2</sub>, Fe<sub>2</sub>O<sub>3</sub>(total), CaO, MgO, Zr, Ce, and La; high U/Th ratio rocks are enriched in B. There is no apparent Na<sub>2</sub>O or K<sub>2</sub>O enrichment in high U/Th ratio rocks.

The average values of trace elements that have been introduced during the mineralizing process at Lupin reveal that these elements are not enriched in the batholith (Au <1 ppb, Ag <0.5 ppm, Cu ~2.3 ppm, S <100 ppm, W ~3 ppm). Arguably these metals could have been pumped through the granite and into the deposit leaving the granite depleted but there is no data to support this assumption and this is purely speculative.

The broad magnetic anomaly in the western part of the batholith appears to be associated with minor amounts of iron oxides (ilmenite) and the weakly paramagnetic properties of other iron-bearing minerals such as biotite. The magnetic low in the eastern part of the batholith near the Lupin mine relates to more oxidized rocks with less total iron and almost no iron oxides. The transition from reduced to oxidized state could be an important feature in mobilizing gold if it had moved through the batholith.

Certain characteristics of the batholith have been alluded to as being possibly favourable for gold mineralization (i.e., proximity to deposit, timing, calcic peraluminous chemistry, development of a late volatile phase, variability in oxidation state from reduced to oxidized). However none of these features can provide a positive link between the batholith and the mineralizing quartz veins. Furthermore the lack of enrichment of metals in the batholith that are found at the deposit is an argument against its direct involvement in the mineralizing process.

More detailed studies will be necessary in order to establish if the Contwoyto Batholith played a role in the mineralizing history at Lupin. Possible lines of investigation could involve age dating of the mineralization itself (if possible) and observations on the relationship of the quartz veins at Lupin and the batholith at depth (below present mining levels) as well as the felsic dykes present at the mine. Fluid inclusion studies of the mineralizing quartz veins and of the batholith may also prove useful. In addition a detailed study of the granite/sediment contact may establish if the granite's intrusion played a role in the quartz veins' emplacement (ground preparation).

## ACKNOWLEDGMENTS

The authors acknowledge the assistance of Hecla Canada Ltd. with logistics in the field, including accommodation at the Contwoyto Lake exploration camp. R. Stone expedited from Yellowknife. P.B. Holman carried out the airborne survey operations and R. Hetu produced the geophysical compilation. The first author wishes to thank Professor A.E. Lalonde from the University of Ottawa for his help and guidance during the writing of the thesis of which this is a brief summary. The paper was critically reviewed by J.E. King and K.H. Poulsen of the GSC.

## REFERENCES

- Bachman, R.L., Campbell, T.J., and Sneyd, D.S.**  
1990: Crook Mountain Granite and its relation to Early Proterozoic gold mineralization at the Homestake mine, northern Black Hills, South Dakota; Geological Society of America, Rocky Mountain Section, Program with Abstracts, p. A2.
- Bostock, H.H.**  
1980: Geology of the Itchen Lake area, District of Mackenzie; Geological Survey of Canada, Memoir 391, 101 p.
- Boyle, R.W.**  
1979: The geochemistry of gold and its deposits (together with a chapter on geochemical prospecting for the element); Geological Survey of Canada, Bulletin 280, 584 p.
- Bristow, Q.**  
1979: Gamma-ray spectrometric methods in uranium exploration – airborne instrumentation; in *Geophysics and Geochemistry in the Search for Metallic Ore*, (ed.) P.J. Hood; Geological Survey of Canada, Economic Geology Report 31, p. 135-146.
- Bullis, R.**  
1990: Geology of the Lupin deposit, N.W.T.; Mineral Deposits of the Slave Province, Northwest Territories, (ed.) W.A. Padgham and D. Atkinson; 8<sup>th</sup> IAGOD Symposium, Geological Survey of Canada, Open File 2168, p. 115-125.
- Charbonneau, B.W.**  
1991: Geophysical signature, geochemical evolution and radioactive mineralogy of the Fort Smith radioactive belt, Northwest Territories, Canada; in *Primary Radioactive Minerals (The textural patterns of radioactive mineral paragenetic associations)*, Theophrastus Publications, Athens, Greece, p. 21-48.
- Charbonneau, B.W. and Legault, M.I.**  
1992: Interpretation of airborne geophysical data for the Lupin and Thor Lake areas, N.W.T.; Project Summaries, Canada-Northwest Territories Mineral Development Subsidiary Agreement 1987-1991, Geological Survey of Canada, Open File 2484, p. 107-112.
- Crouzet, J., Recoing, M. et Tollon, F.**  
1979: Les gisements aurifères du Massif Central français; *Chronique de la Recherche Minière*, no. 452, p. 5-38.
- Davis, W.J.**  
1991: Granitoid geochemistry and Late Archean crustal evolution in the Central Slave Province; Ph.D. thesis, Memorial University of Newfoundland, St. John's, Newfoundland.  
1992: A non-subduction-related origin for ca. 2.6 Ga granitoids in the Slave Province, NWT; Geological Association of Canada – Mineralogical Association of Canada, Program with Abstracts, p. A24.
- Ford, K.L. and O'Reilly, G.A.**  
1985: Airborne gamma ray spectrometric surveys as an indicator of granophile specialization and associated mineral deposits in the granitic rocks of the Meguma Zone of Nova Scotia; in *High Heat Production (HHP) granites, hydrothermal circulation and ore genesis*; Institution of Mining and Metallurgy, St. Austell, p. 113-133.
- Geological Survey of Canada**  
1989: Airborne gamma-ray spectrometric maps, Lupin Mine area, Northwest Territories; Open File 1921, scale 1:150 000.

- Grasty, R.L., Carson, J.M., Charbonneau, B.W., and Holman, P.B.**  
1984: Natural background radiation in Canada; Geological Survey of Canada, Bulletin 360, 39 p.
- Henderson, J.F.**  
1938: Beaulieu River area, Northwest Territories; Geological Survey of Canada, Preliminary Report 38-1.
- Keith, S.B., Laux, D.P., Maughan, J., Schwab, K., Ruff, S., Swan, M.M., Abbott, E., and Friberg, S.**  
1990: Magma chemistry and metallogeny: a case study from Nevada; Geology and Ore Deposits of the Great Basin, Field Trip Number 8 Guidebook, Co-sponsored by the U.S. Geological Survey and the Geological Survey of Nevada.
- Kerswill, J.A.**  
1992: Gold metallogeny of the Contwoyto Lake, Russell Lake and Courageous Lake areas, Slave Province, NWT; Project Summaries, Canada-Northwest Territories Mineral Development Subsidiary Agreement 1987-1991, Geological Survey of Canada, Open File 2484, p. 161-167.
- King, J.E., Davis, W.J., Relf, C., and Avery, R.W.**  
1988: Deformation and plutonism in the western Contwoyto Lake map area, Central Slave Province, District of Mackenzie, N.W.T.; in *Current Research, Part C*; Geological Survey of Canada, Paper 88-1C, p. 161-176.
- King, J.E., Davis, W.J., Van Nostrand, T., and Relf, C.**  
1989: Archean to Proterozoic deformation and plutonism of the western Contwoyto Lake map area, Central Slave Province, District of Mackenzie, N.W.T.; in *Current Research, Part C*; Geological Survey of Canada, Paper 89-1C, p. 81-94.
- King, J.E., Davis, W.J., Relf, C., and Van Nostrand, T.**  
1990: Geology of the Contwoyto-Nose Lakes map area, Central Slave Province, N.W.T.; in *Current Research, Part C*; Geological Survey of Canada, Paper 90-1C, p. 177-187.
- Kitaev, N.A., Bogatyrev, P.V., and Bogdanova, L.A.**  
1985: Tourmalines from gold deposits; *Geologiya i Geofizika*, v. 26, p. 68-74.
- Legault, M.I.**  
1991: Geophysical and geochemical study of a two-mica granite from the Lupin mine area, Contwoyto Lake, N.W.T.; B.Sc. thesis, University of Ottawa, Ottawa, Ontario, 104 p.
- Lhotka, P.G. and Nesbitt, B.E.**  
1989: Geology of unmineralized and gold-bearing iron formation, Contwoyto Lake - Point Lake region, Northwest Territories, Canada; *Canadian Journal of Earth Sciences*, v. 26, p. 46-64.
- MacDonald, M.A. and O'Reilly, G.A.**  
1988: Gold enrichment associated with post-magmatic processes in the South Mountain Batholith, southwestern Nova Scotia; in *Report of Activities, Part B*, Nova Scotia Department of Mines and Energy, Report 89-1, p. 13-25.
- Maurice, Y.T. and Charbonneau, B.W.**  
1987: U and Th concentration processes in Canadian granitoids - their detection by airborne gamma ray spectrometry and their relationship to granophile mineralization; *Revista Brasileira de Geociências*, v. 17, no. 4, p. 644-646.
- Mawer, C.K.**  
1986: The bedding-concordant gold-quartz veins of the Meguma Group, Nova Scotia; in *Turbidite-hosted gold deposits*, (ed.) J.D. Keppie, R.W. Boyle, and S.J. Haynes; Geological Association of Canada, Special Paper 32, p. 135-148.
- Mortensen, J.K., Thorpe, R.I., Padgham, W.A., King, J.E., and Davis, W.J.**  
1988: U-Pb zircon ages for felsic volcanism in Slave Province, N.W.T.; in *Radiogenic and Isotopic Studies: Report 2*, Geological Survey of Canada, Paper 88-2, p. 85-95.
- Nockolds, S.R.**  
1954: Average chemical compositions of some igneous rocks; *Bulletin of the Geological Society of America*, v. 65, p. 1007-1032.
- Pagel, M.**  
1982: The mineralogy and geochemistry of uranium, thorium and rare-earth elements in two radioactive granites of the Vosges, France; *Mineralogical Magazine*, v. 46, p. 123-135.
- Relf, C.**  
1989: Archean deformation of the Contwoyto Formation metasediments, western Contwoyto Lake area, Northwest Territories; in *Current Research, Part C*; Geological Survey of Canada, Paper 89-1C, p. 95-105.  
1990: Archean deformation and metamorphism of metasedimentary rocks in the Contwoyto - Nose Lakes area, central Slave Province, N.W.T.; in *Current Research, Part C*; Geological Survey of Canada, Paper 90-1C, p. 95-105.
- Roscoe, S.M.**  
1985: The Booth River Intrusive Suite, District of Mackenzie; in *Current Research, Part A*; Geological Survey of Canada, Paper 85-1A, p. 141-144.
- Tremblay, L.P.**  
1976: Geology of northern Contwoyto Lake area, District of Mackenzie; Geological Survey of Canada, Memoir 381, 56 p.
- Turkian, K.K. and Wedepohl, K.H.**  
1961: Distribution of the elements in some major units of the Earth's crust; *Geological Society of America Bulletin*, v. 72, p. 175-192.
- Urabe, T.**  
1985: Aluminous granite as a source magma of hydrothermal ore deposits: an experimental study; *Economic Geology*, v. 80, p. 148-157.
- van Breemen, O., King, J.E., and Davis, W.J.**  
1990: U-Pb zircon and monazite ages from plutonic rocks in the Contwoyto - Nose Lakes map area, central Slave Province, District of Mackenzie; in *Radiogenic age and isotopic studies: Report 3*, Geological Survey of Canada, Paper 89-2, p. 29-38.

# Origin of the Sudbury Igneous Complex, Ontario – differentiate of two separate magmas<sup>1</sup>

Gang Chai and O. Roger Eckstrand

Mineral Resources Division

*Chai, G. and Eckstrand, O.R., 1993: Origin of the Sudbury Igneous Complex, Ontario – differentiate of two separate magmas; in Current Research, Part E; Geological Survey of Canada, Paper 93-1E, p. 219-230.*

---

**Abstract:** A geochemical study has been carried out along profiles through the North Range and South Range of the Sudbury Igneous Complex. Major, trace, and rare-earth elements are more or less constant through the North Range norite. In the South Range, these elements decrease slightly from quartz-rich norite to norite and remain constant upward. A sharp change is observed in the transition from norite to granophyre. SiO<sub>2</sub> and K<sub>2</sub>O increase dramatically, while Al<sub>2</sub>O<sub>3</sub>, MgO, and CaO decrease. TiO<sub>2</sub>, Fe<sub>2</sub>O<sub>3</sub>, and P<sub>2</sub>O<sub>5</sub> show very high values in the transitional oxide-rich gabbro.

The compositional contrast between norite and granophyre and the uniformity within these units are considered to indicate that they resulted from two separate sources of magma, norite corresponding to a mantle-derived magma and granophyre representing crustal melt by meteorite impact. The oxide-rich gabbro was the result of mixing of the two magmas.

**Résumé :** On a entrepris une étude géochimique le long de profils dans le North Range et le South Range du complexe igné de Sudbury. Les concentrations d'éléments majeurs, d'éléments en traces et de lanthanides sont relativement constantes dans la norite du North Range; toutefois, elles baissent légèrement dans le South Range, avec passage d'une norite quartzique à une norite, tout en demeurant constante vers le haut. Un changement marqué s'observe dans la transition de la norite au granophyre. Les concentrations de SiO<sub>2</sub> et de K<sub>2</sub>O augmentent brusquement et celles de Al<sub>2</sub>O<sub>3</sub>, de MgO et de CaO diminuent. Les concentrations de TiO<sub>2</sub>, de Fe<sub>2</sub>O<sub>3</sub> et de P<sub>2</sub>O<sub>5</sub> sont très élevées dans le gabbro de transition riche en oxydes.

Le contraste entre la composition de la norite et celle du granophyre et l'uniformité qui règne au sein de ces unités semblent indiquer qu'elles proviennent de deux sources distinctes de magma. La norite correspondrait à un magma mantellique, tandis que le granophyre représenterait un bain crustal produit par l'impact d'une météorite. Le gabbro riche en oxydes est un produit du mélange de ces deux magmas.

---

<sup>1</sup> Contribution to Canada-Ontario Subsidiary Agreement on Northern Ontario Development (1991-1995), a subsidiary agreement under the Economic and Regional Development Agreement.

**INTRODUCTION**

The origin of the Sudbury Igneous Complex (SIC) has always been controversial despite numerous studies (Walker, 1897; Collins, 1934; Naldrett et al., 1970; Kuo and Crocket, 1979; Faggart et al., 1985; Grieve et al., 1991). Even the most essential aspects of the SIC remain uncertain, for instance, its form and nature, whether it formed from a differentiated sill, a funnel-shaped intrusion, a crustal melt sheet by meteorite impact, or from two independent intrusions. It is of critical significance to determine the source of the magma that gave rise to the SIC, for all succeeding consideration of the formation of the phases of the SIC and its ores must proceed from this answer. In particular, the answer would clarify the role of meteorite impact in the formation of the Sudbury Structure.




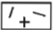
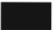

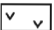
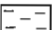
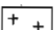
This paper presents results of a systematic geochemical study of the SIC. The study has integrated complete major, trace, and rare-earth elements of the SIC rocks from profiles across the North Range and South Range of the SIC stratigraphy. The geochemical information is used to evaluate previous hypotheses and to construct our tentative interpretation.

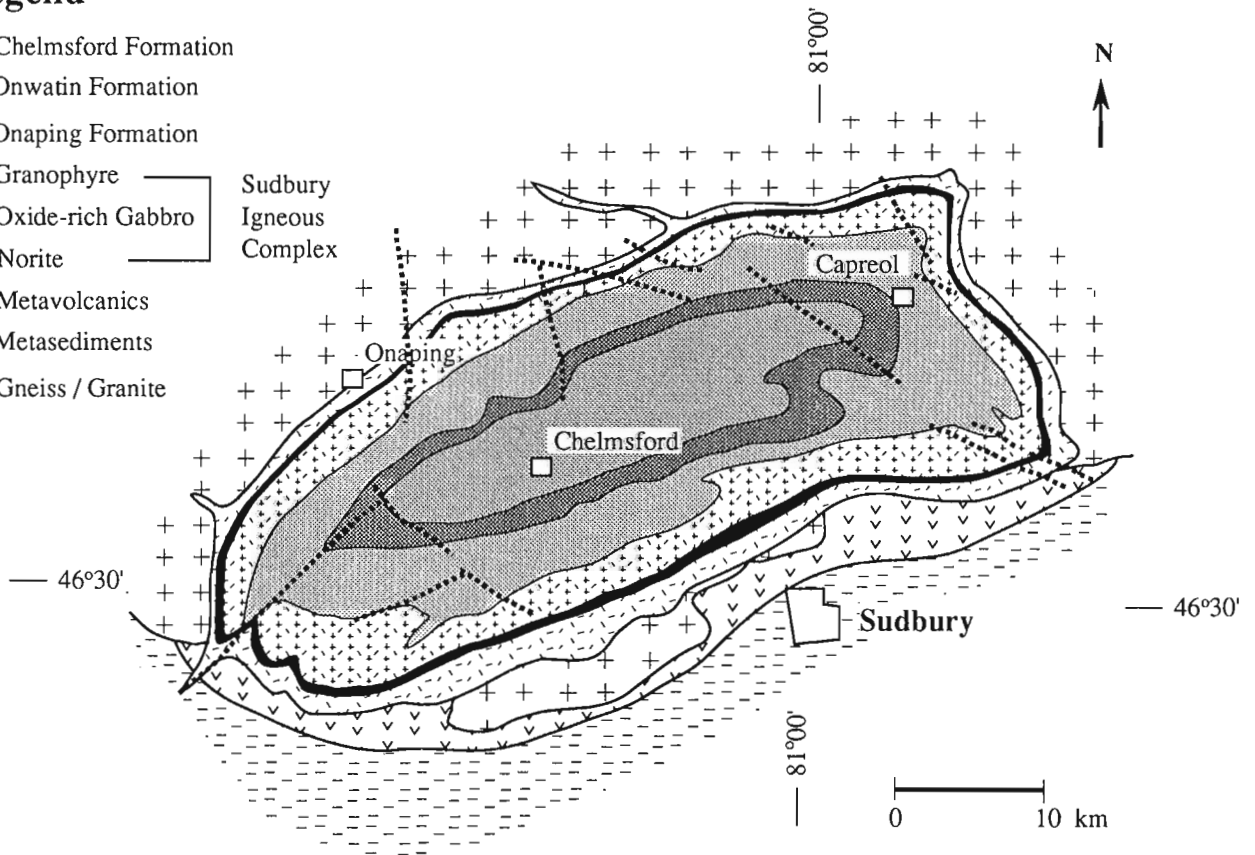
**GEOLOGY OF THE SUDBURY IGNEOUS COMPLEX**

The SIC outcrops as an east-northeast-trending elliptical ring 60 km long by 27 km across (Fig. 1). Generally, it comprises a Lower Zone of noritic rocks, a Transition Zone of oxide-rich gabbro and an Upper Zone of granophyre (Naldrett, 1984).

The Lower Zone comprises a Sublayer and various noritic and gabbroic rocks. The Sublayer is the lowermost unit and consists of noritic, gabbroic, and quartz dioritic rocks that occur as discontinuous basal lenses and radial dykes that extend from the base of the SIC into the footwall rocks. The overlying units of the Lower Zone occur more or less continuously around the ring. On the South Range, these units comprise a marginal quartz-rich norite and the South Range norite. The quartz-rich norite is characterized by 8-20% quartz with a medium- to fine-grained texture. The South Range norite has a medium grained metacumulus texture (Naldrett et al., 1970). Plagioclase and hypersthene constitute the main cumulus phases. Augite is minor in the lower part but increases in amount and becomes a cumulus phase, replacing hypersthene, in the upper part. Other minerals include hornblende, biotite, quartz, and oxides. On the North Range, there is a discontinuous thin layer of mafic norite that

**Legend**

-  Chelmsford Formation
  -  Onwatin Formation
  -  Onaping Formation
  -  Granophyre
  -  Oxide-rich Gabbro
  -  Norite
  -  Metavolcanics
  -  Metasediments
  -  Gneiss / Granite
- Sudbury  
Igneous  
Complex



**Figure 1.** Geological map of the Sudbury region (after Pye et al., 1984).



grades to the overlying felsic norite. The only difference between the two units is that the former contains >40% dark minerals while the latter usually has about 20%. The felsic norite consists of cumulus plagioclase, hypersthene, and largely intercumulus augite, biotite, quartz, and a minor amount of micrographic intergrowth of quartz and feldspar.

The Transition Zone consists of a single unit of oxide-rich gabbro (Naldrett and Hewins, 1984). Ti-Fe oxides compose up to 10% of the rock. Intense alteration of the cumulus phases and a gradual upward increase in the proportion of micrographic intergrowth of quartz and potassic feldspar are typical of this rock type.

The granophyre usually contains 75-80% micrographic intergrowth of quartz and feldspar (Naldrett and Hewins, 1984). Na-rich plagioclase occurs as a cumulus phase and is strongly altered. Dark minerals are much less abundant than in the noritic unit and are dominated by hornblende and biotite.

## CHEMISTRY OF THE IGNEOUS ROCKS

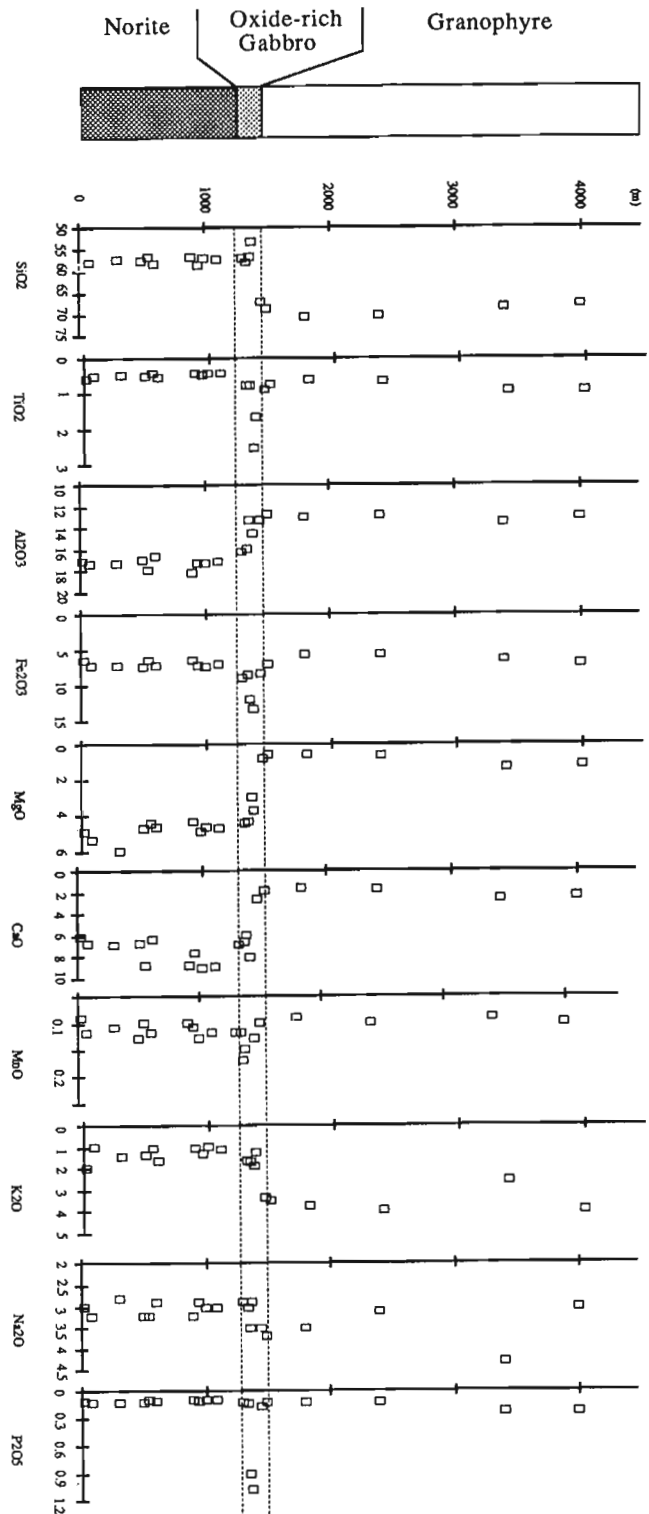
In this study, two traverses across the SIC, corresponding to the North and South ranges, respectively, have been sampled (see Chai et al., 1993, for detailed sample locations). Emphasis has been placed on the North Range because the rocks are fresher and less sheared, and consequently have more colour contrast between dark- and light-coloured minerals than those of the South Range. More samples were collected from the oxide-rich gabbro and adjacent portions of norite and granophyre than in the previous studies in order to better characterize this transition. South Range rocks were sampled and petrological information is presented, but shearing and metamorphism of rocks have rendered the identification of petrological zones more difficult.

### *Elemental variations through stratigraphy*

All the samples have been analyzed for major, trace, and rare-earth elements (data are not presented because of page limitation but are available from the authors). Analyses of major elements were carried out by XRF and other elements by ICP-MS in the Geological Survey of Canada laboratories.

### **North Range profile**

Major elements, such as SiO<sub>2</sub>, TiO<sub>2</sub>, Al<sub>2</sub>O<sub>3</sub>, and Fe<sub>2</sub>O<sub>3</sub>, show minor variation through felsic norite (Fig. 2). MgO increases from 5 wt.% to 6 wt.% over the lower 300 m before it decreases to slightly below 5 wt.% and remains constant in the rest of the felsic norite. CaO is more or less constant, around 6-7 wt.%, in the lower part of the norite; it increases to about 9 wt.% in the upper part of felsic norite. This may be due to an increase in the amount of augite among dark minerals. Naldrett and Hewins (1984) pointed out that though the upper one third of the felsic norite contains almost no hypersthene, it is difficult to determine the transition from norite to gabbro due to severe alteration of pyroxenes. The CaO signature, however, may indicate that the boundary



**Figure 2.** Stratigraphic variation of the contents of major elements of the North Range. The "height" in metres is the horizontal distance measured from the basal contact of the SIC.

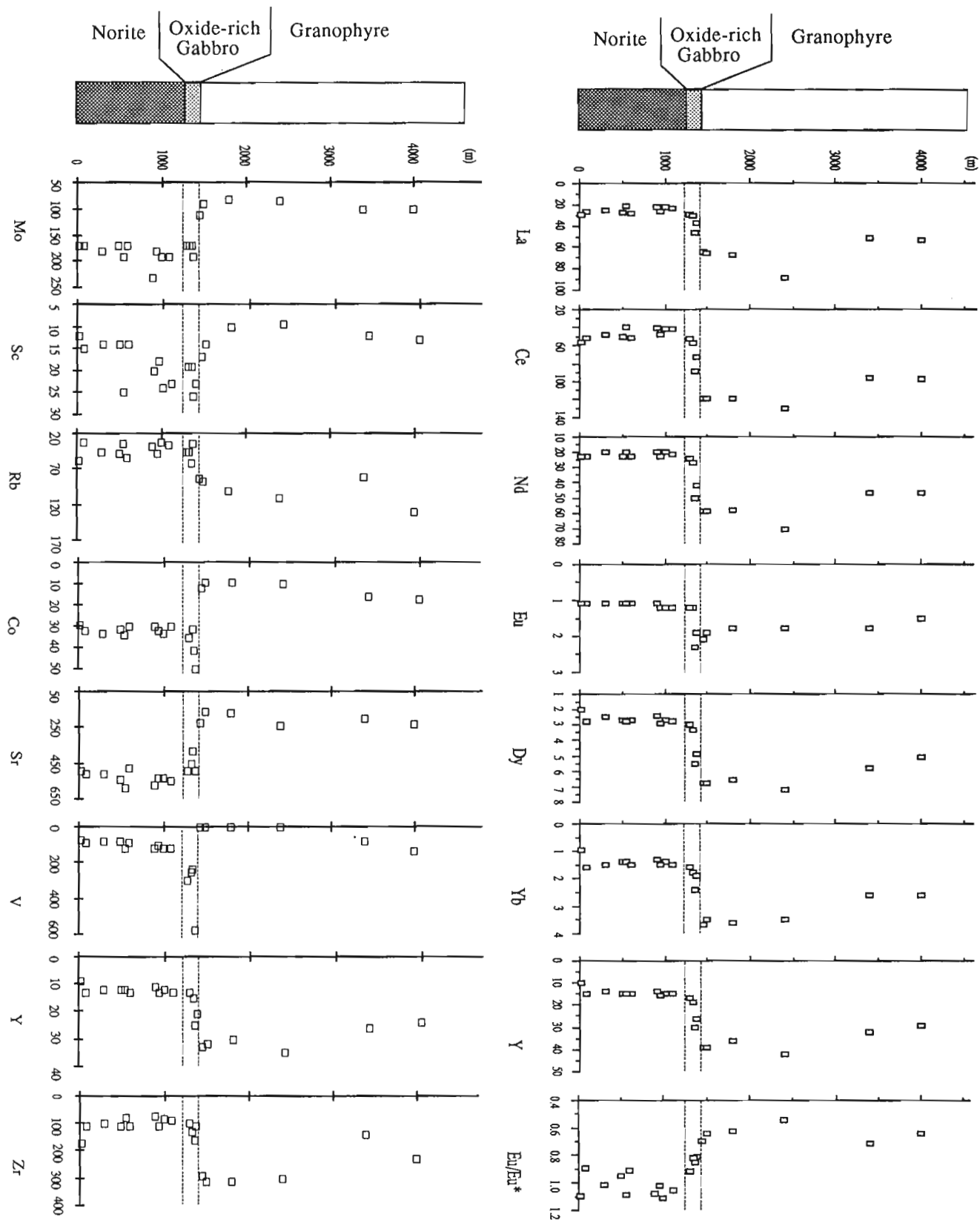


Figure 3. Stratigraphic variation of the contents of selected trace and rare-earth elements of the North Range.

between felsic norite and gabbro is located at about 800 m above the base of the SIC.  $K_2O$  is high at the base and decreases slightly upward in the norite.  $Na_2O$  content, though scattered, also shows a vague upward decrease.

At about 1300 m, there is a sudden change in virtually all the major elements.  $TiO_2$ ,  $Fe_2O_3$ ,  $MnO$ , and  $P_2O_5$  all increase to very high values in the oxide-rich gabbro, reflecting the abrupt increase in magnetite, ilmenite, and apatite.  $SiO_2$  decreases slightly from 57 wt.% to about 56 wt.% and then jumps to more than 67 wt.% in less than 100 m.  $Al_2O_3$  shows a gradual decrease through the oxide-rich gabbro. This probably reflects both a drop in the amount of plagioclase, which is observed in thin sections, and a decrease in anorthite content of plagioclase.  $K_2O$  increases slightly upward, probably due to the increasing abundance of micrographic intergrowth.

Once the granophyre is reached, there is a sharp increase in  $SiO_2$  and  $K_2O$ , and a slight increase in  $Na_2O$ , while  $Al_2O_3$ ,  $MgO$ , and  $CaO$  decrease.  $SiO_2$ ,  $Al_2O_3$ ,  $CaO$ , and  $MgO$  contents vary little in granophyre, while  $Na_2O$  and  $K_2O$  fluctuate more obviously.

Most trace elements are more or less constant in felsic norite (Fig. 3). Sc content increases in the upper part of the felsic norite, similar to that of  $CaO$ , suggesting that this element is mainly incorporated by augite. Abrupt increases in V and Co contents occur at the transition zone, reflecting the similar increases in abundance of oxides and sulphides. In the overlying granophyre, the contents of virtually all trace elements contrast sharply with those of the norite; REE, Rb, Y, and Zr are higher, while Mo, Sc, Co, Sr, and V are lower. All REE contents are more or less constant in the norite and increase sharply to the very high values in the granophyre. The  $Eu/Eu^*$ , near unity in the norite, becomes about 0.66 in the granophyre.

### South Range profile

The compositional variation in the South Range (Fig. 4, 5) is more pronounced than that of the North Range. The basal quartz-rich norite is marked by higher  $SiO_2$ ,  $TiO_2$ ,  $Fe_2O_3$ , and  $MgO$ , and lower contents of other major elements than the South Range norite. The lower  $Al_2O_3$  content may suggest a lower plagioclase content, and high  $MgO$  suggests higher hypersthene, while higher  $SiO_2$  reflects a higher quartz content. These chemical features do not seem to support the interpretation that the quartz-rich norite represents the composition of the primary magma of SIC (Naldrett, 1984). The quartz-rich norite is more likely a hypersthene and plagioclase cumulate with a contaminated, more felsic interstitial liquid (Stevenson and Colgrove, 1968). The South Range norite displays considerable variation in contents of major elements, but is nevertheless distinct from the other rock types. A remarkable increase in  $TiO_2$ ,  $Fe_2O_3$ , and  $P_2O_5$  contents is a typical transition zone feature like that observed in the North Range, but this zone is thicker in the South Range. The chemical features of the granophyre in the South Range are similar to those in the North Range.

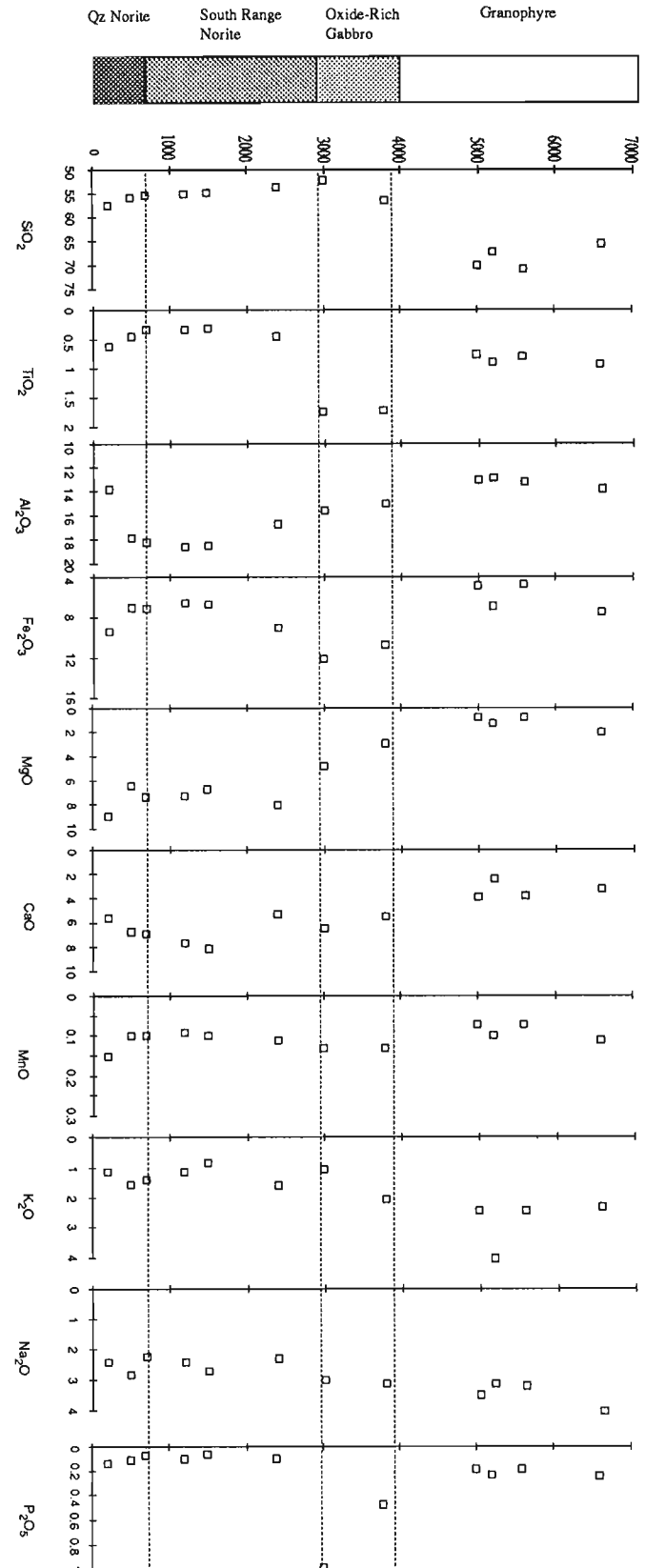


Figure 4. Stratigraphic variation of the contents of major elements of the South Range. "Height" is defined in Fig. 2.

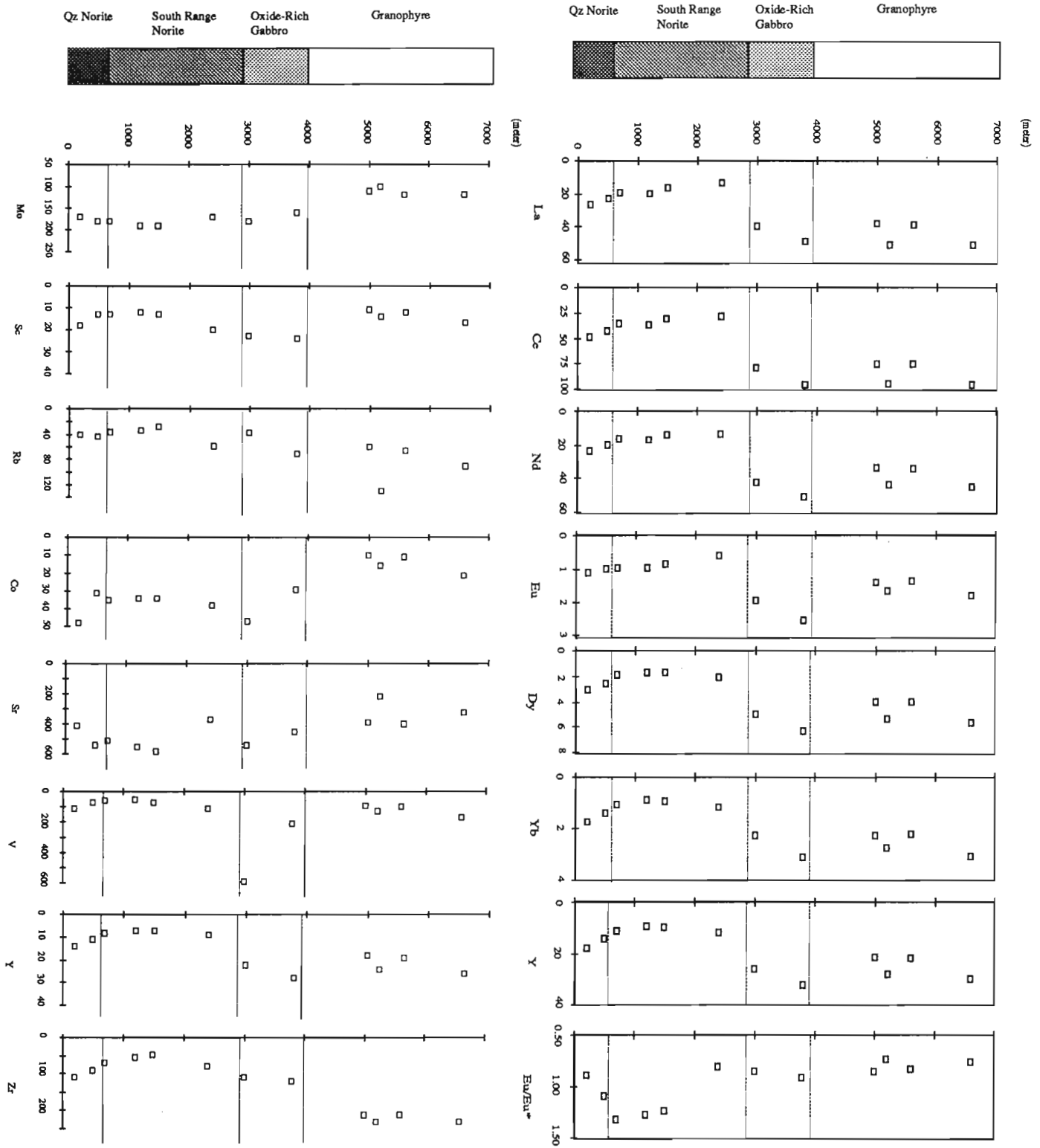


Figure 5. Stratigraphic variation of the contents of selected trace and rare-earth elements of the South Range.

With regard to trace elements in the South Range (Fig. 5), the quartz-rich norite is enriched in Zr, Y, Co, Sc, and V, and weakly depleted in Sr and Mo relative to the overlying South Range norite. Sc in the South Range norite is much lower than that of the North Range norite, and can be ascribed to the lower augite content. Differences in trace element contents between norite and granophyre are more or less similar to those of the North Range, except that the variation is more prominent.

Variation of REE with stratigraphic height for the South Range rocks (Fig. 5) is also similar to that of the North Range rocks. The transition zone samples have REE contents similar to that of granophyre, but because of the sparse sampling and intense deformation of the rocks, the nature of the transition is not well defined. One difference from the North Range is that there is an obvious increase of REE contents towards the base of the quartz-rich norite.

### *Elemental relationships*

One clear chemical feature of the SIC rocks is that there exists two separate populations of data (Fig. 6). One population clusters at a low-SiO<sub>2</sub> content (54-58 wt.%), representing noritic and gabbroic rocks. The other population clusters at a higher SiO<sub>2</sub> content (65-71 wt.%), corresponding to granophyre. Both North Range populations show smaller variation than those of the South Range. There are no intermediate SiO<sub>2</sub> values that would suggest a differentiation trend between the two populations. Furthermore, there is no indication of differentiation within either of the populations. Interestingly, the data for quartz gabbro fall on the lower SiO<sub>2</sub> side of the norite cluster. Considering the variation of SiO<sub>2</sub> upward through the stratigraphy (Fig. 2, 4), its content decreases slightly from around 57 wt.% in felsic norite to about 55 wt.% in oxide-rich gabbro, then increases dramatically to its highest value of 70 wt.% at the base of the granophyre, and thereafter diminishes slightly to 68 wt.% at the top.

Similarly, there is little indication of differentiation trends in the data for the trace and rare-earth elements (Fig. 7). Some elements (Co, Rb, La) in the North Range show weak trends, but like the major elements, data points for norite and granophyre that appear closest in the plot are farthest apart in stratigraphy.

## **PREVIOUS STUDIES ON THE SUDBURY IGNEOUS COMPLEX**

To date, there have been five main hypotheses proposed for the origin of the SIC. These are that the SIC represents: 1) a differentiated sill; 2) a single intrusion in which the upper part was contaminated by roof rocks to form granophyre; 3) a funnel-shaped intrusion; 4) an impact melt sheet; 5) two separate intrusions.

Walker (1897) observed the basin-shaped outline of norite and granophyre, the superposition of granophyre over norite, and the transitional relations between the two rock types. He

suggested that the SIC represents a differentiated sill of a mantle-derived magma. This hypothesis received support from Coleman (1905) and Collins (1934). The latter also defined a transition zone, although very thin in most cases, between norite and granophyre. According to the differentiated sill hypothesis, the relative proportions of the norite, transition zone, and granophyre present in the sill as a whole should be very similar to the proportions that appear at surface.

Wilson (1956) emphasized similarities between the magnetite-rich layer of the SIC and the massive chromite layers of the Bushveld complex, and suggested that the SIC may have a hidden ultramafic zone at its base, implying that the SIC represents a funnel-shaped intrusion. This model overcomes the difficulty of explaining the high proportion of granophyre to norite by suggesting that most of the mafic and ultramafic rock is not exposed at the present level of erosion. Naldrett et al. (1970) observed cryptic variation of pyroxenes in norite, oxide-rich gabbro, and the lower part of granophyre, which they interpreted to be consistent with differentiation by crystal fractionation.

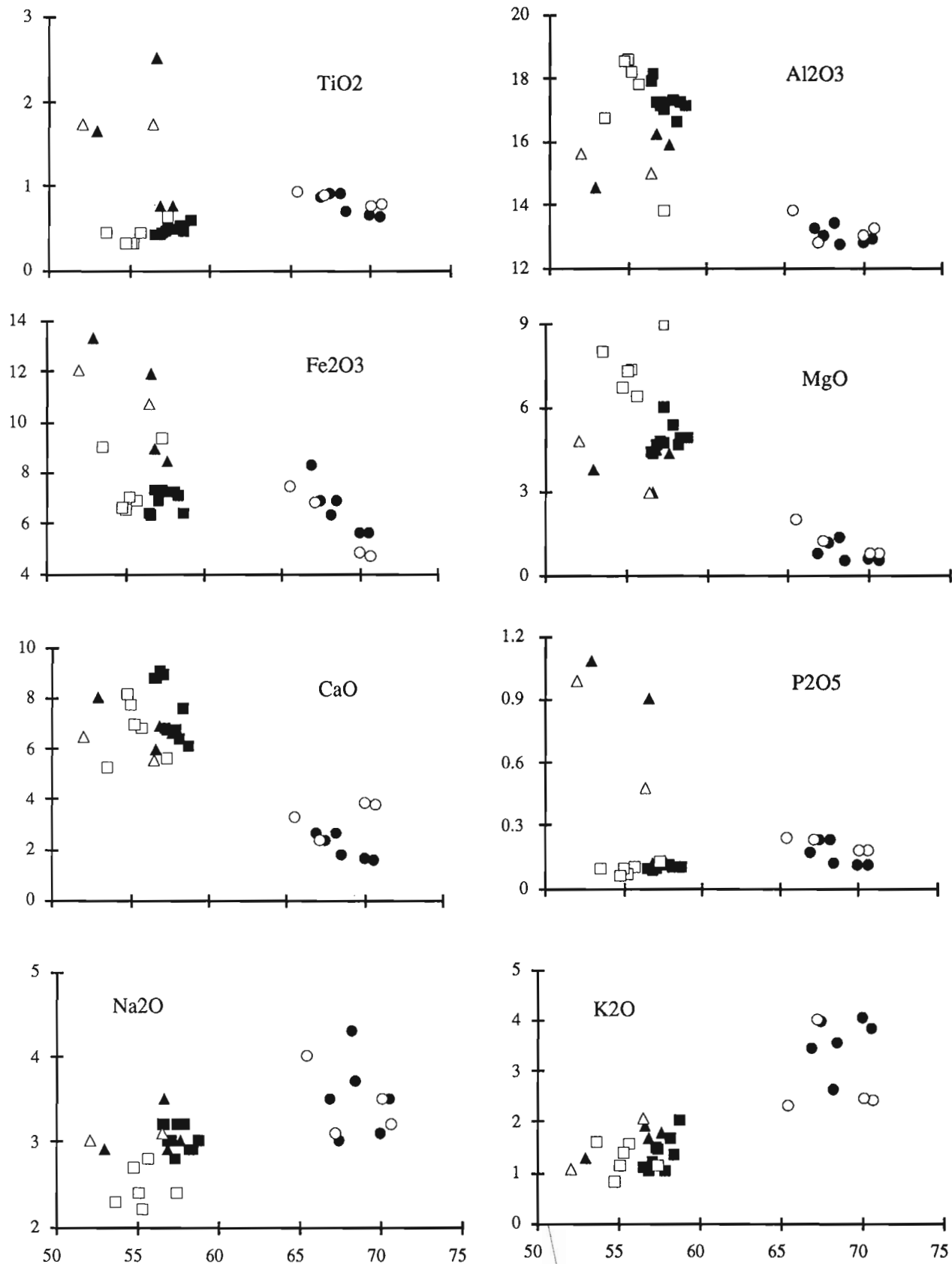
Stevenson and Colgrove (1968) observed inclusions of granite and feldspathic quartzite in the upper part of the granophyre and a gradational variation between granophyre and the Onaping Formation. They suggested that the granophyre represents assimilation of the roof rocks to the SIC magma. This implies that the parent SIC magma could have been as mafic as norite in composition.

Faggart et al. (1985) reported Nd-Sm isotopic results (average  $\epsilon_{Nd} = -7.5$ ) for the SIC norite and gabbro and interpreted them to mean that the magma was derived completely from melting of the Superior Province basement rocks due to meteorite impact. Based on the estimated size of the Sudbury Structure and comparison with other impact sites, Grieve et al. (1991) concluded that the predicted meteorite impact melt is sufficient to generate the SIC.

Although the above hypotheses invoke differing fractionation processes for SIC magma (e.g. source of magma, volume proportion of norite to granophyre, extent of contamination), all of them assume that the SIC represents a single magma before crystallization. These hypotheses can be termed single magma models.

On the other hand, Phemister (1925, 1937) observed that: 1) norite and granophyre are each individually uniform in mineralogy and composition; 2) the transition between the two is abrupt; and 3) there is far too much granophyre to be derived from a basaltic magma. He interpreted the SIC as formed from two independent magmas, and that the granophyre intruded before the noritic magma was completely solidified.

Therefore, the problem of the first order in the genesis of the SIC is whether it was a single differentiated magma or two separately intruded and differentiated magmas.



**Figure 6.** Plot of major element oxides versus  $SiO_2$  for SIC rocks. Square: norite; triangle: gabbro; circle: granophyre; filled: North Range; unfilled: South Range.

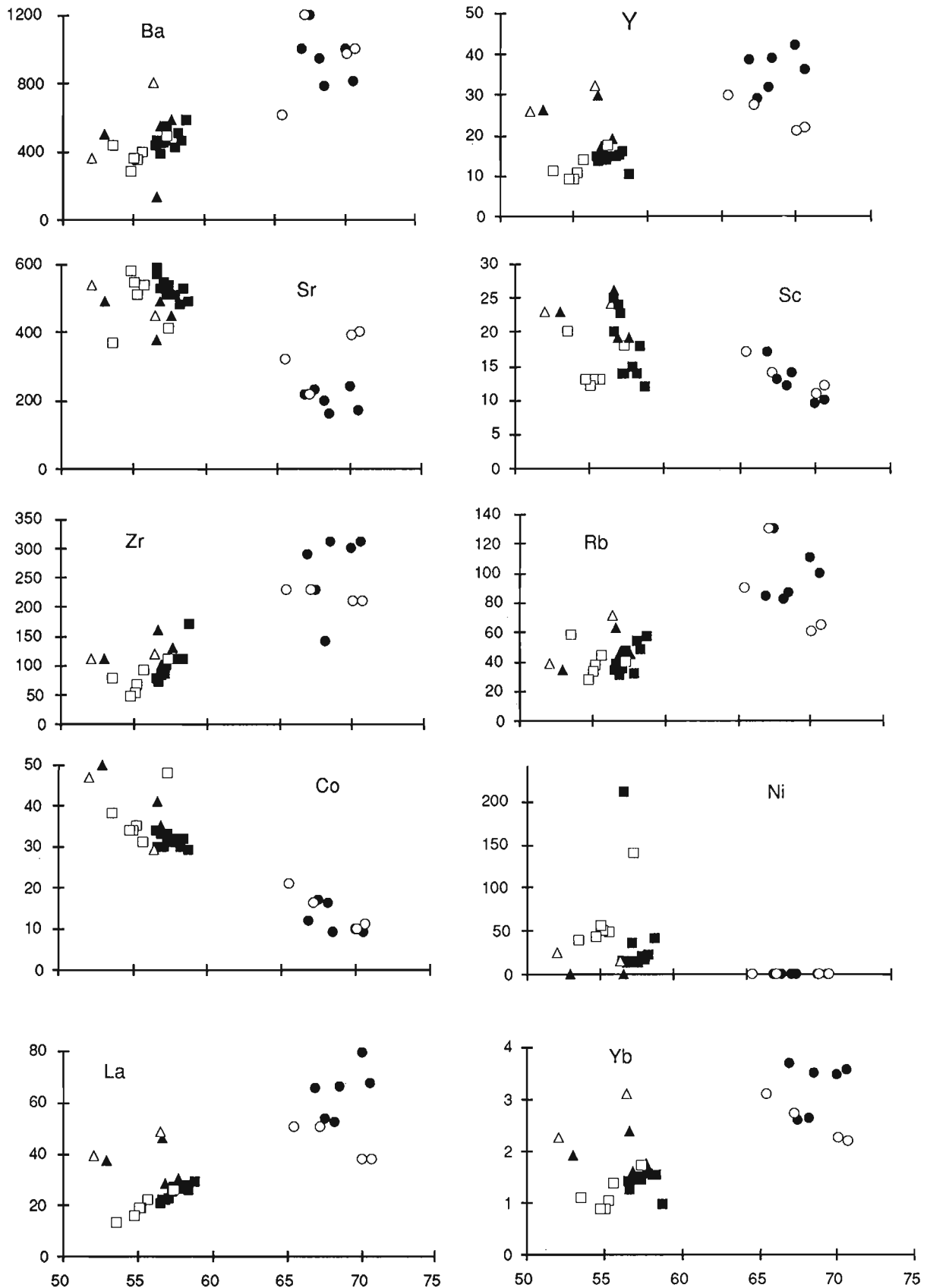


Figure 7. Plot of selected trace and rare-earth elements versus SiO<sub>2</sub> for SIC rocks. See Figure 6 for symbols.

## THE NATURE OF THE SUDBURY IGNEOUS COMPLEX

If the SIC represents a single differentiated intrusion, the crystallization and settling of cumulus minerals must be very efficient, i.e. early crystallized minerals would settle to the bottom of the magma chamber. It seems quite probable that gravitational separation of the pyroxene occurred because of its high density. However, there is no evidence to show that plagioclase is denser than the magma it crystallized from. Campbell et al. (1978) indicated that plagioclase with An<sub>96</sub> has a density greater than basaltic magma, plagioclase with An<sub>55</sub> is less dense than basaltic magma, while that with An<sub>77</sub> is similar in density to basaltic magma. The SIC plagioclase has an anorthite content in the range of 45-55% (Naldrett et al., 1970) and should have densities of 2.63 (1200°C) - 2.68 (25°C) g/cm<sup>3</sup> (Campbell et al., 1978). Collins (1934) found that norite and granophyre have densities of 2.85 and 2.7 g/cm<sup>3</sup>, respectively, both therefore being denser than SIC plagioclase at room temperature. A tholeiitic magma at Kilauea is reported to have a density around 2.65 g/cm<sup>3</sup> at 1 atm at 1200°C (Kushiro, 1980), slightly denser than plagioclase (An<sub>55</sub>) at the same temperature. Even if plagioclase were slightly denser than the SIC magma because of the felsic composition of the SIC magma, plagioclase would not necessarily settle to the bottom of the magma chamber for two reasons. First, the viscosity of a felsic magma, such as the granophyre, is too high. Second, Sparks et al. (1984) indicated that convection of magma, in particular in a large magma chamber, is a common phenomenon if differences in either composition or temperature exist, and magma convection will keep crystals whose density is within 0.5 g/cm<sup>3</sup> of that of the liquid in suspension. Layering in the SIC is poorly developed, but layer thicknesses are probably in the order of 1000 m which is much greater than the values used by Sparks et al. (1984) in their calculation. Consequently, the SIC magma would probably experience significant convection, and plagioclase, being close in density to the magma, remained suspended in the convecting magma. Therefore, it is improbable that cumulus segregation of early separating plagioclase would occur.

Naldrett et al. (1970), in interpreting the formation of granophyre, considered that norite represents the cumulus zone of the SIC magma, and that the magma became too viscous for gravitational settling once it reached granophyre composition. This implies that norite and granophyre represent the two extreme stages in the formation of the SIC. At the beginning, viscosity of the magma was low, and cumulus pyroxene crystals could settle to produce norite, but subsequently the magma became highly viscous so that crystals could not settle, resulting in the formation of granophyre. Pursuing this model, there should have been an intermediate stage with properties between those of norite and granophyre, during which period settling of cumulus minerals became progressively less effective with differentiation. The result should be a decrease in the amount of cumulus phases toward the top of the norite. This is not observed in the norite. It seems that gravitational accumulation of fractionated crystals from a single magma is unable to explain the uniform composition of norite.

Now, let us examine the chemical character of the SIC rocks. It has been demonstrated above that there is a big compositional contrast between norite and granophyre, and also that each rock type tends to have uniform concentrations of major, trace, and rare-earth elements. If the parental magma had differentiated by gravitational settling of the cumulus minerals from a differentiated sill, the residual liquid would be enriched in incompatible elements, and a gradual change in the residual liquid should be expected, in addition to the change of mineral composition. For example, if a differentiated sill model is assumed and the primary magma contains 63 wt.% SiO<sub>2</sub>, crystallization of plagioclase and pyroxenes, with about 53-55 wt.% SiO<sub>2</sub>, will greatly enrich the residual liquid in SiO<sub>2</sub>. Naldrett et al. (1970) envisioned a funnel shaped intrusion for the SIC, in which the majority of the igneous rocks would be norite or other mafic rocks. Thus, when crystallization had reached the top of norite, most of the magma would have been crystallized. The upper part of the norite would have a much more evolved interstitial liquid than in the lower part. Consequently, a well defined differentiation trend should be seen instead of a uniform composition. This is neither observed in the plot of height versus element profiles (Fig. 2-5) nor in the elements versus SiO<sub>2</sub> plots (Fig. 6,7).

REE can be good indicators for a differentiation trend, as they are incompatible during the cumulus process and are not easily affected by metamorphism and alteration. If the SIC had resulted from magma differentiation by crystal accumulation (Kuo and Crocket, 1979), we would expect a gradual upward increase of REE contents in the norite representing enrichment of REE in the evolving magma. Instead, constant, or slightly decreasing REE contents were observed in the norite.

Wilson's (1956) comparison between the SIC and the Bushveld Complex was based partly on the analogy between the SIC oxide-rich gabbro and the Bushveld chromite layers. The formation of the chromite layers is now commonly accepted as the result of mixing of an evolved magma with a new pulse of magma (Campbell and Turner, 1986). If the oxide-rich gabbro can be compared to chromite layers of Bushveld Complex, its formation would be the result of mixing between the noritic magma and the granophyric magma.

From the above discussion, it can be seen that the mineralogical and compositional features of the SIC cannot be explained by a single magma model, at least not by in situ differentiation. A two intrusion model seems more likely.

## A REVISED TWO-INTRUSION INTERPRETATION

Based on the new chemical data and the above discussion, the formation of the SIC can be envisioned as follows. First, a meteorite impact gave rise to the Sudbury Structure (Dietz, 1964), and generated a large volume of crustal melt (Grieve et al., 1991). The granophyre is probably the result of the crystallization of that melt. The REE composition of the granophyre can be modeled by combining suitable



proportions of the immediate country rocks (paper in preparation by authors). The gradual transition from granophyre to the matrix of the Onaping Formation (Stevenson and Colgrove, 1968), which has been interpreted in part as an impact-generated fallback breccia (Peredery, 1972), further supports an impact melt origin of the granophyre.

The meteorite impact could also have been the energy source that led to the emplacement of the mantle-derived magma that gave rise to the norite. This mafic magma could have intruded the chamber occupied by the crustal melt in the following manner: 1) the mafic magma intruded the chamber as a fountain and mixed with the crustal melt on its way up; 2) the higher density of this hybrid magma forced it to fall back to the floor of the chamber and spread out along its base; 3) the difference in temperature and composition between the crustal melt and the hybrid mafic magma would prevent them from mixing with each other, but formed two layers of convected magma.

As the magma cooled, it started to crystallize plagioclase and hypersthene. The plagioclase had about the same density as the magma and would tend to remain suspended in the magma chamber. Pyroxene was much denser than the magma, thus could theoretically sink to the bottom of the magma chamber. However, this type of settling was probably soon impeded by an increasing amount of plagioclase crystals in the magma and the increasing viscosity of the magma that would accompany the decreasing temperature and increasingly felsic composition. Consequently, plagioclase and pyroxene would both crystallize and grow in situ to form norite.

At the stage when the mafic magma was too abundant in suspended crystals and magma convection became slow, the magma would mix with the overlying crustal melt along their mutual boundary. The resulting abrupt change in composition of this hybrid magma might have caused the precipitation of magnetite, apatite, and sulphide, at the contact zone. Thus the oxide-rich nature of the transitional gabbro represents a zone of mixing between norite magma and impact melt.

The granophyre crystallized only after norite crystallization was essentially complete because of the lower liquidus temperature of the former. The liquidus minerals were plagioclase and augite or hornblende. However, the high viscosity of its felsic composition prevented these minerals from settling. When the residual liquid reached cotectic composition, feldspar and quartz crystallized together to form the micrographic intergrowth of the rock.

One of the problems facing the impact model is the coarse grain size of the granophyre, a texture not seen in other impact melt sheets (Grieve et al., 1991). The answer may be that the melt sheet had received a constant heat supply from the underlying mantle-derived magma through latent heat loss during crystallization. Therefore, the crustal melt crystallized slowly and formed the coarse grained granophyre.

## ACKNOWLEDGMENTS

We gratefully acknowledge the helpful discussions and encouragement of geologists of INCO Ltd. and Falconbridge Ltd., in particular, Gordon Morrison, Bob Martindale, Edward Pattison, Walter Peredery, Richard Alcock, Jeffery Scott, and Colin Coates. We also thank Catharine Farrow of Carleton University for providing her assistance in field sampling. We also appreciate the critical review of Robert Baragar of the Geological Survey of Canada. This project is part of Project C1.217, funded by the Geological Survey of Canada under the terms of the Northern Ontario Development Agreement.

## REFERENCES

- Campbell, I. H., Roeder, P.L., and Dixon, J.M.**  
1978: Plagioclase buoyancy in basaltic liquids as determined with a centrifuge furnace; *Contributions to Mineralogy and Petrology*, v. 67, p. 369-377.
- Campbell, I. H. and Turner, J.S.**  
1986: The role of convection in the formation of platinum and chromite deposits in layered intrusions; in *Silicate Melts: Their Properties and Structure Applied to Problems in Geochemistry, Petrology, Economic Geology and Planetary Geology*, (ed.) C.M. Scarfe; Mineralogical Association of Canada, Short Course Handbook, v. 12, p. 236-278.
- Chai, G., Eckstrand, O.R., and Gregoire, C.**  
1993: Platinum group element concentrations in the Sudbury rocks, Ontario – an indicator of petrogenesis; in *Current Research, Part C*; Geological Survey of Canada, Paper 93-1C, p. 287-293.
- Coleman, A.P.**  
1905: The Sudbury nickel field; Report, Ontario Bureau of Mines, v. 14, part 3, 183 p.
- Collins, W.H.**  
1934: Life history of the Sudbury nickel irruptive: Part 1, Petrogenesis; *Transactions, Royal Society of Canada*, v. 28, p. 123-177.
- Dietz, R.S.**  
1964: Sudbury structure as an astrobleme; *Journal of Geology*, v. 72, p. 412-434.
- Faggart, B.E.J., Basu, A.R., and Tatsumoto, M.**  
1985: Origin of the Sudbury Complex by meteoritic impact; neodymium isotopic evidence; *Science*, v. 230, p. 436-439.
- Grieve, R.A., Stoffer, D., and Deutsch, A.**  
1991: The Sudbury Structure: controversial or misunderstood; *Journal of Geophysical Research*, v. 196, no. E5, p. 22753-22764.
- Kuo, H.Y. and Crocket, J.H.**  
1979: Rare earth elements in the Sudbury Nickel Irruptive: comparison with layered gabbros and implications for nickel irruptive petrogenesis; *Economic Geology*, v. 74, p. 590-605.
- Kushiro, I.**  
1980: Viscosity, density and structure of silicate melts at high pressures, and their petrological applications; in *Physics of Magmatic Processes*, (ed.) R.B. Hargraves; Princeton University Press, Princeton, p. 93-120.
- Naldrett, A.J.**  
1984: Mineralogy and composition of the Sudbury ores; in: *The Geology and Ore Deposits of the Sudbury Structure*, (ed.) E.G. Pye, A.J. Naldrett, and P.E. Giblin; Ontario Geological Survey, Special Volume 1, p. 309-325.
- Naldrett, A.J. and Hewins, R.H.**  
1984: The main mass of the Sudbury igneous complex; in *The Geology and Ore Deposits of the Sudbury Structure*, (ed.) E.G. Pye, A.J. Naldrett, and P.E. Giblin; Ontario Geological Survey, Special Volume 1, p. 235-251.
- Naldrett, A.J., Bray, J.G., Gasparrini, E.L., Podolsky, T., and Rucklidge, J.D.**  
1970: Cryptic variation and the petrology of the Sudbury nickel irruptive; *Economic Geology*, v. 65, p. 122-155.

**Peredery, W.V.**

1972: The origin of rocks at the base of the Onaping Formation, Sudbury, Ontario; Ph.D. thesis, University of Toronto, Toronto, Ontario, 366 p.

**Phemister, T.C.**

1925: Igneous rocks of Sudbury and their relation to the ore deposits; Report of the Ontario Department of Mines, v. 34, part 8, p. 1-61.

1937: A review of the problems of the Sudbury Irruptive; Journal of Geology, v. 45, p. 1-47.

**Pye, E.G., Naldrett, A.J., and Giblin, P.E.**

1984: The Geology and Ore Deposits of the Sudbury Structure; Ontario Geological Survey, Special Volume 1, includes Map 2491, District of Sudbury, scale 1:50 000.

**Sparks, R.S.J., Huppert, H.E., and Turner, J.S.**

1984: The fluid dynamics of evolving magma chambers; Philosophical Transactions of the Royal Society of London, v. 310, p. 511-534.

**Stevenson, J.S. and Colgrove, G.L.**

1968: The Sudbury Irruptive – Some petrogenetic concepts based on recent field work; in Reports, 23rd International Geological Congress, v. 5, p. 27-35.

**Walker, T.L.**

1897: Geological and petrographical studies of the Sudbury nickel district, Canada; Quarterly Journal, Geological Society of London, v. 53, p. 40-66.

**Wilson, H.D.B.**

1956: Structure of lopoliths; Bulletin, Geological Society of America, v. 67, p. 289-300.

---

Geological Survey of Canada Project 840050

# Gravity survey of the Sue-Dianne deposit, Northwest Territories<sup>1</sup>

S.S. Gandhi and D. Halliday<sup>2</sup>  
Mineral Resources Division

*Gandhi, S.S. and Halliday, D., 1993: Gravity survey of the Sue-Dianne deposit, Northwest Territories; in Current Research, Part E; Geological Survey of Canada, Paper 93-1E, p. 231-238.*

---

**Abstract:** A local gravity survey was conducted to further investigate resource potential of the magnetite-rich breccia zone of the Sue-Dianne Cu-U-Au-Ag deposit, which is hosted by rhyodacite ignimbrites and contains drill indicated resources of eight million tonnes. Large polymetallic iron oxide-rich deposits of this type occur in a comparable geological setting in South Australia, and have strong gravity expression because of their density contrast with the host rocks.

The survey revealed a Bouguer anomaly of 0.25 mGal over the eastern part of the breccia zone where most of the drilling was done, and a 1.5 mGal anomaly near the little explored western margin of the deposit. The latter anomaly indicates additional potential for iron oxide-rich material, and merits further study. The results support a geological interpretation of mineralization as genetically linked to the felsic volcano-plutonic activity rather than to a mafic plutonic source.

**Résumé :** Un levé gravimétrique local a été fait pour mieux étudier le potentiel minéral de la zone de brèches riches en magnétite du gisement de Sue-Dianne à minéralisation de Cu-U-Au-Ag; le gisement est encaissé dans des ignimbrites rhyodacitiques et ses réserves indiquées par sondage s'élèvent à 8 millions de tonnes. On trouve de gros gisements polymétalliques riches en oxyde de fer de ce type dans des cadres géologiques comparables du sud de l'Australie; leur signature gravimétrique est caractéristique car leur densité diffère de celle des roches encaissantes.

Le levé a révélé la présence d'une anomalie de Bouguer de 0,25 mgal dans la partie orientale de la zone bréchique où la plupart des sondages ont été effectués et d'une anomalie de 1,5 mgal près de la bordure occidentale peu explorée du gisement. Cette deuxième anomalie indique la présence potentielle de lithologies riches en oxyde de fer et justifie la réalisation de travaux additionnels. Les résultats confirment une interprétation géologique selon laquelle la minéralisation serait génétiquement reliée à une activité volcano-plutonique de nature felsique plutôt qu'à une source plutonique mafique.

---

<sup>1</sup> Contribution to Canada-Northwest Territories Mineral Initiatives (1991-1996), an initiative under the Canada-Northwest Territories Economic Development Cooperation Agreement

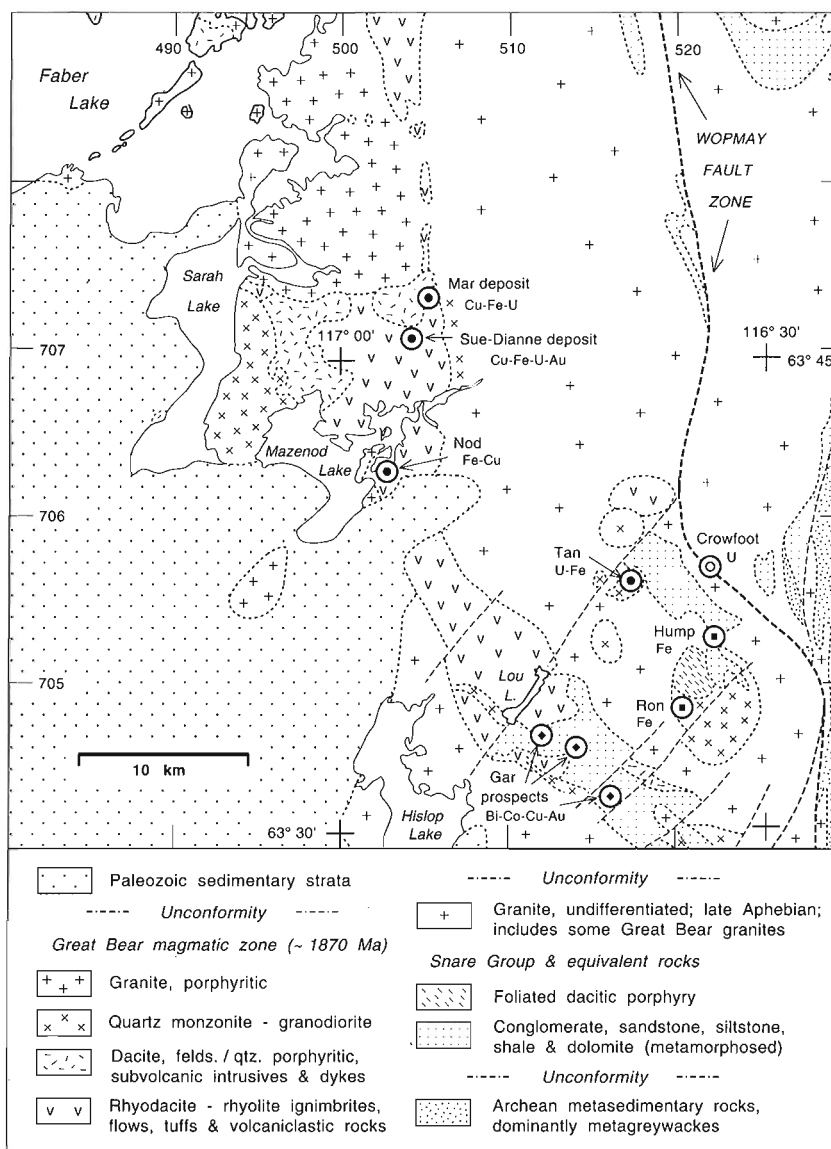
<sup>2</sup> Geophysics Division

## INTRODUCTION

A gravity survey of grid lines over the Sue-Dianne breccia zone and widely spaced localities within 2.5 km of it, was carried out in 1992 to assess the abundance of magnetite-rich breccia matrix that contains copper sulphides and uranium oxide. The breccia zone occurs in a rhyodacite volcanic sequence approximately 1865 Ma in age (Gandhi, 1989; 1992b; Gandhi and Mortensen, 1992). The zone is well exposed on a hill, and contains drill indicated 8 million tonnes averaging 0.8 percent copper and variable amount of uranium, and erratic small values of gold and silver. Magnetite, and associated hematite and specularite, occur in the zone as veins, breccia fillings, and massive pods. Another similar but smaller breccia zone occurs at the Mar deposit, 2.5 km to the north-northeast, and was included in the gravity survey.

The region surrounding the deposits is underlain by rhyodacite ignimbrites, related dacitic and granitic intrusions, and a few small bodies of diorite, all of which belong to the Great Bear magmatic zone (Fig. 1). The density contrast between these igneous rocks (s.g. 2.6-2.9) and the mineralized material containing as much as 50% magnetite and hematite (s.g. 5.2), is sufficient to generate a gravity anomaly if a significantly large tonnage of such material existed at depth. Previously published regional gravity data are from widely spaced (8 to 15 km) stations (Fig. 2). Closer spaced stations are required for resource assessment on local and deposit scales.

The main incentive for the gravity work stemmed from recognition of potential in the study area for large polymetallic deposits similar to the giant Olympic Dam Cu-U-Au-REE deposit in South Australia (Gandhi and Bell, 1990; Gandhi,



**Figure 1.** Regional geology of the Mazenod Lake area showing location of the Sue-Dianne and Mar deposits, Northwest Territories.

1992b), and from the fact that gravity anomalies (8 to 14 mGal) coincident with strong magnetic anomalies played an important role in target definition during exploration of the Olympic Dam and other related deposits in South Australia (Rutter and Esdale, 1985).

## REGIONAL GEOLOGY, GRAVITY, AND MAGNETIC ANOMALIES

The volcanic sequence that hosts the Sue-Dianne deposit forms a northwest- to north-trending belt 10 km wide, and is as much as 5 km thick (Fig. 1). It is a continental volcanic sequence comprised of rhyodacites, rhyolites, and associated volcanoclastic sediments (Gandhi, 1989). It is intruded by related subvolcanic quartz-feldspar porphyritic plutons and dykes, small bodies of diorite and large granitic plutons of the Great Bear magmatic zone. It is affected by gentle folding and faulting. The mineral occurrences genetically related to the volcano-plutonic complex include magnetite-rich veins and breccia fillings carrying notable amounts of copper  $\pm$  uranium and gold, e.g., the Sue-Dianne, Mar, and Nod prospects (Gandhi, 1989, 1992b), and hydrothermal arsenopyrite-rich veins containing bismuth, cobalt, copper, and gold at Gar prospects (Gandhi and Lentz, 1990).

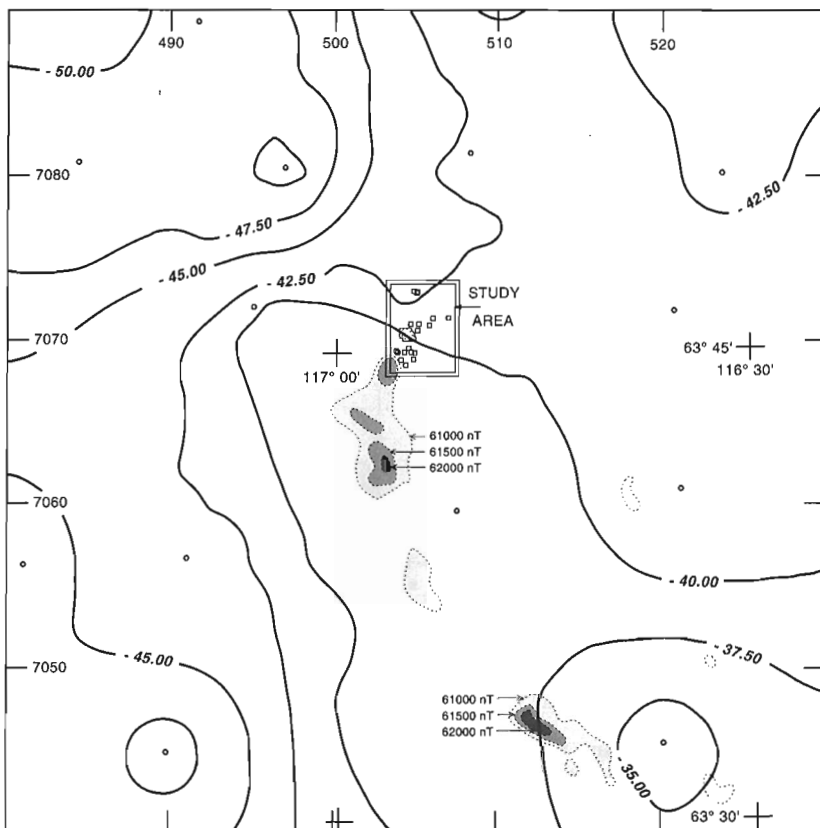
Older rocks exposed in the belt are remnants of an early Proterozoic metasedimentary sequence and granitic intrusives (Fig. 1). The northwest-trending metasedimentary units

include quartzite, metasilstones, argillites, and some carbonate rocks. The metasilstones and argillites contain magnetite-rich beds and lenses (Gandhi, 1992a). The north-trending Wopmay fault zone marks the eastern boundary of the Great Bear magmatic zone. Rocks east of the fault zone are of Archean Slave Craton and ca. 1900 Ma old Hepburn metamorphic and plutonic zone. Flat-lying Paleozoic sedimentary strata, as much as 300 m thick, cover the western part of the Great Bear magmatic zone.

A broad regional Bouguer anomaly defined by the -40.00 mGal contour, extends southeast from the Sue-Dianne deposit area and reaches to -35.00 mGal in the vicinity of the Gar prospects (Fig. 2). Its trend coincides with the regional trend of the volcanic belt and of the metasedimentary rocks in the basement. Strong regional magnetic anomalies occur along the axis of the gravity high, and are associated closely with exposures of the volcanic sequence (Fig. 2). More detailed geophysical surveys and geological mapping are needed to better define these regional anomalies and to isolate local anomalies caused by mineral deposits like the Sue-Dianne deposit.

## DETAILED GRAVITY SURVEY

A total of 70 gravimeter readings were taken during a five day survey in July 1992 (Table 1). Of these, 47 readings were on a 50 m grid over the mineralized zone of the Sue-Dianne



**Figure 2.**

Regional Bouguer anomaly of the Mazenod Lake area, Northwest Territories. Note gravity contours in mGal and magnetic contours in nT.

**Table 1.** Gravimeter readings in the area of Sue-Dianne and Mar deposits, Northwest Territories

Station Number	UTM Northing	UTM Easting	Elevation in metres	Bouguer Anomaly
<i>Sue-Dianne grid</i>				
10501	7070.125	504.300	263.65	-40.71
10501	7070.125	504.300	263.65	-40.73 *
10501	7070.125	504.300	263.65	-40.77 *
10502	7070.175	504.300	259.30	-40.72
10503	7070.225	504.300	252.20	-41.22
10504	7070.275	504.300	243.20	-40.89
10505	7070.300	504.300	237.40	-40.62
10506	7070.325	504.300	236.10	-40.88
10507	7070.086	504.300	274.00	-40.75
10508	7070.075	504.300	275.50	-40.95
10509	7070.025	504.300	279.20	-41.16
10509	7070.025	504.300	279.20	-41.06 *
10510	7069.975	504.300	282.40	-40.89
10511	7069.925	504.300	275.00	-40.94
10512	7069.875	504.300	260.60	-40.38
10513	7069.875	504.200	272.90 †	-40.52
10513	7069.875	504.200	272.90 †	-40.65 *
10513	7069.875	504.200	272.90 †	-40.66 *
10514	7069.925	504.200	279.90 †	-40.76
10515	7069.975	504.200	302.10 †	-40.60
10516	7070.025	504.200	292.40 †	-40.74
10517	7070.075	504.200	285.40 †	-40.75
10518	7070.125	504.200	269.00 †	-40.78
10518	7070.125	504.200	269.00 †	-40.78 *
10519	7070.125	504.250	266.70 †	-40.78
10520	7069.825	504.200	274.40 †	-40.54
10521	7069.775	504.200	274.30 †	-40.17
10522	7069.725	504.200	259.40 †	-41.02
10525	7070.125	504.150	271.90 †	-40.66
10525	7070.125	504.150	271.90 †	-40.68 *
10526	7070.125	504.100	278.90 †	-40.34
10527	7070.125	504.050	274.40 †	-39.05
10528	7070.125	504.000	271.00 †	-39.27
10529	7070.175	504.050	262.00 †	-39.49
10530	7070.225	504.050	250.00 †	-39.93
10531	7070.275	504.050	241.00 †	-40.56
10532	7070.302	504.050	233.00 †	-40.54
10533	7070.317	504.100	233.00 †	-40.81
10534	7070.315	504.154	232.00 †	-41.19
10535	7070.275	504.150	249.00 †	-41.13
10536	7070.225	504.150	248.00 †	-41.03
10537	7070.175	504.150	258.00 †	-40.96
10538	7070.125	504.350	255.40 †	-40.64
10539	7070.125	504.400	251.00 †	-40.78
10539	7070.125	504.400	251.00 †	-40.81 *
10540	7070.175	504.400	246.00 †	-40.84
10541	7070.225	504.400	247.00 †	-40.99
10542	7070.275	504.400	237.00 †	-41.15
10543	7070.325	504.400	235.00 †	-40.98
10544	7070.375	504.400	233.00 †	-41.47
10545	7070.075	504.400	239.00 †	-41.06
10546	7070.025	504.400	246.00 †	-41.29
10547	7069.975	504.400	247.00 †	-41.32
10548	7069.925	504.400	252.00 †	-40.88
10549	7069.875	504.400	253.00 †	-40.36
<i>Dianne Lake shore</i>				
10550	7069.660	504.500	229.00	-39.37
10551	7069.300	504.330	227.00	-39.34
10552	7069.050	504.175	227.00	-39.10
10553	7069.050	503.800	227.00	-38.89
10554	7069.120	503.650	227.00	-38.92
10555	7068.575	503.950	227.00	-38.12
10556	7068.650	504.680	227.00	-38.68
10557	7069.000	504.790	228.00	-38.79
10558	7069.020	504.580	228.00	-38.96
10559	7069.950	504.570	228.00	-40.23
10560	7071.180	506.860	227.00	-41.26
10561	7071.100	505.900	228.00	-41.10
10562	7070.800	505.000	227.00	-41.36
10563	7070.720	504.490	227.00	-41.19
10564	7070.400	504.910	227.00	-40.72
10565	7070.700	505.650	227.00	-40.74
10566	7070.080	504.640	227.00	-40.29
10567	7068.225	504.140	227.00	-37.63
10568	7070.200	504.540	228.00	-40.26
<i>Mar deposit</i>				
10571	7072.800	504.925	241.00 †	-42.65
10572	7072.800	504.940	242.00 †	-42.92
10573	7072.780	504.925	237.00 †	-43.42
10574	7072.780	504.800	236.00 †	-43.74

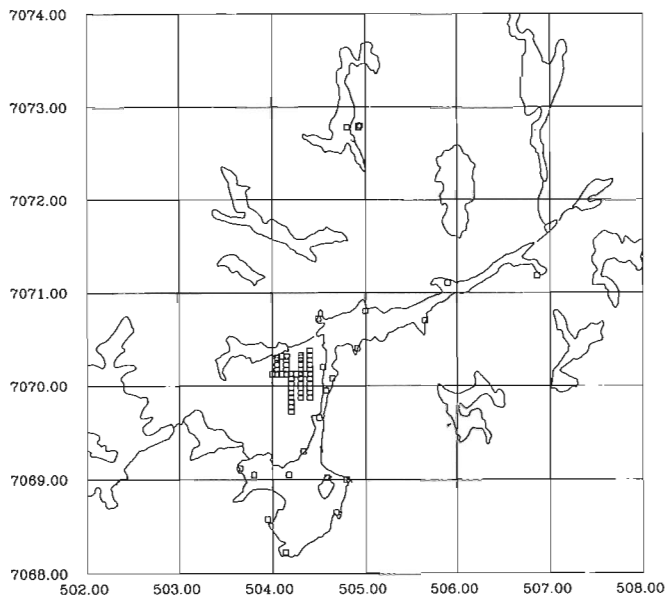
Note : \* denotes duplicate/triplicate readings; † denotes altimeter reading.

prospect, 19 were taken at various intervals on the shore of the nearby Dianne Lake, and the remaining four were on and near the Mar prospect (Fig. 3 and 4).

The gravimeter used was a Lacoste and Romberg, unit G255. Elevations at 22 grid stations on the Sue-Dianne hill were obtained by a Zeiss level. A single level line tied the elevations of these grid stations and Dianne Lake. The remaining 25 sites of the grid were determined by an AIR altimeter with psychrometer. The grid origin at drill hole S-11 has the elevation of 232.2 m according to the drill log (Prest et al., 1977). The elevations derived from this datum are reasonable in comparison with the topographic contours, but it is suggested that a value 5 m less may have been preferable. Relative accuracies estimated for the elevation control are: i) for stations levelled on grid, ±0.5 m; ii) altimetry stations on the grid, ±3.0 m; iii) stations on Dianne Lake, ±1.0 m; and iv) altimetry at Mar prospect, ±5.0 m.

The grid origin at drill hole S-11 has the UTM co-ordinates 7070125 N and 504300 E. The grid was established prior to the survey using an old baseline, and cutting and chaining the cross lines, which required 12 man-days of work. Horizontal positions of the stations on shoreline were scaled from 1:50 000 NTS maps. They were compared several times during the gravity readings with the co-ordinates obtained from a hand-held Ensign GPS unit. Relative accuracies for the horizontal co-ordinates are estimated as: i) on the grid, ±5 m, ii) on shore line, ±50 m, and iii) for Mar stations taken from GPS receiver, ±100 m.

A large closure error of 0.7 mGal was observed in the survey of the grid, and is attributed to the manual transport of the gravimeter. Hence readings on three stations were repeated, and two others were discarded. The stations on Dianne Lake shore were reached by boat. Again a large closure error



**Figure 3.** Gravity stations in the area of Sue-Dianne and Mar deposits, Northwest Territories.

of 1.4 mGal occurred due to insufficient padding to dampen the vibrations. So observations were repeated on ten stations. Other repeat observations produced eight pairs of values with a mean difference of 0.05 mGal and a maximum difference of 0.14 mGal. The spread between the two control stations, Yellowknife and Dianne Lake camp, is 0.036 mGal. The attributed gravity accuracy value is 0.10 mGal.

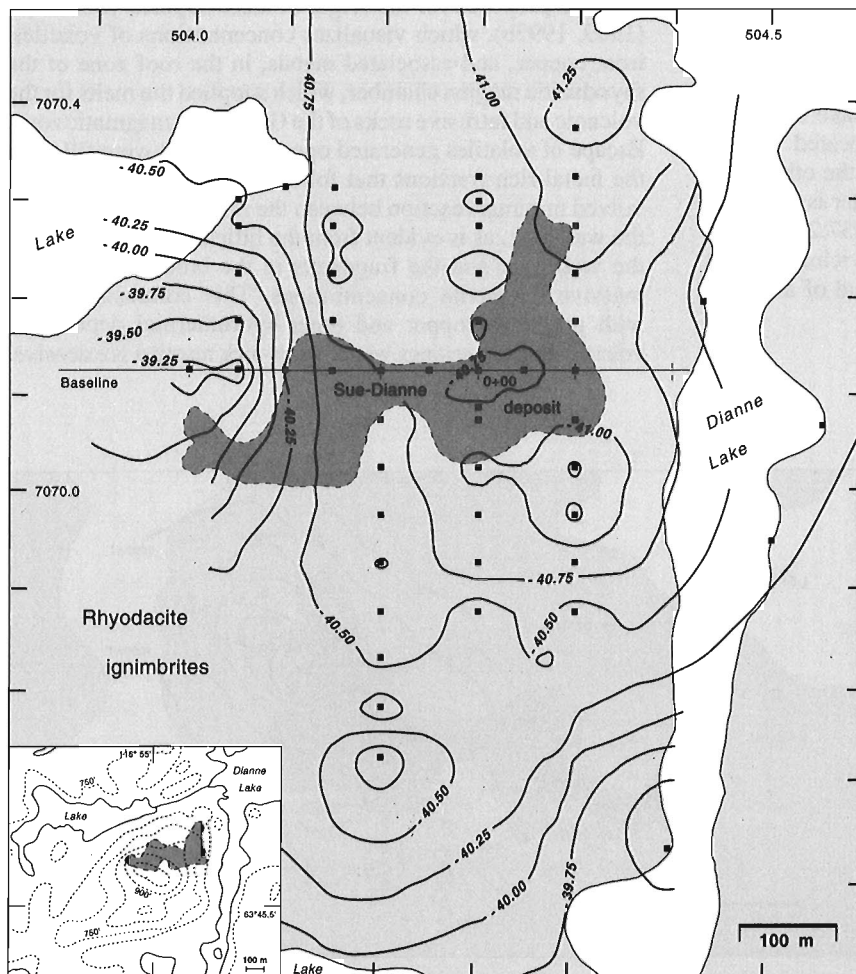
Terrain corrections were computed for all stations. Most stations on the grid are on a prominent hill in an otherwise flat terrain (Fig. 4, inset). To prepare for terrain correction the topography of a 5 km<sup>2</sup> area centred on the Sue-Dianne deposit was digitized from the 1:50 000 scale NTS maps. Points within 100 m of the grid were removed from the data set and replaced with elevations from the gravity survey. The elevations were gridded at 50 m intervals, once with the cells centred on most gravity stations and once not centred. Terrain corrections were computed by three methods: i) using flat-topped prisms not centred on gravity stations, ii) using flat-topped prisms centred on gravity stations, and iii) using sloping triangular prisms with gravity stations at most vertices. Flat-topped prisms have been notorious for giving exaggerated results close to a station unless regridded to a much finer interval than 50 m. In this data set, a good agreement in results from the second and third methods was obtained, and since the second method gave consistently smaller terrain

corrections, they were adopted. The corrections are small, and are probably not needed to detect anomalies of 2 mGals or more in such moderate terrain. Smaller anomalies may be somewhat obscure in contour plots, but they should be more clear in the profile plots.

## DISCUSSION OF DATA

The terrain-corrected gravity readings on the Sue-Dianne grid revealed two noteworthy features: i) a weak gravity anomaly of 0.25 mGal over the eastern part of the breccia zone where most of the tonnage indicated by drilling is located, and ii) a Bouguer anomaly of approximately 1.5 mGal near the west end of the breccia zone (Fig. 4).

The eastern part of the breccia zone is explored by 13 drill holes, the deepest of which is S-5, a vertical hole 80 m east of the grid origin (Fig. 5), that ended in mineralized zone at the depth of 288 m (Climie, 1976; Prest et al., 1977). A ground magnetic survey carried out by Noranda Exploration Company Limited (Climie, 1976), shows a strong anomaly with a peak of 7000 nT at the northeast margin of the Sue-Dianne breccia zone (Fig. 5). The gravity survey, however, shows only a weak Bouguer anomaly of 0.25 mGal over



**Figure 4.**

Gravity contour map of the Sue-Dianne deposit, Northwest Territories. Note contour interval 0.25 mGal, and gravity stations indicated by small squares.

the central part of the eastern lobe of the breccia zone (Fig. 4). Thus the tonnage indicated by the drill data (approximately eight million tonnes) has a very small gravity expression.

The 1.5 mGal Bouguer anomaly at the west end of the breccia zone is significant, particularly when considered in the context of the much smaller gravity expression of the drilled zone in the east. It must however be regarded with caution as it is located on a steep slope facing west, and the elevation of stations in this part of the grid is controlled by altimetry (Table 1). A drill hole 100 m east of the anomaly (S-3, Fig. 5) tested the western lobe of the breccia zone. This 121 m long hole was inclined at 50° towards the south, and intersected weakly mineralized zone at shallow depth. The bedrock exposed at the anomaly peak is barren rhyodacite, hence the source of the anomaly may be at considerable depth. The anomaly lies just outside the ground magnetic coverage over the grid (Fig. 5), hence its magnetic expression is not known. It is apparent that this anomaly merits further scrutiny by gravity and magnetic surveys. Additional gravity readings with levelled elevations are required to the south and west in order to confirm and better define this anomaly. It may be noted that its presence was not apparent during the course of the gravity survey, which emphasizes the desirability of all data reductions to be done in the field.

Gravity readings at the Mar prospect are too few to produce any contour, but they did serve to demonstrate a more positive Bouguer anomaly value over a well-exposed, magnetite-rich lens approximately 2 m wide and 10 m long, located 8 m north of drill hole Mar-1-'78 (Gandhi, 1992b, p. 241). The remainder of the gravity readings show small local variation, and two of these on Dianne Lake shore are significantly anomalous (Table 1). One is located 450 m south-southeast of the grid origin (Fig. 4) and the other is at the south end of Dianne Lake (Fig. 3). The latter is the most positive reading encountered in the survey (-37.25 mGal). There is no evidence of mineralization in its vicinity, but it may be noted that it is situated at the north end of a strong regional magnetic anomaly (Fig. 2).

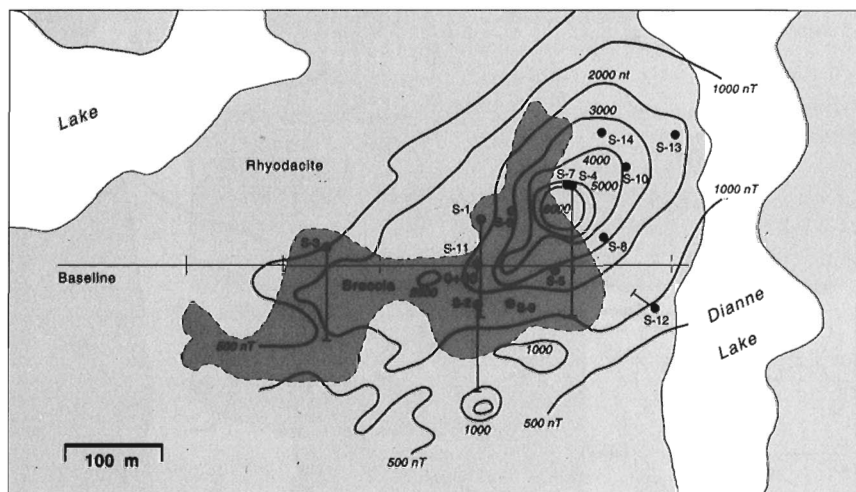
It is apparent that the Sue-Dianne and Mar deposits do not contain concentrations of iron oxides that are sufficiently high to generate large gravity anomalies as is the case with the Olympic Dam and related deposits in South Australia, and hence represent relatively small examples of this group of deposits. The deposits of this group have a wide range in size, and they are highly variable in their metal contents (Gandhi and Bell, 1990). Copper, uranium, gold, and rare-earth elements occur commonly in close association with iron oxides, but their abundances are not necessarily proportional to the amount of iron oxides. It is therefore conceivable that significant values of these metals may occur where iron oxide concentrations are not readily detectable by gravity measurements. This is the case with the eastern part of the Sue-Dianne breccia zone. At the other end of the spectrum are the iron oxide deposits which are essentially monometallic e.g., the magnetite-apatite veins in the western part of Nod prospect (Gandhi, 1992b).

## METALLOGENIC IMPLICATIONS

Results of the gravity survey have some metallogenic implications. The Sue-Dianne and Mar deposits occur in a continental rhyodacitic volcano-plutonic complex (Gandhi, 1989, 1992a). The gravity data show that there is no significant mafic body in their vicinity. This lends credence to the hypothesis proposed for the origin of these deposits by Gandhi (1989, 1992b), which visualizes concentrations of volatiles, iron, copper, and associated metals, in the roof zone of the rhyodacitic magma chamber, which supplied the melts for the volcanic and intrusive rocks of the Great Bear magmatic zone. Escape of volatiles generated open spaces that were filled by the metal-rich fractions that followed the volatiles. This involved minimal reaction between the mineralizing fluids and the wall rock, as is evident from the little altered character of the wall rock and the fragments in the breccia zones with massive magnetite concentrations. This contrasts sharply with porphyry copper and other hydrothermal deposits in volcano-plutonic settings where water-rock reaction is extensive.

**Figure 5.**

Magnetic contours and diamond drill holes of the Sue-Dianne deposit, Northwest Territories (source: Climie, 1976; Prest et al., 1977).





The Sue-Dianne and Mar deposits have many similarities, in terms of regional geological setting and the type of mineralization, with the Olympic Dam deposit and other related deposits namely Acropolis, Oak Dam, and Wirdda Well, in the Stuart Shelf region of South Australia (Gandhi and Bell, 1990; Gandhi, 1992c). These Australian deposits are hosted by, and are genetically related to, the 1.6 Ga old continental, dominantly felsic volcanic rocks of the Gawler Ranges and subvolcanic plutons (Reeve et al., 1990; Johnson and Cross, 1991). This volcano-plutonic activity occurred in extensional environments, following the Sleafordian and Kimban orogenic events in the Gawler Craton between 1.9 and 1.7 Ga ago (Parker, 1990). The deposits are covered by as much as 300 m of flat-lying late Proterozoic and early Paleozoic strata that distinguish the Stuart Shelf region from the Adelaidean geosyncline to the east where equivalent strata are folded.

The coincident strong magnetic and gravity anomalies at the Acropolis and Olympic Dam deposits led to their selection as the prime exploration targets in the Stuart Shelf region (Rutter and Esdale, 1985; Paterson, 1986). The anomalies were tested by drilling in 1975; the first hole RD-1 was drilled at Olympic Dam and the second hole RD-2 was drilled at Acropolis. Subsequent drilling revealed that the Olympic Dam deposit was economically more interesting than the Acropolis deposit and other drilled targets in the Stuart Shelf, and hence most of the work in the region has been concentrated on the Olympic Dam deposit.

The gravity anomalies at the Olympic Dam and Acropolis deposits have amplitudes of 14 and 8 mGal respectively (Rutter and Esdale, 1985; Paterson, 1986). They have been attributed to the presence of large amounts of iron oxides in the two deposits, mainly hematite in the former and magnetite in the latter. The Olympic Dam deposit contains 2000 million tonnes of inferred resources averaging 1.6% Cu, 0.5% U, 0.6 g/t Au, and 3.5 g/t Ag, and notable concentrations of rare-earth elements (Reeve et al., 1990). The proportion of hematite is variable, but commonly ranges between 30 and 50%.

The mineralogical difference between the Olympic Dam and Acropolis deposits is reflected in the coincident magnetic anomalies, approximately 1200 nT in amplitude at Olympic Dam and 6000 nT at Acropolis (Paterson, 1986). It may be pointed out here that the magnetite-rich Sue-Dianne and Mar deposits closely resemble the Acropolis deposit. A common feature of the three deposits is the presence of volcanic fragments in matrix of massive magnetite. Airborne magnetic anomalies at the Sue-Dianne and Mar deposits are in the order of 400 and 200 nT respectively (Geological Survey of Canada Map 2952 G, scale 1:63 360; 1963), and they occur at the margin of a regional magnetic anomaly that exceeds 1000 nT (Fig. 2; Charbonneau, 1988). Ground surveys show much stronger magnetic anomalies, as noted above for the eastern part of the Sue-Dianne breccia zone (Fig. 5).

The Olympic Dam deposit is interpreted as a multistage breccia deposit formed by a variety of processes including repeated faulting, hydrothermal and phreatomagmatic explosions, and epiclastic sedimentation in near surface, eruptive environment (Reeve et al., 1990). The dominant oxide in early hydrothermal assemblages was probably magnetite, but only the minor localized relicts of magnetite-bearing assemblages are preserved within the hematite-rich breccia. Roberts and Hudson (1983) noted that the magnetic anomaly at Olympic Dam is largely unexplained and presumably results from a large magnetic body beyond the current depth of drilling (~700 m). In a recently proposed model, Cross (1991) suggested the presence of a large mafic body at depth below the Olympic Dam deposit. Such a postulated mafic body may explain the magnetic and gravity data better, and provide a source for the iron and copper in the deposit. The gravity survey in the area of the Sue-Dianne and Mar deposits suggests, however, that such a mafic body is not necessary in generation of iron oxide-rich deposits of their size.

The magnetite-rich deposits of the group, like the Sue-Dianne, Mar, and Acropolis deposits, are likely to have formed at a greater depth than the hematite-rich deposits. It is possible that hematite may form by oxidation of magnetite if the deposits are exposed to surficial alteration during their long history. This is apparently the case with the Oak Dam deposit which has hematite-rich cap at the unconformity with the overlying middle Proterozoic Pandura sandstone, and grades at depth into the magnetite-rich main part of the deposit. It is likely that some of the hematite in the Olympic Dam deposit is similarly derived from magnetite. In any case, the Acropolis and Olympic Dam deposits represent, as pointed out by Paterson (1986), a spectrum of mineralizing processes that formed this group of deposits. It is apparent that gravity survey is a useful tool in locating large deposits of this type even if their magnetic signature is weak.

## ACKNOWLEDGMENTS

Exploration data gathered by Noranda Exploration Company Limited in 1970s provided the basis for metallogenic interpretation outlined above, and led to the proposal for the gravity survey. This paper is published with the approval of the company. Field assistance for the gravity survey was provided by J. Morgan, E. Williah, and N. Prasad. Their valuable help is greatly appreciated by the authors. The first author gained familiarity with the Australian deposits and their geological setting during a visit to South Australia in 1991, with the kind help and guidance of K.C. Cross and H.L. Paterson of Western Mining Corporation, and L.R. Rankin of the South Australian Department of Mines and Energy. The gravity survey was a part of project C4.121 supported financially by the Canada-Northwest Territories Minerals Initiative Program for 1991-'96. This paper benefited from the critical reviews by M.D. Thomas and B.W. Charbonneau of the Geological Survey of Canada.

---

**REFERENCES**
**Charbonneau, B.W.**

1988: Gamma spectrometric and magnetic anomalies associated with Cu-U mineralization, Faber Lake volcanic belt, District of Mackenzie, N.W.T.; in *Current Research, Part C*; Geological Survey of Canada, Paper 88-1C, p. 255-258.

**Climie, J.A.**

1976: Geological, geophysical and drill investigations of the Dianne/Sue Groups, District of Mackenzie (85-N-10, 15); Noranda Exploration Company Limited; Department of Indian and Northern Affairs Document 080524, 9 p.

**Cross, K.C.**

1991: The Olympic Dam deposit: Breccia hosted Cu-U-Au-Ag (-REE) mineralization in a high level volcano-plutonic setting; in *Geological Society of Australia, Victorian Division, Annual Selwyn Memorial Symposium 1991*, Melbourne; p. 1-7.

**Gandhi, S.S.**

1989: Rhyodacite ignimbrites and breccias of the Sue-Dianne and Mar Cu-Fe-U deposits, southern Great Bear magmatic zone, Northwest Territories; in *Current Research, Part C*; Geological Survey of Canada, Paper 89-1C, p. 263-273.

1992a: Magnetite deposits in metasilstones of the Snare Group at Hump Lake, Northwest Territories; in *Current Research, Part C*; Geological Survey of Canada, Paper 92-1A, p. 225-235.

1992b: U-Cu-bearing magnetite-matrix breccia of the Mar deposit and veins of the Nod prospect, southern Great Bear magmatic zone, Northwest Territories; in *Current Research, Part C*; Geological Survey of Canada, Paper 92-1C, p. 237-249.

1992c: Metallogeny of the Gawler Craton, South Australia, and its relevance to the southern Great Bear magmatic zone; in *Exploration Overview - 1993*, (ed.) J.A. Brophy, Department of Indian and Northern Affairs, Yellowknife, Northwest Territories, p. 24-26.

**Gandhi, S.S. and Bell, R.T.**

1990: Metallogenic concepts to aid exploration for the giant Olympic Dam-type deposits and their derivatives; Abstracts with Program, Eighth Symposium of the International Association on Genesis of Ore Deposits, Ottawa, August 12-18, 1990, p. A7.

**Gandhi, S.S. and Lentz, D.R.**

1990: Bi-Co-Cu-Au-As and U occurrences in the Snare Group meta-sediments and felsic volcanics of the southern Great Bear magmatic zone, Lou Lake, Northwest Territories; in *Current Research, Part C*; Geological Survey of Canada, Paper 90-1C, p. 239-253.

**Gandhi S.S. and Mortensen, J.K.**

1992: 1.87-1.86 Ga old felsic volcano-plutonic activity in southern Great Bear magmatic zone, N.W.T.; in *Program with Abstracts, Geological Association of Canada-Mineralogical Association of Canada Annual Meeting, Wolfville 1992, May 25-27*, v. 17, p. 37.

**Johnson, J.P. and Cross, K.C.**

1991: Geochronological and Sm-Nd isotopic constraints on the genesis of the Olympic Dam Cu-U-Au-Ag deposit, South Australia; in *Proceedings of the 25th Anniversary Meeting of the Society for Geology Applied to Mineral Deposits: 'Source, Transport, and Deposition of Ore Minerals'*, (ed.) M. Pagel and J.L. Leroy; A.A. Balkema, Rotterdam, p. 395-400.

**Parker, A.J.**

1990: Gawler Craton and Stuart Shelf — Regional Geology and Mineralization; in *Geology of the Mineral Deposits of Australia and Papua New Guinea*, (ed.) F.E. Hughes, Australasian Institute of Mining and Metallurgy, Monograph No. 14, p. 999-1008.

**Paterson, H.L.**

1986: The Acropolis prospect; Eighth Australian Geological Convention, February, 1986; Excursion A1 — Olympic Dam/Stuart Shelf, p. 17-18.

**Prest, S.E., Ronayne, E., and Tilsley, R.**

1977: Diamond drill records, Smith option; Dianne/Sue Groups, District of Mackenzie (85-N-10, 15), N.W.T.; Noranda Exploration Company Limited, 129 p.

**Reeve, J.S., Cross, K.C., Smith, R.N., and Oreskes, N.**

1990: Olympic Dam copper-uranium-gold deposit; in *Geology of the Mineral Deposits of Australia and Papua New Guinea*, (ed.) F.E. Hughes; Australasian Institute of Mining and Metallurgy, Monograph No. 14, p. 1009-1035.

**Roberts, D.E. and Hudson, G.R.T.**

1983: The Olympic Dam copper-uranium-gold deposit, Roxby Downs, South Australia; *Economic Geology*, v. 78, no. 5, p. 799-822.

**Rutter, H. and Esdale, D.J.**

1985: The geophysics of the Olympic Dam discovery; *Bulletin of the Australian Society of Exploration Geophysicists*, v. 16, no. 2/3, p. 273-276.

---

 Geological Survey of Canada Project 750010 KI

# Integrating LANDSAT, aeromagnetic, and geological data for regional bedrock mapping, Winter Lake-Lac de Gras map area, Northwest Territories

A.N. Rencz, D. Baril<sup>1</sup>, and P.H. Thompson<sup>1</sup>

Mineral Resources Division

*Rencz, A.N., Baril, D., and Thompson, P.H., 1993: Integrating LANDSAT, aeromagnetic, and geological data for regional bedrock mapping, Winter Lake-Lac de Gras map area, Northwest Territories; in Current Research, Part E; Geological Survey of Canada, Paper 93-1E, p. 239-246.*

---

**Abstract:** This study demonstrates the utility of integrating digital data from LANDSAT Thematic Mapper imagery, aeromagnetic surveys, and reconnaissance geological maps as an aid to regional bedrock mapping. LANDSAT images enhanced to show structural features and rock outcrop were combined with aeromagnetic and geological data on an image analysis system. Production of integrated maps involves an intensity-hue-saturation (IHS) colour system.

Integration of three data sets across the map area reveals variations in the quality of outcrop and discordance between features on LANDSAT imagery, aeromagnetic anomalies, and lithological contacts derived from previous bedrock mapping. The integrated data assist in planning an optimum distribution and density of traverses. They constrain extrapolation of contacts and structures in areas of poor outcrop and in between geological traverses. Updating of integrated images as new geological data are acquired provides a tool for reassessment of mapping priorities during the project.

**Résumé :** La présente étude démontre qu'il est utile d'intégrer les données numériques des images du capteur Thematic Mapper de LANDSAT, les levés aéromagnétiques et les cartes géologiques de reconnaissance pour faciliter la cartographie régionale du socle rocheux. Des images de LANDSAT, rehaussées pour mettre en évidence les éléments structuraux et les affleurements rocheux, ont été combinées à des données aéromagnétiques et géologiques à l'aide d'un système d'analyse d'image. Les cartes intégrées sont produites à l'aide d'un système IHS (Intensity-Hue-Saturation) couleur.

L'intégration de trois ensembles de données pour la région à l'étude révèle des variations dans la qualité des affleurements et des écarts entre les caractéristiques des images de LANDSAT, les anomalies aéromagnétiques et les contacts lithologiques établis à partir de cartes existantes du socle rocheux. Les données intégrées facilitent la planification d'une distribution et d'une densité optimales des cheminements. Elles limitent l'extrapolation des contacts et des structures dans les zones de faible affleurement et entre les cheminements géologiques. La mise à jour des images intégrées à mesure que de nouvelles données géologiques sont disponibles constitue un outil pour réévaluer les priorités en matière de cartographie dans le cadre du projet.

---

<sup>1</sup> Continental Geoscience Division

## INTRODUCTION

A major responsibility of the Geological Survey of Canada (GSC) is the provision of geoscientific maps representing bedrock and surficial geology. The National Mapping Program (NATMAP) is a GSC program that was designed to promote the production of these geological maps using the most recent computer techniques (CAD/GIS). To offset the high costs of mapping projects, NATMAP has encouraged the development of inter-disciplinary approaches that take advantage of resources, technology and skills from a variety of disciplines.

Remotely sensed imagery from LANDSAT has been used in a variety of geoscience applications, however, there is only limited experience with incorporating digital satellite data into bedrock geological mapping programs. In Canada, masking of bedrock by extensive glacial overburden and vegetation is part of the explanation for this limited use. With a synoptic view of a project area and data in several regions of the electromagnetic spectrum, LANDSAT images can be a useful tool for regional bedrock mapping. Their utility is enhanced when, through data integration, LANDSAT data can be combined with other kinds of information.

Aeromagnetic data are an essential component of regional mapping projects. The technique determines variations in the magnetic field of rocks at the surface and at depth that can be interpreted with respect to rock type and structure. As data are recorded digitally and are processed to a grid format, it is possible to digitally integrate remotely sensed data with aeromagnetic coverage. Researchers have traditionally integrated these data sets on an analog basis; a number of researchers, however, have published on digital integration (Slaney, 1985; Harris et al., 1986, 1990; Kowalick and Glen, 1986; Franklin et al., 1989; Rheault et al., 1991; Broome, 1988). In this study the geology has been integrated as well.

A new NATMAP regional mapping project in the central part of the Archean Slave Province (Thompson, 1992; Thompson et al., 1993) provided an opportunity to develop and test procedures for using combined sets of LANDSAT TM, aeromagnetic and geological data. This paper focuses on the utility of the multi-parameter maps for planning field work. Subsequent papers will assess the integration of this data into the mapping project and the creation of final map products. As the format of Current Research limits figures to black and white, colour images will be made available through a GSC Open File release (Baril et al., in prep.).

## STUDY AREA

Located 250 km north of Yellowknife, the map area (10 800 km<sup>2</sup>) includes parts of three volcano-sedimentary domains (Winter Lake-Contwoyto Lake, Yellowknife-Beaulieu River and Lac de Gras-Courageous Lake) that have produced most of the mineral wealth of the Slave Province (Fig. 1). A better understanding of the origin, evolution and economic potential of the region will be obtained during three field seasons through a combination of 1:250 000 scale mapping,

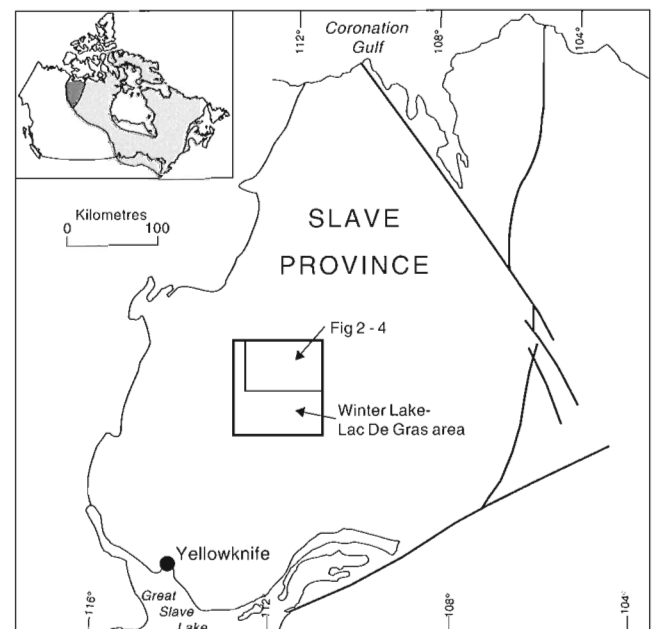
detailed mapping of the Courageous Lake volcanic belt and the western supracrustal domain, and topical studies of metamorphism, structural geology, geochronology, metallogeny and geophysics. Mapping completed in the course of a short reconnaissance in 1991 and during 10 weeks in 1992 expanded the area of known supracrustal rocks, found structural and stratigraphic evidence of potential granitoid basement, and provided new insight into extensive areas of enigmatic granitoid rocks and into the metamorphic and structural history. The area selected to test the integrated image approach is in the north-central part of the Winter Lake-Lac de Gras map area (Fig. 1).

## DATA SETS

### Geology map

The project map area includes the east half of the Winter Lake area (NTS 86A) mapped for the first time by Fraser in 1958 and the west half of the Lac de Gras area (NTS 76D) first mapped by Folinsbee. This work was published at 1:253440 scale (Fraser, 1969; Folinsbee, 1949). Regional mapping outlined four principal lithological packages: 1) low and medium grade metasedimentary rocks; 2) low and medium grade metavolcanic rocks; 3) heterogeneous gneissic and migmatitic rocks derived from granitoid and supracrustal protoliths; 4) homogeneous granitoid rocks.

The regional maps were manually digitized using TYDIG (Intera/Tydac Technologies, Inc., 1991a) software. The resulting vector data were transformed to raster with Intera/Tydac SPANS GIS software (Intera/Tydac Technologies, Inc., 1991b). The two maps were then transferred to an IBM



**Figure 1.** Location of the portion of the Winter Lake-Lac de Gras map area (Slave Structural Province), N.W.T., used in this study.

RISC (Reduced Instruction Set Computer) UNIX workstation to be combined with LANDSAT TM and aeromagnetic data utilizing EASI/PACE (PCI, 1991) image analysis software.

### Aeromagnetic data

The gridded aeromagnetic data were acquired from the National Geophysical Data Centre. The aeromagnetic grid was generated using the standard procedures described by Dods et al. (1985). A sub-grid was then selected to cover the study area. It was converted to an 8 bit (256 levels) image using an histogram-equalized quantization method with GSC software developed by Broome (1988). The resulting raster data were transferred to the RISC workstation and integrated with the LANDSAT data.

### Landsat TM data

The satellite images were acquired on September 11, 1986 by the LANDSAT Thematic Mapper (TM) sensor. They consist of 7 bands of reflected energy from various parts of the electromagnetic spectrum (Table 1) representing 30 x 30 m ground cells; except for the thermal band (#6) which has a spatial resolution of 120 x 120 m.

In the analog to digital conversion (done prior to the user receiving the data) the data were scaled to 8 bits, consequently the data range from 0 to 255. The values are not true reflectance values due to scattering and absorption processes in the atmosphere. The values are generally referred to as digital numbers (DN). For simplicity the digital numbers are considered to be representative of reflectance values with higher numbers indicating a greater reflectance from the surface target.

The Thematic Mapper data, received on 9 inch computer compatible tapes (CCT), were transferred to an ARIES III image analysis system that is part of the joint Canada Centre for Remote Sensing/Geological Survey of Canada (CCRS/GSC) "Storefront Operation". The system consists of a VAX microcomputer with peripherals for reading tapes, plotting the data (TEKTRONIX thermal wax plotter) and archiving data (Magneto optical disk with 400 Mb capacity).

**Table 1.** Types and characteristics of data sets used in the Winter Lake-Lac de Gras mapping project

Image	LANDSAT TM (micrometres)	Aeromagnetic (Gamma)	Geological map
Bands	.45-.52 .52-.60 .63-.69 .76-.90 1.55-1.75 10.35-12.50* 2.08-2.35		15 Geological Units
Spatial resolution (meters)	30x30	200x200	30x30

\* Spatial resolution for band 6 "thermal band" is 120 X 120 m.

## METHODS

### Data analysis resources

All processing of data was done with facilities at the GSC. For the most part the resources are commercially available; however some of the software has been written within the Geomathematics Section (GSC).

The majority of the image processing (image enhancements, classifications and integration) was done on an IBM RISC 6000 with the EASI/PACE image analysis software. The computer is a multi-tasking unit that runs at 32 MIPS with 32 Mb of RAM and 800 Mb of hard drive memory. A powerful workstation is essential for manipulating and displaying large data sets, which in this study were up to 250 Mb in size.

## DATA PROCESSING METHODS/RESULTS

### Landset TM data

The first step in processing the Thematic Mapper data was to geometrically correct the data to fit a common base map. In this case all data were registered to two 1:250 000 NTS topographic map sheets: 86A (Winter Lake) and 76D (Lac de Gras). This was accomplished by identifying common points on the image and on the map. A quadratic relationship was established between the x and y co-ordinates on the map and the corresponding pixel position on the image. The quadratic equation was used to resample the Thematic Mapper image using a bilinear interpolation routine (Lillesand and Kiefer, 1987).

Two types of map products were generated from the TM data: enhancements and classifications. Enhancements attempt to improve the interpretability of images by highlighting features of interest to the user. Classifications attempt to sort the images into user-defined themes (Lillesand and Kiefer, 1987). The images were plotted in colour at a scale of about 1:200 000 and laminated in preparation for field work. Examples of the colour copies can be seen in Baril and Rencz (1992) and the images for these data will be published by Baril et al. (in prep.).

A variety of generally accepted enhancement techniques was applied. The simplest product was a three band combination. "Optimal combinations" were selected subjectively by choosing those which seemed to discriminate the known geological units by highlighting the structure. Each channel was histogram-equalized to optimize the utilization of the colour spectrum and the resulting images were then plotted on an electrostatic plotter. Figure 2 is a black and white image of TM Band 4.

A band ratio image was also prepared for evaluation of the vegetation cover. The ratio Band 4 / Band 3 is a simple and effective vegetation index (VI). As healthy vegetation reflects infra-red (in the spectral region of band 4) and chlorophyll

absorbs red light (band 3) the 4/3 ratio gives high values for healthy vegetation and low values for unhealthy vegetation or absence of vegetation.

Principal component analyses (PCA) were performed within the EASI/PACE software. The principal component analysis was done to concentrate the spectral information from seven channels of Thematic Mapper data into three channels that are uncorrelated. The first principal component contains 87.5% of the all the variance of the seven original Thematic Mapper bands (the first 3 PCA images contain 99.2%).

In addition to enhancements which are designed to assist in the interpretation of features, classifications were done to identify specific features. A map of rock outcrop was produced by extrapolating reflectance statistics from sites of known outcrop to the entire image using a maximum likelihood classification within EASI/PACE (PCI Inc., 1991).

**Aeromagnetic data**

The aeromagnetic data were downloaded by the Geophysical Data Centre as a gridded file onto a VAX. The data were stored as 16 bit signed integers with a grid resolution of 200 m. These data were converted to 8 bits using a program (MAGNETIC) developed within the Geomathematics Section (Bonham-Carter, pers. com.). The 16 to 8 bit conversion was done using a histogram equalization routine (Broome, 1987). The output file from MAGNETIC was downloaded onto the IBM RISC workstation and directly read into the file containing the TM and the geological data.

**Data combinations: IHS**

An intensity, hue, and saturation (IHS) routine was used to overlay the different data types and produce enhanced colour images (Table 2). The IHS colour co-ordinate system was developed over 40 years ago (see Gillespie, 1980) and has been effectively used in a number of applications (Harris and Murray, 1990). In this system, intensity is intuitively interpreted as brightness, hue as colour and saturation as the purity of the colour. An advantage of this method (compared to the

Red, Green, Blue (RGB)) is the ability to directly interpret the colour. For example colour could be derived from aeromagnetic or digital elevation models and then the colour is modified through changes to intensity and saturation which could be derived from other data sources such as Thematic Mapper images. Although this integration can be done with the RGB display, it is more difficult to interpret the meaning of the colours.

Colour maps were found to be the most useful; however due to Current Research printing limitations the figures are presented in black and white. The procedure we followed for this was to simply multiply the digital numbers from each of the channels (LANDSAT TM 4 and aeromagnetic data) and then rescale them to a range of 0 to 255. LANDSAT TM 4 was used because of its broad dynamic range and the raw magnetic channel was divided into 15 classes prior to the multiplication. Although we acknowledge that other procedures may provide a more useful product we did not experiment with this product as we would normally recommend the colour product.

**Vector overlay**

A further enhancement to the images involved overlaying vector files such as geology or a UTM grid on the processed imagery. This was done by "burning" the geological vectors into the raster images. Figures 2, 3 and 4 illustrate overlays of the geology data on raster data.

**MAP PRODUCTION**

The production of colour maps at a specified scale was integral to the success of the project. To accomplish this, images were created on the workstation for image analysis (EASI/PACE). This system created a Post Script file that was transferred to the Synergy electrostatic plotter. For field use, plots without the surrounds were created directly from the image files using a program (PLOTTER) developed within the Geomathematics Section (Tooker et al., 1990). The PLOTTER software permits from one to three channels of input data to be plotted in colour at a user specified scale. Examples of these products can be seen in Baril et al. (in prep.).

**Table 2.** Intensity-Hue-Saturation (IHS) combinations used to make colour images

Parameters	Intensity	Hue	Saturation
Images Used	TM 4,5,7	Geology	Constant=100
	TM 4,5,7	Magnetic Intensity	Constant=100
	TM 4,5,7	Magnetic Shaded Relief (67 degrees)	Constant=100
	TM 4,5,7	Magnetic Shaded Relief (157 degrees)	Constant=100

**DISCUSSION**

Images are produced for each of the three main data layers, (Thematic Mapper, aeromagnetics, and geology) and for combinations of them using the IHS display (Baril et al., in prep.). Each layer is useful on its own but the real power of the approach with respect to regional mapping is in the ability to view various combinations of the data sets. The utility of integrated images, illustrated here in black and white, is greatly enhanced when colour is used (see below). The following discussion involves three combinations, LANDSAT + geology, aeromagnetic + geology, and LANDSAT + aeromagnetic + geology.

LANDSAT TM images (Fig. 2) complement conventional air photo coverage. Together, Bands 1, 2, and 3, provide the equivalent of high level colour air photo coverage, something that is not available for the project area. The images are a cost-effective alternative to air photo mosaics. The size and scale of the image can be varied according to need. Within extensive areas of relatively continuous outcrop, variations in the texture of the Thematic Mapper image as defined by the shape, size, and distribution of bodies of water, swampy terrain, and outcrops, delineate features that may be structures (folds and faults) or contacts between different rock types. LANDSAT images provide a synoptic view of these features that can be compared with aeromagnetic and geological data at the scale of a regional map. Rock units (Folinsbee, 1949) that parallel structural trends on the Thematic Mapper image north of Lac de Gras intersect these features north of Desteffany Lake (Fig. 2). North of the

northwestern arm of Lake Providence, structural trends suggestive of domal features do not correspond to lithological contacts the way they do south of the lake (Fraser, 1969). Outcrop is poor in the area where volcanic rocks extending westward from Desteffany Lake may converge or join with the north-trending volcano-sedimentary belt. These discrepancies between data sets serve as targets for further mapping.

Knowledge of the quality and distribution of outcrop is a useful tool for planning of a regional mapping operation. Creation of an outcrop map from Thematic Mapper data, however, is not straightforward. Various combinations of three TM bands have been tried (see Baril et al., in prep.). High reflectivity is a feature of eskers and snow cover as well as areas of good outcrop. In most cases, highly reflective glacial deposits could be identified by their form. Snow cover is evident from an image that comes closest to the actual

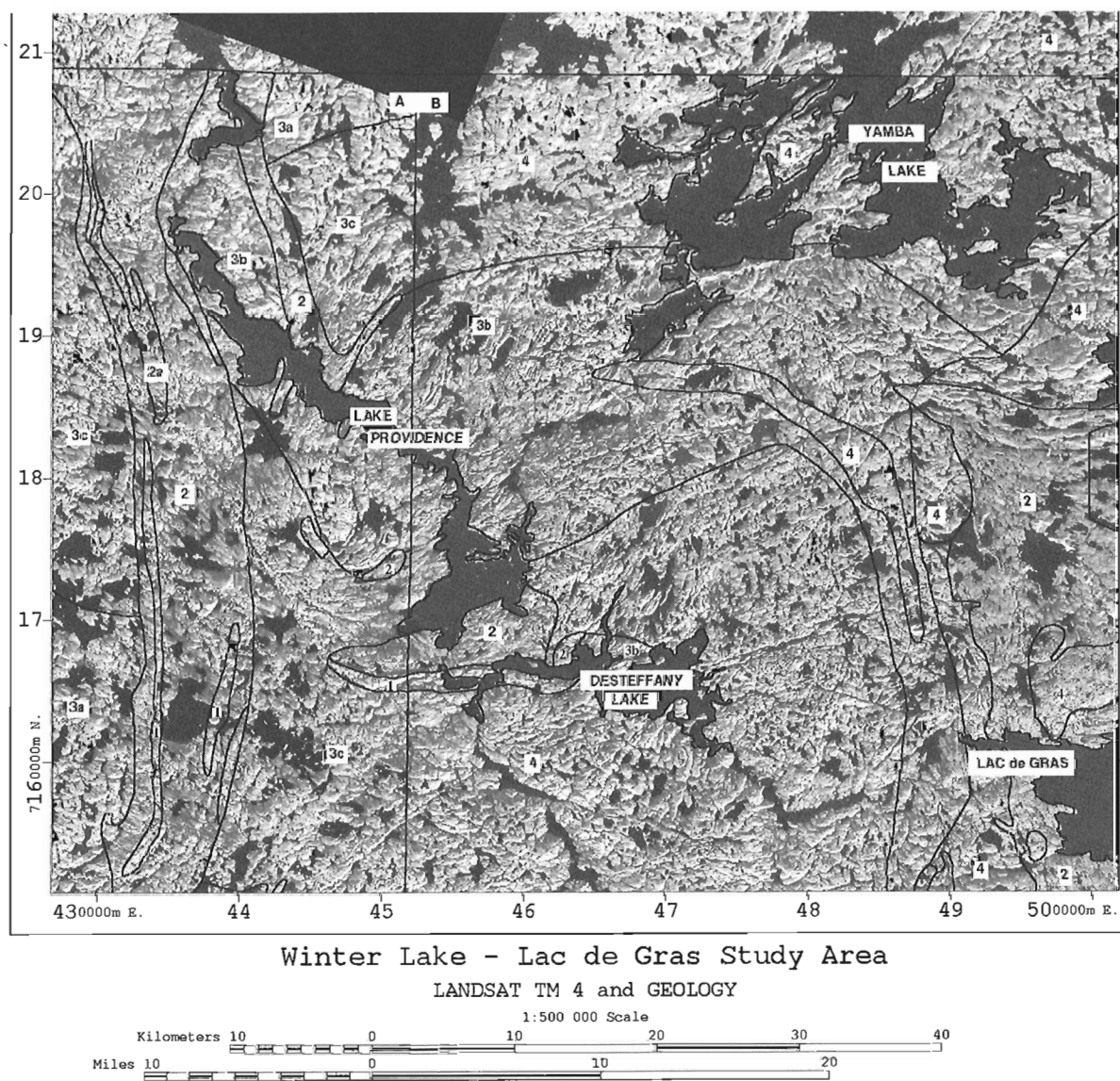


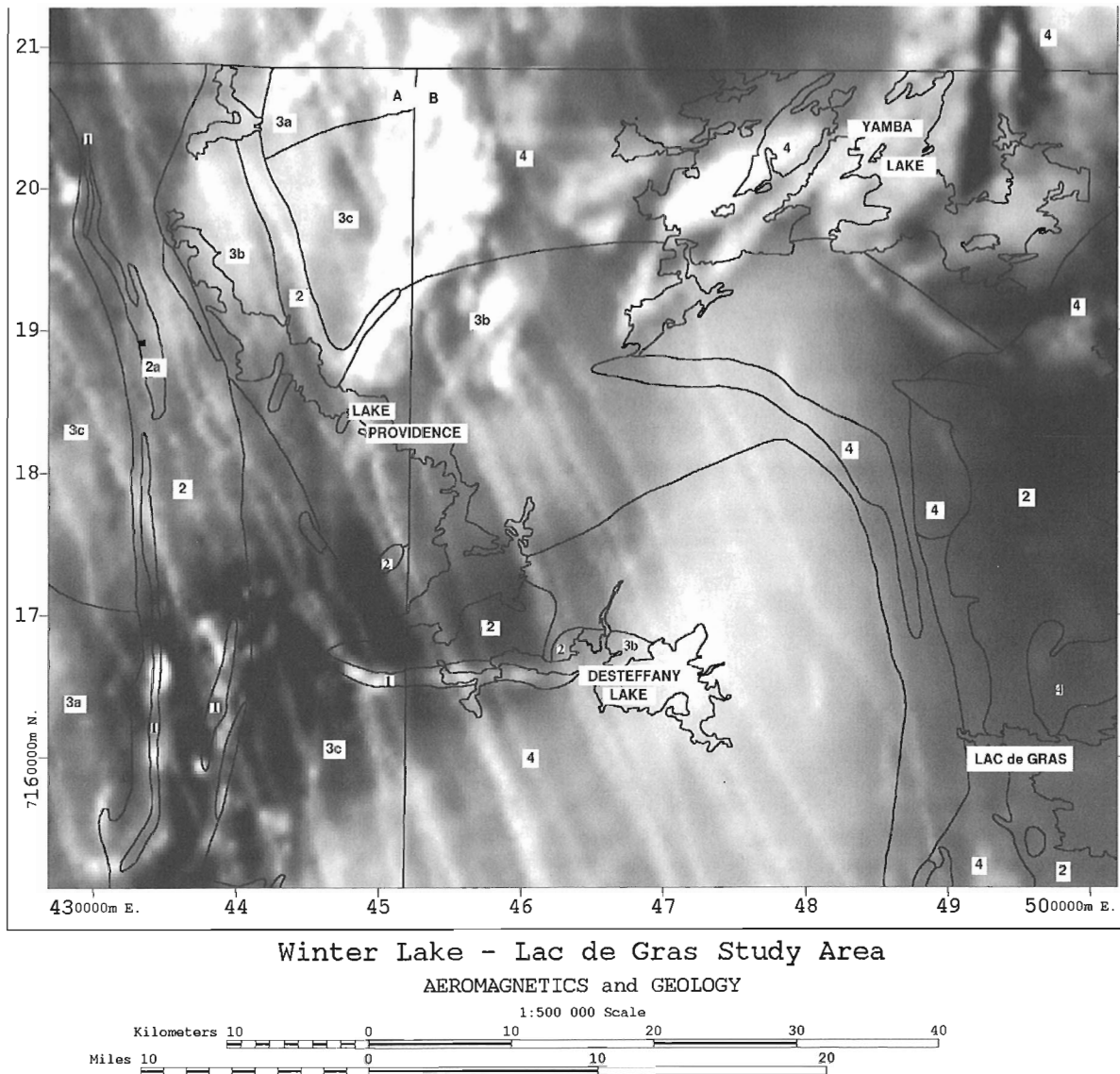
Figure 2. LANDSAT TM data (Band 4) with geological contacts "burned in".

colour of the earth's surface (Bands 1, 2, and 3). Verification with conventional aerial photographs helped to resolve these problems.

Aeromagnetic data are also both concordant and discordant with respect to the reconnaissance geology (Fig. 3). Prominent north-northwest-trending linear highs correspond to mafic dykes too thin (25 m) to be resolved on the geology and Thematic Mapper data layers. A broad positive anomaly elongated north-south parallels contacts northeast of Lac de Gras but it is strongly discordant north of Desteffany Lake. The striking inverted "vee" northeast of Yamba Lake occurs in an area mapped as homogeneous granitoid rocks. The

southeast limit of the prominent aeromagnetic low in the southwest corner of the map cuts across the lithological trends. Discordance between geological and aeromagnetic data reflects both the reconnaissance nature of previous mapping and the possibility of a subsurface source for some magnetic anomalies.

Even on a black and white image (Fig. 4), integration of all three data sets outlines useful targets. There is no indication of the inverted vee-shaped aeromagnetic anomaly in the texture of the TM image east of Yamba Lake. Is the outcrop poor or does the magnetic feature occur deep beneath the surface? The fact that both TM structures and the aeromagnetic



**Figure 3.** Geological contacts have been "burned into" the aeromagnetic data. Geology in part A of map is after (Fraser, 1969) and in part B, after Folinsbee (1949). Rock units: 1 - low- and medium-grade metavolcanic rocks; 2 - low- and medium-grade metasedimentary rocks, 2a - polymictic metaconglomerate; 3 - heterogeneous gneissic and migmatitic rocks derived from granitoid and supracrustal protoliths, 3a - gneissic migmatitic granitoid, 3b - injection gneiss, 3c - foliated granitoid and gneiss; 4 - homogeneous granitoid rocks. With respect to aeromagnetic data, positive anomalies are white and negative anomalies are black.

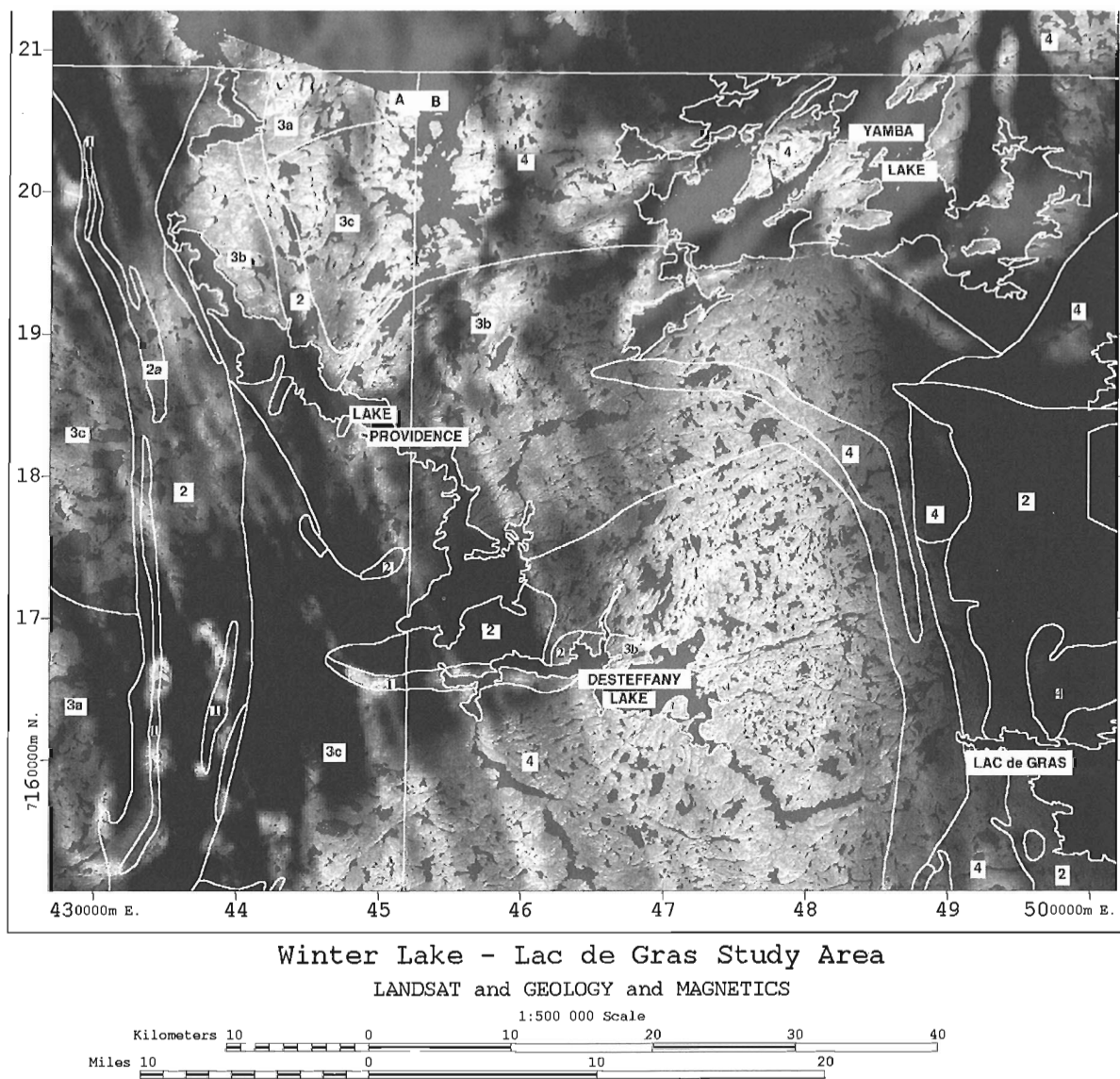


anomaly intersect rock units south of Yamba Lake suggests the reconnaissance geological map is over-simplified. The southwestern aeromagnetic low corresponds with an area of poor outcrop. Have surficial deposits masked the aeromagnetic anomaly or is it also a deep-seated feature? Discordance between geological and aeromagnetic data reflects both the reconnaissance nature of previous mapping and the possibility of a subsurface source for some magnetic anomalies. Mapping every outcrop combined with detailed geophysics would solve many of these problems, at least in areas where bedrock exposure is adequate.

Mapping every outcrop, however, is usually not economically feasible, and it may not be required to reconstruct the geological history. Maps integrating all three types of data help to determine where bedrock mapping will be most effective.

As new data are obtained, updated images provide a basis for modification of priorities, for example, the location of more detailed follow-up mapping.

The colour products were found to be more useful than the black and white products particularly when the products were an integrated set of two or more data sets. The colour is required because it is produced by adding several components to make the final result. In this way information from several sources can be added to produce a final product. The IHS was particularly valuable as it provided hue information from the magnetic data and intensity information (seen as textural differences) from the LANDSAT data. Because black and white is essentially a variation in only one component any combination of information will result in a loss of information from one or the other component. This can be seen in Figure 4



**Figure 4.** Combination of LANDSAT TM data (Band 4), aeromagnetic, and geological data. Necessity of using black and white causes TM texture defined mainly by black bodies of water to disappear in areas where aeromagnetic values are low (black).

in relatively dark areas. In these regions the black colour illustrates areas of low magnetic response but there is only limited, if any, textural information from the LANDSAT data. On the colour imagery there are variations in colour intensity that relate to differences in the LANDSAT imagery.

## CONCLUSIONS

Integration of LANDSAT TM, aeromagnetic, and reconnaissance geology data provides a unique perspective on a map area and on what is known about it before a new project begins. The combination of data sets is more than the sum of its parts because the limitations inherent in each one are more obvious on the integrated map and, to a varying degree, these limitations may be compensated for by contributions of the other two.

Once a map area has been selected for a regional mapping upgrade, integrated data sets assist in planning of an optimum distribution and density of traverses. As the quality and density of geological information increase during mapping, integrated images can be upgraded and mapping priorities reassessed. The information constrains extrapolation of contacts and structures between traverses and in areas of poor outcrop. Integrated data aid in the selection of priority areas for more detailed work.

## ACKNOWLEDGMENTS

We would like to thank D. Graham (Storefront Office at GSC) for his help with the DIPIX ARIES III image analysis system and D. Abbinett (GSC) for the creation of some of the figures. J. King and D. Wright reviewed earlier versions of this paper.

## REFERENCES

### Baril, D. and Rencz, A.N.

1992: LANDSAT TM, ERS1 Radar and aeromagnetic imagery for Lac de Gras, N.W.T.; Geological Survey of Canada, Open File 2572.

### Broome, H.J.

1987: Geophysical imaging software for IBM-compatible microcomputers; Geological Survey of Canada, Open File 1581.

1988: An IBM-compatible microcomputer workstation for modelling and imaging potential field data; *Computers and Geoscience*, v. 14, no. 5., p. 659-666.

### Dods, S.D., Teskey, D.J., and Hood, P.J.

1985: The new 1:1000 000 magnetic anomaly map series of the Geological Survey of Canada-Compilation techniques and interpretation; in *Utility of regional gravity and magnetic maps*, (ed.) W.J. Hinzi; Society of Exploration Geophysicists, p. 69-87.

### Folinsbee, R.E.

1949: Lac de Gras, District of Mackenzie, Northwest Territories; Geological Survey of Canada, Map 977A.

### Franklin S.E., Peddle, D.R., and Gillespie, R.T.

1989: Image processing and data integration techniques for improved geological mapping in the Buchans area, central Newfoundland; in *Proceedings of the Seventh Thematic Conference on Remote Sensing for Exploration Geology*, Calgary, Alberta, p. 1039-1050.

### Fraser, J.A.

1969: Winter Lake, District of Mackenzie; Geological Survey of Canada, Map 1219A.

### Gillespie, A.R.

1980: Digital techniques of Image Enhancement in Remote Sensing in *Geology*; (ed.) B.S. Siegal B.S. and A. R. Gillespie, New York, p. 139-226.

### Harris, J.R. and Murray, R.T.

1990: IHS transform for the integration of radar imagery with other remotely sensed data; *Photogrammetric Engineering and Remote Sensing*, v. 56, no. 12, p. 1631-1641.

### Harris, J.R., Neily, L., Pultz, T., and Slaney V.R.

1986: Principal component analysis of airborne geophysical data for lithologic discrimination using an image analysis system; in *Proceedings of the Twentieth International Symposium on Remote Sensing of Environment*, Nairobi, Kenya, p. 651-657.

### Intera/Tydac Technologies, Inc.

1991a: TYDIG Reference Manual; Intera/Tydac Technologies, Inc., Ottawa, Ontario.

1991b: Spatial Analysis System (SPANS). Reference Guide; Intera/Tydac Technologies, Inc., Ottawa, Ontario.

### Kowalick, W.S. and Glenn, W.E.

1987: Image processing of aeromagnetic data and integration with LANDSAT images for improved structural interpretation; *Geophysics*, v. 52, no. 7, p. 875-884.

### Lillesand, T.M. and Kiefer, R.W.

1987: *Remote Sensing and Image Interpretation*; John Wiley and Sons, Inc., New York. p. 721.

### PCI Inc.

1991: EASI/PACE Users Manual; PCI Inc., Richmond Hill, Ontario.

### Rheault M., Simard, R., Garneau C., and Slaney, V.R.

1991: SAR LANDSAT TM-Geophysical data integration utility of value-added products in geological exploration; *Canadian Journal of Remote Sensing*, v. 17, no. 2, p. 185-190.

### Slaney, V.R.

1985: LANDSAT MSS and airborne geophysical data combined for mapping granite in southwest Nova Scotia; in *Proceedings of the Eleventh International Symposium on Machine Processing of Remotely Sensed Data*, Purdue University, Indiana, p. 198-206.

### Thompson, P.H.

1992: The Winter Lake-Lac de Gras regional mapping project, central Slave Province, district of Mackenzie, Northwest Territories; in *Current Research, Part A*; Geological Survey of Canada, Paper 92-1A, p. 41-46.

### Thompson, P.H., Ross, D., Froese, E., Kerswill, J., and Peshko, M.

1993: Regional Geology in the Winter Lake-Lac de Gras Area, Central Slave Province, District of Mackenzie, N.W.T.; in *Current Research, Part C*; Geological Survey of Canada, Paper 93-1C, p. 61-70.

### Tooker, M., Schewchenko, N., Bonham-Carter, G.F. Rencz, A.N., and Wright, D.F.

1990: Plotter: A Fortran program using UNIRAS for plotting SPANS and EASI/PACE images; Geological Survey of Canada, Open File 2255, 43 p.

Geological Survey of Canada Project 840051

EASTERN CANADA  
AND NATIONAL  
AND GENERAL  
PROGRAMS

EST DU CANADA  
ET PROGRAMMES  
NATIONAUX ET  
GÉNÉRAUX



# Mineralogy and petrology of the stringer sulphide zone in the Discovery Hole at the Brunswick No. 12 massive sulphide deposit, Bathurst, New Brunswick<sup>1</sup>

David R. Lentz<sup>2</sup> and Wayne D. Goodfellow

Mineral Resources Division

*Lentz, D.R. and Goodfellow, W.D., 1993: Mineralogy and petrology of the stringer sulphide zone in the Discovery Hole at the Brunswick No. 12 massive sulphide deposit, Bathurst, New Brunswick; in Current Research, Part E; Geological Survey of Canada, Paper 93-1E, p. 249-258.*

---

**Abstract:** The Discovery Hole (A-1) of the Brunswick No. 12 deposit was selected for petrological analysis of sulphide-rich stringer veins because it intersects the zone of most intense stringer sulphide mineralization within sedimentary and volcanoclastic rocks stratigraphically underlying the massive sulphide deposit. The stringer mineralization is repeated around an F<sub>2</sub> fold that is cored by an infolded massive sulphide lens, and is highly attenuated and asymmetrical around the sulphide deposit. The abundance of sulphide veins generally increase with proximity to the ore body. The veins are composed of quartz, chlorite, sericite, ferroan carbonate, and sulphides (20 to 50%) that consist of pyrite, pyrrhotite, sphalerite, arsenopyrite, chalcopyrite, tetrahedrite, and galena. The core of the vein system is pyrite- and arsenopyrite-rich compared to the more pyrrhotite-rich margins. The footwall stringer zone is interpreted as a hydrothermal fluid conduit that has been structurally transposed during tectonic deformation.

**Résumé :** Le trou Discovery (A-1) du gisement Brunswick n° 12 a été choisi pour fin d'analyse pétrographique des veinules riches en sulfures parce qu'il recoupe la zone de minéralisation filonienne la plus importante à l'intérieur des roches sédimentaires et volcanoclastiques de l'éponte stratigraphique inférieure du gisement de sulfures massifs. La minéralisation filonienne est répétée autour d'un pli P<sub>2</sub>, dont la zone axiale est constituée d'une lentille de sulfures massifs repliée sur elle-même, et est fortement atténuée et asymétrique autour du gisement de sulfures. L'abondance des veinules de sulfures augmente à proximité du corps minéralisé. Les veinules sont composées de quartz, de chlorite, de séricite, de carbonate ferrifère, et de sulfures (de 20 à 50 %) constitués de pyrite, de pyrrhotine, de sphalérite, d'arsénopyrite, de chalcopyrite, de tétraédrite et de galène. La partie centrale du réseau de veinules est riche en pyrite et en arsénopyrite par rapport à la partie externe qui est plus riche en pyrrhotine. La zone de minéralisation filonienne de l'éponte inférieure serait un conduit de fluide hydrothermal qui aurait été transposé structurellement lors de la déformation tectonique.

---

<sup>1</sup> Contribution to Canada-New Brunswick Cooperation Agreement on Mineral Development (1990-1995), a subsidiary agreement under the Canada-New Brunswick Economic and Regional Development Agreement.

<sup>2</sup> Geological Survey of Canada, P.O. Box 50, Bathurst, New Brunswick E2A 3Z1

## INTRODUCTION

There is little published information on the mineralogy and petrology of stringer sulphides in rocks underlying the Brunswick No. 12 massive sulphide deposit. Diamond-drill hole (DDH) A1, the Discovery Hole drilled in 1953 by Anacon Lead Mines Ltd. (Fig. 1 and 2), was selected for an orientation study because it transects weakly altered hanging wall, intensely altered stratigraphic footwall rocks that host the main stringer sulphide mineralization, and moderately altered quartz augen schist at the bottom of the hole. This section represents, therefore, virtually the entire spectrum of stockwork mineralization observed around the ore body.

The massive sulphides at Brunswick No. 12 are underlain by very fine grained, tuffaceous sedimentary rocks that grade laterally into fine grained, crystal-rich tuffs. The coincidence of the stringer zone with this facies change and the juxtaposition of the pelites and quartz wackes of the Patrick Brook Formation with the footwall sedimentary rocks is circumstantial evidence for the existence of a fault-controlled basin hosting the sulphide deposit (cf., Lentz and Goodfellow, 1992). The development of stockwork stringer sulphide mineralization within the Brunswick ore body has been used as evidence for a vent-proximal setting of the Brunswick No. 12 deposit (Jambor, 1979). The stringer sulphide zone is interpreted to be the center of hydrothermal fluid discharge (feeder zone) for the massive sulphide deposit (Goodfellow, 1975; Luff et al., 1992). The spatial association of the stringer sulphide zone with the Cu-rich portion of the orebody is also evidence for the existence of a feeder pipe (Luff et al., 1992). It has also been proposed, however, that the stringer zone sulphides are related to sulphide remobilization during deformation (van Staal and Williams, 1984, 1986). The purpose of this study was, therefore, to obtain textural and mineralogical information that may help constrain the origin of the stringer sulphides. It represents a part of the C-NBCAMD (MDA II) project to document hydrothermal alteration and to determine the environment of ore formation along the Brunswick belt.

## GEOLOGY AND STRUCTURE

The geology of the Brunswick No. 12 deposit has been described by Goodfellow (1975), Luff (1977), van Staal and Williams (1984), and Luff et al. (1992) (Fig. 1 and 2). The primary depositional characteristics of the host rocks to the Brunswick No. 12 deposit have been summarized by Lentz and Goodfellow (1992). Drillhole A1 (Fig. 3) is collared in alkali basalts and associated sedimentary rocks (Boucher Brook Formation; BB Fm), and intersects the hanging wall tuffites, hyalotuffs, and sedimentary rocks of the Flat Landing Brook Formation (FLB Fm) and structural and stratigraphic footwall volcanoclastic and associated sedimentary rocks of the Nepisiguit Falls Formation (NF Fm). A porphyritic dyke occurs at the contact between the Flat Landing Brook and Nepisiguit Falls formations at the inferred Brunswick sulphide horizon. The Nepisiguit Falls Formation has siliceous, chloritic, and sericitic alteration and stringer sulphide mineralization that decreases in intensity with depth. A narrow sequence of thinly bedded graphitic pelites and quartz wackes (<30 m) of the Patrick Brook Formation (PB Fm) is very tightly infolded into the sequence intersected in drillhole A1 (van Staal and Williams, 1984). The drillhole passes through this fold into sedimentary rocks of the Nepisiguit Falls Formation that exhibit increasing intensity of chloritic and silicic alteration and abundance of sulphide veins towards the infolded massive sulphide deposit (Fig. 1 and 2; Luff et al., 1992a). The hole intersects the main sulphide ore zone, which consists of massive pyrite and minor amounts of sphalerite and galena with variable proportions of chalcopyrite, magnetite, and pyrrhotite (SPP or SPPC) (Luff et al., 1992). The sulphide zone intersected in this drillhole represents a structural lens formed by the superposition of a very tight  $F_2$  fold near the nose of a tight  $F_1$  fold (van Staal and Williams, 1984). Therefore, the facing direction changes from downhole to uphole within the core of the sulphide lens without intersecting hanging wall rocks. After this change in the facing direction, moderately altered Nepisiguit Falls Formation sedimentary and volcanoclastic rocks (quartz augen schist) are intersected below the massive sulphide lens (Fig. 1 and 2).

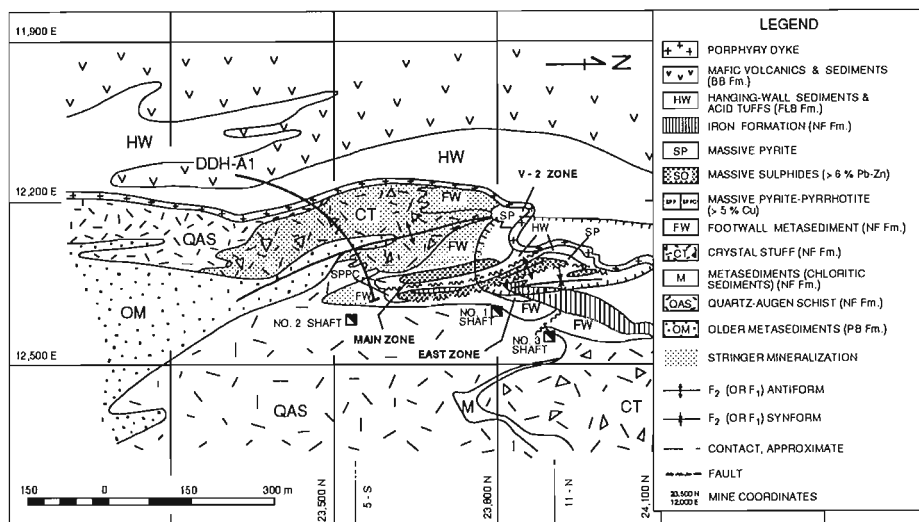


Figure 1.

Surface geology of the Brunswick No. 12 massive sulphide deposit, northern New Brunswick with the location of diamond-drill hole A1 (modified from Luff et al., 1992).

## STRINGER SULPHIDE ZONE

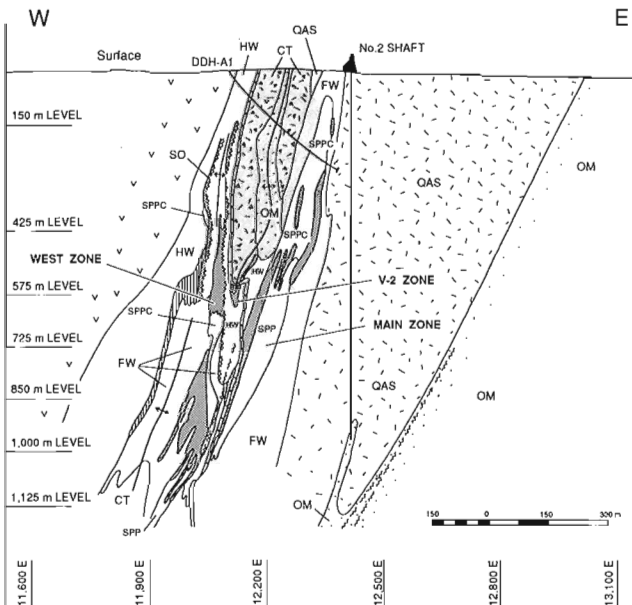
The core of the stringer sulphide zone is dominated by the assemblage quartz-Fe chlorite-pyrite-arsenopyrite and lesser pyrrhotite and chalcopyrite, whereas the peripheral zones of the stringer zone are composed of Fe-Mg chlorite-pyrrhotite-pyrite-sphalerite and rare chalcopyrite and arsenopyrite. The anastomosing nature of the veins is reminiscent of a stock-work vein network (Luff et al., 1992). It is evident that the stringer sulphide mineralization has been transposed and intensely folded, virtually parallel to the strike of the ore horizon. The stringer zone has remained structurally autochthonous relative to the vent facies of the mineralization, at least on the scale of the orebody, since the slightly younger, synvolcanic porphyry dyke that crosscuts the orebody also transects the hanging wall and footwall stratigraphy. This is significant when interpreting alteration facies within the enclosing host rocks (Lentz and van Staal, 1993).

### Petrology and mineralogy

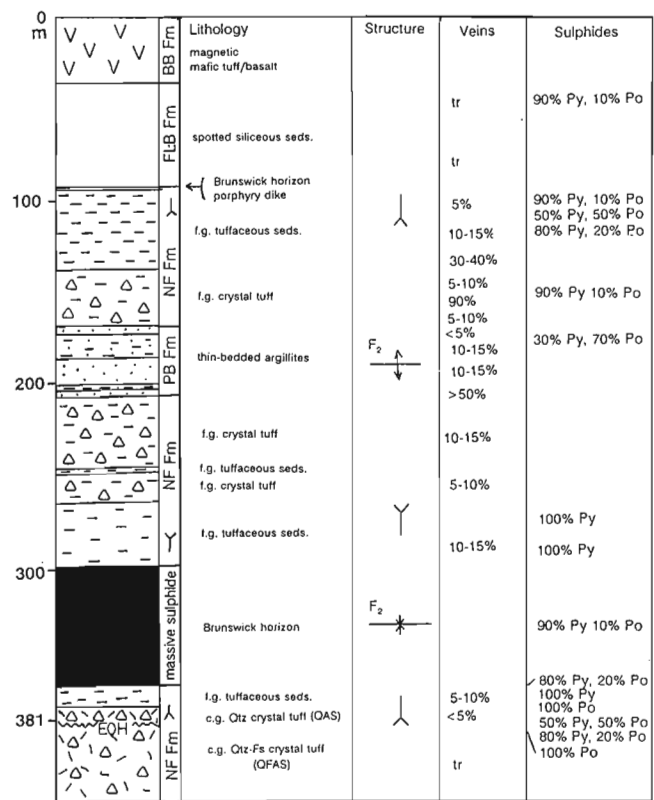
The number of sulphide veins and intensity of alteration increase markedly near the top of the footwall sequence within the vent complex, particularly in the 250 to 300 m interval directly beneath the ore lens (Fig. 3). A few discontinuous, anastomosing pyrite veins and veinlets, and very fine grained disseminated pyrite occur in the hanging wall rocks (Fig. 4A), which are generally devoid of sulphide veins. Within the stratigraphic footwall, the veins contain 20 to 50 vol.% sulphides with abundant hydrothermal quartz, and lesser proportions of chlorite, sericite, and ferroan carbonate (Fig. 4B-G). The veins have variable widths, and may be concordant or shallowly discordant with respect to the primary layering in the host rock (Fig. 4C).

The poorly developed fabrics in the siliceous sedimentary rocks precludes a detailed structural analysis of the vein paragenesis with respect to the deformation. Two samples with sedimentological layering ( $S_0$ ), based on the coherency of the individual laminations, were taken. In these samples, a moderately developed crenulation cleavage ( $S_2?$ ) is present at a high angle to a composite  $S_{0,1}$  fabric that disrupts the veins. However, the veins usually parallel the composite  $S_1, S_2$  fabric (van Staal and Williams, 1984; Luff et al., 1992). The occurrence of sulphide along later ( $S_2?$ ) fabrics that truncate fold hinges indicates that some sulphides have been remobilized during deformation.

Discrete, dark-coloured chloritic wisps occurring in the altered fine grained crystal-rich tuffs are interpreted as chloritized fiamme (Fig. 4B). Although silica occurs in most sulphide-rich veins, siliceous alteration selvages are predominantly developed in association with moderate to intense chloritic alteration (Fig. 4B) and becomes more pervasive with proximity to the exhalative ore facies (Fig. 4D, E). The variably brecciated and pervasively silicified footwall sedimentary rocks directly beneath the ore horizon have little obvious fabric development indicative of competent behaviour during deformation. In these rocks, the mineralization is



**Figure 2.** Geological section 5-South through the No. 2 shaft, Brunswick No. 12 deposit (modified from Luff et al., 1992, see Fig. 1 for location) with diamond-drill hole A1 located.

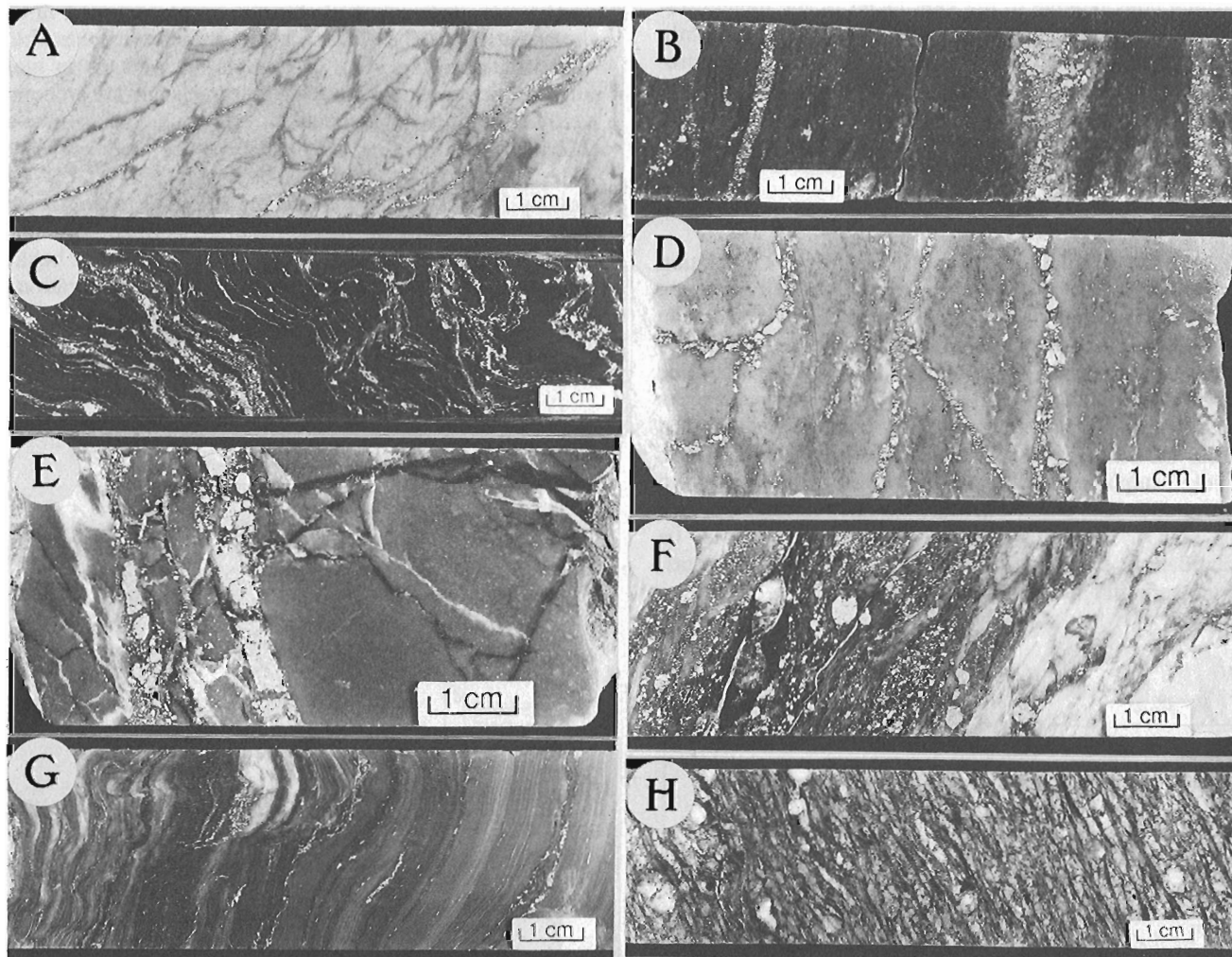


**Figure 3.** Geological profile for diamond-drill hole (DDH) A1 supplemented with three samples from least-altered QFAS 850 m level of the mine at bottom of the hole. BB Fm – Boucher Brook Formation, FLB Fm – Flat Landing Brook Formation, NF Fm – Nepisiguit Falls Formation, PB Fm – Patrick Brook Formation. Note that the massive sulphide intersected in the drill hole represents the synclinal keel of a  $F_1$  and  $F_2$  sheath fold (i.e., note facing directions).

characterized by irregular disseminated sulphides and veins (Fig. 4D, E)). The ore consists predominantly of very fine grained pyrite with irregular replacements of coarser grained pyrite, pyrrhotite, sphalerite, chalcocopyrite, arsenopyrite, and quartz. Irregular, structurally induced brecciation of the ore is infilled with relatively coarse grained quartz, carbonate, and lesser proportions of sulphide minerals (<10%). Stratigraphically and structurally beneath the ore zone, sulphide-rich siliceous veins are cataclastically rounded indicating local intensive shearing parallel to the composite  $S_1S_2$  fabric

(Fig. 4F). Pyrrhotite-rich veinlets occur in the moderately altered, finely layered footwall sedimentary rock (Fig. 4G) and underlying altered crystal-rich tuff (QAS) (Fig. 4H).

Stringer sulphide veins contain Mg-Fe chlorite, phengite, quartz, and sulphide minerals. The sulphides are subhedral to euhedral, fine- to medium-grained pyrite (Fig. 5A-D), pyrrhotite, chalcocopyrite, sphalerite, arsenopyrite, and tetrahedrite. A rare pyritic siliceous vein occurring in the hanging wall (Fig. 5A) contains minor arsenopyrite and minor sericite. Although rare, some veins occur oblique to the fabric



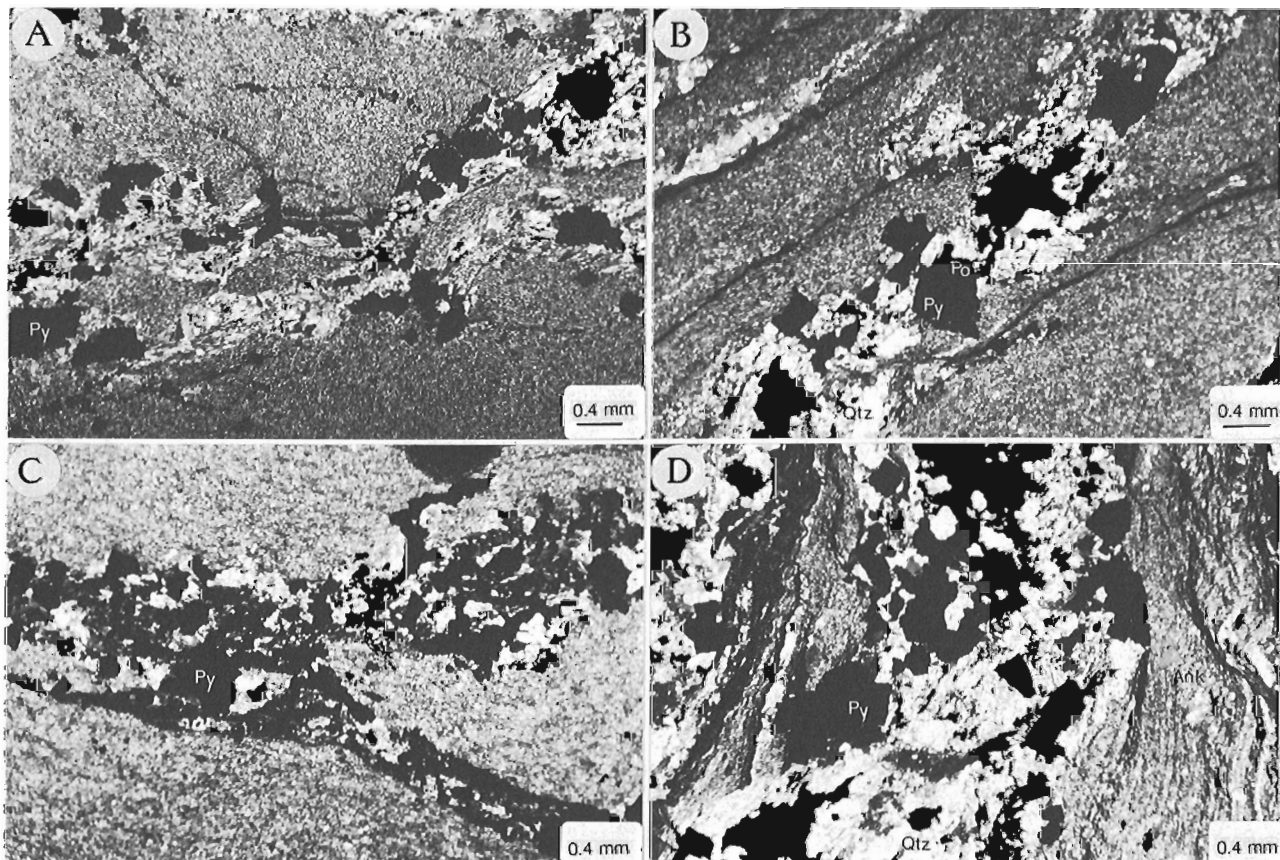
**Figure 4.** Selected polished slabs of drill core from drillhole A1; A) Pyrite-rich veinlets hosted in cream-coloured, weakly altered hanging wall rhyolite (FLB Fm)(LPA-014; A1-57 m), B) Concordant ( $S_1$ ) quartz-bearing, pyrite- and pyrrhotite-rich veins with silicic selvages hosted in a pervasively chloritized fine grained, crystal-rich tuff with dark chloritic fiamme(?) (NF Fm) (LPA-027; A1-146.3 m), C) Quartz-bearing pyrite- and pyrrhotite-rich veins slightly discordant to  $S_0$  defined by graphitic layers in moderately chloritic pelites (PB Fm) (LPA-030; A1-169.8 m), D) Irregular disseminated pyrite and pyrite veins in intensely silicified footwall sediment (NF Fm) with no obvious fabric development that occurs stratigraphically beneath the infolded ore zone (LPA-041; A1-276.5 m), E) Pyrite-rich veins in intensely silicified footwall sediment (NF Fm) or pre-ore exhalative chert horizon(?) with no obvious fabric development and occurs stratigraphically beneath the infolded ore zone (LPA-043; A1-298.4 m) Note that white siliceous veins are secondary and unrelated to the ore system. F) Disseminated pyrite and dismembered pyrite-rich veins in silic, chloritic, and sericitic footwall sediment (NF Fm). The veins are parallel to the composite  $S_1S_2$  fabric (LPA-054; A1-368.5 m). G) Moderately silicic and chloritic footwall sediment with few pyrrhotite-rich veins parallel to  $S_1$  fabric (NF Fm) (LPA-057; A1-372.8 m). H) Moderately altered chlorite-sericite quartz augen schist (QAS) with few per cent pyrrhotite-rich veins parallel to the  $S_1S_2$  fabric (LPA-060; A1-380.7 m).



indicating only partial transposition (Fig. 5B, C). In the thinly layered pelites (Patrick Brook Formation), sulphide veins disrupt the  $S_0$  layering but are, in part, foliated (Fig. 5D). The formation of lenticular quartz ( $\pm$ chlorite) lenses within small discordant sulphide-quartz veinlets parallel to the  $S_1$  fabric is interpreted as sheared quartz associated with fabric development (deformation bands).

The silicate mineralogy is very similar in both veins and host rocks, indicating that pervasive alteration accompanied vein formation or the rocks have been metamorphically re-equilibrated. Quartz is common in the sulphide veins and generally exhibits deformation bands that are consistent with mylonitization. In most places, sulphides constitute between 20 and 50 vol.% of the vein. Several detailed petrographic studies of the ores at the Brunswick deposits have been done (Lea and Rancourt, 1958; Stanton, 1959; Aletan, 1960; Roy, 1961; Boorman, 1975; Fuller, 1968) although no studies have examined the stringer sulphides in detail.

Pyrite is the dominant sulphide phase, commonly comprising greater than 90 vol.% of the sulphide assemblage in the core of the stringer vein system, whereas pyrite is subordinate to pyrrhotite in the less altered zones. The pyrite is very fine grained (<0.01 mm) to medium grained (5 mm). A fine grained, skeletal, arsenopyrite-pyrite-intergrowth texture (Fig. 6A, B) may be indicative of rapid sulphide saturation within the vein. This texture is also evident in the stringer mineralization that characterizes the FAB zone (Lentz and Goodfellow, 1993). Arsenopyrite is commonly very fine- to fine-grained and commonly contains minor inclusions of chalcopyrite and tetrahedrite. Euhedral to subhedral pyrite with minor inclusions of pyrrhotite and chalcopyrite are common and, in some cases, enclose inclusion-rich pyrite. In many cases, pyrrhotite partially to completely replaces subhedral to euhedral pyrite (Fig. 6C). Tetrahedrite forms inclusions in pyrite and, more rarely, in arsenopyrite (Fig. 6D).



**A** – Anastomosing pyrite-sericite-quartz veins in very fine grained felsic tuff/rhyolite with minor disseminated carbonates (LPA-014; DDH A1-57 m).

**B** – Pyrrhotite-pyrite-quartz vein with minor Fe chlorite hosted in a very fine grained footwall sediment (LPA-021; 106.1 m).

**C** – Chlorite-pyrrhotite-quartz-pyrite vein hosted in altered, fine grained crystal tuff (LPA-025; 136.2 m).

**D** – Sulphide-rich carbonate-chlorite-quartz vein discordantly hosted in pelite (PB Fm) (LPA-031; 203.6 m).

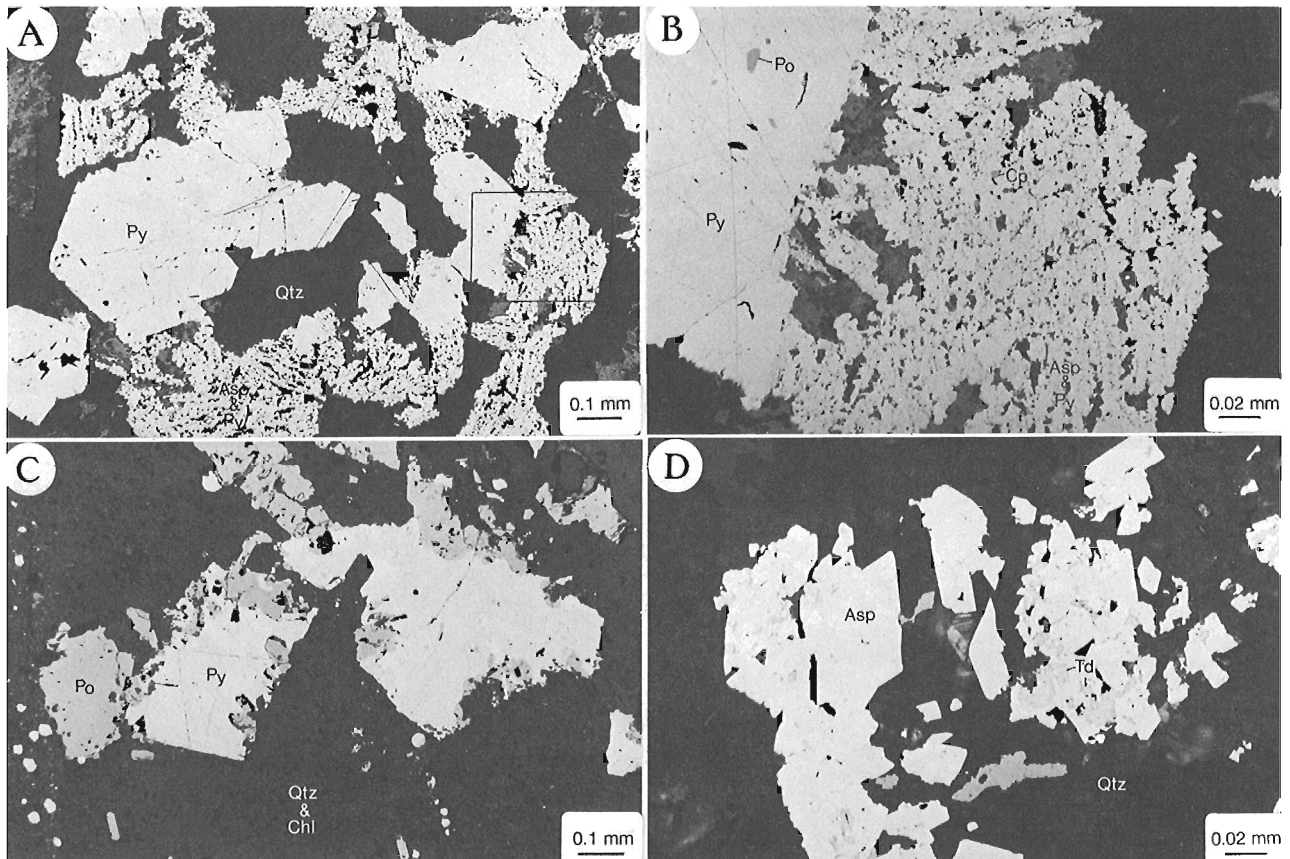
**Figure 5.** Thin section photographs illustrating the sulphide vein/host rock relationships.

Pyrite typically exhibits cataclastic fractures that are filled by pyrrhotite, sphalerite, and chalcopyrite veinlets. Cataclastic textures are related, in some cases, to the development of secondary veinlets within pyrite. In most cases, pyrrhotite is thermally annealed into a foam texture and does not appear to have retained any indications of intracrystalline strain. The ductile behaviour of pyrrhotite, sphalerite, and chalcopyrite under metamorphic conditions may account for their mobilization into cataclastic fractures in pyrite. Sphalerite commonly occurs with pyrrhotite and chalcopyrite, although it is also locally enclosed in pyrite. Sphalerite has a quite uniform medium- to deep-red translucent colour indicative of moderate iron contents irrespective of its association with pyrrhotite and/or pyrite. On the scale of the thin section, this suggests that sphalerite has remained near metamorphic equilibrium. Sphalerite with chalcopyrite disease is rare and occurs in coarse grained pyrite where it is presumably shielded from tectonic stresses that would induce recrystallization.

### Sulphide compositions

The composition of sulphides may be used to constrain hydrothermal and metamorphic conditions within the sulphide stringer zone. The As content of pyrite from the stringer zone is commonly low (<0.25 wt.%; Table 1) and generally increases to values >2 wt.% beneath the ore zone (Table 1). The Co content of pyrite is generally <0.15 wt.% whereas the Co content of pyrrhotite is marginally higher than for co-existing pyrite. Pyrite compositions reported here (Table 1) are similar to previous analyses of pyrite from the Brunswick No. 12 deposit and other massive sulphide deposits in the Bathurst Camp (Sutherland, 1967).

The compositional systematics of arsenopyrite are complex (Kretschmar and Scott, 1976; Scott, 1983) partially due to replacement and zoning within the vent complex (Fig. 7A-C). The cores are usually As-rich (32 to 33 mole% As) whereas the replacement zones are As-poor (30.5 to 32 mole% As) (Table 2). Pyrite overgrowths coexisting



**A** – Fine grained, skeletal (dendritic) arsenopyrite-pyrite intergrowth texture with euhedral pyrites porphyroblasts (?) and interstitial quartz and pyrrhotite (LPA-031; 203.6 m).

**B** – fine grained skeletal arsenopyrite-pyrite intergrowth with minor chalcopyrite (see A for area).

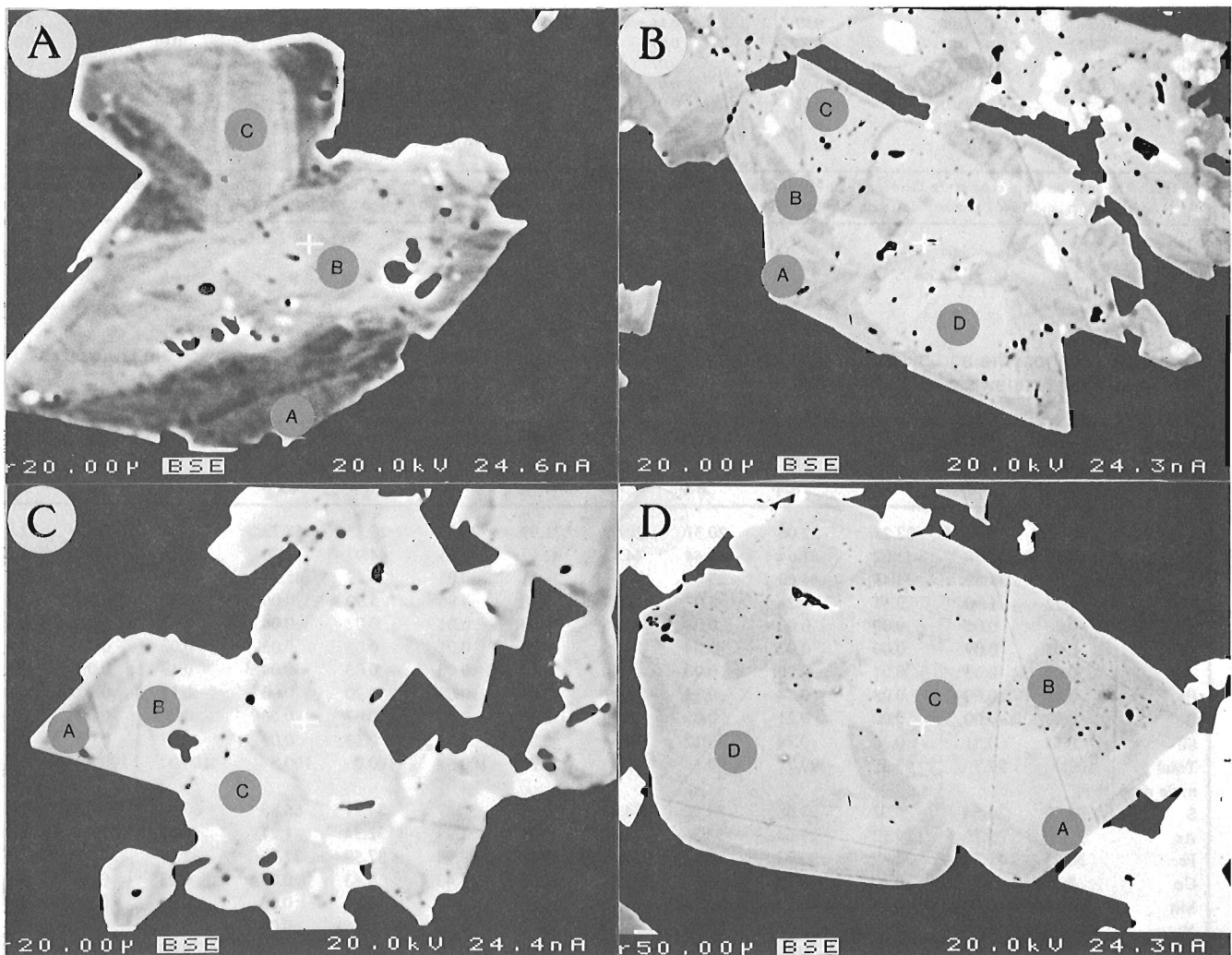
**C** – Pyrrhotite replacement of pyrite (partially recrystallized) (LPA-021; 106.1 m).

**D** – Fine- to medium-grained arsenopyrite with tetrahedrite inclusion in quartz-carbonate matrix (LPA-043; 298.4 m).

**Figure 6.** Thin section photographs of sulphide textural features in the stringer sulphide veins.

with arsenopyrite (Fig. 7C) have higher As contents (Fig. 7D). The preservation of delicate zoning in arsenopyrite (not shown) may be indicative of primary growth. The very high As contents in the cores of arsenopyrite suggests that arsenopyrite saturation probably preceded pyrite and pyrrhotite saturation (cf., Heinrich and Eadington, 1986). This is supported by the absence of pyrite and pyrrhotite inclusions in the cores of As-rich arsenopyrite. The As-poor arsenopyrite coexisting with pyrite and pyrrhotite indicate temperatures of 350° to 425°C at near-surface pressures (cf., Sharp et al., 1985). The lowest As contents, usually associated with the rims of arsenopyrite, correspond to metamorphic temperatures of between 350° to 400°C at 500 MPa (5 kbar) (cf., Sharp et al., 1985) and are consistent with upper greenschist-grade conditions estimated by van Staal (1985).

Sphalerite coexisting with pyrite in pyrrhotite has lower FeS contents (<13 to 14 mole%; sample 019 and 025) than sphalerite hosted in pyrite (16 to 17 mole% FeS; sample 046 and 054) (Table 3). The low-FeS sphalerites are interpreted to be metamorphic, and correspond to pressures of 450 to 550 MPa at an inferred temperature of 400°C (cf., Toulmin et al., 1991). Scott and Kissin (1973) have indicated that hexagonal pyrrhotite is the dominant form at temperatures greater than 254°C. Therefore, if no re-equilibration occurred during retrograde lower greenschist facies metamorphism, these pressure estimates should be realistic. Interestingly, van Staal (1985) determined an average of  $13.10 \pm 0.25$  mole% FeS in sphalerite ( $n = 5$ ) coexisting with pyrrhotite from the main and west ore zones. Similarly, McNulty (1981) determined  $13.6 \pm 0.7$  mole% FeS<sub>sp</sub> from the East Ore Zone. Sphalerite



**A** – As-poor arsenopyrite overgrowth on irregular As-rich arsenopyrite (LPA-042; 290 m).

**B** – As-rich arsenopyrite replaced and corroded by As-poor arsenopyrite (LPA-043; 298.4 m).

**C** – As-rich arsenopyrite overgrown and partially replaced by As-poor arsenopyrite (LPA-043; 298.4 m).

**D** – As-rich pyrite replacing As-poor pyrite (LPA-043; 298.4 m).

**Figure 7.** Scanning electron microscope backscatter images of arsenopyrite and pyrite from selected stringer sulphide samples with probe locations marked as letters (see Table 2).

**Table 1.** Average pyrite and pyrrhotite compositions from selected samples from diamond drillhole A1, Brunswick No. 12 deposit, Bathurst, New Brunswick

Sample Mineral	019		021		021		025		025		042		043		049		12A	12B
	Py	ls	Py	ls	Po	ls	Py	ls	Po	ls	Py	ls	Py	ls	Py	ls	Py	ls
n	4		5		3		11		1		15		10		1		1	1
	$\bar{x}$		$\bar{x}$		$\bar{x}$		$\bar{x}$		$\bar{x}$		$\bar{x}$		$\bar{x}$		$\bar{x}$		$\bar{x}$	
As wt. %	0.08	0.08	0.10	0.04	0.09	0.01	0.22	0.13	0.14	0.46	0.51	0.96	0.77	0.06	0.60	0.02		
S	51.76	0.31	53.57	0.26	39.34	0.18	53.19	0.96	39.24	53.62	0.50	53.12	0.51	52.25	51.84	52.72		
Fe	47.76	0.24	45.83	0.26	58.43	0.08	45.65	0.25	58.57	45.91	0.37	45.41	0.29	47.24	45.86	45.53		
Co	0.06	0.02	0.07	0.02	0.12	0.04	0.21	0.27	0.06	0.08	0.06	0.05	0.02	0.04	0.10	0.05		
Mn	0.02	0.02	0.01	0.01	0.03	0.02	0.01	0.01	0.01	0.02	0.02	0.01	0.01	0.01	0.01	0.01		
Ni	0.03	0.01	0.02	0.02	0.02	0.00	0.03	0.02	0.00	0.02	0.02	0.02	0.01	0.00	0.005	0.005		
Zn	0.20	0.13	0.01	0.01	0.05	0.03	0.02	0.02	0.00	0.02	0.03	0.03	0.04	0.00	0.08	0.29		
Pb	0.00	0.00	0.06	0.06	0.12	0.01	0.05	0.06	0.00	0.06	0.06	0.08	0.07	0.00	0.08	0.09		
Bi	-	-	0.00	0.00	0.00	0.00	0.00	0.00	0.00	0.00	0.00	0.00	0.00	-	-	-		
Sb	0.00	0.00	0.03	0.03	0.08	0.04	0.07	0.04	0.05	0.06	0.03	0.07	0.02	0.00	0.02	-		
Total	100.0		99.7		98.3		99.5		98.1	100.3		99.8		99.6	98.6	98.7		
mole prop.																		
S	65.21		66.96		53.83		66.77		53.77	66.80		66.66		65.79	66.00	66.69		
As	0.04		0.05		0.05		0.12		0.08	0.25		0.52		0.03	0.33	0.01		
Fe	34.54		32.89		45.90		32.90		46.08	32.83		32.71		34.15	33.52	33.06		
Co	0.04		0.05		0.09		0.14		0.04	0.05		0.03		0.03	0.07	0.03		
Mn	0.01		0.01		0.02		0.01		0.01	0.01		0.01		0.01	0.01	0.01		
Ni	0.02		0.01		0.01		0.02		-	0.01		0.01		-	0.00	0.00		
Zn	0.12		0.01		0.03		0.01		-	0.01		0.02		-	0.05	0.18		
Pb	-		0.01		0.03		0.01		-	0.01		0.02		-	0.02	0.02		
Bi	-		-		-		-		-	-		-		-	-	-		
Sb	-		0.01		0.03		0.02		0.02	0.02		0.02		-	0.01	-		

NOTES: The analyses were done at the Geological Survey of Canada, 601 Booth Street, Ottawa, Ontario. Mineral : Py = pyrite and Po = pyrrhotite. n = number of sample points,  $\bar{x}$  = mean, and ls = 1 standard deviation. Samples 12A and 12B are from Sutherland (1967) and contain 0.001 and 0.002 In, respectively.

**Table 2.** Arsenopyrite and pyrite compositions from selected samples in diamond drillhole A1, Brunswick No. 12 deposit, Bathurst, New Brunswick

Sample Fig. 7 Mineral	042B	042C	043A	043B	043C	043D	043A	043B	043C	043A	043B	043C	043D
	A	A	B	B	B	B	C	C	C	D	D	D	D
	Asp	Asp	Asp	Asp	Asp	Asp	Asp	Asp	Asp	Py	Py	Py	Py
S wt. %	20.60	22.04	22.21	22.06	20.31	20.09	21.99	20.57	20.23	52.32	53.66	52.57	52.84
As	44.12	41.88	42.07	41.64	44.44	44.73	42.62	44.55	44.97	2.36	0.14	1.94	1.59
Fe	31.29	32.88	34.45	34.60	28.89	30.26	34.71	30.08	28.42	45.34	45.79	45.51	45.13
Co	3.22	1.90	0.11	0.21	5.03	4.17	0.18	4.86	5.90	0.06	0.04	0.04	0.06
Mn	0.00	0.02	0.00	0.00	0.05	0.05	0.04	0.01	0.02	0.04	0.02	0.01	0.02
Ni	0.05	0.09	0.00	0.07	0.04	0.05	0.00	0.01	0.06	0.03	0.02	0.03	0.01
Zn	0.04	0.03	0.01	0.00	0.00	0.00	0.02	0.03	0.03	0.04	0.13	0.03	0.00
Pb	0.11	0.00	0.08	0.14	0.12	0.11	0.05	0.08	0.20	0.00	0.17	0.10	0.00
Bi	0.09	0.00	0.00	0.21	0.05	0.05	0.07	0.00	0.07	0.00	0.00	0.00	0.00
Sb	0.43	0.81	0.36	0.74	0.17	0.34	0.29	0.33	0.13	0.09	0.07	0.07	0.04
Total	100.0	99.7	99.3	99.7	99.1	99.9	100.0	100.5	100.0	100.3	100.0	100.3	99.7
mole prop.													
S	34.69	36.64	36.92	36.68	34.56	34.03	36.42	34.47	34.21	65.83	66.94	66.03	66.48
As	31.79	29.79	29.92	29.63	32.36	32.42	30.21	31.95	32.54	1.27	0.07	1.04	0.86
Fe	30.25	31.38	32.87	33.03	28.22	29.42	33.00	28.94	27.59	32.75	32.79	32.81	32.59
Co	2.95	1.72	0.10	0.19	4.66	3.84	0.16	4.43	5.43	0.04	0.03	0.03	0.04
Mn	0.00	0.02	0.00	0.00	0.05	0.05	0.04	0.01	0.02	0.03	0.01	0.01	0.01
Ni	0.05	0.08	0.00	0.06	0.04	0.05	0.00	0.01	0.06	0.02	0.01	0.02	0.01
Zn	0.03	0.02	0.01	0.00	0.00	0.00	0.02	0.02	0.02	0.02	0.08	0.02	0.00
Pb	0.03	0.00	0.02	0.04	0.03	0.03	0.01	0.02	0.05	0.00	0.03	0.02	0.00
Bi	0.02	0.00	0.00	0.05	0.01	0.01	0.02	0.00	0.02	0.00	0.00	0.00	0.00
Sb	0.19	0.35	0.16	0.32	0.08	0.15	0.13	0.15	0.06	0.03	0.02	0.02	0.01

NOTES: The analyses were done by John Stirling on the Cameca SX50 at the Geological Survey of Canada, 601 Booth Street, Ottawa, Ontario with analytical conditions are indicated in the photo (Fig. 7). Sample: sample - LPA series. Mineral : Asp = arsenopyrite and Py = pyrite.

analyzed by Sutherland and Halls (1969) from three ore samples and one bulk concentrate from the Brunswick No. 12 deposit contained  $12.9 \pm 0.6$  mole% FeS. Earlier attempts to calculate conditions of formation for these ore bodies (Benson, 1960; Kallikowski, 1961) using sphalerite compositions found  $\text{FeS}_{\text{sp}}$  mole proportions similar to this study. If the pyrite is indeed porphyroblastic (van Staal, 1985), the higher  $\text{FeS}_{\text{sp}}$  would correspond to pressures on the order of 200 MPa (2 kbar) at temperatures of 250 to 350°C. Alternatively, they may represent primary minerals that form during hydrothermal activity in the seafloor vent complex. The preservation of chalcopyrite-diseased sphalerite in pyrite (McNulty, 1981; this study) suggest that at least some of the pyrite euhedra are syngenetic/diagenetic.

## DISCUSSION

Luff et al. (1992) present considerable evidence to support an early or syngenetic origin of sulphide-silicate veins in host rocks stratigraphically underlying the Brunswick No. 12 deposit. Textural evidence can only indicate, however, that most of the veins are pre- $S_2$  fabric development. It is possible, therefore, that peak-metamorphic hydrothermal processes rather than seafloor hydrothermal processes may be responsible for the generation of some veins. The rare syn- to post- $F_2$  "bull" quartz veins ( $\ll 1\%$ ) that occur throughout the mine contain less than 5% sulphides suggesting that sulphide solubilities are low in syn- to late-metamorphic fluids. The stringer veins do not, however, represent remobilized sulphides as they have a very high proportion of low ductility minerals such as pyrite in the stringer zone. It is evident that

pyrite and arsenopyrite deform cataclastically during the later stages of deformation, whereas pyrrhotite, chalcopyrite, galena, and to a lesser extent sphalerite, behave ductily (van Staal, 1985).

The concordant to slightly discordant nature of sulphide veins is consistent with a sulphide stringer zone within the footwall of the Brunswick No. 12 sulphide deposit that has been transposed virtually parallel to bedding ( $S_0$ ) during the  $D_1$  deformation. Layer-parallel veins would be indistinguishable, for the most part, from those transposed into the  $S_0S_1$  fabric. The fine grained intergrowth of pyrite-arsenopyrite, chalcopyrite-diseased sphalerite, and fine grained, inclusion-rich spongy pyrite are similar to textures observed in sub-seafloor epigenetic stockwork hydrothermal systems. As previously mentioned, it is problematic whether the euhedral pyrite is syngenetic, diagenetic, or metamorphic. The preservation of delicate zoning in arsenopyrite, even where enclosed in pyrite, and "skeletal" arsenopyrite-pyrite intergrowths are consistent with a syngenetic origin. These intergrowths appear to nucleate on, rather than replace, euhedral pyrite. The earliest pyrite, however, in the exhalative ores includes framboidal, colloform, and spongy varieties (Lea and Rancourt, 1958; Stanton, 1959; Fuller, 1968). Coarse grained pyrite, partially replaced by pyrrhotite, is quite common in the stringer zone. This is not consistent with metamorphic desulphidation as pyrite is stable where pyrrhotite is absent. This supports a syngenetic/epigenetic origin for at least some of the coarse euhedral pyrite. The replacement of pyrite by pyrrhotite indicates a decrease in  $f(S_2)$  during the discharge of hydrothermal fluids at the seafloor. The higher abundance of pyrite relative to pyrrhotite in the core of the

**Table 3.** Average arsenopyrite and sphalerite compositions from selected samples from diamond drillhole A1, Brunswick No. 12 deposit, Bathurst, New Brunswick

Sample	014		042		043		049		CS		019		025		046		054	
Mineral	Asp		Asp		Asp		Asp		Asp		Sp		Sp		Sp		Sp	
n	16	1s	10	1s	7	1s	10	1s	5	1s	2	1s	6	1s	1	2	1	2
	$\bar{x}$		$\bar{x}$		$\bar{x}$		$\bar{x}$		$\bar{x}$		$\bar{x}$		$\bar{x}$		$\bar{x}$		$\bar{x}$	
As wt.%	42.65	1.48	43.47	1.14	43.57	1.41	44.19	1.05	45.14	0.93	0.00	0.02	0.03	0.00	0.00	0.00		
S	20.97	0.87	21.22	1.10	21.07	0.97	20.02	0.93	20.60	0.29	31.73	31.62	0.20	31.54	31.41			
Fe	34.77	0.49	32.76	1.78	31.63	2.84	35.21	0.59	33.60	0.48	7.60	7.64	0.26	9.53	9.21			
Co	0.09	0.09	1.64	1.48	2.92	2.63	0.16	0.26	-	-	0.01	0.03	0.01	0.01	0.04			
Mn	0.02	0.02	0.01	0.01	0.02	0.02	0.01	0.01	0.01	0.01	0.02	0.01	0.01	0.01	0.09	0.03		
Ni	0.07	0.10	0.04	0.02	0.03	0.03	0.18	0.16	-	-	0.01	0.01	0.02	0.03	0.01			
Zn	0.03	0.02	0.01	0.02	0.01	0.01	0.02	0.03	0.15	0.15	59.02	59.23	0.27	56.74	57.08			
Pb	0.05	0.06	0.07	0.07	0.11	0.05	0.04	0.05	-	-	0.06	0.07	0.08	0.00	0.00			
Bi	0.01	0.02	0.03	0.05	0.06	0.07	-	-	-	-	-	-	-	-	-			
Sb	0.39	0.29	0.38	0.26	0.34	0.20	0.07	0.07	0.54	0.37	0.04	0.02	0.01	0.04	0.01			
Total	99.1		99.6		99.8		99.9		99.2		98.5	98.9		98.1	98.2			
mole prop.																		
As	30.72		31.17		31.28		31.85		32.51	0.67	-	0.01		-	-			
S	35.30		35.56		35.35		33.72		34.66	0.49	48.76	48.57		48.58	48.52			
Fe	33.60		31.52		30.46		34.05		32.46	0.46	6.70	6.74		8.43	8.17			
Co	0.08		1.50		2.66		0.15		-	-	0.01	0.03		0.01	0.03			
Mn	0.02		0.01		0.02		0.01		0.01	0.01	0.02	0.01		0.08	0.03			
Ni	0.06		0.04		0.03		0.17		-	-	0.01	0.01		0.03	0.01			
Zn	0.02		0.01		0.01		0.02		0.12	0.12	44.47	44.61		42.86	43.24			
Pb	0.01		0.02		0.03		0.01		-	-	0.01	0.02		-	-			
Bi	0.00		0.01		0.02		-		-	-	-	-		-	-			
Sb	0.17		0.17		0.15		0.03		0.24	0.16	0.02	0.01		0.02	0.00			

NOTES: The analyses were done at the Geological Survey of Canada, 601 Booth Street, Ottawa, Ontario. Sample: sample number LPA series except CS = van Staal (1985). Mineral: Asp = arsenopyrite and Sp = sphalerite. n = number of sample points,  $\bar{x}$  = mean, and 1s = 1 standard deviation. - = not detected or analysed (CS).

system compared to the outer margins of the stringer zone indicates variable  $f(S_2)$  conditions across the vent complex intersected by drillhole A1. The association and abundance of arsenopyrite and chalcopyrite and their high contents in the stringer zone relative to the exhalative facies of the ore are consistent with their strong prograde temperature-dependant solubilities (cf., Crerar and Barnes, 1976; Heinrich and Eadington, 1986).

## ACKNOWLEDGMENTS

We would like to thank Tim Babin, Jeff Carroll, Paul Giggie, Jeff Hussey, Bill Luff, Dick Mann, and Chris Morton of Brunswick Mining and Smelting Limited for their cooperation and encouragement with this study and continuing studies in the area. John Stirling (GSC) helped with the microprobe analyses. Discussions with John Langton, Steve McCutcheon, Jan Peter, and Cees van Staal were greatly appreciated. The manuscript benefited from reviews by John Langton, Steve McCutcheon, and Cees van Staal.

## REFERENCES

- Aletan, G.**  
1960: The significance of microscopic investigation in the course of beneficiation of the Brunswick ore; Canadian Institute of Mining and Metallurgy, Bulletin, v. 53, p. 945-952.
- Benson, D.**  
1960: Application of the sphalerite geothermometer to some northern New Brunswick sulfide deposits; Economic Geology, v. 55, p. 818-826.
- Boorman, R.S.**  
1975: Mineralogical review of lead-zinc-copper sulphide deposits, Bathurst-Newcastle area, New Brunswick; New Brunswick Research and Productivity Council, Job Report 5128.
- Crerar, D.A. and Barnes, H.L.**  
1976: Ore solution chemistry – V. Solubilities of chalcopyrite and chalcocite assemblages in hydrothermal solution at 200°-350°C; Economic Geology, v. 71, p. 722-794.
- Fuller, B.J.**  
1968: Ore Microscopy of some specimens from Brunswick 6 and 12; New Brunswick Research and Productivity Council, Research Note 15, p. 17.
- Goodfellow, W.D.**  
1975: Rock geochemical exploration and ore genesis at Brunswick No. 12 deposit; Ph.D. thesis, University of New Brunswick, Fredericton, New Brunswick.
- Heinrich, C.A. and Eadington, P.J.**  
1986: Thermodynamic predictions of the hydrothermal chemistry of arsenic, and their significance for the paragenetic sequence of some cassiterite-arsenopyrite-base metal sulfide deposits; Economic Geology, v. 81, p. 511-529.
- Jambor, J.L.**  
1979: Mineralogical evaluation of proximal-distal features in new Brunswick massive-sulphide deposits; Canadian Mineralogist, v. 17, p. 649-664.
- Kalliokoski, J.**  
1961: Temperatures of formation and origin of the Nigadoo and Brunswick Mining and Smelting No. 6 deposits, New Brunswick, Canada; Economic Geology, v. 61, p. 1446-1455.
- Kretschmar, U. and Scott, S.D.**  
1976: Phase relations involving arsenopyrite in the system Fe-As-S and their application; Canadian Mineralogist, v. 14, p. 364-386.
- Lea, E.R. and Rancourt, C.**  
1958: Geology of the Brunswick Mining and Smelting ore bodies, Gloucester County, N.B.; Canadian Institute on Mining and Metallurgy Transactions, v. 61, p. 167-177.
- Lentz, D.R. and Goodfellow, W.D.**  
1992: Re-evaluation of the petrology and depositional environment of felsic volcanic and related rocks in the vicinity of the Brunswick No. 12 massive sulphide deposit, Bathurst Camp, New Brunswick; in Current Research, Part E; Geological Survey of Canada, Paper 92-1E, p. 333-342.
- 1993: Stringer sulphide mineralization and alteration around the FAB base-metal occurrence, Bathurst Mining Camp, New Brunswick; in Current Research; (Comp., ed.) S.A. Abbott; New Brunswick Department of Natural Resources and Energy, Minerals Resources, Information Circular 93-1, p. 91-103.
- Lentz, D.R. and van Staal, C.R.**  
1993: Geological implications of post-ore and pre-deformation emplacement of the "felsic" dike at the Brunswick No. 12 deposit, Bathurst, New Brunswick; Geological Association of Canada-Mineralogical Association of Canada, Program with Abstracts, v. 17, p. A65.
- Luff, W.M.**  
1977: Geology of the Brunswick #12 mine; Canadian Mining Metallurgy Bulletin 70, no. 782, p. 109-119.
- Luff, W., Goodfellow, W.D., and Juras, S.**  
1992: Evidence for a feeder pipe and associated alteration at the Brunswick No. 12 massive sulphide deposit; Exploration and Mining Geology, v. 1, p. 167-185.
- McNulty, D.**  
1981: The east zone of the Brunswick No. 12 deposit, Bathurst-Newcastle area, New Brunswick; B.Sc. thesis, University of New Brunswick, Fredericton, New Brunswick.
- Roy, S.**  
1961: Mineralogy and paragenesis of the lead-zinc-copper ores of the Bathurst-Newcastle district. Geological Survey of Canada, Bulletin 72, 31 p.
- Scott, S.D.**  
1983: Chemical behaviour of sphalerite and arsenopyrite in hydrothermal and metamorphic environments; Mineralogical Magazine, v. 47, p. 427-435.
- Scott, S.D. and Kissin, S.A.**  
1973: Sphalerite composition in the Zn-Fe-S system below 300°C; Economic Geology, v. 68, p. 475-479.
- Sharp, Z.D., Essene, E.J., and Kelly, W.C.**  
1985: A re-examination of the arsenopyrite geothermometer: pressure considerations and applications to natural assemblages; Canadian Mineralogist, v. 23, p. 517-534.
- Stanton, R.L.**  
1959: Mineralogical features and possible mode of emplacement of the Brunswick Mining and Smelting orebodies, Gloucester County, New Brunswick; Canadian Institute of Mining and Metallurgy Transactions, v. LXII, p. 337-349.
- Sutherland, J.K.**  
1967: The chemistry of some New Brunswick pyrites; Canadian Mineralogist, v. 9, p. 71-84.
- Sutherland, J.K. and Halls, C.**  
1969: Composition of some New Brunswick sphalerites; New Brunswick Research and Productivity Council, Research Note 21, 33 p.
- Toulmin, P., III, Barton, P.B., Jr., Wiggins, L.B.**  
1991: Commentary on the sphalerite geobarometer; American Mineralogist, v. 76, p. 1038-1051.
- van Staal, C.R.**  
1985: Structure and metamorphism of the Brunswick Mines area, Bathurst, New Brunswick, Canada; Ph.D. thesis, University of New Brunswick, Fredericton, New Brunswick, 484 p.
- van Staal, C.R. and Williams, P.F.**  
1984: Structure, origin and concentration of the Brunswick 12 and 6 orebodies; Economic Geology, v. 79, p. 1669-1692.
- 1986: Structural interpretation of the Brunswick ore bodies; in Geology in the Real World – The Kingsley Dunham Volume, (ed.) R.W. Nesbitt and J. Nichol; The Institute of Mining and Metallurgy, London, United Kingdom, p. 451-462.

# Geochemistry of the stringer sulphide zone in the Discovery Hole at the Brunswick No. 12 massive sulphide deposit, Bathurst, New Brunswick<sup>1</sup>

David R. Lentz<sup>2</sup> and Wayne D. Goodfellow  
Mineral Resources Division

*Lentz, D.R. and Goodfellow, W.D., 1993: Geochemistry of the stringer sulphide zone in the Discovery Hole at the Brunswick No. 12 massive sulphide deposit, Bathurst, New Brunswick; in Current Research, Part E; Geological Survey of Canada, Paper 93-1E, p. 259-269.*

---

**Abstract:** The distribution of hydrothermal elements within the Discovery Hole at the Brunswick No. 12 deposit shows that the hanging wall rocks are enriched in Hg, Sb, and to a lesser extent, Tl whereas the footwall sequence contains high contents of Cu, Zn, As, Co, Bi, and Au. The abundance of Sb, Pb, Ag, Se, Sn, In, Tl, and Hg, however, are not proportional to sulphide contents indicating different depositional controls. The hydrothermal components are asymmetrically distributed within the stratigraphic footwall of the sheath-folded massive sulphide lens with high contents of Fe, S, Cu, Co, As in the structural hanging wall of the lens, possibly representing vent-proximal mineralization. Elevated contents of Zn, Pb, Sn, In, Ag, and Hg in the structural and stratigraphic footwall of the lens may represent lower temperature, more distal mineralization on the flanks of the main hydrothermal vent.

**Résumé :** La distribution des éléments hydrothermaux à l'intérieur du trou Discovery du gisement Brunswick n° 12 montre que les roches de l'éponte supérieure sont enrichies en Hg, en Sb et, dans une moindre mesure, en Tl, alors que celles de l'éponte inférieure présentent des teneurs élevées en Cu, Zn, As, Co, Bi et Au. Les teneurs en Sb, Pb, Ag, Se, Sn, In, Tl et Hg ne sont pas proportionnelles à l'abondance des sulfures, ce qui indique des contrôles différents. Les composantes hydrothermales sont distribuées asymétriquement dans l'éponte stratigraphique inférieure de la lentille de sulfures massifs, qui a été déformée en un pli en fourreau, avec des teneurs élevées en Fe, S, Cu, Co et As dans l'éponte structurale supérieure, ce qui dénote peut-être une minéralisation proximale par rapport à la zone de sortie des fluides hydrothermaux. Les teneurs élevées en Zn, Pb, Sn, In, Ag et Hg dans l'éponte stratigraphique et structurale inférieure pourraient être l'indication d'une minéralisation de plus basse température et plus distale, qui serait située sur les flancs de la zone principale d'émission des fluides hydrothermaux.

---

<sup>1</sup> Contribution to Canada-New Brunswick Cooperation Agreement on Mineral Development (1990-1995), a subsidiary agreement under the Canada-New Brunswick Economic and Regional Development Agreement.

<sup>2</sup> Geological Survey of Canada, P.O. Box 50, Bathurst, New Brunswick E2A 3Z1

## INTRODUCTION

The distribution of hydrothermal elements in rocks hosting massive sulphide deposits is potentially helpful in litho-geochemical exploration and in interpreting primary and secondary alteration and mineralization. Within zones of stringer sulphide mineralization, the abundance of stringer sulphide veins is a reliable indicator of the proximity to massive sulphides. The composition of stringer sulphides is, however, poorly understood despite its importance in understanding the origin of stockwork mineralization. For example, the exploration for massive sulphides around the FAB stringer zone located south of the Brunswick No. 12 deposit along the Brunswick Belt (Lentz and Goodfellow, 1993a) would benefit from a better understanding of the composition of the stockwork mineralization associated with massive sulphide deposits of the Bathurst Mining Camp.

The geology of the Brunswick No. 12 deposit has been most recently reviewed by Luff et al. (1992a, b) and Lentz and Goodfellow (1993c). The primary depositional, petrological, and geochemical characteristics of the host rocks to the Brunswick No. 12 deposit have been summarized by Lentz and Goodfellow (1992a, b). The alteration at the deposit, including descriptions and interpretation of the stringer sulphides, has also been documented (Goodfellow, 1975a, b; Luff et al., 1992a; Lentz and Goodfellow, 1993b, c). Goodfellow (1975a, b) also documented the distribution of hydrothermal elements in sedimentary and volcanic rocks hosting the sulphide deposit.

Diamond-drill hole (DDH) A1, the 1953 Discovery Hole at the Brunswick No. 12 deposit, was selected for this orientation study because it was drilled from the stratigraphic hanging wall through the footwall sequence and associated sulphide stringer zone, and out into weakly altered footwall pyroclastic rocks (Lentz and Goodfellow, 1993c; Fig. 1). The drillhole intersects an isoclinally folded pyritiferous lens (62.7 m wide) grading 1.22% Pb, 4.26% Zn, 0.46% Cu, and 52 g/t Ag (1.61 oz/tonne) with stratigraphic footwall on either side of the lens. The high Cu/(Zn+Pb) in the upper portion (300.5-315.8 m; 0.33% Pb, 1.86% Zn, 0.67% Cu, and 26 g/t Ag) compared to the lower portion (315.5-363.3 m; 1.45% Pb, 4.90% Zn, 0.40% Cu, and 58 g/t Ag) of the ore lens supports the interpretation that the structural hanging wall (stratigraphic footwall; 300.5-315.8 m interval) represents a vent-proximal mineralization compared to the structural and stratigraphic footwall (363.3 to 382.8 m section). Diamond-drill hole A1 contains most types of alteration and mineralization that are associated with the Brunswick No. 12 ore bodies (Luff et al., 1992a). This geochemical study compliments geological, petrological, and mineralogical results presented for drillhole A1 in a companion paper (Lentz and Goodfellow, 1993c).

## LITHOGEOCHEMISTRY

Major and trace elements were determined on 44 representative samples from drillhole A1 although only results for selected samples are examined because of the scope of this

study. Drillhole A1 samples were supplemented by three samples from the least-altered footwall pyroclastic rocks from the 850 m level of the mine. These samples were appended to the lower section of drillhole A1 (Fig. 1) in order to illustrate the compositional variations from weakly altered, footwall quartz augen schist at the bottom of drillhole A1 into the least-altered footwall pyroclastic rocks of the area.

Major- and trace-element data for the Discovery Hole are presented as geochemical profiles in order to illustrate the spatial distribution of mineralized rocks hosting the Brunswick No. 12 deposit (Fig. 1). The intensity of stringer sulphide mineralization is most closely represented by Fe, and S contents, and increases toward the ore lens (Brunswick Horizon). In general, elevated Cu, Pb, Zn, Ag, and As, which correspond to high Fe and S contents, reflect the association of chalcopyrite, galena, sphalerite, tetrahedrite, and arsenopyrite with pyrite and pyrrhotite in the stringer sulphide zone. Lead and Ag are distributed similar to the other base metals, but are low (<0.1 wt. % and 5 ppm, respectively) relative to Cu and their abundance in the massive sulphide deposit (Luff et al., 1992b). The spatial distribution of S, Fe, Cu, Zn, Cd, and As is interpreted to outline the vent-proximal facies of the stringer sulphide zone. This is consistent with abundance of stringer sulphides. Antimony, Hg, and Tl are enriched in the stratigraphic hanging wall sequence, but are variable within the footwall stringer zone, particularly beneath the main ore lens. Bismuth is variable within the stringer sulphide zone. Arsenic, Au, Sb, and Se contents are high in the stringer zone immediately above the main sulphide lens (Fig. 1), which is considered the most vent-proximal stringer zone. The high content of Co in deeper portions of the stringer sulphide zone just above the infolded metapelites (Patrick Brook Formation) may indicate a host rock control on the distribution of Co. Cobalt is also enriched in the vent-proximal stringer mineralization just above the massive sulphide lens.

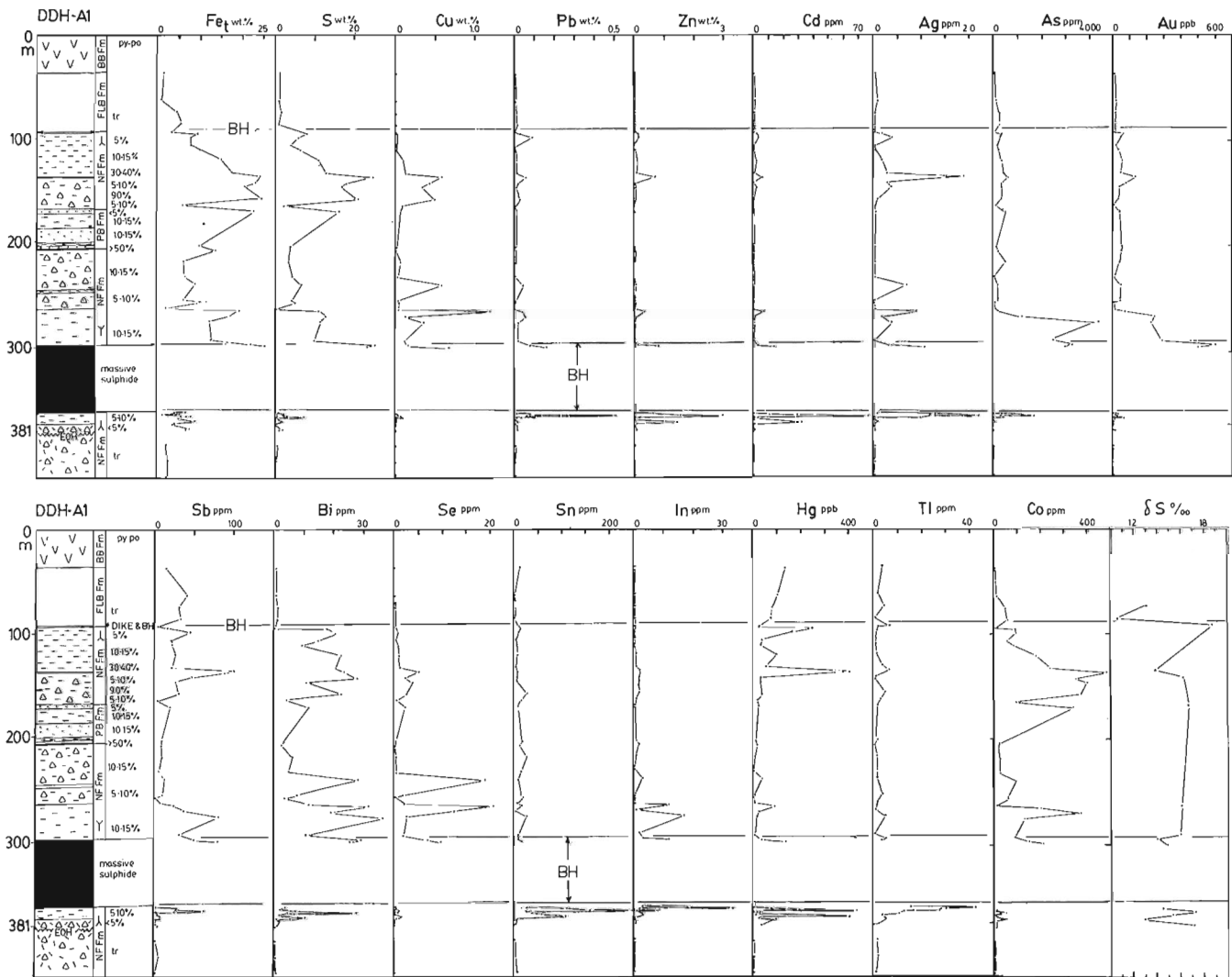
The samples from drillhole A1 were subdivided into seven groups based on sulphur content (Table 1), because there is a general correlation between the abundance of sulphide veins and proximity to massive sulphides. Table 1 presents average data for these groupings (<1% S (least altered), 1-3% S, 3-5% S, 5-10% S, 10-15% S, and >15% S) in order to reveal large scale trends in bulk chemical composition. A rudimentary mass balance analysis of the six subsets without density corrections (10 to 15%), based on aluminum normalization to the least-altered samples (subset 1), was calculated ( $\Delta V\%$ ; Table 1) and indicates large volume increases associated with sulphide veining. Other elements, traditionally considered immobile (e.g., Ti, Zr, Th, Sc, Yb), indicate similar volume changes but have considerably higher variances. Silica decreases with increasing sulphide abundance, however, correction for the volume increases calculated assuming Al immobility ( $\Delta V$ ; Table 1) are consistent with silicification and silica veining observed in the stringer zone.  $\text{Na}_2\text{O}$  is very low throughout whereas  $\text{K}_2\text{O}$  decreases beyond what can be explain by dilution of silicates by stringer sulphides. The highest CaO values correspond to ferroan carbonates that were identified petrographically in the stringer zone. The low  $\text{CO}_2$  contents of these samples are in error, due to the partial extraction of carbonate by acid dissolution.



The least-altered and mineralized footwall pyroclastic rocks (QFAS) from the 850 m level are compositionally similar (Table 1; subset 1) to previously determined background values (Goodfellow, 1975a; Table 2). The low-S subset (#2) (Table 1; 0 to 1 wt.% S) is depleted in alkali elements and enriched significantly in most hydrothermal components, and is similar to weakly altered quartz augen schist (QAS) from the Nepisiguit Falls Formation (Lentz and Goodfellow, 1992b).

The hydrothermal elements (i.e., Cu, Co, Zn, Cd, Sb, Pb, Bi, As, Au, Ag, Se, Sn, In, Tl, Hg) have been ranked according to their relative coherency with respect to the sample groupings that were established on the basis of S contents. The main hydrothermal constituents comprising each subgroup were normalized to the average grades for the

deposit (Luff et al., 1992b) and a bulk ore sample (Petruk and Schnarr, 1981). A spider diagram (Fig. 2) illustrates the principle variations between the subgroups. The average Cu content of the two S-rich subsets (subset 6 and 7) is greater than the values for average ore, whereas Pb and Zn have considerably lower abundances in the stringer zone. The relative steepness of the slopes between elements reflects interelement ratios, for instance the Cu/Pb and Pb/Zn ratios (see also Fig. 3). The As/S ratio (0.02 to 0.2) is two to fifteen times higher in the stringer zone (Table 1) than in bulk ore (As/S  $\approx$  0.006) whereas the Ag/Au ratio (10 to 50) is consistently lower in the stringer zone (Table 1) compared to ore (Ag/Au  $\approx$  140). The Cd/Zn ratio is higher in the low-S subsets compared to the main stringer zone or the ore (Table 1). The high abundance of Fe, Co, Cu, Au, As, Bi, and Ga relative to S within the footwall stringer zone is consistent



**Figure 1.** Geological and geochemical profiles for diamond-drill hole A1 supplemented with three samples from least-altered QFAS 850 m level of the mine at bottom of the hole. BB Fm – Boucher Brook Formation, FLB Fm – Flat Landing Brook Formation, NF Fm – Nepisiguit Falls Formation, PB Fm – Patrick Brook Formation. BH = Brunswick Horizon. Note that the massive sulphide intersected in the drill hole represents the synclinal keel of a F<sub>1</sub> and F<sub>2</sub> sheath fold (i.e., note facing directions).

**Table 1.** Major- and trace-element data on averaged sample subsets from DDH A1 at the Brunswick No. 12 deposit, Bathurst, New Brunswick

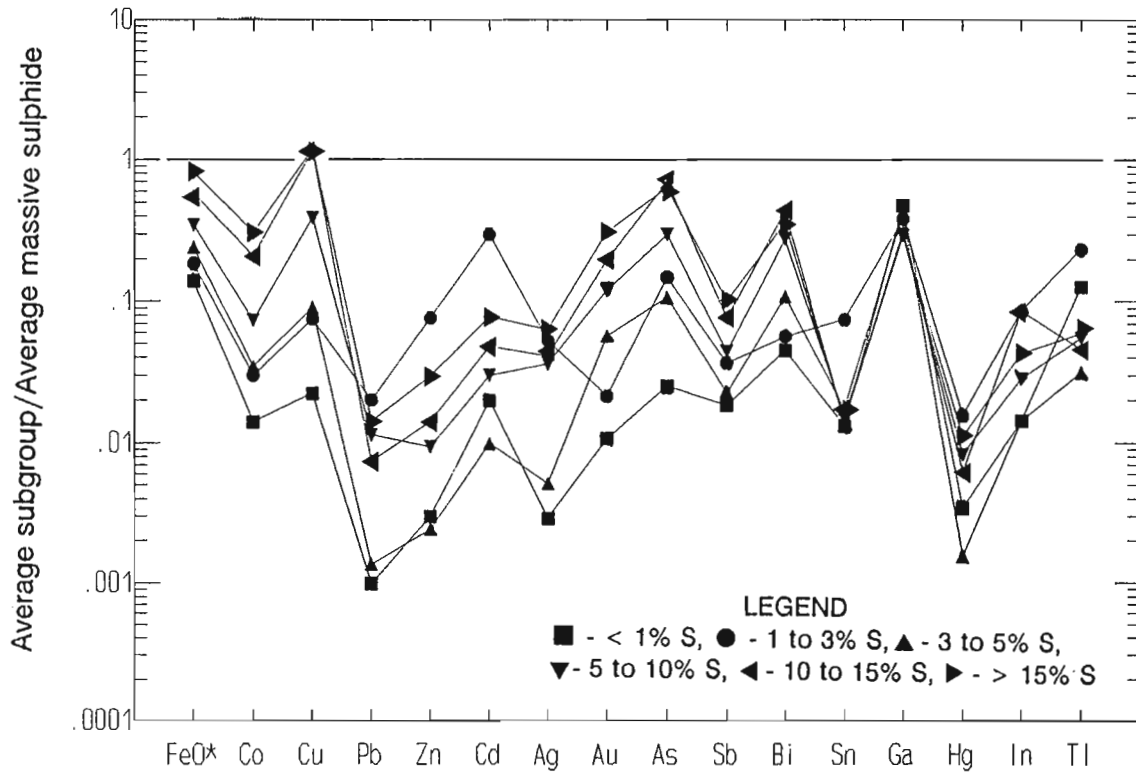
SUBSET	1		2		3		4		5		6		7	
	n		n		n		n		n		n		n	
	$\bar{x}$	1s	$\bar{x}$	1s	$\bar{x}$	1s	$\bar{x}$	1s	$\bar{x}$	1s	$\bar{x}$	1s	$\bar{x}$	1s
SiO <sub>2</sub> wt.%	70.0	1.05	70.9	7.7	68.6	6.3	66.2	9.9	70.1	5.5	59.4	7.7	37.5	12.4
TiO <sub>2</sub>	0.59	0.01	0.46	0.19	0.40	0.18	0.44	0.12	0.25	0.21	0.17	0.05	0.23	0.14
Al <sub>2</sub> O <sub>3</sub>	14.03	0.12	12.37	3.89	12.57	2.80	9.93	2.73	5.76	2.75	5.3	1.89	4.86	1.82
Fe <sub>2</sub> O <sub>3T</sub>	3.63	0.25	6.39	2.91	7.60	3.46	12.35	4.26	14.17	2.62	23.6	3.9	33.6	2.3
MgO	1.85	0.23	2.75	2.77	2.03	1.28	2.17	1.53	1.60	1.27	2.31	1.57	3.00	2.78
MnO	0.05	0.02	0.12	0.14	0.19	0.26	0.09	0.07	0.08	0.02	0.07	0.04	0.10	0.05
CaO	0.33	0.03	0.32	0.26	0.52	0.93	1.19	2.07	0.76	1.14	0.28	0.29	1.70	2.32
Na <sub>2</sub> O	1.60	0.30	0.09	0.08	0.12	0.12	0.07	0.05	0.09	0.04	0.08	0.05	0.07	0.04
K <sub>2</sub> O	4.62	0.52	2.83	1.40	3.10	1.40	1.79	1.21	0.92	0.95	0.23	0.21	0.24	0.26
P <sub>2</sub> O <sub>5</sub>	0.18	0.01	0.16	0.08	0.14	0.06	0.07	0.04	0.14	0.12	0.08	0.06	0.10	0.13
H <sub>2</sub> O	1.8	0.2	3.2	1.2	-	-	-	-	-	-	-	-	-	-
CO <sub>2</sub>	0.2	0.1	0.4	0.6	0.08	0.06	1.19	2.07	0.04	0.08	0.08	0.08	0.01	0.04
S	0.39	0.28	0.48	0.39	1.78	0.49	4.06	0.30	7.06	1.59	11.92	0.96	20.83	3.79
Zr ppm	260	10	220	124	191	73	162	72	88	81	56	16	76	37
Y	36	1	34	14	35	20	21	7	15	9	14	6	14	6
Nb	9	8	24	13	20	7	18	5	-	-	-	-	-	-
Ga	23	5	20	8	17	7	19	4	13	5	14	6	13	4
La	48	3	48.9	20.1	42.8	19.5	37.5	7.7	27.6	13.7	26.4	3.1	26.4	9.8
Yb	3.8	0.2	3.5	1.6	3.4	2.2	1.9	0.7	1.3	0.8	1.2	0.6	0.9	0.5
Ba	593	119	548	783	718	873	603	703	163	143	96	106	661	1432
Rb	150	10	137	62	127	64	89	59	-	-	-	-	-	-
Sr	52	3	18	10	16	10	24	36	9	5	3	5	9	9
Cu ppm	16	4	93	157	248	299	298	189	1290	2070	3830	4688	3929	2197
Zn	102	32	315	239	6761	10028	212	216	830	723	1246	1073	2590	3390
Cd	0.7	0.3	0.7	0.3	15	25	0.5	-	1.5	1.2	2.4	2.6	3.9	4.9
Pb	19	16	94	97	710	1566	48	26	402	387	262	205	503	554
Sb	2.4	2.6	11.4	14.8	18.4	19.1	11.3	5.6	22.1	13.7	38.2	24.6	50.7	29.4
Ag	-	-	0.61	0.22	5.1	7.7	0.5	-	3.5	3.7	4.0	2.9	6.1	6.7
As	3	2	63.0	80.8	283	514	203	151	570	96	1330	1756	1210	1332
Co	10	1	17	17	32	30	37	18	78	25	224	91	329	113
Bi	0.4	0.3	3.4	3.8	3.4	3.3	6.5	4.4	16.7	9.5	26.1	7.5	21.6	7.4
Se	-	-	0.43	0.64	0.40	0.46	0.6	0.5	3.4	6.8	7.6	8.8	4.6	2.9
Au ppb	2	1	8	7	14	10	37	17	78	96	129	98	203	243
Hg ppb	3	1	40	41	142	157	14	12	75	94	56	37	100	139
In ppm	5	1	1	1	6	11	1	1	2	3	6	8	3	4
Tl	1.4	0.4	8.8	9.0	12.7	15.1	1.7	1.0	3	4	2.5	1.8	3.2	2.3
B	37	-	37	17	30	9	23	7	30	20	16	6	5	-
Sn	7	4	15	11	73	83	17	7	15	9	14	10	14	8
Ni ppm	7	3	16	26	11	18	6	5	11	10	10	3	8	7
Sc	9.0	0.1	9.4	2.9	8.5	4.1	7.8	2.3	5.4	3.0	4.1	1.1	4.3	2.2
Cr	21	1	20	10	16	10	23	14	15	6	14	4	13	10
V	38	1	34	18	30	30	39	27	21	17	13	11	19	35
ΔV %	-	-	+13	-	+11	-	+41	-	+143	-	+164	-	+188	-
As/S*100	1.5	1.7	14.5	10.0	13.0	21.1	5.2	4.4	6.7	8.3	11.3	15.3	5.3	5.2
Au/Ag*100	13	11	4	3	13	12	74	35	102	214	46	47	50	51
Cd/Zn*10	0.07	0.02	0.07	0.09	0.03	0.02	0.06	0.06	0.02	0.01	0.02	0.01	0.02	0.01
Se/S*10 <sup>3</sup>	0.02	-	0.17	0.23	0.02	0.02	0.02	0.01	0.05	0.10	0.07	0.08	0.02	0.01

NOTES: SUBSET Represents 1 - least-altered samples 850 M level of the mine , 2 - 0 to 1 wt.% S, 3 - 1 to 3 wt.% S, 4 - 3 to 5 wt.% S, 5 - 5 to 10 wt.% S, 6 - 10 to 15 wt.% S, 7 - >15 wt.% S. Fe<sub>2</sub>O<sub>3T</sub> denotes total Fe reported as Fe<sub>2</sub>O<sub>3</sub>; n = number of samples; - below detection limit. Major- and selected trace-elements were analysed by X-ray fluorescence spectroscopy (XRF) and Inductively-Coupled Plasma Emission Spectroscopy (ICP-ES) in the Geochemical Laboratory at the Geological Survey of Canada, 601 Booth Street, Ottawa, Ontario. As, Au, B, Bi, Cd, Ga, Hg, In, Sb, Se, Sn, and Tl were analysed by X-Ray Assay Ltd., Don Mills, Ontario.

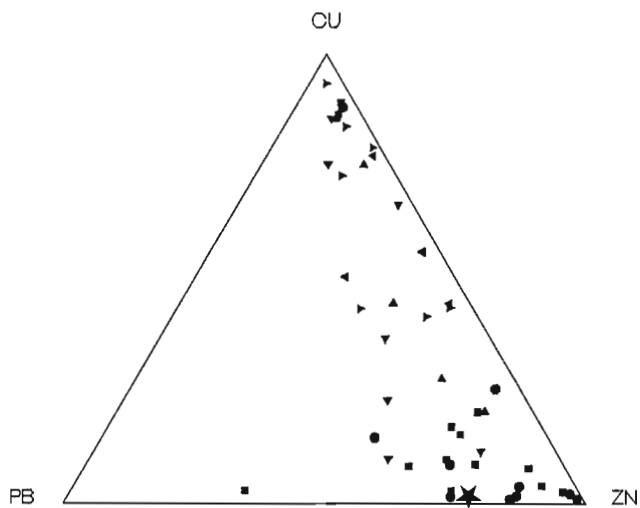
**Table 2.** Average major- and trace-element compositional data on sedimentary and volcanic rocks from the Bathurst Camp, Bathurst, New Brunswick including crustal average abundances for comparison

Ref	1	2	3	4	5	6	7	8	9	10	11	12	13	14	15	16	17
SiO <sub>2</sub> wt.%	57.3	66.0	62.8	40.5	65.9	75.0	68.2	69.5	75.0	74.9	74.1	30.2	58.8	71.5	73.6	71.0	72.4
TiO <sub>2</sub>	0.9	0.5	1.0	3.14	0.54	0.30	0.39	0.64	0.25	0.28	0.34	0.42	0.90	0.52	0.37	0.39	0.74
Al <sub>2</sub> O <sub>3</sub>	15.9	15.2	18.9	-	8.99	5.91	7.63	11.12	10.76	12.61	12.38	-	18.67	13.47	12.56	14.6	12.56
Fe <sub>2</sub> O <sub>3T</sub>	10.1	5.0	7.2	19.85	12.83	10.97	12.10	7.15	3.63	1.85	3.89	47.4	8.27	3.45	4.50	3.05	5.12
MgO	5.3	2.2	2.2	4.52	1.42	1.08	1.51	2.04	1.45	0.64	1.07	1.90	2.21	1.81	1.24	1.23	1.42
MnO	0.18	0.07	0.11	1.62	2.13	1.50	2.18	0.45	0.11	0.01	0.06	2.71	0.11	0.06	0.05	0.04	0.16
CaO	7.4	4.2	1.3	7.17	1.20	0.43	0.61	0.91	0.65	0.27	0.45	3.72	0.52	0.45	0.45	0.66	0.30
Na <sub>2</sub> O	3.1	3.9	1.2	1.06	1.08	1.53	0.36	0.84	1.43	1.97	2.40	0.59	1.22	2.61	1.97	3.29	0.34
K <sub>2</sub> O	1.1	3.4	3.7	1.65	2.06	0.98	1.55	2.46	3.31	5.73	4.18	0.79	5.11	4.11	3.81	4.35	2.41
P <sub>2</sub> O <sub>5</sub>	-	-	0.16	0.98	0.23	0.14	0.34	0.15	0.11	0.11	0.09	1.87	0.12	0.17	0.13	0.23	0.11
H <sub>2</sub> O	-	-	-	3.7	1.7	0.7	2.3	2.0	1.0	1.20	1.00	2.4	2.6	1.4	1.43	1.73	2.9
CO <sub>2</sub>	-	-	-	3.62	0.73	0.21	1.42	0.42	0.74	-	0.17	4.73	0.01	-	0.22	0.05	0.01
S	-	-	-	0.01	0.03	0.01	0.60	0.93	1.2	0.03	-	1.12	0.01	-	-	0.2	0.01
Total	-	-	-	87.8*	98.8	98.8	99.2	98.6	99.6	99.6	101.1	97.9*	98.6	99.6	100.5	100.8	98.5
F ppm	-	550	-	895	528	353	567	524	550	-	-	1398	613	-	-	-	1400
Ba	250	550	650	919	1053	556	1769	1170	966	681	799	866	697	808	752	525	395
Rb	32	112	160	71	119	53	85	143	160	162	127	58	296	145	127	160	200
Sr	260	350	200	161	65	49	37	70	37	47	71	69	61	70	50	73	35
Li	13	20	75	17	15	11	29	39	14	-	12	8	18	-	21	-	44
Zr	100	190	210	378	100	93	100	116	191	191	299	40	194	203	181	230	220
Y	20	22	27	55	25	19	24	28	39	51	59	9	31	16	42	55	25
Nb	11	25	19	43	26	21	23	21	17	14	17	35	24	14	12	15	20
Th	3.5	10.7	14.6	2.8	7.4	5.6	7.3	7.9	12.2	15.4	16.3	3.7	12.7	14.2	12.0	6	11.0
Ni	105	20	55	48	70	44	61	69	6	7	3	49	46	11	8	27	15
Cr	185	35	110	76	31	22	30	74	5	19	10	29	67	16	17	26	49
V	23	60	150	238	88	72	92	213	25	24	23	152	128	44	35	31	97
Co	10	29	23	43	74	50	67	26	4	-	2	20	23	-	4	-	7
Cu	75	25	50	43	48	45	90	61	23	11	7	165	16	14	8	11	22
Pb	8	20	20	344	46	31	281	21	120	19	12	1475	17	27	14	19	8
Zn	80	71	85	229	89	48	475	106	135	41	96	907	126	68	44	40	166
Cd	0.1	0.1	-	0.5	0.5	0.5	1.5	0.8	0.9	-	-	1.6	0.5	-	-	0.4	1.3
Ag	0.08	0.05	-	0.3	0.3	0.3	0.4	0.3	0.2	-	0.4	1.2	0.3	-	0.2	-	0.3
Au ppb	3	1.8	-	1	4	3	6	5	8	-	2.5	7	3	-	1.5	-	1
Sb	0.2	0.2	-	1.3	4.8	3.1	7.6	5.7	4.9	-	0.8	2.9	1.2	0.3	0.7	1.2	0.5
Hg ppb	-	-	-	-	-	-	-	-	-	-	21	-	-	-	19	-	-
Tl	0.36	0.75	-	-	-	-	-	-	-	-	0.79	-	-	-	0.77	-	-
As	1.0	1.5	-	29	16	17	68	32	165	-	4	258	4	-	7	14	33
Sn	2.5	5.5	4.0	80	2	2	3	4	5	-	7	60	4	-	11	-	10
Mo	1.0	1.5	1.0	1	1	1	2	12	2	-	2	33	1	-	1.5	-	0.5
Bi	0.06	0.13	0.25	0.7	0.5	0.6	0.7	0.6	0.6	-	0.3	4.9	0.5	-	0.3	-	0.5

NOTES: Fe<sub>2</sub>O<sub>3T</sub> denotes total FeO reported as Fe<sub>2</sub>O<sub>3</sub>; references; 1 - average bulk continental crust; 2 - average upper continental crust; 3 - average post-Archean shales (Taylor and McLennan, 1985); 4 = altered mafic volcanic rocks (n=9)(BB Fm.), 5 - red argillite (n=52) (BB Fm.), 6 - maroon chert (n=14)(BB Fm.), 7 - green slate (n=30) (BB Fm.); 8 - black slate (n=104) (BB Fm.), 9 - felsic tuff (FLB Fm.) (n=10); 10 - rhyolite (n=13)(FLB Fm.) van Staat et al. (1991); 11 - rhyolite (n=49)(FLB Fm.) Langton and McCutcheon (1993); 12 - iron formation (n=113)(NF Fm.) 13 - Cambro-Ordovician maroon slate (n=7) (NF Fm. ?); 14 - QFAS (n=6) (NF Fm.) McCutcheon (1990); 15 - QFAS (n=26) (NF Fm.) Langton and McCutcheon (1993); 16 - QFAS (n=4)(NF Fm.) Lentz and Goodfellow (1992b); 17 - Cambro-Ordovician black slate & quartzite (n=2) (PB Fm.) (Connell & Hattie, 1990). - No analysis; \* total does not include Al<sub>2</sub>O<sub>3</sub> content.



**Figure 2.** Lognormalized spider diagram illustrating the abundances of the various subgroups (subset) (Table 1) relative to average massive sulphide at the Brunswick No. 12 deposit. Subgrouping based on sulphur contents of the samples: <math>< 1\% S</math>, <math>1-3\% S</math>, <math>3-5\% S</math>, <math>5-10\% S</math>, <math>10-15\% S</math>, and <math>> 15\% S</math> (see Table 1). The average composition of bulk ore used for comparison is 28.2% Fe, 0.31% Cu, 3.55% Pb, 8.82% Zn (Luff et al., 1992b), 1070 ppm Co (Chen and Petruk, 1980). <math>< 100</math> ppm Cd, 105 ppm Ag, 0.7 ppm Au (Lentz et al., 1993), 0.26% As, 450 ppm Sb, 54 ppm Bi, 870 ppm Sn, 44 ppm Ga, 8 ppm Hg, 64 ppm In, 54 ppm Tl (Petruk and Schnarr, 1981; Brunswick Mining and Smelting Corp. Ltd., unpub. data).



**Figure 3.** Ternary diagram illustrating the relative Cu, Zn, and Pb abundances in the variably mineralized samples. See legend in Figure 2 for symbols. The star symbol is the average massive sulphide content (Luff et al., 1992b). This illustrates the relative enrichment Cu versus Pb and Zn within the sample suite, in particular stockwork stringer sulphide vein system, relative to the massive sulphide.

with the lower solubilities of these elements compared to Pb, Zn, Ag, and Sb. Thallium is enriched over background values (Table 2) in the low-S samples (subset 1, 2, 3; Table 1).

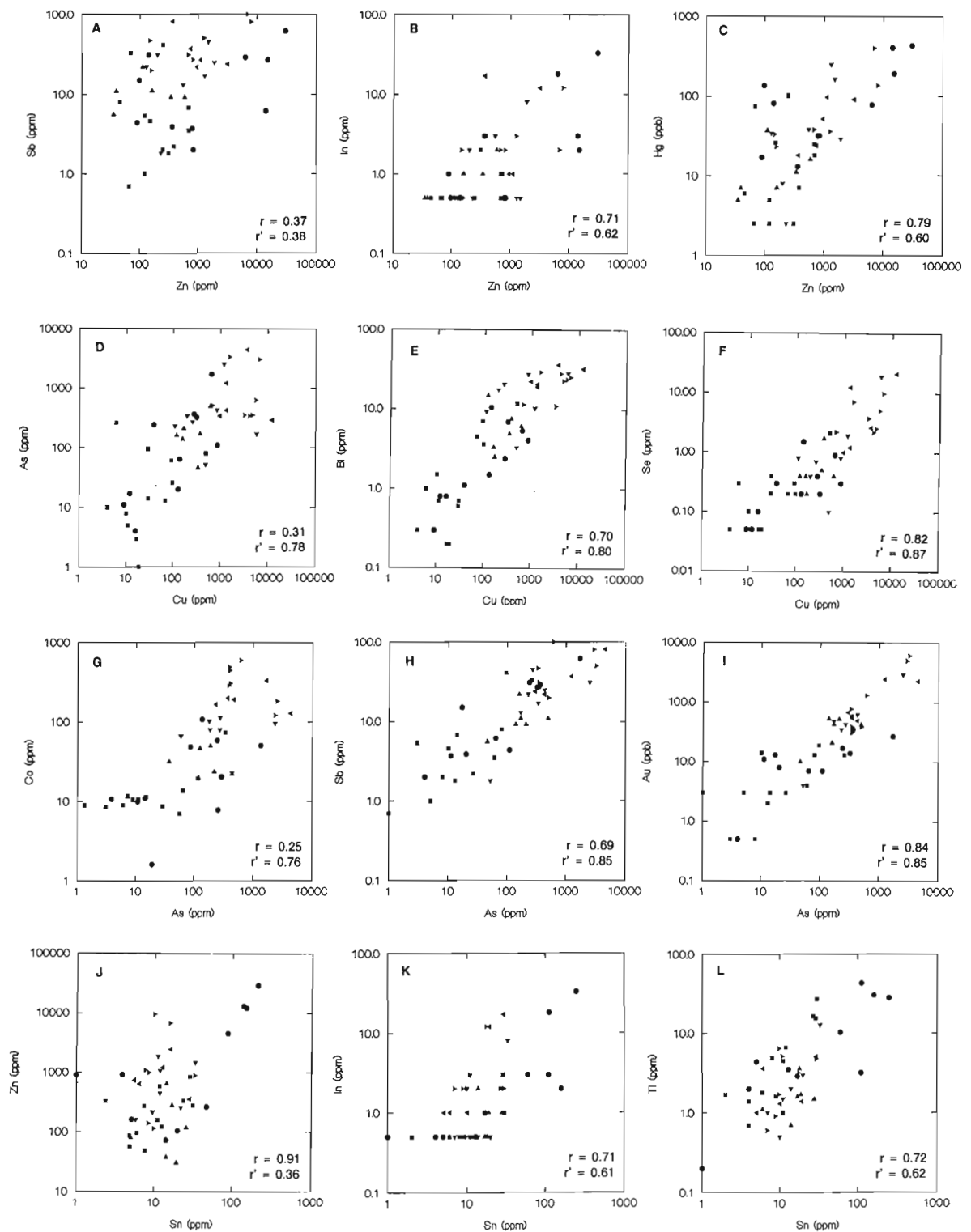
Parametric and nonparametric statistical analyses of selected data reveal numerous elemental associations that reflect the mineralogy and hydrothermal processes within the stringer zone (Table 3). A few elements were included in the statistical analysis that are not typically enriched by hydrothermal processes. In some cases, these elements behave conservatively as they are weakly mobile to immobile and, therefore, have poor correlations with hydrothermal components due to the dilution effect of sulphides. In contrast, the hydrothermal elements usually have higher positive correlations with each other. Strong correlations between Zn and Sb, In, Hg (Fig. 4A, B, C, Table 3), and Cd, and Ag (Table 3) indicate Cd, Hg, and In substitute into sphalerite (Sutherland and Halls, 1969; Jonasson and Sangster, 1974) and that sphalerite is associated with Ag-bearing tetrahedrite. Copper correlates strongly with As, Bi, and Se (Fig. 4D, E, F) due to occurrence of chalcopyrite, arsenopyrite, and bismuthinite in the stringer zone. Selenium substitutes for S in the common sulphides (Cabri et al., 1985). Selenium correlates well with elements preferentially fixed within the vent-proximal stringer zone, however, the Se/S ratio is

**Table 3.** Parametric and nonparametric correlation coefficients computed for selected elements from the suite of samples taken from Diamond Drill Hole (DDH) A1

BOTTOM WEDGE: PEARSON PRODUCT CORRELATION COEFFICIENTS (r)														TOP WEDGE: SPEARMAN RANK CORRELATION COEFFICIENTS (r)													
	AG	AS	AU	BA	BI	CD	CO	CR	CU	FET	HG	IN	LA	MNO	NI	PB	S	SB	SE	SN	TL	V	ZN				
AG	1.00	<b>0.65</b>	<b>0.58</b>	-0.29	<b>0.64</b>	<b>0.84</b>	<b>0.51</b>	<b>-0.44</b>	<b>0.65</b>	0.38	<b>0.61</b>	<b>0.69</b>	<b>-0.62</b>	-0.07	-0.06	<b>0.76</b>	<b>0.58</b>	<b>0.68</b>	<b>0.59</b>	0.30	0.27	<b>-0.53</b>	<b>0.77</b>				
AS	0.31	1.00	<b>0.86</b>	-0.39	<b>0.74</b>	<b>0.43</b>	<b>0.76</b>	-0.28	<b>0.78</b>	<b>0.61</b>	0.38	<b>0.55</b>	<b>-0.67</b>	0.02	0.07	<b>0.65</b>	<b>0.81</b>	<b>0.85</b>	<b>0.77</b>	0.19	0.02	<b>-0.42</b>	<b>0.45</b>				
AU	0.23	<b>0.84</b>	1.00	-0.34	<b>0.75</b>	0.30	<b>0.71</b>	-0.31	<b>0.74</b>	<b>0.67</b>	0.32	<b>0.45</b>	<b>-0.66</b>	0.07	0.00	<b>0.54</b>	<b>0.83</b>	<b>0.78</b>	<b>0.75</b>	0.05	-0.19	<b>-0.50</b>	0.36				
BA	-0.18	-0.21	-0.20	1.00	<b>-0.50</b>	-0.24	<b>-0.45</b>	0.26	-0.37	<b>-0.57</b>	-0.09	-0.32	<b>0.49</b>	-0.27	<b>-0.50</b>	-0.38	<b>-0.45</b>	-0.29	<b>-0.43</b>	0.09	0.25	0.33	-0.31				
BI	<b>0.36</b>	<b>0.54</b>	<b>0.55</b>	-0.19	1.00	<b>0.43</b>	<b>0.78</b>	-0.30	<b>0.86</b>	<b>0.74</b>	0.30	<b>0.53</b>	<b>-0.68</b>	0.00	0.01	<b>0.58</b>	<b>0.81</b>	<b>0.59</b>	<b>0.88</b>	0.22	-0.01	<b>-0.49</b>	<b>0.41</b>				
CD	<b>0.68</b>	0.20	0.01	-0.12	-0.01	1.00	0.29	-0.34	<b>0.41</b>	0.22	<b>0.59</b>	<b>0.61</b>	<b>-0.48</b>	0.00	0.05	<b>0.71</b>	0.33	<b>0.46</b>	<b>0.41</b>	0.38	<b>0.40</b>	-0.37	<b>0.87</b>				
CO	0.28	0.25	0.34	-0.01	<b>0.61</b>	-0.05	1.00	-0.20	<b>0.82</b>	<b>0.79</b>	0.32	0.31	-0.60	-0.01	0.21	<b>0.40</b>	<b>0.88</b>	<b>0.68</b>	<b>0.82</b>	-0.07	-0.23	-0.35	0.27				
CR	<b>-0.43</b>	-0.24	-0.25	0.09	-0.29	-0.25	-0.24	1.00	<b>-0.40</b>	-0.24	-0.12	<b>-0.51</b>	<b>0.41</b>	0.10	<b>0.43</b>	-0.23	-0.34	-0.23	-0.22	-0.38	-0.28	<b>0.82</b>	-0.31				
CU	<b>0.44</b>	0.31	<b>0.36</b>	-0.03	<b>0.70</b>	0.03	<b>0.59</b>	<b>-0.35</b>	1.00	<b>0.72</b>	0.16	<b>0.62</b>	<b>-0.61</b>	-0.19	-0.11	0.47	<b>0.86</b>	<b>0.58</b>	<b>0.87</b>	0.27	-0.03	<b>-0.54</b>	0.38				
FET	0.21	<b>0.41</b>	<b>0.56</b>	-0.08	<b>0.69</b>	-0.11	<b>0.87</b>	-0.23	<b>0.65</b>	1.00	0.15	0.39	-0.53	0.28	0.17	<b>0.45</b>	<b>0.87</b>	<b>0.42</b>	<b>0.68</b>	0.01	-0.24	-0.36	0.38				
HG	<b>0.65</b>	0.09	0.02	-0.07	0.14	<b>0.73</b>	0.18	-0.24	0.14	0.06	1.00	0.20	-0.36	0.29	0.17	<b>0.61</b>	0.28	<b>0.59</b>	0.28	0.00	0.16	-0.21	<b>0.60</b>				
IN	<b>0.74</b>	<b>0.50</b>	0.21	-0.13	0.25	<b>0.74</b>	0.01	-0.40	0.30	0.02	<b>0.41</b>	1.00	<b>-0.50</b>	-0.01	-0.24	<b>0.60</b>	<b>0.42</b>	0.39	<b>0.51</b>	<b>0.61</b>	0.35	<b>-0.60</b>	<b>0.62</b>				
LA	-0.34	<b>-0.44</b>	<b>-0.45</b>	<b>0.50</b>	<b>-0.56</b>	-0.15	<b>-0.41</b>	0.17	-0.34	<b>-0.47</b>	-0.18	-0.28	1.00	0.02	-0.03	<b>-0.59</b>	<b>-0.67</b>	<b>-0.61</b>	<b>-0.65</b>	-0.04	0.06	<b>0.68</b>	<b>-0.45</b>				
MNO	-0.16	-0.05	0.00	0.19	-0.19	-0.09	-0.09	<b>0.37</b>	-0.14	-0.09	0.07	-0.17	0.24	1.00	0.34	0.24	0.04	0.09	-0.08	-0.15	-0.09	0.08	0.21				
NI	-0.18	-0.05	-0.05	-0.16	-0.15	-0.09	-0.03	<b>0.49</b>	-0.14	-0.06	0.01	-0.17	0.01	<b>0.69</b>	1.00	0.09	0.07	0.15	0.04	<b>-0.45</b>	-0.31	0.37	0.06				
PB	<b>0.51</b>	0.18	0.21	-0.12	0.17	0.39	0.02	-0.07	0.11	0.07	0.29	0.18	-0.09	-0.04	-0.07	1.00	<b>0.50</b>	<b>0.63</b>	<b>0.52</b>	0.25	0.22	-0.39	<b>0.79</b>				
S	<b>0.34</b>	<b>0.54</b>	<b>0.69</b>	-0.05	<b>0.76</b>	-0.05	<b>0.86</b>	-0.30	<b>0.63</b>	<b>0.94</b>	0.14	0.11	<b>-0.52</b>	-0.10	-0.10	0.12	1.00	<b>0.67</b>	<b>0.79</b>	0.04	-0.18	<b>-0.49</b>	0.37				
SB	<b>0.66</b>	<b>0.69</b>	<b>0.59</b>	-0.15	<b>0.61</b>	0.30	<b>0.58</b>	-0.30	<b>0.49</b>	<b>0.53</b>	<b>0.48</b>	<b>0.49</b>	<b>-0.49</b>	0.06	0.10	0.28	<b>0.68</b>	1.00	<b>0.67</b>	-0.03	-0.02	-0.39	0.38				
SE	0.32	0.26	<b>0.41</b>	-0.17	<b>0.62</b>	0.02	<b>0.42</b>	-0.21	<b>0.82</b>	<b>0.47</b>	0.05	0.21	-0.34	-0.12	-0.07	0.11	<b>0.45</b>	0.29	1.00	0.11	-0.11	<b>-0.46</b>	0.35				
SN	<b>0.64</b>	0.12	-0.10	-0.05	-0.10	<b>0.92</b>	-0.17	-0.24	-0.08	-0.22	<b>0.59</b>	<b>0.71</b>	-0.08	-0.14	-0.17	<b>0.50</b>	-0.17	0.17	-0.10	1.00	<b>0.62</b>	-0.21	0.36				
TL	<b>0.54</b>	0.02	-0.11	-0.03	-0.15	<b>0.50</b>	-0.23	-0.27	-0.15	-0.26	0.24	<b>0.54</b>	-0.05	-0.09	-0.20	<b>0.49</b>	-0.21	0.07	-0.17	<b>0.72</b>	1.00	-0.13	0.33				
V	<b>-0.37</b>	-0.32	<b>-0.37</b>	0.11	<b>-0.42</b>	-0.14	-0.24	<b>0.86</b>	<b>-0.42</b>	-0.25	-0.16	-0.33	0.34	<b>0.39</b>	<b>0.47</b>	-0.06	-0.34	-0.33	<b>-0.38</b>	-0.13	-0.18	1.00	-0.32				
ZN	<b>0.76</b>	0.21	0.05	-0.13	0.03	<b>0.98</b>	0.01	-0.27	0.08	-0.05	<b>0.79</b>	<b>0.71</b>	-0.17	-0.10	-0.11	<b>0.49</b>	0.02	<b>0.37</b>	0.04	<b>0.91</b>	<b>0.54</b>	-0.16	1.00				

NUMBER OF OBSERVATIONS: 47

NOTES: Bold numbers represent >99% confidence interval (Davis, 1986).



**Figure 4.** Lognormal scatter plots for Zn, Cu, As, and Sn with selected elements with Pearson Product ( $r$ ) and Spearman's Rank ( $r'$ ) correlation coefficients illustrated (see Table 3). See legend in Figure 2 for symbols. These diagrams illustrate elemental associations that may be of mineralogical and/or petrogenetic significance.

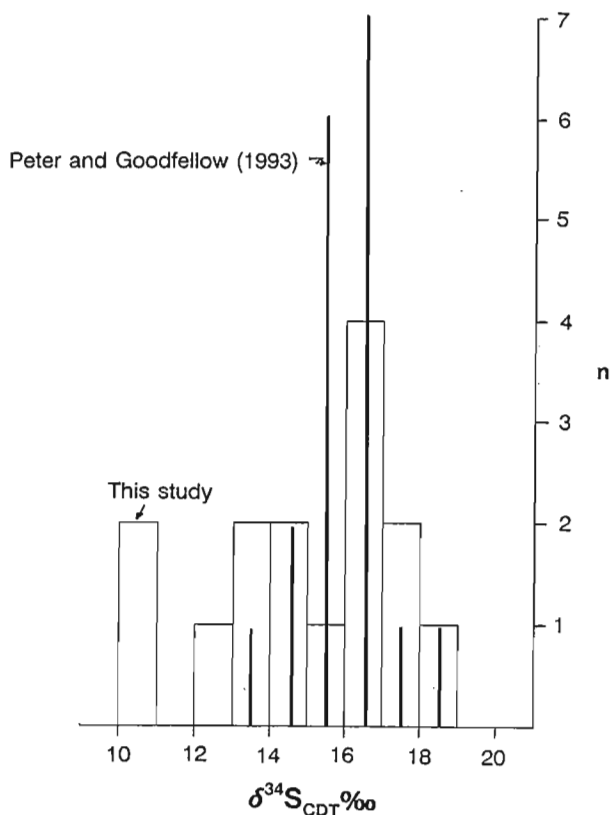
highest in areas of low sulphide abundance (Table 1). Cobalt, Sb, and Au (Fig. 4G, H, I) also display strong positive correlations with As. Cobalt, and a proportion of Sb, substitutes into arsenopyrite (Lentz and Goodfellow, 1993c). Lentz et al. (1993) have suggested that Au occurs within arsenopyrite and, to a much lesser extent, pyrite (cf., Cabri et al., 1989). Tin correlates well with Zn, In, and Tl, possibly because of an association of sphalerite with stannite in sulphide veins. Thallium correlates most strongly with Sn, suggesting that  $Tl^{3+}$  substitutes into stannite at the base of the massive sulphide (Fig. 1).

## SULPHUR ISOTOPES

Sulphur isotope compositions were determined on selected bulk samples from the footwall stringer sulphide zone (drillhole A1), hanging wall volcanoclastic sedimentary rocks and pyritic massive sulphides. The  $\Delta^{34}S$  values between pyrite, pyrrhotite, and sphalerite are typically less than 1‰ due to metamorphic re-equilibration (Lusk and Crocket, 1969; Peter and Goodfellow, 1993). As a result,  $\delta^{34}S$  values for bulk sulphides will not be appreciably affected by the minor variation in relative abundance of pyrite, pyrrhotite, and sphalerite. No obvious relationship between host rock and  $\Delta^{34}S$  composition was found except a moderate correlation with Fe ( $r = 0.52$ ;  $n = 15$ ) reflecting total sulphide abundance. The heaviest  $\delta^{34}S$  value (18.7‰) is in sulphide veins cutting crystal tuff beneath the inferred Brunswick Horizon (Fig. 1), whereas the lightest value (10.6‰) is directly above this horizon in sedimentary rocks of the Flat Landing Brook Formation. The mean  $\delta^{34}S$  of the footwall mineralization is  $15.72 \pm 1.66$ ‰ ( $n = 12$ ) and is indistinguishable from previous results for Brunswick No. 12 massive sulphides ( $\delta^{34}S$  of  $16.0 \pm 1.4$ ‰,  $n = 18$ , Tupper, 1960;  $\delta^{34}S$  of  $15.7 \pm 1.6$ ‰,  $n = 24$ , Peter and Goodfellow, 1993). Peter and Goodfellow (1993) also determined that the host hanging wall rocks have  $\delta^{34}S$  between 14.4 and 16.8‰ ( $n = 4$ ) and that unmineralized footwall rocks have  $\delta^{34}S$  between 2.9 and 6.3‰ ( $n = 7$ ).  $\delta^{34}S$  values for stringer sulphides are between 13.9 and 18.8‰ ( $16.2 \pm 1.3$ ; Peter and Goodfellow, 1993), and are similar to values for massive sulphides reported here (Fig. 5) and Tupper (1960) and Peter and Goodfellow (1993).

## DISCUSSION

The stringer sulphide zone represents a fossilized conduit that carried hydrothermal fluids to the seafloor. The mineralization in the footwall stringer zone probably formed under low  $f(O_2)$  and moderate  $f(S_2)$  conditions, based on the presence of Fe-chlorite, pyrite, pyrrhotite, chalcopyrite, and arsenopyrite. The hydrothermal fluids were moderately acidic (pH  $\approx 4$ ) based on the presence of chlorite and sericite and were probably between 350° and 425°C, based on arsenopyrite geothermometry (Lentz and Goodfellow, 1993c). These general constraints help to better understand the solubility controls on hydrothermal elements in the stringer zone.



**Figure 5.** Histogram of bulk sulphur isotope compositions ( $\delta^{34}S_{CDT}$ ‰) of selected samples from diamond-drill hole A1 including two hanging wall and 12 footwall (stringer and disseminated sulphide) samples. One sample of pyritic massive sulphide (LPA-045; 307 m; 14.7‰) is excluded. The data was determined at the Ottawa-Carleton Geoscience Centre Isotope Facility by Gilles St. Jean. Samples with less than 5% S were determined by the KIBA extraction method whereas the higher S samples were determined by S proportional combustion. The data is compared to the stringer sulphides determined by Peter and Goodfellow (1993).

The solubility of ore-forming elements is dependent on temperature, pressure, pH, and oxygen and sulphur fugacities. These variables must be considered in evaluating what controls mineral zoning (Susak and Crerar, 1982). The Fe-rich nature of the alteration assemblages within the stringer zone (Lentz and Goodfellow, 1993b) suggests that the shallow entrainment of cold Mg-rich seawater into the core of the hydrothermal vent complex was minimal. Within the stockwork mineralization where most of the ore metals are concentrated, temperature and pressure are the most important parameters controlling solubilities, consistent with the overall simplicity of zoning in many hydrothermal systems. In the sulphide-silica veins, for example, the solubility of silica is prograde ( $f(T,P)$ ) above the liquid-vapour curve (Fournier, 1985), although an isothermal decrease in geostatic pressure from lithostatic to hydrostatic conditions drastically reduces silica solubility (>90% efficient at 400°C and 50 to 20 MPa) because of the intersection of the two phase liquid-vapour curve (i.e., boiling). An isobaric decrease in temperature will also result

in silica saturation ( $\approx 50\%$  efficient at 500 MPa and  $400^\circ$  to  $300^\circ\text{C}$ ). However, kinetic effects result in supersaturation of silica in venting hydrothermal fluids indicating that silica deposition in the stringer zone is less than calculated values, which is consistent with the high silica contents in the exhalative ores and iron-formation. Decreasing temperature and geostatic pressure fluctuations are consistent with the dynamics of a subseafloor stockwork system, the dilatant nature of the veins, the large volume increases, and abundance of silica within the veins. Chalcopyrite solubility, as Cu-Cl complexes, is strongly dependant on temperature (Crerar and Barnes, 1976), which is the principle control on its distribution in the stockwork and basal replacement zones of proximal massive sulphide deposits (cf. Jambor, 1979). Within the stringer zone, other elements associated with Cu (Co, As, Bi, and Se) have relatively high abundances. Interestingly, arsenopyrite, and bismuthinite also have strong temperature dependant solubilities (Heinrich and Eadington, 1986; Wood et al., 1987), consistent with their concentration in high-temperature sulphide stringer zones. The early saturation of arsenopyrite may decrease the solubility of trace elements that readily substitute into its structure (i.e., Co, Au, and Sb), regardless of the ligand involved (Lentz et al., 1993). The low Pb, Ag, Zn, and Hg contents of the stringer sulphides, relative to the ore (Fig. 2), indicates that they remained very soluble in the vent complex. The very low abundances of Pb and Ag in the stringer zone relative to the ore is probably a function of the high solubility of galena with respect to Cu, Fe, and Zn sulphides, particularly under the conditions of stringer sulphide formation. Analogous to Pb, Tl is released during hydrolysis of feldspar and alteration of sericite, and is probably mobile as  $\text{Tl}^+$  ions or  $\text{TlCl}$  (Smith and Huston, 1992). The Tl content of the hanging wall sequence is several times greater than background values and may reflect Tl fixation during the sericitic alteration of hanging wall felsic tuff. Mercury anomalies, which are common in the hanging wall rocks of the Brunswick No. 12 deposit (Goodfellow, 1975a) and Australian massive sulphide deposits (Ryall, 1981), probably originated during postdepositional, modification of the ore. Antimony may also have been similarly remobilized from the ore zone into overlying sediments during continued postore hydrothermal activity or during later metamorphism.

The homogeneity of sulphur isotopic compositions in the feeder system is indicative of a relatively uniform  $\text{H}_2\text{S}$  source ( $\delta^{34}\text{S} \approx 15$  to  $17\text{‰}$ ) at high depositional temperatures. Heavy sulphur isotope compositions in the stringer zone are consistent with the entrainment of reduced seawater (low  $\text{SO}_4^{2-}/\text{H}_2\text{S}$ ) into the hydrothermal upflow zone. A reduced seawater source of sulphur (Goodfellow and Jonasson, 1984) could also explain the similarity in  $\delta^{34}\text{S}$  values between stringer sulphides and exhalative massive sulphides.

## ACKNOWLEDGMENTS

We would like to thank the staff of Brunswick Mining and Smelting Limited for their co-operation and encouragement with this study and continuing studies in the area. Peter Belanger supervised the analytical work at the Geological

Survey of Canada. Discussion with Dr. Jan Peter during mapping and sampling of this hole helped considerably in my understanding of stockwork mineralization. The manuscript benefitted from insightful comments by John Langton and Matt Leybourne.

## REFERENCES

- Cabri, L.J., Campbell, J.L., LaFlamme, J.H.G., Leigh, R.G., Maxwell, J.A., and Scott, J.D.**  
1985: Proton-microprobe analysis of trace-elements in sulfides from massive-sulfide deposits; *Canadian Mineralogist*, v. 23, p. 133-148.
- Cabri, L.J., Chryssoulis, S.L., De Villiers, J.P.R., Laflamme, J.H.G., and Buseck, P.R.**  
1989: The nature of "invisible" gold in arsenopyrite; *Canadian Mineralogist*, v. 27, p. 353-362.
- Chen, T.T. and Petruk, W.**  
1980: Mineralogy and characteristics that affect recoveries of metals and trace elements from the ore at Heath Steele Mines, New Brunswick; *Canadian Institute of Mining and Metallurgy Bulletin*, v. 73, p. 167-178.
- Connell, M.D. and Hattie, D.W.**  
1990: Preliminary report on whole-rock analyses from lithochemical study of red manganiferous slate and black slate-chert in the Miramichi Terrane, New Brunswick; (comp.) G.P. Watson, Geological Survey of Canada, Open File 2171, 43 p.
- Crerar, D.A. and Barnes, H.L.**  
1976: Ore solution chemistry – V. Solubilities of chalcopyrite and chalcocite assemblages in hydrothermal solution at  $200^\circ$ - $350^\circ\text{C}$ ; *Economic Geology*, v. 71, p. 722-794.
- Davis, J.C.**  
1986: *Statistical and Data Analysis in Geology*, Second Edition; John Wiley and Sons Ltd. Toronto, Ontario, 646 p.
- Fournier, R.O.**  
1985: The behavior of silica in hydrothermal solutions; in *Geology and Geochemistry of Epithermal Systems*, (ed.) B.R. Berger and P.M. Bethke; *Reviews in Economic Geology*, v. 2, p. 45-61.
- Goodfellow, W.D.**  
1975a: Rock geochemical exploration and ore genesis at Brunswick No. 12 deposit; Ph.D. thesis, University of New Brunswick, Fredericton, New Brunswick.  
1975b: Major and minor element halos in volcanic rocks at Brunswick No. 12 sulphide deposit, N.B., Canada; in *Geochemical Exploration 1974*, (ed.) I.L. Elliot and W.K. Fletcher; Elsevier, Amsterdam, p. 279-295.
- Goodfellow, W.D. and Jonasson, I.R.**  
1984: Ocean stagnation and ventilation defined by  $\delta^{34}\text{S}$  secular trends in pyrite and barite, Selwyn Basin, Yukon; *Geology*, v. 12, p. 583-586.
- Heinrich, C.A. and Eadington, P.J.**  
1986: Thermodynamic predictions of the hydrothermal chemistry of arsenic, and their significance for the paragenetic sequence of some cassiterite-arsenopyrite-base metal sulfide deposits; *Economic Geology*, v. 81, p. 511-529.
- Jambor, J.L.**  
1979: Mineralogical evaluation of proximal-distal features in new Brunswick massive-sulphide deposits; *Canadian Mineralogist*, v. 17, p. 649-664.
- Jonasson, I.R. and Sangster, D.F.**  
1974: Variations in the mercury content of sphalerite from some Canadian sulphide deposits; in *Geochemical Exploration 1974*, (ed.) J.L. Elliot and W.K. Fletcher; Association of Exploration Geochemistry, Special Publication No. 2, Elsevier, Amsterdam, p. 313-332.
- Langton, J.P. and McCutcheon, S.R.**  
1993: Brunswick Project, NTS 21 P/5 West, 21 P/4 West, Gloucester County, New Brunswick; in *Current Research*, (comp. and ed.) S.A. Abbott, New Brunswick Department of Natural Resources and Energy, Minerals and Energy Division, Information Circular 93-1, p. 31-51.
- Lentz, D.R. and Goodfellow, W.D.**  
1992a: Re-evaluation of the petrology and depositional environment of felsic volcanic and related rocks in the vicinity of the Brunswick No. 12 massive sulphide deposit, Bathurst Mining Camp, New Brunswick; in *Current Research, Part E*; Geological Survey of Canada, Paper 92-1E, p. 333-343.



**Lentz, D.R. and Goodfellow, W.D. (cont.)**

- 1992b: Re-evaluation of the petrochemistry of felsic volcanic and volcanoclastic rocks near the Brunswick No. 6 and 12 deposits, Bathurst Mining Camp, New Brunswick; in *Current Research, Part E*; Geological Survey of Canada, Paper 92-1E, p. 343-350.
- 1993a: Stringer sulphide mineralization and alteration around the FAB base-metal occurrence, Bathurst Mining Camp, New Brunswick; in *Current Research, (comp. and ed.) S.A. Abbott*; New Brunswick Department of Natural Resources and Energy, Minerals Resources, Information Circular 93-1, p. 91-103.
- 1993b: Character, distribution, and origin of hydrothermal alteration associated with the Brunswick No. 12 deposit, Bathurst, New Brunswick; Atlantic Geoscience Society Abstracts, Atlantic Geology, v. 29, no. 1.
- 1993c: Mineralogy and petrology of the stringer sulphide zone in the Discovery Hole at the Brunswick No. 12 massive sulphide deposit, Bathurst, New Brunswick; in *Current Research, Part E*; Geological Survey of Canada, Paper 93-1E.
- Lentz, D.R., Giggie, P., Luff, B., and Goodfellow, W.D.**
- 1993: Precious metal distribution in the epigenetic stringer sulphide zone at the Brunswick No. 12 deposit, Bathurst, New Brunswick; Atlantic Geoscience Society Abstracts, Atlantic Geology, v. 29, no. 1.
- Luff, W., Goodfellow, W.D., and Juras, S.**
- 1992a: Evidence for a feeder pipe and associated alteration at the Brunswick No. 12 massive sulphide deposit; *Exploration and Mining Geology*, v. 1, p. 167-185.
- Luff, W., van Staal, C.R., and Lentz, D.R.**
- 1992b: The Brunswick No. 12 and No. 6 mines, Brunswick Mining and Smelting Limited; in *Massive Sulphide Deposits and Geology in northern New Brunswick*, (ed.) J.P. Langton; Geological Association of Canada, Field Trip Guidebook C-6.
- Lusk, J. and Crocket, J.H.**
- 1969: Sulfur isotope fractionation in coexisting sulfides from the Heath Steele B-1 orebody, New Brunswick, Canada; *Economic Geology*, v. 64, p. 147-155.
- McCutcheon, S.R.**
- 1990: Base-metal deposits of the Bathurst-Newcastle district; in *Field guide to massive sulphide deposits in northern New Brunswick*, (ed.) L.R. Fyffe; Base metal Symposium 1990, Minerals and Energy Division, Department of Natural Resources and Energy, New Brunswick, p. 42-71.

**Peter, J.M. and Goodfellow, W.D.**

- 1993: Bulk and stable sulphur and carbon isotope geochemistry of hydrothermal sediments associated with the Brunswick No. 12 deposit, northern New Brunswick; in *Current Research, (comp. and ed.) S.A. Abbott*; New Brunswick Department of Natural Resources and Energy, Mineral Resources, Information Circular 93-1, p. 154-169.

**Petruk, W. and Schnarr, J.R.**

- 1981: An evaluation of the recovery of free and unliberated mineral grains, metals and trace elements in the concentrator of Brunswick Mining and Smelting Corp. Ltd.; Canadian Institute of Mining and Metallurgy Bulletin, v. 74, no. 833, p. 132-159.

**Ryall, W.R.**

- 1981: The forms of mercury in some Australian stratiform Pb-Zn-Ag deposits of different regional metamorphic grades; *Mineralium Deposita*, v. 16, p. 425-435.

**Smith, R.N. and Huston, D.L.**

- 1992: Distribution and association of selected trace-elements at the Rosebery deposit, Tasmania; *Economic Geology*, v. 87, p. 706-719.

**Susak, N.J. and Crerar, D.A.**

- 1982: Factors controlling mineral zoning in hydrothermal ore deposits; *Economic Geology*, v. 77, p. 476-482.

**Sutherland, J.K. and Halls, C.**

- 1969: Composition of some New Brunswick sphalerites; New Brunswick Research and Productivity Council, Research Note 21, 33 p.

**Taylor, S.R. and McLennan, S.M.**

- 1985: *The Continental Crust: Its Composition and Evolution*; Blackwell Scientific Publications, Boston, Massachusetts, 312 p.

**Tupper, W.M.**

- 1960: Sulfur isotopes and the origin of the sulfide deposits of the Bathurst-Newcastle area of northern New Brunswick; *Economic Geology*, v. 55, p. 1676-1707.

**van Staal, C.R., Winchester, J.A., Bedard, J.H.**

- 1991: Geochemical variations in Middle Ordovician volcanic rocks of the northern Miramichi Highlands and their tectonic significance; *Canadian Journal of Earth Sciences*, v. 28, p. 1031-1049.

**Wood, S.A., Crerar, D.A., and Borcsik, M.P.**

- 1987: Solubility of the assemblage pyrite-pyrrhotite-magnetite-sphalerite-galena-gold-stibnite-bismuthinite-argenitite-molybdenite in H<sub>2</sub>O-NaCl-CO<sub>2</sub> solutions from 200° to 350°C; *Economic Geology*, v. 82, p. 1864-1887.



# Evaluation of glacial Lake Iroquois shoreline data from south-central and eastern Ontario<sup>1</sup>

I.M. Kettles and C.G. Rodrigues<sup>2</sup>

Terrain Sciences Division

*Kettles, I.M. and Rodrigues, C.G., 1993: Evaluation of glacial Lake Iroquois shoreline data from south-central and eastern Ontario; in Current Research, Part E; Geological Survey of Canada, Paper 93-1E, p. 271-274.*

---

**Abstract:** The maximum shoreline position of glacial Lake Iroquois and those of later related lakes impounded in the Lake Ontario basin during the last stages of Wisconsinan deglaciation are poorly known north of Belleville and Kingston, Ontario. In this study paleowater planes previously constructed for the Lake Ontario basin are extrapolated to the area north of Kingston and Belleville. When available shoreline data for the same region are evaluated altitudes of shoreline features are found to correspond closely to projected levels of glacial Lake Iroquois and a later related lake.

**Résumé :** La position maximale de la ligne de rivage du Lac glaciaire Iroquois et celles d'autres lacs associés formés plus tard dans la bassin du lac Ontario au cours des derniers stades de la déglaciation du Wisconsinien sont méconnues au nord de Belleville et de Kingston (Ontario). Dans la présente étude, les paléoplans d'eau établis antérieurement pour le bassin du lac Ontario sont extrapolés à la région au nord de Kingston et de Belleville. L'évaluation des données sur la ligne de rivage recueillies dans la même région révèle que les altitudes des formes du rivage correspondent étroitement aux niveaux prévus pour le Lac glaciaire Iroquois et un lac ultérieur associé.

---

<sup>1</sup> Contribution to Canada-Ontario 1985 Mineral Development Subsidiary Agreement under the Economic and Regional Development Agreement.

<sup>2</sup> Department of Geology, University of Windsor, Windsor, Ontario N9B 3P4

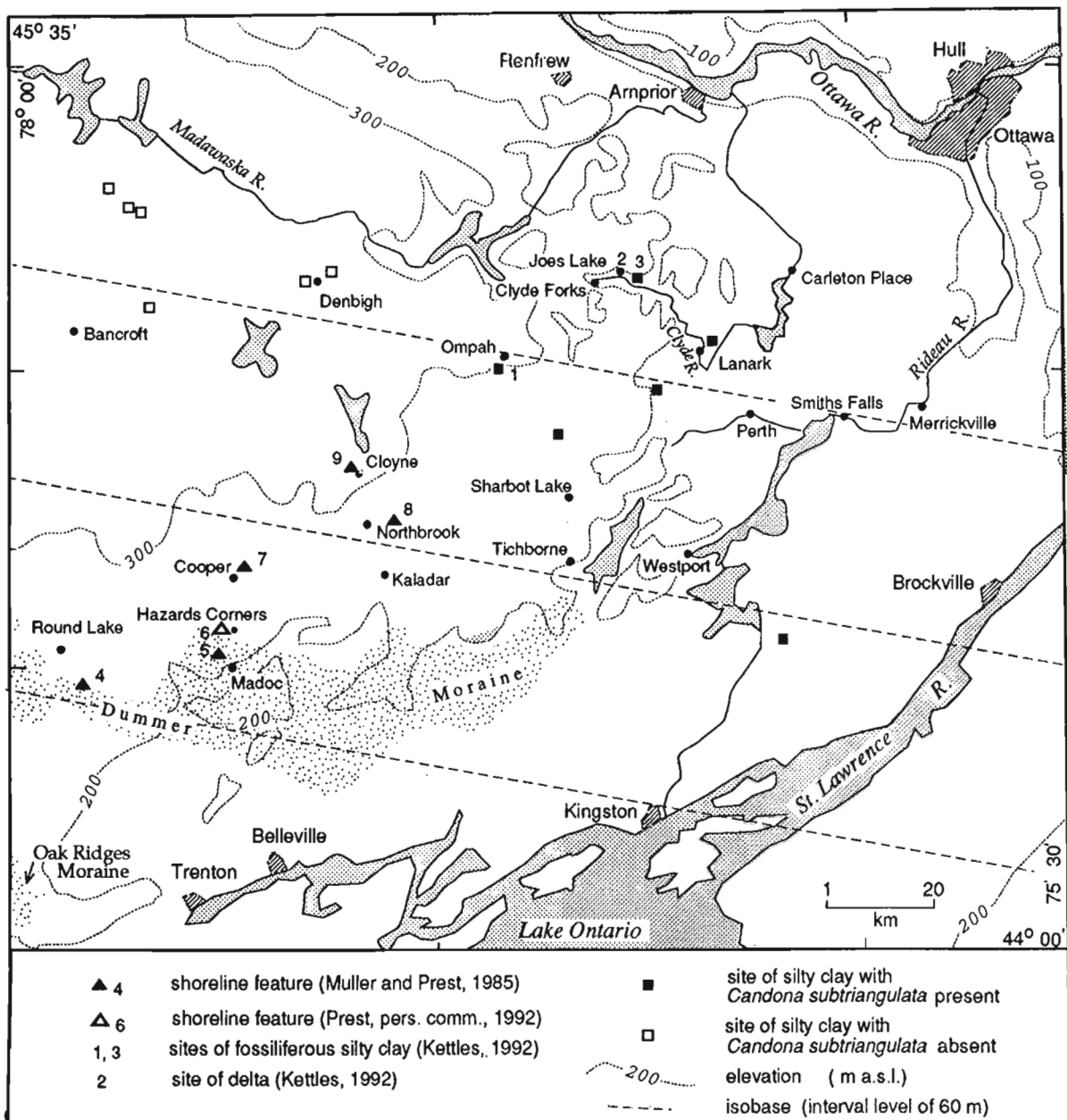
## INTRODUCTION

The maximum shoreline position of glacial Lake Iroquois and those of later related lakes impounded in the Lake Ontario basin during the last stages of Wisconsinan deglaciation are poorly known north of Belleville and Kingston, Ontario (Fig. 1). An understanding of the Quaternary history of this area is needed to interpret Late Wisconsinan events in east-central Canada.

Coleman (1936) and Miryneck (1962) traced the Iroquois shoreline to a maximum level of 225.5 m a.s.l. 15 km south-east of Madoc. Henderson (1973) pointed out that glacial Lake

Iroquois extended at least as far north as Dummer Moraine. Muller and Prest (1985) suggested that shoreline features between Round Lake and Cloyne are related to glacial Lake Iroquois and estimated the extent of the lake based on these data.

More recently, Rodrigues (1992) examined foraminiferal and ostracode assemblages in samples of late glacial and early postglacial sediments collected east of Kingston and Ottawa and suggested that a proglacial lake preceded the Champlain Sea in some parts of the Central St. Lawrence Lowland. Kettles (1992) postulated that Lake Iroquois expanded as far north as Ompah and Clyde Forks, and estimated the limits of



**Figure 1.** Location map showing generalized topography. Also shown are the Oak Ridges and Dummer moraines (after Barnett et al., 1991), sites where samples of laminated silt and clay were collected for microfossil analysis (Kettles, 1992), and shoreline features and isobase lines (after Muller and Prest, 1985).

Iroquois and a later, related lake in that region. These estimated lake limits were based on the following: (1) occurrences of *Candona subtriangulata* in laminated silty clay (C.G. Rodrigues, unpub. data, 1991; Fig. 1). This ostracode species, found in present day Great Lakes, is characteristic of a large oligotrophic lake having few dissolved solids (Delorme, 1970, 1978); (2) occurrences of *Mysis relicta*, a relict species of fresh- or brackish-water shrimp, in modern lakes (Dadswell, 1974); (3) shoreline data for the Clyde Forks-Ompah region; and (4) shoreline studies undertaken near Cloyne (Muller and Prest, 1985). In the present study, shoreline data from both the Clyde Forks-Westport area (Kettles, 1992) and from the Round Lake-Cloyne area (Muller and Prest, 1985, p. 222; V.K. Prest, pers. comm., 1991) are further evaluated.

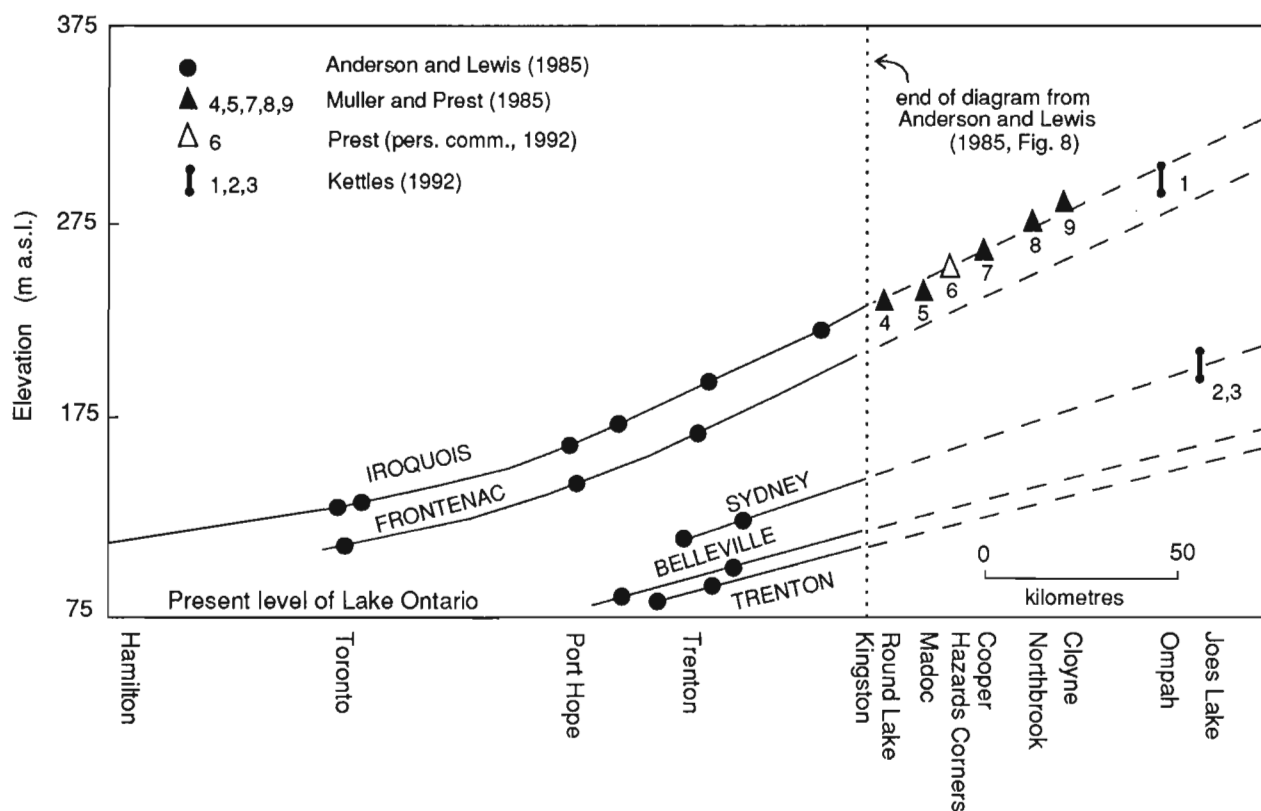
## EVALUATION OF SHORELINE DATA

Anderson and Lewis (1985, Fig. 8) constructed a diagram showing isostatically tilted water planes of the Lake Ontario basin. On their diagram shoreline positions of Lake Iroquois and post-Iroquois phases were calculated using shoreline data from Coleman (1936), Miryech (1962), and Muller and Prest (1985). In order to evaluate further shoreline data from the Clyde Forks-Westport area and the Madoc-Cloyne area, we extrapolated these water planes to the area north of Kingston

using the isobase trend of  $100^\circ$  and the uplift trend of 1.6 m/km calculated by Muller and Prest (1985) for the Belleville-Trenton area (Fig. 1). There are no topographic barriers to prevent flooding from the main Ontario basin; the altitudes of interconnected low-lying areas between Kingston and Ompah and Clyde Forks (Fig. 1) are well below the projected levels of Lake Iroquois and related lower phases (Fig. 2).

The altitude of a subaqueous outwash deposit capped with *Candona subtriangulata*-bearing silty clay (290-305 m a.s.l.) (site 1, Fig. 1) indicates that a proglacial lake with a minimum level of over 305 m a.s.l. covered the Ompah area (Kettles, 1992). As shown on Figure 2, the minimum level of the lake at Ompah is close to the projected level of Lake Iroquois, as are the elevations of shoreline features observed between Round Lake and Cloyne (Muller and Prest, 1985, p. 222; V.K. Prest, pers. comm., 1991).

Twenty-five kilometres northeast of Ompah, the altitude of the topset/foreset contact in a kettled delta (198-213 m a.s.l.) at Joes Lake marks a water plane lower than Lake Iroquois in the Clyde River valley (site 2, Fig. 1; Kettles, 1992). The altitude of the delta at Joes Lake corresponds to the projected level of one of the post-Iroquois lakes, glacial Lake Sydney (Fig. 2). The presence of *Candona subtriangulata*-bearing silty clay capping a subaqueous fan, within the same



**Figure 2.** Extrapolated paleowater-planes of the Lake Ontario basin plotted in section normal to isobases of Glacial Lakes Iroquois and Belleville (after Anderson and Lewis, 1985, Fig. 8). Locations of numbered shoreline features are shown on Figure 1.

elevation range as the delta but 6 km east of it (site 3, Fig. 1), also suggests that the Clyde River valley was flooded by proglacial waters interconnected with the main Ontario basin water (Kettles, 1992).

Although the altitude of the delta at Joes Lake corresponds most closely to glacial Lake Sydney (Fig. 2), too few shoreline features have been identified either near Kingston or in the area north of Kingston to define the paleowater-planes of individual post-Iroquois lakes with confidence.

The close correlation between elevations of shoreline features between Round Lake and Clyde Forks and elevations of extrapolated paleowater-planes of the Lake Ontario basin is further evidence that glacial Lake Iroquois and a related later lake extended more than 85 km north of Kingston.

## ACKNOWLEDGMENTS

The authors would like to thank J. Cousineau and K. Laurus for assisting in the field and office; H.L. Thorleifson, T.W. Anderson, V.K. Prest, and W.W. Shilts for helpful discussions; and R.J. Fulton for reviewing this manuscript.

## REFERENCES

### Anderson, T.W. and Lewis, C.F.M.

- 1985: Post-glacial water-level history of the Lake Ontario basin; in *Quaternary Evolution of the Great Lakes*, (ed.) P.F. Karrow and P.E. Calkin; Geological Association of Canada, Special Paper 30, p. 233-254.

### Barnett, P.J., Cowan, W.R., and Henryk A.P.

- 1991: Quaternary geology of Ontario, southern sheet; Ontario Geological Survey, Map 2556, scale 1: 1 000 000.

### Coleman, A.P.

- 1936: Lake Iroquois; Ontario Department of Mines, 45th Annual Report, v. 2, pt. 7, p. 1-36.

### Dadswell, M.J.

- 1974: Distribution, ecology and postglacial dispersal of certain crustaceans and fishes in eastern North America; National Museum of Natural Sciences, Publication in Zoology, no. 11, 110 p.

### Delorme, L.D.

- 1970: Freshwater ostracodes of Canada, part 111: Family Candonidae; Canadian Journal of Zoology, v. 48, p. 1099-1127.

- 1978: Distribution of freshwater ostracodes in Lake Erie; Journal of Great Lakes Research, v. 4, p. 216-220.

### Henderson, E.P.

- 1973: Surficial geology of Kingston (north half) map-area, Ontario; Geological Survey of Canada, Paper 72-48, 6 p., includes maps 7-1972 and 8-1972, scale 1:250 000.

### Kettles, I.M.

- 1992: Glacial geology and glacial sediment geochemistry in the Clyde Forks-Westport area of Ontario; Geological Survey of Canada, Paper 91-17, 34 p.

### Mirynech, E.

- 1962: Pleistocene geology of the Trenton-Campbellford map area, Ontario; PhD. thesis, University of Toronto, 176 p.

### Muller, E.H. and Prest, V.K.

- 1985: Glacial lakes in the Ontario basin; in *Quaternary Evolution of the Great Lakes*. (ed.) P.F. Karrow and P.E. Calkin; Geological Association of Canada, Special Paper 30, p. 214-229.

### Rodrigues, C.G.

- 1992: Successions of invertebrate microfossils and the late Quaternary deglaciation of the central St. Lawrence Lowland, Canada and United States; *Quaternary Science Reviews*, v. 11, p. 503-534.

Geological Survey of Canada Project 870033

# Geophysical characterization of glacial and postglacial sediments in a continuously cored borehole near Ottawa, Ontario

M. Douma and F.M. Nixon  
Terrain Sciences Division

*Douma, M. and Nixon, F.M., 1993: Geophysical characterization of glacial and postglacial sediments in a continuously cored borehole near Ottawa, Ontario; in Current Research, Part E; Geological Survey of Canada, Paper 93-1E, p. 275-279.*

---

**Abstract:** Borehole conductivity, gamma, and magnetic susceptibility logs have been compared with high resolution seismic reflection data from a site near Ottawa formerly occupied by a number of glacial and postglacial environments. Approximately 58 m of subglacial, proglacial, glaciolacustrine, marine, and fluvial sediments overlie a nearly horizontal bedrock surface. The seismic data show a series of nearly horizontal, parallel reflection events separating units displaying various internal characteristics. The borehole geophysical logs reveal subtle attributes of the strata that will require further investigation.

**Résumé :** Les auteurs ont comparé des diagraphies d'induction, de rayonnement gamma et de la susceptibilité magnétique mesurées dans des trous de forage aux données de sismique réflexion de haute résolution recueillies à un site près d'Ottawa qui avait été le site de divers milieux glaciaires et postglaciaires. Environ 58 m de sédiments sous-glaciaires, proglaciaires, glaciolacustres, marins et fluviaux reposent sur un substratum rocheux quasi horizontal. Les données sismiques montrent une série d'événements parallèles quasi horizontaux qui séparent des unités présentant diverses caractéristiques internes. Les diagraphies géophysiques révèlent que les couches possèdent des attributs ténus qu'il faudra approfondir par d'autres analyses.

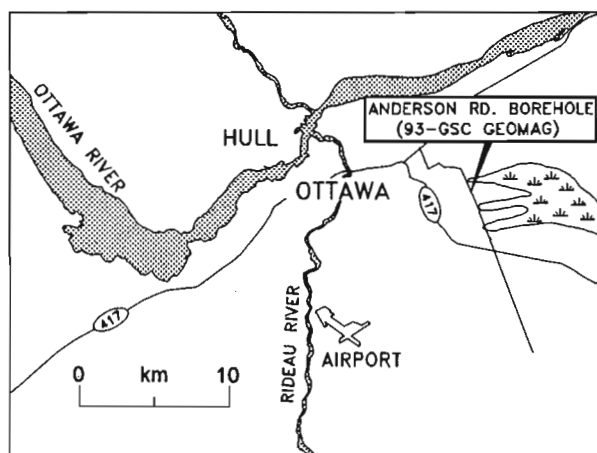
## INTRODUCTION

The Terrain Geophysics and Geothermal Section of the Terrain Sciences Division arranged for the drilling of a continuously sampled borehole at a location 10 km from its Ottawa office for use as a demonstration site when training operators in the operation of the section's EM-39 borehole logging unit (Fig. 1). The site was selected, in part, on the basis of a high resolution seismic reflection line shot over the area which showed a succession of glacial and postglacial strata overlying Paleozoic bedrock. The site is located near the centre of a streamlined 'island' formed in the proto-Ottawa River during the regression of the Champlain Sea and preserved when the river switched channels away from the Mer Bleue area 7650 years ago (Gadd, 1987). This report will present the borehole geophysical data and a portion of the seismic reflection data and provide some preliminary correlations and interpretations.

## SEISMIC METHODS

The seismic section presented in this report is a portion of a 1.6 km line of high resolution reflection data collected in July and October of 1992 in the drainage ditch on the side of Anderson Road 2 km south of Blackburn Hamlet. The complete line, from Blackburn Station south to the GSC's Geomagnetic Laboratory, straddles the transition between Mer Bleue bog, lying in an abandoned channel of the Ottawa River, and a low, elongate, east-west oriented hill which was once an island in that same river. Only the southern-most 324 m of seismic data, from the top of the old island, are included here.

The 'optimum offset' seismic reflection method or presentation of data was designed as a technique for delineating overburden stratigraphy and bedrock topography (Pullan and Hunter, 1990). The technique involves the selection of an optimum source-receiver separation which allows the target reflection to be observed with a minimum



**Figure 1.** Location of the Anderson Road borehole. The high resolution seismic reflection line extends parallel to the road, north-northeastward about 300 m from the borehole.

of interference from other seismic events. The vertical resolution of the subsurface is dependent on the transmission and recording of high frequency seismic energy, and is generally highest when surface sediments are fine grained and water saturated. This area is an excellent site for high resolution seismic surveys, and reflections with a dominant frequency of 500 Hz were recorded (3 m wavelength).

The source-receiver offset for the seismic section shown in this report is 12 m. The source was a 12 gauge Buffalo gun (Pullan and MacAulay, 1987) and the receivers were single, 100 Hz, vertically oriented geophones planted in the bottom of the roadside ditch at intervals of 3 m. A Bison D9000 engineering seismograph was used to collect and record the data. Low cut and high cut filters of 192 and 2000 Hz, respectively, were applied. A 100 ms record, comprised of 1000 samples, was recorded at each geophone location. Final processing prior to presentation consisted of shifting each trace to align the first arrival (the refraction from the water table) to a single datum, applying a 300 to 800 Hz digital band-pass filter, and modifying the display with automatic gain control and time-varying gain tapers.

An average overburden velocity of 1500 m/s, calculated from the moveout of various reflection events on the multichannel records, is confirmed by the agreement between the depth to bedrock determined from the borehole and that calculated from the time of arrival of the bedrock reflection on the seismic record and the overburden velocity.

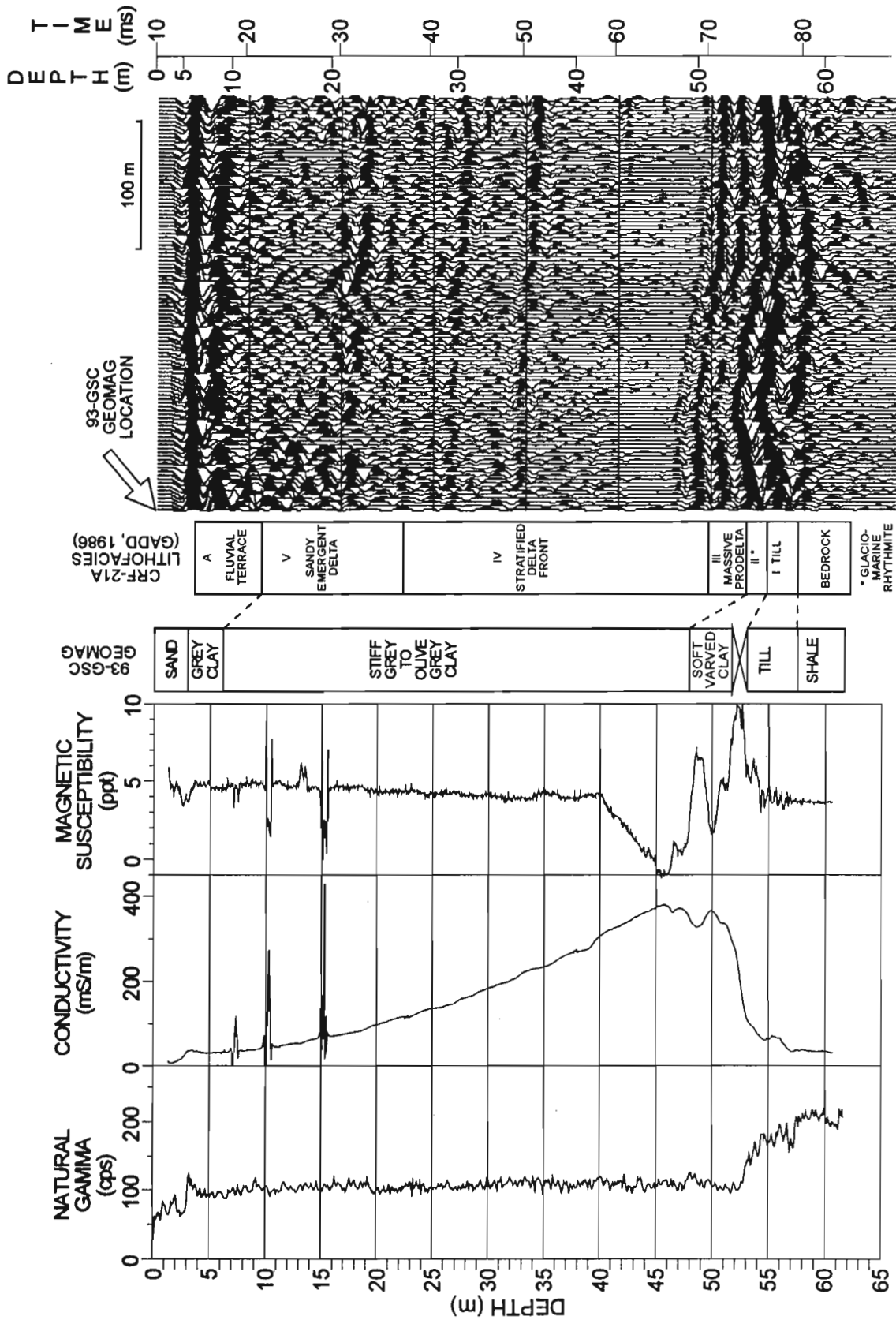
## BOREHOLE GEOPHYSICAL METHODS

In March 1993, a 62.5 m borehole was drilled at the south end of the seismic line, near the intersection of Anderson Road with the driveway of the GSC Geomagnetic Laboratory. The hole is tentatively identified as GSC-93 GEOMAG. Although the hole was continuously sampled using Shelby tubes, at the time of the preparation of this report, the cores have not been extruded. Figure 2 includes a lithological log based on the on-site inspection of the cored material that was exposed at the ends on the tubes, or was observed on the bit between trips to sample. The hole was cased with 2.5 inch I.D. plastic pipe, the bottom 3.3 m of which was perforated to allow the hole to be used as a ground water monitoring well for the bedrock aquifer. After drilling, the hole was logged using a Geonics EM-39 logging system. Successive passes with the conductivity and magnetic susceptibility probes (which utilize an inductive electromagnetic method) and the natural gamma probe, were recorded digitally on a laptop computer linked to the EM-39 logger.

The effective measurement radius of the conductivity probe is estimated to be 1 to 1.5 m, and as the tool is claimed by the manufacturer to be unaffected by fluids in plastic casing, the conductivity measured is taken to be that of the surrounding formation and associated ground water.

The magnetic susceptibility probe measures how strongly the material adjacent to the borehole is affected by a magnetic field, in this case the Earth's field. It is accepted that the





**Figure 2.** EM-39 borehole logs and high resolution seismic section at the Anderson Road borehole. Mis-ties between log depths and the calculated seismic section depth, particularly at shallow depths, are due to the 12 m offset between source and receiver. The lithofacies classification from a borehole CRF-21A is from Gadd (1986).

overall susceptibility of a lithology is dependent only on the amount of ferrimagnetic mineral, such as magnetite, pyrrhotite, and ilmenite, present in the material.

The gamma tool detects the decay of uranium, thorium, and potassium in the environment, although for practical purposes the tool provides a qualitative measurement of the abundance of clay in the strata surrounding the borehole. Low gamma readings are an indication of coarse grained sediments, and high gamma readings are attributable to fine grained materials; although it is important to consider the provenance of the strata when interpreting the results.

## RESULTS

Figure 2 shows the southern-most 324 m of the 1600 m seismic line shot in the ditch adjacent to Anderson Road. An abbreviated lithological log and the results of the EM-39 logging are superimposed at the borehole location to allow comparison of the data. In addition, the figure shows Gadd's (1986) stratigraphic log for borehole CRF-21A, drilled nearby, adjusted to the same bedrock elevation as the new hole.

A reflection event at 79 ms two-way travel time is interpreted to represent the top of bedrock. The calculated depth to bedrock from ground level, based on an average overburden acoustic velocity of 1500 m/s (below the water table), is 58 m. Bedrock consists of very dark grey Ordovician shale, probably of the Carlsbad Formation. It is characterized on EM-39 logs by a high gamma count, low conductivity, and very uniform magnetic susceptibility.

The prominent reflection, at 73 ms (53.5 m, calculated) is interpreted, on the basis of sample and EM-39 logs, to represent the top of ice contact deposits consisting of olive grey to pinkish grey clayey silt with shale clasts and garnet-rich gneiss cobbles. EM-39 logs show low conductivity, variable magnetic susceptibility, and a gamma count which increases from 100 counts per second at the top of the till to 175 counts per second at the bottom. This gamma count is high for a till, and is probably due to the elevated level of radioactivity inherent in the Precambrian material incorporated in the till and to a significant component of radioactive Paleozoic bedrock.

A moderate amplitude reflection event at 66 ms two-way travel time (48 m, calculated), followed by a pair of high amplitude 'rings', marks the top of a clay unit overlying the till. Samples of clay below this contact are recorded as being slightly softer than those above, and some loss of sample due to wash-out indicates less cohesion and more permeability. Conductivity is very high, perhaps because of provenance and mineralogy, or due to the infiltration of saline water from the unit above it. The gamma log indicates that this unit may have a slight fining upward trend, and the magnetic susceptibility is highly variable in this interval. In a nearby borehole, Gadd (1986) assigned this unit to a glaciomarine or glaciolacustrine rhythmic facies of the Leda clay, deposited during an early, freshwater phase of the Champlain Sea.

An acoustically transparent unit exists from 59 to 66 ms two-way travel time (43 to 48 m, calculated). Conductivity is very high at the base of the unit and, if it is interpreted in terms of pore water chemistry, indicates a salinity of approximately 3000 ppm, slightly lower than estimates of salinity based on foraminiferal assemblages in the western basin of the Champlain Sea (Rodrigues, 1987). This unit may correspond to the massive prodelta facies of Gadd (1986). The magnetic susceptibility log shows a uniform and rapid increase upward through this interval. Such a change may indicate a mineralogical change in the sediment due to provenance, subareal weathering environment, depositional environment, or diagenesis.

The reflections above this unit, at 49, 41, 36, and 31 ms (35, 29, 25, and 21 m, calculated), exhibit uniform characteristics and appear to characterize a common lithological unit. The reflections are parallel and conformable. Subordinate reflections visible within each sequence are not well defined. The gamma log records minor coarsening upward sequences throughout this unit. The magnetic susceptibility log shows a slight step-wise increase upward through the unit. This may be correlated with Gadd's (1986) stratified delta front facies. Conductivity declines upward through this sequence, coinciding with Rodrigues' (1987) observation of declining salinity upward through the Leda clay, and perhaps corresponding to the more proximal shift in the depositional environment.

The unit bounded by prominent reflections at 15 and 31 ms (7 to 21 m, calculated), is quite different from underlying units in that it does not exhibit the same amount of internal organization. On the gamma log this unit may be differentiated from that underlying it by the frequency of the changes in the count rate, perhaps due to the thickness of the bedded units. According to the gamma log, the sediment gradually fines downward, to 19.5 m below ground level (approximately 30 ms two-way travel time), where it becomes slightly coarser and the gamma counts begin to fluctuate with greater frequency. This boundary is also recorded by a minor change in magnetic susceptibility. The conductivity log maintains a decrease upward, and if its response is due primarily to the salinity of connate water, then the trend toward declining salinity is again in agreement with Rodrigues (1987). This unit corresponds stratigraphically with Gadd's (1986) sandy emergent delta facies in the nearby Mer Bleue borehole, but the lithology of this unit appears to be predominately silty clay. This unit contains three conductivity and magnetic susceptibility anomalies, at 7, 10, and 15 m, probably not related to borehole lithologies. Each anomaly spans approximately 1.5 m of depth, and none appear on the gamma log. The origin of the anomalies is unknown at present. A positive magnetic susceptibility anomaly at 13 m may be related to a mineralogical change in the sediment.

The seismic record cannot be used to delineate structure in the very shallow subsurface (above 15 ms, or 7 m depth) because of the interference between shallow reflections and refracted wave arrivals. Lithologically the surficial unit consists of 3 m of grey or oxidized sand with minor rhythmic clay overlying 3 m of grey clay containing some brown

organic material and featuring some rounded pebbles of mixed lithology at its base. It is not known yet how much of the surficial material may be fill used to landscape the site, although given the terrain in the immediate vicinity it is unlikely that the fill is more than 1 m thick. The clay unit shows the continuation of the upward diminishing conductivity trend, followed by an abrupt reduction in the conductivity corresponding to the sandy surficial layer. The gamma log marks the upward transition from clay to sand at 3 m with a significant drop in the count rate which would result from a decline in the amount of clay in the surrounding strata. The magnetic susceptibility also decreases in the sandy zone, marking lower concentrations of magnetic material, perhaps through oxidation. Gadd (1986) suggests that this type of lithology represents overbank flooding of proto-Ottawa River floodplains and terraces during progradation into the regressing Champlain Sea.

## SUMMARY

A 62 m borehole drilled to bedrock just east of Ottawa, passed through 57.5 m of unconsolidated sediments. Gamma, conductivity, and magnetic susceptibility logs show good correlation with a high resolution, shallow seismic reflection survey at the site. Cores taken during drilling will be extruded and analyzed at Carleton University. The detailed lithostratigraphy that will be available may explain the conductivity and magnetic susceptibility anomalies at 7, 10, 13, and 15 m below ground level.

Excluding the relatively nonconductive till and bedrock at the bottom of the hole, the conductivity increases, at an increasing rate, with depth. Assuming that the log is reacting primarily to pore water chemistry (i.e. that there is not an increasing concentration of conductive minerals with depth), it indicates increasing salinity with depth. The conductivity at the base of the clay unit suggests a salinity of approximately 3000 ppm. Whether the conductivity trend confirms the decrease, through time, of the salinity of the Champlain Sea determined from foraminiferal assemblages, or marks dilution of saline water by fresh ground water, is unknown.

The gamma log and the seismic record indicate that the 47 m thickness of Leda clay in the borehole may be subdivided into four units. According to Gadd's (1986) lithofacies analysis, these units mark the postglacial immersion of the site in a glaciolacustrine setting, followed by marine incursion by the Champlain Sea. The subsequent regression is recorded in the vertical progression from deep water marine sediments to deltaic overbank deposits.

## ACKNOWLEDGMENTS

Our thanks to R.A. Burns, R. Good, and B.J. Todd who played key roles in the collection of the seismic data in less than perfect weather. S.R. Dallimore stood in at the rig on short notice and his help is gratefully acknowledged. We thank also Molly and Lloyd of Marathon Drilling. The text was improved by S.E. Pullan, and we thank R.J. Fulton and J.A.M. Hunter for critically reviewing the manuscript.

## REFERENCES

- Gadd, N.R.**  
 1986: Lithofacies of Leda clay in the Ottawa basin of the Champlain Sea; Geological Survey of Canada, Paper 85-21.  
 1987: Quaternary evolution of the Ottawa area; in *Quaternary of the Ottawa Region and Guides for Day Excursions*, (ed.) R.J. Fulton; International Union for Quaternary Research, XII<sup>th</sup> International Congress, p. 75-80.
- Pullan, S.E. and Hunter, J.A.M.**  
 1990: Delineation of buried bedrock valleys using the optimum offset shallow seismic reflection technique; in *Geotechnical and environmental geophysics, Volume III: Geotechnical*, (ed.) S.H. Ward; Society of Exploration Geophysicists, p. 75-87.
- Pullan, S.E. and MacAulay, H.A.**  
 1987: An in hole source for engineering seismic surveys; *Geophysics*, v. 52, p. 985-996.
- Rodrigues, C.G.**  
 1987: Late Pleistocene invertebrate microfossils, microfossils and depositional environments of the western basin of the Champlain Sea; in *Quaternary Geology of the Ottawa Region, Ontario and Quebec*, (ed.) R.J. Fulton; Geological Survey of Canada, Paper 86-23, p. 17-23.

Geological Survey of Canada Project 920039.



# Géochimie des roches volcaniques cambro-ordoviciennes du Groupe de Shickshock: incidences sur la stratigraphie et le contexte géotectonique de la Gaspésie septentrionale

G. Camiré, M.R. La Flèche<sup>1</sup>, et M. Malo<sup>1</sup>  
Centre géoscientifique de Québec, Sainte-Foy

*Camiré, G., La Flèche, M.R., et Malo, M., 1993 : Géochimie des roches volcaniques cambro-ordoviciennes du Groupe de Shickshock: incidences sur la stratigraphie et le contexte géotectonique de la Gaspésie septentrionale; dans Recherches en cours, Partie E; Commission géologique du Canada, Étude 93-1E, p. 281-290.*

---

**Résumé :** L'étude des roches volcaniques du Groupe de Shickshock montre que les laves affleurant au lac Matapédia ne sont ni chimiquement ni pétrogénétiquement associées à celles des monts Chic-Chocs et que le Groupe de Shickshock est restreint à la nappe du mont Logan. Les laves du lac Matapédia sont composées de basaltes alcalins à transitionnels, enrichis en terres rares légères ( $[La/Yb]_N = 4,2 \pm 1,9$ ) et en éléments incompatibles (Ti, Ta, Nb, Hf, Zr), et celles du Groupe de Shickshock, de deux unités de basaltes tholéiitiques: l'une, légèrement enrichie en terres rares légères ( $[La/Sm]_N = 1,2 \pm 0,2$ ) et l'autre, appauvrie ( $[La/Sm]_N = 0,8 \pm 0,1$ ). La mise en place des basaltes alcalins du lac Matapédia a marqué l'ouverture d'un rift continental dans lequel la sédimentation clastique était nettement dominante et a vraisemblablement précédé celle des tholéiites du Groupe de Shickshock, extraites à plus faible pression.

**Abstract:** The study of the volcanic rocks of the Shickshock Group reveals that lavas outcropping at Matapédia Lake are neither chemically nor petrogenetically associated with lavas of the Chic-Chocs Mountains and that the Shickshock Group is restricted to the Mount Logan Nappe. The Matapédia Lake lavas are composed of alkaline to transitional basalts, enriched in light rare earth ( $[La/Yb]_N = 4.2 \pm 1.9$ ) and incompatible (Ti, Ta, Nb, Hf, Zr) elements, while those of the Shickshock Group contain two tholeiitic basalt units, one slightly enriched ( $[La/Sm]_N = 1.2 \pm 0.2$ ) and the other, impoverished ( $[La/Sm]_N = 0.8 \pm 0.1$ ) in light REEs. The emplacement of the alkaline Matapédia Lake basalts marked the opening of a continental rift in which clastic sedimentation clearly dominated, and likely preceded that of the Shickshock Group tholeiites, which were extracted at lower pressures.

---

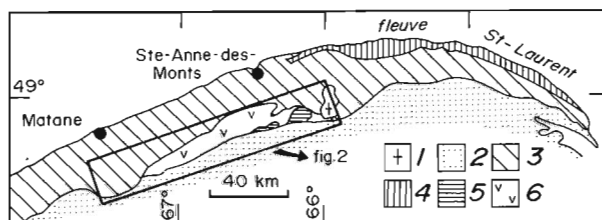
<sup>1</sup> INRS-Géoresources, 2700 rue Einstein, C.P. 7500, Qc, G1V 4C7

## INTRODUCTION

Les roches cambro-ordoviciennes de la partie nord des Appalaches sont réparties entre les zones de Dunnage et de Humber, vestiges respectifs des domaines océanique et continental ordoviciens, amalgamés au cours de l'orogénèse taconienne le long de la ligne Baie Verte – Brompton (Williams et St-Julien, 1982). La géométrie sinueuse de la zone de Humber suit l'ancienne marge du continent nord-américain, formée de promontoires et de rentrants hérités de la taphrogénèse de cette dernière à la fin du Cambrien ou au début du Paléozoïque (ex., Thomas, 1991). Les laves mafiques du Groupe de Shickshock forment le plus important ensemble continu de roches volcaniques de la zone de Humber dans le rentrant de Québec. Sur la base d'associations lithologiques, elles ont été interprétées par St-Julien et Hubert (1975) et Slivitzky et al. (1991) comme des dépôts de rift ou de marge passive appartenant à la zone de Humber et par Lux (1986), comme faisant partie d'une nappe ophiolitique qui aurait été transportée de la zone de Dunnage à sa position actuelle dans la zone de Humber.

Les terrains cambro-ordoviciens de la Gaspésie ont été subdivisés par St-Julien et Hubert (1975) en trois domaines tectoniques qui sont, du nord-ouest au sud-est, le domaine des failles de chevauchement imbriquées, le domaine des nappes externes et le domaine des nappes internes (fig. 1). D'après St-Julien et Hubert (1975) et Vallières (1984), le Groupe de Shickshock est situé à la base stratigraphique du Supergroupe de Québec et du domaine interne taconien, et il serait un équivalent des formations de Tibbit Hill et de la Montagne de Saint-Anselme, des volcanites de Saint-Flavien et du Groupe de Maquereau.

Les roches du Groupe de Shickshock affleurent dans deux régions: sur la rive est du lac Matapédia et dans les monts Chic-Chocs. La position stratigraphique du Groupe de Shickshock a été établie d'après les relations des roches du lac Matapédia avec les séquences sédimentaires environnantes. Or, l'aspect général, les proportions entre roches sédimentaires et volcaniques ainsi que le degré de déformation et de métamorphisme des roches du Groupe de Shickshock sont nettement différents d'une région à l'autre. Afin d'éclaircir ces problèmes de corrélation régionale, on a



**Figure 1.** Unités tectono-stratigraphiques de la Gaspésie septentrionale (d'après Slivitzky et al., 1991). Silurien et Dévonien: 1 = roches intrusives; 2 = roches sédimentaires et volcaniques du synclinorium de Gaspé – Connecticut Valley. Cambrien et Ordovicien: 3 = domaine des nappes externes; 4 = domaine des failles de chevauchement imbriquées; domaine des nappes internes, 5 = nappe du mont Albert, 6 = nappe du mont Logan.

entrepris une étude géochimique des roches volcaniques du Groupe de Shickshock. Les résultats indiquent que les roches du lac Matapédia ne devraient pas être corrélées à celles des monts Chic-Chocs et l'on propose que l'usage du terme «Groupe de Shickshock» soit restreint aux roches volcaniques et sédimentaires de la nappe du mont Logan. Les roches volcaniques et sédimentaires du lac Matapédia, jusqu'à présent attribuées au Groupe de Shickshock, sont ci-après désignées sous le terme d'«unité du lac Matapédia».

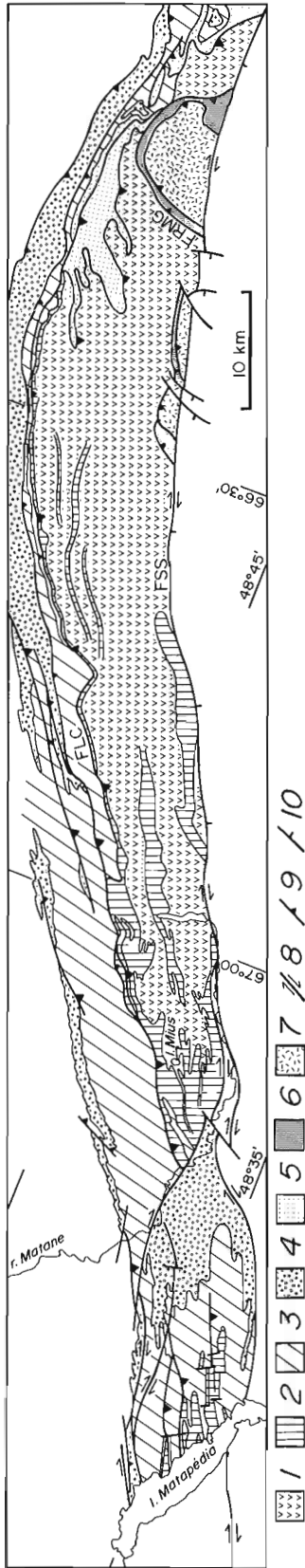
## TRAVAUX ANTÉRIEURS

Des cartes géologiques partielles du Groupe de Shickshock ont été levées par Dresser et Dennis (1944), Osborne et Archambault (1948), MacGregor (1962, 1964), Mattinson (1964), Girard (1967), Ollerenshaw (1967), Aumento (1969), Carrara (1972) et Beaudin (1980, 1984). Les travaux de cartographie les plus détaillés demeurent ceux de Mattinson, d'Ollerenshaw et de Beaudin qui ont subdivisé le Groupe de Shickshock en unités lithologiques informelles.

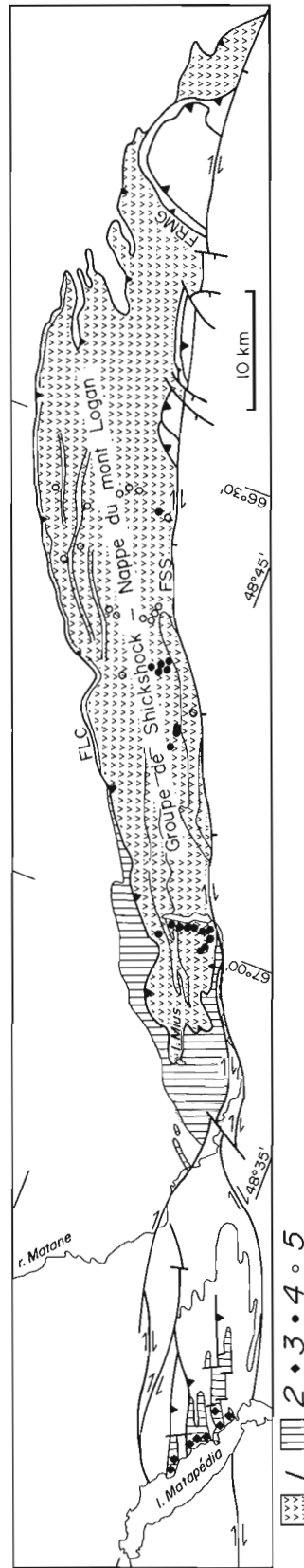
Bien que le Groupe de Shickshock tire son nom de la chaîne des monts Chic-Chocs (toponyme actuel) qui se termine à la rivière Matane (fig. 2), l'unité d'arkoses et de basaltes affleurant sur la rive est du lac Matapédia a généralement été considérée depuis les travaux de Crickmay (1932) comme la section type du groupe. Les cartes géologiques régionales, réalisées avant le début des années 1950, montrent que les roches présentes dans les monts Chic-Chocs se poursuivent jusqu'au lac Matapédia. Considérant que les roches du lac Matapédia ne sont pas typiques des roches de la chaîne des monts Chic-Chocs, McGerrigle a publié, en 1953, une carte géologique de la Gaspésie sur laquelle la «série des Shickshocks» se termine abruptement à l'est de la rivière Matane. Cette interprétation a été reprise par Mattinson en 1958, mais contestée par Ollerenshaw, (1967) qui a soutenu que les roches des deux localités étaient corrélables en dépit du degré de métamorphisme et de déformation plus élevé des roches des monts Chic-Chocs.

## CONTEXTE GÉOLOGIQUE

Le Groupe de Shickshock (Hadrymien ? à Cambrien précoce ?; Slivitzky et al., 1991), tel que défini ci-après, est limité à la nappe du mont Logan (fig. 3). Du nord vers l'ouest, celle-ci chevauche les roches sédimentaires cambriennes et ordoviciennes des formations de l'Orignal et de Rivière-du-Loup (Slivitzky et al., 1991) et les roches volcaniques et sédimentaires de l'unité du lac Matapédia (présent rapport) le long de la faille du lac Cascapédia (Beaudin, 1980; Slivitzky et al., 1991). Elle est à son tour chevauchée par la nappe ophiolitique du mont Albert (fig. 2) (Gagnon et Jamieson, 1985; Lux, 1986) le long de la faille du ruisseau des Marches du Géant. Au sud-est, la nappe du mont Logan se termine à la faille de Shickshock-Sud, une structure composite (Malo et al., 1992) interprétée comme une faille acadienne (Dévonien moyen à tardif) de décrochement dextre



**Figure 2.** Carte géologique simplifiée du Groupe de Shickshock et des unités sédimentaires cambro-ordoviennes environnantes (modifiée de Slivitzky et al., 1991). Groupe de Shickshock: 1 = roches volcaniques (et roches sédimentaires en faible proportion), 2 = roches sédimentaires (et roches volcaniques en faible proportion). 3 = roches sédimentaires de la formation de Rivière-du-Loup. 4 = roches sédimentaires de la formation de Romieu. 5 = roches sédimentaires de la Formation de l'Original. Complexe du mont Albert: 6 = amphibolite du Diable, 7 = roches ultramafiques du mont Albert. 8 = faille de décrochement dextre. 9 = faille de chevauchement. 10 = faille normale. FLC = faille du lac Caspédia; FSS = faille de Shickshock-Sud; FRMG = faille du ruisseau des Marches du Géant.



**Figure 3.** Modifications suggérées aux limites du Groupe de Shickshock et de la nappe du mont Logan. 1 = roches volcaniques et sédimentaires du Groupe de Shickshock (nappe du mont Logan). 2 = roches volcaniques et sédimentaires de l'unité du lac Matapédia (nappe de la rivière Ste-Anne). Localisation des échantillons dont les compositions sont compilées au tableau 1: 3 = basaltes alcalins à transitionnels de l'unité du lac Matapédia; Groupe de Shickshock: 4 = tholéïtes enrichies, 5 = tholéïtes appauvries.

(Berger, 1985; Lebel, 1985) superposée à une faille taconienne (Ordovicien moyen à tardif) plus ancienne dont les mouvements restent à déterminer.

À l'intérieur de la nappe du mont Logan (fig. 3), le Groupe de Shickshock a été affecté par au moins trois phases de plissement. Les deux premières, tout comme le métamorphisme régional, sont attribuées à l'orogénèse taconienne et la dernière à l'orogénèse acadienne (Carrara et Fyson, 1973). Toutes les roches montrent une schistosité régionale  $S_1$  définie par l'alignement des amphiboles et des chlorites dans les roches mafiques et par celle des minéraux micacés, des opaques et des quartz dans les roches sédimentaires. La linéation d'allongement ( $L_1$ ), oblique sur  $S_1$ , est faiblement plongeante et sub-parallèle à la chaîne appalachienne (Camiré et al., 1993). Le métamorphisme augmente vers le sud-est, du faciès des schistes verts au faciès des amphibolites, et culmine aux abords de la faille de Shickshock-Sud. Le Groupe de Shickshock est principalement constitué de roches métavolcaniques mafiques. De minces horizons de roches métasédimentaires (arkoses, pélites, conglomérats et calcaires), aux contacts cisailés ou concordants, sont intercalés dans l'empilement volcanique.

L'unité du lac Matapédia fait partie de la nappe de la rivière Sainte-Anne (Slivitzky et al., 1991) comme les roches sédimentaires de la Formation de Rivière-du-Loup qui la recouvrent en concordance (Ollerenshaw, 1967; Slivitzky et al., 1991). On inclut dans l'unité du lac Matapédia les roches sédimentaires et volcaniques, jusqu'à présent attribuées au Groupe de Shickshock, qui sont situées à l'ouest et au nord du lac Mius dans les monts Chic-Chocs (fig. 3). Contrairement aux roches de la nappe du mont Logan, les roches de l'unité du lac Matapédia, très faiblement métamorphosées (sous faciès des schistes verts ?) sont dominées par la présence de grès arkosiques mal classés plutôt que par celle de roches volcaniques.

## PÉTROGRAPHIE DES ROCHES VOLCANIQUES

Les roches volcaniques du Groupe de Shickshock sont composées de coulées coussinées, par endroits amygdalaires ou bréchiformes, de filons-couches métagabbroïques de quelques mètres d'épaisseur et de rares horizons tuffacés. La schistosité  $S_1$  est très bien développée et aucune microtexture primaire n'a été conservée. On y observe les paragenèses suivantes (compositions déterminées à la microsonde électronique): (1) faciès des amphibolites : magnésio-hornblende + plagioclase ( $An_{17-27}$ ) + quartz + ilménite ± Mg-ripidolite ± épidote ± magnétite, (2) faciès épidote-amphibolite transitionnel: magnésio-hornblende + albite + quartz + épidote + chlorite (brunsvigite ou pycnochlorite) + ilménite ± actinote, (3) faciès des schistes verts : actinote + albite + quartz + chlorite (brunsvigite, pycnochlorite et/ou diabantite) + leucoxène ± épidote ± calcite. Des vestiges d'augite sont présents par endroits dans les schistes verts. La pyrite est une phase accessoire commune mais non abondante.

Les roches mafiques de l'unité du lac Matapédia sont composées de coulées par endroits coussinées, de dykes et de filons-couches. Les microtextures microlitiques ou porphyriques primaires sont bien conservées, mais les phases minérales sont plus ou moins altérées. Des cristaux de labradorite ( $An_{65}$ ) et d'augite (jusqu'à 2 mm de long) ont été conservés sur certains affleurements bien que le plagioclase calcique et le clinopyroxène soient presque partout pseudomorphosés par de l'albite et de la chlorite (brunsvigite ou pycnochlorite). Cette dernière est omniprésente dans la matrice où l'on observe également des plages d'hématite et d'ilménite. L'épidote, le leucoxène, la titanite, le quartz et la calcite sont des phases accessoires communes.

## GÉOCHIMIE

Méthode analytique. Les échantillons ont été pulvérisés dans un mortier en agate et analysés aux laboratoires de l'INRS-Géoresources. Les éléments majeurs et les éléments de Zr, Y, Sr, Nb, Rb, Cr, Ni et V ont été analysés par spectrométrie de fluorescence X; la précision analytique est estimée à plus de 1 % pour les éléments majeurs et à plus de 5 % pour les traces. Les autres éléments traces ont été analysés par activation neutronique; la précision pour le Sc, Ba, Ta, Hf, Th, U, La, Ce, Sm, Eu et Yb est estimée à plus de 5 % et celle pour le Nd, Tb, et Lu entre 5 % et 10 %.

La plupart des échantillons sont peu altérés; leurs indices de peraluminosité sont inférieurs à 1 et leurs indices d'altération (Hashiguchi, et al., 1983) se situent autour de  $A.I. = 35$ , la valeur obtenue pour les basaltes des dorsales médio-océaniques (fig. 4a et 4b). Les échantillons ne montrent pas d'évidence de cumulation (fig. 4c) et ils peuvent être utilisés sur certains diagrammes de discrimination tectonique.

### *Roches volcaniques du Groupe de Shickshock*

Les roches volcaniques du Groupe de Shickshock se divisent en deux sous-unités de basaltes tholéitiques différenciés (tableau 1 et fig. 5) sur la base de leurs contenus en terres rares légères (fig. 6). La première est constituée de tholéites légèrement enrichies ( $[La/Sm]_N = 1,1 \pm 0,2$ ) qui affleurent dans la partie sud-ouest de la nappe du mont Logan (fig. 3) et la seconde, de tholéites appauvries ( $[La/Sm]_N = 0,8 \pm 0,1$ ). L'absence d'anomalies d'Eu (fig. 6) porte à croire qu'il n'y a pas eu de fractionnement significatif ou de cumulation du plagioclase au cours de la différenciation magmatique et que celle-ci s'est produite sous des conditions relativement oxydantes. Les spectres plats des terres rares lourdes indiquent que la source mantellique (lherzolite) se situait à une profondeur moindre que le champ de stabilité du grenat au moment de l'extraction.

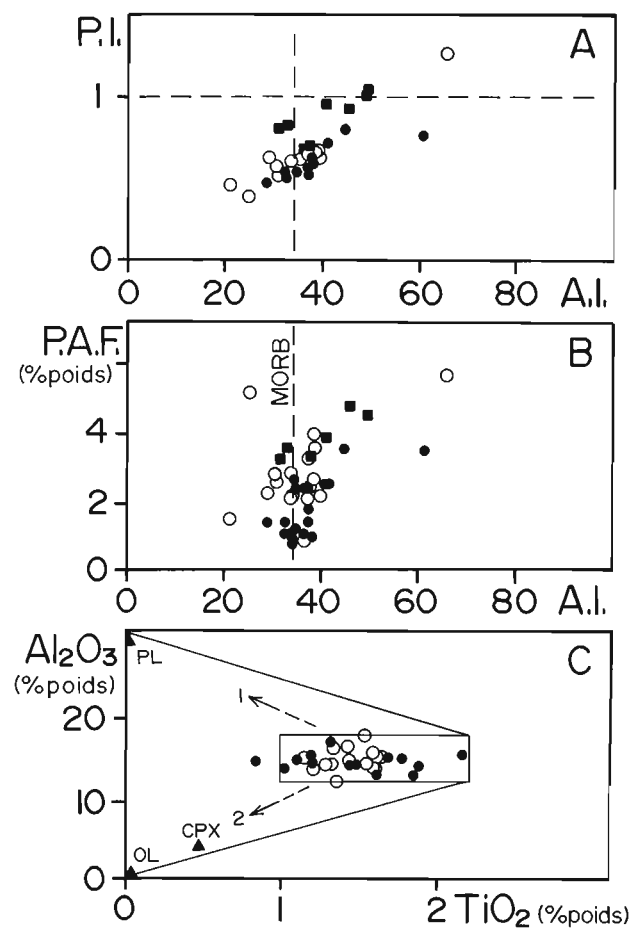
Le rapport Ta/Th moyen des tholéites du Groupe de Shickshock ( $= 1,02$ ) est près de la valeur obtenue pour les basaltes des dorsales médio-océaniques modernes ( $= 1,11$  dans les N-MORB, Sun et McDonough, 1989). Comme pour ces derniers, les rapports Ta/Th élevés des basaltes du Groupe de Shickshock semblent indiquer que leur source mantellique,



appauvrie en terres rares légères et en éléments hautement incompatibles, a été soumise à des processus antérieurs d'extraction magmatique. Toutefois, l'enrichissement relatif en Th et Ta par rapport à Hf des tholéiites du Groupe de Shickshock semble indiquer que leur source, moins appauvrie en éléments incompatibles que celle des N-MORB, a subi un taux moindre de fusion.

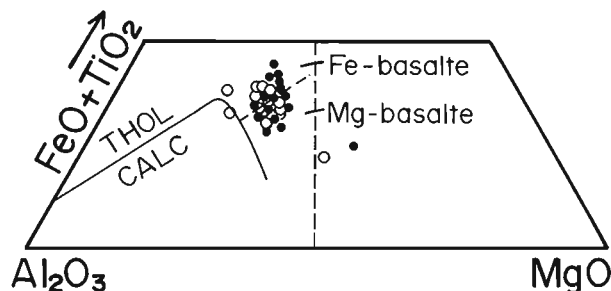
### Roches volcaniques de l'unité du lac Matapédia

La chimie des basaltes transitionnels à alcalins (fig. 7) de l'unité du lac Matapédia contraste nettement avec celle des tholéiites du Groupe de Shickshock. Ils sont enrichis en

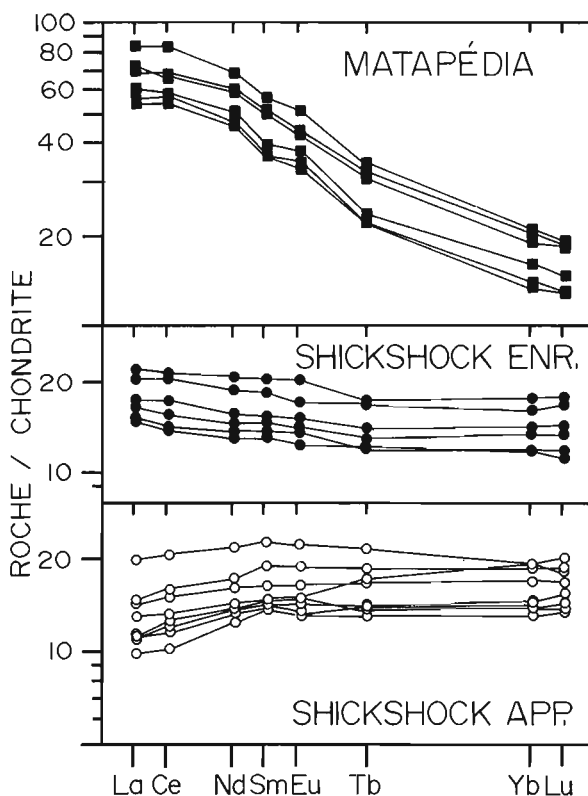


**Figure 4.** a) Variation de l'indice de peraluminosité (P.I. =  $Al_2O_3/[CaO+Na_2O+K_2O]$  mol.) en fonction de l'indice d'altération de Hashiguchi et al. (1983) (A.I. =  $100 \times (MgO+K_2O)/(MgO+K_2O+CaO+Na_2O)$  en % poids). Carrés = basaltes du lac Matapédia; points = tholéiites enrichies du Groupe de Shickshock; cercles = tholéiites appauvries du Groupe de Shickshock. b) Variation de la perte au feu (P.A.F.) en fonction de A.I. c)  $Al_2O_3$  vs  $TiO_2$ . L'encadré représente le champ des basaltes subalcalins non cumulatifs d'après Pearce (1989), le vecteur 1, la direction de cumulation du plagioclase et le vecteur 2, la direction de cumulation de l'olivine (OL) et du clinopyroxène (CPX). Les basaltes alcalins du lac Matapédia, riches en  $TiO_2$ , tombent à l'extérieur de cette figure.

éléments incompatibles, majeurs ( $TiO_2 = 3,94 \pm 0,92$  % poids et  $P_2O_5 = 0,66 \pm 0,28$  % poids) et à l'état de traces (Ta, Nb, Hf, Zr) (tableau 1). Les terres rares sont plus abondantes et les rapports  $[La/Yb]_N (= 4,2 \pm 1,9)$ , beaucoup plus fractionnés (fig. 6). Le fractionnement des terres rares n'est toutefois pas associé à la présence d'anomalies négatives en Ti, Nb et Ta et les roches de l'unité du lac Matapédia ne peuvent pas être interprétées comme des basaltes d'arc (ex. Briquieu et al., 1984). Les rapports  $[Tb/Yb]_N$  relativement élevés indiquent que les magmas parentaux ont probablement été extraits d'une source située dans le champ de stabilité du grenat (ex. lherzolite à grenat). Comme pour les basaltes du Groupe de



**Figure 5.** Diagramme ternaire de classification des roches volcaniques subalcalines (Jensen, 1974). Points = tholéiites enrichies et cercles = tholéiites appauvries du Groupe de Shickshock.



**Figure 6.** Spectres des terres rares normalisées aux valeurs des chondrites de Sun et McDonough (1989).

**Tableau 1.** Compositions moyennes des roches métavolcaniques et métasédimentaires du Groupe de Shickshock et des roches volcaniques de l'unité du lac Matapédia

	Lac Matapédia		groupe de Shickshock					
			THOL. ENR.		THOL. APP.		SÉD.	
	moy.	d.s.	moy.	d.s.	moy.	d.s.	moy.	d.s.
SiO <sub>2</sub>	46,97	2,56	49,42	2,03	48,51	2,80	57,78	3,44
TiO <sub>2</sub>	3,94	0,92	1,44	0,28	1,45	0,24	1,05	0,22
Al <sub>2</sub> O <sub>3</sub>	14,36	1,42	14,04	0,87	14,05	1,21	18,26	1,76
Fe <sub>2</sub> O <sub>3</sub>	13,69	1,93	13,12	1,42	12,57	1,24	7,76	1,35
MnO	0,24	0,06	0,22	0,02	0,21	0,02	0,11	0,03
MgO	6,19	1,39	7,13	0,73	7,08	2,04	2,67	0,57
CaO	4,98	0,64	10,6	1,81	9,66	2,66	3,29	1,99
Na <sub>2</sub> O	4,25	0,83	2,44	1,08	3,12	1,19	3,68	1,35
K <sub>2</sub> O	0,18	0,25	0,23	0,10	0,21	0,11	2,99	1,80
P <sub>2</sub> O <sub>5</sub>	0,66	0,28	0,15	0,03	0,14	0,02	0,24	0,09
p.a.f.	4,26	0,83	1,78	0,76	2,86	1,20	2,46	0,63
Rb	8	5	7	3	7	2	85	59
Sr	180	112	116	36	76	47	307	240
Ba	223	63	146	47			646	283
Zr	246	46	87	18	84	13	213	71
Y	48	9	34	6	34	6	37	10
Nb	35	8	17	3	14	4	16	5
Cr	88	76	217	89	153	85	67	19
Ni	37	21	83	23	69	22	39	14
V	470	134	510	117	481	117	163	60
La	21,6	4,3	6,1	1,2	4,4	1,0	38,6	10,8
Ce	54,4	10,8	15,3	3,2	11,7	2,6	83,9	23,2
Nd	33,9	6,4	10,3	2,2	8,9	1,8	41,0	12,0
Sm	9,1	1,5	3,5	0,7	3,3	0,6	8,5	2,5
Eu	3,15	0,51	1,27	0,24	1,24	0,28	2,15	0,44
Tb	1,40	0,23	0,72	0,17	0,74	0,13	1,07	0,32
Yb	4,07	0,91	3,19	0,71	3,24	0,59	3,42	1,03
Lu	0,59	0,16	0,49	0,11	0,52	0,08	0,49	0,14
Sc	38	6	44	4	48	4	20	5
Hf	6,2	0,9	2,2	0,5	2,1	0,4	6,0	1,7
Ta	1,58	0,50	0,42	0,07	0,42	0,09	0,85	0,16
Th	1,7	0,3	0,5	0,2	0,4	0,1	7,1	2,5
U	0,6	0,1	0,6	0,1	0,6	0,1	1,2	0,4
Zr/Y	5,2	0,8	2,5	0,2	2,5	0,3	5,8	1,4
[La/Yb] <sub>N</sub>	4,2	1,9	1,4	0,3	1,0	0,2	8,7	3,4
[La/Sm] <sub>N</sub>	1,6	0,4	1,1	0,2	0,8	0,1	3,0	0,7
[Tb/Yb] <sub>N</sub>	1,5	0,2	1,0	0,1	1,0	0,1	1,5	0,2
Mg#	51	8	56	4	56	6		
n	8		19		16		7	

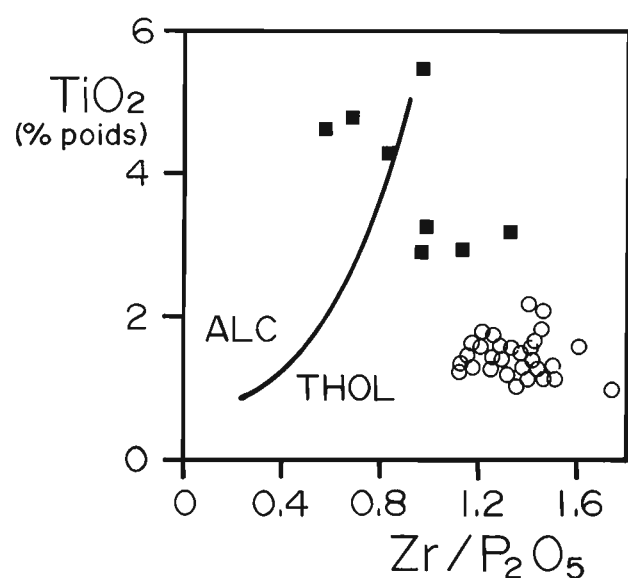
moy. = moyenne; d.s. = déviation standard; n = nombre d'analyses; Fe<sub>2</sub>O<sub>3</sub> = fer total;  
p.a.f. = perte au feu. THOL. ENR.: basaltes tholéitiques légèrement enrichis; THOL. APP.: basaltes tholéitiques appauvris; SÉD.: roches métasédimentaires. Mg# = 100 x (Mg/(Mg+Fe<sup>2+</sup>))(cations).

Shickshock, dont les contenus en terres rares sont inversement corrélés aux teneurs en MgO et Ni, des processus de cristallisation fractionnée à faible pression ont été impliqués dans la pétrogénèse des roches du lac Matapédia.

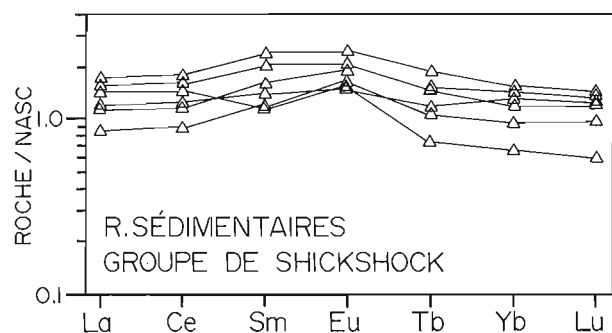
Les basaltes de l'unité du lac Matapédia ne sont pas reliés pétrogénétiquement (c.à.d. par cristallisation fractionnée ou assimilation crustale) aux tholéiites du Groupe de Shickshock, car pour un degré de différenciation à peu près identique ( $Mg\# = 51$ , tableau 1), ils sont très enrichis en éléments incompatibles.

### Roches sédimentaires du Groupe de Shickshock

Des roches sédimentaires du Groupe de Shickshock ont aussi été analysées. Leurs concentrations en terres rares étant comparables à celles du NASC (fig. 8), le «North American Shale Composite» compilé par Gromet et al. (1984), elles



**Figure 7.** Les basaltes alcalins à transitionnels du lac Matapédia (carrés), riches en  $TiO_2$  se distinguent nettement des tholéiites du Groupe de Shickshock (cercles) sur ce diagramme de classification de Winchester et Floyd (1976).



**Figure 8.** Spectres des terres rares normalisés aux valeurs du NASC ("North American Shale Composite" compilé par Gromet et al., 1984).

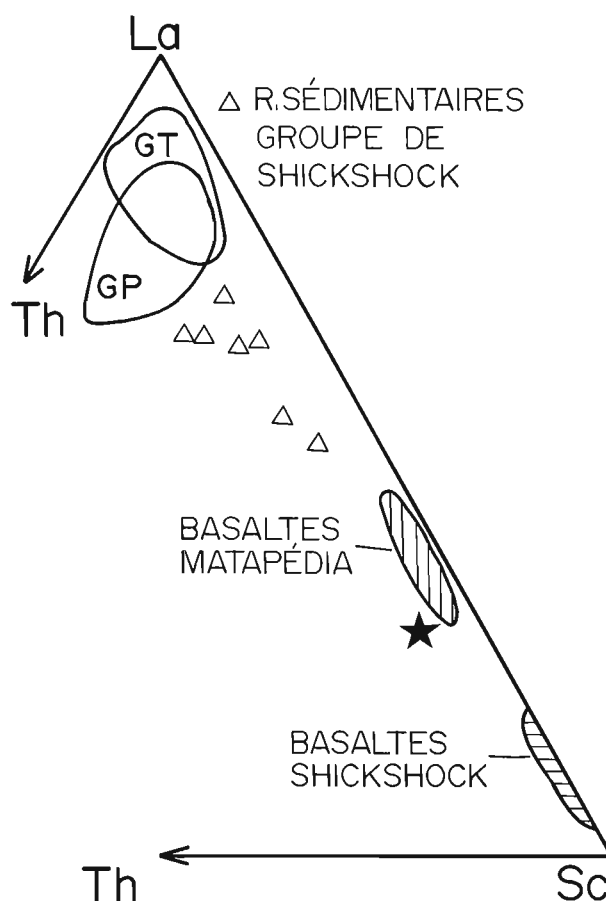
semblent dérivées d'une source évoluée, essentiellement d'origine continentale. Sur le diagramme de la figure 9 (La-Th-Sc), elles se situent près des champs des gneiss potassiques et tonalitiques de la province de Grenville. Sur un tel diagramme, les sédiments des dorsales et des arcs insulaires seraient situés beaucoup plus près du pôle du Sc.

## DISCUSSION ET CONCLUSIONS

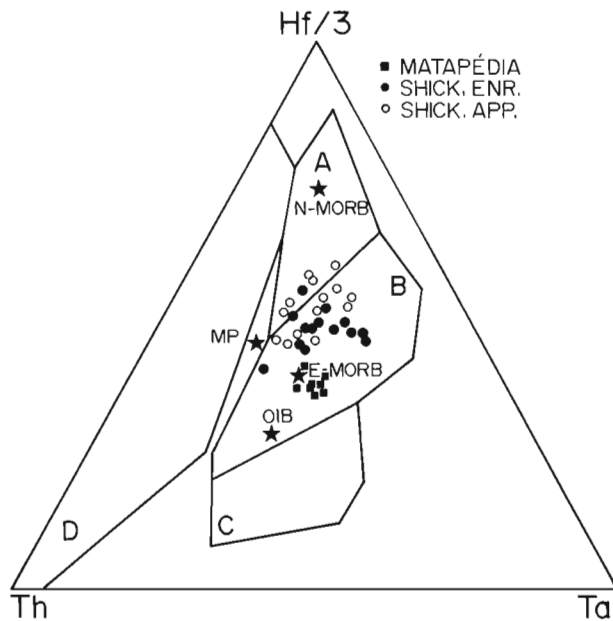
### Environnement géotectonique

Selon toute probabilité le milieu géotectonique de formation des tholéiites du Groupe de Shickshock et des basaltes alcalins à transitionnels de l'unité du lac Matapédia, bien que ces derniers ne soient pas reliés pétrogénétiquement, a été un rift continental.

Sur la figure 10 ( $Hf/3-Ta-Th$ ), les tholéiites du Groupe de Shickshock et les basaltes alcalins de l'unité du lac Matapédia ont des compositions approchant celles des basaltes enrichis des dorsales médio-océaniques (E-MORB) et, à un moindre



**Figure 9.** Diagramme La-Th-Sc. Les roches sédimentaires du Groupe de Shickshock (nappe du mont Logan) sont riches en La et dérivées d'une source sialique. Leurs compositions se situent près des champs des gneiss potassiques (GP, 35 analyses) et tonalitiques (GT, 50 analyses) de la province de Grenville (données non publiées de La Flèche et Birkett). Étoile = sédiments des arcs insulaires (Bhatia et Crook, 1986).



**Figure 10.** Diagramme (Hf/3)-Th-Ta de discrimination d'environnement tectonique de Wood et al. (1979) modifié par Pearce (1989). Les champs sont: A = basaltes normaux des dorsales médio-océaniques (N-MORB); basaltes intraplaques reliés à des plumes: B = basaltes enrichis des dorsales médio-océaniques (E-MORB) et C = basaltes des îles océaniques; D = basaltes d'arc reliés aux zones de subduction. Les compositions moyennes des OIB (basaltes des îles océaniques), N-MORB, E-MORB et MP (manteau primitif) sont tirées de Sun et McDonough (1989).

degré, celles des basaltes des îles océaniques (OIB), deux types de basaltes reliés à la présence de panaches mantelliques enrichies et qu'on retrouve le plus souvent dans des milieux intraplaque. Comparées aux basaltes normaux des rides mid-océaniques (N-MORB), les tholéiites du Groupe de Shickshock sont nettement enrichies en Th et Ta, signe de l'existence d'un milieu géotectonique de formation ou de mécanismes pétrogénétiques différents de ceux des N-MORB (ex., plus faible taux de fusion partielle, ou des deux). Des processus d'assimilation crustale ou de subduction ne semblent pas avoir été impliqués dans la formation des basaltes alcalins de l'unité du lac Matapédia ni dans celle des tholéiites du Groupe de Shickshock.

Les tholéiites du Groupe de Shickshock se distinguent des laves alcalines à transitionnelles des formations de Tibbit Hill (Pintson et al., 1985), de la Montagne de Saint-Anselme, de Saint-Flavien (Lafleche et al., sous presse) et du ruisseau Gagnon (Thivierge, 1992), auxquelles elles sont habituellement comparées, de la même façon qu'elles se distinguent des laves du lac Matapédia. La production de ces basaltes alcalins à l'intérieur d'un rift continental immature est supportée par (1) une source mantellique profonde (champ de stabilité du grenat) et par (2) la sédimentation clastique abondante (les roches sédimentaires dominent dans les formations où on retrouve des laves alcalines à transitionnelles), dérivée d'une source grenvillienne (Dia et al., 1990). Par contre, la chimie

des tholéiites du Groupe de Shickshock témoigne d'une atténuation presque complète de la lithosphère continentale qui a permis la montée de l'asthénosphère à faible profondeur et l'extraction des liquides basaltiques sous une faible pression. L'effusion des tholéiites du Groupe de Shickshock, accompagnée d'une sédimentation clastique peu abondante mais dérivée d'une source continentale, se serait ainsi produite dans un milieu de rift mature, transitionnel vers l'ouverture d'un bassin océanique. Dans un tel milieu, il faut envisager la possibilité que la péridotite du mont Albert puisse être le vestige d'un segment de diapir mantellique relié à l'ouverture, plutôt qu'un vestige ophiolitique relié à la fermeture du bassin.

### Stratigraphie

Puisque les basaltes du lac Matapédia ne peuvent, sur la base de leurs contenus en éléments à l'état de traces et en éléments majeurs, être corrélés à ceux des monts Chic-Chocs à l'est du lac Mius, ils ne devraient pas être inclus dans le Groupe de Shickshock, qui serait ainsi restreint à la nappe du mont Logan. De plus, l'on croit, pour les raisons suivantes, que la nappe du mont Logan se termine dans la région du lac Mius plutôt qu'à la rivière Matane (voir fig. 2 et 3). (1) Les roches volcaniques à l'ouest du lac Mius sont des basaltes alcalins à transitionnels, très peu déformés et métamorphisés dont la composition est en tous points semblable à celle des basaltes du lac Matapédia ( $[La/Yb]_N = 2,5$  et  $TiO_2 = 4,05$  % poids; données non publiées de C. Wilson, communiquées à K. Schrijver, février 1992). (2) Tel que l'a noté Ollerenshaw (1967), la séquence arkoses-roches volcaniques et sills et dykes du lac Matapédia est analogue à celle présente à l'extrémité ouest des monts Chic-Chocs. (3) Le changement dans les proportions relatives entre les roches volcaniques et sédimentaires est bien marqué à la longitude du lac Mius, où la quantité de roches volcaniques augmente brusquement. (4) À l'est du lac Mius, le Groupe de Shickshock ressemble manifestement peu à l'unité du lac Matapédia. Le changement se produit dans une zone où sont distribuées sporadiquement les roches «fraîches» (de type Matapédia) et les roches métamorphisées. Cette zone correspond vraisemblablement à la limite sinueuse de la nappe du mont Logan qui chevaucherait dans ce secteur l'unité du lac Matapédia. Le changement brusque du faciès métamorphique et le contraste lithologique marqué supportent l'existence d'une faille à la longitude du lac Mius, considérée ici comme la continuité probable de la faille du lac Cascapédia (fig. 3).

Puisqu'il existe des contacts concordants entre l'unité du lac Matapédia et la Formation de Rivière-du-Loup, qui font toutes deux partie de la nappe de la rivière Sainte-Anne, l'on suggère que l'unité du lac Matapédia soit incluse dans le Groupe de Trois-Pistoles plutôt que dans le Groupe de Shickshock. De plus, il est possible que l'unité du lac Matapédia soit en partie corrélable à l'unité des Pics, une unité informelle définie par Brisebois et al. (1991) et constituée de volcanites mafiques, de grès et de conglomérats. Dans les régions de Matane et de Dufaultville, l'unité des Pics est recouverte par la Formation de Rivière-du-Loup et contient des laves alcalines à transitionnelles, notamment au ruisseau Gagnon.

Dans un milieu de rift, il est fréquent que le magmatisme alcalin précède le magmatisme tholéiitique. Il est donc tout à fait possible que le Groupe de Shickshock soit plus jeune que l'unité du lac Matapédia en dépit de son degré de métamorphisme et de déformation plus élevé. Par conséquent, le Groupe de Shickshock ne devrait pas être considéré comme étant situé à la base stratigraphique du Supergroupe de Québec tant qu'il n'aura pas été daté.

Les travaux qui suivront au cours de l'année viseront à caractériser et à établir les relations pétrogénétiques, s'il en existe, entre la péridotite du mont Albert, l'amphibolite du Diable et le Groupe de Shickshock qui constituent un ensemble distinct de la zone de Humber et du domaine interne taconien de la chaîne appalachienne.

## REMERCIEMENTS

Isabelle Roy a assisté G. Camiré au cours des travaux de terrain. Les analyses chimiques ont été réalisées par Jean-Pierre Ricbourg, Réal Gosselin et Marc Greendale aux laboratoires de l'INRS-Géoressources. Jean Bédard a aimablement révisé le manuscrit.

## RÉFÉRENCES

- Aumento, F.**  
1969: Serpentine mineralogy of ultrabasic intrusions in Canada and on the mid-Atlantic Ridge; Commission géologique du Canada, étude préliminaire 69-53.
- Beaudin, J.**  
1980: Région du mont Albert et du lac Cascapédia; Ministère de l'Énergie et des Ressources du Québec, DPV-705.  
1984: Analyse structurale du groupe de Shickshock et de la péridotite alpine du mont Albert, Gaspésie; thèse de doctorat, Université Laval.
- Berger, J.**  
1985: Analyse structurale de la faille de Shickshock Sud en Gaspésie occidentale, Québec; mémoire de maîtrise, Université de Montréal.
- Bhatia, M. R. et Crook, K. A. W.**  
1986: Trace element characteristics of graywackes and tectonic setting discrimination of sedimentary basins; Contributions to Mineralogy and Petrology, v. 92, p. 181-193.
- Briqueu, L., Bougault, H. et Joron, J.-L.**  
1984: Quantification of Nb, Ta, Ti and V anomalies in magmas associated with subduction zones: petrogenetic implications; Earth and Planetary Sciences Letters, v. 68, p. 297-308.
- Brisebois, D., Lachambre, G. et Piché, G.**  
1991: Carte géologique de la Gaspésie; Ministère de l'Énergie et des Ressources du Québec, carte 2146 - DV 91-21.
- Camiré, G. E., Malo, M., et Tremblay, A.**  
1993: Étude structurale et métamorphique des roches cambro-ordoviciennes du groupe de Shickshock, Gaspésie septentrionale, Québec; dans: Recherches en cours, partie D; Commission géologique du Canada, étude 93-1D, p. 155-160.
- Carrara, A.**  
1972: Structural geology of Lower Paleozoic rocks, Mount Albert area, Gaspé Peninsula, Québec; thèse de doctorat, Université d'Ottawa.
- Carrara, A. et Fyson, W. K.**  
1973: Taconic and Acadian folds in northern and western Gaspé Peninsula, Québec; Revue canadienne des sciences de la Terre, v. 10, p. 498-509.
- Crickmay, G. W.**  
1932: Evidence of Taconic orogeny in Matapédia Valley, Quebec; American Journal of Science, v. 24, p. 368-386.
- Dia, A., Dupré, B., Gariépy, C. et Allègre, C. J.**  
1990: Sm-Nd and trace element characterization of shales from the Abitibi, Labrador Trough and Appalachian belts – Consequences for crustal evolution through time; Revue canadienne des sciences de la Terre, v. 27, p. 758-766.
- Dresser, J. A. et Dennis, T.**  
1944: Géologie du Québec; Ministère des Mines du Québec, RG-20.
- Gagnon, Y. et Jamieson, R. A.**  
1985: Geology of the Mount Albert region, Gaspé Peninsula, Québec; dans: Recherches en cours, partie A; Commission géologique du Canada, étude 85-1A, p. 783-788.
- Girard, P.**  
1967: Géologie de la région de mont Richardson; Ministère des Richesses Naturelles du Québec; RP-563.
- Gromet, L. P., Dymek, R. F., Haskin, L. A. et Korotev, R. L.**  
1984: The "North American Shale Composite" Its compilation, major and trace element characteristics; Geochimica et Cosmochimica Acta, v. 48, p. 2469-2482.
- Hashiguchi, H., Yamada, R. et Inoue, T.**  
1983: Practical application of low Na<sub>2</sub>O anomalies in footwall acid lava for delimiting promising areas around the Kosaka and Fukazawa Kuroko deposits, Akita Prefecture, Japan; Economic Geology, monograph 5, p. 387-394.
- Jensen, L. S.**  
1974: A new cation plot for classifying sub-alkalic volcanic rocks; Ontario Ministry of Natural Resources, Miscellaneous Paper 66.
- La Flèche, M. R., Schrijver, K. et Tremblay, A.,**  
sous presse: Cambrian alkaline basaltic rocks in and contiguous to a sector of the Appalachian Humber Zone, Canada; American Journal of Science.
- Label, D.**  
1985: Analyse structurale de la déformation acadienne, principalement la faille de Shickshock Sud dans la région de Rimouski-Matapédia; mémoire de maîtrise, Université de Montréal.
- Lux, D. R.**  
1986: <sup>40</sup>Ar/<sup>39</sup>Ar ages for minerals from the amphibolite dynamothermal aureole, mont Albert, Gaspé, Québec; Revue canadienne des sciences de la Terre, v. 23, p. 21-26.
- MacGregor, I. D.**  
1962: Geology, petrology and geochemistry of the Mount Albert and associated ultramafic bodies of central Gaspé, Québec; thèse de maîtrise, Queen's University.  
1964: A study of the contact metamorphism aureole surrounding the Mount Albert ultramafic intrusion; thèse de doctorat, Princeton University.
- Malo, M., Kirkwood, D., De Broucker, G. et St-Julien, P.**  
1992: A reevaluation of the position of the Baie Verte – Brompton Line in the Québec Appalachians: the influence of Middle Devonian strike-slip faulting in Gaspé Peninsula; Revue canadienne des sciences de la Terre, v. 29, p. 1265-1273.
- Mattinson, C. R.**  
1958: The geology of the Mount Logan area, Gaspé, Québec; thèse de doctorat, université McGill.  
1964: Région du mont Logan, comtés de Matane et de Gaspé-Nord; Ministère des Richesses Naturelles du Québec, RG-118.
- McGerrigle, H. W.**  
1953: Carte géologique de la péninsule de Gaspé; Ministère des Mines, Québec, carte 1000.
- Ollerenshaw, N. C.**  
1967: Région de Cuoq-Langis, comtés de Matapédia et de Matane; Ministère des Richesses Naturelles du Québec; RP-465.
- Osborne, F. F. et Archambault, M.**  
1948: Chromiferous chromite chlorite from Mount Albert, Québec; Société royale du Canada, transactions XLII, section IV, mai 1948.
- Pearce, J. A.**  
1989: A 'users guide' to basalt discrimination diagrams; dans: Oceanic basalts, édité par: J. Tarney, Shiva Publications.
- Pintson, H., Kumarapeli, P. S. et Morency, M.**  
1985: Tectonic significance of the Tibbit Hill volcanics: geochemical evidence from Richmond area, Québec; dans: Recherches en cours, partie A; Commission géologique du Canada, étude 85-1A, p. 123-130.
- St-Julien, P. et Hubert, C.**  
1975: Evolution of the Taconian orogen in the Québec Appalachians; American Journal of Sciences, v. 275-A, p. 337-362.

**Slivitzky, A., St-Julien, P. et Lachambre, G.**

1991: Synthèse géologique du Cambro-Ordovicien du nord de la Gaspésie; Ministère de l'Énergie et des Ressources du Québec, ET 88-14.

**Sun, S. S. et McDonough, W. F.**

1989: Chemical and isotopic systematics of oceanic basalts: implications for mantle composition and processes; dans: Magmatism in the ocean basins; édité par: A. D. Saunders and M. J. Norry; Geological Society Special Publication 42, p. 313-345.

**Thivierge, I.**

1992: Géologie et gîtologie du basalte du ruisseau Gagnon, Gaspésie; Ministère de l'Énergie et des Ressources du Québec, MB 92-01.

**Thomas, W. A.**

1991: The Appalachian-Ouachita rifted margin of southeastern North America; Geological Society of America Bulletin, v. 103, p. 415-431.

**Vallières, A.**

1984: Stratigraphie et structure de l'orogénie tectonique de la région de Rivière-du-Loup; thèse de doctorat, Université Laval.

**Williams, H. et St-Julien, P.**

1982: The Baie Verte-Brompton Line: early Paleozoic continent-ocean interface in the Canadian Appalachians; in: Major structural zones and faults of the Northern Appalachians; édité par: P. St-Julien et J. Béland; Association géologique du Canada, publication spéciale 24, p. 177-207.

**Winchester, J. A. et Floyd, P. A.**

1976: Geochemical magma type discrimination: application to altered and metamorphosed igneous rocks; Earth and Planetary Sciences Letters, v. 28, p. 459-469.

**Wood, D. A., Joron, J.-L. et Treuil, M.**

1979: A re-appraisal of the use of trace elements to classify and discriminate between magma series erupted in different tectonic settings; Earth and Planetary Sciences Letters, v. 45, p. 326-336.

---

Projet 92001 GP de la Commission géologique du Canada

# Tectonics along the Dog Bay Line – a Silurian terrane boundary in northeastern Newfoundland<sup>1</sup>

M.A.J. Piasecki<sup>2</sup>  
Continental Geoscience Division

*Piasecki, M.A.J., 1993: Tectonics along the Dog Bay Line – a Silurian terrane boundary in northeastern Newfoundland; in Current Research, Part E; Geological Survey of Canada, Paper 93-1E, p. 291-298.*

---

**Abstract:** In the northeastern Dunnage Zone, the Dog Bay Line is a well defined tectonostratigraphic boundary inclined steeply to the southeast. It separates fundamentally different Silurian successions, implying that it is a Silurian terrane boundary. In the coastal region, it is marked by a ductile shear zone. Inland, deformation becomes less intense and more brittle.

Deformation along the Dog Bay Line began in the Ordovician with the formation of a volcanic mélange. In the Silurian, the line became the site of intense shearing. Kinematic fabrics in the shear zone indicate that an early phase of ductile dextral transpression was followed by extensional relaxation (dip slip), and in turn by transcurrent dextral shearing, in a sequence of movements that extended from ductile to brittle. Minor southeast-over-northwest thrusting extended from ductile-brittle to brittle stages of deformation.

**Résumé :** Dans le nord-est de la zone de Dunnage, la ligne de Dog Bay est une limite tectonostratigraphique bien définie qui s'incline brusquement vers le sud-est. Elle sépare des successions siluriennes fondamentalement différentes, ce qui porte à croire qu'il s'agit d'une limite de terrane silurien. Dans la région littorale, elle se traduit par une zone de cisaillement ductile. Vers l'intérieur du continent, la déformation devient moins marquée et plus cassante.

La déformation le long de la ligne de Dog Bay a débuté à l'Ordovicien avec l'accumulation d'un mélange volcanique. Au Silurien, la ligne est devenue un site de cisaillement intense. Les fabriques cinématiques dans la zone de cisaillement révèlent qu'une phase précoce de transpression dextre ductile a été suivie par un relâchement de distension (déplacement normal), puis par un cisaillement dextre coulissant, dans une série de déplacements variant de ductiles à cassants. Une période de faible chevauchement du sud-est sur le nord-est a eu lieu au cours des étapes de déformation ductile-cassante et de déformation cassante.

---

<sup>1</sup> Contribution to Canada-Newfoundland Cooperation Agreement on Mineral Development (1990-1994), a subsidiary agreement under the Canada-Newfoundland Economic and Regional Development Agreement.

<sup>2</sup> Department of Geology, Keele University, Keele, Staffordshire ST5 5BG, U.K.

## INTRODUCTION

The Exploits Subzone of the Dunnage Zone represents remnants of the southeastern flank of Iapetus. Its ophiolites have been thrust onto the Gander Zone probably in Arenigian time (Colman-Sadd et al., 1992), and were subsequently covered by Ordovician and Silurian sequences. A region of this subzone bounded by Gander Bay in the east and the Reach Fault in the west has long been known as the Botwood Belt (Williams, 1967; Williams et al., in press). This belt was described as containing a striking variety of sediments, ranging from upper Ordovician deep sea turbidites once thought to pass into underlying turbidites of the Davidsville Group, a Silurian shallow marine, fossiliferous limestone-shale-siltstone succession, a Silurian terrestrial volcanic-sedimentary group, and redbeds. There has been no consensus on the interpretation of its stratigraphy. Its major structures have been recorded in several reconnaissance studies, the most notable being those of Karlstrom et al. (1982), Williams et al. (1988), and Lafrance and Williams (1992).

Recent remapping of the ground to the west of the GRUB (Gander River Ultramafic Belt) line (Carmanville and Comfort Cove Map sheets 2E/8 and 2E/7 respectively) has shed new light on the stratigraphy and tectonics of the northern Exploits Subzone. Most significant is the recognition that within the Botwood Belt, fundamentally different Silurian (and late Ordovician-Silurian) sequences are separated by a well defined tectonostratigraphical line, the Dog Bay Line. This line coincides with a zone of mélange (recorded but not discussed by Karlstrom et al. (1982) and a wide zone of shearing, depicted as the Indian Islands Fault (shear zone) in reconnaissance maps, but not discussed by Williams et al. (1988) or Lafrance and Williams (1992).

This paper reports on the tectonic features of the Dog Bay Line based on 1992 fieldwork, complementing the remapping of the Comfort Cove sheet by Drs. K.L. Currie and H. Williams.

## STRATIGRAPHY ACROSS THE DOG BAY LINE

Detailed accounts of lithologies, stratigraphy, and stratigraphic redefinitions have been given by Currie (1993) and Williams (1993). From west to east, the rocks involved in the recognition of the Dog Bay Line belong to the Badger Group, Botwood Group, Duder Group, and the Indian Island Group (Fig. 1).

### *Badger and Botwood groups*

To the west of the Dog Bay Line, late Ordovician to early Silurian deep sea sediments are now assigned to the Badger Group. The Badger Group consists of thin- to medium-bedded greywackes interlayered with siltstones and conglomerates at its base and top, with thicker conglomerates in the middle. Its upper boundary is commonly faulted, but 1 km north of Port Albert, the Badger Group is overlain with a

spectacular erosional disconformity by a markedly contrasting, Silurian terrestrial volcanic-sedimentary sequence, the Botwood Group. The terrestrial rocks consist of a volcanic unit of black and reddened vesicular and amygdaloidal basaltic lava flows, interbedded with tuffs and volcanoclastics, some containing accretionary lapilli. Minor limestone interbeds are locally present, and have yielded Llandovery-early Wenlock fauna (Elliott et al., 1991). The volcanics are stratigraphically overlain by a thick sequence of sandstones, including sandstones with volcanic clasts and tuffaceous layers.

### *Indian Islands Group*

To the east of the Dog Bay Line, the Silurian Indian Island Group, laid down in shallow seas, begins with basal limestone breccias, limestones, and shales. These are followed by thick siltstones with thin limestone beds, then by dark grey shales with siltstones, and finally by red siltstones and sandstones. On Seal Islands, basal limestone breccias with minor shale rests with apparent conformity to the Ordovician Hamilton Sound Group which comprises dark to black deep water shales with coticles (manganese nodules), cherts, and zones of olistostromal mélanges (Currie, 1992, 1993). Lithological contrasts across this contact suggest an erosional disconformity.

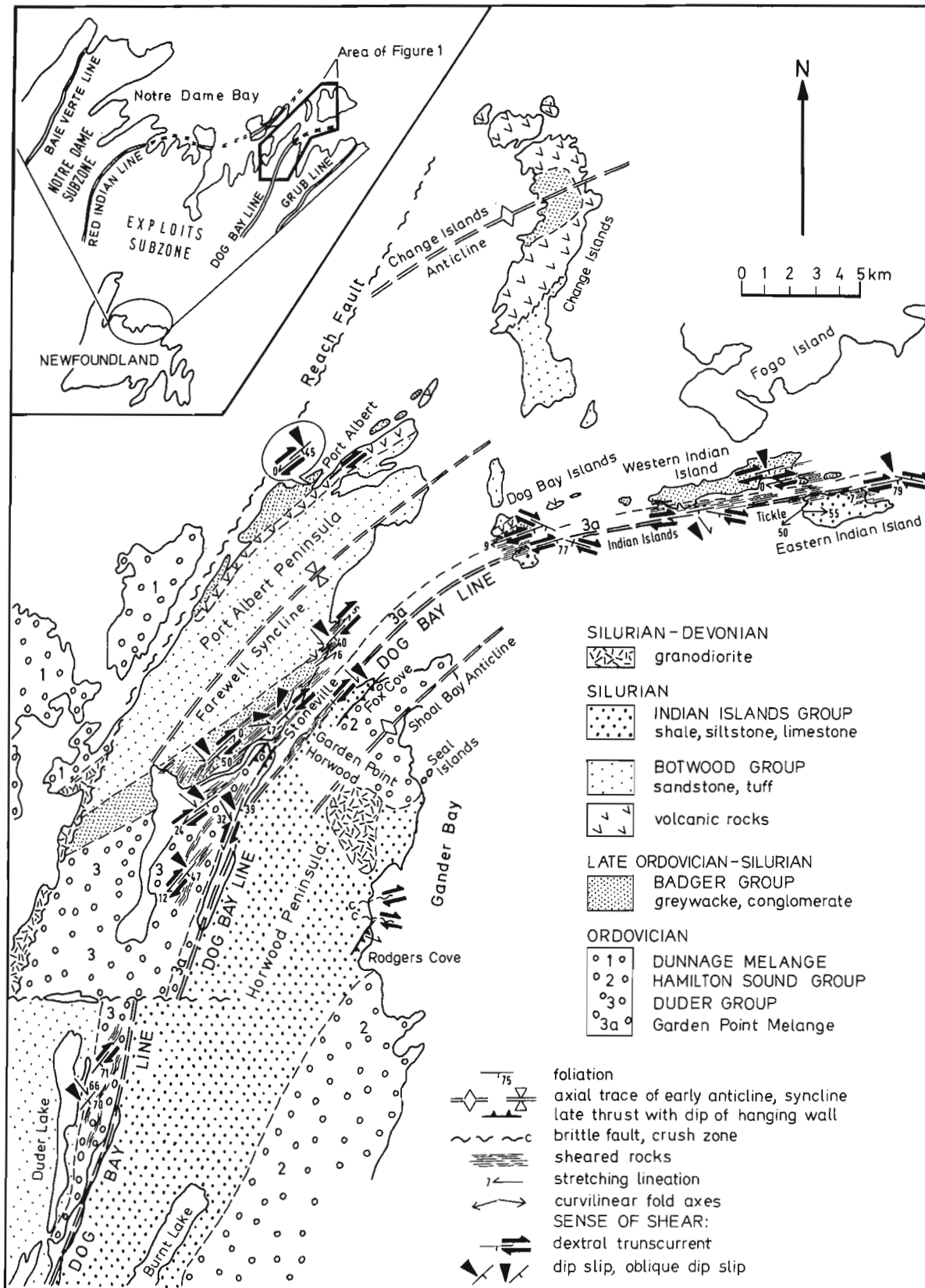
The Dog Bay Line separates the shallow sea Indian Islands Group from the deep sea and terrestrial Badger and Botwood groups. It follows the regional northeasterly trend typical of north-central Newfoundland (Fig. 1), but from Duder Lake northwards this trend progressively curves becoming east-northeasterly in the Indian Islands.

### *Duder group*

Along this regional flexure of outcrop belts, a hitherto apparently unrecorded, major volcanic-sedimentary assemblage, the Duder group of Currie (1993) intervenes between the Badger and Indian Island groups (Fig. 1). On the western shore of Dog Bay, in unshaped rocks under the Pentecostal Church in Stoneville, the Duder Group stratigraphically underlies the base of the Badger Group, suggesting that it is of early- or mid-Ordovician age. On the eastern shore of Dog Bay, its boundary against the Indian Island Group is the Dog Bay Line, coincident with a zone of intense shearing. In this region the Dog Bay Line forms the boundary between the Indian Islands Group and the Garden Point Mélange.

From east to west, the Duder Group comprises a mélange, the Garden Point Mélange, followed by rhythmic units of mafic pillow lavas, pillow breccias, salic lavas, and crystal tuffs interbedded with black shale. Many lavas and fragmental volcanic units contain mafic and salic dykes, and concordant gabbros varying in thickness from 1 m to 100 m, a few containing preserved primary sill-like contacts, albeit without contact chilling. At the top of the group is a tuffaceous shale with pumice clasts and local mélange horizons (Sawmill shale of Currie, 1993).





**Figure 1.** Geological setting of the Dog Bay Line, modified after maps of Williams (1993) and Currie (1993). Symbol for sheared rocks coincides with sectors of the area investigated in this study.

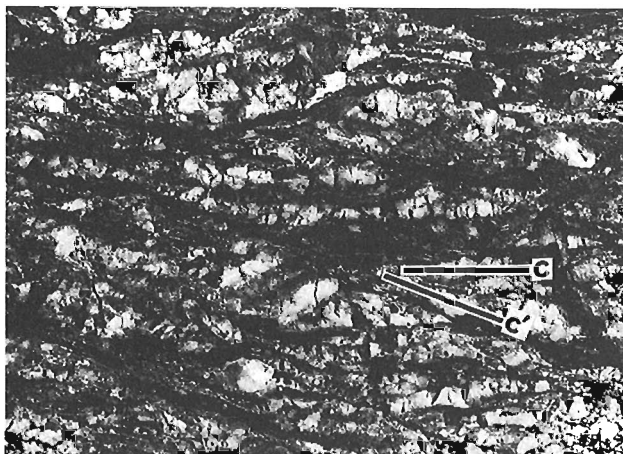
The Garden Point Mélange consists of blocks derived almost entirely from the Duder volcanics in a matrix of disrupted shale. Where best exposed it is generally intensely sheared, and has been interpreted as a tectonic mélange (Karlstrom et al., 1982). However, southwest of Stoneville, where deformation is less intense, the presence of trails of shale-enveloped blocks of gabbro, some of which are mylonitic whereas others are not, indicates that the Garden Point Mélange has been a mélange, probably an olistostromal mélange, prior to the shearing.

In the region of Duder Lake, the wide zone of folded, cleaved, locally sheared, steeply to vertically dipping and sparsely exposed Duder volcanics, narrows due to faulting, but may extend westwards under a cover of younger redbeds (the Ten Mile sandstone of Currie, 1993). The redbeds are regionally gently inclined and hardly deformed: if they belong to the Botwood group, then this would imply the presence of a major unconformity within the group. Preliminary reconnaissance by K.L. Currie and H. Williams suggests that the Dog Bay Line and the zone of disrupted volcanics extends southward to the Trans-Canada Highway, and probably continues farther south where it is truncated by the Mount Payton batholith.

## TECTONICS ALONG THE DOG BAY LINE

The Dog Bay Line is marked by a complex shear zone within which metasediments and volcanics in lowest greenschist metamorphic grade range from protomylonites to mylonites and locally to ultramylonites.

The northern segment of the Dog Bay Line is the most intensely sheared. It corresponds with a thinned-out, 600 m to 1 km wide belt of the Garden Point Mélange and adjacent rocks of the Indian Islands and Badger groups that outcrop



**Figure 2.** Protomylonitic core to a block of sheared gabbro in the Garden Point Mélange. Thin high strain zones of fine grained mylonite (dark stringers) anastomose around "low strain augen" or "buttons" of less affected gabbro (e.g. top centre). An indistinct C-foliation (C) is marked. Slip and rotation on shear bands (C') indicates dextral sense of movement. Indian Islands Tickle.

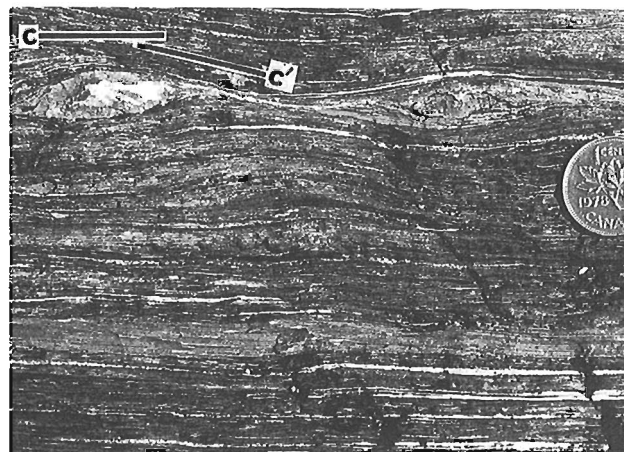
along the Indian Island Tickle and between the southern and middle Dog Bay Islands (Fig. 1). The small, elongate islands within the Indian Islands Tickle are low strain "augen" bounded by mylonite belts. Many are cored by blocks of gabbro with protomylonitic centres in which millimetre-wide shear surfaces bound and displace "buttons" of gabbro (Fig. 2); towards their boundaries with black shale-phyllonite, the gabbros become mylonitic and locally even ultramylonitic.

To the northwest of the Dog Bay Line, progressively rarer belts of weaker shear deformation extend for some 2 km into the Badger and Botwood groups, locally reaching Port Albert, 6.5 km away. To the southeast, within the Indian Islands Group, shear deformation is contained within a zone 100 m to 200 m wide, locally extending to 1 km; only related brittle deformation reaches 7 km.

South of Horwood, the zone of shear deformation widens to some 4 km and the deformation becomes less intense. Narrow belts of shearing anastomose over a wider area, and phyllonites of the Garden Point Mélange in the east, and of black shale farther west bound larger volcanic units (or olistoliths?) sheared along their boundaries and also containing narrow internal belts of shear.

### *Shear fabrics along the Dog Bay Line*

Mylonitic rocks along the Dog Bay Line contain several generations of S-C foliations, shear bands and related lineations, small-scale asymmetric synshearing folds and, in fragmental rocks, rotated pebbles and feldspar porphyroclasts. These fabrics of simple shear deformation can be used as sense-of-shear indicators (Fig. 3 and 4; see also Berthe et al., 1979; Passchier and Simpson, 1986). The mylonitic rocks abound in swarms of concordant and subconcordant quartz veinlets developed on all scales (Fig. 3, 5, 6), as described



**Figure 3.** Early intense, penetrative shear fabric in phyllonite. Mylonitic C-foliation (C) and low-angle shear bands (C') indicate a dextral sense of shear. White concordant veins are synshearing quartz veins. Plane of photograph parallel to subhorizontal stretching lineation. Indian Island Group (Horwood Shale), Horwood shore.

from ductile shear zones elsewhere in Newfoundland (Piasecki 1988), and from Scotland, where they were shown by the geochemical work of Hyslop (1992) to have formed continuously during ductile shearing.

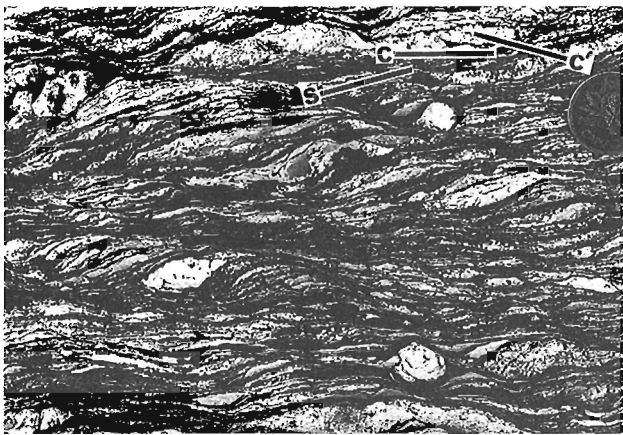
Along the Dog Bay Line, several generations of shear fabrics indicate a complex history of movements in which early dextral transpression was followed by extension and then by progressively more brittle dextral transcurrent shearing. Locally, minor southeast-over-northwest thrusting extended from brittle-ductile to brittle stages of deformation.

### *Early transpressional deformation*

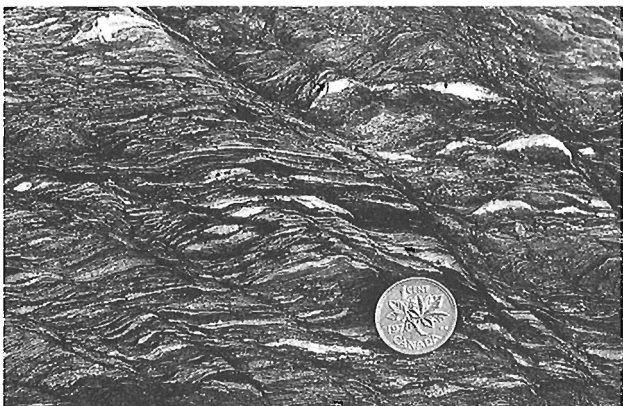
The earliest structures along and adjacent to the Dog Bay Line shear zone are folds of bedding. East of the Dog Bay Line, the Shoal Bay Anticline is a major early fold. West of the Dog



**Figure 6.** Late, discordant shear. Early flattened mylonite fabric (C-foliation along pencil) with an early swarm of boudined quartz veinlets (white lenticles) is transected from top left to bottom right by a less penetrative "strain-slip" cleavage with dextral sense of displacement. The discordant shear surfaces follow earlier shear bands of the late concordant shear. Indian Islands Group, Indian Islands.



**Figure 4.** Early intense, penetrative shear fabric in mylonite derived from a Badger Group conglomerate. Mylonitic S-C foliations and shear bands (S, C, and C' respectively) indicate dextral sense of shear. Quartzose pebbles are stretched and sigmoidal, feldspar clasts are more rounded. Stoneville.



**Figure 5.** Late, discordant shear. Early penetrative, flattened mylonite fabric (C-foliation left to right) with an early swarm of boudined quartz veinlets (white lenticles) is transected clockwise (from top left to bottom right) by a less penetrative "strain-slip" cleavage with dextral sense of displacement. Indian Islands Group, Indian Islands.

Bay Line, there are the Change Islands Anticline and the major Farewell Syncline (Fig. 1). The Farewell Syncline is subhorizontal and overturned to the northwest. In its core, its axial surface cleavage fans within the thickly bedded Botwood sandstones. In its envelope of shales, turbidites and conglomerates of the Badger Group, the axial cleavage, a pressure-solution cleavage in the more siliceous rocks, dips moderately steeply to the southeast. It is steeper than bedding in the northwestern (normal) limb in which rocks are only locally mylonitic, but is subparallel to bedding in the southeastern (inverted) limb which is intensely mylonitic.

In both limbs of the fold, this axial cleavage forms the main mylonitic foliation (C-foliation). Within this foliation, small-scale, penetrative S-C foliations, shear bands, porphyroclasts, and rotated pebbles (Fig. 4) systematically show a dextral sense of movement parallel to a gently plunging to subhorizontal mineral stretching lineation (Fig. 1). Since the shear movement acted along the fold's axial surface in a direction subparallel to its axes, the dextral shearing was clearly superimposed on already existing limbs of the Farewell Syncline.

This small-scale, penetrative dextral shear fabric is commonly very flattened and stretched subparallel to the subhorizontal lineation. Its shear bands and S-foliations are commonly inclined at less than  $10^\circ$  (Fig. 3, 4), and concordant quartz veinlets are boudined and recrystallised from originally long grains into equigranular aggregates (depicted in Piasecki, 1988). It appears that flattening, most likely related to late stages in the development of the Farewell Syncline, overlapped early shearing, implying an early transpressional regime along the Dog Bay Line.

In most mylonitic rocks which exhibit the gently inclined lineation of the early dextral movements, the mylonitic foliation also contains a steep lineation. It is a weak mineral stretching lineation, and in places a crenulation lineation which approximates intersections between the early

mylonitic C-foliation and early flattened shear bands, and of the C-foliation and crests of flattened S-C "buttons". The attitude of this steep lineation locally varies in adjacent exposures from plunging down the dip of foliation to being oblique and even plunging in opposite directions (in Stoneville, Fig. 1). Subparallel to this steep lineation are weak shear bands, rare S-C foliations, rotated porphyroclasts, and pebbles, all systematically indicating down-dip to oblique normal movement (southeast side down) in southeast dipping rocks. The regional mylonitic foliation (cleavage) is thus composite. Where very late kink folding has tilted the rocks to dip northwestwards, as along the Horwood shore, this movement becomes reversed (northwest side up).

The elements of the down-dip fabric are larger, less penetrative, and more widely spaced than those of the early dextral fabric, and the inclination of its shear bands and S-foliations are substantially greater. In places, small sigmoidal domains ("buttons", cf. Fig. 2, 4, 6) bounded by S-C and shear band surfaces of the down-dip fabric, contain modified relics of the flattened dextral fabric. The implication of this is that, while the dextral and down-dip fabrics may at first appear to resemble the components of one strain (Williams et al., 1988, p. 22), the normal, extensional movements postdated the dextral shearing of the transpressional regime.

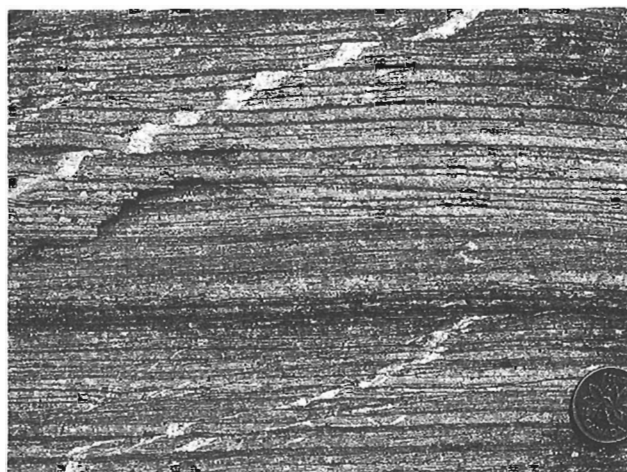
On Eastern Indian Island, in some localities containing the dip-slip fabrics, the early, usually subhorizontal lineation shows large variations in plunge, suggesting that it has been rotated by the dip-slip movements. The earliest megascopic folds on the island are upright, locally curvilinear to sheath-fold in form with a subvertical sense of extension. Some adjacent folds plunge in opposing directions, not unlike  $D_3$  folds in the Hamilton Sound Group in the Carmanville map area (Piasecki, 1992). It is uncertain whether these are the products of early transpression, or modification by the succeeding extensional dip-slip movements.

#### ***Late transcurrent dextral shear***

From Duder Lake northwards, in most mylonitic rocks along the Dog Bay Line, the early small-scale, penetrative dextral shear fabric is overprinted by two phases of later dextral shear fabrics, the first concordant, the second discordant. These differ from the early dextral fabric in that they are more brittle, less penetrative, and are more widely spaced, with steeper dips of S-foliations and shear bands.

#### ***Late concordant transcurrent shear***

From Duder Lake to the Indian Islands, a late dextral shear fabric follows the trend and attitude of the early penetrative dextral fabric. Thus, the main mylonitic foliation, the intense cleavage typical of the Dog Bay Line, is complex and composite. To the north of Stoneville and on Eastern Indian Island, where the regional trend swings towards the east, this is demonstrated by crosscutting fibrous quartz and carbonate veinlets that are offset along spaced surfaces within this composite foliation (Fig. 7).



**Figure 7.** Late dextral shear. Fibrous quartz veinlets crosscut early penetrative mylonite foliation (C-foliation left to right) but are offset along spaced surfaces within this composite foliation. Plane of photograph parallel to subhorizontal stretching lineation. Indian Island Group, Eastern Indian Island.

In the phyllonitic shale at Horwood (in the Horwood formation at grid ref. 7990 8155 on 1:10,000 sheet 2E/7), this late transcurrent dextral movement sigmoidally stretches quartzite pebbles that have been previously stretched up to an aspect ratio of 10:2:1 along the subvertical lineation related to the earlier dip-slip shear movement, indicating that the late transcurrent shear postdated the subvertical extension.

#### ***Late discordant shear***

In the Dog Bay Islands and Indian Islands, where the regional trend has swung to the east-northeast, the regional composite foliation (cleavage) becomes transected clockwise by separated zones of disturbance in the form of a less penetrative mylonitic "strain-slip" cleavage (Fig. 5, 6), in places with related subconcordant quartz veinlets. Dextral slip along this late cleavage displaces and rotates the rocks and the regional cleavage into more easterly trends.

Seven kilometres southeast of the Dog Bay Line, along Gander Bay north of Rodgers Cove, thick siltstones of the Indian Islands Group (Charles Cove formation of Currie, 1993) contain several zones of late fault breccia. Locally more than 50 m thick, the crush zones trend east to northeast and exhibit dextral displacement (Fig. 1). Similar dextral crush zones occur on Western Indian Island, indicating that, on both sides of the Dog Bay Line, the late dextral movements extended from brittle-ductile to the brittle stages of deformation.

#### ***Late minor thrusting and folding***

On southern Dog Bay Island, along the Dog Bay Line, quartz veining is associated with minor, near-upright, subhorizontal chevron folds and apparently related open and curvilinear folds. Individual veinlets follow the folds' axial surfaces but are also folded by the folds, indicating synfolding vein

emplacement. The same veinlets are sigmoided by late dextral transcurrent movements, implying that local minor folding preceded, or was closely associated with the late dextral shearing.

West of the Dog Bay Line, between Horwood and Stoneville, several late, minor brittle thrusts displacing southeast over northwest telescope the Duder Group (Fig. 1). East of the line, a brittle-ductile thrust with the same sense of displacement separates shales and siltstones of the Indian Islands Group 2 km north of Rodgers Cove (Fig. 1: see also Fig. 1 in Currie, 1993); and, at Fox Cove, a brittle thrust marks the boundary between the Indian Island and Hamilton Sound groups (Fig. 1).

The last minor fold structures in the region are gently inclined and gently plunging kink and crenulation folds, some occurring in conjugate sets. They abound on both sides of the Dog Bay Line, in areas of the late southeast-over-northwest thrusting. Their presence on Seal Islands adjacent to the apparently concordant boundary between the Hamilton Sound and Indian Island groups suggests that this boundary may have been tectonized. Generally the late kink folds are very small, but along the Horwood shore and on the middle Dog Bay Island larger scale variants tilt southeast dipping rocks to dip to the northwest. Steeply plunging kink folds are locally well developed in sheared Horwood shale along its mylonitic boundary with the Garden Point Mélange.

### *Late major faults*

One of the last major structures in the Botwood Belt is the rectilinear Reach Fault. Within the fault zone, common brittle fabrics and locally preserved ductile-brittle fabrics indicate sinistral transcurrent motion; and coastal mapping by Williams (1993) suggests sinistral displacement of up to 15 km.

## **ECONOMIC GEOLOGY**

Sheared Duder Group volcanics and shales contain abundant suites of quartz veins and locally of carbonate veins. Earlier suites are concordant and appear to be synshearing (cf. Fig. 3), later ones are discordant, locally netveining the phyllonitic rocks. Many vein suites carry gold mineralization in several prospects, as at Clutha (Churchill and Evans, 1992), an expression of the mobility of gold in shear zones.

## **DISCUSSION**

The scale of displacement along the Dog Bay Line is difficult to ascertain. Silurian stratigraphies do not correlate across the line, implying that the line is a Silurian terrane boundary. Possible Ordovician correlatives may be coticule and mélange-bearing rocks within the regions of the Dunnage Mélange to the west of the line, and Carmanville to the east of it. These occurrences now form an east-trending belt (see Fig. 1 in Williams, 1992). Restoration of a dextral

displacement of a minimum of 60 km along the Dog Bay Line aligns the Ordovician rocks into the regional northeasterly trend prevalent in north-central Newfoundland.

The timing of deformation along the Dog Bay Line can be reasonably assessed. The earliest event, the formation of the Garden Point Mélange, either by shear deformation or, more likely, in the form of an olistostrome derived from the Duder Group, preceded the shearing, and is almost certainly early- or mid-Ordovician, broadly related to the Ganderian, or Penobscottian orogeny (Colman-Sadd et al., 1992).

The protracted history of ductile dextral transpression followed by extensional relaxation (ductile dip-slip), and in turn by progressively less ductile dextral movements, affects the Ordovician Duder Group, Ordovician-Silurian Badger Group, the Silurian Indian Island Group (Ludlowian?), and the lower (northern) part of the Botwood Group; it must be late Silurian. A minimum age is provided by the emplacement of the Mount Payton batholith at 420 Ma (Reynolds et al., 1981) which truncates the Dog Bay Line. This shearing was probably broadly coeval with Silurian sinistral shearing along the GRUB line, the boundary between the Exploits Subzone and the Gander Zone, only 30 km to the southeast (Piasecki, 1992). In the region between Reach Fault and Gander Bay, no evidence was found for the very early west-over-east thrusting suggested by Lafrance and Williams (1992). The late southeast-over-northwest thrusting along the Dog Bay Line and within the Indian Islands Group is late Silurian or younger. The rectilinear, brittle Reach Fault is considerably younger; it truncates the Farewell Syncline and contains a posttectonic lamprophyre dyke belonging to a Jurassic dyke suite (Currie, 1993).

The curvature of the regional trend of outcrop belts and of the Dog Bay Line in the north coastal region resembles a structure complimentary to the Hermitage flexure in southeastern Newfoundland. The very late dextral discordant shear movement has contributed only in a small way to this curvature, as an expression of a more fundamental shearing mechanism that requires further structural investigation, possibly in higher metamorphic grade rocks of the northern Burlington Peninsula.

## **ACKNOWLEDGMENTS**

This contribution is the result of close collaboration with K.L. Currie and H. Williams. I am indebted to them for stimulating discussions, ideas, and logistic support in the field, and the Geological Survey of Canada for financial support under Research Contract 23226-0-0543.

## **REFERENCES**

- Berthe, D., Choukroune, P., and Jegouzo, P.  
1979: Orthogneiss, mylonite and non coaxial deformation of granites: the example of the South Armorican Shear Zone; *Journal of Structural Geology*, v. 69, p. 31-42.

**Churchill, R.A. and Evans, D.T.W.**

1992: Geology and gold mineralization of the Duder Lake gold showings, eastern Notre Dame Bay, Newfoundland; in *Current Research*, Newfoundland Department of Mines and Energy, Geological Survey Branch, Report 92-1, p. 211-220.

**Currie, K.L.**

1992: A new look at the Gander-Dunnage relations in Carmanville map area, Newfoundland; in *Current Research*, Part D; Geological Survey of Canada, Paper 92-1D, p. 27-33.

1993: Ordovician-Silurian stratigraphy between Gander Bay and Birchy Bay, Newfoundland; in *Current Research*, Part D; Geological Survey of Canada, Paper 93-1D, p. 11-18.

**Colman-Sadd, S.P., Dunning, G.R., and Dec, T.**

1992: Dunnage-Gander relationships and Ordovician orogeny in central Newfoundland: a sediment provenance and U/Pb age study; *American Journal of Science*, v. 292, p. 317-355.

**Elliott, C.G., Dunning, G.R., and Williams, P.F.**

1991: New U-Pb zircon age constraints on the timing of deformation in north-central Newfoundland and implications for early Paleozoic Appalachian orogenesis; *Geological Society of America, Bulletin*, v. 103, p. 125-135.

**Hyslop, E.K.**

1992: Strain induced metamorphism and pegmatite development in the Moine rocks of Scotland; Ph.D. thesis, University of Hull, U.K., 300 p.

**Karlstrom, K.E., van der Pluijm, B.A., and Williams, P.F.**

1982: Structural interpretation of the eastern Notre Dame Bay area, Newfoundland: regional post-Middle Silurian thrusting and asymmetrical folding; *Canadian Journal of Earth Sciences*, v. 19, p. 2325-2341.

**Lafrance, B. and Williams, P.F.**

1992: Silurian deformation in eastern Notre Dame Bay, Newfoundland; *Canadian Journal of Earth Sciences*, v. 29, p. 1899-1914.

**Passchier, C.W. and Simpson, C.**

1986: Porphyroclast systems as kinematic indicators; *Journal of Structural Geology*, v. 8, p. 831-843.

**Piasecki, M.A.J.**

1988: Strain-induced mineral growth in ductile shear zones, and a preliminary study of ductile shearing in western Newfoundland; *Canadian Journal of Earth Sciences*, v. 25, p. 2118-2129.

1992: Tectonics across the Gander-Dunnage boundary in northeastern Newfoundland; in *Current Research*, Part E; Geological Survey of Canada, Paper 92-1E, p. 259-268.

**Reynolds, P.H., Taylor, K.A., and Morgan, W.R.**

1981:  $^{40}\text{Ar}/^{39}\text{Ar}$  ages from the Botwood-Mount Payton region, Newfoundland: possible palaeomagnetic implications; *Canadian Journal of Earth Sciences*, v. 18, p. 1850-1855.

**Williams, H.**

1967: Silurian Rocks of Newfoundland; in *Geology of the Atlantic Region*, (ed.) E.R.W. Neale and H. Williams; Geological Association of Canada, Special Paper No. 4, p. 93-137.

1992: Mélanges and coticule occurrences in the northeast Exploits Subzone, Newfoundland; in *Current Research*, Part D; Geological Survey of Canada, Paper 92-1D, p. 121-128.

1993: Stratigraphy and structure of the Botwood Belt and definition of the Dog Bay Line in northeastern Newfoundland; in *Current Research*, Part D; Geological Survey of Canada, Paper 93-1D, p. 19-27.

**Williams, H., Dean, P.L., and Pickering, K.T.**

in press: Botwood Belt; in Chapter 4 in *Geology of the Appalachian-Caledonian Orogen in Canada and Greenland*, (ed.) H. Williams; Geological Survey of Canada, *Geology of Canada*, no. 6 (also *Geological Society of America, The Geology of North America*, v. F-1.

**Williams, P.F., Elliott, C.G., and Lafrance, B.**

1988: Structural geology and mélanges of eastern Notre Dame Bay, Newfoundland; *Geological Association of Canada, Field Trip Guidebook*, Trip B2, 60 p.

---

Geological Survey of Canada Project 730044 AC

# Hydrocarbon charge history of east coast offshore basins: modelling geological uncertainty

M.A. Williamson, T.J. Katsube<sup>1</sup>, Z. Huang, M. Fowler<sup>2</sup>,  
K.D. McAlpine, F.C. Thomas, R. Fensome, and M. Avery  
Atlantic Geoscience Centre, Dartmouth

*Williamson, M.A., Katsube, T.J., Huang, Z., Fowler, M., McAlpine, K.D., Thomas, F.C., Fensome, R., and Avery, M., 1993: Hydrocarbon charge history of east coast offshore basins: modelling geological uncertainty; in Current Research, Part E; Geological Survey of Canada, Paper 93-1E, p. 299-306.*

---

**Abstract:** Efforts to reconstruct the detailed hydrocarbon charging histories of sedimentary basins require that explorationists make numerous geological, geophysical and geochemical assumptions. Many of these assumptions can be made with a fair and defensible degree of certainty (such as the varying proportion of rock components and age-depth relationships within a well); others, however, are accompanied by varying degrees of uncertainty (such as kerogen reaction kinetics or seal permeability evolution) and can potentially, significantly impact the quality and accuracy of predictive models. In our studies of hydrocarbon charge in the Scotian and Jeanne d'Arc basins considerable effort to reduce such uncertainty and risk is being made. This paper demonstrates, through reference to case studies, preliminary results of several uncertainty reduction projects.

**Résumé :** Afin de reconstituer l'histoire détaillée de la formation d'hydrocarbures dans les bassins sédimentaires, les scientifiques chargés de l'exploration doivent formuler de nombreuses hypothèses géologiques, géophysiques et géochimiques. Nombre de ces hypothèses peuvent être faites avec un degré de certitude juste et défendable (comme la proportion variable des composantes des roches et les corrélations entre l'âge et la profondeur dans un puits); d'autres, cependant, s'accompagnent de divers degrés d'incertitude (comme la cinétique de la réaction du kérogène ou l'évolution de la perméabilité des roches étanches) et peuvent avoir des répercussions importantes sur la qualité et l'exactitude des modèles de prévision. Dans le cadre de leurs études sur les hydrocarbures contenus dans les bassins Néo-Écossais et de Jeanne d'Arc, les auteurs s'efforcent de réduire l'incertitude et le risque. À l'aide d'études de cas, le document présente les résultats préliminaires de plusieurs projets visant à réduire l'incertitude.

---

<sup>1</sup> Mineral Resources Division

<sup>2</sup> Institute of Sedimentary and Petroleum Geology, Calgary

## INTRODUCTION

Two decades of co-operative efforts to gather, interpret and assimilate geophysical, geological and engineering data have produced a comprehensive knowledge base for Canada's eastern offshore regions. Whether in the form of specific databases or interpretive reviews/atlasses (Keen and Williams, 1990; Atlantic Geoscience Centre, 1991), this knowledge base underpins the Atlantic Geoscience Centre's current petroleum geoscience research through the Hydrocarbon Charge Modelling Project. The research strategy applies new and emerging technologies and data processing/numerical methods to good quality databases. This allows the derivation of quantitative models explaining the observed distribution (Fig. 1) of petroleum accumulations throughout the basins. More importantly, it allows the development of predictive models of resource emplacement and distribution to assist in the exploration and production of petroleum, basin and play prioritization, and resource assessment and management.

Through the integration of information from a broad range of data types and disciplines we are developing models of the compaction, thermal, organic maturation, diagenetic and pressure histories of basinal source rock, reservoir and seal

systems. Our models range from the molecular (for example, kerogen bond strengths and breakdown into petroleum products) to crustal scales (for example, regional thermal and crustal evolution models).

Numerous assumptions have to be made during the construction of quantitative and semi-quantitative models of many of the processes involved in basin charge histories. Some of these assumptions are reasonably well understood and can be made based on observational data; others, however, have to be made with less certainty. This has the effect, to a greater or lesser degree, of introducing uncertainty into hydrocarbon charge models of particular areas. It is important, therefore, to understand the impact of these uncertainties on model conclusions, or, in other words, the sensitivity of our models to each assumption.

In the Hydrocarbon Charge Modelling Project, we are making considerable effort to minimize, as far as possible, the introduction of uncertainty. Some of our efforts are illustrated in this paper which presents "snapshots" of several case study investigations of specific uncertainties, and reviews the effects of these on some of the basin attributes that we are trying to model.

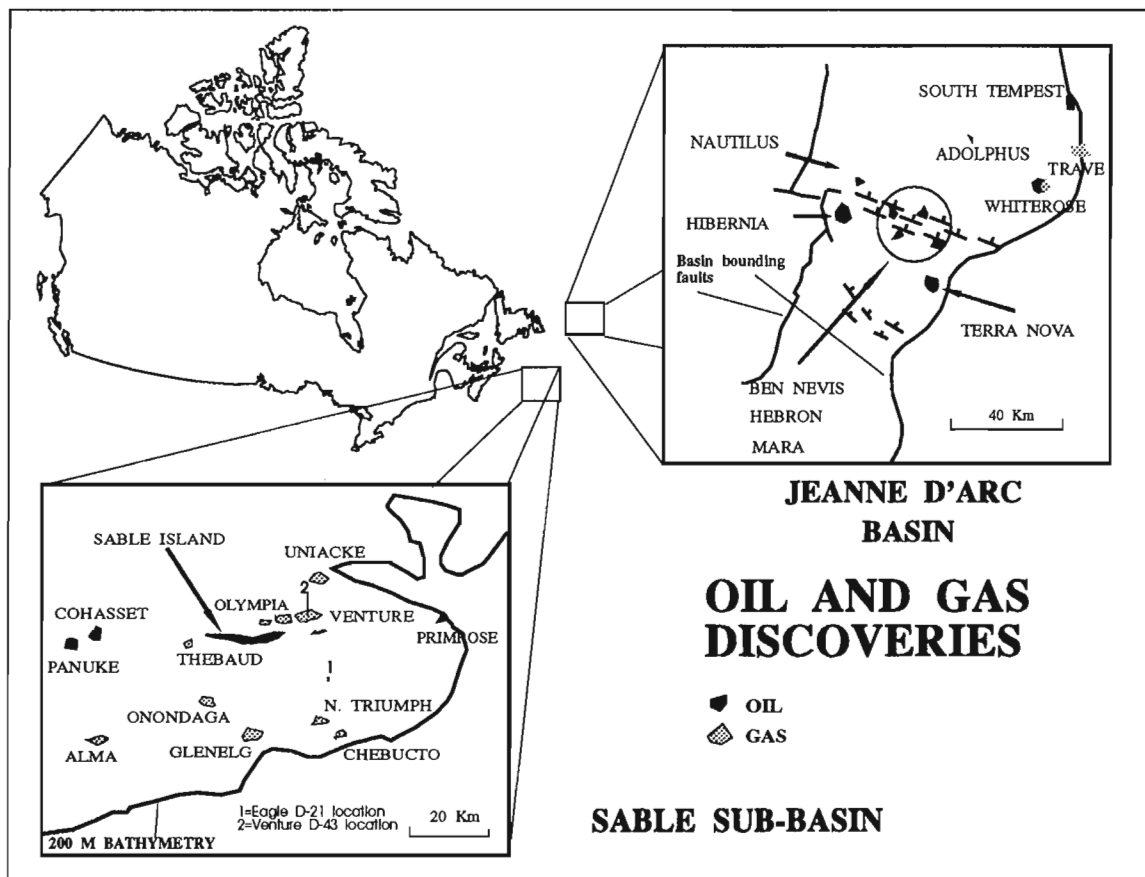


Figure 1. Sketch map of oil and gas distribution offshore eastern Canada.



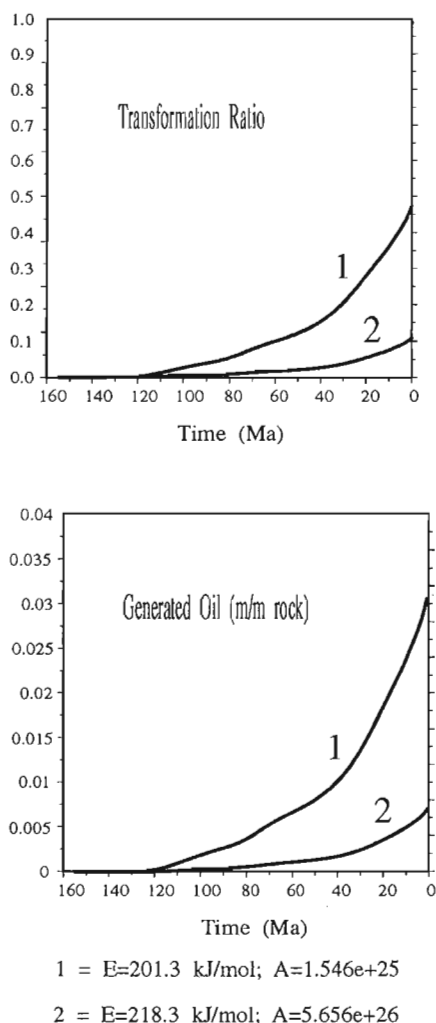
## MODEL UNCERTAINTY 1 – SOURCE ROCK KINETIC PARAMETERS

The rates at which kerogen molecular bonds are broken down during the hydrocarbon generation process are governed by the kinetic parameters A and E of the Arrhenius equation. These quantities show considerable variation among source rocks and control such important events as the timing and volume/composition of generated hydrocarbons. In the absence of measured values of A and E for specific source rocks or kerogens (e.g. the Egret Member source interval of Jeanne d'Arc Basin, offshore Newfoundland) it has been customary

to make assumptions. Figure 2 shows some implications of these assumptions. Curve 2 shows model calculated transformation ratios and volume of hydrocarbon generated for the Egret source interval with A and E parameters assumed to be the same as measured for North Sea Kimmeridgian source rocks. Curve 1 is based on A and E parameters derived for the Egret Member by hydrous pyrolysis analysis of the Egret source (Hunt et al., 1991). Significant discrepancies are seen regarding the transformation timing of the kerogen and generated volumes of oil with clear implications for regional charge analyses. Further reduction of this uncertainty is anticipated through joint research with the Institute of Sedimentary and Petroleum Geology on specific Egret Member kerogen kinetics (Issler and Fowler, pers. comm, 1993).

### *Egret source rock kinetics*

HIBERNIA AREA



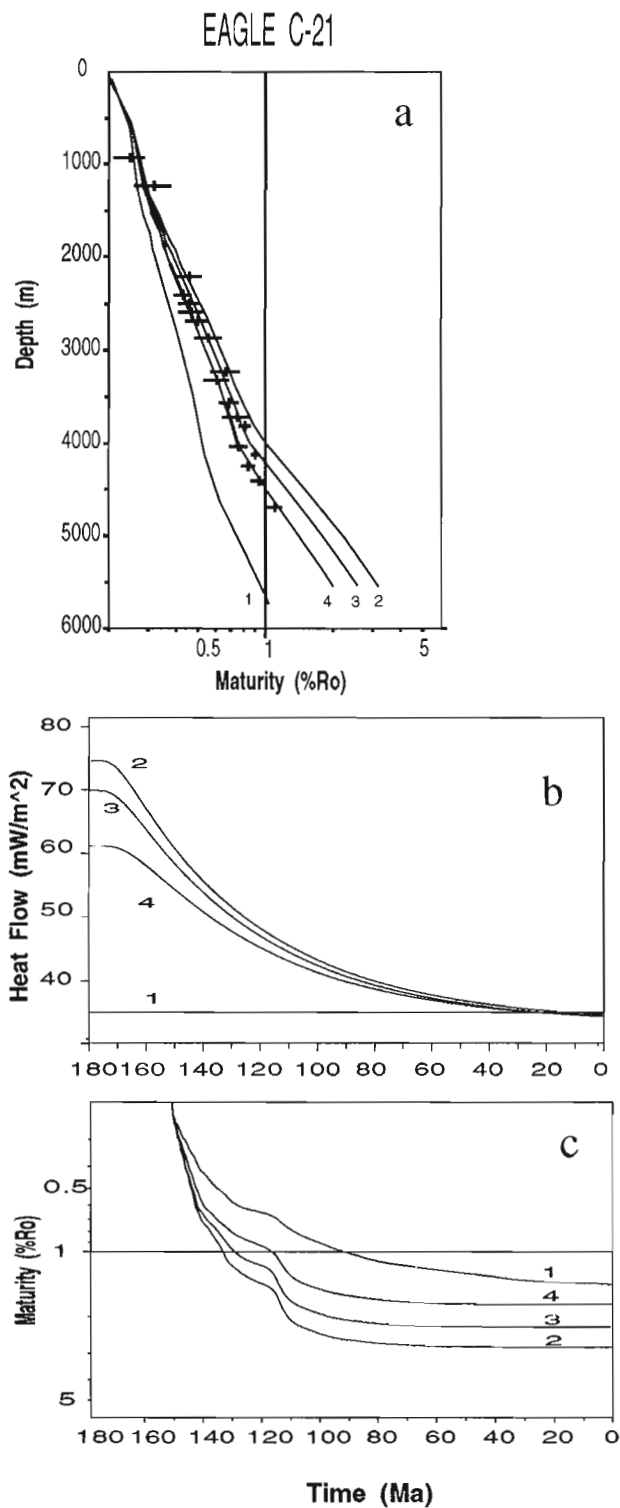
**Figure 2.** Oil generation and kerogen transformation ratio predicted for the Hibernia area. This assumes, for the Egret source rock, kinetic parameters from Hunt et al. (1991, curve 1) (based on hydrous pyrolysis measurements on Egret samples, see text) or from values reported for the Kimmeridgian aged North Sea source rocks (curve 2).

## MODEL UNCERTAINTY 2 – PALEO-HEAT FLOW, SABLE SUBBASIN

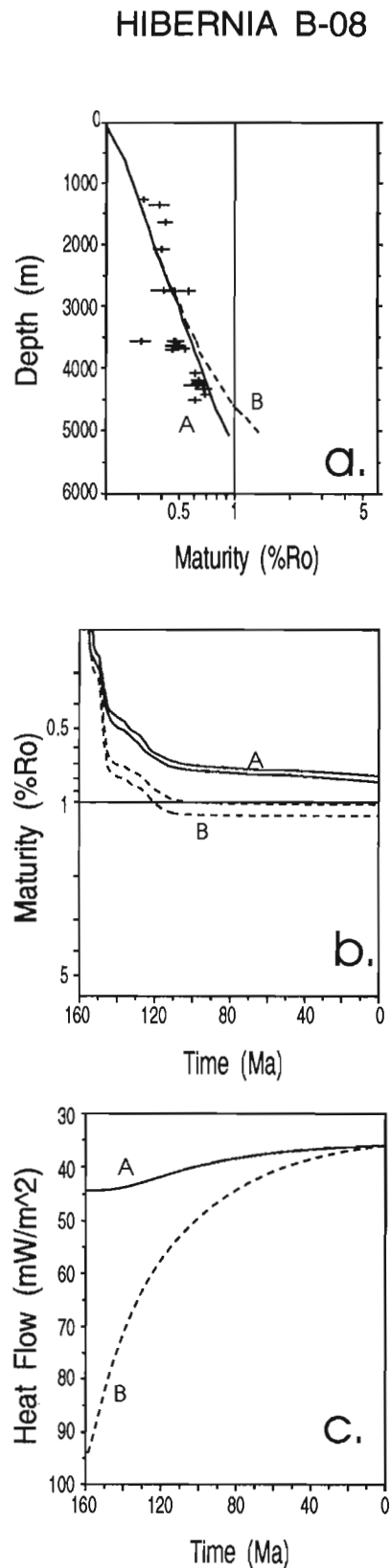
As a guide to the accuracy of our modelled maturity-depth profiles we compare predicted versus measured vitrinite reflectance values. Notwithstanding the accuracy of the latter (see model uncertainty 6), a good fit between measured and predicted values allows confidence in our reconstructions of maturity-time curves and in the thermal assumptions used in our simple thermal reconstructions based on a steady state thermal conductance model. Plots (Fig. 3) for the Eagle C-21 well (Sable Subbasin) show sensitivities of predicted vitrinite-depth to several heat flow curve assumptions with their respective maturity-time curves. In our efforts to constrain paleo-heatflow assumptions we are using, not only measured vitrinite reflectance, but also Apatite Fission Track technologies which can track sediment temperature-time histories. From Figure 3 it is clear that the initial variance of heat flow magnitudes following a rifting event at 180 Ma rapidly declines to negligible differences at the time of the test datum deposition (152 Ma), with concomitant negligible effect on the maturity time curves and maturity-depth present day profiles. The exception to this is the case where the heat flow assumption is for no rifting perturbation (i.e. flat, curve 1), which causes underestimation of measured vitrinite reflectance and delayed maturity.

## MODEL UNCERTAINTY 3 – PALEO-HEAT FLOW, JEANNE D'ARC BASIN

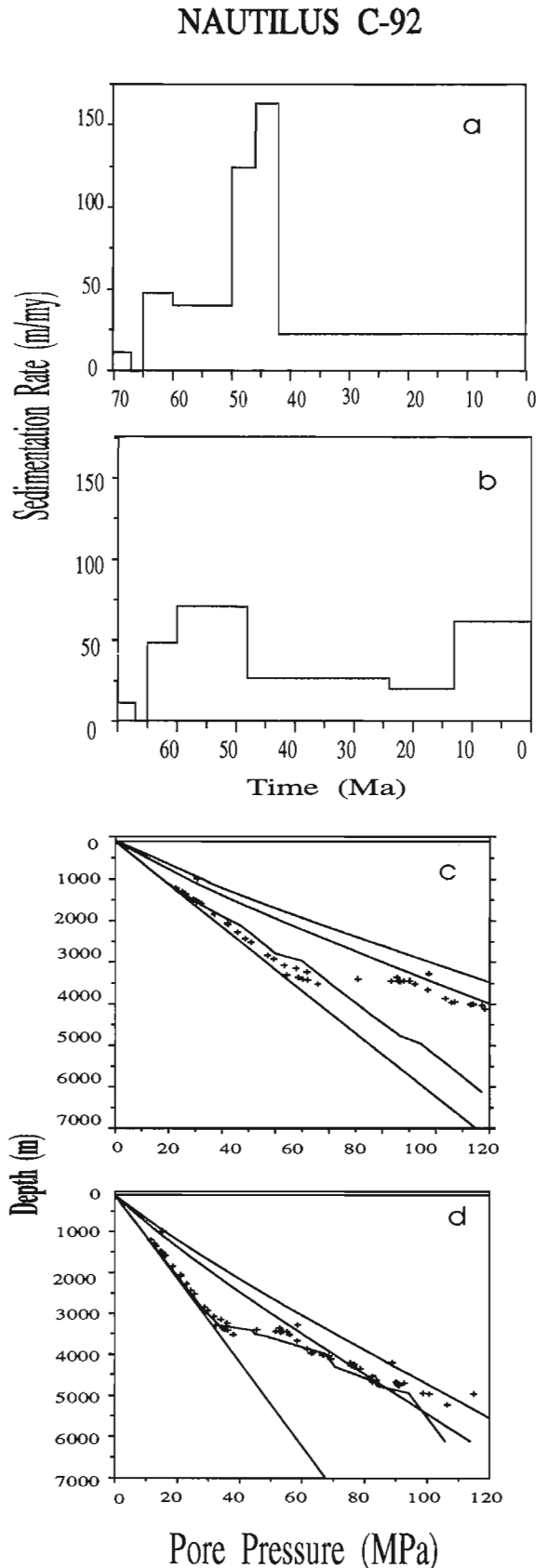
Our thermal models and assumptions for the Jeanne d'Arc Basin have, until recently, assumed a time invariant heat flow (Williamson, 1992). This was originally based on the view that the basin was somewhat offset from the area of maximum rifting/thermal perturbation. The time invariant heatflow assumption is being re-examined in our efforts to reduce uncertainties. Fission Track analyses are underway (Shimeld, pers. comm., 1993) as are attempts to look at heatflow variability as a response to predicted maturity indices. Figure 4 shows a range of heatflow time assumptions (curves A and B) with their impact on maturity timing for the Egret source interval and on present-day maturity-depth predictions. Clearly, curve A more closely fits measured values (Fig. 4a), however,



**Figure 3.** Model predicted maturity (vitrinite) depth profiles (a curves 1-4) and maturity time profiles (c for the 152 Ma datum) assuming time invariant (b curve 1) and variant (b curves 2-4) heat flow at the Eagle location, Sable Subbasin.



**Figure 4.** Model predicted maturity (vitrinite reflectance) depth profiles (a) and maturity time profiles (b, for Egret member, 152 Ma datum) assuming heat flow time curves A and B (c) for the Hibernia B-08 location, Jeanne d'Arc Basin.



**Figure 5.** Influence of biostratigraphic resolution on model predicted pore pressure depth profile at Nautilus C-92, Jeanne d'Arc Basin.

the different implications of each thermal curve are well marked by the modelled maturity-time paths for the Egret datum (Fig. 4b).

#### **MODEL UNCERTAINTY 4 – PORE PRESSURE PREDICTIONS, JEANNE D'ARC BASIN**

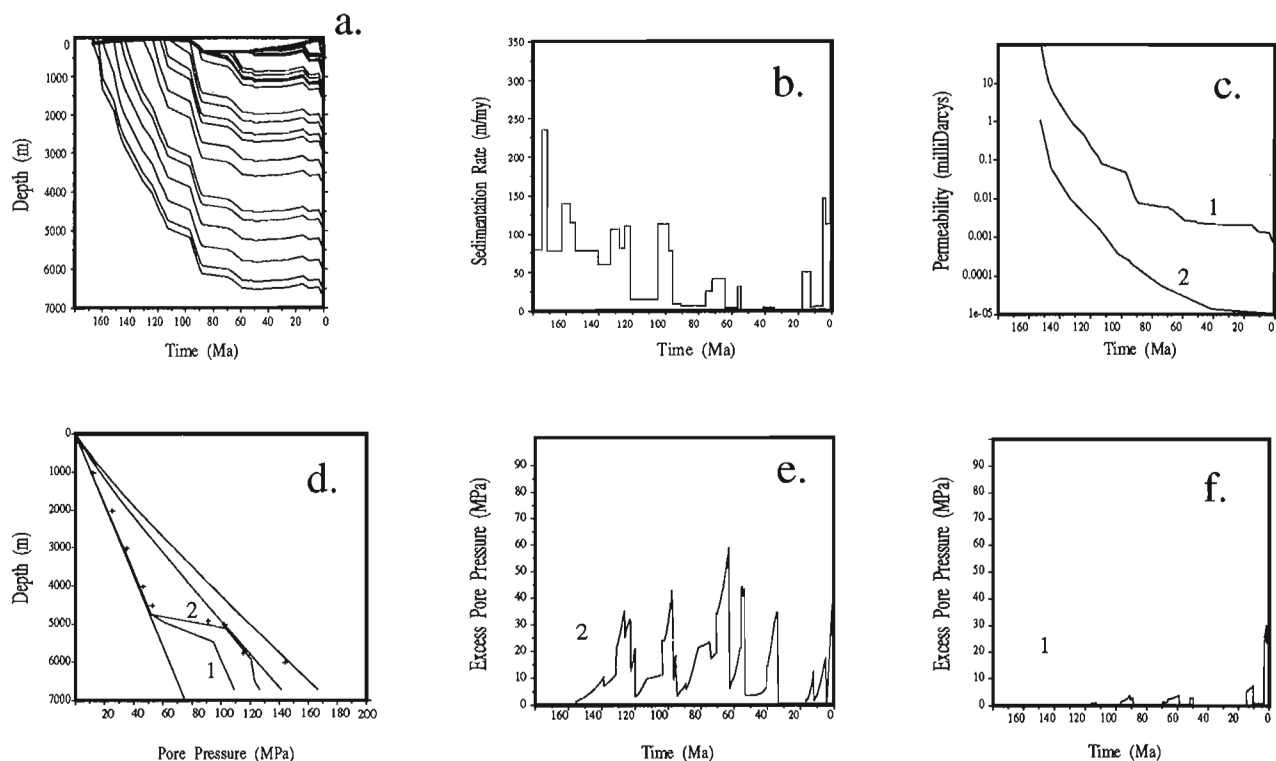
Models of predicted pore pressure-depth profiles and pore pressure time histories are sensitive to a broad variety of assumptions and data (Williamson and Smyth, 1992). The predictive ability of our pore-pressure depth models with respect to biostratigraphic resolution of the Cenozoic wedge offshore eastern Canada is examined in Figure 5. Figure 5a assumes an even sedimentation rate during the 40 Ma to recent interval; this assumption was initially due to poor sample control and little or no paleontological analysis. The sedimentation curve in Figure 5b results from a re-examined biostratigraphy for the uppermost intervals in the well. This increased resolution clearly impacts the predictive ability of the pore pressure model (Fig. 5c-d) allowing a better fit between predicted pressure-depth profiles (solid line) and measured pressures from DSTs and RFTs and mud weight conversions (crosses). Elements of the charge modelling project continue to generate more resolved biostratigraphies coupled with a general seismo- and sequence stratigraphic effort within the Cenozoic interval.

#### **MODEL UNCERTAINTY 5 – ROCK PROPERTIES AND PRESSURING**

The physical and chemical behaviour of muds, particularly their pore structure evolution, as they are transformed to shale through compression and heat have a significant impact on basin charge analyses in several ways. Most obvious are the compaction corrections made to accurately reconstruct interval burial histories, which also affect the thermal models through their influence on assigned sediment thermal conductivity profiles through time. Similarly, accurate imaging of lithological sealing capacities through time is important for reconstructing formation pore pressures as they evolve through time, in response to the sediment compaction disequilibrium processes (Mudford, 1988, 1989; Mudford and Best 1989; Williamson, 1992). Despite their importance, relatively little is known about the physical and chemical behaviour of muds and shales compared to, for example, reservoir intervals (sandstones and limestones).

Figure 6 demonstrates the sensitivity of modelled pore-pressures to assumed permeability-time curves. The compaction corrected burial history and sedimentation rate plots for the Venture B-43 well in Sable Subbasin (Fig. 6a, b) are typical for this basin, showing a rapid, initial subsidence rate (following Mesozoic rifting) that decreases around 90 Ma and builds up again during the last 20 Ma. Permeability-time curves (1 and 2, Fig. 6c) were derived using the so-called modified Kozeny-Carman relationship that is more applicable to low permeability rocks (Ungerer et al., 1990). Both

## VENTURE B-43

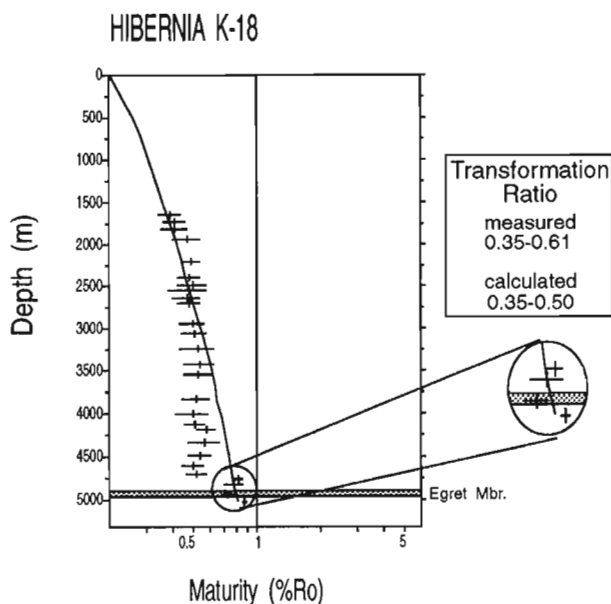


**Figure 6.** **a.** Compaction corrected burial history curve for Venture B-43 (see Fig. 1 for location) offshore Nova Scotia. **b.** Sedimentation rate. **c.** Model assumed permeability-time profiles (1 and 2). **d.** Model predicted pore pressure-depth profiles for the present day (actual measured values are shown as crosses). **e.** Modelled excess pore pressure-time profile for the 152 Ma datum in Venture B-43 and assuming curve 2 permeability profile. **f.** Modelled excess pore pressure-time profile for the 152 Ma datum in Venture B-43 and assuming curve 1 permeability profile.

curves are for the 152 Ma datum for a formation that is currently at a depth of 5500 m and which represent a range of clay grain sizes from 0.002 mm (curve 1) to 0.0002 mm (curve 2).

Reconstruction of pore pressure-time was performed using a transient diffusion formulation based on combining Darcy's law with the continuity equation for the conservation of the total fluid mass. A discussion of these methods is beyond the scope of this paper, for further details and examples of applications see Bear (1972), Shi and Wang, (1986), Mudford (1988), and Williamson (1992). The mathematical models comprise a series of equations that describe fluid pressure evolution through geological time in a compacting sedimentary column (derived in this example using Platte River Associates BasinMod software). Estimates of formation pore pressures using the two permeability-time curves are seen in Figure 6 (d, e, f). Curve 2 model predictions of the present day pore-pressure depth profile provides a better fit (compared to measured DST/RFT/MUD Wts., shown as crosses) than curve 1 (Fig. 6d). However, given the numerical models sensitivity, both curves can be regarded as giving a "good" fit to observations. Figure 6 (e, f) shows, however, important differences in modelled pore pressure through time

for curve 1 and 2 assumptions. Modelled excess pore pressures (i.e. in excess of hydrostatic) are shown for the 152 Ma datum through time (Fig. 5e, f). Using curve 2 permeability-time profile suggests that the formation was subject to excess pressures early in its burial history and that these pressures have often exceeded the lithostatic pressure, implying a fracturing/healing seal history. Very limited excess pressuring is indicated using curve 1 assumptions, with only a late (last 10 Ma) response to disequilibrium compaction pressuring. The simple conclusion to be drawn from this example is that, despite a good fit between modelled and measured present day pressure-depth profiles using both permeability-time curves, there are important differences in respective formation pressure time estimates with significant implications for the formations sealing history. In the absence of measured permeability there would be no significant basis for selection of a preferred model; however, permeability measurements by Katsube et al. (1991) on this well indicate that present day permeabilities are more similar to the curve 2 assumption. Other work reported in this paper, however, indicates that physical property evolution of compacting shales is intimately tied to complex diagenetic processes which our numerical pore pressure models are yet to account for.

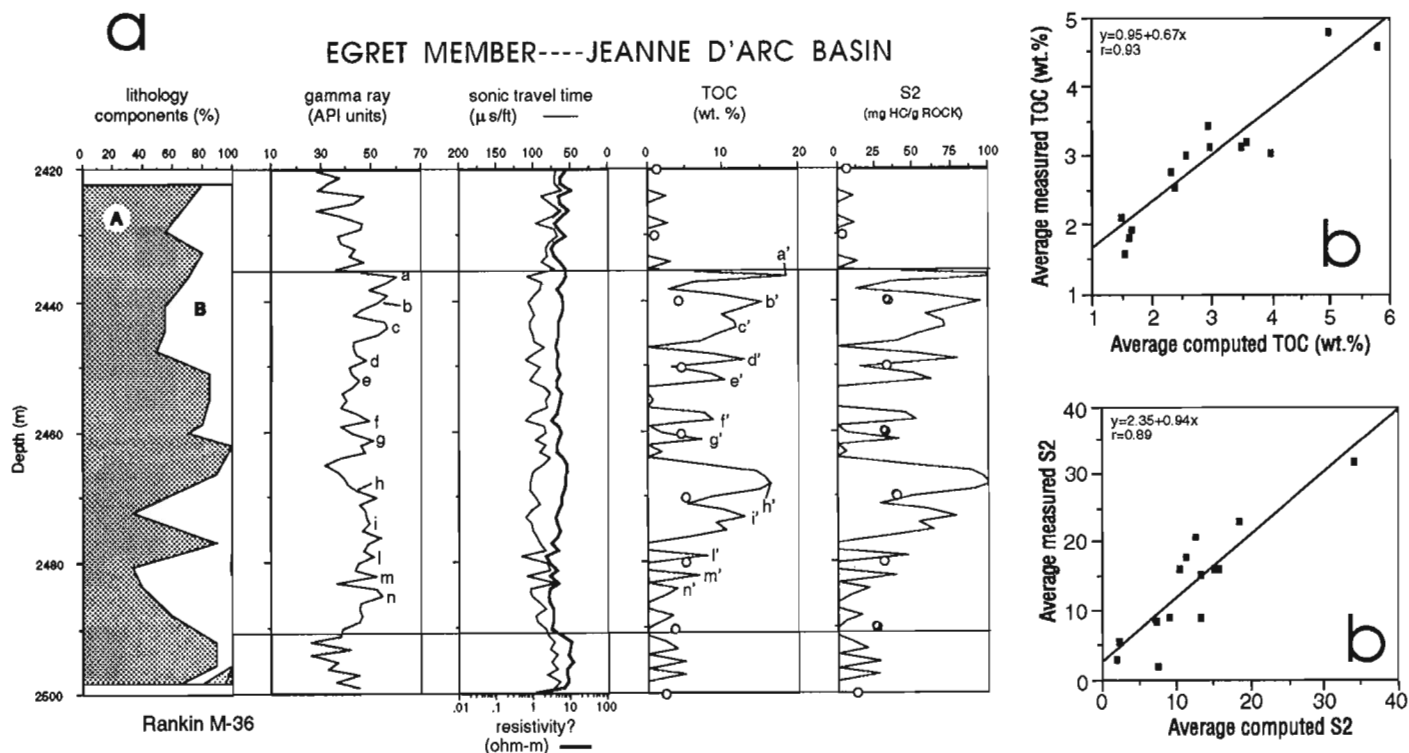


**Figure 7.** Measured vitrinite-depth profile for Hibernia K-18 location (crosses) versus model predicted vitrinite profile (solid line). Rock-Eval measurements on the source interval indicates a production index (transformation ratio) similar to that predicted by the model supporting the predicted maturity-depth profile (see text).

## MODEL UNCERTAINTY 6 – MATURITY INDICATORS

In addition to measured vitrinite reflectance and fission track data as constraints on thermal and maturity models we also utilize, where possible, Rock-Eval data. For example, the measured vitrinite reflectance-depth versus model predicted plot for Hibernia K-18 shows (Fig. 7) an apparent overprediction for a substantial part of the rock column. Predicted values for the Egret Member, however, are similar to the measured values (see magnified section). There is therefore some uncertainty in the quality of the fit and subsequently in the predicted maturity time curves. Rock-Eval measured data of transformation ratios (production index) for the Egret member are of similar magnitudes however, to the model predicted values, i.e. values predicted using the same thermal model that produced the apparent overprediction of the vitrinite in the figure. It is most likely that the vitrinite reflectance measurements seen in this figure have been suppressed through exposure to oils of lower maturities (stained, see Avery et al., 1986). Utilization of several measured maturity and thermal indicators, therefore, reduces uncertainties and increases confidence in our model predictions.

## PREDICTION OF SOURCE ROCK PROPERTIES



**Figure 8.** Digital log derived lithological and geochemical components of the Egret source rock interval at the Rankin M-36 location. Also shown are the high correlation coefficients between measured and predicted average TOC and S2. See text for more details.

## MODEL UNCERTAINTY 7 – KEROGEN DISTRIBUTION

Regional studies of hydrocarbon charge histories will often identify gross and net source rock intervals, with the net comprising the sum total of organic rich layers. It is evident however that the distribution of kerogen within source rocks is an important control on such properties as generation-expulsion efficiencies that in turn may influence hydrocarbon charge timing and magnitude. Playing a significant part in this is the exact nature (shale, carbonate, silt, diagenesis etc.) and extent/continuity of non-organic rich layers within the gross source interval. Ideally, our studies would have access to outcrop or cores to develop a comprehensive understanding of chemical characters and facies of the source rock. In the absence of such for the Jeanne d'Arc Basin we are dependent on cuttings based Rock-Eval and lithology data. In an effort to understand the detailed nature of the kerogen distribution we have applied the delta log R method of Passey et al. (1990) to the Egret source interval (Huang et al., in press). Results of these applications are shown in Figure 8.

Figure 8a shows log derived lithologic components of the Egret interval (A = carbonate, B = shale), the gamma curve and the overlain resistivity log and sonic travel time logs from which are derived predicted TOC and S2 values. Predicted TOC and S2 curves are shown as solid lines; Rock-Eval data (small circles) are from cuttings samples (i.e. averaged values over 10 m intervals, and subject to cavings contamination). The method allows prediction of kerogen distribution in the Egret Member source interval on a more detailed scale than the Rock-Eval method alone permits. The accuracy of the method is illustrated in Figure 8b which shows the correlation between averaged calculated and average measured TOC and S2. At the very least, what is clear from these figures are relative peaks and lows in source quality (see serrated profiles), which provides insight into kerogen distribution throughout the interval.

## ACKNOWLEDGMENTS

Al Grant and Phil Moir (AGC) are thanked for their review and comments on this paper. The performance of this research is expertly aided by numerous individuals including Kevin Coflin (AGC), Scott King, Kevin Desroches, and Art Jackson (AGC).

## SUMMARY

The research activities presented above provide a snapshot of our ongoing efforts to reduce uncertainty in our comprehensive, quantitative hydrocarbon charge models of eastern Canada frontier basins. Results from the projects described above and other ongoing research activities are continually being integrated into the broader hydrocarbon charge models for east coast basins. Ultimately the work will provide more

accurate resource estimates, increased understanding of the presently observed distribution of petroleum occurrences and, importantly, quantitative models with which to provide predictions of further petroleum accumulations.

## REFERENCES

- Atlantic Geoscience Centre**  
1991: East Coast Basin Atlas Series: Scotian Shelf; Geological Survey of Canada, 147 p.
- Avery, M., Bell, J.S., and McAlpine, D.K.**  
1986: Vitrinite reflectance measurements and their implications for oil and gas exploration in the Jeanne d'Arc Basin; in *Current Research, Part A*; Geological Survey of Canada, Paper 86-1A, p. 489-498.
- Bear, J.**  
1972: *Dynamics of fluids in porous media*; American Elsevier Publishing Co., New York.
- Huang, Z., Williamson, M., Fowler, M., and McAlpine, D.K.**  
in press: Predicted and measured petrophysical and geochemical characteristics of the Egret Member oil source rock, Jeanne d'Arc Basin, offshore eastern Canada; *Journal of Marine and Petroleum Geology*.
- Hunt, J.M., Lewan, M.D., and Hennet, R.J.C.**  
1991: Modelling oil generation with time-temperature index graphs based on the Arrhenius equation; *American Association of Petroleum Geologists Bulletin*, v. 75, no. 4, p. 795-807.
- Katsube, J., Best, M.E., and Mudford**  
1991: Petrophysical characterization of shales from the Scotian shelf; *Geophysics*, v. 56, p. 1681-1689.
- Keen, M. and Williams, G. (ed.)**  
1990: *Geology of the Continental Margin of eastern Canada*; Geological Survey of Canada, *Geology of Canada*, no. 2, 853 p. (also *Geological Society of America, Geology of North America* vol. I-1).
- Mudford, B.**  
1988: Modelling the occurrence of overpressures on the Scotian Shelf, offshore eastern Canada; *Journal of Geophysical Research*, v. 93, p. 7845-7855.  
1990: A one-dimensional, two phase model of overpressure generation in the Venture gas field, offshore Nova Scotia; *Bulletin of Canadian Petroleum Geology*, v. 38, no. 2, p. 246-258.
- Mudford, B. and Best, M.**  
1989: Venture gas field, offshore Nova Scotia: case study of overpressuring in region of low sedimentation rate; *American Association of Petroleum Geologists Bulletin*, v. 73, p. 1383-1396.
- Passey, Q.R., Creaney, S., Kulla, J.B., Moretti, F.J., and Stroud, J.D.**  
1990: A practical model for organic richness from porosity and resistivity logs; *American Association of Petroleum Geologists Bulletin*, v. 74, p. 1777-1794.
- Shi, Y. and Wang, C.**  
1986: Pore pressure generation in sedimentary basins- overloading versus aquathermal; *Journal of Geophysical Research*, v. 91, p. 2153-2162.
- Ungerer, P., Burrus, J., Doligez, B., Chenet, P.Y., and Bessis, F.**  
1990: Basin evaluation by integrated two-dimensional modeling of heat transfer, fluid flow, hydrocarbon generation and migration; *American Association of Petroleum Geology Bulletin*, v. 74, no. 3, p. 309-335.
- Williamson, M.A.**  
1992: The subsidence, compaction, thermal and maturation history of the Egret Member source rock, Jeanne d'Arc Basin, offshore Newfoundland; *Bulletin of Canadian Petroleum Geology*, v. 40, no. 2, p. 136-150.
- Williamson, M.A. and Smyth, C.**  
1992: Timing of gas and overpressure generation in the Sable Basin offshore Nova Scotia: implications for gas migration dynamics; *Bulletin of Canadian Petroleum Geology*, v. 40, no. 2, p. 151-169.

# Detection of $^{234}\text{Pa}$ in low-level radioactive waste by gamma-ray spectral logging

P.G. Killeen and K.A. Pflug  
Mineral Resources Division

*Killeen, P.G. and Pflug, K.A., 1993: Detection of  $^{234}\text{Pa}$  in low-level radioactive waste by gamma-ray spectral logging; in Current Research, Part E; Geological Survey of Canada, Paper 93-1E, p. 307-312.*

---

**Abstract:** An example of the advantage of borehole gamma-ray spectral logging over total count logging, for detecting and identifying unexpected radioelements, was demonstrated at the Port Hope landfill site during a Geological Survey of Canada study in conjunction with an investigation by the Low-Level Radioactive Waste Management Office of Atomic Energy of Canada Limited. The dominant source of radioactivity in the low-level radioactive waste at the landfill site is radium ( $^{226}\text{Ra}$ ). However, radioactivity from anomalous concentrations of protactinium ( $^{234}\text{Pa}$ ) at one location was recognized because of unusual logs recorded by the GSC gamma-ray spectral logging system. Identification of the source of radioactivity as  $^{234}\text{Pa}$  was only made possible because the complete spectrum was recorded.

**Résumé :** On a démontré l'avantage que présentent les diagraphies spectrales de rayons gamma par rapport aux diagraphies par comptage total pour la détection et l'identification d'éléments radioactifs lors d'une étude entreprise par la Commission géologique à la décharge de Port Hope. Cette étude a été menée conjointement avec une enquête par le Bureau de gestion des déchets radioactifs de faible activité de l'Énergie atomique du Canada Ltée. Le radium ( $^{226}\text{Ra}$ ) est la source principale de radioactivité dans les déchets radioactifs de faible activité à la décharge. Toutefois, le système de diagraphie spectrale de rayons gamma de la CGC a donné des résultats inhabituels à un endroit, ce qui a permis de reconnaître une radioactivité due au protactinium ( $^{234}\text{Pa}$ ). On a reconnu que la source de cette radioactivité était le  $^{234}\text{Pa}$  uniquement parce que le spectre complet a été enregistré.

**INTRODUCTION**

The municipal landfill site in the town of Port Hope, Ontario, is contaminated with low-level radioactive waste (primarily <sup>226</sup>Ra) originating from a radium refinery which operated from 1933 until the 1950s. Responsibility for clean-up of the waste at the landfill site rests with the Low-Level Radioactive Waste Management Office (LLRWMO) of Atomic Energy of Canada Limited (AECL). During a recent investigation of this site by the LLRWMO, the Borehole Geophysics Section of the Geological Survey of Canada (GSC) carried out a study to assess the application of borehole geophysics to the detection of low-level radioactive waste.

Gamma-ray spectral logging was found to be the most useful technique for this application (Killeen et al, in press). In addition to delineating the contaminated layers, the gamma-ray spectral logs were successfully used to identify the source of radioactivity, including some unexpected sources.

**THE <sup>238</sup>U DECAY SERIES**

The low-level radioactive waste at the Port Hope landfill site is dominantly <sup>226</sup>Ra, which belongs to the <sup>238</sup>U decay series (Fig. 1). When this series is in radioactive equilibrium (i.e., the rate of decay of each element is equal to its rate of production by decay of its parent), the theoretical and experimentally measured (equilibrium reference) gamma-ray energy spectra have characteristic shapes as illustrated in Figure 2. The equilibrium reference spectrum in this figure was acquired with a 32 mm x 127 mm (1.25" x 5") CsI(Na) detector. As this figure shows, most of the gamma rays in the <sup>238</sup>U series spectrum are emitted by <sup>214</sup>Bi, however, because the series is in equilibrium the <sup>214</sup>Bi gamma-ray count rate can be related to the concentration of any radioelement in the series. It is, therefore, customary to define an energy window (the 'uranium window') which includes the 1765 keV and, sometimes, the 2204 keV <sup>214</sup>Bi gamma-ray peaks (see Fig. 2) and determine the concentration of <sup>238</sup>U (or any other radioelement in the series) from the count rate in this window.

Equilibrium throughout the entire <sup>238</sup>U series would not be expected in the waste at the landfill site. It is expected, though, that at least radioelements in the decay series from <sup>226</sup>Ra through to <sup>214</sup>Po, which produce most of the <sup>238</sup>U series gamma rays, generally exist in equilibrium proportions because of their short half-lives. Thus, spectra from radium-contaminated zones will resemble the <sup>238</sup>U series equilibrium reference spectrum shown in Figure 2 and the <sup>226</sup>Ra concentration can be computed from the count rate in the uranium window.

**GAMMA-RAY SPECTRAL LOGGING**

Figure 3 illustrates the principle of gamma-ray spectral logging. In gamma-ray spectral logging, the gamma rays from radioelements within the rock or soil surrounding a borehole are counted and their energies are measured. Gamma-ray

**DISINTEGRATION SERIES OF URANIUM-238**

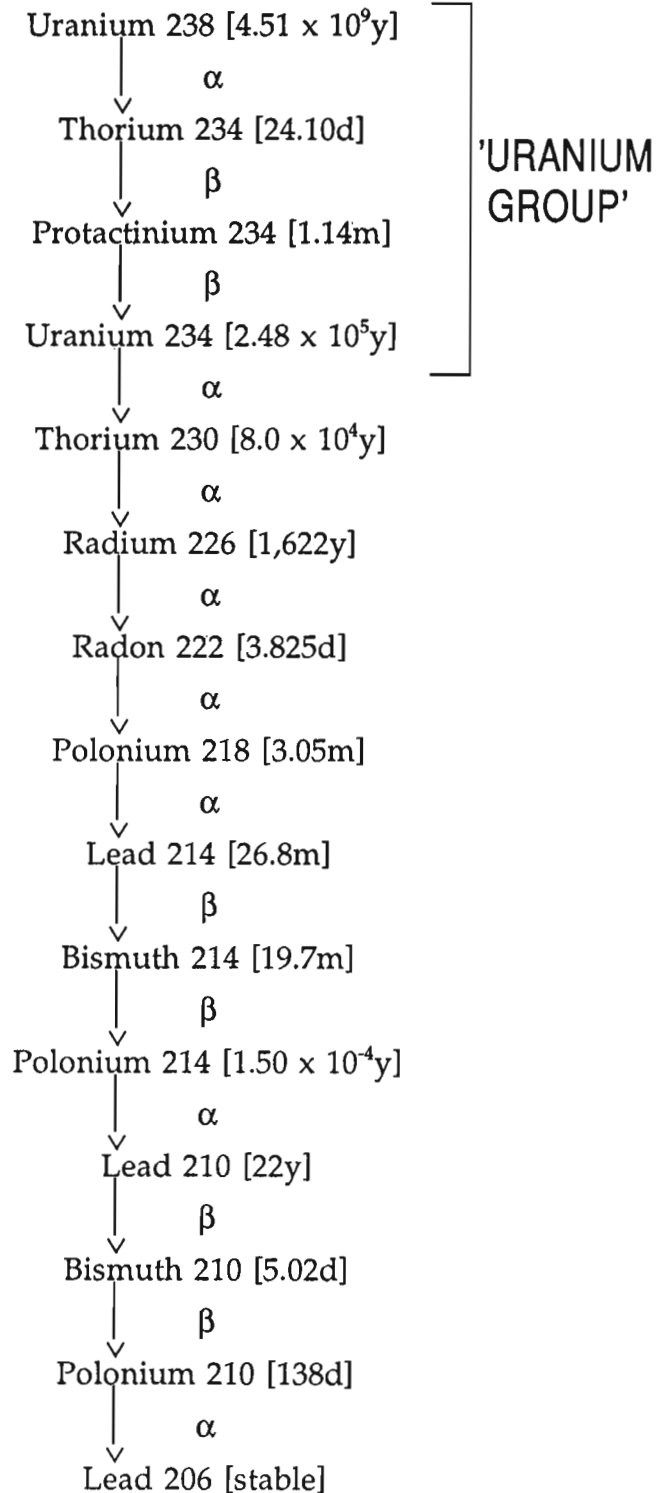
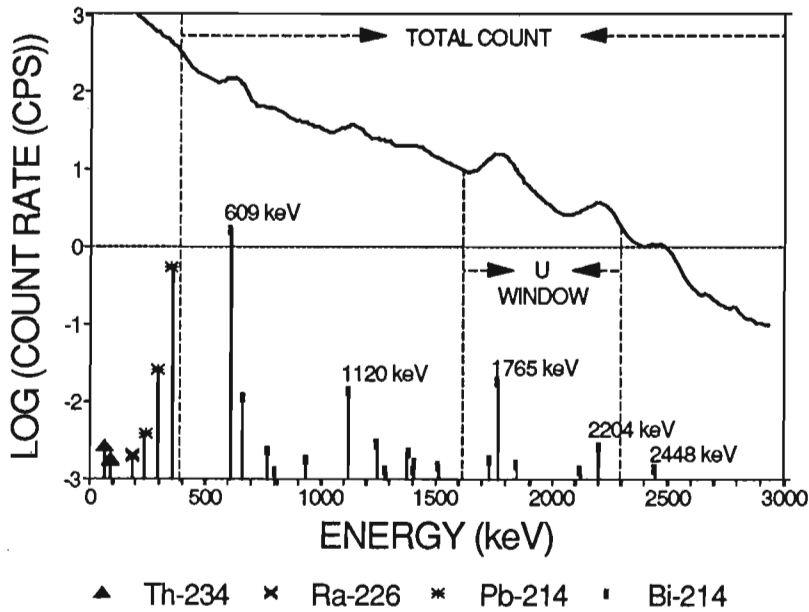


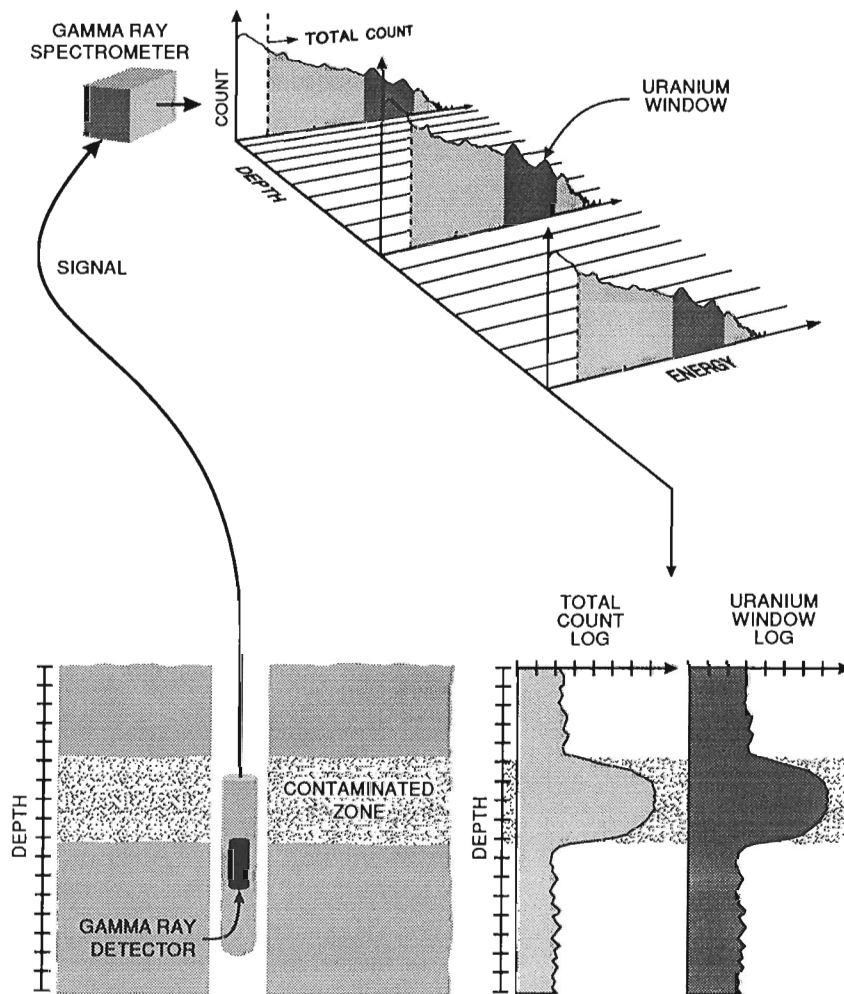
Figure 1. <sup>238</sup>U decay series.





**Figure 2.**

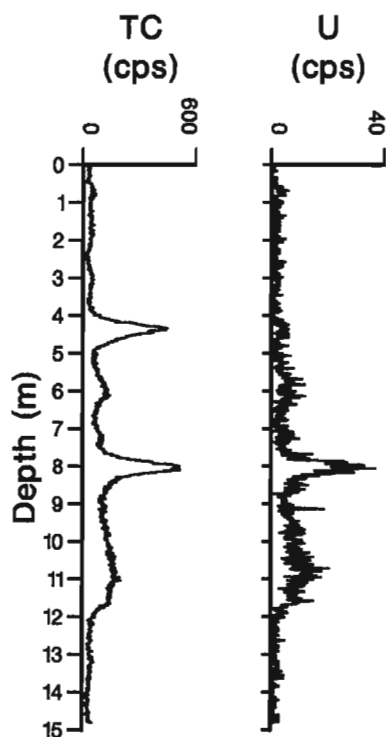
Theoretical (line histogram) and experimentally measured (equilibrium reference, solid line) gamma-ray energy spectra for the  $^{238}\text{U}$  series in equilibrium. No scale is given for the theoretical spectrum since only the relative amplitudes of the peaks are important. The theoretical spectrum is plotted on a linear scale while the equilibrium reference spectrum is on a logarithmic scale.



**Figure 3.** Total count and uranium window logs obtained from a spectral gamma-ray logging probe. Because a complete spectrum is recorded at each sample depth, a log of the count rate in any energy window (within the energy limits measured) can be produced.

energy spectra, containing characteristic peaks which can be used to identify the source of radioactivity, are thus acquired continuously as the detector moves along the borehole. By defining energy windows encompassing specific gamma-ray energy peaks in the spectra and computing the count rates in these windows, the vertical distribution of radioactivity (or gamma-ray logs) due to selected radioelements can be plotted. In contrast, the gamma-ray energies are not measured in total count logging so that identification of the source is not possible. Only the total radioactivity due to all sources along the borehole can be determined. This might include naturally occurring sources of thorium, uranium, and potassium, as well as radium or other sources.

A typical gamma-ray spectral log could consist of spectra (256 channel, 0 to 3 MeV) recorded every second with the probe moving at 0.6 m/min giving a sample length of 1 cm. These individual spectra can be summed on a channel-by-channel basis to produce a 'summed spectrum' over a given depth range with improved counting statistics. Similarly, the probe may be held stationary at a selected depth and the one second spectra can be summed to produce a summed spectrum at a given depth.



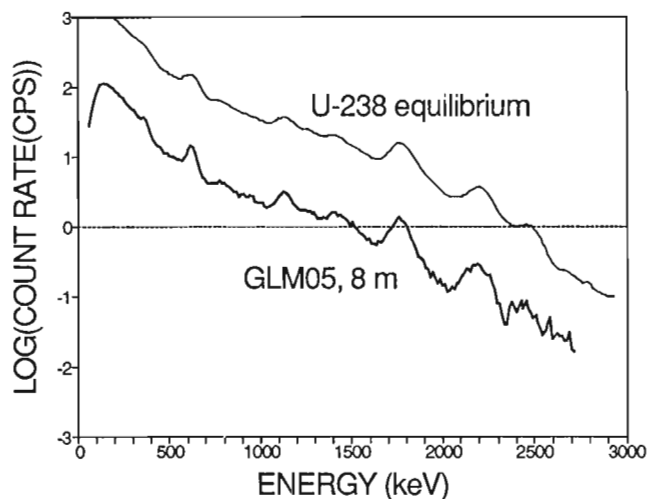
**Figure 4.** Total count and uranium window logs from hole GLM05 at the Port Hope landfill site. The total count log shows two apparently similar anomalies at 4.4 m and 8.0 m. The difference in source of the anomalies is evident from the uranium log which only shows the 8.0 m anomaly.

## LOGGING RESULTS FROM HOLE GLM05

An example of the advantage of spectral logging over total count logging for source identification is the anomaly at a depth of 4.4 m in hole GLM05. Logs of the count rate in the total count and uranium windows for this hole are shown in Figure 4. The total count log contains two anomalies with similar amplitudes at 4.4 m and 8.0 m. From the total count log alone, both anomalies would be attributed to radium contamination. However, the absence of an anomaly at 4.4 m in the (unstripped) uranium log indicates that this anomaly is due primarily to lower energy gamma rays.

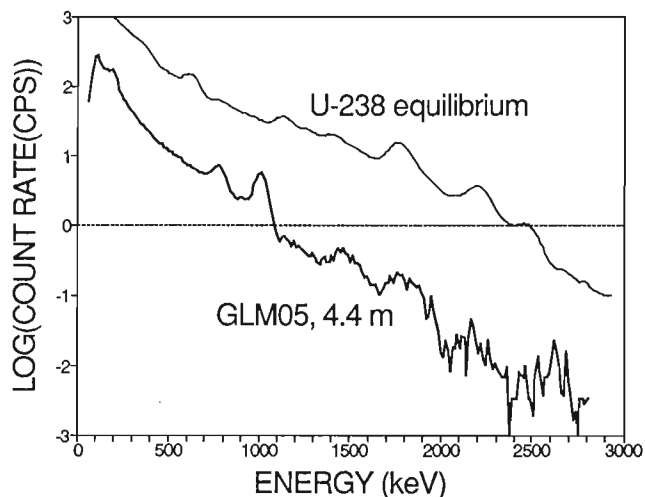
The difference in source of the two anomalies is clearly demonstrated by the spectra at these depths. In Figure 5, the  $^{238}\text{U}$  series equilibrium reference spectrum from Figure 2 is plotted along with the measured spectrum from 8.0 m in hole GLM05. All measured spectra presented in this paper were acquired with a 32 mm x 127 mm CsI(Na) detector. Apart from a difference in overall count rate, the two spectra are the same and, therefore, the 8.0 m anomaly can be attributed to radium contamination. In Figure 6, the  $^{238}\text{U}$  series equilibrium reference spectrum from Figure 2 is plotted along with the 4.4 m spectrum in hole GLM05. Unlike the 8.0 m anomaly, the spectrum from the 4.4 m anomaly has different energy peaks and a different overall shape than the  $^{238}\text{U}$  series equilibrium reference spectrum and, therefore, the source of the 4.4 m anomaly must be different than that of the 8.0 m anomaly.

The second decay product in the  $^{238}\text{U}$  series ( $^{234}\text{Pa}$ , see Fig. 1) emits gamma rays, the two most prominent of which have energies at 766 keV and 1001 keV and are believed to be the cause of the two dominant peaks in the 4.4 m spectrum. Although they are not evident in the  $^{238}\text{U}$  series equilibrium reference spectrum due to their relatively low intensities, they

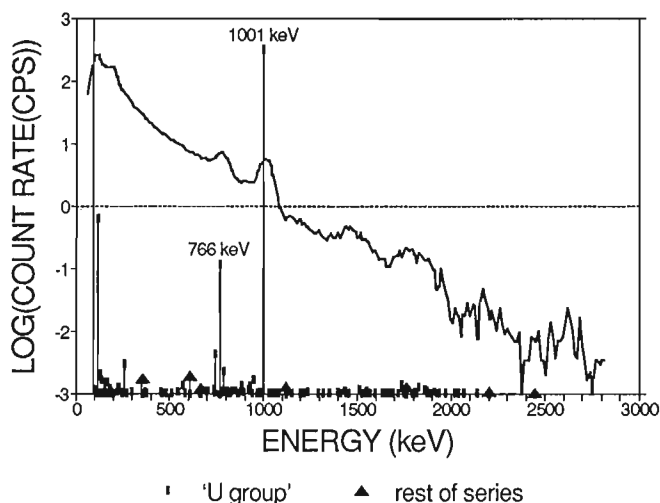


**Figure 5.**  $^{238}\text{U}$  series equilibrium reference spectrum and measured spectrum from the anomaly at 8.0 m in hole GLM05. The same peaks are visible in the two spectra and the shapes of the spectra are similar.

would dominate the spectrum if the concentrations of the 'uranium group' (Rosholt, 1959) nuclides ( $^{238}\text{U}$ ,  $^{234}\text{Th}$ ,  $^{234}\text{Pa}$ , and  $^{234}\text{U}$ ) considerably exceeded equilibrium values relative to the rest of the  $^{238}\text{U}$  series. This situation would also result in a much lower count rate at high energies (as observed in the 4.4 m spectrum) because the intensities of the 'uranium group' gamma rays above 1001 keV are low relative to the intensities of the 766 keV and 1001 keV gamma rays.



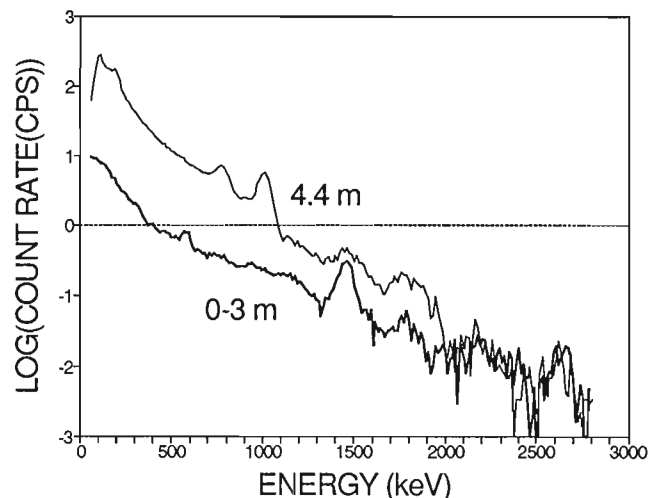
**Figure 6.**  $^{238}\text{U}$  series equilibrium reference spectrum and measured spectrum from the anomaly at 4.4 m in hole GLM05. The difference in shape of the spectra and in the peaks visible in the spectra suggest that the 4.4 m anomaly is not caused by radium contamination. Note the much lower count rate at the high energy end of the 4.4 m spectrum which explains why the anomaly was missed by the uranium window.



**Figure 7.** Measured spectrum (solid line) from the anomaly at 4.4 m in hole GLM05 and theoretical spectrum (line histogram) produced when the 'uranium group' elements in the  $^{238}\text{U}$  series exceed equilibrium proportions by a factor of 1000. No scale is given for the theoretical spectrum which is plotted on a linear scale. The 4.4 m spectrum is plotted on a logarithmic scale.

To confirm the possibility that waste containing an excess of 'uranium group' radioelements might exist at the landfill site, the history of the Port Hope refinery, where the low-level radioactive waste originated, was investigated. At the Port Hope refinery, several experimental methods of uranium extraction were investigated; some early tests produced waste containing up to 20% uranium and high levels of protactinium (Duncan Moffat, pers. comm., 1993). This waste presumably initially contained the radionuclides  $^{238}\text{U}$  and  $^{234}\text{U}$  in approximately equilibrium ratios and protactinium ( $^{235}\text{U}$  can be ignored because of its low relative abundance). Because of the 24.1 d half-life and 1.14 min half-life, respectively, of  $^{234}\text{Th}$  and  $^{234}\text{Pa}$ , after five to six months  $^{234}\text{Th}$  and  $^{234}\text{Pa}$  would equilibrate with the  $^{238}\text{U}$  in the waste. Elements below  $^{234}\text{U}$  would remain insignificant for a long time due to the 80 000 year half-life of  $^{230}\text{Th}$ , the next nuclide in the series. Today this waste would be expected to contain 'uranium group' nuclides in equilibrium with concentrations of up to 20% uranium, but insignificant amounts of the other  $^{238}\text{U}$  series decay products. Allowing for dilution of the waste by 'clean' soil at the landfill site to as low as 1% (or 10 000 ppm) uranium, the 'uranium group' would still be present in far greater concentrations than the other radionuclides in the series, which would be at background levels (9 ppm uranium).

The theoretical spectrum corresponding to this situation is shown in Figure 7 with the 4.4 m spectrum from hole GLM05. The theoretical spectrum is dominated by the 766 keV and 1001 keV  $^{234}\text{Pa}$  gamma rays which correspond with the two prominent peaks in the 4.4 m spectrum. Above 1001 keV, the intensities of the 'uranium group' gamma rays in the theoretical spectrum in this case are comparable to the intensities of gamma rays from the rest of the  $^{238}\text{U}$  series. Above 2100 keV, there are no 'uranium group' gamma rays. Thus, the 4.4 m spectrum above 1001 keV is due to background levels of potassium (K), U, and thorium (Th) in the soil, with increased count rates and distortion of the background spectrum between 1001 keV and 2100 keV due to the gamma rays from the anomalous concentrations of



**Figure 8.** Spectra from the anomaly at 4.4 m and summed from 0 to 3 m (the nonanomalous zone) in hole GLM05.

'uranium group' radioelements. This is demonstrated in Figure 8 which shows the summed spectrum from 0 to 3 m in hole GLM05 (a nonanomalous or background spectrum) and the 4.4 m spectrum. (Note: the 0 to 3 m summed spectrum differs from the  $^{238}\text{U}$  series equilibrium reference spectrum in Figures 2, 5, and 6 due to additional peaks from  $^{40}\text{K}$  (1460 keV) and  $^{232}\text{Th}$  (2614 keV)).

## DISCUSSION AND CONCLUSIONS

Comparison of the anomalous spectrum from a depth of 4.4 m in hole GLM05 with the  $^{238}\text{U}$  series equilibrium reference spectrum and the theoretical spectrum corresponding to an excess of the 'uranium group', indicates that this anomaly is caused by  $^{234}\text{Pa}$  supported by high uranium concentrations. However, samples were not collected from hole GLM05 so it is not possible to confirm the presence of  $^{234}\text{Pa}$ . A drilling and sampling program is planned for the summer of 1993 during which it is expected that samples from near the vicinity of hole GLM05 will be collected for lab analysis of the  $^{234}\text{Pa}$  concentrations. In addition, standard library spectra of potassium, uranium, and thorium are being constructed using measurements in model boreholes (Killeen, 1986) in order to use spectral fitting techniques to better define the individual components making up the spectrum. Results of such a fitting process should clearly show the spectrum of the unexpected radionuclides in the residual spectrum (Grasty, 1985).

The results from hole GLM05 illustrate the effectiveness of a portable 256 channel gamma-ray spectral logging system for the in situ identification of unexpected sources of radioactivity in low-level radioactive waste investigations. The advantages of using gamma-ray spectral logging for this type of application are 1) the equipment is portable, easy to

use, and can be rented or purchased; 2) full spectral information is recorded and available for subsequent processing; and 3) by calibrating in model boreholes with known potassium, uranium, and thorium concentrations, logs of the distribution of potassium and decay products of uranium and thorium along a borehole can be efficiently obtained.

## ACKNOWLEDGMENTS

The authors wish to acknowledge Jonathan Mwenifumbo, Bob Zelmer, and Barry McCallum for their participation in this work. We also thank Duncan Moffat for providing historical information regarding uranium refining methods tested at the Port Hope refinery.

## REFERENCES

- Grasty, R.L.**  
1985: The analysis of multichannel airborne gamma-ray spectra; *Geophysics*, v. 50, p. 2611-2620.
- Killeen, P.G.**  
1986: A system of deep test holes and calibration facilities for developing and testing new borehole geophysical techniques; in *Borehole Geophysics for Mining and Geotechnical Applications*, (ed.) P.G. Killeen; Geological Survey of Canada, Paper 85-27, p. 29-46.
- Killeen, P.G., Pflug, K.A., Mwenifumbo, C.J., Zelmer, R.L. and McCallum, B.A.**  
in press: Application of spectral gamma-ray logging to low-level radioactive waste management studies; *Nuclear Geophysics*.
- Rosholt, J.N., Jr.**  
1959: Natural radioactive disequilibrium of the uranium series; United States Geological Survey, Bulletin 1084-A, p. 1-30.

Geological Survey of Canada Project 880030

# Effect of vacuum-drying and temperature on effective porosity determination for tight rocks

N. Scromeda and T.J. Katsube  
Mineral Resources Division

*Scromeda, N. and Katsube, T.J., 1993: Effect of vacuum-drying and temperature on effective porosity determination for tight rocks; in Current Research, Part E; Geological Survey of Canada, Paper 93-1E, p. 313-319.*

---

**Abstract:** Effective porosity measurements of rock samples usually include an oven-drying procedure at temperatures of 90-116°C (American Petroleum Institute's recommendation), in order to drive out free and adsorbed waters, but leaving structural water intact. However, concern has been raised over possible textural changes occurring for certain clays when drying at temperatures above 50°C, resulting in many laboratories applying vacuum-drying at temperatures well below 100°C. Therefore, a study has been carried out to investigate the effect of low temperature vacuum oven-drying on measurement accuracy of effective porosity.

Results indicate that differences between drying under vacuum and under atmospheric pressures do not influence the effective porosity values when at temperatures above 100°C. However, while larger fractions of free water may be driven out under vacuum compared to atmospheric conditions at lower temperatures, temperatures above 100°C are required to drive off the adsorbed water, implying that measurements at temperatures below 100°C could be inaccurate.

**Résumé :** Pour mesurer la porosité efficace des échantillons de roche, il faut habituellement sécher les échantillons au four à des températures allant de 90 à 116°C (recommandation de l'American Petroleum Institute) pour en extraire l'eau libre et l'eau adsorbée tout en laissant intacte l'eau structurale. Toutefois, certains se sont inquiétés des changements de texture de certaines argiles qui peuvent se produire lorsque le séchage se fait à des températures supérieures à 50°C, nombre de laboratoires allant jusqu'à recourir au séchage sous vide à des températures bien inférieures à 100°C. On a donc entrepris une étude de l'effet du séchage au four sous vide à basse température sur la précision des mesures de la porosité efficace.

Les résultats indiquent que la porosité efficace est la même, que le séchage se fasse sous vide ou à la pression atmosphérique, lorsque la température dépasse 100°C. Toutefois, même si plus d'eau libre est extraite sous vide qu'à la pression atmosphérique à de faibles températures, il faut dépasser une température de 100°C pour extraire l'eau adsorbée, ce qui signifie que les mesures à des températures inférieures à 100°C pourraient être inexactes.

## INTRODUCTION

Effective porosity measurements of rock samples usually include a drying procedure (American Petroleum Institute, 1960). The conventional drying method consists of oven-drying a rock sample at 116°C under atmospheric condition or 93°C under vacuum, both following the recommended practice for core-analysis procedures (American Petroleum Institute, 1960). These temperatures are selected to drive out the free water and adsorbed water on the pore surfaces, but not the structural water. However, concern has been raised over possible textural changes occurring for certain clay types (e.g. Soeder, 1986) when drying rocks at temperatures above 50°C (e.g. partial expulsion of interlamellar water). This could cause reduced measurement accuracy. For this reason, many laboratories servicing the petroleum industry vacuum-dry their samples at temperatures well below 100°C (e.g. Katsube et al., 1992).

The effective porosity of various types of tight (low porosity) rocks have been and are being measured in our laboratory (e.g. Hume and Katsube, 1987; Katsube and Hume, 1987; Katsube and Walsh, 1987; Katsube et al., 1991; Scromeda et al., 1993) using the immersion method, which involves drying the samples at a temperature of 105-116°C. Only atmospheric pressures have been used for drying in the past. In order to find out whether results similar to those at 105-116°C can be achieved at lower temperatures when using vacuum-drying, a series of effective porosity measurements on several rock types has been carried out under vacuum at different temperatures. This paper describes the results of these measurements.

The immersion method used in our studies is described by Katsube et al. (1992). They provide a relatively comprehensive overview of the method, including the advantages and limitations of the various procedures applied. The effective porosity,  $\phi_E$ , is given by the following equation:

$$\phi_E = (W_W - W_D)\delta_E / (W_D\delta_W) \quad (1)$$

where  $W_W$  is the weight of the fluid-saturated rock specimen,  $W_D$  is that of the dry rock sample,  $\delta_E$  is the bulk density of the rock sample, and  $\delta_W$  is the bulk density of the pore water (usually considered to be unity) saturating the specimen. The main subject of this study is how to determine  $W_D$ .

The suite of rock samples used in this study consists of three granites, two gabbros, and three shales. The effective porosity of this suite was previously measured (Katsube and Scromeda, 1991) under atmospheric pressure. The shale sample V-5 was also used in a study (Katsube et al., 1992) similar to this one, that is, effective porosity was measured at various temperatures but under atmospheric conditions, thus creating an adequate comparison for this study. Petrophysical information related to these samples is available in Katsube and Hume (1987) for the granites, in Hume and Katsube (1987) for the gabbros, and in Katsube et al. (1992) for the shales.

## METHOD OF INVESTIGATION

### *Sample preparation*

The granite and the gabbro samples were cut into half-disk specimens with a diameter of 4.10-4.56 cm, and a thickness of 0.91-1.05 cm. The shale samples, cylindrical plugs with a diameter of 2.54 cm, were cored in the vertical direction from 10.16 cm split core samples (Katsube et al., 1991). These plugs were then cut to a thickness of 0.5-1.0 cm for the porosity measurements.

### *Previous experimental projects*

The effective porosities of the three shale samples (V-4, V-5, and V-9) have been measured several times in the past, (Katsube et al., 1990, 1991, 1992). The results labeled "EP-1991(3)" and reported in Katsube et al. (1992) are listed in Table 3 to represent the previous measurements for these samples, since their oven-drying procedures are similar to those in this study. Results of previous effective porosity measurements for the three granite samples (W-1, W-2, and W-3) and two gabbro samples (E-1 and E-2) are reported in Katsube and Scromeda (1991), and are also listed in Table 3.

### *Experimental procedure*

The experimental procedure used in this study is similar to ones used in the past (Katsube and Scromeda, 1991; Katsube et al., 1992), as previously mentioned, except for slight variations made in the drying procedure using the vacuum oven. The procedure used for this study is as follows:

#### **(1) Vacuum saturation**

The rock specimen is placed in a dry beaker using tweezers, before the beaker is placed in a vacuum chamber. Vacuum is then applied at a pressure of 760 mm Hg for 15 minutes, to degas the specimen before it is saturated by introducing purified, deionized water into the chamber. After saturation, vacuum is applied for another 15 minutes for additional degassing, before leaving the immersed specimen under atmospheric pressure for up to 1,490 minutes (approximately 24 hours). Before weighing the specimen, it is removed from the beaker using tweezers, and then the surface moisture films removed using a kimwipe. Considerable care is taken to maintain a consistent surface-drying process. The specimen is then placed in a dry beaker for vacuum-drying.

#### **(2) Vacuum-drying**

The saturated specimen is now in a dry beaker and is placed in the vacuum chamber, once again, in order to evacuate the moisture. It is left under vacuum for periods varying from 195

to about 720 minutes. After each of the specified periods, the sample is weighed. This procedure is repeated until a constant weight is obtained. A constant weight is defined by the specimen weight variation being less than 0.1 mg per hour.

**(3) Vacuum oven-drying**

Once the sample has been removed from the vacuum chamber under room temperature, it is placed in the vacuum oven under a vacuum of 760 mm Hg. The vacuum oven-drying is carried out in five steps at five different temperatures of 50°C, 70°C, 90°C, 100°C, and 116°C. At each temperature level, the specimen is dried for periods of up to 2160 minutes. At certain intervals, the specimen is removed from the oven and cooled in a desiccator for approximately 10 minutes at room temperature. The sample is then weighed and returned to the vacuum oven to be reheated. This procedure is repeated until a constant weight (<0.1 mg/hour) is obtained. Once a constant weight is obtained, the sample is returned to the vacuum oven and heated at the next temperature level. These procedures are repeated until a constant weight at the temperature of 116°C has been attained. This procedure is very similar to that used in a previous study (Katsube et al., 1992).

**Additional parameters**

The duration times for drying and degassing under vacuum, for saturating under atmospheric pressure, and for oven-drying at different temperatures under vacuum are represented by  $t_f$ ,  $t_s$ , and  $t_D$ , respectively, and are expressed in minutes. Duration of saturation,  $t_s$ , is measured from the point that 15 minutes of vacuum-drying and 15 minutes of vacuum-degassing the immersed sample is completed. The weight of a specimen at any given time is represented by  $W_r$  in grams. After  $W_r$  reaches a constant value during the saturation process, the specimen is considered to be fully saturated and its weight is represented by  $W_w$ . When  $W_r$  reaches a constant value during oven-drying at 116°C, the specimen is considered to be completely dried and its weight is represented by  $W_D$ . The weight difference between  $W_r$  and  $W_D$  is  $\Delta W_r$ :

$$\Delta W_r = W_r - W_D \tag{2}$$

Another parameter frequently used in this study is the degree of saturation,  $S_r$ , a parameter used to monitor the water content in the specimen. It is defined as follows:

$$S_r = \Delta W_r / (W_w - W_D) \tag{3}$$

where  $\Delta W_r$  (equation 2) is the weight of the free and bound (or adsorbed) water content at any given time during the test. Since oven-drying will be performed at different temperatures,  $W_r$  will reach a constant value at each temperature level, subsequent to prolonged drying times ( $t_D$ ). These values are represented by  $W_{rD}$ . Similarly, the degree of saturation ( $S_r$ ) will eventually also reach a constant value at each temperature level. These values are represented by constant saturation,  $S_{rD}$ , and derived by

$$S_{rD} = (W_{rD} - W_D) / (W_w - W_D) \tag{4}$$

**EXPERIMENTAL RESULTS**

The results of saturating the samples are listed in Table 1. The samples were saturated for 23 hours or longer, based on previous study (Katsube and Scromeda, 1991) that indicated that this time period is sufficient for achieving full saturation for these three rock types. The values of  $W_w$  are listed in Table 1, and the values of  $t_s$  at which  $W_w$  were determined are 1430-1490 minutes.

Results of vacuum-drying and degassing of the saturated samples at room temperature (23°C) are listed in Table 2a, and those for the vacuum oven-drying at temperatures varying from 50°C to 116°C are listed in Tables 2b to 2f. Since there is a relative similarity of the data within each rock type (e.g.  $\phi_E$  for granites, gabbros, and shales are 0.41-0.67%, 0.12-0.31% and 3.2-11.5%, respectively, Table 3), each of the three rock types are represented by only one sample (W-2 for the granite, E-2 for the gabbro and V-5 for the shale sample) in these tables. The values of  $W_r$  generally decreased with time (Tables 2a to 2f). However, there were cases of slight deviations from this general trend, probably due to experimental error. The  $S_r$  values at the beginning ( $t_D = 0$ ) of each temperature level generally continue to decrease with increasing temperatures (Tables 2b to 2f). This is because, subsequent to the completion of drying at a certain temperature level, and the specimen being removed from the vacuum oven for weighing, the specimen is returned to the vacuum oven without having much exposure to the room atmosphere. The values for  $W_{rD}$  ( $t_D = 1740$  minutes) at 116°C (Table 2f) were used to determine  $W_D$ . The results for  $W_w$  and  $W_D$  are listed in Table 3. The effective porosities ( $\phi_E$ ) derived using equation (1) are also listed in Table 3.

The degree of saturation ( $S_r$ ) versus the vacuum oven-drying times ( $t_D$ ) for the three representative samples are plotted in Figures 1, 2, and 3, illustrating the results for three selected temperatures of 50°, 70° and 100°C. These figures illustrate how  $S_r$  generally decreases with time. In Figure 4, the constant saturation ( $S_{rD}$ ) values are plotted against temperature for the

**Table 1. Water contents at saturation**

Sample	$t_s$ (min)	$W_w$ (g)	$\Delta W$ (mg)	$S_r$ (%)
W-1	1490	18.7902	32.7	100.0
W-2	1490	22.4152	44.8	100.0
W-3	1460	19.0814	44.4	100.0
E-1	1460	20.0648	8.3	100.0
E-2	1430	20.4679	22.1	100.0
V-4	1430	4.0328	159.5	100.0
V-5	1430	2.8819	63.0	100.0
V-9	1430	6.3190	74.2	100.0

$t_s$  = Time required to reach saturation under atmospheric pressure.  
 $W_w$  = Weight of specimen at saturation.  
 $\Delta W$  = Weight difference between  $W_w$  and  $W_D$ .  
 $S_r$  = Degree of saturation.

**Table 2a.** Degree of saturation with vacuum-drying time ( $t_i$ ) at 23°C

Sample	$t_i$ (min)	$W_r$ (g)	$\Delta W_r$ (mg)	$S_r$ (%)
W-2	0	22.4152	44.8	100.0
	195	22.3778	7.4	16.5
	300	22.3771	6.7	15.0
	360	22.3768	6.4	14.3
	480	22.3768	6.4	14.3
	600	22.3765	6.1	13.6
	720	22.3764	6.0	13.4
E-2	0	20.4679	22.1	100.0
	195	20.4574	11.6	52.5
	300	20.4574	11.6	52.5
	360	20.4551	9.3	42.1
	480	20.4547	8.9	40.3
	600	20.4546	8.8	39.8
	720	20.4542	8.4	38.0
V-5	0	2.8819	63.0	100.0
	195	2.8435	24.6	39.0
	300	2.8394	20.5	32.5
	360	2.8409	22.0	34.9
	480	2.8374	18.5	29.4
	600	2.8356	16.7	26.5
	720	2.8351	16.2	25.7

$t_i$  = Time duration of saturation under atmospheric pressure.  
 $W_r$  = Weight of specimen at a given time.  
 $\Delta W_r$  = Weight difference between  $W_r$  and  $W_0$ .  
 $S_r$  = Degree of saturation.

**Table 2b.** Degree of saturation with vacuum oven-drying time ( $t_D$ ) at 50°C

Sample	$t_D$ (min)	$W_r$ (g)	$\Delta W_r$ (mg)	$S_r$ (%)
W-2	0	22.3764	6.0	13.4
	120	22.3748	4.4	9.8
	270	22.3742	3.8	8.5
	390	22.3742	3.8	8.5
	510	22.3747	4.3	9.6
	660	22.3744	4.0	8.9
	780	22.3742	3.8	8.5
E-2	0	20.4533	7.5	33.9
	120	20.4524	6.6	29.9
	270	20.4521	6.3	28.5
	390	20.4521	6.3	28.5
	510	20.4516	5.8	26.2
	660	20.4516	5.8	26.2
	780	20.4516	5.8	26.2
V-5	0	2.8390	20.1	31.9
	120	2.8289	10.0	15.9
	270	2.8269	8.0	12.7
	390	2.8263	7.4	11.7
	510	2.8279	9.0	14.3
	660	2.8262	7.3	11.6
	780	2.8261	7.2	11.4

$W_r$  = Weight of specimen at a given time.  
 $\Delta W_r$  = Weight difference between  $W_r$  and  $W_0$ .  
 $S_r$  = Degree of saturation.

**Table 2c.** Degree of saturation with vacuum oven-drying time ( $t_D$ ) at 70°C

Sample	$t_D$ (min)	$W_r$ (g)	$\Delta W_r$ (mg)	$S_r$ (%)
W-2	0	22.3742	3.8	8.5
	120	22.3742	3.8	8.5
	270	22.3742	3.8	8.5
	390	22.3742	3.8	8.5
	510	22.3742	3.8	8.5
	660	22.3740	3.6	8.0
	780	22.3731	2.7	6.0
	900	22.3733	2.9	6.5
	1170	22.3731	2.7	6.0
	E-2	0	20.4516	5.8
120		20.4514	5.6	25.3
270		20.4510	5.2	23.5
390		20.4494	3.6	16.3
510		20.4506	4.8	21.7
660		20.4504	4.6	20.8
780		20.4493	3.5	15.8
900		20.4508	5.0	22.6
1170		20.4493	3.5	15.8
V-5		0	2.8261	7.2
	120	2.8269	8.0	12.7
	270	2.8242	5.3	8.4
	390	2.8234	4.5	7.1
	510	2.8259	7.0	11.1
	660	2.8239	5.0	7.9
	780	2.8229	4.0	6.3
	900	2.8243	5.4	8.6
	1170	2.8229	4.0	6.3

$W_r$  = Weight of specimen at a given time.  
 $\Delta W_r$  = Weight difference between  $W_r$  and  $W_0$ .  
 $S_r$  = Degree of saturation.

**Table 2d.** Degree of saturation with vacuum oven-drying time ( $t_D$ ) at 90°C

Sample	$t_D$ (min)	$W_r$ (g)	$\Delta W_r$ (mg)	$S_r$ (%)
W-2	0	22.3729	2.5	5.6
	120	22.3727	2.3	5.1
	270	22.3727	2.3	5.1
	390	22.3726	2.2	4.9
	570	22.3729	2.5	5.6
	810	22.3728	2.4	5.4
	1230	22.3726	2.2	4.9
	E-2	0	20.4493	3.5
120		20.4487	2.9	13.1
270		20.4487	2.9	13.1
390		20.4485	2.7	12.2
570		20.4488	3.0	13.6
810		20.4484	2.6	11.8
1230		20.4477	1.9	8.6
V-5		0	2.8229	4.0
	120	2.8230	4.1	6.5
	270	2.8218	2.9	4.6
	390	2.8208	1.9	3.0
	570	2.8218	2.9	4.6
	810	2.8208	1.9	3.0
	1230	2.8207	1.8	2.9

$W_r$  = Weight of specimen at a given time.  
 $\Delta W_r$  = Weight difference between  $W_r$  and  $W_0$ .  
 $S_r$  = Degree of saturation.



**Table 2a.** Degree of saturation with vacuum oven-drying time ( $t_D$ ) at 100°C

Sample	$t_D$ (min)	$W_r$ (g)	$\Delta W_r$ (mg)	$S_r$ (%)
W-2	0	22.3726	2.2	4.9
	120	22.3725	2.1	4.7
	360	22.3725	2.1	4.7
	540	22.3724	2.0	4.5
	780	22.3721	1.7	3.8
	1080	22.3722	1.8	4.0
E-2	2160	22.3720	1.6	3.6
	0	20.4477	1.9	8.6
	120	20.4481	2.3	10.4
	360	20.4478	2.0	9.0
	540	20.4478	2.0	9.0
	780	20.4472	1.4	6.3
V-5	1080	20.4478	2.0	9.0
	2160	20.4466	0.8	3.6
	0	2.8207	1.8	2.9
	120	2.8216	2.7	4.3
	360	2.8208	1.9	3.0
	540	2.8214	2.5	4.0
V-5	780	2.8205	1.6	2.5
	1080	2.8207	1.8	2.9
	2160	2.8196	0.7	1.1

$W_r$  = Weight of specimen at a given time.  
 $\Delta W_r$  = Weight difference between  $W_r$  and  $W_D$ .  
 $S_r$  = Degree of saturation.

**Table 2f.** Degree of saturation with vacuum oven-drying time ( $t_D$ ) at 116°C

Sample	$t_D$ (min)	$W_r$ (g)	$\Delta W_r$ (mg)	$S_r$ (%)
W-2	0	22.3720	1.6	3.6
	360	22.3710	0.6	1.3
	1380	22.3707	0.3	0.7
	1740	22.3704	0.0	0.0
E-2	0	20.4466	0.8	3.6
	360	20.4466	0.8	3.6
	1380	20.4462	0.4	1.8
	1740	20.4458	0.0	0.0
V-5	0	2.8196	0.7	1.1
	360	2.8195	0.6	1.0
	1380	2.8192	0.3	0.5
	1740	2.8189	0.0	0.0

$W_r$  = Weight of specimen at a given time.  
 $\Delta W_r$  = Weight difference between  $W_r$  and  $W_D$ .  
 $S_r$  = Degree of saturation.

**Table 3.** Results of the effective porosity measurements by this study, and a comparison with previous measurements

Sample	$\delta_E$ (g/mL)	$W_w$ (g)	$W_D$ (g)	$\Delta W$ (mg)	$\phi_E$ (%) (I)	(II)
Granite						
W-1	2.66	18.7902	18.7575	32.7	0.46	0.41
W-2	2.65	22.4152	22.3704	44.8	0.53	0.51
W-3	2.66	19.0814	19.0370	44.4	0.62	0.67
Gabbro						
E-1	2.93	20.0648	20.0565	8.3	0.12	0.14
E-2	2.88	20.4679	20.4458	22.1	0.31	0.30
Shale						
V-4	2.80	4.0328	3.8733	159.5	11.5	10.2
V-5	2.64	2.8819	2.8189	63.0	5.9	5.7
V-9	2.69	6.3190	6.2448	74.2	3.2	3.3

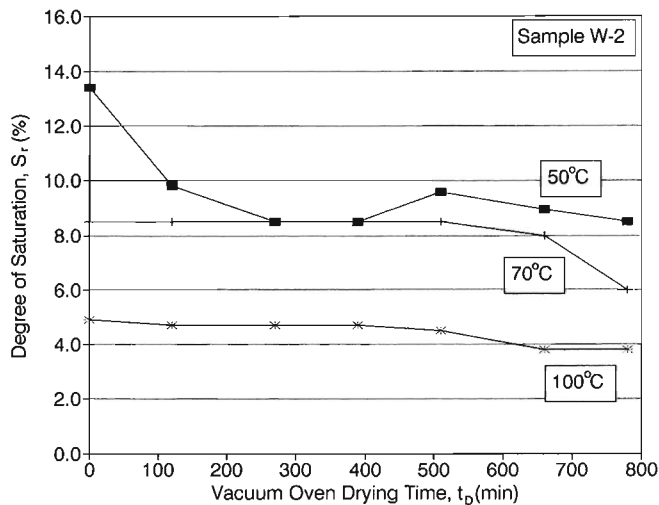
$\delta_E$  = Bulk density.  
 $W_w$  = Wet weight.  
 $W_D$  = Dry weight.  
 $\Delta W$  =  $W_w - W_D$ .  
 $\phi_E$  = Effective porosity.  
(I) = Results of this study.  
(II) = Results from previous studies (Katsube and Scromeda (1991) for samples W-1 through E-2, and Katsube et al. (1992, EP-1991(3) for samples V-4 to V-9).

three representative samples. The curve for Sample E-2 shows significantly larger values for  $S_{rD}$  at lower temperatures, compared to the other samples.

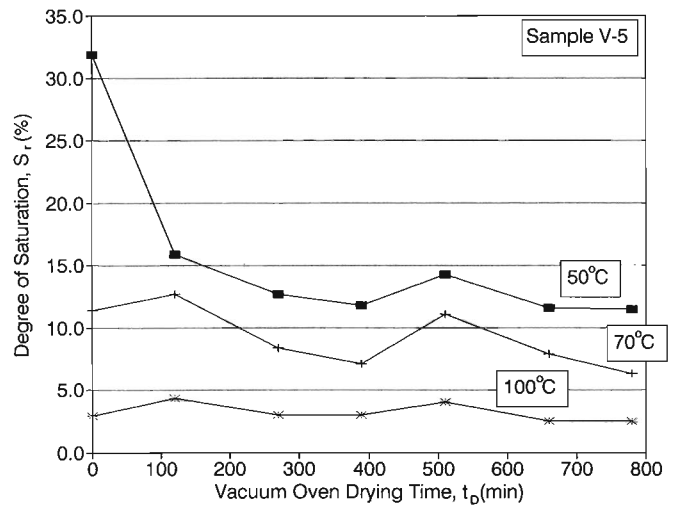
For sample V-5, the  $S_{rD}$  values are listed in Table 4, for both this study under vacuum and for the previous study (Katsube et al., 1992) at atmospheric pressure. The values of  $t_D$  at which  $S_{rD}$  was determined varied between 720 and 2160 minutes (Tables 2a to 2f; Katsube et al., 1992). Curves for constant saturation ( $S_{rD}$ ) with temperature ( $T$ ) for these two studies are plotted in Figure 5. The curve for this study (EP-1992(1), Fig. 5) shows significantly lower  $S_{rD}$  values at the lower temperatures as compared to those of the previous study (EP-1991(3), Fig. 5).

## DISCUSSIONS AND CONCLUSIONS

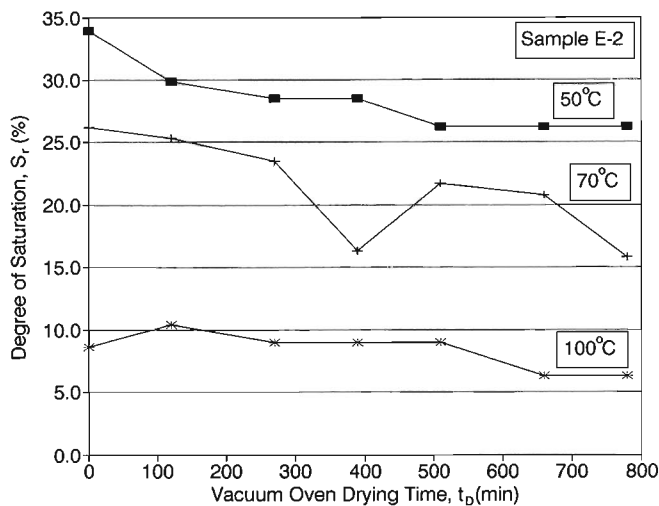
The effective porosity values obtained by this study are generally very similar to those obtained by previous studies (Katsube and Scromeda, 1991; Katsube et al., 1992), as shown in Table 3, indicating that vacuum oven-drying does not significantly affect the effective porosity measurements. However, some values (e.g. V-4) obtained by this study are larger than those obtained previously. The vacuum oven-drying may be the reason for the increase, although damage to the samples due to repeated measurements (Katsube et al., 1992) could also be the cause. This could be the case for the shale sample V-4, since it contains illite, smectite, and organic material (Katsube et al., 1990).



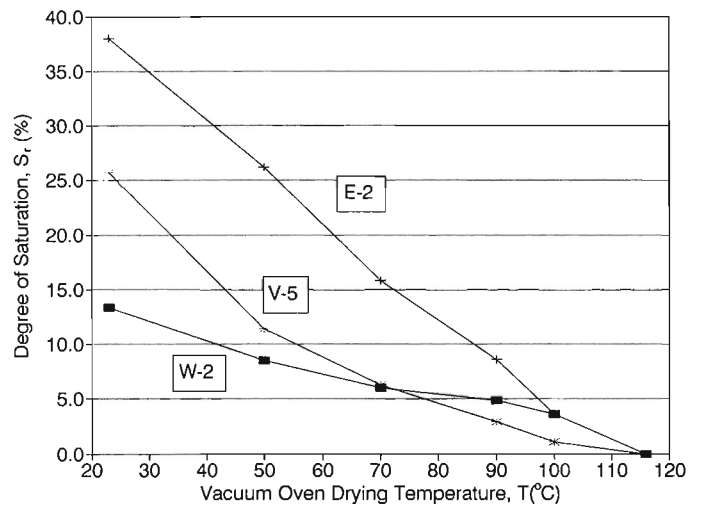
**Figure 1.** Degree of saturation ( $S_r$ ) as a function of vacuum oven-drying time ( $t_D$ ), for three selected temperatures of 50°C, 70°C and 100°C, for sample W-2.



**Figure 3.** Degree of saturation ( $S_r$ ) as a function of vacuum oven-drying time ( $t_D$ ), for three selected temperatures of 50°C, 70°C and 100°C, for sample V-5.



**Figure 2.** Degree of saturation ( $S_r$ ) as a function of vacuum oven-drying time ( $t_D$ ), for three selected temperatures of 50°C, 70°C and 100°C, for sample E-2.



**Figure 4.** Constant saturation ( $S_{rD}$ ) as a function of vacuum oven-drying temperature ( $T$ ) for the three representative samples (W-2, E-2, and V-5).

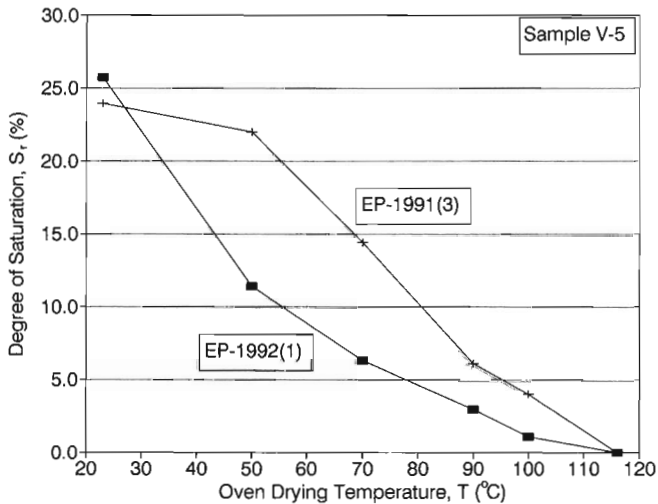
A comparison of the drying curves for the three rock types (Fig. 4, Tables 2a to 2f) represented by samples W-2 (granite), E-2 (gabbro), and V-5 (shale), indicate that the granite dries more quickly than the others at temperatures below 70°C, and the shale dries more quickly than the others at temperatures higher than that. Comparison of the two curves of constant saturation versus temperature for sample V-5 (Fig. 5), EP-1992(1) for this study (vacuum condition) and EP-1991(3) for the previous study (Katsube et al., 1992), shows a considerable difference, with  $S_{rD}$  values for the previous measurements (atmospheric pressures) being considerably larger at the lower temperatures. For example, the  $S_{rD}$  value at 50°C for this study (Table 4) is almost half (11.4%) of that (22.0%) for the previous study.

The difference in the two  $S_{rD}$ - $T$  curves for sample V-5 (Fig. 5), may imply that a larger fraction of the free water is being driven out at lower temperatures when under vacuum, compared to when under atmospheric conditions. However, the fact that temperatures had to reach 116°C before  $S_r$  or  $S_{rD}$  became zero (Tables 2b-2f), suggests that temperatures above 100°C are required to drive off the adsorbed water, even under vacuum conditions. This implies that laboratories performing effective porosity measurements at temperatures below 100°C are probably not obtaining true effective porosity values. A study of the  $S_{rD}$ - $T$  curves for the granites and gabbros is also likely to provide interesting and useful information not only on the free-adsorbed water relationship in these rock types, but also on their pore structure.

**Table 4.** A comparison between two sets of constant saturation ( $S_{rD}$ ) values at different temperatures (T) for sample V-5. The values of  $t_D$  at which the  $S_{rD}$  values were determined varied between 720 and 2160 minutes for both studies (Tables 2a to 2f; Katsube et al., 1992).

T (°C)	$S_{rD}$ (%) (Katsube et al., 1992) <sup>1</sup>	$S_{rD}$ (%) (This Study) <sup>2</sup>
23	23.9	25.7
50	22.0	11.4
70	14.4	6.3
90	6.1	2.9
100	4.0	1.1
116	0.0	0.0

<sup>1</sup> At atmospheric pressure  
<sup>2</sup> Under vacuum



**Figure 5.** Constant saturation ( $S_{rD}$ ) as a function of vacuum oven-drying temperature (T) for sample V-5, for two studies: EP-1992(1) (this study) and EP-1991(3) (previous study of Katsube et al., 1992).

## ACKNOWLEDGMENTS

The authors acknowledge the support provided to this work by K.A. Richardson (Geological Survey of Canada, Ottawa), M.A. Williamson (Geological Survey of Canada, Atlantic Geoscience Centre, Dartmouth, N.S.), and by M.E. Best (Geological Survey of Canada, Pacific Geoscience Centre, Sydney, B.C.). The authors express their sincere thanks to S.W. Adcock (Geological Survey of Canada, Ottawa) for critically reviewing this paper and for his constructive comments.

## REFERENCES

- American Petroleum Institute**  
1960: Recommended practices for core-analysis procedure; in API Recommended Practice 40 (RP 40), First Edition; American Petroleum Institute, Washington, D.C., p. 55.
- Hume, J.P. and Katsube, T.J.**  
1987: Pore structure characteristics; in Geotechnical Studies at East Bull Lake Research Area, (ed.) A.G. Latham; Canada Centre for Mineral and Energy Technology, Report MRL 87-94, p. 39-66.
- Katsube, T.J. and Hume, J.P.**  
1987: Pore structure characteristics of granitic rock samples from Whiteshell research area; in Geotechnical Studies at Whiteshell Research Area (RA-3); Canada Centre for Mineral and Energy Technology, Report MRL 87-52, p. 111-158.
- Katsube, T.J. and Scromeda, N.**  
1991: Effective porosity measuring procedure for low porosity rocks; in Current Research, Part E; Geological Survey of Canada, Paper 91-E, p. 291-297.
- Katsube, T.J. and Walsh, J.B.**  
1987: Effective aperture for fluid flow in microcracks; International Journal of Rock Mechanics and Mining Sciences and Geomechanics Abstracts, v. 24, p. 175-183.
- Katsube, T.J., Best, M.E., and Mudford, B.S.**  
1991: Petrophysical characteristics of shales from the Scotian Shelf; Geophysics, v. 56, no. 10.
- Katsube, T.J., Murphy, T.B., Best, M.E., and Mudford, B.S.**  
1990: Pore structure characteristics of low permeability shales from deep formations; in Proceedings of the 1990 SCA (Society of Core Analysts) 4th Annual Technical Conference, August, 1990, Dallas, Texas; SCA-9010, p. 1-21.
- Katsube, T.J., Scromeda, N., and Williamson, M.**  
1992: Effective porosity of tight shales from the Venture Gas Field, offshore Nova Scotia; in Current Research, Part D; Geological Survey of Canada, Paper 92-1D, p. 111-119.
- Scromeda, N., Katsube, T.J., Salisbury, M.**  
1993: Electrical resistivity and porosity of core samples from the Sudbury Structure, Ontario; in Current Research, Part C; Geological Survey of Canada, Paper 93-1C, p. 279-285.
- Soeder, D.J.**  
1986: Laboratory drying procedures and the permeability of tight sandstone core; SPE Formation Evaluation, p. 16-22.



# Formation factor determination procedure for shale sample V-3 from the Scotian Shelf

T.J. Katsube and N. Scromeda  
Mineral Resources Division

*Katsube, T.J. and Scromeda, N., 1993: Formation factor determination procedure for shale sample V-3 from the Scotian Shelf; in Current Research, Part E; Geological Survey of Canada, Paper 93-1E, p. 321-330.*

---

**Abstract:** According to the Patnode and Wyllie equation:

$$1/\rho_r = 1/(F\rho_w) + 1/\rho_c,$$

where  $\rho_r$ ,  $F$ ,  $\rho_w$ , and  $\rho_c$  are the bulk electrical resistivity, formation factor, pore fluid resistivity, and pore surface resistivity, respectively, the relationship between the two variables,  $1/\rho_r$  and  $1/\rho_w$ , is linear. However, there are cases where deviations from this linearity occur, causing problems in the determination of  $F$ . A study has been carried out to resolve this problem by testing the equation for varied NaCl concentrations and pore fluid saturation times, using a tight shale sample.

Results indicate that the problem is eliminated by using NaCl concentrations larger than 0.02 N, and saturation times larger than 240 minutes, for this sample. However,  $F$  values produced by previous tests, at 80% saturation, varied by 29% from the results of this study, at 97-100% saturation. These discrepancies are within the error range of  $\pm 20-40\%$  claimed for the previous procedures established for crystalline rocks.

**Résumé :** D'après l'équation de Patnode et Wyllie :

$$1/\rho_r = 1/(F\rho_w) + 1/\rho_c,$$

où  $\rho_r$ ,  $F$ ,  $\rho_w$  et  $\rho_c$  sont la résistivité électrique apparente, le facteur de formation, la résistivité du fluide interstitiel et la résistivité de surface des pores, respectivement, la relation entre les deux variables,  $1/\rho_r$  et  $1/\rho_w$ , est linéaire. Toutefois, il y a des cas où cette linéarité n'est pas parfaite, rendant difficile l'évaluation de  $F$ . Une étude a été effectuée pour résoudre ce problème en vérifiant l'équation pour des concentrations de NaCl et des temps de saturation en fluide interstitiel différents, avec un échantillon de shale compact.

Les résultats indiquent que le problème ne se pose pas lorsque la concentration de NaCl dépasse 0,02 N et que les temps de saturation dépassent 240 minutes pour cet échantillon. Toutefois, les valeurs de  $F$  obtenues dans des vérifications antérieures, pour une saturation de 80 %, s'écartent de 29 % des résultats de la présente étude où le taux de saturation est de 97 à 100 %. Ces écarts se situent dans la fourchette d'erreur de  $\pm 20-40\%$  établie dans des études antérieures portant sur des roches cristallines.

## INTRODUCTION

Archie (1942) related the bulk rock electrical resistivity,  $\rho_r$ , to the pore fluid electrical resistivity,  $\rho_w$ , by the formation factor,  $F$ , as follows:

$$\rho_r = F\rho_w \quad (1)$$

However, Patnode and Wyllie (1950) indicated that conductive layers on the pore surfaces of rocks distort the relationship in equation (1) so that accurate information on pore structure can not be obtained by using that equation alone. They introduced the following equation to explain how pore surface resistivity,  $\rho_c$ , affects electrical measurements:

$$1/\rho_r = 1/(F\rho_w) + 1/\rho_c \quad (2)$$

It implies that by measuring  $\rho_r$  for a multiple number of solutions having different values of  $\rho_w$ , and then by inserting them into equation (2), a value of  $F$  free from the surface conduction effects could be obtained. This is referred to as the true formation factor,  $F_T$ , and  $F$  obtained by equation (1) is referred to as the apparent formation factor,  $F_a$ .

Katsube (1981) reported on experimental results using this method, probably for the first time for crystalline rocks. Since then considerable formation factor data for tight crystalline rocks have been reported (e.g. Wadden and Katsube, 1982; Katsube and Kamineni, 1983; Katsube et al., 1985; Hume and Katsube, 1987; Katsube and Hume, 1987a, b). According to equation (2), the relationship between  $1/\rho_r$  and  $1/\rho_w$  should be linear, which is usually the case. However, there are also cases of nonlinearity (e.g. Fig. 7 in Katsube et al., 1992b). In order to find a solution to this discrepancy, electrical properties of six rock samples (three granites, two gabbros, and one shale) representing varied physical and geological characteristics are being studied. The purpose of this paper is to provide information on results obtained, to date, on the tight shale sample. The petrophysical characteristics of this sample, identified as "V-3", were reported previously (Katsube et al., 1990, 1991a, 1992a, c; Katsube and Scromeda, 1991), and are compiled in Table 1.

A rearrangement of equation (2), suggested by Worthington (1975), has been used in the past for formation factor determination:

$$1/F_a = 1/F + \rho_w/\rho_c \quad (3)$$

This equation suggests a linear relationship between  $1/F_a$  and  $\rho_w/\rho_c$ . Typical results showing good and poor linear relationships are given in Figure 1, reproduced from previous publications. The measurements were made at five different NaCl concentrations of 0.02, 0.05, 0.1, 0.2 and 0.5 N, a procedure previously established for tight crystalline rocks (Katsube, 1981). The reason for selecting this concentration range was based on concerns that NaCl concentrations above 0.5 N might damage the pore structure, and that concentrations below 0.02 N could be influenced by ions from remnants of evaporated fluids, or by the dissolution of rock forming

minerals. An example of a good linear relationship between  $1/F_a$  and  $\rho_w/\rho_c$  is shown in Figure 1a. The somewhat poorer linear relationship shown in Figure 1b is suspected of being caused by measurement error. However, the example in Figure 1c represents a systematic error showing increased discrepancy with decreasing fluid resistivity ( $\rho_w$ ). This non-linearity at high NaCl concentrations is observed quite frequently and indicates the possibility of procedural error in the measurement. For this reason, data points displaying systematic deviations are usually eliminated from the formation factor determination procedure (Katsube et al., 1992a).

This paper reports on two tests carried out to investigate this problem. One, referred to as the "Extended concentration test", tests equation (2) for a range of NaCl concentrations (0.001-0.5 N) that exceeds that of previous tests (0.02-0.5 N). The other, referred to as the "Varied  $t_s$  test", tests the same equation for pore fluid saturation times,  $t_s$ , varying from 90 to 1680 minutes. The results of these two tests are also compared with data on sample V-3 from a previous study (Katsube et al., 1990, 1991a) referred to as the "1988 test", and from a recent study (Katsube and Scromeda, in prep.) referred to as the "1992 test". The NaCl concentration range for both of the 1988 and 1992 tests was 0.02-0.5 N, and their saturation times ( $t_s$ ) were 30 minutes and 210-240 minutes, respectively. An identical specimen of sample V-3 was used for all of these tests.

## METHOD OF INVESTIGATION

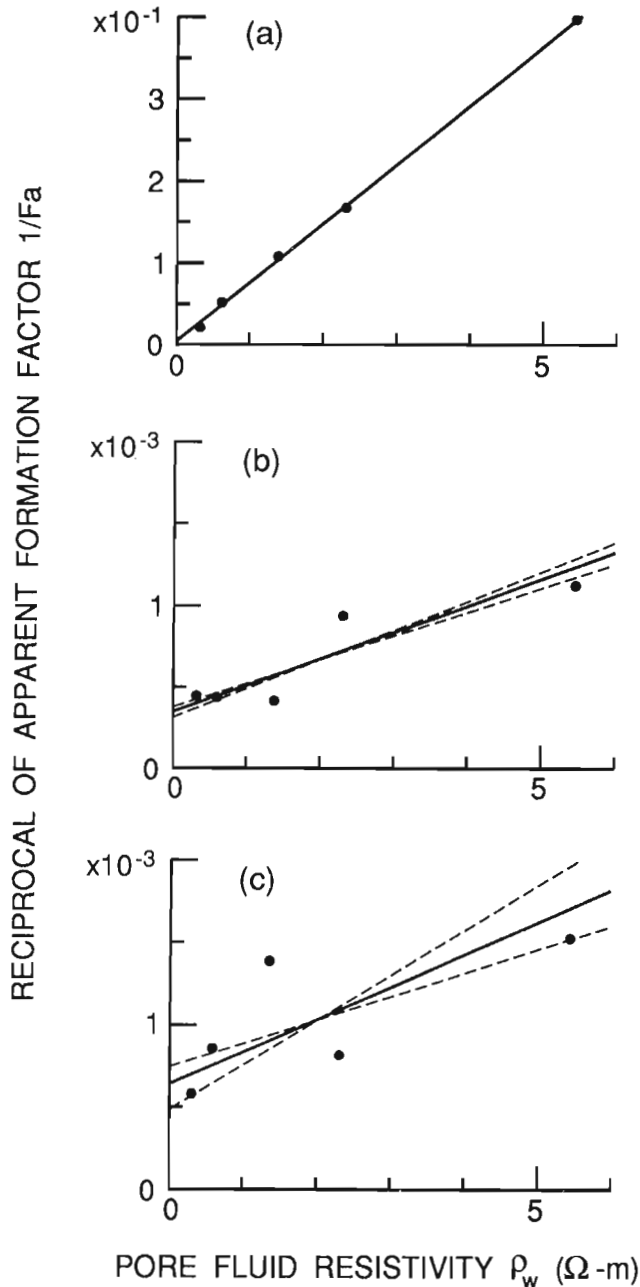
### Sample preparation

The specimen used for these tests is a disc shaped specimen, with a diameter of 2.5 cm and a thickness of 0.57 cm (Table 1), that was cut out from a split core shale sample labeled V-3 (Katsube et al., 1991a, 1992b). First, the dimensions of the specimen were measured using a caliper. The results are used to determine the geometric factor,  $K_G$ , required for the electrical measurements, using the following equation:

$$K_G = (r_D/2)^2\pi/l \quad (4)$$

where  $r_D$  is the diameter and  $l$  is the thickness of the specimen. The geometric factor ( $K_G$ ) has a value of 0.0860 m for this specimen.

Subsequently, the specimen was placed under vacuum for 15 minutes and then immersed in a brine (still under vacuum) for 15 more minutes for degassing. The specimen was then allowed to stand in the brine (in covered beakers) for saturation times ( $t_s$ ) varying from 90 to 1680 minutes under atmospheric pressure, before being subjected to electrical measurements. The fluid resistivity ( $\rho_w$ ) of the brine was measured before saturating the specimen. The basic principles of this preparation generally follow those previously described (Katsube, 1981; Katsube and Walsh, 1987; Katsube and Salisbury, 1991).



**Figure 1.** Typical examples of  $1/F_a$  as a function of  $\rho_w$ , showing good and poor linear relationships: (a) Example of a good linear relationship (Katsube and Salisbury, 1991). (b) Example of a poor linear relationship (Katsube et al., 1991b). (c) Example of a poor linear relationship (Katsube et al., 1992a), with a progressive deviation from linearity with decreasing  $\rho_w$ . The parameter  $\rho_w$  represents the pore fluid resistivity for five different NaCl solutions with concentrations of 0.02, 0.05, 0.1, 0.2, and 0.5 N (right to left in the diagram). The solid lines represent the reduced major axis (RMA), and the broken lines represent the normal regression lines (NRL).

**Table 1.** Petrophysical characteristics of the shale sample (identified by "V-3") used in this study. The data are from the literature (Katsube et al., 1990 [1], 1991a [2], 1992c [3]; Coyner et al., 1993 [4])

Parameter	Values	References
Rock type	Shale	[2]
Dimensions of specimen		[3]
Diameter, $r_D$ (cm)	2.494	
Thickness, $l$ (cm)	0.568	
Bulk density, $\delta$ (g/mL)	2.66	[3]
Effective porosity, $\phi_E$ (%)	4.6-8.6	[3]
True formation factor, $F_T$	260	[1,2]
Bulk resistivity, $\rho_r$ ( $\Omega$ -m)	1800	[1,2]
Surface resistivity, $\rho_o$ ( $\Omega$ -m)	1600	[1]
Apparent tortuosity, $\tau_a$	4.7	[1]
Permeability at zero pressure, $k_0$ ( $m^2$ )	$8.3 \times 10^{-19}$	[4]
Permeability at 60 MPa effective pressure, $k_0$ ( $m^2$ )	$3 \times 10^{-22}$	[4]
Mean pore aperture, $d_{Fk}$ (nm)	51	[*]
Pore path density, $n$ ( $m^{-1}$ )		
True tortuosity, $\tau$	3.3	[2]

[\*]: Calculated by inserting the permeability ( $k_0$ , Katsube, 1993) and formation factor ( $F$ , Katsube et al., 1991a) values at atmospheric pressure into the Walsh and Brace equation (Walsh and Brace, 1984; Katsube and Walsh, 1987; Katsube et al., 1991a, 1992c) for sheetlike pores.

### Electrical measurements

The shale specimen was placed in a capacity type sample-holder with graphite electrodes covering the two parallel faces. The surfaces of the sides of the specimen were dried before measurement. The sample-holder was then placed in an enclosed space in order to reduce movement of air around it. This was a precautionary measure to minimize evaporation of fluid from the rock pores. The sample holder was connected to an automatic electrical impedance system which measures the in-phase and out-of-phase components of the impedance at frequencies of  $1.0 \cdot 10^6$  Hz, as described in Gauvreau and Katsube (1975).

The electrical resistivity was determined by techniques and procedures previously described (Katsube, 1981; Katsube and Walsh, 1987; Katsube and Salisbury, 1991; Katsube et al., 1991b). First, the complex resistivity,  $\rho^*$ , is measured over a frequency range of  $1.0 \cdot 10^6$  Hz:

$$\rho^* = \rho_R + i\rho_I, \quad (5)$$

where  $\rho_R$  is the real resistivity and  $\rho_I$  is the imaginary resistivity, both obtained from impedance  $Z(\theta)$  measurements:

$$\rho^* = K_G Z(\theta), \quad (6)$$

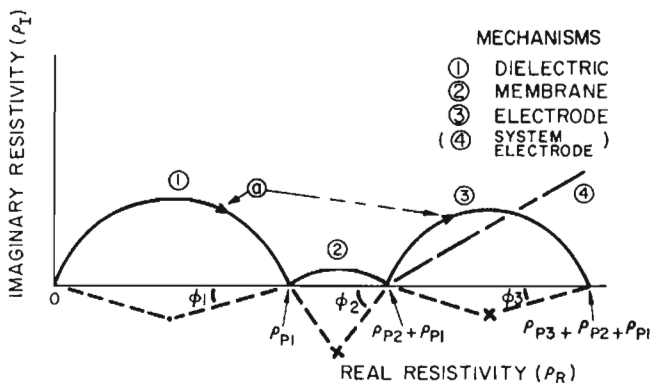
where  $\theta$  is the phase angle.

Then the bulk electrical resistivity,  $\rho_r$ , is determined from the Cole-Cole plots of the complex resistivity ( $\rho^*$ ), by the method described in Katsube (1975), Katsube and Walsh (1987) and elsewhere (e.g. Katsube and Salisbury, 1991; Katsube et al., 1991a). When electrical resistivity is measured over these frequencies, dielectric polarization, Warburg impedance, and electrode polarization effects are reflected in the results (Katsube, 1975, 1977). A simple method applied to distinguish different mechanisms for improvement of the measurement accuracy is to use Cole-Cole plots where imaginary resistivity ( $\rho_I$ ) is plotted against real resistivity ( $\rho_R$ ) (Katsube and Walsh, 1987).

Katsube (1975) considered plots consisting of three arcs and suggested that each arc includes the effect of different groups of electrical conduction mechanisms (Fig. 2). It was proposed that the leftmost arc reflects the effects of the dielectric constant, double layer, pore structure, and pore water chemistry. In accordance with this model, bulk rock resistivity ( $\rho_r$ ) used in this study is determined from the point where the left arc intersects the horizontal axis. The electrical measurements in this study are made at room temperature, with errors estimated to be generally in the ranges of 10-20% percent.

**Varied concentrations – "Extended concentration test"**

Bulk electrical resistivity ( $\rho_r$ ) was determined for the specimen saturated with various brines made up of different NaCl concentrations: 0.001 N, 0.002 N, 0.005 N, 0.01 N, 0.02 N, 0.05 N, 0.1 N, 0.2 N, and 0.5 N. The saturation time was 210 to 240 minutes prior to the electrical measurements. Previous tests on this shale sample (Katsube et al., 1992b), indicate that the specimen is 95% saturated at a saturation time of 120 minutes (Table 2), and 97% at 260 minutes, suggesting that a 210 minute saturation time represents more than a 95% saturation. The bulk electrical resistivity ( $\rho_r$ ) measurements were started at the lowest concentration of 0.001 N, and then



**Figure 2.** Description of method used to determine bulk electrical resistivity,  $\rho_r$  ( $\rho_{P1}$  in this figure), using Cole-Cole complex resistivity plots (Katsube, 1975).

progressed to the higher concentrations. Between measurements, the specimen was rinsed by immersing it overnight (12 hours) in distilled water, prior to the next measurement with a higher concentration.

**Varied saturation times – "Varied  $t_s$  test"**

In order to study the effect of saturation time, the bulk electrical resistivity ( $\rho_r$ ) was determined for saturation times of 90, 240, 315, 1440 and 1680 minutes, at NaCl concentrations of 0.001 N, 0.01 N, 0.1 N, and 0.5 N. After every measurement at each saturation-time interval for the same concentration, the specimen was immediately reimmersed into the solution until the next measurement. Between measurements at different concentrations, the same rinsing procedure, as previously described, is applied.

**Formation factor determination**

Either equation (2) or (3) can be used to determine the true formation factor ( $F_T$ ). In the latter case, which has traditionally been used following the work by Worthington (1975), the apparent formation factor ( $F_a$ ) is determined using equation (1) before inserting it into equation (3) to determine  $F_T$ . In order to reduce errors due to analytical procedures, this two-step calculation using equation (3) is avoided by using equation (2) in this study. The techniques and procedures previously used to determine  $F_T$  are described in the literature (Katsube, 1981; Katsube and Walsh, 1987; Katsube and Salisbury, 1991; Katsube et al., 1991a).

**Table 2.** Extent of saturation with time under atmospheric pressure for shale sample V-3 (from EP-1991(3) experiments in Katsube et al., 1992b)

$t_s$ (min)	$W_t$ (g)	$\Delta W_t$ (mg)	$S_t$ (%)
0	6.8021	93.5	44.0
1	6.8568	148.2	69.7
5	6.8551	146.5	68.9
10	6.8629	154.3	72.6
15	6.8658	157.2	73.9
20	6.8696	161.0	75.7
30	6.8776	169.0	79.5
50	6.8877	179.1	84.2
60	6.8923	183.7	86.4
90	6.9066	198.0	93.1
120	6.9113	202.7	95.3
150	6.9139	205.3	96.6
180	6.9143	205.7	96.8
260	6.9145	205.9	96.9
320	6.9169	208.3	98.0
380	6.9169	208.3	98.0
1465	6.9212	212.6	100.0
1525	6.9212	212.6	100.0

$t_s$  : Saturation time under atmospheric pressure.  
 $W_t$  : Weight of specimen at time t.  
 $\Delta W_t$  : Weight difference between  $W_t$  and  $W_0$ .  
 $W_0$  : Dry weight.  
 $S_t$  : Degree of saturation.



**EXPERIMENTAL RESULTS AND DATA ANALYSIS**

The results of the "Extended concentration test" and "Varied  $t_s$  test" are listed in Tables 3 and 4, respectively. The results of the "1988 test" (Katsube et al., 1990, 1991a) and the "1992 test" (Katsube and Scromeda, in prep.) are listed in Tables 5 and 6, respectively.

The results of the "Extended concentration test" (Table 3), with the reciprocal of bulk electrical resistivity ( $1/\rho_r$ ) plotted as a function of the reciprocal of fluid resistivity ( $1/\rho_w$ ) in accordance to equation (2), are shown in Figure 3. The result for all nine points are shown in Figure 3a. Six points representing the smaller values of  $1/\rho_w$  are plotted in Figure 3b, and the conceptual relationship interpreted from this data is shown in Figure 3c. Although the relationship between the two parameters is linear in both Figures 3a and 3b, the slope, which was 0.0060 in Figure 3a, has decreased to 0.0045 in Figure 3b, and decreases further to 0.0030 for points 1, 3, 4, and 5 (counting from the left), which show the smallest slope. For this reason, the relationship between the two parameters is interpreted to be a curve consisting of a linear section for the larger values of  $1/\rho_w$ , as is expected from equation (2), and a nonlinear section for the smaller values of  $1/\rho_w$  which contradicts that equation.

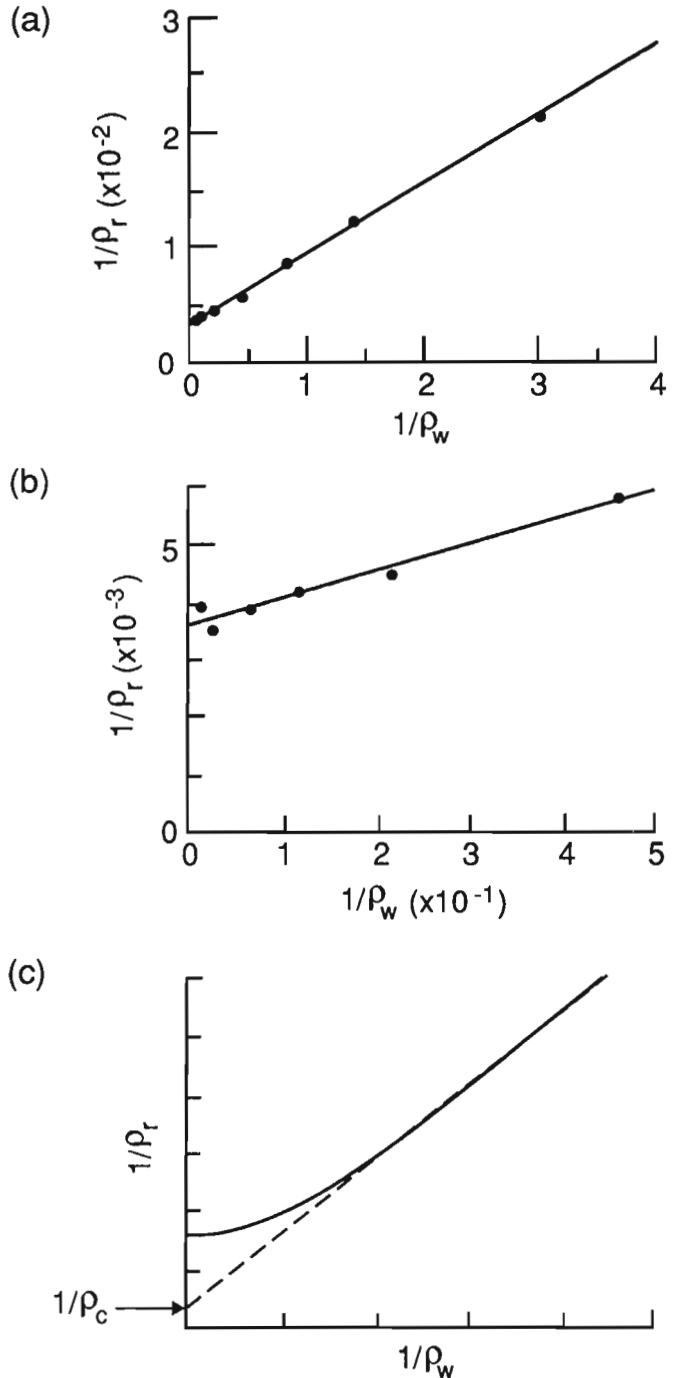
While all nine points are quite representative of the linear relationship existing between the two parameters, the true formation factor ( $F_T$ ) determination using the five points for the larger values of  $1/\rho_w$  produces more accurate results, since they are likely to be free from any nonlinearity. In order to

**Table 3.** Results of the "Extended concentration test" – bulk resistivity ( $\rho_r$ ) as a function of varied NaCl concentration for saturation times ( $t_s$ ) between 210 and 315 minutes, for the tight shale, sample V-3

NaCl (N)	$\rho_w$ ( $\Omega$ -m)	$\rho_r$ ( $\Omega$ -m)	9	5	n	3*	4*
0.001	81.3	255	x				x
0.002	41.6	287	x				
0.005	15.9	261	x				x
0.01	8.81	240	x				x
0.02	4.63	226	x	x	x		x
0.05	2.17	176	x	x	x	x	
0.1	1.22	117	x	x	x	x	x
0.2	0.709	80.4	x	x	x	x	x
0.5	0.333	46.8	x	x	x		
$F_T$			165	157*	163	142	328
$\rho_o$ ( $\Omega$ -m)			292	330*	310	391	265

N = Concentration of pore fluid (NaCl in this case).  
 $\rho_w$  = Resistivity of pore fluid (NaCl in this case).  
 $\rho_r$  = Bulk rock resistivity.  
 n = Number of data points used for formation factor (F) determination.  
 $F_T$  = True formation factor.  
 $\rho_o$  = Surface resistivity.  
 x = Point used for  $F_T$  determination.  
 \*: Values determined by the conventional method, using equation (4) and the five data points (0.02-0.5 N NaCl).  
 \*: Extreme cases selected for determination of error range.

determine the possible error range,  $F_T$  values were determined for two extreme cases: one for points 6, 7, and 8 (left to right) which show the largest slope, and the other for the smallest slope described above. The results are listed in the two columns to the far right of Table 3.



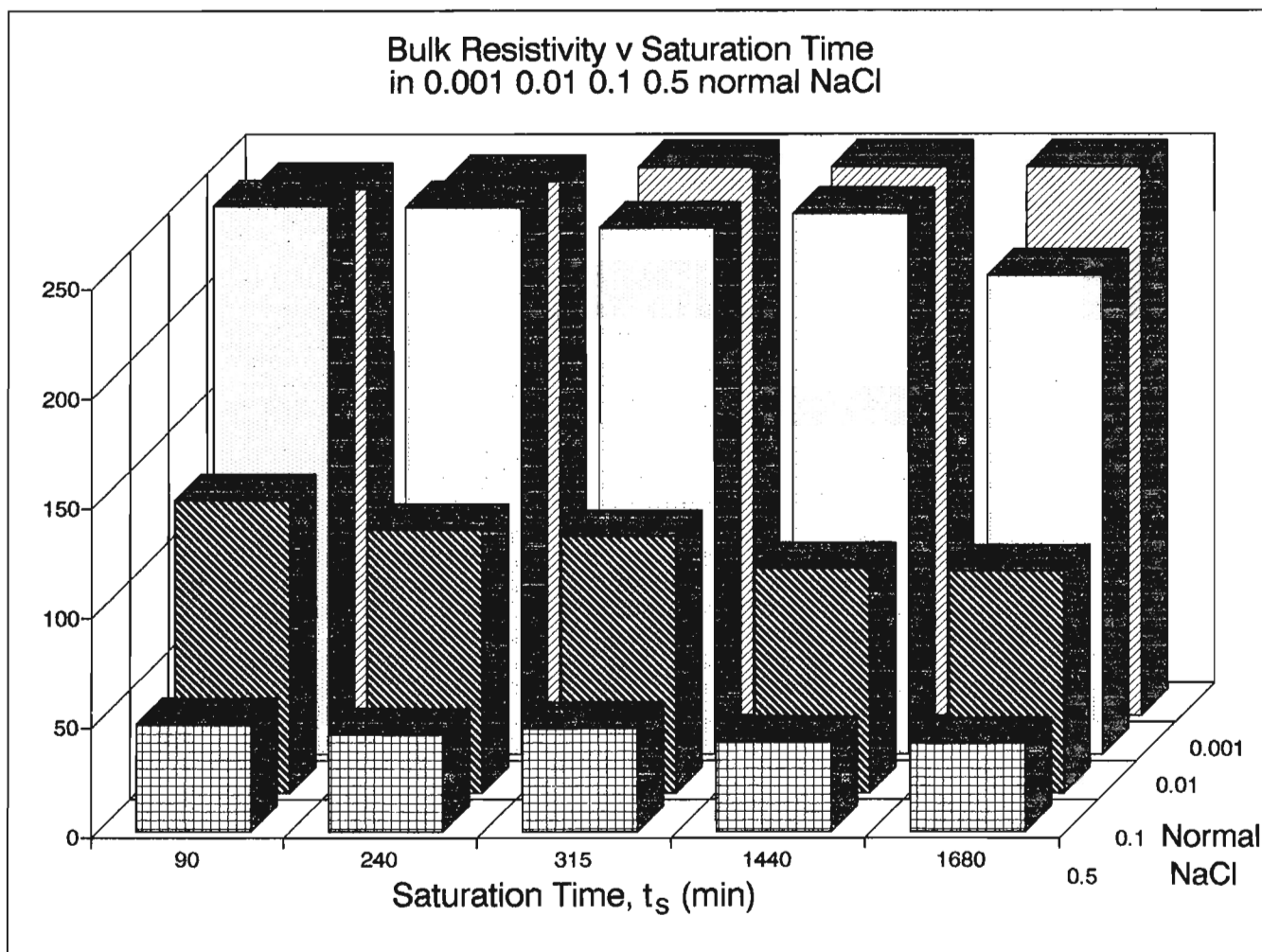
**Figure 3.** Reciprocal of bulk electrical resistivity ( $1/\rho_r$ ) plotted as a function of the reciprocal of fluid resistivity ( $1/\rho_w$ ), for sample V-3, obtained from the "Extended concentration test" in this study. (a) The result for all nine points (slope = 0.0060). (b) Result for six points of the smaller values of  $1/\rho_w$  (slope = 0.0045). (c) The conceptual relationship between  $1/\rho_r$  and  $1/\rho_w$ .

The results of the "Varied  $t_s$  test" (Table 4), are displayed in Figure 4a. Concentrations 0.01, 0.1, and 0.5 N show considerably different levels of bulk electrical resistivity ( $\rho_r$ ) as expected, but concentration 0.001 N shows results similar to that of 0.01 N. This is a trend somewhat consistent with that shown in Figure 3c, where resistivities show little change at lower NaCl concentrations. The reciprocal of bulk electrical resistivity ( $1/\rho_r$ ) plotted as a function of the reciprocal of fluid resistivity ( $1/\rho_w$ ) for the different saturation times ( $t_s$ ) are shown in Figure 5a. The effect of saturation times ( $t_s$ ) on the resistivities is conceptually described in Figure 5b, where the relationship between  $1/\rho_r$  and  $1/\rho_w$  is linear (as expected from equation (2)) at longer saturation times ( $t_s$ ), but is nonlinear, with a smaller slope for the linear portion of the curve, at shorter saturation times ( $t_s$ ). This nonlinear section of the curve resembles that in Figure 3c. The true formation factor ( $F_T$ ) and surface resistivity ( $\rho_c$ ) values determined for the different saturation times ( $t_s$ ) are listed in Table 4 and displayed in Figure 4b. The  $F_T$  and  $\rho_c$  values are determined

**Table 4.** Results of the "Varied  $t_s$  test" - bulk resistivity ( $\rho_r$ ) as a function of saturation time ( $t_s$ ) for different NaCl concentrations (N), for sample V-3

NaCl (N)	$\rho_w$ ( $\Omega$ -m)	$\rho_r$ ( $\Omega$ -m)				
		$t_s=90$	$t_s=240$	$t_s=315$	$t_s=1440$	$t_s=1680$
0.001	81.3	240	243	255	323	294
0.01	8.81	252	249	240	246	218
0.1	1.22	133	120	117	102	101
0.5	0.333	48.8	43.7	46.8	40.1	39.6
$F_T$		179	156	170	138	139
$\rho_c$		286	286	271	301	247
$F_T$		173*	152*			
$\rho_c$		325*	319*			

N = Concentration of pore fluid (NaCl in this case).  
 $\rho_w$  = Resistivity of pore fluid (NaCl in this case).  
 $\rho_r$  = Bulk rock resistivity.  
 $t_s$  = Saturation time (minutes).  
 $F_T$  = True formation factor.  
 $\rho_c$  = Surface resistivity.  
 \*: Eliminated 0.001 N values for formation factor determination.



**Figure 4a.** Results of the "Varied  $t_s$  test" for sample V-3. (a) Bulk electrical resistivity ( $\rho_r$ ) measurements for varied saturation times ( $t_s$ ), at different NaCl concentration levels. (b) Formation factor and pore surface resistivity ( $\rho_c$ ) values for varied saturation times ( $t_s$ ), at different NaCl concentration levels.

only for the linear portion of the curves. That is, the data points for the smallest value of  $1/\rho_w$ , for  $t_s = 90$  and 240 minutes, are excluded.

Results of the "1988 test" (Table 5; Katsube et al., 1990, 1991a), with  $1/\rho_r$  plotted as a function of  $1/\rho_w$  in accordance with equation (2), are shown in Figure 6a. The relationship between the two parameters generally represents a linear relationship, as expected from equation (2). In order to determine the possible error range, the  $F_T$  values were determined for points 2, 3, and 5, showing the largest slope, and for points 1, 2, and 4, showing the smallest slope. These results are listed in the two columns to the far right of Table 5.

Results of the "1992 test" (Table 6; Katsube and Scromeda, in prep.) with  $1/\rho_r$  plotted as a function of  $1/\rho_w$ , are shown in Figure 6b. The relationship between the two parameters generally represents a good linear relationship, as expected from equation (2), indicating that the  $F_T$  value determined from this relationship is an accurate representation of the sample. However, since there is a slight curvature to this relationship, a possible error range is determined using

**Table 5.** Results for sample V-3 in the "1988 test" (Katsube et al., 1990, 1991a)

NaCl (N)	$\rho_w$ ( $\Omega$ -m)	$\rho_r$ ( $\Omega$ -m)	5	5	n	3*	3*
DW	DW	184					
0.02	5.18	146	x	x	x		x
0.05	2.27	136	x	x	x	x	x
0.1	1.25	104	x	x	x	x	
0.2	0.72	96.1	x	x			x
0.5	0.39	55.1	x	x	x	x	
$F_T$			268*	209	205	200	329
$\rho_c$			160*	189	178	187	163

N = Concentration of pore fluid (NaCl in this case).  
 $\rho_w$  = Resistivity of pore fluid (NaCl in this case).  
 $\rho_r$  = Bulk rock resistivity.  
n = Number of data points.  
DW = Deionized water.  
 $F_T$  = True formation factor.  
 $\rho_c$  = Surface resistivity.  
\*: Literature data (Katsube et al., 1990), implying that  $F_T$  and  $\rho_c$  were determined by the conventional method using equation (3) and five data points (0.02-0.5 N NaCl).  
†: Extreme cases selected for determination of error range.

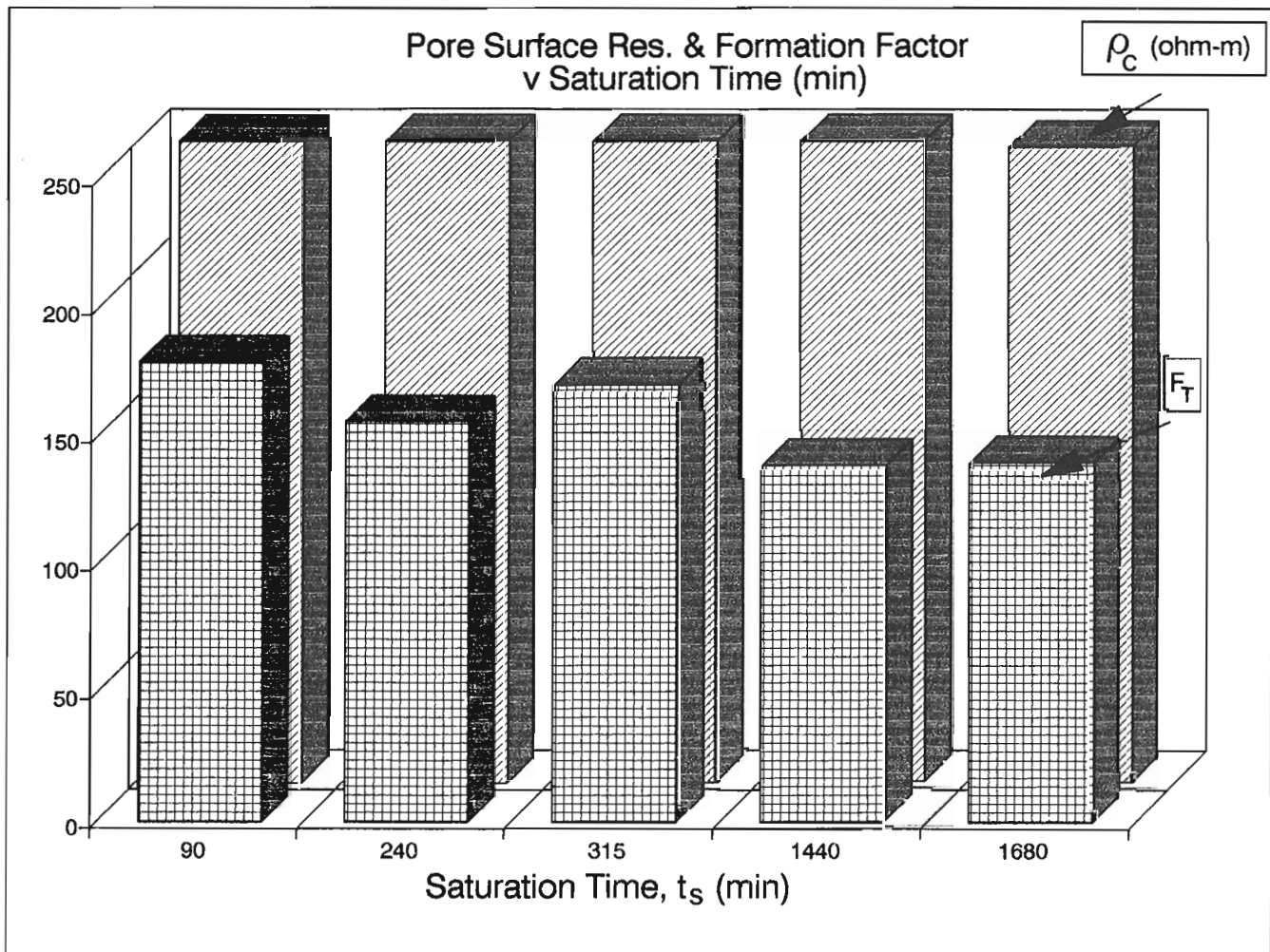


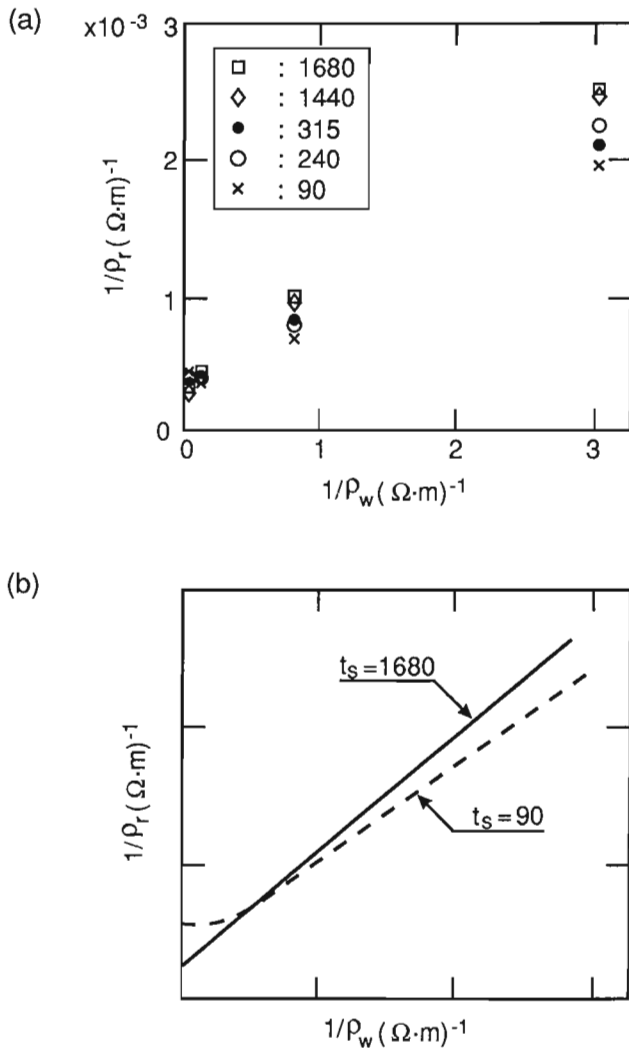
Figure 4b.

points 3, 4, and 5, which show the largest slope, and points 1, 2, and 3, which show the smallest slope. These results are listed in the two columns to the far right of Table 6.

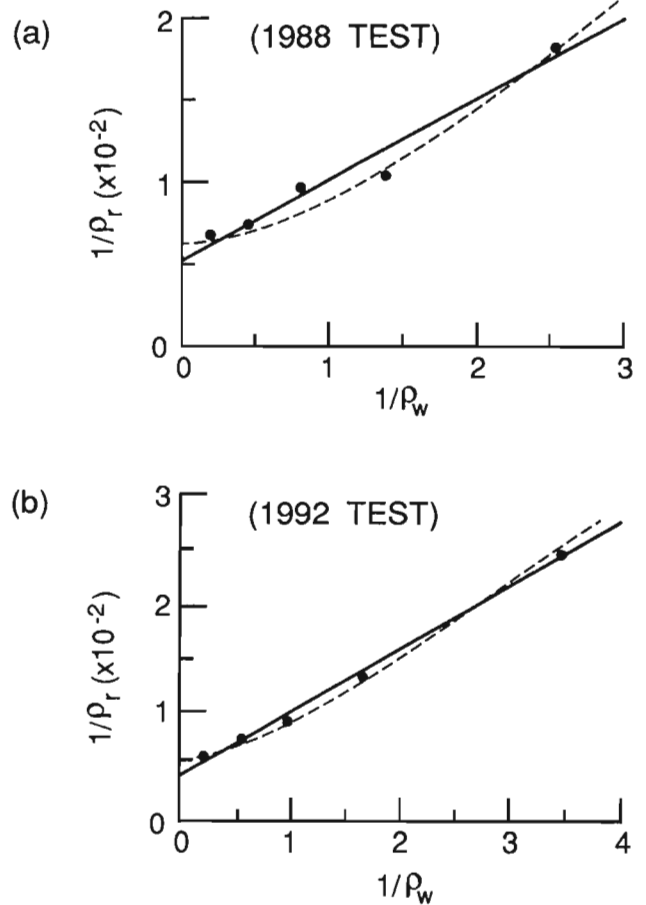
The results of all four tests – the "Extended concentration test" and "Varied  $t_s$  test" (this study), the "1988 test" (Katsube et al., 1990, 1991a), and the "1992 test" (Katsube and Scromeda, in prep.) – are compiled in Table 7.

### DISCUSSION AND CONCLUSIONS

Based on the experimental results of the "Extended concentration test", the conceptual relationship between the reciprocal of bulk electrical resistivity ( $1/\rho_r$ ) and the reciprocal of fluid resistivity ( $1/\rho_w$ ) is a curve, consisting of a linear section



**Figure 5.** Reciprocal of bulk electrical resistivity ( $1/\rho_r$ ) plotted as a function of the reciprocal of fluid resistivity ( $1/\rho_w$ ), for sample V-3, for different saturation times ( $t_s$ ). (a) Results of the actual measurements. (b) Description of the conceptual relationship between  $1/\rho_r$  and  $1/\rho_w$  for different saturation times ( $t_s$ ).



**Figure 6.** Reciprocal of bulk electrical resistivity ( $1/\rho_r$ ) plotted as a function of the reciprocal of fluid resistivity ( $1/\rho_w$ ), for sample V-3: (a) for results of the "1988 test" (Katsube et al., 1990, 1991a); (b) for the results of the "1992 test" (Katsube and Scromeda, in prep.).

**Table 6.** Results for sample V-3 in the "1992 test" (Katsube and Scromeda, in prep.)

NaCl (N)	$\rho_w$ (Ω·m)	$\rho_r$ (Ω·m)	5	5	n	3*	3*
0.02	5.00	161	x	x	x	x	
0.05	1.84	134	x	x	x	x	
0.1	1.03	110	x	x	x	x	x
0.2	0.605	76.4	x	x	x		x
0.5	0.287	40.9	x	x			x
$F_T$			215*	175	208	268	162
$\rho_o$			191*	235	203	183	330

N = Concentration of pore fluid (NaCl in this case).  
 $\rho_w$  = Resistivity of pore fluid (NaCl in this case).  
 $\rho_r$  = Bulk rock resistivity.  
n = Number of data points.  
 $F_T$  = True formation factor.  
 $\rho_o$  = Surface resistivity.  
\*: Values determined by the conventional method, using equation (3) and five data points (0.02-0.5 N NaCl).  
\*: Extreme cases selected for determination of error range.

**Table 7** Summary of data analysis

Type of Test	$F_T$	$F_T$ -Range	$\rho_c$ ( $\Omega$ -m)	$\rho_c$ -Range
Extended concentration	$163 \pm 21$	142-328	$310 \pm 81$	265-391
Varied $t_s$	$151 \pm 20$	138-170	$283 \pm 18$	271-301
1988	$209 \pm 120$	200-329	$189 \pm 20$	163-189
1992	$162 \pm 13$	162-268	$330 \pm 100$	183-330
Interpreted Values	$162 \pm 11$		$310 \pm 50$	

and a nonlinear section (Fig. 3c). The linear section is in accordance with theory as expressed by equation (2), but the reason for the discrepancy shown by the nonlinear section is unknown. One explanation offered is that, ions dissolving into the pore fluid from the rock reduce the pore fluid resistivity below levels expected for the low NaCl concentrations. This would create an intrinsic maximum pore fluid resistivity. This suggests that the data for the larger values of  $1/\rho_w$  are more representative of the true relationship between the two parameters. Therefore, the true formation factor ( $F_T$ ) and surface resistivity ( $\rho_c$ ) values determined using  $1/\rho_r$  for the five largest values of  $1/\rho_w$  (Table 3; Fig. 3a) are the most likely values for the  $F_T$  and  $\rho_c$ . Their most likely error ranges are determined by considering the slope of a line passing through several of the five points that slightly deviate from the rest (Table 3, Fig. 3a). The four points for the smaller values of  $1/\rho_w$  (Table 3, Fig. 3b) constitute the nonlinear section of the curve, making them unlikely to represent the true values of  $F_T$  and  $\rho_c$ . However, they can be used to determine the maximum possible error range of  $F_T$  and  $\rho_c$ . Therefore, the most likely values ( $F_T$ ,  $\rho_c$ ) are 163 and 310  $\Omega$ -m, the most likely error ranges ( $\epsilon_{F1}$ ,  $\epsilon_{\rho1}$ ) are  $\pm 21$  and  $\pm 81$   $\Omega$ -m, and the maximum possible error ranges ( $\epsilon_{F2}$ ,  $\epsilon_{\rho2}$ ) are  $\pm 120$  and  $\pm 81$   $\Omega$ -m for  $F_T$  and  $\rho_c$  (Table 7).

The conceptual relationship between the two parameters for the "Varied  $t_s$  test" shows that shorter saturation times (e.g.  $t_s = 90$  minutes), illustrated in Figure 5b, introduce a non-linearity between  $1/\rho_r$  and  $1/\rho_w$ , similar to that in Figure 3c. This indicates that  $F_T$  and  $\rho_c$  determined using  $1/\rho_r$  for the larger values of  $1/\rho_w$  (Table 4) are more accurate. As saturation time ( $t_s$ ) increases (Fig. 5b), the slope of the linear section increases without any change in the vertical axis intercept, implying that  $F_T$  decreases without any change in  $\rho_c$ . Also, the nonlinearity disappears with increased  $t_s$ , for reasons not known. A possible explanation for this is that, the intrinsic fluid conductivity caused by the dissolving material from the rock has had time to diffuse out of the rock through the pore fluid into the solution surrounding the rock specimen. An explanation offered for the reason that  $F_T$  decreases with time is that, at smaller saturation times ( $t_s$ ) the pores are not fully saturated causing reduced space for ionic flow. This situation would disappear at larger saturation times ( $t_s$ ) where the pores would become fully saturated, thus increasing the space for ionic flow. This implies that larger saturation times ( $t_s$ )

increase the measurement accuracy of  $F_T$  and  $\rho_c$ . Based on the results in Table 2, which indicate that the sample is 97% saturated at  $t_s = 180$ -260 minutes,  $F_T$  is interpreted to have reached stability at  $t_s = 240$  minutes (Table 4, Fig. 4b). Based on this interpretation, the value of  $\rho_c$  is determined by taking the average of all five values in Table 4, and  $F_T$  by averaging the values for  $t_s > 90$  minutes, excluding that for  $t_s = 315$  minutes because it is abnormally large. This results in  $F_T = 151 \pm 20$  and  $\rho_c = 283 \pm 18$   $\Omega$ -m.

The results of the data analysis for  $F_T$  and  $\rho_c$  (Table 7) produce values of  $209 \pm 120$  and  $189 \pm 20$   $\Omega$ -m for the "1988 test" (Katsube et al., 1990, 1991a), and  $162 \pm 13$  and  $330 \pm 100$   $\Omega$ -m for the "1992 test" (Katsube and Scromeda, in prep.). The results of the "1992 test" (Table 7) are consistent with the "Extended concentration test" and the "Varied  $t_s$  test", with the most likely values for  $F_T$  and  $\rho_c$  being  $162 \pm 11$  and  $310 \pm 50$   $\Omega$ -m, respectively. However, the results of the "1988 test", where  $F_T$  and  $\rho_c$  are  $209 \pm 120$  and  $189 \pm 20$   $\Omega$ -m, respectively, are inconsistent with the results of the other three tests to a considerable degree. This inconsistency for  $F_T$  is understandable, because of the shorter saturation time ( $t_s$ ) that was used. However, the reason for the discrepancy related to  $\rho_c$  is not understood because, according to the "Varied  $t_s$  test", the  $\rho_c$  values should not change with time. The only suggestion that can be made, is that some mineralogical change has taken place at the pore surfaces, subsequent to the "1988 test".

The  $F_T$  and  $\rho_c$  values of  $209 \pm 120$  and  $189 \pm 20$   $\Omega$ -m (Table 7), produced by the "1988 test" (80% saturation), vary by 29% and 39% from the averages of the "1992 test" (97-100% saturation), which are  $162 \pm 13$  and  $330 \pm 100$   $\Omega$ -m (Table 7), respectively. These discrepancies are within the error range of  $\pm 20$ -40% claimed at the time that the measurement procedures used in the "1988 test" were established for crystalline rocks (Katsube, 1981). However,  $F_T$  and  $\rho_c$  determined by the conventional method for the same set of data using equation (3) produce values of 268 and 160  $\Omega$ -m respectively, values varying from the interpreted values (Table 7) by 65% and 52%, respectively. Although, these variations are larger than the error ranges previously claimed, they are small when it is considered that the two parameters can vary over a range of seven orders of magnitude (e.g. Katsube and Salisbury, 1991).

## ACKNOWLEDGMENTS

The authors express appreciation to Q. Bristow (Geological Survey of Canada, Ottawa) for critically reviewing this paper and for expressing considerable interest in this study. Special appreciation is expressed for the provision by Dr. Bristow of diagrams containing new methods and ideas for displaying complex data. The authors acknowledge the support provided to this work by M. Williamson (Geological Survey of Canada, Atlantic Geoscience Centre, Dartmouth, N.S.), M.E. Best (Geological Survey of Canada, Pacific Geoscience Centre, Sydney, B.C.), and by K.A. Richardson (Geological Survey of Canada, Ottawa).

---

**REFERENCES**


---

- Archie, G.E.**  
1942: The electrical resistivity log as an aid in determining some reservoir characteristics; Transactions of the American Institute of Mining, Metallurgical and Petroleum Engineers, v. 146, p. 54-67.
- Coyner, K., Katsube, T.J., Best, M.E., and Williamson, M.**  
1993: Gas and water permeability of tight shales from the Venture Gas Field, offshore Nova Scotia; in Current Research, Part D; Geological Survey of Canada, Paper 93-1D, p. 129-136.
- Gauvreau, C. and Katsube, T.J.**  
1975: Automation in electrical rock property measurements; Report of Activities, Part A; Geological Survey of Canada, Paper 75-1A, p. 83-86.
- Hume, J.P. and Katsube, T.J.**  
1987: Pore structure characteristics; in Geotechnical Studies at East Bull Lake Research Area, (ed.) A.G. Latham; Canada Centre for Mineral and Energy Technology, Report MRL 87-94, p. 39-66.
- Katsube, T.J.**  
1975: The electrical polarization mechanism model for moist rocks; Geological Survey of Canada, Paper 75-1C, p. 353-360.  
1977: Electrical properties of rocks; in Induced Polarization for Exploration Geologists and Geophysicists; Short Course Presented by the University of Arizona, Tucson, March 14-16, p. 15-44.  
1981: Pore structure and pore parameters that control the radionuclide transport in crystalline rocks: Proceedings of the Technical Program, International Powder and Bulk Solids Handling and Processing, Rosemont, Illinois, p. 394-409. (Available from: CAHNERS Exposition Group, 222 West Adams Street, Chicago, Illinois 60606 U.S.A.).  
1993: Nano-pore transport mechanism of tight shales from the Scotian Shelf, offshore Nova Scotia; in Current Research, Part D; Geological Survey of Canada, Paper 93-1D, p. 121-127.
- Katsube, T.J. and Hume, J.P.**  
1987a: Pore structure characteristics of granitic rock samples from Whiteshell research area; in Geotechnical Studies at Whiteshell Research Area; (RA-3); CANMET, Report MRL 87-52, 111-158.  
1987b: Electrical properties of granitic rocks in Lac du Bonnet batholith; in Geotechnical Studies at Whiteshell Research Area (RA-3); Canada Centre for Mineral and Energy Technology, Report MRL 87-52, p. 205-220.
- Katsube, T.J. and Kaminen, D.C.**  
1983: Effect of alteration on pore structure of crystalline rocks; core samples from Atikokan, Ontario; Canadian Mineralogist, v. 21, p. 637-646.
- Katsube, T.J. and Salisbury, M.**  
1991: Petrophysical characteristics of surface core samples from the Sudbury structure; in Current Research, Part E; Geological Survey of Canada, Paper 91-E, p. 265-271.
- Katsube, T.J. and Scromeda, N.**  
1991: Effective porosity measuring procedure for low porosity rocks; in Current Research, Part E; Geological Survey of Canada, Paper 91-E, p. 291-297.
- Katsube, T.J. and Walsh, J.B.**  
1987: Effective aperture for fluid flow in microcracks: International Journal of Rock Mechanics; and Mining Sciences and Geomechanics Abstracts, v. 24, p. 175-183.
- Katsube, T.J., Best, M.E., and Mudford, B.S.**  
1991a: Petrophysical characteristics of shales from the Scotian Shelf; Geophysics, v. 56, p. 1681-1689.
- Katsube, T.J., Mareschal, M., and Aucoin, F.**  
1991b: Electrical characteristics of a graphitic rock from the Kapuskasing Structural Zone; Geological Survey of Canada, Paper 91-E, p. 291-297.
- Katsube, T.J., Murphy, T.B., Best, M.E., and Mudford, B.S.**  
1990: Pore structure characteristics of low permeability shales from deep formations; in Proceedings of the 1990 SCA (Society of Core Analysts) 4th Annual Technical Conference, August, 1990, Dallas, Texas; SCA-9010, p. 1-21.
- Katsube, T.J., Percival, J.B., and Hume, J.P.**  
1985: Characterization of the rock mass by pore structure parameters; Atomic Energy of Canada Limited Technical Record, TP-299, p. 375-413.
- Katsube, T.J., Scromeda, N., Mareschal, M., and Bailey, R.C.**  
1992a: Electrical resistivity and porosity of crystalline rock samples from the Kapuskasing Structural Zone, Ontario; in Current Research, Part E; Geological Survey of Canada, Paper 92-1E, p. 225-236.
- Katsube, T.J., Scromeda, N., and Williamson, M.**  
1992b: Effective porosity of tight shales from the Venture Gas Field, offshore Nova Scotia; in Current Research, Part D; Geological Survey of Canada, Paper 92-1D, p. 111-119.
- Katsube, T.J., Williamson, M., and Best, M.E.**  
1992c: Shale pore structure evolution and its effect on permeability; in Symposium Volume III of the Thirty-Third Annual Symposium of the Society of Professional Well Log Analysts (SPWLA), The Society of Core Analysts Preprints, Oklahoma City, Oklahoma, June 15-17, 1992; Paper SCA-9214, p. 1-22.
- Patnode, H.W. and Wyllie, M.R.J.**  
1950: The presence of conductive solids in reservoir rocks as a factor in electric log interpretation; Transactions of the American Institute of Mining, Metallurgical and Petroleum Engineers, v. 189, p. 47-52.
- Wadden, M.M. and Katsube, T.J.**  
1982: Radionuclide diffusion rates in crystalline rocks; Chemical Geology, v. 36, p. 191-214.
- Walsh, J.B. and Brace, W.F.**  
1984: The effect of pressure on porosity and the transport properties of rocks; Journal of Geophysical Research, v. 89, p. 9425-9431.
- Worthington, P.F.**  
1975: Quantitative geophysical investigations of granular aquifers; in Geophysical Surveys, v. 2; D. Reidel, Dordrecht, p. 313-366.

---

 Geological Survey of Canada Project 870057

# Effect of compaction on porosity and formation factor for tight shales from the Scotian Shelf

J.M. Loman<sup>1</sup>, T.J. Katsube, J.M. Correia<sup>1</sup>, and M.A. Williamson<sup>2</sup>  
Mineral Resources Division

*Loman, J.M., Katsube, T.J., Correia, J.M., and Williamson, M.A., 1993: Effect of compaction on porosity and formation factor for tight shales from the Scotian Shelf; in Current Research, Part E; Geological Survey of Canada, Paper 93-1E, p. 331-335.*

---

**Abstract:** The effect of stress on shale porosity and formation factor has been studied to provide information for developing quantitative models of hydrocarbon charge histories. These models are required to improve the accuracy of predicting hydrocarbon distribution in the sedimentary basins of the Canadian Frontier regions. Porosity decreases and formation factor increases with increasing stress, as expected. However, this study indicates that the rate of increase or decrease of these parameters is sample dependent. For example, the effective porosity decrease varies from a reduction of 94% (1.8 to 0.1% ) to 5.6% (7.2 to 6.8%) for the confining pressure range of 3.5 to 51.7 MPa. Similarly, the formation factor increase varies from 220% (298 to 964) to 55% (226 to 351) for the same pressure range. This variation is thought to be related to the diagenetic characteristics of the samples.

**Résumé :** Les auteurs ont étudié l'effet des contraintes sur la porosité et le facteur de formation des shales afin d'obtenir de l'information en vue de l'élaboration de modèles quantitatifs de l'histoire de la migration des hydrocarbures. Ces modèles sont nécessaires pour mieux prévoir la distribution des hydrocarbures dans les bassins sédimentaires des régions pionnières du Canada. Tel que prévu, la porosité diminue et le facteur de formation augmente avec l'accroissement des contraintes. Toutefois, l'étude indique que le taux d'augmentation ou de diminution de ces paramètres varie selon les échantillons. Par exemple, la diminution de la porosité efficace varie de 94 % (de 1,8 à 0,1 %) à 5,6 % (de 7,2 à 6,8 %) dans le domaine des pressions de confinement de 3,5 à 51,7 MPa. De même, l'augmentation du facteur de formation varie de 220 % (de 298 à 964) à 55 % (de 226 à 351) dans le même domaine de pressions. Cette variation serait liée aux caractéristiques diagénétiques des échantillons.

---

<sup>1</sup> K & A Energy Consultants, Inc., 6849 East 13th Street, Tulsa, Oklahoma 74112 U.S.A.

<sup>2</sup> Atlantic Geoscience Centre, Dartmouth

## INTRODUCTION

Quantitative models of the hydrocarbon charge history for the Canadian frontier basins are being developed (Williamson, 1992; Williamson and Smyth, 1992) to improve the accuracy of predicting hydrocarbon distribution in these sedimentary basins. Information on petrophysical characteristics of basin fill is required for this development. Although such information is abundant for reservoir rocks, little exists for shales (Mudford and Best, 1989).

Various studies are currently underway, at the Geological Survey of Canada (GSC), to provide petrophysical information on tight shales (e.g., Katsube et al., 1990, 1991, 1992a, b; Katsube and Best, 1992; Katsube, 1992; Coyner et al., 1993; Katsube, 1993). This paper provides a description of the data obtained to date on the effect of stress on shale porosity and formation factor. These data are required to study the effect of compaction and burial on the shale pore structure and permeability mechanisms. The results contained in this paper are for eight tight shale samples from the Venture Gas Field, offshore Nova Scotia (Table 1, Katsube et al., 1991), and for one unconsolidated sample from the ocean floor in the same region.

## EXPERIMENTAL PROCEDURES

### Samples

The eight tight shale samples used in this study are discs of 2.54 cm in diameter and 0.4-0.8 cm in thickness. Information on their petrophysical characteristics and shale texture can be found in the literature (Katsube et al., 1990, 1991, 1992a, b). Information on the area and depth from which these samples have been taken is found in Table 1.

### Initial measurements (porosity and permeability)

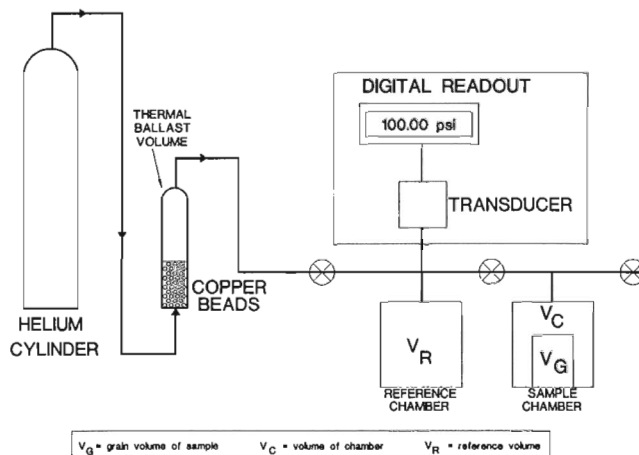
Samples V-3, V-4, V-5, V-6, V-7 and V-9 were cleaned with methylene chloride for 24 hours in a standard reflux-type extractor. These samples, along with Samples V-1-v and V-8,

**Table 1.** Sample information on locations and depths (after Katsube et al., 1991) for the eight tight shale samples from the Venture Gas Field, offshore Nova Scotia

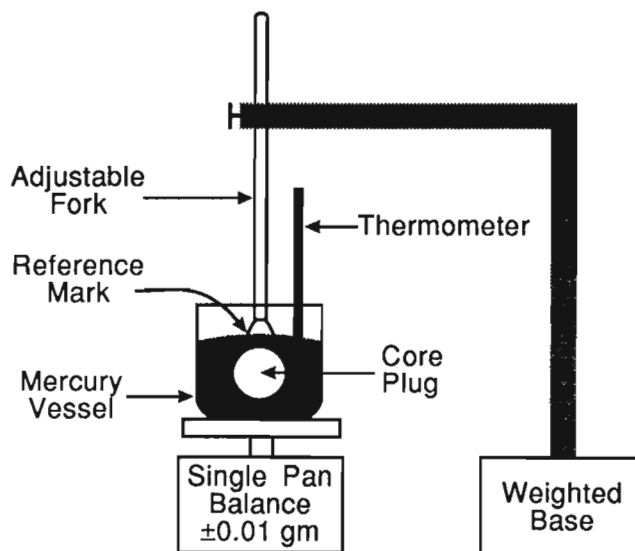
Sample Number	Venture Well (I.D.)	Depth (m)
V-1-v	B-13	4693.40
V-3	B-43	4916.36
V-4	B-43	4962.48
V-5	B-52	5122.35
V-6	B-52	5131.54
V-7	B-52	5271.59
V-8	B-52	5273.53
V-9	B-52	5553.65

I.D. = Well identification number.

were then dried in a convection oven for 24 hours at a temperature of 37.8°C (100°F). This was followed by 24 hours of vacuum drying at approximately 23.9°C (75°F). It was thought that two samples, V-1-v and V-8, were not durable enough to survive the cleaning with methylene chloride without being damaged. Gas permeability was then measured at a confining pressure of 2.76 MPa (400 psi) using a standard gas flow permeameter, with flow pressures ranging from 0.14 to 0.35 MPa (20.0 to 50.00 psi). The gas flow rate through the sample was measured using a microburette and a bubble meniscus. Porosities were determined by first using a Boyles' Law double-celled helium porosimeter to obtain grain volume (Fig. 1). Then the bulk volume of the samples was obtained by using the mercury immersion (Archimedes principle) technique (Fig. 2). These measurements and procedures generally follow the recommended practices of the American Petroleum Institute (API, 1960).



**Figure 1.** Boyles' Law double-celled helium porosimeter used to obtain grain volume of the shale samples.



**Figure 2.** Archimedes Mercury Immersion Apparatus used to determine bulk volume of the shale samples.



### Preparation for electrical measurements

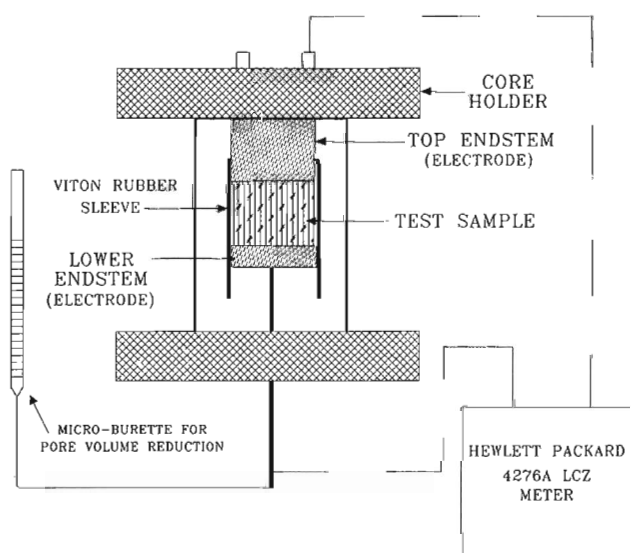
Next, the samples were placed in a saturation vessel and vacuum (76.2 cm of mercury) dried for 12 hours. The saturating brine was then introduced into the saturation vessel and compressed at 6.9 MPa (1000 psi) for 24 hours. A saturating brine of 30 000 ppm sodium chloride was used for samples V-1-v and V-8, to simulate their in-situ conditions. A brine with higher concentration, consisting of 80 000 ppm sodium chloride plus 20 000 ppm calcium chloride dihydrate, was used for the rest of the samples due to concern over possible clay swelling in them. After removal from the saturation vessel, each sample was placed in individual electrically isolated core holders (Fig. 3) and flushed with brine using backpressures to insure 100 per cent brine saturation. The electrical resistivity of the brine is measured using a YSI Model 35 conductance meter with a matched probe.

### Resistivity and porosity versus pressure measurements

Bulk electrical resistivities,  $\rho_b$ , were measured at multiple confining pressures between 3.5 and 51.8 MPa (500 to 7500 psi), at a frequency of 1000 Hz, using a Hewlett Packard Model 4276A LCZ meter. The samples were tested in a two-electrode system using a stainless steel electrode and end piece assembly. As confining pressure was increased, the amount of brine squeezed out of the sample was volumetrically measured and used to determine the porosity value at each of the confining pressures. The temperature variance was approximately  $\pm 1.1^\circ\text{C}$  during the electrical resistivity tests. The apparent formation factor,  $F_a$ , is determined using the following equation (Archie, 1942):

$$F_a = \rho_b / \rho_w \quad (1)$$

where  $\rho_w$  is pore fluid resistivity.



**Figure 3.** High pressure core holder with two-electrode system used to measure electrical resistivities at multiple confining pressures up to 51.8 MPa (7500 psi).

## EXPERIMENTAL RESULTS

The results of the effective porosity ( $\phi_E$ ) and apparent formation factor ( $F_a$ ) measured under varied confining pressures for the eight tight shale samples are listed in Table 2, and in Table 3 for the unconsolidated sample. In Table 4, a comparison is made between the effective porosity ( $\phi_E$ ) and apparent formation factor ( $F_a$ ) values obtained in this study with those from previous studies (Katsube et al., 1990, 1991). The effective porosity ( $\phi_E$ ) values from the previous studies show a wide range of variation for all of the samples. This is because the data consist of values obtained by different methods conducted in different laboratories under different conditions, therefore possibly representing different types of porosities (e.g., some including, others excluding adsorbed water), although all referred to as effective porosity. This is a subject currently under intensive study.

## DISCUSSION AND CONCLUSIONS

The effective porosity ( $\phi_E$ ) values at the lowest pressures (3.5 MPa) are consistent with those of previous measurements, except for sample V-4 which displays a value considerably lower than those obtained in previous studies (Table 4). The effective porosity ( $\phi_E$ ) value for V-6 is below those of previous measurements, but is thought to be within the range of measurement error. As the measurements in this study were made at elevated pressures, it is expected that they would produce values lower than those obtained by previous measurements made at atmospheric pressure. However, such lower values are seen only for samples V-4 and V-6.

The apparent formation factor ( $F_a$ ) values for the lowest pressure (3.5 MPa) are smaller than the true formation factor,  $F$ , values obtained by previous measurements (Table 4), except for samples V-3 and V-5. Apparent formation factor ( $F_a$ ) corrected for pore surface conduction is the true formation factor ( $F$ ), as explained in the literature (e.g., Katsube et al., 1991; Patnode and Wyllie, 1950). Higher pressures, such as attained in this study, are expected to produce apparent formation factor ( $F_a$ ) values larger than the true formation factor values obtained by previous measurements which were made at atmospheric pressure. On the other hand, the lack of pore surface conduction corrections (Patnode and Wyllie, 1950) in this study are expected to produce apparent formation factor values smaller than the true ones. Therefore, it is understandable that this study has produced apparent values both above and below the true values obtained by previous measurements.

The effective porosity ( $\phi_E$ ) decreases and the apparent formation factor ( $F_a$ ) increases with increased confining pressure for the consolidated samples (Tables 2a and 2b), as expected. However, the degree of variation with pressure is very dependent on the sample. For example, the effective porosity ( $\phi_E$ ) decrease varies from a reduction of 94% ( $\phi_E$  change from 1.8 to 0.1% for sample V-6) to 5.6% ( $\phi_E$  change from 7.2 to 6.8% for sample V-7) for the confining pressure increase from 3.5 to 51.7 MPa. Similarly, the apparent formation factor ( $F_a$ ) increase varies from 220% ( $F$  change

**Table 2a.** Petrophysical properties as a function of confining pressure for four tight shale samples (V-1-v to V-5)

Sample	$k_a$ ( $\mu$ D)	P (MPa)	$\phi_E$ (%)	$\rho_w$ ( $\Omega$ -m)	$F_a$
V-1-v	0.87	3.5	3.5	0.205 (23.6 °C)	287.9
		6.9	3.5		319.4
		17.2	2.6	370.7	
		27.6	1.8	438.3	
		41.4	1.4	486.1	
		51.7	1.0	553.1	
V-3	887	3.5	5.8	0.083 (23.2 °C)	364.3
		6.9	5.5		412.7
		13.8	5.1	477.2	
		27.6	4.8	595.6	
		34.5	4.5	736.8	
		51.7	4.4	888.7	
V-4	858	3.5	1.8	0.085 (21.6 °C)	297.6
		6.9	1.3		362.7
		13.8	0.8	464.3	
		27.6	0.4	659.8	
		34.5	0.3	752.0	
		51.7	0.1	963.5	
V-5	2.78	3.5	4.4	0.084 (22.4 °C)	1911
		6.9	4.2		2186
		13.8	4.1	2646	
		27.6	3.9	3350	
		34.5	3.9	3700	
		51.8	3.8	4374	

$k_a$  = Gas permeability.  
 P = Confining pressure.  
 $\phi_E$  = Effective porosity.  
 $\rho_w$  = Pore fluid resistivity.  
 $F_a$  = Apparent formation factor.

**Table 2b.** Petrophysical properties as a function of confining pressure for four tight shale samples (V-6 to V-9)

Sample	$k_a$ ( $\mu$ D)	P (MPa)	$\phi_E$ (%)	$\rho_w$ ( $\Omega$ -m)	$F_a$
V-6	0.645	3.5	0.4	0.084 (22.4°C)	3588
		6.9	0.4		3742
		13.8	0.4	4085	
		27.6	0.3	4615	
		34.5	0.3	4994	
		51.8	0.3	5639	
V-7	1.9	3.5	7.2	0.083 (23.2°C)	383.3
		6.9	7.2		416.2
		13.8	7.1	472.6	
		27.6	7.0	560.3	
		34.5	6.9	661.9	
		51.7	6.8	762.9	
V-8	1.24	3.5	7.7	0.205 (23.6°C)	225.7
		6.9	7.4		236.8
		13.8	7.2	266.8	
		27.6	6.9	301.7	
		34.5	6.6	326.6	
		51.7	6.4	350.5	
V-9	1.61	3.5	2.0	0.085 (21.6°C)	567.4
		6.9	1.8		596.8
		17.2	1.7	666.9	
		27.6	1.4	820.6	
		41.4	1.3	886.6	
		51.7	0.3	1034.2	

$k_a$  = Gas permeability.  
 P = Confining pressure.  
 $\phi_E$  = Effective porosity.  
 $\rho_w$  = Pore fluid resistivity.  
 $F_a$  = Apparent formation factor.

**Table 3.** Petrophysical properties as a function of confining pressure for an unconsolidated seafloor sample from offshore Nova Scotia

Sample	$k_a$ ( $\mu$ D)	P (MPa)	$\phi_E$ (%)	$\rho_w$ ( $\Omega$ -m)	$F_a$
V-SF-1	29.6	3.5	37.8	0.084 (22.2°C)	4.75
		6.9	28.6		7.34
		13.8	19.5	11.8	
		20.7	15.7	14.5	
		27.6	13.1	16.8	
		34.5	10.8	18.9	
		41.4	7.3	22.7	
		48.3	6.1	24.2	
		55.2	5.1	26.7	
		62.1	3.9	28.3	
69.0	2.7	29.5			

$k_a$  = Gas permeability.  
 P = Confining pressure.  
 $\phi_E$  = Effective porosity.  
 $\rho_w$  = Pore fluid resistivity.  
 $F_a$  = Apparent formation factor.

**Table 4.** Comparison of effective porosity ( $\phi_E$ ) and formation factor (F) measurements at the lowest pressures (3.5 MPa) with those of previous measurements for the tight shale samples.

Samples	Effective Porosity ( $\phi_E$ ) (%)		Formation Factor ( $\times 10^3$ )	
	This Study	Previous* Studies	This Study ( $F_a$ )	Previous** Studies (F)
V-1-v	3.5	3.1-7.0	0.29	0.54
V-3	5.8	4.0-11.4	0.36	0.27
V-4	1.8	5.8-15.6	0.30	0.45
V-5	4.4	3.5-6.8	1.91	1.03
V-6	0.4	0.7-2.1	3.59	17.6
V-7	7.2	4.9-9.5	0.38	0.43
V-8	7.7	7.7-12.1	0.23	0.31
V-9	2.0	0.8-3.3	0.57	1.63

\* : Katsube et al. (1992a)  
 \*\* : Katsube et al. (1991)  
 $F_a$  = Apparent formation factor.  
 F = True formation factor.

from 298 to 964 for sample V-6) to 55% ( $F_a$  change from 226 to 351 for sample V-8) for the same pressure range. This variation is thought to be related to the diagenetic characteristics of the samples (Katsube et al., 1992b; Katsube and Williamson, in press). That is, the variation depends on whether the final diagenetic phase of the sample was cementation resulting in most of the pores being filled with cement, or whether it was dissolution resulting in an abundance of pore space consisting of secondary dissolution pores.

The effective porosity ( $\phi_E$ ) decreases and the apparent formation factor ( $F_a$ ) increases with increased confining pressure also for the unconsolidated sample (V-SF-1, Table 3), as expected. It is interesting that the effective porosity ( $\phi_E$ ) value at the maximum confining pressure of 69 Mpa is 2.7%, a value similar to those of the consolidated samples (Table 4). The confining pressure of 69 MPa is equivalent to an overburden pressure for a depth of about 3 km in the Venture Gas Field (Mudford and Best, 1989), a depth of about 50 to 65% of those for the consolidated samples (Table 1). However, the apparent formation factor ( $F_a$ ) value of 29.5 for the unconsolidated sample at the maximum confining pressure is considerably lower than the true formation factor (F) values of the consolidated samples (Table 4), most likely because of it not being corrected for pore surface conduction.

## ACKNOWLEDGMENTS

The authors thank K.A. Richardson (Geological Survey of Canada, Ottawa) for critically reviewing this paper, and for his beneficial comments.

## REFERENCES

- API (American Petroleum Institute)**  
1960: Recommended practices for core-analysis procedure; API Recommended Practice 40 (RP 40) First Edition, American Petroleum Institute, Washington, D.C., p. 55.
- Archie, G.E.**  
1942: The electrical resistivity log as an aid in determining some reservoir characteristics; Transactions of the American Institute of Mining, Metallurgical and Petroleum Engineers, v. 146, p. 54-67.
- Coyner, K., Katsube, T.J., Best, M.E., and Williamson, M.**  
1993: Gas and water permeability of tight shales from the Venture Gas Field offshore Nova Scotia; in Current Research, Part D; Geological Survey of Canada, Paper 93-1D, p. 129-136.
- Katsube, T.J.**  
1992: Statistical analysis of pore-size distribution data of tight shales from the Scotian Shelf; in Current Research, Part E; Geological Survey of Canada, Paper 92-1E, p. 365-372.  
1993: Nano pore transport mechanism of tight shales from the Scotian Shelf; in Current Research, Part D; Geological Survey of Canada, Paper 93-1D, p. 121-127.
- Katsube, T.J. and Best, M.E.**  
1992: Pore structure of shales from the Beaufort-MacKenzie Basin, Northwest Territories; in Current Research, Part E; Geological Survey of Canada, Paper 92-1E, p. 157-162.
- Katsube, T.J. and Williamson, M.A.**  
in press: Effect of diagenesis on shale nano-pore structure and implications for sealing capacity; Clay Mineralogy.
- Katsube, T.J., Murphy, T.B., Best, M.E., and Mudford, B.S.,**  
1990: Pore structure characteristics of low permeability shales from deep formations: in Proceedings of the 1990 SCA (Society of Core Analysts) 4th Annual Technical Conference, August, 1990, Dallas, Texas, SCA-9010, p.1-21.
- Katsube, T.J., Best, M.E., and Mudford, B.S.**  
1991: Petrophysical characteristics of shales from the Scotian shelf; Geophysics, v. 56, p. 1681-1688.
- Katsube, T.J., Scromeda, N., and Williamson, M.**  
1992a: Effective porosity of tight shales from the Venture Gas Field, offshore Nova Scotia; in Current Research Part D; Geological Survey of Canada, Paper 92-1D, p. 111-119.
- Katsube, T.J., Williamson, M., and Best, M.E.**  
1992b: Shale pore structure evolution and its effect on permeability; in Symposium Volume III of the Thirty-Third Annual Symposium of the Society of Professional Well Log Analysts (SPWLA), The Society of Core Analysts Preprints, Oklahoma City, Oklahoma, June 15-17, 1992, Paper SCA-9214, p. 1-22.
- Mudford, B.S. and Best, M.E.**  
1989: Venture Gas Field, offshore Nova Scotia; case study of overpressuring in region of low sedimentation rate; American Association of Petroleum Geologists Bulletin, v. 73, p. 1383-1396.
- Patnode, H.W. and Wyllie, M.R.J.**  
1950: The presence of conductive solids in reservoir rocks as a factor in electric log interpretation; Transactions of the American Institute of Mining, Metallurgical and Petroleum Engineers, v. 189, p. 47-52.
- Williamson, M.A.**  
1992: The subsidence, compaction, thermal and maturation history of the Egret Member source rock, Jeanne D'Arc Basin, offshore Newfoundland; Bulletin of Canadian Petroleum Geology, v. 40, no. 2, p. 136-150.
- Williamson, M.A. and Smyth, C.**  
1992: Timing of gas and overpressure generation in the Sable Basin offshore Nova Scotia; Bulletin of Canadian Petroleum Geology, v. 40, no. 2, p. 151-169.



# Gold occurrences of the Rocky Brook-Millstream fault, northern Appalachians, New Brunswick<sup>1</sup>

Alain Tremblay<sup>2</sup>, Stéphane Faure<sup>2</sup>, and Benoit Dubé  
Quebec Geoscience Centre, Sainte-Foy

*Tremblay, A., Faure, S., and Dubé, B., 1993: Gold occurrences of the Rocky Brook-Millstream fault, northern Appalachians, New Brunswick; in Current Research, Part E; Geological Survey of Canada, Paper 93-1E, p. 337-346.*

---

**Abstract:** In northern New Brunswick, gold occurrences are found in close association with the Rocky Brook-Millstream fault in the Bathurst and Upsalquitch Forks areas. In the Bathurst area, gold is mostly found within sulphide-rich, extensional and shear veins associated with second-order structures of the Rocky Brook-Millstream fault, whereas in the area of Upsalquitch Forks, it is mainly associated with brittle-ductile structures developed in mafic to felsic intrusive rocks. On the basis of their mineralogy and structural/lithological relationships with hosting rocks, gold occurrences are divided into (1) precious and base metal veins, and (2) gold only veins. In northern New Brunswick, the highest potential for economic gold mineralizations appears to be related to mafic intrusions (i.e., Elmtree deposit and Upsalquitch Forks area gold showings) due to favourably rheological and chemical properties of hosting rocks.

**Résumé :** Dans le nord du Nouveau-Brunswick, des indices aurifères sont connus le long de la faille de Rocky Brook-Millstream (RBM) dans les régions de Bathurst et d'Upsalquitch Forks. Dans la région de Bathurst, l'or est principalement associé à des veines, riches en sulfures, représentant des structures d'extension ou de cisaillement de second ordre qui sont génétiquement associées à la faille de RBM. Dans la région d'Upsalquitch Forks, les minéralisations aurifères sont principalement associées à des structures fragiles-ductiles développées au sein de roches intrusives. En fonction de leur minéralogie et de leurs relations lithologiques et structurales avec les roches-hôtes, ces indices aurifères sont divisés en deux types: (1) veines polymétalliques et (2) veines aurifères. A cause d'un contexte rhéologique et chimique favorable, les indices aurifères possédant le potentiel économique le plus intéressant sont associés aux roches intrusives mafiques (i.e. dépôt d'Elmtree et indices de la région d'Upsalquitch Forks).

---

<sup>1</sup> Contribution to Canada-New Brunswick Cooperation Agreement on Mineral Development (1990-1995), a subsidiary agreement under the Canada-New Brunswick Economic and Regional Development Agreement.

<sup>2</sup> INRS-Géorressources, Quebec Geoscience Centre, Sainte-Foy

## INTRODUCTION

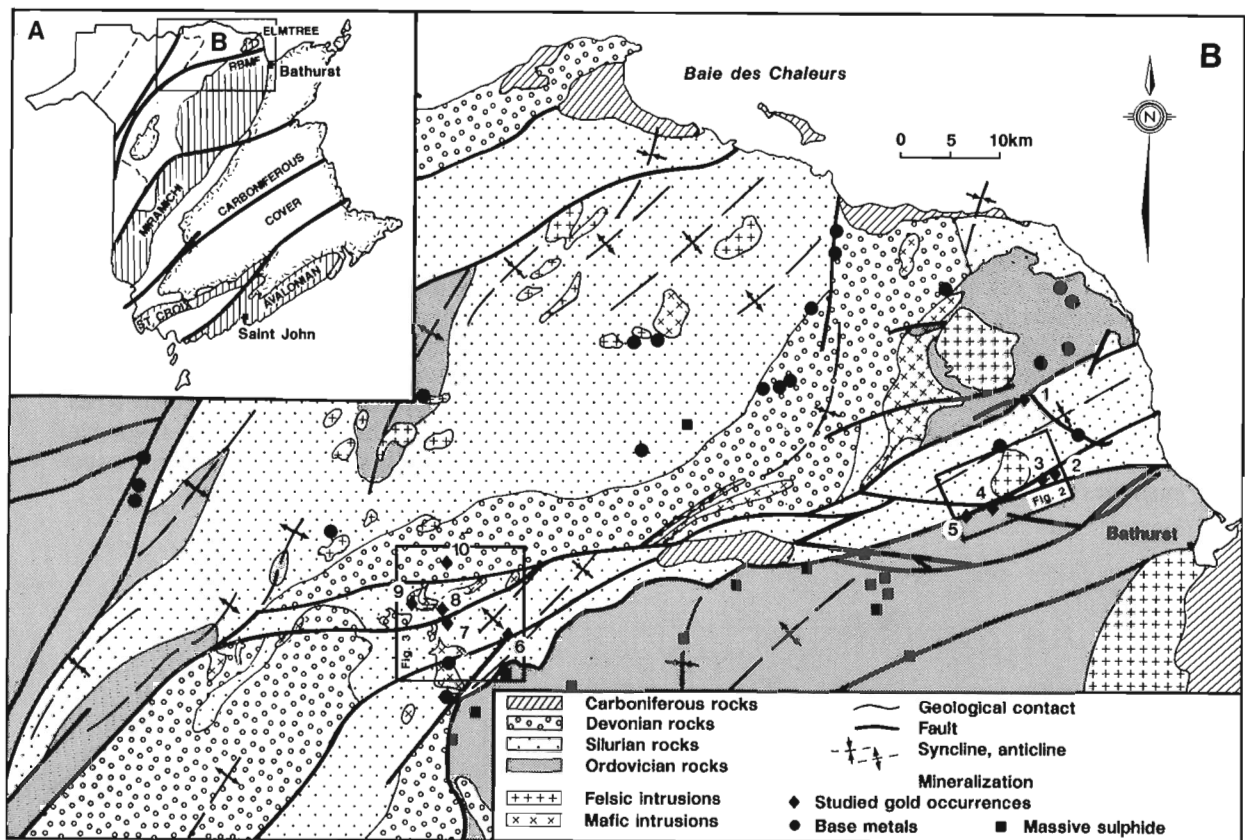
During the past decade, several gold occurrences spatially related to the Rocky Brook-Millstream (RBM) fault were discovered in northern New Brunswick. Previous studies carried out along the fault have revealed a close genetic relationship between brittle-ductile shear zones and gold occurrences (Ruitenberg et al., 1990; Tremblay and Dubé, 1991; Faure et al., 1992).

The Bathurst and Upsalquitch Forks areas are the two principal regions where mining companies have focused their gold exploration program during the last ten years. Most gold showings and prospects of these areas have been described in internal or public reports released by the industry. Since most of these occurrences are poorly exposed, it is difficult to present a definite interpretation for each of them. Therefore, this contribution is intended to provide a summary of ore mineralogy, alteration, and structure for the most significant gold occurrences related to the fault. The resulting classification will be used as a basis for the establishment of a genetic model for gold mineralization in northern New Brunswick.

## REGIONAL GEOLOGY

The northern New Brunswick Appalachians are mainly characterized by two rock packages of contrasting structural styles and facies: the Ordovician Miramichi and Elmtree terranes, and the Late Ordovician to Early Devonian Matapedia cover sequence (Fig. 1A; Ruitenberg et al., 1977; Fyffe and Fricker, 1987). These two lithotectonic units are bounded by Late Ordovician to Early Silurian unconformities or by fault zones associated with the Acadian orogeny (Fig. 1B, McCutcheon and Bevier, 1990).

The Miramichi Terrane (Fig. 1A) consists of poly-deformed Ordovician rocks. It is made up of a quartzite-slate sequence of the Miramichi Group, and of epiclastic and volcanic rocks of the Tetagouche Group (van Staal and Fyffe, 1991). The Elmtree Terrane (Fig. 1A) is essentially made up of the Fournier Group which consists of a mafic-ultramafic intrusive complex overlain by mafic volcanics and clastic rocks. The Miramichi and Elmtree terranes were docked together in Late Ordovician to Early Silurian times (Fyffe and Fricker, 1987), and suffered at least three phases of regional deformation (van Staal, 1987).



**Figure 1.** A) New Brunswick map showing the location of major pre-Silurian terranes. RBMF: Rocky Brook-Millstream fault. B) Simplified geological map of the northern New Brunswick Appalachians. Studied gold occurrences are located on the map. 1: Elmtree deposit, 2: Stephen's Brook showing, 3: Lavigne Brook showing, 4: Rocky Brook deposit, 5: Bradley Brook showing, 6: Simpson's Field showing, 7: McCormack Brook showing, 8: Dalhousie Road showing, 9: Mulligan Gulch showing, 10: Upsalquitch Forks showing.

Rock units of the Matapedia cover sequence disconformably overlie the older Ordovician terranes. The cover sequence has been subdivided into three main zones (Davies, 1979), namely, Aroostock-Matapedia, Tobique, and Chaleurs zones. Studied areas are underlain by the Tobique and the Chaleurs zones which consist of clastic rocks and limestones belonging to the Silurian Chaleurs Group overlain by sedimentary rocks and bimodal mafic-felsic volcanics of the Lower Devonian Tobique and Dalhousie groups (Fig. 1A; Greiner, 1967; Dostal et al., 1989). A single phase of regional deformation has affected the Matapedia cover sequence. Within Late Ordovician and Silurian rocks, the regional schistosity is, however, more penetrative than in the Devonian sequences (Walker and McCutcheon, 1991). Ordovician terranes and the Matapedia cover sequence are crosscut by mafic to felsic intrusions ranging in age from Ordovician to Devonian (Fig. 1B).

The Rocky Brook-Millstream fault is a dextral strike-slip fault that is part of a major transpressive fault system characterizing this segment of the northern Appalachians (Malo and Béland, 1989; Ruitenberget al., 1990; van Staal and Fyffe, 1991). These major faults were commonly associated with the development of both synthetic and antithetic, gold-bearing fault splays and structures (e.g., Tremblay and Dubé 1991). In the Bathurst area, the Rocky Brook-Millstream fault affects Upper Silurian rocks and appears to be cut by the Early to Middle Devonian Nicholas Denys intrusion (381 ± 4 Ma; Davis et al., 1969), thus

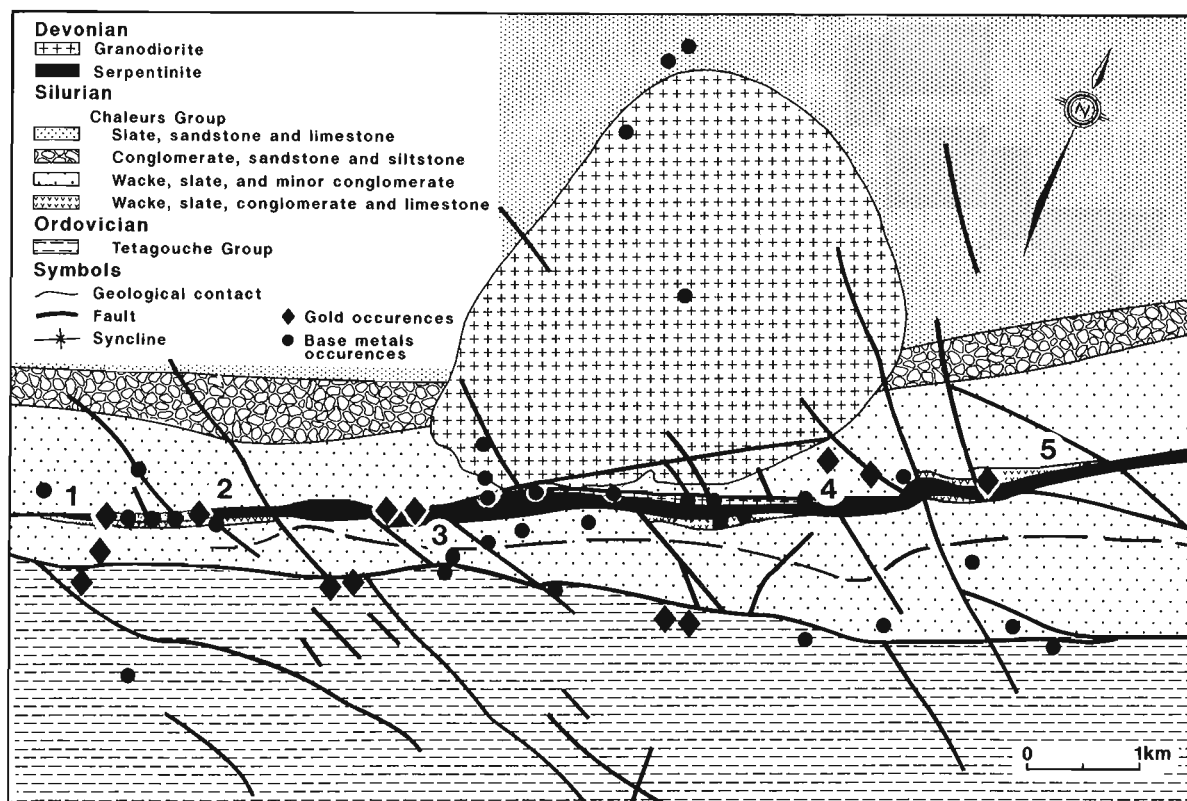
indicating that a significant amount of dextral transpression took place in Early Devonian times (van Staal and Fyffe, 1991).

## GOLD AND BASE METAL OCCURRENCES

Studied gold occurrences are spatially related to the Rocky Brook-Millstream fault in the Bathurst and Upsalquitch Forks areas (Fig. 1, 2, 3). Gold occurs mostly in Silurian and Devonian sedimentary rocks and in Late Silurian to Early Devonian mafic to felsic intrusions. The main characteristics of studied deposits and/or showings are presented in Table 1.

### Bathurst area

Gold occurrences of the Bathurst area are located on Figures 1 and 2. The Elmtree deposit occurs within a gabbroic intrusion spatially related to the Elmtree fault, a major east-northeast-trending structure that belongs to the Rocky Brook-Millstream fault system. The Stephen's Brook, Lavigne Brook, Bradley Brook, and Rocky Brook showings are gold occurrences found along the Rocky Brook-Millstream fault and related faults (Fig. 2). Most of these showings occur within the Chaleurs Group, and are spatially associated with slivers of foliated and brecciated serpentinite (Fig. 2; Philpott, 1987). Hosting rocks and structures were described by Tremblay and Dubé (1991), and summarized below.



**Figure 2.** Detailed map of gold showings associated to the Rocky Brook-Millstream fault in the Bathurst area. See Figure 1B for location. 1-2: Bradley Brook, 3: Rocky Brook, 4: Lavigne Brook, 5: Stephen's Brook.

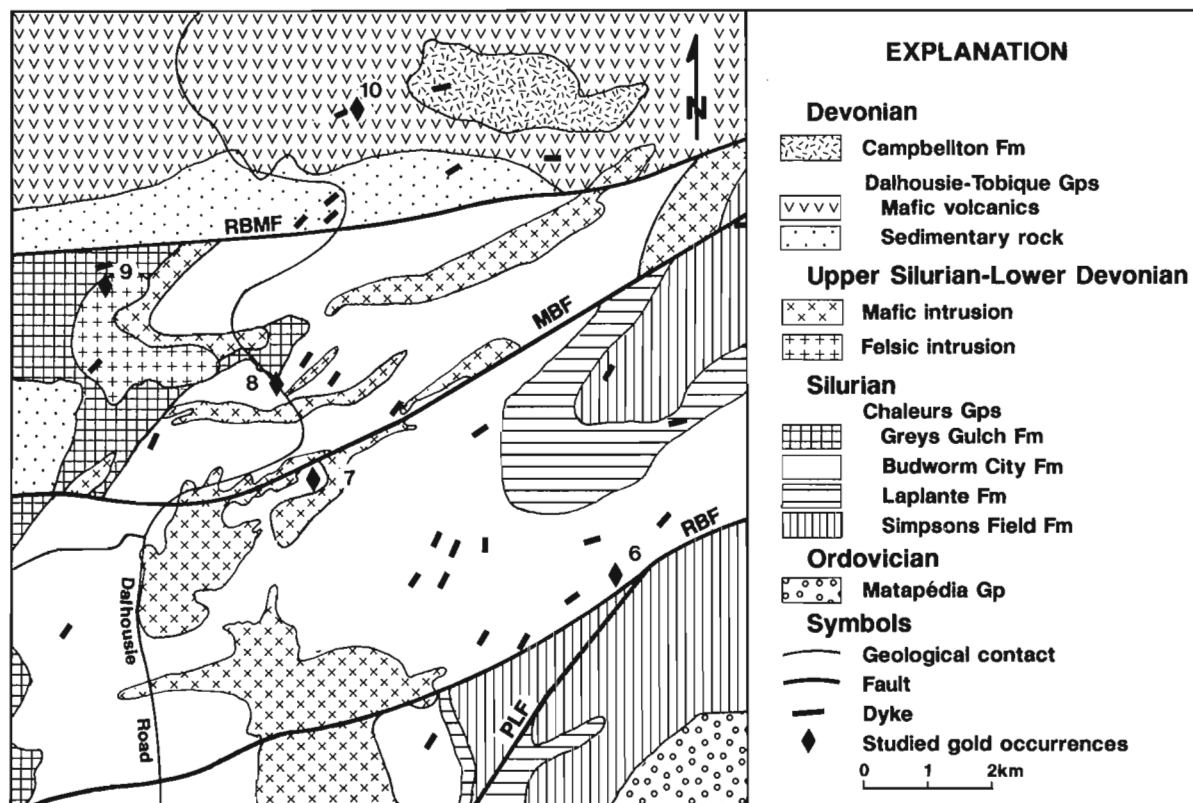


Figure 3. Geological map of gold showings associated with the Rocky Brook-Millstream fault in the Upsalquitch Forks area. See Figure 1B for location and identification of numbered showings. PLF: Portage Lake fault, RBF: Ramsay Brook fault, MBF: McCormack Brook fault, RBMF: Rocky Brook-Millstream fault.

Table 1. Principal lithological and structural characteristics of studied gold occurrences

Occurrences	Host rocks			Age			Structural control	Grades g/t, (references)
	Maf.	Fel.	Sed.	Ord.	Sil.	Dev.		
1- Elmtree	x			?			Dextral brittle-ductile faults; extensional and sheared veins.	4.5 Au, 350 000 t (Dubé, 1990)
2- Stephens Brook			x		x		N-S trending, shear-related sulphides-rich veins (1m-wide).	9.3 Au, 1.2 m (Burton, 1985)
3- Lavigne Brook			x		x		Stockwork and disseminated sulphides related to WNW-trending dextral shear.	1.7 Au & 161 Ag, 3.1 m (Ninacs, 1971)
4- Rocky Brook			x	x			WSW trending dextral shear; sulphides in stringer with quartz.	1.5 Au & 12.2 Ag, 3 m (Davies et al., 1969)
5- Bradley Brook			x		x		NW-trending extensional sulphides-quartz veins.	27.7 Au & 630.5 Ag, Grab (Pearson, 1976)
6- Simpson's Field	x				x		Disseminated sulphides and stockwork along dextral faults; argillic alter.	8.0 Au, 1 m (Fitzpatrick, 1986a)
7- McCormack Brook	x				x		Sheared and extensional veins related to folding and faulting.	1.4 Au, 1.34 m (Fitzpatrick, 1986b)
8- Dalhousie Road	x				x		Sheared and extensional veins related to dextral fault.	1.6 Au, 0.14 m
9- Mulligan Gulch		x			x		Sheared and extensional veins; argillic alteration.	1.7 Au, grab (Pronk & Burton, 1988)
10- Upsalquitch Forks	x					x	Sheared and extensional veins.	10.4 Au, grab (Pronk & Burton, 1988)



The Elmtree deposit is the most significant gold occurrence of northern New Brunswick, estimated reserve reaching 350 000 tonnes and grading up to 4.46 Au g/t (Dubé, 1990). The deposit is hosted by a differentiated gabbroic body (Paktunc and Ketchum, 1989; Tremblay et al., in press) intruding black slates and phyllites of the Elmtree Group. The Elmtree gabbro was interpreted to be deformed by a synthetic splay of the Elmtree fault (Tremblay and Dubé, 1991). Gold is found in the anorthositic part of the intrusion (Paktunc and Ketchum, 1989; Tremblay and Dubé, 1991). It is associated with quartz-carbonate alteration related to brittle-ductile shear zones. Best gold values were found within sulphide-rich, altered shear zones (McCutcheon et al., 1988). The most common sulphide minerals in the hosting gabbro are arsenopyrite and pyrite (up to 35%). Pyrrhotite was found in association with chalcopyrite, sphalerite, and minor stannite. Watson (1988) also described stibnite, jamesonite, boulangerite, and cassiterite. Native gold is present in association with arsenopyrite, less commonly with pyrrhotite (Harris, 1986).

The Stephen's Brook and Bradley Brook showings (Fig. 2) are arsenopyrite-rich gold occurrences (see Table 2). At Stephen's Brook, the mineralization is related to sinistral brittle shear zones underlined by massive to semi massive, arsenopyrite-pyrite-rich shear veins (Fig. 4A). At Bradley Brook showing, gold mineralization occurs in extensional veins consisting of arsenopyrite and galena (Fig. 4B). In both showings, other associated sulphide minerals are sphalerite and chalcopyrite, with minor amounts of pyrrhotite, stannite, and cubanite. In hosting sedimentary rocks, disseminated sulphide minerals consist of pyrrhotite, arsenopyrite, pyrite, and chalcopyrite, with traces of stannite, marcasite, and hematite.

The Lavigne Brook showing is located close to the southeastern border of the Nicholas-Denys granitic intrusion (Fig. 2). The mineralization is found within shear veins associated with dextral brittle faults, and consists of chalcopyrite, pyrite-marcasite, pyrrhotite, arsenopyrite, and

minor sphalerite, covellite, and hematite. Adjacent sedimentary rocks contain diopside and idocrase porphyroblasts, which is consistent with skarn-type gold mineralization (Einaudi et al., 1981).

The Rocky Brook deposit (Fig. 2) consists of massive sulphides hosted by the Tetagouche Group (Philpott, 1987). It is made up of discontinuous lenses of massive to semi massive, sulphides-rich quartz veins associated with brittle-ductile shear zones. Gossan-like alteration, and stringers and veinlets of quartz and sulphides are also found. The ore mineralogy consists of sphalerite, pyrite-marcasite, pyrrhotite, arsenopyrite, and galena. Minor occurrences of chalcopyrite, stannite, and freibergite were observed.

### Upsalquitch Forks area

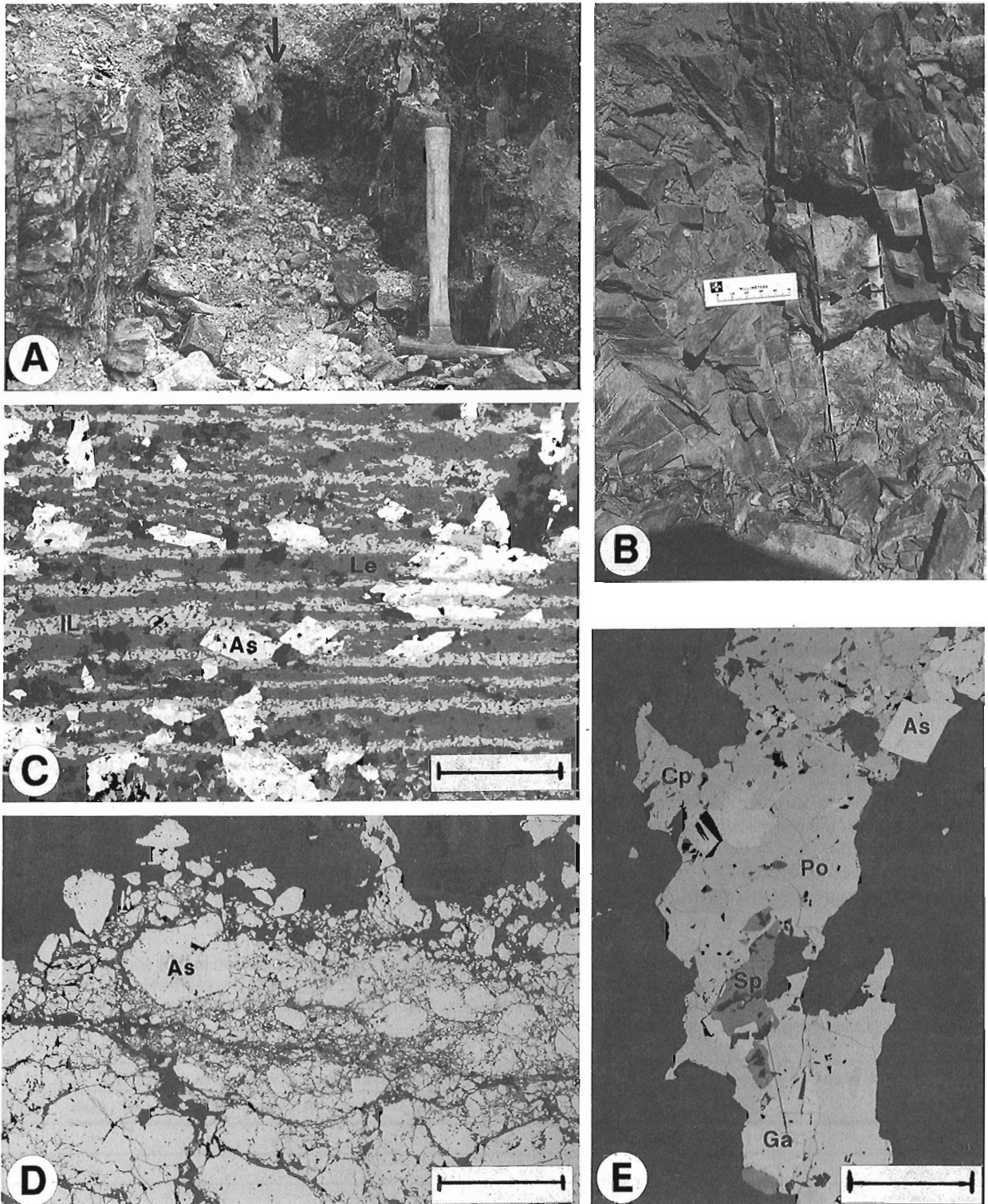
Seven gold showings are known in the Upsalquitch Forks area (Walker and McCutcheon, 1991), most of these being hosted by or closely associated with mafic and felsic intrusions (Fig. 1, 3). In this area, the Rocky Brook-Millstream fault trends almost easterly, and is associated with northeast-trending secondary faults along which most of the above-mentioned gold occurrences are found (Fig. 3). The lithological and structural characteristics of these occurrences were described in detail by Faure et al. (1992).

The Simpson's Field prospect (Fig. 3) is located along the Ramsay Brook fault (RBF). The mineralization (essentially pyrite-rich; see Table 2) is associated with a gabbroic sill-like intrusion crosscutting the Upper Silurian Budworm City Formation (see Fig. 3). The dominant structural feature is a flexural slip fold that was attributed to dextral shearing associated to the Ramsay Brook fault, and to the formation of quartz-sulphide stockworks and extensional veins.

The Dalhousie Road showing (Fig. 3) was the first gold occurrence found in the Upsalquitch area (Ruitenberg et al., 1990). It consists of quartz-ankerite-sericite veins with pyrite

**Table 2.** Ore mineralogy and relative abundances of metallic and alteration minerals observed in thin sections in the studied gold occurrences. S/G: sulphide/gangue ratio, Au: native gold, As: arsenopyrite, Py: pyrite, Po: pyrrhotite, Sp: sphalerite, Cp: chalcopyrite, Cb: cubanite, Ga: galena, St: stannite, Tt: tetrahedrite, Ms: marcasite, Cv: covellite, Cc: chalcocite, Bo: bornite, Hem: hematite, Goe: goethite, Ilm: ilmenite.

Occurrences	Num. of samples	S/G (%)	Modal proportion of observed metallic minerals in thin section (%)																	
			Au	As	Py	Po	Sp	Cp	Cb	Ga	St	Tt	Ms	Cv	Cc	Bo	Hem	Goe	Ilm	
1- Elmtree	7	2-25	tr	33	34	20	7	<1	tr				tr	tr			3		2	
2- Stephens Br.	9	5-10		63	22	7	3	4	tr	tr			<1	<1			tr	<1		
3- Lavigne Br.	4	10-50		4	8	6	tr	71					9	tr			2			
4- Bradley Br.	4	50-90		75	<1	2	3	20					tr	<1			tr			
5- Rocky Br.	5	50-80		14	17	16	37	<1		9			<1	tr	6		tr	<1		
6- Simpsons Field	5	2-10	tr	2	95												2	<1	<1	
7- McCormack Br.	6	5-15	tr	40	55		tr	2					tr					3	tr	
8- Dalhousie Road	4	3-5			60													23		17
9- Mulligan Gulch	2	5-20		tr	99															
10- Upsalquitch Forks	6	2			70	tr		17		10			tr				tr	3		



**Figure 4.** **A)** North-trending, arsenopyrite-rich shear vein (black arrow) at the Stephen's Brook gold showing. Hammer for scale. **B)** Arsenopyrite-rich extensional vein (dashed lines) of the Bradley Brook gold showing. Black arrows point toward the centre of the vein. Scale bar is 5 cm. **C)** Photomicrographic view of arsenopyrite (As) overgrowths within exsolution lamellae of ilmenite (IL; pale lamellae) and leucoxene (Le; dark lamellae). Elmtree gold deposit. **D)** Photomicrograph of the cataclastic texture characterizing arsenopyrite-rich veins of the Stephen's Brook showing. **E)** Photomicrograph of the polymetallic assemblage of the Rocky Brook showing. As: arsenopyrite, Ga: galena, Sp: sphalerite, Cp: chalcopyrite, Po: pyrrhotite. Photomicrographs are shown in reflected light. Scale bars are 0.2 mm.

and minor arsenopyrite found within a 25 m wide mafic intrusion. Anastomosing brittle faults were found in both the intrusive and hosting sedimentary rocks (Faure et al., 1992).

The Upsalquitch Forks showing (Fig. 3) is the only gold occurrence found in the volcanic rocks of the Dalhousie Group (Pronk and Burton, 1988), to the north of the Rocky Brook-Millstream fault. It occurs within an altered dioritic body that is in faulted contact with hosting volcanic rocks. The mineralization forms a stockwork of quartz-calcite veins with abundant pyrite, chalcopyrite, galena, and minor sphalerite, pyrrhotite, chalcocite, and stannite. Gold appears to be concentrated along brittle-ductile shear zones within, and along the boundaries of the intrusion (Hoy, 1987).

The McCormack Brook prospect (Fig. 3) is located along the McCormack Brook Fault (MBF), a east-northeast-trending splay of the Rocky Brook-Millstream fault (Fig. 2). Host rocks are small gabbroic bodies intruded in rocks of the Budworm City Formation. The local structure is characterized by isoclinal folds and anastomosing brittle-ductile shear zones (Faure et al., 1992). Gold mineralization occurs mostly in quartz-carbonate shear veins and associated stockworks, and in adjacent alteration zones. Sulphide minerals include arsenopyrite, pyrite with minor amounts of chalcopyrite, tetrahedrite, and native gold.

The Mulligan Gulch gold showing (Fig. 3) is hosted in a felsic intrusion. It is located approximately 500 m south of the Rocky Brook-Millstream fault. The host rock is a porphyritic monzonite (Murphy, 1989) that intrudes the Late Silurian Grey Gulch Formation. Mineralized quartz veins contain iron-carbonates and pyrite, and minor amounts of arsenopyrite, sphalerite, galena, and chalcopyrite (Fitzpatrick, 1986b). Alteration is characterized by the presence of sericite and/or epidote, and a widespread zone of silicification.

## **ORE MICROSCOPY**

The principal microscopic characteristics of ore minerals are described below. The sulphide/gangue ratio and the relative modal abundance of various sulphides for each studied occurrences are listed in Table 2.

In gabbroic rocks, ilmenite was observed in the Elmtree deposit, the Simpson's Field and the Dalhousie Road showings. It is characterized by a trelliswork texture. As shown in the Elmtree deposit, ilmenite commonly preserves exsolution lamellae within primary titanomagnetite that was totally replaced by leucoxene and anatase (Fig. 4C). Arsenopyrite is the dominant sulphide mineral in vein-type showings spatially related to the Rocky Brook-Millstream fault in the Bathurst area. It occurs as euhedral crystals, usually enclosing, or at the edge of, subhedral to anhedral pyrite. In mafic intrusive rocks, arsenopyrite is frequently disseminated along weakness planes, or closely associated to ilmenite (Fig. 4C). In extensional veins (i.e., Bradley Brook), arsenopyrite was found as free grains between coarse grained quartz, carbonates, sericite, or chlorite. In shear veins (i.e., Stephen's Brook), it shows well-developed cataclastic

textures (Fig. 4D) that are characterized by a progressive decrease of grain size with increasing shear. Native gold was found in the Elmtree deposit (Harris, 1986), the Simpson's Field (Clemson, 1986; Stirling, 1987), and the McCormack Brook showings (this study). Gold is associated with sulphides in altered intrusive rocks, near the contact with hosting sedimentary rocks. Gold is found in four textural sites: (1) infilling of voids in fractured sulphides (arsenopyrite, pyrite); (2) at arsenopyrite grains margins; (3) at grain boundaries between pyrrhotite crystals, and (4) as free grains in coarse grained, equigranular quartz.

Pyrite is abundant in the Elmtree deposit, and the Stephen's Brook and Rocky Brook showings. It is the main sulphide of gold showings of the Upsalquitch Forks area. Pyrite appears to be more common in altered sedimentary and intrusive rocks than in gold-bearing veins. Pyrite grains found in gabbros and sedimentary rocks are mostly euhedral to subhedral and locally show framboidal overgrowths. In extensional veins, pyrite forms both homogenous and zoned crystals, whereas in shear veins, it is characterized by cataclastic textures. Xenomorphic grains of pyrrhotite were mainly observed at the Elmtree deposit and at the Rocky Brook showing (Fig. 4E). They are mostly concentrated along weakness planes and frequently show porphyroblastic textures. Coarse grains of pyrrhotite frequently enclose pyrite and arsenopyrite crystals. Chalcopyrite, sphalerite, and galena are late sulphide phases after arsenopyrite, pyrite, and pyrrhotite. Chalcopyrite is abundant (up to 70%) in the Lavigne Brook showing, and sphalerite is dominant (37%) in the Rocky Brook showing. In extensional veins, these sulphides were found as enclosing pyrite and pyrrhotite grains, or within fractured arsenopyrite crystals. In shear veins, plastic deformation and recrystallization textures have commonly destroyed any primary textural relationships.

Cubanite was locally found as irregular lamellae within chalcopyrite. Stannite is present within arsenopyrite, sphalerite, or pyrite. Tetrahedrite was observed at the Rocky Brook and McCormack showings, in association with chalcopyrite and arsenopyrite. Hematite, chalcocite, and covellite were found as supergene alteration minerals on most of the studied showings and deposits.

## **CLASSIFICATION**

Based on ore mineralogy, relationships with host rocks, structural controls, and the proximity to ultramafic rocks and plutons, we distinguish two main types of gold occurrences in northern New Brunswick: (1) precious and base metal veins, and (2) gold-only veins.

### ***Precious and base metal veins***

Precious and base metal veins are found mainly in the Bathurst area. They are characterized by a significant gold/silver content, and by the relative abundance of sulphides. The ore mineralogy consists mainly of arsenopyrite and pyrite with lesser amounts of pyrrhotite, sphalerite, chalcopyrite, and galena. Gold is found within or closely

related to arsenopyrite. Silver values vary from 12 g/t (Rocky Brook; Davies et al., 1969) to 630 g/t (Bradley Brook; Pearson, 1976). Sulphides are found as semi massive to massive shear veins, in extensional quartz veins, or in altered wall rock close to brittle-ductile shear zones.

Shear veins are found in the Stephen's Brook and Rocky Brook showings. In the Upsalquitch Forks showing, gold-rich zones were found along quartz-calcite-pyrite shear veins. Silver-rich zones were also found in association with quartz-pyrite veins (Hoy, 1987), and gave significant values of lead, mercury, bismuth, and arsenic (Pronk and Burton, 1988). Extensional veins, consisting of arsenopyrite, galena, and quartz, are characteristic of the Bradley Brook showing. In the Elmtree deposit, gold-bearing sulphides are disseminated in altered wall rocks along brittle-ductile shear zones hosting barren stockwork of quartz veinlets.

### **Gold-only veins**

Gold-only veins characterize the Upsalquitch Forks area. They are associated with mafic to felsic intrusions, close to the faulted contacts with surrounding rocks. We have distinguished two mineral associations: (1) auriferous quartz-pyrite veins (Simpson's Field, Dalhousie Road, and Mulligan Gulch), and (2) auriferous quartz-arsenopyrite veins (McCormack Brook).

In the former, gold is found within quartz-carbonates veins and in altered stockwork (Stirling, 1987). It occurs mostly as micrometre-wide inclusions within pyrite grains or along grain boundaries (Clemson, 1986).

Quartz-arsenopyrite veins are the most interesting gold showings of the Upsalquitch Forks area. At McCormack Brook, gold is associated with disseminated sulphides and quartz-carbonate shear veins and stockworks. Gold formed small inclusions hosted by arsenopyrite crystals.

## **DISCUSSION AND CONCLUSION**

Gold deposits and showings of northern New Brunswick were classified as stratiform and epigenetic occurrences (Ruitenberget al., 1990). Stratiform gold deposits are associated to volcanogenic sulphide deposits in pre-Silurian volcano-sedimentary sequences of the Miramichi and Avalon terranes (Davies et al., 1985, Ruitenberget al., 1979). Ruitenberget al. (1990) subdivided the epigenetic gold mineralizations as (1) quartz-carbonate veins and stockworks, (2) polymetallic veins, (3) contact metasomatic porphyry-copper, and (4) volcanic breccias. They also emphasized their genetic relationship with faulting although McCutcheon and Bevier (1990) stressed that plutonism was the main control for gold occurrences of the Upsalquitch Forks area.

All studied occurrences are enclosed in competent rocks such as intrusive rocks and silicified sedimentary rocks, and are in close association to the Rocky Brook-Millstream and associated faults. Precious and base metal veins occur mainly in the Bathurst area within sedimentary Silurian rocks, close to serpentinite fault slivers and granitic plutons. They are

characterized by Au-As-Cu-Zn-Pb minerals and a quartz-carbonate alteration. In the Upsalquitch Forks area, gold is found in close association with mafic to felsic intrusions hosted by Silurian and Devonian sedimentary rocks. They consist of gold-only veins with minor Cp-Zn-Pb minerals and a quartz-carbonate alteration.

Several factors may explain the variation of the ore mineralogy of gold occurrences of the Bathurst and Upsalquitch Forks areas: (1) the nature of hosting rocks, which controlled most of the hydrothermal alteration products, (2) the influence of the spatially-related plutonism, and (3) the crustal level of fluid circulation.

In northern New Brunswick, the plutonism probably acted as a thermal source, heating surrounding sedimentary rocks and creating sufficient fracturation and secondary permeability for enhancing fluid circulation. Syn- to post plutonic shearing in localized fault zones then concentrated the fluids and served as a plumbing system. The structural analysis of most gold occurrences reveals that ore fluids were trapped in various settings related to second order splays and structures of the Rocky Brook-Millstream fault. Ore-bearing structures consist mainly of sub vertical, extensional, and shear fractures lying at high- or low-angle to main faults (e.g., Tremblay and Dubé, 1991). Hosting structures are compatible with a dextral strike-slip motion along the Rocky Brook-Millstream fault and associated splays. Therefore, any gold exploration program in northern New Brunswick must account for this type of geometry. However, because of the relationship between pluton-hosted gold occurrences and major fault zones of the Upsalquitch Forks area (e.g., faults locally postdating the mineralization, gold showings away from faults), McCutcheon and Bevier (1990) argued that the importance of faulting in controlling the distribution of gold occurrences has been over-emphasized. Age constraints indicate that the Rocky Brook-Millstream fault and associated transpressive deformation were mostly active in Early Devonian times but faulting continued in Middle Devonian, and probably post-Middle Devonian times (see van Staal and Fyffe, 1991). This implies that faulting was coeval and postdated plutonic events recorded in the Upsalquitch Forks area (Late Silurian to Early Devonian; McCutcheon and Bevier, 1990). Therefore, it is not surprising to find mineralized structures and plutons crosscut by sterile fault fabrics as described by McCutcheon and Bevier (1990). Therefore, in our opinion, it does not exclude any genetic relationships between faulting and gold mineralization.

In northern New Brunswick, the low grade of the regional metamorphism, the ore-related alteration assemblages and brittle-ductile structures are consistent with an overall mesothermal type of mineralization. However, it is probable that the crustal level of mineralization was slightly different between the Bathurst and Upsalquitch Forks areas. In the former, gold is mainly found at, or near the contact between Ordovician and Silurian rocks whereas in the latter, it occurs in Upper Silurian to Lower Devonian rocks.

The highest potential for economic gold mineralization appears to be related to mafic intrusions (i.e. Elmtree deposit and most gold showings from the Upsalquitch Forks area) due

to their favourably rheological and chemical properties. Competency contrast between the mafic intrusives and the surrounding rocks causes a more brittle response in the former, allowing the development of brittle-ductile shear zones. In addition, the iron-rich composition favoured precipitation of gold (Dubé et al., 1987). This is clearly indicated by the relationship between altered titanomagnetite and arsenopyrite/pyrite in the Elmtree deposit (Fig. 4C) that suggests that the iron content of the gabbro allowed the formation of sulphides and consequently the precipitation of gold. In such a setting, the ore geometry is controlled not only by the hosting structures but also by the distribution and the nature of the mafic intrusions. These mineralizations are similar to many Archean gold deposits (Poulsen et al., 1986; Dubé et al., 1989) and were also found elsewhere in the Maritimes Appalachians of Newfoundland (Dubé, 1990) and Quebec (Malo et al., in press).

The overall relationship between tectonism and plutonism suggests the synchronism of deformation and mineralization. As proposed by Ruitenberg et al. (1990) and McCutcheon and Bevier (1990), we believe that orogenically-driven (Acadian), crustal thickening generated a large volume of mafic to felsic magma. It provided sulphide- and gold-rich fluids derived from the lower crust (Cameron 1988), which were drained by fault-related structures. Carbon dioxide-rich fluids bleached the upper crust and precipitated ore minerals in favourably sites such as fractures related to both major (Rocky Brook-Millstream) fault system, and rheologically-induced faults between intrusives rocks and enclosing rocks.

## ACKNOWLEDGMENTS

Field trips and discussions with S. McCutcheon and J. Walker were helpful. Critical review by Katleen Lauzière was useful and improved the manuscript. Thanks are due to Luce Dubé for drafting the figures.

## REFERENCES

- Burton, D.M.**  
1985: Geology, geochemistry and geophysics of the Stephens Brook claim group, Brunswick Mining and Smelting Corp. Ltd.; New Brunswick Department of Natural Resources and Energy, Minerals and Energy Division, Assessment Report 473204.
- Cameron, E.M.**  
1988: Archean gold: relation to granulite formation and redox zoning in the crust; *Geology*, v. 16, p. 109-112.
- Clemson, J.E.**  
1986: Investigation of gold mineralization in five samples from the Smith Showing, Simpsons Field Property, New Brunswick, Noranda Exploration Company; New Brunswick Department of Natural Resources, Minerals and Energy Division, Annex on Assessment Report #473302, 18 p.
- Davies, J.L.**  
1979: Geological map of northern New Brunswick; New Brunswick Department of Natural Resources and Energy, Mineral and Energy Division, Map NR-3.
- Davies, J.L., Tupper, W.M., Bachinski, D., Boyle, R.W., and Martin, R.**  
1969: Geology and mineral deposits of the Nigadoo River-Millstream River area, Gloucester County, New Brunswick; Geological Survey of Canada, Paper 67-49, 70 p.
- Davies, J.L., van Stall, C.R., Luff, W.M., Archibald, D.E., and Fyffe, L.R.**  
1985: Massive sulphide deposits to the Bathurst-Newcastle area, New Brunswick, Canada; Geological Association of Canada-Mineralogical Association of Canada, Fredericton, New Brunswick, Field guide to Excursion 2, 73 p.
- Dostal, J., Wilson, R.A., and Keppie, J.D.**  
1989: Geochemistry of Siluro-Devonian volcanic rocks in northern and central New Brunswick (Canada): tectonic implications; *Canadian Journal of Earth Sciences*, v. 26, p. 1282-1296.
- Dubé, B.**  
1990: A preliminary report on contrasting structural styles of gold-only deposits in western Newfoundland; in *Current Research, Part B*; Geological Survey of Canada, Paper 90-1B, p. 77-90.
- Dubé, B., Guha, J., and Rocheleau, M.**  
1987: Alteration patterns related to gold mineralization and their relation to CO<sub>2</sub>/H<sub>2</sub>O ratios; *Mineralogy and Petrology*, v. 37, p. 267-291.
- Dubé, B., Poulsen, H., and Guha, J.**  
1989: The effects of layer anisotropy on auriferous shear zones: the Norbeau mine, Quebec; *Economic Geology*, v. 84, p. 871-878.
- Einaudi, M.T., Meinert, L.D., and Newberry, R.J.**  
1981: Skarn deposits; *Economic Geology*, v. 75, p. 317-391.
- Faure, S., Tremblay, A., and Dubé, B.**  
1992: Structural study of relationship between gold occurrences and the Rocky Brook-Millstream fault zone in the Upsalquitch Forks area, northern New Brunswick; in *Current Research, Part D*; Geological Survey of Canada, Paper 92-1D, p. 101-109.
- Fitzpatrick, D.**  
1986a: Report of work on Simpsons Field property (Smith Option), Restigouche county, New Brunswick, Noranda Exploration Company; New Brunswick Department of Natural Resources, Mineral and Energy Division, Assessment Report 473302, 19 p.  
1986b: Report of work on McCormack/Ramsay Property, Restigouche county, New Brunswick, Noranda Exploration Company; New Brunswick Department of Natural Resources, Mineral and Energy Division, Assessment Report 473301, 19 p.
- Fyffe, L.R. and Fricker, A.**  
1987: Tectonostratigraphic terrane analysis of New Brunswick; *Maritime Sediments and Atlantic Geology*, v. 23, p. 113-122.
- Greiner, H.R.**  
1967: Silurian-Devonian relationships of the Charlo map-area, New Brunswick; in *International Symposium of the Devonian*, (ed.) D.H. Oswald; Alberta Society of Petroleum Geologists, v. 2, p. 973-979.
- Harris, D.C.**  
1986: Mineralogic report on samples from the Elmtree deposits; Energy, Mines and Resources Canada, Lacana Mining Corporation, unpublished report.
- Hoy, D.**  
1987: Report on 1986 exploration for the Upsalquitch River Group, Restigouche County, New Brunswick, Lacana Mining Corporation; New Brunswick Department of Natural Resources, Minerals and Energy Division, Assessment Report 473371, 18 p.
- Malo, M. and Béland, J.**  
1989: Acadian strike-slip tectonics in the Gaspé region, Québec Appalachians; *Canadian Journal of Earth Sciences*, v. 26, p. 1764-1777.
- Malo, M., Moritz, R., Chagnon, A., and Roy, F.**  
in press: Géologie et métallogénie du segment est de la faille du Grand Pabos, Gaspésie; Ministère de l'Énergie et des Ressources, Québec.
- McCutcheon, S.R. and Bevier, M.L.**  
1990: Implications of field relations and U-Pb geochronology for the age of gold mineralization and timing of Acadian deformation in northern New Brunswick; *Atlantic Geology*, v. 26, p. 237-246.
- McCutcheon, S.R., Burton, D.M., and Hoy, D.**  
1988: The geologic setting of gold occurrences in northern New Brunswick; Field guide to northern New Brunswick, Gold Symposium 1988, Saint John, New Brunswick, 41 p.
- Murphy, R.B.**  
1989: Geochemistry of Siluro-Devonian mafic volcanic rocks and associated gabbroic intrusions, Upsalquitch Forks area, New Brunswick; M.Sc. thesis, Acadia University, Wolfville, Nova Scotia, 274 p.

- Ninacs, G.**  
1971: Geology, geochemistry, geophysics and diamond drilling of the Mija Mines option, Beresford Mines Ltd.; New Brunswick Department of Natural Resources and Energy, Minerals and Energy Division, Assessment Report 472342.
- Paktunc, A.D. and Ketchum, J.W.F.**  
1989: Petrology, structural geology, and gold mineralization of the Elmtree mafic body, northern New Brunswick in Current Research, Part B; Geological Survey of Canada, Paper 89-1B, p. 75-82.
- Pearson, H.A.**  
1976: Geology, geophysics, geochemistry and diamond drilling of the Nicholas Denys area, Zarina Exploration Ltd.; New Brunswick Department of Natural Resources and Energy, Minerals and Energy Division, Assessment Report 470426.
- Philpott, G.**  
1987: Preliminary map. Bedrock geological compilation of parts of the Bathurst (21P/12) map area; New Brunswick Department of Natural Resources and Energy, Minerals and Energy Division, MP 87-51B.
- Poulsen, H., Ames, D.E., Lau, S., and Brisbin, W.C.**  
1986: Preliminary report on the structural setting of gold in the Rice Lake area, Uchi Subprovince, southeastern Manitoba; in Current Research, Part B; Geological Survey of Canada, Paper 86-1B, p. 213-221.
- Pronk, A.G. and Burton, D.M.**  
1988: Till geochemistry as a technique for gold exploration in northern New Brunswick; CIM Bulletin, v. 81, p. 90-98.
- Ruitenberg, A.A., Fyffe, L.R., McCutcheon, S.R., St. Peter, C.J., Irrinki, R.R., and Venugopal, D.V.**  
1977a: Evolution of pre-Carboniferous tectonostratigraphic zones in the New Brunswick Appalachians; Geoscience Canada, v. 4, p. 171-181.
- Ruitenberg, A.A., Giles, P.S., Venugopal, D.V., Buttimer, S.M., McCutcheon, S.R., and Chandra, J.**  
1979: Geology and mineral deposits, Caledonia area; New Brunswick Department of Natural Resources, Mineral Resources Branch, Memoir 1, 213 p.
- Ruitenberg, A.A., Johnson, C.J., and Fyffe, L.R.**  
1990: Epigenetic gold deposits and their tectonic setting in the New Brunswick Appalachians; CIM Bulletin, v. 83, p. 43-55.
- Stirling, J.A.R.**  
1987: Mineralogy of selected gold deposits in New Brunswick; New Brunswick Department of Natural Resources and Energy, Minerals and Energy Division, Assessment Report 472550.
- Tremblay, A. and Dubé, B.**  
1991: Structural relationships between some gold occurrences and fault zones in the Bathurst area, northern New Brunswick; in Current Research, Part D; Geological Survey of Canada, Paper 91-1D, p. 89-100.
- Tremblay, A., Dubé, B., and Faure, S.**  
in press: Geochemical evidence for flow differentiation of the Elmtree mafic body, northern New Brunswick; in Current Research, New Brunswick Department of Natural Resources and Energy, Mineral Resources, Information Circular 93-1.
- van Staal, C.R.**  
1987: Tectonic setting of the Tetagouche Group in northern New Brunswick: implications for plate tectonic models of the northern Appalachians; Canadian Journal of Earth Sciences, v. 24, p. 1329-1351.
- van Staal, C.R. and Fyffe, L.R.**  
1991: Dunnage and Gander zones, New Brunswick: Canadian Appalachian region; New Brunswick Natural Resources and Energy, Mineral Resources Division, Geoscience Report 91-2, 39 p.
- Walker, J.A. and McCutcheon, S.R.**  
1991: Geology and litho-geochemistry of Upsalquitch Forks, north-central New Brunswick; New Brunswick Department of Natural Resources, Minerals and Energy Division, Open File Report 91-3, 130 p.
- Watson, G.P.**  
1988: Geologic setting, mineralogy and alteration studies, Elmtree Au deposit, northeastern New Brunswick; in Program with Abstracts, v. 13, Geological Association of Canada-Mineralogical Association of Canada Annual Meeting, St. John's, Newfoundland, p. A132.

# Eastern Canadian earthquakes 1992

R.J. Wetmiller and J.A. Drysdale  
Geophysics Division

*Wetmiller, R.J. and Drysdale, J.A., 1993: Eastern Canadian earthquakes 1992; in Current Research, Part E; Geological Survey of Canada, Paper 93-1E, p. 347-350.*

---

**Abstract:** For the 1992 calendar year, 317 earthquakes occurred in or near southeastern Canada. The largest earthquake in this period was a magnitude 4.4 (on the Richter scale) earthquake which occurred in western Quebec north of Buckingham, between Ottawa and Montreal, on the evening of November 17. The tremor was felt from Montreal to Pembroke, and in northern New York State, but caused no damage. In all, 37 earthquakes had magnitude 3.0 or greater and three had magnitude 4.0 or greater. Twenty-nine of the earthquakes in eastern Canada were reported felt by Canadians. In addition to natural seismic activity, the seismograph networks supplied information on 306 rockbursts (mining-induced seismic events) or possible rockbursts in mines in eastern Canada and 378 large blasts or suspected blasts.

**Resume :** Du 1<sup>er</sup> janvier au 31<sup>me</sup> décembre 1992 on a localisé dans le sud-est du Canada 317 tremblements de terre. Le plus fort séisme a été un tremblement de terre de magnitude 4.4 (sur l'échelle Richter) qui s'est produit dans l'ouest du Québec au nord de Buckingham, et entre Montréal et Ottawa, pendant le soir du 17<sup>me</sup> novembre. Ce séisme a été ressenti de Montréal à Pembroke, et dans le nord de l'état du New York, mais n'a causé aucun dégâts matériels. Trent-sept tremblements de terre avaient une magnitude d'au moins 3, et trois avaient une magnitude d'au moins 4. Vingt-neuf séismes ont été ressentis. Parmi les données recueillies par les réseaux sismographiques étaient aussi 306 coups de toit (événements liés à l'activité minière) ou coups de toit possibles et 378 explosions.

## INTRODUCTION

Seismologists at the Geological Survey of Canada record and study the earthquakes that occur in or near Canada every day. Data from more than 100 seismograph stations, operated in all parts of the country, are used to analyze more than 1500 events every year. The information collected is documented for scientific and engineering studies which lead eventually to improvements in the seismic hazard provisions of the National Building Code of Canada (Basham et al., 1982, 1985; Heidebrecht et al., 1983). Strong earthquakes represent a significant, although infrequent, hazard in many parts of the country and adequate preparation through an effective building code is one of the best ways of lessening the impact of damaging earthquakes.

## SEISMOGRAPH NETWORKS

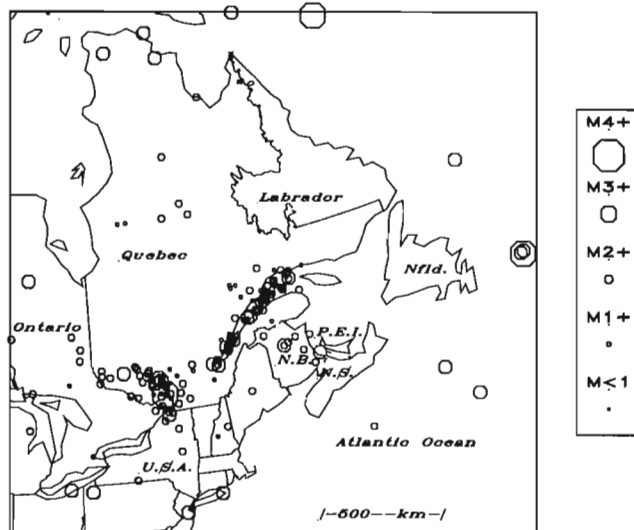
The Geological Survey of Canada operates two seismological research centres, one at the Pacific Geoscience Centre near Sidney, British Columbia, north of Victoria, and the other at the Geophysics Division on the Observatory Campus in Ottawa. Each centre operates a local telemetered seismograph network or networks monitoring the seismic activity in its region and, in addition, the two centres collaborate on the monitoring of earthquakes throughout the rest of the country. The data collected by the telemetered networks are sent via telephone, radio, or satellite links directly to the responsible centre for analysis; in this manner the Geological Survey of Canada can react immediately to strong seismic events. In other areas of the country, seismograph data are recorded on paper records which must be mailed to the responsible centre for analysis (see Munro et al. (1988) for a description of the many seismograph stations being operated by the Geological Survey throughout Canada). Once the paper records have been received and read, and additional data for Canadian earthquakes have been obtained from seismograph networks in neighbouring countries, all the earthquake information is compiled into a national database documenting the seismic activity for all regions of the country (see Wetmiller et al. (1991) for descriptions of the current procedures for collecting, and Wetmiller et al. (1984b) and Drysdale et al. (1985) for the current procedures for analyzing earthquake data from the seismograph networks in eastern Canada). The Geological Survey of Canada is now in the process of modernizing its seismograph network using satellite technology and will soon be able to monitor earthquake activity throughout the whole country in real time with much increased efficiency (North and Anglin, 1993). At the present time, four seismograph stations in Canada's far north (Inuvik, Mould Bay, Resolute, and Iqaluit) have begun transmitting their data directly to Ottawa via satellite allowing, for the first time, same-day locations of earthquakes in northern Canada.

## HIGHLIGHTS FOR EASTERN CANADA

This report presents a summary of the earthquake activity that occurred in eastern Canada for the 1992 calendar year. It is relatively complete for the populated area of southeastern Canada covered by the telemetered seismograph networks operated by the Geophysics Division but is less complete for the northern regions of eastern Canada, although most of the larger events in the remote areas will have been noted here.

In this year, 317 earthquakes were documented in eastern Canada and adjacent areas. Their distribution, shown in Figure 1, is similar to that observed in previous years. Most of the earthquake activity took place in the Province of Quebec in two broad areas: one following the lower St. Lawrence Valley from Quebec City to Sept-Îles (184 events), and the other lying in southwestern Quebec, on the north side of the Ottawa Valley, from Montreal to Timiscaming (58 events). Elsewhere, isolated activity was detected in northern Quebec, Ontario, New Brunswick, and the Atlantic offshore. No earthquakes in Nova Scotia, Prince Edward Island, or Newfoundland and Labrador were large enough to be located by the seismograph network.

Many of the earthquakes occurred in zones that have been previously identified to be seismically active. The most active seismic zone in eastern Canada is the Charlevoix-Kamouraska zone (Anglin, 1984) of the St. Lawrence Valley, located about 100 km northeast of Quebec City, which had 115 earthquakes during 1992. Also active were the West



**Figure 1.** Distribution of earthquake activity in eastern Canada and adjacent areas in 1992.



Quebec seismic zone (Forsyth, 1981), noted above, which had 58 earthquakes and the Lower St. Lawrence seismic zone (Adams et al., 1989) which had 42 events during this period.

Seismic activity often continues to reoccur at the sites where strong earthquakes have taken place in the past. These events, called aftershocks, illustrate the long time period needed by the Earth's crust to reach a new state of equilibrium following a strong earthquake. In 1992 there were a number of examples of this phenomenon. Continuing activity was recorded from the Miramichi, New Brunswick aftershock zone, site of a magnitude 5.8 earthquake on January 9, 1982 (Wetmiller et al., 1984a), and the Mont-Laurier, Quebec aftershock zone, site of a magnitude 5.0 earthquake on October 19, 1990 (M. Lamontagne et al., in prep.). Seven events were located in the Miramichi zone and three in the Mont-Laurier zone in 1992. In contrast, no earthquake activity was detected in the Saguenay, Quebec (November 25, 1988, magnitude 6.5) aftershock zone during 1992 (North et al., 1989).

Earthquakes also can and do occur from time to time in areas outside the active seismic zones and away from the sites of recent strong earthquakes. In 1992 the Quebec City region experienced five minor tremors. The strongest was magnitude 3.6 on August 28.

In addition to the natural earthquake activity, the seismograph networks detected hundreds of other seismic events in 1992: 306 rockbursts or possible rockbursts were documented at Canadian mines (mostly in the Sudbury, Ontario region) and 378 blasts or suspected blasts were investigated. The largest rockburst noted in 1992 was a magnitude 3.1 event at the Creighton Mine in Sudbury on February 6. Blasts and rockbursts produce seismic signals very similar to earthquake activity, therefore the source of such events recorded on the seismograph networks must be confirmed in order that the rate of natural earthquake activity is not biased.

Thirty-seven of the earthquakes detected in 1992 had magnitude 3.0 or greater. The largest earthquakes were three events with magnitudes from 4.0 to 4.4; two of these were located in the Atlantic offshore region where they went unnoticed while the third and largest was located in western Quebec, between Montreal and Ottawa, where it was felt by many people on the evening of November 17.

In all during 1992, 29 earthquakes were reported felt, the largest being the magnitude 4.4 event in western Quebec noted above. Magnitude 5 on the Richter scale is generally considered to be the threshold for damage from earthquakes and none of the earthquakes in 1992 caused any damage. The last event to cause significant property damage in eastern Canada was the magnitude 6.5 Saguenay earthquake of November 25, 1988, centred near Chicoutimi, Quebec, which caused several million dollars worth of damage in the province (Mitchell et al., 1989). The following list gives details of the felt earthquakes and/or those with magnitude 4.0 or greater that occurred in this period.

*Magnitude 4.0 on 13/01/1992:*

Southern Grand Banks, offshore Newfoundland.

*Magnitude 3.3 on 10/03/1992:*

La Malbaie, Charlevoix, Quebec. Felt at Saint-Fidèle.

*Magnitude 1.9 on 11/03/1992:*

Baie-Saint-Paul, Charlevoix, Quebec. Felt at Saint-Joseph-de-la-Rive.

*Magnitude 2.8 on 31/03/1992:*

35 km south of Ottawa, Ontario. Reported felt in Kemptville, North Gower. Also slightly felt 8 km west of North Gower with a rumbling sound following.

*Magnitude 2.9 on 04/04/1992:*

La Malbaie, Charlevoix, Quebec. Felt at Île aux Coudres, Saint-Hilarion, Baie-St-Paul.

*Magnitude 2.5 on 18/04/1992:*

10 km south of Cornwall, Ontario. Felt widely in Cornwall, chiefly in the west end. First of two events within an hour.

*Magnitude 2.4 on 18/04/1992:*

10 km south of Cornwall, Ontario. Felt in Cornwall; Second of two events within an hour.

*Magnitude 3.2 on 01/05/1992:*

Baie-Saint-Paul, Charlevoix, Quebec. Felt strongest at Île aux Coudres. Felt at Saint-Hilarion, Baie-St-Paul, Les Éboulements, Saint-Urbain.

*Magnitude 3.0 on 19/05/1992:*

Western Quebec, 40 km east of Mont-Laurier. Felt at Nominigüe.

*Magnitude 2.9 on 30/05/1992:*

Western Quebec, 40 km east of Mont Laurier. Felt at Lac Nominigüe. Followed by Magnitude 1.6 Aftershock two minutes later.

*Magnitude 3.3 on 03/06/1992:*

Western Quebec, 50 km east of Mont-Laurier. Felt at Lac Nominigüe. People were awakened.

*Magnitude 3.4 on 04/06/1992:*

Lower St. Lawrence, Quebec. Weakly felt at Rimouski and Pointe-au-Pere.

*Magnitude 4.1 on 05/06/1992:*

Labrador Ridge, offshore.

*Magnitude 3.3 on 28/06/1992:*

20 km west of Quebec City. Felt at Valcartier, Stoneham, Val-Belair, Notre-Dame-des-Laurentides, Loretteville, Lac-Saint-Charles, Beauport, Saint-Émile, Sainte-Foy, Village-des-Hurons, Charlesbourg, and Neufchâtel.

*Magnitude 2.5 on 08/07/1992:*

Western Quebec, 30 km southeast of Maniwaki. Felt (heard) at Notre-Dame-du-Laus, Quebec.

*Magnitude 3.5 on 20/08/1992:*

Miramichi, New Brunswick. Felt in Bathurst (crystals rattled), Florenceville, Beechwood, and Centreville. First of three earthquakes.

*Magnitude 3.5 on 20/08/1992:*

Miramichi, New Brunswick. Felt in Bathurst (crystals rattled), Florenceville, Beechwood, and Centreville. Second of three earthquakes.

*Magnitude 2.9 on 20/08/1992:*

Miramichi, New Brunswick. Felt in Beechwood and Centreville. Third of three earthquakes.

*Magnitude 3.1 on 21/08/1992:*

Western Quebec, 25 km southeast of Mont-Laurier. Felt at Lac-des-Îles, Quebec.

*Magnitude 3.4 on 27/08/1992:*

Lower St. Lawrence, Quebec. Felt and heard in Pointe-au-Pere. People were awakened. Felt also in Rimouski, Mont-Joli, and Forestville.

*Magnitude 3.6 on 28/08/1992:*

15 km southeast of Quebec City. Felt in the Quebec City region, Neuville, Beauport, Ancienne-Lorette, Sainte-Foy, and Charlesbourg. Weakly felt at Lévis and Saint-Romuald.

*Magnitude 2.8 on 29/08/1992:*

5 km northeast of Pembroke, Ontario. Felt in the Pembroke Region.

*Magnitude 2.9 on 12/10/1992:*

Western Quebec. Felt (heard) locally at La Minerve.

*Magnitude 3.3 on 11/11/1992:*

Western Quebec, 25 km east of Mont Laurier. Felt at Lac-Saguay, Quebec.

*Magnitude 4.4 on 17/11/1992:*

Western Quebec, 50 km north of Buckingham. Widely felt in the Laurentians, Ottawa-Hull, north of Montréal, Pembroke, and in the U.S. In Vermont and New York State. Three small aftershocks of less than magnitude 2.5 Were recorded in the following 3 hours.

*Magnitude 3.3 on 18/11/1992:*

East of Moncton, New Brunswick near Cap-Péle. Felt by several people in the Moncton, and Cap-Péle, New Brunswick regions.

*Magnitude 2.4 on 23/11/1992:*

20 km north of Quebec City. Felt in the Quebec City region at Beauport and Charlesbourg.

*Magnitude 2.8 on 24/11/1992:*

10 km south of Quebec City. Felt in the Quebec City region at Beauport, Charlesbourg, Neufchâtel, and Portneuf.

*Magnitude 2.8 on 04/12/1992:*

Western Quebec, 80 km northwest of Maniwaki. Felt at Le Domaine.

*Magnitude 2.6 on 27/12/1992:*

5 km south of Moncton, New Brunswick. Felt mildly in Moncton area. Very small unlocated aftershock at 0949.

More information about these earthquakes or any other seismic activity in eastern Canada during 1992 is available on request from the Geophysics Division.

**REFERENCES**

**Adams, J., Sharp, J., and Connors, K.**  
1989: Revised epicentres for earthquakes in the lower St. Lawrence seismic zone: 1928-1968; Geological Survey of Canada, Open File 2072, 82 p.

**Anglin, F.M.**  
1984: Seismicity and faulting in the Charlevoix zone of the St. Lawrence Valley; Bulletin Seismological Society of America, v. 71, p. 595-603.

**Basham, P.W., Weichert, D.H., Anglin, F.M., and Berry, M.J.**  
1982: New probabilistic strong seismic ground motion maps of Canada: a compilation of earthquake source zones, methods and results; Geological Survey of Canada, Earth Physics Branch, Open File Report 82-33, 205 p.  
1985: New probabilistic strong ground motion maps of Canada; Bulletin Seismological Society of America, v. 75-2, p. 563-595.

**Drysdale, J.A., Horner, R.B., Wetmiller, R.J., Stevens, A.E., Rogers, G.C., and Basham, P.W.**  
1985: Canadian earthquakes - 1982 / Tremblements de terre canadiens - 1982; Geological Survey of Canada, Earth Physics Branch, Seismological Series, v. 92, 61 p.

**Forsyth, D.A.**  
1981: Characteristics of the western Quebec seismic zone; Canadian Journal of Earth Sciences, v. 18, p. 103-119.

**Heidebrecht, A.C., Basham, P.W., Ranier, J.H., and Berry, M.J.**  
1983: Engineering applications of new probabilistic seismic ground-motion maps of Canada (1983); Canadian Journal of Earth Sciences, v. 10-4, p. 670-680.

**Mitchell, D., Tinawi, R., and Law, T.**  
1989: The 1988 Saguenay earthquake: a site visit report; Geological Survey of Canada, Open File 1999, 92 p.

**Munro, P.S., Halliday, R.J., Shannon, W.E., and Schieman, D.R.J.**  
1988: Canadian seismograph operations - 1986; Geological Survey of Canada, Paper 88-16, 76 p.

**North, R.G. and Anglin, F.M.**  
1993: Automatic location of earthquakes in eastern Canada; in Current Research, Part E; Geological Survey of Canada, Paper 93-1E.

**North, R.G., Wetmiller, R.J., Adams, J., Anglin, F.M., Hasegawa, H.S., Lamontagne, M., Du Berger, R., Seeber, L., and Armbruster, J.**  
1989: Preliminary results from the November 25, 1988, Saguenay (Quebec) earthquake; Seismological Research Letters, v. 60, p. 89-93.

**Wetmiller, R.J., Adams, J., Anglin, F.M., Hasegawa, H.S., and Stevens, A.E.**  
1984a: Aftershock sequences of the 1982 Miramichi, New Brunswick, earthquakes; Bulletin Seismological Society of America, v. 74, p. 621-653.

**Wetmiller, R.J., Horner, R.B., Stevens, A.E., and Rogers, G.C.**  
1984b: Canadian earthquakes - 1980 / Tremblements de terre canadiens - 1980; Geological Survey of Canada, Earth Physics Branch, Seismological Series, v. 92, 60 p.

**Wetmiller, R.J., Lyons, J.A., Shannon, W.E., Munro, P.S., Thomas, J.T., Andrew, M.D., Lapointe, S.P., Lamontagne, M., Wong, C., Anglin, F.M., Adams, J., Cajka, M.G., McNeil, W., and Drysdale, J.A.**  
1991: Eastern Canadian seismic studies: July 1989 to June 1990, Geological Survey of Canada, Open File 2369, 41 p.

# Automatic location of earthquakes in eastern Canada

R.G. North and F.M. Anglin  
Geophysics Division

*North, R.G. and Anglin, F.M., 1993: Automatic location of earthquakes in eastern Canada; in Current Research, Part E; Geological Survey of Canada, Paper 93-1E, p. 351-360.*

---

**Abstract:** A grid-search location algorithm has been applied to multiple band frequency domain detections generated by postprocessing of digital data from the Eastern Canada Telemetered Network. The resulting locations usually agree well with those produced by an experienced analyst, and can considerably reduce the human effort required to measure seismic arrivals and use them to locate earthquakes. The methods are now being improved so that they can be routinely applied to the data that are being produced by the recently modernized Canadian National Seismograph Network, which covers the whole country.

**Résumé :** Un algorithme de repérage par quadrillage a été appliqué aux réponses en fréquence multibande obtenues par post-traitement de données numériques provenant du Réseau de télémétrie de l'Est du Canada. Les positions obtenues correspondent en général à celles obtenues par un analyste expérimenté, et elles peuvent réduire considérablement l'effort humain requis pour localiser les séismes et mesurer leur intensité. On cherche maintenant à améliorer les méthodes pour pouvoir les appliquer couramment aux données produites par le Réseau sismographique canadien qui vient d'être modernisé et qui s'étend sur l'ensemble du pays.

## INTRODUCTION

Traditional earthquake location methods involve the human analysis of earthquake recordings, either analogue or digital, to identify and time the arrival of different types of phases (P, S, etc.) at several stations and then using these readings in a location program. Several iterations of this rather time-consuming process may be carried out before an acceptable solution is found. In seismically active regions, many events may have to be located each day, and even in less active areas, such as most of Canada east of the Rocky Mountains, larger earthquakes may produce many aftershocks that can defeat the efforts of the analyst to keep up to date.

In eastern Canada, the primary source of waveform data for the detection and location of seismic events, many of which are manmade (quarry and mine blasts) rather than natural, has, since 1980, been the digital Eastern Canada Telemetered Network (ECTN). This network consists of over 20 sites from Manitoba to New Brunswick, telemetered in real time by satellite, telephone, or radio links to a central processing system in Ottawa. Data from each site, or "station" are filtered in a single site-dependent frequency band and then passed to a signal detection algorithm that looks for sudden increases in energy in the selected frequency band.

When the ECTN was designed in the mid 1970s, both computer power and on-line data storage were limited. These constraints precluded saving continuous data from the network and led to high detection thresholds and ratios on the number of daily detections. As a result, small, but potentially useful, signals were not being saved for further analysis. Over the last 15 years, huge advances have been made in both processing power and inexpensive data storage techniques, and the new Canadian National Seismograph Network (CNSN) that is now being installed across the country takes full advantage of these. Routine processing now includes detection in up to four different frequency bands, and the continuous data are permanently archived on optical disk. Because data storage will no longer be dependent upon signal detection, thresholds for detection can be set much lower so that smaller signals are detected, although false alarms will then be more frequent. New techniques can be developed to identify such false alarms, and to automate signal recognition, phase identification, and event location. While it is unlikely that such methods will ever completely replace the experienced human analyst, they will reduce the level of effort needed by providing initial values that are usually reasonable and require only minor corrections.

In preparation for full-scale use of CNSN data, automatic detection and location techniques have been developed and partially tested using data from the ECTN. The results are encouraging, and indicate that such techniques can indeed often produce event locations that are comparable with those achieved by the trained human analyst. This report describes the algorithms employed, compares the results with those produced by the analyst, and outlines work now in progress that is aimed at improving accuracy and reducing the proportion of false events generated.

## SIGNAL DETECTION

As noted above, the ECTN detection processing applies band pass filtering and then calculates exponentially weighted short term average (STA) and long term average (LTA) power estimates. A detection is declared if (STA/LTA) exceeds a specified threshold. Band pass filtering is carried out in the time domain by cascading recursions for two single-pole filters. This extremely simple and computationally efficient filter is rather weak and thus large amplitudes at frequencies outside the nominal passband cause detections. Several ECTN sites are unavoidably located in populated areas, where strongly monochromatic signals from trains and heavy machinery cause frequent detections because it is not always possible to tune these out with an appropriate filter.

With increased computing capacity it is easy to calculate more effective power estimates and to do so in a number of different frequency bands. At any given site, the frequency at which signal-to-noise ratio (SNR) is maximized depends on phase type ( $P_n$ ,  $P_g$ ,  $S_n$ ,  $L_g$ , etc.), distance to the source, and source size. For example, on a relatively wide-band (response flat to velocity from 1 to 10 Hz) system such as the ECTN, the dominant frequency of  $L_g$  ranges from 5 Hz or higher at distances of 100 km or less to lower than 2 Hz at distances of greater than 500 km, while the dominant frequency of  $P_n$  shows much less distance dependence and may be as high as 10 Hz at distances approaching 1000 km. While such variations pose problems for signal detection, they also offer opportunities for phase recognition.

In the time domain, sharp bandpass filters require many recursion coefficients, and if several different filters are to be applied, it may be more efficient to filter in the frequency domain. Only the forward Fourier transform need be calculated since power in a given band can be simply calculated by integrating the spectrum over the desired range of frequencies. Frequency domain detectors were first developed in New Zealand (Gledhill, 1985) and are particularly appropriate for high Q regions such as eastern Canada where the various crustal phases cover a broad range of frequencies over large distances. Whereas Gledhill used integer Discrete Fourier Transforms carried out on a microprocessor at each individual station, we carry out the detection on the central data acquisition system using the Fast Fourier Transform (FFT).

## AUTOMATIC LOCATION SCHEME

Traditional location schemes obtain an epicentre solution by minimizing the travel-time residuals as follows. A reasonable starting solution is determined and the equation of condition is calculated. This equation is inverted to obtain corrections which are added to the starting solution to obtain a better approximation. This procedure is applied iteratively until there is no further improvement or until a specified maximum number of iterations have been performed. While this computationally efficient method usually works well, it can fail to converge because of bad data values or, even when all the input data are good, because the starting solution is poor.

Quite complex, and often ad-hoc, weighting schemes are frequently employed to winnow out bad data, and computer codes for earthquake location are often many thousands of lines long and consequently difficult to modify and maintain.

Simpler and potentially more robust methods that search through a wide range of potential solutions have until recently been impractical because of the computing power required for the very large number of distance and travel time calculations needed. One such brute force method for which the computer code is very simple is the grid search technique. Each point on a grid of possible locations is evaluated and that which provides the best solution (residuals minimized on an L2 least squares, or L1 or other, norm) is chosen. The minimum points of sparse grids can be used in successive searches over finer and finer grids until the desired accuracy is obtained. With increased computing power such methods are becoming increasingly popular (e.g., Sambridge and Kennett, 1986).

Location using automatic detections, rather than readings by a human analyst, poses particular problems. The false alarm rate may be quite high, with a significant proportion of detections being due to noise bursts, telemetry dropouts, and other random factors. The phase type (P, S, etc.) is not known and must be inferred from such properties as frequency content and polarization information if the latter can be measured from three component data. The context of the detection – for example, if several detections arrive in a short time period, the first is more likely to be P and later ones more likely to be of S type – might also be useful.

The CNSN is now starting to provide continuous three-component broad band data from a limited number of stations across Canada, and frequency-domain detection, polarization analysis and grid search location techniques are being developed to take advantage of all these characteristics. These have been stimulated by the quite successful implementation of a subset of these techniques to locate earthquakes in eastern Canada using the single-component time windowed (detections only) data provided by the ECTN.

---

## IMPLEMENTATION WITH ECTN DATA – DETECTION

The ECTN system produces time series files (TSFs) containing digital data from all stations of the network each time there is a detection. The TSF starts 60 seconds before the first detection starts and ends 30 seconds after the last one ends; a single TSF is formed from overlapping detections at different stations, subject to a maximum length of 10 minutes. A very high (95% or more) proportion of TSFs correspond to single station detections and over 80% of these on inspection turn out to be "false" in the sense that no real signal can be discerned. Of the several hundred TSFs that are produced each day, only 10 or so correspond to seismic events and typically only one of these is the subject of further analysis – the others are from distant events (teleseisms) or from the many mine and quarry blasts that take place each day in eastern Canada.

The TSFs produced by the ECTN have been used to develop and test the frequency domain detector and grid search automatic location methods. Each individual station trace in the TSF is passed to the detector, which moves a window 128 samples (2.13 sec) long, with one-third overlap (43 samples) through the data. For each window the mean is removed and the spectrum calculated using a conventional FFT algorithm. Power is calculated in four different frequency bands by integrating the spectrum between the upper and lower band limits. The bands chosen are 1-3, 3-8, 8-15, and 15-26 Hz and cover most of the usable spectrum. The individual power values are saved as the short term average (STA) and the long term average (LTA) is calculated with the simple recursion

$$LTA(i) = A * LTA(i-1) + (1-A) * STA(i-5)$$

A is close to 1 (typically 0.99) and the (i-5) provides a lag of about seven seconds between the LTA update and the current STA. This improves the detectability of emergent signals. Each time a new STA is calculated (every 1.41 sec), the LTA is calculated and the ratio (STA/LTA) is compared to a threshold for the given frequency band. If this threshold is exceeded a single line giving the station, channel, time, STA and LTA in each band, and trigger status (indication of which bands exceeded the threshold) is written to the detection log. When the end of the input data trace is reached, the maximum trace value, and the time at which it occurred, are saved. For each trace the detections are then consolidated so that a series of overlapping detections are merged into one whose duration is saved, together with the maximum STA, LTA, and bands triggered for each discrete detection.

In practice it has been found that signals from close events often produce only one long detection, as the time interval between the different phases is short and energy remains high in most bands. At distances greater than 250 km or so, several discrete detections which often correspond to  $P_n$ ,  $S_n$ , and  $L_g$  are likely. The frequency content of the various detected signals is observed to depend upon both distance and phase type. At short distances, all phases usually produce detections in all four bands, the energy being greatest at the higher frequencies. Beyond 300 km distance,  $L_g$  is preferentially detected in the lower frequency bands and  $P_n$  and  $S_n$  are more likely to be detected at the higher end of the frequency range.

---

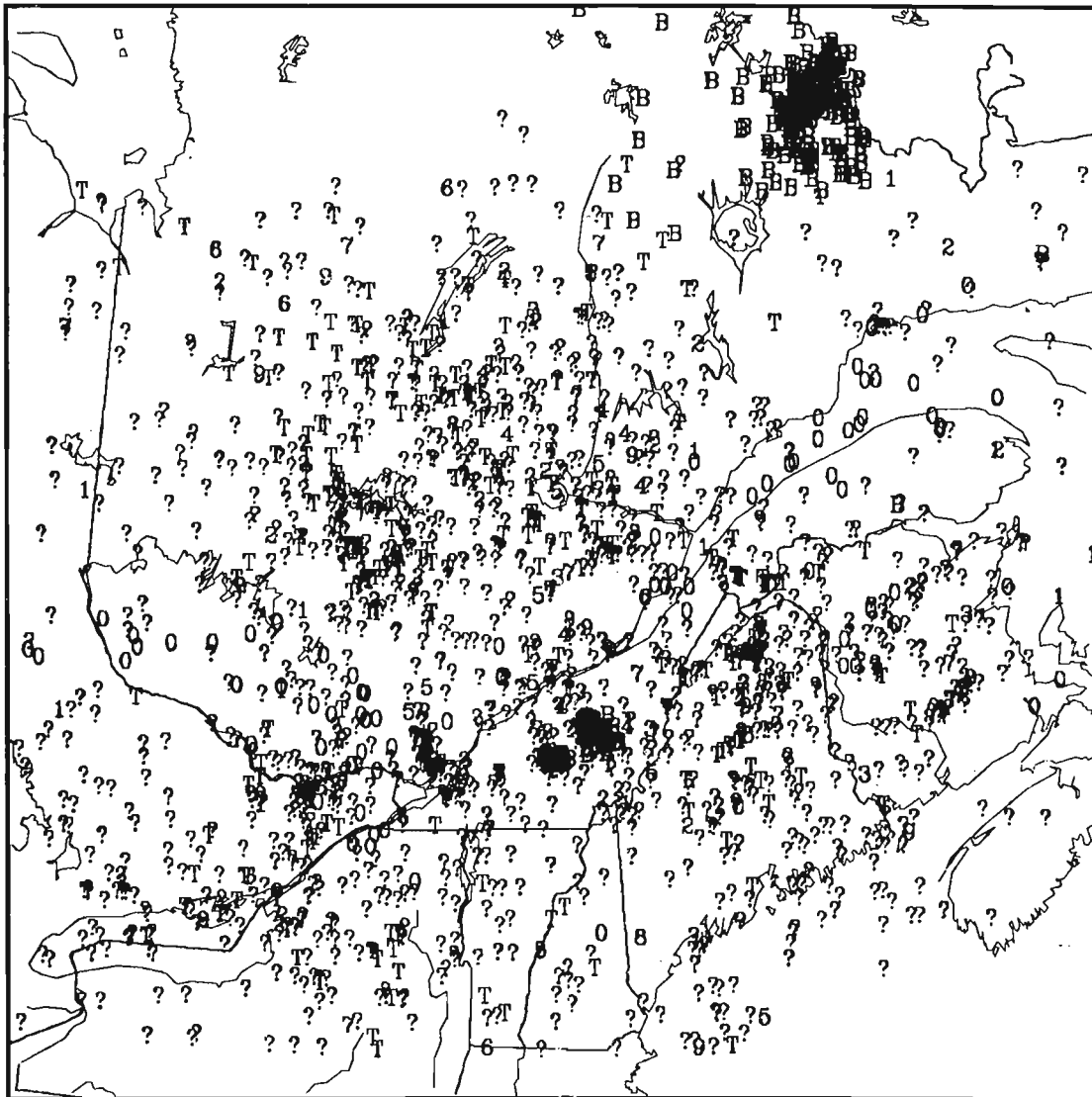
## IMPLEMENTATION WITH ECTN DATA – LOCATION

The detections obtained from all the individual station traces in the TSF are sorted by onset time and passed to the grid search location algorithm. Detections shorter than 10 seconds in duration are rejected and for each of the remaining ones a simple high- to low-frequency ratio (HF/LF) is calculated; it is unity if there were detections in all bands, greater than one if more high frequency than low frequency bands were triggered, and less than one if the reverse is true. If less than three detections meet the minimum duration criterion, the location procedure is abandoned.

The grid search algorithm is now invoked. The starting grid has a spacing of  $0.25^\circ$  and extends from  $43$  to  $60^\circ\text{N}$  and from  $50$  to  $80^\circ\text{W}$ . For every grid point each of the first four detections is tested as a possible P wave onset. Each event hypothesis has the location of the grid point considered and an origin time calculated by subtracting the theoretical travel time for P (for the distance from the station to the grid point) from the detection time. For this trial epicentre, all other detections are tested to see whether they match as either P, S, or  $L_g$ . Certain limitations are applied in this process – all detections from stations at less than  $100$  km distance are tested only as P, and those from stations at distances greater than  $300$  km cannot be  $L_g$  if  $(\text{HF}/\text{LF})$  is greater than  $1$ , or P if  $(\text{HF}/\text{LF})$  is less than  $1$ . The phase with the smallest travel time

residual is chosen and the residual saved. After all detections have been tested, they are sorted by size of residual and the top (largest) one-sixth rejected. The sum of the absolute values (L1 norm; L2 norm was also tried and found to be slightly inferior) of the remaining residuals is calculated, and the grid location and this sum saved if the latter is the smallest yet found.

Once the search has been completed and a minimum found, the corresponding grid location is used as the centre point of a new denser and smaller grid that is  $0.5^\circ$  square and has a grid spacing of  $0.05^\circ$ . The minimum from the search over this grid is in turn used as the centre for a third and final grid  $0.1^\circ$  square and with a  $0.01^\circ$  spacing. Individual station



**Figure 1.** Distribution of 1973 automatic locations produced from ECTN data from January 1992 to February 1993. Events plotted with "B" are believed to be mine blasts, those with "T" arise from P-wave arrivals from distant earthquakes, and those marked by "?" cannot be associated to any known event. Automatic locations that match earthquakes that have been independently located by human analysts are plotted with numbers that indicate the amount by which the automatic event is mislocated; "0" denotes less than  $100$  km error, "1" denotes an error of  $100$ - $200$  km and so on. Events plotted with "9" are mislocated by more than  $900$  km.

magnitudes are calculated by the method, and with the restrictions, described below, and the solution saved in a file. This file is periodically examined to evaluate the quality of the solutions and to determine whether certain stations which become extremely noisy at certain times of year should be excluded during the location processing. The inclusion of such stations with large numbers of false detections from telemetry dropouts and other factors can produce a large number of false events. For larger events, an electronic mail message is sent to members of the earthquake analysis group; it usually arrives about ten minutes after the event has been recorded.

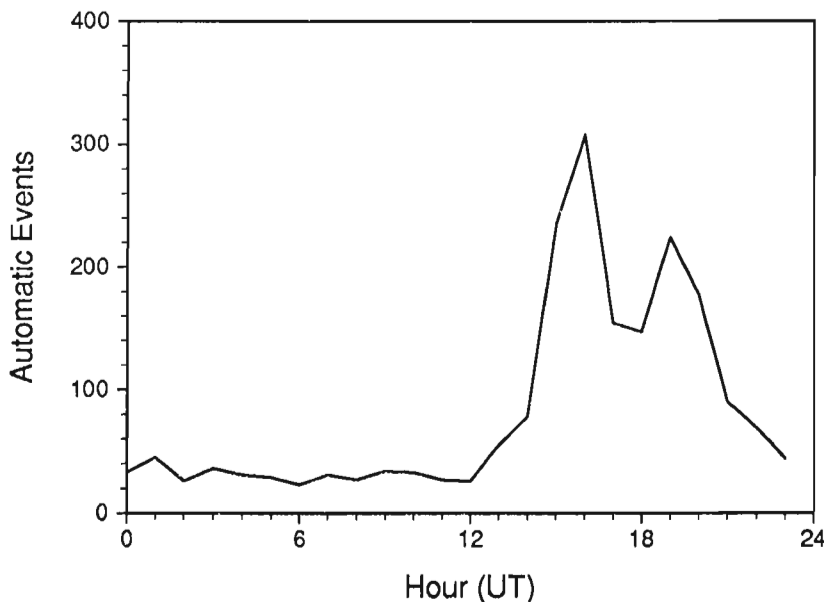
## LOCATION RESULTS

Figure 1 shows the positions of the 1973 automatic locations produced between January 1992 and March 1993. Their distribution bears little resemblance to that of earthquakes in eastern Canada (see, e.g., the report by Drysdale and Wetmiller in this issue of *Current Research*). Only about 10% of the automatic locations were sent in mail messages to the seismologists. Many of the automatic locations are in areas of little natural seismicity, and there are strong concentrations of events near Labrador City and in the Eastern Townships region of Quebec.

These concentrations are easily explained as they correspond to regular blasting activities at the Wabush iron mine in Labrador and at Asbestos and Thetford Mines in Quebec. Of the 185 events plotted near the Quebec-Labrador border, 90 took place within two minutes of 1200, 1300, or 1400 local time and many others occurred close to 15 minutes after these times. The Wabush mine is outside the network and thus the considerable scatter in locations can be attributed to poor azimuthal coverage. Virtually all the 40 events located near the town of Asbestos took place between 1545 and 1600 local time. Blasting times at Thetford Mines appear to be more

variable, but the 62 events here are concentrated between 1200 and 1300, and between 1500 and 1600, local time. Because both Thetford Mines and Asbestos lie within the ECTN, locations of events here are quite good, as evidenced by the strong spatial clustering. The magnitudes of the blasts range from 2.1 to 3.5 at Wabush, 1.7 to 2.6 at Asbestos, and 1.8 to 2.6 at Thetford Mines. In Figure 1, events which from their time and location are clearly blasts are plotted with the letter B. Some of the other events are probably also related to mining or quarrying activity at sites where blasting is less regular. Figure 2 shows the distribution of the automatic locations by (UT) hour of occurrence – 63 percent of all the events take place between 1500 to 2100 and less than one quarter of these can be attributed to the three mines discussed. A comparison of the numbers of Wabush blasts and of natural earthquakes located by analysts produces the interesting statistic that during the 15 months covered by this study, the Wabush mine generated as many events of magnitude 3.0 or greater as there were earthquakes in the whole of eastern Canada, and three times as many events of magnitude 2.5 or greater.

An examination of some of the events plotted in more unusual locations, where little natural seismicity is known, revealed that many were obtained from detections that were closely grouped, generally within 60 seconds, in time. Such grouping could be indicative of P-waves from earthquakes outside Canada, and thus a comparison was made between the times of the automatic locations and the predicted P-wave arrival times from large (magnitude greater than 4.5) teleseismic events during the same time period. It was found that automatic event times matched the predicted arrival times from 197 of the 624 distant earthquakes with magnitude greater than 5 that were located by the Yellowknife array during the same time period, and that a further 62 matched events with magnitudes 4.5 to 5.0. These false hypocentres that were produced from teleseismic signals are plotted in Figure 1 with the letter T.



**Figure 2.**

Automatic locations, by hour of occurrence.

Assigning automatic events on the basis of their time and location to mines, and matching them with large teleseisms, has accounted for only 546 (28%) of the total. The remaining events were compared with the events located in eastern Canada by human analysts over the same time period, and 154 were found to correspond within 200 km in location and within 60 seconds in origin time. These are plotted on Figure 1 with numbers denoting the location difference (see caption). All the remaining events (1273 in number) cannot be associated with mine blasts or confirmed earthquakes, and are plotted with a question mark (?). As shown below, the high proportion of unknown or false events can be greatly reduced with appropriate screening.

### MAGNITUDE DETERMINATION

The analyst obtains the magnitude by measuring the amplitude  $A$  and period  $T$  of the maximum of the  $L_g$  phase, and calculating  $m_{bLg}$  from  $\log(A/T)$  by adding the appropriate distance correction. What is directly measured is the maximum of the velocity trace which is then converted to displacement by dividing by  $(T/2\pi)$  and then corrected for the response of the instrument. For the ECTN, the nominal value of velocity per digital count is valid over a wide range of frequencies (2-10 Hz) where the instrument response is flat to velocity. In this range  $(A/T)$  can be obtained by multiplying the measured velocity by  $2\pi$ .

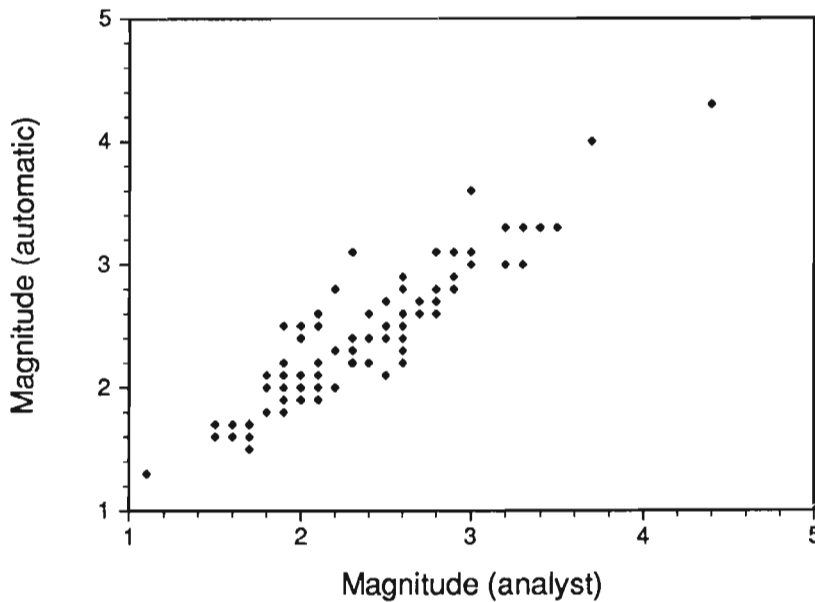
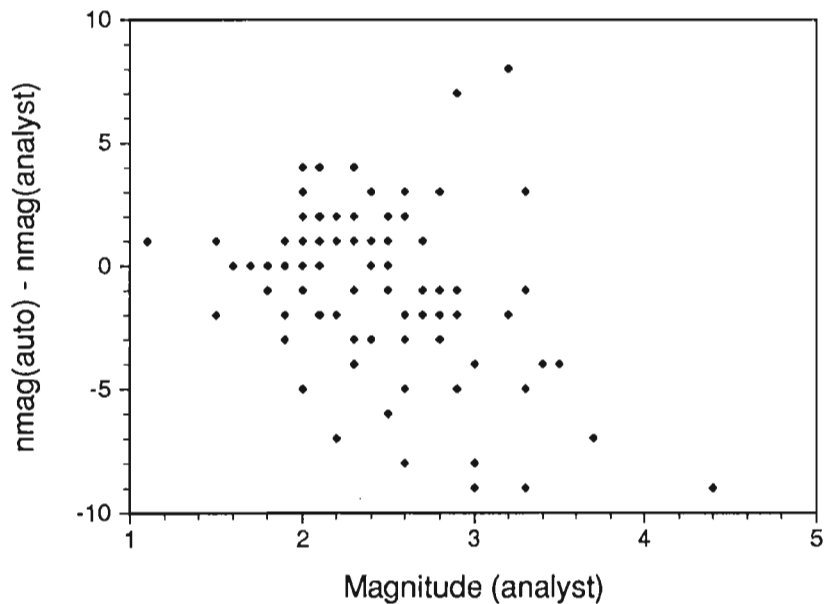


Figure 3a.

Comparison of magnitudes determined by the human analyst and the automatic scheme.

Figure 3b.

Difference between the number of magnitude readings per event made by the automatic scheme and by the human analyst, as a function of magnitude.





While obtaining the value of the trace maximum during a detection is clearly easy to automate, measuring the corresponding dominant period is not, because of the broad band character of the data. It is thus assumed that the period lies in the flat (to velocity) portion of the response. The peak trace amplitude within each detection is obtained and the time at which it occurs is saved. When the detection has been associated to an event, the distance to which is known, the predicted time of arrival of  $L_g$  is calculated using a velocity of 3.6 km/s and the trace amplitude is only used in magnitude calculation if the time of the trace maximum matches this predicted time within 30 seconds. This simple check appears to be very effective.

The event magnitude is calculated by averaging all the individual station magnitudes. Figure 3a compares the automatic event magnitudes with those calculated by the analyst, and it is clear that the agreement is very good. The analyst often adds further station magnitudes, obtained from additional (often analogue) stations and from other agencies. Figure 3b shows that for the larger events, which are recorded to the greatest distance, the analyst determines more station magnitudes than the automatic scheme, but, surprisingly, the latter employs more individual station values than the analyst for over 60% of the events with magnitude less than 3. The analysts presumably do not read all the possible magnitudes because they consider that enough have been measured to obtain a good average value – this may well be true but the more tireless automatic scheme contributes additional data that could prove valuable in other studies, such as improving magnitude formulae.

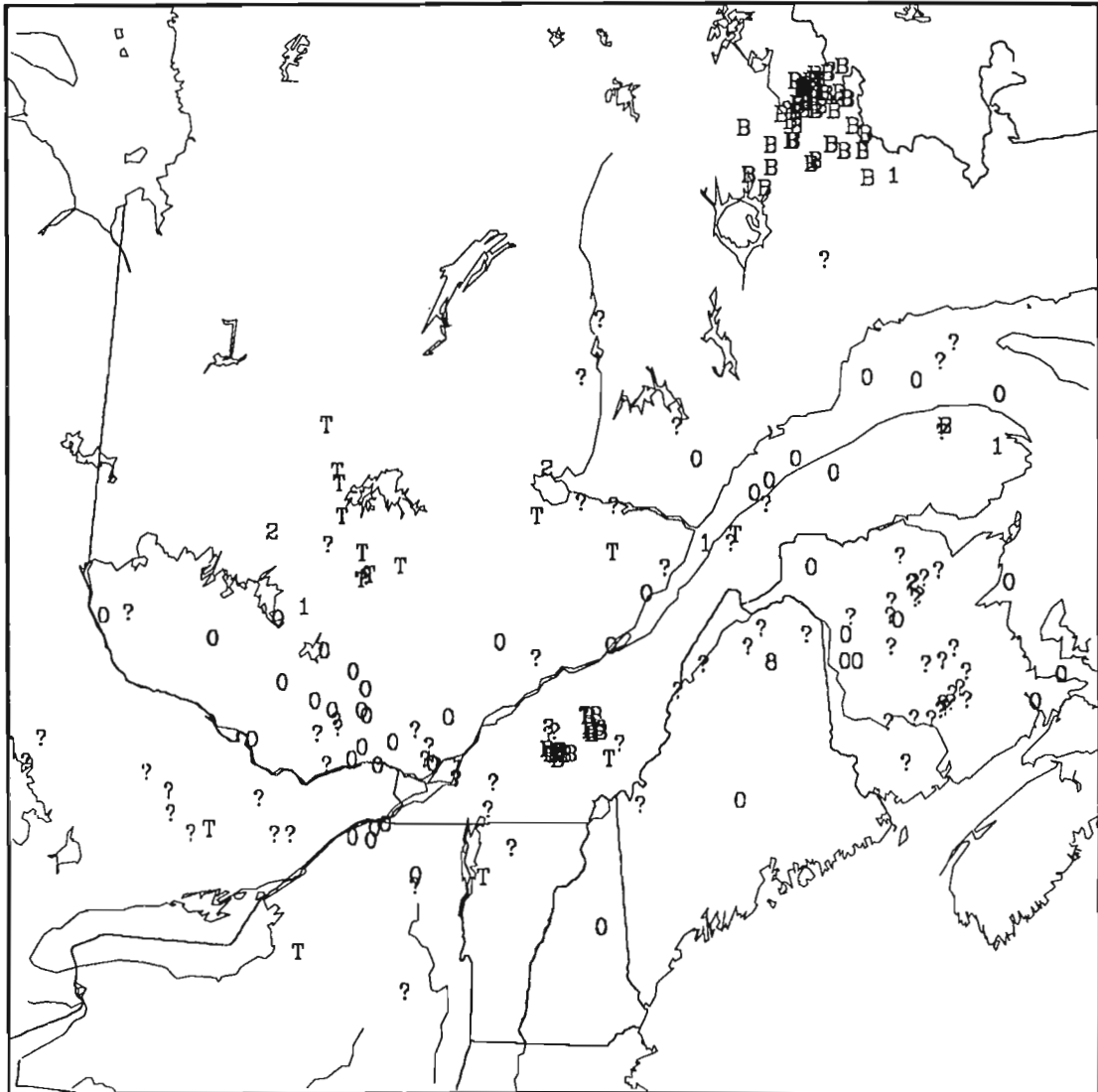
## REDUCING THE PROPORTION OF "FALSE" EVENTS

An automatic location scheme, even if it captures most real events, is not very useful if at the same time it produces a high proportion of false events from spurious detections or signals from distant earthquakes. The events plotted in Figure 1, 64% of which cannot be associated with any known events and 13% of which have been erroneously created from teleseismic signals, do not create confidence in the automatic scheme. While the 14% of events that are probably blasts can be easily identified and flagged as such, the analysts will have little patience with a scheme that presents them with nearly 5 events per day, only 10% of which turn out to be real earthquakes. Clearly some criteria need to be established to reduce the number of false events while retaining the most significant (likely to be felt and/or damaging) earthquakes.

The factors to be considered in establishing these criteria include the fairly obvious ones that are used to assess the quality of an earthquake location – number of stations used, number of phases used, size of the travel-time residuals, etc. Additional characteristics that are particularly relevant to automatic locations include the relative numbers of different types of phases, and the number, or proportion, of unassociated detections, and magnitudes calculated. The last of these is a particularly strong constraint since magnitude is computed only if the time of the maximum amplitude is consistent with that of the predicted  $L_g$  arrival time from the hypothetical epicentre. A wide range of possible combinations of constraints have been considered, the objective being to maximize the number of events of magnitude 2.5 and

**Table 1.** Distribution of automatic event types under no restrictions and after the application of different constraints. In the first column, the brackets contain the codes used for plotting the events in figures 1 and 4. The last three rows list only the earthquakes meeting certain magnitude restrictions. The constraints are as follows: (1) At least 5 stations, 4 P arrivals, and 4 magnitudes required, and no more than 30% of detections unassociated. (2) As (1), but at least 5 magnitudes required. (3) As (1), but at least 6 magnitudes required.

Number of events	No constraint	Constraint		
		1	2	3
(all)	1973	524	391	210
type unknown (?)	1273	226	166	77
from teleseism (T)	259	38	30	16
Labrador Blast (B)	185	118	87	49
Thetford Blast (B)	62	39	23	7
Asbestos Blast (B)	40	33	24	9
earthquake (0, 1,..9)	154	70	61	52
earthquake, M > 2.0	80	60	54	50
earthquake, M > 2.5	34	31	28	28
earthquake, M > 3.0	11	11	11	11



**Figure 4.** Locations of the reduced set of automatic events. Symbols as in Figure 1.

**Table 2.** Distribution, by magnitude and by mislocation, of all the automatic locations that correspond to analyst-located earthquakes. Locations of these events are denoted by numbers in Figure 1. The last column gives the number of events that were not captured by the automatic procedures.

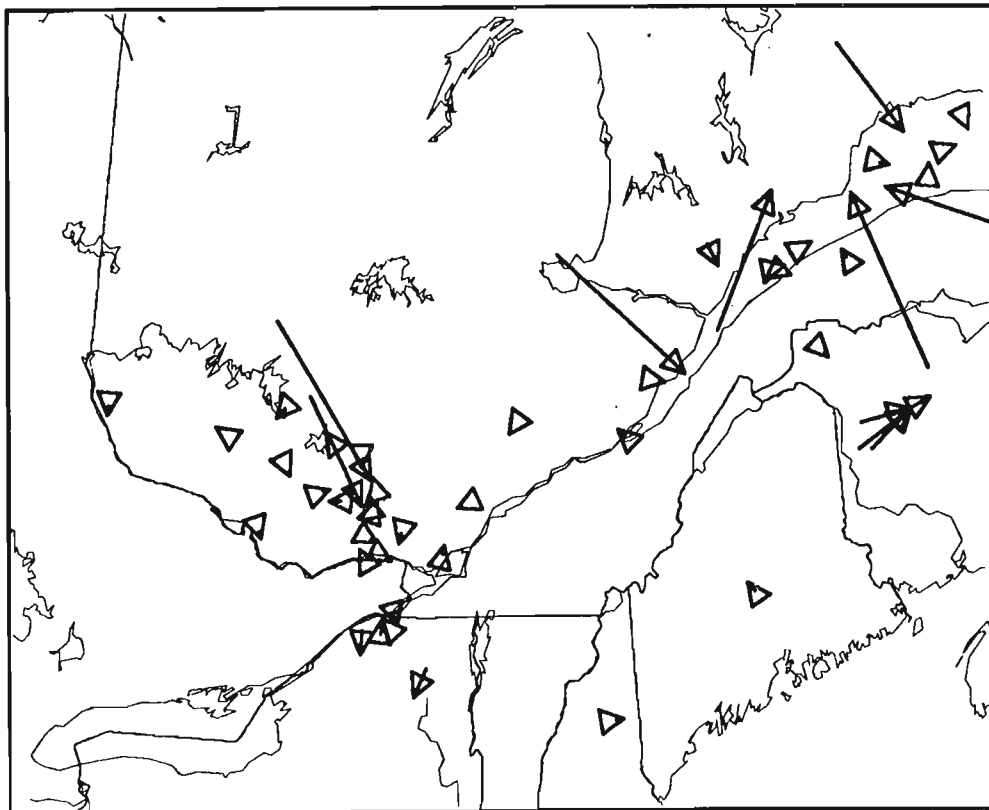
Magnitude	# events	Mislocated by (km)				Missed
		<20	<50	<100	>100	
>4.0	1	1	1	1	0	0
>3.5	2	1	1	1	1	0
>3.0	14	8	8	9	2	3
>2.5	47	20	21	24	10	13
>2.0	120	43	54	60	25	35
>1.5	187	52	64	74	39	74
>1.0	209	54	66	76	48	85

greater and to minimise the number of false events. The results of some of these combinations, including those concluded to be the best, are summarized in Table 1. Constraint 3 retains all confirmed locations for events of magnitude 3 or greater, 82% of those over magnitude 2.5, and 63% of those greater than magnitude 2. At the same time the

proportions of events produced from teleseismic signals, and unidentifiable events, have been greatly reduced. The locations of the events remaining after constraint 3 are plotted in Figure 4; the symbols are the same as in Figure 1. Most of the probably false events (plotted with ?) are at the edges of the network, in New Brunswick and in Ontario. The few

**Table 3.** As Table 2, but only for the events meeting constraint 3 (see caption to Table 1). Locations of these events are denoted by numbers in Figure 4, and the corresponding mislocation vectors are plotted in Figure 5.

Magnitude	# events	Mislocated by (km)				Missed
		<20	<50	<100	>100	
>4.0	1	1	1	1	0	0
>3.5	2	1	1	1	1	0
>3.0	14	8	8	9	2	3
>2.5	47	20	21	24	4	19
>2.0	120	35	39	42	8	70
>1.5	187	35	39	42	9	136
>1.0	209	35	39	42	9	158



**Figure 5.** Mislocation vectors for the earthquakes plotted in Figure 4. The head of the arrow denotes the location made by the human analyst, and the tail the automatic location.

remaining events that have been produced from teleseismic arrivals (T) are mostly restricted to a remote area of Quebec south of Chibougamau.

---

## COMPARISON OF AUTOMATIC AND ANALYST LOCATIONS

---

In Figures 1 and 4 the automatic locations that have been matched to analyst locations are plotted as numbers that indicate the difference between the two. Tables 2 and 3 give these differences as a function of magnitude, the total number of events in each magnitude range, and the number for which there were no automatic locations at all. The analyst-located events used were restricted to lie between 43 and 50°N, and 65 and 80°W – this area was chosen as it is that within which good azimuthal coverage, and thus locations, can be provided by the ECTN. Comparing the two tables, it can be seen that the full set of automatic locations includes more accurately located events, and fewer missed ones, than the reduced set. The latter (Table 3) provides the same detection and location capability for events greater than magnitude 3, and does so with a much lower false alarm rate, as illustrated by Figure 4. Many of the unidentified events (plotted with ?) are at suspicious times (close to the hour or half hour and during the workday) and seem likely to be mine blasts, though this cannot be confirmed. More than two-thirds of the automatic locations match the analyst locations to better than 20 km. Figure 5 shows "mislocation vectors" as arrows – in many cases the arrow is so short that the tail cannot be seen. Most

of the worst automatic locations (longest arrows) are at the edge of the ECTN, in New Brunswick and the lower St. Lawrence region.

---

## CONCLUSIONS

---

A frequency-domain detection scheme and a grid search algorithm have been combined to produce an effective automatic location scheme that can produce good results with a relatively low false alarm rate. While further work is needed, it is clear that such a method can usually provide good starting locations and excellent magnitude estimates. The technique is now being tailored for use with the CNSN that is now being installed; here many stations will be three-component and thus polarization analysis can be used to identify phase type and to provide arrival azimuth as a further constraint.

---

## REFERENCES

---

- Gledhill, K.R.**  
1985: An earthquake detector employing frequency domain techniques; Bulletin of the Seismological Society of America, v. 75, p. 1827-1835.
- Sambridge, M.S. and Kennett, B.L.N.**  
1986: A novel method of hypocentre location; Geophysical Journal of the Royal Astronomical Society, v. 87, p. 679-697.

---

Geological Survey of Canada Project 880015

# Étude de la minéralogie des argiles dans l'encaissant carbonaté du gîte de Gays River, Nouvelle-Écosse

P. St-Antoine, A. Chagnon et M.M. Savard  
Centre Géoscientifique de Québec, Sainte-Foy

*St-Antoine, P., Chagnon, A. et Savard, M.M., 1993: Étude de la minéralogie des argiles dans l'encaissant carbonaté du gîte de Gays River, Nouvelle-Écosse; dans Recherches en cours, Partie E; Commission géologique du Canada, Étude 93-1E, p. 361-368.*

---

**Résumé :** La fraction argileuse contenue dans les dolomies encaissantes est décrite pour trois puits de forage traversant les zones minéralisées de grade élevé et faible du gîte de Gays River. Cet exercice vise à déterminer de façon préliminaire la nature des argiles et leur relation avec la minéralisation. Les résultats obtenus indiquent la présence de smectite, d'illite et de chlorite dans les dolomies. La smectite est peu abondante dans la zone minéralisée de grade élevé, où elle ne contient qu'une seule couche d'eau interfoliaire. Dans les forages traversant les zones de faible grade, elle est proportionnellement plus abondante et contient deux couches d'eau. Pour leur part, l'illite et la chlorite sont uniformément distribuées dans les trois puits étudiés et n'affichent pas de variation systématique de leur indice de cristallinité. En conclusion, les variations des proportions de smectite à l'échelle locale, semblent indiquer que les fluides minéralisants ont laissé une auréole autour de la zone de grade élevé.

**Abstract:** Clays of host dolostones are described in three drill cores going through the mineralized high grade and low grade zones of the Gays River deposit. This work aims to preliminary establish the nature of clays and their relationship to ore minerals. The obtained results indicate presence of smectite, illite and chlorite in the dolostones. Smectite is not abundant in the high grade zone where it contains only one water interlayer. Whereas it is proportionally more abundant and contains two water interlayers in the low grade zone. Illite and chlorite are uniformly distributed in the three drill cores and do not show systematic variation of crystallinity. In conclusion, the distribution and composition of the smectite at a local scale suggest that the mineralizing fluids have left a halo around the high grade zone.

## INTRODUCTION

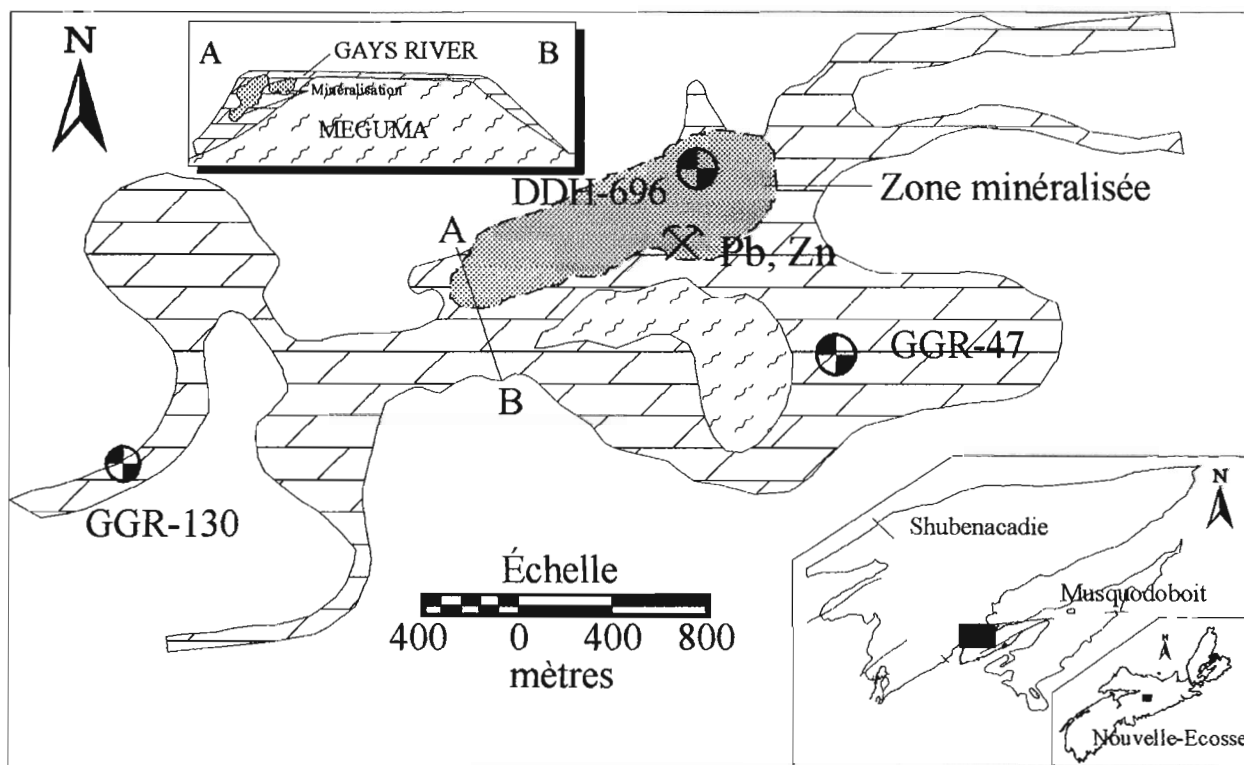
Les carbonates de Gays River encaissent un gisement de Pb-Zn possédant les caractéristiques des gisements du type «vallée du Mississippi» (MacEachern et Hannon, 1974a et b, Hannon, 1980) ou «Irish» (Akande et Zentilli, 1984). Depuis sa découverte au milieu des années 1970, le gîte de Gays River a été soumis à une série d'études pétrographiques et d'analyses chimiques visant à démontrer sa nature et son évolution géologique. Cependant, aucune étude portant sur la composition des argiles n'y a encore été effectuée. Récemment, Gall et Sangster (1991) ont étudié la nature des phyllosilicates, et la cristallinité de l'illite dans les faciès sous-jacents du groupe de Horton et sus-jacents de la Formation de Meaghers Grant dans le but d'établir les trajectoires des fluides minéralisants. Toutefois, leur étude n'a pas permis de caractériser les assemblages des argiles directement associées à la minéralisation. Il est par conséquent souhaitable d'évaluer la composition argileuse de l'encaissant minéralisé, si l'on désire comprendre l'influence des fluides minéralisants, et déterminer les auréoles d'altération susceptibles d'être produites par ces fluides.

Ce rapport propose donc un premier aperçu de la composition minéralogique de la fraction argileuse des roches carbonatées de Gays River. Les variations des assemblages argileux y sont comparées, entre les zones minéralisées de grade élevé et de faible grade (latéralement), ainsi que verticalement dans un même puits.

Ces travaux s'inscrivent dans le cadre d'un projet plus détaillé visant à apporter une meilleure compréhension du modèle métallogénique des gisements et indices de Pb-Zn-Ba retrouvés dans le sous-bassin de Shubenacadie (fig. 1). Les résultats présentés dans ce travail seront combinés à une vaste série de données sur les argiles répartie sur l'ensemble des sous-bassins de Musquodoboit et de Shubenacadie.

## CONTEXTE GÉOLOGIQUE

Les sous-bassins de Musquodoboit et de Shubenacadie dans lesquels on retrouve les roches carbonatées de la Formation de Gays River, recouvrent les roches métasédimentaires plissées et faillées du Groupe de Meguma. Au Viséen moyen, ces sous-bassins ont été le siège d'une invasion marine rapide qui a marqué le début de la mise en place des dépôts marins du Groupe de Windsor. Giles (1981) a reconnu dans ces dépôts marins cinq cycles transgressifs-régressifs majeurs. À la base du Groupe de Windsor, on retrouve des roches carbonatées fossilifères et dolomitisées, appartenant à la Formation de Gays River. Ces faciès calcaires ont été mis en place lors de la première transgression marine au Viséen moyen (Giles et al., 1979; Boehner et al., 1989), soit durant le premier cycle transgressif-régressif du Groupe de Windsor. Les faciès correspondant aux quatre autres cycles sont principalement constitués de gypse, d'anhydrite et de halite.



**Figure 1.** Carte de la région étudiée et position des trois forages par rapport à la zone minéralisée de grade élevé. Modifié de Giles et Boehner (1982).

Les observations pétrographiques effectuées révèlent, à l'instar de Boehner et al. (1989), que les principaux faciès composant la Formation de Gays River se répartissent généralement de la façon suivante, de la base au sommet: 1) brèche de base encroûtée par des ciments et des algues calcaires; 2) bafflestone à algues codiacées; 3) bafflestone et bindstone à bryozoaires et coraux; et 4) bindstone stromatolitique, wackestone et packstone à mollusques et bindstone à algues et bryozoaires. Ces variations de faciès sont le résultat d'une diminution progressive du niveau marin (Boehner et al., 1989). Finalement, il appert que tous ces faciès ont été dolomités. La portion minéralisée des dolomies est située sur le versant donnant sur le sous-bassin de Shubenacadie (Kontak, 1992). Akande et Zentilli (1984) rapportent que la minéralisation se présente sous forme dissiminée ou massive dans le gîte de Gays River.

Récemment, Savard (1992) proposait la séquence para-génétique suivante pour la formation de Gays River: cimentation marine précoce; remplacement dolomitique; micro-fracturation et cimentation dolomitique; début d'une cimentation calcitique et migration d'hydrocarbures, une micro-bréchification, des précipitations de sphalérite, galène, fluorite, anhydrite et barytine se produisant probablement au même moment et, finalement, une micro-fracturation, une cimentation calcitique tardive et une stylolisation.

## MÉTHODE

### Échantillonnage

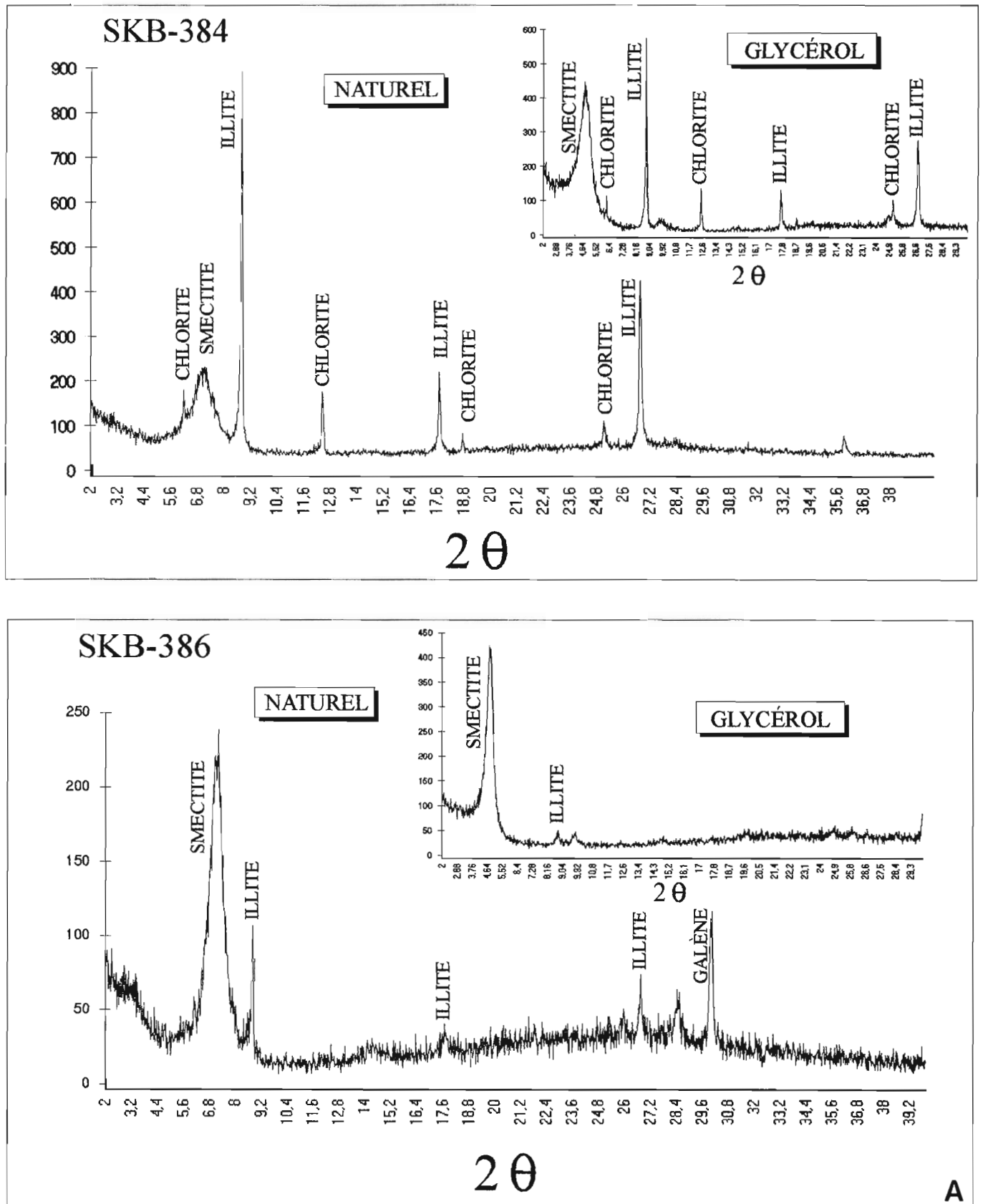
Quinze échantillons ont été utilisés pour des analyses en diffraction des rayons X de minéraux argileux provenant de trois puits de forage ( GGR-130, GGR-47 et DDH-696) et représentant la zone minéralisée de grade élevé (SKB-521, SKB-519, SKB-518 et SKB-516) et celle de faible grade (tous les autres échantillons). Par ailleurs, tous ces échantillons ont été prélevés uniformément de la base au sommet des puits, recoupant ainsi l'ensemble des faciès à carbonates observés. L'échantillonnage permet ainsi d'analyser un matériel appartenant à l'horizon minéralisé.

### Argiles

L'extraction des minéraux argileux se fait par abrasion des fragments obtenus par concassage, dans de l'eau déminéralisée, sous forte agitation. Les suspensions ainsi obtenues sont décarbonatées à l'acide chlorhydrique 1N sous agitation constante, et la fraction inférieure à 2 microns est séparée par centrifugation. Pour la diffraction des rayons X, l'appareil utilisé est un Phillips, à 40 Kv et 20 Ma, la vitesse du goniomètre est de 2 degrés/minute et l'enregistrement des

**Tableau 1.** Tableau synthèse des résultats obtenus pour les 15 échantillons étudiés à partir des forages GGR-130, GGR-47 et DDH-696. Les échantillons ont été positionnés en fonction des faciès auxquels ils appartiennent et en respectant leur position par rapport à la base et le sommet des puits. \* = Smectite à deux couches d'eau interfoliaire. IC = Indice de cristallinité de l'illite. I2/I = intensité relative des pics 002/001 de l'illite. X = présence d'illite. Les valeurs mentionnées pour représenter les proportions de smectite et de chlorite dans les échantillons, sont calculées en effectuant le rapport de l'intensité de la réflexion 001 de la smectite (ou chlorite) sur l'intensité de la réflexion 001 de l'illite plus smectite (ou chlorite) et le tout multiplié par 100. La moyenne des proportions de smectite pour chacun des forages a également été reportée dans le tableau.

FACIÈS	GGR-130					DDH-696					GGR-47							
	Échantillon	smectite	illite	chlorite	IC	I2/I	Échantillon	smectite	illite	chlorite	IC	I2/I	Échantillon	smectite	illite	chlorite	IC	I2/I
Bindstone stromatolitique wackestone et packstone à mollusques et bindstone à algues et bryozoaires.	SKB-389 (124 m)		X		0.29	0.23							SKB-366 (98 m)	47	X		0.36	0.24
	SKB-387 (156 m)	49	X	8	0.20	0.23	SKB-521 (189 m)	X	43		0.35		SKB-363 (125 m)	64	X		0.25	0.21
	SKB-386 (166 m)	92	X		0.15	0.21												
Bafflestone et bindstone à bryozoaires et coraux	absent						SKB-519 (234 m)	62	X		0.26		absent					
							zone de minéralisation massive											
Bafflestone à algue codiacées	SKB-384 (184 m)	44	X	10	0.25	0.20							SKB-362 (133 m)	38	X		0.20	0.18
	SKB-382 (198 m)	66*	X	13	0.12	0.23	SKB-518 (255 m)	Pas d'argiles dans cet échantillon										
Brèche de base	SKB-380 (211 m)	64*	X	12	0.35	0.26	SKB-516 (284 m)	17	X	23	0.25	0.32	SKB-361 (143 m)	66*	X		0.25	0.31
													SKB-359 (159 m)	34.4*	X	12	0.15	0.27
Moyenne des concentrations de smectite	63					39					50							



**Figure 2.** Spectres de diffraction des rayons X de quatre échantillons représentatifs des assemblages argileux présents dans les forages étudiés. Les diffractogrammes des échantillons naturels et traités au glycérol sont représentés pour l'ensemble de ces échantillons.



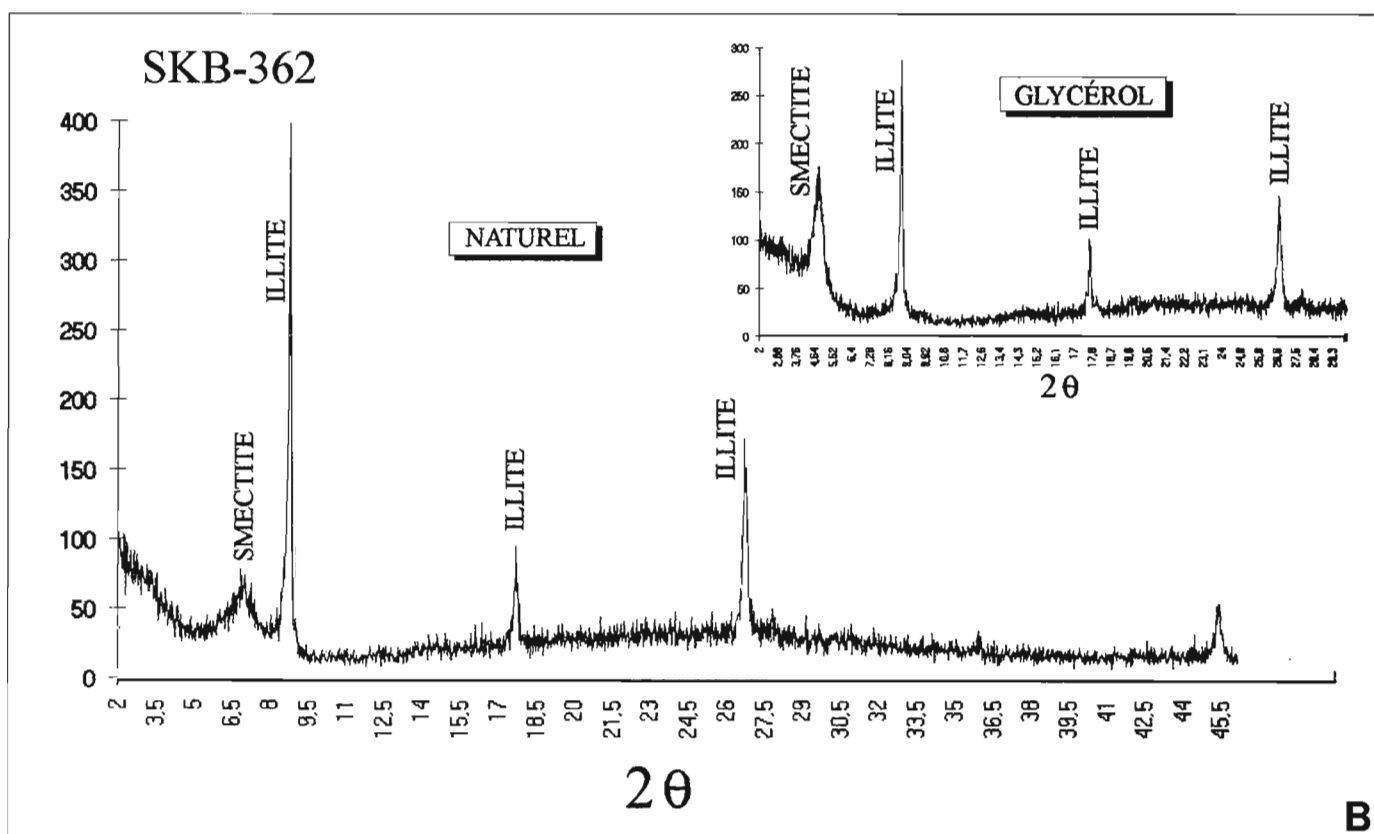
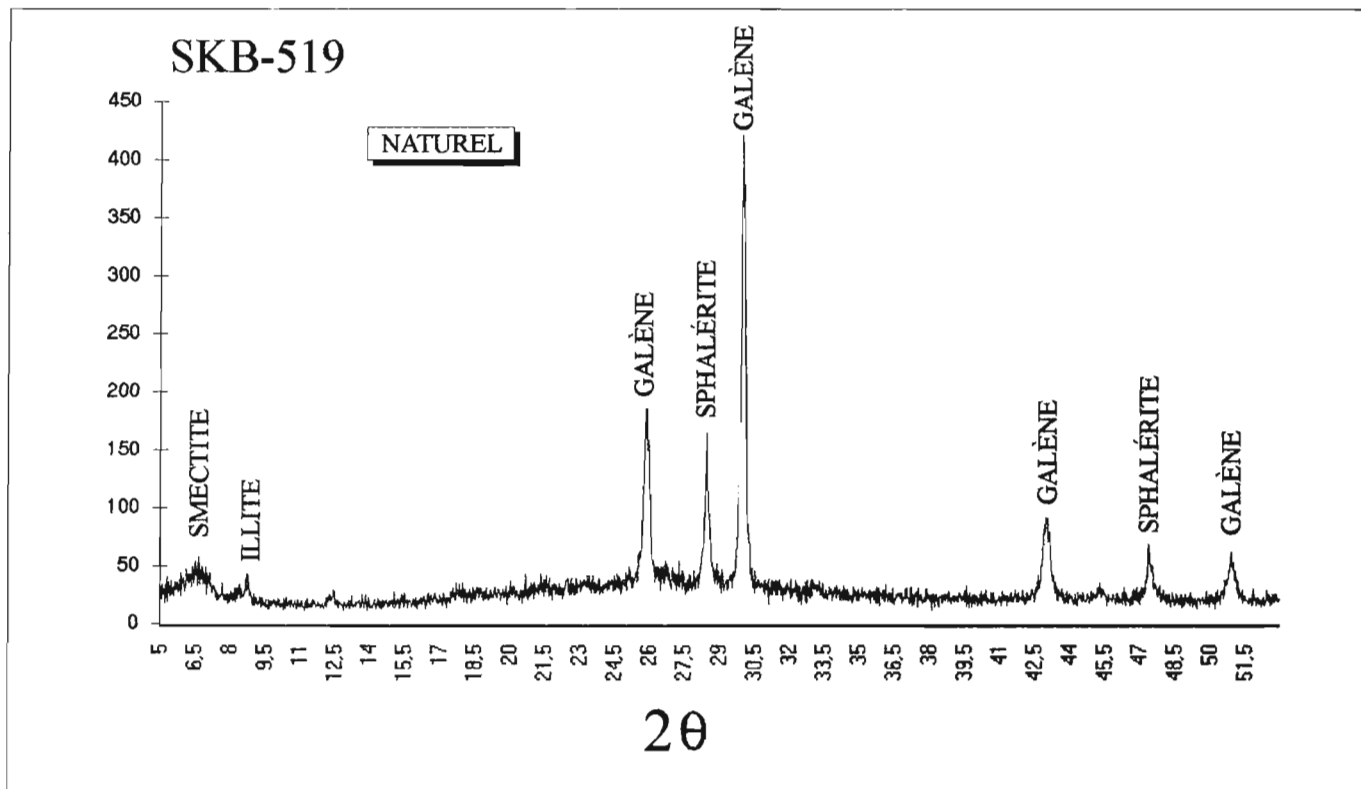


Figure 2. (suite)

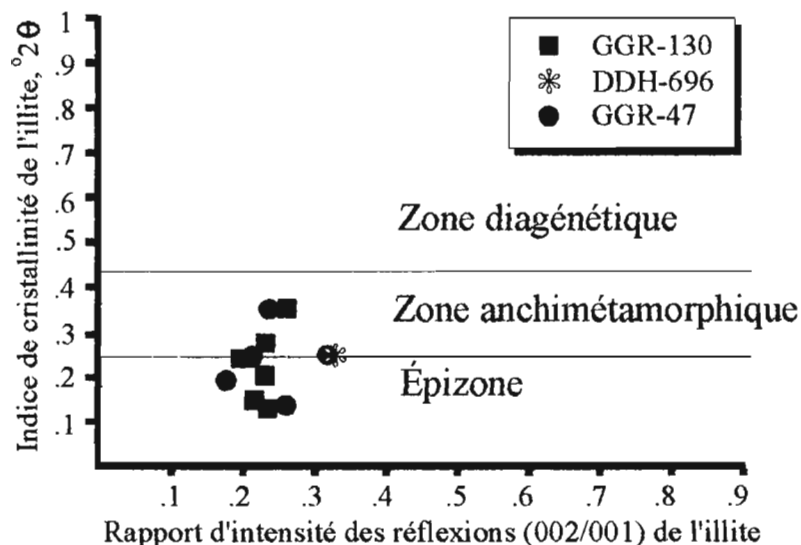


Figure 3.

Diagramme d'Esquevin (1969) présentant l'indice de cristallinité de l'illite en fonction des rapports d'intensité de ses réflexions (002/001).

spectres de diffraction a été obtenu sur un enregistreur à déroulement à un degré/centimètre. Les spectres ont également été compilés sur ordinateur et traités à l'aide du logiciel Jade<sup>MD</sup>. La diffraction est faite sur des lamelles orientées et séchées à l'air ambiant. De plus, elles ont été saturées au glycérol et chauffées durant une heure à 550°C. L'abondance relative des minéraux argileux est évaluée en comparant l'intensité de leur réflexion 001. L'indice de cristallinité de l'illite (indice de Kubler) a été déterminé en mesurant la largeur à mi-hauteur de sa réflexion 001.

## RÉSULTATS

Les minéraux de la fraction argileuse, identifiés dans les roches carbonatées de Gays River sont de l'illite, de la smectite, et de la chlorite (tableau 1). La smectite se retrouve sous deux formes: la première est une smectite à deux couches d'eau interfoliaire présentant une réflexion entre 14 Å et 15 Å pour l'échantillon naturel. Cette smectite se retrouve dans les zones minéralisées de faible grade et plus spécialement à la base des puits. La deuxième smectite ne contient qu'une couche d'eau interfoliaire et présente une réflexion autour de 12 Å et 13 Å pour l'échantillon naturel. Dans les deux cas, lorsque l'échantillon est traité au glycérol, la réflexion passe à une valeur variant de 17 Å à 18 Å (fig. 2). La proportion de smectite dans la zone de grade élevé (DDH-696) affiche une forte diminution comparativement à la zone de faible grade (GGR-130 et GGR-47) (tableau 1). Cette différence atteint un facteur de 3 entre le puits DDH-696 et GGR-130. Dans l'ensemble, les proportions de smectite ne semblent pas afficher de diminution ou de hausse vers la base ou le sommet des puits.

L'illite est présente de façon ubiquiste mais en proportions variables dans tous les échantillons. Le rapport d'intensité de ses réflexions 002/001 (fig. 3) varie de 0,18 à 0,32 et laisse supposer la présence d'une illite ferrugineuse et magnésienne. Son indice de cristallinité varie de 0,12 à 0,36, ce qui situeraient les fractions étudiées dans l'anchizone et l'épizone (fig. 3). Pour sa part, la chlorite est présente dans les trois puits

étudiés, mais pas nécessairement dans tous les échantillons. Elle est d'ailleurs, presque totalement absente du forage GGR-47. Proportionnellement, la chlorite semble plus abondante dans la zone de grade élevé, bien qu'elle soit présente en quantité bien inférieure comparativement à l'illite et la smectite. Les quatre spectres de diffraction présentés à la figure 2 montrent la diversité et les variations des assemblages d'argiles des forages étudiés dans le cadre du présent travail. L'échantillon SKB-519 (forage DDH-696) reflète bien la proportion que prennent les sulfures de plomb et zinc par rapport aux argiles contrairement aux autres échantillons. Dans tous les cas, on constate le haut degré de cristallinité de l'illite et de la chlorite par rapport à la smectite.

## DISCUSSION

Les travaux en cours de Héroux, Chagnon et Savard (en préparation) portant notamment sur l'altération des argiles dans les sous-bassins de Shubenacadie et Musquodoboit, rapportent la présence de kaolinite et de corrensite dans la zone du gîte de Gays River. Ces deux minéraux argileux n'ont pas été observés dans les forages étudiés dans le présent travail (tableau 1). Ceci pourrait s'expliquer par le fait que le matériel étudié par Héroux et al. (soumis) ne provient pas des mêmes forages que ceux présentés ici, et que la kaolinite et la corrensite pourraient être authigènes. En effet, seuls des mécanismes de sédimentation peuvent expliquer l'absence de ces minéraux argileux dans les forages à l'étude puisque ces mécanismes ont tendance à uniformiser les assemblages d'argiles dans les aires de sédimentation (Weaver, 1989). La présence d'illite et de chlorite bien cristallisées avec la smectite dans les mêmes échantillons et la répartition non homogène de ces smectites dans les forages étudiés, semblent indiquer qu'elles sont authigènes. Les valeurs présentées pour exprimer la proportion de smectite (tableau 1) sont évaluées en fonction de l'intensité de la réflexion 001 de l'illite présente dans les mêmes échantillons. Or l'intensité des réflexions 001 de l'illite et de la smectite de l'échantillon SKB-519 est faible et tend à se confondre avec le bruit de

fond, ce qui rend la valeur du rapport de leur intensité peu significative. D'autre part, si l'on compare les moyennes des proportions de smectite d'un puits à l'autre (tableau 1), la présence d'une auréole de smectite autour de la zone de grade élevé est plus perceptible. Ainsi, en termes de proportions, les smectites sont plus abondantes dans les échantillons de la zone de faible grade, c'est-à-dire autour de la zone de grade élevé, et semblent dessiner une auréole autour du gîte.

Sur la base des données présentées au tableau 1, la formation de cette auréole pourrait s'expliquer de deux façons. La première serait que les minéraux argileux de la smectite auraient été précipités dans les dolomies de Gays River bien avant les métaux de base, par un fluide dans lequel l'activité du magnésium, du calcium, de l'aluminium et de la silice aurait été suffisante. Cette idée concorde avec l'hypothèse avancée par Savard (1992), qui avance sur des bases pétrographiques et géochimiques, que des fluides de bassin ont migré dans les roches carbonatées à Gays River avant la mise en place des sphalérites et galènes. Lors de la mise en place du gîte, les smectites auraient été digérées dans la zone de grade élevé par les fluides métallifères. La deuxième hypothèse impliquerait que la formation de la smectite serait directement reliée aux processus de mise en place du gîte, c'est à dire qu'elle aurait été formée par les fluides métallifères en périphérie de la zone de grade élevé en réponse à une neutralisation du pH de ces fluides dans le milieu carbonaté. L'acidification provoquée par la précipitation de sulfures dans la zone de grade élevé aurait, quant à elle, empêché la formation de la smectite ou l'aurait détruite au fur et à mesure de la progression du gîte. La présence de smectite à couche d'eau unique (à savoir, dont la réflexion varie de 12 à 13 Å) dans les forages GGR-130 et GGR-47, porte à croire que les conditions thermiques reliées à la minéralisation pourraient avoir affecté de façon significative l'ensemble des roches carbonatées autour du gîte de Gays River.

Dans tous les échantillons, l'illite présente un haut degré de cristallinité (tableau 1, fig. 2) qui la situe dans l'anchizone et l'épizone. De plus, si l'on considère que la smectite est présente dans les mêmes échantillons, l'on peut raisonnablement croire que l'illite possède une origine détritique. En accord avec les travaux de Gall et Sangster (1991), l'indice de cristallinité de l'illite n'indique aucune variation en réponse à une surchauffe qui serait reliée à la mise en place des gisements plombo-zincifères de Gays River. D'ailleurs, Ravenhurst et al. (1989) proposent une valeur de pouvoir réflecteur qui situe le niveau de maturation de la matière organique dans la zone diagénétique pour les roches carbonatées de Gays River, alors que l'indice de cristallinité de l'illite semble indiquer que ce minéral ait été formé soit dans l'anchizone, soit dans l'épizone, ou soit dans les deux.

La chlorite présente aussi un haut degré de cristallinité comme l'illite, signe qu'elle aurait été formée à des températures pouvant excéder celles qui ont été avancées pour la formation du gîte de Gays River, soit de 215 à 225°C (Ravenhurst et al., 1989 et Akande et Zentilli, 1984). Ceci suppose que, tout comme l'illite, la chlorite pourrait avoir une origine détritique. Un nombre supplémentaire d'analyses en diffraction des rayons X, combiné avec une étude au MEB

des argiles et la modélisation d'un certain nombre de diffractogrammes à l'aide du logiciel Newmod de Reynolds (1985), permettront sans doute d'éclaircir davantage la nature et l'évolution des minéraux argileux dans l'encaissant carbonaté de Gays River.

## CONCLUSION

Ces travaux montrent que les principaux minéraux argileux présents dans les roches carbonatées de la Formation de Gays River sont l'illite, la chlorite et la smectite. Les fluides responsables de la minéralisation ont laissé une signature sur la smectite contenue dans les roches carbonatées à Gays River. La répartition de la smectite dans les trois forages étudiés montre que cette dernière forme une auréole autour de la zone minéralisée de grade élevé (DDH-696). De plus, l'association avec la smectite d'illite et de chlorite bien cristallisées, semble indiquer une origine détritique pour ces deux minéraux, alors que la smectite serait authigène et possiblement reliée aux processus de mise en place du gîte.

## REMERCIEMENTS

Les auteurs tiennent à remercier Richard Filion (Université Laval) pour l'aide précieuse qu'il a apporté lors de l'analyse des échantillons en diffraction des rayons X, ainsi que Greg Lynch et Yvon Héroux pour avoir discuté des résultats avec les auteurs et revu le manuscrit. Les deuxième et troisième auteurs remercient également la Compagnie Westminer pour sa collaboration depuis deux ans. La préparation des échantillons a pu être complétée grâce à la participation de Geneviève Corbeil (Université Laval).

## RÉFÉRENCES

- Akande, O.S. and Zentilli, M.**  
1984: Geologic, fluid inclusion, and stable isotope studies of the Gays River lead-zinc deposit, Nova Scotia, Canada. *Economic Geology*, v. 79, p. 1187-1211.
- Boehner, R.C., Giles, P.S., Murray, D.A., and Ryan, R.J.**  
1989: Carbonate buildups of the Gays River Formation, lower Carboniferous Windsor Group, Nova Scotia. *Canadian society of petroleum geologists, Memoir 13*, p. 609-621.
- Esquevin, J.**  
1969: Influence de la composition chimique des illites sur leurs cristallinités. *Bulletin Centre de Recherche de PAU, SNPA*, v. 3, p. 147-154.
- Gall, Q. and Sangster, D. F.**  
1991: Clay mineralogy in Devonian-Carboniferous basins, mainland Nova Scotia, and its bearing on the genesis of sediment-hosted mineralization. *Geological Survey of Canada, Paper 91-1E*, p. 327-335.
- Giles, P.S.**  
1981: Major transgressive cycles in middle to late Viséan Rock of Nova Scotia. *Nova Scotia Department of mines, Paper 81-2*, 27 p.
- Giles, P.S. and Boehner, R.C.**  
1982: Geological map of the Shubenacadie and Musquodoboit basins central Nova Scotia. *Nova Scotia Department of Mine and Energy*.
- Giles, P.S., Boehner, R.C., and Ryan, R.J.**  
1979: Carbonate banks of the Gays River Formation in central Nova Scotia. *Nova Scotia Department of mines, Paper 97-6*, 57 p.

**Hannon, P.**

1980: Gays River lead-zinc deposit, in Trip 6, Mineral deposits and mineralogenic provinces of Nova Scotia. Geological Association Canada-Mineralogical Association Canada, Ann. Mtg., Halifax, Field Trip Guidebook, p. 74-79.

**Kontak, D.J.**

1992: A preliminary report on geological, geochemical, fluid inclusion and isotopic studies of Gays River Zn-Pb deposit, Nova Scotia. Open file report 92-014.

**MacEachern, S.B. and Hannon, P.**

1974a: The Gays River discovery – A Mississippi Valley Type lead zinc deposit in Nova Scotia. Canadian Mining Metallurgy Bulletin, v. 67, p. 61-66.

1974b: The Gays River discovery. Canadian Mining Journal, v. 95, p. 77-79.

**Ravenhurst, C.E., Reynolds, P.H., Zentilli, M., Krueger, H.W., and Blenkinsop, J.**

1989: Formation of carboniferous Pb-Zn and barite mineralization from basin-derived fluids, Nova Scotia, Canada. Economic Geology, v. 84, p. 1471-1488.

**Reynolds, R.C.**

1985: Description of program Newmod for the calculation of the one-dimensional X-ray diffraction patterns of mixed-layered clays. logiciel disponible de R.C. Reynolds, Departement of Earth Sciences, Dartmouth College, Hanover NH 03755, USA.

**Savard, M.M.**

1992: Diagenèse pré- et post-minéralisation: implication pour le dépôt de Gays River, Nouvelle Écosse. Commission Géologique du Canada, Étude 92-1E, p. 289-298.

**Weaver, C.E.**

1989: Clays, mud, and shales. developments in sedimentology, 44, Elsevier, 819 p.

---

Geological Survey of Canada Project 9200455

## AUTHOR INDEX

Anglin, F.M. . . . .	351	La Flèche, M.R. . . . .	281
Avery, M. . . . .	299	Lamberson, M. . . . .	97
Aylsworth, J.M. . . . .	141	Lawrence, D.E. . . . .	133
Ballantyne, B. . . . .	73	Lee, P.J. . . . .	93
Baril, D. . . . .	239	Legault, M.I. . . . .	207
Barrie, J.V. . . . .	15	Lentz, D.R. . . . .	249, 259
Beauchamp, B. . . . .	105	Linden, R.H. . . . .	41
Bednarski, J.M. . . . .	191	Loman, J.M. . . . .	331
Brisbin, D.I. . . . .	157	Lowe, C. . . . .	23
Burgess, M.M. . . . .	133	Luternauer, J.L. . . . .	67
Bustin, R.M. . . . .	11, 97	MacInnes, K.L. . . . .	133
Cameron, B.I. . . . .	157	Malo, M. . . . .	281
Camiré, G. . . . .	281	Mastalerz, M. . . . .	11
Carter, E.S. . . . .	55	McAlpine, K.D. . . . .	299
Chagnon, A. . . . .	361	Nassichuk, W.W. . . . .	113
Chai, G. . . . .	219	Nixon, F.M. . . . .	275
Charbonneau, B.W. . . . .	207	North, R.G. . . . .	351
Clague, J.J. . . . .	41, 47	Pflug, K.A. . . . .	307
Clarkson, C. . . . .	97	Piasecki, M.A.J. . . . .	291
Conway, K.W. . . . .	15	Plouffe, A. . . . .	73
Correia, J.M. . . . .	331	Rencz, A.N. . . . .	239
Currie, K.L. . . . .	197	Rodrigues, C.G. . . . .	271
Douma, M. . . . .	275	Ruzicka, V. . . . .	175
Drysdale, J.A. . . . .	347	St-Antoine, P. . . . .	361
Dubé, B. . . . .	337	Savard, M.M. . . . .	361
Dunn, C. . . . .	73	Schau, M. . . . .	185
Dyke, L. . . . .	83	Scromeda, N. . . . .	313, 321
Eckstrand, O.R. . . . .	219	Seemann, D.A. . . . .	23
Faure, S. . . . .	337	Shilts, W.W. . . . .	47
Fensome, R. . . . .	299	Shives, R. . . . .	73
Fowler, M. . . . .	113, 299	Skibo, D.N. . . . .	113
Gandhi, S.S. . . . .	231	Slack, J.F. . . . .	33
Gittins, J. . . . .	197	Snowdon, L.R. . . . .	113
Goodfellow, W.D. . . . .	249, 259	Steel, R. . . . .	105
Haggart, J.W. . . . .	55	Stewart, K.R. . . . .	113
Halliday, D. . . . .	23, 231	Tella, S. . . . .	185
Hannington, M.D. . . . .	157	Teskey, D. . . . .	73
Harris, D. . . . .	9, 73	Thériault, P. . . . .	105
Hearty, D.B. . . . .	23	Thomas, F.C. . . . .	299
Hickson, C. . . . .	73	Thompson, P.H. . . . .	239
Huang, Z. . . . .	299	Todd, B.J. . . . .	141
Issler, D.R. . . . .	123	Tremblay, A. . . . .	337
Katsube, T.J. . . . .	123, 299, 313, 321, 331	Tribe, S. . . . .	1
Kettles, I.M. . . . .	141, 165, 271	van der Heyden, P. . . . .	73
Kidd Creek Study Group . . . . .	151	Wetmiller, R.J. . . . .	347
Killeen, P.G. . . . .	307	Williamson, M.A. . . . .	299, 331
Koopman, E.R. . . . .	157	Wolfe, S. . . . .	83
Kostaschuk, R.A. . . . .	67		



### **NOTICE TO LIBRARIANS AND INDEXERS**

The Geological Survey's Current Research series contains many reports comparable in scope and subject matter to those appearing in scientific journals and other serials. Most contributions to Current Research include an abstract and bibliographic citation. It is hoped that these will assist you in cataloguing and indexing these reports and that this will result in a still wider dissemination of the results of the Geological Survey's research activities.

### **AVIS AUX BIBLIOTHÉCAIRES ET PRÉPARATEURS D'INDEX**

La série Recherches en cours de la Commission géologique contient plusieurs rapports dont la portée et la nature sont comparables à ceux qui paraissent dans les revues scientifiques et autres périodiques. La plupart des articles publiés dans Recherches en cours sont accompagnés d'un résumé et d'une bibliographie, ce qui vous permettra, on l'espère, de cataloguer et d'indexer ces rapports, d'où une meilleure diffusion des résultats de recherche de la Commission géologique.

Geological Survey of Canada Current Research, is released twice a year. Paper 93-1, parts A to D were published in January 1993 and Paper 93-1 Part E (this volume) was published in July 1993.

Recherches en cours, une publication de la Commission géologique du Canada, est publiée deux fois par année. Les parties A à D de l'Étude 93-1 ont été publiées en janvier 1993 tandis que le partie E de l'Étude 93-1 (le présent volume) l'a été en juillet 1993.

Part A, Cordillera and Pacific Margin  
Partie A, Cordillère et marge du Pacifique

Part B, Interior Plains and Arctic Canada  
Partie B, Plaines intérieures et région arctique du Canada

Part C, Canadian Shield  
Partie C, Bouclier canadien

Part D, Eastern Canada and national and general programs  
Partie D, Est du Canada et programmes nationaux et généraux

Part E (this volume)  
Partie E (ce volume)